

M.Y.H. Bangash · T. Bangash

---

Explosion-Resistant Buildings

M.Y.H. Bangash · T. Bangash

# **Explosion-Resistant Buildings**

**Design, Analysis, and Case Studies**

With 286 Figures and 83 Tables

 Springer

## Authors

Prof. Dr. M.Y.H. Bangash  
Emeritus Professor of Aerospace & Nuclear Engineering Structures  
Consulting Engineer

Dr. T. Bangash  
Structural Engineering Consultant  
39 Wontner Rd  
SW177QT London  
United Kingdom

ISBN-10 3-540-20618-3 **Springer Berlin Heidelberg New York**  
ISBN-13 978-3-540-20618-7 **Springer Berlin Heidelberg New York**

Library of Congress Control Number: 2005930167

This work is subject to copyright. All rights are reserved, whether the whole or part of the material is concerned, specifically the rights of translation, reprinting, reuse of illustrations, recitation, broadcasting, reproduction on microfilm or in other ways, and storage in data banks. Duplication of this publication or parts thereof is permitted only under the provisions of the German Copyright Law of September 9, 1965, in its current version, and permission for use must always be obtained from Springer. Violations are liable to prosecution under German Copyright Law.

**Springer is a part of Springer Science+Business Media**

springer.com

© 2006 M.Y.H. Bangash & T. Bangash, London, UK  
Published by: Springer-Verlag Berlin Heidelberg 2006  
Printed in Germany

The use of general descriptive names, registered names, trademarks, etc. in this publication does not imply, even in the absence of a specific statement, that such names are exempt from the relevant protective laws and regulations and therefore free for general use.

Cover-Design: Erich Kirchner, Heidelberg  
Printed on acid-free paper 62/3141/Yu - 5 4 3 2 1 0

# Preface

Many nations have become victims of terrorism. Bombs have exploded in and around buildings and other structures. Such events have generated considerable concern over the ability of countries and governments to protect installations and their occupants against a potential threat of terrorism. Many countries have established defence agencies and research councils who are currently examining the structural integrity of existing buildings and other vital installations. In some countries codified methods have been developed together with the design methodologies and construction techniques to try to protect old installations against vehicle bomb effects in particular. The purpose of this book is to give an exhaustive study of buildings structures resisting explosion with and without external/internal impact and fire caused by such effects. A number of case studies with damage scenarios are included. The book is divided into various chapters.

Chapter 1 gives a review of bomb-affected buildings. Case studies including Alfred P. Murrah Federal Building in Oklahoma and World Trade Center (WTC) Twin Towers in New York have been given a wide coverage. Notable explosions in the world with relevant data are tabulated. After these the damage scenario of the Pentagon building is fully described. This chapter now resorts to the availability of data on major explosive elements, their ingredients and material properties. The last part of this chapter covers guidelines for high-rise fire fighting caused by explosion, giving strategy and tactics, modes and tactics of aggressors, duties and responsibilities of managers and security staff, owners and managers, related to security measures, vehicle barrier system requirements, vehicle bomb observation list and selection procedures related to a vehicle barrier. Where certain areas could not, for lack of space, be included, relevant references are given to the reader/researcher for an in-depth study.

Chapter 2 is devoted entirely on blast and explosive loadings on buildings. This gives a comprehensive data on explosive and bombs especially related to the well known damage scenarios. A summary is given on recent terrorist attacks. The phenomenology for blast evading on buildings due to vehicle bomb is given. This is followed by blast wave scaling laws. Blast loads and modelling whether internal or external are summarised giving all analytical and design equations for a reader to assimilate. Basic parameters of a bomb blast including computational aspects of transient over pressures, reflected

shocks in relation to peak pressure loading and total impulse, magnitude in TNT, stand-off distance and altitude, structural orientation with respects to the explosive and the ground are given much in greater detail. Stress waves and blast waves are explained with analytical methods. Explosions of spherical charges with full implementation are given. This is followed by the methodology of explosion in air. Analytical models are given for the impulse of incident pressure, thickness of shock front, stagnation pressure, oblique shock and shock reflection, whether normal or oblique. Next various modes of internal blast and load modelling with respect to building's structural response and modes are given in much greater detail. Various pressures-time relations in graphical shapes based on research work carried out by many scholars are given as novel examples. This chapter is fully supported by references for future individual endeavours.

Chapter 3 gives a comprehensive treatment of fire in buildings with and without explosion/impact. The subject is cleanly introduced. This is followed by loadings and structural restraints. Pre and post flash over designs fires are given a detailed treatment. For the basis of temperature-time relation, tables are showing data and factors for enclosures. Major analysis is given to cover the relevant area. The authors choose the place at this stage to introduce material properties with compressive tables and graphs defining various parameters. Methods of analysis and design are introduced using codified and numerical methods and techniques. They are supported by detailed analyses, tables and graphs. Various design examples based on British, American and European practices are given to explain the usage of analytical and design techniques. Structural elements in different materials are designed against the fire. A detailed chapter is given on the global analysis of buildings under fire using finite element. Since fire is generally associated with structures under impact and impulsive loads and explosion whether internal or external, the reader/researcher/designer can now easily handle any kind of scenario.

Methods of analysis related to structural response to blast loadings are now thoroughly dealt with Chap. 4. A sound introduction to the subject is given. Methods of analysis, numerical and analytical tools are underlined. One of the methods known as discreet element method which has been adopted for Oklahoma building is fully dealt with. The philosophy of structural response analysis to blast loading has been fully exhausted by developing analytical/numerical models while fully supported by examples, graphs and tables. Additional response for shock loading has been introduced. The remaining part of this chapter is devoted entirely to the finite/discrete element of technology which eventually has been applied later on to the damage scenario of the Oklahoma building in the USA.

Chapter 5 now deals with the design of structural elements under blast loads. The main idea is to include in the design the blast response resistance. The subject is briefly introduced. Various charts, graphs and tables containing data and parameters are now acting as design aids. Practical design examples based on British and American practices are given. They show how blasts are

converted into design loads and structural elements in various materials are designed. Apart from steel and concrete elements, an emphasis is placed on the behaviour of glass and glazing materials subject to blast loads. The finite element technique is applied to solve a case study related to glass in the blast environment.

In structural analysis when the structure is located with respect to two or more media, the interactive analysis is needed to integrate the media in the global analysis. The same can be applied to two different materials interacting with each other. The interaction is brought about by contact or gap elements. This subject is nicely covered in Chap. 6. Commercial firms or bureaux have developed various such elements. The major ones are documented in this chapter which have already been tested in other fields of engineering.

Aircraft/missile impact data analysis is now compiled in Chap. 7. Basic impact dynamics is initially introduced. Data on civilian and military aircraft are given in detail so that they can be useful during the imputing of various computer programs. Various equations have been developed for normal and oblique impact. Aircraft impacts on structures are introduced and analytical model is devised for the formulation of various relevant computer programs. The load-time function has been established together with impact modelling developed by a number of researchers. Military, airforce and navy missiles and impactors with their relative data are included. The damage scenario can be checked by various noted empirical formulae devised for structural perforation, penetration, scabbing, spalling and rupture. They are included in this chapter. Comprehensive lists of reference are given at the end for an in-depth study.

Since the collapse of the WTC towers, it is now necessary to include a chapter on aircraft hot fuel-structure interaction during aircraft impact conditions. A comprehensive investigation is reported in Chap. 8. The data on WTC towers and impactors are included in this chapter. The hot fuel interaction analysis with tower components has been thoroughly investigated. The damage scenarios have been established. Relevant references are included for those who are deeply interested to pursue their future research interests in this area.

When impact, explosion alone or in combination, occurs, fire is bellowed, together firing debris, as witnessed in WTC disaster scenario. Scattering flying objects are the results. Chapter 9 examines the identity of the form and location of unknown elements inside a given surrounding medium. It is proposed to measure wave reflection data in space and time. Hybrid finite element/difference method is developed in three dimensions where scattering can be performed with time periodic or known data in the form of short impulses. The basic mathematical tool was devised which amounts to numerically solving the time-dependent elastic wave equation with given material coefficients. Finally the scattering phenomenon of objects was achieved using the TIME-DOMAIN approach. Program FEMVIEW was linked to view the

damage scenario. The computerised version was identical to the actual WTC scenario. This chapter is supported by useful references.

Chapter 10 is a vast chapter of the book which deals with the building global analysis for the damage scenario. Here all the work given for individual research/design areas given in Chaps. 1 to 9 is combined to form a global analysis for tall spatial structures. Linear and non-linear analyses are achieved by modelling prototype structures as assemblages of line and panel members using static and dynamic load influences. Framed and cored structures are considered. Analytical and numerical models are included fully supported by data, graphs, tables and plates.

Various scenarios are considered such as impact-cum-fire, explosion-cum-fire, impact-cum-explosion and in other combinations. On structural sides, methods of analysis for framed and core systems are given in much greater detail. Comparisons are given in each case to validate the methodology and assumptions. Where shear walls are have been introduced as random structures, a comprehensive 3D analysis is separately given. A section is given for the local and global stability analysis. Both finite element and finite/discrete element techniques have been used with the Damage model.

Global analysis with PROGRAM BANGF has been performed. The reader is given a flow chart which indicates how an integrated analysis has been philosophised. Based on this integrated analysis, case studies were selected, the prominent of them is the Twin Tower (WTC, New York) collapse scenario and the Oklahoma building known as The Alfred Murrah Building. The WTC building was chosen for the application of the 3D finite element analysis. Identical damage scenario have been obtained. A comprehensive analytical and numerical works are included on Finite/Discrete Element Method. The computer program given in the Appendix I based on this method is applied on the Oklahoma building. The damage scenario is produced.

Both analytical works are fully supported by comprehensive data, tests, original drawings and charts. The results are meaningful as far as possible.

An up to date references are included in this chapter for future studies.

To crown all, each chapter contains numerous analytical and design examples selected on the basis of existing constructed facilities. Examples from both analysis and design have been selected using various practices. This provides the reader with a wide coverage of the international scene. Wherever new codes are operational, such as the Eurocodes, they have received due consideration. This is clear from the contents of the book where such codes give the reader an opportunity to study the comparative analytical and design tools in buildings and their structural components subject to explosion, impact and fire.

This book is supported by a comprehensive bibliography of each chapter for those who intend to carry out in-depth study in their individual projects.

The book carries a large Appendix which covers the background analyses and computer subroutines required to execute complicated analyses and de-

signs of building structures and their components. With slight adjustments, these can be linked easily to a number of relevant computer packages.

This book will be of use to researchers and practicing engineers, designers, defence agencies, government departments, technologists, mathematicians and specialists in computer-aided techniques of building construction. The major design examples will be beneficial to building, civil, structural and mechanical engineers who are involved in static and transient load analyses. Specialists in wind, earthquake and explosion engineering disciplines will also find this book extremely useful.

The topics covered in this book are within the syllabuses of postgraduate courses at various universities. Both lecturers and students should find the text relevant to their projects and research theses in fields of explosion, impact, shock and fire.

This book acts as a technical guide for defence and disaster agencies, research establishments, computer-aided bureaux, construction companies and for those who wish to validate experimental test results and on-site monitoring data. Many consultants in the building trade would find this book extremely useful in the design of building structures to be checked or designed for explosion, aircraft/missile impact and fire, aircraft impact and fire.

Great effort has been made by the author to highlight all aspects of analysis and design related to explosion in building structures. The contents of the book have been carefully selected to cover major analytical, numerical and design problems associated with building structures. Certain areas could not be presented in this text, but the author has given many references instead, and has included an extensive bibliography to enable the reader to carry out an in-depth study satisfactorily.

In this book, it has been necessary to dispense with chapters and to replace them appendices. This is because each topic is an entity in itself and needs to be encompassed within a chapter. One can, therefore, consider this to a large book comprising a series of mini-books with different titles. A total of ten chapters are included in this volume.

Although the authors have given a separate acknowledgement, they would be failing in their duty if they did not thank those whose names are mentioned in the text. Matina Theodoropoulou for overall work on typing this manuscript.

Finally, but not least the authors would like to thank from the deepest of their heart, Matina's friend and great human being with so many skills and a great driving for progress and success, Mr Vas from Greece, now living in Peckham. Thank you Vas. Vas would like to thank DJ Tiesto for keeping him entertained with his brilliant music during the long hours of working on this manuscript.

London, September 2005

*M. Y. H. Bangash  
T. Bangash*



## Acknowledgements

The authors are indebted to many individuals, institutions, organizations and research establishments mentioned in the book, for helpful discussions and for providing useful practical data and research material.

The authors owe a special debt of gratitude to their families who provided unwavering support, especially Dr. F.N. Bangash for checking some of the hand calculations and for checking the final layout.

We also wish to acknowledge the help given by the following:

Mr Mike Chrimes and his staff, the Institution of Civil Engineers Library, London

The Institution of Structural Engineers Library, London

The American Society of Civil Engineers (ASCE), New York

The American Concrete Institute, Detroit

The Concrete Society, London

The Royal Institute of British Architects, London

The British Cement Association, UK

The British Library, St Pancras, London

The Institute of Chemical Engineers Library, Derby, UK

The MUTO Institute, Tokyo

The Japan Society of Civil Engineers, Tokyo

The Chinese Society of Civil Engineers, Beijing

The Institution of Mechanical Engineers, London

Der Bauingenieur, Germany

Times Index, Research Publications, Reading, UK

The Ministry of the Environment, UK

The British Standards Institution, London

The Building Research Establishment, UK

The European Union Library, Brussels, Belgium

The ASEAN Countries, Central Library, Korea

Bird Air Structures Incorporation, USA

Mero-Raumstruktur GmbH & Co., Germany

The International Journal Shell & Spatial Structures, Madrid, Spain

The International Union of Architects (UIA), New York

The British Steel Corporation, London

The United States Steel Corporation, Pittsburgh

The National Science Foundation, Washington, DC

The Steel Construction Institute, UK

Palai du Centre Naturel des Industries et Technique, Paris

M/S Geodesic Techniques PVT Ltd., Bangalore, India

Council on Tall Buildings and Urban Habitat, Lehigh University, PA, USA

Nippon Steel, Tokyo

Skidmore, Owings & Merrill, Chicago, USA

US Agency for International Development, Washington, DC  
 BCV Progetti Srl, Milan  
 Artech Inc., Taipei  
 Australian Institute of Steel Construction, Brisbane  
 Mitsubishi Estate Co. Ltd., Tokyo  
 Rahulan Zain Associates, Kuala Lumpur, Malaysia  
 Shimizu Corporation, Tokyo  
 Steen Consultants Pty Ltd., Singapore  
 Weidlinger Associates, New York  
 M/S Speco Engineering Ltd., New Delhi, India  
 M/S Octalube Space Structures (India) PVT Ltd., Chennai, India  
 Nihon Sekki Ltd., Tokyo  
 US Federal Emergency Managements Agency, Washington D.C.  
 SRI International, Menlo Park, California, USA  
 Japan Society for Earthquake Research, Tokyo  
 Natural Science and Engineering, Research Council of Canada (NSERC),  
 Quebec  
 ASCE Task Force on Wind Forces, ASCE, New York  
 Beratende Ingenieure VBI, Hamburg, Germany  
 Dr. Ing. Fritz Nötzold, Consulting Engineers, Langen, Germany  
 Michael Joseph Ltd., USA

The authors are indebted to the following for their tremendous help in providing advice and materials in the form of experimental results, data, drawings and background design during this research period:

Dr. W.G. Corley of CTL Laboratories, Skokie 60077, Illinois, USA  
 Dr. J. Bardwell of CTL Laboratories, Skokie 60077, Illinois, USA  
 Edward R. Sturm, President of Sturm Engineering Company, Oklahoma,  
 USA  
 Mr Mike Chrimes, Chief Librarian, The Institution of Civil Engineers, London, UK  
 The American Society of Civil Engineers, Reston, Virginia  
 FEMA, 500 C Street, S W Washington D.C., USA  
 Professor Bachman formerly of the Swiss Federal Institute of Technology,  
 Zurich, Switzerland  
 Mrs Natalie Ammann of the Swiss Federal Institute of Technology, Zurich,  
 Switzerland  
 Dr. Walter Ammann of Eidgenössisches Institut für Schnee-und-Lawinenfor-  
 schung, SLF, Davos, Switzerland  
 Kirkpatrick Consulting Engineers of Oklahoma, USA

The authors also appreciative of the efforts of those authors and researchers mentioned in the references and bibliography.

The authors would also like to take this opportunity to thank the unwavering support provided by their family during this research period.

This acknowledgment would be incomplete without praising the enormous help given by the then computer bureaux STRUCOM Ltd, London, and the FEA, Kingston, Surrey, UK.

The authors are also grateful to Miss Matina Theodoropoulou, Greece, for typing the manuscript and are indebted to all the people named in the text for their valuable research and from whom the authors have received inspiration while writing this book.

To crown all, the authors are grateful to Federal Emergency Agency, Washington D.C., U.S.A., for materials and greater support provided. It will not be out of mention to thank Dr. Karuna from Sri Lanka who provided his program on temperature which he developed for MSc Thesis duly discussed and supervised by the first author.

# Conversion Tables

## Units

<i>Imperial units</i>	<i>SI units</i>	<i>Additional</i>
1 in	= 25.4 mm	
1 in <sup>3</sup>	= 0.003785 (m <sup>3</sup> )	
1 ft	= 30.48 cm	
1 ft <sup>2</sup>	= 0.09290 (m <sup>2</sup> )	1 ft <sup>3</sup> = 0.02832 (m <sup>3</sup> )
10 ga	= 3.57 mm	1 cu yard = 0.765 (m <sup>3</sup> )
18 ga	= 1.27 mm	
1 lb	= 0.454 kg	
1 ton	= 9.964 kN	
1 sq ft	= 929 (cm) <sup>2</sup>	
1 cubic ft	= 16.4 (cm) <sup>3</sup>	
1 psi	= 6.89 kPa	= 6895 Pascal (Pa)
20 T/ft <sup>2</sup>	= 1915.2 kN/m <sup>2</sup>	
1 lb/sq ft	= 992.16 kPa	= 47.88 Pascal (Pa)
1 lb/ft <sup>3</sup>	= 16.02 kg/m <sup>3</sup>	
1 ft lb	= 1.356 Nm	
1 ft/sec	= 0.3048 M/s	
1 slug	= 14.59 kg	
1 in lb	= 0.1129848 Nm	
1 kip/in	= 175.1268 kN/m	
1 bar	= 100 kN/m <sup>2</sup>	
1 kip	= 1000 lb	= 4.448 kN
1 short ton (2000 lb)	= 0.9072 Megagram (Mg)	

<i>MKS units</i>	<i>SI units</i>
1 Pascal (Pa)	= 1 N/m <sup>2</sup>
1 kgm	= 9.807 Nm
1 kgf	= 99.807 N

	Temperature in °C (Celsius)	
1°F (Fahrenheit)	= $t_f = \frac{5}{9} K$	$t_c = (t_f - 32)/1.8$
1°C		$t_f = 1.8 t_c + 32$

# Contents

Preface .....	V
Conversion Tables .....	XIII
<b>1 Explosion and Buildings – A Review of Affected Buildings and General Criteria, Data, and Management .....</b>	<b>1</b>
1.1 General Introduction .....	1
1.2 A Review of Bomb-Affected Buildings .....	1
1.2.1 Case Studies on Bomb Damage to Buildings .....	2
1.3 The Pentagon Building .....	24
1.3.1 Introduction .....	24
1.3.2 Damage Scenario .....	26
1.3.3 Aircraft Crash into the Pentagon .....	30
1.4 Data on Major Explosive Elements. Their Ingredients and Material Properties .....	39
1.4.1 Introduction .....	39
1.5 Explosion Caused by Impact-cum-Fire .....	46
1.5.1 Introduction .....	46
1.5.2 Guide to High-Rise Fire Fighting Caused by Explosion .....	49
1.5.3 Aggressor: Threats and Tactics .....	52
1.6 Vehicle Barrier System Requirements .....	60
1.7 Vehicle Bombs – City of London Police Observation List ...	61
1.8 Selection Procedures for a Vehicle Barrier .....	62
1.8.1 Example 1.1 American Practice .....	63
References .....	64
<b>2 Blast and Explosive Loadings on Buildings .....</b>	<b>67</b>
2.1 Introduction .....	67
2.2 Explosives and Bombs .....	67
2.2.1 A Terrorist Bomb .....	68
2.2.2 Blast Loads on Buildings .....	69
2.2.3 Blast Wave Scaling Laws .....	76
2.2.4 Basic Parameters of a Bomb Blast .....	77

2.2.5	Explosions in Air . . . . .	83
2.2.6	The Impulse of the Incident Pressure . . . . .	87
2.2.7	Thickness of the Shock Front . . . . .	88
2.2.8	Evaluation of Stagnation Pressure, Stagnation, and Post-shock Temperatures . . . . .	88
2.2.9	Oblique Shock . . . . .	89
2.2.10	Shock Reflection . . . . .	93
2.2.11	Oblique Reflection . . . . .	94
2.3	Internal Blast Load Modelling and Structural Response of Buildings . . . . .	95
	References . . . . .	100

**3 Fire and Buildings**

	<b>With and Without Explosion/Impact . . . . .</b>	<b>103</b>
3.1	Introduction . . . . .	103
3.2	Loadings and Restraints . . . . .	105
3.2.1	$t$ -Squared Fires . . . . .	112
3.3	Pre- and Post-flashover Design Fires . . . . .	116
3.3.1	Pre-flashover Design Fires . . . . .	116
3.3.2	Heat Transfer . . . . .	116
3.4	Temperature-Time Relation . . . . .	117
3.5	Material Properties . . . . .	127
3.5.1	Steel . . . . .	127
3.5.2	Concrete and Reinforcing Steel . . . . .	132
3.5.3	Masonry/Brick/Block . . . . .	137
3.6	Methods of Analysis and Design . . . . .	139
3.6.1	Empirical and Code Analytical Equations . . . . .	139
3.6.2	Calculations of Fire Resistance of Steel Members . . . . .	139
3.6.3	Additional Methods of Protection for Hollow Columns . . . . .	148
3.6.4	Summary of Empirical Equations for Steel Columns Fully Protected Against Fire (USA) . . . . .	150
3.6.5	Examples in Steel Structures . . . . .	150
3.6.6	Calculations of Fire Resistance of Concrete Members . . . . .	158
3.7	Deflection of Simple Beams in Reinforced and Prestressed Concrete Exposed to Fire – IStructE Method . . . . .	171
3.8	Limit State and Plastic Analysis . . . . .	179
3.8.1	Basic Theory . . . . .	179
3.8.2	Plastic Analysis and Fire Temperature . . . . .	183
3.8.3	Beams and Temperatures – Tabulated Cases . . . . .	185
3.8.4	Compression Members or Columns . . . . .	185
3.8.5	Portal Frames – Tabulated Cases . . . . .	192
3.9	Multi-bay-Multi-storey Framed Buildings Subject to Fire Loading . . . . .	192

3.10	Finite Element Analysis of Buildings on Fire . . . . .	205
3.10.1	Introduction . . . . .	205
3.10.2	Basic Heat Transfer Analysis . . . . .	206
3.10.3	Computer Subroutines . . . . .	211
3.10.4	Applications . . . . .	211
3.11	Case Study for Global Analysis Based on Finite Element Method – Canary Wharf Building . . . . .	217
3.11.1	Introduction to the Analysis . . . . .	217
3.11.2	Data . . . . .	218
	References . . . . .	227
<b>4</b>	<b>Structural Response to Blast Loadings –</b>	
	<b>Methods of Analysis . . . . .</b>	<b>229</b>
4.1	Introduction . . . . .	229
4.2	Methods of Analysis and Design . . . . .	230
4.3	Structural Response Analysis to Blast Loading . . . . .	230
4.4	Design Examples . . . . .	231
4.4.1	Example 4.1 . . . . .	231
4.5	Finite Element Method of Analysis . . . . .	249
4.5.1	Dynamic Finite Element Technology . . . . .	249
4.5.2	Combined Finite Discrete Element Method . . . . .	249
4.5.3	Element Technology . . . . .	249
4.5.4	Static Condensation . . . . .	272
4.5.5	Forces and Moments Along the Element . . . . .	278
4.5.6	Damping of the Stretching Movement of the Element . . . . .	282
	References . . . . .	288
<b>5</b>	<b>Blast Response Resistance –</b>	
	<b>Design of Structural Elements . . . . .</b>	<b>289</b>
5.1	Introduction . . . . .	289
5.2	Practical Design Examples . . . . .	289
5.2.1	Example on British Practice . . . . .	289
5.2.2	Example on American Practice . . . . .	303
5.2.3	Example on British Practice . . . . .	307
5.2.4	Example on American Practice . . . . .	312
5.3	The Use of Baker et al. Charts for Evaluating Blast Parameters . . . . .	315
5.3.1	Example on American Practice . . . . .	315
5.4	Glass and Glazing . . . . .	319
5.4.1	Introduction . . . . .	319
5.4.2	US Technical Manual 5-1300 . . . . .	320
5.4.3	Keenan and Meyers Method for Hardening Buildings . . . . .	321
	Reference . . . . .	332

<b>6</b>	<b>Contact or Gap Elements for Blast-Fire</b>	
	<b>Structural Interaction</b> .....	333
6.1	Introduction to Bangash T. Contact Elements.....	333
6.2	NBS Contact Detection for Problems of a 2D Nature .....	334
6.3	NBS Contact Detection Algorithm for 3D Problems.....	337
6.4	3D Implementation into the Combined FEM/DEM Method .....	337
6.5	NBS Algorithm – Detection of Contact.....	341
6.6	3D NBS Algorithm – Implementation .....	341
6.7	Hallquist et al. Method .....	349
6.8	DELFT Interface Fraction Type Element .....	351
6.9	ANSYS Contact Elements .....	353
6.10	ABAQUS Gap Contact Element.....	356
6.11	LS-DYNA Gap/Contact Elements .....	362
	References .....	365
<b>7</b>	<b>Aircraft and Missile Impact – Data and Analysis</b> .....	367
7.1	Introduction .....	367
7.2	Direct Impact/Impulse and Momentum .....	367
7.3	Two Columns/Girders Falling and Impacting Each Other in Contact in Elastic Medium .....	380
7.4	Oblique Impact .....	382
7.5	Aircraft Impact on Structures – Peak Displacement and Frequency .....	386
7.6	Aircraft Impact: Load-Time Functions .....	388
	7.6.1 Introduction .....	388
	7.6.2 Stevenson’s Direct Head-On Impact Model .....	388
	7.6.3 Riera Model .....	388
	7.6.4 Model of Wolf et al. ....	389
7.7	Military, Air Force, and Navy Missiles and Impactors .....	394
	7.7.1 Introduction to Bombs, Rockets, and Missiles .....	394
7.8	Empirical Formulae for Structural Elements in Damage Scenario.....	406
	7.8.1 Introduction .....	406
	7.8.2 The National Defence Research Committee (NDRC) Formula.....	406
	7.8.3 The Bechtel Formula .....	408
	7.8.4 The IRS Formulae for Penetration and Complete Protection .....	409
	7.8.5 The ACE Formulae to Prevent Penetration or Perforation.....	409
	7.8.6 The Stone and Webster Formula .....	410
	7.8.7 The CKW-BRL Formula for Penetration and Perforation .....	410
	7.8.8 Modified Ballistic Research Laboratory Formula....	410



7.8.9 Chalapathi, Kennedy, and Wall  
(CKW)-BRL Formula . . . . . 411

7.8.10 Dietrich, Furste (DF)-BRL Formula . . . . . 411

7.8.11 Modified Stone and Webster . . . . . 411

7.8.12 Modified Kar Formula . . . . . 412

7.8.13 Petry Formula . . . . . 412

7.8.14 Modified Barr, Carter, Howe,  
and Neilson Formulae . . . . . 414

7.8.15 Modified CEA-EDF Formula . . . . . 414

7.8.16 Chang Formulae . . . . . 415

7.8.17 Haldar, Miller, and Hatami Method . . . . . 416

7.8.18 Takeda, Tachikawa, and Fujimoto Formula . . . . . 416

7.8.19 Hughes Formulae . . . . . 416

7.8.20 Modified Kar Formulae . . . . . 417

7.8.21 Perry and Brown Formulae . . . . . 417

7.8.22 Formulae for Deformable Missiles Impacting  
on Concrete Targets –  
McMahon, Meyers, Sen Model . . . . . 419

7.8.23 Rotz Damage Model . . . . . 420

7.8.24 Missiles on Steel Targets . . . . . 420

References . . . . . 428

**8 Aircraft Hot Fuel-Structure Interaction**

**During Impact Condition . . . . . 441**

8.1 Introduction . . . . . 441

8.2 Aviation Fuels . . . . . 441

8.3 Fuel-Structural Interaction –  
Basic Analytical Formulations . . . . . 443

8.3.1 Velocity Pressure Formulations . . . . . 444

8.3.2 Stress Vector . . . . . 449

8.4 Output Quantities . . . . . 452

8.5 Input Data and General Analysis of WTC-1 and WTC-2  
(World Trade Center) . . . . . 453

8.5.1 Geometrical Data . . . . . 453

8.5.2 Aircraft Impact Areas and Speed . . . . . 453

8.5.3 Connection Details, Structural Sizes,  
and Other Parameters . . . . . 458

8.5.4 Critical Temperature for Steel . . . . . 462

8.5.5 Walls with Opening . . . . . 463

8.5.6 Stresses in Steel to Be Considered . . . . . 464

8.5.7 Data on Finite Elements and Their Geometry . . . . . 464

8.5.8 Analysis of Hot Fuel-Floor Interaction . . . . . 465

References . . . . . 471

**9 Flying Debris – Elastic Scattering Approach** . . . . . 475

9.1 Introduction . . . . . 475

9.1.1 Nomenclature . . . . . 475

9.1.2 Turbulence Modeling . . . . . 476

9.2 Finite Element/Difference Method  
for Elastic Wave Equations . . . . . 477

9.2.1 Elastic Wave Propagation . . . . . 477

9.3 Three Dimensional Scattering of Elements  
Under Impact/Explosion/Fire . . . . . 491

9.4 Debris Dispersion Relation Using Time-Dependent  
Elastic Waves . . . . . 492

9.4.1 Stability Criterion . . . . . 492

9.4.2 Absorbing Boundary Conditions . . . . . 492

9.4.3 Neumann Boundary Conditions . . . . . 493

9.5 Debris Elements Forced by a 3-D Turbulent Flame . . . . . 493

9.5.1 Introduction . . . . . 493

9.5.2 Turbulent Driven Debris Equations . . . . . 493

9.6 Development of Flight Model . . . . . 498

9.7 Damage Function for a Scenario . . . . . 500

9.8 Test Example on WTC Tower Collapse . . . . . 503

9.8.1 Additional Data Due to Explosion . . . . . 504

References . . . . . 517

**10 Building Global Analysis for Damage Scenario** . . . . . 529

10.1 Introduction . . . . . 529

10.2 Analysis of Buildings in Three-Dimensions . . . . . 531

10.2.1 General Introduction . . . . . 531

10.2.2 Finite Element Analysis  
of Framed Tubular Buildings  
Under Static and Dynamic Loads Influences . . . . . 532

10.3 Multi Multiple-Core Systems . . . . . 552

10.4 Local and Global Stability Analysis . . . . . 560

10.4.1 Flexural Buckling . . . . . 560

10.4.2 Inclusion of Torsional Buckling . . . . . 561

10.5 Formation of Elastic–Plastic Joint Element Using Finite  
Element or Finite Discrete Element Analyses . . . . . 563

10.5.1 Introduction . . . . . 563

10.5.2 The Damage Model . . . . . 565

10.6 Modelling and Behaviour of Masonry Walls . . . . . 569

10.6.1 Introduction . . . . . 569

10.6.2 Thermal Bowing . . . . . 569

10.6.3 Masonry Material Properties . . . . . 571

10.6.4 Wall Geometry . . . . . 571

10.6.5 Boundary Conditions . . . . . 572

10.6.6 Applied Loading on Walls . . . . . 572

10.6.7 The Finite Element Model . . . . . 572

10.7	Global Analysis Based on PROGRAM BANGF .....	572
10.7.1	General Introduction .....	572
10.8	Case Studies .....	574
10.8.1	Introduction .....	574
10.8.2	WTC Towers Collapse in New York .....	574
10.9	World Trade Center (WTC 1 and WTC 2) .....	582
10.9.1	Data for Three-Dimensional Finite Element Modelling .....	582
10.10	Finite Element Modelling of WTC-1 or WTC-2 .....	586
10.10.1	Introduction .....	586
10.10.2	WTC 2 .....	594
10.10.3	Analysis of Results from the Global Analysis .....	595
10.10.4	A Comparative Study of WTC-1 Tower Results .....	597
10.10.5	A Comparative Study of WTC-2 Tower Results .....	599
10.10.6	Practical Solution to Twin Towers .....	599
10.10.7	Conclusion and Future Recommendations .....	599
10.11	Case Study: Alfred P. Murrah Building, Oklahoma, U.S.A. .	601
10.11.1	Introduction .....	601
10.11.2	Experimental Validation of the Combined Finite-Discrete Element Modelling of Structures .....	605
10.11.3	Structural Layout of the Alfred P. Murrah Building .....	613
10.11.4	Structural Damage to the Alfred P. Murrah Building .....	617
10.11.5	Structural Plans for the Floors of the Alfred P. Murrah Building .....	621
10.11.6	Material Properties and Reinforcement Detailing .....	624
10.11.7	Numerical Simulation of Blast Loading .....	630
10.11.8	Conclusions .....	653
	References .....	655
<b>Appendix I</b> .....		659
A.I.A	Related Analysis and Computer Programs Based on Finite Element .....	659
A.I.B	Computer Program Based on FEM/DEM .....	738
A.I.C	Rules for Impact/Explosion and Load Distribution – Time Function .....	764
	References .....	769
<b>Index</b> .....		771

# **1 Explosion and Buildings – A Review of Affected Buildings and General Criteria, Data, and Management**

## **1.1 General Introduction**

Many nations have become victims of terrorism on a grand scale. Bombs have exploded in and around buildings in many countries causing civilian casualties and structural damage. As a result, such events have generated considerable concern over the ability of countries to protect buildings and their occupants from the continued threat of bombings. In response to a potential threat of terrorist bombings against civilian structures, various defence agencies and research councils are examining design methodologies and construction techniques. Protecting the buildings against vehicle bomb attacks has become a priority. The issue of the structural integrity of existing buildings is now a burning one. Analytical, theoretical and design-cum-construction techniques are constantly being reviewed by government agencies and engineering consultants. Bangash [1.13] has given a detailed version of structures subject to impact and explosion. This section is related to bomb explosion in and around buildings only. It covers important case studies of buildings, review of existing knowledge for blast effects and their mitigation and protective design technologies, analytical and computational techniques. Conclusions and recommendations are also given. For impact forces causing the damage a reference is made to Appendix A.1 for detailed methodology of translating impact forces associated with the explosion.

## **1.2 A Review of Bomb-Affected Buildings**

LZA [1.38,1.39] has reviewed the large number of data in this field from the Second World War, drawing attention to some of the more relevant research papers on blast and its effect on both hardened and conventional-bearing framed structures. Referring to the UK, France, Germany and Japan, tens of thousands of records of bomb damage have been compiled.

## 1.2.1 Case Studies on Bomb Damage to Buildings

### 1.2.1.1 Introduction

A bomb explosion within or around a building can have catastrophic effects, damaging and destroying internal or external portions of the building. It blows out large framework, walls and doors/windows and shuts down building services. The impact from the blast causes debris, fire and smoke and hence can result in injury and death to occupants.

Bomb damage to buildings depends on the type and layout of the structure, material used, range of the located explosive device and the charge weight. This section deals with the historical survey of important buildings hit directly by bomb explosion and the collateral damage to building sub-systems. Case studies are chosen from various countries and they are by no means complete as many explosions can occur and more and more collateral damage to building sub-systems can in future, be reported. If a building is not designed 'for a blast', a steel frame might be better under reasonably small bomb scenarios since steel has equal capacity in tension and compression and concrete has capacity only in compression in at one face and tension is taken by the reinforcement at the other face. One doesn't know in which direction the blast effects will occur.

If a building is designed for a blast, the concrete components do better. They have more mass and more damping and energy-absorbing capacity. In the United States, the state department allows only reinforced-concrete buildings in high-risk areas.

### 1.2.1.2 Case Studies

#### 1. *The Alfred P. Murrah Federal Building*

In April 1995, the bombing of the Alfred P. Murrah Federal Building in Oklahoma City was one of the largest terrorist attacks in the USA. A car bomb, estimated to contain about 1800 kg of high explosives and located 3–5 m from the north face of the building and about 12–15 m from the east end, caused 168 fatalities and numerous injuries, and caused an estimated \$50 million in damage. Besides this, the number of surrounding buildings damaged was around 75.

The Murrah Building was a nine-storey building of RC slab/column construction. Measuring 61.5 m × 21.5 m. The frame had 10.7 m × 6.2 m typical bays, created by a column line along each face and one down the centre. Four of the north-face columns, spaced at 12.3 m and unsupported for two storeys, formed an atrium at street level. A 61.5 m spandrel beam at the third floor transferred loads from the columns on floors above the exposed columns at height 8 m. the explosion destroyed three of the four front columns and a centre-line column. With four columns completely destroyed, the upper floor

toppled northward as the 200 mm thick slabs separated from the centre-line columns. As a result, 8 of the 10 bays collapsed in the northern half of the building. Two bays collapsed on either side of the failed centre column in the southern half of the building. Moreover, inside the south entrance slabs in adjacent bays on two floors collapsed. The most recent information is as follows.

The bomb was fertilizer-based (ammonium nitrate fuel oil ANFO) explosive which had the TNT equivalent  $1814 (1.05) = 1905$  kg. Figure 1.1 indicates the Murrah Building prior to blast. Figure 1.2 shows the position of the building along with other buildings in the locality before the blast while Fig. 1.3 shows the extensively damaged part of the Murrah building. The centre column 6-lines of the building was ripped off by blast. Figure 1.4 shows damage to the south east portion of the building.

In addition, the explosion hurled broadside into 30 of 4 two-storey exposed columns along a recessed entrance and a 61 m long third-floor spandrel beam that transferred loads from columns spaced 6.5 m apart on typical floors above to the 8.5 m tall exposed columns spaced every 12 m. The blast kicked the legs out from under the  $0.91 \text{ m} \times 1.5 \text{ m}$  transfer beam and served to expose the  $500 \text{ mm} \times 900 \text{ mm}$  columns. It was also observed that a  $9.1 \text{ m} \times 5 \text{ m}$  slab was hanging precariously over the rubble-covered columns. A mile away window frames had been pushed back 0.61 m and the 610 mm centre-line columns as reported thus failed. The bomb also deformed and in some places ruptured the  $10.7 \text{ m} \times 6.1 \text{ m}$  frames of typical bays.

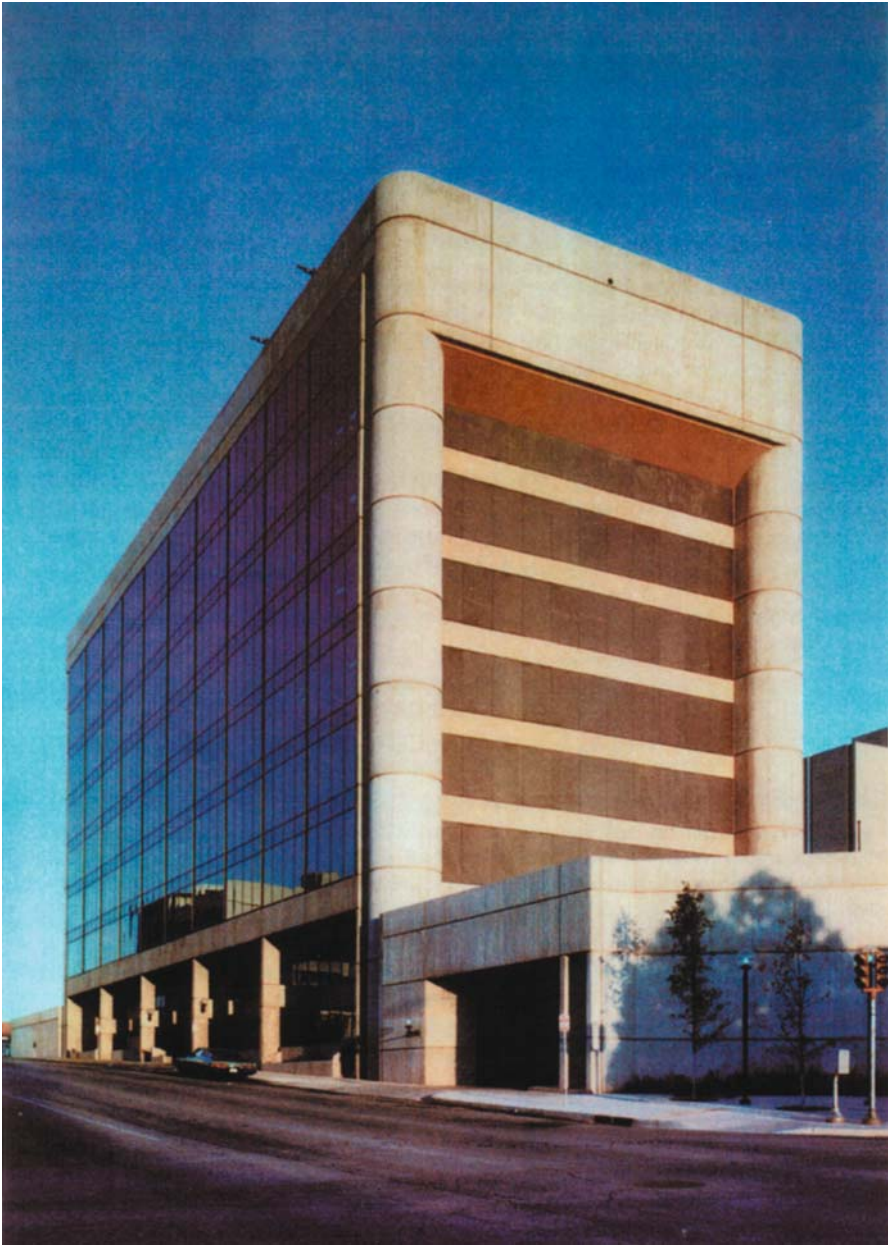
The bomb crater was  $9.15 \text{ m} \times 2.45 \text{ m}$ , and the site needed immediate attention. The building was finally demolished with 220 explosive charges that brought it crashing to the ground. The 4500 tonnes of debris were removed over a period of three weeks.

## *2. The World Trade Center, New York*

The World Trade Center (WTC), New York City, was attacked on 26 February 1992. It was a 110-storey plaza. The damage was extensive. The bomb estimated to be about 900 kg of high explosive, was detonated against the south wall of the north tower in an underground garage two levels below the ground floor. The following gives additional details:

- Severe damage at sub grade levels of the floors.
- Bomb crater across some of the floors 24 m to 36 m.
- Two storeys of RC slabs 280 mm thick blown out.
- Parking floor slabs failed at column capital.
- Segments of the masonry wall along the south wall of the north trade tower were blown out.

The World Trade Center vehicle bomb consisted of properly mixed ordinary ANFO TNT equivalent of  $816.5 (0.7) = 571.6$  kg (1260 lb). This bomb was also fertilizer based. The energy content of this bomb was around 30% of the one used in Oklahoma City. These structures consisting of Twin Towers are shown later on which were collapsed by terrorists using various aircraft.

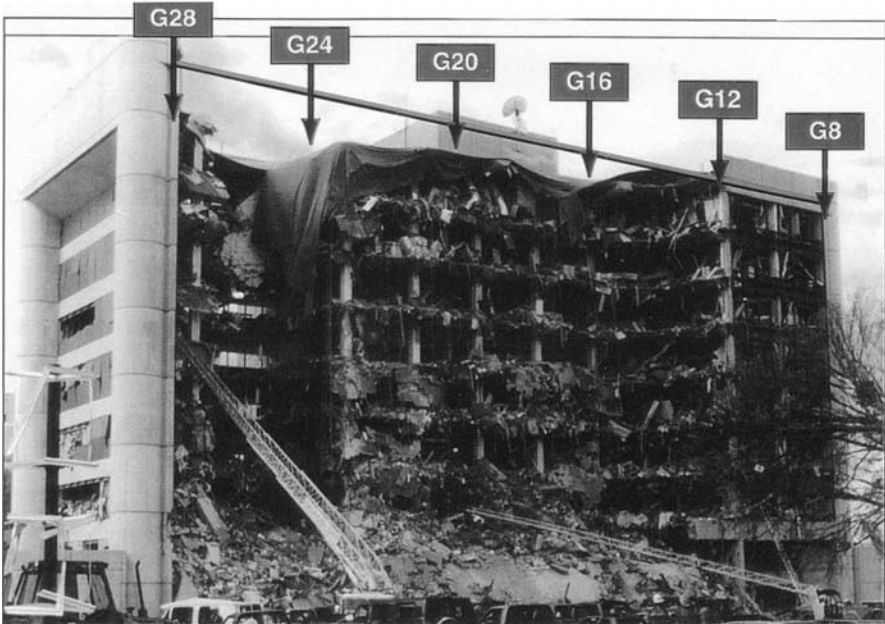


**Fig. 1.1.** Murrah Building prior to blast (courtesy: ASCE 2003, New York; courtesy and permission: Kirkpatrick Engineering Consultants, Oklahoma, U.S.A)



Fig. 1.2. Immediate vicinity of Murrrah Building (courtesy: FEMA 2002, Washington, D.C.)





**Fig. 1.3.** Damage to north and east sides of Murrah Building (courtesy: ASCE 2003, New York; courtesy: Kirkpatrick Engineering Consultants, Oklahoma, U.S.A, 2003)



**Fig. 1.4.** Damage to south-east portion of Murrah Building

### 3. *Jewish Community Centre, Buenos Aires*

A van loaded with 275 kg of high explosives was detonated on 18 July 1994. The explosive range was between 3–5 m from the front face of the building of five storeys of brick masonry construction. The exterior walls supported the floor slabs, which developed progressive failure leading to collapse of a number of them, which were finally destroyed.

### 4. *St. Mary Axe, London*

A car bomb of 350 kg TNT was detonated on 11 April 1992 causing extensive damage to a number of adjacent buildings including the European Development Bank, a ten-storey block with three-storey pedestal. The building was made up of concrete columns and slab construction with non-bearing masonry walls for the lower three levels. Although it was shielded by another building from the explosion, and thus saved from direct blast, the windows of the bank building were completely broken. The windows that survived were on the upwind face of the building, particularly second-floor podium windows (2.5 m × 2.5 m) made of toughened 10 mm thick double-glazed glass.

### 5. *Bishopsgate, London*

The Bishopsgate bomb blast, in April 1993 destroyed several buildings. Load-bearing walls, glazing and cladding were heavily damaged. The mode and the level of damage was very similar to that of St. Mary's. Fittings and claddings had to be replaced. The frames were twisted right down to the foundations. 'Sof-shock' glass was considered rather than laminated glazing since, in future, if such blasts occur, the glass membrane will stretch and thus reduce loads transferred to the structural components. The raised floors and suspended ceilings were distorted by the blast and thus needed realignment and re-levelling. Close to the blast centre, severe internal damage was visible.

### 6. *Docklands, London*

On 9 February 1996, a bomb in London's Docklands caused widespread damage. The cost of destruction was over £ 100 million. Figure 1.5 shows a plan of various buildings close to the blast site. The unusual vehicle carrying the South Quay bomb made it more lethal than the previous bombs. The vehicle was disguised as a small lowloader thus creating a vicious device that produced heavier shrapnel, which scythed through the lightweight cladding, used on many of the buildings shown on Fig. 1.5. Apparently the explosives were packed tightly into a small space and confined between metal sheets eventually turning out to be a pretty potent source of shrapnel. It is estimated, from the blast pattern, that the home-made explosive, (HME) which detonated could have been no more than 500 kg TNT high explosive, about 75% the force of commercially produced TNT. In an open space, the bomb

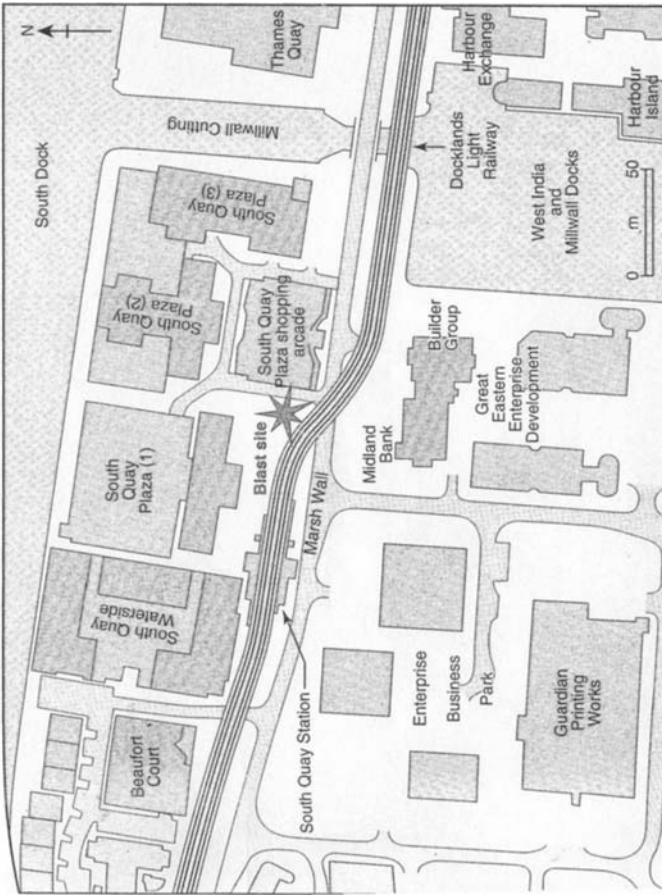


Fig. 1.5. Buildings in London Docklands (courtesy of NCE Feb. 1996)

would have produced a hemi-spherical blast wave and caused havoc despite its being half the size of the earlier London bombings in 1992 and 1993. The bomb detonation released gas at a pressure of 300 kilobar and temperature of 4000°C and consisted of a layer of compressed air, due to gas expansion. Between various buildings, a complex pattern of reflection and refraction waves resulted from the blast, thus varying structural response and damage. The response obviously depends on factors such as the blast energy due to explosion, building geometry, structural form and most importantly, the ranges (distances from the blast centre to the building concerned).

Tall buildings with a greater height/base ratio compared with smaller buildings reacted better. There appears to be no significant difference in performance between concrete and steel-framed buildings. Generally, there is a dependence on the quality of design and detailing.

On the question of individual building and blast effects, the following examines important buildings in the Docklands area and how they sustained damage.

### South Quay Waterside

Here, three tower blocks and a 24-storey tower block are located. Generally, they have steel framed main structures with composite deck floors sitting on an RC-framed basement. Cladding is made of granite and glazing is tinted glass with no protective film. Most of them were unoccupied at the time of the blast. Most of the glass was lost and cladding was slightly damaged. In general the buildings appear to have performed well since the Docklands light railway having received some damage, protected them.

### The South Quay Plaza (SQP) 1, 2, 3

The Arcade consists of a shopping centre and three office buildings. They have RC frames with pitched roofs. The front has, in each case, granite cladding and mirror glass.

SQP1 – Seven storeys extensively damaged and all glass lost. Roof was damaged. Each side of the building stripped of its frame.

SQP2 and SQP3 – Ten storeys and fourteen storeys, respectively. The buildings were completed in 1989. All glass lost from SQP2 and much lost from the other side of SQP3.

These two buildings were otherwise intact. The Plaza shopping centre had to be demolished.

### Thames Quay

This has three inter-connecting blocks with stepped façades. The London Dockyard Council (LDC) occupies the block nearest to the centre of the blast. Windows had a plastic film coating. Due to the blast, the cladding panels were dimpled. The building was completed in 1989.

Great Eastern Enterprise

This is made up of two blocks of five and nine storeys. The damaged part was completed in 1989. Two steel frames were separated by 100 mm. Cladding comprised aluminium panels and semi-reflective tinted glass with no protective film. Total destruction of the front and west façade was visible. There was little damage to the side remote from the blast. The frames, in general, performed well.

Docklands Light Railway

The railway ran only metres from the centre of the blast. Alarming cracks in the concrete bridge deck soffit crossing Marsh Wall were visible. Its elevated structure at South Quay required major reconstruction. Its viaduct structure, in general, has emerged structurally sound. Two circular RC piers supporting a 35 m span of two steel box girders, appear undamaged. Elastomeric bridge bearings appear unaffected. The bomb also destroyed DLR's offices in South Quay Plaza.

Heron Quay. ICE's Office Thomas Telford House, London

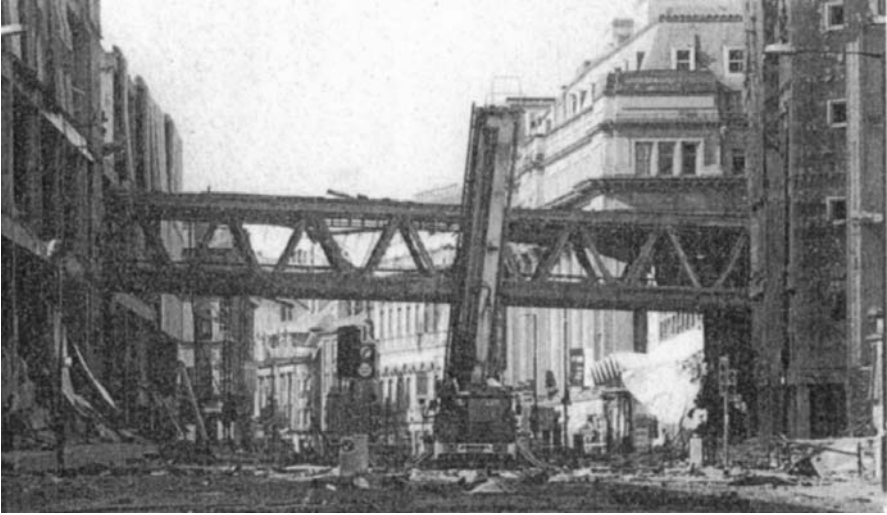
The Institution for Civil Engineers' Dockland office at Heron Quay was approximately 1 km from the centre of the blast. Generally it was sheltered by other structures from the direct force. The structure of the ICE's building took the blast well. The large hinged windows were severely shaken and two panes were plucked out. Flying debris crashed through the glazed canopy and broke two more panes. Light fittings dropped from their holders. No plastic films to the windows existed at the time of the blast.

*7. Staples Corner, London*

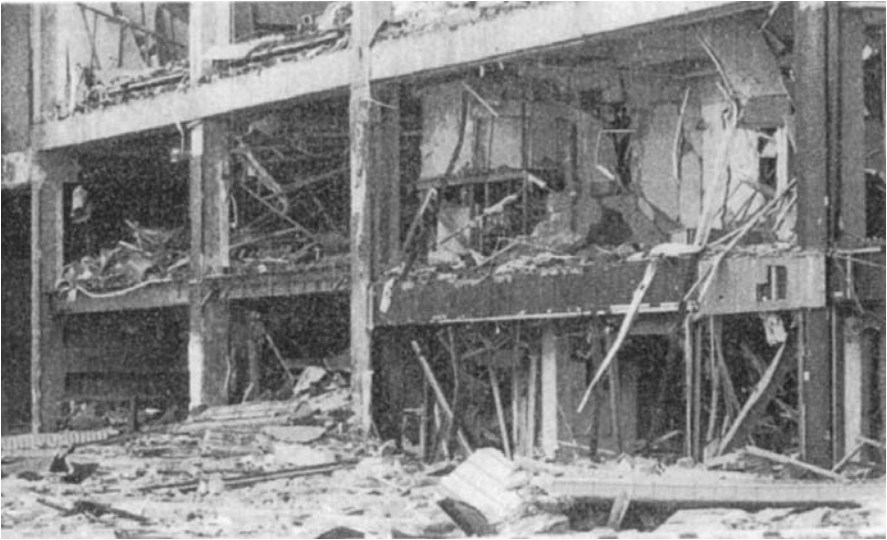
On 11 April 1992 an explosion occurred at Staples Corner damaging a single-storey steel-framed warehouse measuring 56 m × 57 m. A range of 17 m was the nearest from the blast. Severe damage occurred to cladding made of light profiled steel-sheet construction, sheetings, and purlins block-work lining the wall and some fittings and finishes. The main steel frame sustained minor damage. It was estimated that the explosive force was around 100 kg TNT.

*8. Manchester Bomb Blast, UK*

On 15 May 1996 Manchester city centre received a heavy blast from a bomb hidden in a vehicle parked close to the bridge outside the Arndale shopping centre. At the time of writing this case study, engineers and surveyors were eagerly awaiting permission to enter the blast zone since it was still subject to forensic examination. As shown in Fig. 1.6 a 30 m long steel-trussed foot-bridge, providing high-level pedestrian access, seemed to be reaching total collapse. The blast lifted the 200-ton structure from its bearings thus making it unsafe. In the central zone there are around 1000 buildings of widely varying sizes. The 1.5-ton bomb detonated in Manchester left scenes of destruction in the dozens of streets forming the heart of the city. Figures 1.7



**Fig. 1.6.** Murrah Building prior to blast



**Fig. 1.7.** Immediate vicinity of Murrah Building

and 1.8 reveal parts of this devastation. Some buildings were immediately shored up. The worst damage was that to the 220 m<sup>2</sup> Arndale shopping centre consisting of steel and concrete-framed structures supporting concrete-plank flooring and large external cladding panels. Along Corporation Street, the 20 m high frontage lost windows. The 7 m tall heavy concrete panels hung on to the structure above the ground level brickwork infill. Dozens of the tiled

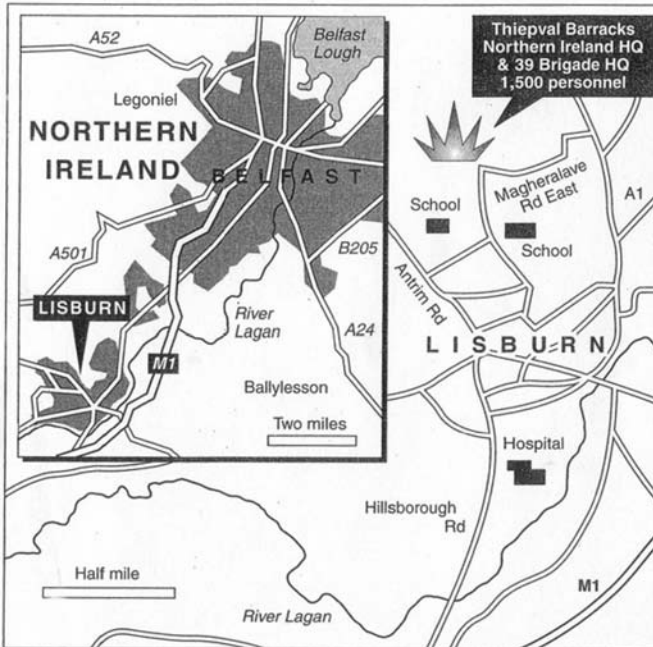


**Fig. 1.8.** Damage to north and east sides of Murrah Building

cladding panels were blasted off by this bomb, which was placed just a few metres away. The frame itself was buckled. A 20-storey office block stood well. The 10-storey Longbridge House, however, was blasted with non-structural concrete infill panels on the lower floors of the steel-framed structure were collapsed. Close to the Arndale Centre, the Royal Exchange building did lose most of its windows and was structurally damaged. Across the road, the Marks and Spencer store lost both its glazed shop fronts and the heavy concrete coping. It is interesting to see that ground floor windows close to the blast remained intact while those higher up a 26-storey office block some 500m away were shattered. Complete shop fronts several streets away from the blast area were blown out but adjacent windows and those on the opposite side of the road were not even cracked.

### *9. Bomb Blast at Lisburn, Northern Ireland*

The bombs exploded within 15 minutes of each other in the Thiepval Barracks of the British Army, eight miles from the south of Belfast. A map shown in Fig. 1.9 indicates the position of the blast. Figure 1.10 shows the scenario, which occurred on 7 October 1996. The two bombs, which produced huge clouds of smoke, were believed to have contained between 250 kg and 500 kg of explosive. A neurological hospital close to the barracks was badly damaged. The approach to the barracks is a four-lane road, two lanes in and two lanes out. At the barriers and further on along the perimeter fencing, there were security cameras which would have filmed the cars. After going through the barriers, however, the two cars carrying the explosives would have faced no further security checks on their way to the car park. It shows the error lies



**Fig. 1.9.** Map showing location of the Lisburn bombings

at the security checks particularly, prior to reaching the car park, although the security layout was perfect to catch the terrorists. The size of the bomb can be derived easily from the damage level and also from the case history of the terrorists given below:

- Aug 31, 1994: IRA suspends campaign temporarily
- Feb 9, 1996: Bomb explodes in London Docklands
- Feb 18, 1996: IRA bomb detonates in a bus, Aldwych, London
- March 9, 1996: Explosion in Fulham, London
- April 17, 1996: Explosion at empty house, South Kensington
- April 24, 1996: Two bombs failed on Hammersmith Bridge, London
- June 15, 1996: Manchester City bombing
- June 28, 1996: Mortars fired at barracks in Germany
- July 13, 1996: Car bombs devastating Enniskilen Hotel, Northern Ireland
- July 15, 1996: Seven arrested in London after bombs components found
- Sept 23, 1996: Police arrests in London and Sussex and recovered bomb making equipment
- Sept 29, 1996: Car bomb containing 250 lb of explosives made safe in Belfast, Northern Ireland
- Aug 7, 2005: 10 kg bombs, London Underground, U.K.





**Fig. 1.10.** Crater from one of the Linsburn bombings

#### *10. Al-Khobar, Saudi Arabia*

Figure 1.11 shows a general view of the building housing US troops in Eastern Saudi Arabia after an explosion. The blast from explosive equivalent to 5000 lb TNT destroyed the horizontal members of the floors and at some levels damaged the verticals. All windows and doors were blasted out. A crater 45 ft long and 35 ft deep was created. Debris from one whole side of the building fell. The wall panels remained intact. A number of people died and some were injured. The bomb was hidden in an abandoned (fuel) truck and ripped off the entire façade of this residential block. The explosion occurred 26 June 1996 at the junction between 8th Street and 31st Street at King Abdul Aziz Air Base at Dhahran.

#### *11. Pakistan and India Bomb Blast*

Between 1993 and 2005 the total number of explosion incidents in Pakistan was 650, including one in the cancer hospital in Lahore, demolishing a large



**Fig. 1.11.** Al-Khobar Building, Saudi Arabia (courtesy Associated Press, France, AFP)

section of the hospital. Around 300 such incidents took place in India including that at the Bombay Stock Exchange and also the Rajasthan bomb blast. The capacities of these bombs have not been reported. Some religious places were targets as well. Bomb blasts in India for the same period turn out to be 210, including the attack on the Indian Parliament.

### *12. Israel and the Other Middle Eastern Countries*

Israel has compiled a database since 1968, called ODS (Observed Damages to Structures). The ODS includes more than 25,000 events recorded throughout the world where structures were attacked. Referring to car explosions or devices placed near these structures, the ODS reports around 1500 events only in Israel. Since the subject is on explosives in or around buildings, the present discussion does not include rockets, anti-tank weapons, recoilless guns, mortars, artillery shells, missiles, and air bombs. The classification of explosives used in the ODS is:

- small explosives – up to 5 kg TNT
- medium explosives – up to 20 Kg TNT
- large explosives – up to 100 kg TNT
- very large explosives – up to 2000 kg TNT

The database of observed effects of terrorist attacks on structures is a useful tool enabling designers to design better and safer structures.

Table 1.1 indicates notable explosions in the world. Table 1.2 shows a comparison of the data on bomb-affected areas in the Middle East with those of some European countries.

### *13. WTC Towers: Impact-cum Fire Explosion and the Collapse Scenario*

Following the September 11, 2001, attacks on New York City's World Trade Center (WTC), the Federal Emergency Management Agency (FEMA) and the structural Engineering Institute of the American Society of Civil Engineers (SEI/ASCE), in association with New York City and several other Federal agencies and professional organizations, deployed a team of civil, structural and fire protection engineers to study the performance of buildings at the WTC site.

The events following the attacks in New York City were among the worst building disasters in history and resulted in the largest loss of life from any single building collapse in the United States. Of the 58,000 people estimated to be at the WTC complex, 2,830 lost their lives that day, including 403 emergency responders. Two commercial airliners were hijacked, and each was flown into one of the two 110-storey towers. The structural damage sustained by each tower from the impact, combined with the ensuing fires, resulted in the total collapse of each building. As the towers collapsed, massive debris clouds consisting of crushed and broken building components fell onto and blew into surrounding structures, causing extensive collateral damage and, in some cases, igniting fires and causing additional collapses. In total, 10 major buildings experienced partial or total collapse and approximately 30 million square feet of commercial office space was removed from service, of which 12 million belonged to the WTC Complex.

As each tower was struck, extensive structural damage, including localized damage, each structure remained standing. However, as each aircraft

**Table 1.1.** Notable explosions in the world

Date	Location	Deaths/Injuries
31/10/1963	State Fair Coliseum, Indianapolis, USA	73
23/7/1964	Harbour munitions, Bone, Algeria	100
4/3/1965	Gas pipeline, Natchitiches, Louisiana, USA	17
9/8/1965	Missile silo, Searcy, Arkansas	53
21/10/1965	Bridge, Tila Bund, Pakistan	80
30/10/1965	Cartagena, Colombia	48
24/11/1965	Armony, Keokuk, Louisiana, USA	20
13/10/1966	Chemical plant, La Salle, Quebec, Canada	11
17/2/1967	Chemical plant, Hawthorne, New Jersey, USA	11
25/12/1967	Apartment building, Moscow	20
6/4/1968	Sports store, Richmond, Indiana, USA	43
8/4/1970	Subway construction, Osaka, Japan	73
24/6/1971	Tunnel, Sylmar, California, USA	17
28/6/1971	School, fireworks, Pueblo, Mexico	13
21/10/1971	Shopping Centre, Glasgow, Scotland	20
10/2/1973	Liquefield gas tank, Stated Island, New York, USA	40
27/12/1975	Mine, Chasnala, India	431
13/4/1976	Munitions works, Lapua, Finland	45
11/11/1976	Freight train, Iri, South Korea	57
22/12/1977	Grain elevator, Westwego, Louisiana, USA	35
24/2/1978	Derailed tank car, Waverly Tennessee, USA	12
11/7/1978	Propylene tank truck, Spanish coastal campsite	150
23/10/1980	School, Ortuella, Spain	64
13/2/1981	Sewer system, Louisville, Kentucky, USA	0
7/4/1982	Tanker truck, tunnel, Oakland, California, USA	7
25/4/1982	Antiques exhibition, Todi, Italy	33
2/11/1982	Salang Tunnel, Afghanistan	1000-3000
25/2/1984	Oil pipeline, Cubatao, Brazil	508
21/6/1984	Naval supply depot, Severomorsk, USSR	200+
19/11/1984	Gas storage area, northeast Mexico City	334
5/12/1984	Coal mine, Taipei, Taiwan	94
25/6/1985	Fireworks factory, Hallett, Oklahoma, USA	21
6/7/1986	Oil rig, North Sea	166
1/6/1988	Coal mine, Brocken, West Germany	-
4/6/1988	Freight train, Arzamar, USSR	-
27/6/1988	Commuter trains, Paris, France	-
3/7/1988	Commercial Iranian Airline, Persian Gulf	-
1/4/1995	Murrah Federal Building, Oklahoma, USA	250
26/2/1992	The World Trade Center, New York, USA	150
18/7/1994	Jewish Community Centre, Buenos Aires, Brazil	125
9/2/1996	Docklands, London, UK	-
4/4/1993	St. Mary's Bishops Gate, London, UK	-
11/4/1992	Staple Corner, London, UK	-
15/6/1996	Manchester, Bomb blast, Manchester, UK	-
7/10/1996	Lisburn, Northern Ireland	-
26/6/1996	Al-Khobar, Saudi Arabia	-
8/1/1968(to date)2003	Israel and Middle Eastern Countries	1600
1/1/1993(to date)2003	Pakistan and India	1200
11/9/2001	World Trade Center (WTC), USA	2630
11/9/2001	Pentagon Building, Washington D.C., USA	189
10/3/2005(to date)	Iraqi Invasion	15005 (reported killed)

**Table 1.2.** Data on bomb-affected areas (1990–2003) in various countries

Target	Countries											
	USA	UK	Iran	Iraq	India	Pakistan	Israel	Europe	Far east	South America	Australia	Afghanistan
Residential	2553*	150	40	300	25	15	110	210	100	200	–	–
Commercial	1468*	315	40	150	200	5	210	115	200	300	–	–
Vehicles	1698	200	–	100	3	–	80	3	11	50	–	–
Educational	573*	16	–	–	–	–	–	–	–	10	–	–
Mail boxes	2712	25	–	3	–	–	10	5	–	20	–	–
Open areas	568	30	10	–	–	–	–	–	10	–	–	–
Utilities	143	40	5	10	2	10	20	–	15	13	–	–
Law enforcement	108	25	15	15	19	50	150	–	10	150	–	–
State and local governments	155	15	–	16	11	20	10	–	–	80	–	–
Federal government	48	40	15	10	–	21	130	–	–	150	–	–
Banks	72	10	–	–	20	5	–	–	–	20	–	–
Military	27	16	10	50	–	–	10	13	10	1110	–	–
Airports and aircraft	10	15	–	5	100	8	20	–	8	13	–	–
Apartments	244*	10	–	–	2	–	16	–	–	10	–	–
Religious facilities†	30	10	5	8	–	50	40	10	–	5	–	–
Energy facilities†	11*	2	–	–	8	–	–	–	–	10	–	–
Parks‡	89	10	–	–	–	–	–	–	–	30	–	–
Medical facilities‡	26	2	–	–	–	2	–	–	–	40	–	–
Other‡	481	–	–	–	–	–	–	–	–	–	–	–
Total	18,200	–	–	30,000§	1300	1000	250	210	1200	250	1500	1700§

\* Around 70% were other explosions.

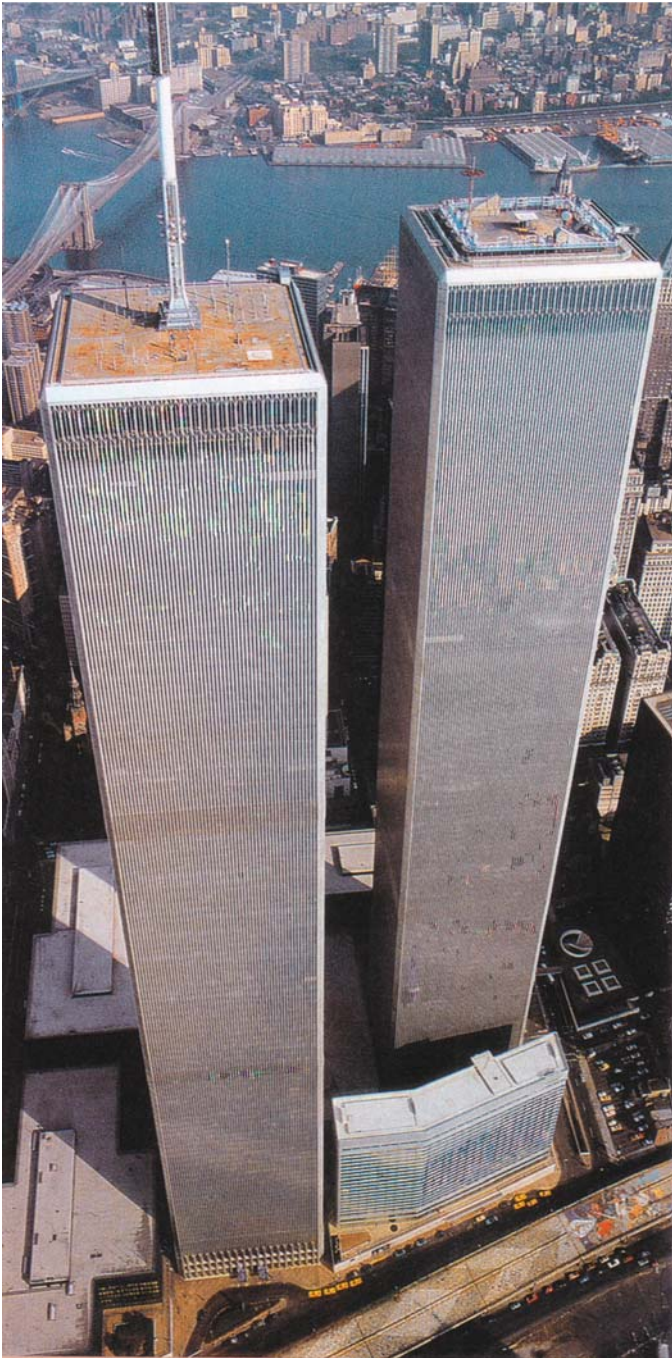
† Hospitals and supply depots, mosques, temples, churches, synagogues.

‡ Shops, restaurants etc.

§ Till Feb. 2005.

impacted a building, jet fuel on board ignited. Part of this fuel immediately burned off in the large fireballs that erupted at the impact floors. Remaining fuel flowed across the floors and down elevator and utility shafts, igniting intense fires throughout upper portions of the buildings. As these fires spread, they further weakened the steel-framed structures, eventually leading to total collapse.

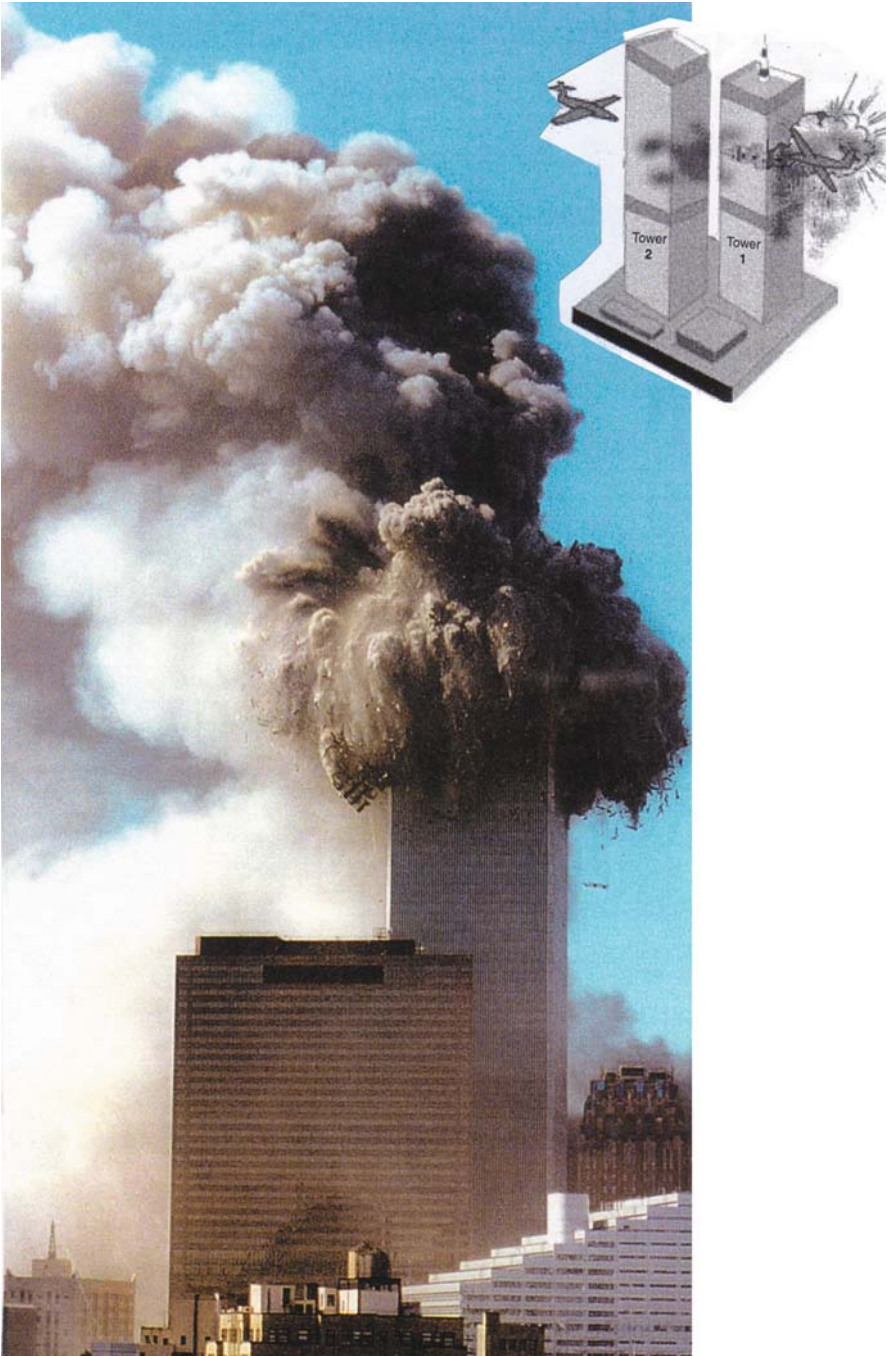
Figure 1.12 gives a bird’s eye view of the World Trade Center (WTC) complex with the towers dominating the Plaza and other buildings, prior to aircraft impact-cum-explosion. Figures 1.13 and 1.14 show the collapse scenario of the two WTC Towers. Figure 1.15 indicates the schematic depiction of collapse debris impact.



**Fig. 1.12.** A bird's eye view of the WTC Complex (courtesy: Yamasaky Associates, Architects, New York, 2002; courtesy: FEMA, New York, Washington, D.C., 2002)

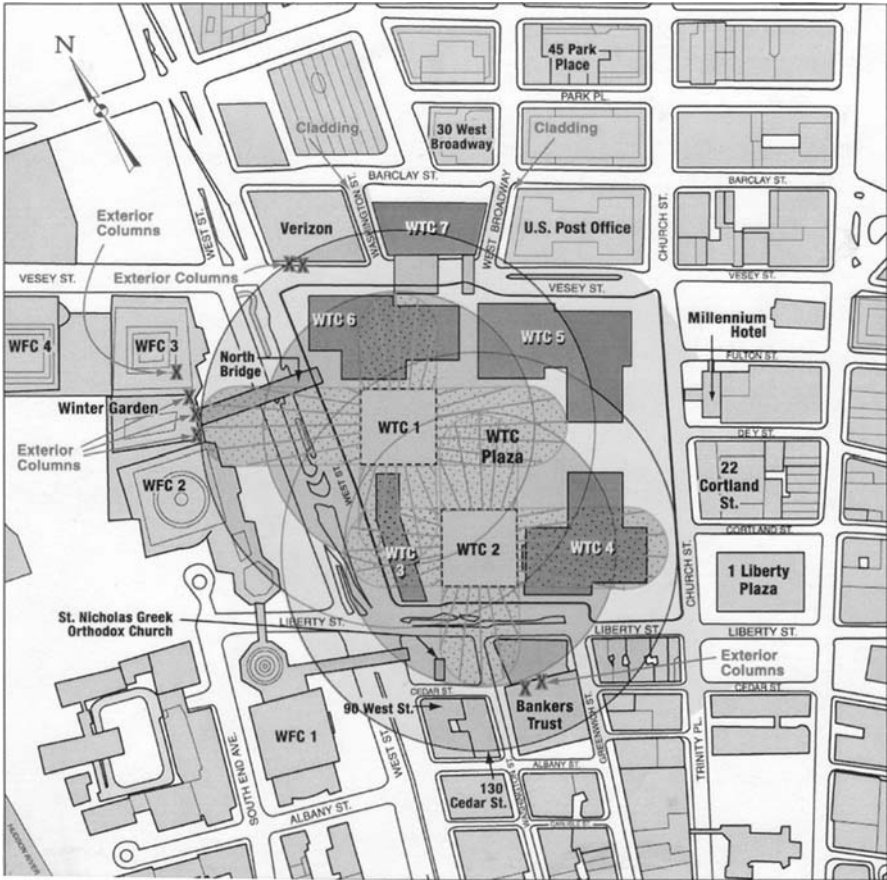


**Fig. 1.13.** WTC Tower with antenna-collapsed scenario: Tower I (courtesy: FEMA 2002, Washington, D.C.)



**Fig. 1.14.** WTC Tower without antenna-collapsed scenario: Tower II (courtesy: FEMA 2002, Washington, D.C.)





**Fig. 1.15.** Schematic depiction of areas of collapse debris impact based on aerial photographs and documented damage. Striped areas indicate predominant locations of exterior steel columns. Inner circles indicate approximate radius of exterior steel columns and other heavy debris. Outer circles indicate approximate radius of aluminum cladding and other lighter debris. Heavy Xs show where exterior steel columns were found outside the predominate debris areas (courtesy: FEMA Report 2001, New York)

The structural damage sustained by each of the two buildings as a result of the terrorist attacks was massive. The fact that the structures were able to sustain this level of damage and remain standing for an extended period of time is remarkable and is the reason that most building occupants were able to evacuate safely. Events of this type, resulting in such substantial damage, are generally not considered in building design, and the ability of these structures to successfully withstand such damage is noteworthy.

Preliminary analyses of the damaged structures, together with the fact the structures remained standing for an extended period of time, suggest

that, absent other severe loading events such as a windstorm or earthquake, the buildings could have remained standing in their damaged states until subjected to significant additional load. However, the structures were subjected to a second, simultaneous severe loading event in the form of the fires caused by the aircraft impacts.

The large quantity of fuel carried by each aircraft ignited into each building. A significant portion of this fuel was consumed immediately in the ensuing fireballs. The remaining fuel is believed either to have flowed down through the buildings or to have burned off within a few minutes of the aircraft impact. The heat produced by this burning jet fuel spread across several floors of the buildings, it ignited much of the buildings' contents, causing simultaneous fires across several floors of both buildings. The heat output from these fires is estimated to have been comparable to the power produced by a large commercial power generating station. Over a period of many minutes, this heat included additional stresses into the damaged structural frames while simultaneously softening and weakening these frames. This additional loading and the resulting damage were sufficient to induce the collapse of both structures.

The ability of the two towers to withstand aircraft impacts without immediate collapse was a direct function of their design and construction characteristics, as was the vulnerability of the two towers to collapse a result of the combined effects of the impacts and the ensuing fires.

#### Chronological Events Leading to the Collapse of WTC Towers

7.59 am (1159 GMT)

American Airlines Flight 11, carrying 92 people, leaves Boston's Logan International Airport for Los Angeles.

8.01 am (1201 GMT)

United Airlines Flight 93, carrying 45 people, leaves Newark, New Jersey, International Airport for San Francisco.

8.14 am (1214 GMT)

United Airlines Flight 175, carrying 65 people, leaves Boston For Los Angeles

8.45 am (1245 GMT)

American Airlines Flight 11 crashes into north tower of World Trade Center

9.03 am (1303 GMT)

United Airlines Flight 175 crashes into south tower of World Trade Center

9.31 am (1331 GMT)

US President George W. Bush calls the crashes an "apparent terrorist attack on our country"

9.40 am (1340 GMT)

American Airlines Flight 77, carrying 64 people from Washington to Los Angeles, crashes into Pentagon. Trading on Wall Street called off.

9.48 am (1348 GMT)

The Capitol and West Wing of the White House are evacuated

9.49 am (1349 GMT)

The Federal Aviation Administration bars aircraft takeoffs across the country. International flights in progress told to land in Canada

9.50 am (1350 GMT)

Two World Trade Center – the South tower – collapses

9.58 am (1358 GMT)

Emergency dispatcher in Pennsylvania receives call from a passenger on United Flight 93, who says: “We are being hijacked, we are being hijacked!”

10 am (1400 GMT)

United Flight 93 crashes 139 kilometres southeast of Pittsburgh

10.29 am (1429 GMT)

One World Trade Center – the North tower – collapses

10–11.30 am (1400–1530 GMT)

Government buildings around the US are evacuated, including the Capitol and the White House. The United Nations closes. The Securities and Exchange Commission closes all US financial markets for the day. New York City mayor Rudolph Giuliani calls for evacuation of Lower Manhattan

11.40 am (1540 GMT)

President Bush arrives at Barksade Air Force base, Louisiana, from Florida after deciding not to return to Washington right away. He later travels to US strategic command at Offutt Air Force Base, Nebraska

2.51 pm (1851 GMT)

The Navy dispatches missile destroyers and other equipment to New York and Washington

5.25 pm (2125 GMT)

Second World Trade Center collapses

### Aircraft Involved Impacting Towers

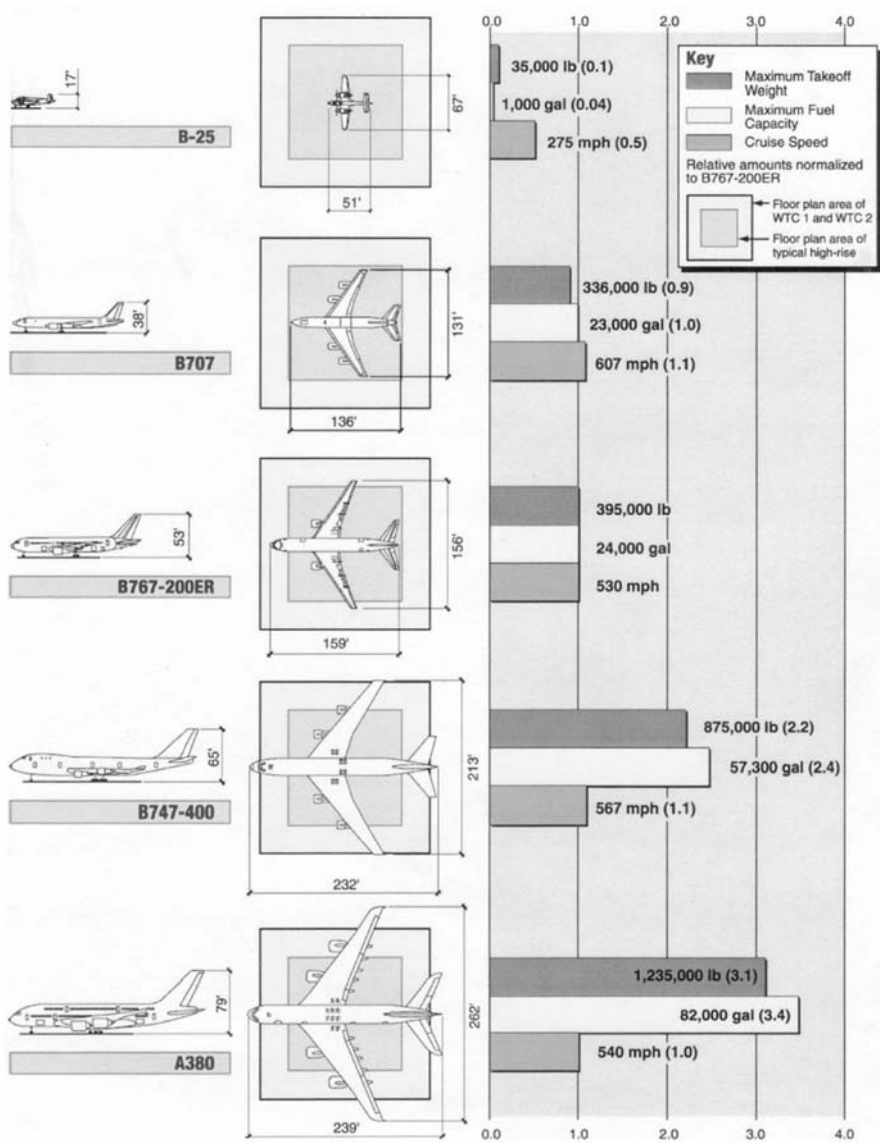
Plate 1.1 indicates the type of aircraft involved in impacting tall towers and Pentagon building. The load-time function for the global analysis for these aircraft are given in the Appendix A.2.

## **1.3 The Pentagon Building**

### **1.3.1 Introduction**

In mid-July 1941 it was ordered that the Pentagon be constructed. Its purpose is to consolidate military personnel with a single structure (Plate 1.2(a)) that would provide a temporary solution to the War Departments critical shortage space. Construction began on September 11, 1941 and was completed on January 1943. The compromise made, due to the Second World War, in the use of materials accelerated not only the speed of construction, but also the

**Plate 1.1.** Comparison of high-rise buildings and aircraft sizes (courtesy: FEMA 2001 Report, Washington, D.C.)



structure's decoration. Since this is one of the world's largest office buildings, the Pentagon covers 29 acres (12 ha) of land and encompasses more than 613,140 m<sup>2</sup> of floor space – three times the floor space of Empire State Building and twice that of Chicago's Merchandise Mart. The structure rests on 41,493 concrete piles – the combined length would be 322 km. The complex has been renovated. Since now it is located on a site of more than 400 acres across the Potomac River from Washington D.C., partly on the old Washington airport and about mile south of the Lincoln memorial. The structure became a 5-storey building with a basement and a sub-basement under apart, and the total enclosed floor space was increased to about  $4 \times 10^6$  sq.ft. The employment of a reinforced concrete frame was decided for his huge building. The framework in which storey heights vary from 11 ft. 4½ inches (3.4671 m) to 21 ft. 1½ inches (6.4389 m) was slab and beam type continuous throughout.

### 1.3.2 Damage Scenario

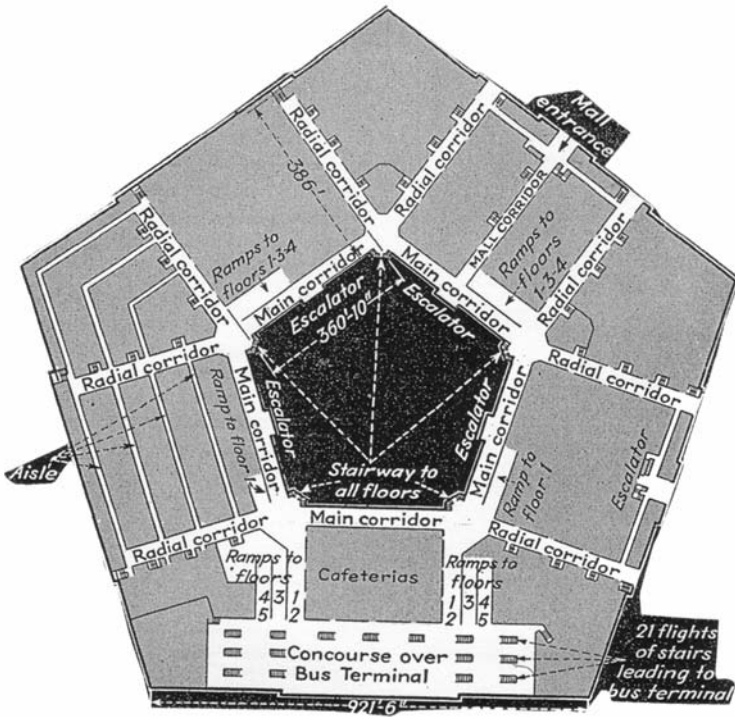
The Pentagon security cameras took some useful shots, which are shown on Plates 1.2 and 1.3. A typical floor is shown in (a) of the Plate 1.2 with aerial photography of the building shown in (b).

At 9:38 A.M. on September 11 an airliner was flown into the first storey of the Pentagon. The impact occurred in the renovated portion of the building approximately 140 ft (46.672 m/s) to the south of the boundary between the renovated section and the next section scheduled to be renovated. A photograph taken by a security camera shows the plane impacting the building at ground level. The aircraft sliced through the building into the section not yet renovated. the impact and the fire initiated by the fuel in the airplane that immediately spread widely in the structure took the lives of all 64 people aboard the aircraft and 125 occupants of the Pentagon.

Plate 1.3(a) shows at 4 s the spread of the fireball. On Plate 1.3(b) presents an exterior view of the extent of the damage from the crash, including a collapsed portion of Ring E at the point of impact, beyond which the impact destruction from the decelerating aircraft continues; the subsequent devastation from the force is also evident. The superior performance of the improved window system incorporated during the renovation is evident on the right. Figure (c) on Plate 1.3 indicates the final damage scenario of the Pentagon Building. Two issues of structural performance commanded attention in this study. First, the collapse that did occur was not immediate; this calls for an examination of the interaction between fire and structural performance. Second, many of the first-storey columns in a portion of the structure that remained standing were destroyed during the crash. Such performance is desirable, and the reasons for it are of interest to the engineering profession.

In general, the first-floor interior columns were severely damaged immediately adjacent to the collapse area on the north side of the expansion joint on column line 11 in Ring E. First-floor columns 11A, 11B and 11C to the North of the expansion joint were missing. Upper columns on the north side of the

**Plate 1.2.** The Pentagon (with compliments of the Pentagon, Washinton, DC, USA)



(a) Plan of the second floor with corridors and aisles. Note: Typical plans of the other floors are similar in the Pentagon



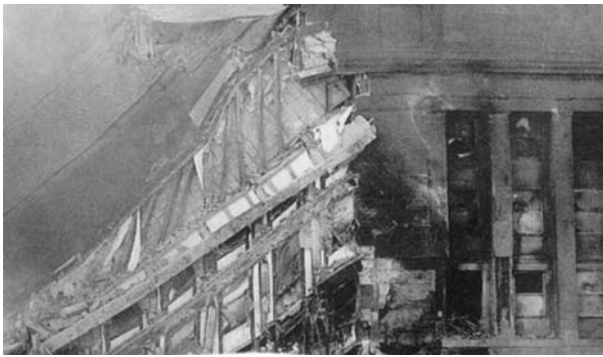
(b) Aerial photograph of the Pentagon showing approaching aircraft

**Plate 1.3.** Fireball, collapse, and damage scenario (with compliments of the Pentagon, Washinton, DC, USA)

---



(a) Fireball and shadow of smoke



(b) Ring E after collapse



(c) Damage scenario

---

**Plate 1.4.** Damage to façade and exterior of the Pentagon building (with compliments of the Pentagon, Washinton, DC, USA)



(a) Façade damage to the south of impact area



(b) Exterior evidence of fire to the north of the impact area



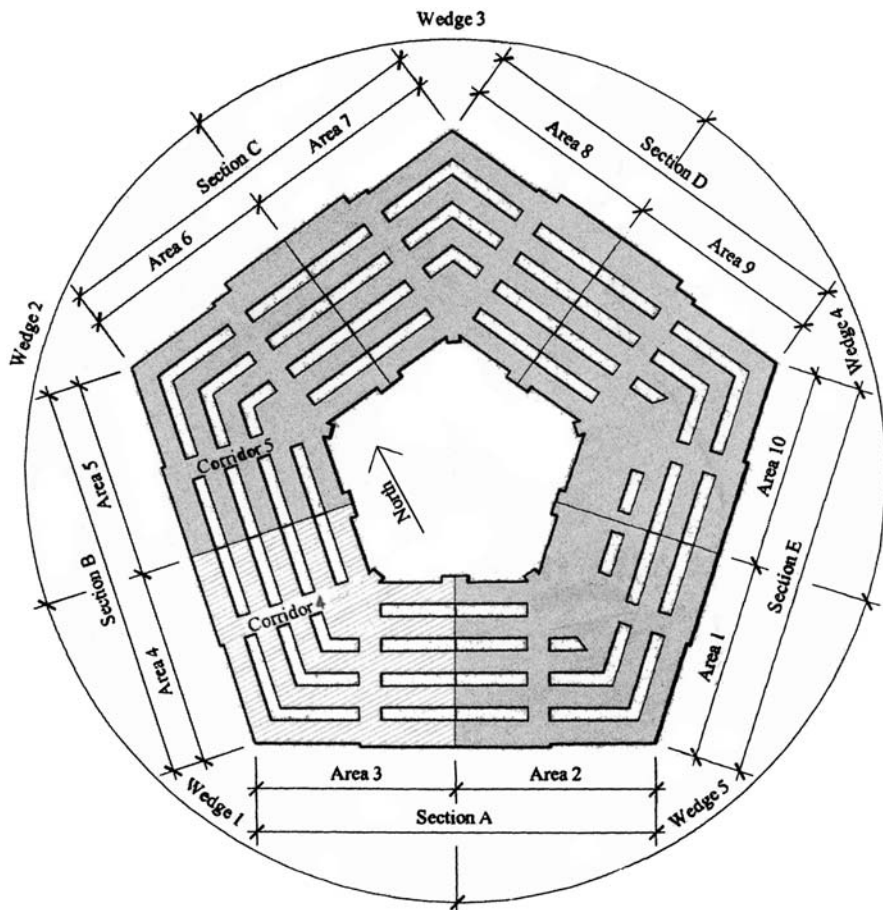
(c) Exterior evidence of fire to the south of the impact area

expansion joint on column line 11 were intact, except for the second-floor columns at 11A and 11B. These columns were severed at the second floor, which was also damaged at this location. To the south, façade panels were also damaged.

The exterior of the building showed clear evidence of the extensive fire that occurred within the building (Plate 1.4(a)). The limestone façade was blackened by smoke for more than 200 ft to the north of the impact point. (Plate 1.4(b)). Evidence of fire damage was less severe to the south and even immediately adjacent to the impact area the façade to the south showed little evidence of fire damage.



**Plate 1.5a.** Pentagon Building structural details (with permission from Pentagon and compliments of ASCE, U.S.A.)



(a) Designation of wedges in the renovation

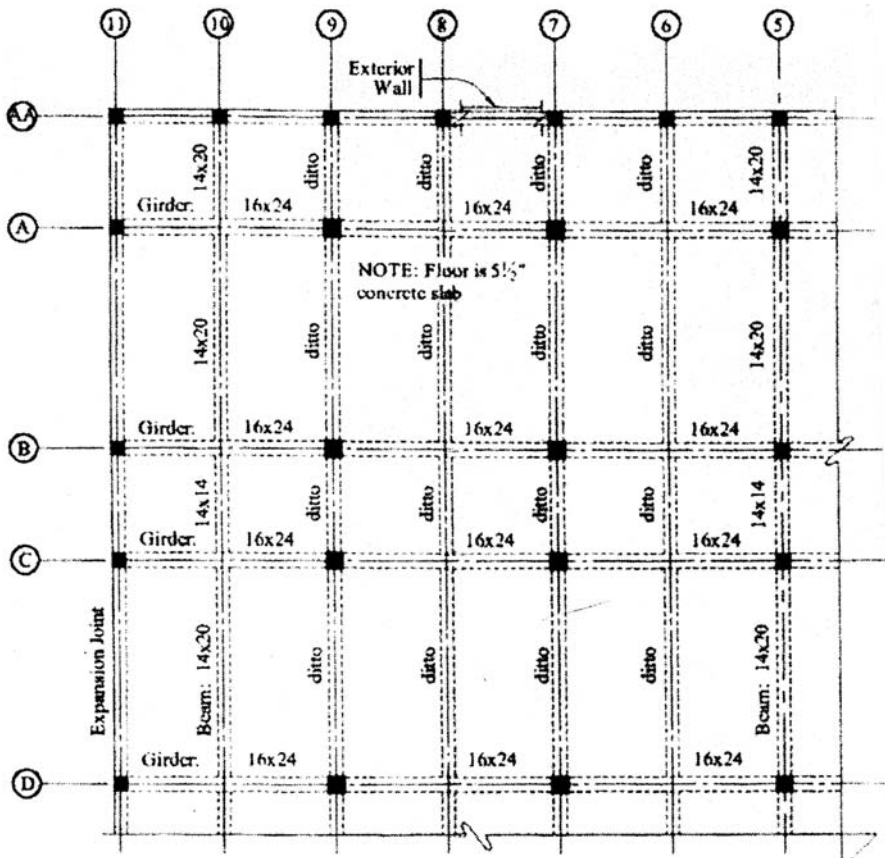
The west façade of the Pentagon was severely scarred by debris impact, particularly to the south of the collapse area. As shown on Plate 1.4(a). In the south of the impact area there is an evidence of fire on the exterior.

### 1.3.3 Aircraft Crash into the Pentagon

#### 1.3.3.1 General Design Description

Plates 1.1. to 1.5a–f show the details of the floor system of the Pentagon Building in the area of interest for this study. Slabs, beams, and girders all

**Plate 1.5b.** Pentagon Building structural details (with permission from Pentagon and compliments of ASCE, U.S.A.)



(b) Floor system

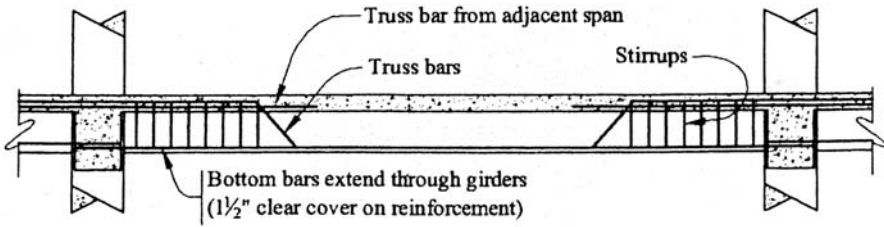
make use of straight and trussed bars. Except for the top reinforcement in the short spans adjacent to longer spans, there are no continuous top bars.

These drawings are taken into consideration in the overall analysis and computer program BANG-F described later on the text.

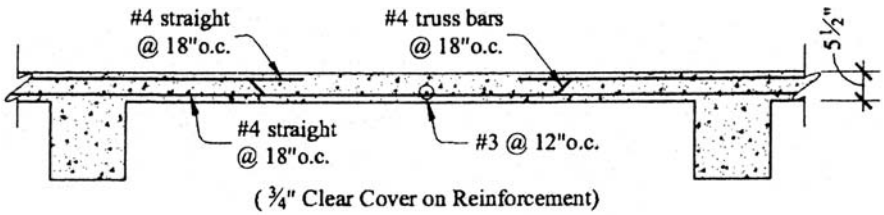
### 1.3.3.2 Aircraft Impact on Pentagon Building

The impacting airplane was a Boeing 757-200 aircraft whose overall dimensions are shown in this text. When the aircraft departed from Washington's Dulles International Airport on the morning of September 11, 2001, it held 64 passengers and crew members. According to the National Transportation

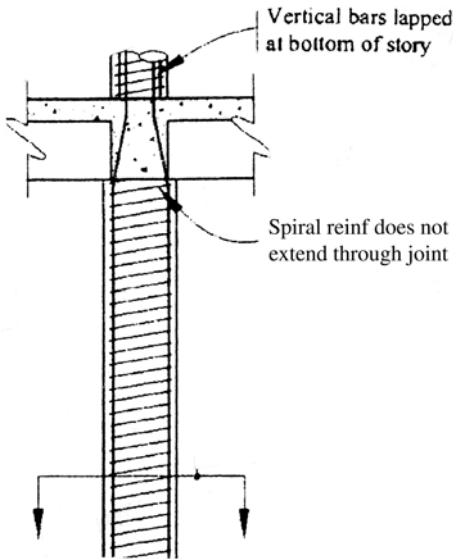
**Plate 1.5c-f.** Pentagon Building structural details (with permission from Pentagon and compliments of ASCE, U.S.A.)



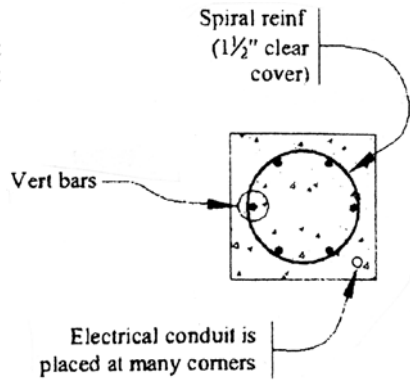
(c)



(d) Typical beam



(e) First-story column



(f) Typical floor slab

Safety Board, the aircraft weighed approximately 181,520 lb (82.34 MN) of which 36,200 lb (16.42 MN) was fuel at the time of impact. It was traveling at 460 knots (780 ft/s or 240 m/s) on a magnetic bearing of  $700^\circ$  ( $1.22$  rad) when it struck the Pentagon.

According to Boeing engineers, much of the aircraft fuel was contained in the wing tanks. The weight in each wing was composed of the following:

Exposed wing structure	13,500 lb	(6.12 MN)
Engine and struts	11,900 lb	(5.40 MN)
Landing gear	3,800 lb	(1.72 MN)
Fuel	14,600 lb	(6.62 MN)
Total	43,800 lb	(19.88 MN)

The balance of the weight was in the fuselage. In the normal course of use the center fuel tank is the last filled and the first used. Thus the weight of the fuselage at the time of impact was  $181,520 - (2 \times 43,800) = 93,920$  lb (42.60 MN). Of this,  $36,200 - (2 \times 14,600) = 7,000$  lb (3.18 MN) was fuel in the center tank. The load-time function for the impact analysis for the Boeing 757-200 aircraft is given later on this text.

The aircraft entered the building at an angle, traveling in a north-easterly direction. With the possible exception of the immediate vicinity of the fuselage's entry point at column line 14, essentially all interior impact damage was inflicted in the first story. The aircraft seems for the most part to have slipped between the first-floor slab on grade and the second floor. The path of damage extended from the west exterior wall of the building in a north-easterly direction completely through Rings E, D, C, and their connecting lower floors. There was a hole in the east wall of Ring C, emerging into AE Drive, between column lines 5 and 7 in Wedge 2 at a point approximately 310 ft (94.5 m) from where the fuselage of the aircraft entered the west wall of the building. The path of the aircraft debris passed approximately 225 ft (68.6 m) diagonally through Wedge 1 and approximately 85 ft (25.9 m) diagonally through a portion of Ring C in Wedge 2 (Plate 1.5a).

Along the path of the movement of aircraft debris through the building, most of the serious structural damage was within a swath that was approximately 75–80 ft (22.9–24.4 m) wide and extended approximately 230 ft (70.1 m) into the first floor of the building. This swath was oriented at approximately  $35$ – $40^\circ$  to the perpendicular to the exterior wall. Within the swath of serious damage was a narrower, tapering area that contained most of the very severe structural damage. This tapering area can be represented approximately by a triangle centered on the trajectory of the aircraft in plan, with a base width at the aircraft entry point of approximately 90 ft (27.4 m) and a length along the aircraft path of approximately 230 ft (70.1 m).

### *Conclusions*

In this text, fuel structure interaction analysis is fully justified: After impact the fuel-interaction with floors combined with air due to ventilation caused

by the debris shall be a responsible factor in the collapse of certain parts of the Pentagon Building structural elements.

Paul F. Mlakar of the U.S. Corps of Engineers of Vicksburg, MS, U.S.A., along with his other colleagues (Journal of Performance of Constructed Facilities, ASCE, August 2005) described the structural damage caused by the terrorist attack on the Pentagon is as follows:

“Even though essentially all the destroyed columns were within this triangular damage area, there were also a few relatively lightly damaged columns interspersed with heavily damaged columns along the path of the aircraft debris through the building. Column 1K, located 200 ft (61 m) from the impact point, was the last severed column along the path of the aircraft. Note that columns on grids E and K are much weaker than the other columns because they support only one floor and a roof.

There were two areas of severe impact damage in the first story. The first area along the path of the aircraft was within approximately 60 ft (18.3 m) of the impact point and corresponds generally to the area that collapsed. In the collapse area and for approximately 20 ft (6.1 m) beyond the collapse area along its northern and eastern edges, columns were removed or very severely damaged by impact. In addition, there was serious second-floor beam and slab damage for 60 ft (6.1 m) to the north of the collapse area, especially along a strip bounded approximately by column lines B and C.

The second area of severe damage was bounded approximately by column lines E, 5, G, and 9. In this region, which was beyond a field of columns that remained standing, several columns were severed and there was significant second-floor beam and slab damage. In both areas, severe slab damage appeared to be caused by moving debris rather than by overpressure from a blast.

Impact damage to the structure above the second-floor slab did not extend more than approximately 50 ft (15.2 m) into the building. This shows that the aircraft slid between the first-floor slab on grade and the second-floor slab for most of its distance of travel after striking the building.

Most likely, the wings of the aircraft were severed as the aircraft penetrated the facade of the building. Even if portions of the wings remained intact after passing through the plane of the facade, the structural damage pattern indicates that the wings were severed before the aircraft penetrated more than a few dozen feet (several meters) into the building. Ultimately, the path of the fuselage debris passed between columns 9C and 11D, which were separated by approximately 28 ft (8.5 m) at a depth of approximately 65 ft (19.8 m) along the aircraft’s path. Columns 9C and 11D were severely distorted but still in place: hence the wings clearly did not survive beyond this point.

At a depth of approximately 160 ft (48.8 m) into the building, columns 3G, 3H, 3J, and 5J were damaged but still standing, although in the direct path of

the fuselage. With a maximum spacing of less than 14 ft (4.3 m) between pairs of these columns in a projection perpendicular to the path of the fuselage, it is highly unlikely that any significant portion of the fuselage could have retained structural integrity at this point in its travel. More likely, the fuselage was destroyed much earlier in its movement through the building. Therefore the aircraft frame most certainly was destroyed before it had traveled a distance that approximately equaled the length of the aircraft.

The debris that traveled the farthest traveled approximately twice the length of the aircraft after entering the building. To come to rest at a point 310 ft (94.5 m) from the area of impact at a speed of 780 ft/s (238 m/s), debris experienced an average deceleration of approximately 30 g.

Several columns exhibited severe bends. However, the predominant evidence suggests that these columns generally did not receive impact from a single, rigid object. Instead, the deformed shapes of these columns are more consistent with loads that were distributed over the height of the columns.

The analyses of the available data reveal that the wings severed exterior columns but were not strong enough to cut through the second-floor slab upon impact. (The fight wing did not enter the building at the point where it struck the second-floor slab in its plane.) The pattern of structural damage throughout the impact zone, together with the deformed shape of columns (smooth, without cusps), suggest that the aircraft disintegrated rapidly as it moved through the forest of columns on the first floor. As the moving debris from the aircraft pushed the contents and demolished exterior wall of the building forward, the debris from the aircraft and building most likely resembled a rapidly moving avalanche through the first floor of the building.”

### **1.3.3.3 Response of Fire Exposure of the Structural Elements of the Pentagon Building**

At 9:38 a.m. on September 11, 2001, a Boeing 757 airliner was flown into the first story of the Pentagon and impacted its west façade. The impacted section, located in Wedge 1, is composed of two reinforced-concrete structural systems separated by an expansion joint. Immediately upon impact, a large fireball engulfed the exterior of the building in the impact area. Interior fires also began immediately. The impact caused the Wedge 1, (Plate 1.5a), Ring E structure to deflect downward along the line of the expansion joint. According to eyewitness accounts, the structure survived the initial aircraft impact, that is, it was able to maintain this deformed shape and did not collapse immediately. However, portions of the structural system south of the expansion joint, directly above where the aircraft impacted (which had the largest unsupported floor area because of loss of first-story columns), eventually collapsed approximately 19 min after the impact and exposure to the ensuing fire.

Within the interior, fire damage in areas that did not collapse generally was similar to that normally resulting from substantial fires in office buildings. Most of the serious structural damage was within a swath that was approximately 75–80 ft (23–24.5 m) wide and extended approximately 230 ft (70 m) into the first floor of the building. Columns and beams along the path of the debris and within the fire area were damaged to varying degrees. Many columns and beams in the impact zone were completely destroyed (broken, disconnected, or with large deformation), whereas others in and adjacent to the impact zone sustained from heavy cracking and spalling to partial loss of concrete cover for reinforcement, with loss of concrete cover being typical for the beams and columns in the impact zone.

Prior to the partial collapse, the fire that was first ignited by the ejected Jet A aviation turbine fuel had transitioned from the growth stage and become a ventilation-controlled “fully developed” or “postflashover” fire. This is evidenced in several photographs by the Pentagon, which was taken prior to the collapse and shows the flames projecting from the windows. In a ventilation-controlled postflashover fire, the flames typically project from windows and openings because there is insufficient air in the burning rooms to allow all the combustible gases to burn inside the rooms.

Estimation of the fire intensity, that is, maximum temperatures and time-temperature characteristics, of postflashover fires is important in understanding the effect of fire on exposed structural elements. However, the accuracy of such estimation depends on a correct estimation of the fire fuel load (hydrocarbon-based building and aircraft contents and Jet A fuel) and the ventilation factor. This cannot be done with a high degree of exactness even in a typical building fire. In the case of the Pentagon attack, it is further complicated by the lack of complete knowledge of the available fuel load (besides the ejected Jet A fuel) and by the unconventional ventilation factor.

In the vicinity of the impact zone, fire damage to columns, beams and slabs was limited to cracking and spalling. The methodology of the estimation of cracking and spalling can be seen in the senior authors’ following book:

*M.Y.H. Bangash: Manual of Numerical Methods in Concrete*  
(Thomas Telford, London 2001) pp. 918

The fire intensity can also be estimated if the fire fuel load ( $\text{MJ}/\text{m}^2$ ), and the ventilation factor,  $F_v$  ( $\text{m}^{1/2}$ ) are known. According to information provided by the National Transportation Safety Board, the aircraft had on board about 5,300 gal (20,200 L) of Jet A fuel, or approximately 36,200 lb (16,000 kg) of fuel based on the density of 6.8 lb/gal ( $0.79 \text{ g}/\text{cm}^3$ ), at the time of impact. Based on images captured by the Pentagon security camera, which showed the aircraft approaching and the subsequent explosion and fireball, it is estimated that about 4,900 lb (2,200 kg) of jet fuel was involved in the prompt fire and was consumed at the time of impact outside the building. This leaves about

30,400 lb (13,800 kg) as the estimated mass,  $M$ , of the Jet A fuel that entered the building and contributed to the fire fuel load within the building.

The net calorific value or heat of combustion – that is, the amount of heat released during complete combustion of a unit mass of fuel,  $\Delta H_c$  – measured for Jet A fuel is 18,916.6 Btu/lb (44 MJ/kg). Thus, the maximum possible energy,  $E$ , that could have been released inside the building by the complete burning of 30,400 lb (13,800 kg) of Jet A fuel is

$$\begin{aligned} E &= M\Delta H_c = 30,400 \times 18,916.6 \\ &= 575,064,488 \text{ Btu (607,200 MJ)} \end{aligned}$$

It is assumed that the fuel was initially contained within the first floor, in a “room” bounded by the path of damage caused by the impact of the airplane. The estimated total surface area,  $A_t$  (floor, ceiling, and bounding walls including windows and openings), of the room is about 36,597 ft<sup>2</sup> (3,400 m<sup>2</sup>). The fire fuel load,  $e_{f,a}$ , contributed by the available Jet A fuel alone can be computed as

$$e_{f,a} = \frac{E}{A_t} = \frac{575,064,488}{36,597} = 15,713 \text{ Btu/ft}^2 \text{ (178 MJ/m}^2\text{)}$$

As indicated, within the first half an hour of the aircraft impact, the fire had become fully developed within some compartments of the Pentagon. This means combustible building and aircraft contents had begun to burn and therefore contributed to the fire fuel load. The exact fire fuel load contributed by the building and aircraft contents,  $e_{f,b}$ , is not known because of insufficient information on the type of occupancy in this particular section of the Pentagon. However, a lower-bound estimate can be made using data recommended by the International Council for Research and Innovation in Building and Construction, or CIB, which lists average fuel loads for different types of occupancy. The lower bound fuel load contributed by the building and the aircraft contents,  $e_{f,b}$ , can be about 200 MJ/m<sup>2</sup> (17611 Btu/ft<sup>2</sup>). The combined total fuel load due to fire,  $e_f$ , is about 378 MJ/m<sup>2</sup> (33,325 Btu/ft<sup>2</sup>).

The ventilation factor  $F_v$  can be equal to

$$\frac{A_v\sqrt{h}}{A_t}$$

where

- $A_v$  = area
- $h$  = height of opening
- = 75% accounted for existing windows
- $A_t$  = area of windows



**Plate 1.6.** Pentagon: Fireball and disaster scenario (with compliment of Pentagon and ASCE, Joournal of Performance of Constructed Facilities, August 2005)



(a) (Color) Fireball within 2s of impact



(b) (Color) Northern portion of impact area before collapse

Hence

$$h = 3.05 \text{ m (10 ft)}$$

$$A_v = 0.75 \times 1098 = 824 \text{ ft}^2 (77 \text{ m}^2)$$

A Pentagon security camera located near the northwest corner of the building recorded the aircraft as it approached and crashed into the building (Plate 1.6a). The photographs taken approximately 1 s apart show the approaching aircraft and the ensuing fireball associated with the initial impact. The series of photographs suggest that the top of the fuselage of the aircraft was approximately 20 ft (6.1 m) above the ground as it approached the building.

A photograph, (Plate 1.6b) taken by the Associated Press before the building to the south of an expansion joint at column line 11 collapsed, provides useful information. This shows that the portion of the building that subsequently collapsed was displaced vertically by approximately 18–24 in. (460–610 mm) relative to the building north of the expansion joint. The façade was missing on the first floor as far north as column line 8. On the second floor the façade was missing between column lines 11 and 15. The photograph also shows that the only column missing on the second floor in the West exterior wall of the building was at column line 14. The spandrel beam for the third floor and all third floor exterior columns appeared to be intact.

### 1.3.3.4 Conclusions

In the Pentagon Building the hot fuel structural elements interaction combined with fire due to ventilation caused the collapse scenario. The structural debris shall be treated as a responsible factor in the collapse of parts of the building. The analytical methodology given in the text justified the hot fuel-structural interaction as the main aspect of the disaster scenario of the Pentagon Building.

## 1.4 Data on Major Explosive Elements. Their Ingredients and Material Properties

### 1.4.1 Introduction

Explosives are capable of exerting sudden pressure on their surroundings as a rapid conversion of the substance into hot gases. Their pressure, which is raised by the generation of heat during explosion, overbalances the restraining pressure of the surroundings. Explosions generate shock waves. Typical terrorist bombs are home made types and tend to be economical and are easy to obtain from readily available fertilizers, liquid and solid fuels. Bomb affected buildings are summarised earlier. Here Tables 1.3 to 1.7 give the summary of data on major explosives and their properties.

Table 1.3. Data on major explosives

Explosive	Composition	$V_{sp}$ (l/kg)	$Q_E$ (kcal/kg)	Temperature at explosion ( $^{\circ}\text{C}$ or $\text{K}$ )	$V_E$ (m/s)	Properties
Abbeite (ammonia dynamites)	Ammonium nitrate (58); nitroglycerine (8); dinitrotoluene (2); sodium chloride (23); wood meal (9).					As a blasting explosive in coal Mining.
AG dynamite	Ammonium nitrate (45); nitroglycerine (45); ammonia gelatine wood flour dynamite (7.5); collodian cotton (2.5).	635	1200	4050	6600	Mining operations, underground quarrying, tunneling in hard rock; submarine work.
Amatol (mixture of TNT and ammonium nitrate)	Ammonium nitrate (80); TNT (20); or ammonium nitrate (50); TNT (50);					As a bursting charge for high explosive shells/bombs.
Ammonal	Ammonium nitrate (65); TNT (15); charcoal (33); aluminium powder (17).					Shell filler; blasting tunneling.
Ammonite	Potassium nitrate (10); ammonium nitrate (77); solid hydrocarbon (1); naphthalene (10); gelatinized nitroglycerine (2).	860 to 915	938 to 1020	2310 to 2600	3500 to 5100	Ammonites are the main explosive used in the USSR.
Belgian permite	Ammonium nitrate (78); TNT (8); calcium silicide (14).					Dark-grey powder set off by service detonators
Black powder	Potassium nitrate (70-75); sulphur (10-14); charcoal (14-16).	260	588	2615	400	Class A (pellet), class B (powder); bombs used in the USA
DD 60/40 (LE)	Picric acid (60); dinitrophenol (40).					Bursting charge for shells used by the French.
Gelignite	Ammonium nitrate (70); nitroglycerine (29.3); nitro cotton (0.7).					Used for blasting.
MDPC (HE)	Picric acid (55); dinitrophenol (35); trinitro-cresol (10).					Bursting charge for shells used by the French.
PETN	PETN (70); TNT (30).	780	1410	4010	8200	High explosive charge for sea mines, drop bombs and torpedoes.
Wetter-astralit	Gelatinized nitroglycerine (12); ammonium nitrate (57); wood meal (2); coal powder (2); sodium chloride (27).					A German explosive used in many countries.

$V_{sp}$  = specific volume for explosive gases;  $Q_E$  = specific heat of explosion;  $V_E$  = velocity at explosion.

Table 1.4. Data on major explosives elements

Explosive element	Composition	Density (kg/m <sup>3</sup> )	V <sub>sp</sub> (l/kg)	Q <sub>E</sub> (kcal/kg)	Temperature at explosion (°C or K)	V <sub>E</sub> (m/s)	3kg load dropped at which explosions occurred	Impact sensitivity (mm)
Ammonium nitrate	NH <sub>4</sub> NO <sub>3</sub>	1600		1090				
Charcoal	Black powder or lump coal (95%) and ash (5%)	1600	—	—	—	—	—	—
Dinitroglycol	(CH <sub>2</sub> ) <sub>2</sub> (NO <sub>3</sub> ) <sub>3</sub>	1400	738	1690	4230	8300	104	
Dinitrophenol	C <sub>6</sub> H <sub>3</sub> OH(NO <sub>2</sub> ) <sub>2</sub>	1400	—	—	—	—	—	
Gun cotton	Cellulose nitrate (high nitration)	300	936	810	2640	6300	270	
Hexogen	—	1700	908	1500	3850	8300	435	
Nitroglycerine	C <sub>3</sub> H <sub>5</sub> (NO <sub>3</sub> ) <sub>3</sub>	1600	717	1470	4110	8000	60	
PETN	C(CH <sub>2</sub> ONO <sub>2</sub> ) <sub>4</sub>	1750	—	—	See table A4.3	—	420	
Picric acid	—	900	685	920	3620	7250	900	
Potassium nitrate	KNO <sub>3</sub>	—	—	—	—	—	—	
Sodium nitrate	NaNO <sub>3</sub>	—	—	—	—	—	—	
Trinitroresol	C <sub>6</sub> HCH <sub>3</sub> (OH)(NO <sub>2</sub> ) <sub>3</sub> CH <sub>3</sub>	—	—	—	—	—	—	
Trinitrotoluene (TNT)	C <sub>6</sub> H <sub>2</sub> (CH <sub>3</sub> )(NO <sub>2</sub> ) <sub>3</sub>	1600	728	1000	2950	6800	2200	

Table 1.5. Non-aluminized explosive mixtures

Name	Apparent formula	Composition	(g/mol)	Density (g/cm <sup>3</sup> )	Explosive strength (% TNT)	Gurney constant (m/s)
Amatol	C <sub>0.62</sub> H <sub>4.44</sub> N <sub>2.26</sub> O <sub>3.53</sub>	80/20 Ammonium nitrate/TNT	100	1.60	143b, 130m,123t	2908
Anfo	C <sub>0.365</sub> H <sub>4.713</sub> N <sub>2.000</sub> O <sub>3.000</sub>	96/6 Ammonium nitrate/ No.2 diesel oil	85	1.63	142b	2763
Black powder	C <sub>1.25</sub> K <sub>1.92</sub> N <sub>5.36</sub> O <sub>14.4</sub> S <sub>0.31</sub>	75/17/10 Potassium nitrate/ carbon/sulphur			17s, 50m, 10t	
Comp A-3	C <sub>1.87</sub> H <sub>3.74</sub> N <sub>2.46</sub> O <sub>2.46</sub>	91/9 RDX/WAX	100	1.65	157b, 135m, 126p, 109a	2727
Comp B-3	C <sub>6.854</sub> H <sub>8.740</sub> N <sub>7.650</sub> O <sub>9.300</sub>	64/36 RDX/TNT	347	1.713	133m, 130t, 132p, 149b	2843
Comp C-4	C <sub>4.82</sub> H <sub>3.54</sub> N <sub>2.46</sub> O <sub>2.54</sub>	91/5.3/2.1/1.6 RDX/ di-(2-ethylhexyl) sebacate/ polyisobutyl/motor oil	100	1.66	160b, 130m, 115p	2801
Cyclotol	C <sub>5.045</sub> H <sub>7.464</sub> N <sub>6.876</sub> O <sub>7.753</sub>	77/23 RDX/TNT	288	1.743	159b, 112u, 133p	2979
Dynamite (MVD)	–	75/15/10RDX/TNT/plasticizers	–	–	105s, 122m	–
LX-14	C <sub>4.51</sub> H <sub>2.92</sub> N <sub>2.59</sub> O <sub>2.66</sub>	95.5/4.5 HMX/estane 5702-F1	100	1.83	167b	3033
Octol	C <sub>2.332</sub> H <sub>2.366</sub> N <sub>1.293</sub> O <sub>3.2155</sub>	76.3/23.7 HMX/TNT	388	1.809	115m, 158b, 160p	2965
PBX-9011	C <sub>5.696</sub> H <sub>10.476</sub> N <sub>8.062</sub> O <sub>8.589</sub>	90/10 HMX/estane	329	1.767	153b, 140p	2815
PBXC-116	C <sub>1.968</sub> H <sub>10.476</sub> N <sub>2.356</sub> O <sub>2.474</sub>	86/14 RDX/binder	100	1.65	117b	2970
Pentolite	C <sub>2.332</sub> H <sub>2.366</sub> N <sub>1.293</sub> O <sub>3.215</sub>	50/50 TNT/PETN	100	1.65	126m, 122t, 156b, 116a, 108p	–
Smokeless powder	C <sub>6</sub> H <sub>7</sub> N <sub>2.5</sub> O <sub>10</sub>	99/1Nitrocellulose/diphenylamine	275	–	93s	–

Table 1.6. Ingredients of explosives and their properties

Formula	Name	(g/mol)	Density (g/cm <sup>3</sup> )	Explosive strength (% TNT)	Gurney constant (m/s)
C <sub>6</sub> H <sub>6</sub> N <sub>4</sub> O <sub>7</sub>	Ammonium picrate (explosive D)	246	1.72	100t, 99m, 84s, 87b, 91p, 85a	2137
(C <sub>6</sub> H <sub>7</sub> N <sub>2.25</sub> O <sub>9.5</sub> ) <sub>n</sub>	Nitrocellulose 12% N (NC)	263(n)	—	82b	2189
(C <sub>6</sub> H <sub>7</sub> N <sub>2.5</sub> O <sub>10</sub> ) <sub>n</sub>	Nitrocellulose 13.35% N (NC)	274(n)	1.67	102b, 140t	2473
(C <sub>6</sub> H <sub>7</sub> N <sub>3</sub> O <sub>11</sub> ) <sub>n</sub>	Cellulose trinitrate 14.1% N (NC)	297(n)	1.66	95s, 138b	2966
C <sub>6</sub> H <sub>8</sub> N <sub>2</sub> O <sub>6</sub>	2,2-Dinitropropylacrylate (DNPA)	204	1.47	50b	1478
(C <sub>6</sub> H <sub>8</sub> N <sub>6</sub> O <sub>9</sub> ) <sub>n</sub>	Cellulose dinitrate 11.1% N (NC)	252(n)	1.66	87b	2170
C <sub>6</sub> H <sub>8</sub> N <sub>6</sub> O <sub>18</sub>	Mannitol hexanitrate	452	1.73	170t, 156b	3451
(C <sub>6</sub> H <sub>9</sub> N <sub>3</sub> O <sub>11</sub> )	Glycerol monolactate trinitrate (GLTN)	299	1.47	115m, 148b	2952
C <sub>7</sub> H <sub>5</sub> N <sub>5</sub> O <sub>7</sub>	2,4,6-Trinitrobenzaldehyde	241	—	125t, 94b	2307
C <sub>7</sub> H <sub>5</sub> N <sub>3</sub> O <sub>6</sub>	2,4,6-Trinitrotoluene (TNT)	227	1.65	100t, 100m, 100s, 100b	2315
C <sub>7</sub> H <sub>5</sub> N <sub>3</sub> O <sub>6</sub>	2,4,6-Trinitrotoluene (liquid TNT)	227	1.447	103b	2356
C <sub>7</sub> H <sub>5</sub> N <sub>3</sub> O <sub>7</sub>	2,4,6-Trinitroanisole	243	1.41	112t, 93b	2202
C <sub>7</sub> H <sub>5</sub> N <sub>3</sub> O <sub>7</sub>	2,4,6-Trinitro- <i>m</i>	243	1.68	98t, 87b	2131
C <sub>7</sub> H <sub>5</sub> N <sub>3</sub> O <sub>8</sub>	<i>N</i> -Methyl- <i>N</i> , 2, 4, 6-tetraaminoiline (TETRYL) <i>o</i> -cresol	287	1.73	131t, 131m, 123s, 130b, 116p	2710
C <sub>10</sub> H <sub>16</sub> N <sub>5</sub> O <sub>19</sub>	Dipentaerythritolhexanitrate (DPEHN)	524	1.63	128t, 142m, 123s, 182b	3268
C <sub>12</sub> H <sub>4</sub> N <sub>6</sub> O <sub>12</sub>	2,2', 4,4', 6,6' Hexanitrobiphenyl (MNBP)	424	1.74	114b, 116t	2588
C <sub>12</sub> H <sub>4</sub> N <sub>8</sub> O <sub>8</sub>	1,3,8,10 Tetraamino-1,2,4-benzotriazole (T-TACOT)	388	1.81	108b	2655
C <sub>12</sub> H <sub>4</sub> N <sub>8</sub> O <sub>8</sub>	1,3,7,9 Tetraamino-1,2,4-benzotriazole (Z-TACOT)	388	1.85	108b	2656
C <sub>12</sub> H <sub>4</sub> N <sub>8</sub> O <sub>8</sub>	5,7-Dinitro-1-picrylbenzotriazole (BTX)	420	1.74	110b	2611
C <sub>12</sub> H <sub>4</sub> N <sub>8</sub> O <sub>12</sub>	2,2', 4,4', 6,6' Hexanitroazobenzene (HNAB)	452	1.78	122b	2693
C <sub>12</sub> H <sub>6</sub> N <sub>8</sub> O <sub>2</sub>	Diaminohexanitrobiphenyl (dipicramide)/(DIPAM)	454	1.79	105b	2431
C <sub>13</sub> H <sub>2</sub> N <sub>5</sub> O <sub>14</sub>	2,2', 4,4', 6-Pentanitrobenzophenone (PENCO)	407	1.86	92b	2352
C <sub>14</sub> H <sub>6</sub> N <sub>6</sub> O <sub>12</sub>	2,2', 4,4', 6,6' Hexanitrostilbene (HNS)	450	1.74	108b	2524
C <sub>17</sub> H <sub>6</sub> N <sub>13</sub> O <sub>16</sub>	2,6-Bis (picrylazo)-3,5-dinitro-pyridine (PADP)	647	1.86	122b	2738
C <sub>18</sub> H <sub>2</sub> N <sub>9</sub> O <sub>18</sub>	2,2', 2'', 4,4', 4'', 6,6', 6'' Nonanitroterphenyl (NONA)	635	1.78	113b	2608
C <sub>18</sub> H <sub>6</sub> N <sub>8</sub> O <sub>16</sub>	2,2', 2'', 4,4', 4'', 6,6', 6'' Octanitroterphenyl (ONT)	590	1.80	106b	2537
C <sub>18</sub> H <sub>7</sub> N <sub>11</sub> O <sub>18</sub>	1,3-Bis (picrylamino) 2,4,6-trinitrobenzene	665	1.79	101b	2427
C <sub>21</sub> H <sub>6</sub> N <sub>15</sub> O <sub>18</sub>	2,4,6-Tris (picrylamino), <i>r</i> -triazine	759	1.75	86b	2261
C <sub>22</sub> H <sub>6</sub> N <sub>15</sub> O <sub>20</sub>	2,4,6-Tris (picrylamino) <i>s</i> -nitropyrimidine	803	1.88	82b	2210
C <sub>23</sub> H <sub>6</sub> N <sub>15</sub> O <sub>22</sub>	2,4,6-Tris (picrylamino) 3,5-dinitropyrimidine	847	1.80	98b	2400
C <sub>24</sub> H <sub>6</sub> N <sub>12</sub> O <sub>24</sub>	2,2', 2'', 2''', 4,4', 4'', 6,6', 6''', 6'''' dodecanitro- <i>m</i> '-quaterphenyl	846	1.81	114b	2625
C <sub>24</sub> H <sub>6</sub> N <sub>14</sub> O <sub>24</sub>	Azobis (2,2', 4,4', 4'', 6,6', 6'' hexanitrobiphenyl) (AHH)	874	1.78	120b	2699
C <sub>24</sub> H <sub>6</sub> N <sub>16</sub> O <sub>24</sub>	Dodecanitro-3,3-bis (phenylazo)-biphenyl (BisHNAB)	902	1.81	127b	2785
C <sub>24</sub> H <sub>6</sub> N <sub>9</sub> O <sub>18</sub>	1,3,5-Triperylbenzene (TPB)	711	1.67	81b	2242
NO	Nitric oxide	30	1.30	69b	2212

**Table 1.7.** Explosive and crater formation data

Type of soil/rock	Type of explosives	Charge data				Crater data			
		Weight (kg)	Length (m)	Diameter (m)	Radius (m)	Depth (m)	Angle (degrees)	Volume (m <sup>3</sup> )	
Sandstone	<i>Type A</i> Semi-gelatine	3.632	0.22	0.132	1.25	0.400	134	0.454	
		3.632	0.25	0.132	2.44	0.700	148	4.26	
		3.632	0.30	0.132			no crater		
	<i>Type A</i> Gelatine	3.632	0.18	0.132	1.83	0.850	132	341	
		3.632	0.2	0.132			no crater		
		3.632	0.12	0.132	0.750	0.310	130	0.176	
	Ammonia-gelatine	3.632	0.152	0.132	1.83	0.920	130	330	
		3.632	0.152	0.132			no crater		
		3.632	0.23	0.132	1.02	0.310	142	0.937	
	Ammonia-dynamite	3.632	0.23	0.132	1.0	1.700	124	0.5	
	Granite	<i>Type A</i> Semi-gelatine	2.80	0.25	0.10	1.25	0.310	150	0.46
			2.80	0.25	0.10	1.83	0.310	158	0.937
			2.80	0.3048	0.10	0.75	0.1524	154	0.08
<i>Type B</i> Semi-gelatine		14.50	0.62	0.1524	1.83	0.457	105	1.306	
		1.48	0.25	0.16	0.10	1.230	152	2.90	
		4.355	0.60	0.10	1.20	0.620	152	0.90	
<i>Type B</i> Gelatine		14.50	0.62	0.1524	3.0	0.62	154	3.55	
		8.62	0.47	0.128	3.20	0.40	164	5.26	
Marlstone		<i>Type A</i> Semi-gelatine	1.544	0.308	0.10	1.0	0.308	138	0.44
			1.544	0.308	0.10	1.80	0.62	118	1.58
			1.544	0.308	0.10	0.16	0.150	112	0.0044
			3.620	1.37	0.13	1.82	1.37	108	5.210
			6.130	0.32	0.13	1.82	1.22	114	5.210
Chalk		<i>Type A</i> Semi-gelatine	0.908	0.22	0.08	1.01	0.4	138	0.510
	0.908		0.20	0.08	1.24	0.77	114	2.08	
	2.040		0.22	0.13	2.10	1.524	106	7.39	
	3.632		0.20	0.152	3.45	1.53	112	11.36	
	Ammonia-gelatine	3.632	0.125	0.152	1.70	0.9	130	2.70	
		3.632	0.10	0.152	1.70	1.02	118	7.73	
		3.632	0.152	0.152	2.10	1.52	106	8.86	
		3.632	0.13	0.152			no crater		

**Table 1.7.** Continued

Charge depth (m)					Particle (a) or flyrock (b) velocity (m/s)					Additional data and velocity $V_E$ of detonation (m/s) of explosive	
0.1	0.2	0.3	0.4	0.5	0.6	0.9	1.5				Density = 1153.44 kg/m <sup>3</sup> $V_E$ = 3657.6
	b	b			b	b	b				
	60.0	60.0			30.5	15.0	2.0				
							1.5				
							b				
							2.0				
					0.6						Depth 3.05 m and greater Density = 1361.7 kg/m <sup>3</sup> $V_E$ = 6095.7
					b						
					30.5						
							1.5				Just broke surface
							b				
							2.0				
				0.5							Density = 1410 kg/m <sup>3</sup> $V_E$ = 2591
				b							
				25.0							
						0.9					
						b					
						29.0					
	0.2										Depth 3.15 m and greater $V_E$ = 1981 Density = 1121.4 kg/m <sup>3</sup>
	b										
	90.0										
		0.3									
		b									
		75.0									
		0.3									
							0.9				
											Charge depth 2 m
					0.6						
							1.5				
0.1	0.2	0.3	0.4	0.5	0.6	0.7	0.9	1.5	3.0		Charge depth 2 m Density = 1153.44 kg/m <sup>3</sup> $V_E$ = 3657.6
b											
60.0											
								1.5			
									3.0		
								1.5			
								1.5			
											Density = 1121.44 kg/m <sup>3</sup> $V_E$ = 1981
			0.4					1.5			
								1.5			
0.1	0.2	0.3	0.4	0.5	0.6	0.7	0.9	1.5	3.0		Density = 1153.44 kg/m <sup>3</sup> $V_E$ = 3657.6
					0.6						
								1.5			
									3.0		



## 1.5 Explosion Caused by Impact-cum-Fire

### 1.5.1 Introduction

Fire is the primary cause of loss of life and property throughout the world. During the past two decades fire has damaged hundreds of thousands of structures. Significant advances have been made in controlling or mitigating the effects of fire. Various methods have been developed to protect buildings. New materials have been developed or invented. A considerable time is spent by various researchers on the development of mathematical models to simulate the behaviour of structural members in fire. This is possible only if one uses numerical and computer techniques. A large number of computer programmes that calculate the fire resistance of structural members now exist. The input data for these computer programmes require, apart from loading and fire density, thermal and mechanical properties of various building materials at elevated temperatures. In addition, the expected severity of building fires and temperature-time relations has also been developed. Most of these properties have been codified. The closet measures related to building design are probably those for the confinement of fire. These measures include fire barriers capable of delaying or preventing spread of fire, dimension and locations of buildings. All these measures are directly related to the detailed knowledge of the mechanics and severity of fire. It is, therefore, essential to outline some areas outside the domain of a structural engineer, which he or she should be aware of. Some of these are described below:

- Mechanics of fluids and building aerodynamics applicable to fire engineering.
- Conduction of heat in solids.
- Convection and radiation heat transfer.
- Thermochemistry
- Chemical equilibrium and thermal decomposition.
- Fire dynamics.
  - Flame height and fire plumes.
  - Air entrainment into buoyant jet flames.
  - Ceiling jet flows, vent flows and natural convection wall flows.
  - Combustion conditions, and smouldering combustion.
  - Flammability limits and flaming ignition of solids
  - Smoke production, smoke and heat venting.
- Burning rates and calorimetry
- Compartment fire modelling and fire models for enclosures.
- Stochastic models for fire growth
- Explosion protection.
- Detection systems, automatic sprinkler systems.
- Foam system and foam agents.

Within the non-structural analysis, structural analysts must be aware of hazard calculations, risk analysis and probability methods.

**Table 1.8.** Calorific values of typical materials (Source: Eckert ERG and Drake RM (1972) Analysis of Heat and Mass Transfer, McGraw-Hill, New York. Reprinted by permission of McGraw-Hill, Inc.)

Metal	Thermal conductivity k, W/m × °C													
	$\rho$ , kg/m <sup>3</sup>	$c_p$ , KJ/kg × °C	k, W/m × °C	$\alpha$ , m <sup>2</sup> /s × 10 <sup>5</sup>	-100°C	0°C	100°C	200°C	300°C	400°C	600°C	800°C	1000°C	1200°C
Aluminium pure	2707	0.896	204	8.418	215	202	206	215	228	249				
Lead	11373	0.130	35	2.343	36.9	35.1	33.4	31.5	29.8					
Iron:														
Pure	7897	0.452	73	2.034	87	73	67	62	55	48	40	36	35	36
Wrought iron														
0.5% C	7849	0.46	59	1.626		59	57	52	48	45	36	33	33	33
Steel														
(C max ≈ 1.5%):														
Carbon steel														
C ≈ 0.5%	7833	0.465	54	1.474		55	52	48	45	42	35	31	29	31
1.0%	7801	0.473	43	1.172		43	43	42	40	36	33	29	28	29
1.5%	7753	0.486	36	0.970		36	36	36	35	33	31	28	28	29
Copper:														
Pure	8954	0.3831	386	11.234	407	386	379	374	369	363	353			
Aluminium bronze														
95% Cu, 5% Al	8666	0.410	83	2.330										
Molybdenum	10220	0.251	123	4.790	138	125	118	114	111	109	106	102	99	92
Nickel:														
Pure (99.9%)	8906	0.4459	90	2.266	104	93	83	73	64	59				
Ni-Cr 90% Ni,														
10% Cr	8666	0.444	17	0.444		17.1	18.9	20.9	22.8	24.9				
Silver:														
Purest	10524	0.2340	419	17.004	419	417	415	412						
Pure (99.9%)	10524	0.2340	407	16.563	419	410	415	374	362	360				
Tin, pure	7304	0.2256	64	3.884	74	65.9	59	57						
Tungsten	19350	0.1344	163	6.271		166	151	142	133	126	112	76		
Zinc, pure	7144	0.3843	112.2	4.106	114	112	109	106	100	93				

**Table 1.9.** Recommended values for characteristic live load densities in various occupancy types (Source: Holman JP (1966) Heat Transfer, McGraw-Hill, New York. Reprinted by permission of McGraw-Hill, Inc.)

Substance	Temperature °C	k, W/m × °C	ρ, kg/m <sup>3</sup>	C, kJ/kg × °C	α, m <sup>2</sup> /s × 10 <sup>7</sup>
Insulating material					
Asbestos					
Loosely packed	-45	0.149			
	0	0.154	470-570	0.816	3.3-4
	100	0.161			
Asbestos-cement boards	20	0.74			
Sheets	51	0.166			
Balsam wool, 2.2lb/ft <sup>3</sup>	32	0.04	35		
Cardboard, corrugated	...	0.064			
Celotex	32	0.048			
Corkboard, 10lb/ft <sup>3</sup>	30	0.043	160		
Cork, regranulated	32	0.045	45-120	1.88	2-5.3
Ground	32	0.043	150		
Fiber, insulating board	20	0.048	240		
Glass wool, 1.5lb/ft <sup>3</sup>	23	0.038	24	0.7	22.6
Structural and heat-resistant material					
Asphalt	20-55	0.74-0.76			
Brick:					
Building brick, common	20	0.69	1600	0.84	5.2
Face		1.32	2000		
Carborundum brick	600	18.5			
	1400	11.1			
Chrom brick	200	2.32	3000	0.84	9.2
	550	2.47			9.8
	900	1.99			7.9
Diatomaceous earth, moulded and fired	200	0.24			
	870	0.31			
Fireclay brick	500	1.04	2000	0.96	5.4
burnt 2426°F	800	1.07			
	1100	1.09			
Insulating material					
Fireclay brick, burnt 2642°F	500	1.28	2300	0.96	5.8
	800	1.37			
Cement, Portland		0.29	1500		
Mortar	23	1.16			
Concrete, cinder	23	0.76			
Stone, 1-2-4 mix	20	1.37	1900-2300	0.88	8.2-6.8
Glas, window	20	0.78 (avg)	2700	0.84	3.4
Corosilicate	30-75	1.09	2200		
Plaster, gypsum	20	0.48	1440	0.84	4.0
Metal lath	20	0.47			
Wood lath	20	0.28			
Stone					
Granite		1.73-3.98	2640	0.82	8-18
Limestone	100-300	1.26-1.33	2500	0.90	5.6-5.9
Marble		2.07-2.94	2500-2700	0.80	10-13.6
Sandstone	40	1.83	2160-2300	0.71	11.2-11.9
Wood (across the grain):					
Balsa 8.8lb/ft <sup>3</sup>	30	0.055	140		
Cypress	30	0.097	460		
Fir	23	0.11	420	2.72	0.96
Maple or oak	30	0.166	540	2.4	1.28
Yellow pine	23	0.147	640	2.8	0.82
White pine	30	0.112	430		

The main concern of the structural engineer is the properties of the various materials involved and the analytical tools available for the design of structural elements in fire. They are given later on in this text under various sections.

No matter how many precautions are taken to improve the fire safety design of buildings, they will not be complete without sufficient availability of training in professional education and practice. The main objective is to prepare sufficient manuals of awareness and to transfer knowledge of fire safety of buildings to the building design practitioners by way of courses and seminars at various institutions. Architects and engineers must place importance on fire safety provisions and allow funds for training facilities.

The explosion can be generated due to earthquakes and aeroplane/missile impact. For example, aircraft full of fuel can accidentally impact vital building installations and can cause fire-cum-explosion. A typical example was the World Trade Center (WTC) in New York when the aircraft hit the WTC buildings and fuel around to 1000°C poured in the building creating explosion and fire. The shear temperature (+700°C can melt the steel section and can produce magma) and loosening of members and joints due to impact load produced by aircraft crashes, resulted the collapse of WTC Towers. Loading member restraints and calorific values of typical materials involved are vital information for the assessment and re-evaluation and retrofitting of the elements of buildings. A reference is made to Appendix A.I for the aircraft/missile data and a separate section in this text on the fire analysis.

It is necessary to present various calorific values of materials. The recommended values for the characteristic fire load densities in various occupancy types. Tables 1.8 and 1.9 give the summary of the findings.

## **1.5.2 Guide to High-Rise Fire Fighting Caused by Explosion**

### **1.5.2.1 Introduction**

The purpose is to provide a complete functional command organisation designed to allow for single or multi-agency use. It shows how to combine command strategy with organisational procedures and should be designed to be used primarily for high rise fire incidents.

The key elements of the system are:

- The systematic development of a complete, functional organisation with the major functions being Command, Operations, Planning, Logistics and Finance/Administration.
- Designed to allow for multi-agency adoption in federal, state, provinces and local fire agencies. Therefore, organisational terminology used in the Incident Management System is designed to be acceptable at all levels of government.
- Designed to be the basic operating system for all high-rise incidents within each agency.

- The organisation builds from the ground up, with the management of all major functions initially being the responsibility of one or just a few persons. Functional units are designed to handle the most important incident activities.
- Designed on the premise that the jurisdictional authority of the involved agencies will not be compromised. Each agency having legal responsibility within its jurisdiction is assumed to have full command authority within its jurisdiction at all times.
- Multi-jurisdictional incidents will normally be managed under a Unified Command management structure involving a single incident command post and a single incident action plan.
- The system is intended to be staffed and operated by qualified personnel from any agency.
- The system expands and contracts organisationally based upon the needs of the incident. Span-of-control recommendations are followed closely.

### 1.5.2.2 Strategy and Tactics

Extinguishing high-rise fires requires aggressive fire fighters advancing 45 mm to 65 mm hand lines. The high-rise fires are labour intensive and provide many obstacles to rapid-fire extinguishment. Hence strategic and tactical considerations for high-rise building fires must be proactive. Because of the operational problems involved to control a vertically extending fire, containment on the floor of origin must be the main objective.

Empirical evidence reveals that flashover can occur at 10 minutes, and the loss of elevators typically occurs approximately 20 minutes into the operation. The cause of elevator failure is run-off water from hose lines entering the elevator shafts and shorting out electrical contacts. Water usage at serious high-rise fires will result in elevator loss more than 90% of the time.

If possible, enough resources to handle the incident should be in place at the 20-minute mark. Serious high-rise fires require a minimum of three handlines. When necessary, this allows parallel lines on the fire floor and a line on the floor above to cover extension.

Fire environment, fire floor location, building construction, and unreliable water supply dramatically increase operational problems in high-rise buildings. The fire environment is severely affected by:

- Slab construction
- Heavy, sealed windows
- Intense heat and smoke
- Limited means of ventilation

Water delivery must be maximized to attain the most effective cooling action. The height of the fire area requires the fire service to rely on an unreliable means of transportation during firefighting operations. We are at the mercy of elevators and the probability that they will not operate properly during

fire operations. The task of multi-floor ascent via stairwells will slow down operations considerably.

### *Operating Guidelines*

The following suggested basic strategic operating guidelines for the high-rise buildings:

- Locate a fire
- Simultaneously, or as soon as possible, begin the process of controlling evacuation.
- Gain control of the building systems
- Elevators, HVAC systems, communications equipment, fire pumps
- Confine and extinguish the fire. Experience indicates any serious fire will require a large commitment of personnel and a need for frequent relief of personnel. Judicious placement of hose streams will facilitate the confinement and extinguishing phase.
- Operate a large-calibre water appliance into the fire area from the stairwell on the fire floor.
- Open the floor below or ceiling above the fire floor, and direct water into the fire area.
- Flood the floor above the fire with hoselines operating from the stairwell. This procedure will not be effective on hidden fire.
- Deploy lines on the floor above the fire to control extension. The number of personnel and hoselines needed to accomplish this will vary depending on the size of the building and the severity of the fire conditions.

### *Engine Company Operations*

The many variables and complexities built into high-rise buildings may be compounded by both the fire location and the fire load within the tenant space on the floor. Pairing of engine companies should be considered. Companies operating in tandem will facilitate hose stretching and relief for personnel operating hoselines. Many fires will be within easy reach of hose streams operated in the immediate stairway enclosure area. Other fires may require extending hoselines, using rolled up lengths, and personnel from more than one company to advance the first hose line. The initial commitment of engine companies in two remote standpipe-equipped stairwells will allow the following:

- An engine company in the best position to commence aggressive fire attack.
- Two handlines may be operated in tandem.
- Increased stream coverage on fire floor.
- Fire may be prevented from wrapping around the core.
- Maintains the integrity of both stairwells to protect companies operating above the fire.

- Firefighters to assist occupants if the fire stairwell is an evacuation stair, and ensure that the stairwell door remains closed.
- Increased fire attack options and flanking movements are made possible.
- Standby line to be available to attack fire extension on the floor above.
- Operating lines must never oppose each other.

### *Ladder Company Operations*

Ladder companies are normally assigned to the following responsibilities at a high-rise fire:

- Determine the life hazard on the fire floor, and initiate evacuation procedures where required.
- Conduct a primary search of the fire floor.
- Provide support to the advancing engine company by:
  1. Removing obstructions
  2. Forcing entry.
  3. Opening ceiling to expose plenum.
    - Determine the number of stairways serving the fire floor and the floor above.
    - Proceed to the floor above the fire via a stairway other than the attack stairway.
    - Determine which is the best stairway to be used by the occupants for evacuation and advise IC/ Operations.
    - Examine the floor above the fire, and report to the IC/ Operations the following:
      - a) The heat and smoke conditions.
      - b) The status of the evacuation.
      - c) Any extension of the fire.
      - d) Presence of stairs – down to fire floor or upward to floor above.
        - Examine all floors for occupants and smoke conditions.

### **1.5.3 Aggressor: Threats and Tactics**

Aggressors are those who carry out hostile acts against personnel and assets and steal vehicles, arms, ammunition, explosives, money etc. They can be criminals, protesters, terrorists and subversives. Their main object is to inflict death and injury, destroy or damage facilities, steal equipment, material and information and finally create adverse publicity. Hence, the models and tactics of aggressors have to be translated into the design of structures, particularly buildings, and their important structural components.

#### *Classification: Modes and Tactics*

The offensive strategies used by aggressors reflect the function of each group. The designers consider these strategies when selecting the modes and tactics

of aggression that form the ‘design basic threat’. Tables 1.10 to 1.12 give a complete picture of the modes and tactics. The flow charts given in Figs. 1.16 to 1.18 form the basis of these tables.

**Table 1.10.** Modes and tactics of aggressors

- 
- *Vehicle mode: vehicle laden with explosives*
  - Cars, trucks, vans – moving or stationary
  - Targets: high density of personnel, expensive symbolic value.
  
  - *Moving car/truck bomb tactic*  
 Aggressor tactic effective when they are driven with high explosive and when an unobstructed approach to the targeted facility is available.
    - Answer: Obstructions are created which are capable of stopping vehicles with minimum penetration to barriers.
  
  - *Stationary car/truck or van bomb tactic*  
 The vehicle is carrying high explosives and is parked near the facility. Explosives are detonated by either of the following:
    1. Time-delaying system
    2. Remote control
 Answer: The barriers shall be designed to control the energy due to the blast effect by the following list of strategies:
    1. As stand-off distance is maintained using statistics of bomb-blasts between the installations, assets and facilities and the exploding vehicle bomb.
    2. Design or strengthen that given (1) to withstand the explosion.
    3. Investigate from the current available statistics improvised explosive devices, incendiary devices and their effects.
    4. For exterior mode hardening of installations is essential but cannot prevent local damage, deaths and injuries. The hardening process shall be combined with architectural and landscaping techniques that can detect explosives or bombs.
    5. A properly designed fence to provide both visual obscuration, conceal the asset and prevent throwing explosives and other objects.
  
  - *Surveillance mode*  
 The terrorist compromises information from outside using the following for recording and for the operation of installations:
    1. Visual surveillance to monitor installations by ocular and photographic devices.
    2. Electronic emanation to monitor frequency waves.
    3. Acoustical eavesdropping to monitor voice communication and transmitted data.
 Answer: The answer for this strategy is:
    1. To eliminate or minimize sight lines between vantage points and the installations – part of assets
    2. Inspect and eliminate listening devices and other acoustical eavesdropping techniques from sound areas, floors, ceilings and shielded rooms and equipment



- *Foot mode*

The terrorists in particular can enter installations and facilities by overt, covert or forceful means using any tools. They can penetrate walls, windows, doors, and utility openings. Explosives are concealed in targeted areas. The terrorist can use false credentials for legitimate access

- *Delivery mode*

In this case, explosive and incendiary are delivered to the proposed targets by using letters, packages and regular material supplies

Answer to foot and delivery modes

The strategy adopted shall have the adoption of the following:

1. Detection at the earliest possible stage and providing information to the response force.
2. Delaying the aggressor or terrorist to give the response force sufficient time to engage and to neutralise the suspect.
3. Creating restricted areas, validating personnel and visitors.
4. Checking the premises, hand-carried items and storage locations installed away from the main asset or installation.
5. Where detonation cannot be avoided, a bomb disposal squad shall remove the item(s) from the asset.

- *Computerised database, terrorist activities and threat*

A computerised database of terrorist incidents can provide the basis for a logical, efficient and cost-effective design of installations as counter measures. Several approaches are studied

Answer:

1. To concentrate on the review of literature related to terrorism and guerrilla theories in order to provide an idea of possible motivations of those groups who leave printed materials behind and are prepared to be interviewed.
  2. To carry out a quantitative analysis studying characteristics of terrorist campaigns and their pitfalls and to accumulate data in greater detail which are valuable to both the analyst and the structural engineer.
  3. To collect data from terrorist events and discrete incidents as the unit of analysis, thus including actual acts.
  4. To select parameters for the terror database listed as:
    - Year, month and day.
    - City, country.
    - Terrorist group number and its activity past and present.
    - Weaponry used
    - Target attacked.
    - Incident description, methods and case history.
    - Basic data for examination
    - Main building.
    - Secondary building.
    - Underground archives with electro-mechanical services.
    - Parking complex underground and on ground.
-

**Table 1.11.** Managers and security staff

- 
- I. Security staff duties and responsibilities
    - a) Maintenance and vigilance to spot criminal activities
    - b) Securing the premise at business hours
    - c) Controlling the access and egress of staff, visitors and vehicles
    - d) Ensuring the perimeter fencing is in good condition at all times
    - e) Checking the functioning of the security lightings and equipment
    - f) Switching on and switching off alarm systems
    - g) Constantly in touch with police and fire brigade
  - II. Security staff integrity, training and status
    - a) Credentials should be carefully checked
    - b) A proper and effective training should be given
    - c) The absolute integrity of the security staff is essential
    - e) The senior security staff should have properly established contacts with management at all levels and should report to a member of top management
    - d) The discipline of the security staff and assignment instructions must be clearly adhered to
    - e) All security staff should be immediately acquainted with changes in the instructions
    - f) A log book for the security staff shall be maintained along with a security manual
  - III. Accommodation
    - a) Security staff must be given satisfactory accommodation at a good vantage point with a direct view of routes
    - b) The security control room in the main buildings must be sited in view of all measures described elsewhere
    - c) The gatehouse staff should be in the direct or video screen view of the control room
- 

**Table 1.12.** Owners and managers

---

Owners and managers

Security measures should be continuously checked by management for efficacy. The following are important points, which should be noted for record:

1. Check that the quality of gates, doors and shutters within the building has been established and are in line with the new risk.
2. All keys and controls for vehicles and equipment are in possession of owner and manager.
3. Check that all windows are properly secured and their systems are based on codes and insurance guarantees.
4. Check that walls, roof, roof lights, fixing and fastening have been secured for vulnerable areas. No deteriorations exist. Where there is a possibility, all defects have been removed for which records must be kept.
5. Check that good sight lines from the security office are not obstructed by vehicles etc. and no parts of the premises are hidden from passers-by. Where such premises need visibility from the street, they should be promptly adhered to prior to handing over to security staff.

6. Check that surveillance equipment is operational and in good order. Everyday check is necessary.
7. Check that the means of signalling an alarm condition, and telephones are appropriate for the new risk established.
8. Check that crime prevention officer and other police liaison contact have been briefed on local crime pattern and the senior security officer is also aware.
9. Check that existing security measures do not negate fire precautions agreed with local Fire Authority and in no circumstances infringe safety requirements.
10. Check that no other security exists which depend on local environments and emergency procedures are followed.
11. Where buildings contain dangerous substances, check that explanation to hazard warnings are installed.

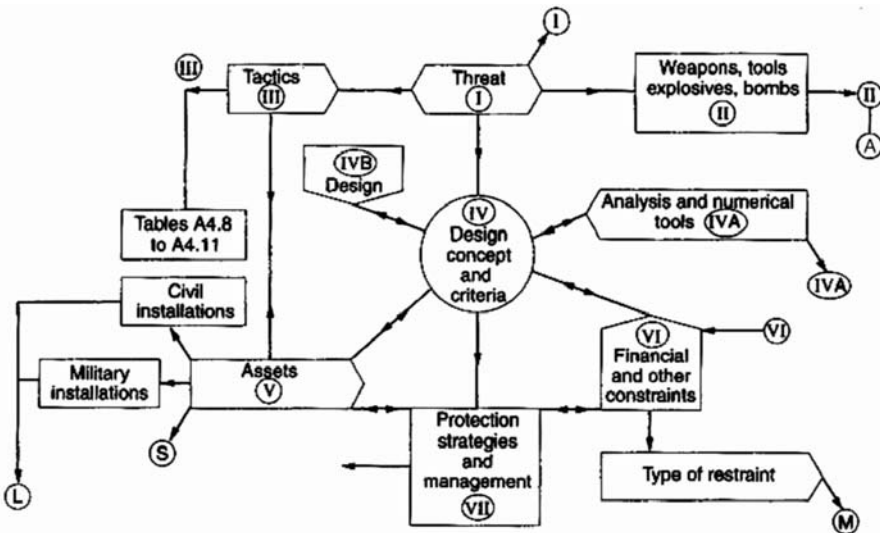


Fig. 1.16. Modes and tactics: flow chart A

*Site Problems and Management*

Any building site has special problem areas and they should be identified and then thoroughly analysed. The type of the building concept and various facilities associated with a building play a great part in providing a range of counter measure to a potential set of terrorist attacks. Some of the measures are given broadly below:

- A provision of active security systems involving access control systems combined with intrusion detection systems, alarm systems and surveillance systems.
- A provision of physical protection and hardening features.

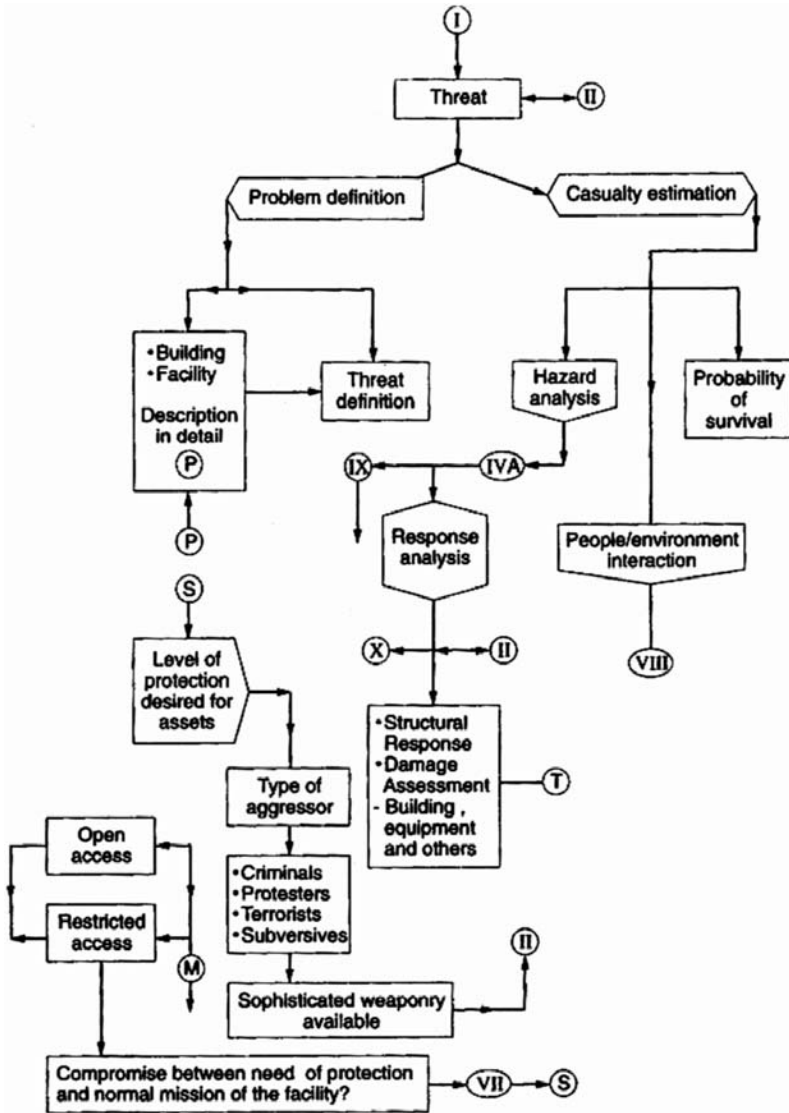


Fig. 1.17. Modes and tactics: flow chart B

- Emergency measures and crisis management.
  - Evacuation, fire fighting and personnel protection including first aid
  - Paramedic access
- Management of the attack-included damages to equipment and building structure.
- Security guards to respond to attack and deter additional attacks.

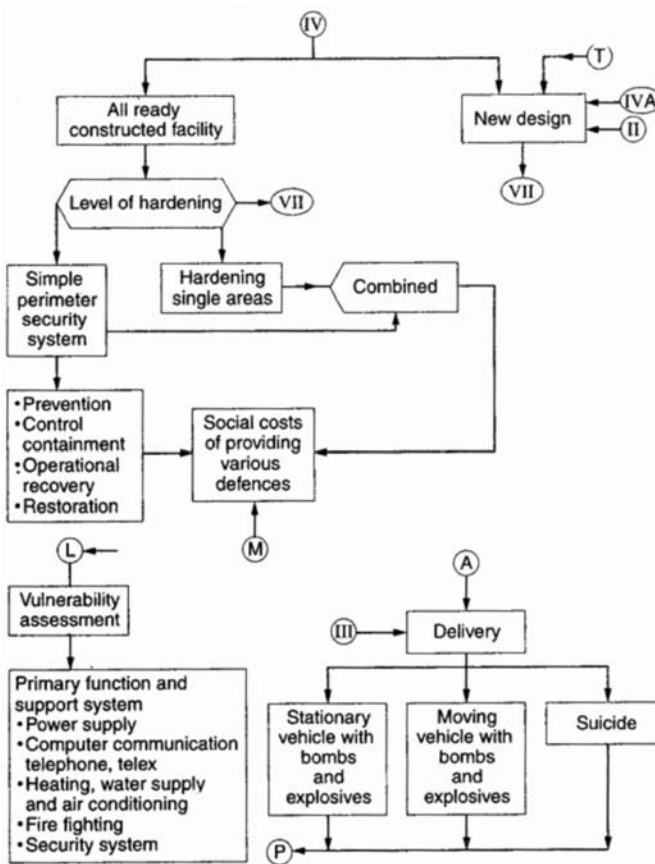


Fig. 1.18. Modes and tactics: flow chart C

Engineering measures are needed to protect buildings, and landscape consultants are needed to give a thorough site management. The architectural/engineering measures are as follows.

- 1) The entrance corridor is closed or access is denied by steps, large concrete planters and other kinds of barriers.
- 2) Parking adjacent to the exterior walls is prohibited by means of concrete planters.
- 3) Existing doors between the car park and service floor are strengthened.
- 4) Site control must be provided by means of the following:
  - a) Security systems and security guards as mentioned above;
  - b) A fence is designed to reduce direct attack on facilities and strengthened to act as a barrier against vehicle access and vehicle impact with or without explosives;

- c) A main entrance that has been designed and strengthened using a combination of active barriers and non-direct access roads
- d) The building's envelope, i.e., external walls, windows, doors, strengthened for at least three to four floors of the building;
- e) A more secured glass such as laminated glass, laminated glass with anti-fragmentation film, polycarbonates or a combination of these glasses, to replace the existing ordinary glass;
- f) Protection of the vital internal areas and exposed equipment;
- g) A transformer unit located apart from the primary transformer, with the addition of adding separate direct lines to diesel generators;
- h) Prevention of unauthorised access to a protected structure by means of security hardware such as lights, alarms, radios, phones, CCTV, vaults, card readers and IDS systems in association with (a) to (g) above;
- i) Where a new facility is to be conceived, all components in a building must be designed against internal and external blast effects;

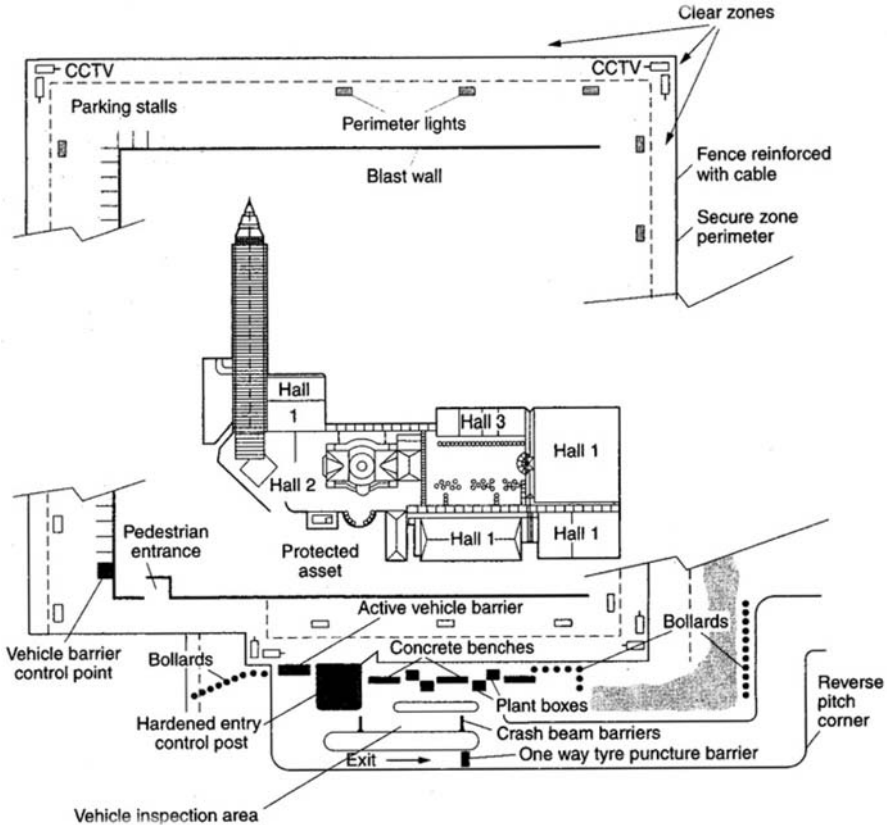


Fig. 1.19. Installation or facility security protection plan

- j) The use of SIFCON (slurry infiltrated fibre concrete), an excellent material that resists perforation by ballistics, bomb fragments and rocket propelled grenade;
- k) All systems described in (a) to (h) must not create a fortress effect.

A typical layout shown in Fig. 1.19 is the best choice of layout for the protection of the facility or installation. The layout shown on Fig. 1.19 shall be the basis (with slight changes) of the answers to all site problems posed below.

### 1.6 Vehicle Barrier System Requirements

The configuration and layout of the entrance/exit route to the vehicle barrier most certainly has an influence. It is necessary to have one route for the entrance and one for the exit. The landscape engineer should look into the provision for passive barriers to direct traffic with a small radius for turning prior to the barrier location. This measure offers the following:

- a) The vehicle speed is reduced by one-half owing to the kinetic energy absorbed by the barrier which is proportional to the square of the vehicle speed will thus be by a factor of one-quarter.
- b) In turning, the velocity or speed of the vehicle is limited by the friction coefficient between the tyres and the road surface. The vehicle will skid when the centrifugal force exceeds the friction. The smaller the radius of the turn in the roadway, the lower the vehicle speed would have to be without skidding. It is therefore vital to plan a curved entrance roadway.
- c) In the landscape layout, in order to achieve passive barriers, it is essential to provide a reserve curve slope together with speed bumps and S-curves.

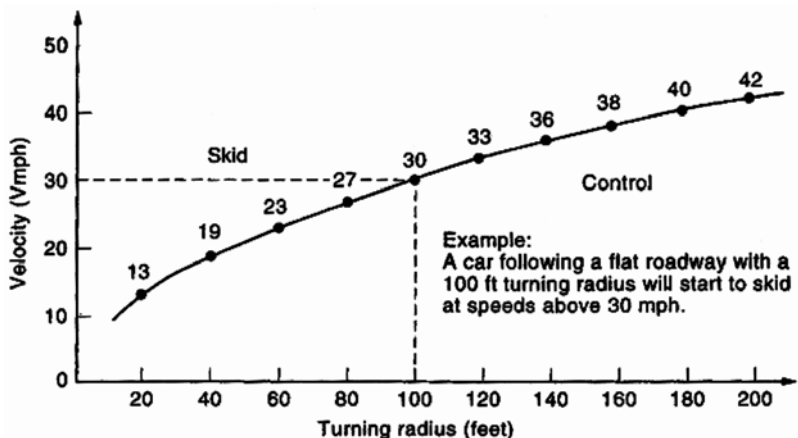


Fig. 1.20. Installation approach design: relationship between turning radius and attainable velocity without skidding

These measures would, potentially, deter the terrorists. Figure 1.20 shows the relationship between the turning radius and attainable velocity without skidding.

## 1.7 Vehicle Bombs – City of London Police Observation List

When designing barriers, the type of potential vehicle bomb must be considered. The list below provides items that should be observed.

- Beware: Terrorist criminals use flat-backs, box vans, skip lorries and cars. Do you know what to look for when you stop an HGV?
- Beware of unprofessional re-sprays. Are there paint splashes in unusual places? Can you still see the previous operator's name under the new paint? It could indicate where the vehicle was acquired or last operated.
- Is the rear registration plate obscured to avoid recognition?
- Are there signs of sections having been cut and welded? Does the underside or floor section look unusually deep?
- Did you know that the floor of most flat-back box lorries is made of wood? If the one you stop has a metal floor, are the rivets new?
- Does it look properly manufactured?
- The Department of Transport Plate is; laminated paper, which can be green, red or blue. Green indicates HGVs approved for international use, red for UK use and blue for general use pre-1980.
- An unusually large gap between the cab and the box/container may indicate that the vehicle has been converted and the hydraulics behind the cab removed.
- Beware: On rigid vehicles there should be no cables or wires from the cab into the box container. The manufacturer will always channel them under the floor.
- Is the vehicle clean where it should be dirty, especially on the underside body frame?
- The Vehicle Identification Number (VIN plate) will be found in or around the driver's cab. This plate is riveted to the vehicle at the time of manufacture and should stay with the vehicle throughout its life.
- Beware of plates that appear to have new rivets or if the plate is unusually clean for the vehicle.
- HGVs supplied by bona-fide dealers will in virtually every case have either the name of the dealer or the manufacturer of the plates immediately under the INDEX NUMBER. This may even indicate the city or town from which the vehicle originated.
- Beware of plates that appear new and do not display the dealer/maker's name.



- Beware of new nuts or rivets on old plates or extra drilled holes or plates held in place by Velcro.
- Does the driver's cab look 'lived in' or is it unusually clear of paper such as delivery invoices, etc? Does the vehicle show signs of carrying what it appears to trade in?
- Any HGV over 3.5 tonnes will usually be fitted with a tachograph. You should be suspicious if the tachograph has been removed.
- All HGVs must have wing mirrors on each side of the cab. The near-side may have two, or one convex mirror with the bottom portion allowing the footway to be seen.
- All HGVs must display a current road tax disc and possibly a London Borough's Transport Scheme disc.
- Remember the vehicle registration should be shown on all the discs. Check that they all correspond.
- The operator's licence will also have the area code of issue at the start of the number SE or OK indicating it was issued in the South East region.
- If the disc is faded contact a traffic officer who will be able to help.
- London Borough's Transport Scheme Permit Plates are displayed on the front and rear bumpers if the owner or operator of the vehicle wants to use it in London at night or at weekends. UK hauliers are aware of these London regulations, so be suspicious of non-compliant vehicles during those times.
- All HGVs must comply with Construction and Use Regulations, as outlined in the Road Traffic Act, so look out for:
  - I. Cracked or broken wing mirrors
  - II. Cracked windscreens
  - III. Broken headlights, etc.
  - IV. Bald tyres.

## 1.8 Selection Procedures for a Vehicle Barrier

When the threat for the barrier has been established, including explosive load and vehicle type, a suitable vehicle can be selected. The decision should be based on:

- a) Can absorb deadly forces including impact loads.
- b) Can be reliable for repair parts and manufacturer's service policy.
- c) Can be operational and shall have emergency capability.
- d) The availability of power and working with alternative sources of power.
- e) The manufacturer's operator training and handling of equipment.
- f) Cyclic and access control frequency including explosive manual for remote control.
- g) Manufacturer's responsibility on legal issues.

**1.8.1 Example 1.1 American Practice**

A terrorist weighing 15,000 lb is to be impact a barrier with a maximum speed of 40 mph with enough road impediments. Develop the kinetic energy based on the crash-test formula:

$$KE = 33.44 \times 10^{-3} WV^2,$$

where

$KE$  = kinetic energy (ft lb),

$W$  = vehicle weight (lb),

$V$  = velocity in mph.

$$KE = 33.44 \times 10^{-3}(15,000)(40)^2 = 802,560 \text{ ft lb (1088.3 kNm)}$$

The vehicle barrier must be designed to withstand this kinetic energy.

## References

- [1.1] Skinner P, Wallace M (2002) World Trade Center. The giants that defied the sky. White Star s.r.l., p. 123
- [1.2] The Daily Telegraph/The Independent (London), The Times (London) (2001) Extract from features on WTC. 2001 Sept. 16, 50 pp.
- [1.3] Hopkinson J (2001) Fire-safety engineering: the consultant's view. *J. Instruct Eng.*, London, 2001 Oct. 2
- [1.4] Subramanian N (2002) Collapse of WTC. Its impact on skyscraper construction. *J. Indian Concrete* (March 2002):165–169
- [1.5] Scleich J-B (2002) Auswirkungen des WTC-Schocks auf den europäischen Stahlgeschoßbau. *Stahlbau* 71(4):289–293
- [1.6] Anon (2002) 11 September. The official report on WTC. *The New Civil Engineer* (2002, May 9):5–7
- [1.7] ABC (2001) Planes attack US targets. A report on 9/11/2001. 12 pp.
- [1.8] Hunkele LM (2001) The Pentagon project. *Civil Engineering* (June 2001):85
- [1.9] Mlakar PF et al. (2003) The Pentagon building performance report. January 2003. Two Appendices, ASCE, 61 pp.
- [1.10] Prieto, R (2002) The 3Rs: lessons learned from September 11th. The Royal Academy of Engineering, London (Oct. 2002) 20 pp.
- [1.11] FEMA (Federal Emergency Agency) (2002) The World Trade Center building performance study (data collection preliminary observations and recommendations). FEMA region II, New York and ASCE, May 2002, p. 435
- [1.12] Baker WE, Cox PA, Westine PS, Kulesz JJ (eds.) (1982) Explosion hazards and evaluation. *Fundamental studies in engineering*. Elsevier Scientific publishing Company, NY
- [1.13] Bangash M (1993) Impact and explosion, analysis and design. CRC Press 1993, Sect. 4.3
- [1.14] International Organization for Standardization (1999) Fire resistance tests – elements of building construction. ISO 834
- [1.15] National Fire Protection Association (1999) Standard methods of fire tests of building construction and materials. NFPA 251, Quincy, MA
- [1.16] U.S. Department of Energy (1996) Accident analysis for aircraft crash into hazardous facilities. DOE Standard 3014-96, October 1996
- [1.17] Zalosh RG (2002) Explosion protection In: SFPE handbook of fire protection engineering. 3rd edn, Quincy, MA
- [1.18] Bangash T (2003) Ph.D. Thesis, London University
- [1.19] Harris B (2001) The World Trade Center, a tribute. Courage Books, Philadelphia
- [1.20] Isner M, Klem T (1994) The World Trade Center explosion and fire. February 26, 1993, Fire Investigation Report, National Fire Association
- [1.21] Rubin D, Tuchman J (2001) WTC engineers credit design in saving thousands of lives. *Engineering News Record* 247(16):12 (2001 Oct. 15)
- [1.22] Skidmore, Owings & Merrill LLP (1979) Drawing A-11, WTC hotel, New York, NY
- [1.23] Skidmore, Owings & Merrill LLP (1979) Drawing A-12, WTC hotel, New York, NY
- [1.24] Skidmore, Owings & Merrill LLP (1981) Drawing A-6C, New York, NY

- [1.25] United States Fire Administration (1993) The World Trade Center bombing: report and analysis. Technical Reports Series. Prepared in Association with the Federal Emergency Management Agency, October 1993
- [1.26] AISC (2001) Manual of steel construction. LRFD, 3rd edn. Chicago
- [1.27] ASTM (2000) Standard test methods for fire tests of building construction and materials. ATM E119. West Conshohocken, PA
- [1.28] Smith D (2002) Report from Ground Zero: the story of the rescue efforts at the World Trade Center, Viking Press
- [1.29] Worthington, Skilling, Helle, Jackson (1968) The World Trade Center Northeast Plaza building. Structural drawings
- [1.30] Zalosh RG (1995) Explosion protection. In: SFPE handbook of fire protection engineering, 2nd edn
- [1.31] Flack and Kurtz, Inc. (2002) Oral communication providing engineering explanation of the emergency generators and related diesel oil tanks and distribution systems. April 2002
- [1.32] Lombardi FJ (Port Authority of New York and New Jersey) (2002) Letter concerning WTC7 fireproofing. 2002 April 25
- [1.33] Odermatt, J.T. (New York City Office of Emergency Management) (2002) Letter regarding OEM tank at WTC7
- [1.34] Rommel, J. (New York State Department of Environmental Conservation) (2002) Oral communication regarding a November 12, 2001 letter about diesel oil recovery and spillage. April 2002
- [1.35] Salvarinas JJ (1986) Seven World Trade Center, New York, fabrication and construction aspects. Canadian Structural Engineering Conference
- [1.36] Silverstein Properties (2002) Annotated floor plans and riser diagrams of the emergency generators and related diesel oil tanks and distribution systems, March 2002
- [1.37] Guy Nordenson and Associates and Simpson, Gumpertz, and Heger, Inc. (2001) Draft structural evaluation for the New York Department of Design and Construction (DDC). Prepared for LZA Technology, Oct. 2001
- [1.38] LZA/Thornton-Tomasetti and Gilsanz Murray Steficek LLP (2001) Interim life safety report, 30 West Broadway, New York, NY. Prepared for New York City Department of Design and Construction, 2001 Nov. 21
- [1.39] LZA Technology/Thornton-Tomasetti, Structural Engineers Association of New York, and Guy Nordenson et al. (eds.) (2002) WTC emergency damage assessment of buildings. Structural Engineers Association of New York Inspections of September and October 2001, Draft prepared for the New York City Department of Design and Construction. New York, NY, est. April 2002
- [1.40] Bangash MYH (1993) Impact and explosion: Analysis and design. Blackwell
- [1.41] GuideLines on explosion – City of London Police (1999) Updated 2003
- [1.42] Data and extract (2003), Reuters

# 2 Blast and Explosive Loadings on Buildings

## 2.1 Introduction

Blast is a sudden release of energy and explosions can be identified as being due to gas, nuclear, bombs or explosives. Bangash [1.13] gave an extensive treatment of explosion dynamics and blast wave characteristics related to structural loading. However, it is not intended to repeat this work here.

This section deals with the formation of blast waves by condensed high explosives and bombs. Both explosives and bombs are categorized as small, medium and high or large:

- Small explosive devices – up to 5 kg TNT
- Medium explosive devices – up to 20 kg TNT
- Large explosive devices and bombs – up to 100 kg TNT
- Very large explosive devices and bombs – up to 2500 kg TNT.

These explosives or bombs are sometimes given in lbf TNT or ton TNT designated as YIELD. This is discussed later on in the chapter. The last load – time relation is important for determining the blast resistance of buildings and their components. A number of such relations for both external and internal blasts is given. Gas and nuclear explosions do not frequently occur, however.

## 2.2 Explosives and Bombs

Safety, reliability and performance of explosives and bombs are difficult to assess for commercial explosives that are made from cheap ingredients such as TNT or nitroglycerine mixed with low-cost nitrates. Military explosives and bombs are made from expensive materials like TNT and RDX or HMX with TNT. A reference is made to Chap. 1 for detailed texts on various explosives. Terrorists often manufacture their own military explosives using Semtex in order to attack buildings and other structures. The blast can be external or internal. The basic characteristics of abnormal loads produced on buildings subjected to explosives are of:

- Stationary randomness

**Table 2.1.** Explosives and charge factors (CF)

Explosives	Mass specific energy (kJ/kg)	TNT equivalent (CF)
TNT	4520	1.000
GDN (glycol dinitrate)	7232	$\frac{7232}{4520} = 1.6$
Pyroxilene	4746	1.05
Pentritone	6689.6	1.48
Dynamite	5876	1.30
Schneiderite	3164	0.70
Dinitrotoluene (DNT)	3164	0.70
Ethylenedinitramine	5650	1.25*
Compound B [0.6RDX + 0.4TNT]	5190	1.148
RDX (cyclonite)	5360	1.185
HMX	5650	1.256
Semtex	5660	1.25*
Dentolite <sup>50</sup> / <sub>50</sub>	–	1.129
DENT	–	1.282

\* Identical

- Transient or dynamic nature
- Short duration with time histories from milliseconds to a few seconds.

The model simulations of some of these techniques are described later on in the chapter.

The use of TNT (trinitrotoluene) is generally considered as a reference. When the high explosive is other than TNT, the equivalent energy is obtained by using the *charge factor*. This will form the value of the scaled distance  $Z = R/W^{1/3}$ . The charge factor is equal to

$$\frac{\text{actual mass of the charge}}{\text{mass of the TNT equivalent}}$$

It is designated CF. Table 2.1 shows these factors. Table 2.2 show attacks on previous sites and explosion loads.

Referring to the work done by Baker WE et al. [1.12], the CF for RDX is computed as  $5360/4520 = 1.185$ . Hence 100 kg of RDX is converted to  $1.185 \times 100 = 118.5$  kg of TNT.

### 2.2.1 A Terrorist Bomb

Table 2.2 summarizes some recent terrorist attacks on buildings with bombs of variable magnitudes and intensity. Some terrorists prefer to use vehicles for bombing targets. A complete history is given in Chap. 1.

**Table 2.2.** Terrorist attacks with explosives

No.	Site/country	Explosion load
1. April 1995	Oklahoma City/USA	4800 lbf (33.1 ton of TNT)
2. Feb 1993	The World Trade Center, NY/USA	1200 lbf (0.6 ton of TNT)
3. July 1994	The Jewish Community Centre, Buenos Aires/Argentina*	275 kg of TNT
4. April 1992	St. Mary Axe, London/UK†	350 kg of TNT
5. July 1994	Apartments, Israeli Embassy, London/UK	350 kg of TNT
6. April 1992	Staples Corner, London/UK‡	300 kg of TNT
7. Feb 1993	The World Trade Center, NY/USA	900 kg of TNT

## Additional details

Determination of range or distance (R.B. Philips, REN 558, 1945)

$$R = \frac{KW^{0.333}}{\{1 + (3175/W)^2\}^{0.1667}}$$

$R$  = range in m

$W$  = mass of explosives in kg of TNT

$K$  = constant  $\approx 5.6$

Blast resistance in terms of the quantity scaled distance

$$Z = \frac{R}{W^{1/3}}$$

\* 3 to 5 m range

† 115–160 m range

‡ 17 m nearest corner range

### 2.2.2 Blast Loads on Buildings

There are many threats to be considered in the design of civilian structures. The most serious threat against buildings and other important civilian structures has been the explosives located inside and a large external explosion due to the ‘car bomb’. Apart from ‘deterrence’, ‘keep out’, deception and other measures, the idea of resisting explosive blast loads with minimum structural modifications is to be promoted among civil and structural engineers. When a bomb explodes, a rapid release of stored energy is characterized by an audible blast. The energy released is divided into two distinct phenomena – thermal radiation, and coupling with air and soil, known as *air blast* and *ground shock*, respectively. Air blast is the principal cause of the damage to buildings. On the other hand the ground shock-wave propagates by compressing the air molecules in its path, thus producing the *ambient overpressure* or the *incident pressure*. The waves propagate with supersonic velocity and finally hit the building. They reflect from the building with amplified overpressures. The air blast penetrates through windows and doors and other openings in the building. Floor slabs, partitions, and contents are subjected to these pres-

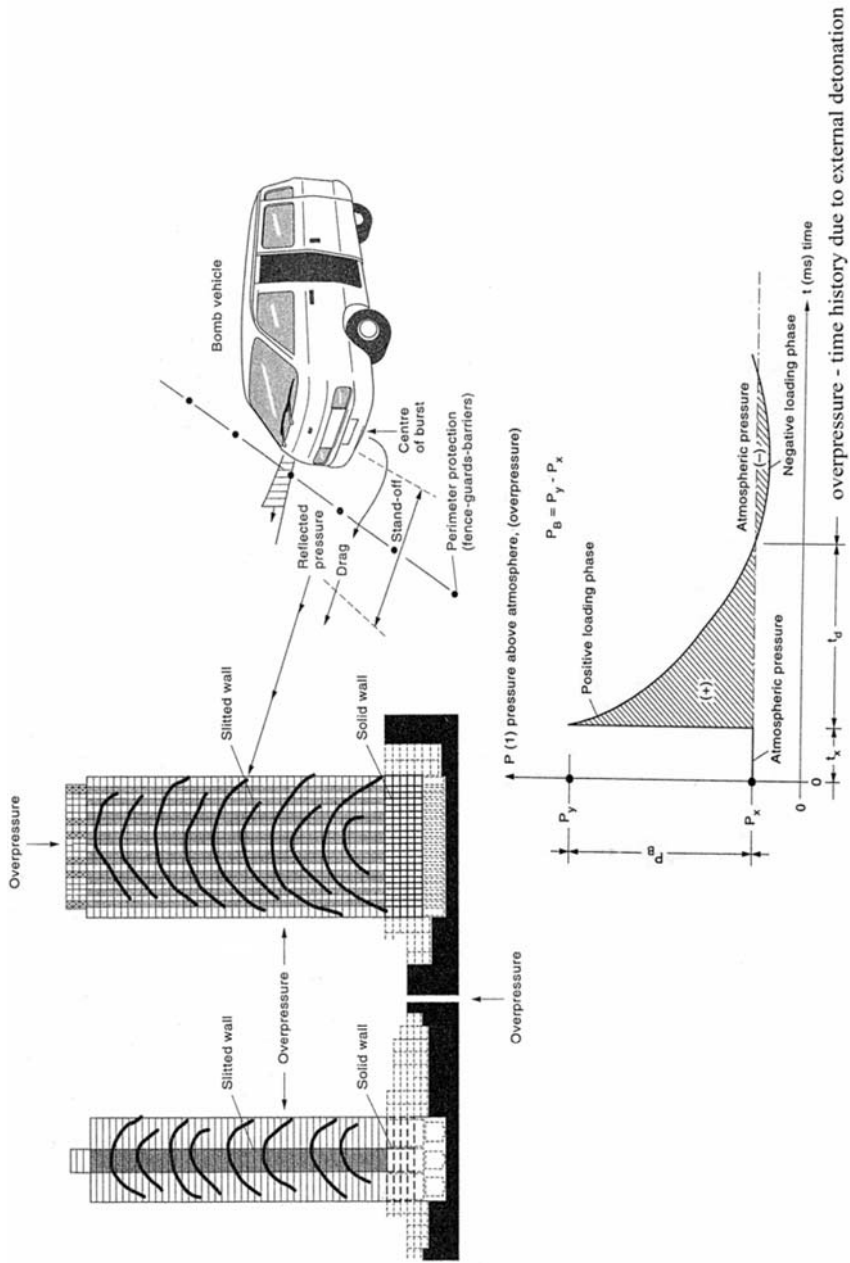


Fig. 2.1. Blast loads on buildings: typical scenarios



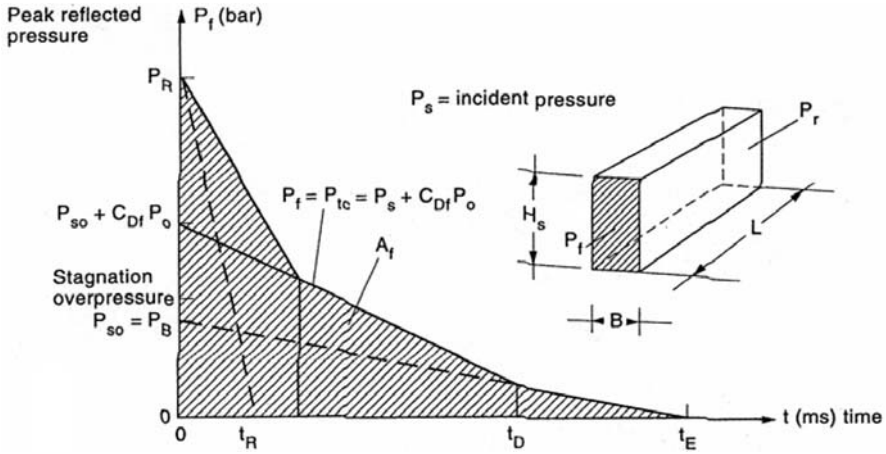


Fig. 2.2. Pressure on the front face versus time

tures. Columns and walls are either damaged or totally destroyed. During this process, *diffraction* of the wave occurs as the shock propagates around corners increasing or reducing pressures in these regions. The process continues until the entire building is engulfed by shock-waves and all surfaces in a building are covered by the overpressure. Figure 2.1 shows a complete scenario on blast loads on buildings. The pressure decays exponentially and is time and space dependent and in some areas suction forces occur. These are bracketed as a *negative loading phase* and Fig. 2.2 shows both positive and negative phases and the behaviour of the travelling shock-wave giving the instantaneous relationship between the overpressure and the stand-off distance.

A secondary effect of the air blast as given by Bangash MYH [2.27] is the *dynamic pressure* or *drag loading* which has a very high velocity that also propels debris as projectiles. The air-blast phenomenon takes place in very short time intervals, measured in milliseconds. The magnitude of the pressure  $P$  is roughly proportional to the size of the explosive or bomb  $W$  and is related as

$$P \propto \frac{W}{R^3}, \tag{2.1}$$

where  $R$  is the stand-off distance from the centre of the charge and  $W$  is the *charge weight* or *yield* measured in equivalent lbs, tonne, or kg of TNT.

A typical *car yield bomb* ranges from 0.1 ton of TNT. The bomb on usual civilian targets as stated in Table 2.2 seldom goes beyond 500–2000 lb (0.25–1 ton) of TNT. Table 2.3 gives various expressions for blast-load evaluation and modelling.

**Table 2.3.** Blast loads and modelling**(A) External blast and load modelling***(i) Overpressure  $P_{SO} = P_B$* 

The overpressure  $P_{SO}$  in its peak form acting dynamically on walls or front faces of a building can be written as

$$P_{SO} = 6784 \frac{W}{R^3} + 93 \left( \frac{W}{R^3} \right)^{1/2}, \quad (i)$$

where  $W$  = total charge weight in TNT (tonne),  $R$  = stand-off distance to the centre of the detonation in metres.

For example

$$W = 1.1 \text{ tonne}$$

$$R = 90 \text{ m}$$

$$P_{SO} = 0.1244 \text{ bar}$$

$$q_0 = \text{peak drag} = 2.5 C_D P_{SO} / (7 P_{SO} + P_O) \quad (ii)$$

$$P_R = \text{peak pressure of a reflected shock} \quad (iii)$$

$$= 2 P_O + 6 / (7 P_O + P_{SO}) \text{ when } P_{SO} < 10 \text{ bar}$$

or

$$= 4 \log_{10} P_{SO} + 1.5 \text{ when } P_{SO} \geq 10 \text{ bar} \quad (iv)$$

where

$$P_O = \text{ambient atmospheric pressure} \approx 1 \text{ bar},$$

$$C_D = \text{drag coefficient} = 1.0 \text{ in general.}$$

In detail

$$C_{Dr} = \text{drag coefficient for the rear face} = 0.25 \text{ to } 0.5 \quad (v)$$

$$C_{Df} = \text{drag coefficient for the front face} = 0.8 \text{ to } 1.6 \quad (vi)$$

*(ii) Pressure-time relation*

Notation

$$T_C = \frac{3S}{U} \quad S = H_S \leq \frac{1}{2}B \quad T_C = \text{reflected pulsetime} \quad (vii)$$

$$S = H_S \text{ when } B \geq H$$

$$P_f = \text{pressure at front face}$$

$$P_r = \text{pressure at rear face}$$

$$B = \text{building width}$$

$$H_S = \text{building height}$$

$$t_R = \text{time for reflected wave} = 2i_r / P_R$$

$$i_r = \text{total reflected pressure impulse}$$

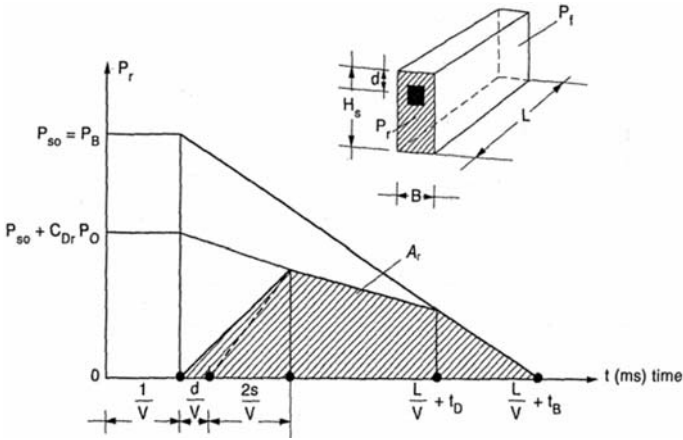


Fig. 2.3. Pressure on the rear face versus time

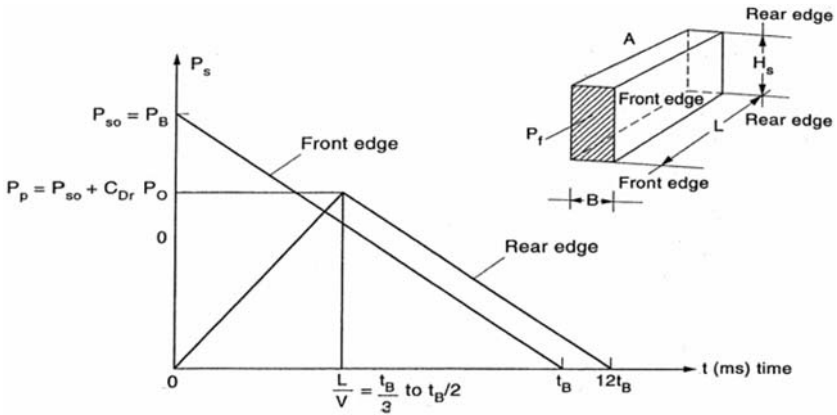


Fig. 2.4. Pressure on the side face versus time

(B) Duration

$$\begin{aligned}
 t_B = \text{shock pulse duration} &= 10.23 \frac{W^{1/3}}{\sqrt{P_{SO}}} \quad P_{SO} < 70 \text{ bar} \\
 &= 20.77 \frac{W^{1/3}}{\sqrt{P_{SO}}} \quad P_{SO} \geq 70 \text{ bar}
 \end{aligned}
 \tag{viii}$$

$$t_D = \text{time of drag} = 20.77 \left( \frac{W}{P_{SO}} \right)^{1/3} \quad \text{for } P_{SO} < 2 \text{ bar}
 \tag{ix}$$

$$t_D = 14.35 \frac{W^{1/3}}{\sqrt{P_{SO}}} \quad \text{for } P_{SO} \geq 2 \text{ bar}
 \tag{x}$$

Notation

$P_p$  = peak impulsive load

Note: 1 bar = 100 kN/m<sup>2</sup>

**(C) US Army Corps of Engineers TM5-855-1**

The principle adopted in Section (A) of this table is adopted. Figure 2.5 shows a section through a building with average pressure-time variation.

The bomb is located close to the structure. The average pressure-time curve is constructed over a length of the building  $1.3 \times$  normal  $R$ , the stand-off distance  $\neq 2S$ . The portion of the surface loaded is  $L_w$ .

- $C_E$  = equivalent factor for load
- $\frac{D}{L}$  = blast wave location ratio (Refer to Fig. 2.6.)
- $\frac{L_{wb}}{L}$  = wavelength and span ratio

The pressure build-up is linear from  $t_f$  at  $f$  point to the time  $t_d + t_f$  when blast wave reaches point  $d$ .

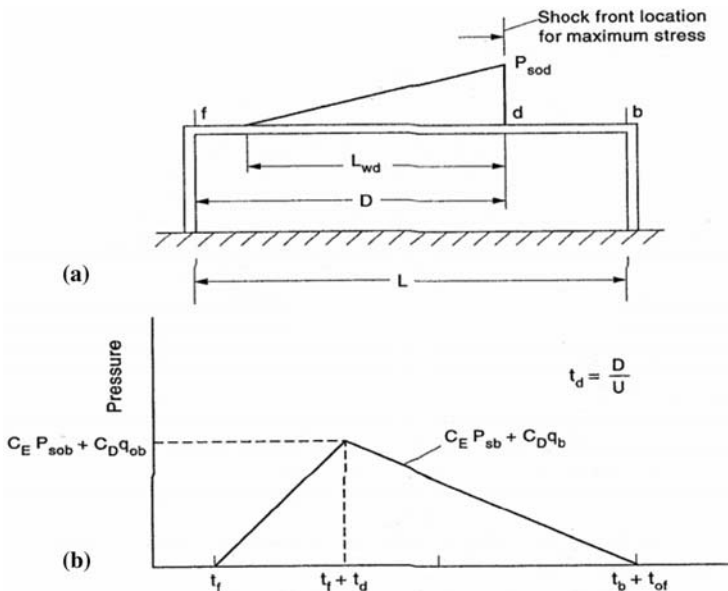
$$P_{or} = \text{peak pressure} = C_E P_{SO_b} + C_D q_0$$

The drag coefficient  $C_D$  for the roof and wall:

<i>Peak dynamic pressure psi</i> (kN/m <sup>2</sup> )	$C_D$
0-25 (0-172.37)	-0.40
25-50 (172.37-344.738)	-0.30
50-130 (344.738-896.32)	-0.20

Equivalent load factor as shown in Fig. 2.6 is given by

$$C_E = \frac{P_{SO}}{P_{SO_b}}$$



**Fig. 2.5.** Roof and side wall loading (span direction perpendicular to shock front). (a) Section through structure, (b) average pressure – time variation. Taken from TM5-855-1 (courtesy US Army Corps of Engineers)

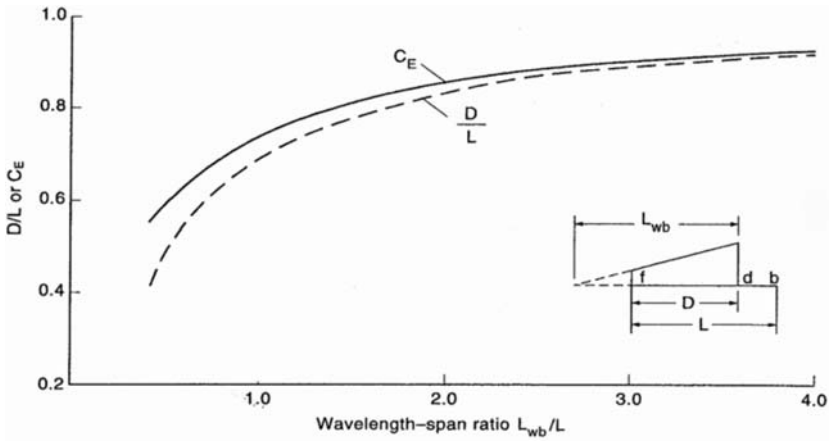


Fig. 2.6. Equivalent load factor and blast wave location ratio versus wave-length-span ratio (courtesy: US Army Corps of Engineers)

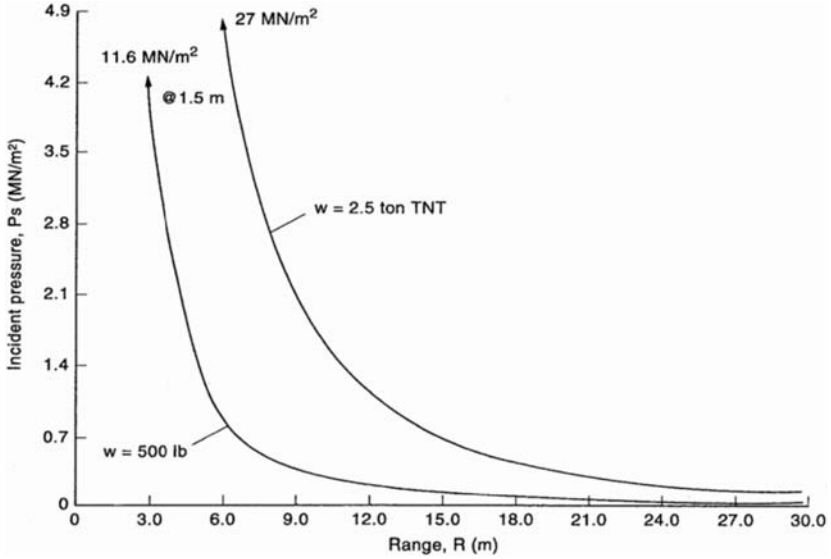


Fig. 2.7. Load-range-time relations: incident pressure versus range

and blast wave location ratio

$$\frac{D}{L},$$

where  $L$  is the width of the strip or element being considered.

The incident pressure  $P_s$  for two bombs of yield 500 lb and 2.5 ton TNT for ranges  $R$  normally required for Table 2.3 is given in Fig. 2.7.

### 2.2.3 Blast Wave Scaling Laws

The Hopkinson–Cranz scaling law is commonly known as ‘cube-root’ scaling. Two bombs of weights  $W_1$  and  $W_2$  having diameters  $d_1$  and  $d_2$ , respectively, are made up of the same explosive materials. The charge weights  $W_1$  and  $W_2$  are related as

$$\frac{d_1}{d_2} = \left( \frac{W_1}{W_2} \right)^{1/3} \quad (2.2)$$

since  $W_1$  and  $W_2$  are proportional to  $d_1^3$  and  $d_2^3$ , respectively. Assuming the two bombs of charge weights  $W_1$  and  $W_2$  produce the same overpressure  $P_{SO}$  and at certain ranges  $R_1$  and  $R_2$  respectively, with  $d_1/d_2$  constant and with positive phase duration and impulse ratios.

Pressure-duration-stand-off for one tonne TNT explosion is given by

$$\frac{R_1}{R_2} = \left( \frac{W_1}{W_2} \right)^{1/3} \quad (2.3)$$

This leads to a scale distance  $Z = R/W^{1/3}$  which is a constant of proportionality. Curves can be plotted, for nuclear or chemical explosives, for overpressures and scale distances.

The impulse of the incident pressures associated with the blast wave is the integrated area under the pressure-time curve. Consequently, the positive phase impulse,  $i_s$ , is defined as follows:

$$\begin{aligned} i_s &= \int_{t_a}^{t_a+t_0} P(t) dt \\ &= cP_{SO}t_0, \end{aligned} \quad (2.4)$$

where  $P(t)$  represents the pressure – time relationship;  $P_{SO}$  is the peak incident overpressure;  $t_0$  is the duration of positive phase;  $t_a$  is the blast wave arrival time;  $c$  is the value between 0.2 and 0.5 depending on the equation used to describe the variation of pressure with time  $P(t)$ . Figure 2.2 gives the exact positioning of these values.

As the blast wave propagates through the atmosphere, the air behind the shock front is moving outward at lower velocity. The velocity of the air particles, and hence the wind pressure, depends on the peak overpressure of the blast wave. This later velocity of air is associated with the *dynamic (blast wind) pressure*,  $q$ . For typical conditions, standard relationships have been established between the peak incident pressure,  $P_{SO}$ , the peak dynamic pressure,  $q_0$ , the wind velocity, and the air density behind the shock front and these quantities are dependent on  $P_{SO}$ . The net dynamic pressure is the product of  $q$  and the drag coefficient  $C_D$ .

When the shock front strikes a building, it produces large pressures on exposed surfaces and penetrates to the inside through openings. The overpressure causes hydrostatic-type loads, and the dynamic pressure causes drag

load. High *reflected pressures* are generated on surfaces due to reflection of the shock wave on the front face of the building. The reflected pressure-time variation and the peak *reflected pressure*,  $P_r$ , are shown in Fig. 2.2. At a given distance from the point at which burst occurred overpressure and dynamic pressure decay with time.

As pointed out earlier, it is customary to characterize the pressure loadings in terms of scaled range  $Z$  as

$$Z = \frac{R}{W^{1/3}}, \quad (2.5)$$

where  $R$  is the radial distance between the centre of explosion and  $W$  is the explosive weight in TNT.

### 2.2.4 Basic Parameters of a Bomb Blast

The analysis for blast effects include the following:

- (a) Computation of transient overpressure from the blast wave front
- (b) Reflected shocks to evaluate peak pressure loading and total impulse.

In case of buildings, the following parameters need urgent attention:

1. The magnitude of the explosion in TNT
2. The stand off distance and altitude
3. The geometry of a building structural system
4. The structure orientation with respect to the explosive and the ground.

Generally, for the design purposes a simplified blast-structure interaction shall be developed depending upon the building location and orientation (front, rear, sides and roof) relative to the point of burst. Where a comprehensive analysis suggested later on in the text, shall be adopted.

For the purpose of computational analysis, Fig. 2.2 is idealized in terms of straight dotted positive and negative phases with positive specific impulse “ $i_s$ ” area such that the accuracy being a parabolic curve is not sacrificed. The idealised pressure-time relation for a blast wave profile is shown in Fig. 2.5. A similar idealised pressure-time relation can be achieved for other case studies exhibited in Figs. 2.3 to 2.7.

In terms of incident pressures and phase durations the following two cases define the blast loadings:

- I. Peak positive incident (side-on) pressure  $P_{SO}^+$  positive phase duration  $t_O^+$  and the corresponding positive incident impulse  $i_s^+$ .
- II. Peak negative incident pressure  $P_{SO}^-$  (suction), negative phase duration  $t_O^-$ , and the corresponding negative incident impulse  $i_s^-$ .

The negative phase is comparatively longer, the pressure will essentially return to ambient. The peak values of the under-pressure are generally small compared with the peak positive overpressures.

Since the degree of blast damage depends largely on the drag force associated with strong winds and is influenced by the shape and size of the structure, the net pressure acting on the structure is called the *dynamic pressure* and is proportional to the square of the wind velocity and to the density of the air behind the shock front.

When the incident blast wave from an explosion in air strikes a more dense medium such as land or water, it is reflected. The front of the blast wave in the air will assume a hemispherical shape. Since there is a region of regular reflection, all structures on the surface, even close to ground zero, are subjected to air blast. Some of the blast wave energy is transferred into the ground. A minor oscillation of the surface is experienced and a ground shock is produced. For large overpressures with a long positive-phase duration, the shock will penetrate some distance into the ground and will damage buried structures.

When the front of the air blast wave strikes the face of the structure, reflection occurs. As the wave front moves forward, the reflected overpressure on the face drops rapidly to that produced by the blast wave without reflection, plus an added drag force due to wind. At the same time, the air-pressure wave diffracts around the structure and is entirely engulfed by the blast. The damage caused by diffraction will be determined by the magnitude of the loading and by its duration. If the structure has openings, there will be a rapid equalization of pressure between the inside and outside of that structure. The diffraction loading of the structure as a whole will be decreased. Since large structures have openings, diffraction and drag must not be ignored.

The loads computed for the surface explosion shall be  $P_{SO}$  and  $2.3 P_{SO}$  for roof/floors and walls respectively, where  $P_{SO}$  is the peak incident wave pressure. Figure 2.7 and Table 2.4 show the damage-distance relationship and peak overpressure failure effects on structural components, respectively.

#### 2.2.4.1 Stress Waves and Blast Waves

Stress waves represent the basis of explosion in the surrounding medium, be it gaseous, liquid or solid. They are defined as moving parts of the medium, being in a state of stress such that the boundaries are *waves* and the rest of the medium consists of *wave fronts*. Stress waves are sometimes called *deformation waves*. These stress waves are divided into normal and tangential waves representing stresses in those directions. Normal waves may be divided into *pressure waves* and *tensile waves* or *rarefaction waves*. The normal waves are also known as *P* (longitudinal) waves and the *S* (tangential) waves as *transverse waves*. In geological media, the surface is the interface of individual layers of rock and soil or air and soil/rock. The interface between them is known as the *free surface*. The surface waves are then classified according to the shape and sense of the trajectories followed by movements in a medium. The surface waves are given below.



- (1) *The Rayleigh wave (R wave)*. This wave exhibits a planar elliptic motion in the medium such that its semi-axes decrease rapidly at a certain distance from a given depth.
- (2) *The Love wave (Q wave)*. These waves exhibit a spatial motion in a medium and their components are parallel and normal to the plane of propagation.
- (3) *The hydrodynamic wave (H wave)*. These waves are similar to *R* waves and propagate along the surface of the liquid and are free from shear stresses.
- (4) *The composite wave (C wave)*. The surface particles exhibit a complex phenomenon when compared with others.

The *R* wave propagation is expressed as:

$$\delta_x = W_{E(t)} L' \{ \exp(-qz) - 2q\bar{s} [(\bar{s})^2 + (L')^2 \exp(-\bar{s}z)] \} \times \sin(\omega t - L'x) \quad (2.6)$$

$$\delta_x = W_{E(t)} L' \{ \exp(-qz) - 2(L')^2 [(\bar{s})^2 + (L')^2 \exp(-\bar{s}z)] \} \times \cos(\omega t - L'x) \quad (2.7)$$

where *x*, *y* and *z* are the co-ordinate axes

$$L' = \omega / v_{SR}$$

$$\omega = \text{circular frequency}$$

$$v_{SR} = \text{velocity of sine wave in the } Y\text{-direction}$$

$$t = \text{time}$$

$$\delta = \text{particle displacement}$$

$$q = \omega^2 (v_{SZ}^2 - v_{RZ}^2) / v_{PZ}^2 v_{SZ}^2$$

$$\bar{s} = \omega^2 (v_{SZ}^2 - v_{RZ}^2) / v_{SZ}^2 v_{RZ}^2$$

$$W_{E(t)} = \text{work done}$$

$$v_{SZ} = \text{propagation velocities of transverse waves}$$

$$v_{PZ} = \text{propagation velocities of longitudinal waves}$$

$$v_{RZ} = \text{propagation velocities of Rayleigh waves}$$

The *Q* wave is generally propagating in the *Y*-direction if the *x*, *y* plane lies on the interface of the layer and on the mass medium. The displacement  $\delta_y$  is a function of time *t* and the co-ordinates *x* and *z*. The *Q* wave is expressed as

$$\delta_y(x, z, t) = (A \cos \alpha' z + B \sin \alpha' z) \exp [L' (v_z t - x)] , \quad (2.8)$$

where

$$L' = \text{a wave number}$$

$$A, B = \text{constants}$$

$$v_z = \text{phase velocity}$$

$$\alpha' = L' \sqrt{[v_z^2 / (v_{sz}^2 - 1)]}$$

The phase velocity  $v_z$  is determined from:

$$v_z = \frac{G_m}{G_s L' d} \times v_{szs} \times \sqrt{\left\{ \left[ \tan^{-1} \sqrt{\left( 1 - \frac{v_z^2}{v_{szsn}^2} \right) / \left( \frac{v_z^2}{v_{szsn}^2} - 1 \right)} \right]^2 + 1 \right\}} \quad (2.9)$$

where

- $v_{szs}$  = propagation velocity of the explosion
- $v_{szsn}$  = propagation velocity in the mass half space
- $G_m, G_s$  = moduli of elasticity in shear and mass half space, respectively.

*Explosion of a Spherical Charge*

When a charge is located at a sufficient depth below the surface, the explosion causes vibrations to propagate in the form of spherical wave fronts in a longitudinal direction, with mass particles displaced radially. This displacement is generally calculated as:

$\delta_r$  = radial displacement

$$\begin{aligned}
 &= \frac{r_s^2 v_{zp} a}{r_s^2 (\beta r_s - v_{zp})} \\
 &\times \left\{ \frac{r_s}{v_{zp}} \left[ 1 - \left( t - \frac{r_s}{v_{zp}} - \frac{r_s}{\beta r_s - v_{zp}} \right) \beta \right] + t - \frac{r_s}{\beta r_s - v_{zp}} \right\} e^{-\beta(t-r_s/v_{zp})}
 \end{aligned}
 \tag{2.10}$$

where

- $v_{zp}$  = velocity in m/s
- $r_s$  = radius of the cavity of the charge (sometimes known as  $t$  = time)
- $\alpha, \beta$  = constants for the particular type of charge

*Explosion of a Cylindrical Charge*

The following gives displacements  $\delta_r, \delta_\theta$  and  $\delta_\phi$  in cylindrical co-ordinates for a cylindrical cavity:

$$\delta_R = \frac{R_0^2 h p}{4 m_R v_{zp} R} \left( 1 - \frac{2 v_{zs}^2}{v_{zp}^2} \cos^2 \phi \right) \frac{\partial F(t - R/v_{zp})}{\partial t}
 \tag{2.11}$$

$$\delta_\theta = 0; \quad \delta_\phi = \frac{R_0^2 h p \sin 2\phi}{4 v v_{zs} R} \left[ \frac{\partial F(t - R/v_{zs})}{\partial t} \right]
 \tag{2.12}$$

where

- $R_o$  = base of a cylinder with height
- $m_R$  = relative mass
- $\delta_R, \delta_\theta, \delta_\phi$  = displacements in cylindrical co-ordinates  $R, \theta$  and  $\phi$ , respectively
- $\nu$  = Poisson's ratio
- $t$  = time

**2.2.4.2 Damping of Stress Waves**

When a stress wave caused by an explosion propagates in a material it is damped at a certain  $x$  and its amplitude  $X(x)$  is given by

$$X(x) = X_0 e^{(-\gamma x)}
 \tag{2.13}$$

where

$$\begin{aligned} X(x) &= \text{amplitude at a distance} \\ xX_0 &= \text{amplitude of the wave at a source} \\ \gamma &= \text{damping ratio} \end{aligned}$$

For a chemical explosion, the relationships between explosion overpressure and ambient atmosphere, duration time and impact load are compared with those for a nuclear explosion in Table 2.4. Impulse or impact depends on the peak overpressure,  $P_{so}$ , in the shock front and on the duration of the wave. In some cases, the rate of decay of the overpressure can influence the impulse/impact load. The scaling principle to explosion has also been given earlier. The scaling law for explosion is defined for the distance for uniform atmosphere as

$$\text{scaled distance} = x \times \rho_{\text{TNT}}^{1/3} / E_{\text{R}}^{1/3} \quad (2.14)$$

where

$$\begin{aligned} c_f &= \text{charge size factor } V, \\ V_{\text{TNT}} &= \text{actual and required TNT volumes, respectively} \\ \rho, \rho_{\text{TNT}} &= \text{actual and standard TNT atmosphere densities, respectively.} \end{aligned}$$

For a non-uniform atmosphere the scaled distance will be different. The energy release,  $E_{\text{R}}$ , is almost equal to the weapon yield.

The *scaling of the overpressure* is given by

$$\text{actual pressure} = \text{overpressure} \times P_o \quad (2.15)$$

where  $P_o$  is the atmospheric pressure.

The *scaling time*,  $t_{sc}$ , is given by

$$t_{sc} = t_a \times f_t / Y^{-1/3}, \quad (2.16)$$

where  $f_t$ , the transmission factor for time, is given by

$$f_t = \left( \frac{\rho}{\rho_{\text{TNT}}} \right)^{1/3} \left( \frac{T}{T_{\text{TNT}}} \right)^{1/6} \quad (2.17)$$

and is expressed in terms of atmospheric pressure and temperature, where  $T$ ,  $T_{\text{TNT}}$  = actual and TNT temperatures, respectively  $Y$  = weapon yield,  $W$ .

The *direct impulse/impact scaling* per unit area is written as

$$F_t(t)/\text{unit area} = (\text{scaled impulse/area})(P_{so}/p_s(t_z/t_{sc})), \quad (2.18)$$

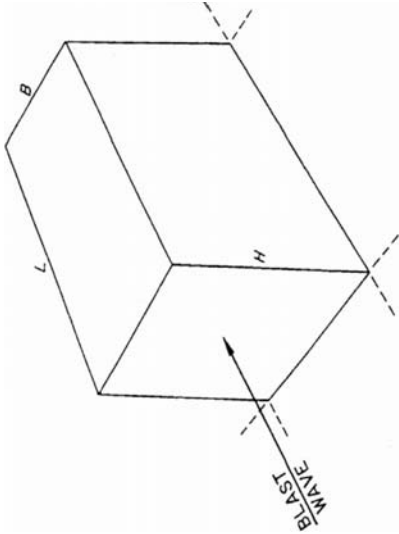
where  $P'_3$  = standard overpressure for reference explosion.

Transmission factors for distance and time for large explosions, with large path distances and variations in atmospheric pressure and temperature, can be written in integral form:

$$\text{scaled distance} = \frac{1}{Y^{1/3}} \int_{x_1}^{x_2} \left( \frac{\rho}{\rho_{\text{TNT}}} \right)^{1/3} dx \quad (2.19)$$

A transmission factor to conform to variations of pressures and temperatures will be given by

**Table 2.4.** A comparison of overpressures, time duration and impact loads for chemical and nuclear explosions

Chemical	Nuclear
$\frac{P_{so}}{P_o} = \frac{40.4x^2 + 810}{\sqrt{[(1 + 434x^2)(9.77x^2)(1 + 0.55x^2)']}}$	$\frac{P_{so}}{P_o} = \frac{5.12}{x^2} \times \sqrt{(1 + 0.00013x^2)}$
$\frac{t_d}{Y^{1/3}} = \frac{990 + 4.65 \times 10^5 x^{10}}{(1 + 125 \times 10^3 x^3)(1 + 6.1x^6)} \times \frac{1}{\sqrt{(1 + 0.02x^2)}}$	$\frac{t_d}{Y^{1/3}} = (200\sqrt{1 + 1 \times 10^{-6} x^3})(1/Z)$
$F - 1(t)/\text{unit area} = \frac{0.7}{x^2} \times \frac{2}{\sqrt{(1 + 360x^4)}}$	$Z = \sqrt{(1 + 0.025x)} \left[ \sqrt[6]{(1 + 5.25 \times 10^{-13} x^5)} \times \sqrt{(1 + 2 \times 10^{-5} x)} \right]$
$F - 1(t)/\text{unit area} = \frac{0.92}{x^3} \times \frac{2}{\sqrt[3]{(1 + 0.135x^3)}}$	$F - 1(t)/\text{unit area} = \frac{0.92}{x^3} \times \frac{2}{\sqrt[3]{(1 + 0.135x^3)}}$
$t_d$ = duration time in seconds for a distance = 0.7 $x$ = distance in m	where
<i>Example</i> Transmission factor for a distance = 0.7 Energy release = 100 kg TNT at a height of 12 000 m Atmospheric pressure = 260 mbar A point is 15 m away Scaled distance = $0.7(15/100^{1/3}) \approx 2.30$ Peak overpressure ratio = 1.51 Transmission factor = 0.615 Scaled duration = 1.32 ms Actual duration = $100^{1/3}(1.32/0.615) = 9.97$ ms Overpressure = $1.52 \times 260 = 390$ mbars = 0.39 bars	

$\bar{f}_d$  = transmission factor for distance

$$\bar{f}_d = \frac{1}{x} \int_{x_1}^{x_2} \left( \frac{\rho}{\rho_{\text{TNT}}} \right)^{1/3} dx \quad (2.20)$$

where  $x$  represents the actual distance. Similarly, the transmission for time is given by

$$\bar{f}_d = \frac{1}{x} \int_{x_1}^{x_2} \left( \frac{\rho}{\rho_{\text{TNT}}} \right)^{1/3} \left( \frac{T}{T_{\text{TNT}}} \right)^{1/2} dx \quad (2.21)$$

The subjects of open air, underground and underwater explosions are fully discussed under different headings in this chapter. The above elements are common to all of them.

### 2.2.5 Explosions in Air

Explosion characteristics, including duration, are based on the sudden release of energy. An explosion maybe due to nuclear detonation, explosives, gas or dust. As stated, the magnitude of an explosion in relative values is known as the explosive yield. One generally accepted standard is the energy released in an explosion of TNT (symmetrical 2,4,6-trinitrotoluene). As stated earlier, the front of the shock wave is quite steep and, as a result, the pressure may be treated as instantaneous. The dynamic load is then characterized by a rapidly reached peak value which decreases as the blast wave decays. The net effect of the load depends on the structure of the blast wave and on the geometry and construction of the structure. The basic relationship for such a blast wave having a steep front is given by Rankine-Hugonist, and is based on the conservation of mass, energy and momentum at the shock front. Using Fig. 2.13 and the above conditions together with the equation of state for air, the blast wave pressure is written as

$$\frac{U}{v_s} = \left( 1 + \frac{6 P_{\text{so}}}{7 P_a} \right)^{1/2} \quad (2.22)$$

$$\frac{u}{v_s} = \frac{5}{7} \frac{p_{\text{so}}}{p_a} \left( 1 + \frac{6 P_{\text{so}}}{7 P_o} \right)^{-1/2} \quad (2.23)$$

$$\frac{\rho}{\rho_a} = \frac{7 + 6P_{\text{so}}/P_o}{7 + P_{\text{so}}/P_o} \quad (2.24)$$

$$\frac{p_r}{p_{\text{so}}} = 2 \frac{7P_o + 4P_{\text{so}}}{7P_o + P_{\text{so}}} \quad (2.25)$$

$$\frac{q}{p_{\text{so}}} = \frac{5}{2} \frac{P_{\text{so}}}{7P_o + P_{\text{so}}} \quad (2.26)$$

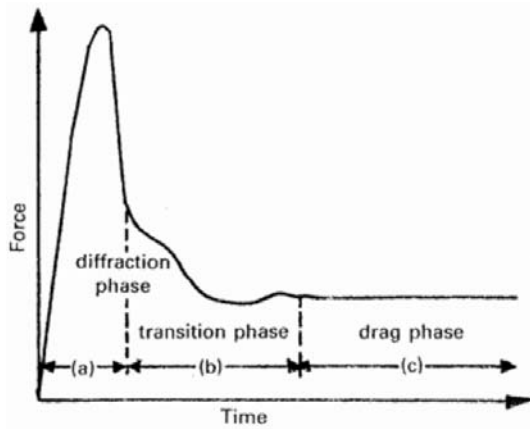


Fig. 2.8. Force-time history

$$\left(\frac{v_{so}}{v_s}\right)^2 = \frac{(P_{so} + P_a)(P_{so} + 7P_o)}{6P_{so} + 7P_o} \quad (2.27)$$

$$M^2 = \left(\frac{u}{v_{so}}\right)^2 = \frac{25}{7} \frac{P_{so}^2}{(P_{so} + P_o)(P_{so} + 7P_o)} \quad (2.28)$$

$$\frac{\bar{R}}{\bar{R}_a} = 0.727 P_{so}/P_o \quad (2.29)$$

$$\frac{P_r}{q_{do}} = \frac{4}{5} (4 + 7P_o/P_{so}) \quad (2.30)$$

where

$v_{so}$  = speed of sound in the air behind the shock front

$v_s$  = speed of sound in ambient air

$M$  = Mach number

$P_o$  = pressure of ambient air

$P_{so}$  = overpressure

$P_r$  = reflected pressure

$q_{do}$  = dynamic pressure =  $1/2 \rho u^2$

$\bar{R}$  = Reynolds number per foot (flow behind shock front)

$\bar{R}_a$  = Reynolds number per foot for ambient air sea level ( $6.89 \times 10^6$ )

$u$  = particle velocity of flow behind the shock front

$U$  = shock front velocity

$\rho$  = density of air behind shock front

$\rho_a$  = density of ambient air

In general the force-time relation given in Fig. 2.8 represents a true picture which involves diffraction transition and drag phases.

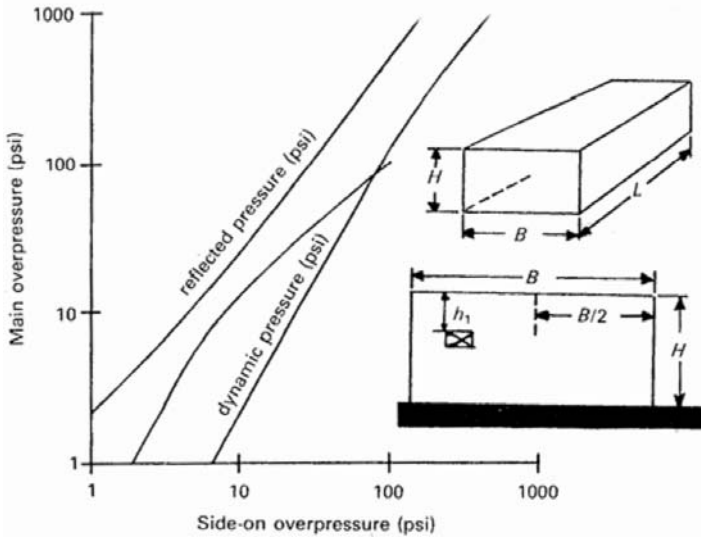


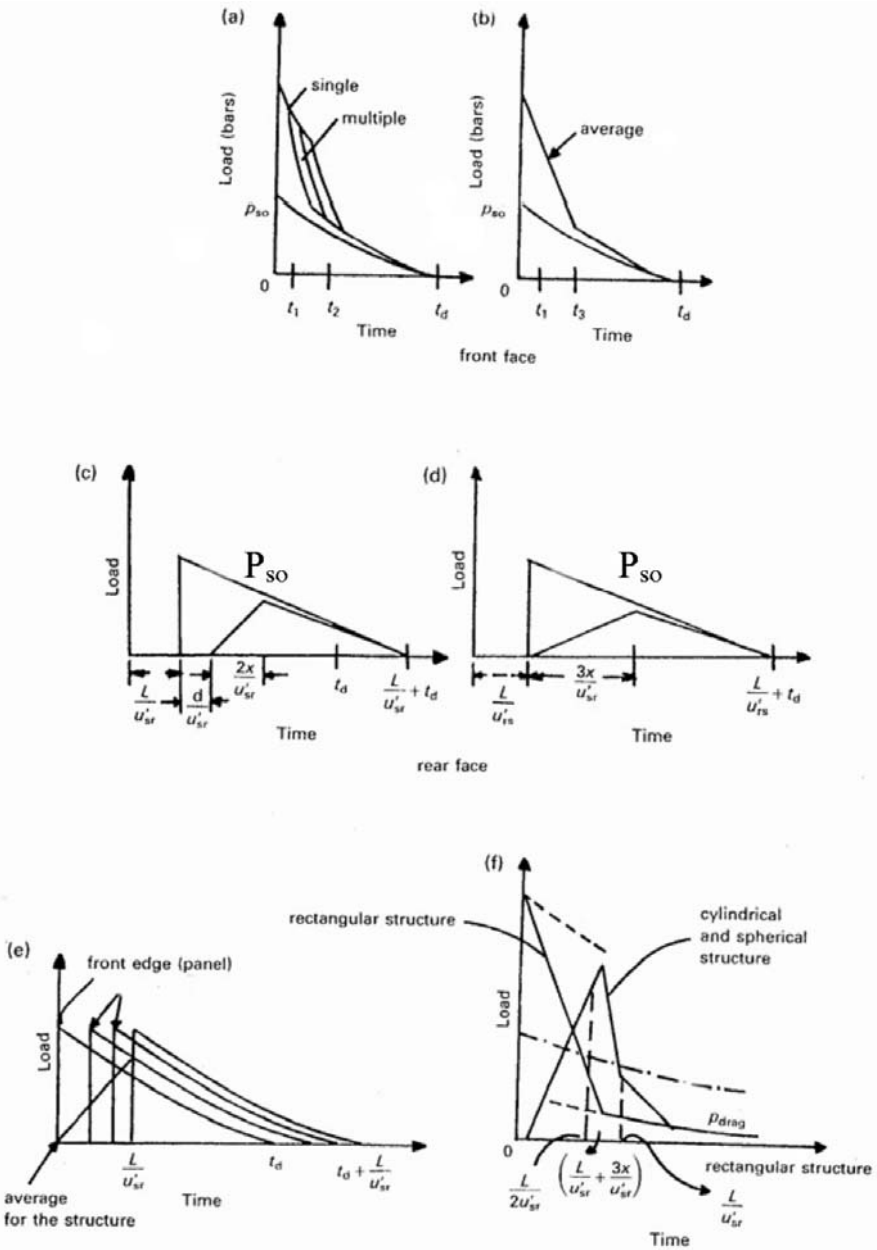
Fig. 2.9. Overpressure  $P_{SO}$  versus  $P_r$ ,  $M$ , and  $q_{do}$  for a building

Figure 2.9 shows reflected pressure, dynamic pressure and Mach number for side-on overpressure. When the blast wave is vertical and strikes the front face of the structure, normal reflection occurs and the entire facade of the building or structure is instantly subjected to the reflected overpressure,  $P_{ro}$ , which is greater than  $P_{so}$ , the overpressure in the immediate surroundings. As a result, the blast air flows from the region of high pressure to the one of low pressure, forming a rarefaction wave with a velocity  $u_{rr}$  over the front of the structure. It then progresses inward from the edges of the structure, moving with a velocity  $v_s$  in the reflected medium. This speed varies with time as the blast wave decays. For example, as shown in Fig. 2.9 if one takes a small panel of a structure, the wave varies at this panel with a corresponding time  $h_1/u_{rr}$ , where  $h_1$  is the distance from the top to that panel and  $u_{rr}$  is the rarefaction velocity. Assuming this time is  $t_1$ , the relieving time,  $t_r$ , is about twice that required for the sound wave, which is  $t_2 - t_1 = 2x/u_{rr}$ , where  $t_2$  is the forward time and  $x$  is the distance through which the pressure relief is obtained for the length of the structure,  $L$ , width,  $B$ , and height,  $H$ . Figure 2.10 gives load distributions on various faces against time. The peak diffraction pressure,  $P_{df}$ , and peak drag load,  $P_d$ , are given by

$$P_{df} = P_r A \tag{2.31}$$

$$P_d = P_D C_D A \tag{2.32}$$

where  $A$  is the projected area,  $C_D$  is the drag coefficient,  $P_r$  is the reflected pressure and  $P_D$  is the dynamic pressure  $\approx P_{so}$ .



**Fig. 2.10.** Load-time relationships for blasts in open air. (a) Several panels; (b) average for the structure; (c) one panel; (d) average for the rear face; (e) side or top face; (f) drag type loads



The blast wind from an explosion exerts loads on structures which are quite similar to those developed by natural winds. Nevertheless, these wind load surfaces are transient in nature and of considerably greater magnitude than those developed by conventional winds."The drag coefficient is also defined as

$$C_D = \text{drag energy/kinetic energy} = (P_d/\rho)/\frac{1}{2}u^2 \quad (2.33)$$

For an ideal gas explosion in air

$$\rho = \text{density} = p_a/RT \quad (2.34)$$

where  $R$  is the gas constant,  $T$  is temperature,  $P_d$  is the drag load and  $P_o$  is the pressure. The value of  $R$  is equal to 287 J/kg-K.

The value of  $C_D$  is also written in terms of Mach numbers as

$$C_D = 2 P_d/k_r M^2 P_o \quad (2.35)$$

The value of  $P_d$  is then written as

$$P_d = \frac{1}{2} C_D \rho u^2 = \frac{1}{2} k_r M^2 C_D p_a \quad (2.36)$$

where

$$k_r = \text{heat capacity ratio} = C_p/C_v \approx 1.4$$

$$C_p = \text{specific heat capacity at constant pressure}$$

$$C_v = \text{specific heat capacity at constant volume}$$

The Mach number may be written as

$$M = u/(kRT)^{1/2} \quad (2.37)$$

An individual small panel experiences load from an explosion when the shock front has traversed the distance  $L$ , the entire length of the structure, and a compression wave has travelled a distance  $h_r$  from the near edge into the panel. The time for the shock will be  $L/u'_{sr}$ , where  $u'_{sr}$  is the speed of the shock, a value close to  $U$ . After these times the pressure on the panel increases and becomes instantaneous pressure on the rear face equal to  $P_{\text{stag}} - P_{\text{drag}}$ . Figure 2.10c and d show the load-time function for the rear face for a small panel and an average for the entire rear face. Similarly, for the panels along the side or top of a structure, ignoring reflection and  $p_{\text{stag}}$  (stagnation), the overpressure diagram is as shown in Fig. 2.10. Figure 2.10f illustrates dynamic drag type loading.

## 2.2.6 The Impulse of the Incident Pressure

The impulse of the incident pressures associated with the blast wave is the integrated area under the pressure-time curve. Consequently, the positive phase impulse,  $i_s$ , is defined as follows:

$$\begin{aligned}
 i_s &= \int_{t_a}^{t_a+t_o} P(t) dt \\
 &= cP_{so}t_o
 \end{aligned}
 \tag{2.38}$$

where  $P(t)$  represents the pressure–time relationship;  $P_{SO}$  is the peak incident overpressure;  $t_o$  is the duration of positive phase;  $t_a$  is the blast wave arrival time; and  $c$  is a value between 0.2 and 0.5 depending on the equation used to describe the variation of pressure with time  $P(t)$ .

As stated earlier the blast wave propagates through the atmosphere, the air behind the shock front is moving outward at lower velocity. The velocity of the air particles, and hence the wind pressure, depends on the peak overpressure of the blast wave. This latter velocity of air is associated with the *dynamic (blast wind) pressure*,  $q$ . For typical conditions, standard relationships have been established between the peak incident pressure,  $P_{so}$ , the peak dynamic pressure,  $q_o$ , the wind velocity, and the air density behind the shock front. These relationships state that the magnitude of the dynamic pressure, shock front velocity and air density are solely a function of the peak incident overpressure, and, hence, independent of the explosion size.

The net dynamic pressure on a structure is computed as the product of the dynamic pressure,  $q$ , and a drag coefficient,  $C_D$ . The drag coefficient depends on the geometry of the structure and its orientation relative to the direction of the wind produced by the dynamic pressure. For a rectangular building, the drag coefficient may be taken as +1.0. For the roof, front and rear walls, the drag coefficient is a function of the peak dynamic pressure and may vary from  $-0.4(q_o < 170 \text{ kPa})$  to  $-0.2(q_o > 350 \text{ kPa})$ .

The dynamic pressure  $q$  plays an important role in generating the blast loading.

### 2.2.7 Thickness of the Shock Front

The thickness of the shock wave is the ratio of the velocity jump between two points  $u_1$  and  $u_2$  divided by the maximum velocity gradient  $(du/dx)_{\max}$  in a specific zone. In terms of Mach number, the thickness  $t_{sh}$  of the shock front using the Rankine-Hugonist equation is given by

$$t_{sh} = [(11 + 7M)/\rho(M - 1)]10^{-8} \tag{2.39}$$

### 2.2.8 Evaluation of Stagnation Pressure, Stagnation, and Post-shock Temperatures

The stagnation pressure, is generally, is given in (2.40) in terms of ambient pressure and is now defined in terms of the velocity of sound,  $v_s$ , and  $v_{so}$ , which is the speed of sound after the shock front. The value of  $p_{stag}$  is given by

$$p_{stag} = p_2 \left[ 1 + \frac{(k-1)(v_{so}/v_s)^2}{2(T_2/T_a)} \right]^{k/k-1} \tag{2.40}$$

where

- $p_2$  = shock-generated pressure
- $T_2$  = shock-generated temperature
- $T_a$  = ambient temperature
- $v_{so}$  = blast-generated velocity

The temperature known as the blast stagnation temperature obeys the relationship

$$\frac{T_{stag}}{T_o} = \frac{T_2}{T_a} + \frac{1}{2}(k - 1) \left( \frac{v_{so}}{v_s} \right)^2 \tag{2.41}$$

The value of  $k$  is generally taken as 1.4. The post-shock temperature  $T_{ps}$  is given for  $k = 1.4$  by

$$\frac{T_{ps}}{T_a} = \left( \frac{v_{so}}{v_s} \right)^2 = \frac{(p_2/p_a + 6)(p_2/p_a)^{5/7}}{6(p_2/p_a) + 1} \tag{2.42}$$

where  $T_{ps}$  is the temperature under post-shock.

Equations (2.40) to (2.42) are extremely useful when explosion occurs and at the same time generates temperature leading to fire.

### 2.2.9 Oblique Shock

A shock wave may occur in a plane that is oriented at an angle  $\theta$  to the direction of the blast windflow. Let that velocity be  $v_{so}$ ; its components are  $v_1$  and  $v_2$  as shown in Fig. 2.11. In this oblique shock phenomenon, the velocity vectors are related in terms of the angle  $\theta$  and the angle  $\alpha$  of the shock plane with respect to the on-coming stream by

$$v_{so2}/v_2 = \tan(\alpha - \theta) \tag{2.43}$$

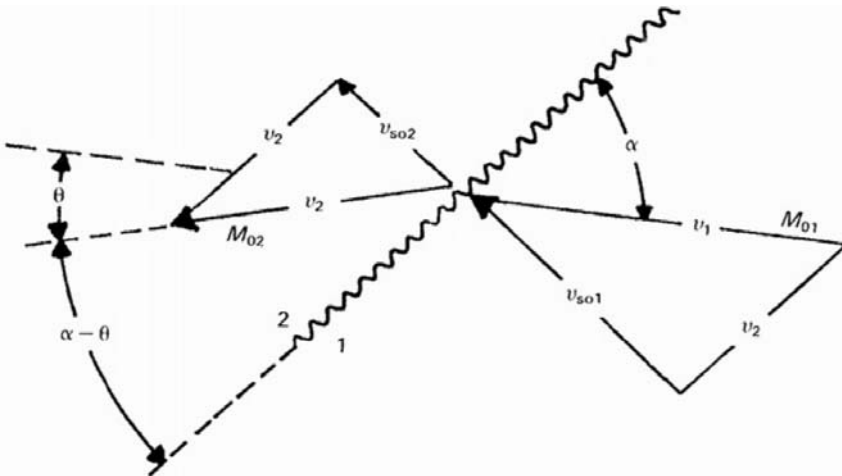


Fig. 2.11. Oblique shock

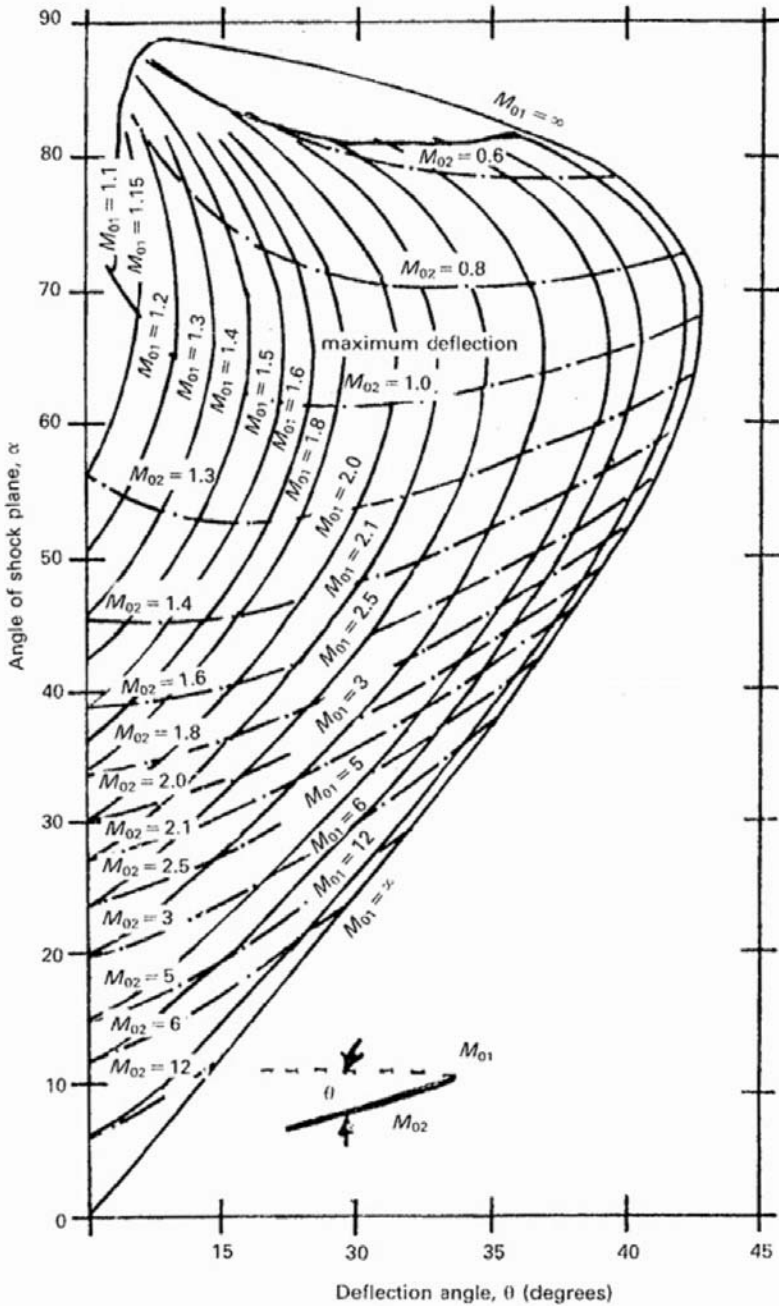


Fig. 2.12. Numerical relationships of  $\theta$  and  $\alpha$  for given values of  $M_{01}$  and  $M_{02}$

where  $v_{so2}$  and  $v_2$  are the velocities after shock of the normal and parallel components, respectively. The Mach number is given by

$$\begin{aligned} M_1 \text{ (normal to the shock plane)} &= v_{so1} \sin \alpha / v_{s1} \\ &= M_{o1} \sin \alpha \end{aligned} \tag{2.44}$$

For the downstream component  $v_{so2}$ :

$$\begin{aligned} M_2 \text{ (normal to the shock plane)} &= v_{so2} \sin(\alpha - \theta) / v_{s2} \\ &= v_{so2} / v_s \\ &= M_{o2} \sin \alpha (\alpha - \theta) \end{aligned} \tag{2.45}$$

where  $v_{s1}$  and  $v_{s2}$  are shock velocities in planes 1 and 2.

The following equations may be derived along the same lines as (2.40) to (2.42):

$$p_2 / p_a = \frac{k M_{o1}^2 \sin^2 \alpha - \frac{k-1}{2}}{\frac{k+1}{2}} \tag{2.46}$$

For the temperature and the speed-of-sound effects,  $T_2 / T_a$  is given by

$$T_2 / T_a = (v_{s2} / v_{s1})^2 = \frac{1 + \frac{k-1}{2} (M_{o1}^2 \sin^2 \alpha) \left( k M_{o1}^2 \sin^2 \alpha - \frac{k-1}{2} \right)}{\left( \frac{k+1}{2} \right)^2 M_{o1}^2 \sin^2 \alpha} \tag{2.47}$$

The Mach numbers of the upstream and downstream velocities, before and after the shock, are related by

$$[M_{o2} \sin(\beta - \theta)]^2 = \frac{2 + (k-1) M_{o1}^2 \sin^2 a}{2k M_{o1}^2 \sin^2 a - (k-1)} \tag{2.47a}$$

The values of  $p_a$  and  $T_a$  are in plane 1, i.e.,  $P_o = P_2$  and  $T_a = T_1$ . The value of  $k$  is generally taken as 1.4.

The relation between the angle of the shock plane,  $a$ , and the angle of deflection  $\theta$  may be found from

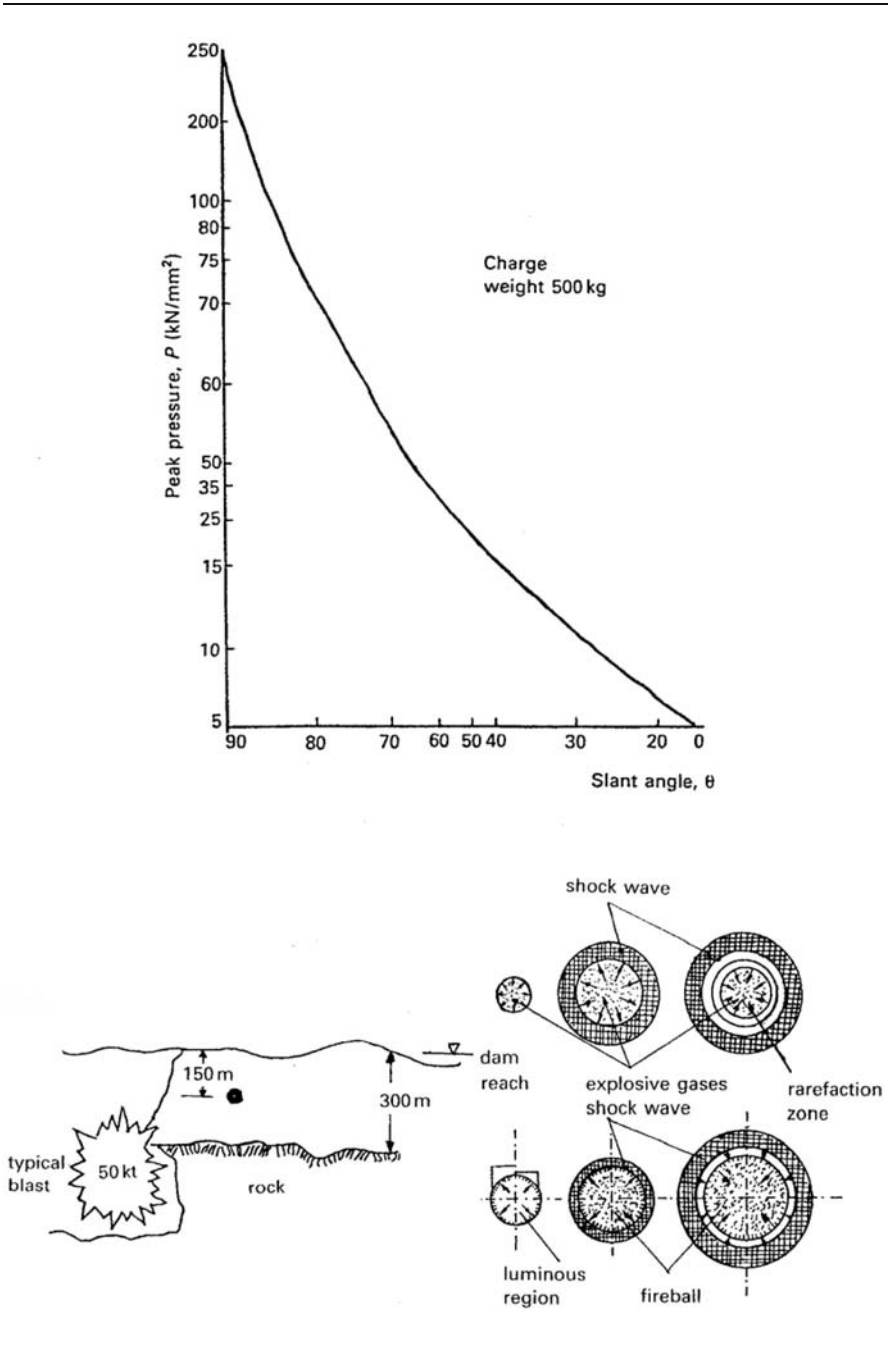
$$\frac{\tan(a - \theta)}{\tan a} = \frac{2 + (k-1) M_{o1}^2 \sin^2 a}{(k+1) M_{o1}^2 \sin^2 a} \tag{2.48}$$

The maximum deflection can easily be obtained from Fig. 2.12 for a given Mach number. Using the manipulated version of (5.47), the value of  $\alpha$  is computed as

$$\begin{aligned} \sin^2 a &= \frac{1}{4k M_{o1}^2} \times (K + 1) M_{o1}^2 - 4 \\ &\quad + \sqrt{\{(k+1) [(k+1) M_{o1}^4 + 8(k-1) M_{o1}^2 + 16]\}} \end{aligned} \tag{2.49}$$

A typical example for a charge weight of 500 kg versus slant angle is given on Plate 2.1.

Plate 2.1. Shock wave peak pressure versus slant range



## 2.2.10 Shock Reflection

### 2.2.10.1 Normal Shock Reflection

The reflected shock front exhibits the same particle velocity as that of the incident shock. Nevertheless, the characteristics of the two shocks moving through different media are different. In a similar manner, the particle velocity ratio  $v_{so}/v_{sol}$  is related to  $P_2/P_o = P_r/P_2$  such that

$$(v_{so}/v_{sol})^2 = \frac{\left(\frac{2}{k}\right) \left(\frac{P_r}{P_2} - 1\right)^2}{(k+1) \left(\frac{P_r}{P_2}\right) + (k-1)} = \left(\frac{v_{so}}{v_{sol}}\right) \left(\frac{T_2}{T_a}\right) \quad (2.50)$$

where  $P_r$  is the absolute pressure generated in the reflected shock.

Equation (2.50) can easily be written in terms of  $P_r/P_2$  as

$$P_r/P_2 = \frac{(3k-1)(P_2/P_1) - (k-1)}{(k-1)(P_2/P_1) + (k+1)} \quad (2.51)$$

where  $P_1$  is the pressure of the unshocked air  $\approx P_o$ .

The Mach number,  $M_r$ , for the reflected shock can similarly be related to the Mach number for the incident shock,  $M_{o1}$ , by

$$M_r^2 = \frac{2kM_{o1}^2 - (k-1)}{(k-1)M_{o1}^2 + 2} \quad (2.52)$$

The relationship between  $P_r$  and  $P_1$ , the incident shock, and the Mach number can be written in the following form:

$$\begin{aligned} P_r/P_1 &= \frac{(P_2/P_1)[(3k-1)(P_2/P_1) - (k-1)]}{(k-1)(P_2/P_1) + (k+1)} \\ &= \frac{[(3k-1)M_1^2 - 2(k-1)][2kM_1^2 - (k-1)]}{(k^2-1)M_{o1}^2 + 2(k+1)} \end{aligned} \quad (2.53)$$

Using  $k = 1.4$ , (2.51) to (2.53) can be modified. For example, (2.52) becomes

$$M_r^2 = \frac{7M_{o1}^2 - 1}{M_{o1}^2 + 5} \quad (2.54)$$

and (2.52) becomes

$$\frac{P_r}{P_1} = \frac{(4M_{o1}^2 - 1)(7M_{o1}^2 - 1)}{3(M_{o1}^2 + 5)} \quad (2.55)$$

The temperature after the shock is greater than the ambient temperature  $T_1 = T_a$ . The reflected value  $T_r$ , can easily be derived after algebraic manipulation similar to (2.42).

$$T_r/T_1 = T_a = \left(\frac{v_{sr}}{T_a}\right)^2 = \frac{\left[(k-1) \left(\frac{P_2}{P_1}\right) + 1\right] \left[3(k-1) \left(\frac{P_2}{P_1}\right) - (k-1)\right]}{k \left[(k+1) \left(\frac{P_2}{P_1}\right) + (k-1)\right]} \quad (2.56)$$

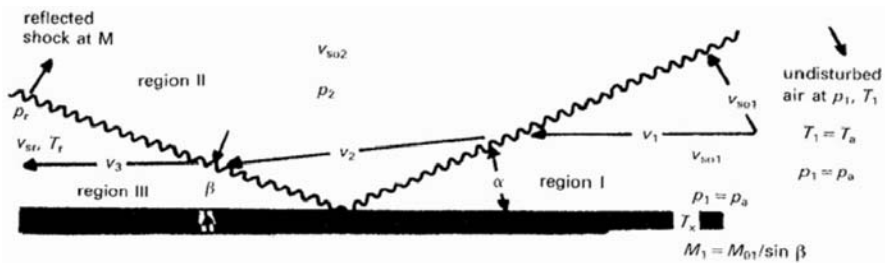


Fig. 2.13. Oblique reflection of shock waves

The reflection coefficient is defined by

$$\begin{aligned}
 C_r &= \frac{P_r - P_1}{P_2 - P_1} = \frac{\text{reflected overpressure}}{\text{overpressure in the incident shock}} \\
 &= \frac{(3k - 1)(P_2/P_1) + (k + 1)}{(k - 1)(P_2/P_1) + (k + 1)} \tag{2.57} \\
 &= \frac{(3k - 1)M_{o1}^2 + (3 - k)}{(k - 1)M_{o1}^2 + 2}
 \end{aligned}$$

For  $k = 1.4$

$$C_r = \frac{8M_{o1}^2 + 4}{M_{o1}^2 + 5} \tag{2.58}$$

### 2.2.11 Oblique Reflection

Figure 2.13 illustrates the basic concept of oblique reflection. An incidental shock at  $M_{o1}$  with an incident angle of  $\alpha$  causes a corresponding reflect shock in Mach number:

$$M_r = M_{o1} \sin \alpha \tag{2.59}$$

The angle  $\beta$  of this reflected shock is given by

$$\beta = (\alpha - \theta), \tag{2.60}$$

where  $\theta$  is the deflection angle. From (2.54), the value of  $P_r/P_1$  becomes

$$P_r/P_1 = (7M_r^2 - 1)(7M_{o1}^2 - 1) - 36 \tag{2.61}$$

The reflection coefficient is derived using (2.56) and (2.61) with  $k = 1.4$ :

$$\begin{aligned}
 C_r &= \frac{P_r - P_1}{P_2 - P_1} \\
 &= \frac{(7M_r^2 - 1)(7M_{o1}^2 - 1) - 36}{42(M_{o1}^2 - 1)} \tag{2.62}
 \end{aligned}$$

The Mach number  $M_{o2}$  in region II for  $k = 1.4$  will be

$$[M_{o2} \sin(\alpha - \theta)]^2 = \frac{5 + M_{o1}^2}{7M_{o1}^2 - 1} \tag{2.63}$$



## 2.3 Internal Blast Load Modelling and Structural Response of Buildings

Plate 2.2 describes in logical and mathematical terms the modelling of the ternal blast.

The response of a building to a large explosion occurs in some distinct phases which, in turn, depend on the building layout, various materials itsed, design and fixing of structural components, bomb yield, its range and duration, etc. These are some of the variables. A number of buildings subjected to large explosions have been examined and the following are the common features observed.

### Mode (1)

As the blast wave encounters the nearest external wall of the building, windows are found shattered and walls and columns are deflected under reflected pressure.

### Mode (2)

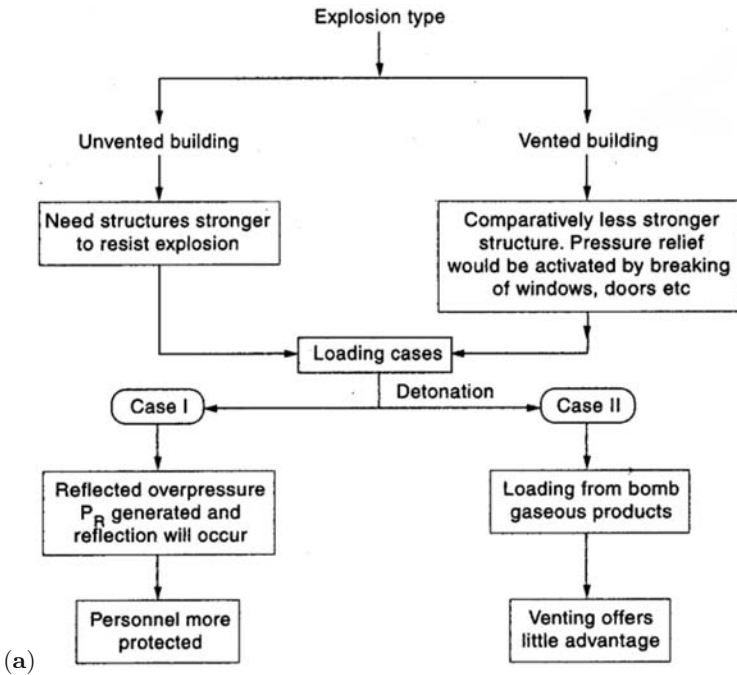
When the blast wave expands and finally diffracts around the building, it exerts an overpressure on the roof, side walls and on the walls of the far side. Not knowing the exact location of the bomb, each face of the building must be designed for the worst case including the explosion normal to the face. The internal pressure penetrating through openings, generally, is found to exert a downward arid an upward pressure on floor slabs. All columns, beams and slabs must be designed or checked for these pressures. In the design, if it is possible, the number of openings must be reduced and where openings and windows and their sizes are known, a provision for blast-resistant glazing would be needed.

### Mode (3)

The frame of the building is the last structure to respond to the blast load. In precast concrete buildings designers are particularly aware that in tlfeevent of explosion the buildings should not behave as a 'house of cards'. Where large panel construction is used, this problem becomes acute. The progressive failure'Iequence is based on initial cricks, loss of support and failure progression due to debris loading. In order to prevent such failure, connections and special tension, compression reinforcement and shear and bending steel should be provided.

**Plate 2.2** Explosion type

When an explosion occurs within a structure such as buildings, the requirement is slightly different than the one at the outside. The following chart explains the requirement:



The incident and reflected waves are approximated as triangular pressure pulses (Fig. b) with a pressure-time history can be written as

$$P_R(T) = P_R \left( 1 - \frac{t}{T_R} \right) \tag{a}$$

$$i_R = \frac{1}{2} T_R P_R \tag{b}$$

$$T_R = \frac{2i_R}{P_R} \tag{c}$$

$$P_{R1} + P_{R2} + P_{R3} \approx 1.75 P_{R1} = P_{RT} \tag{d}$$

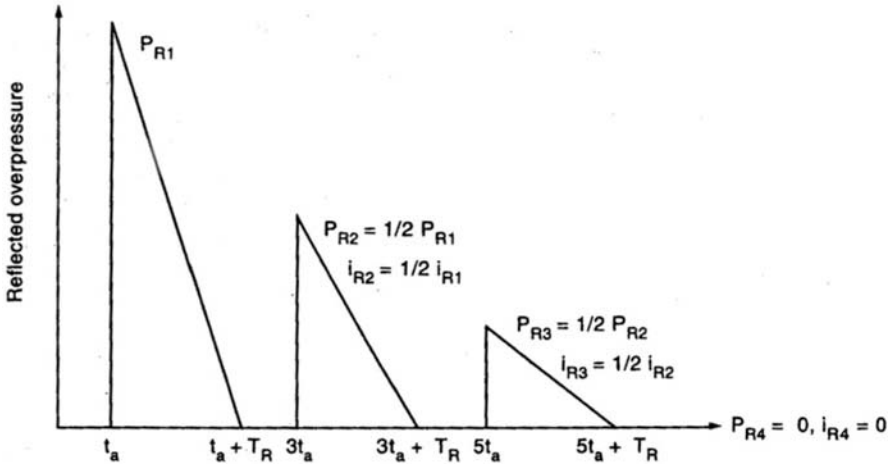
$$i_{R1} + i_{R2} + i_{R3} \approx 1.75 i_{R1} = i_{RT} \tag{e}$$

Reverberation time ( $RT$ ) = time delay between each blast wave arriving at the inner face of the building  
 = constant when  $t_R = 2t_a$  (f)

where

$t_a$  = arrival time at first blast wave at the inner reflecting surface

Reverberation phase =  $(St_a + T_R)$



(b) Internal blast wave propagation (Baker et al. [1.12])

The pressure-time history for the internal blast loading of the bomb gaseous pressure decay is given as

The value of

$$P(t) = (P_{Qs} + P_o)e^{-2.13\tau}$$

where

$$\tau = \frac{\alpha_e A_s t \alpha_0}{V} \tag{g}$$

$$\alpha_e = \frac{\text{vent area}}{\text{wall area}} \tag{h}$$

$t_{\max}$  = blow down time

$$i_g = \text{bomb gas impulse} = \int_0^{t_{\max}} [P(t) - P_o] dt \tag{i}$$

$$= \frac{P_{Qs} + P_o}{2.13 \alpha_e \frac{A_s \alpha_0}{V}} \left[ 1 - e^{-\{2.13 \alpha_e A_s \alpha_0 / V\} t_{\max}} \right] - P_o t_{\max}$$

$A_s$  = total internal surface area

$V$  = volume of the structural part subject to blast wave

$\alpha_0$  = speed of sound at ambient condition

$t$  = time

Notation:

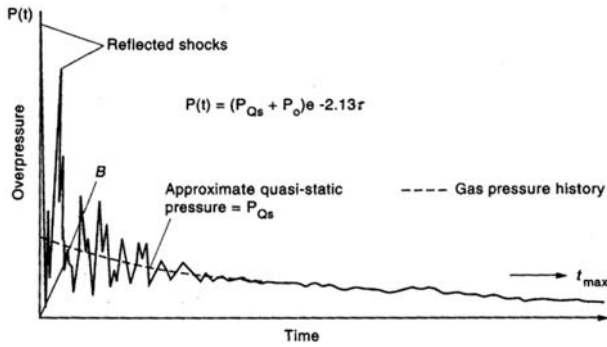
$P_{Qs}$  = quasi-static pressure

$P_o$  = atmospheric pressure

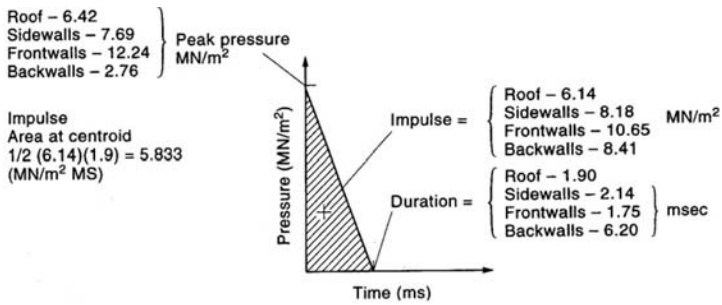
$P_a$  = pressure at ambient temperature

$P_i = P_{Qs} + P_o$

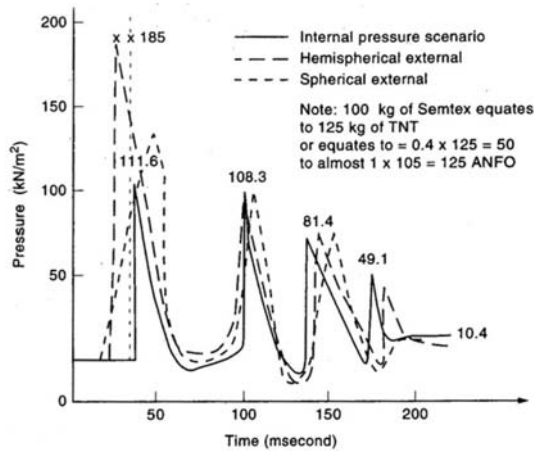
$i_g$  = bomb gas impulse



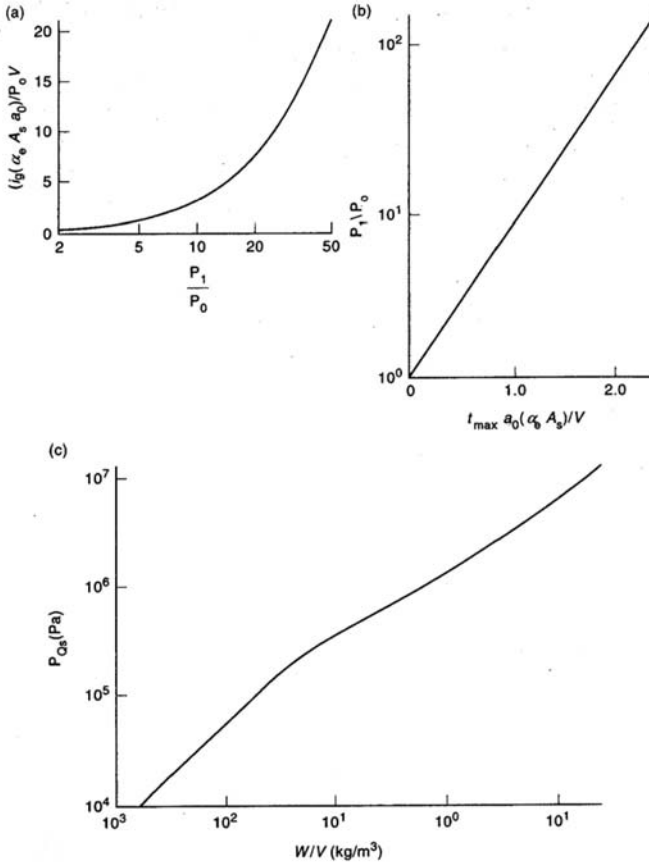
(c) Typical pressure-time profile for internal blast loading of a partially-vented structure (US Army Corp of Engineers, TM5-1300)



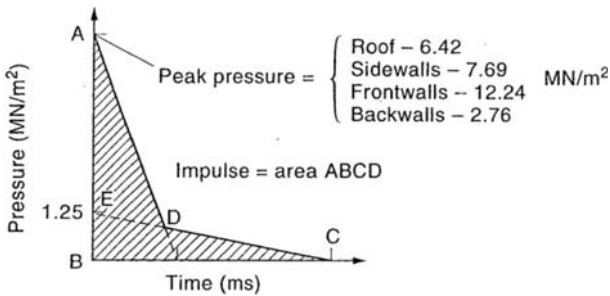
(d) Shock overpressure



(e) Load-time function for 100 kg of Semtex



(f) Prediction of gas pressure impulse ( $i_g$ ), 'blowdown' time ( $t_{max}$ ), and peak quasi-static pressure ( $P_{Qs}$ ) (Baker et al. [1.12])



(g) Bilinear blast loading

## References

- [2.1] American Society of Civil Engineers (1985) Design of structures to resist nuclear weapons effects. ASCE Manuals and Reports on Engineering Practice 42, New York, ASCE
- [2.2] American Society of Civil Engineers (1961) Design of structures to resist nuclear weapons effects. Manuals of Engineering Practice 42, New York, ASCE
- [2.3] American Society of Civil Engineers. Research Council of the Performance of Structures (1975) A comparative study of structural response to explosion-induced ground motions. ASCE project 210.03/17.2.72-3, New York, ASCE
- [2.4] Tillotson E (1974) Earthquakes, explosions and the deep underground structure of the United Kingdom
- [2.5] Bangash MYH (1993) Impact and explosion: analysis and design. Oxford: Blackwell Scientific Publications
- [2.6] SCI (1992) Computerised analysis tools for assessing the response of structures subjected to blast loading, London, HMSO
- [2.7] SCI (1992) The prediction of the pressure loading on structures resulting from an explosion. London, HMSO
- [2.8] SCI (1992) Interim guidance notes for the design and protection of topside structures against explosion and fire. Ascot, SCI
- [2.9] Singhal, AC and others (1994) Simulation of blast pressure on flexible panel. ASCE Journal of Structural Engineering (SCI, Publication 112)
- [2.10] James RT and Partners (1993) How to minimise bomb damage. Architects Journal; ASCE Journal of Structural Engineering 120(7):2001–2020 (July 1994)
- [2.11] Smith PD, Hetherington JG (1994) Blast and ballistic loading of structures. Oxford: Butterworth-Heinemann Ltd.; Structural assessment of bomb damage for World Trade Center 1994. New York, ASCE, JPCF (Nov, 1994)
- [2.12] Dharaneepathy MV and others (1995) Critical distance for blast-resistant design; Computers and structures (1994) ASCE Journal of performance constructed facilities 8(4): 229–242 (Nov. 1994)
- [2.13] Batsanov SS (1994) Effects of explosions on materials: modification and synthesis under high-pressure shock compression. Springer-Verlag, New York; Computers and Structures 54(4):587–595 (1995 February 17)
- [2.14] I.Struct.E. (1978) Symposium on stability of low-rise buildings of hybrid construction. London, IstructE
- [2.15] I.Struct.E. (1978) Structural damage in buildings caused by gaseous explosions and other accidental loadings, 1971–1977. London. HMSO
- [2.16] Mainstone RJ and others (1995) Blast effects on buildings: design of buildings to optimize resistance to blast loading. London, Thomas Telford
- [2.17] Mays GC, Smith PD (eds.) (1995) The structural engineer's response to explosion damage. London, IstructE
- [2.18] ASCE (1961) Design of structures of resist nuclear weapons effects. New York, ASCE
- [2.19] ASCE (1998) Blast and fire engineering for topside structures – Phase 2: final summary report. Ascot, Steel Construction Institute

- [2.20] Selby CA, Burgan BA (1997) Methodology for estimating the explosion yield of incidents involving conventional or improvised explosives (SCI Publication 253)
- [2.21] Merrifield R, MacKenzie J (1998) Reinforced earth protective structures for industrial and military applications. Reinforced Earth Group (Paper from the 8th International Symposium on The Effects of Interactions of Munitions with Structures, Washington, DC, April 1997)
- [2.22] Bulson P (1984) Structures to resist the effects of accidental explosions. St. Louis, Missouri, U.S. Army AG Publications Center (Taken from lectures for projected course at MIT, Cambridge, Mass, Aug. 1984)
- [2.23] United States, Department of the Army and others (1998) Tunnel structures. Proc. of a Colloquium held in Stockholm 1998, Zurich, IABSE; 1984 reprint of 1969 edition. Army Technical Manual TM 5-1300; Navy publication NAVFAC P-397; Air Force Manual AFM 88-22
- [2.24] IABSE (1998) Eurocode 1: Basis of design and actions on structures – Part 2-7: Actions on structures – accidental actions due to impact of explosions. Brussels, CEN (IABSE Report 78)
- [2.25] European Committee for Standardization (1998) Structures under shock and impact VI. Papers from the 6th International Conference held in Cambridge, England July 2000, Southampton, Boston, WIT Press,
- [2.26] Jones N, Brebbia CA (2000) Restoration of some bomb damaged marine structures
- [2.27] Bangash MYH (1990) Prototype building structures: analysis and design. London, Thomas Telford
- [2.28] Braid JG (1999) The effect of tamped explosions on the side walls of underground structures. CUPPD ICE Library
- [2.29] Gulvanessian J, Menzies JB
- [2.30] United States. Army Corps of Engineers (1990) Explosions on domestic structures. Part 1: The relief of gas and vapour explosions in domestic structures. Part 2: The relationship between containment characteristics and gaseous reactions; and discussion. London, IstructE
- [2.31] Hinman EE (1995) Guidance on the design of domestic accommodation in load bearing brick work and block work to avoid collapse following an internal explosion. London
- [2.32] Hinman EE (1995) Piper Alpha technical investigation: Interim report, September 1988 + Annex D: photographs, London, Department of Energy; Fire Engineering 148(10): 14–15 (Oct. 1995)
- [2.33] Department of Energy (1998) Piper Alpha technical investigation: Further report. London, Department of Energy, December 1988
- [2.34] Department of Energy (1988) Structure response and damage produced by airblast from surface mining. Pittsburgh, U.S. Department of the Interior
- [2.35] Siskind, DE and others (1980) Protection of buildings against explosions. Report of Investigations 8485, The Steel Construction Institute

# 3 Fire and Buildings With and Without Explosion/Impact

## 3.1 Introduction

Fire is the primary cause of loss of life and property throughout the world. During the past two decades fire has damaged hundreds of thousands of structures. Significant advances have been made in controlling or mitigating the effects of fire. Various methods have been developed to protect buildings. New materials have been developed or invented. A considerable time is spent by various researchers on the development of mathematical models to simulate the behaviour of structural members in fire. This is possible only if one uses numerical and computer techniques. A large number of computer programs that calculate the fire resistance of structural members now exist. The input data for these computer programs require, apart from loading and fire density, thermal and mechanical properties of various building materials at elevated temperatures. In addition, the expected severity of building fires and temperature-time relations have also been developed. Most of these properties have been codified. The closet measures related to building design are probably those for the confinement of a fire. These measures include fire barriers capable of delaying or preventing spread of fire, dimensions and locations of buildings. All these measures are directly related to the detailed knowledge of the mechanics and severity of fire. It is, therefore, essential to outline some areas outside the domain of a structural engineer which he or she should be aware of. Some of these are described below:

- (a) Mechanics of fluids and building aerodynamics applicable to fire engineering.
- (b) Conduction of heat in solids.
- (c) Convection and radiation heat transfer.
- (d) Thermochemistry.
- (e) Chemical equilibrium and thermal decomposition.
- (f) Fire dynamics.
  - i. Flame height and fire plumes.
  - ii. Air entrainment into buoyant jet flames.
  - iii. Ceiling jet flows, vent flows and natural convection wall flows.
  - iv. Combustion conditions, and smouldering combustion.
  - v. Flammability limits and flaming ignition of solids.



- vi. Smoke production, smoke and heat venting.
- (g) Burning rates and calorimetry.
- (h) Compartment fire modelling and fire models for enclosures.
- (i) Stochastic models for fire growth.
- (j) Explosion protection.
- (k) Detection systems, automatic sprinkler systems.
- (l) Foam system and foam agents.

Within the non-structural analysis, structural analysts must be aware of hazard calculations, risk analysis and probability methods.

The main concern of the structural engineer is the properties of the various materials involved and the analytical tools available for the design of structural elements in fire. They are given later on in this text under various sections.

No matter how many precautions are taken to improve the fire safety design of buildings they will not be complete without sufficient availability of training in professional education and practice. The main objective is to prepare sufficient manuals of awareness and to transfer knowledge of fire safety of buildings to the building design practitioners by way of courses and seminars at various institutions. Architects and engineers must place importance on fire safety provisions and allow funds for training facilities.

Building codes are different in every country. In a prescriptive code environment, designers have little choice but to follow a book of rules. With more modern performance-based codes, designers have unlimited freedom to design innovative solutions to fire safety problems, provided that the required levels of safety and performance can be demonstrated to the satisfaction of the approving authorities. Whatever type of code is used, design for fire safety will include a combination of reducing the probability of ignition, controlling the spread of fire and smoke, allowing for occupant escape and fire-fighter access, and preventing structural collapse. One framework for demonstrating fire safety is scenario analysis. In this method a number of “worst case” scenarios are analysed. In each scenario the likely growth and spread of fire and smoke is compared with detection and occupant movement, taking into account all the active and passive fire protection features and structural behaviour, to establish whether the performance requirements have been satisfied. As stated earlier, fire safety objectives are usually met with a combination of active and passive fire protection systems. Active systems control the fire or fire effects by some action taken by a person or an automatic device. Passive systems control the fire or fire effects by systems that are built into the structure or fabric of the building.

The objectives for providing fire resistance need to be established before making any design, recognizing that fire resistance is only one component of the overall fire safety strategy. Structural elements can be provided with fire resistance for controlling the spread of fire or to preventing structural collapse, or both, depending on their function. The term fire design time

is not precisely defined. Depending on the importance of the building, the requirements of the owner, and the consequences of a structural collapse or spread of fire, the fire design time will be selected by the designer as one of the following:

- (1) the time required for occupants to escape from the building,
- (2) the time for fire-fighters to carry out rescue activities.

## 3.2 Loadings and Restraints

The load-bearing structures must be subjected to the characteristic dead loads  $G_K$  and the characteristic imposed loads  $Q_K$  having the same values as for normal design. The partial safety factors for dead and imposed loads according to BS 8110 are 1.4 and 1.6 respectively. In case of fire they are 1.05 for dead load and 1.0 for composed load. In major analysis, it is essential to impose temperature load due to fire. Where dynamic analysis is performed, the fire load will be treated as an accidental overload. The American Society of Civil Engineers' Standard ASCE7-93 is not explicit about such a load, as fire is not treated as a permanent load. The best combination is based on the total of the combined effects multiplied by a factor  $P_F$ :

$$P_F(L + L_r + *T) + D \quad (3.1)$$

where

$$P_F = 0.75 \text{ or } 0.66$$

\* $T$  = forces due to temperature changes, etc.

$L$  = live loads

$L_f$  = roof loads

$D$  = dead loads.

The other indication is to include a factored \* $T$ , i.e.,  $1.2*T$  in the above assessment of combined loads. The best combination will then be:

$$1.2D + 1.6L + 0.5L_T + 1.2*T \quad (3.2)$$

Where thermal properties of the structural materials are known, an approximate relationship has been by the Council of Tall Buildings as

$$L = t_f \sqrt{A_W A_T} \quad (3.3)$$

where

$L$  = total weight of fireload in kilograms

$t_f$  = fire resistance in minutes

$A_W$  = windowed area in square metres

$A_I$  = surface area of the enclosed walls and ceiling of the compartment or room containing the fire in square metres.

Generally the fire grading of buildings has been directly related to fire load per unit floor area. Fire loads for domestic, office and hospital buildings are considered as low, for shops and department stores as medium and for storage buildings as high. For modern buildings, based on recent surveys, an average of  $25 \text{ kg/m}^2$  ( $5.751 \text{ bf/ft}^2$ ) is used. The logical conclusion would be to keep full dead weight and reduced live load due to occupancy and its reduction in level and full load of the fire:

$$(P_F L + L_r + F_L) + l.2D \quad (3.4)$$

where  $F_L$  = fire load.

The BSI (British Standards Institute) in their draft code 96/540837 indicate that the fire load is influenced by duration and severity of fire and the fire load density is related to a number of different types of occupancy. The effective fire load density is expressed in  $\text{MJ/m}^2$  of the floor area as discussed above in other cases. It is suggested that it can also be expressed in terms of equivalent weight of wood as a function of floor area. Several methods may be used to establish the effective fire load in a room or a compartment:

- (a) direct measurement/assessment
- (b) statistical survey
- (c) use of characteristic fire load density.

*(a) Direct Measurement/Assessment*

Where the fire loading in the direct measurement is unlikely to change over the design life of the building, the fire load density may be estimated from a knowledge of the weight and calorific values of the contents.

The following expressions are adopted:

$$q_{ki} = \frac{\sum m_c H_c}{A_f} \quad (3.5)$$

where

$q_{ki}$  = fire load density of the compartment ( $\text{MJ/m}^2$ )

$m_c$  = total weights of each combustible material in the compartment (kg)

$H_c$  = calorific value of each combustible material ( $\text{MJ/kg}$ )

$A_f$  = total internal floor area of the compartment ( $\text{m}^2$ ).

In the case that wet or damped materials are present, the effective calorific value  $H_c$  is modified by:

$$H_c = H_u(l - 0.01M) - 0.025M \quad (3.6)$$

where

$H_c$  = effective calorific value of the wet material ( $\text{MJ/kg}$ )

$H_u$  = calorific value of the dry material ( $\text{MJ/kg}$ )

$M$  = moisture content (in % by dry weight).

Table 3.1 gives calorific values of typical materials.

**Table 3.1.** Calorific values of typical materials (Source: Eckert ERG and Drake RM (1972) Analysis of Heat and Mass Transfer, McGraw-Hill, New York. Reprinted by permission of McGraw-Hill, Inc.)

Metal	Thermal conductivity k, W/m × °C													
	$\rho$ , kg/m <sup>3</sup>	$c_p$ , KJ/kg × °C	k, W/m × °C	$\alpha$ , m <sup>2</sup> /s × 10 <sup>5</sup>	-100°C	0°C	100°C	200°C	300°C	400°C	600°C	800°C	1000°C	1200°C
Aluminium pure	2 707	0.896	204	8.418	215	202	206	215	228	249				
Lead	11 373	0.130	35	2.343	36.9	35.1	33.4	31.5	29.8					
Iron:														
Pure	7 897	0.452	73	2.034	87	73	67	62	55	48	36	35	36	36
Wrought iron														
0.5% C	7 849	0.46	59	1.626		59	57	52	48	45	33	33	33	33
Steel														
(C max ≈ 1.5%):														
Carbon steel														
C ≈ 0.5%	7 833	0.465	54	1.474		55	52	48	45	42	35	31	29	31
1.0%	7 801	0.473	43	1.172		43	43	42	40	36	33	29	28	29
1.5%	7 753	0.486	36	0.970		36	36	36	35	33	31	28	28	29
Copper:														
Pure	8 954	0.3831	386	11.234	407	386	379	374	369	363	353			
Aluminium bronze														
95% Cu, 5% Al	8 666	0.410	83	2.330										
Molybdenum	10 220	0.251	123	4.790	138	125	118	114	111	109	106	102	99	92
Nickel:														
Pure (99.9%)	8 906	0.4459	90	2.266	104	93	83	73	64	59				
Ni-Cr 90% Ni,														
10% Cr	8 666	0.444	17	0.444		17.1	18.9	20.9	22.8	24.9				
Silver:														
Purest	10 524	0.2340	419	17.004	419	417	415	412						
Pure (99.9%)	10 524	0.2340	407	16.563	419	410	415	374	362	360				
Tin, pure	7 304	0.2256	64	3.884	74	65.9	59	57						
Tungsten	19 350	0.1344	163	6.271		166	151	142	133	126	112	76		
Zinc, pure	7 144	0.3843	112.2	4.106	114	112	109	106	100	93				

**Table 3.2.** Recommended values for characteristic fire load densities in various occupancy types

Substance	Temperature °C	k. W/m × °C	ρ. kg/m <sup>3</sup>	C, U/kg-°C	a. m <sup>2</sup> /s × 10 <sup>7</sup>
Insulating Material					
Asbestos					
Loosely packed	-45	0.149			
	0	0.154	470-570	0.816	3.3-4
	100	0.161			
Asbestos-cement boards	20	0.74			
Sheets	51	0.166			
Balsam wool, 2.2lb/ft <sup>3</sup>	32	0.04	35		
Cardboard, corrugated		0.064			
Celotex	32	0.048			
Corkboard, 10lb/ft <sup>3</sup>	30	0.043	160		
Cork, regranulated	32	0.045	45-120	1.88	2-5.3
Ground	32	0.043	150		
Fiber, insulating board	20	0.048	240		
Glass wool, 1.5lb/ft <sup>3</sup>	23	0.038	24	0.7	22.6
Structural and heat-resistant materials					
Asphalt	20-55	0.74-0.76			
Brick:					
Building brick, common	20	0.69	1600	0.84	5.2
Face		1.32	2000		
Carborundum brick	600	18.5			
	1400	11.1			
Chrom brick	200	2.32	3000	0.84	9.2
	550	2.47			9.8
	900	1.99			7.9
Diatomaceous earth, moulded and fired	200	0.24			
	870	0.31			
Fireclay brick, burnt 2426°F	500	1.04	2000	0.96	5.4
	800	1.07			
	1100	1.09			
Insulating material					
Fireclay brick, burnt 2642°F	500	1.28	2300	0.96	5.8
	800	1.37			
Cement, Portland		0.29	1500		
Mortar	23	1.16			
Concrete, cinder	23	0.76			
Stone 1-2-4 mix	20	1.37	1900-2300	0.88	8.2-6.8
Glass, window	20	0.78 (avg)	2700	0.84	3.4
Corosilicate	30-75	1.09	2200		
Insulating material					
Plaster, gypsum	20	0.48	1440	0.84	4.0
Metal lath	20	0.47			
Wood lath	20	0.28			
Stone					
Granite		1.73-3.98	2640	0.82	8-18
Limestone	100-300	1.26-1.33	2500	0.90	5.6-5.9
Marble		2.07-2.94	2500-2700	0.80	10-13.6
Sandstone	40	1.83	2160-2300	0.71	11.2-11.9
Wood (across the grain):					
Balsa 8.8lb/ft <sup>3</sup>	30	0.055	140		
Cypress	30	0.097	460		
Fir	23	0.11	420	2.72	0.96
Maple or oak	30	0.166	540	2.4	1.28
Yellow pine	23	0.147	640	2.8	0.82
White pine	30	0.112	430		

*(b) Statistical Survey*

A statistical survey is needed for the characteristic fire load density of similar buildings in question. The following points are recommended:

- (a) a minimum of five buildings
- (b) buildings investigated should have comparable use and similar size and contents
- (c) the buildings should be located in the same country in regions of similar socio-economic conditions.

*(c) Characteristic Fire Loads*

Recommended values for characteristic fire load densities in various occupancy types are determined from data collected in European countries. They are given in Table 3.2. For the deterministic study it is recommended that the 80% fractile be taken as the characteristic value for design purposes. If only the average value is available, the 80% fractile may be estimated by  $1.5q_{ki}$ .

In the case of *protected fire loads* (combustible material stored within a container such as a steel filing cabinet), the effective fire load may be less and will depend upon the fire temperature and duration, container integrity and the nature of the combustibles. In such circumstances, with a calorific value of 40% of that of the total contents, the equivalent fire load density may be expressed as:

$$q_e = \frac{q_{ki}}{H_w} \quad (3.7)$$

where

- $q_e$  = equivalent fire load density of wood ( $\text{kg}/\text{m}^2$ )
- $q_{ki}$  = measured fire load density ( $\text{MJ}/\text{m}^2$ )
- $H_w$  = calorific value of dry wood ( $18 \text{ MJ}/\text{kg}$ ).

*(d) Safety Factors*

Safety factors have already been discussed under loads. If a fire may put a large number of people at risk, it may be appropriate to include additional safety factors within the design. In buildings where large numbers of people are unaware of exit routes (e.g. shopping centres), it will be appropriate to include additional safety factors to take account of uncertainties in the distribution of occupants between the available exits. The design can be considered acceptable if the available safe escape time (ASET) is:

$$\text{ASET} \geq t_{\text{det}} + \Delta t_{\text{pre}} + (\lambda_{\text{flow}} \Delta t_{\text{flow}}) \quad (3.8)$$

where

- $t_{\text{det}}$  = detection time  
 $\Delta t_{\text{pre}}$  = pre-movement time  
 $\Delta t_{\text{flow}}$  = flow time  
 $\lambda_{\text{flow}}$  = design factor applied to flow time  
     1 for offices and industrial premises  
     2 for large and complex public buildings

such that

$$\text{ASET} \geq t_{\text{sec}} = t_{\text{det}} + \Delta t_{\text{pre}} + \lambda_{\text{flow}}, \quad (3.9)$$

where dynamic analysis using finite element technique for large buildings is required, the value of ASET must be considered in time-steps and overall time required for the resistance. A reference is made to Appendix 1.

Where the occupants remain in tall and complex buildings for an extended period while fire fighting operations take place and where structural failure threatens the life of the occupants, it is recommended that the adequacy of the structural fire resistance should be evaluated as follows:

$$L_{\text{crit}} \geq \lambda_{\text{str}} L, \quad (3.10)$$

where

- $L_{\text{crit}}$  = fire load at structural failure  
 $L$  = design fire load (80% fractile)  
 $\lambda_{\text{str}}$  = design factor  
     = 1.5 for tall and unsprinklered buildings > 30 m  
     = 1.0 for low-rise < 30 m  
     = 1.0 for sprinklered buildings > 30 m).

However, if  $\Delta t_{\text{flow}}$  is estimated at 2<sup>1/2</sup> minutes with an inherent factor of 2, the ASET value will be 5 min. If the travel distance is increased and  $\Delta t_{\text{flow}}$  is raised to 3 min, it will be necessary to increase ASET to 6 min such that

$$\frac{\text{ASET}}{\Delta t_{\text{flow}}} (\text{base care}) \leq \frac{\text{ASET}}{\Delta t_{\text{flow}}} (\text{new design}) \quad (3.11)$$

This increase in ASET may be achieved by a large smoke reservoir, smoke extract system or by controls on combustible materials that would reduce the expected rate of fire growth. If

$$\frac{\text{ASET}}{\Delta t_{\text{flow}}} (\text{base care}) < 1.0 \quad (3.12)$$

it should be checked that the base case is not unsafe and that an appropriate fire growth rate has been chosen for the calculations. The traditional criteria can also be looked at in the following manner.

*Travel distance* may be increased by a factor of 2 if a smoke control system is provided.

*Fire resistance:* The required fire resistance is increased by:

- i.  $1/2$  hour for every 10 m height to a maximum of 30 m
- ii. 1 hour for basement 10 m deep and  $1/2$  hour at the basement level with sprinkler systems.

*Compartment sizes:* The floor area is increased by a factor of 2 where a sprinkler system is provided.

The Russians define the fire resistance of the building as the ability of the structure to retain its operating functions in the period of fire for some definite time, after which the structure loses its carrying or protecting capacity. Lyalin reported that the heat of the fire,  $q$ , which he calls warmth of the fire, is given as:

$$q = z\beta_c Q_H n, \quad (3.13)$$

where

- $z$  = factor for chemical burning
- $\beta_c$  = coefficient of the speed of burning
- $Q_H$  = the lowest warmth of burning
- $n$  = weight speed of burning.

The fire load or the 'heat load' can be found by:

$$Q_\tau = Q_a f(\text{Bi}; \text{Fo}), \quad (3.14)$$

where

- $Q_\tau$  = fire heating load during the period of time
- $Q_a$  = maximum heat content of the structure
- $f(\text{Bi}; \text{Fo})$  = function of the Bio and Fourie criteria.

The fire resistance limit corresponding to these fire load equations is given by:

$$L_F = K_0 \tau \quad (3.15)$$

where

- $L_F$  = required fire resistance limits in hours
- $\tau$  = time of the fire in hours
- $K_0$  = factor for fire resistance
  - = 1.5 for vertical structures
  - = 2.5 for fire-proof structures
  - = 1.25 for horizontal structures.

This criterion is taken from 'Building Standards and Rules' SNi 11-A.5 85.

Japan, in its State of the Art Report No. 5A 1978, recommends a fire load of  $36\text{kg/m}^2$ , provided the duration of the fire does not exceed 45 min and the fire temperature does not exceed  $150^\circ\text{C}$ .



The Swedes, in their State of the Art Report 5B (1987), assume that tall buildings cannot be evacuated during a fire: they insist that the buildings should be provided with fire protection measures. They have established a relation between effective fire load  $q$  and resistance time  $\tau$  for a structure in a fire compartment. The fire load  $q_c$  initially is given by:

$$q_c = \frac{1}{A_f} \sum m_\nu H_\nu; (\text{Mcal/m}^2) \quad (3.16)$$

where

$A_f$  = floor area ( $\text{m}^2$ )

$m_\nu$  = the total weight (kg)

$H_\nu$  = effective heat value (Mcal/kg) for each individual material  $\nu$

$q_c$  is also given in terms of an equivalent amount of wood per unit area  $A_f$ . A modified formula exists for  $q_c$ :

$$q_c = \frac{1}{A_f} \sum m_\nu H_\nu \quad (3.17)$$

in which  $A_t$  is the total area of the surfaces bounding the compartment ( $\text{m}^2$ ). The connection between the different fire load definitions is given by:

$$q_c = \frac{A_t}{A_f} q (\text{Mcal/m}^2) \quad \text{and} \quad q_c = \frac{A_t}{4.5A_f} q (\text{kg/m}^2) \quad (3.18)$$

A further development, leads to a more differentiated characterization of the fire load. The value of  $q$  is:

$$q_c = \frac{1}{A_f} \sum \mu_\nu m_\nu H_\nu \quad (3.19)$$

in which  $m_\nu$  denotes a dimensionless coefficient between 0 and 1, giving the real degree of combustible for each individual component  $\nu$  of the fire load. The coefficient  $\mu_\nu$  depends on the duration of the fire and the temperature-time characteristics of the fire compartment.

*The range of fire load density.* It is concluded that for  $q$  the temperature-time relation is very important.

### 3.2.1 $t$ -Squared Fires

The growth rate of a design fire is often characterized by a parabolic curve known as a *t-squared fire* such that the heat release rate is proportional to the time squared. The *t-squared fire* can be thought of in terms of a burning object with a constant heat release rate per unit area, in which the fire is spreading in a circular pattern with a constant radial flame speed. The *t-squared* heat release rate is given by:

$$Q = (t/k)^2 \quad (3.20)$$

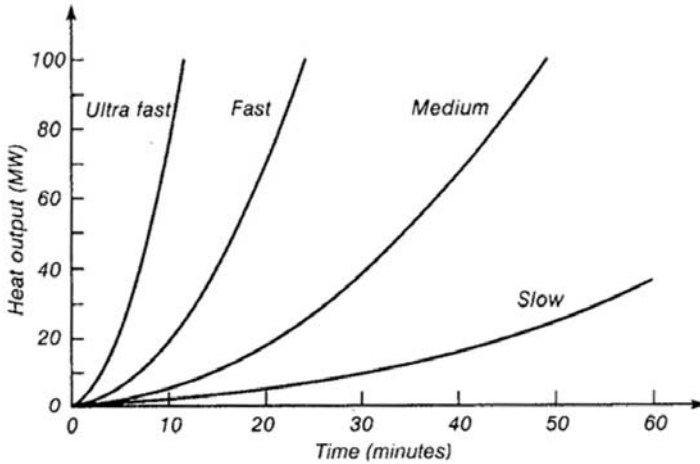


Fig. 3.1. Heat release rate for  $t^2$  fires

Table 3.3. Fire growth rates for  $t^2$  fires

Fire growth rate	Value of A:	Value of $a$	Typical real fire
Slow	600	0.00293	Densely packed wood products
Medium	300	0.0117	Solid wood furniture such as desks Individual furniture items with small amounts of plastic
Fast	150	0.0466	Some upholstered furniture High stacked wood pallets Cartons on pallets
Ultrafast	75	0.1874	Most upholstered furniture High stacked plastic materials Thin wood furniture such as wardrobes

where  $Q$  is the heat release rate (MW),  $t$  is the time (s), and  $k$  is a growth constant ( $s/\sqrt{\text{MW}}$ ).

Values of A are given in Table 3.3 for slow, medium, fast and ultrafast fire growth, producing the heat release rates shown in Fig. 3.1. The numerical value of  $k$  is the time for the fire to reach a size of 1.055 MW. The choice of growth constant depends on the type and geometry of the fuel. Values of A and peak heat release rate for many different burning objects are given in Table 3.3 (Babraukas (1995)). An alternative formulation is given as:

$$Q = \alpha t^2 \quad (3.21)$$

where  $\alpha$  is the fire intensity coefficient ( $\text{MW}/\text{s}^2$ ). Values of  $\alpha$  are also given in Table 3.3.

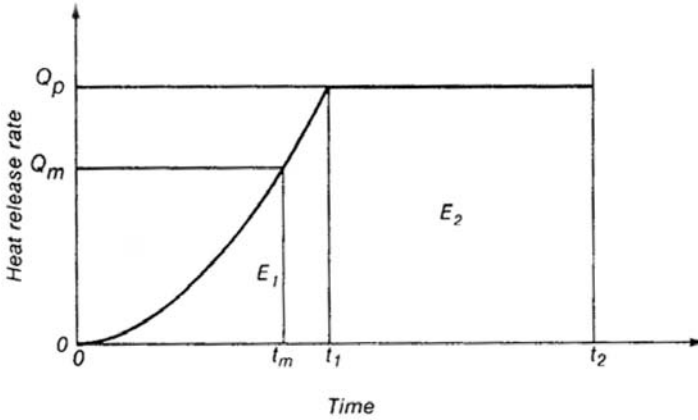


Fig. 3.2. Calculation of heat release rate (Reproduced from Buchanan (2001))

Calculations for a  $t^2$  fire are given below with reference to Fig. 3.2. Using (3.20), the time  $t_1$  (s) for the fire to reach the peak heat release rate  $Q_p$  (MW) is given by  $Q_p = (t/k)^2$ .

The energy released is the area under the curve of heat release rate vs. time. Because the area under a parabola is one third of the enclosing rectangle, the energy  $E_1$  released to time  $t_1$  is given by

$$E_1 = t_1 Q_p / 3 \tag{3.22}$$

If the total energy  $E$  (MW) in the fuel has not been released at time  $t_1$  the energy released in the steady burning phase  $E_2$  (MW) is given by

$$E_2 = E - E_1 \tag{3.23}$$

and the duration  $t_b$  (s) of the steady burning phase is given by

$$t_b = t_2 - t_1 = E_2 / Q_p \tag{3.24}$$

If the fuel has insufficient time to reach its peak heat release rate, all of the fuel will be consumed in time  $t_m$  (s) where

$$t_m = (3Ek^2)^{1/3} \tag{3.25}$$

and the burning rate  $Q_m$  at time  $t_m$  is given by

$$Q_m = (t_m/k)^2 \tag{3.26}$$

Figure 3.2 shows the resulting heat release rates for a fire in office furniture with slow, medium and fast fire growth rates. The peak heat release rate has been taken from Fig. 3.2.

Plate 3.1. Channel four building on fire



### 3.3 Pre- and Post-flashover Design Fires

#### 3.3.1 Pre-flashover Design Fires

The  $t$ -squared fires described above can be used to construct pre-flashover design fires, as input for calculating fire growth in rooms.

The fires described above are generally used to describe the heat release rate for burning of a single object. Fire can spread from the first burning object to a second object by flame contact if it is very close, or by radiant heat transfer if it is further away. The time to ignition of a second object depends on the intensity of radiation from the flame and the distance between the objects. When the time to ignition of the second object has been calculated, the combined heat release rate can be added at any point in time to give the total heat release rate for these two, and subsequent objects. This combined curve then becomes the input design fire for the room under consideration. There may be many more items involved, and the resulting combination may itself be approximated by a  $t$ -squared fire for simplicity.

#### 3.3.2 Heat Transfer

Some knowledge of heat transfer is essential to the understanding of fire behaviour. Heat transfer occurs by the three processes of conduction, convection and radiation, which can occur separately or together depending on the circumstances.

##### Conduction

Several material properties are needed for heat transfer calculations in solid materials. These are the *density*, *specific heat* and *thermal conductivity*. Density,  $\rho$ , is the mass of the material per unit volume in  $\text{kg}/\text{m}^3$ . Specific heat  $c_p$  is the amount of heat required to heat a unit mass of the material by one degree, with units of  $\text{J}/\text{kgK}$ . Thermal conductivity,  $k$ , represents the rate of heat transferred through a unit thickness of the material per unit temperature difference, with units  $\text{W}/\text{mK}$ . In the steady-state situation, the transfer of heat by conduction is directly proportional to the temperature gradient between two points, with a constant of proportionality known as the thermal conductivity,  $k$ , so that

$$\dot{q}'' = kdT/dx \quad (3.27)$$

where  $\dot{q}''$  is the heat flow per unit area ( $\text{W}/\text{m}^2$ ),  $k$  is the thermal conductivity ( $\text{W}/\text{mK}$ ),  $T$  is temperature ( $^{\circ}\text{C}$  or  $\text{K}$ ), and  $x$  is distance in the direction of heat flow ( $m$ ). The steady-state calculation does not require consideration of the heat required to change the temperature of material that is being heated or cooled.

## Radiation

Radiation is the transfer of energy by electromagnetic waves which can travel through a vacuum, or through a transparent solid or liquid. Radiation is extremely important in fires because it is the main mechanism for heat transfer from flames to fuel surfaces, from hot smoke to building objects and from a burning building to an adjacent building. The radiant heat flux  $\dot{q}''$  ( $\text{W}/\text{m}^2$ ) at a point on a receiving surface is given by

$$\dot{q}'' = \varphi \varepsilon_e \sigma T_e^4 \quad (3.28)$$

where  $\varphi$  is the configuration factor,  $\varepsilon_e$  is the emissivity of the emitting surface,  $\sigma$  is the Stefan-Boltzmann constant ( $5.67 \times 10^{-8} \text{ W}/\text{m}^2\text{K}^4$ ), and  $T_e$  is the absolute temperature of the emitting surface (K).

The resulting heat flow  $\dot{q}''$  ( $\text{W}/\text{m}^2$ ) from the emitting surface to the receiving surface is given by

$$\dot{q}'' = \varphi \varepsilon \sigma (T_e^4 T_r^4) \quad (3.29)$$

where  $T_r$  is the absolute temperature of the receiving surface (K), and  $\varepsilon$  is the resultant emissivity of the two surfaces, given by

$$\varepsilon = \frac{1}{1/\varepsilon_e + 1/\varepsilon_r - 1} \quad (3.30)$$

The configuration factor  $\varphi$  is given by

$$\varphi = \frac{1}{90} \left[ \frac{x}{\sqrt{1+x^2}} \tan^{-1} \left( \frac{y}{\sqrt{(1+x^2)}} + \frac{y}{\sqrt{(1+y^2)}} \tan^{-1} \left( \frac{x}{\sqrt{1+y^2}} \right) \right) \right] \quad (3.31)$$

## 3.4 Temperature-Time Relation

A great deal of research, involving theory, experiment and data monitoring on site, has been carried out and is still continuing with regard to the time-temperature relation. In this section a few examples are given to show different practices.

In general it is widely believed that the temperature course of fire may be divided into the following three periods:

- (a) the growth period
- (b) the fully developed period
- (c) the decay period.

To determine the temperature course, it is necessary to know at each moment during a fire the rate at which heat is produced and the rate at which heat is lost to exposed materials and surroundings. Several of the parameters that determine heat production and heat losses can be categorized as follows:

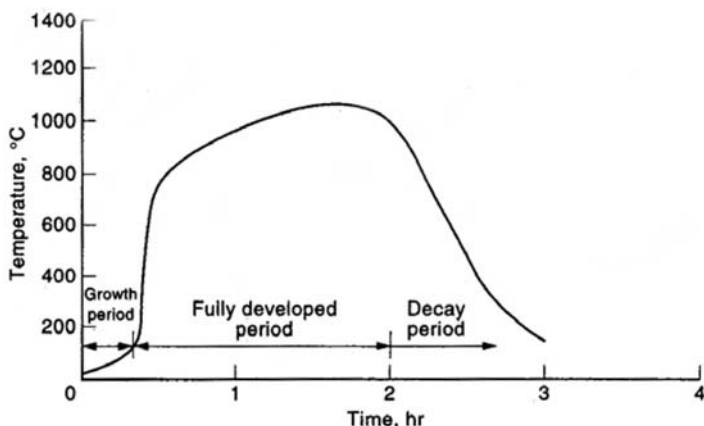


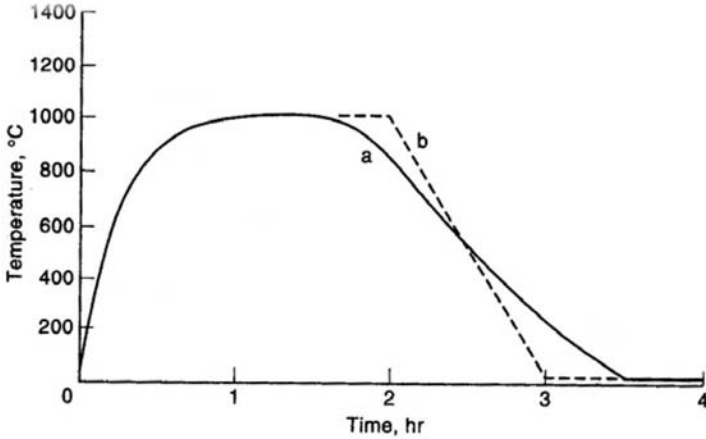
Fig. 3.3. Idealized temperature course of fire (reproduced from Report No. 5A, 1978)

- |   |   |   |
|---|---|---|
| (a) material properties   | } | predicted with reasonable accuracy      |
| (b) room dimensions   |   |   |
| (c) emissivity of flames  |   |   |
| (d) exposed materials   |   |   |
| (e) gases that burn outside the room  | } | predicted with less reasonable accuracy |
| (f) loss of unburnt particles through window                                |   |   |
| (g) temperature difference in the room                                      | } | difficult to predict                    |
| (h) temperature change with time during the fire, which in turn depends on: |   |   |
| (i) amount  |   |   |
| (ii) surface area   |   |   |
| (iii) arrangement of combustible contents                                   |   |   |
| (iv) velocity and direction of wind   |   |   |
| (v) outside temperatures  |   |   |

Various unpredictable and variations in approaches exist for computing fire load densities. However, it is possible to indicate for any compartment a characteristic temperature-time curve whose effect will not be exceeded during the lifetime of the building. Such curves are useful for the fire-resistance design of buildings. A number of Japanese researchers have produced results. Figs. 3.3 and 3.4 summarize the results of the temperature-time curve for the resistance design.

Where  $\epsilon_r$  is the emissivity of the receiving surface,  $x = H/2r$  and  $y = W/2r$ .

The emissivity  $\epsilon$  indicates the efficiency of the emitting surface as a radiator, with a value in the range from zero to 1.0. A so-called 'black-body' radiator has an emissivity of 1.0. In fire situations, most hot surfaces, smoke



**Fig. 3.4.** Temperature curves for fire resistance design (reproduced courtesy of ASCE)

particles or luminous flames have an emissivity between 0.7 and 1.0. The emissivity can change during a fire; for example zinc-coated steel (galvanized steel) has a very low emissivity until the temperature reaches about  $400^{\circ}\text{C}$  when the zinc melts and the bare steel is exposed to the fire. Some times the value of

$$\varphi = A_1/\pi r^2 \quad (3.32)$$

is written, where

$r$  = a distance between emitting and receiving surfaces

$A_1$  = radiating surface area.

### Example 3.1

Calculate the average heat release rate when 250 kg of paraffin wax burns in half an hour.

Mass of fuel	$M = 250 \text{ kg}$
Calorific value	$\Delta H_c = 46 \text{ MJ/kg}$
Energy contained in the fuel	$E_I = M\Delta H_c = 250 \times 46 = 11500 \text{ MJ}$
Time of burning	$\tau = 2000 \text{ s}$
Heat release rate	$Q = E_I/\tau = 11500/2000 = 5.75 \text{ MW}$

Calculate the fuel load energy density in an office  $5 \text{ m} \times 3 \text{ m}$  containing 170 kg of dry wood and paper and 80 kg of plastic materials. Assume calorific values of 16 MJ/kg and 30 MJ/kg respectively.



Mass of wood	$M_{\text{wood}} = 170 \text{ kg}$
Calorific value	$\Delta H_{c,\text{wood}} = 16 \text{ MJ/kg}$
Energy contained in the wood	$E_{\text{I wood}} = M\Delta H_c = 170 \times 16 = 2720 \text{ MJ}$
Mass of plastic	$M_{\text{plastic}} = 80 \text{ kg}$
Calorific value	$\Delta H_{c,\text{plastic}} = 30 \text{ MJ/kg}$
Energy contained in plastic	$E_{\text{plastic}} = M\Delta H_c = 80 \times 30 = 2400 \text{ MJ}$
Total energy in fuel	$E_\tau = E_{\text{I wood}} + E_{\text{I plastic}}$ $= 2720 + 2400 = 5120 \text{ MJ}$
Floor area	$A_f = 5 \times 3 = 15 \text{ m}^2$

**Example 3.2**

A room in a storage building has 2500 kg of polyethylene covering the floor. Calculate the heat release rate and duration of burning after the roof collapses in a fire. The room is 6.0 m by 10.0 m. Take  $q = 0.031$  and  $Q_s = 1.36$  and  $A_f = 60$ . Determine the duration  $\tau$  of burning.

Mass of polyethylene	$M = 2500 \text{ kg}$
Calorific value	$\Delta H_c = 43.8 \text{ MJ/kg}$ $E_1 = M\Delta H_c = 109500 \text{ MJ}$
Specific heat release rate	$Q_s = q\Delta H_c = 0.031 \times 43.8 = 1.36 \text{ MW/m}^2$
Total heat release rate	$QQ_s A_f = 1.36 \times 60 = 81.6 \text{ MW}$
Duration of burning	$\tau = E/Q = 109,500/81.6 = 1.342 \text{ sec}$ $\approx 22.5 \text{ minutes}$

**Example 3.3**

Calculate the radiant heat flux from a window in a burning building to the surface of an adjacent building 5.0 m away. The window is 2.0 m high by 3.0 m wide and the fire temperature is  $800^\circ\text{C}$ . Assume an emissivity of 0.9.

Emitter height	$H = 2.0 \text{ m}$
Emitter width	$W = 3.0 \text{ m}$
Distance from emitter	$r = 5.0 \text{ m}$
Height ratio	$x = H/2r = 2/(2 \times 5) = 0.20$
Width ratio	$y = W/2r = 3/(2 \times 5) = 0.30$
Configuration factor	$\varphi = \frac{1}{90} \left[ \frac{x}{\sqrt{1+x^2}} \tan^{-1} \left[ \frac{y}{\sqrt{1+x^2}} \right] \right.$ $\left. + \frac{y}{\sqrt{1+x^2}} \tan^{-1} \left( \frac{x}{\sqrt{1+x^2}} \right) \right]$
Emitter temperature	$T = 800^\circ\text{C} = 1073 \text{ K}$

Emissivity	$\varepsilon = 0.9$	${}^2\text{K}^4$
Stefan-Boltzmann constant	$\sigma = 5.67 \times 10^{-8}$	$\text{W/m}^2$
Radiant heat flux	$\dot{q}'' \varphi \varepsilon \sigma T^4 = 0.0703 \times 0.9 \times 5.67 \times 10^{-8} \times 1073$	$= 0.000003849$

The opening factor  $F$  which has an effect on the temperature-time relation is given by:

$$F = \frac{A_W \sqrt{H^*}}{A_t} \quad (3.33)$$

where

$A_W$  = area of the openings in compartments or enclosures

$H^*$  = height of the opening

$A_t$  = area of the bounding surfaces ( $A_T$  or  $A_f$  in British codes).

The rate of burning  $R$  of the combustible materials in an enclosure is given by:

$$R = 330 A_W \sqrt{H^*} \quad (3.34)$$

The duration time

$$\tau = \frac{q_c A_t}{330 A_W \sqrt{H^*}} = \frac{Q_c}{330 F} \quad (3.35)$$

where  $q_c$  = the fire load/unit area.

Here

$$q_c = 330 F \tau. \quad (3.36)$$

Table 3.4 gives information for various factors regarding the enclosure needed in the above equations. If  $R = K A_W \sqrt{H^*}$  then the value of  $K$  in imperial units is 330; 5.5 to 6 kg/(min-m<sup>5/2</sup>) for  $1/4 A_t$  and 9 to 10 kg/(min-m<sup>5/2</sup>) for small area  $A_t$  has been adopted in Denmark, Japan, the USA, the UK and the former USSR.

As an example if the window height  $H^*$  is 1.8 m,  $A_W$  = total opening = 356 m<sup>2</sup> and  $A_t$  = 6337 m<sup>2</sup>, the temperature opening factor  $F$  will be 0.0754.

The temperature curves for the fire resistance design can be described by:

$$T = 250(10F)^{0.1/F^{0.3}} e^{-F^2 t} [3(1 - e^{-0.6t}) - (1 - e^{-3t}) + 4(1 - e^{-12t})] + C \left( \frac{600}{F} \right)^{0.5} \quad (3.36a)$$

where

**Table 3.4.** Factors for an enclosure

Factor	Description
$k$	Thermal conductivity of bounding material: 1.16 W/mK for a heavy material ( $\rho \geq 1600 \text{ kg/m}^3$ ) 0.58 W/mK for a light material ( $\rho < 1600 \text{ kg/m}^3$ )
$pc$	Volumetric specific heat of bounding material: $2150 \times 10^3 \text{ J/m}^3 \times \text{K}$ for a heavy material ( $\rho \geq 1600 \text{ kg/m}^3$ ) $1075 \times 10^3 \text{ J/m}^3 \times \text{K}$ for a light material ( $\rho < 1600 \text{ kg/m}^3$ )
$A_T$	Total inner surface area bounding the enclosure including window area: $1000 \text{ m}^2$
$H$	Window height: 1.8 m
$\varepsilon$	Emissivity for radiation transfer between hot gases and inner bounding surface of the enclosure: 0.7
$\alpha_c$	Coefficient of heat transfer by convection between fire and inner bounding surface area: $23 \text{ W/m}^2 \times \text{K}$
$\alpha_u$	Coefficient of heat transfer between outer bounding surface area and surroundings: $23 \text{ W/m}^2 \times \text{K}$
$c$	Specific heat of combustion gases: $1340 \text{ J/Nm}^3 \times ^\circ\text{C}$
$G$	Volume of combustion gas produced by burning 1 kg of wood: $4.9 \text{ Nm}^3/\text{kg}$
$q$	Heat released in the enclosure by burning 1 kg of wood: $10.77 \times 10^6 \text{ J/kg}$
$T_0$	Initial temperature: $20^\circ\text{C}$
$V$	Volume of enclosure*: $1000 \text{ m}^3$
$\Delta x$	Thickness of elementary layers of bounding material: 0.03 m
$\Delta t$	Tune increment: 0.0004167 hr
$D$	Thickness of bounding material: 0.15 m

\* It can be shown that the influence of the volume of the enclosure on the fire temperature is negligible. Courtesy: ASCE.

$T$  = the fire temperature ( $^\circ\text{C}$ )

$t$  = time (hr)

$F$  = opening factor ( $\text{m}^{1/2}$ )

$C$  = constant based on the properties of the bounding material in fire

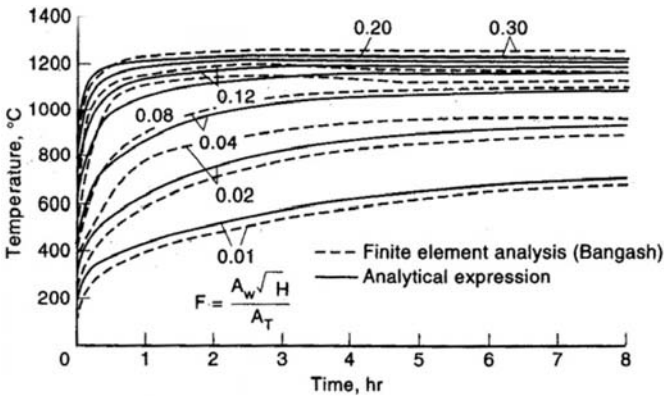
= 0 for heavy materials with  $\rho \geq 1600 \text{ kg/m}^3$

= 1 for light materials with  $\rho < 1600 \text{ kg/m}^3$

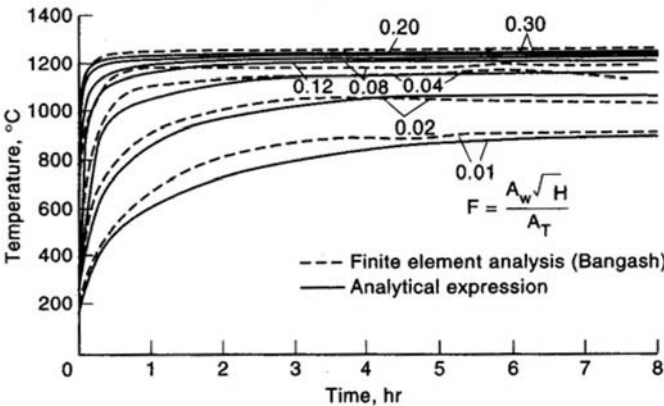
$\rho$  = density

$t$  = time  $\leq \frac{0.08}{F} + 1$ .

$$t > \frac{0.08}{F} + 1 \quad \text{assume } t = \frac{0.08}{F} + 1. \quad (3.36b)$$



**Fig. 3.5.** Comparison between temperature-time curves obtained by solving a heat balance and those described by an analytical expression for ventilation-controlled fires in enclosures bounded by dominantly heavy materials ( $\rho \geq 1600 \text{ kg/m}^3$ )



**Fig. 3.6.** Comparison between temperature-time curves obtained by solving a heat balance and those described by an analytical expression for ventilation-controlled fires in enclosures bounded by dominantly light materials ( $\rho \geq 1600 \text{ kg/m}^3$ )

If  $F > 0.15$  take  $F = 0.15$  for design purposes. Figures 3.5 to 3.8 show some temperature-time curves for design purposes.

The temperature course of fire during the decay period is given by:

$$T = -600 \left( \frac{t}{\tau} - 1 \right) + T\tau \tag{3.37}$$

$$T = 20 \quad \text{if } T < 20^\circ\text{C}$$

The International Standards Organisation (ISO) give the following expression for their standard curves

$$T - T_0 = 345 \log_{10}(8t + l) \tag{3.38}$$

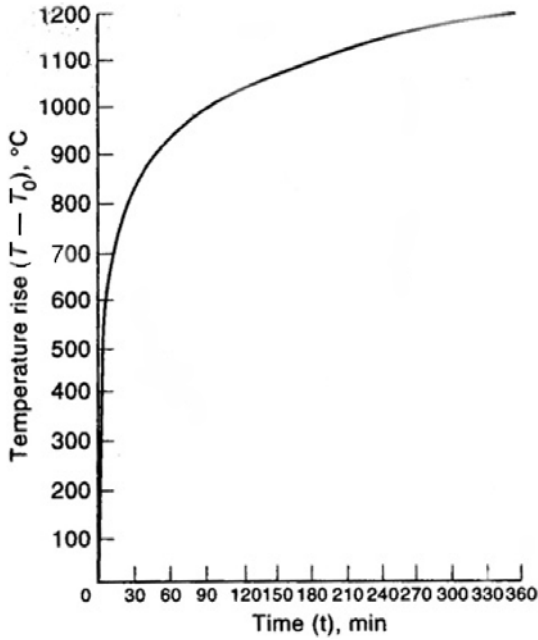


Fig. 3.7. Standard time-temperature curve

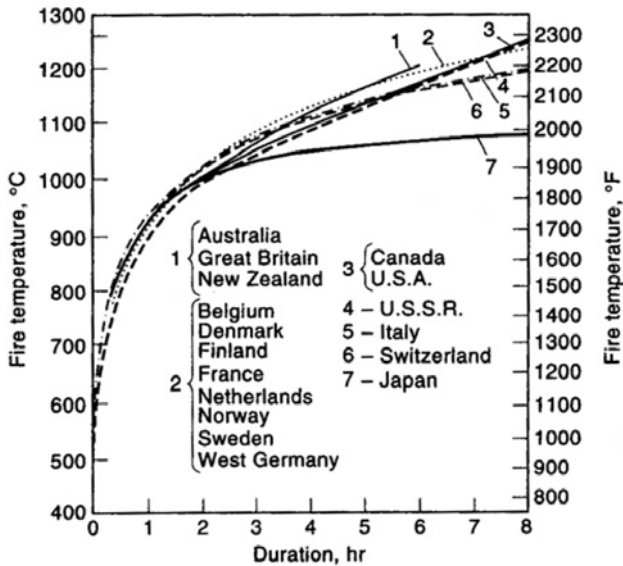


Fig. 3.8. Standard fire temperature-time used in various countries for testing of building elements (reproduced courtesy of ASCE)

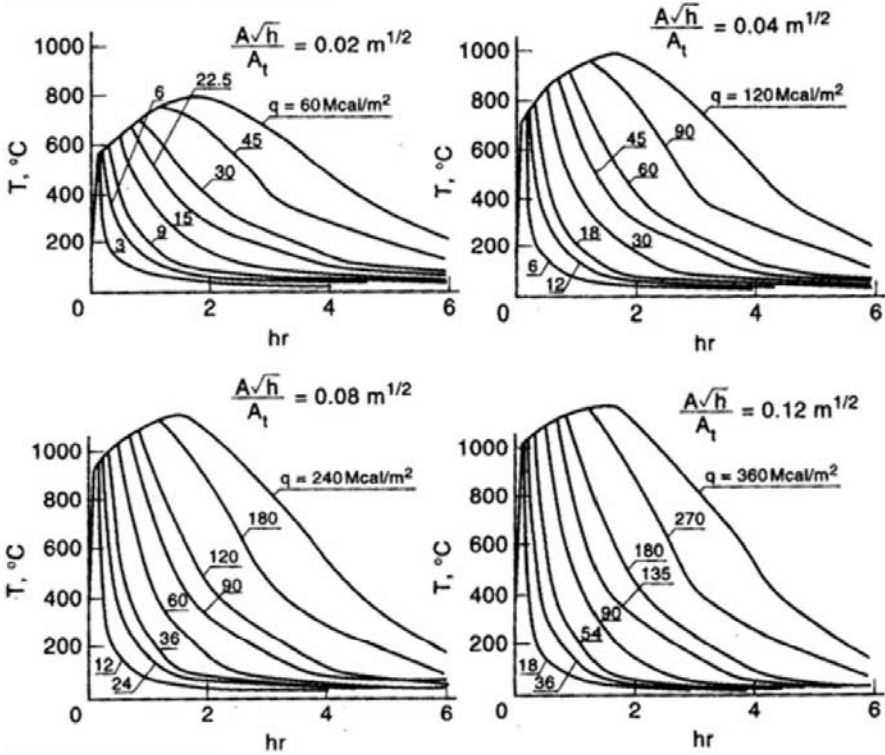


Fig. 3.9. Temperature-time- $q_c$  curves for F-values after Pettersson

where

- $t$  = time (min),
- $T$  = fire temperature ( $^{\circ}\text{C}$ ) =  $T_f$ , and
- $T_0$  = initial temperature ( $^{\circ}\text{C}$ ).

In North America an analytical expression exists for temperature-time curves in the form of an exponential function:

$$T - T_0 = a_1(1 - e^{a_4 t}) + a_2(1 - e^{a_5 t}) + a_3(1 - e^{a_6 t}) \tag{3.39}$$

where

- $a_1 = 532$  for  $^{\circ}\text{C}$ , 957 for  $^{\circ}\text{F}$ ;
- $a_2 = -186$  for  $^{\circ}\text{C}$ , -334 for  $^{\circ}\text{F}$ ;
- $a_3 = 820$  for  $^{\circ}\text{C}$ , 1476 for  $^{\circ}\text{F}$ ;
- $a_4 = -0.6$ ;
- $a_5 = -3$ ;
- $a_6 = -12$ .

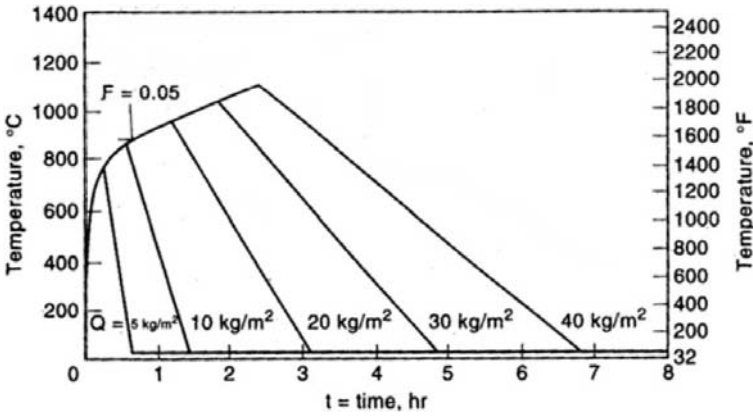


Fig. 3.10. Temperature-time- $q_c$  curves for  $F = 0.05$ , British and American practice

This heat transfer equation is integrable and is used in the finite element analysis.

A number of countries have been involved in fire-temperature-time analysis and research. Harmathy is the first researcher to have collected data from some countries and presented a comparative study graph for the temperature-time relation. Figure 3.8 shows the graph by Harmathy with data from a few other countries added.

The last step is to see how the fire loads  $q_c$  can be graphically related to the temperature-time curve. For design purposes, it is important for the load to be algebraically added to other loads. Petterson [3.1] has presented four graphs for temperature-time- $q_c$  relations, for

$$\begin{aligned}
 F = \frac{A_w \sqrt{H^*}}{A_T} &= 0.02\sqrt{m} \\
 &= 0.04\sqrt{m} \\
 &= 0.08\sqrt{m} \\
 &\text{and } 0.12\sqrt{m}
 \end{aligned}$$

He has taken heat capacity  $\gamma c_p = 400 \text{ kcal/m}^3 \times \text{°C}$ , thermal conductivity  $\lambda = 0.7 \text{ kcal/m} \times \text{h} \times \text{°C}$ . The value of  $q_c$  is in  $\text{Mcal/m}^2$ . Figures 3.7 and 3.8 show such relationships for four different openings.

British practice allows the opening factor  $F = 0.05\sqrt{m}$  for heavy bounding materials. Figure 3.7 shows a simplified temperature-time-fire load  $q_c$  curve for the opening factor  $F = 0.05\sqrt{m}$ . This curve is in full agreement with American practice. The standard temperature-time curve adopted by BS476: Part 8, 1972 is shown in Fig. 3.5 and is compared with other countries in Fig. 3.6.

## 3.5 Material Properties

Now that the fire-time relation has been thoroughly reviewed, it is necessary to look at various materials and how they react to the fire environment. The most common materials are steel, concrete, timber and brick. The properties of these materials must be known prior to design of building structures.

### 3.5.1 Steel

The material properties that affect the temperature rise and distribution in a structural steel section are

- (a) thermal conductivity
- (b) specific heat.

The thermal conductivity  $K$  is given by the USDA Agricultural Handbook No. 72 1987 as

$$\begin{aligned} K &= -0.022T + 48 & \text{for } 0 \leq T \leq 900^\circ\text{C} \\ &= 28.2 & \text{for } T > 900^\circ\text{C}, \end{aligned} \quad (3.40)$$

where  $T$  = temperature in steel ( $^\circ\text{C}$ ).

Specific heat is the characteristic that describes the amount of heat input required to raise a unit mass of material a unit of temperature. A constant of  $600\text{J}/(\text{kg}\times\text{K})$  of the specific heat of steel for the entire temperature range is a reasonable approximation.

Where thermal conductivity and specific heat are involved, thermal diffusivity of the material cannot be ignored, since it is a measure of how the heat is dissipated through the material and is the ratio of the thermal conductivity to the volumetric specific heat of the material. The relationship for thermal diffusivity ' $\alpha$ ' is given by

$$a = K/\rho c, \quad (3.41)$$

where

$K$  = thermal conductivity,

$\rho$  = density, and

$c$  = specific heat.

In British practice

$$c = c_s = 0.52 \text{ kJ}/(\text{kg}\cdot^\circ\text{C})$$

$$\rho = \rho_s = 7850 \text{ kg}/\text{m}^3$$

$$K = K_s = 50 \text{ W}/(\text{m}\cdot^\circ\text{C})$$

At  $20^\circ\text{C}$ , the elastic limit (Young's modulus) is:

	$E_{20} = 206 \text{ kN}/\text{mm}^2$	}	Grade 43 A (BS4360)
Elastic limit at $20^\circ\text{C}$ stress:	$f_y = 250 \text{ N}/\text{mm}^2$		
Ultimate strength:	$f_t = 450 \text{ N}/\text{mm}^2$		



From these basic values, the properties at other temperatures are as given below.

Elastic properties	Temperature range		
	20–300°C	300–700°C	700–900°C
$\frac{fy_T}{fy_{20}}$	$1 - \frac{T^0}{3000}$	$0.9 - \frac{T^0 - 300}{500}$	$0.9 - \frac{T^0 - 700}{200}$
$\frac{E_T}{E_{20}}$	$1 - \frac{T^0}{3000}$	$0.9 - \frac{T^0 - 300}{500}$ (300–900°C)	

Thus it is shown that the modulus of elasticity of steel decreases with increasing temperature. The strength of hot-rolled steel depends on yield and tensile strength. Figures 3.11 and 3.12 show these relations for British and American practices respectively. Lie and Stanzak [3.2–3.4] give the yield strength of steel with temperature as

$$Fy = Fy_0(1 - 0.78\theta - 1.89\theta^4) \tag{3.42}$$

where

$$\theta = (T_F - 68)/1800 \text{ and}$$

$$Tf = \text{temperature of steel (°F)}.$$

European Convention for Constructional Steelwork utilizes the same concept:

$$Fy = Fy_0(1 + T_c/(767 \ln(T_c/1750))) \quad 0 < T_c \leq 600^\circ\text{C} \tag{3.43}$$

$$Fy = Fy_0((108 - T_c/1000)/(T_c - 440)) \quad 600^\circ < T_c \leq 1000^\circ\text{C} \tag{3.44}$$

where

$$Fy = \text{yield stress at elevated temperature}$$

$$Fy_0 = \text{yield stress at room temperature}$$

$$T_c = \text{temperatures of steel (°C)}.$$

Figure 3.11 shows steel strength versus temperature as used in fire resistance based on the British practice. Figure 3.12 evaluates *E* values for elevated temperatures based on the American practice. Figure 3.13 shows the relationship between steels for various temperatures in F°.

The American Iron and Steel Institute gives the thermal expansion  $\alpha$  (temperatures up to 650°C) as:

$$\alpha = (11 + 0.0062T) \times 10^{-6}$$

where *T* = steel temperature (°C).

The Eurocode ENV1993-1-2 has an approach originally specified by ECCS as a design guide (1983, 1985) which calculates the ratio of the required

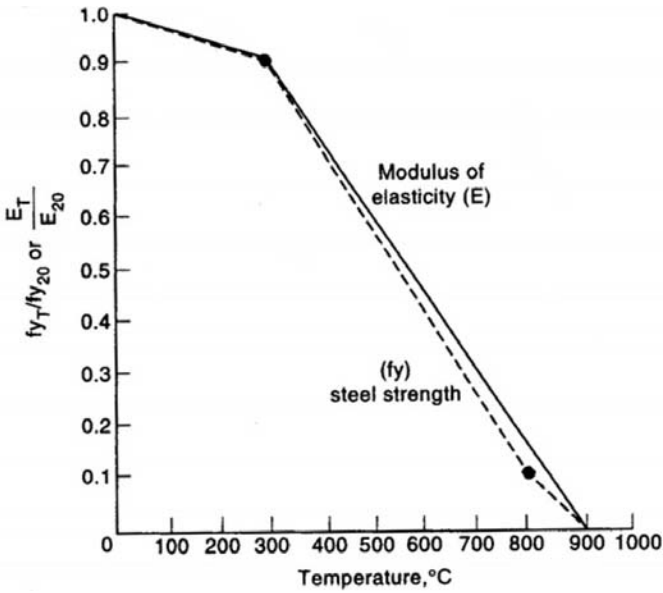


Fig. 3.11. Relationship between steel material properties and temperatures in °C (British practice)

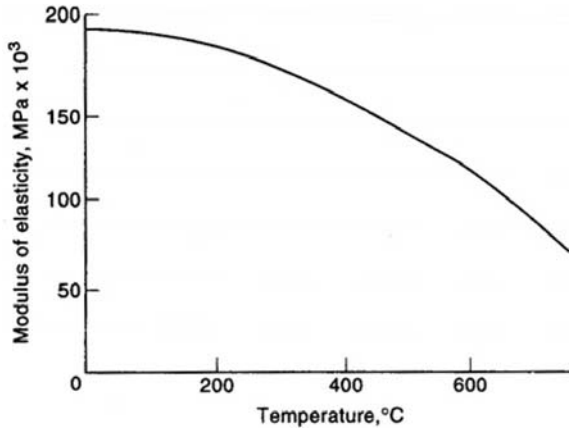
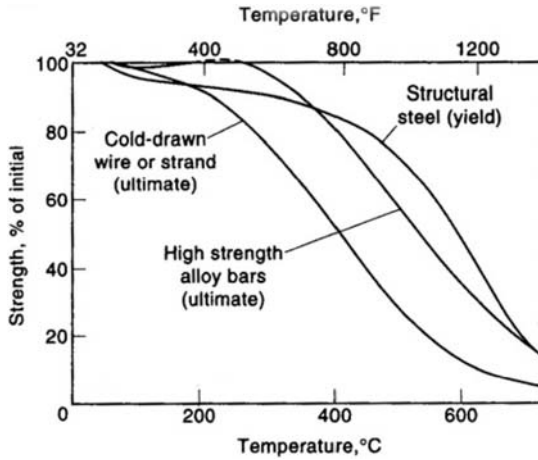


Fig. 3.12. Modulus of elasticity of steel at elevated temperatures (American practice)

strength at elevated temperatures to that at ambient in order to ensure that the structural steel components do not collapse. Hence, for beams, the elastic design should be based on:

$$\frac{f_{amax,\theta cr}}{f_{ay,20^\circ C}} = \left(\frac{\kappa}{\theta}\right) \left(\frac{W_{el}}{W_{pl}}\right) \left(\frac{q_{sd,el}}{q_{fi,d}}\right) \tag{3.45}$$



**Fig. 3.13.** Strength of some steels at high temperature (based on American practice)

where  $f_{amax,cr}/f_{ay,20^{\circ}C}$  is the stress ratio,  $\kappa$  is a factor allowing for the non-uniform temperature distribution, geometric imperfections and strength variations,  $\theta$  is a factor, greater than unity, allowing for redistribution between the elastic ambient moment distribution and the plastic distribution under fire,  $W_{pl}/W_{el}$  is the ratio between the plastic and elastic section moduli (known as the shape factor), and  $q_{fi,d}/q_{sd,el}$  is the ratio of the design load (action) in the fire to the elastic design load (action). In order to design a beam plastically, the relationship is given as:

$$\frac{f_{amax,\theta cr}}{f_{ay,20^{\circ}C}} = \kappa \left( \frac{q_{sd}}{q_{fi,d}} \right) \tag{3.46}$$

where  $q_{fi,d}/q_{sd}$  is the ratio of the fire action to the ultimate action.

The Eurocode now gives two methods for steelwork design:

- (a) load-carrying capacity
- (b) limiting temperature criterion.

*(a) Load-Carrying Capacity*

$$S_{d,F} \leq R_{d,F(t)} \tag{3.47}$$

where  $S_{d,f}$  is the design value of the internal force to be resisted and  $R_{d,F(t)}$  is the design resistance at time  $t$  and should be calculated in accordance with ENV 1992-1-1 except for the use of temperature-modified mechanical properties of steel.

For **tension members** (clause 4.2.21)

$$R_{d,F(t)} = k_{amax,\theta} R_d \tag{3.48}$$

where  $k_{\text{amax},\theta}$  is the normalized strength reduction at a temperature of  $\theta_a$  and  $R_d$  is the ambient design resistance. Note that if  $\theta$  is less than  $550^\circ\text{C}$  at any cross-section, the member may be assumed to be able to carry the fire-induced loading. Where the temperature in a member is non-uniform, then  $\theta$  should be taken as the maximum value in the cross-section.

For **beams** (Class 1 and 2, clause 4.2.2.2), under uniform temperature, the rules for tension and bending are the same except that  $R_d$  is the design bending resistance.

Under non-uniform temperature distribution, the temperature distribution  $R_{d,F(t)}$  is:

$$R_{d,F(t)} = \frac{R_{d,F(\theta)}}{\kappa} \quad (3.49)$$

where  $\kappa$  is a factor allowing for temperature gradient and varying end conditions (Pettersson and Witteveen), and  $R_{d,F(\theta)}$  is the design resistance calculated from the maximum temperature in the cross-section:

$$\left. \begin{aligned} \kappa &= 1.0 && \text{exposed on 4 sides} \\ &= 0.7 && \text{exposed on 3 sides} \end{aligned} \right\} \text{ simple beams}$$

$$\left. \begin{aligned} &= 0.85 && \text{exposed on 4 sides} \\ &= 0.60 && \text{exposed on 3 sides} \end{aligned} \right\} \text{ hyperstatic beams}$$

For **compression members** (Class 1 or 2 section classification; clause 4.2.2.3)

$$R_{d,F(t)} = \frac{k_{\text{max},\theta} R_d}{1.2} \quad (3.50)$$

where  $R_d$  is the ambient design strength calculated using the buckling curve  $c$  of ENV 1993-1-1, and the 1.2 factor is an empirical correction factor.

$\theta$  here is less than  $510^\circ\text{C}$ ; for members other than tension members  $\theta < 350^\circ\text{C}$ .

*(b) Limiting Temperature Criterion*

For a member to perform adequately in a fire, ENV 1993-1-2 requires that

$$\theta \leq \theta_{a,\text{cr}} \quad (3.51)$$

where

$\theta$  = actual temperature

$\theta_{a,\text{cr}}$  = critical temperature which depends on degree of loading  $\mu_{(0)}$ .

The following formulae are suggested using plastic theory and strength reduction due to temperature:

$$\theta_{a,\text{cr}} = 78.38 \ln \left[ \left( \frac{1}{0.9674(\mu_{(0)})^{3.833}} \right)^{1/2} \right] + 482 \quad (3.51a)$$

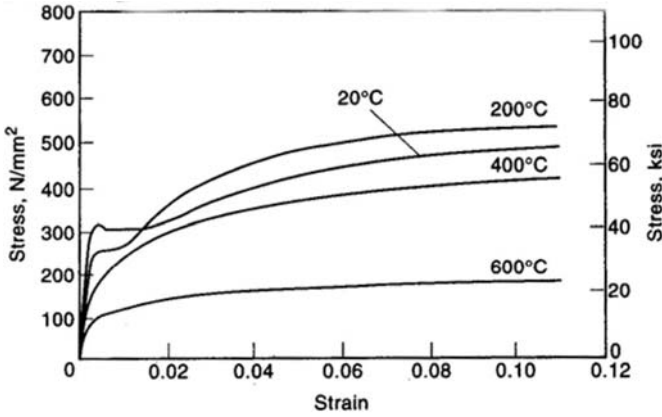


Fig. 3.14. Stress-strain curves for a mild steel (ASTM A36) at various temperatures

The parameter  $\mu_{(0)}$  is the degree of utilization and is given by:

$$\mu_{(0)} = \frac{S_{d,f}}{R_{d,F(0)}} \quad (3.52)$$

The ASTM stress-strain curve of mild steel under various temperatures is shown in Fig. 3.14.

### 3.5.2 Concrete and Reinforcing Steel

Thermal properties of concrete vary with the type and quantity of the aggregate in the concrete. Bangash provides a comprehensive treatment of this subject. The thermal conductivity of concrete is invariant with respect to the direction of heat flow and is dependent on the degree of crystallinity of aggregate. The higher the crystallinity, the higher the thermal conductivity, which decreases with temperature. Figure 3.15 shows the relationship between thermal conductivity and temperature for normal and lightweight concretes. It is difficult to establish a constant value for *specific heat* – a value of  $1170 \text{ J}/(\text{kg} \cdot ^\circ\text{C})$  ( $0.28 \text{ Btu}/(\text{lb} \cdot ^\circ\text{F})$ ) is commonly chosen. Figures 3.16 and 3.17 show specific heat values for different concretes.

The modulus of elasticity and strength of concrete have a direct bearing on the fire-resistance design of building structures. Again Bangash has dealt with this subject in greater detail. British Standard 8110 gives the following expression prior to any fire effects being involved.

$$E = 5.5 \sqrt{\frac{f_{cu}}{\gamma_m}} \text{ kN} / \text{mm}^2 \quad (3.53)$$

The compressive strength of concrete is defined in terms of Grades C, i.e., C2.5, C5, C7.5, C10, C12.5, C15, C20, C25, C30, C35, C40, C45, C50, C55,

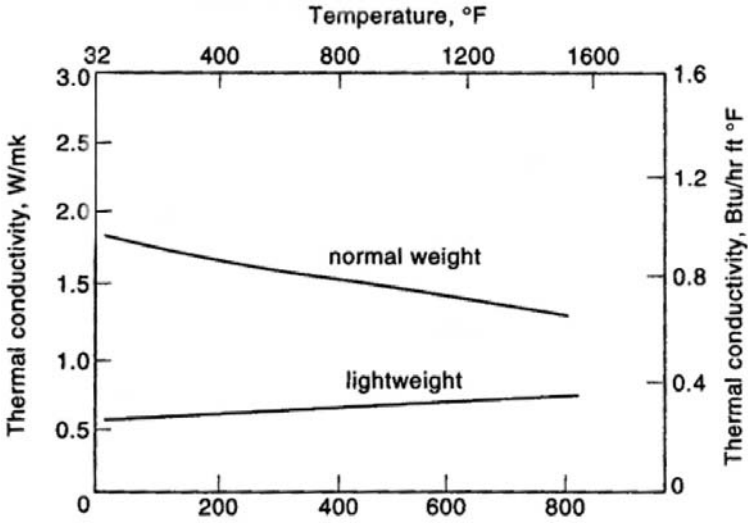


Fig. 3.15. Thermal conductivity of normal weight and lightweight concrete as a function of temperature

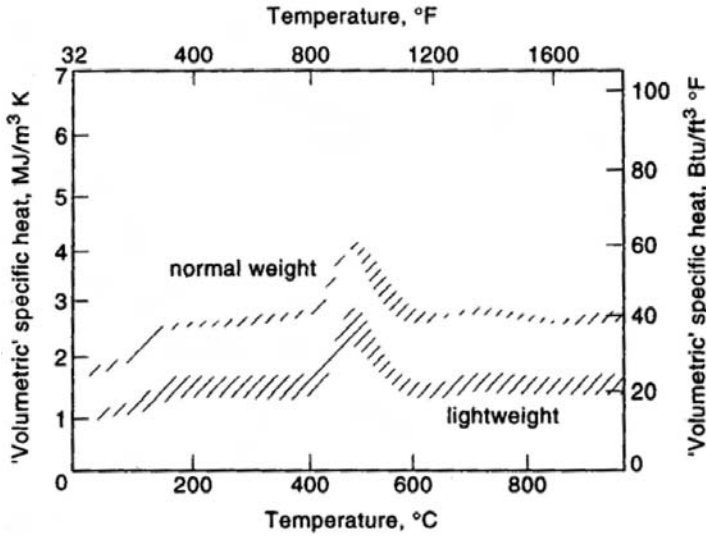


Fig. 3.16. Ranges of volumetric specific heats of normal weight and lightweight concrete

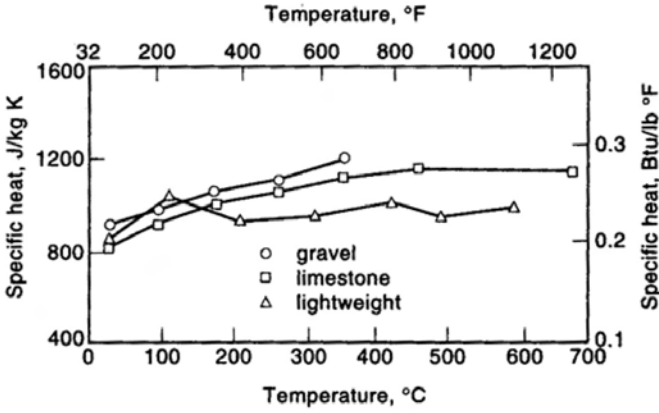


Fig. 3.17. Specific heat for different types of concrete

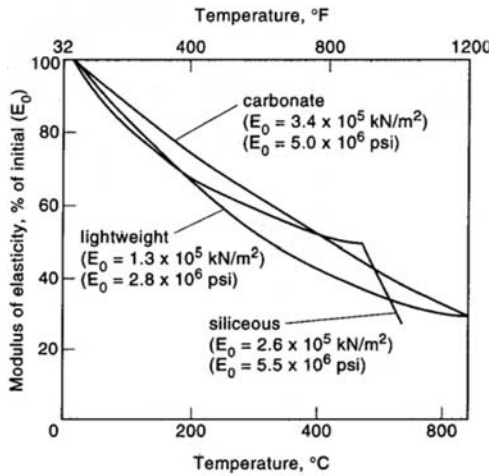
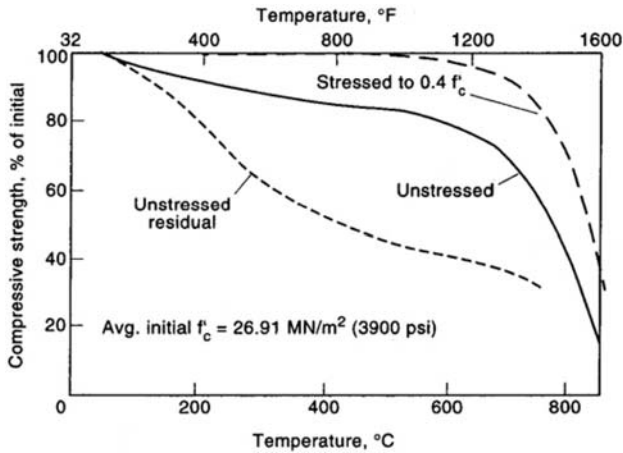


Fig. 3.18. Modulus of elasticity of concrete

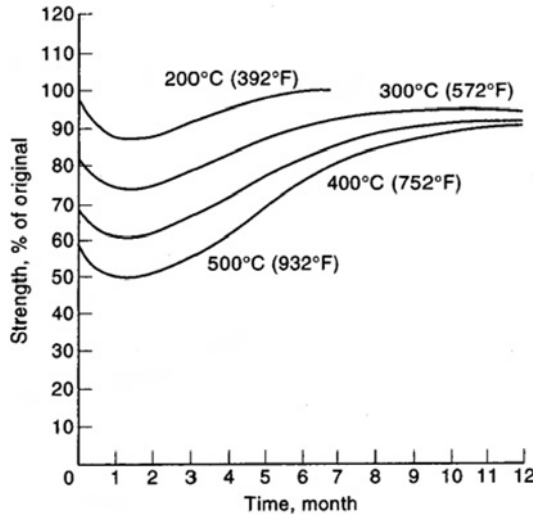
C60. The numerical figures are the compressive strength of concrete in N/mm<sup>2</sup> = MPa.

The ultimate strength of concrete is  $f_{cu}/\gamma_m = 0.67f'_{cu}$  ( $f'_c$  cylindrical strength =  $0.78f_{cu}$ ). The steel reinforcement has a characteristic strength  $f_y$  of 250 and 460 N/mm<sup>2</sup> for mild steel and high-yield steel respectively. The ultimate strength of the reinforcement is  $f_y/\gamma_m = 0.87f_y$ .

Since modulus of elasticity  $E_c$  is reduced with temperature, Fig. 3.18 shows the relationship between  $E_c$  for three different aggregates and temperature. Figures 3.19 to 3.21 summarize the compressive strength of concretes. Reference is made to Bangash for an extensive treatment of this aspect of research. The tensile strength of concrete is dealt with in detail by Bangash. Figure 3.22 shows the tensile strength of concrete at various temperatures.



**Fig. 3.19.** Compressive strength of carbonate aggregate concrete at high temperatures and after cooling



**Fig. 3.20.** Natural recovery of the compressive strength of the normal-weight concrete, heated at various temperatures

Creep of concrete is determined by various factors, the most important being the fire temperature on concrete. For an extensive study on creep, reference is made to Bangash. Harmathy shows creep information for two stress levels, 22.5% and 45% of the concrete strength, and several concrete temperatures for a period of three hours. The creep plays a significant role when the temperature exceeds 400°C (752°F). The Eurocode ENV 1992 *Design* work is not repeated in this section. However, a design example based on ENV 1992-1-2 with BS 8110 will be considered.



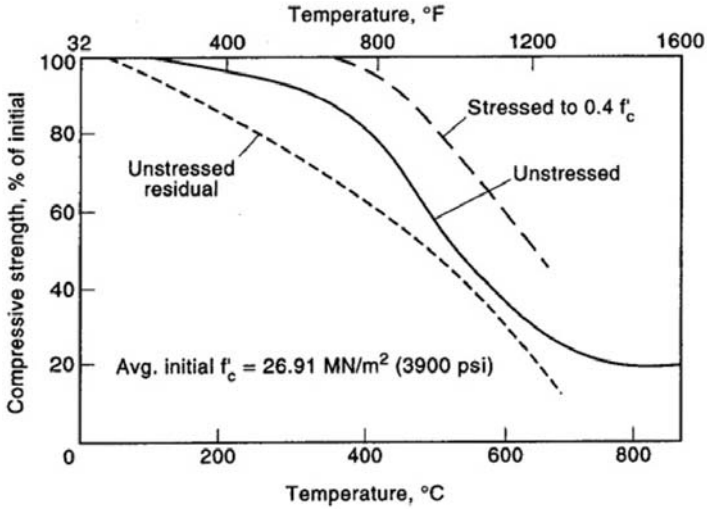


Fig. 3.21. Compressive strength of siliceous aggregate concrete at high temperatures and after cooling

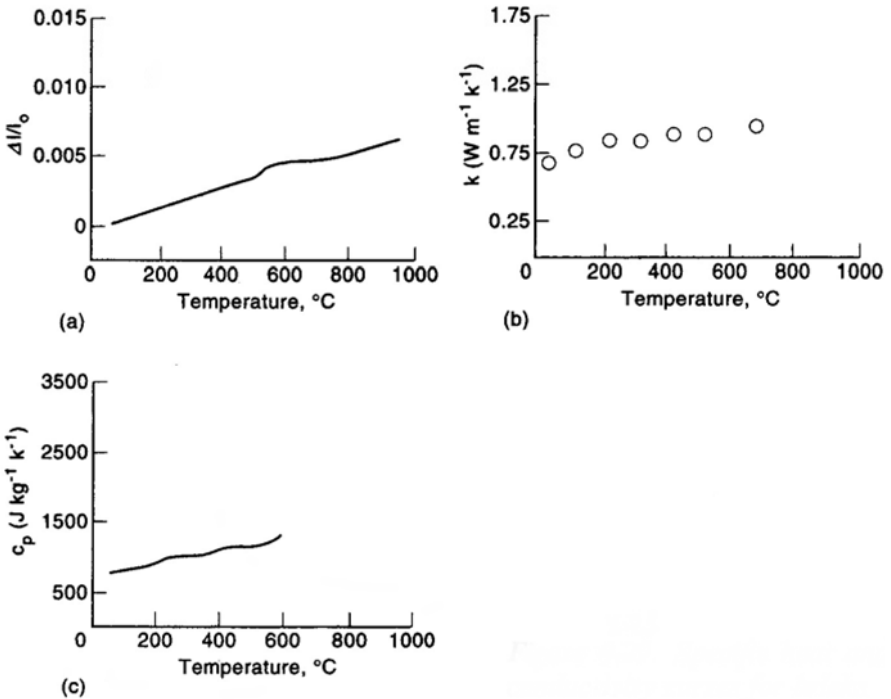


Fig. 3.22. Specific heat and thermal conductivity curves for bricks

### 3.5.3 Masonry/Brick/Block

Building brick materials do not undergo substantial physicochemical changes on heating. The density  $\rho$  of the brick ranges from 1660 to 2270 kg/m<sup>3</sup>, depending on the raw material used on moulding and firing technique. The porosity of the brick is from 19 to 36%. The modulus of elasticity,  $E$ , of the brick is between  $10 \times 10^3$  and  $20 \times 10^3$  MPa. Its compressive strength varies from 10 to 110 MPa. Purkiss [3.5] takes the compressive strength as 50 MPa. At room temperature, the coefficient of thermal expansion  $\alpha$  of brick is about  $5.5 \times 10^{-6}/(\text{mm} \times \text{K})$ . Harmathy [3.6,3.7] developed an empirical equation for the specific heat  $c_p$  of the medium density brick (1935 kb/m<sup>3</sup>) as:

$$c_p = 710.87 + 0.512T - \frac{8.676 \times 10^6}{T^2} \tag{3.54}$$

At room temperature, 298 K (298 Kelvin):

$$c_p = 710.87 + 0.512(298) - \frac{8.676 \times 10^6}{(298)^2} = 765.75 \text{ J}/(\text{kg} \times \text{K}) \tag{3.55}$$

Figure 3.22a shows the dilatometric curve. Figure 3.22b shows the thermal conductivity versus fire temperature of the brick wall. Figure 3.22c shows  $f$  specific heat versus fire temperature of a brick wall.

BS 5628 *Code of practice for use of masonry* (1989) covers materials and components, unreinforced, reinforced and prestressed masonry.

The materials used in the construction of masonry walls are bricks, blocks, mortar and wall ties.

Bricks are walling units not exceeding 337.5 mm in length, 225 mm in width and 112.5 mm in height. ‘Specification for Clay Bricks’ (BS 3921) has a standard format for a clay brick of 225 × 112.5 × 75 mm. This includes allowance for a 10 mm mortar joint. The worksize of the actual brick is 215 × 102.5 × 65 mm. Concrete bricks (BS 6073: Part 2: Precast Concrete Masonry Units) may have the following dimensions:

Length (mm)	thickness (mm)	height (mm)	
290	90	90	Add 10 mm to
215	103	65	all dimensions
190	90	90	for mortar joints
190	90	65	

Masonry walls can also be of blocks which are walling units that exceed the sizes specified for bricks. They are solid, hollow, cellular and insulating blocks and are of the following dimensions:

Length (mm)	hight (mm)	Thickness (mm)
390	190	
440	215	Varies from 60 to 250
590	215	

**Table 3.5.** Capacity factor  $\beta$  (BS5628 Part I, Table 7) 1978

$SR = \frac{h_{ef}}{t_{ef}}$	Eccentricity of top wall $e_x = \text{wall} = e_x$			
	Up to 0,05t	0,1t	0,2t	0,3t
0	1.0	0.88	0.66	0.44
6	1.0	0.88	0.66	0.44
8	1.0	0.88	0.66	0.44
10	0.97	0.88	0.66	0.44
12	0.93	0.87	0.66	0.44
14	0.89	0.83	0.66	0.44
16	0.83	0.77	0.64	0.44
18	0.77	0.70	0.57	0.44
20	0.70	0.64	0.51	0.37
22	0.62	0.56	0.43	0.30
24	0.53	0.47	0.34	–
26	0.45	0.38	–	–
27	0.40	0.33	–	–

For general purpose masonry construction a 1:1:6 cement: lime: sand mortar will be sufficient. For high-strength load-bearing masonry a 1: 1/2:3 cement: lime: sand mortar is more appropriate. For reinforced masonry a mix not weaker than 1: 1/2: 4 1/2 cement: lime: sand is normally adopted. The characteristic loads are given below:

- (a) design and imposed loads
- (b) dead, imposed and wind loads
- (c) accidental damage (this may be considered for a fire situation).

Ultimate design load

$$\begin{aligned}
 &= \gamma_f \text{ characteristic load} \\
 &= \gamma_f (\text{dead load}) + \gamma_f (\text{imposed load}) \\
 &= 1.5G_k + 1.6Q_k
 \end{aligned} \tag{3.56}$$

The characteristic compressive strengths of masonry,  $f_k$ , give the values of  $f_k$  for bricks and block in conjunction with the designated mortar mix. The ultimate compressive strength is equal to  $f_k/\gamma_m$  where  $\gamma_m$  = partial safety factor given by BS 5628: Part 1.

Vertically loaded walls and brick columns can fail by crushing or, if they are slender, by lateral buckling. The slenderness ratio (SR) is needed if the walls fail by buckling to crushing during a fire.

$$SR \text{ (wall)} = \frac{\text{effective height } (h_{ef})}{\text{effective thickness } (t_{ef})} \quad \text{or} \quad \frac{\text{effective length } (l_{ef})}{\text{effective thickness } (t_{ef})} \tag{3.57}$$

For a masonry column the slenderness ratio is:

$$SR = \frac{h_{ef}}{t_{ef}} \not\geq 27 \quad (3.58)$$

SR (wall)  $\not\geq 20$  if  $t_{ef} < 90$  mm in two storeys.

If the load occurring on walls is eccentric and the load capacity is reduced by buckling, then the capacity reduction factor  $\beta$  which is dependent on  $e_x/t_f$  ratio must be applied. Table 3.5 gives the reduction factor  $\beta$ .

$$\text{The vertical design strength of the wall} = \frac{\beta_f f_k}{\gamma_m} \quad (3.59)$$

$$\text{The vertical design strength of the column} = \frac{\beta t f_k}{\gamma_m} \quad (3.60)$$

All symbols have previously been defined except  $b$  and  $t f$ .

$b$  = width of column

$t$  = actual thickness of wall or leaf and column.

## 3.6 Methods of Analysis and Design

A number of numerical and analytical techniques are available along with computer packages for the analysis of building structures, with particular reference to the fire environment. Practically every country has a fire code. Analytical, empirical and design equations are available to assess the fire protection of structural components in major materials such as steel, concrete, timber and masonry. In this text, the author has classified these equations in the following manner.

1. Empirical and code analytical equations.
2. Limit state and plastic analysis.
3. Finite element analysis, finite difference analysis and boundary element analysis.

### 3.6.1 Empirical and Code Analytical Equations

All calculations of fire resistance involve the determination of the temperatures, deformations of the structural components and their strength during exposure to fire. The temperature distribution analysis is generally done by finite element, boundary element and finite difference methods since it is time-dependent and the calculation procedure is always complex. In order to simplify these complex procedures, numerical methods such as finite element method and high-speed computers are very convenient.

### 3.6.2 Calculations of Fire Resistance of Steel Members

The temperature rise in a steel structure or its elements can be estimated using quasi-steady-state equations by Malhotra. The equations are derived from one-dimensional heat transfer equations.

*(a) Unprotected steel members*

The equation for temperature rise during a short time period  $\Delta t$  is given by:

$$\Delta T_s = \frac{\alpha}{c_s(W/D)}(T_f - T_s)\Delta t \quad (3.61)$$

$\Delta T_s$  = temperature rise in steel ( $^{\circ}\text{F}/^{\circ}\text{C}$ )

$a$  = heat transfer for coefficient from exposure to steel member  
( $\text{Btu}/(\text{ft}^2 \times \text{sec})$  or  $\text{W}/\text{m}$ )

$D$  = heated perimeter (ft or m)

$c_s$  = specific heat for steel ( $\text{Btu}/(\text{lb} \times ^{\circ}\text{F})$ ) or  $\text{J}/(\text{kg} \times ^{\circ}\text{C})$

$W$  = weight of steel ( $\text{lb}/\text{ft}$  or  $\text{kg}/\text{m}$ )

$T_f$  = fire temperature ( $\bar{R}$  or  $K$ )

$T_s$  = steel temperature ( $\bar{R}$  or  $K$ )

$\Delta t$  = time step (sec)

where

$$a = \alpha_r + \alpha_c \quad (3.62)$$

$\alpha_r$  = radiative portion of the heat transfer.

(Mulhotra considers:

$$= \frac{1}{W/D} = \frac{S}{m_s \rho_s A_s} \quad (3.63)$$

where  $S$  = area,  $m_s$  = mass).

$\alpha_c$  = convective portion of heat transfer

$$= 9.8 \times 10^{-4} \text{ to } 1.2 \times 10^{-3} \text{Btu}/(\text{ft}^2 \times \text{sec})$$

$$= 20 \text{ to } 25 \text{ W}/(\text{m}^2 \times ^{\circ}\text{C})$$

$$\Delta t < \begin{cases} 15.9 W/D & \text{Imperial units} \\ 3.25 W/D & \text{SI units} \end{cases}$$

$P_s/A_s$  = shape factor

$A_r$  (based on the Stefan-Boltzman law for radiation)

$$= \frac{5.77w_r}{T_f - T_s} \left[ \left( \frac{T_f + 273}{100} \right)^4 - \left( \frac{T_s + 273}{100} \right)^4 \right] \text{ W}/(\text{m} \times ^{\circ}\text{C}) \quad (3.64)$$

$w_r$  = emissivity of flames = 0.7 for steel surfaces.

In American practice  $w_r = \varepsilon_f$  and  $\alpha_r$  is given as:

$$\alpha_r = \frac{C_1 E_f}{T_f - T_s} (T_f^4 - T_s^4) \quad (3.65)$$

$$C_1 = 4.76 \times 10^{-13} \text{ Btu}/(\text{sec} \times \text{ft}^2) R^4 \\ = 5.77 \times 10^{-8} \text{ W}/\text{m}^3 K^4.$$

The values of  $w_r$  or  $E_f$  are given for more cases in Table 3.6 along with the shape factor  $P_s/A_s$ .

Table 3.6. Emissivity  $\omega_r$  or  $\epsilon_r$ , heated perimeters and shape factors for steel shapes

Type of construction exposed to fire	$\omega_r$ or $\epsilon_r$	Shapes	Heated perimeter*	Shape factor unprotected steel†
1. Columns on all sides	0.7		$D = 4b_f + 2d - 2t_w$	$\frac{D \text{ or } P_s}{A_s}$
2. Columns outside face	0.3		$D = 3b_f + 2d - 2t_w$	$\frac{D \text{ or } P_s}{A_s}$
3. Girder with $\frac{\text{width}}{\text{depth}} \leq 0.5$	0.5		$D^2 = \frac{(b_f + d)}{b_f d}$	$\frac{D \text{ or } P_s}{A_s}$
4. Girder with $\frac{\text{width}}{\text{depth}} < 0.5$	0.7		$D = \frac{b_f + d}{t_w (b_f + d - 2t_w)}$	$\frac{D \text{ or } P_s}{A_s}$
5. Box or lattice girders	0.7		$D = \frac{4d}{d^2 - (D - 2t_w)^2}$	$\frac{D \text{ or } P_s}{A_s}$
6. Girder with concrete floor slab, only underside of the bottom flange exposed	0.5		$D = 8b_f + 2d + 2a - 4t_w$	$\frac{D \text{ or } P_s}{A_s}$
7. Floor girder with slab on the top flange	0.5		$D = 4a + 2b + 2c$	$\frac{D \text{ or } P_s}{A_s}$

\* Indicates the surface through which the heat is flowing through the steel.

† The shape factor is the rise of temperature of a steel section.

$A_s$  = surface area.

The fire temperature  $T_f$  is evaluated at time  $t$  according to ASTM E-119 test

$$T_f = C_1 \log_{10}(0.133t + 1) + T_0 \quad (3.66)$$

where  $t$  is time and

$$\begin{aligned} C_1 &= 620 \text{ with } T_f, T_0 \text{ in } ^\circ\text{F} \\ &= 34.5 \text{ with } T_f, T_0 \text{ in } ^\circ\text{C} \\ T_0 &= \text{initial temperature.} \end{aligned}$$

*(b) Protected steel members*

Here the insulating material is considered along with steel for the overall thermal resistance. If the thermal capacity of the insulating material is neglected, the value of  $\Delta T_s$  is given as

$$\Delta T_s = \frac{k}{c_s h W / D} (T_f - T_s) \Delta t \quad (3.67)$$

All symbols are defined above, except  $k$  and  $h$ :

- $k$  = thermal conductivity of the insulating material (Btu/(ft  $\times$  sec  $\times$   $^\circ\text{C}$ ) or W/(m  $\times$   $^\circ\text{C}$ ),  
 $h$  = protection thickness (ft or m).

*Conditions*

- (a) If the thermal capacity of the material, then the following inequality is true:

$$c_a = \frac{W}{D} > 2c_i \rho_i h \quad (3.68)$$

- (b) If the thermal capacity is considered when gypsum and concrete are used as insulating materials, the value of  $\Delta T_s$  can be written as:

$$\Delta T_s = \frac{k}{h} \left( \frac{T_f - T_s}{(c_s h W / D) + 1/2c_i \rho_i h} \right) \Delta t \quad (3.69)$$

All symbols are defined above except  $c_i$ , and  $\rho_i$ .

- $c_i$  = specific heat of insulating material (Btu/(lb  $\times$   $^\circ\text{F}$ ) or J/(kg  $\times$   $^\circ\text{C}$ )  
 $\rho_i$  = density of insulating material (lb/ft<sup>3</sup> or kg/m<sup>3</sup>).

Figure 3.23a–d shows the relationship between  $D/A_s$  versus temperatures and durations for various values of  $h/k$  values.

The European Commission suggests in Eurocode that the value of  $\Delta t$  can be defined as follows:

$$\Delta t \not\leq \frac{25000}{D/A_s}.$$

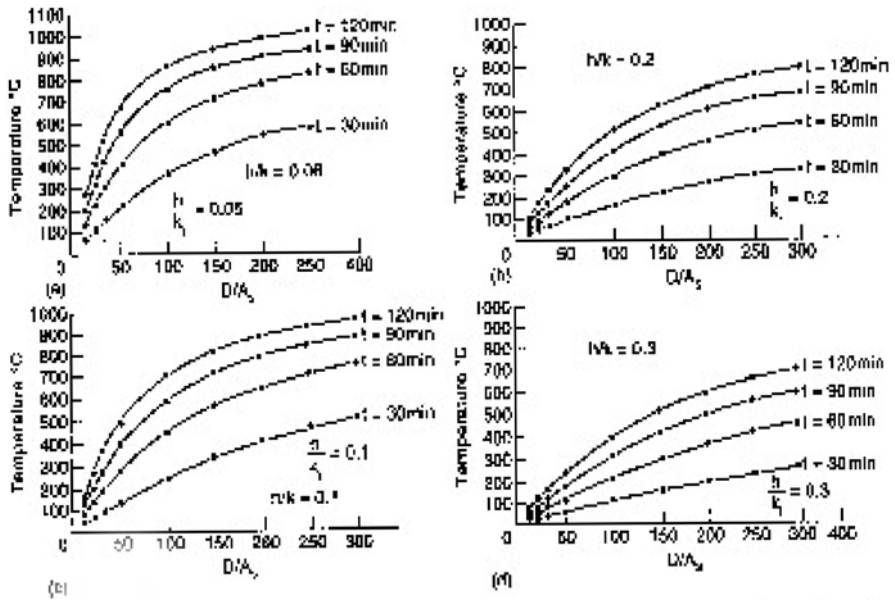


Fig. 3.23. Relations between  $D/A_s$  versus temperature versus duration for  $h/k$  ratios

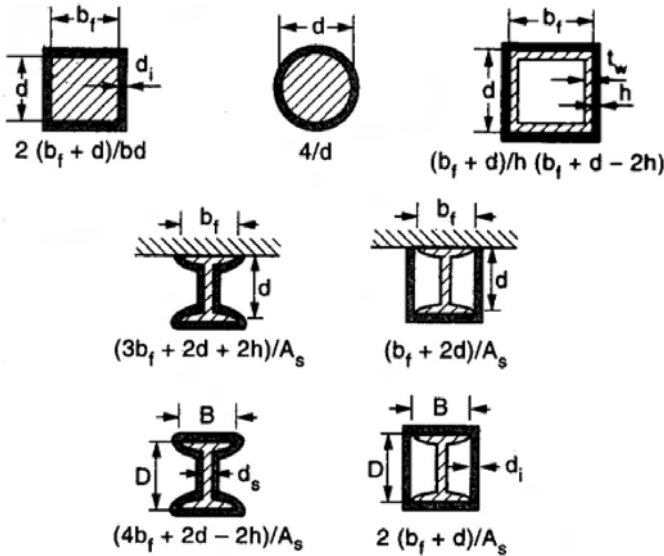
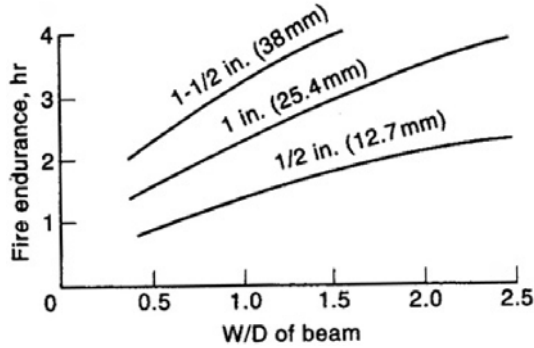
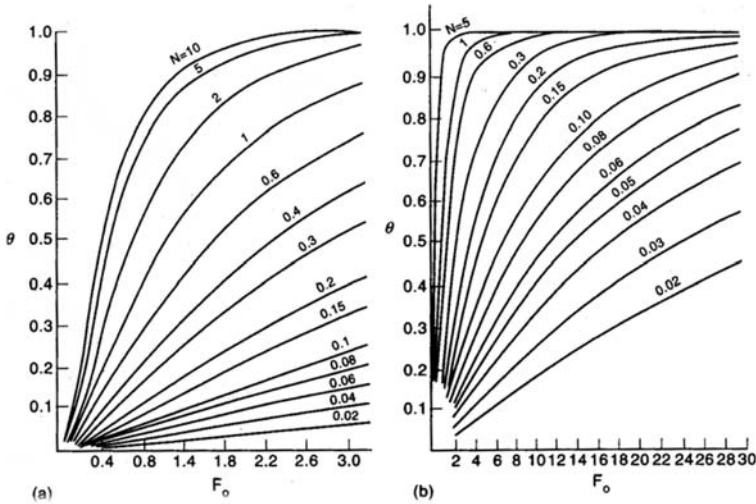


Fig. 3.24. Shape factors for protected steel





**Fig. 3.25.** Fire protection and endurance of steel beams (average section temperature 10000°F), ASTM E-119



**Fig. 3.26.** Lie's Graphs: dimensionless steel temperatures versus Fourier numbers

Generally, the shape factor for  $D/A_s$  is in the range of 10 to 300 for an average resulting emissivity ( $w_f$  or  $E_f$ ) = 0.5. Figure 3.23 shows the shape factors for protected steel sections. Figure 3.24 gives shape factors for protected steel.

Heat transfer analyses can be very tedious and involved. Computer programs have been developed and the outputs are translated into graphs. Two of such graphs are known as Jeanes' Graph and Lie's Graphs. Jeanes formulated a series of time-temperature graphs of protected steel beams. The protection is generally provided by a specific spray-applied cementitious material with a range of 0.5 in. (12.7 mm) to 1.5 in. (38 mm). They are commonly used for wide-flanged beams. Figure 3.25 shows  $W/D_s$  of the beam versus fire endurance for various insulation thicknesses.

Lie's Graphs are shown in Fig. 3.26. In order to use these graphs, some dimensionless parameters have to be evaluated: Fourier number  $F_0$  for the layer, and  $N$  and  $\theta$ , defined below:

$$F_0 = \frac{dt}{h^2} \quad (3.69a)$$

$$N = \frac{\rho_t c_t h}{c_s (W/D)} \quad (3.70)$$

$$\theta = \frac{T - T_0}{T_m - T_0} \quad (3.71)$$

The mean temperature  $T^m$  with a heating time  $t$  for these graphs is calculated from the standard time-temperature curve:

$$\begin{aligned} T_m &= 150(\ln 480t - 1) - \frac{30}{t}, \quad T(^{\circ}\text{C}) \\ &= 270(\ln 480t) - 238 - \frac{54}{t}, \quad T(^{\circ}\text{F}) \end{aligned} \quad (3.72)$$

(c) *Steel columns*

In steel columns, the temperature due to fire is still a function of  $W/D$ , weight-to-heated-perimeter ratio. Hence, to avoid rapid loss of strength in a column it is necessary to insulate it. Similar to beam sections, the heated perimeter  $D$  of some steel columns is shown in Tables 3.7a and 3.7b along with their fire resistance formulae. Concrete encasement is another form of protection for steel columns. Lie and Harmathy have developed methods of protection. Figure 3.27 gives three cases for which the following equations are given for both normal and lightweight concrete.

(a) Normal concrete protection on all sides. The resistance  $R$  is given as:

$$R = 11 \left( \frac{W}{D} \right)^{0.7} + 19h^{1.6} \left\{ 1 + 94 \left[ \frac{H}{\rho_c h(L+h)} \right]^{0.8} \right\} \quad (3.73)$$

(b) Lightweight concrete protection on all sides. The resistance  $R$  is given as:

$$R = 11 \left( \frac{W}{D} \right)^{0.7} + 23h^{1.6} \left\{ 1 + 94 \left[ \frac{H'}{\rho_c h(L+h)} \right]^{0.8} \right\} \quad (3.74)$$

All notations have been defined previously, except

$H'$  = thermal capacity of steel column at ambient temperature  
(0.11 WBtu/(ft - °F))

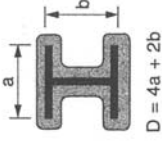
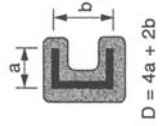
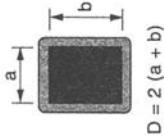
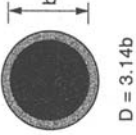
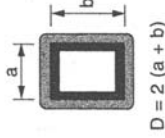
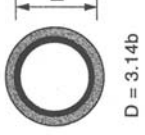
$\rho_c$  = concrete density (lb/ft<sup>3</sup> or kN/m<sup>3</sup>).

Table 3.7a. Steel columns, heated perimeter and fire resistance

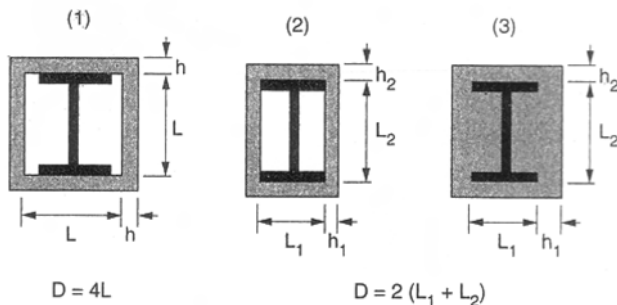
Type	Heated perimeter fully protected box type	Fire resistance <i>R</i>
(1) Low density box protection		(1) $R = (C_1(W/D) + C_2)h$
(2) Density range $20 < \rho \leq 50 \text{ lb/ft}^3$ $320 \leq \rho \leq 800 \text{ kg/m}^3$		(2) $R = (1200(W/D_p) + 30)h$ Chemically stable materials such as vermiculite, perlite, sprayed mineral fibres and dense mineral wool
(2a) As above in (2)		(2a) Cement paste, gypsum, cementitious mixtures and plasters
(3) Density range as above in (2)		(3) $R = (1200(W/D_p) + 72)h$ Pastes or gypsum such as cementitious mixture and plasters

\*  $C_1, C_2$  = material constants;  $W$  = weight of steel column lb/ft (kg/m);  $D$  = heated perimeter inches (mm or m);  $h$  = thickness of protection in (mm or m).

Table 3.7b. Steel columns, heated perimeter and fire resistance

Type	Heated perimeters fully protected; contour protection	Fire resistance, $R$
(4) Density $10 \leq \rho \leq 20 \text{ lb/ft}^3$ $(160 \leq \rho \leq 320 \text{ kg/m}^3)$	  $D = 4a + 2b$	(4) $R = (45(W/D) + 30)h$ Small round and square columns (width < 6 in. (152 mm)) $h \leq 1.5 \text{ in. (35 mm)}$
(5) As in (4)	 $D = 2(a + b)$  $D = 3.14b$	(5) $R = (60(W/D) + 30)h$ All other shapes, sizes and thickness of protection
(6) Gypsum wall board AISI 1980	 $D = 2(a + b)$  $D = 3.14b$	(6) $R = 130(hW'/2D)^{0.75}$ $W' = W + 50(hD/144)$

Note: All parameters as before.  $W'$  = weight of steel column with gypsum wall board protection (lb/ft or kg/m).



**Fig. 3.27.** Concrete-protected structural steel columns. (1) square shape protection with a uniform thickness of concrete cover on all sides; (2) rectangular shape with varying thickness of concrete cover and (3) encasement having all re-entrant spaces filled with concrete

### 3.6.3 Additional Methods of Protection for Hollow Columns

There are two types of hollow column protection arrangements, as follows.

- (a) Filling the hollow columns and carrying a share of the load at room temperature. Concrete acts as a heat sink and takes more load as steel strength is reduced.
- (b) Filling the hollow columns with water. Water inside absorbs the heat transferred from the fire to the column. The heat is dissipated by evaporation of the water. Flemington R.A. [3.8] has done research on the quantity of water necessary to prevent excessive temperature rise of steel. The quantity of external storage water required to achieve fire resistance is given by

$$V_w = 3.92 \times A \times \bar{q} \times 10^{-7} \tag{3.75}$$

where

$V_w$  = required external storage water ( $m^3$ ),

$A$  = surface area of the column ( $m^2$ ),

$\bar{q}$  = heat transferred to the column during a fire test per unit surface area ( $kJ/m^2$ )

= 150740 for  $\frac{3}{3}$  hour fire rating

= 225260 for 1 hour fire rating

= 580 960 for 2 hour fire rating

= 785460 for 3 hour fire rating

= 1014460 for 4 hour fire rating.

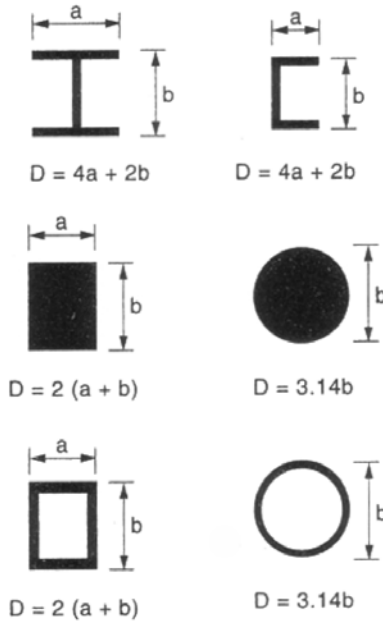


Fig. 3.28. Sections of unprotected steel columns

### Column-Water Interaction

A comprehensive finite element analysis is required for the heat transfer to water while interacting with columns in the fire environment. Appendix I gives a guidance in this direction.

### Unprotected Steel Columns

Figure 3.28 shows data on unprotected steel shapes used in this section. The AISC gives the following formulae for the fire resistance of unprotected steel columns:

$$R = 10.3 \left( \frac{W}{D} \right)^{0.7} \quad \text{for } W/D < 10 \quad (3.76)$$

$$R = 8.3 \left( \frac{W}{D} \right)^{0.8} \quad \text{for } W/D \geq 10 \quad (3.77)$$

where

$R$  = resistance in minutes

$W$  = weight of steel column per ft length

$D$  = heated perimeter of steel section (in).

The values of  $D$  are given in Tables 3.7a,b and also in Fig. 3.28.

### 3.6.4 Summary of Empirical Equations for Steel Columns Fully Protected Against Fire (USA)

Table 3.8 provides a summary of the empirical equations of columns when they are protected by various insulations. In each case the resistance  $R$  is given.

### 3.6.5 Examples in Steel Structures

#### Example 3.4 American Practice

A wide-flange WF 24 × 76 steel beam with 1 in (25.4 mm) of spray-applied cementitious material (British equivalent 610 × 229 × 113 kg/m). The beam has  $W/D = 1.03$  lb/ft and nowhere does the temperature exceed 1000°F (538°C) or 811 K. The insulation temperature is to be 750°F while keeping the steel temperature at 538°C. The results obtained from

- (a) Malhotra's quasi-steady state approach
- (b) Jeanes' graph
- (c) Lie's graph

are compared. To calculate the fire resistance  $R$  for the spray-applied beam, the following data are used:

	Steel	Insulation
$K$ (Btu/ft × hr × °F)	25.6	0.067
$C_p$ (Btu/lb × °F)	0.133	0.305
$\gamma$ (density/ft <sup>3</sup> )	480	14.9

(a) *Malhotra's Method*

$$c_s W/D > 2c_i \rho_i d$$

$$0.133 \times \frac{1.03}{1/12} > 2 \times 0.305 \times 14.9 \times \frac{1.0}{12}$$

$$1.644 > 0.757$$

The thermal capacity of insulation is therefore neglected. The steel temperature rise for each time step is:

$$\Delta T = \frac{0.067/3600}{10.132 \times \frac{1.0}{12} \times \frac{1.03}{1/12}} (T_f - T_s) \Delta t$$

$$= 1.37 \times 10^{-4} (T_f - T_s) \Delta t$$

$$\Delta t(\max) = 15.9 \frac{w}{d} = 15.9 \times \frac{1.03}{1/12} \approx 195 \text{ sec}$$

**Table 3.8.** Empirical equations for protected columns

Protection	Empirical equation	Protection	Empirical equation
Column/unprotected	<p><math>R = 10.3(w/d &gt;)^{0.7}</math>, (for <math>W/D &lt; 10</math> (for critical temperature of 100°F))</p> <p><math>R</math> = fire endurance time (min)</p> <p><math>W</math> = weight of steel section per linear foot (lb/ft)</p> <p><math>D</math> = heated perimeter (in.)</p>	Column/spray-applied materials and board products – wide flange shapes	<p><math>R = [C_1(W/D) + C_2]h</math></p> <p><math>C_1</math> and <math>C_2</math> = constants for specific protection material</p>
Column/gypsum wall-board	<p><math>R = 130 \left( \frac{hW/D}{2} \right)^{0.75}</math></p> <p>where</p> <p><math>W' = W + \left( \frac{50hD}{144} \right)</math></p> <p><math>H</math> = thickness of protection (in.)</p> <p><math>W'</math> = weight of steel section and gypsum wall-board (lb/ft)</p>	Column/concrete cover	<p><math>R = R_0(1 = 0.03 \text{ m})</math></p> <p>where</p> $R_0 = 10(W/D)^{0.7} + 17 \left( \frac{h^{1.6}}{k_c^2} \right) \times \left\{ 1 + 26 \left[ \frac{H}{\rho_c C_c h(L+h)} \right]^{0.8} \right\}$
Column/spray-applied materials and board products – hollow	<p><math>R = C_1(A/P)h + C_2</math></p> <p><math>C_1</math> and <math>C_2</math> = constants for specific protection material</p> <p>The <math>A/P</math> ratio of a circular pipe is determined by: <math>A/P</math> pipe = <math>(t(d-t)/d)</math></p> <p>where</p> <p><math>d</math> = outer diameter of the pipe (in)</p> <p><math>t</math> = wall thickness of the pipe (in)</p> <p>The <math>A/P</math> ratio of a rectangular or square tube is determined by:</p> $A/P \text{ tube} = \frac{t(a+b) - 2f}{a+b}$ <p>where</p> <p><math>a</math> = outer width of the tube (in)</p> <p><math>b</math> = outer length of the tube (in)</p> <p><math>t</math> = wall thickness of the tube (in)</p>	Column/concrete en-cased	<p><math>D = 2(b_t + d)</math></p> <p><math>R_0</math> = fire endurance at zero moisture content of concrete (min)</p> <p><math>m</math> = equilibrium moisture content of concrete (% by volume)</p> <p><math>b_t</math> = width of flange (in)</p> <p><math>d</math> = depth of section (in)</p> <p><math>k_c</math> = thermal conductivity of concrete temp. (Btu/(hr-ft<math>\times</math>°F))</p> <p>For concrete-encased columns use:</p> $H = 0.11W + \rho_c C_c / 144(b_t d - A_s)$ $D = 2(B_t + d)$ $L = (b_t + d - )/2$ <p><math>H</math> = thermal capacity of steel section at ambient temp. <math>\times = 0.11tT(\text{Btu}/(\text{ft}\text{-}\text{°F}))</math></p> <p><math>C_c</math> = specific heat of concrete at ambient temp. (Btu/(lb<math>\times</math>°F))</p> <p><math>L</math> = inside dimension of one side of square concrete box protection (in)</p> <p><math>A_s</math> = cross-sectional area of steel column (in<math>^2</math>)</p>



One hour allowable time is prescribed by various codes for fire resistance. At  $T_0$  the room temperature is around  $21^\circ\text{C}$  ( $70^\circ\text{F}$ ). The time step is chosen to be 3 min. The results are as follows:

Time (min)	$(T_f - T_s)^\circ\text{F}$	$\Delta T_s(^\circ\text{F})$	$T_s(^\circ\text{F})$
0			70
3	690	18.53	*88.53
6	937	25.16	113.69
$\vdots$	$\vdots$	$\vdots$	$\vdots$
185	764	39	1000

The fire endurance is 106 min.

(Note: To convert to  $^\circ\text{C}$ , use  $^\circ\text{C} \frac{^\circ\text{F}-32}{1.8}$  for all values.)

(b) *Jeane's Graph*

$W/D = 1.03 \text{ lb/ft}$  in with an insulation thickness of 1 in. The fire endurance is estimated to be 2 hr or 120 min.

(c) *Lie's Graph*

Figures and equations are used.

*Dimensionless Parameters*

$$\begin{aligned}
 F_0 &= \frac{at}{h^2} & a &= \frac{K}{\rho_i c_i} = \frac{0.067}{14.9 \times 0.305} = 0.014 \text{ ft}^2/\text{hr} \\
 &= \frac{0.0147t}{(1/12)^2} = 2.12t \quad (t \text{ in hours}) \\
 N &= \frac{\rho_i c_i h}{c_s(W/D)} = \frac{14.9 \times 0.305 \times (1/12)}{0.133(1.03/(1/12))} = 0.2304
 \end{aligned}$$

Adopting a trial and error method with a critical temperature of  $1000^\circ\text{F}$ , the fire endurance time is 115 min.

Jeane's and Lie's approaches are in close agreement. Malhotra's method is methodical and the small difference may be attributed to the equations being dependent on one-dimensional heat transfer.

### Example 3.5 British Practice

Calculate the time or duration for a beam of  $457 \times 152 \times 60 \text{ kg/m}$  fully protected by 25 mm sprayed fibre insulation for a temperature rise in the steel of  $270^\circ\text{C}$ . Use the following data and the relevant European Codes including the Eurocode 3 and the ISO formula for the furnace temperature  $T_f$ .

Steel:

$$\begin{aligned}A_s &= 75.8 \text{ cm}^2, \\ \rho_s &= 7850 \text{ kg/m}^3, \\ p_s \text{ or } D &= 1.254 \text{ m}, \\ \bar{c}_s &= 520 \text{ J/kg}^\circ\text{C}\end{aligned}$$

Insulation:

$$\begin{aligned}D_i &= 0.025 \text{ m}, \\ k_i &= 0.11 \text{ W/m}^\circ\text{C}, \\ c_i &= 1050 \text{ J/kg}^\circ\text{C}, \\ \rho_i &= 300 \text{ kg/m}^3.\end{aligned}$$

ISO formula for furnace temperature  $T_f$ :

$$\begin{aligned}T_f &= 345 \log_{10}(8t + 1) + T_0, \\ \Delta t &> \frac{25000}{(P_s \text{ or } D)/A_s}, \\ T_0 &= \text{initial temperature} = \text{ambient temperature} = 20^\circ\text{C}, \\ \frac{P_d}{A_s} &= \frac{1.254}{75.8 \times 10^{-4}} = 16.5 \text{ m}, \\ \Delta t &= \frac{25000}{1.254/75.8 \times 10^{-4}} 152 \text{ sec} = 2.5 \text{ min}, \\ c_s \rho_s A_s &= 520 \times 7850 \times 75.8 \times 10^{-4} = 30942, \\ 2c_i \rho_i d_i P_i &= 2 \times 1050 \times 300 \times 0.025 \times 1.254 = 19.750.\end{aligned}$$

$30942 > 19750$ : The insulation has a low heat capacity.

$$\begin{aligned}\Delta T_s &= \frac{165 \times 2.5 \times 60}{520 \times 7850} (T_f - T_s) \times \frac{0.11}{0.025} = 0.027(T_f - T_s), \\ T_f &= 345 \log_{10}(8t + 1) + T_0.\end{aligned}$$

Table 3.9 shows a step-by-step calculation. It can be seen that, for a value of  $270^\circ\text{C}$ , the duration is around 150 minutes or  $2\frac{1}{2}$  hours.

### Example 3.6 American Practice

A steel column is protected by 1 in thick (25.4 mm) spray-applied cementitious material. Using the American practice and the following data, determine the fire resistance  $R$  for the column:

$$C_1 = 63 \quad C_2 = 36 \quad \frac{W}{D} = 1.4 \text{ 5 lb/ft} \times \text{in}$$

**Table 3.9.** Step-by-step calculations

t (min)	$T_f$ (°C)	$T_f - T_s$ (°C)	$\Delta T_s$ (°C)	$T_s$ (°C)
0				20
$\frac{2.5}{2} = 1.25$		359	9.70	29.70
2.5	486	486.3	12.32	42.02
5.0	598.43	556.41	15.02	57.04
7.5	672.98	615.94	16.63	73.67
10.0	732.1	658.43	17.78	
20.0	852.8	761.35	20.56	91.45
30.0	913.25	821.8	22.20	113.65
40.0	978.4	864.75	23.35	137
60.0	1062.34	925.34	25.00	162
90.0	1148.00	986.00	26.62	188.62
95.0	1182.72	994.10	26.84	215.46
100.0	1217.46	1002.00	27.05	242.51
150	1305.01	1062.5	28.70	271.21

Protection: contour profile type

$$\begin{aligned}
 R &= \left( 63 \frac{W}{D} + 36 \right) h \\
 &= (63 \times 1.44 + 36) \times 1 \\
 &= 126.72 \text{ min} \approx 2 \text{ hr}
 \end{aligned}$$

**Example 3.7 American Practice**

A column W 8 × 28 is encased in a normal concrete with all spaces duly filled in. Using the American practice and the following data, determine the fire resistance time for the column. Using ASTM data:

$$\begin{aligned}
 h_2 = h_1 = h &= 1.5 \text{ in} & b_f &= 6.535 \text{ in} & d &= 8.060 \text{ in} \\
 \frac{W}{D} &= 0.67 \text{ lb}/(\text{ft} \times \text{in})
 \end{aligned}$$

Protection: contour profile type

$$A = 8.25 \text{ in}^2$$

Thermal properties of concrete at 70°F(21°C):

	Normal concrete	Lightweight concrete
$K$ (btu/(hr×ft×°F))	0.95	0.35
$C_p = C_c$ (Btu/(lb×°F))	0.20	0.20
$\rho_c =$ density of concrete	= 100 lb/ft <sup>3</sup> for lightweight concrete = 150 lb/ft <sup>3</sup> for normal concrete	

concrete cover = 1.5 in

moisture content in both concretes = 5% } for lightweight concrete  
for normal concrete

If this column has a lightweight concrete for protection, what is the fire protection time for the same column?

$$R = R_0(1 + 0.03 m)$$

$$m = 5\%$$

$$R = 1.15 R_0 \text{ for both lightweight and normal concrete}$$

$$R_0 = 10 \left( \frac{W}{D} \right)^{0.7} + 17 \left( \frac{h^{1.6}}{K_c^{0.2}} \right) \left\{ 1 + 26 \left[ \frac{H}{\rho_c c_c h(L + h)} \right]^{0.8} \right\}$$

$$h = 1.5$$

$$H = 0.11 W + \frac{\rho_c c_c}{144} (B_f D - A_s)$$

$$= 0.11 \times 28 + \frac{\rho_c \times 0.2}{144} (6.535 \times 8.060 - 8.25).$$

For  $\rho_c = 100 \text{ lb/ft}^2$ : lightweight concrete:  $H = 9.25$ .

For  $\rho_c = 150 \text{ lb/ft}^3$ : normal concrete:  $H = 10.484$ .

$$L = 1/2(b_f + d) = 1/2(6.535 + 8.060) = 7.30 \text{ in (185 mm)}$$

$R_0$  (lightweight concrete)

$$= 10(0.67)^{0.7} + 17 \left( \frac{(1.5)^{1.6}}{(0.2)^{0.2}} \right) \left\{ 1 + 26 \left[ \frac{9.25}{100 \times 0.2 \times 1.5(7.3 + 1.5)} \right]^{0.8} \right\}$$

$$= 199 \text{ min}$$

$R_0$  (normal concrete)

$$= 10(0.67)^{0.7} + 17 \left( \frac{(1.5)^{1.6}}{(0.2)^{0.2}} \right) \left\{ 1 + 26 \left[ \frac{10.484}{100 \times 0.2 \times 1.5(7.3 + 1.5)} \right]^{0.8} \right\}$$

$$= 87 \text{ min}$$

Adopting lightweight concrete 1.5 in thick for insulation,  $R$  duration time is 1.37 times more than that for normal concrete.

**Example 3.8 American Practice**

The thickness of the sprayed applied protection material for the steel beam is calculated on the basis of the following scaling relationship provided by the American practice:

$$h = \left( \frac{W_2/D_2 + 0.6}{W_1/D_1 + 0.6} \right) h_2$$

where

subscript 1 = substitution of beam and required thickness,

subscript 2 = specified beam and protection thickness in the referenced tested design or tested assembly  $R \not\leq 1$  hr.

Restrictions:  $W/D \geq 0.37$  and  $h \geq \frac{3}{8}$  in

The existing beam is  $W 12 \times 16$  with 1.44 in protection, having  $W/D = 0.54$ ; it is to be replaced by  $W 24 \times 76$  with  $W/D = 1.03$  /ft in owing to damage in a fire. Determine the thickness of the spray-applied fire protection to provide a 2-hr protection for the same rating.

$$W_2/D_2 = 0.54 \quad \text{for } W 12 \times 16$$

$$W_1/D_1 = 1.0 \quad \text{for } W 24 \times 76$$

$$h_2 = 1.44$$

$$h_1 = \frac{(0.54 + 0.6)}{(1.03 + 0.6)} \times 144 = 1.0 \text{ in}$$

This is only for the beam and if it is a part of the floor or roof assembly, the deck thickness must not be altered.

**Example 3.9 British Practice**

A steel column  $254 \times 254 \times 167$  kg/m is fully exposed to temperature changes. Using the following data and the relevant Eurocode 3, calculate a step-by-step temperature rise and evaluate the final collapse of this column:

$$A_s = 212 \text{ cm}^2$$

$$D \text{ or } P_s = 1.636 \text{ m}$$

$$\text{ambient temperature} = 20^\circ\text{C}$$

$$\text{gas temperature } T_f = 345 \log_{10}(0.133t + 1) + T_0$$

$$t = \text{time (min)}$$

$$T_0 = \text{initial temperature } (^\circ\text{C})$$

$$a = a_c + a_r$$

$$a_c = 25 \text{ W}/(\text{m}^2 \times ^\circ\text{C})$$

$$a_r = \frac{5.75 w_r}{(T_f - T_s)}$$

$$\times \left[ \left( \frac{T_f + 273}{100} \right)^4 - \left( \frac{T_s + 273}{100} \right)^4 \right] \text{ W}/(\text{m}^2 \times ^\circ\text{C})$$

Steel properties:

$$\begin{aligned}
 C + s &= 520 \text{ J}/(\text{kg}^\circ\text{C}) \\
 \rho_s &= 7850 \text{ kg}/\text{m}^3 \\
 \Delta t &\not\geq \frac{25000}{P_s} \text{ or } D/AS \\
 \tau_s &= \text{steel temperature rise at time } t^\circ\text{C} \\
 w_r &= \text{average emissivity} = 0.5
 \end{aligned}$$

### Example 3.10 European Practice

Determine the sprayed plaster protection to a unival beam Grade S355JR  $406 \times 178 \times 74$  kg/m UB for a 90-minute fire duration. Use the following data:

beam span = 9 m

bending moments from each simple end at 3 m are 236 and 184 kNm, respectively

partial safety factors 1.0 and 0.8 on permanent (dead) load action and live load, respectively

$$\text{concentrated} \left\{ \begin{array}{ll} \text{load on one side} & \begin{array}{l} \text{dead load } 40 \text{ kN} \\ \text{imposed load } 70 \text{ kN} \end{array} \\ \text{load on other side} & \begin{array}{l} \text{dead load } 40 \text{ kN} \\ \text{imposed load } 70 \text{ kN} \end{array} \end{array} \right.$$

$$\text{gypsum plaster } p_p = 800 \text{ kg}/\text{m}^3 \quad \lambda_p = 0.2 \text{ W}/(\text{m}^\circ\text{C})$$

$$p = 20\%$$

$$= \frac{M_{fi}}{M_c} \leq \frac{mM_{fi}}{M_b}$$

$$R = \text{load ratio } \frac{236}{532.5} = 0.433 \leq \frac{0.89 \times 236}{378}$$

$$\theta_{lim} \text{ (Eurocode 3)} = 633^\circ\text{C}$$

$$I_f = \left\{ \frac{t_{fi,d}}{40(\theta_{lim} - Ap/Vi = 140/m)} \right\}^{1.3} = 0.06 \times 10^{-4}$$

$$\rho'_p = \text{effective density} = \rho_p(1 + 0.03p) = 1280 \text{ kg}/\text{m}^3$$

$$\mu = \lambda_p \left( \frac{\rho'_p}{\rho_a} \right) I_f \left( \frac{Ap}{Vi} \right)^2 = 0.20 \left( \frac{1280}{7850} \right) (9.06) \times 10^{-4} (140)^2 = 0.579$$

$$\mu_{(0)} = \frac{S_{d,f}}{R_{d,F}} \frac{K S_{d,f}}{R_{d,F}}$$

$$\mu_{(0)} = 0.7 \times 0.556 = 0.389$$

$$\theta_{a,cr} = 78.38 \ln \left\{ \left( \frac{1}{0.967(\mu_0)^{3.833}} - 1 \right)^{1/2} \right\} + 482$$

For a 90-minute fire duration, temperature  $607^\circ\text{C}$  and the spray thickness should be 21 mm.

Check

$$F_w = \frac{(1 + 4\mu)^{1/2} - 1}{2\mu} = \frac{(1 + 4 \times 0.389)^{1/2} - 1}{2 \times 0.389} = 0.76$$

$$d_P = \text{thickness (m)}$$

$$= \lambda_P I_f F_w \left( \frac{AP}{V_i} \right)$$

$$= 0.2 \times 9.06 \times 10^{-4} \times 0.76 (140)$$

$$= 0.0193 \text{ m}$$

$$= 19.3 \text{ mm}$$

Adopt 21 mm as proposed.

### 3.6.6 Calculations of Fire Resistance of Concrete Members

#### Introduction

Various approximate formulae have been developed for reinforced and prestressed concrete elements. The situation is not the same as for steel. Concrete properties vary not only with time but with the location in the section and its non-uniform character. More complicated factors become apparent when fire resistance calculations are performed. The reinforcement and concrete can resist different temperatures within the same section. An average rise in temperature of 250°F (121°C) on unexposed surface is regarded in American practice (ASTM, 1985) as failure. Hence in this case the thermal fire resistance is the time elapsed to reach a temperature rise of 250°F (121°C). In a composite slab or beam, the failure due to fire is defined when steel temperature reaches 1100°F (532°C) for reinforcement and 800°F for prestressing steel. A reference is made to the properties of concrete and reinforcing steel in the fire environment.

#### American Code

##### *Reinforced Concrete Columns*

Based on Lie and Allen [3.9] and Lie et al. [3.10], the minimum dimensions of the column are as given below:

$$t_{\min} \text{ (in)} = 3.2 f(R + 1) \quad \text{rectangular shape} \quad (3.78)$$

$$*t_{\min} \text{ (in)} = 3.2 f(R + 0.75) \quad \text{normal weight} \quad (3.79)$$

$$*t_{\min} \text{ (in)} = 4.0 f(R + 1) \quad \begin{array}{l} \text{siliceous aggregate} \\ \text{normal weight} \end{array} \quad (3.80)$$

$$\dagger t_{\min} \text{ (in)} = 3.0 f(R + 1) \quad \text{carbonate aggregate}$$

\* Design conditions columns (2) and (4), Table 3.10.

† Design Conditions column (3), Table 3.10.

**Table 3.10.** Factor  $f$

(1)	(2)	Where $kh$ is more than 12 ft but not more than 24 ft	
		(3) $t$ is not more than 12 in and $p$ is not more than 3%	(4) All other cases
1.00	1.0	1.2	1.0
1.25	0.9	1.1	0.9
1.50	0.8	1.0	0.8

For found columns the diameter must not be less than 1.2 times the value determined above.

† Overdesign factor is the ratio of the calculated load carrying capacity of the column to the column strength required to carry the specified loads determined in conformance with ACI 318-89 ‘Building Code Requirements for Reinforced Concrete’.

- $k$  = the effective length factor obtained from ACI 318-89 ‘Building Code Requirements for Reinforced Concrete’
- $p$  = the area of vertical reinforcement in the column as a percentage of the column area
- $h$  = unsupported length of the column (ft)
- $C_{\min}$  = minimum cover (in) to vertical reinforcements
  - for  $R \leq 3$  hr  $C_{\min} = R$  or 2 in., whichever is less
  - for  $R > 3$  hr  $C_{\min} = \frac{1}{2}(R - 3) + 2$

### Concrete Slabs

Harmanthy [3.7] and Lie and Harmanthy [3.11] give the semi empirical formula for a *monolithic concrete slab* (Fig. 3.29a), for which the failure temperature rise is 250°F (121°C) at the unexposed surface, as:

$$R_1 = 0.205 \frac{(pc)^{1.2} L^{1.85}}{k^{0.65}} \tag{3.81}$$

where

- $R_1$  = fire resistance of slab based on heat transmission criterion (hr)
- $L$  = thickness of slab (ft)
- $\rho$  = density of concrete (lb/ft<sup>3</sup>)
- $c$  = specific heat of concrete (Btu/lb × °F)
- $k$  = thermal conductivity of concrete (Btu/ft × hr × °F)



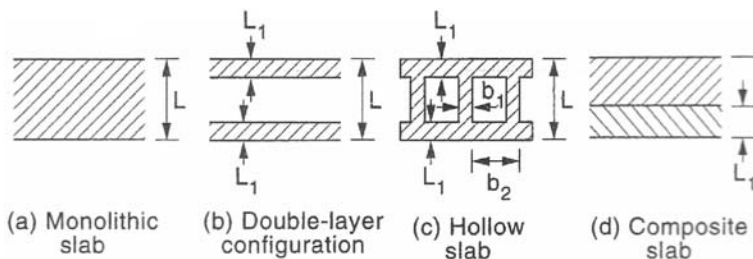


Fig. 3.29. Different slab shapes

If

$$\begin{aligned}
 k &= 1.0 \text{ Btu}/(\text{ft} \times \text{hr} \times ^\circ\text{F}) && \text{normal concrete} \\
 &= 0.45 \text{ Btu}/(\text{ft} \times \text{hr} \times ^\circ\text{F}) && \text{lightweight concrete} \\
 c &= 0.20 \text{ Btu}/(\text{LB} \times ^\circ\text{F}) && \text{both types of concrete}
 \end{aligned} \tag{3.82}$$

then

$$R_2 = 0.03\rho^{1.2}L^{1.85} \tag{3.83}$$

normal concrete

$$R_1 = 0.05\rho^{1.2}L^{1.85} \tag{3.84}$$

lightweight concrete

For a *double-layer slab* (Fig. 3.29b), for a failure temperature rise of 250°F

$$R_2 = 0.75 \frac{(pc)^{1.1}L_1^{1.6}}{k^{0.5}} \tag{3.85}$$

where

- $R_2$  = thermal fire resistance of the slab (hr)
- $L_1$  = thickness of one layer of the slab (ft)
- $\rho$  = density of the concrete (lb/ft<sup>3</sup>)
- $c$  = specific heat of the concrete (Btu/(ft×hr×°F))
- $k$  = thermal conductivity of the concrete (Btu/(ft × hr × °F))

where no data are available for  $k$  and  $c$ , (3.81) can be used, then

$$R_2 = sp^{1.1}L_1^{1.6} \tag{3.86}$$

where

- $s = 0.13$  for normal concrete
- $= 0.216$  for lightweight concrete.

For a *hollow concrete slab* in dry conditions, for a temperature, for a temperature rise of 250°F (121°C), the value of  $R$  is given by Harmanthy [3.7] as:

$$R + \left[ \frac{1}{\frac{b_1/b_2}{(R_1)^{1/2}} + \frac{1 - (b_1/b_2)}{(R_2)^{1/2}}} \right]^2 \tag{3.87}$$

**Table 3.11.** Multiplying factor for equivalent thickness

Material of top layer	Base slab of normal-weight concrete	Base slab of lightweight concrete
Type X gypsum wallboard	3	2 <sup>1</sup> / <sub>4</sub>
Cellular concrete (density 25-35 lb/ft <sup>3</sup> )	2	1 <sup>1</sup> / <sub>2</sub>
Vermiculite and perlite con- crete (density 35 lb/ft <sup>3</sup> or less)	1 <sup>3</sup> / <sub>3</sub>	1 <sup>1</sup> / <sub>2</sub>
Gypsum sand plaster	1 <sup>1</sup> / <sub>4</sub>	1
Portland cement with sand aggregate	1	3/4
Terazzo	1	3/4

$R$  = thermal fire resistance of the hollow slab (hr)

$R_1$  = thermal fire resistance of the monolithic slab (hr)

$R_2$  = thermal fire resistance of the double-layer slab (hr)

$b_1$  = thickness of a web (ft)

$b_2$  = distance between the centrelines of two webs (ft).

All the locations of web and cavity this slab may be considered as monolithic and double-layer respectively. Lie [3.12] and Abrams and Gustaferro [3.13] have carried out theoretical and experimental studies on *composite slabs* (layers of normal and lightweight concrete); with a failure temperature of 250°F (121°C) at the unexposed face, the value  $R$  is given as:

$$R = 0.057 \left( 2l^2 - dl - \frac{6}{l} \right) \quad \text{normal concrete} \quad (3.88)$$

$$R = 0.063 \left( l^2 - dl - d^2 + \frac{4}{l} \right) \quad \text{lightweight concrete} \quad (3.89)$$

where

$R$  = fire resistance of slab (hr)

$l$  = slab thickness (in)  $l - d \geq 1$  in

$d$  = base slab thickness (in).

In some cases the top layer on the base slab is different from normal or lightweight concrete. The top layer is converted to an equivalent thickness of concrete and is added to the base slab in order to calculate fire resistance  $R$  given above in (3.88) and (3.89). Table 3.11 gives a multiplying factor for that top layer which has to be used to obtain equivalent thickness.

### Simply-Supported Unstrained Beams and One-Way Slab

Assuming the underside of the slab is exposed to fire, the bottom of this slab will expand more than the top, resulting in its deflection. As the temperature increases, the tensile strength of concrete and steel will decrease. At the elevated temperature, when the strength of steel reaches its limit, flexural collapse will occur. The nominal moment strength will be constant through the length:

$$M_n = A_s f_y \left( d - \frac{a}{2} \right) \quad (3.90)$$

where

$A_s$  = area of reinforcing steel

$f_y$  = yield stress of reinforcing steel

$d$  = distance from centroid of reinforcing steel to extreme compressive fibre

$a$  = depth of equivalent rectangular compressive stress block at ultimate load, is equal to  $A_s f_y / 0.85 f'_c b$  where  $f'_c$  = cylinder compressive strength of concrete and  $b$  is width of slab.

The normal  $BM$  is:

$$BM = M = m = \frac{\omega L^2}{8} \quad (3.91)$$

where

$\omega$  = uniformly distributed load per unit length

$L$  = span length.

After the material strength has reduced, the retained moment capacity  $M_{\eta\theta}$  is

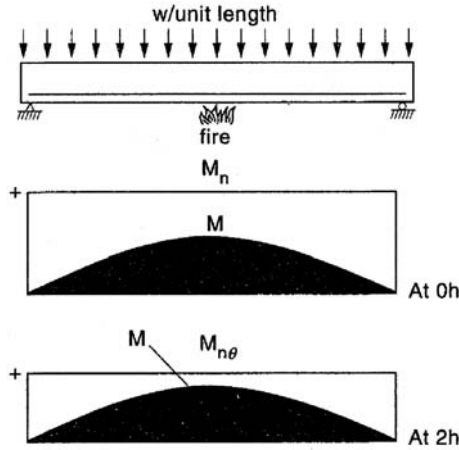
$$M_{\eta\theta} = A_s f_{y_\theta} \left( d - \frac{a_\theta}{2} \right) \quad (3.92)$$

where subscript  $\theta$  defines the effects of temperature.

$A$  and  $d$  are not affected but  $\alpha_\theta$  is reduced. Assuming the imposed and dead loads are constant and the concrete strength at the top is not reduced, Fig. 3.30 shows the two moments at zero hour and at 2 hours. Flexural failure occurs when  $M_{\eta\theta} = M$ . The equations indicate that the fire resistance depends on the load intensity, strength-temperature characteristics and fire duration. In general the cover to reinforcement is a protection and in some cases other materials are added. Table 3.12 shows the cover in American practice.

### Continuous Beams and Slabs

A statical indeterminacy can create additional reactions of the indeterminate supports due to fire. There will be an increase in the negative moments.



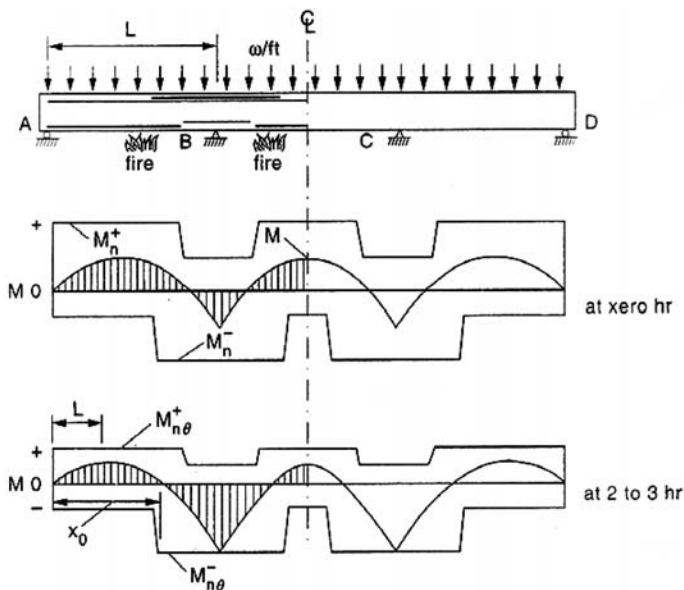
**Fig. 3.30.** Moments for a simple beam of slab under loads and fire.  $M$  due to loads only;  $M_{n\theta}$  due to fire

**Table 3.12.** Minimum cover: American practice

Base slab concrete type	Fire resistance (hr)							
	1/2	3/3	1	1 1/2	2	3	4	
Reinforced concrete (all types)	0.65	0.65	0.8	0.83	1.1	1.65	2.2	
Prestressed-concrete, normal-weight concrete (dominantly siliceous aggregate)	0.8	0.85	1.1	1.45	1.75	2.25	2.65	
Normal-weight concrete (dominantly carbonate aggregate)	0.8	0.85	1.1	1.45	1.75	2.25	2.65	
Lightweight concrete	0.8	0.8	0.9	1.25	1.55	2.0	2.35	

Courtesy: ASCE.

These are due to differential heating which causes lifting of the supports at the ends, thus increasing the reactions at the interior supports. There will be a redistribution of moments. Hence, the negative moments increase, while the positive moments decrease. The negative moments will cause yielding of the reinforcement. It is vital that compressive failure in the negative moment region is avoided, i.e. reinforcement should be small enough so that, based on the ACI [3.14],  $A_s f_y / b d f'_c$  is  $< 0.3$ . A decrease in the positive moment will mean that the reinforcement in that region can be heated to a higher temperature before failure occurs.



**Fig. 3.31.** A three-span continuous beam under external loads and internal temperature

Figure 3.31 shows a continuous beam slab loaded externally with uniform load and subjected to fire from underneath. The reduced moment capacity  $M_e$  is given as follows. Let

- $M_{\eta\theta}^+$  = positive moment due to fire
- $M_{\eta\theta}^-$  = negative moment due to fire
- $\omega$  = uniform load.

At a distance  $x_1$  from the outer support,  $A = M_{x_1}$  is given as:

$$M_{x_1} = \frac{\omega L}{2}x_1 - \frac{\omega x_1^2}{2} - \frac{M_{\eta\theta}^- x_1}{L} = M_{\eta\theta}^+ \tag{3.93}$$

Hence

$$x_1 = \frac{L}{2} - \frac{M_{\eta\theta}^-}{\omega} \tag{3.94}$$

$$M_{\eta\theta}^- = \frac{\omega L^2}{8} - \omega L^2 \sqrt{\frac{2M_{\eta\theta}^+}{\omega L^2}} \tag{3.95}$$

$$x_0 = 2x_1 \tag{3.96}$$

In the spans are symmetrical, then  $x_1 = L/2$ :

$$M_{x_1} = \frac{\omega L^2}{8} - M_{\eta\theta}^- \tag{3.97}$$

but

$$M_{x_1} = M_{\eta\theta}^+ \quad (3.98)$$

$$M_{\eta\theta}^- = \frac{\omega L^2}{8} - M_{\eta\theta}^+ \quad (3.99)$$

### Other Beams/Slabs with Different Loadings and Restraints

Other beams/slabs under loads can similarly be examined. In this chapter, various structures under plastic analysis are examined later on under a separate section.

#### Example 3.11 American Practice

A two-span continuous reinforced is to be analysed and designed for reinforcement to provide three-hour fire resistance. Use the following data and the ACI Code 318:

- slab thickness: 150 mm (6 in)
- positive reinforcement: #4 Grade 60 bars @ 150 mm (6 in) spacing
- concrete grade: 28 Mn/m<sup>2</sup> (4000 lb/in<sup>2</sup>) compressive strength
- concrete aggregate: siliceous
- concrete cover: 19 mm (0.75 in)
- each span: 4.88 m (16 ft)
- concrete density: 2400 kg/m<sup>3</sup> (150 lb/ft<sup>3</sup>)
- superimposed load: 1.914 kN/m<sup>2</sup> (40 lbf/ft<sup>2</sup>).

Material properties of steel and concrete in fires are given in Fig. 3.32.

#### Negative Reinforcement. Moments and Reinforcement

$M_n^+$  = positive nominal moment strength for 3-hr fire exposure

$$= A_s f_{y\theta} \left( d - \frac{a_\theta^+}{2} \right)$$

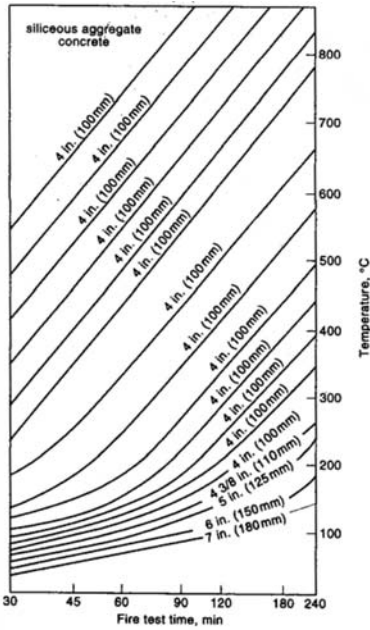
$\theta$  and  $f_{y\theta}$ :

$$\alpha_\theta^+ = \frac{A_s f_{y\theta}}{0.85 f'_c b} \quad (3.100)$$

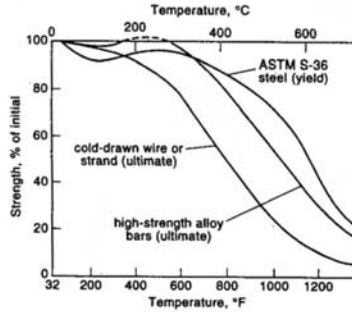
$M_{\eta\theta}^-$  = negative moment at the interior support

$$= \frac{\omega L^2}{2} - \omega L^2 \sqrt{\frac{2M_{\eta\theta}^+}{\omega L^2}} \quad (3.101)$$

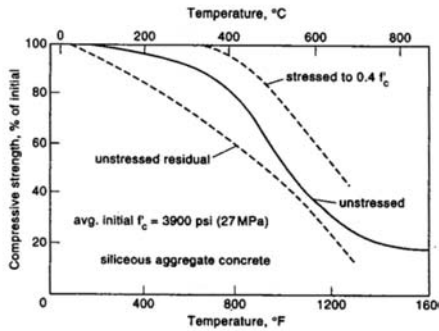
$$A_s^- = \frac{M_{\eta\theta}^-}{f_{y\theta}} (d'_\theta - \alpha_\theta^- / 2) \quad (3.102)$$



Temperatures within slabs during tests-siliceous aggregate concrete



Strength of certain steels at high temperatures



Compressive strength of siliceous aggregate concrete at high temperatures and after cooling

**Fig. 3.32.** Material properties under high temperatures

$$\omega_\theta = \frac{A_s f_y \theta}{b(eff \times d') f'_c \theta} \leq 0.30 \tag{3.103}$$

$$x_0 = \text{bar top length} = 2x_1 = 2 \left( \frac{L}{2} - \frac{M_{\eta\theta}}{\omega L} \right) \tag{3.104}$$

$$f_y = 460 \text{ N/mm}^2 \quad A_b = 129 \text{ mm}^2 (0.2 \text{ in}^2) \quad d_b = 12.7 \text{ mm} (0.5 \text{ in})$$

$$f_{y\theta} / f_y = 0.20 \quad l_d = \text{developing length} = 0.3 \text{ m.}$$

Calculations are performed in SI units, derived from the Imperial units.

$$A_s = \left( \frac{1000}{150} \right) 129 = 860 \text{ mm}^2$$

loading:

$$\omega_1 = 1.914 \text{ kN/m}^2 (401 \text{ bf/ft}^2)$$

$$\omega_d = 2400 \text{ kg/m}^3$$

$$\omega = \left( \frac{150}{1000} \right) (2400)(9.8)/1000 + 1.914 = 5.442 \text{ kN/m width}$$

$$M_{\eta\theta}^+ = (3\text{-hr exposure}) = A_s f_{y\theta} \left( d - \frac{a_\theta^+}{2} \right)$$

$\theta$ ,  $f_{y\theta}$  and  $a_\theta^+$  are taken from the Table given in the Code.

$$u = 25 \text{ mm}$$

$$t = \text{time} = 3 \text{ hr} = 180 \text{ min}$$

$$\theta = 750^\circ\text{C}$$

$$f_{y\theta}/f_y = 0.2 \quad \text{or} \quad f_{y\theta} = 0.20 \times 460 = 93 \text{ mN/m}^2$$

$$d = h - \text{cover} - 1/2 \quad d_b = 150 - 19 - \frac{12.7}{2} = 125 \text{ mm}$$

$$\alpha_\theta^+ = \frac{A_s f_{y\theta}}{0.85 f'_{c\theta} b} = \frac{860 \times 93}{0.85(28)(1000)} = 3.36 \text{ mm}$$

$$M_{\eta\theta}^+ = \frac{860 \times 93}{1000} = \left( 125 - \frac{3.36}{2} \right) / 1000 = 9.86 \text{ kNm/m width}$$

$$M_{\eta\theta}^- = 5.442(4.88)^2 \left[ \frac{1}{2} - \sqrt{\frac{2(9.86)}{5.442(4.88)^2}} \right]$$

$$= 129.6(0.5 - 0.39) = 19.44 \text{ kNm/m width}$$

$$d' = 150 - 19 - \frac{12.7}{2} = 125 \text{ mm.}$$

From the Table:

$$\theta = 190^\circ\text{C}$$

$$f_{y\theta}/f_y = 94\%$$

$$f_{y\theta} = 0.9 \times 460 = 432.4 \text{ mN/m}^2$$

25 mm of concrete is  $760^\circ\text{C}$  or higher

$$d'_{\text{eff}} = 150 - 25 - 19 - \frac{1}{2}(12.7) = 100 \text{ mm}$$

$$a_0^- = 25 \text{ mm}$$

$$A_s = \frac{19.44(1000 \text{ N/kN})(1000 \text{ mm/m})}{432.4(100 - 25/2)} \approx 514 \text{ mm}^2/\text{m width}$$

bars 140 mm c/c  $> 514 \text{ mm}^2/\text{m}$ .

At a concrete temperature of  $760^\circ\text{C}$ :

$$0.38(\text{eff}d') = 0.38(100) + 25 = 63 \text{ mm}$$

$$t = 180 \text{ min}$$



$$\theta = 430^\circ$$

For

$$\theta = 600^\circ\text{C}$$

$$f'_{c\theta}/f'_c = 64\%$$

$$f'_{c\theta} = 0.64 \times 28 = 18\text{mN/m}^2$$

$$a_\theta^- = \frac{921(432.4)}{0.85(18)(1000)}$$

$$= 26\text{ mm}$$

Therefore, 25 mm is assumed to be acceptable.

$$\omega_\theta \text{ verification: } \omega_\theta = \frac{921(432.4)}{1000(100)(18)} = 0.22 < 0.30$$

Both

$$A_s = 432.4\text{ mm}^2$$

are satisfactory.

$x_o$  = length of the top bar

$$= 2x_1 = 2 \left( \frac{L}{2} - \frac{M_{\eta\theta}}{\omega l} \right)$$

$$= 2 \left( \frac{4.88}{2} - \frac{19.44}{5.442 * (4.88)} \right)$$

$$= 3.416 \approx 3.42\text{ m}$$

Theoretically, the bars should be cut a distance  $l - x_o + l_d$

$l_d$  = development length of the bar

$$4.88 - 3.42 + l_d = 1.46 + l_d$$

$$= 488 - \frac{1}{2}x_o + l_d$$

$$\text{Theoretical} = 488 - \frac{3.42}{2} + l_d = 3.17 + l_d$$

$$= 3.17 + 0.3 = 3.47\text{ m.}$$

This is recommended for a 40% cut on either side of the intermediate support with 20% extended to external supports (ACI 318-83).

### Example 3.12 British Practice on Continuous Slab

A reinforced concrete solid slab of 175 mm thickness, 5 m width, is continuous over 5 m spans. The nominal cover provided everywhere is 20 mm. Using the

following data and the British Code BS8110, design this slab for bending, shear, deflection and cracking such that the maximum fire resistance is not less than 1 hr and hence ignore individual material properties for bars and type of concrete.

dead weight	=	47 kN/m <sup>2</sup>
imposed load	=	4 kN/m <sup>2</sup>
span internal	=	5 m
concrete density	=	24 kN/m <sup>3</sup>
$f_{cu}$	=	40 N/mm <sup>2</sup>
$f_y$	=	460 N/mm <sup>2</sup>
$d$	=	effective depth
	=	175-20-6 for half diameter of steel
	=	149 mm.

### Fire Resistance

Table 3.6 (BS 81 10) indicates that the fire resistance for a 175 mm thick slab with 20 mm cover = 1½ hr > 1 hr.

$$F = \text{design load} = (1.4 \times 4.7 + 1.6 \times 4) \times 5 = 65 \text{ kN/m width}$$

From Table 3.14 (clause 3.5.2.4)

$$\begin{aligned} M &= \text{ultimate bending moment for interior span} \\ &= 0.063 \times 65 \times 5 \approx 20.5 \text{ kNm/m.} \end{aligned}$$

### Reinforcement

$$K = \frac{M}{bd^2 f_{cu}} = \frac{20.5 \times 10^6}{1000(149)^2 \times 40} = 0.0231$$

$$\begin{aligned} z &= d \left[ 0.5 + \sqrt{\left( 0.25 - \frac{K}{0.9} \right)} \right] > 0.95d \\ &= 149 \left[ 0.5 + \sqrt{\left( 0.25 - \frac{0.0231}{0.9} \right)} \right] = 145 > 0.95 \times 149 = 141.5. \end{aligned}$$

Use  $z = 141.5$

$$A_s = M / 0.87 f_{yz} = \frac{20.5 \times 10^6}{0.87 \times 460 \times 141.5} = 362 \text{ mm}^2$$

T12-300[as prov. 377 mm<sup>2</sup>/m].

### Check for Shear

$$\frac{0.5F}{bd} = \frac{0.5 \times 65 \times 10^3}{1000 \times 149} = 0.22 \text{ N/mm}^2 < V_c = 0.41$$

*Deflection*

Span depth ratio = 26

$$\frac{M}{bd^2} = \frac{2.05 \times 10^6}{1000 \times (149)^2} = 0.92$$

 $f_s = 275 \text{ N/mm}^2$  (clause 3.4.6)

modification factor for tension reinforcement = 1.48

allowable span/depth =  $26 \times 1.48 = 38.48$  (Table 3.12)

$$\text{actual span/depth} = \frac{5000}{149} = 33.56 < 38.480.$$

*Cracking*

$$3d = 3 \times 149 = 447 \text{ mm}$$

spacing between bars =  $300 - 12 = 288 < 447 \text{ mm}$  $h = 175 \text{ mm} < 200 \text{ mm}$  (clause 3.12.11.2.7).

The cracking condition is satisfied. The slab will stand  $1\frac{1}{2}$  hour maximum fire duration.

**Example 3.13 British Practice**

A reinforced concrete T-beam is shown in Fig. 3.33a. Using the following data, determine the strength reduction factor for reinforcement and concrete of this beam and the temperature. What is the duration of the fire resistance?

Applied moment = 50 kNm

$$f_{cu} = 41 \text{ N/mm}^2 \quad f_y = 460 \text{ N/mm}^2$$

$$A_s = 6 \times 804 = 4824 \text{ mm}^2 \text{ for 6 T 32 bar}$$

At ambient temperature

$$M = F_y A_s z$$

$$Z = 0.95d$$

$$= 0.95 \times 390 = 370.5$$

$$M = 460 \times 4824 \times 370.5 \times 10^{-6}$$

$$= 822 \text{ kNm.}$$

Allowable strength reduction coefficient for tensile reinforcement

$$= \frac{50}{822} = 0.426 = \sigma_{ST}$$

$\sigma_{ST}$  occurs at  $600^\circ\text{C}$  (Fig. 3.33b).  $\sigma_{CT}$  occurs at 0.426 at  $600^\circ\text{C}$ . From Fig. 3.33b, the duration of the fire resistance is 4 hours and 30 min.

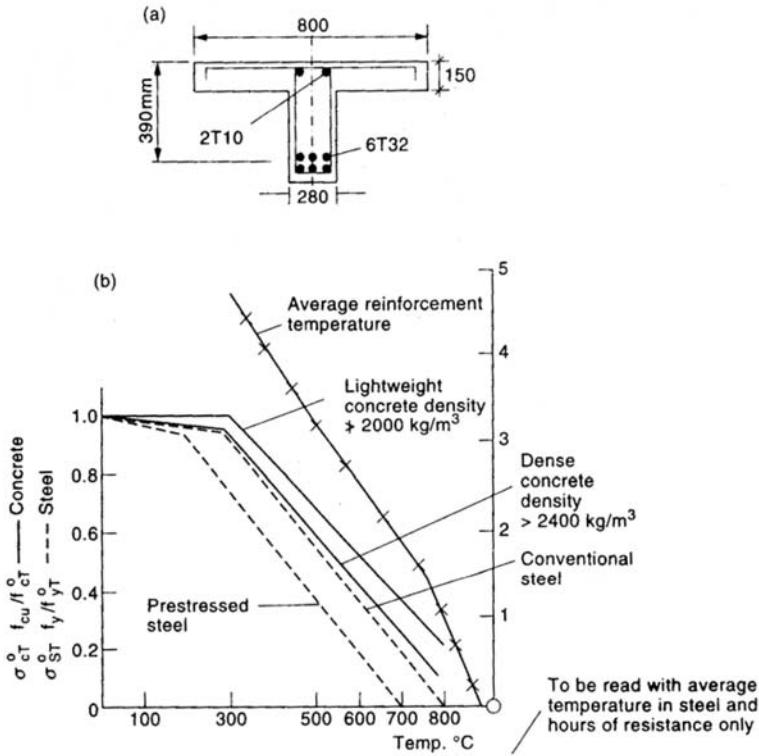


Fig. 3.33. (a) A reinforced concrete T-beam. (b) Reduction in strength, average temperature in the reinforcement and fire resistance duration

### 3.7 Deflection of Simple Beams in Reinforced and Prestressed Concrete Exposed to Fire – IStructE Method

#### External Loads as Point Loads

Figure 3.34 shows the loadings  $W$ . Take a distance  $z$  from  $R_A$  and determine deflection  $y_p$ . Let  $E_{C(T)}$  and  $I_{(T)}$  be the Young’s modulus and second moment area respectively.

$$R_0 \times l = w_1(l - a) + w_2(l - b) + \dots w_n(l - n) \tag{3.105}$$

$$M_z = R_0z - \{w_1(z - a) + w_2(z - b) + \dots w_n(z - n)\} \tag{3.106}$$

$$E_{C(T)} I_{(T)} \frac{d^2y}{dz^2} = -M_z \tag{3.107}$$

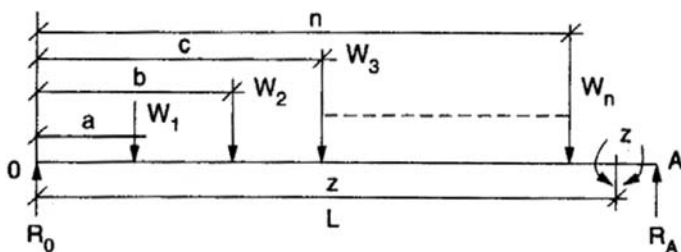


Fig. 3.34. Point loads on simple beam

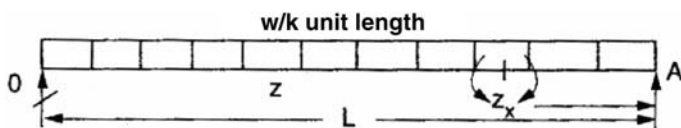


Fig. 3.35. Uniformly distributed load on simple beam

$$E_{C(T)}I_{(T)} - y = \left\{ \frac{w_1}{6}(z - a)^3 + \frac{w_2}{6}(z - b)^3 + \frac{w_n}{6}(z - n)^3 \right\} - R_0 \frac{z^3}{6} + AZ + B$$

$$x = 0 \quad y = 0 \quad \therefore B = 0$$

$$x = L \quad y = 0$$

$$A = \frac{1}{L} \left\{ \frac{R_0 L^3}{6} - \frac{w_1}{6}(L - a)^3 - \frac{w_2}{6}(L - b)^3 - \frac{w_n}{6}(L - n)^3 \right\}$$

$$\begin{aligned} \therefore y_P = \frac{1}{E_{C(T)}I_{(T)}} & \left[ \frac{1}{6} \{w_1(z - a)^3 + w_2(z - b)^3 + \dots w_n(z - n)^3\} \right. \\ & - \frac{z}{LL} \{w_1(L - a)^3 + w_2(L - b)^3 + \dots w_n(L - n)^3\} \\ & \left. + \frac{(L^2 z - z^3)}{6L} \{w_1(L - a)^3 + w_2(L - b)^3 + \dots w_n(L - n)^3\} \right] \end{aligned} \quad (3.108)$$

**External Loads as Distributed Loads (Fig. 3.35)**

Moments and deflections are computed in a similar manner to that above. See Fig. 3.34. The deflection  $y_d$  is given by

$$M_z = \frac{wL - z}{2} - \frac{w - z - z}{2} \quad (3.109)$$

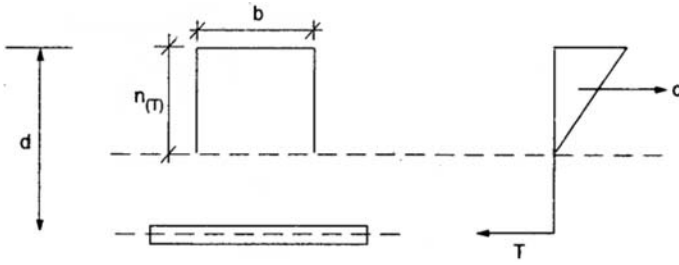


Fig. 3.36. Determination of neural axis

### Deflection Due to Fire Temperature $\gamma_\tau$

The force exerted by fire can be written as:

$$\begin{aligned}
 F &= E_{C(T)} a_c (T - T_0) \delta_A \\
 &= E_{C(T)} a_c (T - T_0) \frac{A}{N}
 \end{aligned} \tag{3.110}$$

$$\text{moment } M_T = \frac{1}{N} [E_{C(T)} a_c (T - T_0) A] (\gamma = N A_{(T)}) \tag{3.111}$$

$$E_{C(T)} I_{(T)} \frac{d^2 y}{dz^2} = -M_T \tag{3.112}$$

$$\therefore y_T = \frac{M_T z (L - a)}{2 E_{C(T)} I_{(T)}} \tag{3.113}$$

All parameters have been defined previously.

When all three such displacements or deflections occur, then the total deflection is:

$$\delta = y_p + y_d + y_t \tag{3.114}$$

It becomes necessary to know the second moment of area  $I_{(T)}$  in the above expressions, while  $E_{(T)}$  can be found elsewhere in this chapter. Figure 3.36 shows the neutral axis and  $I_{(T)}$  can be found as:

$$\begin{aligned}
 m_{(T)} &= \frac{E_{S(T)}}{E_{c(T)}} \\
 n_{(T)} &= \frac{m_{(T)} A_s}{b} \left( \sqrt{1 + \frac{2bd_1}{m_{(T)} A_s}} - 1 \right)
 \end{aligned} \tag{3.115}$$

$$l_{(T)} = \frac{bn_{(T)}^3}{3} + m_{(T)} - A_s (d_1 - n_{(T)}) \tag{3.116}$$

In Eurocode 2, the elastic modulus is based on the following derivations. A reference is made to Fig. 3.37 for the concrete stress-strain curve.

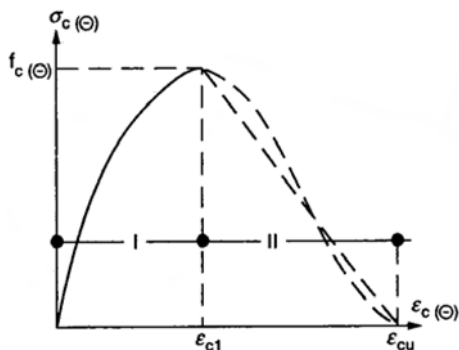


Fig. 3.37. Stress-strain under compression at elevated temperature

**Range I**

$$\sigma_c = f_{c\theta} \left[ \left( \frac{\epsilon_{c\theta}}{\epsilon_{c1\theta}} \right) \left( \frac{3}{2 + \left( \frac{\epsilon_{c\theta}}{\epsilon_{c1\theta}} \right)^3} \right) \right] \tag{3.117}$$

$$\frac{f_{c(\theta)}}{f_{c(20^\circ\text{C})}} = \frac{3}{2} \frac{f_{c(\theta)}}{\epsilon_{c1(\theta)}} \left[ \frac{\epsilon_{c(\theta)}}{\left( \frac{\epsilon_{c1(\theta)}}{\epsilon_{c1(20^\circ\text{C})}} \right)^3} \right] \tag{3.118}$$

and  $\epsilon_{c1(\theta)}$  to be chosen according to the values of Table 3.1 of the Report.

**Range II**

For numerical purposes a descending branch should be adopted. Linear and non-linear models are permitted.

$$N_T = \int_A E\alpha\theta dA_T = \int_A E\alpha\theta y dA \tag{3.119}$$

$N$  = number of nodes       $A = \sum \Delta A = N\Delta A$

$N\Delta A$  = number of equal areas.

Hence

$$\sigma_1 = \frac{1}{N} \sum E_{c(\theta)} a_c \Delta\theta = -\frac{1}{N} \sum E_{c(\theta)} a_c (\theta - \theta_{20}) \tag{3.120}$$

$$\sigma_2 = \frac{1}{N^2} \left[ \sum E_{c(\theta)} a_c (\theta - \theta_{20}) \right] \tag{3.121}$$

$$\begin{aligned} \sigma_3 &= \frac{1}{N} \left[ \sum E_{c(\theta)} a_c \Delta\theta y \Delta A \right] \frac{Y_j}{I(\theta)} \\ &= \frac{1}{N^2} \left[ \sum E_{c(\theta)} a_c (\theta - \theta_{20}) (y - NA(\theta)) \right] \frac{AY_c}{I(\theta)} \end{aligned} \tag{3.122}$$

Hence

$$\begin{aligned} \sigma_{P1} &= \text{stresses due to direct prestressing} \\ &= -F_{(\theta)}/A \\ \sigma_{P2} &= \text{stresses due to prestressing moment} \\ \sigma_{P3} &= \text{stresses due to elongation of the prestressing tendon} \\ &= \frac{E_{(\theta)}\alpha_{(\theta)}(\theta - \theta_{20})}{A}A_{ps} \end{aligned}$$

where

$$A_{ps} = \text{area of the prestressing tendons.}$$

All other parameters have been defined above.

### Stresses Due to External Loads

A similar analysis is done previously, except that the loads are denied by 1 for point loads and 2 for uniformly distributed loads respectively and the stresses are:

$$\begin{aligned} \sigma_{L1} &= -\left( M_{z1} \times \frac{Y_j}{I_{(\theta)}} \right) \tag{3.132} \\ \sigma_{L2} &= -\left( M_{z2} \times \frac{Y_j}{I_{(\theta)}} \right) \end{aligned}$$

The total stresses are algebraically added as

$$\sigma_{Total} = \sigma_1 + \sigma_2 + \sigma_3 + \sigma_{P1} + \sigma_{P2} + \sigma_{P3} + \sigma_{L1} + \sigma_{L2} \tag{3.133}$$

The neutral axis depth and the *I*-value can be similarly computed.

$$\begin{aligned} E_{c(\theta)} &= \frac{d\sigma_{c(\theta)}}{d\sum c(\theta)} \\ &= \frac{3f_{c(\theta)}}{\sum c1(\theta)} \left[ \frac{\left\{ 2 + \left( \frac{\sum c(\theta)}{\sum c1(\theta)} \right)^3 \times 1 - \sum c(\theta) \left\{ \frac{3\sum c(\theta)^2}{\sum c1(\theta)^3} \right\} \right\}}{\left[ 2 + \left( \frac{\sum c(\theta)}{\sum c1(\theta)} \right)^3 \right]^3} \right] \end{aligned} \tag{3.134}$$

$$\begin{aligned} E &= \frac{3}{2} \times \frac{f_{c(\theta)}}{\sum c1(\theta)} \\ \sigma_{c(\theta)} &= 0 \quad \sum_{c(\theta)} = 0 \end{aligned} \tag{3.135}$$

Karuna [3.15] developed a computer program on the basis of the concept. This program has been linked to the program ISOPAR given in Appendix I. This program is flexible enough to be part of, or simulated into any existing computer package on the market.



### Prestressed Concrete Beams

A few changes are necessary when a simply supported prestressed concrete beam is exposed to fire. For the purpose of analysis, a straight tendon is adopted. Where the cables are cured, the analysis requires a cable profile which is used for locating temperature zones. A piece-by-piece analysis of the work described below is required. For a simply-supported beam the stresses induced by temperature changes, using the symbols for the EC2, are:

$$\sigma_{\text{Total}} = \sigma_1 + \sigma_2 + \sigma_3 \quad (3.135a)$$

where

$$\sigma_1 = -E\alpha\theta$$

$$\sigma_2 = NT/A$$

$$\sigma_3 = M_T(f/I)$$

Notes

$\theta$  =  $T$  in the above work

$\theta$  is used in EC2

$$\theta_{20} = T_0$$

$$m_{(\theta)} = \frac{E_{p(\theta)}}{E_{c(\theta)}} \quad (3.136)$$

$$n_{(\theta)} = \frac{A(h/2) + (m_{(\theta)}A_{ps} - A_{ps})d}{A_c + (m_{(\theta)} - 1)A_{ps}} \quad (3.137)$$

$$I_{(\theta)} = \frac{1}{12}bh^3 + bh(y_{(\theta)} - h/2)^2 + (m_{(\theta)} - 1)A_{ps}(d - y_{(\theta)}) \quad (3.137a)$$

where

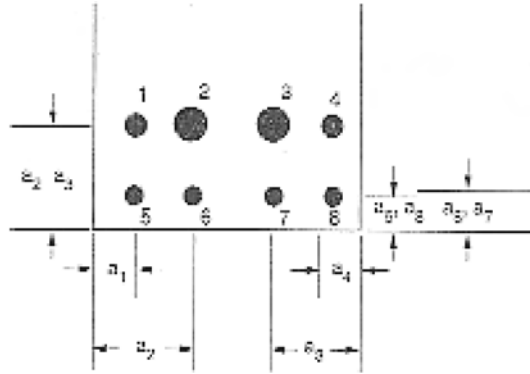
$A$  = gross concrete area

$h$  = height of the beam.

All other parameters have been defined previously.

### Temperature Distribution

The temperature distribution in concrete exposed to fire for slabs and ribs or beams was first given by the Institution of Structural Engineers, London, in *Design and Detailing of Concrete Structures for Fire Resistance* in April 1978. In slabs, both dense and lightweight concrete are used. It is suggested that where lightweight concrete is used the numerical value of temperature ( $^{\circ}\text{C}$ ) corresponding to the distance from an exposed surface should be reduced by 20%. These curves are based on data obtained from the Portland Cement Association (PCA, 1978). It is permissible to interpolate for intermediate sizes. The average distance from the exposed surface  $a_m$  is computed as:



**Fig. 3.38.** Determination of average axis distance (reproduced courtesy of the Institution of Structural Engineers)

**Table 3.13.** Beam parameters

Width of beam	$B_1, B, B_2$
Time of fire exposure	$t_1, T, T_2$
Depths of fire exposed surface	$D_1, D, D_2$
Temperature of char points:	
$TE1 = TE(B_1, D_2, T_1)$	
$TE2 = TE(B_2, D_2, t_1)$	
$TE3 = te(b_1, D_2, T_2)$	
$TE4 = TE(B_2, D_2, T_2)$	
$TE5 = TE(B_1, D_2, T_2)$	
$TE6 = TE(B_2, D_1, T_2)$	
$TE7 = TE(B_1, D_1, T_1)$	
$TE = TE(B_2, D_1, T_1)$	
By interpolation:	
$TE57 = (T - T_2)(TE5 - TE7)/(T_2 - T_1) + TE5$	
$TE13 = (T - T_2)(TE3 - TE1)/(T_2 - T_1) + TE3$	
$TE86 = (T - T_2)(TE6 - \times TE8)/(T_2 - T_1) + TE6$	
$TE24 = (T - T_2)(TE4 - TE2)/(T_2 - T_1) + TE4$	
$TE91 = (D - D_2)(TE57 - TE13)/(D_1 - D_2) + TE13$	
$TE92 = (D - D_2)(TE86 - TE24)/(D_1 - D_2) + TE24$	
Hence:	
$TEa = (B - B_i)(TEa2 - Tea1)/(B_1 - B_2) + Tea1$	

**Table 3.14.** Below and overleaf

<i>b</i> <sub>1</sub> = 300																
<i>T</i>	<i>D</i>															
	0	10	20	30	40	50	60	70	80	90	100	110	120	130	140	150
1hr	860	675	530	430	350	290	240	200	160	140	110	90	70	50	49	30
1½hr	925	750	630	530	450	380	330	280	250	220	190	170	150	140	120	100
2hr	1000	850	730	610	530	450	400	350	310	280	260	240	220	210	200	190
3hr	1025	870	750	670	600	540	480	440	400	360	330	310	290	270	260	240
4hr	1070	900	860	710	650	600	550	500	460	430	400	370	350	340	320	300
<i>b</i> <sub>2</sub> = 250																
<i>T</i>	<i>D</i>															
	0	10	20	30	40	50	60	70	80	90	100	110	120	130	140	150
1hr	900	720	570	460	320	320	270	230	190	160	140	120	110	100	100	100
1½hr	950	800	660	550	460	390	340	290	260	230	200	190	170	160	150	140
2hr	1000	880	752	640	550	480	420	370	340	300	280	260	240	230	220	200
3hr	1060	940	800	700	620	550	500	460	430	390	360	340	330	320	310	300
4hr	1100	950	830	730	680	610	660	520	490	460	440	420	400	390	380	370
<i>b</i> <sub>3</sub> = 200																
<i>T</i>	<i>D</i>															
	0	10	20	30	40	50	60	70	80	90	100	110	120	130	140	150
1hr	910	760	620	500	400	350	300	260	230	200	180	170	150	140	120	100
1½hr	970	840	700	570	490	420	370	340	300	270	260	240	220	200	190	180
2hr	1060	910	790	670	580	510	460	430	400	360	350	330	310	300	290	280
3hr	1100	960	840	730	650	590	550	520	500	470	460	440	430	420	400	390
4hr	1100	1000	870	760	700	650	620	590	560	540	520	510	500	480	460	440
<i>b</i> <sub>4</sub> = 150																
<i>T</i>	<i>D</i>															
	0	10	20	30	40	50	60	70	80	90	100	110	120	130	140	150
1hr	950	800	660	530	430	370	350	320	300	280	260	250	230	220	200	
1½hr	1010	870	730	620	520	470	450	420	400	390	370	360	350	340	330	
2hr	1030	940	820	780	620	560	530	510	500	480	460	440	450	440	430	
3hr	1100	1000	900	790	700	660	640	610	600	590	580	570	560	550	540	
4hr	1100	1030	930	830	750	700	660	640	640	620	610	600	600	590	570	
<i>b</i> <sub>5</sub> = 100 mm wide rib																
<i>T</i>	<i>D</i>															
	0	10	20	30	40	50	60	70	80	90	100	110	120	130	140	150
1hr	990	860	730	600	510	470	450	440	420	410	400	400	390	380	370	360
1½hr	1070	940	800	700	630	600	580	570	560	550	540	535	530	525	520	510
2hr	1100	1000	870	780	720	680	670	660	650	640	635	630	625	620	615	610
3hr	1100	1040	940	860	820	780	760	760	740	730	725	720	715	715	710	710
4hr	1100	1050	950	880	840	800	780	780	760	750	740	735	730	725	720	715
<i>b</i> <sub>6</sub> = 125 mm wide rib																
<i>T</i>	<i>D</i>															
	0	10	20	30	40	50	60	70	80	90	100	110	120	130	140	150
1hr	970	720	690	560	460	420	380	360	340	320	310	305	300	290	280	270
1½hr	830	900	760	650	560	530	500	480	460	450	440	430	420	410	405	400
2hr	1100	970	850	740	660	630	600	580	560	550	540	530	525	520	515	510
3hr	1100	1020	920	820	760	730	700	690	680	670	660	650	645	640	630	625
4hr	1100	1040	940	840	780	750	730	710	700	700	690	670	665	660	655	650

$$\alpha_m = \frac{\sum A_s \alpha}{\sum A_s} \quad (3.138)$$

where

$A_s$  = area of tensile steel bars or tendons

$a$  = axis distance as shown in Fig. 3.38.

There are two ways to simulate graphs into a computer program:

- (a) by curve fitting technique
- (b) by transforming them into tables of numerical figures.

The former method is well known and a number of computer programs are available on curve fitting. Karuna [3.15] has developed a computer routine to read tables prepared from these graphs. The temperature distribution is tabulated in Table 3.13 indicating  $B$ ,  $D$  and time or duration. In order to find temperature for a width  $b$ , time  $t$  and depth  $d$ , the computational technique shown in Table 3.13 is adopted. A typical output for the temperature distribution is given in the Appendix and in Table 3.14.

### 3.8 Limit State and Plastic Analysis

The resisting capacity of steel beams, girders, columns, frames and their joints decreases as they are heated in the fire environment. Failure occurs when stresses at reduced capacity equal those produced by the applied loads. The strains can increase at a rapid rate without increase in stress. When the deformation reaches its critical value, the limit state is then also reached. This limit state of failure depends on the stress level, sectional properties and attainment of a particular temperature. The failure of steel members follows an elasto-plastic behaviour, after passing through the elastic limit, and collapse does not take place until a mechanism with *plastic hinges* is formed. Figures 3.39 to 3.42 give a vivid picture.

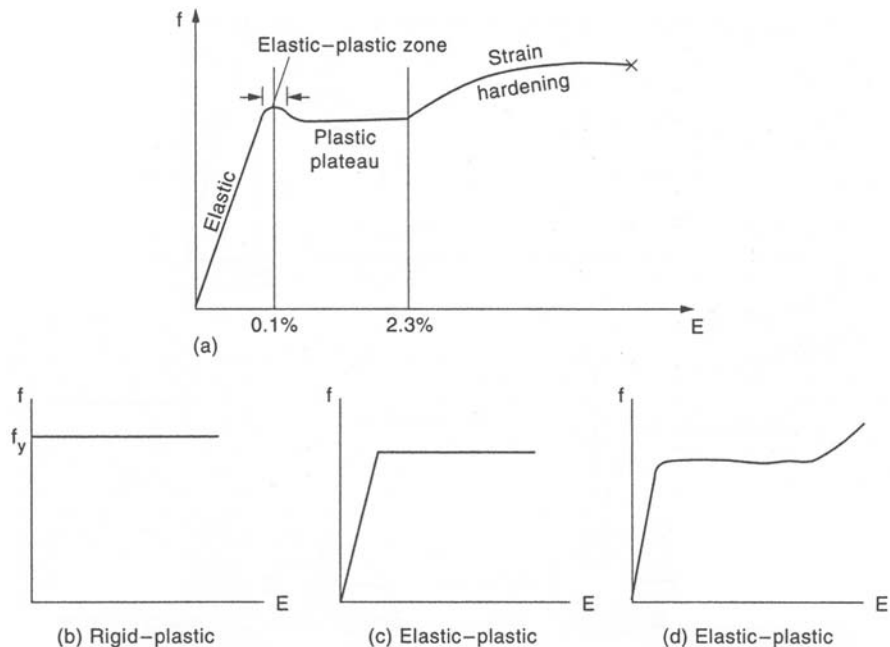
#### 3.8.1 Basic Theory

Each phenomenon is given a numerical status.

Elastic:

$$M = \int_{-d/2}^{d/2} (f d dy) y \quad (3.139)$$

$$f = \frac{E}{R} y$$



**Fig. 3.39.** (a) Plastic analysis. (b)–(d) There are basically three idealized relationships

$$\begin{aligned}
 M &= \int \frac{E}{R} b y^2 \, dy \\
 &= \frac{EI}{R} = \frac{fI}{y} = f z_e
 \end{aligned}
 \tag{3.140}$$

where  $z_e$  is the elastic modulus. (See Fig. 3.40a.)

First yield:

$$M y = f_y z_e
 \tag{3.141}$$

(See Fig. 3.40b)

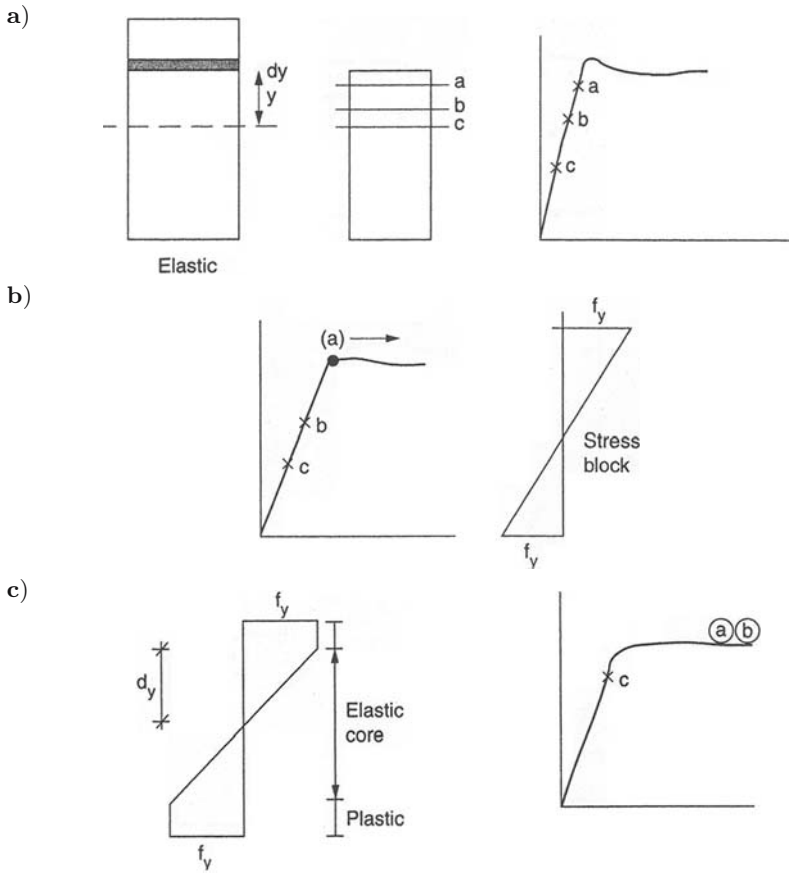
Partially plastic: in plastic theory the load can continue to increase.

$$M = \int_{-d_y}^{+d_y} f_1 b y \, dy + 2 \int_{d_y}^{d/2} f_2 b y \, dy
 \tag{3.142}$$

elastic
plastic

$$f_1 = \frac{E}{R} y \quad f_2 = f_y
 \tag{3.143}$$

$$M = f_y z_{ez} + f_y z_{pz}
 \tag{3.144}$$



**Fig. 3.40.** (a) Elastic phenomenon. (b) Yield conditions. (c) Partially plastic phenomenon

where

$z_e$  = elastic modulus, inner core

$z_{pz}$  = first moment area, plastic zone.

An elastic inner core provides stiffness. (See Fig. 3.40c.)

Fully plastic:

$$M_p = f_y z_p \tag{3.145}$$

where

$M_p$  = fully plastic moment of resistance

$z_p$  = first moment area of whole section.

(See Fig. 3.41.)



Fig. 3.41. Fully plastic phenomenon

Shape factor:

$$\frac{M_p}{M_y} = \frac{\sigma_y z_p}{\sigma_y z_e} = \frac{z_p}{z_e} \tag{3.146}$$

$z_p$ , and  $z_e$  are both related to the geometry of the section.

Rectangular section:

$$z_p = \frac{bd^2}{4} \quad z_e = \frac{bd^2}{6} \quad \left( z_c = \frac{1}{y} \right) \tag{3.147}$$

$$\frac{M_p}{M_y} = 1\frac{1}{2} \tag{3.148}$$

Therefore, if a plastic design is used, 50% more strength is obtained out of a rectangular section.

See Fig. 3.42 for examples of section types.

$$\begin{aligned} z_e &= \frac{1}{2} = 2 \left( \frac{BT^3}{12} + BT \left( \frac{d}{2} + \frac{T}{2} \right) \right)^2 \\ &= \frac{BT(D+T)}{D+27} \\ z_p &= ydA = 2 \int_{d/2}^{d/2+T} By dy = BT(d+T) \\ \frac{z_p}{z_e} &= \frac{d+2T}{d+T} \approx 1. \end{aligned} \tag{3.149}$$

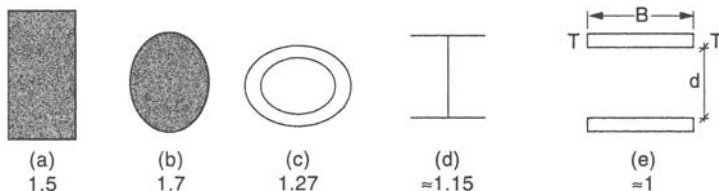


Fig. 3.42. Shapes and shape factors

### 3.8.2 Plastic Analysis and Fire Temperature

There is a definite relationship between the steel strength and temperature. Constrado (UK) and the BRE (Garston) have carried out tests. Table 3.15 shows the effect of temperature on the elastic properties of steel.

**Table 3.15.** Effect of temperature on the elastic properties of steel

Elastic properties	Temperature range (°C)		
	20–300	300–700	700–900
$\frac{F_{yT}}{f_{y20}}$	$1 - \frac{T^\circ}{3000}$	$0.9 - \frac{T^\circ - 300}{500}$	$0.1 - \frac{T^\circ - 700}{200}$
$\frac{E_{yT}}{E_{20}}$	$1 - \frac{T^\circ}{3000}$	$0.9 - \frac{T^\circ - 300}{500}$ for 300–900°C	

Grade 43

Elastic limit at ambient temperature 20°C  $f_{y20} = 250 \text{ N/mm}^2$   
 Ultimate strength at ambient temperature 20°C  $F_{t20} = 450 \text{ N/mm}^2$   
 Young’s modulus at ambient temperature 20°C  $E_{20} = 206 \text{ kN/mm}^2$

The following steps are adopted for structures built of steel.

1. Work out moment at ambient temperature.
2. Compute

$$\begin{aligned}
 M_e &= \text{elastic moment capacity} \\
 &= f_y z_e
 \end{aligned}
 \tag{3.150}$$

where

$f_p$  = yield stress  
 $z_e$  = elastic modulus.

3. Develop various possible mechanisms ( $M_e \leq M_p$ ) and compute greatest plastic moment:

$$M_p = f_p z_p$$

where

$f_p$  = stress failure in the extreme fibre  
 $z_p$  = plastic modulus.

4. 
$$\frac{M_p}{M_{ew}} = \frac{z_p f_{yT}}{z_e f_{y20}} \tag{3.151}$$

The strength reduction factor  $\sigma_s$  is:

$$\sigma_s = \frac{f_{yT}}{f_{20}} \tag{3.152}$$



5. There is no gain in fire resistance if the section is plastically designed. A correction factor is applied when determining the fire resistance analytically. EC3 gives the following correction factors/ when the service load  $P_s$  is in the range of  $0.2-0.85 P_u$ , the ultimate load or the collapsed load:

$$\text{determinate beams:} \quad f = 0.77 + 0.15 \frac{P_s}{P_u} \quad (3.153)$$

$$\text{indeterminate beams:} \quad f = 0.25 + 0.77 \frac{P_s}{P_u} \quad (3.154)$$

$$\text{columns:} \quad f = 0.85 \quad (3.155)$$

Buildings generally consist of floors with beams of simple and continuous types and/or mixed types. Different restraints can be provided to suit the building layout and other imposed conditions. It therefore becomes necessary to give examples of how unprotected steel beams in the temperature environment due to fire can fail when plastic analysis is considered. Example 3.13 shows a typical simply-supported beam subjected to uniformly distributed load. Various steps are presented in order to arrive at a temperature which, in conjunction with loads, can result in failure of this beam. Tables 3.13 and 3.14 show tabulated results of beams and columns with different boundary conditions and loads using the plastic analysis.

### Example 3.14 British Practice

A simply supported steel beam is loaded with 25.0 kN/m service load. Using the following data and plastic analysis, determine the critical temperature at which this beam would fail (see Fig. 3.43).

section: 406 mm  $\times$  178 mm  $\times$  74 kg/m

UB Grade 43

$\omega_s$  = service load = 25 kN/m

section moduli:

$z_e$  = elastic = 1058 cm<sup>3</sup>

$z_p$  = plastic = 1510 cm<sup>3</sup>

allowable bending stress = 165 N/mm<sup>2</sup>

$f_y = f_{y20}$  = yield stress or strength at ambient temperature = 250 N/mm<sup>2</sup>.

Shape and load factor are ignored.

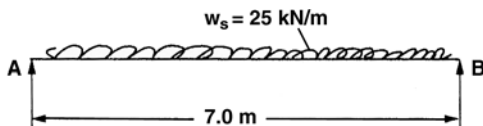


Fig. 3.43. Simply-supported beam with uniformly distributed load

- (a) The plastic hinge occurs at the middle  
Under service load:

$$M_{\max} = \frac{\omega_s L^2}{8} = \frac{25.0 \times 7^2}{8} = 153.125 \text{ kN/m}$$

$$\text{maximum bending stress} = f_{s \max} = \frac{M}{z_e} = \frac{153.125 \times 10^6}{1330 \times 10^3} = 115.132$$

$$M_p = \text{plastic moment} = f_{y20} \times z_p = \frac{250 \times 1510 \times 10^3}{10^6} = 377.5 \text{ kN/m}$$

$$P_u = \text{load developed due to} = M_p = \frac{8M_p}{L^2} = \frac{8 \times 377.5}{(7)^2} = 61.63 \text{ kN/m}$$

(without a load factor)

$$\sigma_s = \frac{115.132}{250} = 0.46$$

- (b) The hinge is formed at the centre (failure conditions)

$$\frac{f_{yT}}{f_{y20}} = \frac{z_e}{z_p} \times \frac{P_s}{P_u} = \frac{1330}{1510} \times \frac{25.0}{61.63} = 0.357$$

$$\text{correction factor } f = 0.77 + 0.15(P_s/P_u) = 0.77 + 0.15 \times 0.4056 = 0.83$$

$$\sigma_s = 0.83 \times 0.357 = 0.3.$$

The temperature at which this beam would fail is 680°C.

### 3.8.3 Beams and Temperatures – Tabulated Cases

See Table 3.16 for these tabulated cases.

### 3.8.4 Compression Members or Columns

The buckling curves for a steel column at high temperatures for Grade 43 and 50 steel relate the axial stress  $f_y$  to the slenderness ratio  $\lambda$ . For normal design purposes, the effective height is  $0.7L$  with  $0.5L$  between the nodes. If the column expands, the resultant expansion  $\delta L$  is as follows:

$$\delta L = aT_s \times L - \frac{P_L}{A_s} \left( \frac{1}{E_0} - \frac{1}{f_T} \right) m \quad (3.156)$$

where

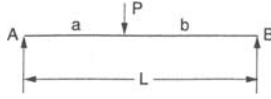
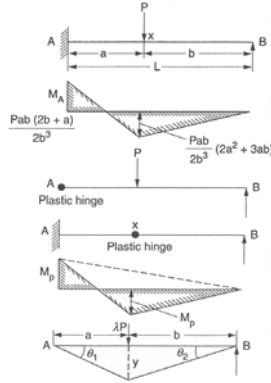
$a$  = coefficient of expansion (m/°C)

$T_s$  = steel temperature (°C)

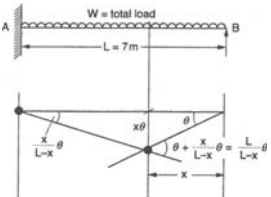
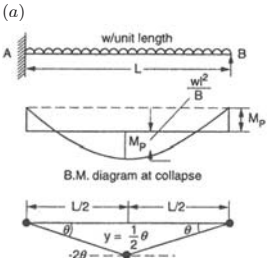
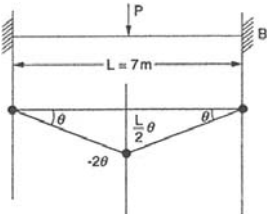
$L$  = exposed length (m)

$E_0 E_T$  = modulus of elasticity at ambient and steel temperatures respectively (kN/mm<sup>2</sup>).

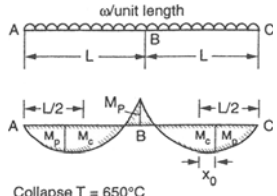
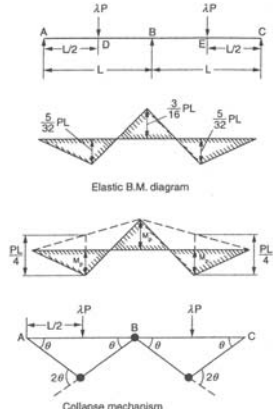
**Table 3.16a.** (below and facing). Beams and temperature at failure

Case	Plastic analysis and temperature at failure	Beams, loadings and restraints
I	<p>Cases</p> <p>(a) <math>M_p = \frac{\gamma Pab}{L} = \gamma(42.857)</math>  <math>P = 25 \text{ kN}, a = 3 \text{ m}, b = 4 \text{ m}, L = 7 \text{ m},</math>  <math>\gamma = 1.75</math></p> <p>(b) <math>M_p = \gamma PL/4</math>  <math>= \gamma(43.75)</math>  <math>\gamma = 1.75</math>                      when <math>a = b = L/2</math>, load at the centre</p> <p>(a) <math>M_p = 75 \text{ kN/m}</math>                      (b) <math>M_p = 76.563 \text{ kN/m}</math>  <math>z_p = \frac{76.56 \times 10^6}{250} = 306252 \text{ mm}^3 = 306 \text{ cm}^3</math>                      Adopt for both cases <math>z_p = 336 \text{ cm}^3</math> and  <math>z_e = 286 \text{ cm}^3</math>                      Steel tables: <math>T = 610^\circ\text{C}</math></p>	 <p>Beam <math>305 \times 102 \times 25 \text{ kg/m}</math>                      UB Grade 43  <math>f = a857</math>  <math>\sigma_s = 0.42</math>  <math>T = 610^\circ\text{C}</math>                      corresponding to  <math>\sigma_s = 0.42</math></p>
II	<p>Case (a):</p> <p>Propped cantilever</p> $\gamma = \frac{M_p}{P} \left( \frac{2\theta_1 + \theta_2}{y} \right)$ $y = a\theta_1 = b\theta_2$ $\gamma = \frac{M_p}{P} \left[ \frac{2\theta_1}{a\theta_1} + \frac{\theta_2}{b\theta_2} \right]$ $= \frac{M_p}{P} \left[ \frac{2}{b} + \frac{1}{b} \right] = \frac{M_p(2b + a)}{Pab}$ <p><math>P = 25 \text{ kN}, \gamma = \text{load factor}, a = 3 \text{ m},</math>  <math>b = 4 \text{ m}, L = 7 \text{ m}, \gamma = 1.75</math></p> <p>Case (b):</p> <p>If <math>a = b = L/2</math></p> $\lambda = \frac{M_p \left( \frac{3}{2}L \right)}{P(L^2/4)} = \frac{6M_p}{PL}$ <p>Case (a):</p> $M_p = \frac{1.75 \times 25 \times 3 \times 4}{11} = 47.73 \text{ kN/m}$ <p>Case (b):</p> $M_p = \frac{1.75 \times 23 \times 7}{6} = 51.04 \text{ kN/m}$ <p>The different is small, take case (b):</p> $z_p = \frac{51.04 \times 10^6}{250} = 204166,67 \text{ mm}^3 \approx 204 \text{ cm}^3$ <p>Adopted:</p> $\left. \begin{aligned} z_p &= 232 \text{ cm}^3 \\ z_e &= 206 \text{ cm}^3 \end{aligned} \right\} \text{ steel tables}$ <p><math>T = 600^\circ\text{C}</math></p> <p>Case (c): The load is <math>25 \text{ kN/m}</math> udl over the entire span. The problem of finding a hinge, distance <math>x</math> from the top</p>	 <p>Beam <math>305 \times 102 \times 25 \text{ kg/m}</math>                      Beam <math>305 \times 102 \times 23 \text{ kg/m}</math>                      UB Grade 43  <math>f = 0.856</math>  <math>\sigma_s = 0.434</math>  <math>T = 600^\circ\text{C}</math>                      corresponding to  <math>\sigma_s = 0.434</math></p>

**Table 3.16a.** Continued

Case	Plastic analysis and temperature at failure	Beams, loadings and restraints
Propped Cantilever (continued)	Assume $w_v = 25L = 25 \times 7 \times 1.75 = 306.25 \text{ kN}$ $M_p = \frac{W_x(L-x)}{2(L+x)} \quad \lambda = 1.75$ The maximum occurs at $x = (\sqrt{2} - 1)L$ $M_p = 0.686 \frac{w_v L}{8} = 0.686 \times \frac{x7}{8} = 183.83 \text{ kN/m}$ $z_p = \frac{183.83 \times 10^6}{250} = 753306 \text{ mm}^3 \approx 753 \text{ cm}^3$ Adopted $z_p = 483 \text{ cm}^3$ $z_e = 752 \text{ cm}^3$ $T = 590^\circ$	 <p>Beam 305 × 165 × 54 kg/m                      UB Grade 43  <math>f = 0.856</math>  <math>\sigma_s = 0.436</math>  <math>T = 590^\circ \text{C}</math>                      corresponding to  <math>\sigma_s = 0.436</math></p>
Fixed beams	(a) = Uniform load $w = 25 \text{ kN/m}$ , $L = 7 \text{ m}$ , $\lambda = 1.75$ $P_u = 1.75 \times 25 = 43.75 \text{ kN/m}$ The central hinge rotation is $-2\theta$ , the uniform load moves through an average distance $\frac{1}{4}L\theta$ $v = \omega L$ $M_p = w \left(\frac{1}{4}L\theta\right) = M_p(4\theta)$ $M_p = \frac{\omega L^2}{16} = 153.125 \text{ kN/m}$  (b) = $\left(\frac{1}{2}L\theta\right) = M_p(\theta) + M_p(2\theta) + M_p(\theta)$ $M_p = \frac{P_u L}{8} = \frac{306.25 \times 7}{8} = 265 \text{ kN/m}$ $P_u = 1.75 \times 25 \times 7 = 306.25 \text{ kN}$ $M_e = \frac{\omega L^2}{12}$ at ends = $\frac{25 \times 7^2}{12} = 102.1 \text{ kNm}$ $z_e = \frac{102.1 \times 10^6}{165} = 619 \text{ cm}^3$ Case (a): $z_p = \frac{153.125 \times 10^6}{250} = 612500 \text{ mm}^3 = 612.5 \text{ cm}^3$ Adopted: $z_p = 706 \text{ cm}^3$ $z_e = 613 \text{ cm}^3$ } steel tables Case (b): $z_p = \frac{265 \times 10^6}{250} = 106 \text{ mm}^3 \approx 1072 \text{ cm}^3$ Adopted: $z_p = 1200 \text{ cm}^3$ $z_e = 1060 \text{ cm}^3$ } > 619 cm <sup>3</sup> min. } steel tables	(a)  (b)  <p>Case (b) section governs                      406 × 178 × 60 kg/m                      UB Grade 43  <math>\sigma_s = 0.432</math>  <math>T = 580^\circ \text{C}</math></p> <p>Case (a) for the same total load                      406 × 178 × 60 kg/m  <math>f = 306.25 \text{ kN}</math>  <math>\sigma_s = 0.425</math>  <math>T = 610^\circ \text{C}</math></p>

**Table 3.16b.** Two-span continuous beams at failure

Case	Plastic analysis and temperature at failure	Beams, loadings and restraints
Two-span continuous beams	<p>Case (1):</p> $M_p = \frac{\lambda \omega L^2}{11.656} = z_p f_y$ $x_0 = \frac{L}{11.656}$ <p><math>\omega = 25.5 \text{ kN/m}</math>, <math>L = 7.5 \text{ m}</math> <math>\lambda = 1.5 \text{ m}</math>                      Beam ABC (for example)                      406 mm <math>\times</math> 178 mm <math>\times</math> 60 kg/m                      UB Grade 43  <math>z_e = 1058 \text{ cm}^3</math>  <math>z_p = 1194 \text{ cm}^3</math></p> <p>At yield = <math>M_s</math>, service moment = <math>\frac{\omega_0 L^2}{8} = \tau_i f_{y23}</math></p> <p>When a plastic hinge is formed:</p> $M_p = \frac{1.5 \times 25.5 \times 7.5^2}{11.656} = 184.6 \text{ kNm}$ $z_p \text{ (calculated)} = \frac{184.6 \times 10^6}{250} = 738354$ <p><math>738.354 \text{ cm}^3 &lt; 1194 \text{ cm}^3</math> – satisfactory</p> $\sigma'_s = \text{reduction factor at yield}$ $= \frac{f_{yT}}{f_{20}} \frac{z_e}{z_p} \frac{P_s}{P_l}$ $= \frac{8}{11.656} \frac{1058}{1198} \times \frac{25.5}{1.5 \times 25.5}$ $= 0.4041$ $f = 0.77 + 0.15 \times \frac{25.5}{1.5 \times 25.5} = 0.87$ <p><math>\sigma_s</math> (plastic case) = <math>0.87 \times 0.4041 = 0.352</math>  <math>T = 650^\circ\text{C}</math></p>	<p>Case (1)</p> <p>Beam 406 <math>\times</math> 78 <math>\times</math> 60 kg/m                      UB Grade 43</p>  <p>Collapse <math>T = 650^\circ\text{C}</math></p>
	<p>Case (2):</p> <p><math>P = 25.5 \times 7.5</math>  <math>2 \times p \left( \frac{L}{2} \right) = 6M_p(\theta)</math>  <math>\lambda = 6M_p/PL</math></p> $M_p = \frac{1.5 \times 25.5 \times 7.5 \times 7.5}{6} \approx 358.6 \text{ kNm}$ $z_p \text{ (calculated)} = \frac{358.6 \times 10^6}{250}$ $= 1434375 \text{ mm}^3 \approx 1434 \text{ cm}^3$ <p>Adopted:</p> $\left. \begin{matrix} z_p = 1470 \text{ cm}^3 \\ z_e = 1300 \text{ cm}^3 \end{matrix} \right\} \text{ steel tables}$	<p>Case (2)</p> <p>Beam 4576 <math>\times</math> 191 <math>\times</math> 67 kg/m                      UB Grade 43  <math>f = 0.87</math>  <math>\sigma_s = \text{reduction factor} = 0.513</math>  <math>T = 550^\circ\text{C}</math></p>  <p>Elastic B.M. diagram</p> <p>Collapse mechanism</p>

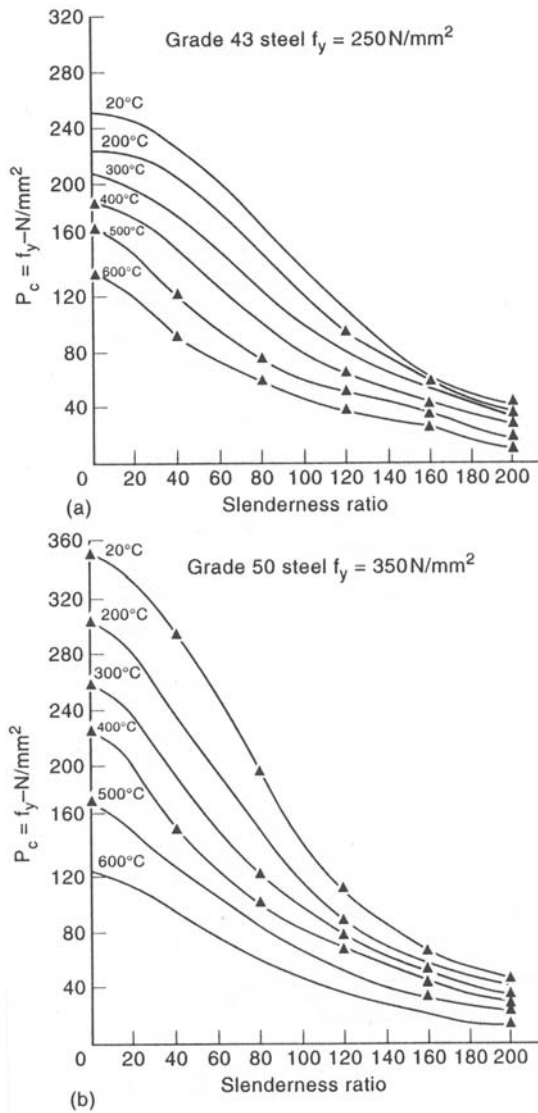


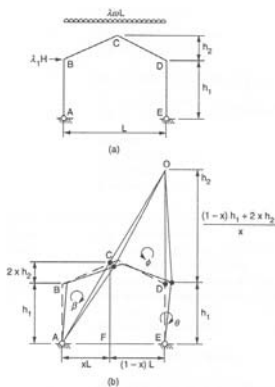
Fig. 3.44. Buckling curves for axially loaded steel columns

The value of  $f$ , the correction factor, is between 0.85 and 0.69. The EC3 recommends  $f = 0.85$  with  $\lambda = 1.75$ . Figure 3.44a and 3.44b shows buckling curves for axially loaded columns for various temperatures. The failure temperature is between 500 and 550°C. Example 3.15 is given to explain the use of these curves for a column.

**Table 3.17.** (below and overleaf). Portal frames

*A single-bay frame-pitched portal with and without horizontal loads*

I



(a) Loads:

- $\lambda\omega L$  vertical uniform load
- $\lambda_1 H$  horizontal load

*Pinned supports:*

$$M_p = \frac{\lambda\omega L^2}{8} \left[ \frac{\bar{Y}(2 + \bar{Y})}{N^2 + 2N - \bar{Y}K^2 + 1} \right]$$

$$x = (N - 1)/K \quad K = h_2/h_1$$

$$\bar{Y} = 2\lambda_1 H h_2 / \lambda\omega L^2 = \sqrt{[(1 + K)(1 - \bar{Y}K)]}$$

(b)  $\lambda_1 H = 0$ , i.e. no horizontal loading: as a result  $\bar{Y} = 0$

$$M_p = \frac{\lambda\omega L^2}{8} \left[ \frac{1}{1 + K + \sqrt{1 + K}} \right]$$

*Numerical example based on (a)*

Data:

$$\lambda_1 = \lambda = 1.75$$

$$h_2 = \frac{1}{4} h_1 \quad K = \frac{1}{4}$$

$$h_1 = 5 \text{ m} \quad h_2 = \frac{5}{4} = 1.25 \text{ m}$$

$$L = 10 \text{ m} \quad H = 1.75 \times 20 = 35 \text{ kN}$$

$$\lambda\omega = 1.75 \times 20 = 35 \text{ kN/m}$$

$$\bar{Y} = \frac{2 \times 1.75 \times 20 \times 5}{1.75 \times 20 \times 10^2} = 0.1$$

$$K = \frac{1.25}{5} = 0.25$$

$$N = \sqrt{(1 + 0.25)(1 \times 0.1 \times 0.25)} = 0.177$$

$$M_p = \frac{35 \times 100}{8}$$

$$\times \left[ \frac{0.1(2.10)}{(0.177)^2 + 2 \times 0.177 - 0.1(0.25)^2 + 1} \right]$$

$$= \frac{3500}{8} \left[ \frac{0.21}{0.1322821} \right] = 694.54 \text{ kN/m}$$

$$z_p = \frac{694.54 \times 10^6}{250} = 2778160 \text{ mm} \approx 2780 \text{ cm}^3$$

$$553 \times 210 \times 109 \text{ kg/m}$$

UB Grade 43

$$\frac{f_{yT}}{f_{y20}} = 0.50$$

$$f = 0.8557 \text{ (beam)} = 0.85 \text{ (leg)}$$

$$T_s = 610^\circ\text{C at failure}$$

$$z_p \text{ (adopted)} = 2830 \text{ cm}^2$$

$$z_e \text{ (adopted)} = 2480 \text{ cm}^2$$

$$z_e \text{ (elastic calculation)} = 2450 \text{ cm}^2$$

II Loads  $\lambda\omega L^2 = \lambda P$ ,  $\lambda_1 H$  is the same. The pitched portal is symmetrical. Supports are fixed. Various failure modes are investigated and from the interaction diagrams, the final failure mode is established.

### Single and Multi-storey Frames in Steel

The work is extended from a one-bay, one-storey frame to multi-storey, multi-bay frames in the fire environment, using, of course, the plastic analysis concept. Details are given in Tables 3.16 to 3.17.

**Table 3.17.** Continued

	$h_1 \frac{L}{2} = \frac{5}{2} \quad h_2 = \frac{1}{4} h_1 - \frac{L}{8} = 1.25$
	<p>Mechanism (1):</p> $\lambda P = \frac{10M_p}{L} \quad \text{or} \quad M_p = \frac{\lambda PL}{10} = 350 \text{ N/m}$
	<p>Mechanism (2):</p> $\lambda H + \lambda P = \frac{14M_p}{L}$ <p>or</p> $M_p = \frac{L}{14} (\lambda P + \lambda_1 H) = 275 \text{ kN/M}$
	<p>Mechanism (3):</p> $\lambda_1 H = \frac{8M_p}{L} \quad \text{or} \quad M_p = \frac{\lambda_1 HL}{8} = 43.75 \text{ kN/M}$
	<p><math>\lambda_1 = \lambda_2 = 1.75</math> as an example; for the other values, graphs can be modified.</p> <p><math>z_p</math> (computed) = <math>1400 \times 10^3 \text{ mm}^3 = 1400 \text{ cm}^3</math>  <math>z_p</math> (adopted) = <math>1470 \text{ cm}^3</math>  <math>457 \times 191 \times 67 \text{ kg/m}</math> UB Grade 43  <math>z_e</math> (calculated) = <math>1100 \text{ cm}^3</math>  <math>z_p</math> (adopted) = <math>1300 \text{ cm}^3</math></p> <p><math>T_s = 610^\circ\text{C}</math>  <math>f = 08557</math> beam  <math>f = 0.85</math> leg</p> $\frac{f_{YT}}{f_{20}} = 0.505$

**Example 3.15 British Practice**

A column of dimensions  $203 \times 203 \times 86 \text{ kg/m}$  is loaded with  $1400 \text{ kN}$ , which is the ultimate load. Using the following data and BS 5950 code of practice, determine the fire temperature at which this column collapses with sufficient buckling.

- $L = 5\text{m}$
- $Ag = 110 \text{ cm}^2$
- flange thickness:  $T = 20.5 \text{ mm}$  radii of
- gyration:  $r_2 = 9.27 \text{ cm}$
- $r_y = 5.32 \text{ cm}$
- failure length approaching =  $0.5L$
- $f =$  correction factor =  $0.85$  fire conditions:  $L_{\text{eff}} = 0.7L$ .

The column is restrained in position (pinned) at both ends but is not restrained in direction.



Since the flange thickness,  $T = 20.5$  mm, is greater than  $16 \text{ mm}^2$ ,  $p_y = 265 \text{ N/mm}^2$ , the following slenderness ratios apply:

$$i_x = \frac{L_{ex}}{\gamma_x} = \frac{0.7 \times 5000}{92.7} = 37.756 < 180$$

$$i_y = \frac{L_{ey}}{\gamma_y} = \frac{0.7 \times 5000}{53.2} = 65.79 < 180$$

for

$$i_x = 37.757, \quad p_y = 265 \text{ N/mm}^2, \quad p_c = 223 \text{ N/mm}^2$$

$$i_y = 65.79, \quad p_y = 265 \text{ N/mm}^2, \quad p_c = 133 \text{ N/mm}^2$$

The case of  $p_c = 133 \text{ N/mm}^2$  is considered:

$$P = Agp_c = 110 \times 10^2 \times 133 \times 10^{-3} = 1463 \text{ kN}$$

which is greater than  $1400 \text{ kN}$ , therefore satisfactory.

$$P_C > F$$

$203 \times 203 \times 86 \text{ kg/m}$ , UC Grade 43 adopted.

At failure the effective length  $= 0.5L = 0.5 \times 5000 = 2500$

$$i_T \text{ at failure} = \frac{2500}{53.2} \approx 47.$$

The buckling temperature of the steel column at failure is, for  $i_r = 47$  and  $p_c = 133 \text{ N/mm}^2$ :

$$T_s \quad \text{due to fire} = 480^\circ\text{C}$$

$$f = 0.85 \quad \text{correction factor}$$

$$p_c = 0.85 \times 133 = 113.05$$

$$T_s = 550^\circ\text{C}, \text{ failure conditions.}$$

### 3.8.5 Portal Frames – Tabulated Cases

See Tables 3.18 to 3.21 for these tabulated cases.

## 3.9 Multi-bay-Multi-storey Framed Buildings Subject to Fire Loading

### Summary of Formulae Based on EC3 I.1 and I.2

Plastic analysis combined with EC3 have been suggested. It is assumed the reader is now fully familiar with plastic analysis. EC3 introduced earlier, specifies the following.

**Table 3.18.** Single-storey tow-bay frame

Single-storey two-bay frame in steel	$\frac{P_u}{P} = \lambda$
	load factor = 1.75 shape factor = 1.15 $P$ is shown on the diagram $1.75P = P_u$ all loads are vertical 40 kN at 7 80 kN at 8 40 kN at 2
	$M_p = 32 \times 1.75 = 57.225 \text{ kN/m}$ $z_p \text{ (computed)} = \frac{57.225 \times 10^6}{250}$ $= 228900 \text{ mm}^3 = 229 \text{ cm}^3$
Final collapse mechanism $\frac{F_{yT}}{F_{y0}} = 0.5074 \quad \sigma_s = 0434$ for beams $f \text{ (beams)} = 0.856 \quad T_s = 620^\circ\text{C}$ Adopted: $T_s$ at failure $620^\circ\text{C}$	Section adopted throughout: 203 × 102 × 23 kg/m UB Grade 43 $z_p = 232 \text{ cm}^3$ $z_e$ for this section is $206 \text{ cm}^3$ $z_e \text{ (computed)} = \frac{57.225 \times 10^6}{250 \times 1.5} = 199 \text{ cm}^3$ $z_e \text{ (adopted)} = 206 \text{ cm}^3$ $f \text{ (column)} = 0.85$ Based on buckling requirements: $T_s = 610^\circ\text{C}$

Partial safety factors

(1) Action	Ultimate limit state		Fire limit state	
	EC	BS5950	EC	BS5950
Self+dead loads	1.35	1.40	1.0	1.0
Imposed loads				
(permanent)	1.50	1.60	1.0	1.0
(variable)	1.50	1.60	0.5–0.9	0.80
Materials	1.05	1.0	1.0	1.0
Structural steel				

(2)  $n_{fl,T}$  = load level at time  $t$ , at the fire limit state

$$\frac{E_{fl,d,t}}{R_d} \leq \frac{R_{fl,d,t}}{R_d} \tag{3.157}$$

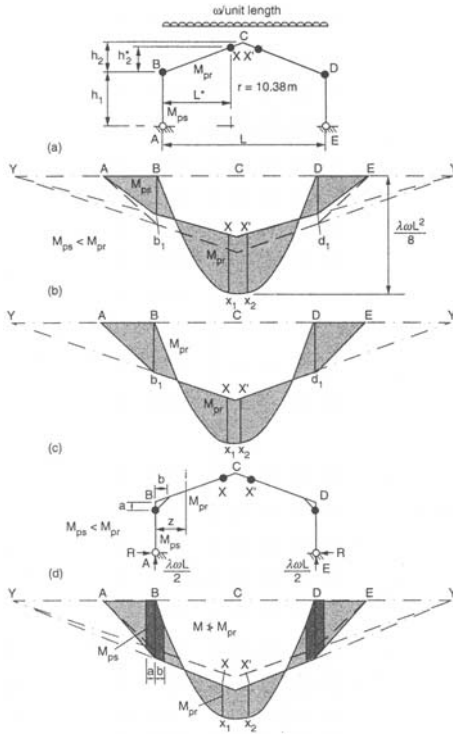
where

$E_d$  = action at ultimate limit state

$E_{fl,d,t}$  = action at fire limit state

**Table 3.19.** (below and overleaf). Portal frames

A pinned portal frame under uniform load on plane projection. Rafter and columns vary in sizes.  
Plastic analysis



Numerical solution:

$$\omega_{\text{elastic}} = P = D + I = 2.58 + 4.5 = 7.08 \text{ N/m}$$

$$\omega = 10.8 \text{ kN/m}$$

$$\text{ratio} = 0.656$$

$$h_1 = 7.0 \text{ m}$$

$$h_2 = 4 \text{ m} \quad b =$$

$$L = 30 \text{ m} \quad a = D_b = 0.53 \text{ m}$$

Rafter:

$$406 \times 178 \times 54 \text{ UB Grade 43}$$

$$M_{ps} = 564 \text{ kN/m}$$

Leg AB or ED:

$$533 \times 210 \times 82 \text{ kg/m UB}$$

$$z_{xx} = 1800 \text{ cm}^3$$

$$z_{yy} = 192 \text{ cm}^3 \quad A = 104 \text{ cm}^2$$

$$s_{xx} = 2060 \text{ cm}^3 \quad r_x = 21.3 \text{ cm}$$

$$s_{yy} = 300 \text{ cm} \quad r_y = 4.38 \text{ m}$$

$$T = 13.2 \text{ mm}$$

Rafter:

$$406 \times 178 \times 54 \text{ kg/m UB GRade 43}$$

$$T = 10.9 \text{ cm}^3$$

$$z_{xx} = 925 \text{ cm}^3$$

$$z_{yy} = 114 \text{ cm}^3$$

$$s_{xx} = 1050 \text{ cm}^3$$

$$s_{yy} = 177 \text{ cm}^3$$

$$A = 68.4 \text{ cm}^2$$

$$M_{pt} = M_{rb} = 287 \text{ kN/m}$$

$$s_{xy} = s_{xx} = 2860 \text{ n}^2$$

$$n = 0.057$$

$$s_{rx} = 2050.8 \text{ cm}^3$$

$$P_f = 275 \text{ N/mm}^2$$

$$R + \frac{\frac{1}{2}\lambda\omega L^2 + M_{ps}}{h} + h_2 = H = 86.96 \text{ kN}$$

$$M_{ps} = (h_1 - u)R \quad \text{columns plastic moment}$$

$$M_p \text{ moment at any point} = R \left( h_1 + \frac{2z}{L} \cdot z \right) - \frac{\lambda\omega}{2} (L - z)(z)$$

$$M_{pt} = \text{plastic moment in a rafter}$$

$$F_c = V = \frac{\lambda\omega L}{2} = 162.15 \text{ kN}$$

$$P_z = AgPy = 104 \times 275 \times 10^{-1} = 2860 \text{ kN}$$

$R_d$  = member resistance at ultimate limit state

$R_{f1,d,t}$  = reduced member resistance at fire limit state for exposure time  $t$

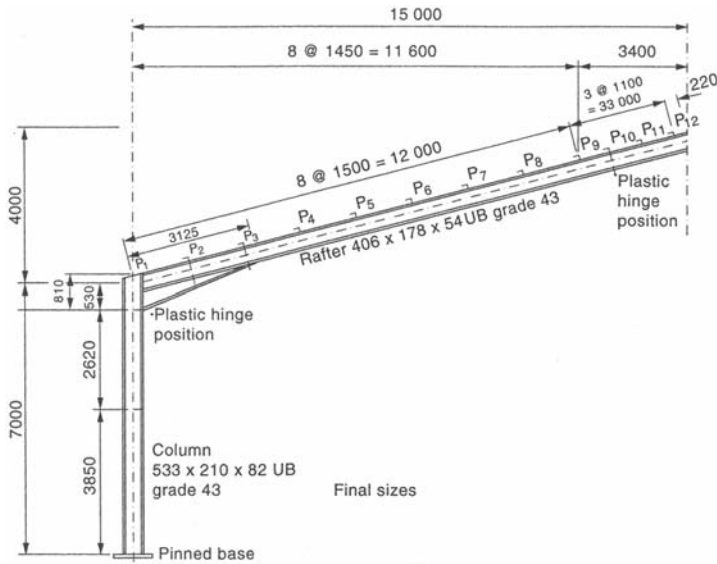
(3) Strength reduction factor and elastic modulus. (See Table 3.21.)

Lateral torsional buckling resistance, is defined as  $M_{b,Rd}$

$$M_{b,Rd} = \frac{\beta_w f_b w_{pl,y}}{\gamma_{M1}} \tag{3.158}$$

where

Table 3.19. (Continued)



Rafter:

$$F = 0.868 \quad f_{yt} = 0.58 \quad p_y = 275 \text{ N/mm}^2$$

$$\sigma = 0.504 \quad T = 540^\circ\text{C}$$

Leg or column:

$$p_y = 275 \text{ N/mm}^2 \quad p_c = 140 \text{ N/mm}^2$$

$$p_y = 119 \text{ N/mm}^2 \quad T = 600^\circ\text{C} \quad f = 0.85$$

The purlin and rafters fail first, in 2 hours. The legs fail in  $2\frac{1}{2}$  hours with temperature of  $600^\circ\text{C}$ .

Note: Since more than one component is involved and the frame varies in size at different places, a comprehensive analysis is demanded using 3D finite element method. An isolated analysis for joints where plastic hinges are predicted must be carried out using finite element or other appropriate methods.

$\beta_w$  = parameter (Eurocode) for class section

$W_{p1,y}$  = major axis plastic modulus =  $z_p$

$\gamma_{M,1}$  = parameter for steel material

$f_b$  = bending strength to be determined by EC3

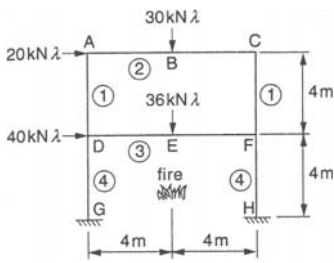
$I_{LT} = \frac{i_z}{u} = \frac{\text{minor axis radius of gyration}}{\text{buckling parameter}}$

$a_{LT} = i_z \times \text{torsional index}$

$$\bar{\lambda}_{LT\theta} = \sqrt{\frac{k_{y\theta}}{k_{E\theta}}} \times \bar{\lambda}_{LT} \tag{3.159}$$

$$\Phi_{LT} = 0.5 \left[ 1 + 0.21\bar{\lambda}_{LT\theta} - 0.2 \right] + \bar{\lambda}_{LT\theta}^2$$

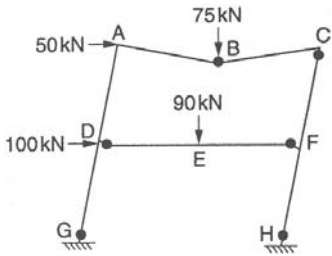
**Table 3.20.** Single-bay multi-storey frames



(a) Single-bay two-storey frame

$\lambda = 2.5$ ; ①  $z_p = 320$ ; ②  $z_p = 400$ ; ③  $z_p = 800$ ;  
 ④  $z_p = 680$   
 $p_y$  for fire =  $250 \text{ N/mm}^2$

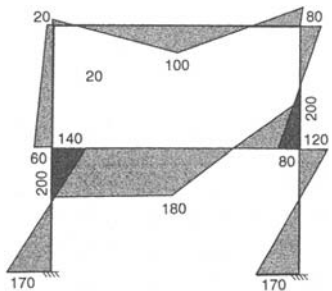
The plastic mechanism (combined) is shown in Fig. (b) and the final plastic moment diagram is given in Fig. (c). A series of computations for each member resulted in the following fire temperature distribution,  $T_s$  (Ref. BS 5950)



(b) Final mechanism (combined) with plastic loads

Columns

- AD → at A =  $150^\circ\text{C}$
- D =  $250^\circ\text{C}$  outside
- =  $400^\circ\text{C}$  inside
- DE → at G =  $560^\circ\text{C}$  outside
- CF → at C =  $350^\circ\text{C}$  outside
- F =  $350^\circ\text{C}$  inside
- FH → at F =  $500^\circ\text{C}$  outside
- H =  $560^\circ\text{C}$  inside



(c) Plastic moment diagram (kN/m)

Beams

- AC → at C =  $350^\circ\text{C}$
- at AD =  $150^\circ\text{C}$
- at B =  $435^\circ\text{C}$
- DF → at D =  $800^\circ\text{C}$
- at F =  $800^\circ\text{C}$
- at E =  $580^\circ\text{C}$

$$x_{LT} = \frac{1}{\phi + (\phi^2 - \lambda^2)^{0.5}} \tag{3.160}$$

$$\bar{\lambda} \text{ for column} = \frac{\lambda}{\chi} (\beta_A)^{0.5} \tag{3.161}$$

$$\lambda = \frac{L}{r} \quad \lambda_1 = \pi \left( \frac{E}{f_y} \right)^{0.5}$$

$$N_{b,Rd} = \text{axial resistance} \tag{3.162}$$

$$= \frac{\chi \beta_A A f_y}{\gamma_{M1}}$$

**Table 3.21.** Strength reduction of temperatures

Temperature (°C)	Eurocodes 3 and 4			BS5950: Part 8			Elastic modulus $K_{E\theta}$	
	$K_{y\theta}$	$K_{x\theta}$	$K_{\theta}$	2%	1.5%	0.5%		
100	← 1.0 →							
200	↑	0.92	0.81	←	1.0	→	0.94	0.9
300	1.0	0.84	0.61	←	1.0	→	0.85	0.8
400	↓	0.77	0.42	0.97	0.96	0.78	0.78	0.7
500	0.78	0.61	0.36	0.78	0.75	0.62	0.62	0.6
600	0.47	0.35	0.18	0.47	0.46	0.38	0.38	0.31
700	0.23	0.17	0.08	0.23	0.22	0.18	0.18	0.13
800	0.11	0.09	0.05	0.11	0.10	0.07	0.07	0.09
900	0.06	0.05	0.04	0.06	0.06	0.04	0.04	0.06

$K_{y\theta}$  corresponds to 2% strain.

$K_{x\theta}$  corresponds to 0.5% strain.

$K_{\theta}$  corresponds to 0.1% strain.

$$K_{E\theta} = \frac{\text{initial tangent modulus}}{200 \text{ kN/mm}^2}; K_{x\theta} = \frac{f_{x,\theta}}{f_{y,20}} \quad K_{y\theta} = \frac{f_{y,\theta}}{f_{y,20}}$$

$\chi$  = reduction factor based on slenderness and imperfection

$\beta_A$  = factor depending on section

$\gamma_{M,1}$  = partial factor for material

$$N_{b,fi,tRd} = \frac{\chi_{fi} A K_{y,\theta} f_y}{\gamma_{M,fi}} \text{ column fire limit state}$$

**Example 3.16 Based on Plastic Analysis and Eurocode EC3 Part 1.2**

A four-storey steel building has a plan area 48 m × 48 m. A typical steel frame is shown in Fig. 3.45 which is part of the steel work of this building. The spacings between such frames are 6 m. Steel beams support concrete floors. Using the following additional data, determine the failure of beams and columns where critical temperatures exceed the allowable.

Floor slab: 350 mm supported by steel beams

Fire duration: 1/2 hour allowed.

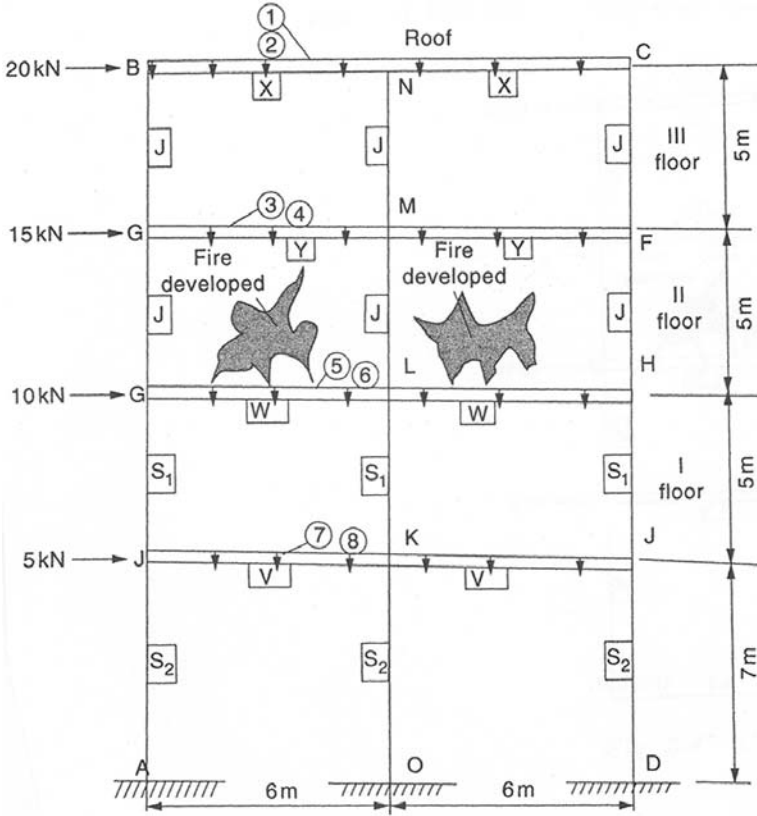


Fig. 3.45. Unprotected steel frame

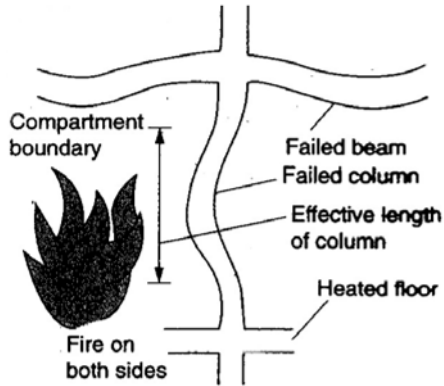


Fig. 3.46. Floor deformation and column effective length at fire limit state

Data (refer to Fig. 3.45):

Load characteristics		Lateral loads	
① $G_K = 1-5 \text{ kN/m}^2$	⑤ $G_K = 3 \text{ kN/m}^2$	at B	20 kN
② $G_K = 6.0 \text{ kN/m}^2$	⑥ $G_K = 6 \text{ kN/m}^2$	at E	15 kN
③ $Q_K = 1.5 \text{ kN/m}^2$	⑦ $G_K = 3.5 \text{ kN/m}^2$		$\lambda = 1.75$
④ $Q_K = 4.5 \text{ kN/m}^2$	⑧ $Q_K = 5 \text{ kN/m}^2$		

Beams/girders	* $z_p$ ( $\text{cm}^3$ )	$z_e$ ( $\text{cm}^3$ )	Columns	* $z_p$ ( $\text{cm}^3$ )	$z_e$ ( $\text{cm}^3$ )
☒ $305 \times 102 \times 33 \text{ kg/m}$ UB Grade 43	481	416	☒ $254 \times 254 \times 73 \text{ kg/m}$ UB Grade 43	X-X	X-X
☒ $406 \times 178 \times 67 \text{ kg/m}$ UB Grade 43	1350	1190	☒ same as ☒ UB Grade 43	Y-Y	Y-Y
☒ $533 \times 210 \times 82 \text{ kg/m}$ UB Grade 43	2060	1800			
☒ $686 \times 254 \times 170 \text{ kg/m}$ UB Grade 43	5630	4920	☒ same as ☒ UB Grade 43		

\*  $z_p = w_{pl}$  (Eurocode 3 symbol for plastic modulus).  
Reduction load in the column for fire limits is ignored based on number of storeys alone.

$$W = P = \text{axial load} = b_1 b_2 (\gamma_G G_K + \gamma_{Q,1} Q_{K,1})$$

See Fig. 3.46.

### Sample Calculations for a Typical Area

#### Third Floor

(a) Fully restrained beam (torsional buckling is ignored) (Fig. 3.47)

#### Beam EM

$M_{fi}$  = maximum moment at fire limit state

$$\begin{aligned} \text{fire load} &= \gamma_{GA} G_K + \psi_{1,1} Q_{K,1} \\ &= (1.0 \times 3 + 0.5 \times 3.5) \\ &= 4.75 \text{ kN/m}^2 \\ M_{fi} &= \frac{4.75 \times 3 \times 6^2}{8} = 64.125 \text{ kN/m} \end{aligned}$$



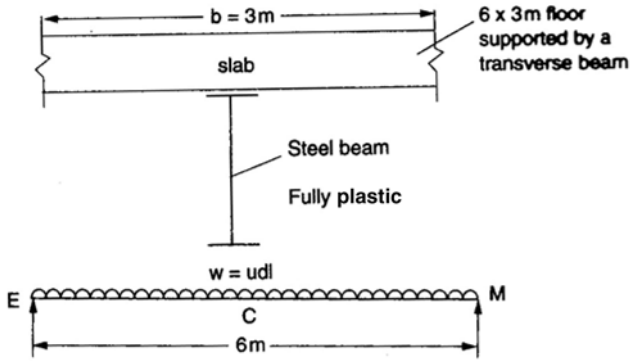


Fig. 3.47. Steel concrete composite beam

Fire limit state

$$\begin{aligned}
 n_{fi} &= \text{load level} \\
 &= \frac{K_{y,\theta}}{K_I} \left( \frac{\gamma_{M,1}}{\gamma_{M,fi}} \right) = \frac{M_{fi}}{M_{c,Rd}} \\
 &= \frac{K_{y,\theta}}{K_I} \times \frac{1.05}{1.0} = \frac{64.125}{232.83} = 0.275 \\
 K_{y\theta} &= \text{strength reduction} = 0.1835 \\
 &= \frac{f_{y,\theta}}{f_{y,2\theta}} = \frac{f_{y,T}}{f_y} \\
 \theta_\alpha &= \text{critical temperature of fire} = 0.1835 \\
 &= T_s \text{ corresponding to } K_{y\theta} = 0.1835 \\
 &= 739^\circ\text{C} \\
 M_p &= 244.475 \text{ kNm} \\
 z_p &= \frac{244.475}{275} \times 10^6 \\
 &= 889 \times 10^3 = w_{p1} \text{ (Eurocode symbol)} \\
 M_{c,Rd} &= \frac{w_{p1} f_y}{\gamma_{M0}} = \frac{244.475 \times 10^3}{1.05 \times 10^6} \\
 &= 232.83 \text{ kNm}
 \end{aligned}$$

Fully restrained steel beam size:

- 406 × 140 × 46 UB
- BS Grade 43
- EC3 Part 1,2 (Grade S275).

*(b) Laterally unrestrained beam (lateral buckling method)*

From the transverse beam supporting  $6 \times 3$  m concrete floor would obviously increase the value of total load: this will be point load  $P$ . Lateral buckling will occur.

$$P = b_1 b_2 (\gamma_G G_{K+Q,1} \underline{Q_{K,1}})$$

$$P = 167.4 \text{ kN} \quad M_{\max}(\text{elastic}) = \frac{PL}{4} = 251 \text{ Knm}$$

Lateral restraints are at E, C, and M. New section:

$$z_p = w_p = \frac{371.25 \times 10^6}{275} = 1350 \times 10^3 \text{ mm}^3 = 1350 \text{ cm}^3$$

section (steel tables):  $406 \times 178 \times 67$  UB

$$b_1 = 3$$

$$b_2 = 6$$

$$\gamma_{Q1} = 1.5$$

$$\gamma_{Q2} = 1.35$$

$$l = \text{buckling length} = 3 \text{ m}$$

$$M_p = 371.25 \text{ kNm}$$

$$T = T_f(\text{flange}) = 14.3$$

$$T = t_w(\text{web thickness}) = 8.8$$

$$\varepsilon = \left( \frac{235}{f_y} \right)^{0.5} = 0.9235$$

$$T > 16 \text{ mm}^2$$

$$F_y = 275 \text{ N/mm}^2$$

Class 1 (Table 5.3.1 Part 1.1):

$$\frac{d}{t} \leq 73\varepsilon = 72 \times 0.9235 = 66.492$$

$$\frac{C}{T} \leq 10\varepsilon = 9.235$$

From steel tables:

$$\frac{d}{t} = 41 \leq 66.492$$

$$\frac{C}{T} = 6.25 \leq 9.235$$

This is acceptable, and so the class 1 section is satisfactory.

*Lateral torsional buckling resistance (based on EC3)*

$M_{b,Rd}$  = bending moment at the major axis at the fire limit state due to buckling, i.e. buckling resistance moment

$$= \frac{\beta_w f_b w_{pl,s}}{\gamma_{M1}}$$

$$b_w = 1.0 \quad \text{for class 1}$$

$$w_{pl,y} = 1350 \times 10^3 \text{ mm}^3 = bz_p$$

$$\gamma_{Mi} = 51.05$$

$f_b$  = bending strength

based on Table 5.21 EC-3,  $K = 1.0$ :

$$\left(\frac{K}{C_1}\right)^{0.5} = 0.729 \quad (\text{Table 5.22 of EC-3})$$

Determination of  $f_b$ :

$$i_{LT} = i_z = \frac{\text{minor axis radius of gyration}}{\text{buckling parameter}} = \frac{39.9}{0.88} = 45.341$$

$$a_{LT} = \text{minor axis radius of gyration} \times \text{torsional index } x \text{ (steel tables)} \\ = 39.9 \times 30.5 = 1216.95$$

$$\beta_w^{0.5} \left(\frac{K}{C_1}\right)^{0.5} \frac{L}{i_{LT}} = (1.0)^{0.5} (0.729)^{0.5} \times \frac{3000}{45.341} = 48.28$$

$$\frac{L}{a_{LT}} = \frac{3000}{1216.95} = 2.465$$

Using Table 5.20 of the code,  $f_b = 251.45 \text{ N/mm}^2$ .

Hence

$$M_{b,Rd} = \frac{1.0 \times 251.45 \times 1350 \times 10^3}{1.05 \times 10^6} = 323.3 \text{ kNm} \\ > M_{\max} = 251 \text{ kNm}.$$

The beam is used for normal temperature design.

*Calculation for critical temperature for beam  $406 \times 178 \times 67 \text{ kg/m UB}$*

Beam loading at fire limit state:

$$\gamma_{GA} G_K + \psi_{l,1} Q_{K,1}) \times \text{floor area} \\ = 4.75 \times 6 \times 3 = 85.5 \text{ kN}$$

$$M_{\max} = \frac{(85.5 \times 6)}{4} = 128.25 \text{ kNm}.$$

$K(x, \theta]$  method (non-iterative method approximation):

Normal slenderness = temperature dependent slenderness

$$\bar{\lambda}_{LT} = i_{LT} = \bar{\lambda}_{L,T,\theta} = \frac{45.31}{85.5} = 0.53$$

$$\text{load level} = n_{fi} = \frac{K}{KI} \frac{\gamma_{M,1}}{\gamma_{M,fi}} = \frac{M_{fi}}{M_{b,Rd}} = M_{\max}$$

$$K_{z,\theta} \times \frac{1.05}{1.0} = \frac{128.25}{323.3}$$

$$K_{x,\theta} = 0.38.$$

Using Eurocode EC-3 Table 3.1.

$$\theta_{a_{\max}} = T_s = 600^\circ\text{C}.$$

Similar calculations have been carried out for other zones and members. Malhotra [3.16] carried out experiments and suggests that unprotected steel members collapse between temperatures of 550–600°C.

### Columns

Axial load/storey

$$\begin{aligned} w &= b_1 \times b_2(\gamma_G G_K + \gamma_{Q,1} Q_{K,1}) \\ &= 6 \times 6(1.35 \times 3.0 + 1.50 \times 3.5) \\ &= 334.8 \text{ kN} \end{aligned}$$

maximum load on single column line acting axially

$$\begin{aligned} &= \text{No. storeys} \times 334.8 \text{ kN} \\ &= 4 \times 334.8 = 1339.2 \text{ kN}. \end{aligned}$$

*Normal design of column prior to fire limit state (based on EC3 Parts 1.1 and 1.2).*  $M_p$  from the plastic analysis of the frame for the column:

$$\begin{aligned} M_{p_{\max}} &= 124 \text{ kNm} \\ \text{computed } z_p &= \frac{124 \times 10^6}{275} = 45090909 \text{ mm}^3 \approx 451 \text{ cm}^3 \\ z_p(Y - Y) &= 463 \text{ cm}^3 \\ A &= 92.9 \text{ cm}^2 \\ \frac{d}{t} &= \frac{d}{t_w} = 23.3 \\ \frac{D}{T} &= 8.94 = \frac{c}{t_f} \end{aligned}$$

Initial section:

254 × 254 × 73 kg/m UC Grade 43; class I section:

column  $f_{y,20} = 275 \text{ N/mm}^2$

$$\varepsilon = \left( \frac{235}{f_{y,20}} = 275 \right)^{0.5} = 0.924$$

$i$  = radius of gyration = 6.46 cm (from steel tables)

$$N_{b,Rd} = \frac{\chi \beta_A A F_y}{\gamma_{M1}}$$

$$\bar{\lambda} = \text{normalized slenderness} = \frac{\lambda}{\lambda_1} (\beta_A)^{0.5}$$

$$\lambda = \left( \frac{E}{f_y} \right)^{0.5} \beta_A = 1.0 \text{ (class 4.3 section)} \quad \gamma_{M1} = 1.05$$

$\lambda$  = slenderness

$$\begin{aligned} \frac{L}{C} &= \frac{\text{buckling length}}{\text{radius of gyration}} \\ &= \frac{5000}{64.6} = 77.34 \end{aligned}$$

$$\bar{\lambda} = \frac{77.34}{93.9 \times 0.924} (1.0)^{0.5} = 0.892$$

$$\phi = 0.5(1 + a(\bar{\lambda} - 0.2) + \bar{\lambda}^2) = 1.067$$

$a$  (buckling curve C, Eurocode) = 0.49.

Hence

$$\chi = \frac{1}{\phi + (\phi^2 \bar{\lambda}^2)^{0.5}} = 0.605$$

$$N_{b,Rd} = \frac{0.605 \times 1.0 \times 9290 \times 275}{1.05 \times 10^3} = 1472 \text{ kN,}$$

which is greater than  $P = 1339.2$  kN.

Adopt column section

254 × 254 × 73 kg/m UC.

Fire resistance

$$w_{f,1} = b_1 \times b_2.$$

Fire limit state (approximation method):

$$\begin{aligned} w_{f,1} &= b_1 \times b_2 (\gamma_G G_K + \psi_{1,1} Q_{K,1}) \\ &= 6 \times 6(1 \times 3.0 + 0.5 \times 3, 5) = 171 \text{ kN} \end{aligned}$$

$$P_{\max} \text{ on column} = 4 \times w_{f1} = 4 \times 171 = 684 \text{ kN}$$

buckling length  $l_{fi} = 0.7L$

$$\bar{\lambda}_{\theta \max} = \bar{\lambda}_{f1} = \left( \frac{k_{y\theta}}{k_{E\theta}} \right)^{0.5} = 0.7 \bar{\lambda}_{f1} = 0.7 \times 0.892 = 0.6244$$

$$\phi_{\theta} = 0.5 [(1 + 0.49(0.6244 - 0.2) + (0.6244)^2)]$$

$$\chi_{fi} = \frac{1}{\{0.7989 + [(0.7989)^2 - (0.6244)^2]^{0.5}\}} = 0.771$$

adaptation factor = 1

$$\begin{aligned}
 N_{b,f1,r,Rd} &= \frac{\chi_{fi}}{1.0} A k_{x\theta} f_{y,20} \\
 &= \frac{0.771}{1.0} \left( \frac{9290}{10^3} \right) k_{x,\theta}(275) = 792.9 \text{ kN} \\
 K_{x\theta} &= 0.364 \\
 \theta &= T_s = 620^\circ\text{C}
 \end{aligned}$$

If the entire frame is enveloped by fire, the temperatures on beam and column at failure will be 600 and 620°C. The maximum 620°C is adopted.

Where the fire is on one floor, such as floor II, all other components have been reanalyzed and the following table gives the developed temperatures and temperatures they can sustain at failure:

	$T_s = \theta$	$\theta_\alpha =$ capacity at failure temp
	(developed)	$= T$
Beams:		
BN and NC	50°C	(580°C)
EM and MF	600°C	(600°C)
GL and LH	80°C	(750°C)
IK and KJ	30°C	(850°C)
Columns:		
BE, NM and CF	50°C	(600°C) buckling
EG, ML and FH	620°C	(620°C) criteria
GI, LK and HJ	30°C	(620°C)
JA, KO and JD	20°C	(620°C)

## 3.10 Finite Element Analysis of Buildings on Fire

### 3.10.1 Introduction

Structural solutions of building response to fire have been demonstrated in earlier sections. A comprehensive analysis of fire response of buildings is needed for the following reasons.

1. Evaluation of the temperature distribution history of buildings in fire environments. This involves:
  - (a) heat transfer analysis of both linear and non-linear planar and ax-symmetric heat conduction problems
  - (b) type of analysis such as steady-state or transient with initial and boundary conditions using one-, two-, and three-dimensional elements.
2. Thermal properties and dimensional changes due to the intensity of fire. Types of changes characterizing degradation and the influence of both convective and radiative mechanisms.

3. Partial and complete damage of the overall building structure predicted by the finite element package, involving correlation and corroborative results.

A number of finite element packages can offer such options. The best package should indicate the following major evaluations:

- (a) material behaviour and dimensional changes caused by temperature differentials;
- (b) non-linear direct stiffness evaluation coupled with time-step integration should form the basis of the program;
- (c) correct formulation of fire environment;
- (d) efficiency in producing complex results using a combination of a variety of elements where possible;
- (e) it should be interactive.

### 3.10.2 Basic Heat Transfer Analysis

The governing equation for heat conduction is the heat balance equilibrium equation:

$$\rho c = \left( \frac{\partial T}{\partial t} + \{\nu\}^{T''} \{L\}T \right) + \{L\}^{T''} \{q\} = \bar{q}$$

where

- $\rho$  = density
- $c$  = specific heat
- $T$  = temperature (=  $T(x, y, z, t)$ )
- $t$  = time

$T''$  = transpose of the matrix

$$\rho c \frac{\partial T}{\partial t} = \dot{e} \tag{3.163}$$

$$\frac{\partial T}{\partial t} = \dot{T} \tag{3.164}$$

$$\{L\} = \left\{ \begin{array}{c} \frac{\partial}{\partial x} \\ \frac{\partial}{\partial y} \\ \frac{\partial}{\partial z} \end{array} \right\} = \text{vector operator} = \nabla \tag{3.165}$$

$$\{L\}T = \nabla T \quad \text{or} \quad [L]^{T''} \{q\} = \nabla \times \{q\}$$

$\{q\}$  = heat flux vector

$\bar{q}$  = heat generation rate per unit volume.

The heat flux vector to the thermal gradients can be determined using Fourier's Law:

$$\{q\} = -[K]_t \nabla T$$

$$[K]_t = \text{conductivity matrix} = \begin{bmatrix} K_{xx} & 0 & 0 \\ 0 & K_{yy} & 0 \\ 0 & 0 & K_{zz} \end{bmatrix}_t \quad (3.166)$$

$K_{xx}$ ,  $K_{yy}$ ,  $K_{zz}$  = conductivity in the element  $x$ ,  $y$  and  $z$  directions, respectively.

Combining (3.160) and (3.166) and writing in a more familiar form:

$$\begin{aligned} & \rho c \left( \frac{\partial T}{\partial t} - v_x \frac{\partial T}{\partial x} + v_y \frac{\partial T}{\partial y} + v_z \frac{\partial T}{\partial z} \right) \\ & = \bar{q} + \frac{\partial}{\partial x} c + \left( K_x \frac{\partial T}{\partial x} \right) + \frac{\partial}{\partial y} \left( K_y \frac{\partial T}{\partial z} \right) + \frac{\partial}{\partial z} \left( K_z \frac{\partial T}{\partial z} \right) \end{aligned} \quad (3.167)$$

### Boundary Conditions

(a) Specified temperatures acting on surface 1 (S1):

$$T^* = T_1 \quad (3.168)$$

(b) Specified heat flows acting on surface 2 (S2):

$$\{q\}^T \{\bar{n}\} = -q^* \quad (3.169)$$

where

$\{\bar{n}\}$  = unit outward normal vector

$q^*$  = specified heat flow.

(c) Specified convection surfaces acting on surface 3 (S3):

$$q^* = -h_f(T_B - T) \quad (3.169a)$$

where

$h_f$  = film coefficient at temperature  $\frac{T_B + T_s}{2}$  for the element

$T_B$  = bulk temperature

$T_s$  = temperature at the surface of the model

Equation (3.169a) for  $q^*$  can now be written as:

$$\{\bar{n}\}^T [k]_t \nabla T = q^* = h_f(T_B - T) \quad (3.169b)$$

Integrating (3.167) over the volume of the element and combining with the finite element formulation:



$$\int_{\text{vol}} \left( \rho c \delta T \left( \frac{\partial T}{\partial t} + \{v\}^T \{L\} T \right) + \{L\}^T (\delta T) ([D] \{L\} T) \right) d(\text{vol}) \tag{3.170}$$

$$= \int_{S_2} \delta T q^* d(S_2) + \int_{S_3} \delta T h_f (T_B - T) d(S_3) + \int_{\text{vol}} \delta T \bar{q} d(\text{vol})$$

vol = volume of the element

$\delta T$  = an allowable virtual temperature (=  $\delta T(x, y, z, t)$ ).

*Heat Flow.* In a fire situation, temperature  $T$  varies in both space and time. In the finite element formulation given in the Appendix, the following equations assume a major role.

The temperature  $T$  is written as:

$$T = \{N\}^{T''} \{T_e\} \tag{3.171}$$

Where

- $T = T(x, y, z, t)$  = temperature
- $\{N\} = \{N(x, y, z)\}$  = element shape functions
- $\{T_e\} = \{T_e(t)\}$  = nodal temperature vector
- $T''$  = transpose.

The time variation is written as:

$$\dot{T} = \frac{\partial T}{\partial t} = \{N\}^T \{\dot{T}_e\} \tag{3.172}$$

$\delta T$  has the same form as  $T$ :

$$\delta T = \{\delta T_e\}^{T''} \{N\}. \tag{3.173}$$

The combination  $\{L\}T$  is written as:

$$\nabla T = \{L\}T = [B] \{T_e\} \tag{3.174}$$

where  $[B] = \{L\} \{N\}^{T''}$ .

The variational equation (3.170) can now be written as:

$$\int_{\text{vol}} \rho c \{\delta T_e\}^{T''} \{N\} \{N\}^{T''} \{N\} \{\nu\}^{T''} \{\dot{T}_e\} d(\text{vol})$$

$$+ \int_{\text{vol}} \rho c \{\delta T_e\}^{T''} \{N\} \{\nu\}^{T''} [B] \{T_e\} d(\text{vol})$$

$$+ \int_{\text{vol}} \{\delta T_e\}^{T''} [B]^{T''} [D] [B] \{T_e\} d(\text{vol})$$

$$\begin{aligned}
 &= \int_{S_2} \{\delta T\}^{T''} \{N\} q^* d(S_2) \\
 &+ \int_{S_3} \{\delta T\}^{T''} \{N\} h_f (T_B - \{N\}^{T''} \{T_e\}) d(S_3) \\
 &+ \int_{\text{vol}} \{\delta T_e\}^{T''} \{N\} \bar{q} d(\text{vol})
 \end{aligned} \tag{3.175}$$

The quantities outside the matrix symbols,  $c$  and  $\hat{\cdot}$  in particular, do vary over the element.  $\{T_e\}$ ,  $\{\dot{T}\}$  and  $\{\delta T_e\}$  are nodal quantities which do not vary and they are taken outside the integral. Equation (3.175) is to be multiplied by an arbitrary term  $\{\delta T_e\}$  and may be dropped where  $\{\delta T_e\} \{\delta T_e\}^{T''}$  appears out of the rest.

Equation (3.175) is reduced to:

$$\begin{aligned}
 &\rho \int_{\text{vol}} c \{N\} \{N\}^{T''} d(\text{vol}) \{\dot{T}_e\} + \rho \int_{\text{vol}} \{N\} \{\nu\}^{T''} [B] d(\text{vol}) \{T_e\} \\
 &+ \int_{\text{vol}} [B]^{T''} [D] [B] d(\text{vol}) \{T_e\} \\
 &= \int_{S_2} \{N\} q^* d(S_2) + \int_{S_3} T_B h_f \{N\} d(S_3) \\
 &- \int_{S_3} h_f \{N\} \{N\}^{T''} \{T_e\} d(S_3) + \int_{\text{vol}} \bar{q} \{N\} d(\text{vol})
 \end{aligned} \tag{3.176}$$

Equation (3.178) now assumes the following form, involving element specific heat, total conductivity and heat flow matrices:

$$[C_e^t] \{\dot{T}_e\} + ([K_e^{tm}] + [K_e^{tb}] + [K_e^{tc}]) \{T_e\} = \{Q_e\} + \{Q_e^c\} + \{Q_e^g\} \tag{3.177}$$

where

$$\begin{aligned}
 [C_e^t] &= \rho \int_{\text{vol}} c \{N\} \{N\}^{T''} d(\text{vol}) = \text{element specific heat (thermal damping)} \\
 &\hspace{15em} \text{matrix evaluated from enthalpy curve} \\
 [K_e^{tm}] &= \rho \int_{\text{vol}} c \{N\} \{\nu\}^{T''} [B] d(\text{vol}) \\
 [K_e^{tb}] &= \rho \int_{\text{vol}} [B]^{T''} [D] [B] d(\text{vol}) \\
 [K_e^{tc}] &= \int_{S_3} h_f \{N\} \{N\}^{T''} d(S_3)
 \end{aligned} \left. \vphantom{\begin{aligned} [C_e^t] \\ [K_e^{tm}] \\ [K_e^{tb}] \\ [K_e^{tc}] \end{aligned}} \right\} = \text{total element conductivity matrix}$$

$$\left. \begin{aligned} [Q_e^f] &= \int_{S_2} \{N\} q^* d(S_2) \\ [Q_e^c] &= \int_{S_2} T_B h_f \{N\} d(S_3) \\ [Q_e^g] &= \int_{vol} \bar{q} \{N\} d(vol) \end{aligned} \right\} = \text{total element heat flow vector}$$

Based on the Stefan-Boltzmann Law, the *radiation heat* flux from the surface, i.e. heat transfer rate,  $Q$ , between two surfaces ‘ $i$ ’ and ‘ $j$ ’ due to radiation is given as:

$$Q_i = \sigma \varepsilon_i F_{ij} A_i (T_i^4 - T_j^4) \tag{3.178}$$

where

- $Q_i$  = heat transfer rate from surface  $i$
- $\sigma$  = Stefan-Boltzmann constant
- $\varepsilon_i$  = effective emissivity
- $F_{ij}$  = view factor from surface to surface  $j$
- $A_i$  = area of surface  $i$
- $T_i, T_j$  = absolute temperature at surface  $i$  and surface  $j$ , respectively.

If the surface considered is small compared with the surrounding environment at uniform temperature  $T_j$ , the effective or resultant emissivity  $\varepsilon_i = \varepsilon_s$ , the surface emissivity. The effective value of  $\varepsilon_i$  is calculated when radiation is between two infinitely long parallel planes as

$$\varepsilon_i = \frac{1}{\frac{1}{\varepsilon_i} + \frac{1}{\varepsilon_g} - 1} \tag{3.179}$$

where  $\varepsilon_g$  = gas or flame emissivity.

The total heat flux at a boundary

$$= q^* + Q_i \quad \text{convection and radiation.} \tag{3.180}$$

The shape functions and other parameters are given for elements in the Appendix. The heat flow equilibrium equation in matrix form given above can be solved by time integration. The critical time increment  $\Delta t_{cr}$  is taken to be:

$$\Delta t_{cr} = \frac{2}{\lambda_{max}} \tag{3.181}$$

When  $\lambda_{max}$  is the maximum eigenvalue and is given by:

$$\lambda_{max} \leq \max_i \left[ c_{ii}^t / \left( K_{ii}^{tb} + \frac{1}{2} \sum_j K_{fij} \right) \right] \tag{3.182}$$

the upper limit to the critical time increment is:

$$\Delta t_{cr} = \min_i \left[ c_{ii}^t / \left( K_{ii}^{tb} + \frac{1}{2} \sum_j K_{f_{ij}} \right) \right] \quad (3.183)$$

where

$c_{ii}^t$  = specific heat matrix given above

$K_{ii}^{tb}$  = element conductivity matrix

$K_{f_{ij}}$  = stiffness matrix.

All these parameters are fully discussed in the preamble of this section on fire.

### 3.10.3 Computer Subroutines

Some important subroutines given in the Appendix are reproduced from TASEF-2, a two-dimensional FE program on temperature analysis of structures exposed to fire, linked with the program ISOPAR, the description of this 3D finite element analysis program (Appendix).

### 3.10.4 Applications

(a) *Concrete beams and columns.* The program ISOPAR has been tested on beams and columns. Heat is transferred from three faces. The temperature rise and isotherms are examined. Figures 3.48 and 3.49 show a more rapid rise in beams than in slabs. The I-beam has a much higher temperature rise than do rectangular beams or square beams. The higher temperature exists in the central part of the I-beam. Figures 3.50a and b show isotherms for various RC columns. The finite element results shown indicate that inside of these columns the temperature rise is more rapid than that in beams of the same cross-section.

(b) *Steel and composite beams and columns.* Figures 3.51a and b show isotherms for steel and composite sections. In the case of composite columns with embedded steel profiles, and due to reduction in strength and stiffness in the outer part of concrete portions with temperatures above 300°C, the stresses in steel are enhanced or augmented and early collapse occurs before the steel reaches temperatures up to 500°C, a critical temperature. The failure theory of concrete is chosen to be the Ottoson failure criterion in the three-dimensional finite element analysis given in the Appendix.

(c) *Full-scale prototype building under fire using three-dimensional finite element analysis.* Two types of buildings have been examined; the description of each of them is given prior to the analysis. The following points are kept in mind when a building is on fire.

(a) A finite element method in connection with a time-step integration is used to calculate the temperature distribution in any component of a building. The Appendix gives the basic finite element technique.

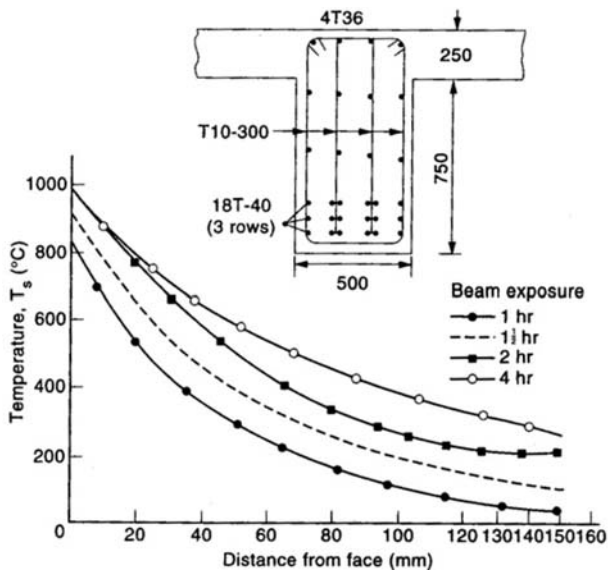


Fig. 3.48. Temperature versus distance for T-beams

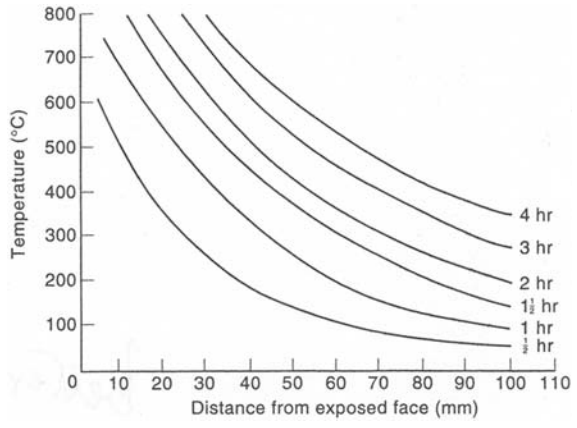


Fig. 3.49. Temperature versus distance for reinforced concrete beams and slabs

- (b) Knowing the temperature distribution, it is possible to determine the relations between loads and deflections of the building system.
- (c) The procedure takes into account the geometric effects, thermal material laws and material non-linearity.
- (d) Any frame composed of interconnected columns and beams is divided into discrete elements. The beam elements are given in the Appendix. In order to decide what type of element is used, it is necessary to take into account the heat balance between adjacent mesh elements.

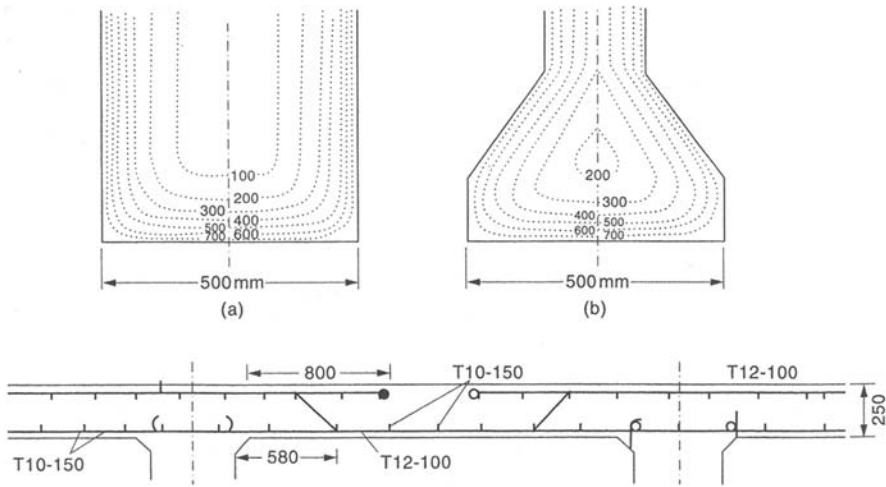
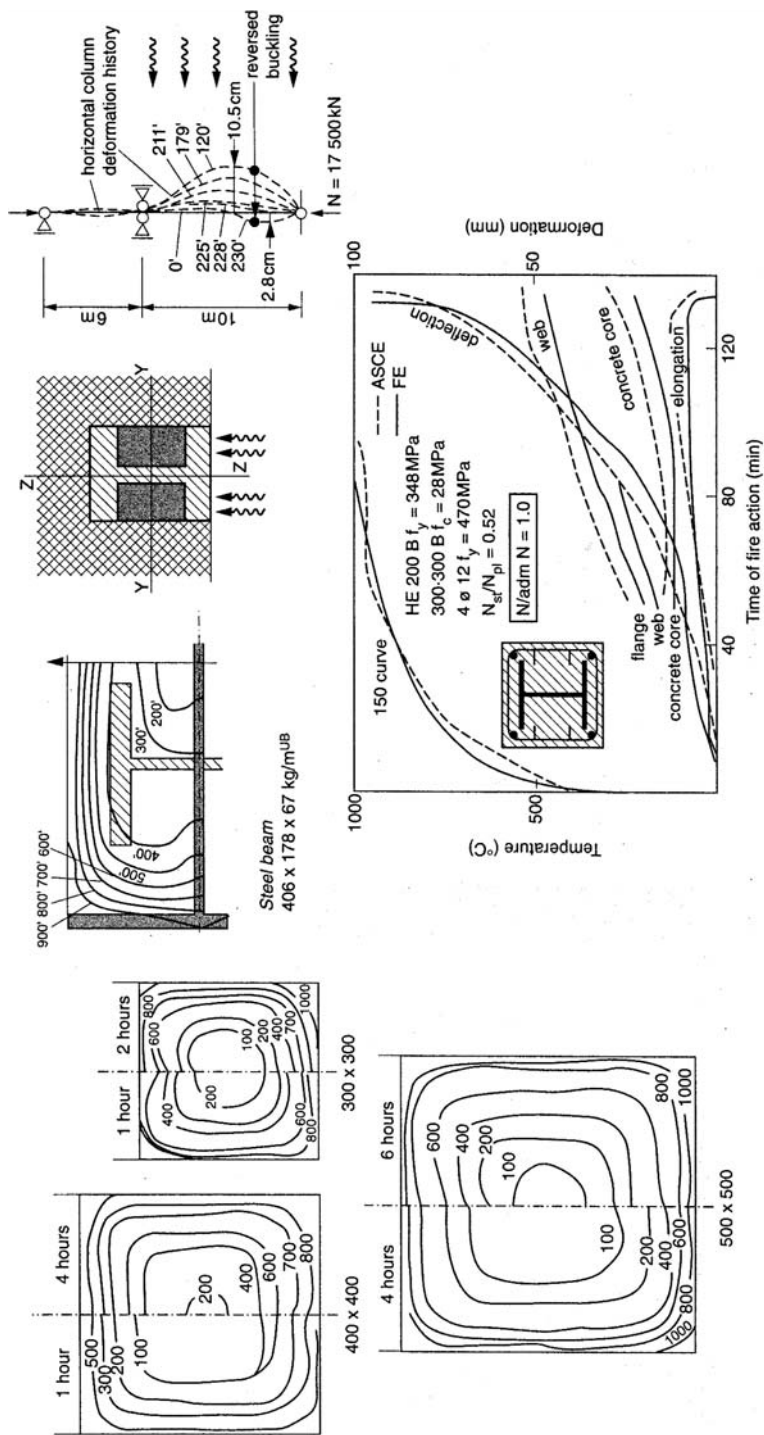


Fig. 3.50. Isotherms for various reinforced concrete columns

- (e) At ambient temperature the fire resistance of composite concrete slabs with profiled steel sheets as shown in Table 3.22 can, in the absence of a suitable flooring system, be simulated into the finite element program. Such composite slabs transmit tensile stresses due to positive bending moments. The temperature of the steel sheets will increase in fire, and material properties will decrease. At a certain temperature, dependent on load level and frame static system, the steel may no longer be able to transmit tensile force and, as a result, the slab fails for no load-bearing capacity. These facts include the failure associated with the insulation, if any.
- (f) All research work indicates that static continuity of beams or columns has an explicitly favorable, increasing effect on the fire-resistance time of these structural elements. The global behavior of real structures during fires, although fires remain localized through the use of building compartments, is important, since there is a probability of not inducing global collapse at an early stage of the fire. All structural components are assumed interconnected.
- (g) It is assumed no wind and snow loads occur simultaneously during fire. Generally, the global safety factor recommended must not exceed 1.9 for 100 minutes of fire, after which global equilibrium failure occurs due to structural mechanisms. The service loads, in that case, are to be increased by 1.9.
- (h) The same conditions are considered in composite construction for the local fire simulation.



Note  
 Steel columns: 254 x 254 x 73 kg/muc  
 Grade 43 or 2755

Experimental data of a 4.20 m (13.7 ft)  
 composite column with embedded file, tested  
 with one end fixed and the other pin-jointed

Fig. 3.51a. Steel and composite beams and columns

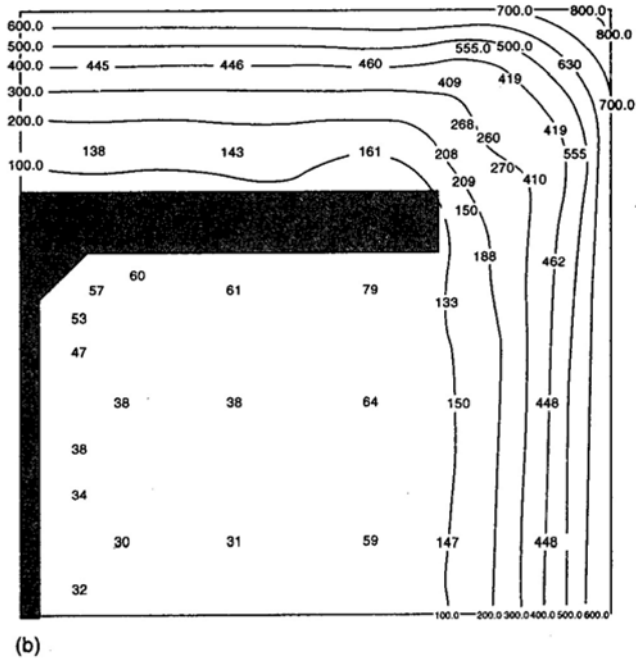
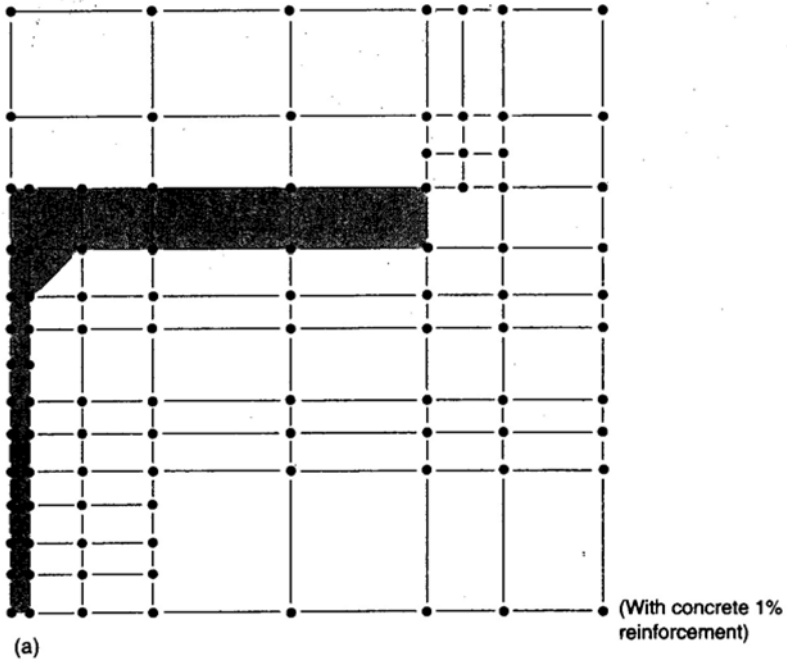


Fig. 3.51b. Isotherms for steel and composite sections (three-dimensional finite-element analysis)



**Table 3.22.** (Below and facing). Fire resistance of composite concrete slabs with profiled steel sheet without additional means of fire protection

Laboratory tests and report no. (country)	Cross-section* (dimensions in mm)	Statical system (span in m)	Live load (m/m <sup>2</sup> )	Fire resistance criteria regarding load-bearing capacity	Fire resistance time (min)
1 TNO BV73-74 (The Netherlands)			2700	$\frac{\delta}{L} > \frac{L'}{900H}$	40
2 EMPA 66356/1 (Switzerland)			4800	$\frac{\delta}{L} > \frac{1}{20}$	55
3 EMPA 66356/2 (Switzerland)			10100	$\frac{\delta}{L} > \frac{1}{20}$	69
4 CTICI 74V58/T41 (France)			2500	$\frac{\delta}{L} > \frac{1}{20}$	33
5 CTICI 74V64/T47 (France)			2500	$\frac{\delta}{L} > \frac{1}{30}$	35
6 CTICI 74V59/T42 (France)			2500	$\frac{\delta}{L} > \frac{1}{30}$	37
7 CSTB 66.2385D (France)			3830	$\frac{\delta}{L} > \frac{1}{30}$	38
8 CSTB 66.2478A (France)			3800	$\frac{\delta}{L} > \frac{1}{20}$	44
9 CSTB 70.4018 (France)			6880	$\frac{\delta}{L} > \frac{1}{30}$	38
10 CSTB 69.2595 (France)			10100	$\frac{\delta}{L} > \frac{1}{30}$	40
11 EMPA 11009 (Switzerland)			3300	$\frac{\delta}{L} > \frac{1}{30}$	40
12 VTI/PAL A8378 (Finland)			3500	$\frac{\delta}{L} > \frac{1}{30}$	43

\* Dense concrete, unless otherwise stated.

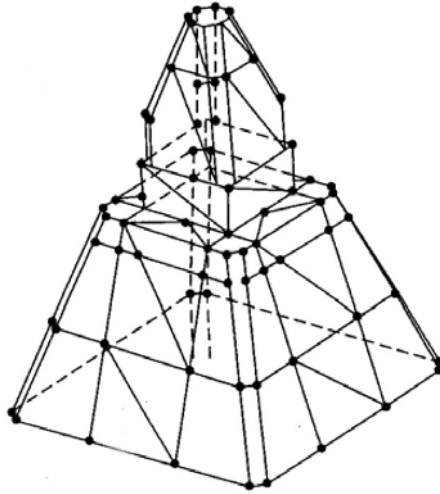


Fig. 3.52. Typical finite element mesh for the pyramid

### 3.11 Case Study for Global Analysis Based on Finite Element Method – Canary Wharf Building

#### 3.11.1 Introduction to the Analysis

The Canary Wharf tower shown in Fig. 3.53 is located in the East London docklands area. Figures 3.54 and 3.55 show particular features of this tower. The tower consists of a three-level substructure. Plant floor level is on the 2nd floor.

The tower is a square of 58.5m sides in plan, with its reentrant corners rising to 235.8m above ground level. There is a total of 49 floors, 45 of which are allocated for offices. The total height at the tip is 245.8m above ground level. The remaining floors are allocated for penthouses, mechanical plant and cooling towers. Figure 3.56 shows floor-to-floor height and structural details. Typical floor height is 4.11m, including an allowance of 140 mm for an access floor. Two setbacks all around are considered, one on the 45th floor of about 4 m and the other of 3.5 m at penthouse level. The perimeter framing consists of closely spaced columns and deep girders of the dimensions shown in Fig. 3.57. The wind-resisting system is located on the perimeter of the floors. In each tube, identical tree-like framing units exist. A floor system identical to that shown in Fig. 3.57 is used for all office floors. The interior framing of the service core takes only gravity loads. The lower portion of the substructure consists of concrete floors, columns, encased steel columns and walls. The building is assumed to have a fire somewhere in the uppermost levels.



**Fig. 3.53.** Canary Wharf building

### 3.11.2 Data

structural steel: Grade 50 for perimeter tube, others Grade 43

maximum column plate: 150 mm

composite deck: 60 mm acting with 465 mm deep floor beams at 3 m on centre spanning from the core to the perimeter tube

office floor area:  $32.51 \times 29$  m with spans 14.23 and 12.17 m

total gravity load on foundation:  $2664 \times 10^3$  kN.

Figure 3.58 shows the finite element mesh scheme of the entire building. The steel sections are three-noded isoparametric elements; each node has a two-degrees of freedom system. All concrete elements are represented by four-noded brick elements. A reference is made to the Appendix for steel and concrete failure criteria. Based on tables given earlier, the fire resistance time is taken to be 35 minutes. The following data for the elements are taken into consideration:

Steel 350 000 elements

Concrete 290 000 elements

Others 15 000 elements.

The program ISOPAR covers material criteria given in the Appendix and in the above mentioned paragraphs. Pseudo-fire is assumed to occur on and on

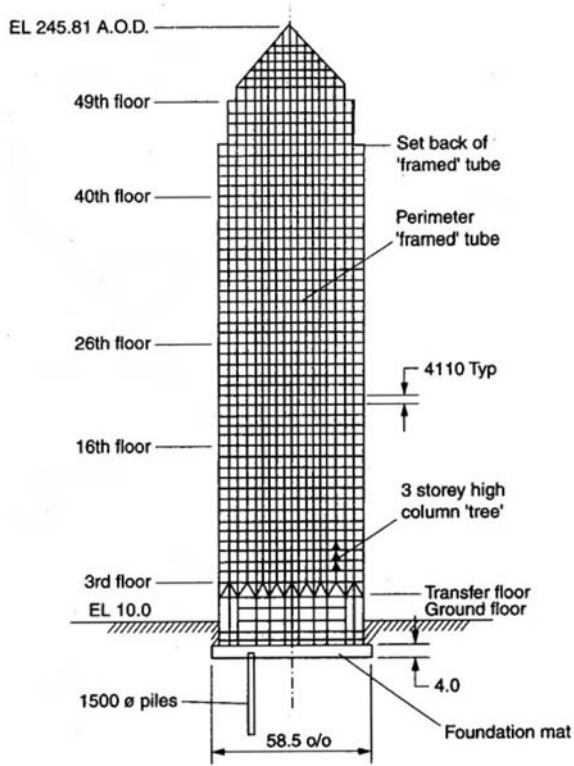


Fig. 3.54. Diagrammatic elevation of tower using finite element mesh

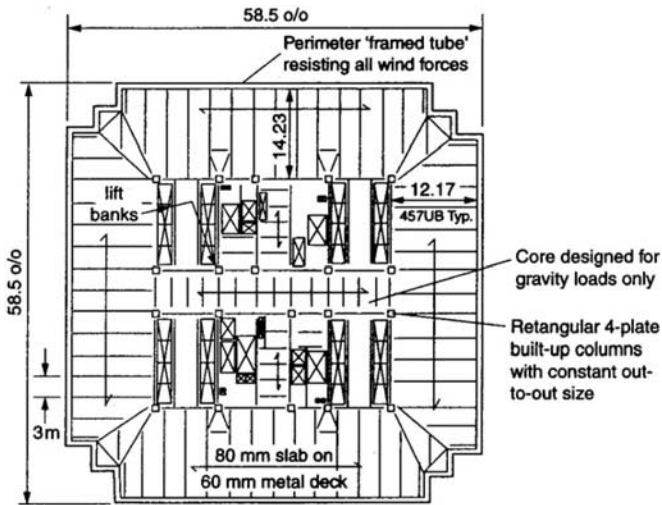


Fig. 3.55. Typical low-rise floor framing plan

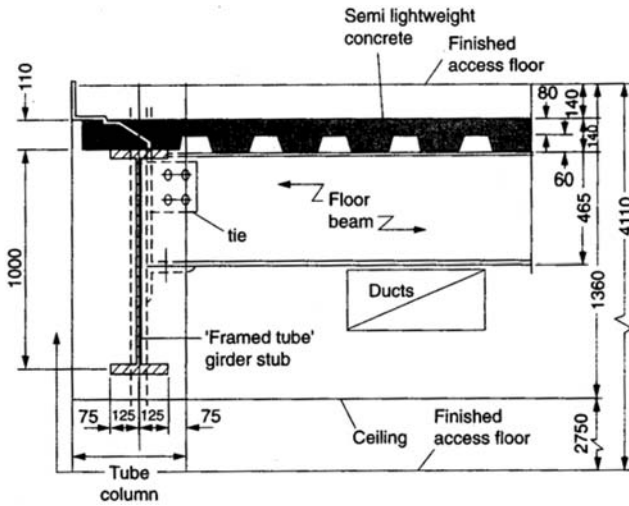


Fig. 3.56. Floor-to-floor height and structural details

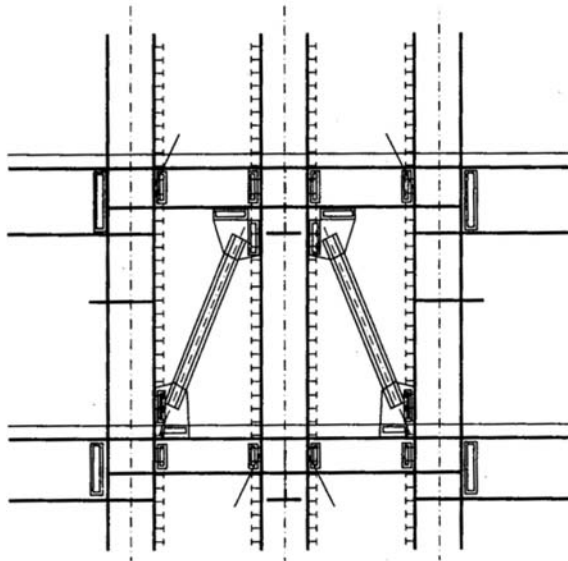
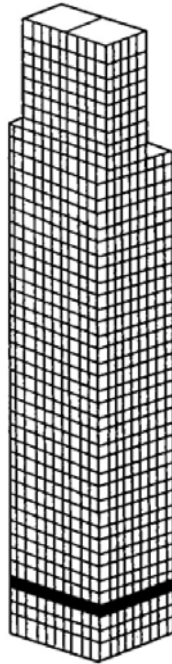


Fig. 3.57. Closely placed steel columns



**Fig. 3.58.** Finite element mesh scheme for the Canary Wharf building (with-out canopy) – 3D layout from the East/West side

the 25th floor and on the 45th floor simultaneously. The time assumed prior to the arrival of fire fighters is 35 minutes. The black band on the finite element scheme is the area of the transfer floor. The temperature developed in the concrete of the flooring system is  $360^{\circ}\text{C}$  (see Table 3.23) and a great deal of the yielding has occurred in the steel complex. The floor system has collapsed but no serious damage has occurred to the tubing system. Some additional floors shown by hatched zones have been affected. The steel complex has reached  $600^{\circ}\text{C}$  within half an hour in most areas on the 25th and 45th floors. Floors 24 and 23 have reached  $55^{\circ}\text{C}$  to  $65^{\circ}\text{C}$  in all areas. The pyramid is not affected but the temperature in most areas is  $45^{\circ}\text{C}$ . This example was computed in 75 minutes of a Cray 3.

The computer program FIRES-T3 (Fire Response of Structures – Thermal, Three-dimensional),\* in association with ISOPAR, which conducts the fire scenario at the floor level, is demonstrated by Fig. 3.59. The fire scenario is illustrated in Fig. 3.60.

The procedure is to excite fire at a specific floor and then produce a scenario and damage at floors above and below. The procedure is continued from the bottom floor/basement to the canopy in successive stages by artificial generation of fire. A 1-hr limit is established prior to the arrival of the

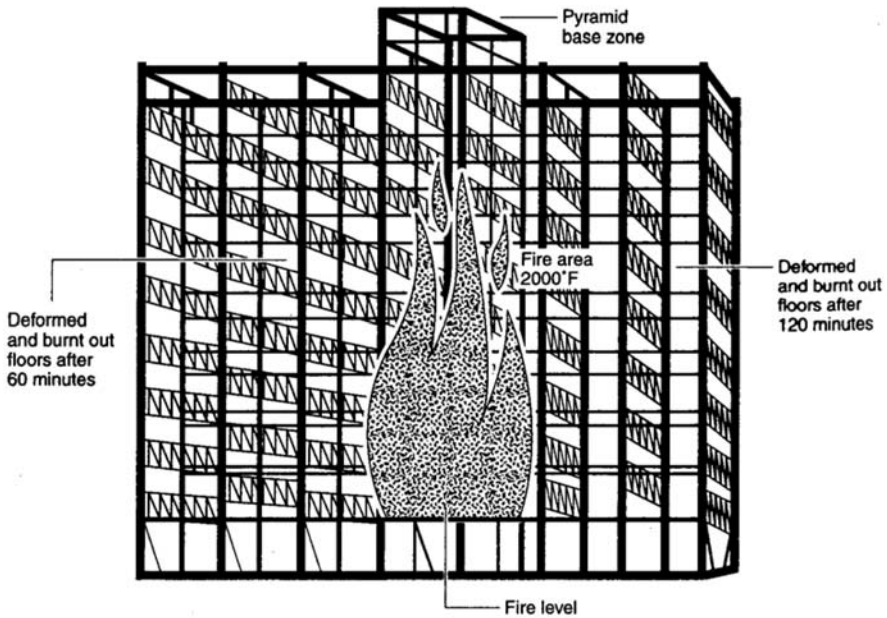


Fig. 3.59. Fire damage at particular floor levels for a portion of the building

fire ambulances. A typical damage zone of the floor and verticals is shown by brown colours. In the elevations, the green colour represents floor levels which show temperatures from  $80$  to  $120^{\circ}\text{C}$  and are still robust. No damage of serious consequence occurs. It appears that the structure has been designed for much worse conditions. Concrete elements in the floor receive cracking, as shown by blue lines along the walls. Again no bursting of reinforcement occurs elsewhere. Overall, conditions of the building for a 1-hr continuous fire affect very little. If the fire is extended for 4 hr, the floor segments fall where the red rectangles are shown. The corresponding temperature rise to  $550^{\circ}\text{C}$ . Yellow total indicate total damage in areas at  $550^{\circ}\text{C}$  but the steel has yielded and is not collapsed. The limiting time of 4hr is sufficient. The overall performance of this build-up is very satisfactory.

This program is similar to TASEF given in the Appendix has been modified extensively to link with BANG-FIR and FEMVIEW in order to create a disaster scenario due to fire in the said building as a formal test case. This is shown in Fig. 3.60.



**Fig. 3.60.** Fire scenario (typical example on assumed calculated fire) – initial example on Canary Wharf, London 2003



**Table 3.23.** Initial temperature distribution for columns-atypical example

A column  $203 \times 203 \times 60$  kg/m is protected on all four sides by 25mm insulation of vermiculite slabs. Using the following data and the relevant Eurocodes, calculate the time for protection such that for the furnace temperature  $T_f$  of  $950^\circ\text{C}$ , the temperature rise  $T_s$  on the assembly is no more than  $340^\circ\text{C}$ , which is the temperature for column collapse.

Column  $203 \times 203 \times 60$  kg/m

$$\text{Steel properties } \begin{cases} A_s = 76 \text{ cm} \\ C_s = 250 \text{ J}/(\text{kg} \times ^\circ\text{C}) \\ \rho_s = 7850 \text{ kg}/\text{m}^3 \end{cases} \quad \begin{array}{l} \text{depth of section} = 209.2 \text{ mm} \\ \text{breadth of section} = 205.2 \end{array}$$

$$\text{Insulation properties } \begin{cases} d_i = 0.025 \text{ m} \\ k_i = 0.15 \text{ W}/(\text{m} \times ^\circ\text{C}) \\ c_i = 1200 \text{ J}/(\text{kg} \times ^\circ\text{C}) \\ \rho_i = \Delta t \not\propto \frac{25000}{D \text{ or } P_s/A_z} \end{cases}$$

$T_f$  = initial furnace temperature =  $330^\circ\text{C}$

for 1 minute based on ISO standard  $T_f = 345\log(8t + 1) + T_0$

$T_0$  or  $T_s$  = ambient or initial temperature =  $20^\circ\text{C}$  at zero time.

*European practice*

Column size  $254 \times 254 \times 60$  kg/m

$$P_s \text{ or } \frac{D}{A_s} = \frac{1.636}{21.2 \times 10^{-3}} = 77.17 \text{ m}$$

$$\Delta t \not\propto \frac{25000}{77.17} = 324 \text{ sec}$$

Adopt

$$\Delta t = 300 \text{ sec}(5 \text{ min})$$

$$\Delta T_s = \frac{\alpha(300)(77.17)}{520 \times 7850} (T_f - T_s) = 0.00596 \text{ or } (T_f - T_s)$$

$T_s$  = temperature rise ( $^\circ\text{C}$ )

$$T_f = 3451\log_{10}(0.133 \times t + 1) + T_{0.36.80} = 113.20$$

At  $t = 5$  min

$$T_f = 3451\log(0.133 \times 5 + 1) + 20$$

$$a = a_c + a_y$$

$$\alpha_y = \frac{5.77 \times 0.5}{(T_f - T_s)} \left[ \left( \frac{T_f + 273}{100} \right)^4 - \left( \frac{T_s + 273}{100} \right)^4 \right] \text{ W}/(\text{m}^2 \times ^\circ\text{C})$$

According to the temperature rise ( $500\text{--}600^\circ\text{C}$ ), this column when fully loaded will collapse after about 85 minutes.

$$D \text{ or } P_i = 2(\alpha + b) = 2(205.2 + 209.2) = 828.8 \text{ mm} = 0.8288 \text{ m}$$

$t$ (min)	$T_f$ ( $^{\circ}\text{C}$ )	$\alpha = \alpha_c + \alpha_r$ ( $\text{W}/(\text{m}^2 \times ^{\circ}\text{C})$ )	$T_f - T_s$ ( $^{\circ}\text{C}$ )	$\Delta T_s$ ( $^{\circ}\text{C}$ )	$T_s$ ( $^{\circ}\text{C}$ )
0.00					20
5.00	113.20	29.92	76.40	16.80	$\vdots$ 36.80
10.00	163.54	31.17	126.74	23.55	$\vdots$ 60.35
15.00	224.71	33.6	164.36	32.92	$\vdots$
$\vdots$	$\vdots$	$\vdots$	$\vdots$	$\vdots$	93.27
25.00	312.69	38.0	219.48	49.75	$\vdots$
$\vdots$	$\vdots$	$\vdots$	$\vdots$	$\vdots$	143.02
35.00	402.61	44.83	259.59	69.36	$\vdots$
$\vdots$	$\vdots$	$\vdots$	$\vdots$	$\vdots$	212.38
44.00	529.73	57.70	317.36	109.14	$\vdots$
$\vdots$	$\vdots$	$\vdots$	$\vdots$	$\vdots$	321.52
75.00	680.46	81.38	358.94	174.1	$\vdots$
$\vdots$	$\vdots$	$\vdots$	$\vdots$	$\vdots$	495.62
100.0	894.21	134.08	398.59	318.52	$\vdots$ 814.14

$$\frac{d_i}{K_i} = \frac{0.025}{0.15} = 0.17 \quad \frac{D \text{ or } P_i}{A_s} = \frac{0.8288}{76 \times 10^{-4}} = 109$$

$$\Delta t = \frac{25000}{109} = 229 \text{ sec} \quad A_s = 76 \times 10^{-4} \text{ m}^2$$

$\Delta t = 4 \text{ min}$  as time interval

$$\Delta T_s = \frac{P_i}{A_s} \frac{T_f - T_s}{c_s \rho_s} \times \Delta t \frac{c_s \rho_s}{c_s \rho_s + c_i \frac{\rho_i d_i P_i}{2 A_s}} \times \frac{k_i}{d_i}$$

$$= \frac{109 \times 4 \times 60 (T_f - T_s)}{520 \times 7850}$$

$$\times \left[ \frac{520 \times 7850}{520 \times 7850 + 1200 \times 300 \times 0.025 \times \frac{109}{2}} \right]^{[\frac{0.15}{0.025}]}$$

$$= 0.064 (T_f - T_s) (0.8) (6)$$

$$= 0.0307 (T_f - T_s)$$

$$\Delta T_s = 0.0307 (330 - 20) = 9.5^{\circ}\text{C} \approx 10^{\circ}\text{C}.$$

Hence

$$T_s = 20 + 10 = 30^{\circ}$$

On the lines suggested the following table can be utilized

Time (min)	$T_f$ ( $^{\circ}\text{C}$ )	$T_f - T_s$ ( $^{\circ}\text{C}$ )	$\Delta T_s$ ( $^{\circ}\text{C}$ )	$T_s$ ( $^{\circ}\text{C}$ )
0				20
	330	310	10	30
$\vdots$	$\vdots$	$\vdots$	$\vdots$	$\vdots$
60	950	632	25	340

*Check*

$$\frac{P_i}{A_s} = 109 \text{ ignoring thermal capacity of the insulation}$$

$$\frac{d_i}{K_i} = 0.17$$

$T_s$  at 60 minutes =  $360^{\circ}\text{C}$

Hence the protection time is around 60 minutes.

---

## References

- [3.1] Peterson O (1986) Structure for behavior – development trends. In: Grant CF, Pagni PJ (eds.): 1st Int. Symp. for fire safety science, Hemisphere Publishing Corp., Washington, DC; also Lund University (1988) Report LU TVDG/CTVBB-3040, Lund, Sweden
- [3.2] Lie TT, Stanzak WW (1973) Engineering. J. Am. Inst. Steel Construction, 34d Qtr.
- [3.3] Lie TT, Stanzak WW (1974) Eng. J. 57:5–6
- [3.4] Lie TT, Stanzak WW (1976) AISC Eng. J. 13:2
- [3.5] Purkiss JA (1996) Fire safety engineering. Design of structures, Butterworth-Heinemann, Oxford
- [3.6] Harmathy TZ (1965), Ten rules of fire endurance rating. Fire Technology 1(2):93–102
- [3.7] Harmathy TZ (1970), Thermal performance of concrete masonry walls and fire. Special Publication 464, American Society for Testing and Materials, Philadelphia, PA
- [3.8] Flemington RA (1980) Fire protection of hollow structural sections. Tech. Bulletin 21, STELCO Inc. Toronto, Canada
- [3.9] Lie TT, Allen DE (1972) Calculation of the fire resistance of reinforced concrete columns. Technical Paper No. 378, Division of Building Research, Council of Canada
- [3.10] Lie et al. (1984) Fire resistance of reinforced concrete columns. Technical Paper No. 379, Division of Building Research, National Research Council of Canada
- [3.11] Lie TT, Harmathy TZ (1974) Fire endurance of concrete-protected steel columns. Journal of the American Concrete Institute 1
- [3.12] Lie TT (1982) Fire and Buildings. Applied Science Publishers Ltd., Barking, UK
- [3.13] Abrams MS, Gustafero AH (1969) Fire endurance of two-course floors and roofs. Journal of the American Concrete Institute 66(2):92–102
- [3.14] American Concrete Institute (1987) Guide for determining the fire endurance of concrete elements. ACI 216R81
- [3.15] Karuna E (1996) MSc Thesis, City University, London, UK
- [3.16] Malhotra HL (1982) Design of fire-resisting structures. Survey University Press, London

# 4 Structural Response to Blast Loadings – Methods of Analysis

## 4.1 Introduction

It is important to check that all plans for safety are in agreement with the proposed measures to be adopted which include protection to receive to the occupants, contents, essential building functions, emergency functions and essential repairs and retrofitting etc. The most important items under observation are:

- (a) exterior walls and columns inside the buildings,
- (b) exterior columns in buildings,
- (c) elastic, plastic instability and  $P - \Delta$  effect.
- (d) *Roof structures*

The roofstructure, apart from normal design, shall consider the following loading cases:

- (i) down ward overpressure – primary load
  - (ii) suction due to negative pressure (negative loading phase)
  - (iii) upward blast pressure arriving from penetration through windows, doors and other openings.
- (e) *Floor structures*
- The floors are to be designed to withstand blast loadings and pressures acting from above and from below independently.
- (f) *Framed structures and shear walls*

The frame must be designed to withstand both the total blast on the building and also the ground shock. Soil structure, interaction must be the basis for the analysis and design. Both vertical and lateral loadings must be considered simultaneously. Progressive collapse criteria must be satisfied as part of the global analysis.

Where shear walls and a lift core are used, they must adequately resist the blast and assist the frame in transmitting the total load to the foundations, thus minimizing the  $P - \Delta$  effect.

- (g) *Foundation structures*

Foundations are not directly in line of blast loads unless the bomb explodes in the basement or underground car parks. All vulnerable areas are to be included in the overall performance of the building. The design

of such components of the foundation must include anchors, piles and embedded items such as prestressing cable galleries, pipes and others.

In the design of all these elements, the blast loads are combined with dead loads with a partial safety factor for load of 1.0 when upward pressures due to blast are considered. For downward pressures, regular partial safety factors must be added. For  $P - \Delta$  and lateral effects, all loads in given design codes are to be considered. The inelastic deformation is also considered. For strain rate effects, a reference is made to Appendix for detailed input on a specific material.

Since bombs, plastic explosives and other incendiary devices are extremely sensitive to the geometry of the target, the analysis becomes complex and costly. Diffraction becomes a big problem. Therefore, finite element and other numerical methods are adopted for the analysis of the global behaviour of the building subjected to blast.

## 4.2 Methods of Analysis and Design

Methods of analysis have been fully explained in Chaps. 2 and 3 and sections elsewhere of this text. However, there is an additional proviso that whatever methods are used they require adequate resolution in space and time to account for high intensity and short duration loading. The following methods are recommended:

- (a) The modelling of components such as beams, slabs, columns and walls can be carried out by a single or two-degree-of-freedom system. The response of such components can be found by using standard charts and handbooks. Limit state analysis and a plastic method of analysis can be useful tools.
- (b) For complex structural components, or for the entire building, nonlinear finite element analysis using explicit or implicit or mixed hybrid modelling on micro- or main-frame computers should be carried out. The Appendix provides guidance for such an analysis of complex building problems.
- (c) The use of discrete elements or a mixture of discrete and finite element method described later on in this text.

Any numerical and analytical methods cannot be justified exclusively unless they are coupled with the structural response analysis. It is also essential to develop some simple structural response analysis.

## 4.3 Structural Response Analysis to Blast Loading

Bangash and TM5-1300 have given detail the response of building structures to explosions. The structural response is dependant on a number of factors including layout, structural detailing, damping characteristics, material

properties, explosive charge source and its range and degrees of freedom and individual components and the entire structure. The vibrations produced can be based on single-degree-of-freedom situations. The vibration can be free or damped. Sometimes to simplify the analysis the analysis, standard charts are prepared to evaluate certain parameters needed for the explosion analysis. Based on Table 4.1 where single-degree-freedom equations are summarized, a blast load with triangular load approximation is taken into consideration. Figure 4.1 gives the elastic-plastic response in which resistance and displacement functions and the  $C_w$  work done ratio are given for the blast load with triangular formation. Similarly Fig. 4.2 gives a similar plot for a rectangular formation of the blast load. These graphs have been produced by the USA Army Corps of Engineers. Referring to Table 4.1, and the idealised blast load impulse given in Fig. 4.3 (the details of which are given in Fig. 4.1, a derivation for the dynamic load factor (DLF) was developed and plotted by Baker et al. for a single degree in Fig. 4.4 and for a corresponding  $t_m/T_n$  relation in Fig. 4.5 for all value of  $t_d/T_n$  where  $t_d$  and  $T_n$  are the maximum blast time and natural period, respectively. Examples 4.1 and 4.3 explain these concepts in detail.

## 4.4 Design Examples

### 4.4.1 Example 4.1

Define step-function and ramp-function loads. Determine in both cases the response equations for a single-degree-of-freedom system. If the step-load response with time-rise is given in various figures, determine the maximum response.

*Solution:* Responses for step-function and ramp-function loads.

#### (a) Step-function load

This is a suddenly applied load that remains constant and is non-periodic (see Fig. 4.6). The equations of motion with and without damping are given below:

$$\begin{aligned} M\ddot{\delta} + C\dot{\delta} + K\delta &= F && \text{damped} \\ M\ddot{\delta} + K\delta &= F && \text{undamped} \end{aligned} \quad (4.1)$$

#### (b) Ramp-function load

A ramp load increases linearly with time (Fig. 4.7). The equation representing this situation is given by

$$F_r = \frac{t}{t_1} \quad (4.2)$$

where  $t_1$  = time to reach  $F$ .

**Table 4.1.** Response analysis equations

1. *Single-degree of freedom systems*

Equation of motion

$$F(t) = M\ddot{\delta} + C\dot{\delta} + K\delta \tag{a}$$

$M$  = mass

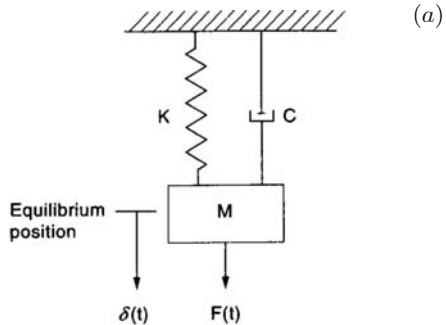
$\delta$  = displacement

$\dot{\delta}$  = velocity

$\ddot{\delta}$  = acceleration

$C$  = damping

$K$  = structural resistance  
(spring constant)



If  $C = 0$ , the structure is *undamped*.  $F(t)$  = applied force; if  $F(t) = 0$  the structure of the building will have fundamental vibration.

(A) *For free vibration*

At  $t =$  time = 0,  $\dot{\delta}_0$  = velocity at time 0. The complete solution for displacement is

$$\delta(t) = \frac{\dot{\delta}_0}{\omega} \sin \omega t + \delta_0 \cos \omega t \tag{b}$$

where

$$\omega = \sqrt{\frac{K}{M}} \quad (\text{undamped circular frequency})$$

Where damping is not ignored, the damping factor  $\xi$  is involved, the value of  $\xi = C/2M\omega$ . The displacement  $\delta(t)$  can be written as

$$\delta(t) = e^{-\xi\omega t} [C_1 \sin \omega \sqrt{1 - \xi^2} t + C_2 \cos \omega \sqrt{1 - \xi^2} t] \tag{c}$$

Consider  $\omega_d$  = damped frequency then

$$\frac{\omega_d}{\omega} = \sqrt{1 - \xi^2}$$

if  $\xi < 1$  underdamping

$> 1$  overdamping

$\xi = 0$  undamped

$\xi = 1$  critical damping =  $2M\omega$

$C_1$  and  $C_2$  are coefficients. The larger the value of  $\xi$ , the greater is the recovery period.

(B) *For forced vibration*

If  $\delta = 0$ , then  $\dot{\delta}_0$  is the initial velocity, and the displacement at time  $\tau$  is

$$\Delta x = \frac{F f(\tau) d\tau}{M\omega} \sin \omega(t - \tau) \tag{d}$$

The total displacement between  $t = 0$  and  $t$  can be written by substituting the right-hand side



$$\delta(t) = \int_0^i \Delta x dr = \delta_{st} \omega \int_0^i f(\tau) \sin \omega(t - \tau) d\tau \quad (e)$$

where

$$\delta_{st} = \text{static deflection due to } F = \frac{F}{\omega^2 M} \quad (f)$$

The *blast load* is generally idealized as a triangular load. The displacement  $\delta(t)$  is then

$$\delta(t) = \delta_0 \cos \omega t + \frac{\dot{\delta}_0}{\omega} \sin \omega t + \delta_{st} \omega \int_0^t f(\tau) \sin \omega(t - \tau) d\tau \quad (g)$$

$$f(\tau) = 1 - \frac{\tau}{t_d} \quad (h)$$

After integration and simplifications

$$\delta(t) = \frac{F}{K} \left[ 1 - \frac{t}{t_d} - \cos \omega t + \frac{1}{t_d \omega} \sin \omega t \right] \quad (i)$$

The dynamic load factor (DLF) or dynamic increasing factor is given by

$$\text{DLF} = \frac{\delta_{\text{dyn}}}{\delta_{\text{st}}} = 1 - \cos \omega t + \frac{\sin \omega t}{\omega t_d} - \frac{t}{t_d} \quad (j)$$

Note:  $\delta = x$  or  $y$  on graphs.

For second-stage response for times in excess of the positive-phase duration of the blast load

$$\delta_0 = \text{initial displacement} = \frac{F}{K} \left( \frac{\sin \omega t_d}{\omega t_d} - \cos \omega t_d \right) \quad (k)$$

$$\dot{\delta}_0 = \text{initial velocity} = \frac{F}{K} \left( \omega \sin \omega t_d + \frac{\cos \omega t_d}{t_d} - \frac{1}{t_d} \right) \quad (l)$$

and  $f(\tau) = 0$ .

Substituting into the  $\delta(t)$  equation, the dynamic load factor is

$$\text{DLF} = \frac{1}{\omega t_d} [\sin \omega t_d - \sin \omega(t - t_d)] - \cos \omega t \quad (m)$$

If  $T_n = (2\pi/\omega)$  is the natural response period, the  $\text{DLF}_{\text{max}}$  versus  $t_d/T_n$  plot can be given in graphical form as shown in Fig. 4.3. Similarly time to reach maximum displacement ( $t_m$ ) can be related to  $t_d/T_n$  and is shown in Fig. 4.3.

Types of classification

$$0.4 > \omega t_d \frac{t_d \text{ short}}{T_n \text{ long}} \rightarrow \text{Impulsive } I \text{ or } i$$

$$40 < \omega t_d \frac{t_d \text{ long}}{T_n \text{ short}} \rightarrow \text{Quasi-static}$$

$$0.4 < \omega t_d < 40 \left[ \frac{t_d}{T_n} \approx 1 \right] \rightarrow \text{Dynamic}$$

(C) For forced vibrations of a damped structure

The incremental *displacement*  $\Delta x$  due to an elemental impulse and the final *displacement*  $\delta$  at time  $t$  can easily be derived and are given below:

$$\Delta x = \frac{Ff(\tau)d\tau}{M\omega_d} e^{-\xi\omega(t-\tau)} \sin \omega_d(t-\tau) \quad (n)$$

$$\delta(t) = e^{-\xi\omega t} \left[ \frac{\dot{\delta}_0 + \omega\xi\delta_0}{\omega_d} \sin \omega_d t + \delta_0 \cos \omega_d t \right] + \delta_{st} \frac{\omega^2}{\omega_d} \int_0^t f(\tau) e^{-\xi\omega(t-\tau)} \sin \omega_d(t-\tau) d\tau \quad (o)$$

The dynamic load factor (DLF) can also here assume the form

$$\frac{\delta_{\max}}{(F/K)} = \frac{1}{\left[ 1 - \left( \frac{\omega_f}{\omega} \right)^2 \right]^2 + \left[ 2\xi \frac{\omega_f}{\omega} \right]^2} \quad (p)$$

where  $\omega_f$  = forced vibration frequency.

Other relevant blast loading cases can be gathered from examples.

#### 4.4.1.1 Step-Function Load

A complete solution is the sum of complementary and particular solutions

$$\delta = e^{-\omega\xi t} (A \cos \omega_f t + B \sin \omega_f t) + \frac{F}{K} \quad (4.3)$$

where  $A$  and  $B$  are constants from a stage at rest; the arbitrary constants are:

$$A = -\frac{F}{K}; \quad B = -\frac{F}{K} \frac{\omega\xi}{\omega_f} \quad \text{with damping}$$

Hence

$$\delta = \frac{F}{K} \left\{ 1 - e^{-\omega\xi t} \left( \cos \omega_f t + \frac{\omega}{\omega_f} + \xi \sin \omega_d t \right) \right\} \quad (4.4)$$

Here  $\omega_f = \omega_d$ , the frequency with damping or delay, Generally  $\delta/FK$  is plotted against  $t/T_n$  where  $T_n = 2\pi/\omega_f$  (Fig.4.8).

The time over which the maximum peak occurs,  $t_p$ , is computed from

$$\frac{F}{K} e^{-\omega\xi t} \left\{ \frac{(\omega\xi)^2}{\omega_f} + \omega_f \right\} \sin \omega_f t_p = 0 \quad (4.5)$$

or  $t_p = N\pi/\omega_f$   $N = 0, 1, 2, \dots$

The peak occurs when  $N = 1$  (see Fig. 4.9);  $t_p = \pi/\omega_f$ . The equation for  $\delta_{\max}$  is given as

$$\delta_{\max} = \frac{F}{K} (1 + e^{-\omega\xi\pi/\omega_f}) \quad (4.6)$$

The response can also be evaluated using Duhamel's Integral

$$\delta(t) = \frac{1}{M\omega_f} \int_0^t F e^{-\omega\xi(t-\tau)} \sin \omega_f(t-\tau) d\tau \quad (4.7)$$

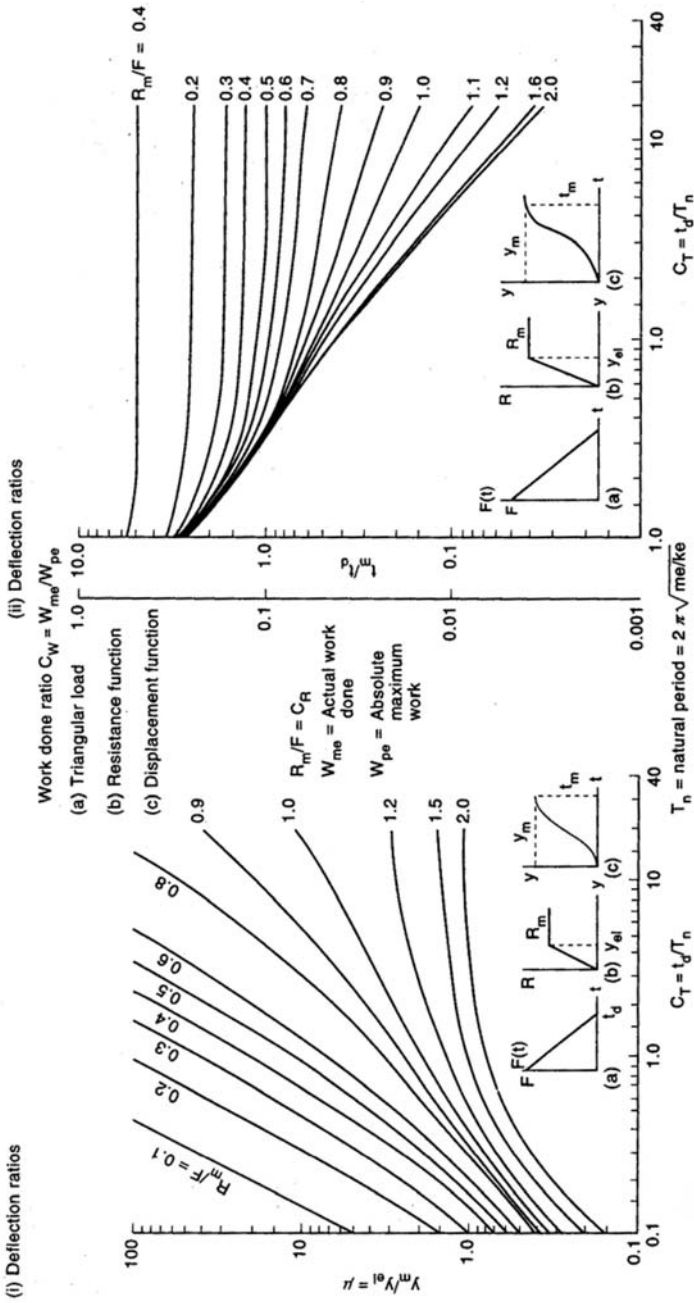


Fig. 4.1. Maximum response of elastic-plastic one-degree-of-freedom system – triangular load

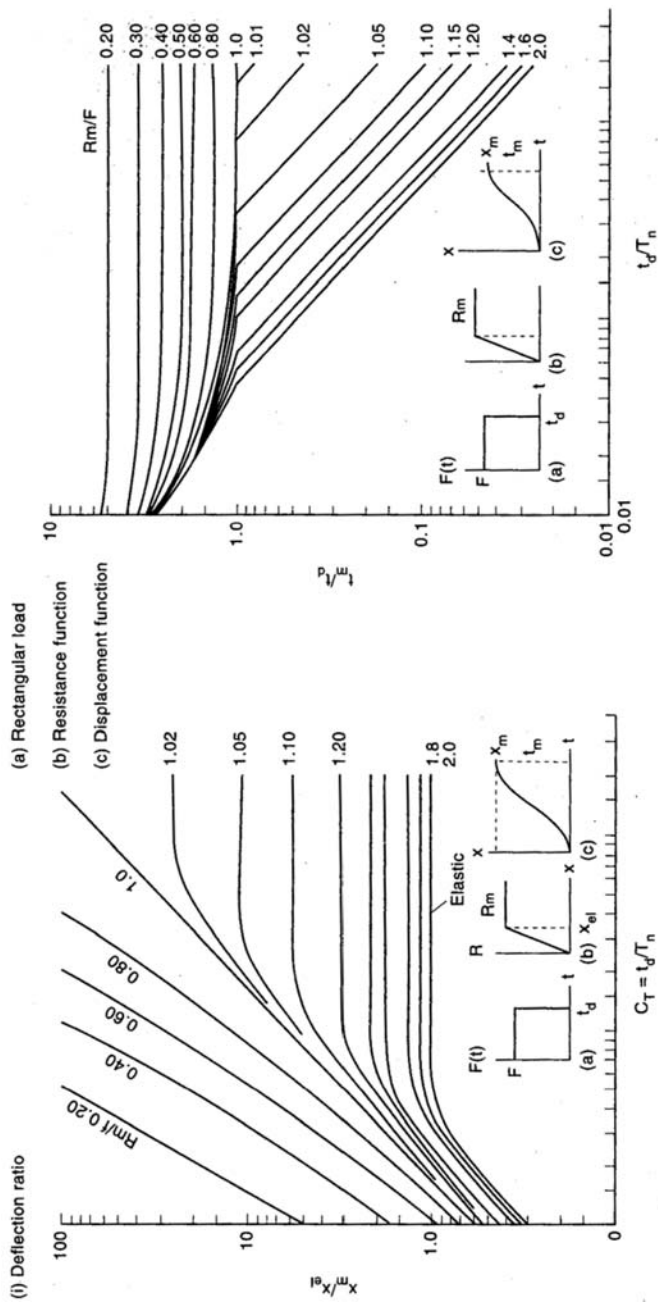


Fig. 4.2. Maximum response of elastic-plastic one-degree-of-freedom system – rectangular load

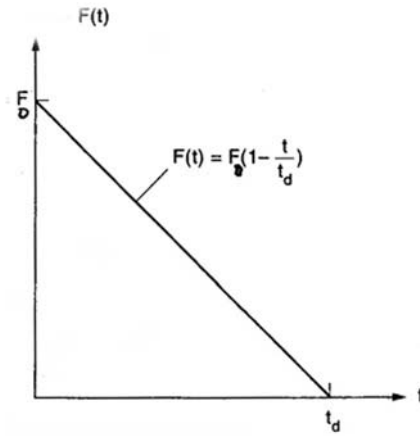


Fig. 4.3. Idealized blast load impulse

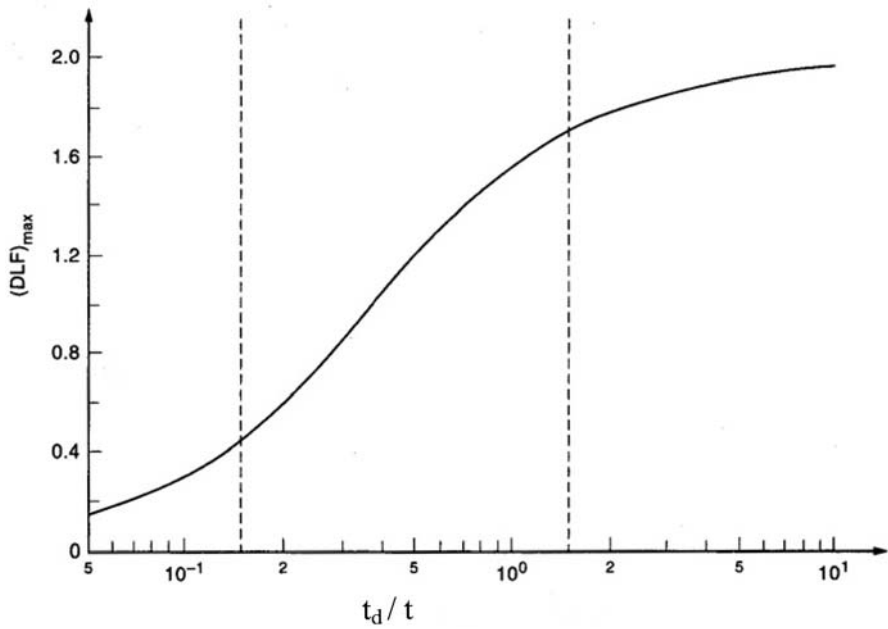


Fig. 4.4. Maximum dynamic load vs  $t_d/T_n$  for elastic SDOF system

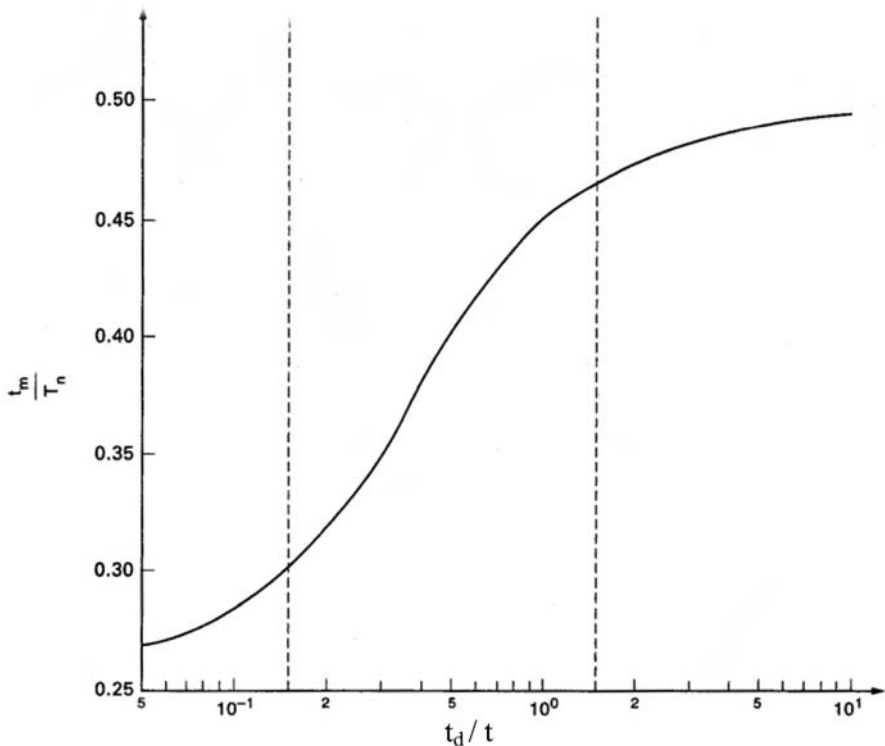


Fig. 4.5. Time to reach maximum displacement vs  $t_d/T_n$  for elastic SDOF system

### Ramp-Function Load

The response is obtained from (4.7). For an undamped system, the Duhamel’s Integral can be simplified to

$$\delta(t) = \frac{1}{M\omega} \int_0^t \frac{F_\tau}{t_1} \sin \omega(t - \tau) d\tau \tag{4.8}$$

Equation (4.8) can also be written as for the displacement at  $t$  caused by the impulse of  $\tau$

$$d\delta(t) = e^{-\xi\omega(t-\tau)} \left[ \frac{F(\tau)d\tau}{M\omega} \sin \omega(t - \tau) \right] \tag{4.9}$$

Each impulse in Fig. 4.6c will assumingly produce a vibration of this form. Since the vibration equations are linear in this case, each impulse is independent of another one and the total resulting motion can be calculated by the principal of superposition. Equation (4.9) maybe integrated form to give vibration at time  $t$ . Looking at (4.8), the following comparable equation is obtained.

$$\delta(t) = \frac{1}{M\omega} \int_0^t F(\tau) \sin \omega(t-T) e^{-\xi\omega(t-T)} dt \quad (4.10)$$

Equation (4.10) is the Duhamel Integral. This equation is useful evaluating response of the structures to impact and blast loading of the damping is neglected ( $\xi = 0$ ), then

$$\begin{aligned} \delta(t) &= \frac{F_0}{M\omega} \int_0^t \sin \omega(t-T) d\tau \\ &= \delta_{st}(1 - \cos \omega t) \end{aligned} \quad (4.11)$$

$$\sin ce = \frac{F_0}{M\omega} = \left( \frac{F_0}{k} \right) \omega = \delta_{st}\omega \quad (4.12)$$

The displacement curve is shown in Fig. 4.6b, in Fig. 4.4, where DLF is 2.0, it is an upper bounce. With the shock loading is often a finite rise time before maximum load is reached, it reduces the value DLF.

If (4.8) is directly used, then the solution is given by

$$\delta(t) = \frac{F}{K} \left( \frac{t}{t_1} - \frac{\sin \omega t}{\omega t_1} \right)$$

Note that  $\omega = \omega_p$  for damped cases, and that  $t_1 = t_d$  on the graphs.

#### 4.4.1.2 Step-Function with Time

For an undamped system where  $t \leq t_1$  and  $t > t_1$  the responses can from previous equations be derived as

$$\delta(t) = \frac{F}{K} \left( \frac{t}{t_1} - \frac{\sin \omega t}{\omega t_1} \right); \quad t \leq t_1 \quad (4.13)$$

$$\delta(t) = \frac{F}{K} \left( 1 - \frac{\sin \omega t}{\omega t_1} + \frac{\sin \omega(t-t_1)}{\omega t_1} \right); \quad t > t_1 \quad (4.14)$$

The maximum value of the response occurs for time  $t_p$  by equating the time differential of (4.14) to zero

$$\frac{F}{K} \{ -\cos \omega t + \cos \omega(t-t_1) \} = 0 \quad (4.15)$$

$$\frac{\tan \omega t}{\tan \omega \frac{t_1}{2}} = 1 \quad (4.16)$$

$$t_p = \frac{N\pi}{\omega} + \frac{t_1}{2} \quad N = 0, 1, 2, \dots \quad (4.17)$$

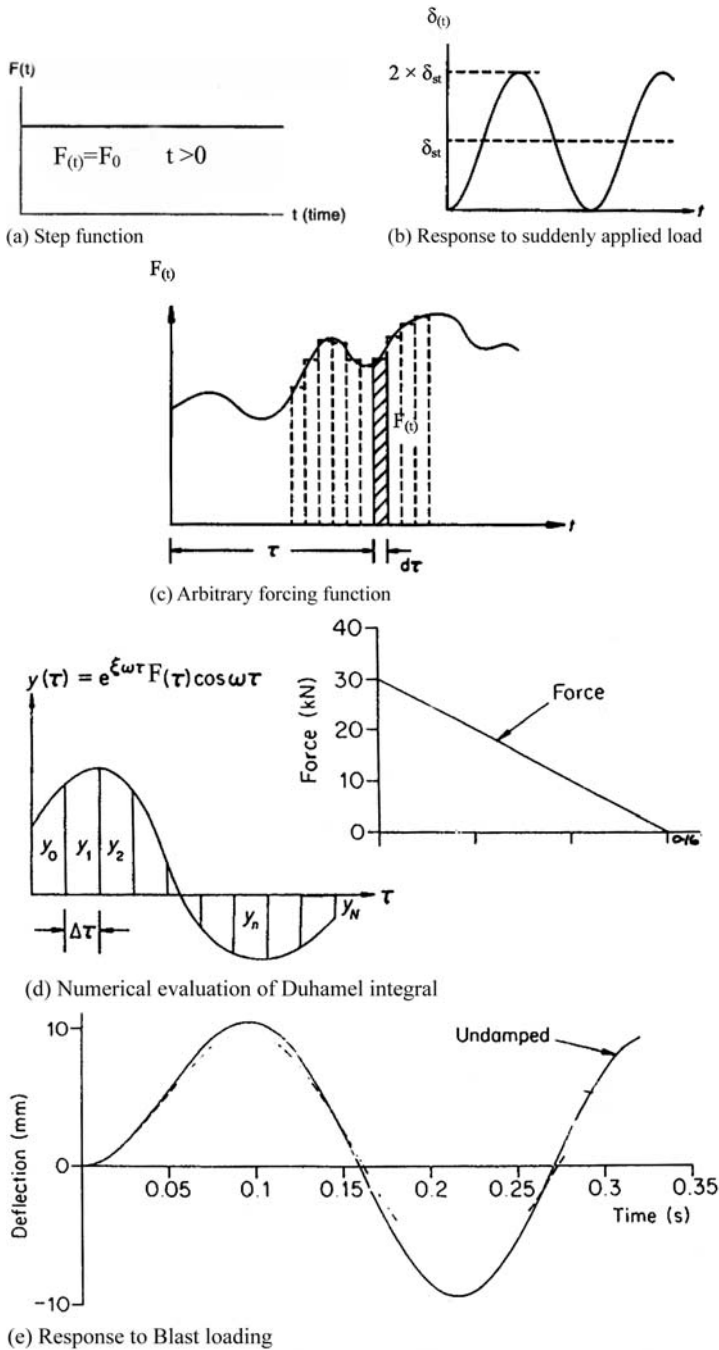


Fig. 4.6. Response and numerical solution method



When  $t = t_p$

$$\delta_{\max} = \frac{F}{K} \left\{ 1 + \frac{2 \sin(N\pi - \omega(t_1/2))}{\omega t_1} \right\} \quad (4.18)$$

A proper value of  $N$  giving  $(2 \sin(N\pi - \omega(t_1/2))/\omega t_1) = \alpha$  positive value will give a true maximum value of  $\delta_{\max}$ .

Numerically, for example, an explosion load is represented by a triangular forcing function as shown in Fig. 4.3 and decays linearly to zero. Assuming the structure is of a one-of-freedom and keeping  $\xi = 0$ , determine maximum response when  $F_0 = 30$  kN and  $t_d =$  duration of the impulse  $= 0.165$ .

Basic theory:

The forcing function must be described in two parts, namely during the application of the force, and after it has decayed to zero. Therefore

$$F(t) = F_0(1 - t/t_d); \quad 0 \leq t \leq t_d \quad (4.19)$$

$$= 0; \quad t \leq t_d \quad (4.20)$$

Neglecting damping, the displacement while the load is being applied is given by

$$\delta_t = (F_0/M\omega) \int_0^t (1 - \tau/t_d) \sin \omega(t - \tau) d\tau \quad (4.21)$$

$$= \delta_{st} [1 - (t/t_d) + (1/\omega t_d) \sin \omega t_d - \cos \omega t_d]; \quad 0 \leq t \leq t_d$$

The vibration after the loading has decayed to zero may be found by first obtaining the displacement and velocity at  $t_d$ . These can be determined

$$\delta_{(t_d)} = \delta_{st} [(1/\omega t_d) \sin \omega t_d + \cos \omega t_d] \quad (4.22)$$

$$\dot{\delta}_{(t_d)} = \delta_{st} [\omega \sin \omega t_d + (1/t_d)(\cos \omega t_d - 1)] \quad (4.23)$$

Substituting  $(t - t_d)$  for the elapsed time while neglecting the damping

$$\delta_{(t)} = \delta_{st} \left\{ \left[ \sin \omega t_d + \left( \frac{1}{\omega t_d} \right) (\cos \omega t_d - 1) \sin \omega(t - t_d) \right] \right. \\ \left. + \left[ \left( \frac{1}{\omega t_d} \right) \sin \omega t_d - \cos \omega t_d \right] \cos \omega(t - t_d) \right\} \quad t > t_d \quad (4.24)$$

A graph of  $t_d/t$  against DLF as stated earlier can be plotted:

- If the blast duration is long compared with the period of vibration – a case for constant suddenly applied load – a case for a constant suddenly applied load and the DLF i.e.  $\delta_{(t)}/\delta_{st}$  tends towards 2.0.
- If the blast is for a brief duration compared with period of vibration the inertia of the structure will play part to prevent it to respond to the load quickly, the  $DLF < 2.0$

When damping is considered, (4.24) can be written as

$$\delta_{(t)} = \frac{e^{-\xi\omega t}}{M\omega} \{c_1(t) \sin \omega t - c_2(t) \cos \omega t\} \quad (4.25)$$

Where

$$C_1(t) = \int_0^t e^{\xi\omega\tau} F(\tau) \cos \omega\tau d\tau \quad (4.25a)$$

$$C_2(t) = \int_0^t e^{\xi\omega\tau} F(\tau) \sin \omega\tau d\tau \quad (4.25b)$$

The integral  $C_1(t)$  and  $C_2(t)$  need numerical integration. Trapezoidal Rule for these integral is suited better. Now consider the integral  $C_1(t)$ , evaluate (see Fig. 4.6b), the value  $pfY = e^{\xi\omega\tau} F(\tau) \cos \omega\tau$  at equally spaced interval.  $C_1(t)$  for a complete response history is evaluated by performing summation incrementally

$$C_1 t = C_1(t - \Delta t) + \frac{\Delta t}{2}(y_{n-1} + y_n) \quad (4.26)$$

/

value of the integral  
at the previous step

By replacing  $\cos \omega t$  and  $\sin \omega t$ , the integration of  $C_2(t)$  is simply performed on the lines suggested for  $C_1(t)$ . The displacement  $\delta(t)$  in (4.25) is evaluated at each time step. Program D. RESPONSE is written to solve Duhamel Integral numerically is documented on Plate 4.1. Referring to Plate 4.1, the frequency  $f$  computed as 4.50 Hz, the period  $T$  is

$$T = \frac{1}{f} = \frac{1}{4.5} = 0.2222 \text{ s}$$

$$t_d(\text{given}) = 0.165$$

$$\frac{t_d}{T} = \frac{0.16}{0.2222} = 0.72$$

$K = 4 \times 10^3 \text{ kN/m}$ ;  $M = 4000 \text{ Kg}$

Using Fig. 4.4, the DLF is computed as

$$\text{DLF} = 1.41$$

$$\frac{\delta(t)}{\delta_{st}} = \text{DLF} = 1.41$$

$$\delta(t) = 10.6 \text{ mm}$$

Figure 4.6e gives then the response to this blast loading.

**Plate 4.1.** Computer programs Simpson approach for blast load cases

---

```

10 REM PROGRAM LOADING
20 REM N = NO. OF STEPS
30 REM L = STEP OF LENGTH
40 REM W = CIRCULAR FREQU.
50 REM M = MASS
60 REM D =CRIT.DAMPING
70 REM F = FORCE
80 REM Δ =DISP.
90 DIM F
100 DIM Δ
110 READ N, L, W, M
120 DATA 32, 0.01, 28.2600, 5000
130 FOR =1 TO N + 1
140 READ F
150 DATA 30, 28.125, 26.25, 24.375, 22.5, 20.625, 18.75, 16.875
160 DATA 15, 13.125, 11.25, 9.375, 7.5, 5.625, 3.75, 1.875, 0
170 DATA 0, 0, 0, 0, 0, 0, 0, 0, 0, 0, 0, 0, 0, 0, 0
180 NEXT 1
190 PRINT "Type in crit. damping"
200 INPUT D
210 IF L < 0 GOTO 460
220 C1 = 0 : C2 = 0
230 YO = F(1): ZO = 0
240 Δ(1) = 0
250 FOR I = 2 TO N + 1
260 P = W * (I - 1) * L
270 E = EXP (D * P)
280 C = COS(T) : S = SIN(T)
290 Y1 = E * F(I) * C
300 Z1 = E * F(I) * S
310 = C1 + (YO + Y1) * L/2
320 = C2 + (ZO +Z1) * L/2
330 Δ(I) = (C1 * S - C2 * C) / (M * W * E)
340 YO = Y1 : ZO = Z1
350 NEXT 1
360 PRINT "TIME DISP."
370 J =0
380 FOR I = 1 TO N+1
390 J = J+1
400 IF J < 20 GOTO 430
410 INPUT "–more–", J$
420 J = 0
430 PRINT Δ(I) * 1000000!
440 NEXT I
Go to
Simpson
450 GOTO 180
460 STOP

```

---

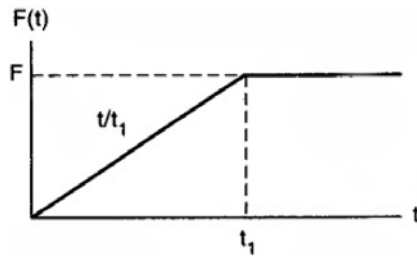


Fig. 4.7. Ramp function

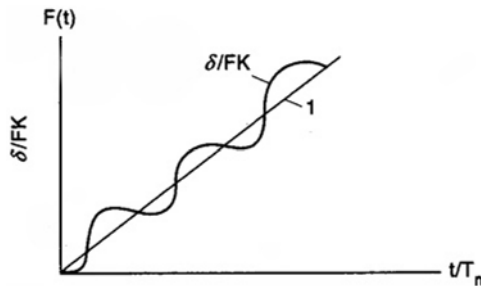


Fig. 4.8. Step function load  $\delta/PK$  and  $t/T_n$  relations

### 4.4.1.3 Additional Response for Shock Loading

The response to shock loading is vital and evaluation is required if the loading is represented by a rectangular pulse load or a triangular pulse load. Since these loads are of short duration the effect of damping shall be ignored. Define clearly these loads and derive expressions for both cases for maximum response.

#### *Rectangular Pulse Load*

A rectangular pulse load of duration  $t_1$  is shown in Fig. 4.9. When  $t \leq t_1$ , it is in fact giving the same response as that indicated by the step-function load (zero damping)

$$\delta(t) = \frac{F}{K}(l - \cos \omega t)t \leq t \quad \text{or} \quad t_d < \frac{T_n}{2} \tag{4.27}$$

where  $t_d$  is the duration of a rectangular pulse. For  $t_1$  will be

$$\begin{aligned} \delta(t) &= \frac{F}{K}(l - \cos \omega t_1) \\ \delta(\dot{t}) = \text{velocity} &= \frac{F}{K}\omega(\sin \omega t_1) \end{aligned} \tag{4.28}$$

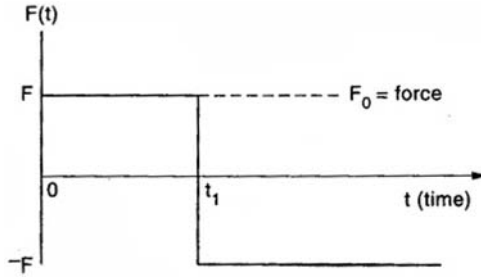


Fig. 4.9. Rectangular pulse

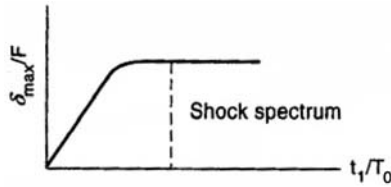


Fig. 4.10. Shock spectrum location

Forced time vibration  $0 \leq t \leq t_d$

$$R_1(t) = 1 - \cos \omega t \tag{4.29}$$

Second forced-time era:  $t > t_1$  or  $t_d < t$

$$\delta = \delta(t_1) \cos \omega(t - t_1) + \frac{\delta(t)}{\omega} \sin \omega(t - t_1) \tag{4.30}$$

Residual vibration era:

$$\delta = R_2(t); \quad \delta(t_1) = R_1(t_d); \quad \delta(\dot{t}) = \dot{R}_1(t_d) \tag{4.31}$$

Substituting various values in (4.30)

$$\delta = \frac{F}{K} \{ \cos \omega(t - t_1) - \cos \omega t \} \quad t > t_1 \text{ or } t_d < t \tag{4.32}$$

The maximum response (Fig. 4.10) will be at the maximum time  $t_p$

$$\begin{aligned} \frac{F\omega}{K} \sin \omega t_p &= 0 \\ t_p &\equiv \frac{\pi}{\omega} < t_1 \text{ or } t_d \end{aligned} \tag{4.33}$$

$t_1$  or  $t_d > \frac{1}{2}T_n$  where  $T_n$  is the natural period. When

$$\begin{aligned} t &= t_p \\ \delta_{\max} &= 2\frac{F}{K} \end{aligned}$$

Differentiating (4.19),  $t_p$  becomes

$$t_p = \frac{T_n}{4} + \frac{t_1}{2}$$

$$\delta_{\max} = 2 \frac{F}{K} \sin \omega \frac{t_1}{2} = \frac{2F}{K} \sin \pi \frac{t_1}{T_n}$$
(4.34)

Note that  $t_1 = t_d$  on the graphs.

*Triangular Pulse Load*

The pulse load is of triangular shape of total duration  $t_1 = t_d$  and it is a superposition of a three-ramp function. The first ramp has a slope of  $2Ft/t_1$  at time  $t = 0$ . The secondary function applied at  $t = t_1/2$  has a slope of  $-4F/t_1$ . The third ramp has a slope of  $2F/t_1$  at  $t = t_1$  (see Fig. 4.11).

$$\delta(t) = \frac{2F}{K} + \left( \frac{t}{t_1} - \frac{\sin \omega t}{\omega t_1} \right) \quad t \leq \frac{t_1}{2}$$
(4.35)

$$\delta(t) = \frac{2F}{K} \left[ 1 - \frac{t}{t_1} - \frac{2 \sin \omega(t - (t_1/2))}{\omega t_1} \right]$$
(4.36)

$$\delta(t) = \frac{2F}{K} \left[ -\frac{\sin \omega t}{\omega t_1} + \frac{2 \sin \omega(t - (t_1/2))}{\omega t_1} - \frac{\sin \omega(t - t_1)}{\omega t_1} \right] \quad t_1 < t$$
(4.37)

Maximum response  $\delta_{\max}$  for  $t = t_p$  in (4.37) obtained as

$$\cos \left( \omega t_p - \frac{\omega t_1}{2} \right) = 0$$
(4.38)

$$t_p = \frac{\pi}{2\omega} + \frac{t_1}{2} = \frac{1}{2}(t_1 + 2T_n)$$

$$\delta_{\max} = \frac{F}{K} \left[ \frac{4}{\omega t_1} \left( 1 - \cos \frac{\omega t_1}{2} \right) \right] \quad \text{for } \frac{t}{T_n} > \frac{1}{2} \text{ within } \frac{t_1}{2} \leq t \leq t_1$$
(4.39)

The ratio of  $\delta_{\max}/(F/K)$  can now be plotted against  $t_1/T_n$ . Thus:

$$R_{\max} = \frac{\delta_{\max}}{(F/K)}$$
(4.40)

The term is a response.

*Special Application of Duhamel Integral for Impulse Load*

Referring to (4.10) using Duhamel Integral. The responses of a system for undamped damped cases are summarised as:

Undamped:

$$\delta(t) = \frac{1}{M\omega} \int_0^t F(\tau) \sin \omega(t - \tau) d\tau$$
(4.41)

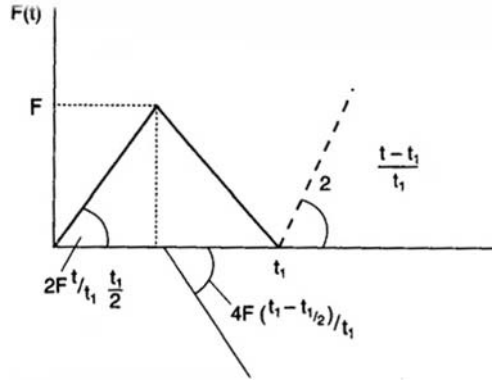


Fig. 4.11. Triangular pulse load

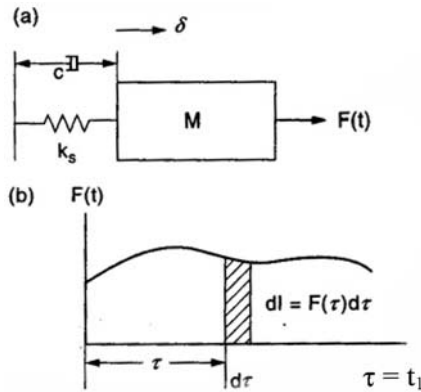


Fig. 4.12. Duhamel's integral method

Damped: Referring to Fig. 4.12 it follows

$$\delta(t) = \frac{1}{M\omega_f} \int_0^t F(\tau) e^{-\xi\omega_f(t-\tau)} \sin \omega_f \tau d\tau \tag{4.42}$$

Referring to Fig. 4.6 when  $t_1 = 0.5$  sec of a triangular impulse for a portal frame displaces by 8 mm.

$$(a) \quad F(t) = F \left( 1 - \frac{t}{t_1} \right) \quad 0 \leq t \leq t_1 \tag{4.43}$$

$$(b) \quad F(t) = 0 \quad t_1 < t \tag{4.44}$$

When  $0 \leq t \leq t_1$

$$\delta(t) = \frac{F}{K} \sin \omega t \int_0^t \left(1 - \frac{\tau}{t_1}\right) \times \cos \omega \tau d(\omega \tau) - \frac{F}{K} \cos \omega t \int_0^t \left(1 - \frac{\tau}{t_1}\right) \sin \omega \tau d(\omega \tau) \tag{4.45}$$

Upon integration

$$\delta(t) = \frac{F}{K} \left[ \sin \omega t \left\{ \sin \omega t - \left(\frac{t}{t_1}\right) \sin \omega t - \frac{1}{\omega t_1} \cos \omega t + \frac{1}{\omega t_1} \right\} - \cos \omega t \left\{ \cos \omega t + 1 + \frac{t}{t_1} \cos \omega t - \frac{1}{\omega t_1} \sin \omega t \right\} \right] \tag{4.45a}$$

Simplifying

$$R_1(t) = 1 - \frac{t}{t_1} - \cos \omega t + \frac{1}{\omega t_1} \sin \omega t \quad R = \frac{K\delta}{F}; \quad f = \frac{\omega}{2\pi} \tag{4.45b}$$

$$\begin{matrix} ft_1 = 0 & 0.5 & 1.50 & 1.80 & 2.0 & 2.10 \\ R_{\max} = 2 & 1.25 & 1.0 & 1.50 & 2.0 & 2.50 \end{matrix} \tag{4.46}$$

When  $t_1 \leq t$

Same as above but it is evaluated at time  $t_1$  since  $F(\tau) = 0$ .

When  $t = t_1$

$$\delta(t) = \frac{F}{K} \left[ \sin \omega t \left\{ -\frac{1}{\omega t_1} \cos \omega t_1 + \frac{1}{\omega t_1} \right\} - \cos \omega t \left\{ 1 - \frac{1}{\omega t_1} \sin \omega t_1 \right\} \right] \tag{4.47}$$

On simplification

$$R_2(t) = \frac{1}{\omega t_1} \left[ \sin \omega t (1 - \cos \omega t_1) - \cos \omega t (\omega t_1 - \sin \omega t_1) \right] \tag{4.48}$$

With damping,  $\xi = 0.05$ .

*Numerical case*

$$\omega = \sqrt{\frac{K}{M}} = \sqrt{\frac{2 \times 10 \times 10^9}{20 \times 10^6}} = 31.623 \approx 31.6$$

$$f = \frac{\omega}{2\pi} = 5.03 \text{ Hz}$$

$$ft_1 = 5.03 \times 0.5 = 2.515$$

substituting into the above expression and/or by interpolation of the values computed for  $R_{\max}$  against  $ft_1$  gives:

$$\begin{aligned} \delta_{\max} &= K \frac{\delta_{\max}}{R_{\max}} = \left( \frac{2 \times 5 \times 10^9 \times 8}{2.10} \right) \times 10^{-3} \\ &= 31.095 \text{ MN} \end{aligned}$$



## 4.5 Finite Element Method of Analysis

### 4.5.1 Dynamic Finite Element Technology

Bangash M.Y.H. 3D Finite Element analysis BANG-BLAST in order to assess the structural integrity and structural response. Appendix I gives through analytical study of the dynamic finite element analysis using Blast Loads with and without fir loading. The program BANG-BLAST can be applied to structural elements and global or prototype structures. Loading defined in Chaps. 1 and 2 can be simulated and create damage scenarios. The detailed study on WTC Buildings New York has been carried out using BANG-BLAST. A separate section on case studies on the collapsed scenario of the World Trade Canter in New York.

### 4.5.2 Combined Finite Discrete Element Method

Bangash T. has developed a combined finite-discrete element modelling of structures when they are in distress. This method which was originally initiated several researchers for rock mechanics has been thoroughly modified by Bangash T. for his Ph.D. work and applies to concrete structures under blast loading. Bangash T. analysed the Alfred Murrah Building and used blast pressure loading provided by Kirkpatrick Consulting Engineers of Oklahoma, U.S.A. the detailed case study on Murrah Building is included in this text.

### 4.5.3 Element Technology

#### 4.5.3.1 Introduction

In this chapter a simple element is introduced which can be used in the discretization of structural elements.

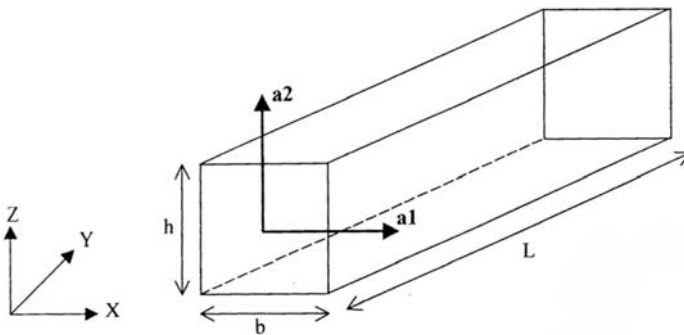


Fig. 4.13. Beam structural element

A structural beam is shown in Fig. 4.13. It's orientation is described by local element axis  $a1$  and  $a2$ .

This beam can be discretised into nodes and elements as shown in Fig. 4.14.



Fig. 4.14. Discretised beam structural element

The mass of each node is taken to act across half of the adjoining elements to either side of the node, as shown in Fig. 4.15.

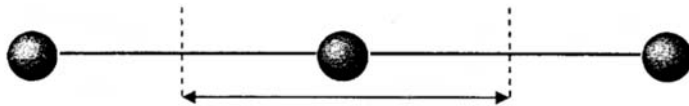


Fig. 4.15. Area over which mass of node acts

Each element has end nodes  $i$  and  $j$  at either end. The local orientation of the nodes is described by the local nodal axis. For example, at node  $i$  this would be  $e_{1(i)}$  and  $e_{2(i)}$ . The element length is represented by vector  $r_i$ .  $r(i)$  and  $r(j)$  are the respective nodal vectors in the global axis as illustrated in Fig. 4.16.

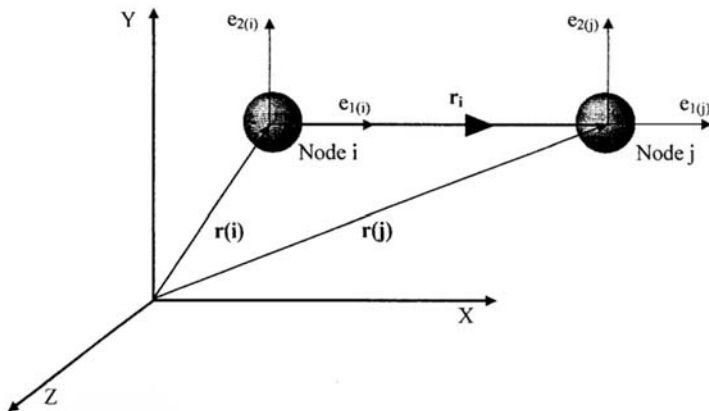


Fig. 4.16. Typical element with nodes-showing local nodal and global axis

This element can then be used to discretise walls, beams, columns and slabs, as illustrated with a simple structure as shown in Fig. 4.17.

The nodal rotation is found as follows. Figure 4.17 shows a simple element with applied moments at each node. The nodal orientations are thus found.

If the element length,  $L$  is small it can be asserted that

$$L = 2\phi r \tag{4.49}$$

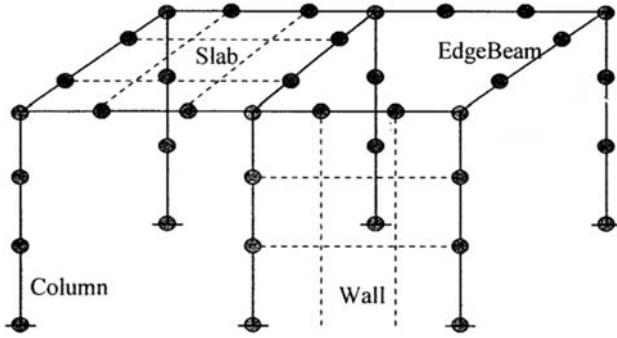


Fig. 4.17. A simple discretised structure

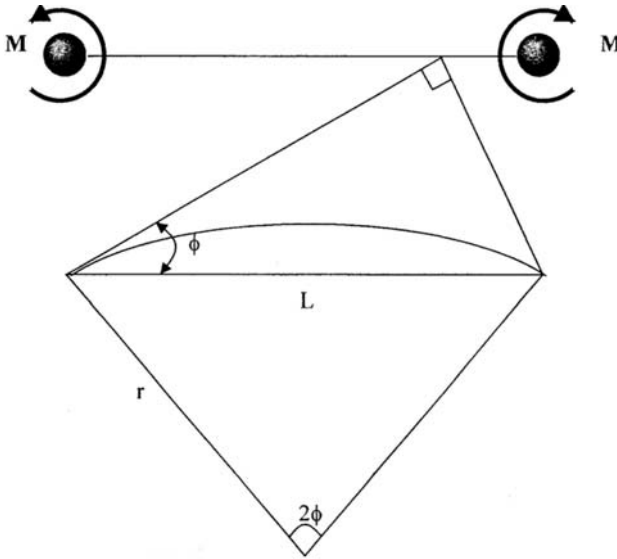


Fig. 4.18. Derivation of the formula for nodal rotation

where  $\phi$  is the angle and  $r$  is the radius of curvature. Rearranging (4.49) gives

$$\frac{1}{R} = \frac{2\phi}{L} \tag{4.50}$$

The first term in (4.49) is equal to the curvature  $\phi_u$ .

$$\phi_u = \frac{1}{R} \tag{4.51}$$

Hence the moment,  $M$  can then be computed using (4.42)

$$M = \frac{EI}{R} = \phi_u EI \tag{4.52}$$

Therefore by substituting (4.50) and (4.51) into (4.52) the expression for moment can be given as

$$M = \frac{2\phi}{L} EI \quad (4.53)$$

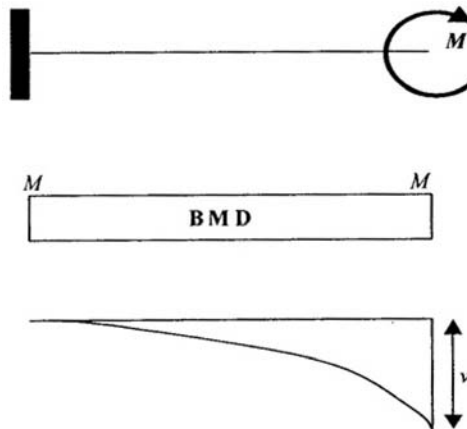
Rearranging (4.53) gives

$$\phi = \frac{ML}{2EI} \quad (4.54)$$

#### 4.5.3.2 Element Accuracy for Various Loading and Support Conditions

In the following examples the deflection is derived for particular loading cases, each with a varying number of elements. In each case the error is calculated and compared with the exact result.

##### Example 1. Cantilever with a Moment at the Free End



**Fig. 4.19.** The BMD and deflected shape for a cantilever with end moment

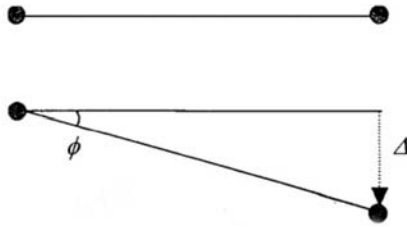
The exact deflection,  $\nu$  in the standard case is given by (4.55)

$$\nu = \frac{ML^2}{2EI} \quad (4.55)$$

*Case with 1 Element*

The angle  $\phi$  is found using (4.54).

$$\phi = \frac{ML}{2EI} \quad (4.56)$$



**Fig. 4.20.** Deflection using one element

The deflection, as given in (4.57) is derived by multiplying the angle  $\phi$  with the length of the element, which in this particular case is  $L$

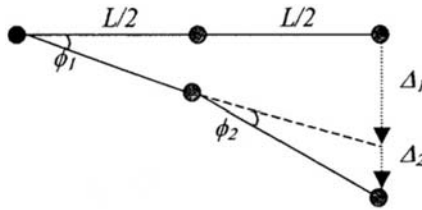
$$\Delta = \frac{ML}{2EI} L = \frac{ML^2}{2EI} \tag{4.57}$$

where  $\Delta$  = the deflection in our case,  $E$  = the Youngs modulus of elasticity,  $I$  = the second moment of inertia.

As is seen this expression for deflection is the same as the theoretical prediction for the deflection and hence no error is found.

*Case with 2 Element*

A similar principle is employed for the case where two elements are used, to calculate the deflections  $\Delta_1$  and  $\Delta_2$  of the first and second elements respectively.



**Fig. 4.21.** Deflection using two elements

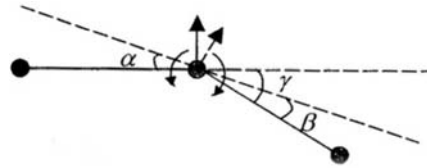
For equilibrium at the middle node as shown in Fig.4.22 the following conditions apply.

$$\alpha = \beta \quad \text{and} \quad \beta = 0.5\gamma \tag{4.58}$$

The respective element rotations  $\phi_1$  and  $\phi_2$  are obtained using (4.53) and is shown in (4.59) and (4.60)

$$\phi_1 = \frac{M}{2EI} \frac{L}{2} = \frac{ML}{4EI} \tag{4.59}$$

$$\phi_2 = \frac{M}{2EI} \frac{L}{2} = \frac{ML}{4EI} \tag{4.60}$$



**Fig. 4.22.** Moment equilibrium

The respective element deflections are  $\Delta_1$  and  $\Delta_2$  are obtained using equation and is shown in (4.61) and (4.62)

$$\Delta_1 = \frac{M}{2EI} \frac{L}{2} = \frac{ML^2}{4EI} \tag{4.61}$$

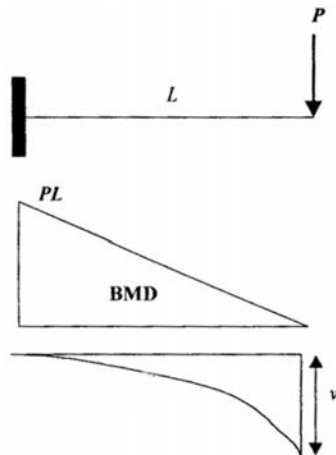
$$\Delta_2 = \frac{M}{4EI} \frac{L}{2} = \frac{ML^2}{4EI} \tag{4.62}$$

Therefore the total deflection is found from the sum of the individual element deflections.

$$\Delta = \Delta_1 + \Delta_2 = \frac{ML^2}{4EI} + \frac{ML^2}{4EI} = \frac{ML^2}{2EI} \tag{4.63}$$

As in the first case a zero percent error is found to exist between the obtained and exact deflection values.

**Example 2. Cantilever with an End Point Load**



**Fig. 4.23.** The BMD and deflected shape for a cantilever with end point load

The exact deflection,  $\nu$  in the standard case is given by (4.63a).

$$\nu = \frac{PL^3}{3EI} \tag{4.63a}$$

Case with 1 Element

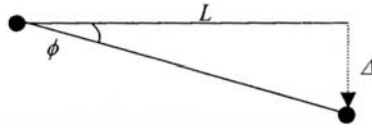


Fig. 4.24. Deflection using one element

The moment,  $M$  is calculated as

$$M = PL \tag{4.64}$$

Hence referring to (4.53) the element rotation is calculated according to (4.65)

$$\phi = \frac{PL}{2EI} L = \frac{PL^2}{2EI} \tag{4.65}$$

Thus the deflection is found as

$$\Delta = \frac{PL^2}{2EI} L = \frac{PL^3}{2EI} \tag{4.66}$$

The error between the obtained deflection and the exact deflection is now calculated

$$\left| \frac{\frac{PL^3}{2EI} - \frac{PL^3}{3EI}}{\frac{PL^3}{3EI}} \right| \times 100 = \left| \frac{3}{2} - 1 \right| \times 100 = 50\% \tag{4.67}$$

Case with 2 Elements

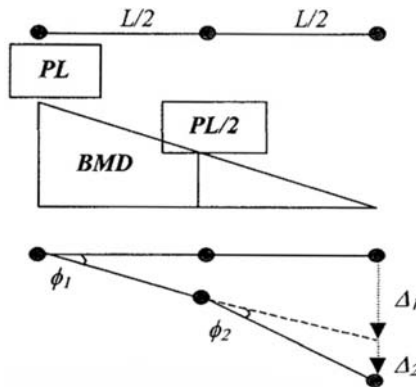


Fig. 4.25. Deflection using two elements

Using the above procedures the element angles and deflections are as follows. The element length in this case is  $L/2$ .

$$\phi_1 = \frac{PL}{2EI} \frac{L}{2} = \frac{PL^2}{4EI} \quad (4.68)$$

For the second element a moment of  $PL/2$  acts at the node. Hence accounting for this in the calculation for the element rotation  $\phi_2$  gives

$$\phi_2 = \frac{1}{2} \frac{PL}{2EI} \frac{L}{2} \cdot 2 = \frac{PL^2}{4EI} \quad (4.69)$$

The deflections are found by multiplying the element rotations by the distance of the rotated node to the deflected end of the beam

$$\Delta_1 = \frac{PL^2}{4EI} L = \frac{PL^3}{4EI} \quad (4.70)$$

$$\Delta_2 = \frac{PL^2}{8EI} \frac{L}{2} = \frac{PL^3}{8EI} \quad (4.71)$$

The total deflection is then found to be as

$$\Delta = \Delta_1 + \Delta_2 = \frac{PL^3}{4EI} + \frac{PL^3}{8EI} = \frac{3PL^3}{8EI} \quad (4.72)$$

The error between the deflection given in (4.72) and the exact deflection is

$$\left| \frac{\frac{3}{8} - \frac{1}{3}}{\frac{1}{3}} \right| \times 100 = 12.5\% \quad (4.73)$$

#### *Case with 4 Elements*

Each element length is now  $L/4$ . The bending moments at each node are shown in bold in the boxes in Fig. 4.26. The respective element rotations and displacements are given in (4.74) to (4.81)

$$\phi_1 = \frac{PL}{2EI} \frac{L}{4} = \frac{PL^2}{8EI} \quad (4.74)$$

$$\phi_2 = \frac{1}{2} \frac{3PL}{4EI} \frac{L}{4} \cdot 2 = \frac{3PL^2}{16EI} \quad (4.75)$$

$$\phi_3 = \frac{1}{2} \frac{PL}{2EI} \frac{L}{4} \cdot 2 = \frac{PL^2}{8EI} \quad (4.76)$$

$$\phi_4 = \frac{1}{2} \frac{PL}{4EI} \frac{L}{4} \cdot 2 = \frac{PL^2}{16EI} \quad (4.77)$$

$$\Delta_1 = \frac{PL^2}{8EI} L = \frac{PL^3}{8EI} \quad (4.78)$$



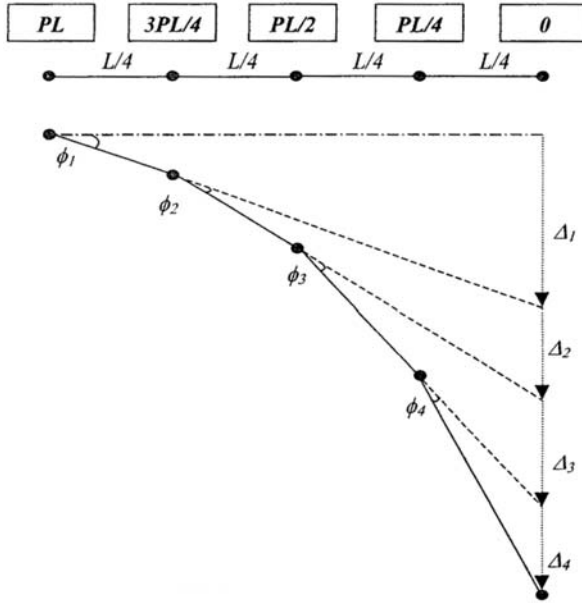


Fig. 4.26. Deflection using four elements

$$\Delta_2 = \frac{9PL^3}{64EI} \tag{4.79}$$

$$\Delta_3 = \frac{PL^3}{16EI} \tag{4.80}$$

$$\Delta_4 = \frac{PL^3}{64EI} \tag{4.81}$$

Hence the total deflection will be

$$\Delta = \Delta_1 + \Delta_2 + \Delta_3 + \Delta_4 = \frac{11PL^3}{32EI} \tag{4.82}$$

The values for  $\omega_\phi$  and  $\omega_\alpha$  obtained are exactly the same as in the first case. The values of area and mass have reduced in proportion.

It is also seen that  $\omega_\alpha$  is less than  $\omega_\phi$ . This will mean that rotation will govern the time step. Therefore the time step  $1/2 m\omega$  will be smaller. This will result in greater CPU time. If they are both equal we then

$$\omega_\phi = \omega_\alpha \tag{4.82a}$$

$$\sqrt{\frac{4Eh^2}{\rho L^4}} = \sqrt{\frac{2E}{\rho L^2}}$$

Thus

$$L = h\sqrt{2}.$$

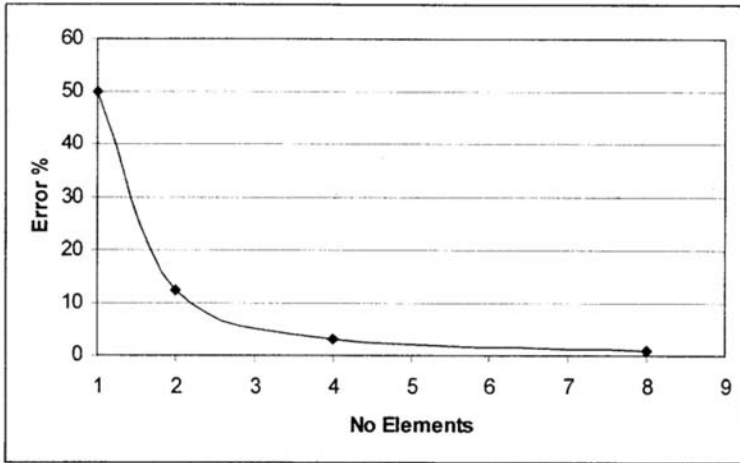


Fig. 4.27. Error versus No elements

Therefore as long as  $L < h\sqrt{2}$  axial rotation will govern.

The error in this case is calculated as previously and found to be 3.125%.

$$\left| \frac{\frac{11}{32} - \frac{1}{3}}{\frac{1}{3}} \right| \times 100 = 3.125\% \tag{4.83}$$

The error is estimated to be of the order of  $L^2$ .

**Example 3. Cantilever with a Distributed Load**

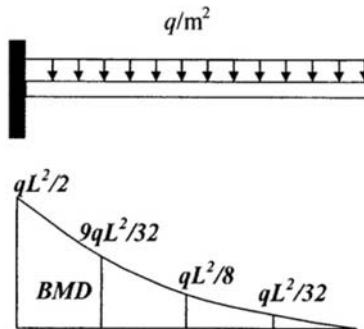


Fig. 4.28. The BMD for a cantilever with distributed load

The exact deflection,  $\nu$  in the standard case is given by (4.83).

$$\nu = \frac{qL^4}{8EI} \tag{4.84}$$

Case with 1 Element

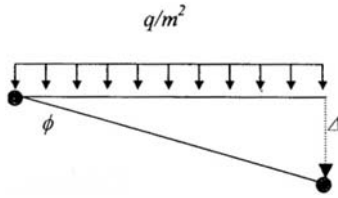


Fig. 4.29. Deflection using one element

Referring to (4.53) the element rotation is calculated according to (4.85)

$$\phi = \frac{qL^2}{2} \frac{1}{2EI} L = \frac{qL^3}{4EI} \tag{4.85}$$

From this we can find the deflection to be as per equation

$$\Delta = \frac{qL^3}{4EI} L = \frac{qL^4}{4EI} \tag{4.86}$$

The error difference is calculated as

$$\left| \frac{\frac{1}{4} - \frac{1}{8}}{\frac{1}{4}} \right| \times 100 = 50\% \tag{4.87}$$

Case with 2 Elements

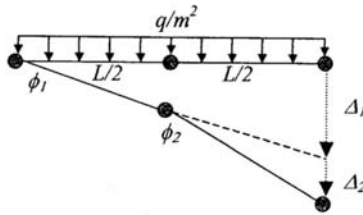


Fig. 4.30. Deflection using two elements

The element angles and deflections are derived as shown in (4.88) to (4.91)

$$\phi_1 = \frac{qL^2}{2} \frac{1}{2EI} \frac{L}{2} = \frac{qL^3}{8EI} \tag{4.88}$$

$$\phi_2 = \frac{qL^2}{8} \frac{1}{2EI} \frac{L}{2} 2 = \frac{qL^3}{16EI} \tag{4.89}$$

$$\Delta_1 = \frac{qL^4}{8EI} \tag{4.90}$$

$$\Delta_2 = \frac{qL^4}{32EI} \tag{4.91}$$

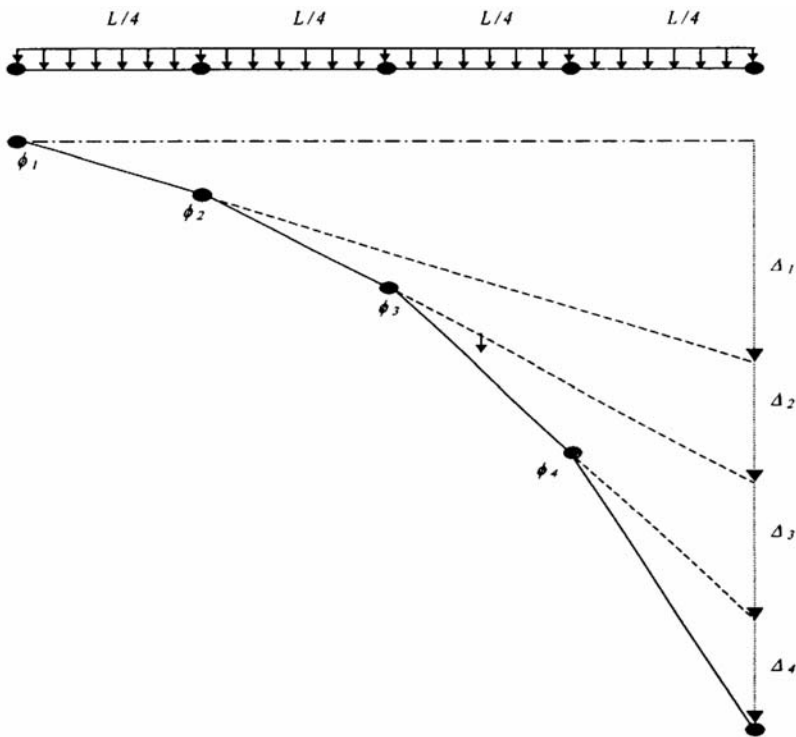
The total deflection is then found to be as per equation

$$\Delta = \Delta_1 + \Delta_2 = \frac{5qL^4}{32EI} \tag{4.92}$$

The error between the deflection and the exact deflection is

$$\left| \frac{\frac{5}{32} - \frac{1}{8}}{\frac{1}{8}} \right| \times 100 = 25\% \tag{4.93}$$

*Case with 4 Elements*



**Fig. 4.31.** Deflection using four elements

The element angles and rotations for this case is described as per (4.94) to (4.101)

$$\phi_1 = \frac{qL^2}{2} \frac{1}{2EI} \frac{L}{4} = \frac{qL^3}{16EI} \tag{4.94}$$

$$\phi_2 = \frac{9qL^2}{32} \frac{1}{2EI} \frac{L}{4} 2 = \frac{9qL^3}{128EI} \tag{4.95}$$

$$\phi_3 = \frac{qL^2}{8} \frac{1}{2EI} \frac{L}{4} \cdot 2 = \frac{qL^3}{32EI} \quad (4.96)$$

$$\phi_4 = qL^2 \frac{1}{2EI} \frac{L}{4} \cdot 2 = \frac{qL^3}{128EI} \quad (4.97)$$

$$\Delta_1 = \frac{qL^4}{16EI} \quad (4.98)$$

$$\Delta_2 = \frac{27qL^4}{512EI} \quad (4.99)$$

$$\Delta_3 = \frac{qL^4}{64EI} \quad (4.100)$$

$$\Delta_4 = \frac{qL^4}{512EI} \quad (4.101)$$

Hence the sum of the individual deflections gives the total deflection

$$\Delta = \Delta_1 + \Delta_2 + \Delta_3 + \Delta_4 = \frac{17qL^4}{128EI} \quad (4.102)$$

The error in this case is

$$\left| \frac{\frac{17}{128} - \frac{1}{8}}{\frac{1}{8}} \right| \times 100 = 6.25\% \quad (4.103)$$

The error in all cases so far reduces as the number of elements employed is increased and appears to be converging to the exact result.

In the subsequent examples the bending moments are calculated at the nodal points and compared to the standard result.

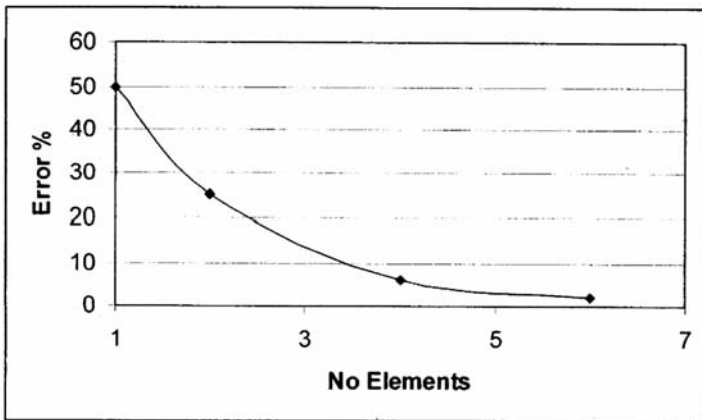
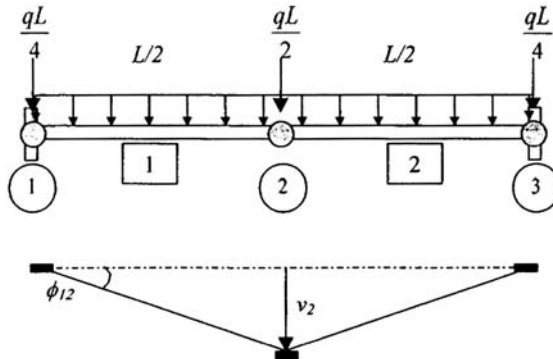


Fig. 4.32. Error versus No elements

**Example 4. A Simply Supported Beam Under Distributed Load**

*Case with 2 Elements*



**Fig. 4.33.** Simply supported beam with distributed load using two elements

The distributed load is made equivalent to point loads using the equivalent load theorem.

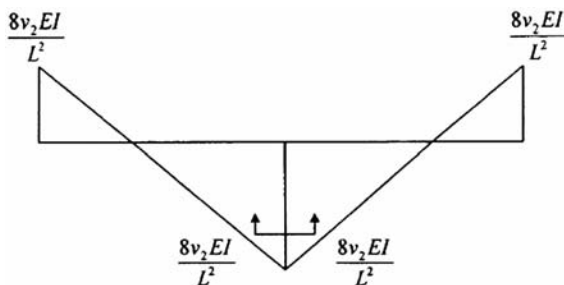
Assuming rotations are small the angle  $\phi_{12}$  is found to be

$$\phi_{12} = \frac{v_2}{(L/2)} = \frac{2v_2}{L} \tag{4.104}$$

The moment  $M_{12}$  is found as

$$M_{12} = \frac{2EI}{L} \phi = \frac{2EI}{(L/2)} \frac{2v_2}{L} = \frac{8v_2EI}{L^2} \tag{4.105}$$

By symmetry  $M_{12}$  is equal to  $M_{32}$ . Therefore the provisional bending moment diagram in terms of deflections will be as shown in Fig. 4.34.



**Fig. 4.34.** Provisional BMD for simply supported beam with distributed load using two elements

The shear at node 2 is given by (4.56)

$$\left( \frac{8\nu_2 EI}{L^2} + \frac{8\nu_2 EI}{L^2} \right) \div \frac{L}{2} = \frac{32\nu_2 EI}{L^3} \tag{4.106}$$

The shear at node 2 is now equated with load as per (4.107)

$$\begin{array}{c} \frac{32\nu_2 EI}{L^3} \quad \frac{qL}{2} \quad \frac{32\nu_2 EI}{L^3} \\ \uparrow \quad \downarrow \quad \uparrow \\ \text{---} \end{array}$$

$$2 \left( \frac{32\nu_2 EI}{L^3} \right) = \frac{qL}{2} \tag{4.107}$$

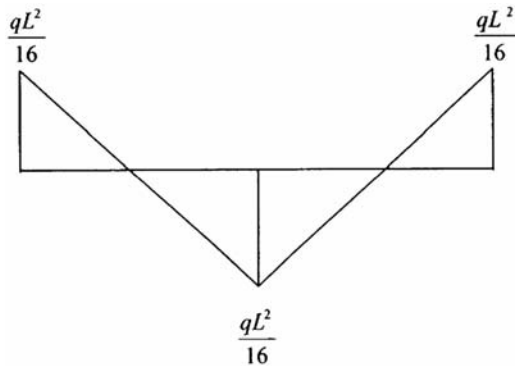
Rearranging (4.107) gives the deflection  $\nu_2$  as

$$\nu_2 = \frac{qL^4}{128EI} \tag{4.108}$$

Therefore (4.58) is substituted into the values shown in Fig. 4.23 to produce the final bending moment diagram illustrated in Fig. 4.35

$$M = \frac{8EI}{L^2} \frac{qL^4}{128EI} = \frac{qL^2}{16} \tag{4.109}$$

The end moments are found to differ from the exact result by 25% and the centre moment is found to differ by 50%.



**Fig. 4.35.** Final BMD for simply supported beam with distributed load using two elements

*Case with 3 Elements*

Once again rotations are assumed small, hence the rotation of element one  $\phi_{e1}$  is

$$\phi_{e1} = \frac{3\nu_2}{L} \tag{4.110}$$

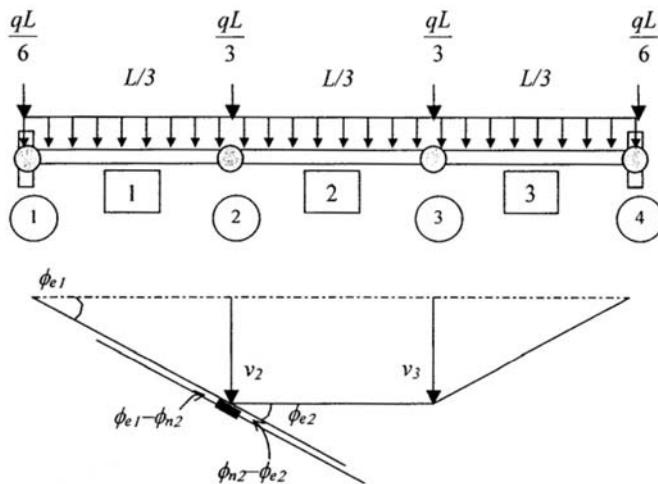


Fig. 4.36. Simply supported beam with distributed load using three elements

The nodal rotation at 2 is represented as  $\phi_{n2}$ . The rotation of element 2 is zero, hence

$$\phi_{e2} = 0 \tag{4.111}$$

Taking the basic equation for moment to be

$$M = \frac{2EI}{L} \phi \tag{4.112}$$

And equating moments at node 2 gives

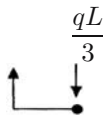
$$\frac{2EI}{(L/3)} \left( \frac{3v_2}{L} - \phi_{n2} \right) = \frac{2EI}{(L/3)} \phi_{n2} \tag{4.113}$$

This gives the nodal rotation at 2,  $\phi_{n2}$  as

$$\phi_{n2} = \frac{3v_2}{2L} \tag{4.114}$$

Therefore our provisional BMD in terms of deflections is shown in Fig. 4.37.

The shear at 2 is

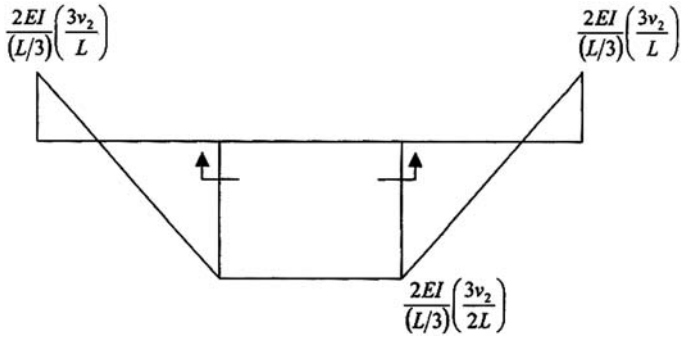


$$\left( \frac{9v_2EI}{L^2} + \frac{18v_2EI}{L^2} \right) \frac{3}{L} = \frac{qL}{3} \tag{4.115}$$

Hence

$$\left( \frac{27v_2EI}{L^2} \right) \frac{3}{L} = qL \tag{4.116}$$



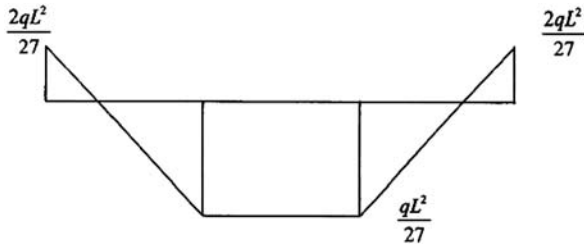


**Fig. 4.37.** Provisional BMD for simply supported beam with distributed load using three elements

By rearranging (4.65) the deflection  $v_2$  will be

$$v_2 = \frac{qL^4}{243EI} \tag{4.117}$$

Combining this result with the provisional bending moment diagram in Fig. 4.37 results in the final BMD as illustrated in Fig. 4.38.



**Fig. 4.38.** Final BMD for simply supported beam with distributed load using three elements

The error at node 1 is

$$\left| \frac{\frac{2}{27} - \frac{1}{12}}{\frac{1}{12}} \right| \times 100 = 11\% \tag{4.118}$$

The error at node 3 is

$$\left| \frac{\frac{2}{27} - \frac{1}{12}}{\frac{1}{12}} \right| \times 100 = 14\% \tag{4.119}$$

The error is seen to reduce significantly by just adding one element to the analysis.

Case with 4 Elements

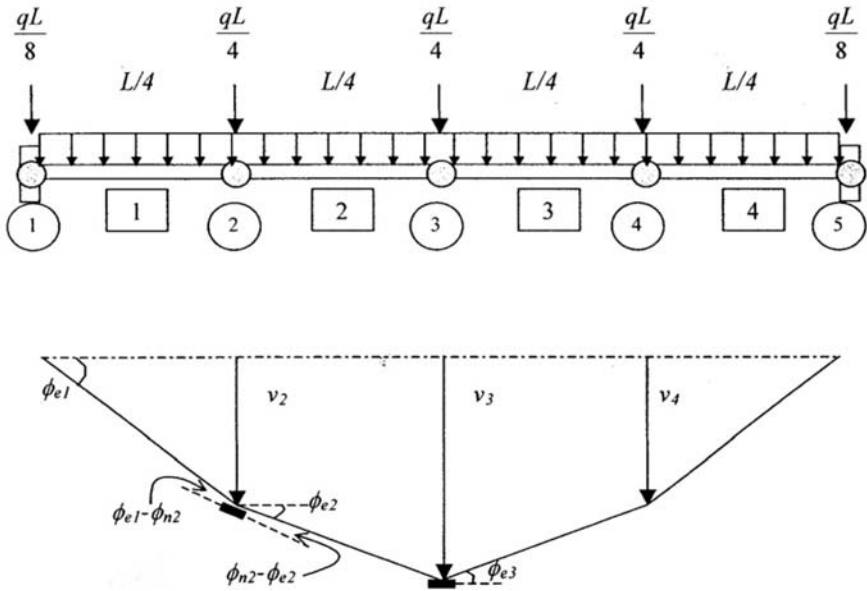


Fig. 4.39. Simply supported beam with distributed load using four elements

The rotated angles are calculated as follows

$$\phi_{e1} = \frac{4\nu_2}{L} \tag{4.120}$$

$$\phi_{e2} = \frac{\nu_3 - \nu_2}{(L/4)} = \frac{4}{L}(\nu_3 - \nu_2) \tag{4.121}$$

By equating moments about node two \$\phi\_{e3}\$ is found to be zero

$$\frac{2EI}{L/4} = \left( \frac{4}{L}(\nu_3 - \nu_2) \right) = \frac{2EI}{L/4} \left( \frac{4}{L}(\nu_3 - \nu_2) \right) \tag{4.122}$$

As the equation is the same on both sides the rotation at node three is zero.

$$\phi_{e3} = 0 \tag{4.123}$$

By equating moments at node three

$$\frac{2EI}{L/4} \left( \frac{4\nu_2}{L} - \phi_{n2} \right) = \frac{2EI}{L/4} \left( \phi_{n2} - \frac{4}{L}(\nu_3 - \nu_2) \right) \tag{4.124}$$

This gives

$$\phi_{n2} = \frac{2\nu_3}{L} \tag{4.125}$$

Equating moments about node three proves that our assumption in (4.125) is correct

$$\frac{2EI}{L/4} = \left( \phi_{n2} - \frac{4}{L}(\nu_3 - \nu_2) \right) = \frac{2EI}{L/4} \left( \phi_{n2} - \frac{4}{L}(\nu_3 - \nu_2) \right) \quad (4.126)$$

This now gives the bending moment diagram in terms of deflections as described by Fig. 4.40.

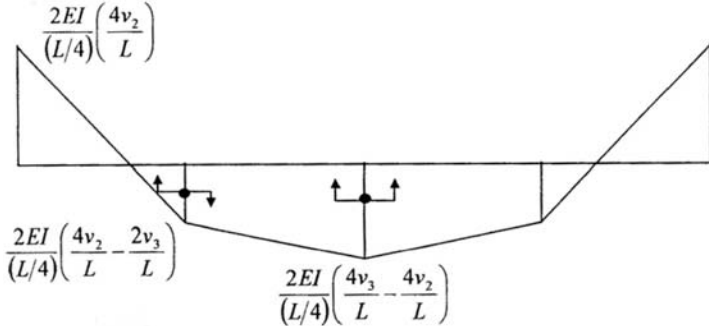


Fig. 4.40. Provisional BMD in terms of deflection using four elements

The shear on the left of node 2 is found as



$$\left[ \frac{32EI}{L^2} + \frac{8EI}{L^2}(4\nu_2 - 2\nu_3) \right] \frac{4}{L} \quad (4.127)$$

Which gives

$$\left[ \frac{64EI\nu_2}{L^2} - \frac{16EI\nu_3}{L^2} \right] \frac{4}{L} \quad (4.128)$$

The shear on the left of node 2 is found as



$$\left[ \left( \frac{8EI}{L^2}(4\nu_3 - 4\nu_2) \right) - \left( \frac{8EI}{L^2}(4\nu_2 - 4\nu_3) \right) \right] \frac{4}{L} \quad (4.129)$$

Which gives

$$\left[ \frac{8EI}{L^2}(6\nu_3 - 8\nu_2) \right] \frac{4}{L} \quad (4.130)$$

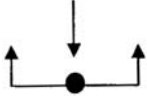
By subtracting Eq. (4.128) from Eq. (4.130) and equating them with the load gives

$$\left[ \frac{8EI}{L^2}(6\nu_3 - 8\nu_2) \right] \frac{4}{L} \quad (4.131)$$

This simplifies to

$$128\nu_2 - 64\nu_3 = \frac{qL^4}{16EI} \quad (4.132)$$

Equating the shear with load at node three gives



$$\left[ \left( \frac{8EI}{L^2} (6\nu_3 - 8\nu_2) \right) \frac{4}{L} \right] 2 = \frac{qL}{4} \tag{4.133}$$

This simplifies to

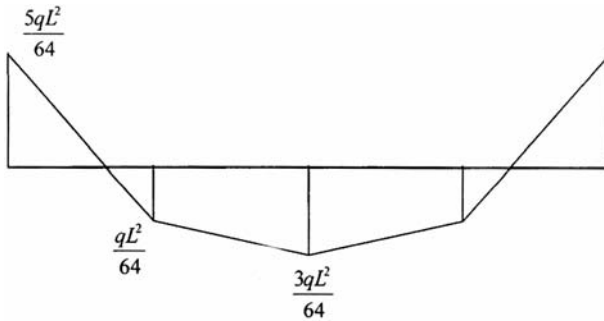
$$96\nu_3 - 128\nu_2 = \frac{qL^4}{16EI} \tag{4.134}$$

Solving Eqs. (4.132) and (4.136) will give us  $\nu_2$  and  $\nu_3$ .

$$\nu_2 = \frac{5qL^4}{2048EI} \tag{4.135}$$

$$\nu_3 = \frac{qL^4}{256EI} \tag{4.136}$$

Combining these results with the provisional BMD in Fig. 4.40 give the final BMD as shown in Fig. 4.41.



**Fig. 4.41.** Final BMD using four elements

The end moment error is

$$\left| \frac{\frac{5}{64} - \frac{1}{12}}{\frac{1}{12}} \right| \times 100 = 6.25\% \tag{4.137}$$

The centre moment error is

$$\left| \frac{\frac{3}{64} - \frac{1}{12}}{\frac{1}{12}} \right| \times 100 = 12.5\% \tag{4.138}$$

They are again seen to converge to the exact result.

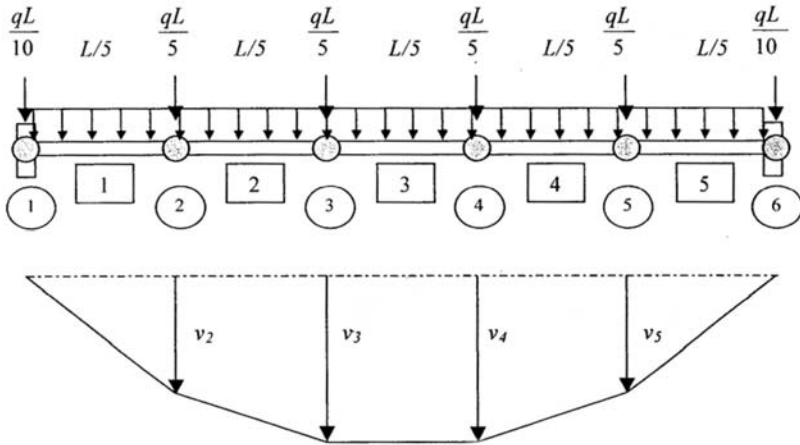


Fig. 4.42. Simply supported beam with distributed load using five elements

Case with 5 Elements

The rotations are given in (4.139) and (4.140)

$$\phi_{e1} = \frac{5\nu_2}{L} \tag{4.139}$$

$$\phi_{e2} = \frac{\nu_3 - \nu_2}{(L/5)} = \frac{5}{L}(\nu_3 - \nu_2) \tag{4.140}$$

Equating moments about node 2 gives

$$\frac{2EI}{L/4}(\phi_{e1} - \phi_{n2}) = \frac{2EI}{L/4}(\phi_{n2} - \phi_{e2}) \tag{4.141}$$

Solving (4.141) gives

$$\phi_{n2} = \frac{5\nu_3}{2L} \tag{4.142}$$

Equating moments about node three

$$\frac{2EI}{L/5}(\phi_{ne2} - \phi_{n3}) = \frac{2EI}{L/5}(\phi_{n3}) \tag{4.143}$$

Solving this gives

$$\phi_{n3} = \frac{5}{2L}(\nu_3 - \nu_2) \tag{4.144}$$

Therefore the provisional bending moment diagram in terms of deflections is as shown in Fig. 4.45.

The shear on the left of node 2 is found as



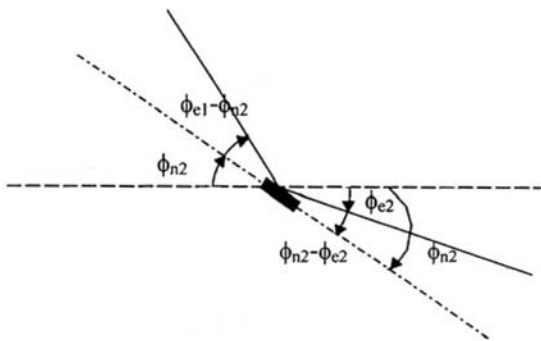


Fig. 4.43. Rotation at node 2

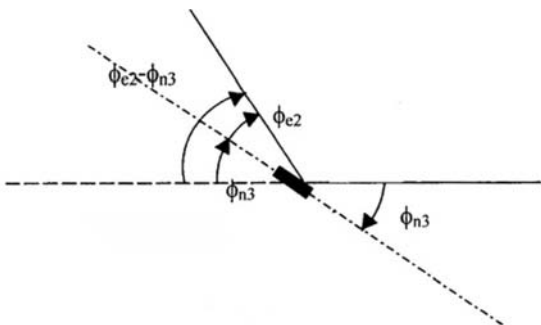


Fig. 4.44. Rotation at node 3

$$\left[ \frac{50EI\nu_2}{L^2} + \frac{50EI}{L^2} \left( \nu_2 - \frac{\nu_3}{2} \right) \right] \frac{5}{L} \tag{4.145}$$

Which gives

$$\frac{125EI}{L^3} [4\nu_2 - \nu_3] \tag{4.146}$$

The shear on the left of node 2 is found as



$$\left[ \left( \frac{25EI}{L^2} (\nu_3 - \nu_2) \right) - \left( \frac{50EI}{L^2} \left( \nu_2 - \frac{\nu_3}{2} \right) \right) \right] \frac{5}{L} \tag{4.147}$$

Which gives

$$\frac{125EI}{L^3} [3\nu_3 - 3\nu_2] \tag{4.148}$$

By subtracting (4.147) from (4.146) and equating them with the load gives

$$\frac{125EI}{L^3} (7\nu_2 - 3\nu_3) = \frac{qL}{5} \tag{4.149}$$

This simplifies to

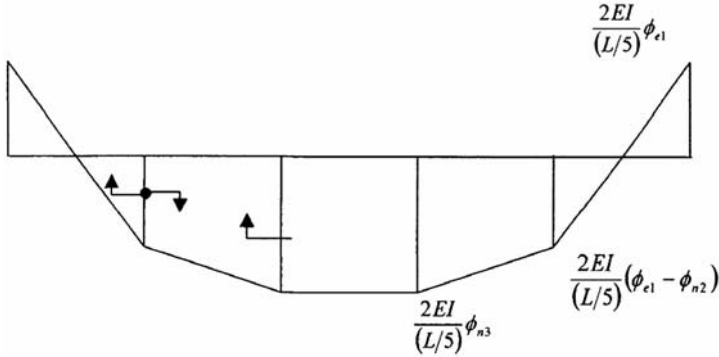


Fig. 4.45. Provisional BMD in terms of the deflections

$$7\nu_2 - 3\nu_3 = \frac{qL^4}{625EI} \tag{4.150}$$

Equating the shear with load at node three gives

$$\frac{125EI}{L^3}(2\nu_3 - 3\nu_2) = \frac{qL}{5} \tag{4.151}$$

This simplifies to

$$2\nu_3 - 3\nu_2 = \frac{qL^4}{625EI} \tag{4.152}$$

Solving (4.150) and (4.152) will give us  $\nu_2$  and  $\nu_3$ .

$$\nu_2 = \frac{qL^4}{625EI} \tag{4.153}$$

$$\nu_3 = \frac{2qL^4}{625EI} \tag{4.154}$$

Combining these results with the provisional bending moment diagram gives the final bending moment diagram as illustrated in Fig. 4.46.

The end moment error is

$$\left| \frac{\frac{2}{25} - \frac{1}{12}}{\frac{1}{12}} \right| \times 100 = 4\% \tag{4.155}$$

The centre moment error is

$$\left| \frac{\frac{1}{25} - \frac{1}{12}}{\frac{1}{12}} \right| \times 100 = 4\% \tag{4.156}$$

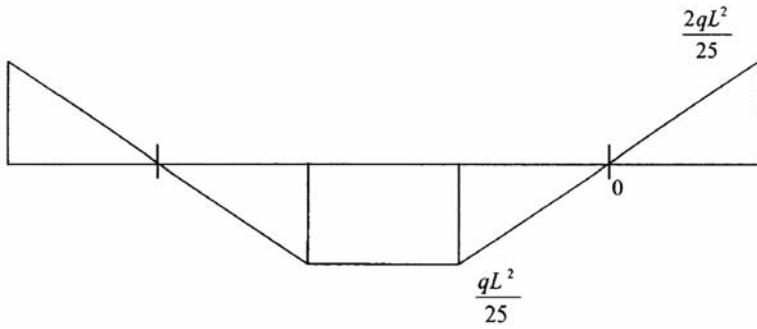


Fig. 4.46. The BMD and deflected shape for a cantilever with end moment

### 4.5.3.3 Error Convergence Result

Figures 4.47 and 4.48 give plots for errors versus central and end moments. Here too it is seen that the results appear to be converging to their exact values.

### 4.5.4 Static Condensation

Let us say that our applied load is  $p$  and that our equation of motion is given in (4.157)

$$Kx + M\ddot{x} = p \tag{4.157}$$

Equation (4.157) can be written more fully as

$$\begin{bmatrix} M_{tt} & 0 \\ 0 & 0 \end{bmatrix} \begin{bmatrix} \ddot{x}_t \\ \ddot{x}_\theta \end{bmatrix} + \begin{bmatrix} k_{tt} & k_{t\theta} \\ k_{\theta t} & k_{\theta\theta} \end{bmatrix} \begin{bmatrix} x_t \\ x_\theta \end{bmatrix} = \begin{bmatrix} p \\ 0 \end{bmatrix} \tag{4.158}$$

The suffix  $t$  denotes translation and rotation is referred to using suffix  $\theta$ .  $k_{tt}$  are the forces on the translational degrees of freedom due to translation.  $k_{t\theta}$  are the forces on translation degrees of freedom due to rotation. Other  $k$  matrices are hence easily inferred.

The rotational degrees of freedom in the mass matrix can be eliminated by static condensation, because the kinetic energy corresponding to the rotational degrees of freedom is insignificant compared with those corresponding to translation. This assumes that there are no loads in the rotational degrees of freedom and hence no spring forces along these degrees of freedom.

Equation (4.147) can now be written as

$$M_{tt}\ddot{x}_t + k_{tt}x_t + k_{t\theta}x_\theta = p \tag{4.159}$$

and

$$k_{\theta t}x_t + k_{\theta\theta}x_\theta = 0 \tag{4.160}$$

Equation (4.160) is rearranged to give  $x_\theta$  and then substituted into (4.161) gives



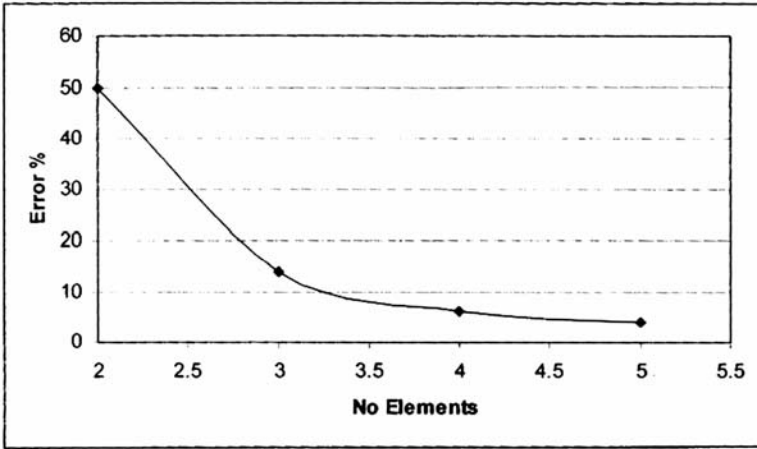


Fig. 4.47. Centre moment versus No elements

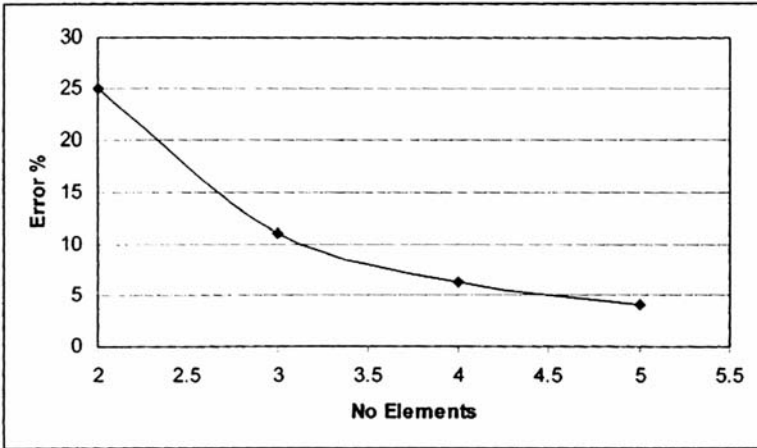


Fig. 4.48. End moment error versus No elements

$$M_{tt}\ddot{x}_t + k^* x_t = p \tag{4.161}$$

$k^*$  is the condensed stiffness matrix, given by

$$k^* = k_{tt} - k_{t\theta}k_{\theta\theta}^{-1}k_{\theta t} \tag{4.162}$$

The stiffness matrix for a general element shown in Fig. 4.49 will now be derived.

The force displacement relationship is now given in (4.163).

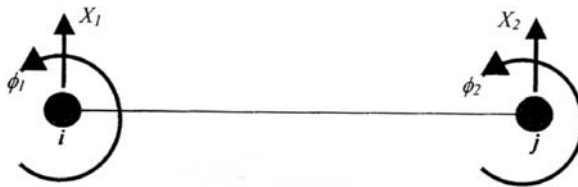


Fig. 4.49. Simple general element

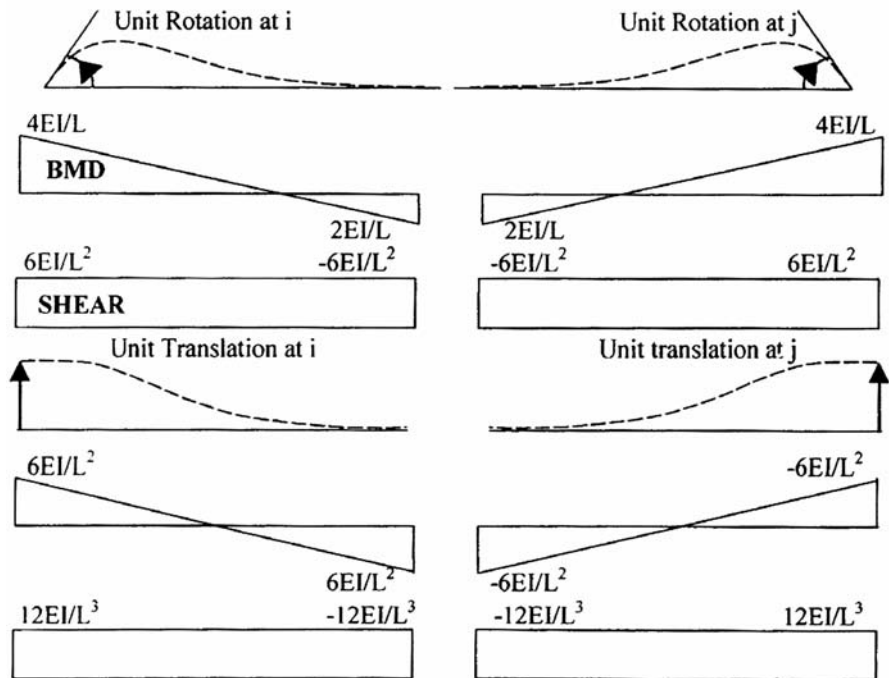


Fig. 4.50. Bending moment and shear diagrams due to unit translation and rotation at each node

$$\begin{bmatrix} F_1 \\ F_2 \\ M_1 \\ M_2 \end{bmatrix} = \begin{bmatrix} \frac{12EI}{L^3} & \frac{-12EI}{L^3} & \frac{6EI}{L^2} & \frac{-6EI}{L^2} \\ \frac{-12EI}{L^3} & \frac{12EI}{L^3} & \frac{-6EI}{L^2} & \frac{6EI}{L^2} \\ \frac{6EI}{L^2} & \frac{-6EI}{L^2} & \frac{4EI}{L} & \frac{2EI}{L} \\ \frac{-6EI}{L^2} & \frac{6EI}{L^2} & \frac{2EI}{L} & \frac{4EI}{L} \end{bmatrix} \begin{bmatrix} X_1 \\ X_2 \\ \phi_1 \\ \phi_2 \end{bmatrix} \quad (4.163)$$

Referring to Fig.4.49 the force displacement relationship for the adopted element will now be derived.

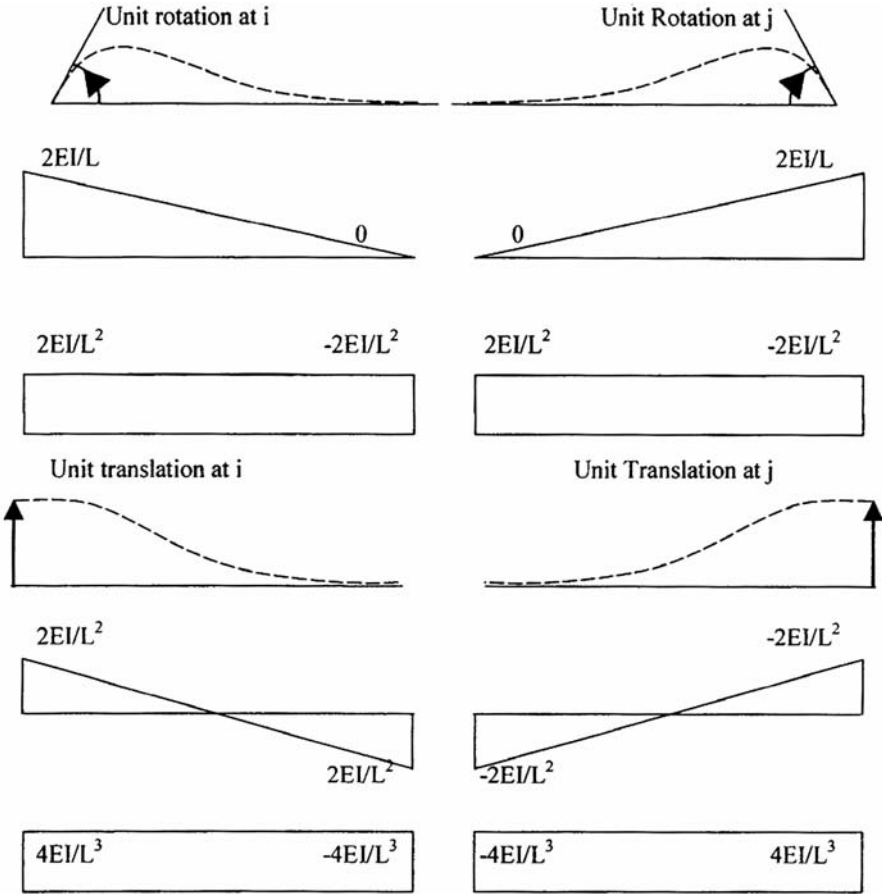


Fig. 4.51. Bending moment and shear diagrams due to unit translation and rotation at each node

The force displacement relationship for this element is

$$\begin{bmatrix} F_1 \\ F_2 \\ M_1 \\ M_2 \end{bmatrix} = \begin{bmatrix} \frac{4EI}{L^3} & \frac{-4EI}{L^3} & \frac{2EI}{L^2} & \frac{-2EI}{L^2} \\ \frac{-4EI}{L^3} & \frac{4EI}{L^3} & \frac{2EI}{L^2} & \frac{-2EI}{L^2} \\ \frac{2EI}{L^2} & \frac{-2EI}{L^2} & \frac{2EI}{L} & 0 \\ \frac{-2EI}{L^2} & \frac{2EI}{L^2} & 0 & \frac{2EI}{L} \end{bmatrix} \begin{bmatrix} X_1 \\ X_2 \\ \phi_1 \\ \phi_2 \end{bmatrix} \quad (4.164)$$

It can be seen from (4.163) that the  $k_{\theta\theta}$  part of the global stiffness matrix is completely full. Inverting this to obtain the condensed stiffness will require complex coding and take up much CPU time.

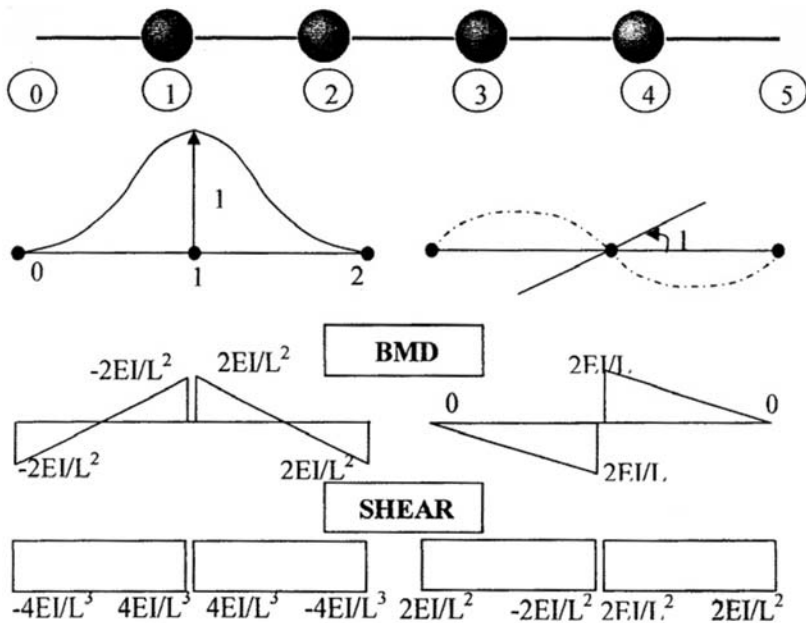


Fig. 4.52. Unit translation and rotation at node 1 of the five element beam

As shown in Fig. 4.50 the element used will assume zero moment at the opposite end to the applied moment. Equal moments at each end will be assumed for applied translation. This results in the  $k_{\theta\theta}$  matrix being diagonal. Hence it is much simpler to invert. Using the lumped mass matrix also contributes to saving on computation.

Taking the five element beam which has already been dealt with earlier the condensed stiffness matrix can be derived as follows.

Figure 4.52 shows the unit translation and rotation as applied to node one. The unit translations and rotations as applied to the other nodes will result in similar bending moment and shear diagrams.

For the example under consideration the global stiffness matrix is described by (4.165)

$$\begin{bmatrix} F_1 \\ F_2 \\ F_3 \\ F_4 \\ M_1 \\ M_2 \\ M_3 \\ M_4 \end{bmatrix} = \begin{bmatrix} k_{tt} & k_{t\theta} \\ k_{\theta t} & k_{\theta\theta} \end{bmatrix} \begin{bmatrix} X_1 \\ X_2 \\ X_3 \\ X_4 \\ \phi_1 \\ \phi_2 \\ \phi_3 \\ \phi_4 \end{bmatrix} \tag{4.165}$$

where

$$[\mathbf{k}_{tt}] = \begin{bmatrix} \frac{8EI}{L^3} & \frac{-4EI}{L^3} & 0 & 0 \\ \frac{-4EI}{L^3} & \frac{8EI}{L^3} & \frac{-4EI}{L^3} & 0 \\ 0 & \frac{-4EI}{L^3} & \frac{8EI}{L^3} & \frac{-4EI}{L^3} \\ 0 & 0 & \frac{-4EI}{L^3} & \frac{8EI}{L^3} \end{bmatrix} \quad (4.166)$$

$$[\mathbf{k}_{t\theta}] = \begin{bmatrix} 0 & \frac{2EI}{L^2} & 0 & 0 \\ \frac{-2EI}{L^2} & 0 & \frac{2EI}{L^2} & 0 \\ 0 & \frac{-2EI}{L^2} & 0 & \frac{2EI}{L^2} \\ 0 & 0 & \frac{-2EI}{L^2} & 0 \end{bmatrix} \quad (4.167)$$

$$[\mathbf{k}_{\theta t}] = \begin{bmatrix} 0 & \frac{-2EI}{L^2} & 0 & 0 \\ \frac{2EI}{L^2} & 0 & \frac{-2EI}{L^2} & 0 \\ 0 & \frac{2EI}{L^2} & 0 & \frac{-2EI}{L^2} \\ 0 & 0 & \frac{2EI}{L^2} & 0 \end{bmatrix} \quad (4.168)$$

$$[\mathbf{k}_{\theta\theta}] = \begin{bmatrix} \frac{4EI}{L} & 0 & 0 & 0 \\ 0 & \frac{4EI}{L} & 0 & 0 \\ 0 & 0 & \frac{4EI}{L} & 0 \\ 0 & 0 & 0 & \frac{4EI}{L} \end{bmatrix} \quad (4.169)$$

Substituting for (4.116) to (4.118) in (4.112) will give the condensed stiffness matrix as in (4.120).

$$[\mathbf{k}^*] = \frac{EI}{L^3} \begin{bmatrix} 7 & -4 & 1 & 0 \\ -4 & 6 & -4 & 1 \\ 1 & -4 & 6 & 0 \\ 0 & 1 & -4 & 7 \end{bmatrix} \quad (4.170)$$

This example has shown the relative ease with which the condensed stiffness matrix is obtained. Thus the main advantage of this new simple element is the fact that static condensation is easily performed to eliminate the rotational

degrees of freedom with the need for complex matrix inversion. This reduces the overall CPU time without any appreciable loss in accuracy providing a suitable number of elements are used.

### 4.5.5 Forces and Moments Along the Element

The element presented is intended for use in the numerical simulation of structures and structural elements subjected to hazardous loading. Such hazardous loading will induce stresses and forces along the length of the element. They are calculated as follows.

Vector  $\mathbf{r}_i$  represents an element in its initial position, with coordinates  $\alpha, \beta, \gamma$  global axis. The local axis is shown as  $e_1, e_2$  and  $e_3$ .

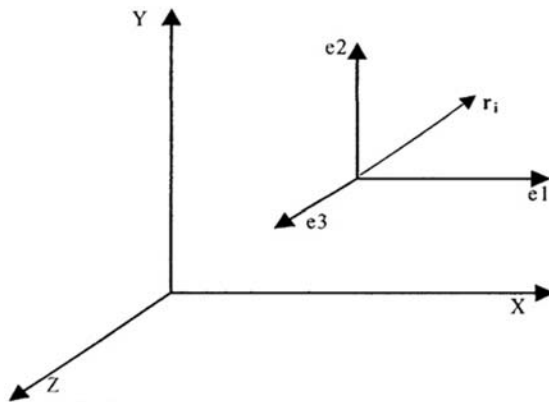


Fig. 4.53. Initial vector in the local and global axis

Initially the projection of  $\mathbf{r}_i$  on to the local axis is the same as its projection on to the global axis. Therefore initially

$$\mathbf{r}_i = \alpha \mathbf{e}_1 + \beta \mathbf{e}_2 + \gamma \mathbf{e}_3 = \alpha \mathbf{X} + \beta \mathbf{Y} + \gamma \mathbf{Z} \tag{4.171}$$

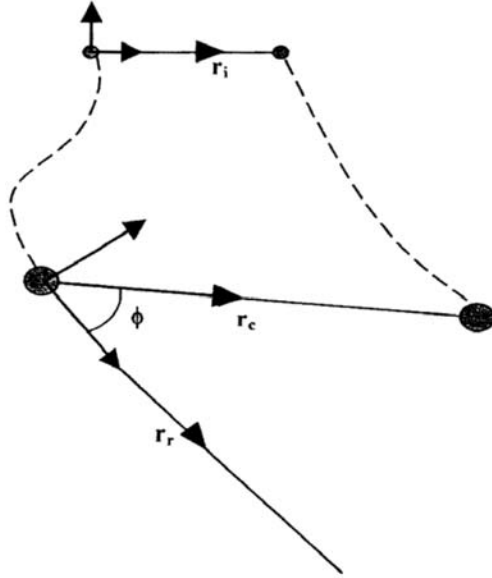
Once  $\mathbf{r}$  has rotated the coordinates will change only in the global axis, provided that there is no relative rotation between the node and the element.

The current position of vector  $\mathbf{r}_c$  can be found from

$$[\mathbf{r}_c] = \begin{bmatrix} e_{x1} & e_{x2} & e_{x3} \\ e_{y1} & e_{y2} & e_{y3} \\ e_{z1} & e_{z2} & e_{z3} \end{bmatrix} \begin{bmatrix} \alpha \\ \beta \\ \gamma \end{bmatrix} = \begin{bmatrix} e_{x1} & e_{x2} & e_{x3} \\ e_{y1} & e_{y2} & e_{y3} \\ e_{z1} & e_{z2} & e_{z3} \end{bmatrix} \begin{bmatrix} \mathbf{r}_x \\ \mathbf{r}_y \\ \mathbf{r}_z \end{bmatrix}_i \tag{4.172}$$

The  $e$  matrix is known as the rotation matrix where  $e_{x1}$  is the projection of  $e_1$  on to the  $x$  axis,  $e_{x2}$  is the projection of  $e_1$  on to the  $y$  axis and  $e_{x3}$  is the projection of  $e_1$  on to the  $z$  axis. The others are similarly inferred.

Therefore since the initial projection on to the local axis is the same as to the global axis the initial rotation matrix  $[\mathbf{R}]$  for the element is



**Fig. 4.54.** Current position of stretched element with relative nodal rotation

$$\begin{bmatrix} 1 & 0 & 0 \\ 0 & 1 & 0 \\ 0 & 0 & 1 \end{bmatrix} \tag{4.173}$$

If we now assume that along with stretching of the element there is relative rotation of the node, then the calculation to obtain  $\mathbf{r}_e$  is as follows.

Figure 4.54 shows that the element has moved to its current position,  $\mathbf{r}_c$  but the node has also rotated to vector  $\mathbf{r}_r$ . This can be substantiated from the coordinates of the nodes.

$$[\mathbf{r}_r] = [\mathbf{R}] [\mathbf{r}_i] \tag{4.174}$$

where  $[\mathbf{R}]$  is the rotation matrix.

The vector  $\mathbf{r}_r$  is used to calculate  $\mathbf{r}_c$  using vector product. The cross product of  $\mathbf{r}_r$  and  $\mathbf{r}_c$  will produce a vector acting out of the plane of paper. If this is taken as a unit vector, then the sin of the angle between  $\mathbf{r}_r$  and  $\mathbf{r}_c$  is derived as follows

$$\sin \phi = \frac{\mathbf{r}_r \times \mathbf{r}_c}{(\mathbf{r}_r)(\mathbf{r}_c)} \tag{4.175}$$

As the angle is considered small the  $\sin \phi$  can be taken as  $\phi$ , thus giving

$$\phi = \frac{\mathbf{r}_r \times \mathbf{r}_c}{(\mathbf{r}_r)(\mathbf{r}_c)} \tag{4.176}$$

After obtaining the  $\mathbf{r}_i$ ,  $\mathbf{r}_r$  and  $\mathbf{r}_c$  the nodal mass,  $m_n$  for both nodes are subsequently calculated.

$$m_n = r_i \times 0.5A\rho \tag{4.177}$$

The second moment of inertia,  $I_n$ , is found by integrating over the length of half the element as shown in Fig. 4.55.

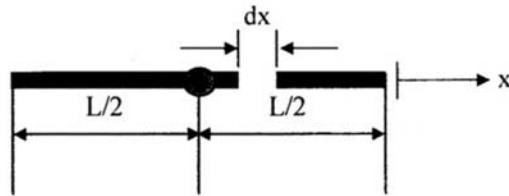


Fig. 4.55. Element rotational velocity

$$I_n = \int_0^{L/2} x^2 \rho A dx = \left[ \rho A \frac{x^3}{3} \right]_0^{L/2} = \rho A \frac{L^3}{24} \tag{4.178}$$

In this case the initial length of the element is  $r_i$  thus (4.178) becomes

$$I_n = \frac{A\rho r_i^3}{24} \tag{4.179}$$

The next step is to calculate the relative velocity of the nodes along the element,  $\nu_a$ , and then to calculate the damped axial force,  $f_a$ .

$$\nu_a = (\nu_{rx} \times r_{cx}) + (\nu_{ry} \times r_{cy}) + (\nu_{rz} \times r_{cz})$$

Where  $\nu_{rx}$  is the relative velocity of the two nodes of the element and  $r_{cx}$  is the component of the  $r_c$  vector projected on to the  $x$  axis. The other notations of equation are similarly inferred. The axial force is given by

$$f_a = EA \times \left( \frac{r_c - r_i}{r_i} \right) \tag{4.180}$$

Cross product of the  $r_c$  and  $r_r$  vectors will give the rotation  $\phi$  in the global system.

$$\varphi = r_c \times r_i \tag{4.181}$$

The rotation vector is then found in the local element coordinate system to give  $\phi_L$ . The local element rotations are then obtained

The cross product of the unit vectors  $\nu_{n0}$  and  $r_0$  will give the direction of the element rotational velocity. The magnitude is found by multiplying by the ratio  $\nu_n/r$

$$\omega = (r_0 \times \nu_{n0}) \left( \frac{\nu_n}{r} \right) \tag{4.182}$$

This therefore gives

$$\omega = (r_0 \times \nu_n) \left( \frac{1}{r} \right) \tag{4.183}$$



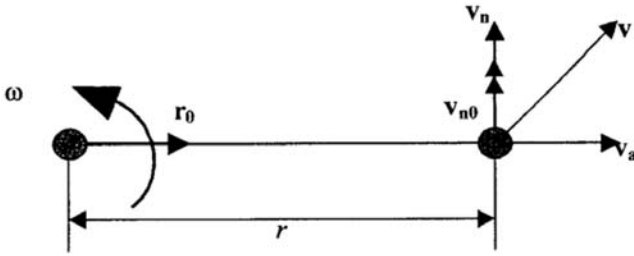


Fig. 4.56. Element rotational velocity

The horizontal component of velocity,  $v_a$  has no influence on the rotational element velocity and hence is not included.

The resultant rotational velocity of the nodes,  $\omega_{res}$  is then found

$$\omega_{res} = \omega_1 - \omega_0 \tag{4.184}$$

The local moments,  $M$ , at any point along the element, in each of the axis direction is calculated using

$$M = \frac{2\phi EI}{r_i} \tag{4.185}$$

If node one is assumed to rotate by 1 then the stiffness of the node is

$$k_i = \frac{2EI}{r_i} \tag{4.186}$$

The moment due to the rotational velocity is damped by multiplying it by (4.187). The final equation is shown in (4.192).

$$C = 2m\omega \tag{4.187}$$

Since

$$\omega = \sqrt{\frac{k}{m}} \tag{4.188}$$

The damping coefficient  $C$  is given by

$$C = 2m\sqrt{\frac{k}{m}} \tag{4.189}$$

Taking the equivalent mass to be given by (4.178) and combing it with (4.186) gives

$$C = \sqrt{\frac{A\rho EIr_i^2}{3}} \tag{4.190}$$

A parameter  $s$  is introduced to the equation. At  $\xi = 0$  the damping is non-existent and at  $\xi = 1$  the damping is critical.

$$C = \xi\sqrt{\frac{A\rho EIr_i^2}{3}} \tag{4.191}$$

The local moments are thus calculated

$$M = C\omega r_i \tag{4.192}$$

These local moments are then found in the global system,  $M_G$ . Shear is found from

$$s = M_G \frac{1}{r_c} \tag{4.193}$$

This procedure is first applied to node 0 and then to node 1. Then nodal forces and moments are then updated with the calculated moments, shear and axial forces. A generalised flow chart is shown in Fig. 4.58.

### 4.5.6 Damping of the Stretching Movement of the Element

Damping is introduced when the element is stretched. The element is assumed to be equivalent to a node attached to a spring as shown in Fig. 4.57.

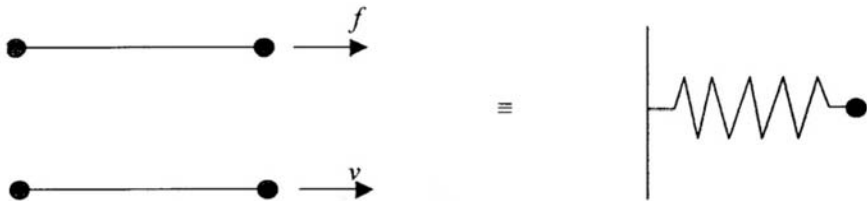


Fig. 4.57. Equivalent spring and node

The force  $f$  is found from

$$f = \frac{\Delta EA}{L} \tag{4.194}$$

The element forces and moments are now calculated flowchart shown in Fig. 4.58 has been devised.

The applied nodal velocities can be split as shown if Fig. 4.59. The bending component does not contribute to the stretching of the element and therefore we will ignore it for now. The velocity of stretch,  $\nu_s$  is found from the dot product of the resultant velocity with  $r_c$ .

$$\nu_s = (\mathbf{v}_1 - \mathbf{v}_2) \cdot \mathbf{r}_c \tag{4.195}$$

Let us now assume that the axial velocity components are the equivalent of one node moving away from a fixed node as shown in Fig. 4.60.

The velocity of stretch will move the node in one second a displacement of  $\Delta$ .

$$\Delta = \nu_s dt \tag{4.196}$$

Where  $dt$  is the time step.

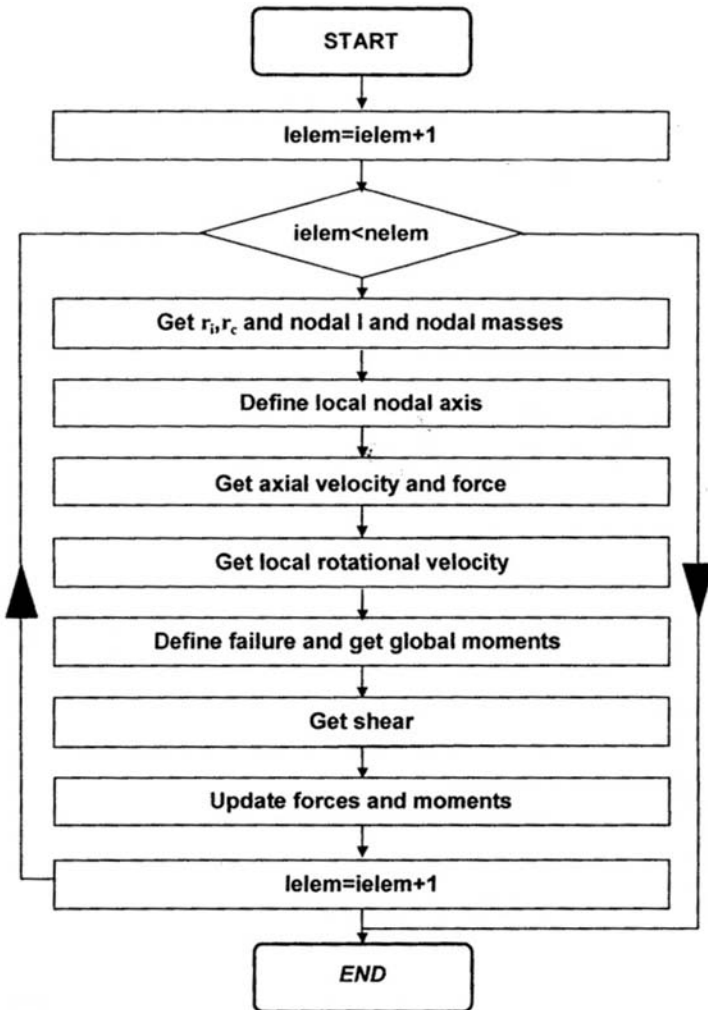


Fig. 4.58. Generalised flow chart to calculate element forces and moments

The strain rate can be calculated as

$$\epsilon = \frac{d\epsilon}{dt} = \frac{v_s}{r_i} \tag{4.197}$$

The stress can be found from

$$\sigma = \epsilon c \tag{4.198}$$

where  $c$  is the damping constant. If the initial displacement is one then the stiffness is calculated as

$$k = \frac{1}{r_i} EA \tag{4.199}$$

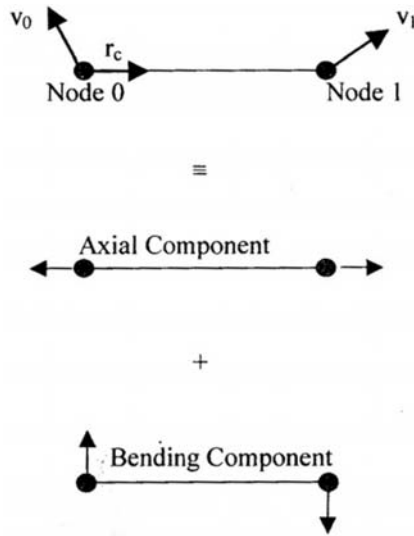


Fig. 4.59. Components of applied velocity

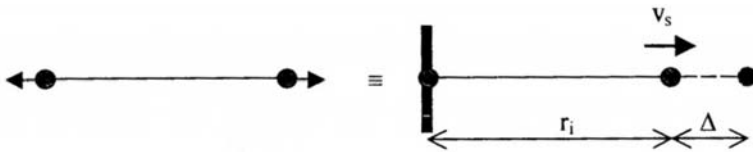


Fig. 4.60. Equivalent velocity of stretch

The mass of each node is taken as the elements’s cross sectional area multiplied by its initial length and its density split across two nodes

$$k = \frac{Ar_i\rho}{2} \tag{4.200}$$

Hence the frequency  $\omega$ , will be given by

$$\omega = \sqrt{\frac{k}{m}} = \sqrt{\frac{2EA}{r_i A \rho}} = \frac{1}{r_i} \sqrt{\frac{2E}{\rho}} \tag{4.201}$$

The element is now replaced with a spring system.



Fig. 4.61. Equivalent spring system

The equation of motion of such a system is

$$kx + m\ddot{x} + C\dot{x} = 0 \quad (4.202)$$

Critical damping will occur when the damping coefficient  $C = 2m\omega$ . Equation (4.202) is divided through by  $m$  giving

$$\frac{k}{m}x + \frac{m}{m}\ddot{x} + \frac{2m\omega}{m}\dot{x} = 0 \quad (4.203)$$

Since

$$\frac{k}{m} = \omega^2 \quad (4.204)$$

Equation (4.202) reduces to

$$\omega^2x + \ddot{x} + 2\omega\dot{x} = 0 \quad (4.205)$$

If

$$x = e^{\lambda t} \quad (4.206)$$

Then

$$\dot{x} = \lambda e^{\lambda t} \quad \text{and} \quad \ddot{x} = \lambda^2 e^{\lambda t} \quad (4.207)$$

Therefore

$$\omega^2 + \lambda^2 + 2\omega\lambda = 0 \quad (4.208)$$

The solution of the quadratic equation becomes

$$x = -e^{\omega t} \quad (4.209)$$

This shows that at critical damping there is no oscillation. Therefore for one element there would be no oscillation if the critical damping were:

$$C_{\text{crit}} = 2m\omega = 2 \frac{Ar_i\rho}{2} \frac{1}{r_i} \sqrt{\frac{2E}{\rho}} = A\sqrt{2E\rho} \quad (4.210)$$

The force due to damping is found as

$$f = A\varepsilon c = A \frac{\nu_s}{r_i} c = A \frac{1}{r_i} cx \quad (4.211)$$

Where

$$\nu_s = \dot{x} \quad (4.212)$$

Therefore the critical force at which damping will occur is

$$f_{\text{crit}} = 2m\omega\dot{x} = C_{\text{crit}}\dot{x} = A \frac{1}{r_i} c\dot{x} \quad (4.213)$$

$$f_{\text{crit}} = 2m\omega\dot{x} = C_{\text{crit}}\dot{x} = A \frac{1}{r_i} c_{\text{crit}}\dot{x} \quad (4.214)$$

Hence critical damping at which no oscillation occurs is

$$c_{\text{crit}} = \frac{r_i}{A} C_{\text{crit}} = \frac{r_i}{A} A\sqrt{2E\rho} = r_i\sqrt{2E\rho} \quad (4.215)$$

The actual damping force,  $f$  is then given as

$$f = \xi f_{\text{crit}} = \xi A\sqrt{2E\rho}x \quad (4.216)$$

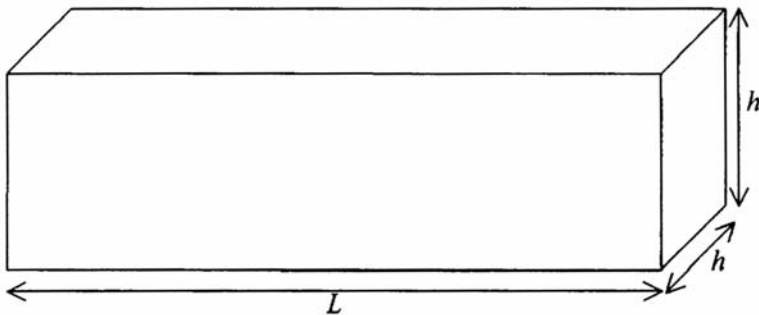
$\xi$  is assigned a value of zero if there is no damping or 1 if damping is critical. The equivalent mass can be found from

$$I_m = \frac{A\rho r^3}{24} \quad (4.217)$$

The rotational stiffness is given by

$$k = \frac{2EI}{r_i} \phi \quad (4.218)$$

where  $I$  is the second moment of Inertia.



**Fig. 4.62.** Structural beam member

If the rotational and axial displacements are one then the axial and rotational velocities are calculated as follows. The second moment of inertia,  $I$  is

$$I = \frac{bh^3}{12} = \frac{h^4}{12} \quad (4.219)$$

The stiffness of the beam element is then

$$k = 2EI \frac{\phi}{L} = 2EI \frac{1}{L} = \frac{2h^4}{12} \frac{1E}{h} = \frac{Eh^3}{6} \quad (4.220)$$

The generalised mass,  $m_g$  can be taken as

$$m_g = \frac{A\rho r^3}{24} \quad (4.221)$$

Hence the rotational velocity,  $\omega_\phi$  is found from

$$\omega_\phi = \sqrt{\frac{k}{m_g}} = \frac{1}{h} \sqrt{\frac{4E}{\rho}} \quad (4.222)$$

A similar approach is taken to calculate the rotational velocity along the axis,  $\omega_a$ . Assuming the mass to be split equally across the two end nodes of the beam this becomes

$$m = \rho A \frac{h}{2} \quad (4.223)$$

The stiffness,  $k$  is found from

$$k = \varepsilon A = \frac{1}{h} E h^2 = E h \quad (4.224)$$

Hence  $\omega_a$  becomes

$$\omega_a = \sqrt{\frac{k}{m}} = \frac{1}{h} \sqrt{\frac{2E}{\rho}} \quad (4.225)$$

The above calculations are now repeated for the situation where the cross sectional width is now reduced to  $h/2$ . Therefore  $\omega_a$  is found from

$$\begin{aligned} m &= \rho A \frac{h}{2} = \rho \frac{h}{2} \frac{h^2}{2} = \frac{\rho h^3}{4} \\ k &= \varepsilon A = \frac{1}{h} E \frac{h^2}{2} = \frac{E h}{2} \\ \omega_a &= \sqrt{\frac{k}{m}} = \frac{1}{h} \sqrt{\frac{4E}{\rho}} \end{aligned} \quad (4.226)$$

The value of  $\omega_\phi$  is found as follows

$$\begin{aligned} I &= \frac{bh^3}{12} = \frac{h}{2} \frac{h^3}{12} = \frac{h^4}{24} \\ k &= 2EI \frac{\phi}{L} = 2EI \frac{1}{h} \frac{h^4}{24} = \frac{Eh^3}{12} \\ m_g &= \frac{A\rho r^3}{24} = \frac{h^2}{2} \rho h^3 \frac{1}{24} = \frac{\rho h^5}{48} \\ \omega_\phi &= \sqrt{\frac{k}{m_g}} = \frac{2}{h} \sqrt{\frac{E}{\rho}} \end{aligned} \quad (4.227)$$

## References

- [4.1] Humar (1992) Dynamics of structures. Butterworth-Heinemann
- [4.2] Kong et al. (1984) Structural analysis. Nelson Publishing Company
- [4.3] Bangash MYH (2002) Manual of numerical methods in concrete. Thomas Telford Publishing
- [4.4] Timoshenko (1990) Mechanics of materials. Chapman and Hall
- [4.5] Kanchi MB (1993) Matrix methods of structural analysis. Wiley Eastern
- [4.6] Atkins KE (1989) Numerical analysis. Wiley
- [4.7] Dawe DJ (1984) Matrix finite element displacement analysis of structures. Wiley
- [4.8] Bangash T (2004) The combined finite element/discrete element method in transient dynamics of reinforced concrete structures under blast loading. Ph.D. Thesis, University of London



# 5 Blast Response Resistance – Design of Structural Elements

## 5.1 Introduction

The influence of assumed deformed shapes on the stresses and strains is well known. A number of attempts have been made on simple beams subjected to elastic and plastic bending. Several tables and charts have been prepared. The resistance  $R_{\max}$  is related to dynamic design factors such as load factor  $K_L$ , mass factor  $K_M$ , load-mass factor  $K_{LM}$  and assumed spring constants  $K$  and  $K_E$ . Ultimate moment capacity  $M_p$  is determined, which will reveal whether or not the structure or its components can have the capacity to resist blast loads. Tables 5.2 to 5.7 indicate these factors and the resisting capacity of structures having various boundary conditions. These tables are equally applied to steel-plated structures. Baker et al. [5.1] have in addition developed P-I diagrams based on extensive databases containing blast damage observations for typical homes and factory buildings in Britain during the Second World War. Table 5.1 including Figs. 5.1 to 5.4 summarize the background to these iso-damage diagrams.

For global and integrated analysis, dynamic finite element analysis and discrete element analysis in which the entire building structure can be analysed for damage assessment is utilized. Material non-linearity, failure criteria and critical distance for the bomb are just some of the factors to be included in the global analysis. This aspect is included in the text and is recommended only for prestigious and expensive buildings since the costs involved in the finite element damage analysis are very high.

## 5.2 Practical Design Examples

### 5.2.1 Example on British Practice

- (a) A reinforced concrete wall is loaded by a blast from a vehicle bomb of 100 kg actual mass. The wall is rigidly connected at the foundation and free at the top. Using the following data, calculate the required reinforcement for the wall:

**Table 5.1.** The P-I diagram

The  $P-i$  or  $P-I$  diagrams are based on both mathematical and experimental results obtained from a variety of bomb-damaged structures. With reasonable confidence they can predict the damage to structures such as small office buildings and light-framed structures. Jarrett (1968) curve fitted an equation

$$R = \frac{KW^{1/3}}{[1 + (\bar{K}/W)^2]^{1/6}} \tag{i}$$

where

$R$  is the range in metres or feet. i.e. the stand-off distance

$W$  is the weapon yield in kg of TNT;

$\bar{K} = 3175$

$K$  = an empirical constant that changes with various level of damage.

In empirical units the same equation is valid but the value of  $\bar{K} = 7000$ .

Applying the Jarrett curve fit to bomb-damaged houses resulted in the establishment of the *Isodamage curves* produced by Baker et al. [5.1]. Examples are shown in Figs. 5.1 and 5.2.

The damage curves based on bombs dropped in Britain have been plotted and are categorized as

Category A – Almost complete demolition

Category B – Such severe damage as to necessitate demolition of external brickwork destroyed or unsafe

Category  $C_b$  – Damage rendering house temporarily uninhabitable – partial collapse of roof and one or two external walls. Loadbearing partitions severely damaged

Category  $C_a$  – Relatively minor structural damage yet sufficient to make house temporarily uninhabitable

Category D – Damage calling for urgent repair but not so as to make house uninhabitable. Damage to ceilings and tiling.

Simple equations describing the damage curves (single-degree-freedom system) based on pressure-pulse are explained below.

$$\frac{\delta_{\max}}{\left(\frac{F}{K}\right)} = 2 \quad \text{or} \quad \frac{\delta_{\max}}{\delta_{st}} = 2 \tag{ii}$$

To acquire velocity  $\dot{\delta}_0$ , the impulse

$$I \text{ or } i = \dot{\delta}_0 M \tag{iii}$$

and its kinetic energy

$$KE = \frac{1}{2} M \dot{\delta}_0^2 = \frac{I^2 \text{ or } i^2}{2M} \tag{iv}$$

then

$$\frac{I^2 \text{ or } i^2}{2M} = \frac{1}{2} K \dot{\delta}_{\max}^2 \tag{v}$$

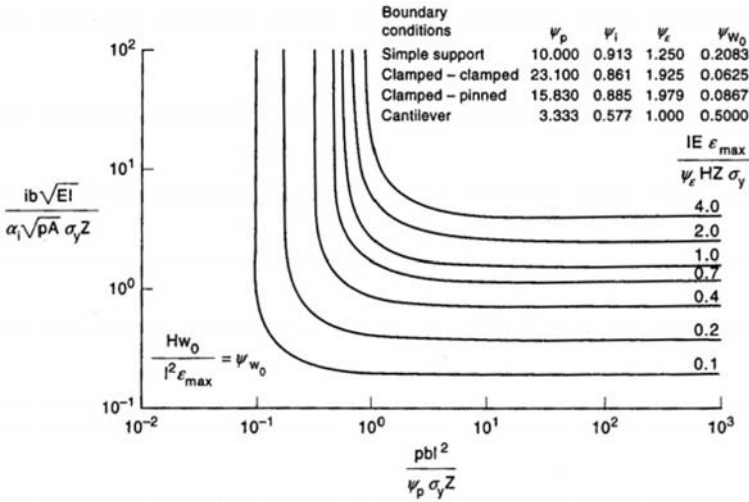


Fig. 5.1. Elastic-plastic solution for bending of blast-loaded beams. From Baker et al. [5.1]

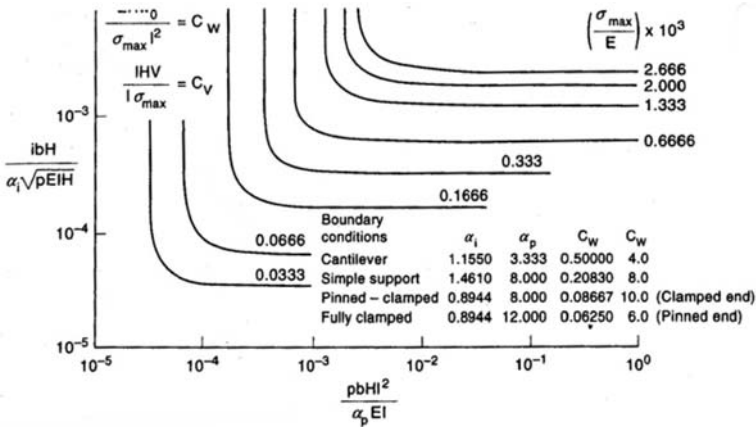


Fig. 5.2. Stresses, shears and deflections in bending of blast-loaded elastic beams. From Baker et al. [5.1]

It is now easy to superimpose on these curves range-weapon or resistance-weapon yield ( $R-W$ ) overlay. The effects of weapons at different ranges can be assessed. Take GP 2000 bomb weighing 895 kg. The explosives it contains amounts to 542 kg.

Note that in order to bring continuity of symbols,  $x = \delta$  and it follows that

$$\frac{\delta_{max}}{F/K} = \frac{1}{\sqrt{KM}} \left(\frac{F}{K}\right) = \frac{1}{2}\omega t_d \tag{vi}$$

The equation is asymptotic and  $\delta_{max}/(F/K)$  versus  $\omega t_d$  can be drawn for all load regimes. From here several  $P-i$  or  $P-I$  curves are drawn in Fig. 5.3 and 5.4 as predicted in Figs. 5.1 and 5.2. In order to assess a specified level of damage, the following procedure is adopted:

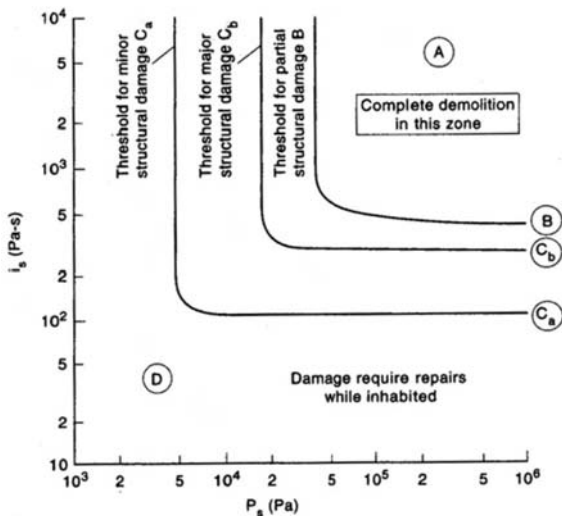


Fig. 5.3. Impulse versus pressure diagram for a constant level of building damage. From Baker et al. [5.1]

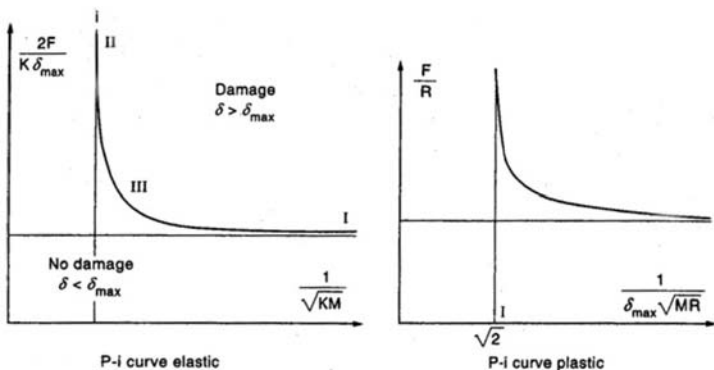


Fig. 5.4.  $P-i$  curves for elastic and plastic cases. From Baker et al. [5.1]

$$\frac{K\delta_{max}}{2F} = 1$$

The blast force  $F$  moving to a distance  $\delta_{max}$  is then equated to the strain energy

$$F\delta_{max} = R\delta_{max} = \frac{I^2}{2M} \text{ or } i^2 \tag{vii}$$

or

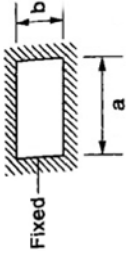
$$\frac{F}{R} = 1 \tag{viii}$$

Hence

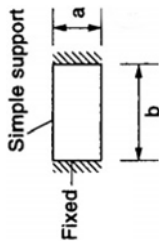
$$\frac{I \text{ or } i}{\sqrt{\delta_{max}MR}}$$

Using  $F/R$  and  $I$  or  $i/\sqrt{\delta_{max}MR}$  axes, the *iso-damage* curves are drawn with further explanatory notes in Fig. 5.1.

**Table 5.2.** Slabs fixed on all sides (courtesy US Army Corps of Engineers),  $M_{Psa}$ ,  $M_{Psb}$  = total negative ultimate moment capacity along edges  $a$  and  $b$ , respectively;  $M_{Psa}$ ,  $M_{Psb}$  = negative ultimate moment capacity per unit width at edges  $a$  and  $b$ , respectively

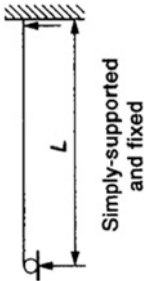


Strain range	$a/b$	Load factor $K_L$	Mass factor $K_M$	Load-mass factor $K_{LM}$	Maximum resistance	Spring constant $k$	Dynamic reactions		
							$V_A$	$V_B$	
Elastic	1.0	0.33	0.21	0.63	$29.2M_{Psb}^0$	$810EI_a/d^2$	$0.10P + 0.15R$	$0.10P + 0.15R$	
	0.9	0.34	0.23	0.68	$27.4M_{Psb}^0$	$743EI_a/d^2$	$0.09P + 0.14R$	$0.10P + 0.17R$	
	0.8	0.36	0.25	0.69	$26.4M_{Psb}^0$	$703EI_a/d^2$	$0.08P + 0.12R$	$0.11P + 0.19R$	
	0.7	0.38	0.27	0.71	$26.2M_{Psb}^0$	$692EI_a/d^2$	$0.07P + 0.11R$	$0.11P + 0.21R$	
	0.6	0.41	0.29	0.71	$27.3M_{Psb}^0$	$724EI_a/d^2$	$0.06P + 0.09R$	$0.12P + 0.23R$	
	0.5	0.43	0.31	0.72	$30.2M_{Psb}^0$	$806EI_a/d^2$	$0.05P + 0.08R$	$0.12P + 0.25R$	
	Elasto-plastic	1.0	0.46	0.31	0.67	$\frac{1}{a}[12(M_{Psa} + M_{Psb}) + 12(M_{Psa} + M_{Psb})]$	$252EI_a/d^2$	$0.07P + 0.18R$	$0.07P + 0.18R$
		0.9	0.47	0.33	0.70	$\frac{1}{a}[12(M_{Psa} + M_{Psb}) + 11(M_{Psa} + M_{Psb})]$	$230EI_a/d^2$	$0.06P + 0.16R$	$0.08P + 0.20R$
		0.8	0.49	0.35	0.71	$\frac{1}{a}[12(M_{Psa} + M_{Psb}) + 10.3(M_{Psa} + M_{Psb})]$	$212EI_a/d^2$	$0.06P + 0.14R$	$0.08P + 0.22R$
		0.7	0.51	0.37	0.73	$\frac{1}{a}[12(M_{Psa} + M_{Psb}) + 9.8(M_{Psa} + M_{Psb})]$	$201EI_a/d^2$	$0.05P + 0.13R$	$0.06P + 0.24R$
0.6		0.53	0.39	0.74	$\frac{1}{a}[12(M_{Psa} + M_{Psb}) + 9.3(M_{Psa} + M_{Psb})]$	$197EI_a/d^2$	$0.04P + 0.11R$	$0.09P + 0.26R$	
0.5		0.55	0.41	0.75	$\frac{1}{a}[12(M_{Psa} + M_{Psb}) + 9.0(M_{Psa} + M_{Psb})]$	$201EI_a/d^2$	$0.04P + 0.09R$	$0.09P + 0.28R$	
Plastic		1.0	0.33	0.17	0.51	$\frac{1}{a}[12(M_{Psa} + M_{Psb}) + 12(M_{Psa} + M_{Psb})]$	0	$0.09P + 0.16R_{max}$	$0.09P + 0.16R_{max}$
		0.9	0.35	0.18	0.51	$\frac{1}{a}[12(M_{Psa} + M_{Psb}) + 11(M_{Psa} + M_{Psb})]$	0	$0.08P + 0.15R_{max}$	$0.09P + 0.18R_{max}$
		0.8	0.37	0.20	0.54	$\frac{1}{a}[12(M_{Psa} + M_{Psb}) + 10.3(M_{Psa} + M_{Psb})]$	0	$0.07P + 0.13R_{max}$	$0.10P + 0.20R_{max}$
		0.7	0.38	0.22	0.58	$\frac{1}{a}[12(M_{Psa} + M_{Psb}) + 9.8(M_{Psa} + M_{Psb})]$	0	$0.06P + 0.12R_{max}$	$0.10P + 0.22R_{max}$
	0.6	0.40	0.23	0.58	$\frac{1}{a}[12(M_{Psa} + M_{Psb}) + 9.3(M_{Psa} + M_{Psb})]$	0	$0.05P + 0.10R_{max}$	$0.10P + 0.25R_{max}$	
0.5	0.42	0.25	0.59	$\frac{1}{a}[12(M_{Psa} + M_{Psb}) + 9.0(M_{Psa} + M_{Psb})]$	0	$0.04P + 0.08R_{max}$	$0.11P + 0.27R_{max}$		



**Table 5.3.** Slabs fixed at shorter sides and simply supported on longer sides (courtesy US Army Corps of Engineers)

Strain range	a/b	Load factor $K_L$	Mass factor $K_M$	Load-mass factor $K_{LM}$	Maximum resistance	Spring constant $k$	Dynamic reactions		
							$V_A$	$V_B$	
Elastic	1.0	0.39	0.26	0.67	$20.4M_{Fpb}^0$	$575EI_b/d^2$	$0.09P + 0.16R$	$0.07P + 0.18R$	
	0.9	0.41	0.28	0.68	$10.2M_{Fpb}^0 + \frac{11}{a}M_{Fpb}$	$476EI_b/d^2$	$0.08P + 0.14R$	$0.08P + 0.20R$	
	0.8	0.44	0.30	0.68	$10.2M_{Fpb}^0 + \frac{10.3}{a}M_{Fpb}$	$396EI_b/d^2$	$0.08P + 0.12R$	$0.08P + 0.22R$	
	0.7	0.46	0.33	0.72	$9.3M_{Fpb}^0 + \frac{9.7}{a}M_{Fpb}$	$328EI_b/d^2$	$0.07P + 0.11R$	$0.08P + 0.24R$	
	0.6	0.48	0.35	0.73	$8.5M_{Fpb}^0 + \frac{9.3}{a}M_{Fpb}$	$283EI_b/d^2$	$0.06P + 0.09R$	$0.09P + 0.26R$	
	0.5	0.51	0.37	0.73	$7.4M_{Fpb}^0 + \frac{9.0}{a}M_{Fpb}$	$243EI_b/d^2$	$0.05P + 0.08R$	$0.09P + 0.28R$	
	Elasto-plastic	1.0	0.46	0.31	0.67	$\frac{1}{a}[12(M_{Fpb} + M_{Fpa}) + 12(M_{Fpb})]$	$271EI_b/d^2$	$0.07P + 0.18R$	$0.07P + 0.18R$
		0.9	0.47	0.33	0.70	$\frac{1}{a}[12(M_{Fpb} + M_{Fpa}) + 12(M_{Fpb})]$	$248EI_b/d^2$	$0.06P + 0.16R$	$0.08P + 0.20R$
		0.8	0.49	0.35	0.71	$\frac{1}{a}[12(M_{Fpb} + M_{Fpa}) + 10.3(M_{Fpb})]$	$228EI_b/d^2$	$0.06P + 0.14R$	$0.08P + 0.22R$
		0.7	0.51	0.37	0.72	$\frac{1}{a}[12(M_{Fpb} + M_{Fpa}) + 9.7(M_{Fpb})]$	$216EI_b/d^2$	$0.05P + 0.13R$	$0.08P + 0.24R$
0.6		0.53	0.37	0.70	$\frac{1}{a}[12(M_{Fpb} + M_{Fpa}) + 9.3(M_{Fpb})]$	$212EI_b/d^2$	$0.04P + 0.11R$	$0.09P + 0.26R$	
Plastic	0.5	0.55	0.41	0.74	$\frac{1}{a}[12(M_{Fpb} + M_{Fpa}) + 9.0(M_{Fpb})]$	$216EI_b/d^2$	$0.04P + 0.09R$	$0.09P + 0.28R$	
	1.0	0.33	0.17	0.51	$\frac{1}{a}[12(M_{Fpb} + M_{Fpa}) + 12(M_{Fpb})]$	0	$0.09P + 0.16R_{max}$	$0.09P + 0.16R_{max}$	
	0.9	0.35	0.18	0.51	$\frac{1}{a}[12(M_{Fpb} + M_{Fpa}) + 11(M_{Fpb})]$	0	$0.08P + 0.15R_{max}$	$0.09P + 0.18R_{max}$	
	0.8	0.37	0.20	0.54	$\frac{1}{a}[12(M_{Fpb} + M_{Fpa}) + 10.3(M_{Fpb})]$	0	$0.07P + 0.13R_{max}$	$0.10P + 0.20R_{max}$	
	0.7	0.38	0.22	0.58	$\frac{1}{a}[12(M_{Fpb} + M_{Fpa}) + 9.7(M_{Fpb})]$	0	$0.06P + 0.12R_{max}$	$0.10P + 0.22R_{max}$	
0.6	0.40	0.23	0.58	$\frac{1}{a}[12(M_{Fpb} + M_{Fpa}) + 9.3(M_{Fpb})]$	0	$0.05P + 0.10R_{max}$	$0.10P + 0.25R_{max}$		
0.5	0.42	0.25	0.59	$\frac{1}{a}[12(M_{Fpb} + M_{Fpa}) + 9.0(M_{Fpb})]$	0	$0.04P + 0.08R_{max}$	$0.11P + 0.27R_{max}$		

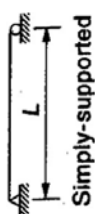

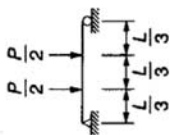


**Table 5.4.** Transformation factors for beams and one-way slabs, simply supported and fixed-end boundary conditions (courtesy US Army Corps of Engineers).  $M_{Ps}$  = Ultimate moment capacity at support;  $M_{Pm}$  = Ultimate moment capacity at midspan

Loading diagram	Strain range	Load factor $K_L$	Mass factor $K_M$	Load-mass factor $K_{LM}$		Maximum resistance $R_{max}$	Spring constant $k$	Effective spring constant $k_E$	Dynamic reaction $V$
				Concentrated mass*	Uniform mass				
	Elastic	0.58	0.45	0.78	$8M_{Ps}/L$	$185EI/L^3$		$V_1 = 0.26R + 0.12P$ $V_2 = 0.43R + 0.19P$ $V = 0.39R + 0.11F \pm M_{Ps}/L$	
	Elasto-plastic	0.64	0.50	0.78	$\frac{4}{L}(M_{Ps} + 2M_{Pm})$	$\frac{384EI}{5L^3}$	$\frac{160EI}{L^3}$		
	Plastic	0.50	0.33	0.66	$\frac{4}{L}(M_{Ps} + 2M_{Pm})$	0		$V = 0.38R_{max} + 0.12F \pm M_{Ps}/L$	
	Elastic	1.0	1.0	1.0	$16M_{Ps}/3L$	$107EI/L^3$		$V_1 = 0.25R + 0.07F$ $V_2 = 0.54R + 0.14F$ $V = 0.78R - 0.28F \pm M_{Ps}/L$	
	Elasto-plastic	1.0	1.0	1.0	$\frac{2}{L}(M_{Ps} + 2M_{Pm})$	$48EI/L^3$	$\frac{160}{L^3}$		
	Plastic	1.0	1.0	1.0	$\frac{2}{L}(M_{Ps} + 2M_{Pm})$	0		$V = 0.75R_{max} - 0.25F \pm M_{Ps}/L$	
	Elastic	0.81	0.67	0.83	$6M_{Ps}/L$	$132EI/L^3$		$V_1 = 0.17R + 0.17P$ $V_2 = 0.33R + 0.33P$ $V = 0.52R - 0.025F \pm M_{Ps}/L$	
	Elasto-plastic	0.87	0.76	0.87	$\frac{2}{L}(M_{Ps} + 3M_{Pm})$	$\frac{56EI}{L^3}$	$\frac{122EI}{L^3}$		
	Plastic	1.0	1.0	1.0	$\frac{2}{L}(M_{Ps} + 3M_{Pm})$			$V = 0.52R_{max} - 0.02F \pm M_{Ps}/L$	

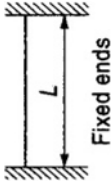
\* Concentrated mass is lumped at the concentrated load.

Table 5.5. Dynamic-design factors for beams and one-way slabs (courtesy US Army Corps of Engineers)

Loading diagram	Strain range	Load factor $K_L$	Mass factor $K_M$		Load-mass factor $K_{LM}$		Maximum Resistance $R_{max}$	Spring constant $k$	Dynamic reaction $V$
			Concentrated mass*	Uniform mass	Concentrated mass*	Uniform mass			
	Elastic	0.64	...	0.50	...	0.78	$\frac{8M_p}{L}$	$\frac{384EI}{5L^3}$	$0.39R + 0.11P$
	Plastic	0.50	...	0.33	...	0.66	$\frac{8M_p}{L}$	0	$0.39R_{max} + 0.12P$
	Elastic	1.0	1.0	0.49	1.0	0.49	$\frac{4M_p}{L}$	$\frac{48EI}{L^3}$	$0.78R - 0.28P$
	Plastic	1.0	1.0	0.33	1.0	0.33	$\frac{4M_p}{L}$	0	$0.75R_{max} - 0.25P$
	Elastic	0.87	0.76	0.52	0.87	0.60	$\frac{6M_p}{L}$	$\frac{56.4EI}{L^3}$	$0.62R - 0.12P$
	Plastic	1.0	1.0	0.56	1.0	0.56	$\frac{6M_p}{L}$	0	$0.75R_{max} - 0.25P$

\* Equal parts of the concentrated mass are lumped at each concentrated load.



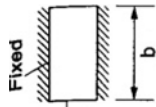


**Table 5.6.** Dynamic-design factors for beams and one-way slabs (courtesy US Army Corps of Engineers)

Loading diagram	Strain range	Load factor $K_L$	Mass factor $K_M$		Load-mass factor $K_{LM}$		Spring constant $k$	Effective spring constants $k_E$		Dynamic reaction $V$
			Concen- trated mass*	Uniform mass	Concen- trated mass	Uniform mass		Elastic	Plastic	
<p><math>P = p/l</math></p>	Elastic	0.53	...	0.41	...	0.77	$\frac{384EI}{5L^3}$	Elastic	$0.36R + 0.14P$	
	Elasto-plastic	0.64	...	0.50	...	0.78	$\frac{384EI}{5L^3}$	Elastic	$0.39R + 0.11P$	
<p><math>P</math></p>	Plastic	0.50	...	0.33	...	0.66	0	$\left( R_{max} = \frac{22MP}{L} \right)$	$0.39R_{max} + 0.12P$	
	Elastic	1.0	1.0	0.37	1.0	0.37	$\frac{192EI}{L^3}$	...	...	$0.71R - 0.21P$
	Plastic	1.0	1.0	0.33	1.0	0.33	0	...	...	$0.75R_{max} - 0.25P$

\* Concentrated mass is lumped at the concentrated load.

**Table 5.7.** Slabs simply supported on shorter sides and fixed on longer sides (courtesy US Army Corps of Engineers)



Strain range	a/b	Load factor $K_L$	Mass factor $K_M$	Load-mass factor $K_{LM}$	Maximum resistance	Spring constant $k$	Dynamic reactions		
							$V_A$	$V_B$	
Elastic	1.0	0.39	0.26	0.67	$20.4M_{Pbb}^0$	$575EI_n/a^2$	$0.07P + 0.187R$	$0.09P + 0.16R$	
	0.9	0.40	0.28	0.70	$19.5M_{Pbb}^0$	$600EI_n/a^2$	$0.06P + 0.16R$	$0.10P + 0.18R$	
	0.8	0.42	0.29	0.69	$19.5M_{Pbb}^0$	$610EI_n/a^2$	$0.06P + 0.14R$	$0.11P + 0.19R$	
	0.7	0.43	0.31	0.71	$20.2M_{Pbb}^0$	$662EI_n/a^2$	$0.05P + 0.13R$	$0.11P + 0.21R$	
	0.6	0.45	0.33	0.73	$21.2M_{Pbb}^0$	$731EI_n/a^2$	$0.04P + 0.11R$	$0.12P + 0.23R$	
	0.5	0.47	0.34	0.72	$22.2M_{Pbb}^0$	$850EI_n/a^2$	$0.04P + 0.09R$	$0.12P + 0.25R$	
	Elasto-plastic	1.0	0.46	0.31	0.67	$\frac{1}{d}[12M_{Pfs} + 12(M_{Pfb} + M_{Pfb})]$	$271EI_n/a^2$	$0.07P + 0.18R$	$0.07P + 0.18R$
		0.9	0.47	0.33	0.70	$\frac{1}{d}[12M_{Pfs} + 11(M_{Pfb} + M_{Pfb})]$	$248EI_n/a^2$	$0.06P + 0.16R$	$0.08P + 0.20R$
		0.8	0.49	0.35	0.71	$\frac{1}{d}[12M_{Pfs} + 10.3(M_{Pfb} + M_{Pfb})]$	$228EI_n/a^2$	$0.06P + 0.14R$	$0.08P + 0.22R$
		0.7	0.51	0.37	0.73	$\frac{1}{d}[12M_{Pfs} + 9.8(M_{Pfb} + M_{Pfb})]$	$216EI_n/a^2$	$0.05P + 0.13R$	$0.06P + 0.24R$
0.6		0.53	0.39	0.74	$\frac{1}{d}[12M_{Pfs} + 9.3(M_{Pfb} + M_{Pfb})]$	$212EI_n/a^2$	$0.04P + 0.11R$	$0.09P + 0.26R$	
0.5		0.55	0.41	0.74	$\frac{1}{d}[12M_{Pfs} + 9.0(M_{Pfb} + M_{Pfb})]$	$216EI_n/a^2$	$0.04P + 0.09R$	$0.09P + 0.26R$	
Plastic		1.0	0.33	0.17	0.51	$\frac{1}{d}[12M_{Pfs} + 12(M_{Pfb} + M_{Pfb})]$	0	$0.09P + 0.16R_{max}$	$0.09P + 0.16R_{max}$
		0.9	0.35	0.18	0.51	$\frac{1}{d}[12M_{Pfs} + 11(M_{Pfb} + M_{Pfb})]$	0	$0.08P + 0.15R_{max}$	$0.09P + 0.18R_{max}$
		0.8	0.37	0.20	0.54	$\frac{1}{d}[12M_{Pfs} + 10.3(M_{Pfb} + M_{Pfb})]$	0	$0.07P + 0.13R_{max}$	$0.10P + 0.20R_{max}$
		0.7	0.36	0.22	0.58	$\frac{1}{d}[12M_{Pfs} + 9.8(M_{Pfb} + M_{Pfb})]$	0	$0.06P + 0.12R_{max}$	$0.10P + 0.22R_{max}$
	0.6	0.40	0.23	0.58	$\frac{1}{d}[12M_{Pfs} + 9.3(M_{Pfb} + M_{Pfb})]$	0	$0.05P + 0.10R_{max}$	$0.10P + 0.25R_{max}$	
0.5	0.42	0.25	0.59	$\frac{1}{d}[12M_{Pfs} + 9.0(M_{Pfb} + M_{Pfb})]$	0	$0.04P + 0.08R_{max}$	$0.11P + 0.27R_{max}$		

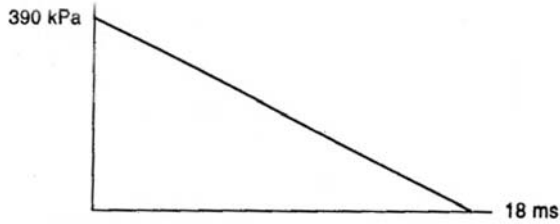


Fig. 5.5. Triangular pressure-pulse function

Wall height = 4 m

Vertical reinforcement  $\rho_{SU} = 0.5\%$  at each face

$R = R' = \text{range} = 4.0 \text{ m}$

Hemispherical charge factor = 1.8

$f_y = \text{Static yield stress of the reinforcement} = 460 \text{ N/mm}^2$

$f_{dy} = \text{Dynamic yield stress of the reinforcement} = 1.2f_y$

Concrete grade = 40

Type III category rotation of the base allowed during explosion:  $\theta = 12^\circ$ .  
Justify the impulsive load analysis.

- (b) If the same wall is fixed at the top as well as at the bottom and is subjected to a quasi-static load of a triangular shape' shown in Fig. 5.5 and adopting BS 8110 and other relevant criteria, check the reinforcement and the wall thickness while behaving as a single-degree elastoplastic system.
- (c) If the wall is subject to vehicle bombs of 50, 100, 150, 200, 250 and 300 kg of TNT at a random range  $R'$  of 1 m to 10 m from the explosion to the centre of the wall, draw curves for

$$\frac{x}{L} \left( \frac{\text{wall deflection}}{\text{wall span}} \right) \text{ versus } R'$$

for various vehicle bombs given. The wall is assumed damaged when

$$\frac{x}{L} = \frac{1}{60}.$$

### Calculations

The vehicle bomb mass produces a hemispherical charge of mass  $1.8 \times 100 \text{ kg} = 180 \text{ kg}$  where 100 kg is the actual mass.

$$R' = \text{range} = 4.0 \text{ m}$$

$$Z = \text{the scaled distance} = \frac{4.0}{180^{1/3}} = 0.705 \text{ m/kg}^{1/3}$$

$$i_r = I_r = \text{reflected overpressure}$$

$$\text{impulse} = 5095 \text{ kPa}\cdot\text{ms}.$$

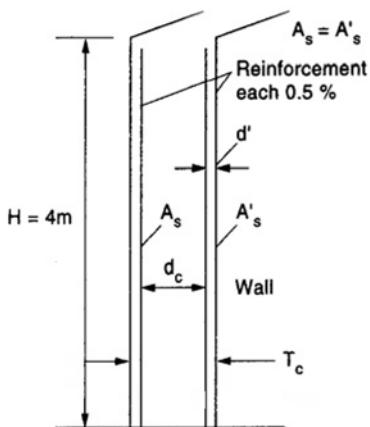


Fig. 5.6. Reinforced concrete wall

For category type III behaviour, the material properties are:

$$f_y = \text{reinforcement yield stress} = 460 \text{ N/mm}^2 \text{ (static value)}$$

$$f_{dy} = 1.2f_y = 1.2 \times 460 = 552 \text{ N/mm}^2 \approx f_{ds} \text{ (dynamic value)}$$

$$\frac{I_r^2}{2K_{LM}\rho d_c} = \left( \frac{2}{H} \rho_v f_{ds} d_c^2 \right) \tan \theta$$

$$\theta = \text{rotation of the base of the wall} = 12^\circ \text{ (Type III category)}$$

$$\tan \theta = 0.2126$$

$$\rho_v = 0.5\%, \text{ i.e. reinforcement on both sides is equal}$$

$$K_{LM} = \text{load-mass factor} = 0.66$$

$$\frac{(5095)^2}{2 \times 0.67 \times 2400d_c} = \frac{2}{4.0} \times \frac{0.5}{100} \times 552 \times 10^6 d_c^2 \times 0.2126$$

$$d_c = 0.302 \text{ m} = 302 \text{ mm}$$

$$T_c = d = \text{overall thickness}$$

$$= d_c + 2 \times \text{cover of } 40 + 2 \text{ assumed-size bar halves}$$

$$= 302 + 80 + 25$$

$$= 407 \text{ mm}$$

Adopt 425 mm or 17 in RC wall ( $T_c$ ) (see Fig. 5.6)

$$A_s = 0.005 \times 302 \times 1000 = 1510 \text{ mm}^2/\text{m} = \text{width of wall.}$$

The reinforcement should be generously placed to account for the cover variations of the material and blast load and is a principal design assumption. A total of 25% steel on top is recommended.

$$\text{Adopt T25-250 where } A_{S_{prov}} = 1963 \text{ mm}^2/\text{m} = \text{width of wall.}$$

When checking for shear:

$$\begin{aligned}\nu &= \frac{r_u(4.0 - 0.302)}{0.302} = 12.245 r_u \\ r_u &= \frac{2}{(4)^2} \times 0.005 \times 552 \times 10^6 (0.302)^2 \\ &= 31465.38 \\ \nu &= 0.3853 \text{ N/mm}^2\end{aligned}$$

$$\frac{100A_s}{bd} = 0.65 \quad f_{cu} = 40 \text{ N/mm}^2 \quad \nu_c = 0.59 \quad (\text{BS8110, Table 3.9})$$

Using Table 13 of B88110

$$\nu < 0.5 \nu_c \not\prec \frac{0.59}{2} = 0.295 \text{ N/mm}^2$$

A minimum shear link is needed when

$$\begin{aligned}\frac{0.59}{2} &< \nu < \nu_c + 0.4 \\ 0.295 &< 0.3853 < 0.7853 \text{ N/mm}^2 \\ A_{Sv} &= \frac{0.4b_v s_v}{0.87f_y} \\ &= 45 \text{ mm}^2\end{aligned}$$

Take

$$\begin{aligned}f_{ds} &= 1.1 \times 250 \\ &= 275 \text{ N/mm}^2 \\ b_v &= 150 \\ s_v &= 300\end{aligned}$$

Then, the ultimate shear =  $31465.38 \times 4 = 125861.52 \text{ N/m}$   
 $= 126 \text{ N/mm}^2$

$$\begin{aligned}f_{ds} &= 1.1 \times 460 = 506 \text{ N/mm}^2 \\ b &= 1.50 \text{ mm} \quad \text{to match up with stirrups}\end{aligned}$$

$$\begin{aligned}A_d &= \text{area of the diagonal bars @}45^\circ \\ &= \frac{126 \times 150}{506} \approx 37.35 \text{ mm}^2\end{aligned}$$

Therefore, 1 row of R8-1.50 bars needed.

For the delay time =  $t_d = T_s = 50 \text{ ms}$ :

$$\frac{t_m}{t_d} = \frac{I}{r_u t_d} = \frac{5095 \times 1000}{31465.38 \times 50} = 3.24 > 3.0$$

Hence the impulsive load analysis is valid.

For the instance where a quasi-static load is applied to the wall restrained at top and bottom, it follows:

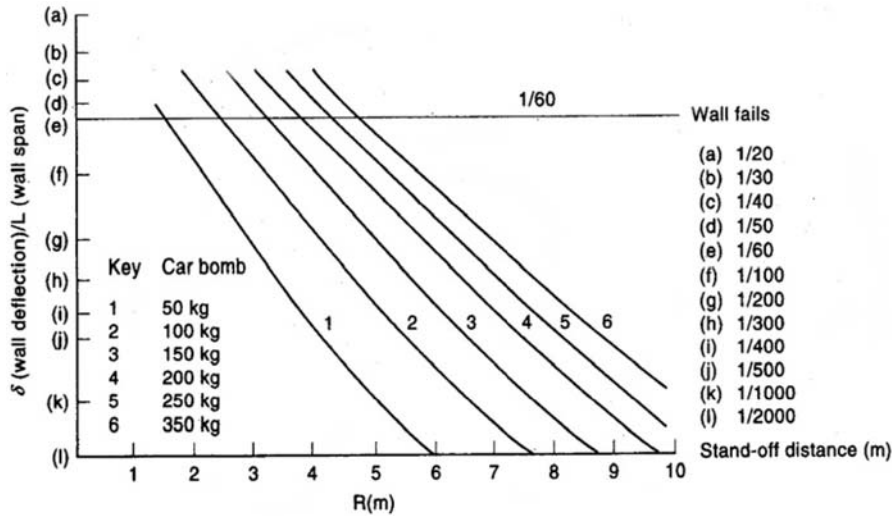


Fig. 5.7.  $\delta/L$  versus stand-off damage assessment

$$r_u = \frac{8(M_{Ps} + M_{Pm})}{H^2}$$

$$M_p = M_{Ps} + M_{Pm}$$

$$A_S = A'_S = 1.963 \text{ mm}^2/\text{m}$$

$x$  = depth of neutral axis

$$= \frac{d - z}{0.45} = \frac{d - 0.95d}{0.45}$$

$$0.05d = 0.45x$$

$$x = \frac{0.05 \times 302}{0.45} = 33.6 \text{ mm}$$

Ignoring the contribution of the compression reinforcement ( $K = K' = 0.156$ )

$$M_p = 1963 \times 552(302 - 0.45 \times 33.6) \times 10^{-3}$$

$$= 310856.28 \text{ Nm/m}$$

Hence

$$r_u = \frac{(M_{ps} + M_{Pm})^8}{(4)^2} = \frac{2 \times 310856.28 \times 8}{4^2}$$

$$= 310856 \text{ N/m}^2$$

$$\rho_s = 0.005 \quad n = \frac{200 \text{ GN}}{30 \text{ GN}} = 6.67$$

$$I = Fbd^3$$

$$F = 0.0246 \quad T = 2\pi \sqrt{\frac{K_{LM} M_d}{K_E}}$$

$$M_d = 2400 \times 0.425 = 1020 \text{ kg/m}^2$$

$$K_{LM} = 0.66$$

$K_E$  (for both ends fixed) = equivalent stiffness

$$= \frac{307 EI}{H^4} = 1.51 \times 10^6 (\text{N/m}^2)/\text{m}$$

$$T = 0.025 = 20 \text{ ms}$$

For a single-degree-of-freedom system (elastoplastic system)

$$\frac{r_u}{P_r} = \frac{310856}{390 \times 10^3} = 0.797 \approx 0.8$$

$$t_d = 18 \text{ ms} \quad \frac{t_d}{T} = \frac{18}{20} = 0.9$$

$$\frac{X_m}{X_E} = 3.0 \quad X_E = \frac{r_u}{K_E} = 0.206 \text{ m or } 206 \text{ mm}$$

$$X_m = 3.0 \times 206 = 618 \text{ mm} < 4000 \times \tan 12^\circ = 850 \text{ mm}$$

Similar analyses have been carried out for various ranges or stand-off distances and explosive weights. The final results are plotted in Fig. 5.7.

### 5.2.2 Example on American Practice

A laterally restrained, simply supported W16 × 50 beam (wide-flanged type; see Fig. 5.8) is subjected to a blast load caused by a bomb detonation. A triangular load-time function Fig. 5.9 is assumed for the elastic analysis. A check is required for any rectangular load-time function as given in the following data:

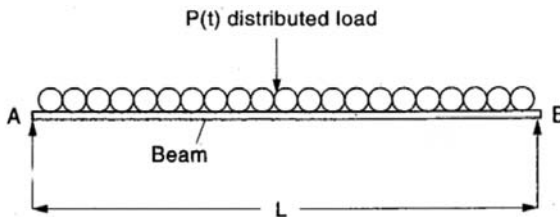


Fig. 5.8. A simply supported laterally restrained beam

(a) Elastic analysis

$$F = 5000 \text{ lb/ft}$$

$$\text{Weight/ft of the beam} = 600 \text{ lb}$$

$$L = 13 \text{ ft}$$

(b) Plastic analysis

$$F = 15000 \text{ lb/ft}$$

$$L = 12 \text{ ft}$$

(c) Confirmation is required if, at some location, the same beam span ( $L$ ) receives  $F = 15000 \text{ lb/ft}$  based on a rectangular load-time function of  $T = 0.1 \text{ sec}$  of the same duration.*Numerical data*

$$E = 30 \times 10^6 \text{ psi}$$

$$I = 659 \text{ in}^4$$

For the real beam:

$$R_m = \frac{R_{me}}{K_R} = \frac{74880}{0.64} = 117000 \text{ lb}$$

$$\text{dynamic load} = 1.8(65000) = 117000 \text{ lb}$$

$$\text{maximum bending moment} = \frac{R_m \times L}{8} = \frac{117000 \times 13}{8}$$

$$= 190125 \text{ ft lb}$$

$$\text{maximum bending stress} = \frac{M}{Z_x} = \frac{190125 \times 12}{80.70} = 2356 \text{ psi}$$

$$\text{dead load stress} = 1706 \text{ psi}$$

$$\text{total bending stress} = 29873 \text{ psi}$$

$$\text{shear in the beam} = \text{dynamic reaction at } t_m(\text{max}) = 0.02 \text{ sec} :$$

$$R_m = 117000 \text{ lb}$$

$$F = P = \left( \frac{0.01 - 0.02}{0.1} \right) \times 65000 = 52000 \text{ lb}$$

$$\text{Max } V = 0.39R_m + 0.11P = 51350 \text{ lb}$$

$$\text{dead load reaction} = 3900 \text{ lb}$$

$$\text{maximum shear stress} = \frac{(51350 + 3900)}{(d = 16.25) \times (t_w = 0.38)} = 8947 \text{ psi}$$

(b) *Plastic analysis*

The span is decreased by 1 ft and a bomb capacity with 15000 lb/ft peak over-pressure is considered.



Plastic analysis is performed based on the following data:

$$\sigma_{dy} \text{ (steel)} = 41.6 \text{ ksi}$$

$\sigma_p$  (max) bending stress can now be evaluated

$$\begin{aligned} M_p &= 1.05\sigma_{dy} \times z_p \\ &= 1.05 \times 41600 \times 80.7 = 3.525 \times 10^6 \text{ in lb} \end{aligned}$$

$$\begin{aligned} R_m &= \frac{8M_p}{L} \quad \text{for a beam under UDL} \\ &= \frac{8 \times 3.5 \times 25 \times 10^6}{12 \times 12} = 1.9584 \times 10^5 \text{ lb} \end{aligned}$$

$$x_{el} = \text{limiting deflection} = \frac{1.9584 \times 10^5}{4.8 \times 10^6} = 0.0408 \text{ ft}$$

For transformation factors  $K_L$  and  $K_M$  in the equivalent system:

$$F = P_i = K_L \times 15000 \times 12 = 0.57 \times 15000 \times 12 = 102600 \text{ lb}$$

$$m_e = K_M \times m_t = 0.415 \times 242 = 100.431 \text{ lb sec}^2/\text{ft}$$

$$f = T_n = \text{fundamental frequency} = 2\pi \sqrt{\frac{100.43}{4.77 \times 10^6}} = 0.029 \text{ sec}$$

$$R_{me} = K_L R_m = 0.57 \times 1.9584 \times 10^6 = 1.1163 \times 10^5 \text{ lb}$$

$$\frac{T}{T_n} = \frac{0.10}{0.029} = 3.45$$

$$C_R = \frac{R_{me}}{P_i} = \frac{1.1163 \times 10^5}{102600} = 1.088$$

weight per foot = 600 lb

$$K_L = 0.57$$

$$K_R = 0.64$$

$$\sigma_{dy} = \text{dynamic yield stress} = 41.65 \text{ ksi}$$

$$\text{DLF} = 1.8$$

For case (c)  $K_L = 0.50$ ,  $K_M = 0.33$ .

A dead load of 1000 lb/ft plus the *weight of the beam* are to be added.

*Note the following conversions for changing these figures into SI units:*

$$1 \text{ in} = 25.4 \text{ mm}$$

$$1 \text{ lbft} = 0.4536 \text{ kg} = 4.448 \text{ N}$$

$$1 \text{ psi} = 6.89476 \text{ kN/m}^2$$

$$1 \text{ ft} = 0.3048 \text{ m}$$

$$1 \text{ ft lb} = 1.356 \text{ kNm}$$

$$1 \text{ in lb} = 0.113 \text{ Nm}$$

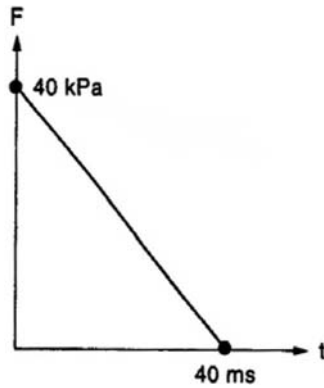


Fig. 5.9. Load-time function

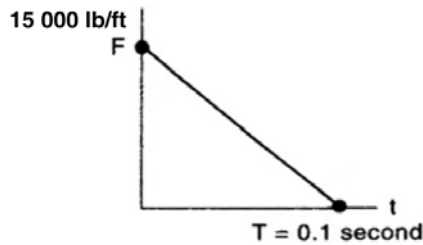


Fig. 5.10. Load-time function – triangular

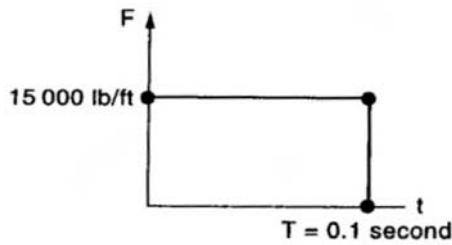


Fig. 5.11. Load-time function – rectangular

Asimilar operation can be performed using a specific bomb yield for which load-time triangular function of 40 kpa on 40 ms as shown in Fig. 5.9. These calculations can be performed again for a specific load-time function replacing that of Figs. 5.10 or 5.11.

(a) For weight/ft of 600 lb

$$\text{Total mass} = M_d \text{ or } m_t = \frac{600 \times 13}{32.2} = 242 \text{ lb sec}^2 / \text{ft}$$

$$E = 30 \times 10^6 \text{ psi}$$

$$I = 659 \text{ in}^4$$

$$\text{total peak load } F = p_i = 5000 \times 13 = 65000 \text{ lb}$$

$$k = \frac{384EI}{5L} = \frac{384 \times 30 \times 10^6 \times 659}{5(13)^3 \times 144} = 4.8 \times 10^6 \text{ lb/ft}$$

For the equivalent system:

$$\text{mass } m_e = K_M m_t = 0.50 \times 242 = 121 \text{ lb sec}^2 / \text{ft}$$

$$F = p_i = 65000 K_L = 65000 \times 0.64$$

$$= 41600 \text{ lb}$$

$$k_e = K_R k = 0.64 \times 4.8 \times 10^6 = 3.072 \times 10^6 \text{ lb/ft}$$

$$T_n = \text{natural period} = 2\pi \sqrt{\frac{m_c}{k_e}} = 0.039 \text{ sec}$$

$$\frac{T}{T_n} = \frac{0.10}{0.039} = 2.56$$

$T$  = duration of load

$T_n$  = fundamental frequency

$$\text{DLF}_{\max} \quad (\text{dynamic load factor}) = 1.80$$

$$\frac{t_m}{T} = 0.20$$

$$R_{me} = 1.8 \times 41600 = 74880$$

$$x_m = \frac{R_{me}}{k_e} = \frac{74880}{3.072 \times 10^6} = 0.0244 \text{ ft}$$

Assume initial deadload of the beam is stress  $\sigma_{\text{dead}} = 5$  ksi. Then:

$$\begin{aligned} z_p &= \frac{M_p}{1.05(\sigma_{dy} - \sigma_{\text{dead}})} = \frac{120.25 \times 12}{1.05(41.6 - 5)} \\ &= 37.55 \text{ in}^2 \\ &< 80.7 \text{ in}^2 \end{aligned}$$

Therefore, best available beam is W16  $\times$  50.

### 5.2.3 Example on British Practice

A simply supported steel beam is one of a number at 1.5 m centres making up a roof structure. The beams carry a cladding material of density 23.4 kg/m<sup>2</sup> and a span of 8 m. Imposed load from the roof is calculated at 42.5 kN/m. Assume initially the self weight of the beam to be 1.125 kN/m. The beam is

restrained at the centre and at the ends. Design this steel beam in a grade 43 material, using the following initial data:

$$\begin{aligned}
 \text{Moment capacity } M_{cx} &= p_y S_x \\
 &= \text{torsional buckling resistance (lateral)} \\
 \bar{M} &= \bar{m} M \leq M_b = p_b = S_x \\
 M_b &= \text{lateral buckling resistance} \\
 \bar{M} &= \text{equivalent uniform movement}
 \end{aligned}$$

After designing this beam, it is the client’s requirement that due to bombing incidents, all structural components of a building need to be checked. This beam is one part of this requirement. The consultant specified the following blast load-time function for the building components. Check that this beam is adequate for the potential blast effects. Take the increasing dynamic factor as 1.3. The ductility factor,  $\mu$ , is 3.0:

$$\begin{aligned}
 E &= 200 \text{ GN/m}^2 \\
 \frac{r_u}{F} &= 1.0 \\
 \text{imposed load} &= 42.5 \text{ kN/m} \\
 \text{assumed self weight of the beam} &= 1.125 \text{ kN/m}
 \end{aligned}$$

(a) Suitable Grade 43 section

Referring to Fig. 5.12, it follows:

$$\begin{aligned}
 M_{\max} &= \frac{WL^2}{8} \\
 &= (42.5 + 1.125) \times \frac{8^2}{8} \\
 &= 349 \text{ kNm}
 \end{aligned}$$

Trial section: 457 × 152 × 74 kg/mUB ( $S_x = z = 1620 \text{ cm}^3$ )

$$\begin{aligned}
 M_{cx} &= p_y S_x \\
 &= 265 \times 1620 \times 10^3 \times 10^{-6} = 429.3 \text{ kNm} > 349 \text{ kNm} \\
 p_y &= 265 \text{ N/m}^2 \text{ for } T > 16 \text{ mm}
 \end{aligned}$$

The section is adequate for bending torsional buckling resistance, i.e. the following expression is met:

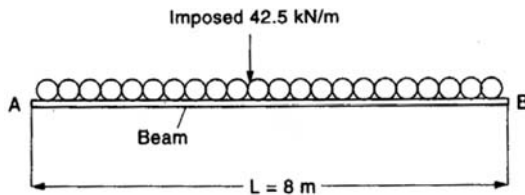


Fig. 5.12. A simply supported beam with unrestrained length

$$\begin{aligned}\bar{M} &= \bar{m}M \leq M_b = p_b S_x \\ \frac{x_m}{x_{el}} &= 2.45 \\ x_m &= 2.45 \times 0.0408 = 0.10 \text{ ft}\end{aligned}$$

The maximum resistance at peak load is now considered. The following equation in the absence of a more rigorous analysis will give a conservative maximum dynamic reaction:

$$\begin{aligned}\max V &= 0.39 R_m + 0.11 F \\ &= 0.39(1.9584 \times 10^5) + 0.11(15000 \times 12) \\ &= 96177.6 \text{ lb} \\ \text{shear stress} &= \frac{V_{\max}}{dxt_w} = \frac{96177.6}{16.25 \times 0.38} \\ &= 15575 \text{ psi}\end{aligned}$$

(c) For a deadload of 1000 lb/ft

Dead weight of the beam = 600 lb/ft

$DL_{\text{total}} = 1.6 \text{ kip/ft}$

$$m_t + \frac{1.6 \times 13}{32.2} = 0.646$$

$m_e = \text{equivalent mass} = 0.646 \text{ kip-sec}^2/\text{ft}$

$I_{\text{total}} = \text{total impulse} = 15 \times 13 \times 0.1 = 19.5 \text{ kip-sec}$

$I_{\text{eq}} = \text{equivalent impulse} = I_{\text{total}} \times 0.5 = 9.75 \text{ kip-sec}$

$$W_{pe} = \text{maximum work done} = \frac{I_{\text{eq}}}{2m_e} = \frac{9.75}{2 \times 0.646} = 7.55 \text{ kip/ft}$$

Practically for the designer  $W_{me}/W_{pe}$  shall be taken as 0.2

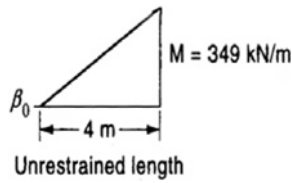
$W_{me} = \text{energy absorbed by the beam}$

$$W_{me} = 0.2W_{pe} = 0.2(9.75) = 1.95 \text{ kip/ft}$$

Since the behaviour is largely plastic

$$\begin{aligned}W_{me} &= R_{me}(x_m) \quad \text{or} \\ R_{me} &= \frac{W_{me}}{x_m} = \frac{1.95}{0.0408} \\ &= 47.8 \text{ kips}\end{aligned}$$

$$\begin{aligned}x_m &= \text{maximum allowable deflection} \\ &= 0.0408 \text{ ft} \approx \frac{1}{2} \text{ in}\end{aligned}$$



**Fig. 5.13.** Load-time function for the unrestrained length of a simply supported beam

Thus, for the actual beam:

$$R_m = \frac{37}{0.5} = 74 \text{ kips}$$

$$\begin{aligned} M_p \text{ (plastic moment required)} &= \frac{R_m L}{8} = \frac{74 \times 13}{8} \\ &= 120.25 \text{ kip/ft} \end{aligned}$$

For a simply supported beam, the end moment is zero (Fig. 5.13)

$$\beta = \frac{\text{smaller end moment} = 0}{\text{larger end moment} = 349} = 0$$

$$\bar{m} = (\text{Table 18 BS 5950}) = 0.57$$

$$n = 1.0 \quad (\text{Table 5.8}) \text{ BS 5950}$$

$$\begin{aligned} M &= \text{equivalent uniform moment} = mM = 0.57(349) \\ &= 198.93 \text{ kNm} \end{aligned}$$

$$M_b = \text{buckling resistance} = p_b S_x$$

$$p_y = 265 \text{ N/mm}^2 \quad (\text{Table 5.5 BS 5950})$$

Now

$$\begin{aligned} \lambda_{LT} &= nu\nu\lambda \\ &= 1.0 \times 0.87 \times 0.856 \times 122.7 \\ &= 91.38 \end{aligned}$$

$L$  = distance between restraints

$$p_b = 138.24 \text{ N/mm}^2 \quad (\text{Interpolation of Table 5.5 BS5950})$$

$$\begin{aligned} \lambda &= \frac{L_E}{r_y} = \frac{1.0L}{3.26 \text{ cm}} \\ &= \frac{1 \times 4000}{3.26 \times 10} \\ &= 122.7 \end{aligned}$$

$$\frac{\lambda}{x} = \frac{122.7}{30} = 4.09$$

$$\nu = 0.856 \quad (\text{Tables 5.6, 5.7 BS 5950})$$

$$\begin{aligned} M_b &= 138.24 \times 1620 \times 10^3 \times 10^{-6} \\ &= 223.95 \text{ kNm} > 198.93 \text{ kNm} \end{aligned}$$

Therefore with  $\bar{M} < M_b$  the lateral buckling resistance of the section is adequate.

(b) Beams at 1.5 centres

$$\frac{r_u}{F} = 1.0$$

This value is assumed for a new beam replacing the damaged one, i.e.

$$\begin{aligned} R_u &= r_u = 1,0 \times 40 \times 8.0 \times 1.5 \\ &= 480 \text{ kN} \end{aligned}$$

$$\begin{aligned} M_p &= \text{plastic moment} = \frac{r_u L}{8} = 480 \text{ kNm} \\ (S_x + z_e)\sigma_{dy} &= 2M_p \quad (\text{from the plastic analysis}) \\ (S_x + z_e) &= \frac{2 \times 480 \times 10^3}{1.3 \times 265 \times 10^6} = 2.787 \times 10^{-3} \text{ m}^3 \text{ or } 2787 \text{ cm}^3 \end{aligned}$$

The existing section is  $457 \times 152 \times 74 \text{ kg/m}$ . Therefore:

$$(S_x + z_e) = (1620 + 1410) = 3030 \text{ cm}^3 > 2787 \text{ cm}^3$$

Mass of the beam + weight of cladding is given by:

$$\begin{aligned} M_d &= \bar{m} = 74 \times 8.0 + 23.4(8 \times 1.5) \\ &= 592 + 280.8 = 872.8 \text{ kg} < 1.125 \text{ kN/m}. \end{aligned}$$

Taken initially:

$$\begin{aligned} T_n &= 2\pi \sqrt{\frac{K_{LM} \bar{m}}{k_e}} \\ &= 2\pi \sqrt{\frac{0.72 \times 872.8}{975 \times 10^4}} \\ &\approx 0.0505 \text{ sec or } 50.5 \text{ ms} \\ k_e &= \frac{384EI}{5L^3} = \frac{384 \times 200 \times 10^9 \times 32500 \times 10^{-8}}{5(8)^3} \\ &= 975 \times 10^4 \text{ N/m} \end{aligned}$$

$$K_{LM} = 0.72$$

$$\frac{t_d}{T_n} = \frac{40}{50.5} = 0.792$$

$$\begin{aligned}
 r_u = R_u &= \frac{8MP}{L} = \frac{8 \times 3030 \times 10^{-6} \times 265 \times 10^6 \times 1.3}{16(\text{or } 2 \times 8)} \\
 &= 5.22 \times 10^5 \text{ N} \quad \text{or} \quad 5.22 \times 10^2 \text{ kN} \\
 \frac{r_u}{F_1} &= \frac{522}{480} = 1.0875
 \end{aligned}$$

The beam can be used. Check for shear:

$$\begin{aligned}
 V_u &= \text{ultimate shear capacity} = \sigma_{dv} A_w \\
 &= 1725 = 172.25 \times 4028.31 \times 10^{-3} = 693.876 \text{ kN} \\
 &\quad \left( \begin{array}{l} \sigma_{dv} = \text{dynamic yield stress in shear} \\ = 0.51 \times 1.3 \times 265 = 172.25 \text{ N/mm}^2 \end{array} \right)
 \end{aligned}$$

$$A_w = \text{area of the web} = (9.9 \times 406.9) = 4028.31$$

But

$$\begin{aligned}
 V &= 0.393r_u + 0.107F \\
 &= 0.393 \times 5.22 \times 10^2 + 0.107 \times 480 = 256.506 \text{ kN} < 693.876 \text{ kN}
 \end{aligned}$$

The beam is therefore adequate.

### 5.2.4 Example on American Practice

A roof slab of dimensions 15 ft  $\times$  10.5 ft restrained on an edges is subject to a peak pressure  $p_{so} + p_{drag}$ . Calculate using the following data:

- the velocity of the shock front,
- clearing time  $t_c$  and rising time  $t_r$ ,
- the maximum resistance  $R_m$ ,
- the final thickness of the slab.

$$\begin{aligned}
 \frac{a}{b} &= \text{aspect ratio} = \frac{10.5}{15} = 0.70 \\
 R_m &= \text{maximum resistance based on } \frac{a}{b} \approx 0.7 \\
 &= \frac{1}{a} [(12M_{Pfa} + M_{Psa}) + 9.8(M_{Pfb} + M_{Psb})] \\
 &= \frac{1}{10.5} [12(2M_p \times 10.5) + 9.8(2M_p \times 15)] \\
 &= 52M_p
 \end{aligned}$$

$M_p$  = bending resistance of slab per unit width, i.e. plastic moment per unit width. Thus:



$$M_p = \frac{406080}{52} = 7809.231 \text{ lb ft/ft}$$

$$= 7.809231 \text{ kip ft} \approx 7.81 \text{ kip ft}$$

$$M_p = \rho_s b d^2 \sigma_{dy} \left( 1 - \frac{\rho_s \sigma_{dy}}{1.7 \sigma'_{dc}} \right)$$

$$\sigma'_{dc} = 3.9 \text{ ksi}$$

$$\sigma_{dy} = 52 \text{ ksi}$$

$$\rho_s = 0.015$$

$$M_p = 0.015(52)(12)d^2 \left[ 1 - \frac{0.015(52)}{1.7(3.9)} \right] = 8.25d^2 \text{ kip in}$$

Now

$$8.25d^2 = 7.81 \times 12 \text{ kip in}$$

$$d = 3.37 \text{ in; take } d = 3.5 \text{ in}$$

$$h = 5 \text{ in}$$

$$I_{\text{Gross}} = \frac{bd^3}{12} = \frac{12(5)^3}{12} = 125 \text{ in}^4$$

Transformed moment of inertia (cracked section)

$$I_t = 38.8 \text{ in}^4$$

$$\text{slab } \frac{x_m}{x_{el}} = 5$$

$I_a$  = average moment of inertia

$$= \frac{1}{2}(125 + 38.8) = 81.9 \text{ in}^4$$

$$k = \text{stiffness} = \frac{216EI_a}{a^2} = \frac{216 \times 3 \times 10^6 \times 81.9}{(10.5)^2 \times 144} = 33.43 \times 10^5 \text{ lb/in}$$

$$m_t = \text{mass of the slab} = \frac{150 \times \frac{7}{12} \times 10.5 \times 15}{386} = 35.7 \text{ lb-sec}^2/\text{in}$$

The required data are:

$$p_{so} + p_{\text{drag}} = 20 - 4p_{do} = 20 - 0.4 \times 7.8 = 16.88 \text{ psi}$$

$$U = \text{velocity front} = 1120 \left( 1 + \frac{6p_{so}}{103} \right)^{1/2}$$

$$t_c = \frac{3}{U}$$

$$t_r = \frac{\text{slab short side}}{U}$$

$$\mu = \text{ductility factor} = 5.0$$

$$R_{m_{\max}} = \frac{1}{a} [(12M_{Pfa} + M_{Psa}) + 9.8(M_{Pfb} + M_{Psb})]$$

$$R_{m_{\text{required}}} = P_i \left( \frac{1}{1 - \frac{1}{2}\mu} \right)$$

$$M_p = \rho_s b d^2 \sigma_{dy} \left( 1 - \frac{\rho_s \sigma_{dy}}{1.7 \sigma'_{dc}} \right)$$

$$\sigma'_{dc} = 3.9 \text{ ksi} \quad \rho_s = 0.015$$

$$\sigma_{dy} = 52 \text{ ksi}$$

The blast is along the short direction of 10.5 ft. Roof slab dimensions are 15 ft  $\times$  10.5 ft restrained on all edges.

total pressure on the RC roof slab = overpressure + drag

$$\begin{aligned} \text{peak pressure} &= P_i \text{ (initially)} = p_{so} + p_{\text{drag}} = 20 - 0.4p_{do} \\ &= 20 - 0.4 \times 7.8 \\ &= 16.88 \text{ psi} \end{aligned}$$

$U$  = velocity of the shock front

$$= 1120 \left( 1 + \frac{6p_{so}}{103} \right)^{1/2} = 1650 \text{ ft/sec}$$

$t_c$  = clearing time for the pressure  $p_r$

$$p_r = 2p_{so} \left( \frac{103 + 4p_{so}}{103 + p_{so}} \right) = 59.4 \text{ psi}$$

$$t_c = \frac{3 \times 12}{1650} = 0.022 \text{ sec or } 22 \text{ ms}$$

$t_r$  = the rising time of the loading on roof slab

$$= \frac{\text{spanning short length}}{U} = \frac{10.5}{1650} = 0006 \text{ sec}$$

The load on the slab in this short transit time is assumed to be uniform. Now

$$\mu = \text{ductility factor} = 5.0$$

$R_m$  = resistance required, i.e. strength calculated based on ductility

$$= P_i \left( \frac{1}{1 - \frac{1}{2}\mu} \right) = 18.8 \text{ psi}$$

$$\begin{aligned} \text{Total resistance of the slab} &= R_{m_{\text{total}}} = 18.8 \times 10 \times 15 \times 144 \\ &= 406080 \text{ lb} \end{aligned}$$

$K_{LM}$  = the load mass factor = 0.73

$$T = 2\pi \sqrt{\frac{0.73 \times 35.7}{33.43 \times 10^5}} = 0.018 \text{ sec}$$

the appropriate response chart is used

$$\frac{t_{de}}{T} = \frac{0.48}{0.018} = 26.67$$

$$\frac{R_m}{F_i = P_i} = \frac{18.8}{16.88} = 1.11$$

and read

$$\mu = 5.0$$

$$\frac{t_m}{t_d} = 0.1$$

$$t_m = 0.1 \times 0.48 = 0.048 \text{ sec}$$

A slab of 5 in (125 mm) thickness is sufficient since the computed  $\mu$  is close to the desired value.

### 5.3 The Use of Baker et al. Charts for Evaluating Blast Parameters

Figures 5.14 and 5.16 give scaled distances versus  $T_s/W^{1/3}$ ,  $t_s/W^{1/3}$ ,  $i_s/W^{1/3}$ ,  $t_a/W^{1/3}$  and  $P_s$  and  $P_r$ .

Figure 5.14 is developed to a side-on blast; Figure 5.15 is for a normally reflected blast; and Fig. 5.16 is for an additional side-on blast. In each case the above parameters are evaluated. Figure 5.17 shows  $z$  versus all other parameters in S.I. units developed by Bangash.

Several examples are given in order to allow the reader to become familiar with the computations of these parameters, using these semi-graphical methods.

#### 5.3.1 Example on American Practice

Determined for the stand-off distance  $R = 6$  m when  $W = 27$  Kg of TNT, determine the scaled distance  $z$ ,  $t_a$ ,  $P_s$ ,  $T_s$ ,  $i_r$  and  $P_r$  using Bakers charts of 27 kg RDX at the same standing distance  $R = 6$  m, calculate  $P_s$ ,  $i_s$ ,  $T_s$  and  $t_a$ .

$$R = 6 \text{ m}, W = 27 \text{ Kg}$$

$$z = \frac{6}{27^{1/3}} = 1.998 \frac{\text{m}}{\text{Kg}_{\text{TNT}}^{1/3}}$$

$$P_s = \text{the incidence overpressure} = 1.649 \times 10^5 \text{ Pa}$$

$$\frac{t_a}{W_{\text{TNT}}^{1/3}} = 1.8455 \times 10^{-2} \frac{\text{s}}{\text{kg}_{\text{TNT}}^{1/3}}$$

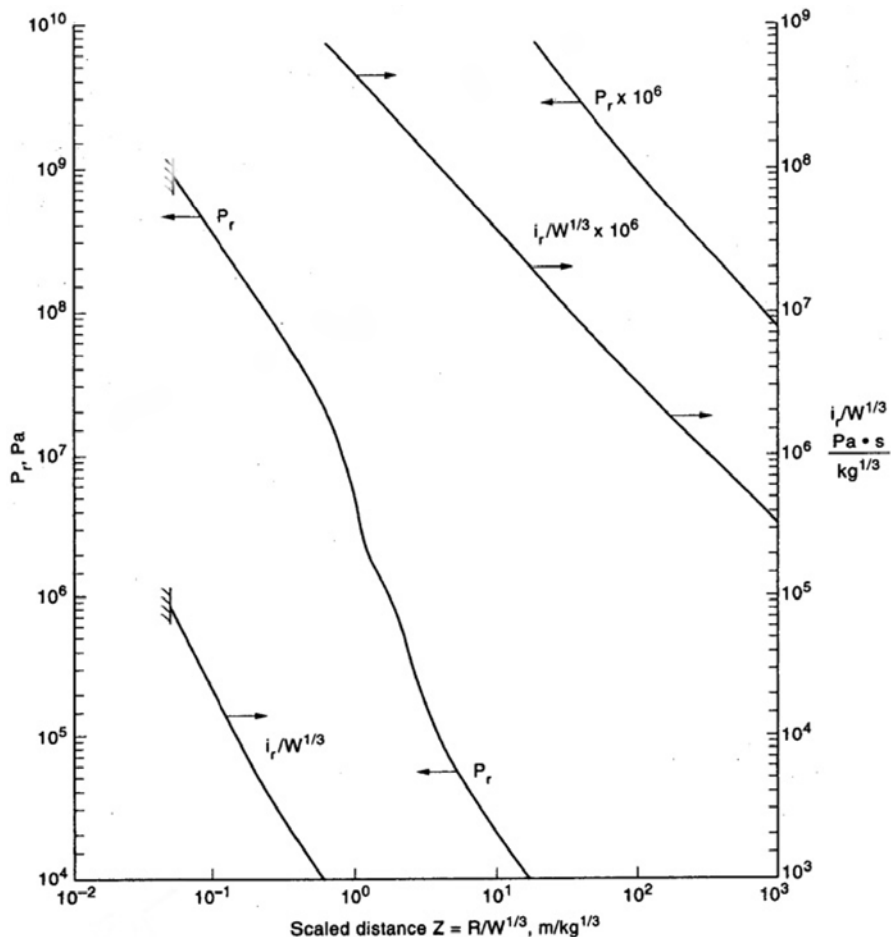


Fig. 5.14. Normally reflected blast parameters for TNT

where  $t_a$  = arrival time (sec)

$$t_a = 1.8455 \times 10^{-2} \frac{\text{s}}{\text{kg}_{\text{TNT}}^{1/3}} \times 3\text{kg}_{\text{TNT}}^{1/3} = 5.434 \times 10^{-2} \text{s}$$

$$\frac{T_s}{W_{\text{TNT}}^{1/3}} = 1.8455 \times 10^{-2} \frac{\text{s}}{\text{kg}_{\text{TNT}}^{1/3}} \times 3\text{kg}_{\text{TNT}}^{1/3} = 5.434 \times 10^{-2} \text{s} = t_a$$

where  $T_s$  = time in seconds.

Figure 5.15 now gives reflected pressure  $P_r$  and scaled reflected specific impulse  $i_r/W^{1/3}$ :

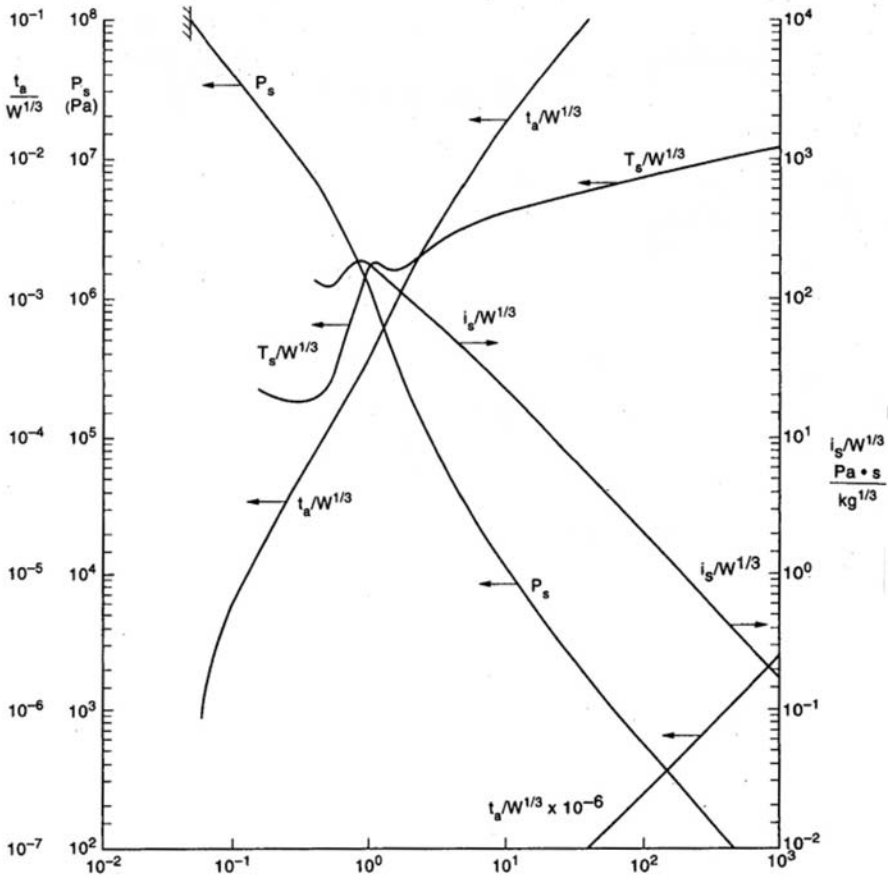


Fig. 5.15. Side-on blast parameters for TNT

$$P_r = 7.3291 \times 10^5 \text{ Pa}$$

$$\frac{i_r}{W_{\text{TNT}}^{1/3}} = 2.795 \times 10^2 \frac{\text{Pa} \cdot \text{s}}{\text{Kg}_{\text{TNT}}^{1/3}}$$

$$i_r = \frac{2.795 \times 10^2 \cdot \text{Pa} \times \text{s}}{\text{Kg}_{\text{TNT}}^{1/3}} \times 3 \text{ Kg}_{\text{TNT}}^{1/3} = 8.385 \times 10^2$$

- (b) The bomb charge 27 Kg RDX (spherical charge)
- in TNT =  $1.185 \times 27 = 32.0 \text{ Kg}_{\text{TNT}}$
- $P_s = 4.0 \times 10^4 \text{ Pa (N/m}^2\text{)}$
- $i_s = 24 \times 10 = 240 \text{ Pa}\cdot\text{s}$
- $T_s = 8.0 \text{ ms}$
- $t_a = 5.5 \text{ ms}$

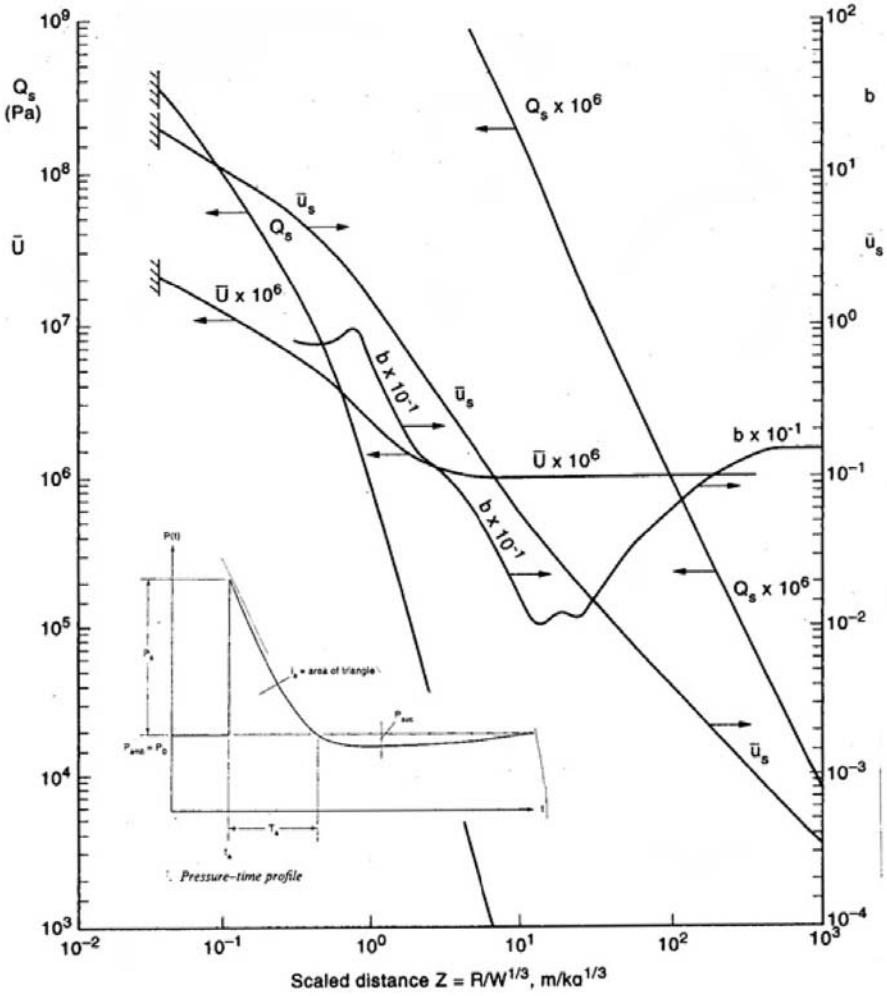


Fig. 5.16. Additional side-on blast pressure in TNT

using Fig. 5.16

$$P_{suc} = \frac{-0.35}{z}$$

$$z > 1.6$$

$$\frac{-0.35}{1.89} = 0.185 \text{ Pa}$$

$$T_{suc} = 1.25W^{1/3} = 3.91 \approx 4.0$$

$$I_{suc} = i_s \left( 1 - \frac{1}{2z} \right) = 176.5 \text{ Pa-s}$$

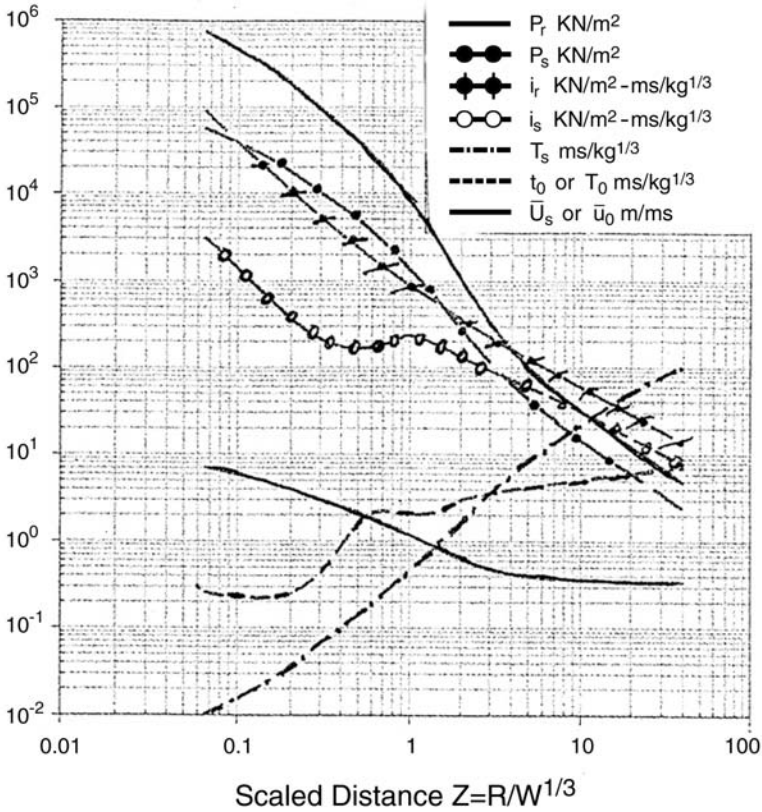


Fig. 5.17.  $z$  versus parameters in S.I. units (calculated converted in S.I. units by Bangash from Baker's chart)

## 5.4 Glass and Glazing

### 5.4.1 Introduction

Glass, plastic glazing sheet and glazing must be designed to receive some impact of the explosive load. The performance of glazing under explosive loading depends upon type, thickness, pane size and support conditions. The glazing specification chosen should meet the design and performance requirement of any code of practice. Glass and plastic glazing sheet material must be secured to the window or door structure in such a manner that it cannot easily be removed. The following describes types of glass used generally in various buildings.

- (a) Annealed glass
- (b) Toughened (tempered) glass
- (c) Laminated glass

- (d) Blast-resistant glazing using US Technical Manual 5-1300: *Structures to Resist the Effects of Accidental Loads* (1990).
- (e) Keenan and Meyers method using a suspended polycarbonate shield in windows and doors.
- (f) Global finite element method

#### 5.4.2 US Technical Manual 5-1300

The US design is based on toughened glass for a load duration of less than one second. The following gives design stress criteria:

% failure	toughened glass (psi)
< 1%	110 MN/m <sup>2</sup> (16000)
50%	160 MN/m <sup>2</sup> (23150)
> 99%	209 MN/m <sup>2</sup> (30300)

The US regulation recommends that the glass needed to resist the blast load (for toughened glass) must involve charge weight, stand offs and the static design resistance  $r_u$  of the selected glass pane at the design stress, using thin-plate large deflection concepts. Graphs and charts are included. Similar to the design of the frame to resist the equivalent static load  $r_u$  transmitted by the glass while sustaining it must have:

- (i) serviceability deflection limit  $\frac{1}{264}$  span or  $\frac{1}{8}$  in (3.2mm),
- (ii) a factor of safety of 1.65 on the yield stress,
- (iii) a factor of 2 on the fixings, and
- (iv) a value of load as if  $r_u$  were acting on the exposed frame

in order to achieve a probability of failure, i.e. cracking, of less than  $\frac{1}{1000}$  (in effect to attain survival with the glass uncracked and frame serviceable).

The US method uses simply charge weight, stand offs and frame load. The most popular pane is 1.55 m × 1.25 m. The following gives frame loads and stand off for this pane dimension:

Glass thickness (mm)	Stress (N/mm <sup>2</sup> )	Frame load* (kN/m <sup>2</sup> )	100 kg TNT @ stand off in metres
Toughened <sup>†</sup> (8)	110	25	85
Laminated toughened <sup>†</sup> (9.5)	110	25	85

\* The values are to be multiplied by 1.65 or 2.0 where appropriate as stated above.

<sup>†</sup> It should have a resistance 75% of the equivalent monolithic thickness.



### 5.4.3 Keenan and Meyers Method for Hardening Buildings

The main purpose of this method is to harden the envelope of buildings so that a full spectrum of protection is provided against blast, fragments and debris. Keenan and Meyers indicate the main objective is the use of suspended polycarbonate shield to increase the resistance capacity to tolerate increased blast loads. The Naval Civil Engineering Laboratory, Port Hueneme, California conducted blast load effects on glazing. The shield is made up of polycarbonate layers with a polyurethane or silicon interlayer. The shield is mounted in a steel frame and is suspended from two steel cables behind the window opening which are connected to the ceiling above. The glass in the glazed window is generally covered with plastic security film. Figure 5.18 to 5.20 show shield components for blast resistance and their available parameters.

#### 5.4.3.1 Explanatory Notes on Shield Design

- (a) Figure 5.18a shows a design chart prepared by the US Army Corp of Engineers for predicting incident blast overpressure  $P_i$  inside a room by a blast overpressure  $P_o$  outside. This involves parameters such as the opening area =  $A$  and  $A = ab$ ,  $P_i = 0.25 P_o$ .
- (b) Figure 5.18b gives a chart to reduce the value of  $P_i$  by a suspended polycarbonate shield behind the opening. This involves the positive pressure gap  $X_T$  needed for the shield to provide some prescribed reduction in  $P_i$ . The parameter  $X_T$  is the horizontal shield displacement,  $X$ , at time of zero overpressure,  $T$ , outside the building.

Additional pressure reduction

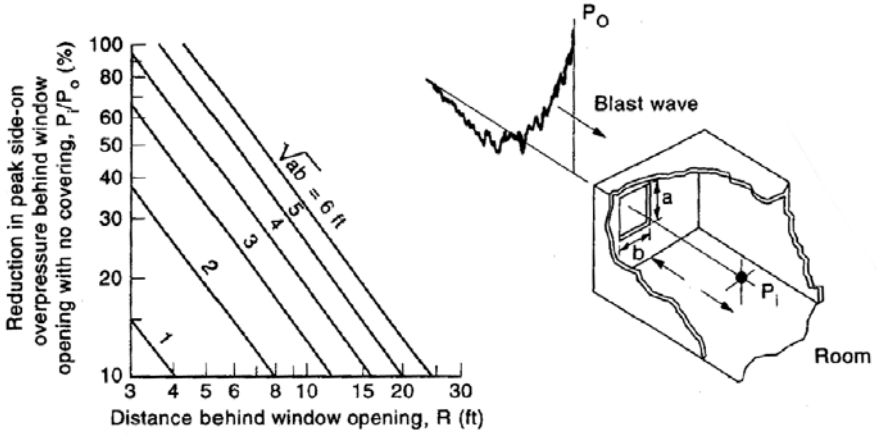
$$P_{\text{red}} = 1 - \frac{P_{\text{design}}}{P_i}$$

$$P_{\text{design}} = 2.4 \text{ psi} \quad (16.55 \text{ kN/m}^2)$$

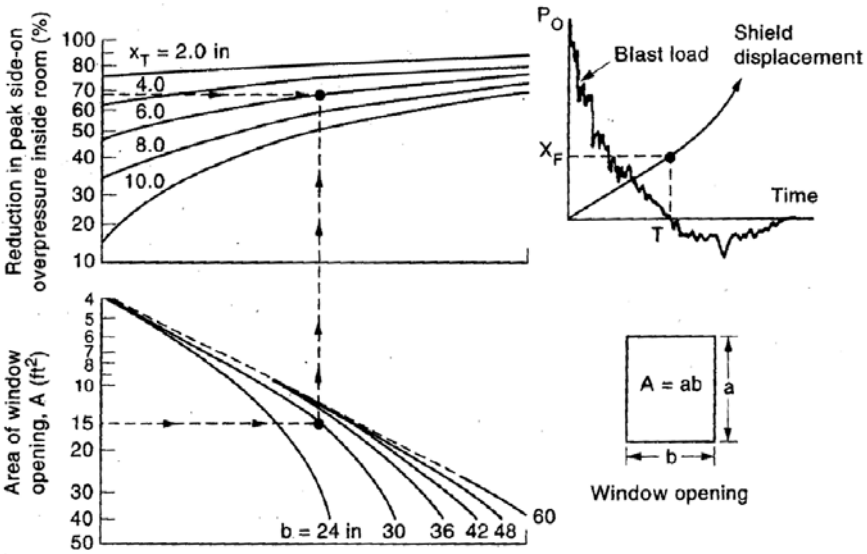
- (c) The shield weight or load (unit weight =  $\gamma$ ) is needed to achieve the prescribed value of the displacement  $X_T$ . A bomb at a stand-off distance  $R$  detonates. The bomb NEW ( $t = T$ ) will give the volume of  $X_T$  using the chart in Fig 5.18b. While knowing  $\gamma$ , it is easy to obtain the value  $\gamma A$ . The sequence for the path is to be found.
- (d) Figure 5.21 gives the design of the suspension cable, knowing the value of the cable force  $T_C$  and design stress  $F_C$  or  $F_S$ . Design diameter of the cable is therefore determined. A practical cable diameter available in the market is then chosen.

*Design Example: On Keenan and Meyers Method*

A terrorist bomb equivalent to 2000 lbf (8.896 kN) detonates 6.10 m (20 ft) from a building having glass windows. Using the Keenan and Meyers method,



(a)



(b)

Fig. 5.18. (a) Peak-side overpressure inside room compared to peak overpressure outside window opening with no cover; (b) Reduction in peak overpressure inside room caused by suspended polycarbonate shield

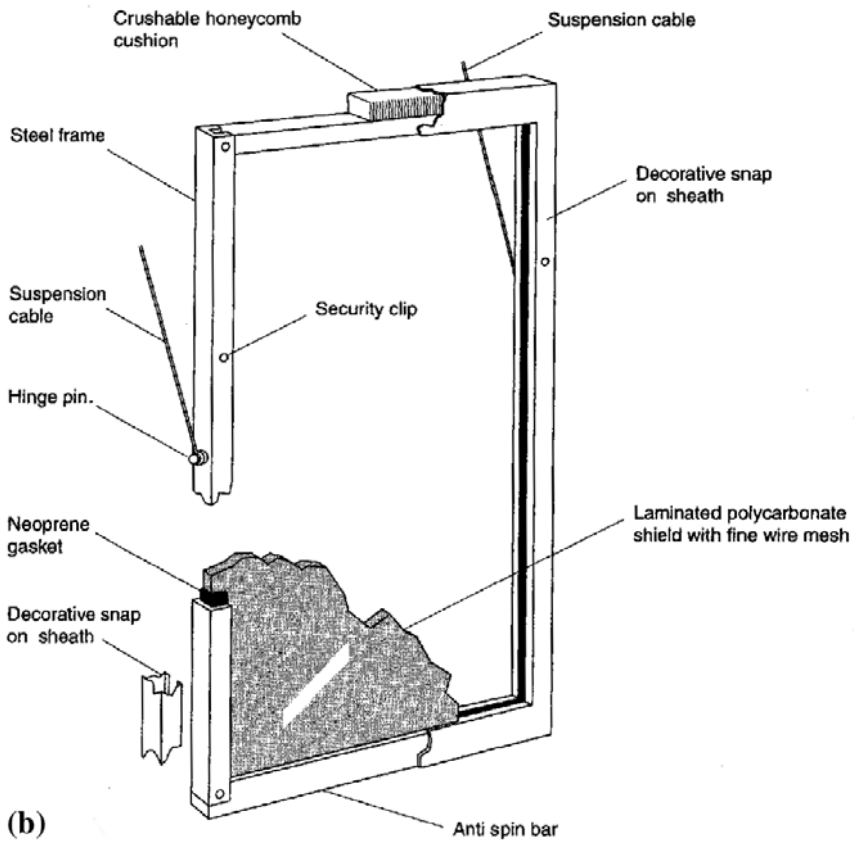
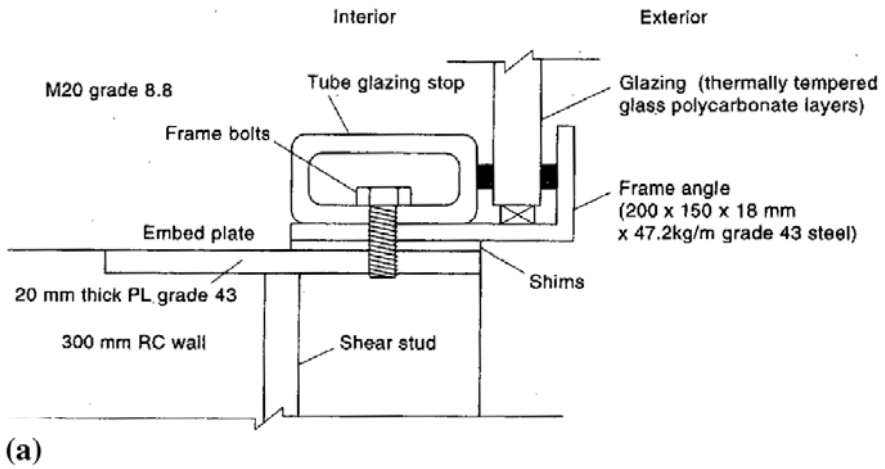


Fig. 5.19. (a) Generic-blast window glazing and frame detail; (b) Shield components for blast testing according to Keenan and Meyers

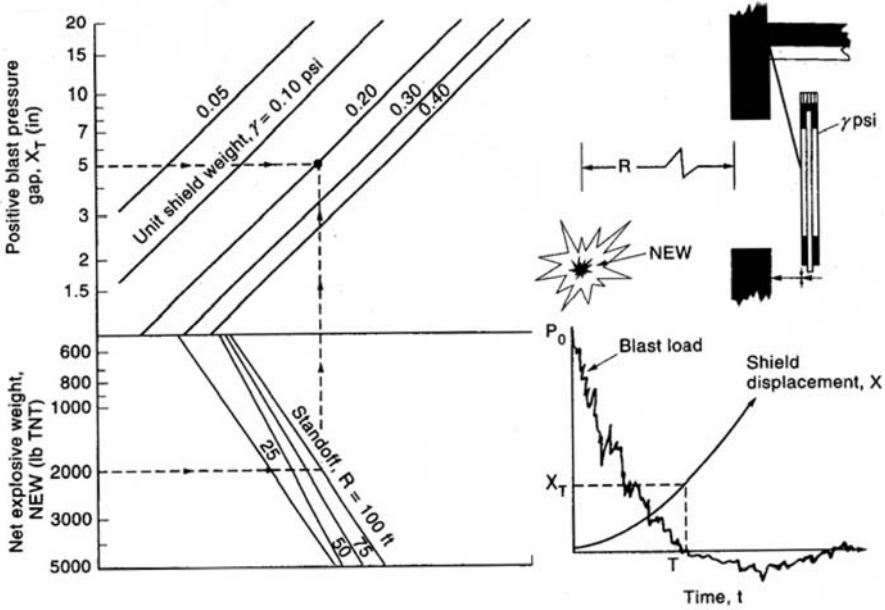


Fig. 5.20. Design criteria for shield weight

design a suspended polycarbonate shield to protect glass from having fragments. Use Keenan and Meyers graphs and the following data:

explosion at the exterior face as an incident blast overpressure  
 $= 172.369 \text{ kN/m}^2 (25 \text{ psi})$

window dimension/opening =  $1.83 \text{ m} \times 0.762 \text{ m}$

work space located behind window ( $R$ ) =  $2.38 \text{ m}$

maximum incident blast pressure limitation =  $16.55 \text{ kN/m}^2 (2.4 \text{ psi})$

$P_i = 0.25 \times 172.369 = 43.1 \text{ kN/m}^2 > 16.55 \text{ kN/m}^2$

window area  $A = 1.395 \text{ m}^2$

cable tensile force =  $T_C$  to determine

$P_o$  = leaking pressure is related as

$$P_i = 0.25P_o$$

$$P_{\text{red}} = \text{pressure reduction} = 1 - \frac{P_{\text{design}}}{P_i}$$

$$P_{\text{design}} = 2.4 \text{ psi} = 16.55 \text{ kN/m}^2$$

$$f_s = f_C = \text{cable design stress}$$

$$= 100000 \text{ lbf/in}^2 (\text{psi}) = 689.5 \text{ MN/m}^2$$

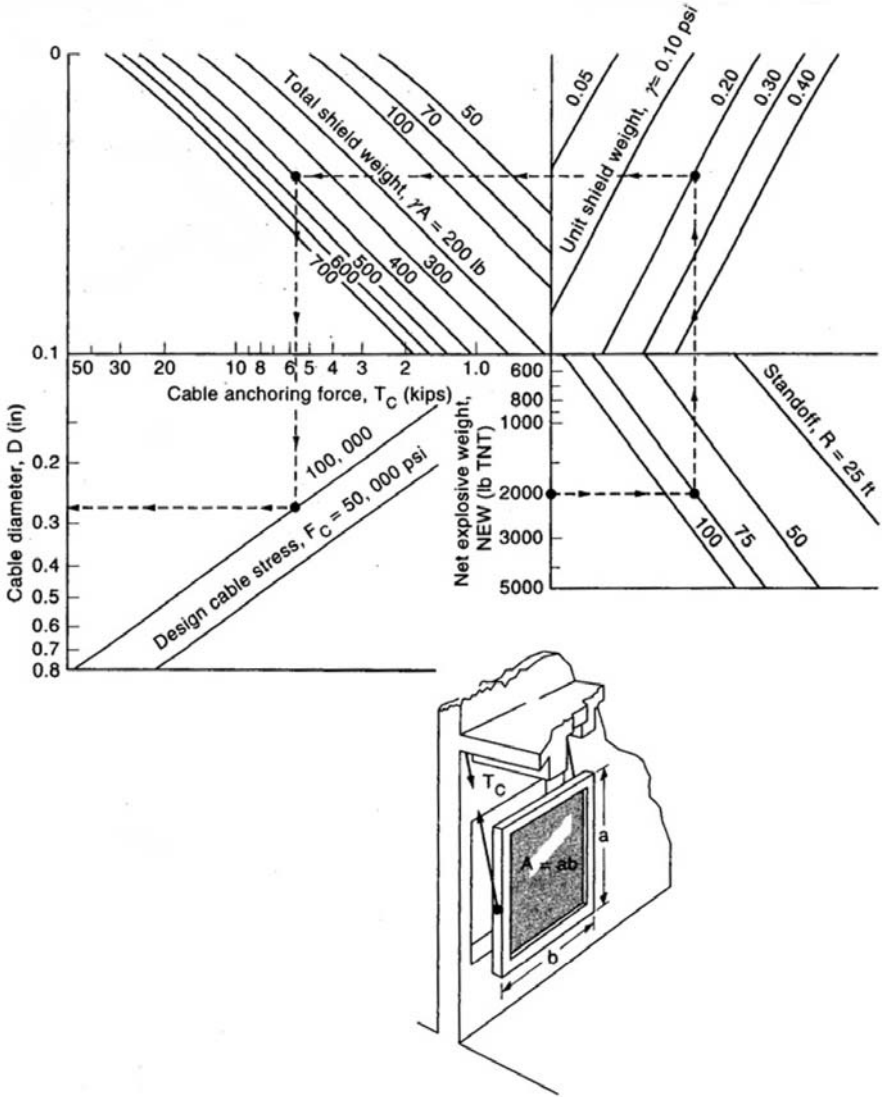


Fig. 5.21. Design criteria for cable anchoring force and cable diameter

*Step 1*

If no shield exists

$$a = 1.83 \text{ m}$$

$$b = 0.762 \text{ m}$$

$$\sqrt{ab} = \sqrt{1.83 \times 0.762} = 1.181 \text{ m}$$

$$R = 2.38 \text{ m}$$

$$\frac{P_i}{P_o} = 25\%$$

Using Fig. 5.18, the value

$$\begin{aligned} P_i &= 0.25P_o \\ &= 0.25 \times 172.369 \\ &= 43.1 \text{ kN/m}^2 \\ &> 16.55 \text{ kN/m}^2 \quad (2.4 \text{ psi}) \end{aligned}$$

The shield is designed to provide required mitigation.

*Step 2*

Controlling maximum overpressure in a protected room.

Use Fig. 5.18 for maximum blast gap  $X_T$  for the shield loaded during time  $T$  by a positive blast pressure.

Additional pressure reduction within the interior room is:

$$1 - \frac{P_{\text{design}}}{P_i} = 1 - \left( \frac{16.55}{43.1} \right) = 0.62, \quad \text{i.e. } 62\%$$

From Fig. 5.18  $A = 1.395 \text{ m}^2$  and the smaller dimension  $b = 0.762 \text{ m}$ . Read in the upper panel  $X_T$  for a 62% reduction:

$$X_T = 127 \text{ mm} \quad \text{or} \quad 0.127 \text{ m}$$

A maximum bottom swing of the shield of 0.127 m will probably contain glass fragments. In practice fragment hazards affect the design.

*Step 3*

Weight of the shield per square metre  $\gamma$  to control the effects of the blast.

From Fig. 5.18 a net explosive load of  $8.896 \text{ kN} = \text{NEW}$  equivalent to the net explosive weight and a stand-off distance  $R = 2.38 \text{ m}$ , gives a value of  $\gamma = 1.38 \text{ kN/m}^2$ .

*Step 4*

Cable size and the load with  $\gamma = 1.38 \text{ kN/m}^2$ .

Calculate the load on the shield

$$\gamma A = 1.38 \times 1.395 = 1.924 \text{ kN}$$

Read across to ' $\gamma A$ ' and note each cable force  $T_C$  for  $\gamma A = 1.924 \text{ kN}$ .

From Fig. 5.21

$$T_C = \text{cable force} = 25 \text{ kN}$$

Cable diameter for  $f_S$  design stress  $689.5 \text{ MN/m}^2$  (100000 psi) = 7 mm diameter.

Therefore, adopt 10 mm HTS bars.

*Stand-off Distances R*

Small packets to suitcases	10–30 m
cars	60 m
vans and lorries	150 m

The above criteria were used throughout for the 150 samples analysed. Panels having areas  $0.6 \text{ m}^2$ ,  $1.934 \text{ m}^2$ ,  $2 \text{ m}^2$  and  $3 \text{ m}^2$  were chosen. The finite element mesh scheme was kept the same for all these windows; only sizes and material properties and loads due to blast effects were varied. A 30 m stand-off distance was adopted for all cases of hidden explosives in cars. The distance chosen for vans and lorries was between 60 and 150 m.

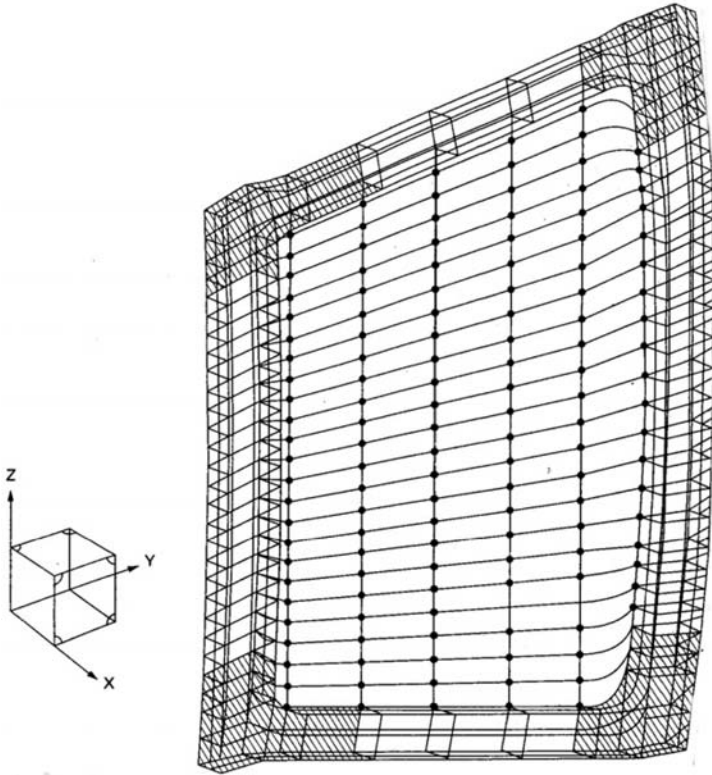
*Finite Element Analysis Parameters*

The following lists provide the thickness ( $t$ ) and area ( $A$ ) dimensions of the glazing used in the analysis. The stand-off distance is 30 m.

Single glazing		Double glazing	
$t$ (mm)	$A$ ( $\text{m}^2$ ) max	$t$ (mm)	$A$ ( $\text{m}^2$ ) max
4	0.2	4 + 4	0.6
6	1.8	5 + 5	1.2
10	3.3	6 + 6	2.5
12	5.0	10 + 10	5.0

Loads up to elastic conditions =  $1.5 \text{ kN/m}^2$  are permitted and in addition:

For window pane dimensions  $1.55 \text{ m} \times 1.25 \text{ m}$ , i.e.  $A = 1.934 \text{ m}^2$  (8 mm toughened glass ( $T^*$ ) and 10 mm laminated glass ( $L^*$ ))



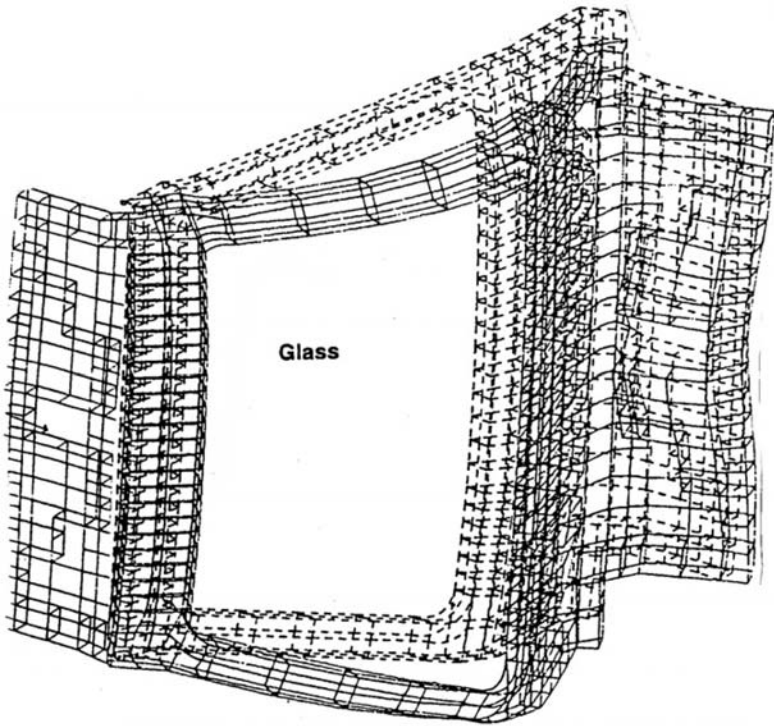
**Fig. 5.22.** Finite element mesh

$$\begin{aligned}
 &\text{frame loads} \times 2.0 \text{ (SF* = safety factor)} = 50 \text{ kN/m}^2 \\
 &\text{equivalent static yield stress} = 1.65 \times 110 = 181.5 \text{ N/mm}^2 \text{ for the frame} \\
 &\text{deflection limitation} \neq \frac{1}{264} \text{ span} \\
 &\text{the average edge reaction at edge nodes (kN/m)} \\
 &\quad \text{(equivalent ultimate static load)} \\
 &= \frac{\text{equivalent ultimate static load} \times \text{area}}{\text{perimeter of the panel}}
 \end{aligned}$$

*Global Finite Element Analysis of Doors and Windows*

Windows and doors are important functional elements, but they represent weak links in the blast resistant design. The blast resistant design for doors is usually accomplished with a single degree of freedom model. This is due to the fact that in many cases the resistance of the door matches that of the wall in which it is located. An important consideration in the door analysis is the life safety egress requirement. The simplest way to treat the door is as a plate supported around its frame. In this case the rebound phase of the





**Fig. 5.23.** Mode shape with glass window panel

blast response is sometimes important to keep the facility secure following a blast event.

Windows with certain products can resist blast pressures of certain magnitudes. The adaption of window products to resist blast pressure or to minimize the amount of fenestration, plays a great part in controlling fragments of flying glass.

A generic blast resistant window system has been shown in earlier accounts. A reference is made to the Appendix for finite element literature. Figure 5.22 shows a typical finite mesh scheme for window and window steel/aluminium frame design. A typical damaged window system is demonstrated in Fig. 5.23 under the blast effects from the explosive SEMTEX. A layered polycarbonate system described earlier was not used in this case. The rolled-steel frame was anchored to the wall. Toughened and laminated glass was used and their material properties form an input to the finite element analysis. These data are given in the next section.

### 5.4.3.2 Finite Element Analysis of the Windows

A 3-D finite element with four nodes on each face is considered.

#### *Material Properties*

Glass:

$$\begin{aligned}
 E &= 61 \text{ GN/m}^2 \\
 \nu &= 0.25 \\
 t &= \text{varies from 6 mm to 12 mm} \\
 \rho &= \text{density} = 2224 \text{ kg/m}^3
 \end{aligned}$$

Steel frame and fixings:

$$\begin{aligned}
 E &= 209 \text{ GN/m}^2 \\
 \nu &= 0.3 \\
 t &= \text{varies from 0.8 mm up} \\
 \rho &= 7800 \text{ kg/m}^3
 \end{aligned}$$

Minimum load to satisfy the protective system criteria for a minimum centrally applied load without:

- (a) fracturing       $\rightarrow$   $\left[ \begin{array}{l} = 1.35 \text{ kN if any length is 900 mm or} \\ = 1.1 \text{ kN if under 900 mm length} \end{array} \right.$   
 (b) deflecting  
 (c) permanent distortion  
 (d) displacement of the whole system.

#### *Nodes and Elements*

The window is made up of a finite element mesh:

Glass:	four-noded solid element isoparametric	
	constant thickness and single layer	115 mm
Frame elements:	four-noded solid element isoparametric	138 mm
	four-noded trapezoidal	84 mm
	four-noded triangular	84 mm
	nodes	4300 mm

Various case studies involving blast resistant glass windows or pans have been examined using 3D F.E. Standard Rc30 is taken into consideration. A graph is plotted for glass thicknesses versus an equivalent static loads representing blast loads for quick solutions available to the designers. However for accurate analysis, a comprehensive numerical method of the designer's choice shall be considered.

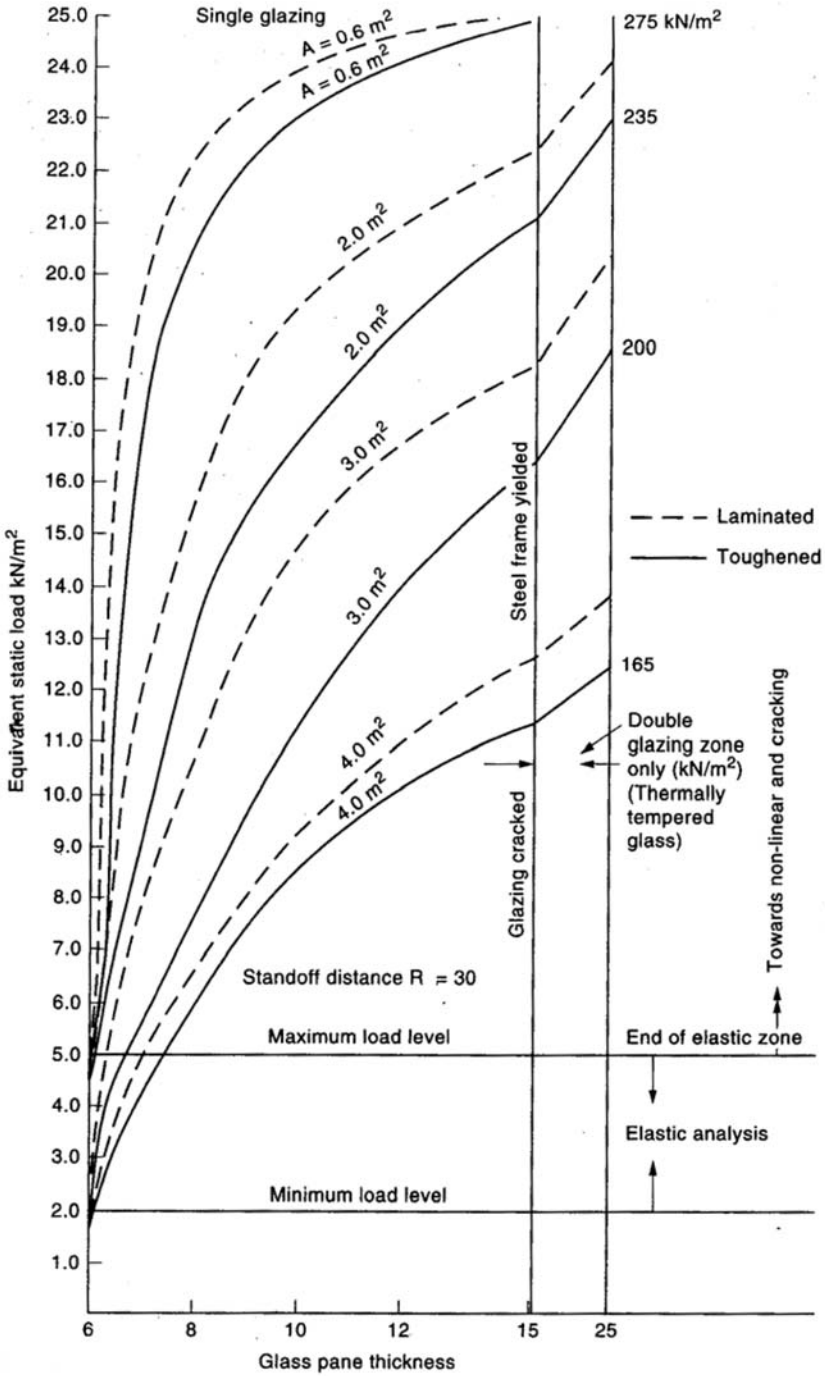


Fig. 5.24. Blast resistant glass window panes: case studies

## Reference

- [5.1] Baker et al. (1983) Explosion hazards and evaluation. Elsevier Scientific Publications, Amsterdam

# 6 Contact or Gap Elements for Blast-Fire Structural Interaction

## Introduction

The contact or gap elements are the interface elements in engineering disciplines. In soil-structure interaction in blast-and fire these elements play a very important role in bringing about close relations between various structural elements under stress and between structural and other elements of a medium. In concrete mechanics example, bond between concrete and reinforcement, aggregate interlock in discrete cracks, friction in concrete, steel and aluminium connections (rigid and semi rigid), structural composites, aircraft/missile impact on vital installations and many other vital cases. This section reviews some methods which are well known and are recommended for static, dynamic impact and blast load analysis. Some are listed below:

- (a) “Bangash T Contact-Element” using Finite Discrete Element Analysis.
- (b) Hallquist et al. Method
- (c) DELFT Interface Friction Type Element
- (d) ANSYS Contact Elements
- (e) ABAQUS Gap Contact Elements
- (f) LS-DYNA Gap/Contact Elements

## 6.1 Introduction to Bangash T. Contact Elements

Discrete Element Method relies on the free interaction of a large number of separate and unconnected bodies. Each body can then be discretized using the finite element method. The number of discrete elements, their density and their shape will change in time.

Various contact detection algorithms are suited only to particular problems such as quasi-static or dense packing. Most algorithms are suited to quasi-static problems where the relative motion of the bodies is restricted. Dynamic problems, however, involve a large number of bodies with no significant restriction on their motion. This will inevitably increase the CPU time,  $T$  (total detection time), generated by such algorithms, as contact detection will now be performed a number of times as opposed to just the single occasion for quasi-static problems.

Hence the optimum algorithm would need to minimise the CPU time and memory requirements,  $M$ , in terms of the number of elements and their packing density. It will also need to be flexible enough to account for the change in  $M$  and  $T$  with packing density.

Most of the algorithms referred to above have total detection time  $T$  directly proportional to

$$T \propto N \ln(N) \tag{6.1}$$

where  $N$  is the total number of discrete elements.

In the case of the NBS algorithm the time  $T$  is found to be directly proportional to the number of bodies,  $N$ .

$$T \propto N \tag{6.2}$$

The memory requirements are

$$M \propto N \frac{1}{\sqrt[2]{\rho}} \quad \text{for 2D} \tag{6.3}$$

$$M \propto N \frac{1}{\sqrt[3]{\rho}} \quad \text{for 3D} \tag{6.4}$$

where  $\rho$  is the packing density.

The NBS algorithm is equally effective for dense and loose packing, while CPU time is not influenced by packing density. For example in the case of 3D a 125 fold decrease in packing gives a less than 5 fold increase in memory requirement.

This sections presents the NBS algorithm as applied to problems of a multidimensional nature. Examples are run on a medium size workstation for purposes of algorithm demonstration.

## 6.2 NBS Contact Detection for Problems of a 2D Nature

The reader is referred to [6.1], where a more detailed delineation of this topic is presented.

In this instance the system will consist of a number of discs, which represent the discrete element system, within a defined rectangular shape. The rectangle is then divided into smaller shapes of dimension  $ncelx$  by  $ncely$ .

Each disc will have its centre within one of the smaller rectangular shapes (Fig. 6.1).

Each of the numbered discs is mapped

$$E = \{0, 1, 2, 3, \dots N\} \tag{6.5}$$

to the set of cells

$$C = \left\{ \begin{array}{cccc} (0, 0) & (0, 1) & \dots & (0, ncely - 1) \\ (1, 0) & (1, 0) & \dots & (1, ncely - 1) \\ (ncelx - 1, 0) & (ncelx - 1, 1) & \dots & (ncelx - 1, ncely - 1) \end{array} \right\} \tag{6.6}$$

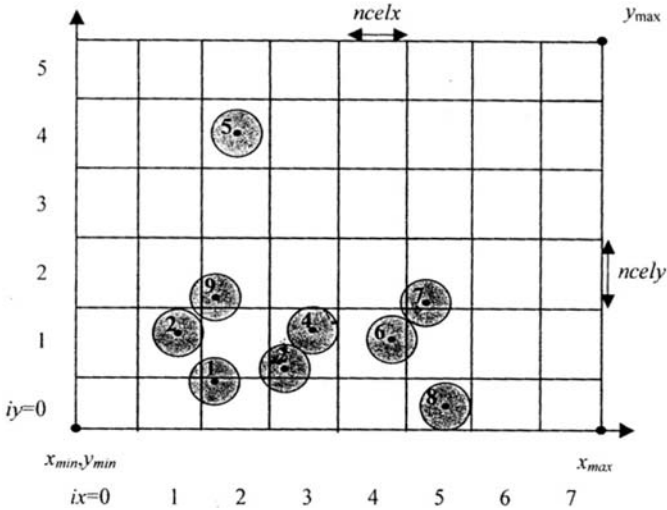


Fig. 6.1. Mapping of discs onto cells

For example the cell  $(ix, iy)$  may have disc with centre coordinates  $(x, y)$ . Therefore from Fig. 6.1 we may say disc 5 is assigned to cell (2,4). The discs are numbered and then assigned to a particular row and then to a particular column of cells.

Incorporating the use of linked lists reduces memory requirements. Firstly each disc is looped over in ascending numerical order and it's integerised  $iy$  coordinate is found. Therefore from Fig. 6.1 we can see the disc 0 is the first to be found when  $iy = 1$ . The next disc found will be disc 2 and then disc 4 followed by disc 6. At each disc is found, it will push along the previous disc as shown in Fig. 6.2. Here only the sequence for  $iy = 1$  is shown. Such lists will further be referred to as  $Y$  lists.

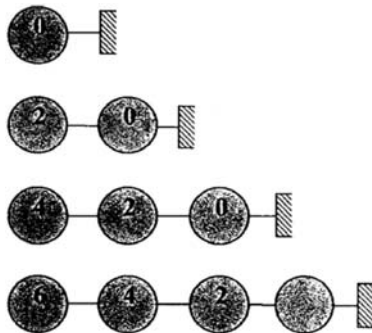


Fig. 6.2. List formation sequence for  $iy = 1$

heady		nexty
0	0	-1
6	1	-1
-1	2	0
	3	-1
-1	4	15
-1	5	1
-1	6	4

Fig. 6.3. Numerical representation of single dimension arrays used for the 2D case

The negative one indicates the end of the list. This process is effectuated by the use of two single dimension arrays as shown in Fig. 6.3.

The heady array is  $ncely$  large and the nexty array is  $N$  large, where  $ncely$  is the number of cells in the  $y$  direction. In the case of  $iy = 1$  the head array begins as  $heady[1] = 6$ . The nexty array represents the next disc in the list for  $iy = 1$ . Therefore it can be read as  $nexty[6] = 4$ ,  $nexty[4] = 2$ ,  $nexty[2] = 0$ , and  $nexty[0] = -1$ .

A loop over each particular  $Y$  list is now performed in order to create a 2D  $(X, Y)$  list by checking it's integerised  $ix$  coordinate. This is shown in Fig. 6.4. Each disc for the  $Y_1$  list is placed by it's integerised  $ix$  coordinate thus creating a 2D list as illustrated in Fig. 6.4.

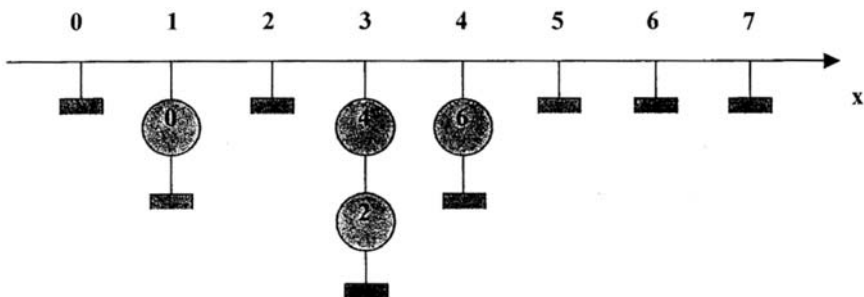


Fig. 6.4. 2D  $(X, Y)$  list



As no loops over cells is carried out we can assume that CPU time required is not a function of  $ncelx$  or  $ncely$  and hence not a function of packing density  $\rho$ .

Contact detection is carried out where the cell has one or more discs mapped to it. A check of the neighbouring cells for contact detection is then carried out. Once again in all operations involved  $T$  is not a function of  $ncelx$  or  $ncely$ .

As no loop over the cells is performed at any stage we can assume CPU time,  $T$  to be directly proportional to the number of discs,  $N$ .

### 6.3 NBS Contact Detection Algorithm for 3D Problems

The NBS algorithm for three dimensions replaces the discs with spheres in a finite defined cubic system as shown in Fig. 6.5. The boundaries are defined by  $x_{min}$ ,  $y_{min}$ ,  $z_{min}$ ,  $x_{max}$ ,  $y_{max}$ , and  $z_{max}$ . The centres of each sphere will never fall outside these boundaries. Once again the NBS algorithm will find spheres with distances between their closest points less than or equal to zero, i.e. they touch or they overlap (Fig. 6.5).

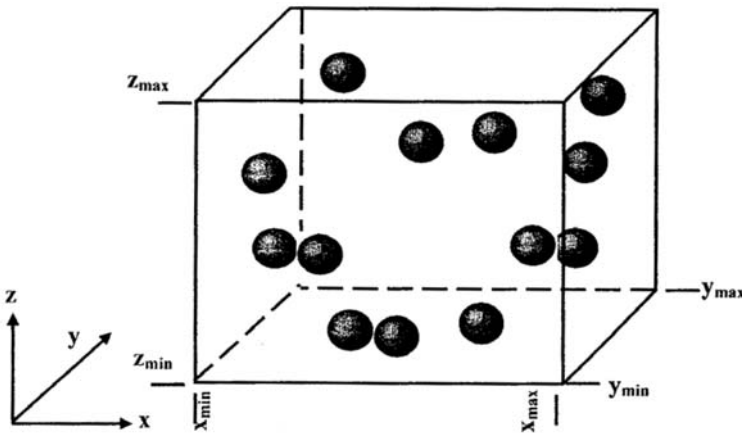


Fig. 6.5. 3D contact detection problem

### 6.4 3D Implementation into the Combined FEM/DEM Method

The NBS algorithm as has been shown relies upon space decomposition. In this case the cube is subdivided into smaller cubes of dimension  $ncelx$  by  $ncely$  by  $ncelz$ . Each sphere is identified by an integer number  $\{0, 1, 2, 3, \dots, N - 1\}$ . Similarly each cell is recognised by integer co-ordinates  $(ix, iy, iz)$ ,

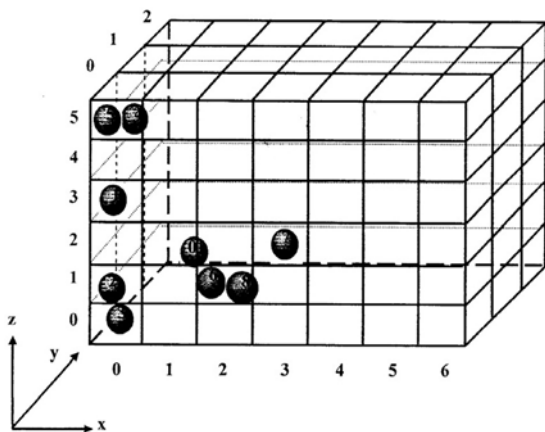


Fig. 6.6. Mapping of spheres on to cubic cells

where  $ix = 0, 1, 2, \dots, ncelx - 1$  and  $iy = 0, 1, 2, \dots, ncely - 1$  and  $iz = 0, 1, 2, \dots, ncelz - 1$ .  $ncelx - 1$ ,  $ncely - 1$ , and  $ncelz - 1$  are the maximum number of cubes in the  $x$ ,  $y$  and  $z$  directions.

$$ncelx = \frac{x_{max} - x_{min}}{2r} \tag{6.7}$$

$$ncely = \frac{y_{max} - y_{min}}{2r} \tag{6.8}$$

$$ncelz = \frac{z_{max} - z_{min}}{2r} \tag{6.9}$$

Mapping from the set of spheres

$$E = \{0, 1, 2, 3, \dots, N\} \tag{6.10}$$

to the set of cubes

$$C = \left\{ \begin{array}{llll} (0, 0, 0) & (0, 1, 0) & \dots & (0, ncely - 1, ncelz - 1) \\ (1, 0, 0) & (1, 0, 0) & \dots & (1, ncely - 1, ncelz - 1) \\ (ncelx - 1, 0, 0) & (ncelx - 1, 1, 1) & \dots & (ncelx - 1, ncely - 1, ncelz - 1) \end{array} \right\} \tag{6.11}$$

is defined in such a way that each discrete element is assigned to one and only one cell. For instance, the sphere with co-ordinates  $(x, y, z)$  is assigned 0 the cubic cell  $(ix, iy, iz)$ , where

$$ix = Int \left( \frac{x - x_{min}}{2r} \right) \tag{6.12}$$

$$iy = Int \left( \frac{y - y_{min}}{2r} \right) \tag{6.13}$$

$$iz = Int \left( \frac{z - z_{min}}{2r} \right) \tag{6.14}$$

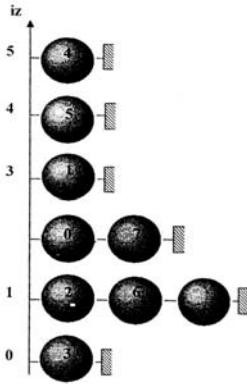


Fig. 6.7. Linked lists,  $Z_i$

$iz$ ,  $iy$  and  $ix$  are said to be integerised relative co-ordinates, here on referred to as integerised co-ordinates. For example sphere eight can be seen to map on to layer 1, column 3 and cell (3,0,1) (Fig. 6.6).

Mapping may also be represented by a 3D array

$$ncel = ncelx.ncely.ncelz \tag{6.15}$$

This undoubtedly would require increased memory, especially for cases where the number of spheres is thinly spread over the cubic space.

This problem is solved, as in the two dimensional case, by using linked lists. Firstly the spheres are mapped on to layers in the  $z$  direction. For each layer in the  $z$  direction a linked list  $iz$  is constructed. For example layer  $iz = 2$  is referred to as  $Z_2$ . This is shown in Fig. 6.7.

A loop over each of the spheres is used to place them on to their respective  $z$  layer by ascertaining the integerised  $iz$  coordinate.. For example when  $iz = 1$  i.e.  $Z_1$ , the sphere 8 is first placed and then pushed along by sphere 6 and further pushed along by sphere 2 once found to lie on this layer.

This done using two 1D arrays which we will call  $headz$  and  $nextz$  as shown in Fig. 6.8. Hence for  $iz = 1$   $headz[1] = 2$ ,  $nextz[2] = 6$ ,  $nextz[6] = 8$  and  $nextz[8] = -1$ . Similar analogous methods are used to form  $X, Y$  and lists for any other dimension.

Loops over the non empty  $Z$  lists are done to obtain a list of spheres in the  $y$  direction –  $Y$  list. These will be placed according to their integerised  $iy$  co-ordinate. A loop over the non empty  $Y$  lists is next performed to place each sphere onto an  $X$  list by using its  $ix$  value. By this procedure each individual sphere is placed onto a list in each of the axis directions.

Once the  $X, Y$  and  $Z$  or  $N$  then the head and next arrays are reset to  $-1$  indicating no spheres present. The subsequent layer is then formed. It can be seen no loop over the cubic cells is carried out and so the CPU time is not a function of  $ncelx, ncely$  or  $ncelz$  and so is not a function of the packing density  $\rho$ .

headz		nextz
-1	0	-1
2	1	-1
-1	2	6
-1	3	-1
-1	4	2
-1	5	4
-1	6	8
-1	7	-1
-1	8	-1

Fig. 6.8. Formation of linked list  $Z_i$

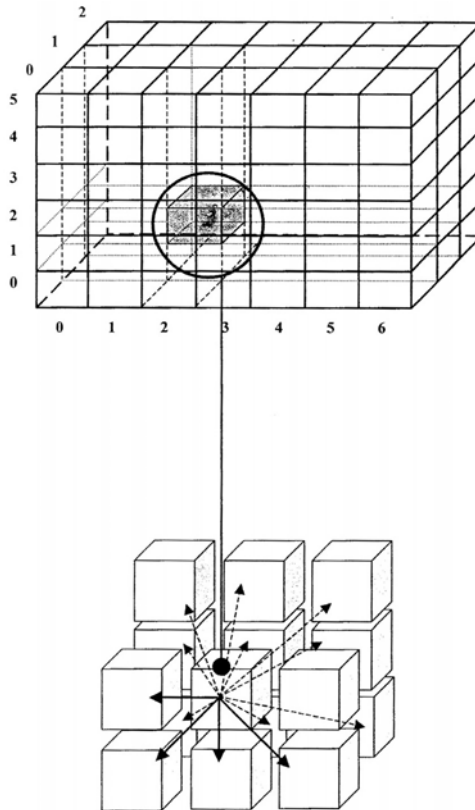


Fig. 6.9. Contact detection in neighbouring cells

## 6.5 NBS Algorithm – Detection of Contact

Each sphere can only be mapped on to a single cubic cell and only neighbouring cells can have any contact. The next stage is to detect contact between the spheres. Once the sphere has been mapped it is marked so that the check against neighbouring cells is not repeated in the loop.

The next step is to search for contacts with spheres in surrounding cubic cells. For example (0,0,2) will check itself against cells (0,0,2), (0,0,1), (1,0,1) and (2,0,1). It will also check itself against all the cells directly beneath each of it's neighbouring cells lying on the same layer.

## 6.6 3D NBS Algorithm – Implementation

The code is able to identify which particular nodes are in contact with each other. A flow chart of the algorithm is shown in Fig. 6.10.

This algorithm ensures no cell is checked twice, thus keeping CPU time to an optimum.

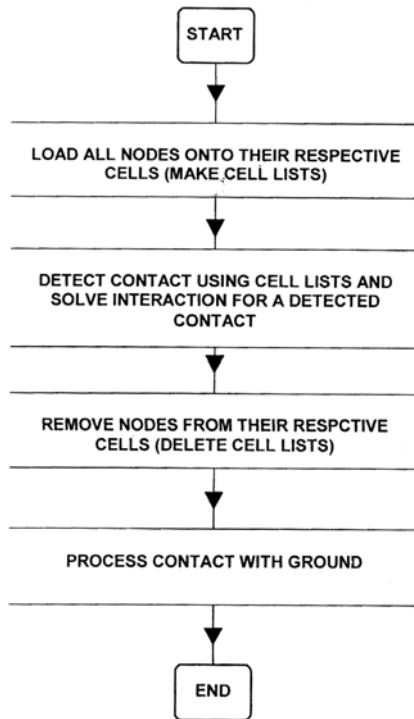


Fig. 6.10. Flow chart of contact algorithm

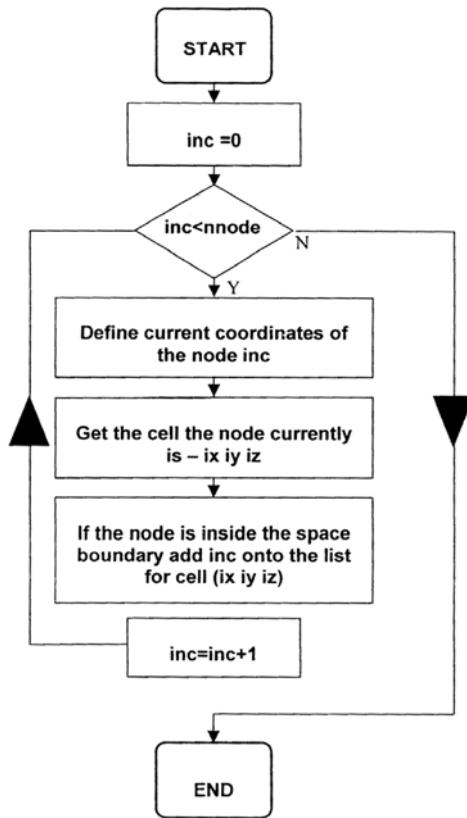


Fig. 6.11. Flow chart detailing the procedure for creating nodal lists for each cell

The algorithm, next processes the interaction between the “contactor” node and the “target” node, once they have been found.

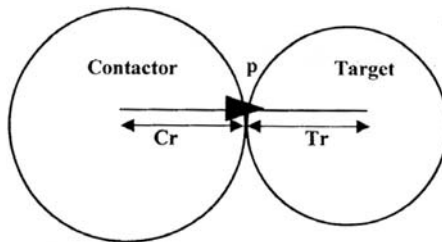


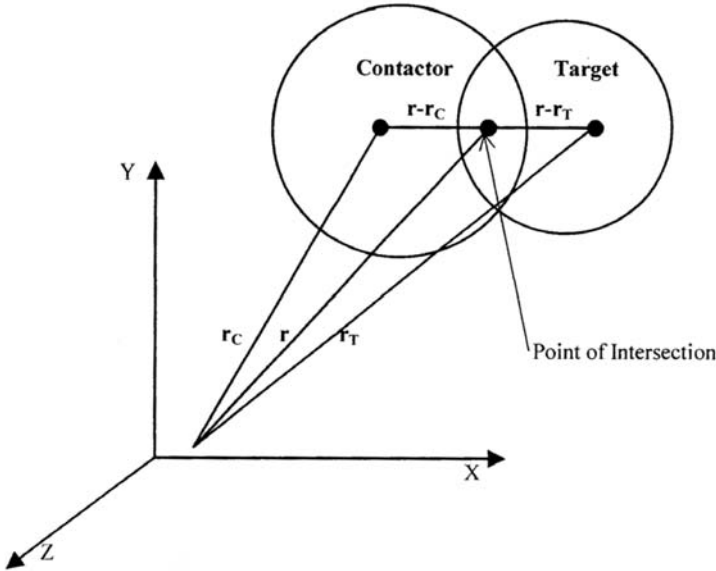
Fig. 6.12. Contact between contactor and target node

The vector  $p$  is found by adding the vector radii of the two nodes.

$$p = C_r + T_r \tag{6.16}$$

It is then transformed into a unit vector.

Contact will occur if there is overlap between the two nodes and  $\mathbf{p}$  is less than the sum of the vector radii.



**Fig. 6.13.** Point of intersection between contacting nodes

The  $\mathbf{r}$  vector at the point of intersection is obtained from the vectors  $\mathbf{r}_C$  and  $\mathbf{r}_T$ . The component of rotational velocity for both nodes contributing to contact is obtained by cross product of the rotational velocity and the respective  $\mathbf{r}$  vector. This is shown in (6.17).

$$\mathbf{h}_C = \boldsymbol{\omega} \times (\mathbf{r} - \mathbf{r}_C) \tag{6.17}$$

A similar equation applies for the target.

$$\mathbf{h}_T = \boldsymbol{\omega} \times (\mathbf{r} - \mathbf{r}_T) \tag{6.18}$$

These components are then combined with the translational velocities to obtain the relative velocities in the  $x$ ,  $y$  and  $z$  directions (6.19).

$$\mathbf{v} = \mathbf{h}_C + \mathbf{v}_C - \mathbf{h}_T - \mathbf{v}_T \tag{6.19}$$

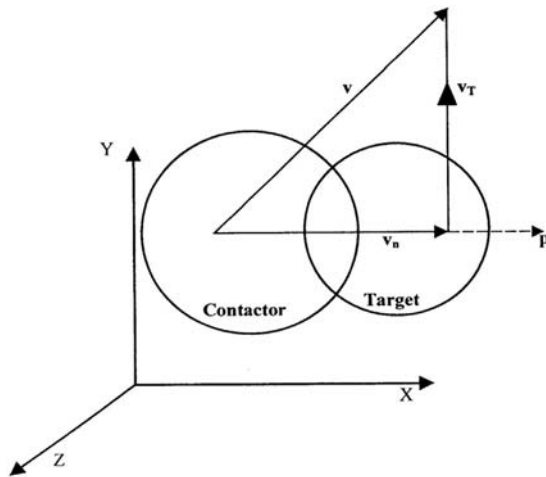
Dot product between the relative velocities and the unit vector  $\mathbf{p}$  will give axial component of velocity in the direction of  $\mathbf{p}$ ,  $\mathbf{v}_n$ .

$$\mathbf{v}_n = \mathbf{v} \cdot \mathbf{p} \tag{6.20}$$

The tangential velocity,  $\mathbf{v}_T$  in the  $x$ ,  $y$  and  $z$  directions is found from

$$\mathbf{v}_T = \mathbf{v} - \mathbf{v}_n \cdot \mathbf{p} \tag{6.21}$$

The next step is to obtain the frictional and normal forces ( $\mathbf{f}_f$  and  $\mathbf{f}_n$  respectively), from the penalty function method[].

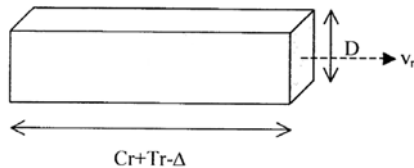


**Fig. 6.14.** Tangential and axial components of relative velocity

The penalty function method in simple form is

$$f = \alpha \times \Delta \tag{6.22}$$

where  $\Delta$  is the overlap. In our case let us assume the overlapping spheres to be represented by a cuboid.



**Fig. 6.15.** Cuboid representation of contacting spheres

Where

$$D = Cr + Tr \tag{6.23}$$

Assuming the overlap is small the force is easily calculated as

$$f = EAD \tag{6.24}$$

The damped force is calculated as

$$f_d = c\xi D\sqrt{km} v_n \tag{6.25}$$

However we know

$$\omega = \sqrt{\frac{k}{m}} \tag{6.26}$$

and



$$k = \frac{1}{D} D^2 E = DE \quad (\text{if the displacement is } 1)$$

and

$$c = 2m\omega$$

$$f_d = 2\xi\sqrt{DEm} \tag{6.27}$$

Therefore in our case  $\alpha$  will be

$$\alpha = \tag{6.28}$$

The normal force is multiplied by  $\mathbf{p}$  to give it direction. The friction force is multiplied by  $\mathbf{v}_T$  to obtain it's direction. The result is then combined to obtain the force vector  $\mathbf{f}$ .

$$\mathbf{f} = \mathbf{f}_n \cdot \mathbf{p} - \mathbf{f}_f \cdot \mathbf{v} \tag{6.29}$$

The contribution of each node to the moment are then found by Cross product of  $\mathbf{f}$  and  $\mathbf{r}$ .

$$\mathbf{M}_{tC} = \mathbf{f} \times (\mathbf{r} - \mathbf{r}_{Cr})$$

$$\mathbf{M}_{tT} = \mathbf{f} \times (\mathbf{r} - \mathbf{r}_{Tr}) \tag{6.30}$$

The resulting  $\mathbf{M}$  and  $\mathbf{f}$  vectors are then added to the applied moments and forces respectively to update the global force and moment vectors.

The procedure is illustrated in the flow charts of Figs. 6.16 and 6.17.

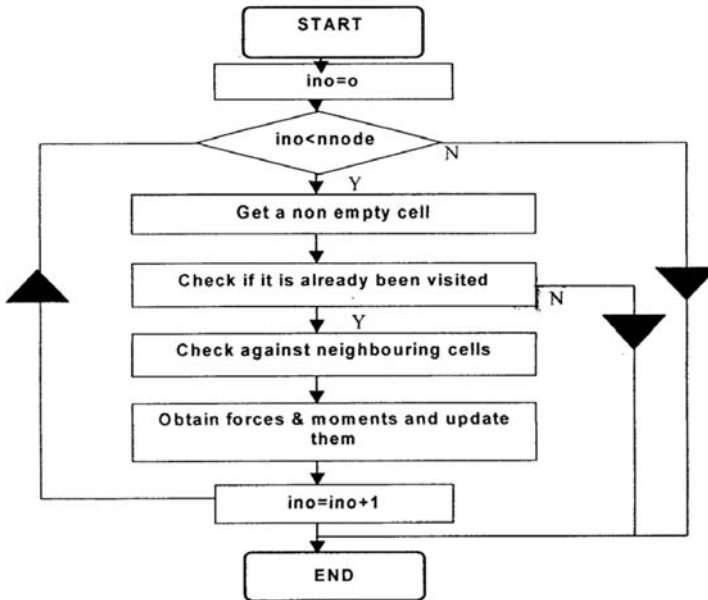
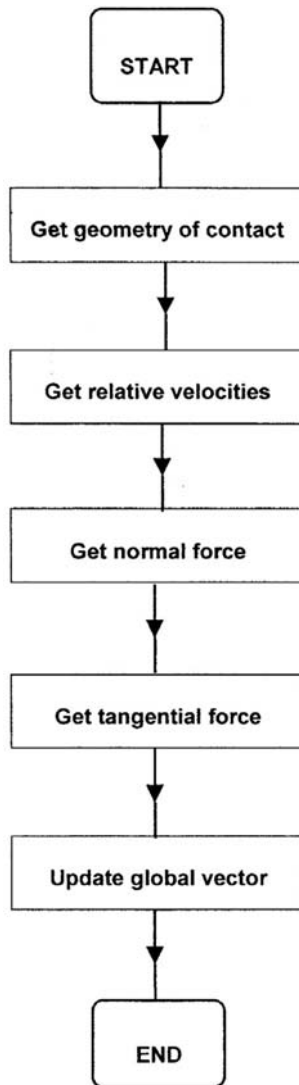


Fig. 6.16. Detecting contact between spheres



**Fig. 6.17.** Procedure to update global force and moment vector

At this point contact with the wall of the box needs to be considered. To do this the lists for each cell must first be deleted as shown in Fig. 6.18.

In the case of contact with the the box wall the node is now regarded as the target. A similar procedure, as outlined before, is followed to obtain the friction and normal forces. A force vector is then obtained using (6.29). The moments are obtained using the second equation of (6.30). The global target force and moment vector is then updated.

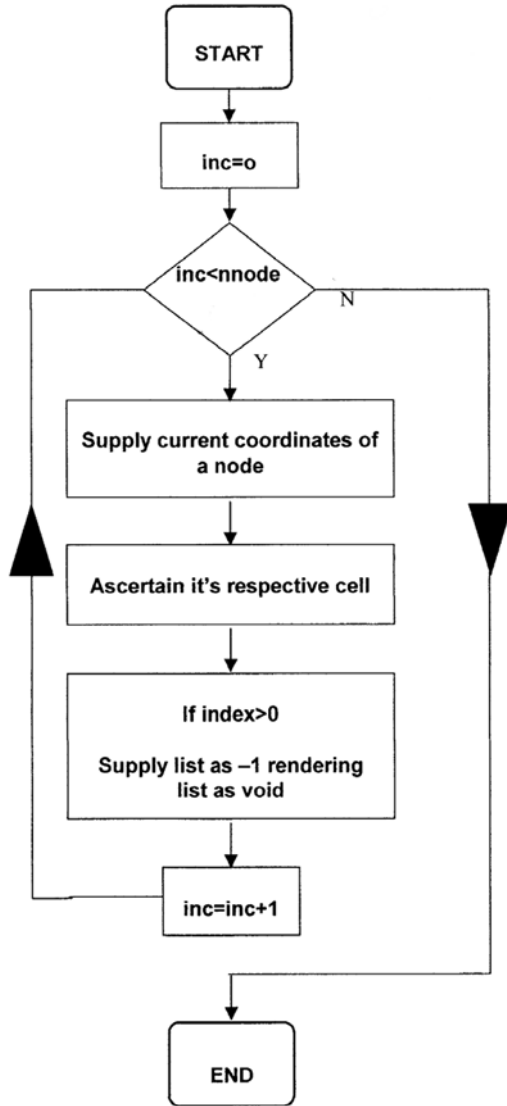


Fig. 6.18. Deleting cell lists

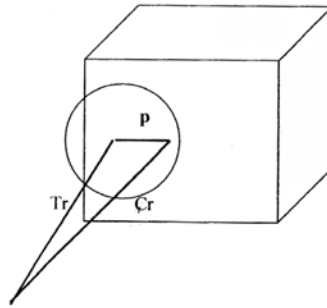


Fig. 6.19. Contact with the box

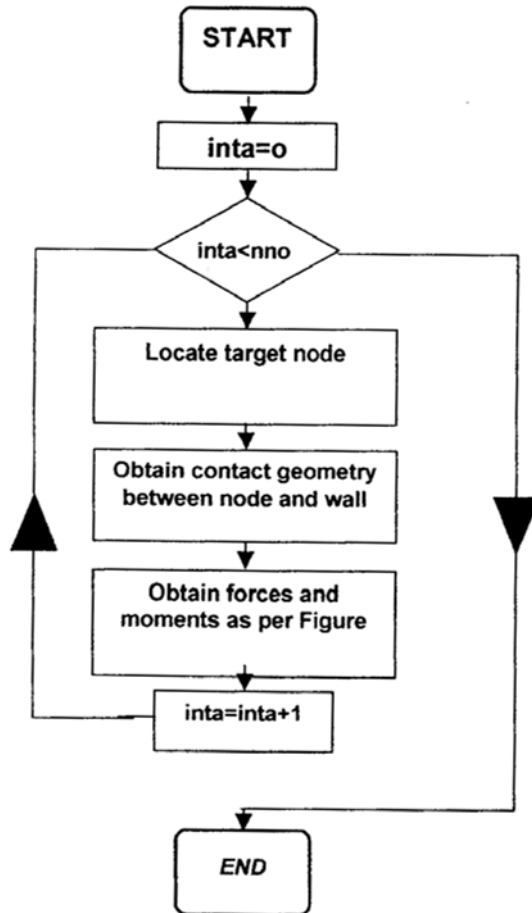


Fig. 6.20. Flow chart for contact with the box

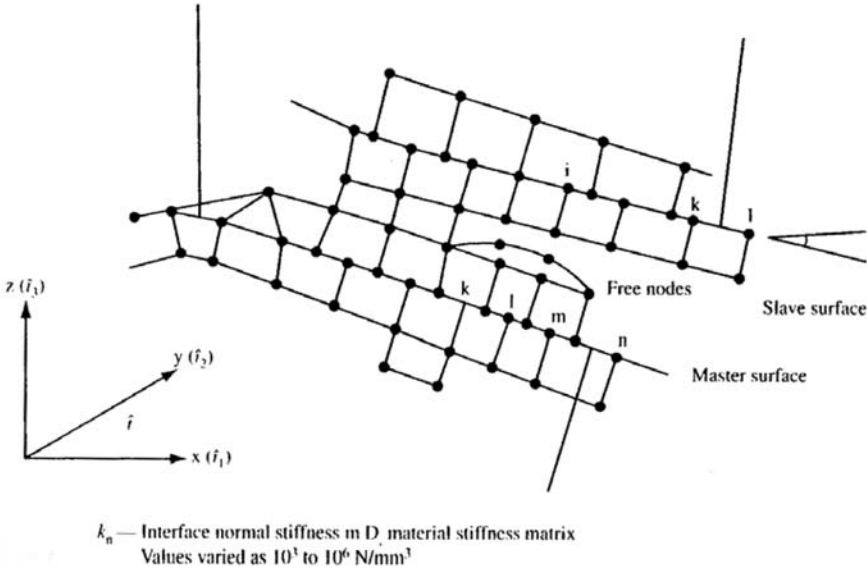


Fig. 6.21. Hallquist contact method (modified by Bangash)

## 6.7 Hallquist et al. Method

Hallquist et al. developed a useful concept of master and slave nodes sliding on each other. As shown in Fig. 6.21 slave nodes are constrained to slide on master segments after impact occurs and must remain on a master segment until a tensile interface force develops. The zone in which a slave segment exists is called a slave zone. A separation between the slave and the master line is known as void. The following basic principles apply at the interface:

- (a) update the location of each slave node by finding its closest master node or the one on which it lies.
- (b) for each master segment, find out the first slave zone that overlaps.
- (c) show the existence of the tensile interface force.

Constraints are imposed on global equations by a transformation of the nodal displacement components of the slave nodes along the contact interface. Such a transformation of the displacement components of the slave nodes will eliminate their normal degrees of freedom and distribute their normal force components to the nearby master nodes. This is done using explicit time integration, as described in the finite element solution procedures. Thereafter impact and release conditions are imposed. The slave and master nodes are shown in Fig. 6.21. Hallquist et al. gave a useful demonstration of the identification of the contact point which is the point on the master segment to the slave node  $n_s$  and which finally becomes nontrivial during the execution of

the analyses. When the master segment  $\hat{t}$  is given the parametric representation and  $t$  is the position vector drawn to the slave node  $n_s$ , the contact point co-ordinate must satisfy the following equations:

$$\begin{aligned} \frac{\partial \hat{r}}{\partial \xi}(\xi_c, \eta_c) \times [\hat{t} - \hat{r}(\xi_c, \eta_c)] &= 0 \\ \frac{\partial \hat{r}}{\partial \eta}(\xi_c, \eta_c) \times [\hat{t} - \hat{r}(\xi_c, \eta_c)] &= 0 \end{aligned} \quad (6.31)$$

where  $(\xi_c, \eta_c)$  are the co-ordinates on the master surface segment  $S_i$ . Where penetration through the master segment  $S_i$  occurs, the slave node  $n_s$  (containing its contact point) can be identified using the interface vector  $f_s$

$$f_s = -lk_i n_i \quad \text{if } l < 0 \quad (6.32)$$

to the degree of freedom corresponding to  $n_s$ , and

$$f_m^i = N_i(\xi_c, \eta_c) f_s \quad \text{if } l < 0 \quad (6.33)$$

where

$$l = \hat{n}_i \cdot [\hat{t} - \hat{r}(\xi_c, \eta_c)] < 0 \quad (6.34)$$

A unit normal

$$\hat{n}_i = \hat{n}_i(\xi_c, \eta_c); \quad \hat{t}_i = \hat{n}_i \sum_{j=1}^n N_j (F_1)^j(t) \quad (6.35)$$

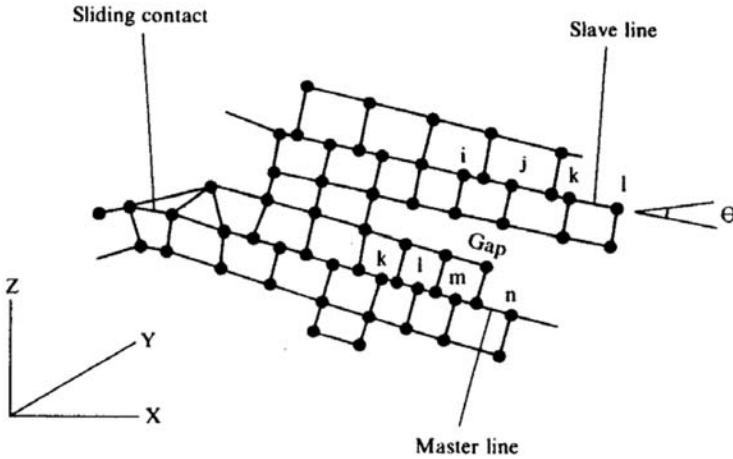
$$k_i = f_{si} K_i A_i^2 / V_i \quad (6.36)$$

where

- $(F_1)^j(t)$  = impact at the  $j$ th node
- $K$  = stiffness factor
- $K_i, V_i, A_i$  = bulk modulus, volume and face area, respectively
- $f_{si}$  = scale factor normally defaulted to 0.10
- $N_i = \frac{1}{4}(1 + \xi\xi_i)(1 + \eta\eta_i)$  for a 4-node linear surface

Bangash extended this useful analysis for other shape functions, such as  $N_i$  for 8-noded and 12-noded elements. On the basis of this theory and owing to the non-availability of the original computer source, a new sub-program CONTACT was written in association with the program ISOPAR. The subprogram CONTACT is in three dimensions.

Gap Element



$$\begin{aligned} \{\hat{\mathbf{F}}_N\} &= [\mathbf{K}_{\gamma',\gamma'}]_i \{U_{\gamma'}\}_i = [\Sigma k] \{\Sigma \Delta_i, \Delta_j, \dots\} \\ &= \{\hat{\mathbf{F}}_{i,j}, \dots\} + \{\pm \mu \hat{\mathbf{F}}_n, \dots \pm k \Delta_i, \dots\} \end{aligned}$$

$$\begin{aligned} \Delta_{sl} &= \text{distance sliding} \\ &= (\Delta_j - \Delta_i) - \frac{\mu |\hat{\mathbf{F}}_n|}{[\mathbf{K}_{\gamma',\gamma'}]} \end{aligned}$$

$\mu$  = friction

$$\begin{aligned} \{\hat{\mathbf{F}}_{SN}\} &\leq \mu \{\hat{\mathbf{F}}_N\} \text{ no sliding} \\ &\geq \mu \{\hat{\mathbf{F}}_N\} \text{ sliding} \\ &= \text{contact broken} \\ \theta &= 0 \cos^{-1} \frac{X}{\gamma} \text{ or } \sin^{-1} \frac{Y}{\gamma} \end{aligned}$$

### 6.8 DELFT Interface Fraction Type Element

This is suited to isoparametric quadrilateral two-dimensional elements as shown in Fig. 6.22. This gap or contact element is dealt with in detail by Rots and Schellekens using traction profile.

Consider the general case of an isoparametric two-dimensional interface element that connects two isoparametric solid elements. Figure 6.22 shows one example. The element geometry  $x$  and the element displacement field  $u$  are interpolated as

$$x = Hx_i \tag{6.37}$$

$$u = Hu_i \tag{6.38}$$

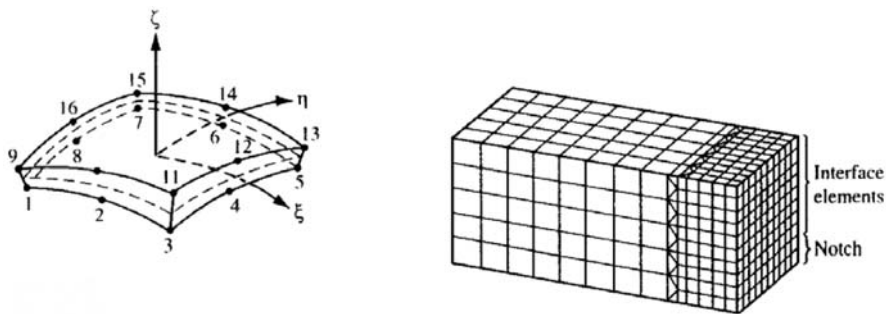


Fig. 6.22. Quadratic two dimensional quadrilateral interface element

where  $x_i$  is the nodal geometry vector in global co-ordinates,  $u_i$  is the nodal displacement vector in global co-ordinates and  $H$  is a logical grouping of the shape functions  $N$  which are expressed in the natural co-ordinates  $\xi$  and  $\eta$  along the surface. The same interpolations are adopted for top and bottom sides of the interface, which implies that the nodes should overlap. If the nodes do not overlap, interpolations should be set up with reference to mid-plane.

The relative displacement field  $\Delta u$  is defined as

$$\Delta u = Lu \tag{6.39}$$

with  $L$  being a  $3 \times 6$  matrix, filled with 1,  $-1$  and 0 such that the relative displacement is the displacement at the top side minus the displacement at the bottom side. Here, the interface elements deviate from continuum elements, where  $L$  contains differential operators.

The interface constitutive behaviour is described in terms of a traction-relative displacement law in the local co-ordinate system at integration points. This requires the global relative displacements  $\Delta u$  to be transformed to local relative displacements  $u$  as

$$\Delta \bar{u} = \Theta^T \Delta u \tag{6.40}$$

$\Theta$  contains the normalised local axes  $n$ ,  $s$  and  $t$  as columns. These local axes are set up according to (6.37).

Substitution of (6.38) into (6.39) and of the result thereof into (6.40) yields

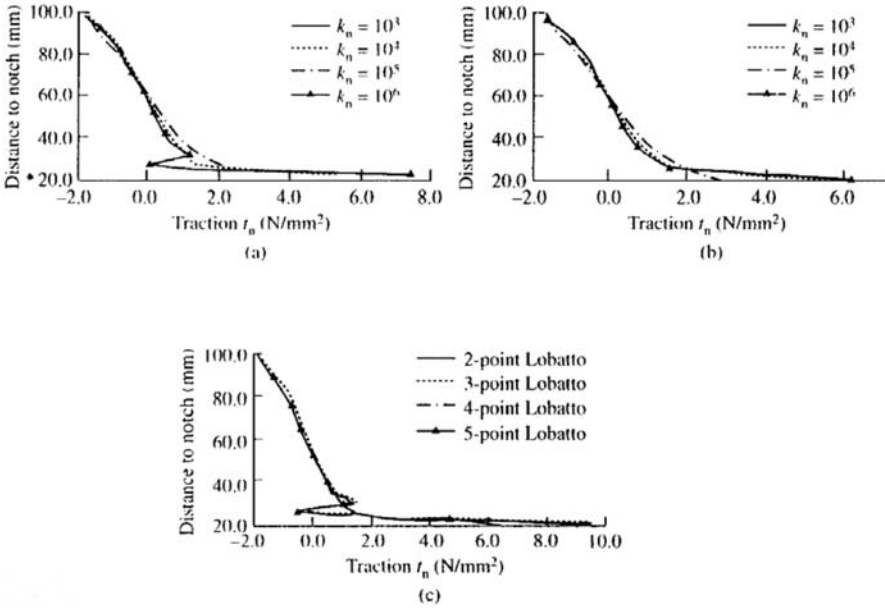
$$\Delta \bar{u} = Bu_i \tag{6.41}$$

where the notation  $B = \Theta^T LH$  has been introduced for the local relative displacement–nodal displacement matrix. Introducing the local traction-relative displacement law as

$$\hat{t} = D\Delta \bar{u} \tag{6.42}$$

the stiffness matrix can be written in standard form:





**Fig. 6.23.** Interface element – behaviour checked with other researchers based on DELFT

$$K = \int_{\xi=-1}^{\xi=+1} \int_{\eta=-1}^{\eta=+1} B^T DB \det(J) d\xi d\eta \tag{6.43}$$

with  $\det J$  being the determinant of the Jacobian operator.

In the case of three-dimensional analysis, Fig.6.23 shows the interface element for three-dimensional elastic analysis of a beam. Element interaction schemes are described in the text. This element has been tested with other methods of analysis by Newton-Cotes, Lobatto, Gauss and node-lumping schemes, The comparative study of results is given in Fig.6.23.

## 6.9 ANSYS Contact Elements

### CONTAC52 – Three-Dimensional Point to Point Contact Element

CONTAC52 represents two surfaces which may maintain or break physical contact and may slide relative to each other. The element is capable of supporting only compression in the direction normal to the surfaces and shear (Coulomb friction) in the tangential direction. The element has three degrees of freedom at each node: translation in the nodal  $x$ ,  $y$  and  $z$  directions as shown in Fig.6.24.

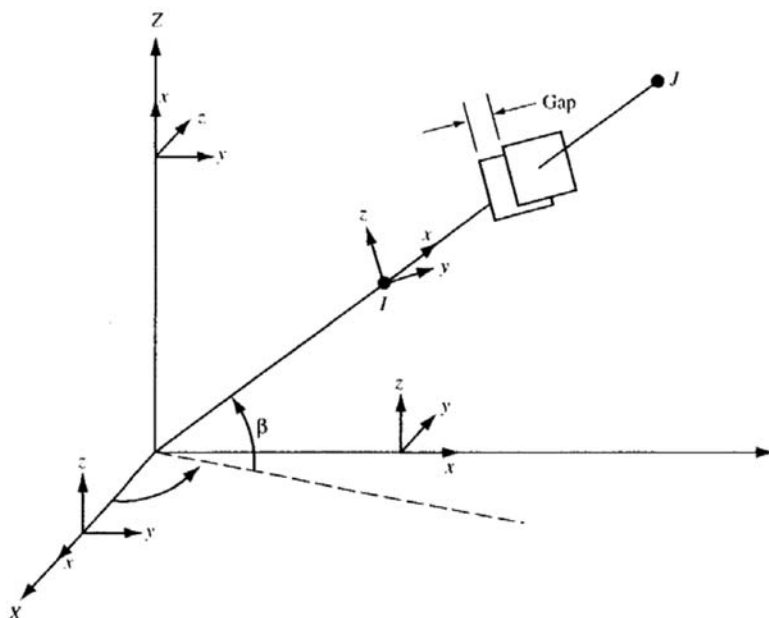


Fig. 6.24. CONTAC52 three-dimensional point-to-point contact element

The element may initially be preloaded in the normal direction or it may be given a gap specification. A specified stiffness acts in the normal and tangential directions when the gap is closed and not sliding.

The geometry node locations and the co-ordinate system for this element are shown in Fig. 6.24. The element is defined by two nodes, two stiffnesses (KN and KS), an initial gap or interference (GAP) and an initial element status (START). The orientation of the interface is defined by the node locations. The interface is assumed to be perpendicular to the  $I$ - $J$  line. The element co-ordinate system has its origin at node  $I$  and the  $x$ -axis is directed towards node  $J$ . The interface is parallel to the element  $y$ - $z$  plane.

The normal stiffness KN should be based on the stiffness of the surfaces in contact. The sticking stiffness KS represents the stiffness in the tangential direction when elastic Coulomb friction is selected ( $\mu > 0.00$  and KEYOPT(1) = 0). The coefficient of friction  $\mu$  is input as material property MU and is evaluated at the average of the two node temperatures. Stiffness may also be computed from the maximum expected force divided by the maximum allowable surface displacement. KS defaults to KN.

The initial gap defines the gap size (if positive) or the displacement interference (if negative). An interference causes the nodes to separate. The only material property used is the interface coefficient of friction  $\mu$ . A zero value should be used for frictionless surfaces.

**Table 6.1.** CONTAC52 input summary

Element name	CONTAC52
Nodes	I, J
Degree of freedom	UX, UY, UZ
Real constants	KN, GAP, START, KS A negative value of GAP assumes an initial interference condition If START = 0.0 or blank, initial status of element is determined from gap input If START = 1.0, gap is initially closed and not sliding (if MU ≠ 0.0), or sliding (if MU = 0.0) If START = 2.0 gap is initially closed and sliding If START = 3.0, gap initially open
Material properties	MU
Surface loads	None
Body loads	Temperatures: T(I), T(J)
Special features	Nonlinear, adaptive descent
KEYOPT(1)	Used only with MU > 0.0 0 Elastic Coulomb friction (KS used for sticking stiffness) 1 Rigid Coulomb friction (resisting force only)
KEYOPT(4)	0 Gap size based on gap real constant 1 Gap size determined from initial node locations (ignore gap real constant)
KEYOPT(7)	Used with automatic loading to control contact time predictions 0 Predictions are made to achieve the minimum time (or load) increment whenever a change contact status occurs 1 Predictions are made to maintain a reasonable time (or load) increment (recommended)

**Table 6.2.** Output for gap element

Name	Definition	O	R
UT(Y, Z)	Displacement (node J-node 1) in element <i>y</i> and <i>z</i> directions	2	2
FS	Tangential (friction) force (vector sum)	2	2
ANGLE	Principal angle of friction force in elementary- <i>z</i> plane	2	2

- 1 – if the value of START is:  
 2 – siding contact  
 3 – gap open (not given in Table AXIII.2)  
 2. If MU > 0.0

The force-deflection relationships for the interface element can be separated into the normal and tangential (sliding) directions as shown in Fig. 6.21. The element condition at the beginning of the first sub-step is determined from START parameter. If the interface is closed and sticking, KN is used in the gap resistance and KS is used for sticking resistance. If the interface is closed but sliding, KN is used in the gap resistance and the constant friction force  $\mu FN$  is used for the sliding resistance.

In the normal direction when the normal force (FN) is negative, the interface remains in contact and responds as a linear spring. As the normal force becomes positive, contact is broken and no force is transmitted.

In the tangential direction for  $FN < 0$  and the absolute value of the tangential force (FS) less than  $\mu|FN|$ , the interface sticks and responds as a linear spring. For  $FN < 0$  and  $FN = \mu|FN|$  sliding occurs. If contact is broken,  $FN = 0$ .

A summary of the element input is given in a step-by-manner in Table 6.1.

### *Output Data*

The solution output associated with the element is in two forms:

- (a) nodal displacements included in the overall nodal solution, and
- (b) additional element output as shown in Table 6.2.

The force displacement curves are generally illustrated.

## 6.10 ABAQUS Gap Contact Element

The following overview underlines various sters and options for gap elements.

### **Overview**

Gap elements:

- allow for contact between two nodes;
- allow for the nodes to be in contact (gap closed) or separated (gap open) with respect to particular directions and separation conditions;
- are always defined in three dimensions but can also be used in two-dimensional and axisymmetric models;
- allow contact to be defined on any type of element, including superelements and user-defined elements;
- provide the contact forces, not stresses between two points in a local basis system;
- require that some limitations be placed on the rotation of the contact direction (GAPUNI and GAPCYL elements only) and
- can be used to stimulate an inextensible cable (by using GAPSPHER elements).

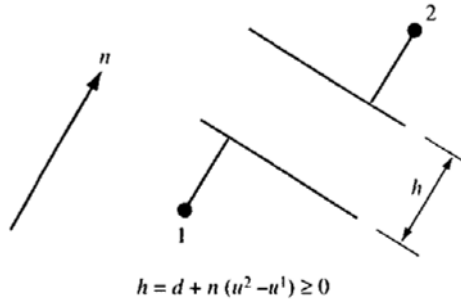


Fig. 6.25. GAPUNI contact element

### Choosing and Defining a Gap Element

- GAPUNI elements model contact between two nodes when the contact direction is fixed in space.
- GAPCYL elements model contact between two nodes when the contact direction is fixed in a plane.
- GAPSPHER elements model contact between two nodes when the contact direction is arbitrary in space.
- Gap elements are defined by specifying the two nodes forming the gap and providing geometric data defining the initial state of the gap.

### GAPUNI Elements

The behaviour of the interface being modelled with a GAPUNI element is defined by the initial distance (clearance)  $d$  of the gap and the contact direction,  $n$ .

#### *Clearance between GAPUNI Nodes*

ABAQUS defines the current clearance between two nodes of the gap  $h$  as

$$h = d + n(u^2 - u^1)$$

where  $u^1$  and  $u^2$  are the total displacements at the first and the second node forming the GAPUNI element. Figure 6.25 shows the configuration of the GAPUNI element. When  $h$  becomes the gap contact element it is closed only when the constraint  $h = 0$  is imposed.

#### *Gap Element Library*

This section defines the gap elements available in ABAQUS.

#### *References*

- GAP contact elements
- \*GAP.

*Element Types*

GAPUNI unidirectional gap between two nodes  
 GAPCYL cylindrical gap between two nodes  
 GAPSPHER spherical gap between two nodes

Active degrees of freedom  $-1, 2, 3(u_x, u_y, u_z)$ .

Additional solution variables – three additional variables relating to the contact and friction forces.

*Nodal Co-ordinates Required*

GAPUNI: if the contact direction  $n$  is specified on the \*GAP option, the nodal co-ordinates are not relevant; however, it is useful to define the co-ordinates of the two nodes for plotting purposes.

GAPCYL and GAPSPHER:  $X, Y, Z$

*Element Property Definition*

Use the \*GAP option to specify the initial clearance or overclosure in GAPUNI elements; a negative value indicates an initial overclosure. For GAPCYL and GAPSPHER elements, specify the maximum separation as a positive number or the minimum separation as a negative number.

*Element loading*

None.

*Element Output*

S11 force in the gap  
 S12 first friction force normal to the gap direction  
 S13 second friction force normal to the gap direction  
 E11 current opening  $h$  of the gap element  
 E12 relative displacement (slip) in the first direction orthogonal to the contact direction  
 E13 relative displacement (slip) in the second direction orthogonal to the contact direction.

The increments of shear slip are the relative displacement increments projected onto the two local directions that are orthogonal to the contact direction.

In two-dimensional or axisymmetric models when the contact direction is along the first ( $X$  or  $r$ ), the active slip direction is E13 and the active shear force is S13. In any other two-dimensional or axisymmetric case the active slip direction is E12 and the active shear force is S12.

*Nodes Associated with the Element*

Two nodes: the ends of the gap.

The behaviour of a GAPCYL element is defined by the initial separation distance between nodes,  $d$ ; the current positions of the element's nodes, and the axis of the GAPCYL element. The axis of the GAPCYL element defines the plane in which the contact direction  $n$  lies. Specify  $d$  and the direction cosines of the GAPCYL element axis on the data line of the \*GAP option.

The value  $d = 0$  is not allowed: it would enforce the distance between the nodes to be exactly zero at all times, which does not correspond to a contact problem.

*Case 1. Defining the Gap Clearance When  $d$  Is Positive*

If  $d$  is positive, the GAPCYL element models contact between two rigid tubes of different diameter where the smaller tube is located inside the larger tube. In this case,  $d$  is the maximum allowable separation. Each tube is represented by a node on its axis with the axes connected by the GAPCYL element and  $d$  corresponds to the difference between the radius of the tubes. The gap between the tubes closes when the two nodes become separated by more than  $d$  in any direction in the plane defined by the axis of the GAPCYL element.

ABAQUS defines the current gap opening,  $h$  in GAPCYL elements for Case 1 as

$$h = d - |\bar{x}^2 - \bar{x}^1| \quad \text{with} \quad \bar{x}^N = x^N - a(ax^N) \quad (6.44)$$

where  $x^N$  is the current position of node  $N$ ;  $d$  is the specified initial separation and  $a$  is the axis of the GAPCYL element.

If the initial position of the tube axes is such that the distance between them is less than  $d$  the GAPCYL element is open initially. If the distance is equal to  $d$  the element is closed initially and if the distance is greater than  $d$  an initial overclosure (interference) is defined.

*Case 2. Defining the Gap Clearance When  $d$  Is Negative*

If  $d$  is negative, the GAPCYL element models external contact between two parallel rigid cylinders. In this case,  $d$  is the minimum allowable separation of the nodes.

Each cylinder is represented by a node on its axis connected by the GAPCYL element and  $d$  corresponds to the sum of the radii of the cylinders. The gap closes when the two nodes approach each other to within  $d$  in any direction in the plane defined by the axis of the GAPCYL element.

ABAQUS defines the current gap opening  $h$  in GAPCYL elements for Case 2 as

$$h = |x^2 - x^1| - |d| \quad \text{with} \quad x^N = x^N - a(ax^N) \quad (6.45)$$

if the initial position of the cylinder axes is such that the distance between them is greater than  $|d|$  the GAPCYL element is open initially. If the distance is equal to  $|d|$  the element is closed initially; and if the distance is less than  $|d|$  an initial overclosure (interference) is defined. Details about modelling interference fit problems with GAP elements are discussed below.

#### *Local Basis System for GAPCYL Element Output*

ABAQUS reports the force across the gap and the shear forces that are orthogonal to the contact direction as element output for GAPCYL elements. It also reports the current clearance in the gap,  $h$ , and the relative motions of the elements' nodes that are orthogonal to the contact direction. The relative motions and the shear forces are reported in local surface directions that are formed using the standard ABAQUS convention for defining directions on surfaces in space. The contact direction defines a surface in space on which the local axes are formed and the slip is calculated from the relative motions in the surface directions.

ABAQUS updates the contact direction for GAPCYL elements based on the motion of the nodes forming the elements. However, the orientation of  $a$  is not updated during the analysis.

### **GAPSPHER Elements**

GAPSPHER elements can be used to model two very different contact situations: contact between two rigid spheres where the smaller sphere is inside the larger, hollow sphere and contact between two rigid spheres along their external surfaces.

The behaviour of a GAPSPHER element is defined by the minimum or maximum separation distance between the nodes  $d$  and the current positions of the element's nodes. Specify the minimum or maximum separation distance  $d$  on the data line of the \*GAP option. The contact direction is defined by the current position of the nodes.

The value  $d = 0$  is not allowed: it would enforce the distance between the nodes to be exactly zero at all times, which does not correspond to a contact problem.

#### *Case 1. Defining the Gap Clearance When $d$ Is Positive*

If  $d$  is positive, the GAPSPHER element models contact between a rigid sphere inside another (larger) hollow rigid sphere. In this case  $d$  is the maximum allowable separation of the nodes forming the gap. Each sphere is represented by a node at its centre, with the centres connected by the GAPSPHER element; and  $d$  corresponds to the difference between the radii of the spheres. The gap closes when the two nodes become separated by more than  $d$ .



ABAQUS defines the current gap opening  $h$  for Case 1 as

$$h = d - |x^2 - x^1| \quad (6.46)$$

with  $x^N$  the current position of node  $N$  and  $d$  the specified separation.

If the initial position of the tube axes is such that the distance between them is less than  $d$ , the GAPSPHER element is open initially. If the distance is equal to  $d$ , the element is closed initially, and if the distance is greater than  $d$  an initial overclosure (interference) is defined.

#### *Case 2. Defining the Gap Clearance When $d$ Is Negative*

If  $d$  is negative, the GAPSPHER element models extend contact between two rigid spheres. In this case  $d$  is the minimum allowable separation of the nodes forming the gap. Each sphere is represented by a node at its centre connected by the GAPSPHER element and  $|d|$  corresponds to the sum of the radii of the spheres. The gap closes when the two nodes approach each other to within  $|d|$ .

ABAQUS defines the current gap opening  $h$  for Case 2 as

$$h = |x^2 - x^1| - |d| \quad (6.47)$$

If the initial position of cylinder axes is such that the distance between them is greater than  $|d|$ , the GAPSPHER element is open initially. If the distance is equal to  $|d|$  the element is closed initially and if the distance is less than  $|d|$  an initial overclosure (interference) is defined.

#### *Local Basis System for GAPSPHER Element Output*

ABAQUS reports the force across the gap and the shear forces that are orthogonal to the contact  $h$  and the relative motions of the elements node that are orthogonal to the contact direction. The relative motions and the shear forces are reported in local surface directions that are formed using the standard direction that formed using the standard ABAQUS convention for defining direction on surfaces in space. The contact direction defines a surface in space on which the local axes are formed, and the slip is calculated from the relative motion in the surface directions.

ABAQUS updates the contact direction for GAPSPHER elements based on the motion of the nodes forming the elements.

#### *Defining Nondefault Mechanical Interactions with Gap Elements*

The default mechanical surface interaction model for problems modelled with gap elements is hard frictionless contact. Optional mechanical surface interaction models can be assigned by using the appropriate options in conjunction with the \*GAP option defining the elements properties. The following mechanical surface interaction models are available:

- (a) friction
- (b) modified 'hard' contact, softened contact and viscous damping.

*Modelling Large Initial Interference with Gap Elements*

Specifying a large negative initial overclosure (interference) may lead to convergence problems as ABAQUS tries to resolve the overclosure in a single increment. Use the \*CONTACT INTERFERENCE, TYPE = ELEMENT option to allow ABAQUS to resolve the overclosure gradually.

Usage: \*CONTACT INTERFERENCE, TYPE = ELEMENT

Specify  $d$  on the data line of the \*GAP option. If a positive value is provided the gap is open initially. If  $d = 0$  the gap is initially closed. If  $d$  is negative, the gap is considered overclosed at the start of the analysis and an initial interference fit problem is defined.

*Specifying the Contact Direction*

The user can specify the contact direction on the data line of the \*GAP option. Otherwise ABAQUS will calculate the gap direction  $n$  by using the initial positions of the two nodes forming the element,  $X^1$  and  $X^2$ :

$$n = (X^2 - X^1)/|X^2 - X^1| \quad (6.48)$$

An error message is issued if  $X^3 = X^1$  (if the two gap element nodes have the same initial co-ordinates). In this situation the user must define  $n$  on the \*GAP option. The normal  $n$  usually points from the first node of the element to the second, unless the gap is overclosed at the start of the analysis. In that case, specify  $n$  so that the correct contact direction is used for the gap element.

If the user specifies the gap direction  $n$  rather than allowing ABAQUS to calculate it, the contact calculations consider only the displacements of the gap elements nodes and the ordering of the nodes in the element definition. The initial co-ordinates of the nodes play no role in the calculations.

The output from the GAPUNI gives force across the gap and shear forces orthogonal to the contact direction. GAPCYL elements and GAPSPHER elements are treated as outside the scope of this book since contact examples between rigid steel tubes internally or externally contacted have not been included in the text. For an in-depth study the reader is referred to analytical and users' manuals of ANSYS, available from Swanson's Incorporation of USA.

## 6.11 LS-DYNA Gap/Contact Elements

### Introduction

The gap elements or contact elements are based on the Hallquist method given above. The number of slave segments and number of master segments are defined by interface control cards. IREAD flag is to read additional control

cards. Ties interface contact definitions are based on offset option which can be used with rigid bodies. Typical letters and numbers are given below as:

Type number (the letters ‘a’, ‘m’, ‘o’ and ‘p’ must be in col. 13)

- 1 – sliding without penalties
- p1 – symmetric sliding with penalties (recommended)
- 2 – tied
- 02 – tied with offsets permitted, see note 1 below
- 3 – sliding, impact, friction
- a3 – sliding, impact, friction, no segment orientation
- m3 – sliding, impact, friction-metal forming option
- 4 – single surface contact
- 5 – discrete nodes impacting surface
- a5 – discrete nodes impacting surface, no segment orientation
- m5 – discrete nodes impacting surface-metal forming option
- 6 – discrete nodes tied to surface, see note 1 below
- 06 – discrete nodes tied to surface with offsets permitted
- 7 – shell edge tied to shell surface, see note 1 below
- 07 – shell edge tied to shell surface with offsets permitted
- 8 – nodes spot welded to surface
- 9 – tiebreak interface
- 10 – one way treatment of sliding, impact, friction
- a10 – one way treatment, no segment orientation
- m10 – one way treatment of sliding, impact, friction-metal forming option
- 11 – box/material limited automatic contact for shells
- 12 – automatic contact for shells (no additional input required)
- 13 – automatic single surface with beams and arbitrary orientations
- a13 – like above but with extra searching for airbag contact
- 14 – surface to surface eroding contact
- 15 – single surface eroding contact
- 16 – node to surface eroding contact
- 17 – surface to surface symmetric/asymmetric constraint method
- 18 – node to surface constraint method
- 19 – rigid body to rigid body contact with arbitrary force/deflection curve  
(this option may be used with deformable bodies)
- 20 – rigid nodes to rigid body contact with arbitrary force deflection curve  
(this option may be used with deformable bodies)
- 21 – rigid body to rigid body contact with arbitrary force/deflection curve;  
unlike option 19 this is a one-way treatment (this option may be used  
with deformable bodies)
- 22 – single edge treatment for shell surface edge to edge treatment
- 23 – simulated draw bead
- 25 – force transducer contact for penalty based contact types – not for  
types 2, 6, 7, 17 and 18, see type 27 below for the constraint type

- 26 – automatic single surface, beams to beams, beam to shell edge  
 27 – force transducer contact for constraint based contact types; applies to types 2, 6, 7, 17 and 18 only.

Static coefficient of friction  $\mu_s$

EQ.-1: part based friction coefficients are used. Applies to contact types a3, a5, a10, 13, 15 and 26 only.

Tying will only work if the surfaces are near each other. The criteria used to determine whether a slave node is tied down is that it must be ‘close’. For shell elements, ‘close’ is defined as distance  $\delta$ , less than:

$$\begin{aligned}\delta_1 &= 0.60 * (\text{thickness\_slave\_node} + \text{thickness\_master\_segment}) \\ \delta_2 &= 0.05 * \min (\text{master\_segment\_diagonals}) \\ \delta &= \max(\delta_1, \delta_2)\end{aligned}\tag{6.49}$$

If a node is further away it will not be tied and a warning message will be printed. For thermal control card

$h_{\text{rad}}$  = radiation conductance

$l_{\text{gap}}$  = length or thickness of gap between sliding surfaces

$h$  = heat transfer conductance

$$h = h_{\text{cont}}, \text{ if the gap thickness is } 0 \leq l_{\text{gap}} \leq l_{\text{min}}\tag{6.50}$$

$$h = h_{\text{cond}} + h_{\text{rad}}, \text{ if the gap thickness is } l_{\text{min}} \leq l_{\text{gap}} \leq l_{\text{max}}\tag{6.51}$$

$$h = 0, \text{ if the gap thickness is } l_{\text{gap}} > l_{\text{max}}\tag{6.52}$$

## References

- [6.1] Munjiza A, Andrews KRF (1998) NBS contact detection algorithm for bodies of a similar size. *Int. Jour. Numer. Meth. Eng.* 43:131–149
- [6.2] Lemos J, Hart RD, Cundall PA (1985) A generalised distinct element program for modelling jointed rock mass. In: Stephenson O (ed.) *Fundamentals of rock joints*. Centek Publishers
- [6.3] Williams JR, Hocking G, Mustoe GGW (1985) The theoretical basis of disc elements. *NUMETA '85 numerical methods in engineering. Theory and applications*. Balkema, Rotterdam
- [6.4] Williams JR, Mustoe G (1993) *Proc. 2nd U.S. Conf. on Discrete Element Methods*. MIT, MA
- [6.5] Williams JR, Mustoe G (1989) *Proc. 1st U.S. Conf. on Discrete Element Methods*. Golden, Colorado
- [6.6] Hua SG and Goodman RE (1988) Discontinuous deformation analysis – A new method for computing stress, strain and sliding of block systems. In: *Key questions in mechanics*. Balkema, Rotterdam, pp. 381–393
- [6.7] Munjiza A, Owen DRJ, Bicanic N (1995) A combined finite-discrete element method in transient dynamics of fracturing solids. *Int. Jour. Eng. Comput.* 12:145–174
- [6.8] Oldenburg M, Nilsson L (1994) The position code algorithm for contact searching. *Int. Jour. Numer. Meth. Eng.* 37:359–386
- [6.9] Bonnet J, Peraire J (1991) An alternative digital tree (ADT) algorithm for 3D geometric searching and intersection problems. *Int. Jour. Numer. Meth. Eng.* 31:1–17
- [6.10] O'Connor R, Gill J, Williams JR (1993) A Linear complexity contact detection algorithm for multi body simulations. *Proc. 2nd U.S. Conf. on Discrete Element Methods*. MIT, MA
- [6.11] Preece DS, Burchell SL (1993) Variation of element packing angle and its influence on computer simulations of blast induced rock motion. *Proc, 2nd U,S, Conf. on Discrete Element Methods*. MIT, MA
- [6.12] Mirtich B (1998) *Impulse-based dynamic simulation of rigid body systems*. PhD Thesis, University of California, Berkeley
- [6.13] Bangash MYH (2002) *Manual of numerical methods in concrete*. Thomas Telford, London
- [6.14] Bangash T (2004) *The combined finite/discrete element method in transient dynamics of reinforced concrete structures under blast loading*. PhD Thesis London University

# 7 Aircraft and Missile Impact – Data and Analysis

## 7.1 Introduction

Impact of aircraft and missiles is considered. Basic impact dynamics is initially introduced. About the free falling bodies and missiles ejecting out of the building structures. The impactor can be an aircraft or a missile. It is therefore essential for a reader to have a readily available data of all these impactors so that he/she can easily simulate them in the finite element analysis in the form of a load-time function. They are given in Tables 7.1 to 7.3. Program BANG-F has been developed which is an extended version of ISOPAR, reported earlier in which facilities exist for the direct interaction of Blast or Fire effects. When the aircraft/missile impacts a building structure and its elements, columns, frames, floors and other parts are scanned for dislocation, plasticity, cracking and damage scenario in the main zones and at joints. A stability check is asked for whether or not the time-dependent projectiles ejecting and pulling under impactive force with and without fire effects and finally impacting targets at certain distances. PROGRAM BANG-F written in Fortran and FEM/DEM written in 'C' have such facilities.

## 7.2 Direct Impact/Impulse and Momentum

An impactor in the forming the form of missile is first given an initial velocity and it is then possible to assume that it is moving under the action of its own weight. If the initial velocity is not vertical, the missile will move in a curve and its flight can be evaluated in terms of horizontal and vertical components of displacement, velocity and acceleration.

An impulse is defined as a force multiplied by time, such that

$$F_1(t) = \int F dt \quad (7.1)$$

where  $F_1(t)$  is the impulse,  $F$  is the force and  $t$  is the time. The momentum of a body is the product of its mass and its velocity:

$$\text{momentum} = mv \quad (7.2)$$

where  $m$  is the mass and  $v$  is the velocity =  $dx/dt$ . Both velocity and momentum are the vector quantities; their directions are the same. If a body is

moving with constant velocity, its momentum is constant. If velocity is to be changed, a force  $F$  must act on the body. It follows that a force  $F$  must act in order to change the momentum.

$$F = m dv/dt$$

or

$$F dt = m dv$$

$$\int_{t_1}^{t_2} F dt = \int_u^v m dv$$

$$F_1(t) = m(v - u) \tag{7.3}$$

Where  $u$  and  $v$  are the velocities at times  $t_1$  and  $t_2$  respectively. If the initial velocity  $u = 0$ , (7.3) becomes

$$I = mv \tag{7.3a}$$

Thus the impulse of a force is equal to the change in momentum which it produces.

## Data on Civilian and Military Aircraft

**Table 7.1.** Civilian aircraft

Civilian aircraft normally in service include Concorde, Airbus, Boeing, Antonov, Ilyushin and Tupolov.

$S$  = span;  $L$  = length;  $H$  = height;  $A_w$  = wing area;  $P_L$  = payload;  
 $V$  = speed;  $w_a$  = weight at take-off or landing.

Basic parameters of Concorde	
Power plant	
	4 × 38050 lb (169 kN)
	Rolls-Royce/Sneema Olympus 593 Mk60 two-spool turbojet
$S$ (m)	25.61
$L$ (m)	62.10
$H$ (m)	12.19
$A_w$ (m <sup>2</sup> )	358
$P_L$ (kg)	11340
$V$ (km/h)	2150
$w_a$ (kg)	186800

**Table 7.1a.** Data on the Airbus family

Type	Power plant	<i>S</i> (m)	<i>L</i> (m)	<i>H</i> (m)	<i>A<sub>w</sub></i> (m <sup>2</sup> )	<i>P<sub>L</sub></i> (kg)	<i>V</i> (km/h)	<i>w<sub>a</sub></i> (kg)
A300B2-100	2 × 51000 lb (227 kN) GE CF6-50C turbofans	44.84	53.75	16.53	260	14900	869	34585
A300B2-200	2 × 51000 lb (227 kN) GE CF6-50C turbofans	44.84	53.57	16.53	260	34585	869	142900
A300B2-100	2 × 51000 lb (227 kN) GE CF6-50C turbofans	44.84	53.57	16.53	260	35925	869	158400
A300B4-200	2 × 52500 lb (233.5 kN) CF6-50C1 turbofans	44.84	53.57	16.53	260	35600	869	165900
A310-202	2 × 48000 lb (218 kN) GE CF6-80A turbofans	43.9	46.66	15.80	219	32400	780	132000

**Table 7.1b.** Data for Antonov aircraft

Type	Power plant	<i>S</i> (m)	<i>L</i> (m)	<i>H</i> (m)	<i>A<sub>w</sub></i> (m <sup>2</sup> )	<i>P<sub>L</sub></i> (kg)	<i>V</i> (km/h)	<i>w<sub>a</sub></i> (kg)
An-12	4 × 4000 ehp Ivchenko AI-20K turboprops	38	37	9.83	119.5	10000	550	54000
An-22	4 × 15000 ehp Kuznetsov NK-12MA turboprops	64.4	57.8	12.53	345	80000	679	250000
An-24	2 × 2500 ehp Ivenchenko AI-24 Seviiny 11 turboprops	29.2	23.53	8.32	74.98	13300	450	21000
An-26*	2 × 2800 ehp Ivenchenko AI-24T turboprops	29.4	23.8	8.575	74.98	5500	435	24000
An-28	2 × 970 ehp Glushkov TVD-10B turboprops (similar to An-14)	21.99	12.98	4.6	39.72	1550	350	6100
An-72	2 × 14330 lb (6500 kg) Lotarev D-36 turbofans	25.83	26.58	8.24	74.98	7500	720	30500

\* An-30 and An-32 have similar status to An-26.

**Table 7.1c.** Data for Boeing aircraft

Type	Power plant	<i>S</i> (m)	<i>L</i> (m)	<i>H</i> (m)	<i>A<sub>w</sub></i> (m <sup>2</sup> )	<i>P<sub>L</sub></i> (kg)	<i>V</i> (km/h)	<i>w<sub>a</sub></i> (kg)
727-200	3 × 16000 lb (71.2 kN) Pratt and Whitney JT8D-17 turbofans	32.9	46.7	10.4	153.2	18594	883	95238
737-200	2 × 16000 lb (71.2 kN) Pratt and Whitney JT8D-17 turbofans	28.3	30.5	11.4	91	15422	775	53297
767	2 × 44300 lb (1.97 kN) Pratt and Whitney JT9D-7R 4A turbofans	47.24	48.46	15.38	200	40224	800	128030
757	2 × 37400 lb (166.43 kN) Rolls-Royce RB211-535C turbofans	37.95	47.32	13.56	181.25	71530	899	298880
747-200B	4 × 50000 lb (222 kN) Pratt and Whitney JT9D-7F (wet) turbofans	59.6	70.5	19.3	512	71530	907	366500
747-200B	4 × 53000 lb (236 kN) Pratt and Whitney JT9D-7Q turbofans	59.6	70.5	19.3	512	69900	907	373300
747-200B	4 × 52500 lb (234 kN) General Electric CF6-50E2 turbofans	59.6	70.5	19.3	512	69080	907	373300

\* For B767-200ER 46.55 48.46 16.155 For other details reference is made to Section 4

° For B747-400 65.00 70.71 19.18 For other details reference is made to Section 4



**Table 7.1d.** Data on the Ilyushin aircraft

Type	Power plant	$S$ (m)	$L$ (m)	$H$ (m)	$A_w$ (m <sup>2</sup> )	$P_L$ (kg)	$V$ (km/h)	$w_a$ (kg)
Ilyushin II-18	4 × Ivenchenko AI-20M turboprops	37.4	35.9	10.17	140	14000	625	64000
Ilyushin II-62	4 × 25000 lb (113 kN) Solovier							
Ilyushin II-76T	20-30-KU turbofans 4 × Solovier D.30KP turbofans, each with 26455 lb St (12000kg)	43.2	53.1	12.4	280	23000	860	165000
Ilyushin II-86	4 × Kuznetsov turbofans, each with 28635 lb St (13000kg)	50.5	46.59	14.76	300	40000	850	157000
		48.06	59.54	15.81	320	42000	900	206000

**Table 7.1e.** Data on the Tupolev series of aircraft

Type	Power plant	$S$ (m)	$L$ (m)	$H$ (m)	$A_w$ (m <sup>2</sup> )	$P_L$ (kg)	$V$ (km/h)	$w_a$ (kg)
TU-104	2 × 21385 lb (97 kN) Mikulin AM 3M500 turbojet	34.54	25.85	11.9	174.4	900	800	76000
TU-124	2 × 11905 lb (54 kN) Soloviev D-20P turbofans	25.5	30.58	8.08	1.19	3500	800	26300
TU-134	2 × 15000 lb (66.5 kN) Soloviev D-30 turbofans	29	34.9	9	127	77000	849	45200
TU-144	4 × 44000 lb St (20000kg) with Kuznetsov NK-144 turbofans	28.8	65.7	12.85	438	14000	2500	180000
TU-154	3 × 21000 lb (93.5 kN) Kuznetsov NK-8-2 turbofans	37.5	48	11.4	202	20000	900	91000

**Table 7.2.** Military aircraft

$S$  = span;  $L$  = length;  $H$  = height;  $A_w$  = wing area;  $P_L$  = payload;  $V$  = speed;  $w_a$  = weight at take-off or landing.

**Table 7.2a.** Data on the Tornado IDS and ADV aircraft

	Power plant	
	Interdictor Strike (IDS)	Air Defence Variant (ADV)
	Turbo-Union RB 199-34R (101 or 103) after burning turbofan MK 8090 lb (3670 kg) to 15950 lb (7253 kg) after burning thrust	As for IDS, with MK 104
$S$ (m)	8.60 max swept 13.90 max unswept	8.60 at 67° sweep 13.90 at 25° sweep
$L$ (m)	16.67	18.68
$H$ (m <sup>2</sup> )	5.95	5.95
$A_w$ (m)	–	–
$P_L$ (kg)	9000	9000
$V$ (Mach)	Mach 2 at high level Mach 1 at low level	Mach 2.2
$w_a$ (kg)	28000	28000
Armament	4 × MK 13/15 1000 lb (454.74 kg) bombs 2 AIM-9L missiles 8 MK 83 retarded bombs 2 CBLS-200 practice bomb containers 4 Kormoram ASM 8 × BL755 cluster bombs	

**Table 7.2b.** Basic parameters for the F-5E and F-20 aircraft

	Power plant	
	Engine 2GEJ 85-21 5000lb (2268 kg) thrust each	Engine GEF404-GE100 1800lb (8164 kg) thrust each
$S$ (m)	7.98 with missiles 8.53 without missiles	8.5 with missiles
$L$ (m)	14.45	14.42
$H$ (m)	4.07	4.10 (4.73 with wheels)
$A_w$ (m <sup>2</sup> )	28.1	27.5
$P_L$ (kg)	6350	7263
$V$ (miles/h)	850	1300
$w_a$ (kg)	11213.8	12700
Armament	Air-to-air	2 No. 20 mm guns and AIM 9 Sidewinder missiles
	Air-to-ground	2 No. 20mm guns and 9 bombs of 3020 kg

**Table 7.2c-1.** Data on the F-16 series of aircraft

	F-16A and F-16B	F-16C and F-16D	F-16N	TF-16N
Power plant	Pratt and Whitney turbofan two shaft 24000 lb (10885 kg) thrust F100-PW-100	F100-PW-200 F100-PW-220 F110-GE-100 25000 lb (11340 kg) thrust	F110-GE-100 25000 lb (11340 kg) thrust	F110-GE-100 25000 lb (11340 kg) thrust
$S$ (m)	9.45 10.01 (with Sidewinder)	9.45 10.01 (with Sidewinder)	9.895 (without Sidewinder)	
$L$ (m)	14.52	15.03	15.10	
$H$ (m)	5.01	5.09	5.10	
$A_w$ (m <sup>2</sup> )	27.87	27.87	27.87	
$P_L$ (kg)	33000 lb (14969 kg)	37500 lb (16781 kg)	37500 lb (16781 kg)	
$V$ (miles/h)	1300	1300	1300	
$w_a$ (kg)	12000 lb (5443 kg)	12430 lb (5638 kg)	17278 lb (7836 kg)	

**Table 7.2c-2.** Data on the F-15

	Power plant
	2 No. Pratt and Whitney F-100-PW-220 each with 24000 lb thrust
$S$ (m)	13.05
$L$ (m)	19.45
$H$ (m)	5.64
$A_w$ (m <sup>2</sup> )	–
$P_L$ (kg)	7000
$V$ (km/h)	2500
$w_a$ (kg)	20000
Armament	4 AIM-9L/M infra-red-guided Sidewinder missiles; 4 AIM-7F/M radar-guided Sparrow missiles; 8 advanced medium-range air-to-air missiles (AMRAAMs); M-61 20mm Gatling gun with 940 rounds of ammunition. Accommodates a full range of air-to-ground ordnance.

**Table 7.2d.** Data on the F/A-18 Hornet

	Power plant
	2 No. F404-GF-400 low bypass turbofan engines each in 1600 lb (70.53 kN) thrust and with a thrust/weight ratio of 8:1
$S$ (m)	11.43
$L$ (m)	17.06
$H$ (m)	4.7
$A_w$ (m <sup>2</sup> )	37.2
$P_L$ (kg)	–
$V$ (km/h)	2700
$w_a$ (kg)	24402
Armament	Up to 7711 kg maximum on nine stations: two wing-tips for Sidewinder heat-seeking missiles; two outboard wings for air-to-ground ordnance; two inboard wings for Sparrow radar-guided missiles, air-to-ground, or fuel tanks; two nacelle fuselage for Sparrow missiles or sensor pods; one centreline for weapons, sensor pods or tank. Internal 20 mm cannon mounted in nose.

**Table 7.2e.** Data for the Grumman F-14 Tomcat

		Power plant
	F-14A	F-14B, C
	2 × 20900 lb (9480 kg) thrust Pratt and Whitney TF30-1412A	2 × 28090 lb (12741 kg) thrust Pratt and Whitney F401-400
	Two shaft after-burning turbofans	
$S$ (m)	11.630 (68° sweep) 19.54 (20° sweep)	safely landing
$L$ (m)	18.89	
$H$ (m)	4.88	
$A_w$ (m <sup>2</sup> )	–	
$P_L$ (kg)	17010	
$V$ (km/h)	Mach 2.3 or 1564 mph maximum speed, 400–500 km/h cruise speed, 125 km/h approaching speed	
$w_a$ (kg)	27216	
Armament	AIM-54 Phoenix missiles AIM-7 Sparrow missiles AIM-9 Sidewinder missiles	

**Table 7.2f.** Comparative data for MIG aircraft

Power plant	MIG-19 (Mikoyan)	MIG-21	MIG-23 (Flogger)	MIG-25 (Foxbat)	MIG-27	MIG-29
(Engines)	<i>Single-seater</i>	<i>Single-seater</i>	<i>Single-seater</i>	<i>Single-seater</i>	<i>Single-seater</i>	<i>Single-seater</i>
	2 × 6700 lb (3040 kg) to 2 × 7165 lb (3250 kg) Kimov RD-9B turbojets	Range turbojet 11240 lb (5100 kg) to 14500 lb (6600 kg) Tumansky single shaft	17640 lb (8000 kg) to 25350 lb (11500 kg) thrust, 1 Tumansky turbofan	27000 lb (12250 kg) to thrust, 2 Tumansky R-266 after-burning turbojets	17640 lb (8000 kg) to 25350 lb (11500 kg) thrust, 1-Tumansky after-burning turbofan	
$S$ (m)	9.00	7.15	8.7 (72° sweep) 14.4 (16° sweep)	14.0 Foxbat A	8.7 (72° sweep) 14.4 (16° sweep)	
$L$ (m)	13.08 (S-5F)	14.35	16.15	22.3 (Foxbat A) 22.7 (Foxbat R) 23.16 (Foxbat U)	16.15	
$H$ (m)	4.02	4.50	3.96	5.60	4.60	
$A_w$ (m <sup>2</sup> )	—	—	—	—	—	—
$P_L$ (kg)	3760	4600	7050	14970	9900	
$V$ (km/h)	Mach 1.3 or 1480 km/h (920 mph)	Mach 2.1 or 2070 km/h (1285 mph)	Mach 1.1 or 1350 km/h (840 mph)	Mach 3.2 or 3380 km/h (2100 mph)		
$w_a$ (kg)	9500	9800	15000	34930		17750

**Table 7.2g.** Data on the British Aerospace Jaguar

Power plant	
2 No. Rolls-Royce Turboméca Adour two shaft turbofans	
7305 lb (3313 kg) to 8000 lb (3630 kg) thrust	
$S$ (m)	8.69
$L$ (m)	15.4 to 16.42
$H$ (m)	4.92
$A_w$ (m <sup>2</sup> )	–
$P_L$ (kg)	6800
$V$ (km/h)	1450
$w_a$ (kg)	1550
Armament and other data	
2 No. 30 mm DFA 553 each with 150 rounds	
5 No. pylons with total external loads of 4536 kg with guns	
2 No. 30 mm Aden for its T-2 model	
Matra 550 Magic air-to-air missiles	
<i>Jaguar A and B and EMK</i>	102 Adour engines
<i>Jaguar S</i>	MK 104s } Adour engines
	MK 108s }
<i>Jaguar Act</i>	} Using digital quadruplex fly-by-wire control system
<i>Jaguar FBW</i>	

**Table 7.2h.** Data on the Dassault aircraft

Type and power plant	$S$ (m)	$L$ (m)	$H$ (m)	$A_w$ (m <sup>2</sup> )	$P_L$ (kg)	$V$ (km/h)	$w_a$ (kg)
Dassault Breguet F1							
Single-seater multi-mission fighter, 7200 kg thrust, SNECMA Atar, 9K-50 single shaft turbojet	8.4	15	4.5	–	7400	1472	14900
Estendard IVM and IVP							
Single-seater strike fighter, 4400 kg thrust, SNECMA Atar, 8B single shaft turbojet	9.6	14.4	4.26	–	5800	1083	10000
Super Estendard							
Single-seater strike fighter, 5110 kg thrust, SNECMA Atar, 8K-50 single shaft turbojet	9.6	14.31	4.26	–	6300	1200	11500
Mirage 3 and 5							
Single-seater or two-seater interceptor, trainer and reconnaissance aircraft, 6000 kg thrust, SNECMA Atar, 9B single shaft turbojet	8.22	15.5	4.25	–	6156	1390	12000
Mirage 2000							
Mirage 315 and F-1 improved version of these aircraft with engines SNECMA turbofans	9	15	4.5	–	7800	2200	9000
Mirage 4000							
SNECMA M53, single shaft bypass turbofan 8 stage axial compressor 2 × 14500 lb (2 × 6579 kg) thrust	12	18.7	4.5	–	13000	2300	16100
Armament							
Mirage 4000							
Internal cannons 2 × 30 mm							Bombs: anti-runway Durandal up to 27 clean or retarded (250 kg) up to 27 laser guided (250 kg) up to 27
4 long-range missiles							Rockets 68 mm
4 air-to-ground missiles							
2 air-to-surface missiles							

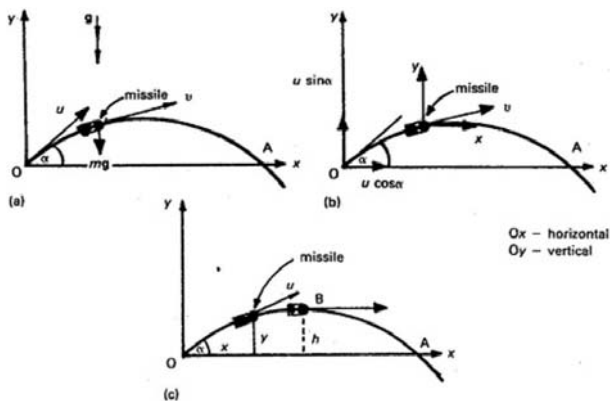
## Helicopters

Helicopters are more vulnerable than aircraft in warfare. In peace time a helicopter may crash after losing a rotor or hitting objects such as offshore platforms, bulidings, helipads or their surrounding structures. Table 7.3 gives useful data for some types of helicopters.

**Table 7.3.** Comparative data of some important combat aircraft

Type	Power plant	S (m)	L (m)	H (m)	$P_L$ (kg)	V mach (mph)	$w_a$ (kg)
BAe Harrier	1 × 21500 lb (9752 kg) thrust	7.7	13.87	3.43	6200	1.2	11793
GR-3 model	Rolls-Royce Pegasus 103		17.0 (GR-3)			(860)	
T-Mark 4 model	two shaft turbofan						
(AV-8A, TAV-8A)	(US designation F-400)						
FRS-I model							
Single-seater							
Two-seater							
F-6 Shenyang (or	2 × Axial turbojets	10.2	15.25	3.35	4500	1.0	10700
NATO's name	MD manufactured					(760)	
FANTAN 'A')							
Single-seater							
Rockwell B-I	4 × 30000 lb (13610 kg)	41.4	45.6	10.24	115670	0.85	179170
Four-seater	General Electric					(646)	
	F101-100 two shaft						
	augmented turbofans						
Saab 37 AJ, JA	1 Svenska flying motor RMB;	10.6	AJ: 10.6	5.6	4500	2.0	16000
Viggen SF, SH,	Pratt and Whitney two shaft					(1320)	
SK versions	25970 lb (11790 kg) to 28086 lb						
Single-seater	(12750 kg) thrust						
SU-9 Fishpot B	1 Lyulka single shaft	8.43	SU-9: 18.5				
SU-11 Fishpot C	turbojet; 19840 lb (9000 kg)		SU-11: 17.4	4.9	4540	0.95	13610
Single-seater	thrust (SU-9) and 22040 lb					(1195)	
	(10000 kg) thrust (SU-11)						
SU-15 (Flagen A	2 × Tumonsky R-25	9.5 D Model	21.50	5.0	10100 (D)	2.3	21000 (D)
to E models)	turbofans; 16530 lb (7500 kg)				5100 (A)	(1520)	16000 (A)
Single-seater	thrust after burner						
SU-17, SU-20 and	(17) 1-Lyulka AL-21 F-3	14 (28° sweep)	18.75	4.75	9000	1.05	19000
SU-22 models	thrust single shaft 17200 lb	10.6 (62° sweep)				(798)	
Single-seater	(7800 kg) (20-22) AL-7F					to	
	22046 lb (10000 kg)					2.17	
						(1432)	

**Table 7.4.** Simplified missile analysis



**Fig. 7.1a–c.** Simplified analysis for missile as a projectile

Figure 7.1a shows a missile projected at a velocity  $u$  from a position 0. At 0,  $x$ ,  $\dot{x}$  and  $\ddot{x}$  are all zero. The only force on the flight is equal to  $mg$ . Hence  $y$ , the acceleration in the vertical direction, is  $-g$ .

The general forms of the velocity and distance equations are:

$$v = u + at \tag{1}$$

$$s = ut + \frac{1}{2}at^2 \tag{1}$$

$$\dot{x} = u \cos \alpha, \quad \dot{y} = u \sin \alpha - gt \quad (\text{Fig. 7.1b}) \tag{2}$$

$$x = (u \cos \alpha)t; \quad y = (u \sin \alpha) - \frac{1}{2}gt^2 \tag{3}$$

$$\ddot{x} = 0; \quad \ddot{y} = -g \tag{4}$$

By elimination of  $t$  from (3), the trajectory equation is written in a parabolic form as

$$y = x \tan \alpha - (gx^2 \sec^2 \alpha / 2u^2) \tag{5}$$

The velocity  $v$  of the missile during flight at any instant in time is given by

$$v = \sqrt{(\dot{x}^2 + \dot{y}^2)} \quad \text{with} \quad \alpha = \tan^{-1} (\dot{y}/\dot{x}) \tag{6}$$

since

$$\dot{y}/\dot{x} = (dy/dt)/(dx/dt) = dy/dx.$$

The direction of the velocity at any instant is along the tangent to the path for that particular instant. If the missile is projected from the aircraft at an angle below its level in order to hit the target at the ground level (the aircraft level is treated as horizontal), (5) becomes

$$y = x \tan \alpha + (gx^2 + \sec^2 \alpha / 2u^2) \tag{7}$$

and all negative signs in (2) and (3) related to  $g$  are *positive*.

Case 1

If the missile is projected from the aircraft impact at an angle of  $\alpha' = 30^\circ$ , from a distance of 700 m, and hits the target at 200 m distance, the speed and the direction are computed from Fig. 7.1d.

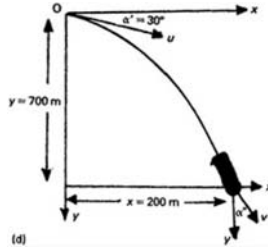


Fig. 7.1d

$$\begin{aligned}
 y &= x \tan 30^\circ + (gx^2/2u^2) \sec^2 30^\circ \\
 700 &= (200/\sqrt{3}) + \frac{9.8 \times 200^2}{2u^2} \times 1.34 \\
 u &= 21.2 \text{ m/s} \\
 dy/dx &= \tan 30^\circ gx \sec^2 30^\circ / u^2 \\
 &= (1/\sqrt{3}) + \frac{9.8 \times 200}{21.2^2} \times 1.34 \\
 &= 6.42 \\
 \alpha'' &= \tan^{-1} 6.42 = 81.15^\circ
 \end{aligned}$$

Case 2

If the missile is projected 4 m above the basic level of impact with a velocity of 100 m/s at an angle of  $45^\circ$  to the horizontal, the horizontal distance  $x$  at which it hits the ground is computed follows:

$$\begin{aligned}
 y &= x \tan \alpha - gx^2 \sec^2 \alpha / 2u^2 \\
 \text{or } -4 &= x - (gx^2/2u^2) \\
 \text{or } -4 &= x - (gx^2/2 \times 100^2)
 \end{aligned}$$

Rejecting the negative root,  $x = 2045 \text{ m}$ .

Case 3: flight time

As shown in Fig. 7.1a, the time taken by a missile to travel along its path from 0 to A is to be computed. At any time  $t$ :

$$y = (u \sin \alpha)t - \frac{1}{2}gt^2$$

At A,  $y = 0$

$$t = 2u \sin \alpha / g \tag{8}$$

The other value of  $t = 0$  cannot be true at A, as was assumed to be the case at 0.

Case 4: maximum height and horizontal range

Reference is made to Fig. 7.1c. At any time  $t$ , at any point B,

$$\dot{y} = 0 = u \sin \alpha - gt$$



Hence

$$t = u \sin \alpha / g \tag{9}$$

Substituting  $t$  into (3) of  $y$

$$\begin{aligned} y &= u \sin \alpha t - \frac{1}{2}gt^2 \\ h &= (u^2 \sin^2 \alpha / g) - \frac{1}{2}g(u \sin \alpha / g)^2 \\ h &= u^2 \sin^2 \alpha / 2g \end{aligned}$$

The maximum range  $x$  is obtained as

$$\begin{aligned} x &= ut \cos \alpha = u(2u \sin \alpha / g) \\ &= 2u^2 \sin \alpha \cos \alpha / g \\ &= u^2 \sin 2\alpha / g \end{aligned} \tag{10}$$

When  $\sin 2\alpha = 1$  or  $\alpha = 45^\circ$

$$x_{\max} = u^2 / g \tag{11}$$

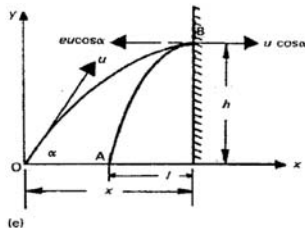


Fig. 7.1e

Case 5

A missile hits the target at a distance  $x$  when travelling horizontally. The distance  $l$  at which the missile hits the ground after bouncing is computed below.

As shown in Fig. 7.1d, by using the coefficient of restitution  $e$ , the speed after hitting the wall =  $eu \cos \alpha$  in a horizontal direction. The maximum height reached is given by

$$h = su \sin \alpha / g$$

The time taken to reach ground level is calculated by

$$\begin{aligned} y = h &= ut + \frac{1}{2}gt^2 = 0 + \frac{1}{2}gt^2 \\ t &= \sqrt{(2h/g)} = \sqrt{(2u^2 \sin^2 \alpha / 2g^2)} \\ &= u \sin \alpha / g \end{aligned} \tag{12}$$

When the missile hits the ground level at a distance  $l$  from the wall

$$\begin{aligned} l/x &= e(u \cos \alpha) / u \cos \alpha \\ l &= ex \end{aligned} \tag{13}$$

where  $e$  is the coefficient of restitution.

It can easily be proved that if the same missile hits a building floor vertically of height  $h$  with a velocity  $v$ , rebounds from there with coefficient of restitution  $e$  and rebounds to the floor with a coefficient of restitution  $f$ , when the value of  $v$  is given by

$$v = [2gh(1 - f^2 + e^2 f^2)]/e^2 f \quad (14)$$

### Example 7.1

A windborne missile of mass  $m$  strikes a building wall and ricochets off at  $120^\circ$  to its original direction. The speed changes from  $u = 40$  m/s to  $v = 35$  m/s. Calculate the resultant impulse of the system. Assume no damage occurs.

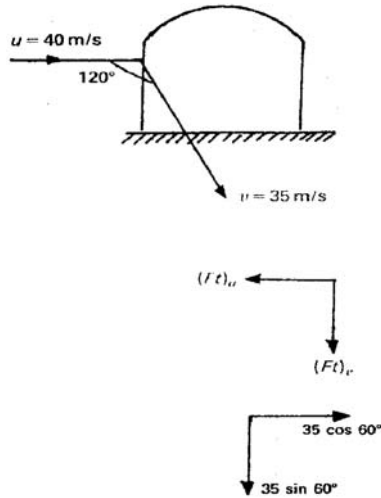


Fig. 7.2. Missile striking a wall

Since the direction of  $u$  and  $v$  are different before and after the impulse, the components of the impulse and the velocities in two perpendicular directions are considered.

$$\begin{aligned} (Ft)_u &= m(+35 \cos 60^\circ) - m(-40) \\ &= m[40 + (35/2)] = 22.5 m \quad \text{where } m = \text{mass} \\ (Ft)_v &= m(35 \sin 60^\circ - 0) \\ &= m35(\sqrt{3}/2) = 30.31 m \end{aligned}$$

Therefore the resultant impulse or impact

$$\begin{aligned} F_1(t) &= \sqrt{\{[(Ft)_v]^2 + [(Ft)_u]^2\}} \\ &= 64.9 m \end{aligned}$$

### 7.3 Two Columns/Girders Falling and Impacting Each Other in Contact in Elastic Medium

When two columns/girders are in contact, they exert equal and opposite forces or impulses on each other and they are in contact for the same time. If no external force affects the motion, the total momentum in the specific direction remains constant. This is known as the *principle of conservation of linear momentum*. When two bodies,  $m_1$  and  $m_2$  collide (Fig. 7.3), the mass ratios are then calculated from (7.1):

$$\begin{aligned} F_{I1}(t) &= m_1(\nu_1 - u_1) = \int F_1 dt \\ F_{I2}(t) &= m_2(\nu_2 - u_2) = \int F_2 dt \end{aligned} \quad (7.4)$$

Since  $\int F_1 dt + \int F_2 dt = 0$ , the relationship between velocity change and mass becomes:

$$m_2/m_1 = (\nu_1 - u_1) / -(\nu_2 - u_2) \quad (7.5)$$

During the collision process knowing the momentum is conserved there is a loss of energy on impact, which is determined using the concept of coefficient of restitution,  $e$ .



Fig. 7.3. Desect-impact

#### Example 7.2

Under impact, one of the falling girders weighing 1195 kg and travelling at 50 km/h comes to rest in 10 seconds at the ground level; calculation is necessary for the ground reaction.

$$\begin{aligned} \text{Total mass} &= 1195 \text{ kg}; u = 50 \text{ km/h} = 13.89 \text{ m/sec} \\ F(t) &= Ft = m\nu - mu \\ &= 0 - 1195(-13.89) \\ &= 16.598 \times 10^3 \\ &= 2F \end{aligned}$$

Hence

$$\begin{aligned} F &= 8.3 \times 10^3 \text{ kg} \\ &= 9.0856 \times 8.3 \times 10^3 \text{ N} \\ &= 0.07541 \text{ KN} \end{aligned}$$

This is the force that the ground soil must tolerate if it necessary to avoid penetration.

Which is defined as the relative velocity of the two masses after impact divided by the relative velocity of the two masses before impact. Before impact:

$$e = (\nu_1 - \nu_2) / -(u_1 - u_2) = 0$$

when the relative velocity vanishes, and

$$e = (\nu_1 - \nu_2) / -(u_1 - u_2) = 1 \quad (7.6)$$

Where  $e < 1$ , it is related to the loss in kinetic energy, and where  $u_2 = 0$  (refer to (7.6))

$$m_1(\nu_1 - u_1) + m_2(\nu_2) = 0 \quad (7.7)$$

$$\nu_1 - \nu_2 = -e u_1$$

hence

$$\nu_1 = u_1(m_1 - e m_2) / (m_1 + m_2) \quad (7.8)$$

$$\nu_2 = u_1 [(1 + e)m_1 / (m_2 + m_1)] \quad (7.9)$$

The original kinetic energy (KE)' =  $\frac{1}{2} m_1 u_1^2$

The final kinetic energy (KE)'' =  $\frac{1}{2} (m_1 \nu_1^2 + m_2 \nu_2^2)$

$$(KE)' - (KE)'' = \frac{1}{2} (m_1 u_1^2 - \frac{1}{2} (m_1 \nu_1^2 + m_2 \nu_2^2)) \quad (7.10)$$

Substituting the values of  $\nu_1$  and  $\nu_2$ :

$$(KE)' - (KE)'' = (KE)' [m_1(1 - e^2) / (m_1 + m_2)] \quad (7.11)$$

The displacement resulting from a short-duration ( $\tau$ ) impact is given by

$$x = b(t - \tau) \quad (7.12)$$

where  $t$  is the time beyond  $\tau$ .

For dynamic analysis, the impact time is divided into  $n$  small segments and, using (7.3a)

$$\begin{aligned} x &= \frac{1}{m} \sum_0^n \nu_n I_n (t - \tau_n) \\ &= \frac{1}{m} \int_0^t F(t - \tau) d\tau \end{aligned} \quad (7.13)$$

If the impact is divided into two phases such that in the first, from time  $t_1$  to  $t_0$ , there will be compression and distortion until  $(\nu_1 + \nu_2)$  are both reduced to zero (the two bodies moving together), in the second, the elastic strain energies in the bodies are restored and are separated by a negative velocity,  $-V_2 = (\nu_1 + \nu_2)$ . During the second phase the impulse relation between the bodies ( $F_T - F_{T0}$ ) will be proportional to  $F_{T0}$  and the coefficient or restitution  $e$  defined above is written as

$$e = (F_T - F_{T0})/F_{T0} \quad (7.14)$$

where  $F_T$  is the total impulse during the impact and  $F_{T0}$  is the impulse in phase one.

At time  $t_0$

$$V_0 = \nu_{10} + \nu_{20} = \nu_1 + \left( \frac{F_{T0}}{m_1} + \nu_2 - \frac{F_{T0}}{m_2} \right) = 0 \quad (7.15)$$

hence

$$V = \nu_1 + \nu_2 = \left( \frac{1}{m_1} + \frac{1}{m_2} \right) F_{T0} \quad (7.16)$$

Similarly, at time  $t_2$  the relationship becomes

$$V_0 - V_2 = F_T \left( \frac{1}{m_1} + \frac{1}{m_2} \right) \quad (7.17)$$

Using (7.14), the expression given in (7.6) may be written in the form:

$$-(V_2/V) = e \quad (7.18)$$

Equations (7.7) and (7.9) result from the above method. However, from (7.14) the total impulse is rewritten as

$$\begin{aligned} F_T &= \frac{m_1 m_2}{m_1 + m_2} (1 + e) (\nu_1 + \nu_2) \\ &= M(1 + e)V \end{aligned} \quad (7.19)$$

where  $M$  is the equivalent combined mass of the bodies.

The changes in velocity after impact of the bodies are written as

$$\begin{aligned} \Delta V_1 &= \frac{M}{m_1} (1 + e) (\nu_1 + \nu_2) = \frac{M}{m_1} (1 + e) V \\ \Delta V_2 &= \frac{M}{m_2} (1 + e) V \end{aligned} \quad (7.19a)$$

## 7.4 Oblique Impact

When two bodies collide and their axes do not coincide, the problem becomes more complex. With oblique impact, as shown in Fig. 7.4 two impulses are generated: the direct impulse,  $F_T$ , and the tangential impulse,  $F'_T$ . The latter is caused by friction between the impacting surfaces and by local interlocking of the two bodies by  $\theta_1$  and  $\theta_2$  respectively. If  $F'_T/F_T = \lambda'$  and the body's centre of gravity has a coordinate system  $X$  and  $Y$ , the components of the vector velocity,  $\nu_1$  and  $u_1$ , normal to the impact surface may be written as follows  $x_1 - y_1$  system

$$\nu_1 = |\bar{\nu}_1| \cos \theta_1 \quad (7.20)$$

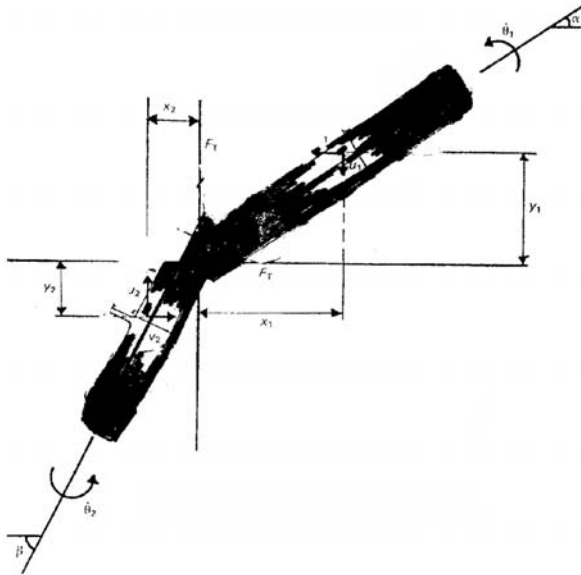


Fig. 7.4. Oblique impact

$$u_1 = |\bar{\nu}_1| \sin \theta_1 \tag{7.20a}$$

where

$$|\bar{\nu}_1| = \sqrt{\nu_1^2 + u_1^2}$$

$$\alpha = \tan^{-1}(u_1/\nu_1)$$

Similarly,  $\nu_2$  written as

$$|\bar{\nu}_2| = \sqrt{\nu_2^2 + u_2^2} \tag{7.21}$$

$$\beta = \tan^{-1}(u_2/\nu_2) \tag{7.21a}$$

The momentum equations for the bodies are summarized below:

$$\left. \begin{aligned} m_1 \nu_1' - F_T &= m_1 \nu_2' \\ m_1 u_1' - \lambda' F_T &= m_1 u_2' \\ m_1 R_1^2 \theta_1' + F_T y_1 - \lambda' F_T x_1 &= m_1 R_1^2 \theta_2' \end{aligned} \right\} \text{body 1} \tag{7.22}$$

where  $\nu_1', \nu_2', u_1'$  and  $u_2'$  are for  $t_1$  and  $t_2$ .

$x_2 - y_2$  system

$$\left. \begin{aligned} m_2 \nu_1'' - F_T &= m_2 \nu_2'' \\ m_2 u_1'' - F_T &= m_2 u_2'' \\ m_2 R_2^2 \theta_2' + F_T y_2 - \lambda' F_T x_2 &= m_2 R_2^2 \theta_2' \end{aligned} \right\} \text{body 2} \tag{7.23}$$

where  $mR_1^2$  and  $mR_2^2$  are the second moment of inertia about the vertical axis passing through the centre of gravity. The rate of approach and the sliding of the two surfaces at the point of contact can be written as

$$\Delta V_1 = v_1 + v_2 - \dot{\theta}_1 y_1 - \dot{\theta}_2 y_2 \quad (7.24)$$

$$\Delta V_2 = u_1 + u_2 - \dot{\theta}_1 x_1 + \dot{\theta}_2 x_2 \quad (7.25)$$

The addition to these equations is the restitution given by (7.18) in which, when (7.24) is substituted and then, in the final equation, (7.22) is substituted, the value of  $F_T$  is evaluated as

$$F_T = \frac{V(1+e)}{c_1 - \lambda c_2} \quad (7.26)$$

where

$$c_1 = \frac{1}{m_1} \left( 1 + \frac{y_1^2}{R_1^2} \right) + \frac{1}{m_2} \left( 1 + \frac{y_2^2}{R_2^2} \right) \quad (7.26a)$$

$$c_2 = \left( \frac{x_1 y_1}{m_1 R_1^2} + \frac{x_2 y_2}{m_2 R_2^2} \right) \quad (7.26b)$$

Using (7.22) and (7.23):

$$v'_2 = v'_1 - (F_T/m_1) \quad (7.27)$$

$$u'_2 = u'_1 - (\lambda' F_T/m_1)$$

$$\begin{aligned} \dot{\theta}_2 &= \dot{\theta}_1 + \frac{y_1 - \lambda' x_1}{m_1 R_1^2} F_T \\ \nu''_2 &= \nu''_1 - \frac{F_T}{m_2} \end{aligned} \quad (7.28)$$

$$u''_2 = u''_1 - \frac{\lambda' F_T}{m_2}$$

$$\dot{\theta}'_2 = \dot{\theta}'_1 + \frac{y_2 - \lambda' x_2}{m_2 R_2^2} F_T$$

Figure 7.5 shows plots for (7.27) and (7.28). It is interesting to note that larger values of  $\lambda'$  show greater interlocking of the surfaces of the two bodies and with  $e$  reaching zero, a greater plastic deformation occurs.

### Case Studies

(1) One body impacting a rigid barrier with no angular velocity.

$$1/m_2 = 0; \quad v_1 = 0; \quad u_1 = 0; \quad \dot{\theta}_1 = 0 \quad (7.29)$$

$$c_1 = \frac{1}{m_1} \left( 1 + \frac{y_1^2}{R_1^2} \right); \quad c_2 = \frac{x_1 y_1}{m_1 R_1^2} \quad (7.29a)$$

$$\nu'_2 = \nu'_1 (y_1^2 - \lambda' x_1 y_1 - e R^2) / \bar{\lambda} \quad (7.29b)$$

$$u'_2 = u'_1 - \nu'_1 \left( \frac{\lambda' (1+e) R^2}{\bar{\lambda}} \right); \quad \dot{\theta}'_1 = \frac{(1+e)(y_1 - \lambda' x_1)}{\bar{\lambda}} \quad (7.29c)$$

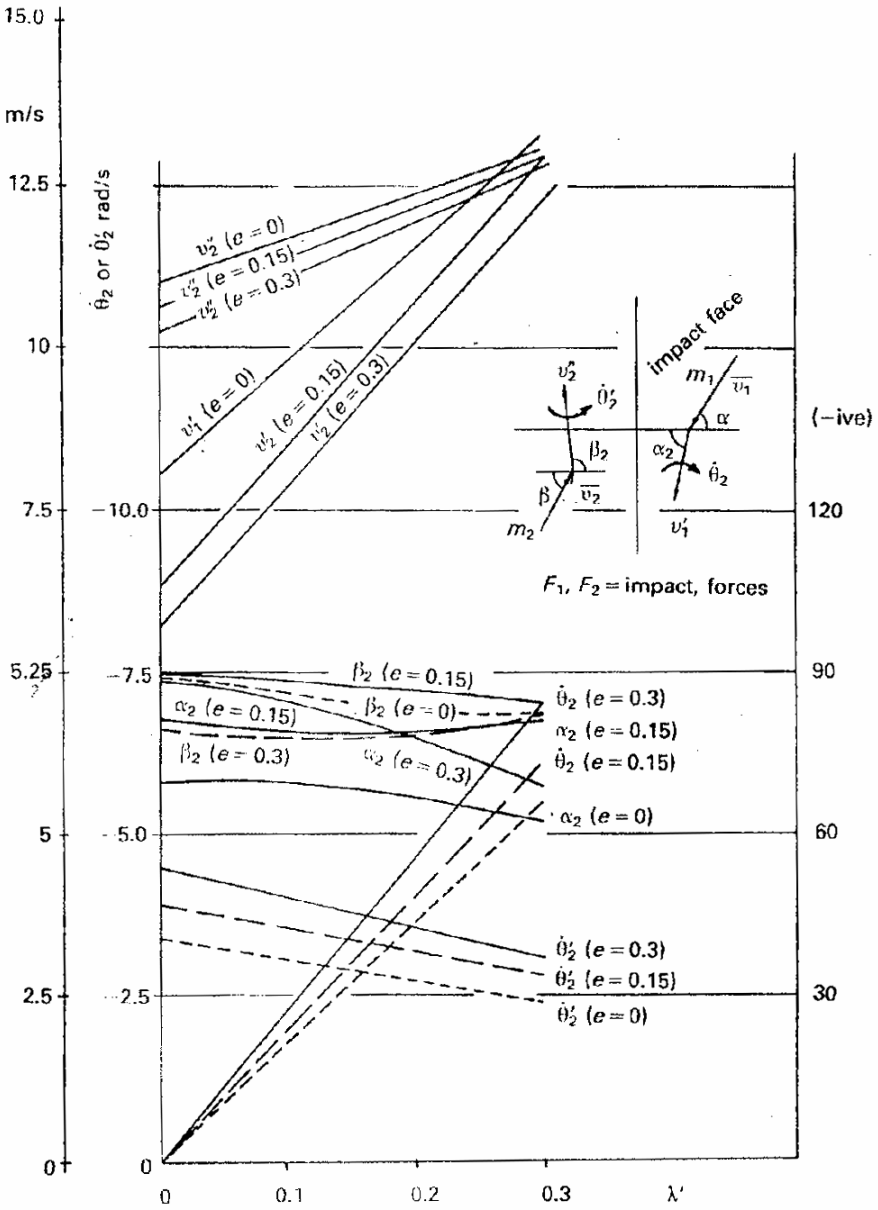


Fig. 7.5. Velocity versus  $\lambda'$  for obliqu. Problems

where

$$\bar{\lambda} = y_1^2 - \lambda' x_1 y_1 + R^2 \tag{7.29d}$$



(2) Circular impactor with radius  $r_1$ .

$$x_1 = r_1 \quad \text{and} \quad y_1 = 0 \quad (7.30)$$

$$v'_2 = e v'_1 \quad (7.30a)$$

$$u'_2 = u_1 - \lambda' v'_1 (1 + e) \quad (7.30b)$$

$$\dot{\theta}_1 = -v'_1 \lambda' r_1 (1 + e) / R^2 \quad (7.30c)$$

For a circular impactor,  $R^2 = 2r_1^2/5$

$$\dot{\theta}_1 = -v'_1 (5\lambda' (1 + e) / 2r_1) \quad (7.30d)$$

(3) Inelastic collisions. The value of  $e = 0$  in the above case studies.

Case study (1)

$$\begin{aligned} v'_2 &= v'_1 (y_1^2 - \lambda' x_1 y_1) / \bar{\lambda} \\ u'_2 &= u'_1 - v'_1 (\lambda' R^2 / \bar{\lambda}) \end{aligned} \quad (7.31)$$

$$\dot{\theta}_1 = (y_1 - \lambda' x_1) / \bar{\lambda}$$

Case study (2)

$$\begin{aligned} v'_2 &= 0; \quad u'_2 = u_1 - \lambda' v'_1 \\ \dot{\theta}_1 &= -v'_1 \lambda' r_1 / R^2 = -2.5 v'_1 \lambda' / r_1 \end{aligned} \quad (7.32)$$

(4) Where no interlocking exists,  $\lambda' = 0$  in the above expressions.

## 7.5 Aircraft Impact on Structures – Peak Displacement and Frequency

A great deal of work has been carried out on the subject of missile and aircraft impact. Tall structures are more vulnerable to civilian, wide-bodied jets or multi-role combat aircraft. A great deal of work on this subject will be reported later. In this section a preliminary analysis is given for the determination of peak displacement and frequency of a tall structure when subject to an aircraft impact. As shown in Fig. 7.6 the overall dimensions of the building are given. Let  $A$  be the base area and  $h$  be the maximum height of the building. According to the principle of the conservation of momentum, if  $m$  is mass and  $v_1$  is the velocity of the aircraft approaching the building, then using a linear deflection profile:

$$F_1(t) = m v_1 = (\rho A h / 2g) v_{20} \quad (7.33)$$

where  $\rho$  is the density or average specific weight and  $v_{20}$  is the velocity of the tip of the building.

The initial velocity,  $v_{20}$ , of the building can thus be evaluated from (7.5). The time

$$\begin{aligned}
 \delta(t) &= (\nu_{20}/\omega) \sin \omega t \\
 &= [\nu_{20}/(2\pi/T)] \sin \omega t \\
 &= [\nu_{20}/\sqrt{(k_c/m_c)}] \sin \omega t
 \end{aligned}
 \tag{7.34}$$

where  $\omega$  is the circular frequency and  $k_c$  and  $m_c$  are the equivalent building stiffness and mass, respectively.

Using (7.33) for  $\nu_{20}$  and  $\sin \omega t = 1$  for  $\delta_{\max}(t)$ , the *peak dynamic displacement*,  $\delta_{\max}(t)$ , is given by

$$\delta_{\max}(t) = m\nu_1 gT/\pi\rho Ah \tag{7.34a}$$

The equivalent point load generated for the peak dynamic displacement is given by (7.34a). If that load is  $F_1(t)$ , then work done is equal to the energy stored and

$$F_1(t) \times \delta_{\max}(t) = \frac{1}{2}k_c \delta_{\max}^2(t) \tag{7.35}$$

from which

$$F_1(t) = \frac{1}{2}k_c \delta_{\max}(t) \tag{7.35a}$$

While momentum is conserved, a portion of energy of the aircraft is lost on impact. The loss of energy  $E_1$  is then written as

$$E_1 = \frac{1}{3}(\rho Ah/mg)(\nu_{20}/\nu_1)^2 \tag{7.36}$$

Equations in case study (1) and (7.31) for inelastic collisions are applied with and without the interlocking parameter,  $\lambda'$ .

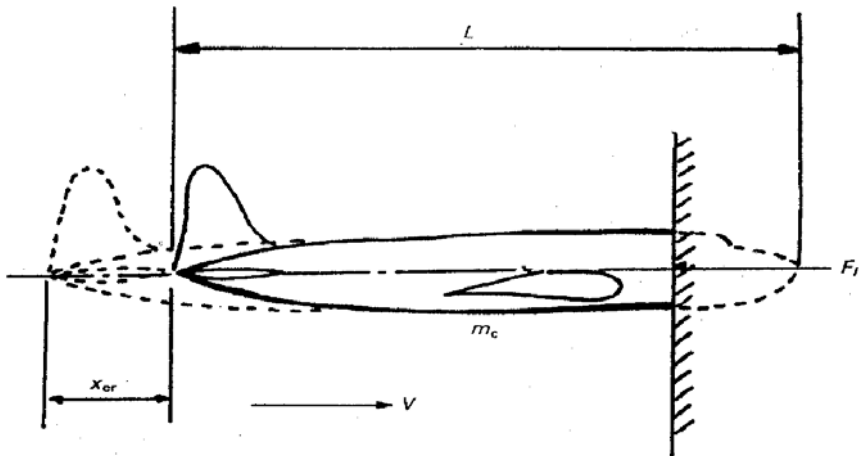


Fig. 7.6. Model aircraft impacting against a rigid surface

## 7.6 Aircraft Impact: Load-Time Functions

### 7.6.1 Introduction

Many sensitive installations are to be found in areas where heavy air traffic exists. Hence aircraft crashes cannot be entirely ruled out in such areas. Much effort is now being devoted to studies of aircraft impact with a clear aim of facilitating design to minimize damage to the aircraft and to the installations. Accident investigations, experiences and records are briefly discussed in Chap. 1. In this section some useful impact models are given which can be easily linked to both simplified and complex methods.

### 7.6.2 Stevenson's Direct Head-On Impact Model

Work has been carried out on the remaining undamaged length of 45 m (150 ft) long DC-8 jet which crashed into a rigid-surface, as shown in Fig. 7.4. A simplified equation of motion is written as

$$V(dV/dx)[k(L - x_{cr}) + m_c] = F_1(t) \quad (7.37)$$

where

$V$  = speed of the aircraft at time  $t$  after impact

$x_{cr}$  = crushed length

$k$  = mass per unit length of fuselage

$m_c$  = concentrated mass at wings including engines and others

$F_1$  = impact force or resistance at the crash level.

Equation (7.37) is integrated:

$$F_1(t) = \frac{1}{2} kV_0^2 \left[ \left( \frac{V}{V_0} \right)^2 - 1 \right] / \log [1 - x_{cr}/(L + m_c/k)] \quad (7.38)$$

where  $V_0$  is the aircraft speed prior to impact.

### 7.6.3 Riera Model

The response of the structure was assessed by Riera. The aircraft was replaced by an equivalent force-time function. The aircraft impinges perpendicularly on a rigid target and it is assumed that it crashes only at the cross-section next to the target. The cross-sectional buckling load decelerates the remaining rigid uncrushed portion. The total impact force  $F_1(t)$  is the sum of the buckling load and the force required to decelerate the mass of the impinging cross-section. Since it is a one-dimensional ideal plastic impact approach, in his model only the buckling load and the distribution of mass are needed. The equation of motion is written as:

$$F_1(t) = R_{cr}x_{cr} + m_c x_{cr} (dx_{cr}/dt)^2 \quad (7.39)$$

where

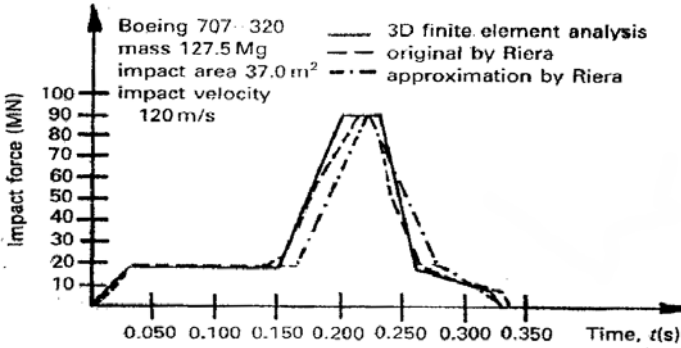


Fig. 7.7. Force as a function of time (Boeing 707-320)

$m_c$  = mass per unit length of the uncrushed aircraft at impact

$x_{cr}$  = crushed length

$dx_{cr}/dt = V_{un}$  = velocity of uncrushed portion

$R_{cr}$  = resistance to crushing, i.e. crushing strength.

Non-linear equations for  $R_{cr}$  and  $m$  are set up and numerical procedures are adopted for the applied forces at discrete time steps. The deceleration of the uncrushed mass  $m$  is written as:

$$G_d = \ddot{x} = -R_{cr}(x_{cr})_n / \int_{(x_{cr})_n}^L m_c x_{cr} dx_{cr} \tag{7.40}$$

In order to determine the current acceleration, current states of  $(x_{cr})_n$  and  $R_{cr}$  at time  $t_n$  can be used. Similarly, the common kinematics relationship between acceleration, velocity, displacement and time can be used to determine conditions at time  $t_{n+1} = t_n + \delta t$ .

$$(\dot{x}_{cr})_{n+1} = (\dot{x}_{cr})_n + \ddot{x}_n \delta t \tag{7.41}$$

$$(x_{cr})_{n+1} = (x_{cr})_n + \dot{x}_{cr} \delta t + \frac{1}{2} \ddot{x}_n \delta t^2 \tag{7.42}$$

Equation (7.39) is used to calculate the current force. The force-time history can thus be determined. A typical force-time history is given in Figs. 7.7 and 7.8.

### 7.6.4 Model of Wolf et al.

Wolf et al. developed a lumped mass, elasto-plastic model, as shown in Fig. 7.9. Just prior to impact on a target of mass  $m_t$ , Fig. 7.9a, spring stiffness  $k_t$  and damping coefficient  $c$ , the model has the mass of the fuselage which is lumped in  $n$  nodes Fig. 7.9b. The mass  $m_w$  or the part of the wing will be assumed to break away when a certain crushing length is achieved. The

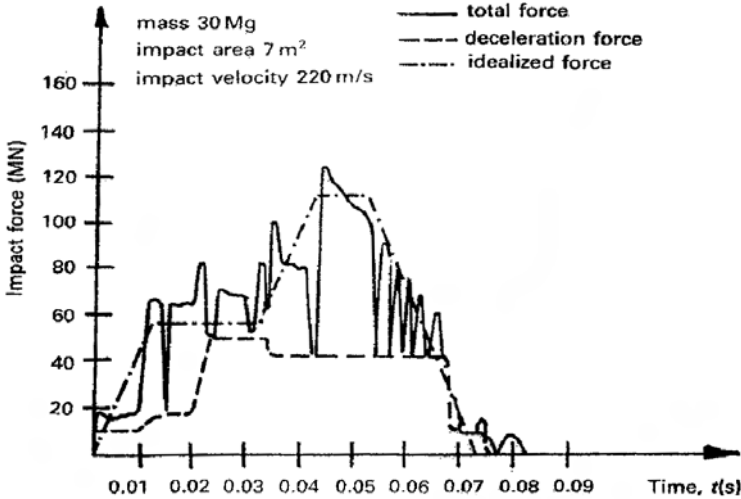


Fig. 7.8. Force as a function of time (Phantom)

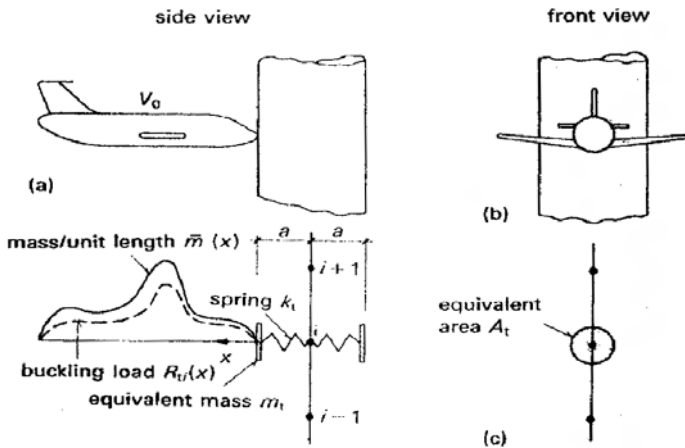


Fig. 7.9. Aircraft impact on chimney

nodes are connected by springs  $k_i$  of length  $L_i$ . The springs work in tension and compression. For a spring next to the target, only contact in compression is allowed. In tension, after reaching the yielding force  $R_{yi}$ , the spring ideally become plastic, with a rupturing strain  $\varepsilon_r$ . At the buckling load  $R_{ti}(x)$  the springs are allowed to crush completely at  $\varepsilon_i = -1$ . When the spring  $k_j$  (Fig. 7.9c) reaches the value of  $-1$ , the masses  $m_j$  with mass  $m_j + m_{j+1}$  (Fig. 7.9c). The spring stiffness  $k_j$  and its  $j$ th degree of freedom are deleted. Using the conservation of momentum, the velocity  $u_{j+1}^+$  just after impact is computed:

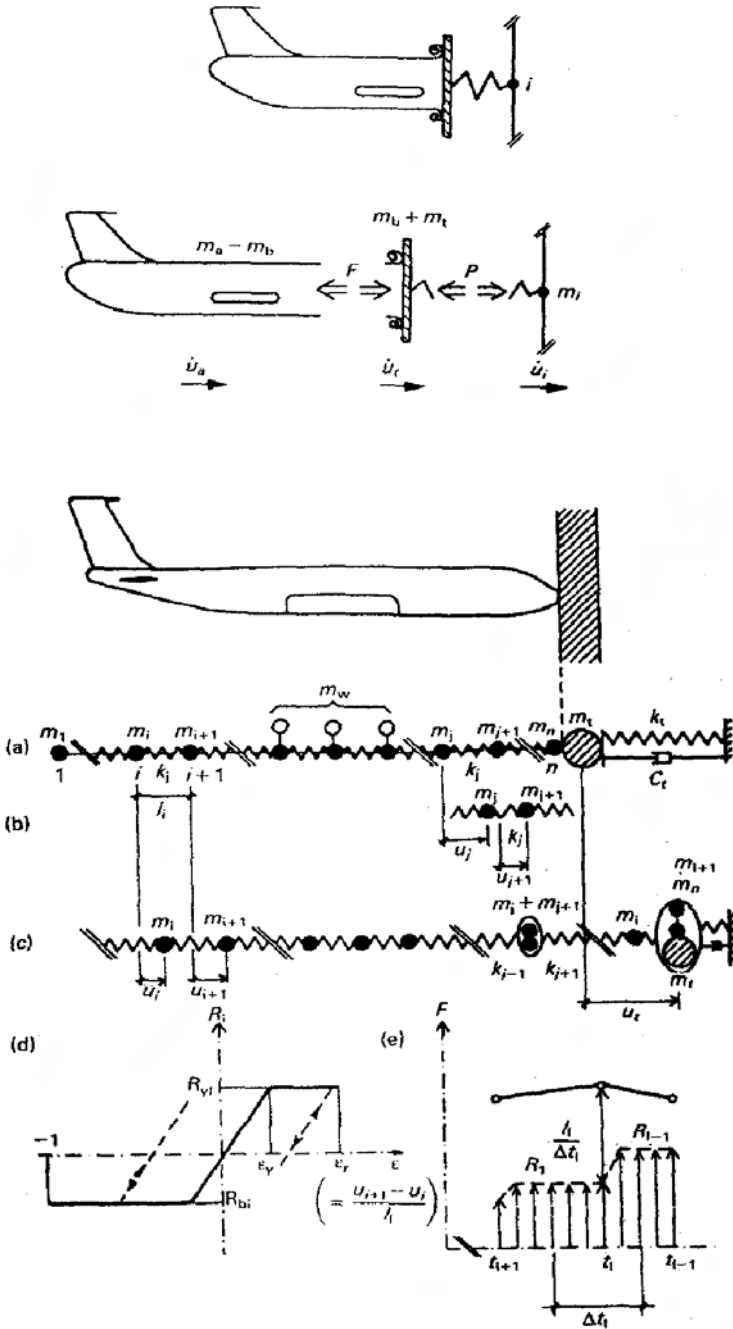


Fig. 7.10. Aircraft impact on deformable target (lumped-mass model)

$$u_{j+1}^+ = (\dot{u}_{j+1}^- m_{j+1} + \dot{u}_j^- m_j) / (m_{j+1} + m_j). \quad (7.43)$$

where  $\dot{u}_j^-$  is the displacement of the  $j$ th node, and  $-$  and  $+$  superscripts for before and after impact. (*Note:* the symbol  $u$  for displacement adopted here is the same as  $x$ , in this text.)

The equations of motion with discrete time steps are adopted for the force-time relationship. The total impulse  $I(t)$  from the individual mass point  $m_1$  to the target at time  $t_1$  is given by

$$I_1(t) = m_\ell [\dot{u}_t^+ - u_1^-] = (m_t + m_b) [\dot{u}_t^+ - u_t^-]. \quad (7.44)$$

Since the mass  $m_\ell$  is distributed along the axis of the aircraft, the time for the momentum transfer  $\delta t_\ell$  is given by

$$\delta t_\ell = \frac{1}{2}(t_{\ell-1} - t_{\ell+1}) \quad (7.45)$$

where  $t_{\ell-1}$  and  $t_{\ell+1}$  are the times of impact of the mass points  $m_{\ell-1}$  and  $m_{\ell+1}$ . Hence the value of  $F_1(t_\ell)$  is given by

$$F_1(t_\ell) = R_\ell + I_1(t) / \delta t_\ell \quad (7.46)$$

where  $R_\ell$  is the force in the spring  $k_\ell$ .

For a deformable target, as shown in Fig. 7.10,

$$F_1(t) = R_B(t) + \bar{m}(t) [\dot{u}_a(t) - \dot{u}_t(t)]^2 \quad (7.47)$$

where

$$R_B(t) = [m_a - m_b(t)] \ddot{u}_a(t) \quad (7.48)$$

where  $m_a$ ,  $m_b$  and  $m$  are the total mass of the aircraft, the mass of the crushed part of it and the mass per unit length of the crushed part next to the target, respectively and  $\dot{u}_a$  and  $\dot{u}_t$  are the velocities of the aircraft and the target respectively. The equation of motion is written as

$$[m_b(t) + m_t] \ddot{u}(t) = P(t) - F(t) \quad (7.49)$$

where  $P$  denotes the force in the impact spring transmitted to nodes of the target. The velocity of the new target for the ideal plastic impact is given by

$$\dot{u}_t = [(m_b(t) + m_t) \dot{u}_i^- + m_t \dot{u}_i^-] / [m_b(t) + 2m_t] \quad (7.50)$$

Again the superscripts  $+$  and  $-$  indicate just after and just before impact.

Wolf et al. tested their work on rigid and deformable targets. Data used in their work are reproduced below:

*Rigid target*

Boeing 707-320

$m_a = 127.5 \text{ Mg}$

$m_w = 38.6 \text{ Mg}$  included in  $m_a$

$\varepsilon_y = 2 \times 10^{-3}$ ;  $\varepsilon_r = 5 \times 10^{-2}$

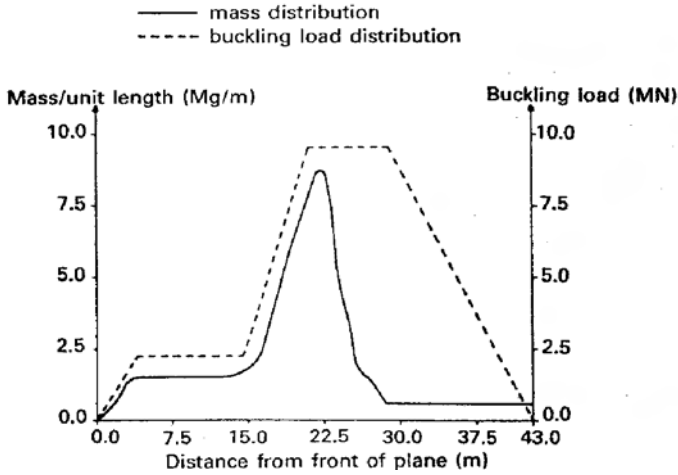


Fig. 7.11. Assumed properties of a Boeing 707-320

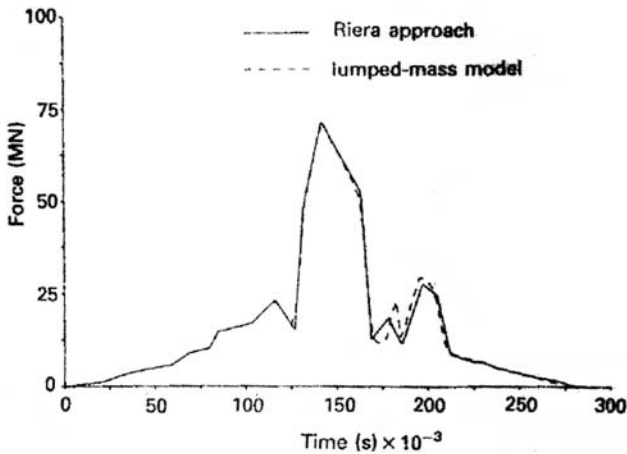


Fig. 7.12. Force-time diagrams for an FB-111

*Deformable target*

Impact area = 37.2 m<sup>2</sup>

$R_T$  = yielding moment/elastic moment

Figures 7.11 and 7.12 show a comparative study for two aircraft, a Boeing 707-320 and a combat aircraft FB-111, impacting on rigid targets, Figures 7.11 and 7.12 illustrate force-time relationships for deformable targets, such as these two aircraft.



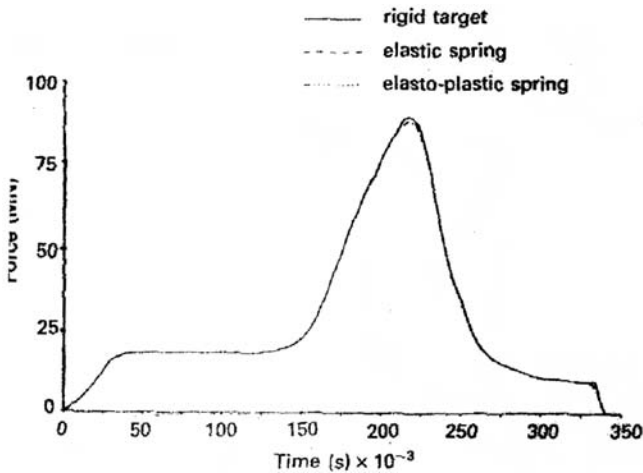


Fig. 7.13. Force-time diagram for a deformable target (frequency 50 Hz) mass model

## 7.7 Military, Air Force, and Navy Missiles and Impactors

### 7.7.1 Introduction to Bombs, Rockets, and Missiles

Different versions of bombs, rockets and missiles are available in the defense markets. Table 7.5 summarizes the characteristics of a number of shells and bombs.

Different missile systems exist in a number of countries. The range capability determines their category. Missiles with a maximum range exceeding 550 km are classified *strategic* and those with ranges between 1000 and 5500 km are known as *intermediate missiles*. Missile systems with ranges less than 1000 km are called *short-range* missile systems. Above these are the inter-continental missiles.

Certain symbols used in the explanatory notes for the missiles are defined as follows:

- ICBM Intercontinental ballistic missiles or strategic missile
- IRBM Intermediate range ballistic missile
- SRM Short-range missile
- SSM Surface-to-surface missile
- NSA Naval surface-to-air missile
- ADM Air defense missile
- AAM Air-to-air missile
- ASM Air-to-surface missile
- RO Rocket
- B Bomb

- Parameters  $L$ : Length;  $S$ : span;  $d$ : diameter;  $w_L$ : weight;  $V$ : speed;  $R$ : range in miles (km); SG: self-guided;  $P_L$ : payload

It is important to mention a few of the missiles. A typical example of the ICBM/IRBM is Patriot, a SAM, and three shoulder-mounted missiles, namely Stinger, Blow Pipe and Javelin missiles. Others are described in Tables 7.5 to 7.14.

### 7.7.1.1 Patriot: A SAM

In March 1972, Patriot was underway with modifications in radar, computer and guidance hardware. In July 1973, demonstration model fire control group (DMFCG) was tested. In January 1979, the program was redesigned XMIM-104 Patriot. A full-scale development commenced in August 1979. First firing in CM electronic counter measures (ECM) was carried out in December 1976. A Patriot fire unit consists of a fire section (FSC) and its launchers. The individual sections of the weapon from nose to tail are given below:

- (1) nose redone
- (2) terminal guidance system
- (3) warhead section
- (4) propulsion system
- (5) control section

The nose random is fabricated from 12 mm thick slip-cast fused silica and tipped with cobalt alloy.

Table 7.5. Guns, shells and bombs

Types of shells and bombs	Manufacturer	Dimensions	$w_L$ (kg)	Shape and guidance	$R$	$V$ (m/s)	Warhead (kg)	Mechanisms
Double base shot gun	International	$d = 1.25$ $t = 0.150$	–	Porous disc	Short	–	–	Guns
Single or double base rim fire	International	$d = 0.875$ $t = 0.10$	–	Porous disc	Short	–	–	Guns
Double base revolver	International	$d = 1.00$ $t = 0.125$	–	Porous disc	Short	–	–	Gun
Single base rifle	International	$d = 1.25$ $d = 0.375$ $t = 0.045$	–	Tubular	Short	–	–	Gun
GBU-15	Rockwell	$L = 3.75$	$MK84$	The forward guidance system	Medium	–	–	Free fall
HOBOS guided bomb	International USA	$MK84$ $S = 112$ $d = 46$ $(M118)$	2240 (1016) $M118$ 3404	is KMU-353 or 390 electro-optical with TV camera or target seeker optics	–	–	–	bomb from
Bofor	Sweden	–	0.120	5500 kg guns	3.7 km	10005	0.88	Trajectory fall
ZSU-23-4	USSR	$L = 654$ $d = 29.5$ 3400 rounds	20.50	SPAA vehicles 4 × 3 automatic	Short	7000	–	Gun
GBU-15(V)2 glide bomb (smart bomb)	USA	$L = 388$	–	Imaging infra-red	Short	–	1111.0	–

$d$  = diameter (mm);  $t$  = web thickness (mm);  $L$  = length (cm);  $w_L$  = weight;  $S$  = span (cm);  $R$  = distance;  $V$  = velocity.

Table 7.6. Missiles for Armed Forces (ICBM and IRBM) (China, USSR)

Types of missiles/rockets	Manufacturer/ country of manufacture	Dimensions	$w_L$ lb (kg)	Power plant and guidance	$R$ miles (km)	$V$ mach	Warhead	Mechanisms
BGM-109	General dynamics/ Convair, San Diego, USA	$L = 5.56$ $S = 2.45$ $d = 0.53$	2200 (1000) to 4000 (1814)	Williams Research F107 Turbofan 600 lb (272 kg) Thrust Guidance MD Tercom and Inertial	1727 (2780)	0.72 (550 mph/ 885 km/h)	Thermo- nuclear 1000 lb (454kg)	SG
CSS-2	China	—	—	Liquid propellant Stage 2	(12000)	0.8	Nuclear 2Mt	SG
CSS-3 (IRBM)	China	—	—	Stage 3 Liquid propellant Two stages	(1200) (2700)	0.7	1-3 Mt Nuclear 20kt 1-3 Mt 1 Mt	SG
Sandal (IRBM)	—	—	—	Two stages	(2000)	—	—	—
SSBS S-3	France	—	—	Solid propellant Two stages	(3000)	0.65	Nuclear 1.2Mt	—
SS-N-20 Sturgeon (IRBM)	USSR	—	—	Solid propellant	(3000)	0.65	Nuclear 1.2Mt	—
UGM-73 Poseidon missile (IRBM)	Lockheed Missiles and Space Company, California, USA	$L = 10.36$ $d = 1.88$	65000 (295000)	Solid motor Thiokol as first stage; Hercules as second stage; guidance: inertial	3230 (5200)	10.0	Lockheed MIRV carrying 50 kt Rvs	Submarine launch
UGM-27 Polaris (ICBM) missile	Lockheed, California, USA	$L = 9.45$ $d = 1.37$	35000 (15850)	Aerojet solid motor with jetavator control as first stage; Hercules motor with liquid injection as second stage	2875 (4630)	10.0	MIRV 200kt	Submarine launch

$d$  = diameter (m);  $L$  = length (cm);  $S$  = wingspan (m);  $w_L$  = launch weight;  $R$  = range;  $V$  = speed; SG = self-guided.

Table 7.7. Missiles for Armed Forces (ICBM and ALCM) (USA, USSR)

Types of missiles/rockets	Manufacturer/ country of manufacture	Dimensions $w_L$ lb (kg)	Power plant and guidance	$R$ miles (km)	$V$ mach	Warhead	Mechanisms
AGM-86A air-launched cruise missile (ALCM)	Boeing, Aerospace, Seattle, USA	$L = 4.27$ $S = 289$ $d = 64$	Williams Research F107-turbofans 600 lb (272 kg) thrust; McDonnell Douglas Tercom with inertial system	760 (1200)	0.6 to 0.8	Thermo-nuclear 200kt	B-52
LGM-30 Minuteman (ICBM) missile, located in silos	Boeing Aerospace, Ogden, USA	$L = 18.2$ $d = 183$	I-Stage: Triokol TU-120 (M55E), $2 \times 10^5$ lb ( $9 \times 10^3$ kg) thrust II-Stage: Hercules rocket III Stage: $35 \times 40^3$ lb ( $16 \times 10^3$ kg) thrust <i>Model II</i> 70116 (31800) <i>Model III</i> 76015 (34475)	II Stage: 7000 (11250) III Stage: 8000 (12875)	1500 mph	Thermo-nuclear 1–5 Mt II-Stage: AVCO MK IIC III-Stage: GE MK-12 MIRV Nuclear 750kt	SG
RS-12/SSI3 Savage (ICBM)	USSR	–	III-Stage: Aerojet $35 \times 10^3$ lb ( $16 \times 10^3$ kg) thrust Solid fuel propellant; three stages	(9400)	0.8	3.6Mt mode 2 or MIRV $4 \times 200$ kt	SG
RS-16/SSI7 (ICBM)	USSR	–	Liquid cold launch; two stages	(11000) (10000)	0.8	3.6Mt mode 2 or MIRV $4 \times 200$ kt	SG
RS-20/SS18 (ICBM)	USSR	–	Liquid propellant; two stages	(10000)	1.0	5–10 Mt mode 2	SG
SS-23 Scalpel (ICBM)	USSR	–	Solid cold launch propellant; three stages	(10000)	1.0	Nuclear MIRV 8–10× 300–500 kt	Rail; mobile
SS-25 Stickle (IRBM)	USSR	–	Solid cold launch propellant; three stages	(10500)	1.0	Nuclear 550kt	

$L =$  length (m);  $S =$  wingspan (cm);  $d =$  diameter (cm);  $w_L =$  launch weight;  $R =$  range;  $V =$  speed; SG = self-guided.

**Table 7.8.** Missiles for Armed Forces (SRM, SCUD, RBS, HJ) (USSR, France, UK, USA, China, Sweden)

Types of missiles/rockets	Manufacturer/ country of manufacture	Dimensions $w_L$ lb (kg)	Power plant and guidance	$R$ (km)	Warhead	Mechanisms
M Type (SRM)	China	$L = 910$	Solid propulsion; inertial	600	Nuclear	SSM
Frog-7 (SRM)	France	$L = 910$ $d = 85$	Solid propulsion	70	Nuclear	SSM
SS-1C Scud B	USSR	$L = 1125$ $d = 85$	Storable liquid; inertial	280	Nuclear	
SS-23 Spider (SRM)	USSR	$L = 605$ $d = 100$	Solid propulsion; inertial	525 miles	Nuclear	SSM
Exocet MM 10	France	$L = 578$ $S = 100$	Solid propulsion; two stages; inertial and active radar homing	70	165 kg Conventional	SSM ship
RBS 15	Sweden	$d = 35$ $L = 435$ $d = 50$	Turbojet and boosters	150	Conventional	SSM ship
Arrow 8 (HJ-8)	China	$L = 99.8$ $S = 47$ $d = 10.2$	Solid propulsion; wire-guided	0.1 to 3	Heat	SSM anti-tank
Spandrel	USSR	$L = 100$ $d = 16$	Solid propulsion; semi-automatic	4	Heat	SSM anti-tank
Vigilant	UK	$L = 107$ $S = 28$ $d = 11$	Solid propulsion; two stages; wire manual or auto	1.375	Heat 6 kg	
Dragon 1 M 47	USA	$L = 74$ $S = 33$ $d = 13$	Multiple solid propulsion; wire manual	1.0	Heat	SSM anti-tank

$L =$  length (cm);  $d =$  diameter (cm);  $S =$  wingspan (cm);  $w_L =$  launch weight;  $R =$  range.

**Table 7.9.** Missiles for Armed Forces (BGM, M, MK, ROM, etc.) (USA, France, Israel)

Types of missiles/rockets	Manufacturer/ country of manufacture	Dimensions	$w_L$ lb (kg)	Power plant and guidance	$R$ (km)	Warhead	Mechanisms
TOW 2 (BGM-71 D)	USA	$L = 140$ $d = 15$	(21.5)	Solid propulsion; wire manual or auto	3.75	Heat conventional	SSM anti-tank
Copperhead (M712)	USA	$L = 137$ $d = 15$	63.5	Cannon launched; laser homing	16	Heat 6.4 kg	SSM anti-tank
Gabriel	Israel	$L$ $S$ $d$		Two stage solid propulsion; auto	18	Conventional 100 kg	SSM shipborne
MK I		335   135   34	430	propulsion; auto	36	100 kg	
MK II		341   135   34	430	pilot/command	36+	150 kg	
MK III		381   135   34	560		200		
MK IV		381   135   34	560	Turbojet propulsion; inertial and active radar homing			
SS-N-3 Shaddock (SRM)	USSR	$L = 1020$ $d = 86$	4700	Solid boosters; internal turbojet radio command	460 to 735	Nuclear and conventional	SSM shipborne
Harpoon (RGM-84A)	USA	$L = 384$ $S = 830$ $d = 34$	519	Solid booster turbojet cruise; inertial and radar	90	Conventional	SSM shipborne
Deadeye 5	USA	$L = 384$ $d = 12.7$	47.5	Solid propulsion; laser homing	24	–	Guided projectile, shipborne NSA
Crotale	France	$L = 290$ $S = 54$ $d = 15$	80	Solid propulsion; radio command	18	15 kg Conventional	NSA
Sadral	France	$L = 180$ $d = 16$	17	Solid propulsion; infra-red homing	0.3-6	3 kg Heat conventional	NSA

$L$  = length (cm);  $d$  = diameter (cm);  $S$  = wingspan (cm);  $w_L$  = launch weight;  $R$  = range.

Table 7.10. Missiles for Armed Forces (mixed) (Israel, USSR, France, Italy)

Types of missiles/rockets	Manufacturer/ country of manufacture	Dimensions	$w_L$ lb (kg)	Power plant and guidance	$R$ (km)	Warhead	Mechanisms
Barak missile	Israel Aircraft Industries (IAI)	$L = 217$ $d = 17$	(86)	Semi-active radar-homing missile with disposable launch canister, manually fitted to an 8-round launcher based on the MBT TCM-30 twin 30 mm anti-aircraft gun mounted	10	Conventional 2 nuclear 7 kg	NSA small patrol boats
SA-N-3 Goblet	USSR	$L = 620$ $S = 150$ $d = 33.5$	550	Solid propulsion; semi-active homing	55	80 kg Conventional	NSA
SA-N-4	USSR	$L = 320$ $d = 21$	190	Solid propulsion; semi-active homing	14.8	50 kg	NSA
Roland 3	France and Italy	$L = 260$ $S = 50$ $d = 27$	85	Solid propulsion and command	8	9 kg Conventional	ADM
SA-4 Ganef (SRM)	USSR	$L = 880$ $S = 290$	100000	Ramjet and solid boosters; radio command	70	135 kg	ADM
SA-10 Grumble MM 10	USSR	$L = 700$ $S = 10$ $d = 45$	1500	Solid propulsion	100	Nuclear	ADM
SA-12 Gladiator	USSR	$L = 750$ $S = 350$ $d = 50$	2000	Solid propulsion; semi-active radar	80	150 kg Conventional	ADM
SA-13 Gopher (HJ-8)	USSR	$L = 220$ $S = 40$ $d = 12$	55	Solid propulsion; infra-red homing	10	4 kg Conventional	ADM

$L$  = length (cm);  $d$  = diameter (cm);  $S$  = wingspan (cm);  $w_L$  = launch weight;  $R$  = range.



Table 7.11. Missiles for Armed Forces (medium type) (UK, USA, China, France)

Types of missiles/rockets	Manufacturer/ country of manufacture	Dimensions	$w_L$ (lb)	Power plant and guidance	$R$ (km)	Warhead	Mechanisms
Bloodhound	UK	$L = 846$ $S = 283$ $d = 55$	–	Ramjet and solid boosters; semi-active radar homing	80	Conventional	ADM
Blow Pipe	UK	$L = 139$ $S = 270$	20.7	Solid propulsion; radio command	Any short distance	Conventional	ADM, shoulder-fixed
Javelin	UK	$L = 140$ $d = 8$	–	Solid propulsion; Saclos	3+ 4+	Conventional	ADM, shoulder-fixed
Hawk MIM-23B	USA	$L = 503$ $S = 119$ $d = 36$	627.3	Solid propulsion; semi-active homing	40	Conventional	ADM
Stinger FIM-92A	USA	$L = 152$ $S = 14$ $d = 7$	15.8	Solid propulsion; infra-red homing	Short range	Conventional	ADM
MIM Hercules L-5B	USA China	$L = 1210$ $d = 80$ $L = 289$ $S = 66$ $d = 13$	4858 85	Solid propulsion; command Solid propulsion; infra-red	140 5	Nuclear and conventional Conventional	ADM AAM
L-7	China	$L = 275$ $S = 66$ $d = 16$	90	Solid propulsion; infra-red	5	Conventional	AAM
Mistral	France	$L = 180$ $d = 9$	18	Solid propulsion; infra-red	3	3 kg Conventional	AAM
Super 530	France	$L = 354$	250	Solid propulsion	25	30 kg	AAM

$L =$  length (cm);  $S =$  wingspan (cm);  $d =$  diameter (cm);  $w_L =$  launch weight;  $R =$  range.

Table 7.12. Missiles for Armed Forces (missiles and rockets) (France, USA, USSR)

Types of missiles/rockets	Manufacturer/ country of manufacture	Dimensions $w_L$ lb (kg)	Power plant and guidance	$R$	Warhead	Mechanisms
550 Magic	France	$L = 275$ $S = 66$ $d = 16$	Solid propulsion; infra-red	5 km	Conventional	AAM
AJM-9 Sidewinder	Naval Weapon Centre, Philco-Ford, Ford Acro- Space, General Electric, USA	up to 190 (86) $S = 56$ to 64 $d = 12.7$	Rocket dyne, Thiokol, Bermite or Naval propellant; Single Grain solid MK 17, 36, 86; guidance: 9E to 9L, high power servo-system, AM/ FM IR conical scan head or Raytheon track via missile	2.5+ miles cruise 6.0 miles max	XM 248 high explosive (150 lb)	AAM (F-16, F-20, F-5E aircraft)
Alamo AA-10	USSR	$L = 400$ $S = 70$ $d = 19$	Solid propulsion; semi-active or infra-red	30 km	Conventional	AAM
AMBAAM	USA	$L = 357$ $S = 63$ $d = 18$	Solid propulsion; command and inertial	12 km	Conventional	AAM
Falcon	USA	$L = 213$ $S = 639$ $d = 29$	Solid propulsion; semi-active radar	8 km	Conventional	AAM
Phoenix	USA	$L = 396$ $S = 92$ $d = 38$	Solid propulsion; semi-active radar	150 km	Conventional	AAM
Sparrow AIM-7M	USA	$L = 366$ $S = 102$ $d = 20$	Solid propulsion; infra-red	140 km	Conventional	AAM

$L$  = length (cm);  $S$  = wingspan (cm);  $d$  = diameter (cm);  $w_L$  = launch weight;  $R$  = range.

**Table 7.13.** Missiles for Armed Forces (mixture ASM and rockets) (China, USSR, USA)

Types of missiles/rockets	Manufacturer/ country of manufacture	Dimensions	$w_L$ lb (kg)	Power plant and guidance	$R$	$V$ mach (mph)	Warhead	Mechanisms	
C-601	China	$L$ 738	2440	Liquid propulsion	100 km	–	400 kg	ASM	
HY-4		$S$ 280							92
C-801		736							280
		480	165	55	1025	–	500 kg	ASM	
				All active radar	150 km	–	Conventional		
S-9	USSR	$L$ 600	750	Solid propulsion;	150 km	–	Conventional	ASM	
S-10		$S$ 350	300	semi-active laser					
AS-11	USSR	$L$ = 350	300	Solid propulsion;	300 km	–	Conventional	ASM	
		$S$ = 90		infra-red	min				
		$d$ = 30							
Sea Eagle	UK	$L$ = 414	600	Turbofan inertial;	110 km	–	Conventional	ASM	
		$S$ = 120		active radar					
		$d$ = 40							
AGM-65	Hughes	$L$ = 246	462	Thiokol TX-481 solid	8 miles	6–10	Mk 19	ASM	
Maverick	Aircraft, Tulson USA	$S$ = 71	(210)	motor; AGM-65C	(13 km) to		113 kg		
		$d$ = 44.5		laser guidance	14 miles				
					(22.5 km)				
AGM-69A	Boeing	$L$ = 4127	2230	LPC (Lockheed	High	(200)	Conventional	ASM	
SRAM	Aerospace, Seattle, USA	$S$ = 89	(1010)	Company)	105 miles		Nuclear	Rocket	
		$d$ = 44.5		propulsion two-pulse	(170 km);		170 kT		
				solid motor;	low				
				guidance: inertial	35 miles				
					(56 km)				
ASLAM	McDonnell	$L$ = 4127	2700	Internal rocket/		6–10	170 kt	ASM	
Missile	Douglas	$S$ = 89	(1200)	ramjet;			Nuclear and		
MK III	USA	$d$ = 44.5		guidance; inertial			conventional		
MK IV				with Tercom					

$L$  = length (cm);  $S$  = wingspan (cm);  $d$  = diameter (cm);  $w_L$  = launch weight;  $R$  = range.

Table 7.14. Missiles for Armed Forces (ADM and NSA types) (UK, USA)

Types of missiles/rockets	Manufacturer/ country of manufacture	Dimensions $w_L$ lb (kg)	Power plant and guidance	$R$ miles (km)	$V$ mach (mph)	Warhead	Mechanisms
MGM-31A Pershing missile	Martin, Orlando, USA	$L = 10.51$ $S = 202$ $d = 101$	2 No. Thiokol solid motors; first stage – M105, second stage – M106; guidance: inertial	100 (160) to 520 (840)	8	Nuclear 400 kt	Mobile tactical system, ADM/SSM
MGM-51C Shillelagh missile	Ford, New Post Beach, USA	$L = 1.14$ $S = 29$ $d = 15.2$	Amoco single- stage solid jetavators; guidance: optical tracking and infra-red command link	3.0	(800)	Octal shaped charge 15 lb (6.8 kg)	Battle tank, ADM/SSM
BGM-71 TOW missile	Hughes Aircraft, Culver City, USA	$L = 1.17$ $S = 34$ $d = 14.7$	Quad boost motor for recoil-less launch; guidance: with optical sighting and trailing wire	up to (3.75)	(620)	Shaped charge containing 5.3 lb (2.4 kg) high explosive	Vehicles, aircraft, ADM/SSM
Sea Dart missile	British Aerospace, UK	$L = 4.4$ $d = 42$	Marconi radar 805 SW tracker with type 909 illuminator; guidance: semi- active	(30)	–	Conventional and nuclear	NSA patrol boats and ships

## 7.8 Empirical Formulae for Structural Elements in Damage Scenario

### 7.8.1 Introduction

It is important first to define certain terms prior to their influence on concrete structures. This section pertains only to local effects largely independent of the dynamic characteristics of the building structures. Local effects consist of missile penetration into and perforation through building structures, and spalling and scabbing of particularly concrete structures. They are defined below.

- (a) Penetration – the measure of the depth of the crater formed at the level of impact.
- (b) Perforation – full penetration through the structure.
- (c) Scabbing – the peeling off of the material from the opposite face to that at which the impact occurred.
- (d) Spalling – the ejection of target material from the face at which the impact occurs.

Analytical and rational mathematical prediction of these effects is extremely difficult. This is due to the complex nature of the transient loads. Various papers have been published in recent years which have described new ideas and methods for analysing and designing against impact on concrete structures connected with nuclear plant facilities. Owing to complexities in evaluating structural damage due to impact loading, design criteria so far developed have been mainly dependent on experimental tests and empirical formulae.

There are various empirical formulae that used to be employed in connection with missile impact problems on nuclear plant structures, but most of them have been discarded because over the years new, more relevant test data have been made available and these empirical formulae did not give good or realistic results in comparison.

However, there are some older and newer formulae which are still very much applicable. Of these, some empirical formulae are given in the next few paragraphs.

### 7.8.2 The National Defence Research Committee (NDRC) Formula

This formula is really the only one of the older formulae still applicable to nuclear plant facilities for design against impacts. It was put forward in 1946 by the National Defence Research Committee (USA), and proposed a theory of penetration for a non-deforming missile penetrating a massive concrete target. This theory enabled one to calculate the penetration, scabbing and perforation thickness for given missile data, and also gave the thickness that would be required to prevent scabbing and perforation.

The modified NDRC formula for penetration is given below

$$x = \left[ 4KNW_d \left( \frac{V_0}{1000d} \right)^{1.8} \right]^{1/2} \quad \text{for } \frac{x}{d} \leq 2.0 \quad (7.51)$$

$$x = \left[ KNW \left( \frac{V_0}{1000d} \right)^{1.8} + d \right] \quad \text{for } \frac{x}{d} \geq 2.0 \quad (7.52)$$

where all the symbols are defined below.

The NDRC formula for perforation thickness is given by

$$\frac{e}{d} = 3.19 \left( \frac{x}{d} \right) - 0.718 \left( \frac{x}{d} \right)^2 \quad \text{for } \frac{x}{d} \leq 1.35 \quad (7.53)$$

This formula is applicable for  $x : d$  ratios less than 1.35 only, and for other  $x : d$  ratios the results are very conservative. For other  $x : d$  ratios the US Army Corps of Engineers put forward the formula

$$\frac{e}{d} = 1.32 + 1.24 \left( \frac{x}{d} \right) \quad \text{for } 1.35 \leq \frac{x}{d} \leq 13.5 \quad (7.54)$$

where

- $W$  = missile weight (lb)
- $x$  = penetration depth (in.)
- $e$  = perforation thickness
- $e_{sc}$  = scabbing thickness
- $d$  = missile diameter (in.)
- $V_0$  = impact velocity (ft/s)
- $f'_c$  = concrete cylinder compressive strength (psi)
- $K = 180/\sqrt{f'_c}$
- $N$  = missile shape factor
  - = 0.72 for flat-nosed bodies
  - = 0.84 for blunt-nosed bodies
  - = 1.00 for spherical-ended bodies
  - $N = 1.14$  for very sharp-nosed bodies.

The formula for scabbing and perforation thickness  $x_{sc}$  and  $x_p$  respectively for a solid cylindrical steel missile and infinite thickness of the target are given below

$$x_{sc}/d = 2.12 + 1.36x_p/d \quad \text{for } 3 \leq t_{sc}/d \leq 18 \quad (7.55)$$

$$x_p/d = 1.32 + 1.24x_p/d \quad \text{for } 3 \leq t_p/d \leq 18 \quad (7.56)$$

$$x_{sc}/d = 7.91(x_p/d) - 5.06(x_p/d)^2 \quad \text{for } t_{sc}/d < 3 \quad (7.57)$$

$$x_p/d = 3.19(x_p/d) - 0.718(x_p/d)^2 \quad \text{for } t_p/d < 3 \quad (7.58)$$

*Modified NDRC Formula*

A modification of the NDRC formula to take into account the finite thickness of a target is proposed. For large diameter missiles impacting on targets of finite thickness the perforation and scabbing thicknesses are given below

$$\begin{aligned}x_p/d &= 3.19(x/d) - 0.718(x/d)^2 && \text{for } x/d \leq 1.35 \\x_{sc}/d &= 7.91(x/d) - 5.06(x/d)^2 && \text{for } x/d \leq 0.65\end{aligned}\tag{7.59}$$

Equations will have a range of  $0.65 \leq x/d \leq 11.75$  and  $1.35 \leq x/d \leq 13.5$ , respectively. In any case,  $t/d \leq 3$  gives comfortable results.

It should be stressed that the above formula for perforation within the stated  $x : d$  ratios are not strictly NDRC formulae but are based on the penetration thickness  $x$ , as obtained from the original NDRC formula.

The values of  $x$  and  $x_{sc}$  in the formulae are the calculated values of the target thickness to prevent perforation and scabbing, respectively. It has been suggested that a factor of safety be used with these values so that the design thickness of the concrete target is 20% or 30% greater than the value calculated.

For example, if a 20% safety factor is used, the design thickness to prevent perforation,  $t_4$  would be given by

$$t_4 = 1.2x\tag{7.60}$$

Similarly, the thickness to prevent scabbing is given by

$$t_4 = 1.2x_{sc}\tag{7.61}$$

where  $x_{sc}$  = scabbing thickness.

It is up to the designer what he or she considers most important for design: the perforation thickness or the scabbing thickness. Usually the larger of two values obtained is used.

In most cases, if the structure is designed against perforation then it is automatically made adequately safe against punching, and further analysis for punching shear is not necessary. This is strictly true for non-deformable missiles such as steel rods but also holds good for most deformable missiles.

**7.8.3 The Bechtel Formula**

This formula is sometimes used to determine the thickness to prevent scabbing. It was developed by the Bechtel Corporation and is based on recent test data applicable to missile impacts on nuclear plant structures. However, the formula is restricted to essentially non-deformable missiles such as solid steel slugs and rods. It is only moderately applicable to hollow pipe missiles. There are two formulae for scabbing thickness which are given below. The Bechtel formula for scabbing thickness for solid steel missiles

$$x_{sc} = \frac{15.5}{\sqrt{f_c}} \left( \frac{W^{0.4} V_0^{0.5}}{d^{0.2}} \right)\tag{7.62}$$

The Bechtel formula for steel pipe missiles (scabbing)

$$x_{sc} = \frac{5.42}{\sqrt{f'_c}} \left( \frac{W^{0.4} V_0^{0.65}}{d^{0.2}} \right) \quad (7.63)$$

The variables given above are in imperial units. The Bechtel formulae are also written for scabbing and perforation thickness in metric units using a new reference velocity  $\nu^*$  (60.96 m/s):

$$t_{sc} = 1.75 \left( \frac{\nu^*}{\nu} \right)^{0.13} \frac{(m\nu^2)^{0.4}}{(df'_c)^{0.4}} \quad (7.64)$$

$$t_p = 0.90 \left( \frac{\nu^*}{\nu} \right)^{0.25} \frac{(m\nu^2)^{0.5}}{(df'_c)^{0.5}} \quad (7.65)$$

where  $\nu = V_0$ .

The variables given above are in imperial units. The symbols again are defined earlier.  $d$  is the nominal missile diameter. The formula was strictly developed with 200 mm (8 in.) diameter pipes but also holds true for other diameters.

Again,  $x_{sc}$  obtained from the formula is the target thickness to prevent scabbing. A factor of safety may also be used to convert to design-target thickness.

#### 7.8.4 The IRS Formulae for Penetration and Complete Protection

The IRS formula for penetration is expressed as

$$x = 1183 f'_c{}^{-0.5} + 1038 f'_c{}^{-0.18} \exp(-0.82 f'_c{}^{0.18}) \quad (7.66)$$

The IRS formula for total protection of a target against penetration, perforation and scabbing is:

$$SVOLL = 1250 f'_c{}^{-0.5} + 1673 f'_c{}^{-0.18} \exp(-0.82 f'_c{}^{0.18}) \quad (7.67)$$

where SVOLL is the minimum wall thickness to provide complete protection. (Note: the units of the penetration and concrete strength are not imperial. The penetration is in units of centimetres and  $f'_c$  is in the units kg force/cm<sup>2</sup> – 1 kg force/cm<sup>2</sup>  $\approx$  100 N/m<sup>2</sup>).

In the IRS formula the value of SVOLL is the equivalent of design thickness as obtained from the other formulae. The penetration depth is the same as those in the other above-mentioned formulae.

#### 7.8.5 The ACE Formulae to Prevent Penetration or Perforation

The formulae for penetration and perforation are as follows.

(a) The formula for penetration

$$x = \frac{2.82}{\sqrt{f'_c}} \left( \frac{W}{d^2} \right) d^{0.215} \left( \frac{V_0}{1000} \right)^{1.5} + 0.5d \quad (7.68)$$



(b) The formulae for perforation and spalling thicknesses are

$$\begin{aligned} e &= 1.23d + 1.07x & \text{(i)} \\ e_{\text{sp}} &= 2.12d + 1.36x & \text{(ii)} \end{aligned} \tag{7.69}$$

The symbols used are those previously defined. The units of the variables are imperial. The ACE formula for perforation gives the thickness of target to prevent perforation. Together with a factor of safety of, say, 1.2, the value of  $e$  can be used to determine the target design thickness.

$$t_a = 1.2e \tag{7.70}$$

This is because  $e$  is the minimum wall thickness of the target to prevent perforation.

### 7.8.6 The Stone and Webster Formula

$$\text{Scabbing thickness } (s) = (W\nu_0/C)^{1/3} \tag{7.71}$$

$C$  is a coefficient (Table 7.15).

### 7.8.7 The CKW-BRL Formula for Penetration and Perforation

$$x = \frac{6Wd^{0.2}}{d^2} \left( \frac{V_0}{1000} \right)^{4/3} \quad (\text{imperial units}) \tag{7.72}$$

The perforation thickness is given by

$$e = 1.3x \tag{7.73}$$

$e$  is the minimum thickness to prevent perforation.

Table 7.15 shows comparisons of scabbing thicknesses.

### 7.8.8 Modified Ballistic Research Laboratory Formula

The modified Ballistic Research Laboratory formula gives the perforation thickness of infinitely thick targets impacted by a non-deformable missile with high velocity as

$$t_p = (427Wd^{0.2}) / (d^2 \sqrt{f'_c} V_0 / 1000)^{1.33} \tag{7.74}$$

where

- $t_p$  = perforation thickness (in.)
- $W$  = missile weight (lb)
- $d$  = missile diameter (in.)
- $f'_c$  = concrete compressive strength (psi)
- $V_0$  = missile velocity (ft/s)
- $x_{\text{sp}} = 2x$  is the spalling thickness.

**Table 7.15.** Comparison of predicted scabbing thickness and known low velocity test results

Missile	Missile velocity (m/s)	Test results scabbing thickness (mm)	Calculated scabbing thickness			
			NDRC (mm)	Bechtel (mm)		
200 mm slug 0.95 kN	60	305	360	315		
75 mm pipe schedule-40 0.35 kN	61	300	285	343		
300 mm pipe 3.3 kN	60	450–600	607	627		
75 mm slug 0.06 kN	30	127	129	129		
75 mm diameter pipe 0.005 kN	59	133	141	151		
Stone and Webster: <i>C</i> coefficients lb/in./s						
	<i>s/d</i>	1	1.5	2.0	2.5	3.0
Solid	<i>C</i>	←	900	—	950	→
Hollow	<i>C</i>					
	$2t/d =$	0.125	2.250	2.450	2.500	2.550
	$=$	0.08	3.00	3.250	3.350	3.400
	$=$	0.06	3.600	3.750	3.900	4.050

**7.8.9 Chalapathi, Kennedy, and Wall (CKW)-BRL Formula**

The penetration depth is calculated using the CKW-BRL method as

$$t_p = (6Wd^{0.2}/d^2)(V_0/1000)^{1.33} \tag{7.75}$$

where  $t_p$  = thickness to prevent perforation =  $1.3x_p$ . All units are imperial, as defined earlier.

**7.8.10 Dietrich, Furste (DF)-BRL Formula**

The formula [Dietrich F., personal communication] gives the thickness to prevent perforation as

$$t_p = (3 \times 10^{-4}/\sqrt{f_{ci}})(Wd^{1.8})(\nu/1000)^{4/3} \tag{7.76}$$

where  $d$  and  $t_p$  are in m,  $W$  is in kN,  $f_{ci}$  is in kN/cm<sup>2</sup> and  $\nu$  is in km/h.

**7.8.11 Modified Stone and Webster**

The scabbing thickness is given, as for the infinitely thick concrete targets, by

$$t_{sc} = (W\nu^2/c'_0) \tag{7.77}$$

where the values of  $W$  and  $\nu$  are in lb and ft/s respectively and  $c'_0$  is a coefficient depending on the ratio of  $t_{sc}/d$ . The range for which this formula is considered is  $3000 \text{ psi} \leq f'_c \leq 4500 \text{ psi}$  and  $1.5 \leq t_{sc}/d \leq 3$ .

### 7.8.12 Modified Kar Formula

The equation for predicting the penetration depth,  $X$ , in concrete structures is given as

$$G(X/d) = [\bar{\alpha}/(f'_c)^{0.5}] N_2 (E^m/E_s)^{1.25} [W/D(d^{1.8})(V/1000)^{1.8}] \quad (7.78)$$

where

$$\begin{aligned} G(X/d) &= (X/2d)^2 & \text{for } X/d \leq 2.0 \\ G(X/d) &= X/d - 1 & \text{for } X/d > 2.0 \end{aligned}$$

$N = 0.72$  for flat-nosed solid bodies, and

$N = 0.72 + 0.25(n - 0.25)^{0.5} \leq 1.17$  for missiles with special nose shapes;  
 $n$  is the ratio of the radius of the nose to the diameter of the missile,  
 and

$N = 0.72 + [(D/d) - 1](0.0306) \leq 1.17$ , for hollow pipe or irregular sections  
 $E^m$  is the modulus of elasticity of the material of the missile (psi)

$E_s$  is the modulus of elasticity of mild steel (psi)

$f'_c$  is the ultimate compressive strength of the concrete test cylinder (psi)

$d$  is the projectile diameter (in.)

$D$  is the outside diameter of a circular section (in.)

$W$  is the weight of the missile (lbs)

$V$  is the impact velocity of the missile (ft/s)

$\bar{\alpha}$  is a constant depending on the type of units used  
 ( $\bar{\alpha} = 180.0$  when using imperial units)

The thickness  $x_a$  to prevent perforation, and the thickness  $x_{sc}$  to prevent backface scabbing are determined by

$$(x_a - a_1)/d = 3.19(X/d) - 0.718(X/d)^2 \quad \text{for } X/d < 1.35 \quad (7.79)$$

$$\rho(x_{sc} - a_1)/d = 7.91(X/d) - 5.06(X/d)^2 \quad \text{for } X/d \leq 0.65 \quad (7.80)$$

in which  $\rho = (E_s/E^m)$  ( $\rho = 1$  for steel missiles), and  $a_1$  is half the aggregate size in concrete (in.)  $x_a = e$  in this case.

For  $X/d$  ratios larger than those shown in the previous equations, the perforation depth and the scabbing thickness can be calculated using the following equations:

$$(x_a - a_1)/d = 1.32 + 1.24(X/d) \quad \text{for } 3 < x_a/d \leq 1.8 \quad (7.81)$$

$$\beta'(x_{sc} - a_1)/d = 2.12 + 1.36(X/d) \quad \text{for } 3 < x_{sc}/d \leq 1.8 \quad (7.82)$$

### 7.8.13 Petry Formula

Petry's formula is used for predicting the penetration depth  $x_p$  for infinitely thick concrete targets. This formula is derived from tests concerning high velocity impact on infinitely thick concrete targets. Where thickness governs

the failure mode or the impact response is influenced by the size and shape of the missile and the presence of the reinforcement, this formula gives accurate assessments.

$$x_p = K_m AV'R \tag{7.83}$$

where

- $x_p$  = depth of penetration in a concrete slab of thickness  $h$
- $K_m$  = material property constant ( $L^3/F$ )  
 $= 4.76 \times 10^{-3} \text{ ft}^3/\text{lb} = 2.97 \times 10^{-4} \text{ m}^3/\text{kg}$
- $A$  = sectional mass weight of the missile per unit cross-sectional area of contact ( $F/L^2$ )
- $V'$  = velocity factor =  $\log_{10} [1 + (V_0^2/V^{*2})]$
- $V_0'$  = initial velocity of missile at impact
- $V^{*2}$  = reference velocity equal to  $215000 \text{ ft}^2/\text{s}^2 (19973 \text{ m}^2/\text{s}^2)$
- $R$  = thickness ratio
- $x_p/D_p = 1 + \exp[-4(\alpha' - 2)]$

where  $\alpha' = h/D_p = h/K_m AV'$  and  $D_p$  is the penetration depth of an infinitely truck slab. The penetration depth is restricted to less than  $h$ , to satisfy the inequality below. In order to prevent penetration and spalling

$$h \geq C_1 A \times 10^{-5} \text{ ft or an equivalent value in SI units}$$

where  $C_1$  is taken from Fig. 7.14. The time required for penetration is derived from the modified Petry formula

$$F = mx = m\nu(d\nu/dx) = -1.15(V^{*2}/K_m A) \exp(2.3x_p/K_m A) \tag{7.84}$$

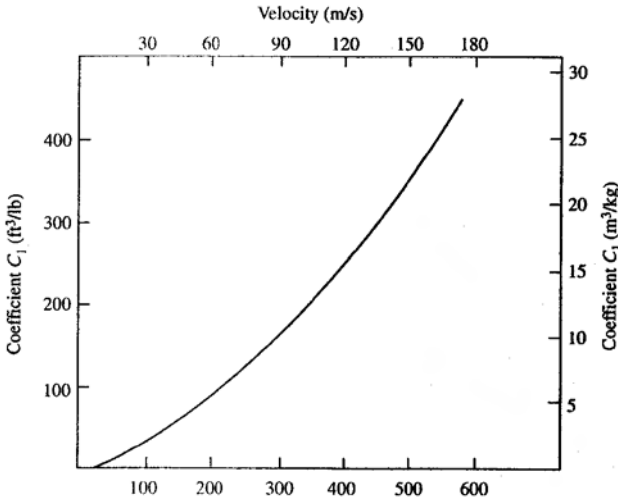


Fig. 7.14. Minimum thickness needed to prevent penetration and spalling

### 7.8.14 Modified Barr, Carter, Howe, and Neilson Formulae

Experiments were undertaken on circular reinforced concrete slabs at three different scales ( $1\times$ ,  $0.38\times$  and  $0.128\times$  prototype). Transient loads, deflections and impactor velocities were measured during impact. The bending reinforcement in the targets varied between 0 and 0.5% each way on each face and the missile velocity varied from 50 m/s to 300 m/s. Based on these tests, a modification of the CEA-EDF formula was suggested. Thus, the velocity to cause perforation  $V$  can be calculated by

$$V = 1.3\sigma^{1/2}D_c^{1/6}(de^2/m_5)^{2/3}r_b^{0.27}. \quad (7.85)$$

Because of the limited test data, it was proposed that the formula be restricted to the following range:

$$\begin{aligned} 160 \text{ kg/m}^3 &< \text{reinforcing steel} \\ 20 \text{ m/s} &< \text{impact velocity} < 230 \text{ m/s} \\ 0.5 &\leq \text{slab thickness/projectile diameter.} \end{aligned}$$

### 7.8.15 Modified CEA-EDF Formula

Tests were carried out for the French Atomic Energy (CEA) and Electricité de France by Berriaud on a series of slabs subject to impactors with varying velocities (from 20 m/s to 200 m/s), thickness, concrete strength and reinforcement quantities. The empirical formula for a thickness to resist perforation is given by

$$x = 0.82(f'_c)^{-3/8}(\rho_c)^{-1/8}(W/d)^{0.5}V_0^{3/4} \quad (7.86)$$

where  $\rho_c$  is the density of concrete and the following ranges apply

$$\begin{aligned} 30 \text{ MPa} &< f'_c < 45 \text{ MPa} \\ 0.3 &< x_p/d < 4 \\ 75 \text{ kg/m}^3 &< p_1 < 300 \text{ kg/m}^3 \end{aligned}$$

where  $p$  is the reinforcement quantity. The perforation velocity  $\nu_p$  for the target thickness is given by

$$\nu_p 1.7 f'_c (\rho_c)^{1/3} (dh^2/W)^{4/3} \quad (\text{metric}). \quad (7.87)$$

The CEA-EDF residual velocity formula  $\nu_r$  based on several tests with a correction factor  $K_0$  is given below with all values in imperial units:

$$\nu_r = \left[ \frac{1}{1 + \frac{W_1}{W}} (\nu^2 - \nu_p^2) \right] \quad (7.88)$$

$$K_0 \nu_p = \left[ \nu_p^2 - \nu_r^2 \left( 1 + \frac{W_1}{W} \right) \right]^{1/2} \quad (7.89)$$

where

$F$  = the resisting force, equal to  $R_m$

$x$  = penetration at any time

$V^*$  = missile velocity at any time

$h$  = penetration depth.

Due to the nonlinear nature of the equation of motion, a numerical integration is necessary to determine the velocity as a function of distance. Then

$$Y = -1.15(V^{*2}/K_m A) \exp[2.3(x - \delta)/K_m A] \quad (7.90)$$

hence

$$m_x = m_t \delta + k \delta \quad (7.91)$$

where

$x$  = missile displacement

$\delta$  = target displacement

$k$  = target stiffness

$m, m_t$  = mass of the missile and target respectively.

### 7.8.16 Chang Formulae

Chang has proposed two semi-analytical formulae for predicting perforation and scabbing thickness of concrete targets impacted by hard steel missiles of non-deformable type:

$$t_p = (u/\nu)^{0.25} (m\nu_0^2/d f'_c)^{0.5} \quad (7.92)$$

$$t_{sc} = 1.84(u/\nu_0)^{0.18} (f'_c)^{0.4} (d)^{0.2} (m\nu_0^2)^{0.4} \quad (7.93)$$

These formulae are probably validated over the following range based on random variable by Bayesian statistics:

$$16.7 \text{ m/s} < \nu_0 < 311.8 \text{ m/s}$$

$$0.11 \text{ kg} < W < 343 \text{ kg}$$

$$2.0 \text{ cm} < d < 30.4 \text{ cm}$$

$$232 \text{ kg/cm}^2 < f'_c < 464.2 \text{ kg/cm}^2$$

$$5.0 \text{ cm} < h < 60.9 \text{ cm}$$

where  $u$  is a reference velocity (200 ft/s or 60.96 m/s) and  $f'_c, d, m$  and  $\nu_0$  are defined in other sections. The scabbing velocity  $V_{sc}$  ft/s, is written as

$$V_{sc} = [(1/2 \times 469)(d^{0.2} f'_c h/W^{0.4})]^{3/2} \quad (7.94)$$

where  $\nu_r, \nu_p, K_0$  and  $W_1$  are the residual velocity of the missile, perforation velocity, correction factor and the weight of the target material removed by impact, respectively. The mean and minimum values of  $K_0$  are 1.45 and 1.225 respectively.

### 7.8.17 Haldar, Miller, and Hatami Method

The impact formula of the NDRC type associated with a non-dimensional impact factor  $I$  are presented in imperial units as

$$I = WN\nu^2gd^3f'_c \quad (7.95)$$

where  $g = 32.2 \text{ ft/s}^2$  and, when substituted, the above equation becomes

$$I = 12NW\nu^2/32.2d^3f'_c$$

where  $N$  is the missile nose-shaped factor and all other notations are as defined earlier.

For various impact factors, the NDRC test results were examined using linear regression analysis for  $x_p/d$  and  $t_{sc}/d$  ratios.

$$\begin{aligned} t_{sc}/d &= -0.0308 + 0.2251I & 0.3 \leq I \leq 4.0 & \text{(a)} \\ t_{sc}/d &= 0.6740 + 0.0567I & 4.0 \leq I \leq 21.0 & \text{(b)} \\ t_{sc}/d &= 1.1875 + 0.0299I & 21.0 \leq I \leq 455 & \text{(c)} \\ t_{sc}/d &= 3.3437 + 0.0342I & 21.0 \leq I \leq 385 & \text{(d)} \end{aligned} \quad (7.96)$$

### 7.8.18 Takeda, Tachikawa, and Fujimoto Formula

Takeda et al. proposed a formula for predicting the penetration depth into reinforced concrete slabs subject to hard missiles:

$$x_0 = [\alpha/(\beta + 1)](\nu_0)^{\beta+1} \quad (7.97)$$

where

$$a = 2^n m^{l-n} / c' \psi$$

$$\beta = 1 - 2n$$

$x_p$  = maximum depth of penetration (cm)

$m$  = mass of projectile ( $\text{kg-s}^2/\text{cm}$ )

$\nu_0$  = impact velocity (cm/s)

$\psi$  = circumference of projectile (cm)

$c', n$  = constants.

Since the formula is based on the kinetic energy as input, it is valid for an energy range from  $20 \times 100 \text{ kg/cm}$  to  $200 \times 10^5 \text{ kg/cm}$ .

### 7.8.19 Hughes Formulae

These formulae have been developed using the dimensional analysis and test analysis results of NDRC and ACE described earlier. Front and back faces are reinforced (front face 0–0.15%; back face 0.3–1.7% each way). The penetration depth calculated for a concrete barrier, assuming no scabbing or perforation occurs, is given by

$$x_p/d = 0.19NI/s' \quad (7.98)$$

where

$N$  = nose-shaped coefficient = 1, 1.12, 1.26 and 1.39 for flat, blunt, spherical and very sharp noses, respectively

$I$  = impact parameter =  $(m\nu^2/0.63\sqrt{f'_c})d^3$

$s'$  = strain-rate factor =  $1 + 12.3 \log(1 + 0.03I)$ .

The thickness of the concrete target necessary to prevent scabbing and perforation is written as

$$x_{sc}/d = 1.74(x_p/d) + 2.3 \quad (7.99)$$

$$x_p/d = 1.58(x_p/d) + 1.4 \quad (7.100)$$

### 7.8.20 Modified Kar Formulae

It is claimed that most of the formulae described earlier do not include dimensions, shapes of the missiles, material properties of the missiles and targets and the size of the coarse aggregate in concrete. Kar gives the penetration depth (in inches) in the concrete targets as

$$G(x_p/d) = \alpha K_p N(W/D)(\nu/10000d)^{1.8} \quad (7.101)$$

where the range for  $G(x_p/d)$  is given as

$$\begin{cases} (x_p/2d)^2 & \text{for } x_p/d \leq 2.0 \\ (x_p/2d) - 1 & \text{for } x_p/d \geq 2.0 \end{cases} \quad (7.102)$$

and where  $D$  = diameter of the actual missile in the case of a circular section or is equal to the projectile diameter  $d$  in the case of a rectangular section.

### 7.8.21 Perry and Brown Formulae

For solid missiles on concrete targets, the penetration depth is given in Fig. 7.15 by

$$x_p/d = 9.605\sqrt{m}[\nu\sqrt{(E_0d^3)}] + 0.06 \quad (7.103)$$

where  $x_p$ ,  $d$  and  $\nu$  are as defined earlier and  $m$  is the missile mass. If  $L < 50$ , the scabbing thickness does not occur. If  $L > 70$  the scabbing thickness certainly occurs.

$$L = [\sqrt{m}(\nu/\sqrt{d})h(1 + h/d)]\sqrt{E_c\sigma_s} \quad (7.104)$$

where



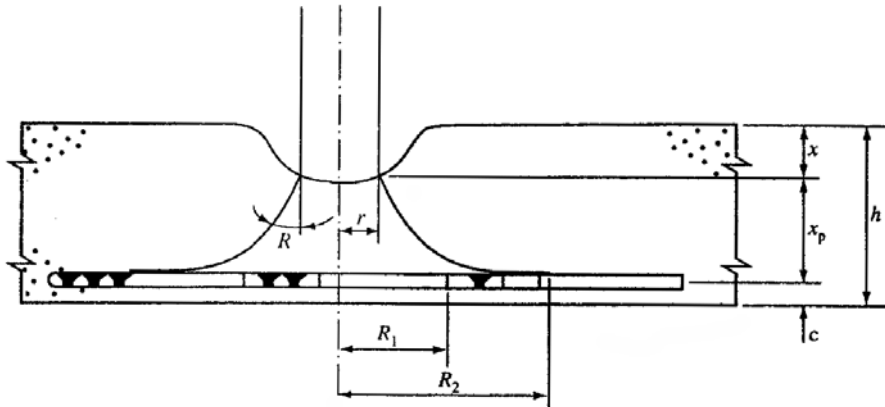


Fig. 7.15. Assumed barrier failure mechanism and derivation of hinge radius

- $h$  = target thickness
- $E_c$  = Young's modulus
- $\sigma_s$  = maximum value of nominal shear stress before damage  
 $= \sigma_{tm} \sqrt{[1 + (\sigma_{cm}/\sigma_{tm})]}$
- $\sigma_{tm}$  = mean tensile stress in concrete
- $\sigma_{cm}$  = compressive stress
- $\sigma_{cr} = 0.90\sigma'_{cr}$   
 $= 0.9[0.52(1 - \nu^2)/(1 - \nu_p^2)]^{1/2}(E_t/E)^{1/2}E_s(t_p/r)$
- $E$  = Young's modulus
- $E_t$  = tangent modulus
- $E_s$  = secant modulus
- $t_p$  = pipe thickness (in.)
- $r$  = pipe radius (in.)
- $\nu, \nu_p$  = Poisson's ratios for elastic and plastic, respectively.

Geometry

$$\begin{aligned} \tan \theta &= R_1 \times r/x = 2 \\ 2x &= R_1 \times r \\ R_1 &= 2(htx_p) + r \\ R_2 &= C_L t_3 \\ R_u &= M_u D_h \end{aligned}$$

where

$$\begin{aligned} M_u &= \text{ultimate curvature} = eu/C_h \approx x_p/C_h \\ D_h &= \text{hinge length (or } R_2 R_1) \\ (R_2 \text{ or } R_1)_{\max} &= r_u/M_u = 0.07/0.003 = 23.3 \\ (R_2)_{\max} &= R_1 + 23 \end{aligned}$$

The thickness to prevent spalling is given by

$$t_{sp} = x_p + x + c \quad (7.105)$$

$$x(x+r)^2 > \left[ \frac{6W^2V_m^2 - W}{2g\pi r_u M_u} \right] \left( \frac{1728}{\rho_c \pi} \right) - R_2^2 C \quad (7.106)$$

where

$$\rho_c = 0.15 \text{ kips/ft}^3$$

$r_u$  = ultimate rotational capacity at hinge (rad)

$C$  = cover (in.)

$M_u$  = ultimate moment capacity at hinge (in kips/in.) (1 kip = 1000 lbf)

$$R_2 = R_1 + 23$$

$$\nu = \nu_2 \text{ if } \nu_2 > \nu'_2$$

$$\nu = \nu'_2 \text{ if } \nu_2 < \nu'_2 < \nu_1$$

if  $\nu'_2 > \nu_1$  not applicable

the spalling equations are not applicable if  $t_{sp} = h < 12$  in.

For pipe missiles on concrete targets, the penetration depth is given by

$$x_p/d = 8[\sqrt{mv}/\sqrt{(Ed^3)}] + 0.24 \quad (7.107)$$

where  $d$  is not outside the diameter of the pipe missile. The scabbing thickness can be achieved if  $L > 60$  and is unlikely to occur if  $L < 50$ . The value of  $L$  in this case is expressed by

$$L = \sqrt{md\nu}/[dh(1+h/d)](\sqrt{E_c/\sigma_s}) \quad (7.108)$$

where the various elements of the equations have been defined previously.

### 7.8.22 Formulae for Deformable Missiles Impacting on Concrete Targets – McMahan, Meyers, Sen Model

The model evaluates local damage including penetration and back face spalling of reinforced concrete targets subject to the impact of deformable, tornado-generated missiles such as pipes, etc. The total penetration is given by

$$x_p = x_1 + x_2 + x_3 \quad (7.109)$$

where

$$x_1 = \text{penetration during time } t_1 = Ft_1^2/6m) + \nu_0 t_1$$

$$F = \text{interface body} = \sigma_{cr} \times A$$

$$t_1 = \text{rise time} = 3.2 \times 10^{-6} F$$

$A$  = pipe area

$\nu_0$  = missile velocity at the initial time  $t_0$

$m$  = mass of the missile

$$\begin{aligned} x_2 - x_1 &= x_c \text{ (plastic missile deformation during } t_2 - t_1) \\ &= \frac{m}{2F}(\nu_2 - \nu_1)^2 + \frac{m\nu_1}{F} \\ &= \frac{m}{2F}(\nu_2^2 - \nu_1^2) \end{aligned} \quad (7.110)$$

$\nu_1, \nu_2 =$  missile velocity at times  $t_1$  and  $t_2$

$$\nu_1 = (Ft_1/2m) + \nu_2 \quad (7.111)$$

$$\nu_2 = (F/m)(t_2 - t_1)t\nu_1$$

$$\begin{aligned} x_3 &= x_2(\text{penetration during } t_3 - t_2) \\ &= -m\nu_2^2/2F \end{aligned} \quad (7.112)$$

$$t_2 = l/\sqrt{(E_T/\rho)} + l/\sqrt{(E/\rho)} = \text{wrinkling duration} \quad (7.113)$$

plastic wave                  elastic wave

$$t_3 = (-m\nu_2/F) + t_2 = \text{final time} \quad (7.114)$$

where

$\rho =$  material density

$l =$  missile length

### 7.8.23 Rotz Damage Model

Rotz predicted scabbing thickness using Bayesian estimators as

$$t_{\text{sp}} = \bar{K}_p(W^{0.14}\nu^{0.65}/\sqrt{f'_c d^{0.2}}) \quad (7.115)$$

where

$\bar{K}_p =$  empirical constant = 5.42

$\nu =$  impact velocity in imperial units (ft/sec)

$d =$  missile diameter (in)

$f'_c =$  concrete compression strength (lb/in<sup>2</sup>)

$W =$  missile weight (lbf)

### 7.8.24 Missiles on Steel Targets

#### Missiles and Targets

Missiles as projectiles with non-deformable nose shape are given in Fig. 7.16. Non-deformable projectiles are assumed to be either spherical or cylindrical, with a nose of one of the shapes shown in Fig. 7.17. The calibre or ballistic density  $\rho$  is generally given as  $W/d^3$ , where  $W$  is the weight of the missile and  $d$  is the diameter. Owing to changes in the value of  $W$ , a longer missile is, therefore, more dense than a short one with the same diameter and material. Metal targets are generally restricted to hard missiles of non-deformable type striking the plate.

#### Slow Speed Indentation of Steel Targets

##### (1) Conical Missile

Assume a conical missile is striking a steel target with a low velocity,  $\nu_0$ , leaving a permanent indentation of diameter  $d_0$  (Fig. 7.17). The yield stress

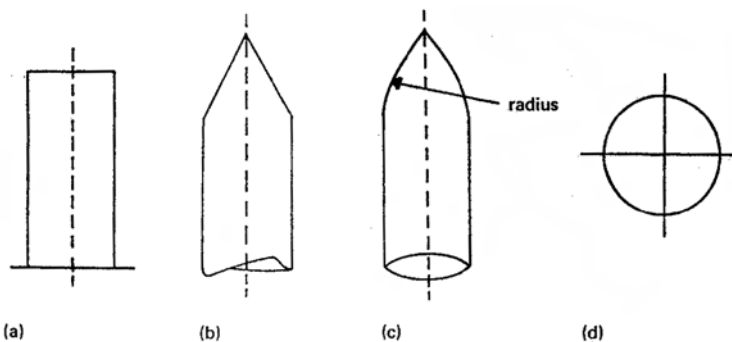


Fig. 7.16. Projectile shapes. (a) flat; (b) conical; (c) ogival; (d) spherical

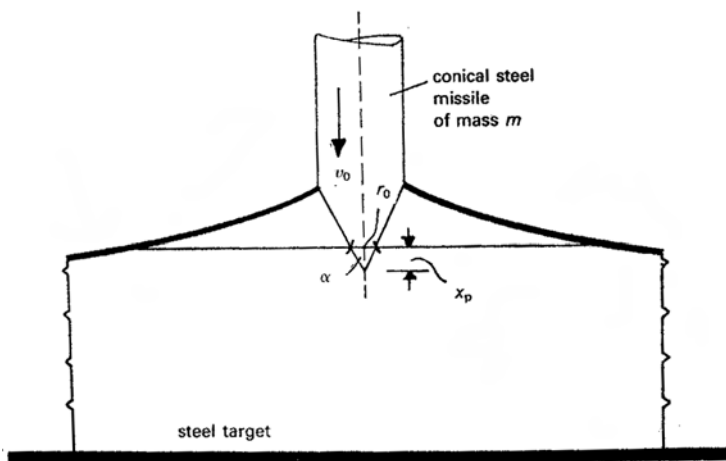


Fig. 7.17. Conical missile striking steel target

of the target steel  $\bar{\sigma}_e = 3\sigma_t$ , where  $\sigma_t$  is the uni-axial stress flow of the target material. The equation of motion is written as

$$m\ddot{x}_p = m\nu(d\nu/dx_p) = -\bar{\sigma}_e\pi r_0^2 \tag{7.116}$$

where  $\nu$  is the missile speed after penetration  $x_p$  is achieved and  $r_0$  is the final radius of the crater  $= x_p \tan \alpha$ .

After substitution of the value of  $r_0$  into (7.116) and integration, the crater radius and depth are written as

$$r_0 = (0.4772m/\bar{\sigma}_e \tan^2 \alpha)^{1/3}(\tan \alpha)\nu_0^{2/3} \tag{7.117}$$

$$x_p = 2r_0 \cot \alpha/2 \tag{7.118}$$

(2) *Spherical Missile*

Equation (7.116) is still applicable when  $x_p/d$  is small. It is assumed that  $r_0 \approx x_p d$ , the equation of motion expressed in (7.116) is integrated and the final penetration obtained as

$$x_p = \sqrt{[(m/\sigma_c)\pi d] \nu} \quad (7.119)$$

where  $\nu$  is the final velocity at the time of the formation of the crater.

(3) *Calder and Goldsmith Velocity Model (Preliminary Report, 1979)*

The impact velocity at which the projectile penetrates a steel target completely, but comes to rest in the process, defines the ballistic limit. The formula for the residual velocity,  $\nu_r$ , developed is based on both impact velocity and ballistic limit and is given for a *sharp-nosed* missile as

$$\nu_r = \sqrt{(\nu_0^2 + \nu_B^2)} \quad (7.120)$$

where  $\nu$  is the initial velocity and  $\nu_B$  is the ballistic limit.

In (7.120) it is assumed that the missile carries no material from the steel target. The residual velocity for a *blunt-nosed* missile carrying a plug of material ejected from the steel target is given by

$$\nu_r = \sqrt{\left[ \frac{m}{m + m'_p} (\nu_0^2 - \nu_B^2) \right]} \quad (7.121)$$

where  $m$  and  $m'_p$  are the masses of the missile and the plug, respectively.

(4) *Ballistic Research Laboratory Formula (BRL)<sup>2</sup>*

This formula is based on the impact of small-diameter, high-calibre, high-density non-deformable missiles striking thin steel targets:

$$(t_p/d)^{3/2} = D\nu^2/1120000\bar{K}_p^2 \quad (7.122)$$

where

- $t_p$  = perforation thickness (in or mm)
- $d = 4A_m/\pi$  = effective missile diameter (in or mm)
- $A_m$  = missile area (in<sup>2</sup> or cm<sup>2</sup>)
- $\nu$  = impact velocity (ft/s or m/s)
- $D$  = missile diameter (in or mm)
- $W/d^3$  = calibre density of missile (lb/in<sup>3</sup> or kg/m<sup>3</sup>), from which  $d$  can be evaluated
- $\bar{K}_p$  = steel penetrability constant depending upon the grade of the steel target; the value of  $\bar{K}_p$  is generally taken as 1.0

(5) *The Stanford Research Institute (SRI) Equation*

Like BRL's formula, the following equation is for small-diameter, hard missile striking a thin steel target.

$$(t_p/d)^2 + (3/128)(B/d)(t_p/d) = 0.0452D\nu/\sigma_{tu} \quad (7.123)$$

where  $t_p$ ,  $d$ ,  $D$  and  $\nu$  are as defined in the BRL formula

$B$  = width of the steel target  
 $\sigma_{tu}$  = ultimate tensile strength of the target steel (lb/in<sup>2</sup> or Pascals)

The formula is based upon tests with the following range of parameters:

$$\begin{aligned} 0.1 &\leq t_p/d \leq 0.8 \\ 21\text{lb/in}^3 \ (550 \times 10^2 \text{ kg/m}^3) &\leq D \leq 12\text{lb/in}^3 \ (3300 \times 10^2 \text{ kg/m}^3) \\ 0.062 \text{ in} \ (1.6 \text{ mm}) &\leq d \leq 3.5 \text{ in} \ (89 \text{ mm}) \\ 70 \text{ ft/s} \ (21 \text{ m/s}) &\leq \nu \leq 400 \text{ ft/s} \ (120 \text{ m/s}) \\ 2 \text{ in} \ (50 \text{ mm}) &\leq B \leq 12 \text{ in} \ (300 \text{ mm}) \\ 5 &\leq B/d \leq 8 \\ 8 &\leq B/t_p \leq 100 \end{aligned}$$

For design purposes, the design thickness due to  $t_p$  or  $t_{sc}$  must be increased by 20%.

(6) *Kar Steel Target Formula*

For mid-to-medium-hard homogeneous steel plates, the barrier may have a ductile failure. When steel target Brinell hardness numbers are above 350, failure by plugging may occur. For inferior quality steel, flaking may occur on the back face of the steel targets. According to Kar, for a good quality steel, back face phenomena do not generally influence the depth of penetration. The penetration or thickness to prevent perforation is given by the following:

$$t_p = \alpha(E/29000)(0.72 + N)\bar{K}_p(m\nu^2)^{0.667}/1067(D + d) \quad (7.124)$$

where  $m$  is the mass of the missile (lb-s<sup>2</sup>/ft) and  $\nu$  (ft/s),  $D$  (in) and  $d$  (in) are as defined.

The penetrability coefficient  $\bar{K}_p$  is determined from the following:

$$\bar{K}_p = (0.632\text{BHN} + 94.88)/275 \quad (7.125)$$

where BHN is the brittle hardness number of the steel target material and is limited to between 0.37 and 1.0. The above equation is still relevant if BHN < 0.37 or > 1.0.

$\alpha = 1.0$  if imperial units are used  
 $= 0.0035$  for  $m$  (kg-s<sup>2</sup>/m),  $\nu$  (m/s),  $d$  (cm),  $E$  (kN/m<sup>2</sup>),  $t_p$  (cm)

(7) *de Marre Modified Formula*

de Marre proposed a relationship between the specific limit energy  $h/d$  and the target penetration:

$$m\nu_1^2/d^3 = \bar{\alpha}(h/d)^{\bar{\beta}} \tag{7.126}$$

where

- $m$  = missile mass (g)
- $\nu_1$  = limit velocity (m/s)
- $d$  = missile diameter (cm)
- $h$  = steel target thickness (cm)
- $\bar{\alpha}$  = constant between 1 and 2
- $\bar{\beta}$  = constant approximately 1
- $h$  is replaced by  $hf(\theta)$
- $\theta$  = incidence angle
- $f$  = a function of obliquity, usually secant

(8) *Taub and Curtis Model*

A perceptive analysis by Taub and Curtis derived the following formula for back-face spalling or petalling type of failure:

$$m\nu_1^2/d^3 = \bar{\alpha}[(h/\bar{\alpha}) + \bar{\beta}] \quad \bar{\beta} < 0 \tag{7.127}$$

(9) *Lambert Model*

The development assumes back-face thickness where petalling occurs and  $d$  to be constant and  $\beta$  becomes complex as a quadratic function. To overcome this, Zukas replaced  $\bar{\beta}$  by  $e^{-h/d} - 1$ ;  $d^3$  by  $d^{3-c} l^c$  and  $\theta$  as stated in the case of the de Marre formula, by  $h \sec^{k'} \theta$ . Both  $c$  and  $k'$  are constants. Using Lambert's limit velocity database containing limit velocities for 200 cases involving:

range of mass	$\frac{1}{2}$ to 3630 g
diameter	$\frac{1}{5}$ to 5 cm
$l/d$	4 to 30
$h$	$\frac{3}{5}$ to 15 cm
$\theta$	$0^\circ$ to $60^\circ$
$\rho_s$ (rod material density)	7.8 to 19 g/cm <sup>3</sup>
$\bar{\alpha} = 4000^2$ ; $c = 0.3$ ; $k' = 0.75$	

the following predicted model is established for the limit velocity  $\nu_\ell$ :

$$\nu_\ell = u(l/d)^{0.15} \sqrt{\left[ \int (z)d^3/m \right]} \text{ m/s} \tag{7.128}$$

where  $z = h(\sec \theta)^{0.75}/d$ ,  $u = 4000$  for rolled homogeneous armour (RHA) and  $m$  depends on the density  $\rho_s$

$$\begin{aligned}
 f(z) &= z + e^{-z} - 1 = \sum_{j=2} (-z)^j / j \\
 \nu &= \begin{cases} 0, & 0 \leq \nu \leq \nu_\ell \\ \alpha(\nu^2 - \nu_\ell^2)^{1/2}, & \nu > \nu_\ell \end{cases} \\
 \nu_\ell &= \max\{\nu : \nu_r = 0\} = \inf\{\nu : \nu_r > 0\} \\
 \nu_r &= \begin{cases} 0, & 0 \leq \nu \leq \nu_\ell \\ \bar{\alpha}(\nu^p - \nu_\ell^p)^{1/p}, & \nu > \nu_\ell \end{cases}
 \end{aligned} \tag{7.129}$$

where the value of  $p$  is generally 2 and  $\nu$ ,  $\nu_\ell$  and  $\nu_r$  are striking velocity, ballistic limit and missile residual velocity, respectively.

*(10) Winfrith Perforation Energy Model*

Using dimensional analysis, the perforation energy of the steel pipe is related to the geometric parameters and material properties by

$$E_p / (\sigma_u d^3) = A(h/d)^a (d/D)^b \tag{7.130}$$

where

- $E_p$  = perforation energy
- $\sigma_u$  = characteristic strength of the material =  $\sigma_c$
- $d, D$  = missile and pipe diameter, respectively
- $h$  = target thickness
- a, b, A = constants given in Table 7.16

Tests have been carried out on target thicknesses of 7.1 mm and 11 mm. For a 25 mm diameter missile the perforation energy varied as the 1.8 power of the target pipe thickness and for a 60 mm diameter missile an exponent of 1.4 was obtained. At an impact energy of 41.5 kJ, the 60 mm diameter missile displaced a shear plug in the pipe wall thickness by a distance of 3 to 11 mm. Figure 7.18 shows a graph of the perforation energy plotted against pipe wall thickness and the missile diameter. In the case of  $E_p$  versus  $d$ , an exponent of 1.9 is obtained for a 7.1 mm pipe wall and 1.7 for an 11 mm pipe wall thickness, averaging both sets to 1.8. Exponents ranging from 1.5 to 1.7 have been suggested for plain steel targets. The test results based on the BRL formula are also plotted. On the basis of these tests, the perforation energy is assumed to vary as

$$E_p = Bh^{1.7}d^{1.8} \tag{7.131}$$

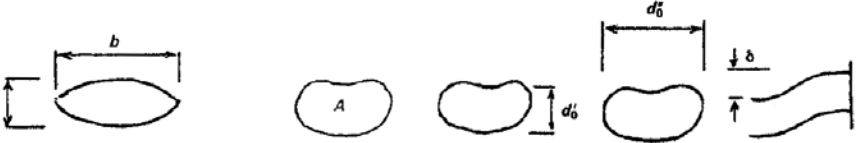
where B is a constant.

In another expression, the exponent is given as 1.7. If this normalized perforation energy variation is imposed on the pipe perforation, the correlation as shown in Fig. 7.18 becomes

$$E_p / \sigma_u d^3 = A(h/d)^{1.7} (d/D)^{1.5} \tag{7.132}$$

where the parameter  $A\sigma_u$  has a value of  $8 \times 10^9$ , if SI units are chosen for  $E_p$ ,  $d$ ,  $h$  and  $D$ .



**Table 7.16.** Permanent deformation of pipe


Test	$a$ (mm)	$b$ (mm)	$A$ (cm <sup>2</sup> )	$d_0'$ (mm)	$\delta$ (mm)	$m$ (kg)	$\nu$ (m/s)	$h$ (mm)
255	75	115	–	–	–	1.7	93	7.4
256	70	100	170	148	21	1.7	67	7.4
257	140	215	158	115	65	7.5	75	7.3
258	170	310	99	77	112	7.3	108	7.2
259	140	250	172	114	60	7.39	69	7.1
260	165	325	113	86	104	7.29	104	7.1
264	130	220	151	111	64	4.0	105	7.3
265	135	200	159	113	67	4.0	104	7.4
266	145	280	121	93	94	4.0	136	7.1
267	135	225	–	–	–	4.0	142	7.0
268	105	–	–	–	–	4.0	117	7.2
269	130	–	–	–	–	4.0	112	7.2
270	105	–	–	–	–	4.0	108	7.2
271	100	110	108	144	35	4.0	108	7.6
272	–	–	–	–	–	4.0	108	7.7
273	120	220	–	100	83	4.0	114	7.5
274	135	250	–	100	82	4.0	114	6.9
275	140	300	135	92	93	4.0	113	7.0
276	100	120	–	–	–	4.0	108	7.4
477	80	90	–	–	–	1.7	130	10.5
478	45	50	–	–	11	1.7	203	18.2
479	70	80	–	–	–	1.7	129	10.7
480	55	60	–	–	17	0.6	325	18.6
481	110	–	–	–	–	4.0	180	10.6
482	105	–	–	–	–	4.0	236	18.6
483	135	200	–	–	–	4.0	136	11.0
484	90	125	–	–	36	4.0	144	18.6
485	110	165	–	–	–	4.0	143	7.2
486	110	140	–	–	–	4.0	87	7.1
487	110	145	–	–	–	4.0	113	8.1
488	105	130	–	–	–	4.0	67	7.2
489	90	160	–	–	36	3.1	75	7.4
400	95	180	–	–	46	3.1	84	7.2
491	100	200	–	–	55	3.1	99	7.2
492	110	220	–	–	–	3.1	143	7.2
493	} oblique impact		–	–	–	4.0	180	7.3
494			–	–	–	4.0	120	7.0
495	185	230	–	–	231	43.0	78	7.4
496	105	180	–	–	55	34.9	49	7.5
497	155	250	–	–	95	37.5	46	7.4
498	170	380	–	–	196	44.0	78	7.3
499	170	270	–	–	350	54.2	100	10.9
500	175	385	–	–	150	29.5	70	7.1

Courtesy of A.J. Neilson, UKAEA, Winfrith, UK.

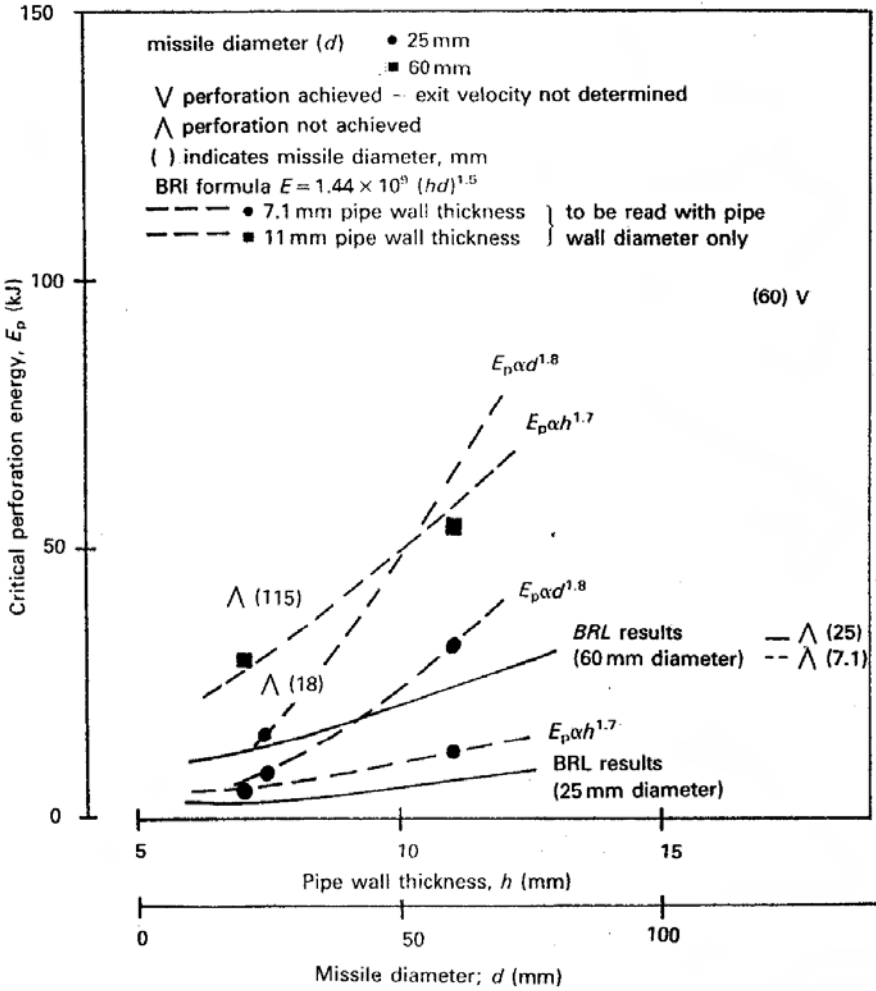


Fig. 7.18. Effect of pipe wall thickness on perforation energy of solid billet missiles (Courtesy of A.J. Neilson, UKAEA, Willfrith, UK)

## References

- [7.1] Davie TN, Richgels AM (1983) An earth penetrator code. Sandia Report – (SAND-82-2358), Sandia National Laboratories, Livermore, California
- [7.2] Kar AK (1978) Projectile penetration into buried structures. J. Struct. Div., ASCE, paper 13479STI
- [7.3] Henrych J (1979) The dynamic of explosion and its use. Elsevier, Amsterdam
- [7.4] Glasstone S, Dolan PJ, The effects of nuclear weapons. US Department of Defense, Washington
- [7.5] Jones N, Wierzbicki T, Structural crash worthiness. Butterworths, London
- [7.6] Morrow CT, Smith MR (1961) Ballistic missile and aerospace technology. Proc. 6th Symp., Academic Press, New York
- [7.7] FIP Concrete for hazard protection. 1st Int. Conf. Concrete Society, Edinburgh
- [7.8] Abaham LM, Structural design of missiles and space-craft. McGraw Hill, New York
- [7.9] BAM (1982) Concrete structures under impact and impulsive loading. Bundesanstalt für Materialprüfung, Berlin
- [7.10] Macmillan RH, Dynamics of vehicle collisions. Special Publications SP5, Inderscience Enterprises, Jersey, UK
- [7.11] Taylor DW, Whitman RV (1953) The behaviour of soils under dynamic loadings. 2. Interim report on wave propagation and strain-rate effect, MIT Report AFSWP-117
- [7.12] Maurer WC (1959) Impact crater formation in sandstone and granite. Master's thesis submitted to Colorado School of Mines
- [7.13] Rinehart JS (1980) Stresses associated with lunar landings. Contribution no. 11, Mining Research Laboratory Colorado School of Mines
- [7.14] Tolch NA, Bushkovitch AV (1947) Penetration and crater volume in various kinds of rocks as dependent on caliber, mass and striking velocity of projectile. BRL Report no. 641, UK
- [7.15] NDRC (1946) Effects of impact and explosion. Summary Technical Report of Div. 2, National Design and Research Corporation (NDRC), Vol. 1. Washington DC
- [7.16] Lang HA (1956) Lunar instrument carrier – landing factors. Rand RM-1725, ASTIA Doc. no AD 112403
- [7.17] Palmore JI (1961) Lunar impact probe. ARS J.:1066–1073
- [7.18] Rinehart JS (1960) Portions of traite de balistique experimentale which deal with terminal ballistics. Chapters III, IV, V and XIV, Félix Hélie, Paris (1884), Naval Ordnance Test Station TM RRB-75
- [7.19] Dennington RJ (1958) Terminal ballistics studies. Proj. Doan Brook Tech. Memo. no 20 Case Inst., ASTIA AD 146 913
- [7.20] Kornhauser M (1958) Prediction of cratering caused by meteoroid impacts. J. Astron. Sci. V(3–4)
- [7.21] Rinehart JS, Pearson J (1954) Behaviour of metals under impulsive loads. American Society for Metals, Cleveland
- [7.22] Rinehart JS (1950) Some observations on high-speed impact. Naval Ordnance Test Station RRB-50. Félix Hélie, Paris, France

- [7.23] Rinehart JS, White WC (1952) Shapes of craters formed in plaster-of-paris by ultra-speed pellets. *Am. J. Phys.* 20(1)
- [7.24] Gazley C Jr (1957) Deceleration and heating of a body entering a planetary atmosphere from space. RAND Corporation Report P-955, USA
- [7.25] Lees L, Hartwig FW, Cohen CB (1959) Use of aerodynamic lift during entry into the earth's atmosphere. *ARS J.*:633–41
- [7.26] Lowe RE, Gervais RL (1961) Manned entry missions to Mars and Venus. In: *ARS Space Flight Report to the Nation*, paper 2158-61, New York
- [7.27] Turnacli RD, Hartnett JP (1957) Generalized trajectories for free-falling bodies of high drag. *ARS paper 543-57*, 12th annual meeting, New York, 2-5 December 1957
- [7.28] Creighton DC (1982) Non-normal projectile penetration in soil and rock: User's guide for computercode PENC02D. Technical Report SL-82-7, US Army Engineering Waterways Experiment Station, Vicksburg, Miss.
- [7.29] Young CW (1972) Empirical equations for predicting penetration performance in layered earth materials for complex penetrator configurations. Development Report No SC-DR-72-0523, Sandia National Laboratory, Albuquerque, NM
- [7.30] Young CW (1985) Simplified analytical model of penetration with lateral loading. SAND84-1635, Sandia National Laboratory, Albuquerque, NM
- [7.31] Matuska D, Durrett RE, Osborn JJ (1982) Hull user's guide for three-dimensional linking with EPIC 3. ARBRL-CR-00484, Orlando Technology, Shalimar, FL
- [7.32] Ito YM, Nelson RB, Ross-Perry FW (1979) Three-dimensional numerical analysis of earth penetration dynamics. Report DNA 5404F, Defense Nuclear Agency, Washington DC, USA
- [7.33] Johnson GR, Stryk RA (1986) Dynamic-Lagrangian computations for solids, with variable nodal connectivity for severe distortions. *Int. Num. Methods Eng.* 23:509–22
- [7.34] Hallquist JO (1984) User's manual for DYNAM – An explicit two-dimensional hydrodynamic finite element code with interactive rezoning. Report UCID-18756, Revision 2, University of California, Lawrence Livermore National Laboratory, USA
- [7.35] Hallquist JO, Benson DJ (1986) DYNA3D user's manual (nonlinear dynamic analysis of structures in three dimensions). Report UCID-19592, Revision 2, University of California, Lawrence Livermore National Laboratory
- [7.36] Carr HH (1948) Analysis of head failure in aircraft torpedoes. NOTS Navord Report 1019, Patent Office Library, London
- [7.37] Reissner E (1946, 1947) Stresses and small displacements of shallow spherical shells. *J. Math. Phys.* XXV 1 and 4
- [7.38] Friedrichs KO (1941) On the minimum buckling load for spherical shells. In: *Theodore von Kàrmàn Anniversary Volume*, CIT, Pasadena, USA, pp. 258–272
- [7.39] Tsein HS (1942) A theory for the buckling of thin shells. *J. Aero. Sci.*, 9:373–384
- [7.40] Payton RG (1962) Initial bending stresses in elastic shells impacting into compressible fluids. *Quart. J. Mech. Appl. Math.* 15:77–90

- [7.41] Office of the Scientific Research and Development (1946) Aircraft torpedo development and water entry ballistics. OSRD Report 2550, CIT, Pasadena, USA
- [7.42] Kornhauser M (1958) Impact protection for the human structure. Am. Astron. Soc., Western Regional Meeting, 18-19 August 1958, Palo Alto, California
- [7.43] Kornhauser M (1960) Structural limitations on the impulsiveness of astronomical maneuvers. ARS Conf. Structural Design of Space Vehicles, 6 April 1960, Santa Barbara, California
- [7.44] ANC-5; Depts of Air Force, Navy and Commerce (1955) Strength of metal aircraft elements. Republican Press, Hamilton, Ohio
- [7.45] Coppa A (1960) On the mechanics of buckling of a cylindrical shell under longitudinal impact. 10th Int. Congress App. Mech., September 1960, Stressa, Italy
- [7.46] Polentz LM (1959) Linear energy absorbers. Machine Design
- [7.47] Martin ED (1961) A design study of the inflated sphere landing vehicle, including the landing performance and the effects of deviations from design conditions. NASA TN D-692
- [7.48] Esgar JB, Morgan WC (1960) Analytical study of soft landings on gas-fill bags. NASA TR R-75
- [7.49] Fisher LJ. Jr (1961) Landing-impact-dissipation systems. NASA TN D-975
- [7.50] Schrader CD (1962) Lunar and planetary soft landings by means of gas-filled balloons. ARS Lunar Missions Meeting, Cleveland, 17-19 July 1962, paper 2480-62
- [7.51] Bethe HA (1941) Attempt of a theory of armor penetration. Frankford Arsenal Rep., Philadelphia
- [7.52] Taylor GI (1941) Notes on H.A. Bethe's theory of armor penetration, II. Enlargement of a hole in a flat sheet at high speeds. Home Ministry Security Report, R.C. 280 UK
- [7.53] Taylor GI (1948) The formation and enlargement of a circular hole in a thin plastic sheet. Quart. J. Mech. Appl. Math. 1
- [7.54] Kineke JH, Vitali R (1963) Transient observations of crater formation in semi-infinite targets. In: Proc. 6th Symp. Hypervelocity Impact, Vol. II. part 2. Springer-Verlag, Berlin, Germany
- [7.55] Eichelberger RJ, Kineke JH (1967) Hypervelocity impact. In: Vollrath K, Thomer G (eds.) High speed physics, Springer-Verlag, Wien, New York
- [7.56] Turpin WC, Carson J.M. (1970) Hole growth in thin plates perforated by hypervelocity pellets. Air Force Materials Lab. Rep. 70-83, Wright-Patterson AFB, Ohio
- [7.57] Holloway LS (1963) Observations of crater growth in wax. BRL Rep., USABRL-M-1526
- [7.58] Freiburger W (1952) A problem in dynamic plasticity: The enlargement of a circular hole in a flat sheet. Proc. Cambridge Phil. Soc. 48
- [7.59] Fraiser JT, Karpov BG, Holloway LS (1965) The behavior of wax targets subjected to hypervelocity impact. In: Proc. 7th Hypervelocity Impact Symp., Vol. V. Springer-Verlag, Berlin, Germany
- [7.60] Rolsten RF, Wellnitz JN, Hunt HH (1964) An example of hole diameter in thin plates due to hypervelocity impact. J. Appl. Phys. 35

- [7.61] Allison FE (1965) Mechanics of hypervelocity impact. In: Proc. 7th Hypervelocity Impact Symp., Vol. I. Springer Verlag, Berlin, Germany
- [7.62] Wilkins M, Guinan M (1973) Impact of cylinders on a rigid boundary. *J. Appl. Phys.* 44
- [7.63] Whiffin AC (1948) The use of flat-ended projectiles for determining dynamic yield stress, II, Tests on various metallic materials. *Proc. R. Soc. London Ser. A*, 194
- [7.64] Goldsmith W (1960) *Impact. The theory and physical behaviour of colliding solids.* Edward Arnold, London
- [7.65] Johnson W (1972) *Impact Strength of Materials.* Edward Arnold, New York
- [7.66] Walters W (1979) Influence of material viscosity on the theory of shaped-charge jet formation. BRL Rep., BRL-MR-02941
- [7.67] Chhabildas LC, Asay JR (1979) Rise-time measurements of shock transitions in aluminum, copper and steel. *J. Appl. Phys.* 50
- [7.68] Birkhoff G, MacDougall D, Pugh E, Taylor G (1948) Explosives with lined cavities. *J. Appl. Phys.* 19
- [7.69] Scott B, Walters W (1984) A model of the crater growth-rate under ballistic impact conditions. In: Proc. Southeastern Conf. on Theoretical and Applied Mechanics, Georgia
- [7.70] Rohani B (1975) Analysis of projectile penetration into concrete and rock targets. S-75-25. US Army Engineer Waterways Experimental Station
- [7.71] Housen K, Schmidt R, Holsapple K (1983) Crater ejecta scaling laws: Fundamental forms based on dimensional analysis. *J. Geophys. Res.* 88
- [7.72] Glass J, Bruchey W (1982) Internal deformation and energy absorption during penetration of semi-infinite targets. In: Proc. 8th Int. Symp. Ballistics, NASA, Langley, USA
- [7.73] Wang WL (1971) Low velocity projectile penetration. *Journal of the Soil Mechanics and Foundations Division, ASCE* 97, no SM12, Proc. paper 8592
- [7.74] Young CW (1969) Depth prediction for earth-penetrating projectiles. *Journal of the Soil Mechanics and Foundations Division, ASCE* 95, no SM3, Proc. paper 6558
- [7.75] Petry L (1910) *Monographies de systèmes d'artillerie.* Brussels
- [7.76] Hakala WW (1965) Resistance of a granular medium to normal impact of a rigid projectile. Thesis presented to the Virginia Polytechnic Institute, Blacksburg, Va, in partial fulfillment of the requirements for the degree of doctor of Philosophy
- [7.77] Thigpen L (1974) Projectile penetration of elastic-plastic earth-media. *Journal of the Geotechnical Engineering Division, ASCE* 100, no GT3, Proc. paper 10414
- [7.78] Butler DK (1975) An analytical study of projectile penetration into rock. Technical Report S-75-7, Soils and Pavements Laboratory, US Army Engineer Waterways Experiment Station, Vicksburg, Miss.
- [7.79] Butler DK (1975) Pretest penetration for DNA rock penetration experiments at a sandstone site near San Ysidro. New Mexico. Soils and Pavements Laboratory, US Army Engineer Waterways Experiment Station, Vicksburg, Miss.

- [7.80] Butler DK (1975) Development of high-velocity powder gun and analysis of fragment penetration tests into sand. Misc. paper S-75-27, Soils and Pavements Laboratory, US Army Engineer Waterways Experiment Station, Vicksburg, Miss.
- [7.81] Bernard RS, Hanagud SV (1975) Development of a projectile penetration theory, Report I, Penetration theory for shallow to moderate depths. Technical Report S-75-9, Soils and Pavements Laboratory, US Army Engineer Waterways Experiment Station, Vicksburg, Miss.
- [7.82] Bernard RS (1976) Development of a projectile penetration theory, Report 2, Deep penetration theory of homogeneous and layered targets. Technical Report S-75-9, Soils and Pavements Laboratory. US Army Engineer Waterways Experiment Station, Vicksburg, Miss.
- [7.83] Hammel J (1979) Impact loading on a spherical shell. 5th Int. Conf. on Structural Mechanics in Reactor Technology (SMiRT), Berlin
- [7.84] Barber EM et al. (1972) A study of air distribution in survival shelters using a small-scale modelling technique. Report 10689, USA National Bureau of Standards
- [7.85] Barneby HL et al. (1963) Toxic gas protection. Paper to ASHRAE Symp. Survival Shelters, 1962
- [7.86] Barthel R (1965) Research on the climate in an underground shelter. *Ingenieur* 77:143–7 (in Dutch)
- [7.87] Barthel R (1965) Theoretical and experimental research regarding the indoor climate in an underground shelter. *Ingenieur* 77:6143–7 (in Dutch)
- [7.88] Cooper J (1980) After the bomb. *Journal of the Chartered Institution of Building Services* 2:48–9
- [7.89] Dasler AR, Minrad D (1965) Environmental physiology of shelter habitation. *ASHRAE Trans* 71:115–24
- [7.90] Drucker EE, Cheng HS (1963) Analogue study of heating in survival shelters. *ASHRAE Symp. Survival Shelters, 1962*, ASHRAE
- [7.91] Bigg JM (1964) Introduction to structural dynamics. McGraw Hill, New York
- [7.92] Gates AS (1963) Air revitalization in sealed shelters. *ASHRAE Symp. Survival Shelters, 1962*, ASHRAE
- [7.93] Gessner H (1961) The ventilation of air-raid shelters. *Schweizerische Blätter für Heizung und Lüftung* 28:1–12 (in German)
- [7.94] Hanna GM (1962) Ventilation design for fallout and blast shelters. *Air Engineering* 4:19–21
- [7.95] Home Office (1981) Domestic nuclear shelters (DNS) – Technical guidance. HMSO
- [7.96] Home Office (1981) Domestic nuclear shelters. HMSO
- [7.97] Eibl J (1982) Behaviour of critical regions under soft missile impact and impulsive loading. IBAM, June
- [7.98] Hughes G, Speirs D (1982) An investigation of the beam impact problem. Technical Report 546, C & CA, UK (now British Cement Association)
- [7.99] Bate S (1961) The effect of impact loading on prestressed and ordinary reinforced concrete beams. *National Building Studies Research Paper* 35
- [7.100] Billing I (1960) *Structure concrete*. Macmillan, London
- [7.101] Watson A, Ang T (1982) Impact resistance of reinforced concrete structures. In: *Designs for dynamic loading*, Construction Press, London, UK

- [7.102] Watson A, Ang T (1984) Impact response and post-impact residual strength of reinforced concrete structures. Int. Conf. and Exposition of Structural Impact and Crashworthiness, Imperial College, London, UK
- [7.103] Perry S, Brown I (1982) Model prestressed slabs subjected to hard missile loading. In: Design for dynamic loading, Construction Press, London, UK
- [7.104] Perry S, Brown I, Dinic G (1984) Factors influencing the response of concrete slabs to impact. Int. Conf. and Exposition of Structural Impact and Crashworthiness, Imperial College, London, UK
- [7.105] Kufuor K, Perry S (1984) Hard impact of shallow reinforced concrete domes. Int. Conf. and Exposition of Structural Impact and Crashworthiness, Imperial College, London, UK
- [7.106] Burgess W, Campbell-Allen D (1974) Impact resistance of reinforced concrete as a problem of containment. Research Report no R251, School of Civil Engineering, University of Sydney
- [7.107] Stephenson A (1976) Tornado-generated missile full-scale testing. In: Proc Symp. Tornadoes, Assessment of Knowledge and Implications for Man. Texas University
- [7.108] Jankov Z, Turnham J, While M (1976) Missile tests of quarter-scale reinforced concrete barriers. In: Proc. Symp. Tornadoes, Assessment of Knowledge and Implications for Man, Texas University, June 1976
- [7.109] Stephen A, Silter G (1977) Full-scale tornado-missile impact tests. 5th Int. Conf. on Structural Mechanics in Reactor Technology (SMiRT), Berlin, 1977, paper J10/1
- [7.110] Jonas W, Rudiger E (1977) Experimental and analytical research on the behaviour of reinforced concrete slabs subjected to impact loads. 5th Int. Conf. on Structural Mechanics in Reactor Technology (SMiRT), Berlin, paper J7/6
- [7.111] Beriaud C et al. (1977) Local behaviour of reinforced concrete walls under hard missile impact. 5th Int. Conf. on Structural Mechanics in Reactor Technology (SMiRT), Berlin, 1977, paper J7/9
- [7.112] Gupta Y, Seaman L (1977) Local response of reinforced concrete to missile impacts. 5th Int. Conf. on Structural Mechanics in Reactor Technology (SMiRT), Berlin, 1977, paper J10/4
- [7.113] Barr P et al. (1982) An experimental investigation of scaling of reinforced concrete structures under impact loading. In: Design for dynamic loading, Construction Press, London, UK
- [7.114] Barr P et al. (1983) Experimental studies of the impact resistance of steel faced concrete composition. 7th Int. Conf. on Structural Mechanics in Reactor Technology (SMiRT), 1983, paper J8/4, Chicago, USA
- [7.115] Det Norske Veritas (1981) Rules for classification of mobile offshore units
- [7.116] Minorsky VV (1959) An analysis of ship collisions with reference to nuclear power plants. Journal of Ship Research 3:1–4
- [7.117] Soreide TH (1981) Ultimate load analysis of marine structures. Tapir, Trondheim
- [7.118] JABSF (1983) Ship collision with an offshore structure. IABSE Colloquium, Copenhagen
- [7.119] Woisin G (1977) Conclusion from collision examinations for nuclear merchant ships in the FRG. In: Proc. Symp. Naval Submarines, Hamburg



- [7.120] Reckling KA (1977) On the collision protection of ships. PRADS Symp., Tokyo
- [7.121] Nagasawa H, Arita K, Tani M, Oka S (1977) A study on the collapse of ship structure in collision with bridge piers. *J. Soc. Nav. Arch. Japan* 142
- [7.122] Macaulay MA, Macmillan RH (1968) Impact testing of vehicle structures. In: *Proc. 12th FISITA Congress, Barcelona*
- [7.123] Emori RI (1968) Analytical approach to automobile collisions. SAE Paper 680016, Society of Automobile Engineers, USA
- [7.124] Neilson ID et al. (1968) Controlled impact investigations. TRRL Report LR 132, Transport Road Research Laboratory, Crowthorne, UK
- [7.125] Grime G, Jones IS (1969) Car collisions – The movement of cars and their occupants. *Proc. I. Mech. Eng.* 184(5)
- [7.126] Emori RI, Tani M (1970) Vehicle trajectories after intersection collision impact. SAE Paper 700176, Society of Automobile Engineers
- [7.127] Wall JG et al. (1970) Comparative head-on impact tests. TRRL Report LR 155, Transport Road Research Laboratory, Crowthorne, UK
- [7.128] Jones IS (1975) Mechanics of roll-over as the result of curb impact. SAE Paper 750461, Society of Automobile Engineers
- [7.129] Wagner R (1978) Compatibility in frontal collisions. In: *Proc. 17th FISITA Congress, Budapest*
- [7.130] Rouse H, Howe JW (1953) *Basic mechanics of fluids*. Wiley
- [7.131] Kinslow R (ed.) (1970) *High velocity impact phenomena*. Academic Press
- [7.132] Nowacki WK (1978) *Stress waves in non-elastic solids*. Pergamon
- [7.133] Hurty WC, Rubinstein MF (1964) *Dynamics of structures*. Prentice-Hall
- [7.134] Morrow CT (1963) *Shock and vibration engineering*. Wiley
- [7.135] Biggs JM (1964) *Introduction to structural dynamics*, Chapter 2, McGraw-Hill
- [7.136] Snowdon IC (1968) *Vibration and shock in damped mechanical systems*. Wiley
- [7.137] Craig RR (1981) *Structural dynamics: An introduction to computer methods*. Wiley
- [7.138] Davies GA (1984) *Structural impact and crashworthiness*. Vol. I, Chapter 7, Elsevier
- [7.139] Andrews KPF et al. (1983) Classification of the axial collapse of cylindrical tubes under quasi-static loading. *Int. J. Mechanical Sciences* 25:678–96
- [7.140] Bodner SR, Symonds PS (1972) Experimental and theoretical investigation of the plastic deformation of cantilever beams subjected to impulsive loading. *Journal of Applied Mechanics* (December):719–28
- [7.141] Conway MD, Jakubowski M (1969) Axial impact of short cylindrical bars. *Journal of Applied Mechanics* 36:809
- [7.142] Hagiwara K et al. (1983) A proposed method of predicting ship collision damage. *Int. J. of Impact Engineering* 1:257–80
- [7.143] Lee EH, Morrison JA (1956) A comparison of the propagation of longitudinal waves in rods of viscoelastic materials. *Journal of Polymer Science* 19:93–110
- [7.144] Samuelides E, Frieze PA (1983) Strip model simulation for low energy impacts on flat-plated structures. *Int. J. Mechanical Sciences* 25:669–86
- [7.145] Backman ME, Goldsmith W (1978) The mechanics of penetration of projectiles into targets. *Int. J. Eng. Sci.* 16:1–99

- [7.146] Bernard RS, Hanagud SV (1975) Development of a projectile penetration theory. Technical Report S-75-9, US Army Waterways Experiment Station
- [7.147] Bernard RS (1976) Development of a projectile penetration theory report 2: Deep penetration theory for homogeneous and layered targets. Technical Report S-75-9, US Army Waterways Experiment Station, Virginia, USA
- [7.148] Byers RK, Chabai AJ (1977) Penetration calculations and measurements for a layered soil target. *Int. J. for Numerical and Analytical Methods in Geomechanics* 1:107–138
- [7.149] Bjork RL (1975) Calculations of earth penetrators impacting soils. AD-AO46 236, Pacifica Technology Hawaii, USA
- [7.150] DNA/SANDIA (1975) Soil penetration experiment at DRES: Results and analysis. SAND.75.0001, Sandia Laboratories, Albuquerque
- [7.151] Hadala PF (1975) Evaluation of empirical and analytical procedures used for predicting the rigid body motion of an earth penetrator. Technical Report S-75-15, US Army Waterways Experiment Station, Virginia, USA
- [7.152] Norwood FR, Sears MP (1982) A nonlinear model for the dynamics of penetration into geological targets. *Journal of Applied Mechanics* 49:26–30
- [7.153] Rohani B (1972) High velocity fragment penetration of a soil target. In: *Proc. Conf. on Rapid Penetration of Terrestrial Materials*, Texas A & M University
- [7.154] Triandafilidis GE (1976) State of the art of earth penetration technology, 2 volumes, Technical Report CE-42(76) DNA-297, The University of New Mexico
- [7.155] Wagner MH, Kreyenhagen KN, Goerke WS (1975) Numerical analysis of projectile impact and deep penetration into earth media. WES Contract Report S-75-4, California Research and Technology Inc.
- [7.156] Yankelevsky DZ (1979) Normal penetration into geomaterials. Research Report 30, Faculty of Civil Engineering, Technion, Israel
- [7.157] Yankelevsky DZ (1983) The optimal shape of an earth penetrating projectile. *Int. J. Solids and Structures* 19:25–31
- [7.158] Yankelevsky, DZ (1985) Cavitation phenomena in soil projectile interaction. *Int. J. Imp. Eng.* 3:167–78
- [7.159] Young CW, Ozanne GM (1966) Low velocity penetration study. SC-RR-66-118, Sandia Laboratories, USA
- [7.160] Young CW (1969) Depth prediction for earth penetrating projectiles. *J. Soil Mech. Found. Div., Proc. Am. Soc. Civ. Eng.* 95:803–17
- [7.161] Young CW (1976) Status report on high velocity soil penetration. SAND 76-0291, Sandia Laboratories, USA
- [7.162] Yarrington P (1977) A one dimensional approximate technique for earth penetration calculations. SAND 77-1126, Sandia Laboratories, USA
- [7.163] Alekseevskii VP (1966) Penetration of a rod into a target at high velocity. *Comb. Expl. Shock Waves* 2:99–106 (English translation)
- [7.164] Backman ME, Goldsmith W (1978) The mechanics of penetration of projectiles into targets. *Int. J. Eng Sci.* 16:1–99
- [7.165] Forrestal MJ, Rosenberg Z, Luk VK, Bless SJ (1986) Perforation of aluminum plates with conical-nosed rods. SAND 86-02921, Sandia National Laboratory, Albuquerque, USA

- [7.166] Frank K, Zook J (1986) Energy-efficient penetration and perforation of targets in the hyper-velocity regime. Hypervelocity Impact Symp., San Antonio, 1986
- [7.167] Levy N, Goldsmith W (1984) Normal impact and perforation of thin plates by hemispherically-tipped projectiles – I. Analytical considerations. *Int. J. Impact Eng.* 2:209–29
- [7.168] Pidsley PH (1984) A numerical study of long rod impact onto a large target. *J. Mech. Phys. Sol.* 32:315–34
- [7.169] Tate A (1986) Long rod penetration models – part I. A flow field model for high speed-long rod penetration. *Int. J. Mech. Sci.* 28:525–48
- [7.170] Zukas JA, Jones GH, Kinsey KD, Sherrick TM (1981) Three-dimensional impact simulations: Resources and results. In: Park KC, Jones RF (eds.) *Computer analysis of large scale structures*, AMD-49, New York, pp. 35–68
- [7.171] Asay JR, Kerley GI (1987) The response of materials to dynamic loading. *Int. J. Impact Eng.* 5(1-4):69–99
- [7.172] Holian KS, Burkett MW (1987) Sensitivity to hypervelocity impact simulation to equation of state. *Int. J. Impact Eng.* 5(1-4):333–41
- [7.173] Maiden CJ (1963) Experimental and theoretical results concerning the protective ability of a thin shield against hypervelocity projectiles. In: *Proc. 6th Symp. Hypervelocity Impact, III*, Springer-Verlag, Berlin, pp. 69–156
- [7.174] Ravid M, Bodner SR, Holeman I (1987) Analysis of very high speed impact. *Int. J. Eng. Sci.* 25(4):473–82
- [7.175] Tillotson JH (1962) *Metallic equations of state for hypervelocity impact*. General Atomic, Division of General Dynamics, GA-3216, San Diego
- [7.176] Chen JK, Sun CT (1985) On the impact of initially stressed composite laminates. *J. Comp. Mat.* 19:490–504
- [7.177] Tsai SW, Hahn HT (1980) *Introduction to composite materials*. Technical Publishing Company, Pennsylvania
- [7.178] Brook N, Summers DA (1969) The penetration of rock by high-speed water jets. *Int. J. Rock Mechanics and Mining Science* 6:249–258
- [7.179] Haimson B (1965) High velocity, low velocity, and static bit penetration characteristics in Tennessee marble, Master's thesis, University of Minnesota
- [7.180] Haimson BC, Fairhurst C (1970) Some bit penetration characteristics in pink Tennessee marble. In: *Proc. 12th Symp. Rock Mechanics*, University of Missouri School of Mines, USA, pp. 547–59
- [7.181] Simon R (1963) Digital machine computations of the stress waves produced by striker impact in percussive drilling machines. In: *5th Symp. Rock Mechanics*, Pergamon, Oxford
- [7.182] Vijay MM, Briery WH (1980) Drilling of rocks with rotating high pressure water jets: An assessment of nozzles. In: *Proc. 5th Int. Symp. Jet Cutting Technology*, Hanover
- [7.183] Watson RW (1973) Card-gap and projectile impact sensitivity measurements, a compilation. US Bureau of Mines Information Circular No 8605
- [7.184] Wells ES (1949) Penetration speed of percussion drill bits. *Chem. Eng. Mineral Rev.* 41(10):362–364
- [7.185] Winzer RR, Ritter AP (1980) Effect of delays in fragmentation in large limestone blocks. Report No MML TR 80-25, Martin Marietta Laboratories, USA

- [7.186] O'Connell WJ, Fortney RA (1974) Turbine missile impact analysis: A detailed treatment. Transactions of the American Nuclear Society 19, 31; EDS Nuclear Inc. Report, 27 October 1974
- [7.187] Moody FJ (1969) Prediction of blowdown thrust and jet forces. ASME Transaction 69-HT-31, American Society of Mechanical Engineers
- [7.188] Norris CH et al. (1959) Structural design for dynamic loads. McGraw-Hill, New York
- [7.189] Emori RI (1968) Analytical approach to automobile collisions. Automotive Engineering Congress, Detroit, Michigan, paper no 680016
- [7.190] Ivey DL, Ruth E, Hirsch TJ (1970) Feasibility of lightweight cellular concrete for vehicle crash cushions. Paper presented at the Annual Meeting of the Highway Research Board, Washington DC
- [7.191] Chen EP, Sih GC (1977) Transient response of cracks to impact loads. In: Elasto-dynamic crack problems. Vol. 4. Noordhoff, Gröninge, Leyden
- [7.192] Davison L, Graham RA (1979) Shock compression of solids. Phys. Rep. 55:255–379
- [7.193] Meyer MA, Aimonc CT (1983) Dynamic fracture (spalling) of metals. Prog. Mat. Sci. 28:1–96
- [7.194] Grady DE (1981) Fragmentation of solids under impulsive stress loading. J. Geophys. Res. 86:1047–54
- [7.195] Grady DE (1981) Application of survival statistics to the impulsive fragmentation of ductile rings. In: Meyers MA, Murr LE (eds.) Shock waves and high-strain-rate phenomena in metals, Plenum, New York, pp. 181–192
- [7.196] Grady DE, Bergstresser TK, Taylor JM (1985) Impact fragmentation of lead and uranium plates. SAND85-1545 (technical report), Sandia Laboratories
- [7.197] Grady DE, Kipp ME (1979) The micromechanics of impact fracture of rock. Int. J. Rock Mech. Min. Sci. 16:293–302
- [7.198] Cour-Palais BG (1987) Hypervelocity impact in metals, glass and composites. Int. J. Impact Eng. 5:221–238
- [7.199] Holsapple KA (1987) The scaling of impact phenomena. Int. J. Impact Eng. 5:343–356
- [7.200] Johns Hopkins University (1961) The resistance of various metallic materials to perforation by steel fragments, Empirical relationships for fragment residual velocity and residual weight. Ballistic Res. Lab. Proj. Thor TR no 47, Johns Hopkins University, Baltimore, Md.
- [7.201] Johns Hopkins University (1961) The resistance of various non-metallic materials to perforation by steel fragments, Empirical relationships for fragment residual velocity and residual weight. Ballistic Res. Lab. Proj. Thor TR no 47, Johns Hopkins University, Baltimore, Md.
- [7.202] Yatteau JD (1982) High velocity penetration model. NSWU TR, 82-123, New South Wales University, Australia
- [7.203] Piekutowski AJ (1987) Debris clouds generated by hypervelocity impact of cylindrical projectiles with thin aluminum plates. Int. J. Impact Eng. 5:509–518
- [7.204] Rinehart JS, Pearson J (1965) Behaviour of metals under impulsive loading. Dover, New York
- [7.205] Al-Hassani S.T.S., Johnson W. and Nasim M. (1972) Fracture of triangular plates due to contact explosive pressure. J. Mech. Eng Sci. 14(3), 173–83

- [7.206] Al-Hassani S.T.S. and Silva-Gomes J.F. (1979) Internal fracture paraboloids of revolution due to stress wave focussing. *Conf. Ser. – Inst. Phys.* 47, 187–96
- [7.207] Al-Hassani S.T.S. and Silva-Gomes J.F. (1986) Internal fractures in solids of revolution due to stress wave focussing. In: *Shock Waves and High-strain-rate Phenomena in Metals*, (Ed. by M.A. Meyers and L.E. Murr), chapter 10. Plenum, New York
- [7.208] Al-Hassani S.T.S. (1986) Fracturing of explosively loaded solids. In: Reid SR (ed.) *Metal forming and impact mechanics*, Chap. 18, Pergamon, Oxford
- [7.209] Swain MV, Lawn BR (1976) Indentation fracture in brittle rocks and glasses. *Int. J. Rock Mech. Min. Sci. Geomech. Abstr.* 13:311–319
- [7.210] Jones N, Liu JH (1988) Local impact loading of beams. In: *Intense dynamic loading and its effects*, Science Press, Beijing, and Pergamon Press, pp. 444–449
- [7.211] Liu JH, Jones N (1988) Dynamic response of a rigid plastic clamped beam struck by a mass at any point on the span. *Int. J. Solids Struct.* 24:251–270
- [7.212] Liu JH, Jones N (1987) Experimental investigation of clamped beams struck transversely by a mass. *Int. J. Impact Eng.* 6:303–335
- [7.213] Liu JH, Jones N (1987) Plastic failure of a clamped beam struck transversely by a mass. Report ES/31/87. Department of Mechanical Engineering, University of Liverpool
- [7.214] Jones N (1979) Response of structures to dynamic loading. *Conf. Ser. – Inst. Phys.* 47:254–276
- [7.215] Recht RF, Ipson TW (1963) Ballistic perforation dynamics. *J. Appl. Mech.* 30:384–390
- [7.216] Lindholm US, Yeakley LM, Davidson DL (1974) Biaxial strength tests on beryllium and titanium alloys. AFML-TR-74-172, Air Force Systems Command, Wright-Patterson Air Force Base, Oh.
- [7.217] Jones N (1970) The influence of large deflections on the behavior of rigid-plastic cylindrical shells loaded impulsively. *J. Appl. Mech.* 37:416–425
- [7.218] Lindberg HE, Anderson DL, Firth RD, Parker LV (1965) Response of reentry vehicle-type shells to blast loads. SRI project FGD-5228, Stanford Research Institute, Menlo Park, Ca.
- [7.219] Cronkhite JD, Berry VL (1983) Investigation of the crash impact characteristics of helicopter composite structure. USA AVRADCDM-TR-82 D.14
- [7.220] Farley GL (1987) Energy absorption of composite materials and structures. 43rd American Helicopter Society Annual Forum, New York
- [7.221] Hull D (1983) Axial crushing of fibre reinforced composite tubes. In: Jones N, Wierzbider T (eds.) *Structural crashworthiness*, Butterworth, London, pp. 118–135
- [7.222] Schmeuser DW, Wickliffe LE (1987) Impact energy absorption of continuous fibre composite tubes. *Trans ASME* 109:72–77
- [7.223] Thornton PH, Edwards PJ (1982) Energy absorption in composite tubes. *J. Comp. Mat.* 16:521–45
- [7.224] Hull D (1982) Energy absorption of composite materials under crush conditions. In: Hayashi T, Kawata K, Umekawa S (eds.) *Progress in science and engineering of composites*, Vol. I, ICCM-IV, Tokyo University, pp. 861–870

- [7.225] Fairfull AH (1986) Scaling effects in the energy absorption of axially crushed composite tubes. PhD thesis, University of Liverpool
- [7.226] Price JN, Hull D (1987) The crush performance of composite structures. In: Marshall IH (ed.) *Composite structures*, Elsevier, Amsterdam, pp. 2.32–2.44
- [7.227] Price JN, Hull D (1987) Axial crushing of glass fibre-polyster oomposite cones. *Comp. Sci. Technol.* 28:211–230
- [7.228] Berry JP (1984) Energy absorption und failure mechanisms of axially crushed GRP tubes. PhD thesis. University of Liverpool
- [7.229] de Runtz JA, Hodge PG (1963) Crushing of tubes between rigid plates. *J. Appl. Mech.* 30:381–395
- [7.230] Abramowicz W, Jones N (1984) Dynamic axial crushing of square tubes. *Int. J. Impact Eng.* 2(2):179–208
- [7.231] Soreide TH, Amdahl J (1982) Deformation characteristics of tubular members with reference to impact loads from collisions and dropped objects. *Norw. Marit. Res.* 10:3–12
- [7.232] Soreide TH, Kavlie D (1985) Collision damage and residual strength of tubular members in steel offshore structures. In: Narayanan R (ed.) *Shell structures stability and strength*, Elsevier Applied Science, London, pp. 185–220
- [7.233] Taby J, Moan T (1985) Collapse and residual strength of damaged tubular members. BOSS '85, paper B8
- [7.234] Durkin S (1987) An analytical method for predicting the ultimate capacity of a dented tubular member. *Int. J. Mech. Sci.* 29:449–67
- [7.235] Ellinas CO, Valsgård S (1985) Collisions and damage of offshore structure: A state-of-the art. In: *Proc. 4th Int. Symp. OMAE, Organisation of Motor Association for Engineering, USA*
- [7.236] de Oliveira JG (1981) Design of steel offshore structures against impact loads due to dropped objects. Report No 81-6, Department of Ocean Engineering, Massachusetts Institute of Technology, Cambridge, Ma.
- [7.237] Adamchak J (1984) An approximate method for estimating the collapse of a ship's hull in preliminary design. In: *Proc. Ship Struct. Symp.*, SNAME, Arlington, Va.
- [7.238] Furness O, Amdahl J (1979) Computer simulation study of offshore collisions and analysis of ship platform impacts. Paper presented at The 2nd Int. Symp. Offshore Structures, Brazil, October 1979; also In: *Applied Ocean Research* 2(3):119–27 (1980)
- [7.239] Furness O, Amdahl J (1980) Ship collisions with offshore platforms. DnV paper 80-PO80, presented at Intermaritee '80 Conf., Hamburg, September 1980
- [7.240] Brown and Root Incorp. (1990) Design of steel offshore structures against impact loads due to dropped objects. Private communication
- [7.241] Knapp AE, Green DJ, Etie RS (1984) Collision of a tanker with a platform. OTC paper 4734, presented at the 16th Annual Offshore Technology Conf., Houston, Texas
- [7.242] Kochler PE, Jorgensen L (1985) Ship impact ice analysis. In: *Proc. 4th Symp. Offshore Mechanics and Arctic Engineering, ASME-Omae, Dallas, Texas, February 1985*, pp. 344–350

- [7.243] Guttman SI, Pushar FJ, Bea RG (1984) Analysis of offshore structures subject to arctic ice impacts. In: Proc. 3rd Symp. Offshore Mechanics and Arctic Engineering, New Orleans, Louisiana, pp. 238–245

# 8 Aircraft Hot Fuel-Structure Interaction During Impact Condition

## 8.1 Introduction

Finite element formulations for the dynamic analysis of aircraft hot fuel structure interaction are presented and evaluated. The hot fluid is assumed to be incompressible and viscous and is described using updated Lagrangian formulation. Three dimensional isoparametric elements with lumped or consistent mass idealisations are employed in the finite element discretisation. Dynamic equilibrium equations are solved using explicit/implicit time integrations. The interaction is assumed entirely mechanical which means that – they are needed to describe the fluid response. The body fluid is assumed to undergo large deformations and the solutions are dependant on discrete time points. On the transient analysis of hot fuel structure systems the employment of hybrid or isoparametric elements discretisation with lumped and consistent mass idealisations are effective in the representation of the hot fluid.

## 8.2 Aviation Fuels

The fire hazard properties of aviation fuels are identified according to susceptibility or ease of ignition, flash points, flammability limits, distillation range (initial and end boiling point), and electrostatic susceptibility. (Note: octane rating has no relation to the degree of fire hazard of a fuel). Table 8.1 summarizes the characteristics of the more common aviation fuels.

After an impact when major structural damage occurs to aircraft fuel tanks, the fuel may be released as a mist due to forward momentum, splashing, and wind shearing. Regardless of the type of fuel involved, this mist is easily ignitable from disrupted electrical circuits, hot engine surfaces, or ignition sources on the ground. The resulting fireball then acts as the ignition source for other combustibles in the area, including pools of high flashpoint Jet A fuel. If antimisting additives can be successfully developed, they are intended to reduce misting and ease of ignition, or if ignition does occur, to prevent the propagation of flame throughout the mist cloud. In some aircraft accidents where deceleration forces are low, liquid fuel flowing from ruptures



**Table 8.1.** Summary data on the fire hazard properties of aviation fuels

	Gasoline	Kerosane Grades
Characteristics	AVGAS	JET A, JET A-1, JP-5, JP-6, JP-8
Freeze Point*	-76°F	-40°F -58°F
Vapor Pressure† (Reid-ASTM D323-58)	5.5 to 7.0 psi	0.1 psi
Flash Point* (By Closed-Cup Method at Sea Level)	-50°F	+95°F to 145°F
Flash Point* (By Air Saturation Method)	-75°F to -85°F	None
Flammability Limits		
Lower Limit	1.4%	0.74%
Upper Limit	7.6%	5.32%
Temp. Range for Flam. Mixtures*	-50°F to +30°F	+95°F to +165°F
Autoignition Temperature*	+825°F to +960°F	+440°F to 475°F
Boiling Points*		
Initial	110°F	325°F
End	325°F	450°F
Pool Rate of Flame Spread‡,§	700-800 fpm	100 fpm (or less)

Note: Figures vary for some of these values in different data sources. Those shown herein are average figures based on the latest available measures

\*  $5/9 (\text{°F}-32) = \text{°C}$

† psi = 6.894 kPa

‡ 1 fpm = 0.3 m/min

§ In mist foam, rate of flame spread in an fuels is very rapid.

fuel tanks or broken fuel has been vapourised and ignited by hot-engine surfaces, hot brakes, heavy electrical arcs etc. thus, antimisting additives solve only a portion of the post crash fuel spill fire problem.

Most aircraft make extensive use of the internal wing volume to store fuel. In larger aircraft, the wing structure is sealed and forms the fuel tank. This is commonly called integral tank, or wet wing construction. Older and light aircraft may incorporate a flexible bladder to contain the fuel within the wing structure, using the wing structure only for support. Separate metal tanks or fiber reinforced nonmetallinc tanks are not widely used, and they are mainly located in light aircraft and older transports.

With integral tank construction, and only to a slightly lesser extent with thin wall bladder tanks, it becomes apparent that disruption of the wing structure by ground impact or other damage will result in the release of fuel and the potential for ignition. This may occur even though occupied portions of the aircraft may be only slightly damaged. Thus, fire becomes the prime threat to the occupants.

Open called foam blocks, cut to fit and placed meticulously in the tank, are used on some military aircraft. While primarily intended for explosion protection after projectile penetration (incendiary bullets, etc.) of the vapor space, they also were tested for improvement of the postcrash fire situation. The tests showed some resulting improvement for tank interior maintenance and loss of available fuel volume have precluded their use in large, long range, civil, and military aircraft.

Several design principles which affect basic aircraft firesafety and crash-worthiness (excluding cabin furnishings and evacuation systems) are mentioned in the Federal Air Regulations and were developed as a result of accident investigations. They include:

1. When the same structure supports fuel tanks and landing gear, shear pins must be incorporated in the landing gear support structure, allowing the gear to be wiped off without applying structural loads to the fuel tanks.
2. The metal aircraft structure must have electrical continuity to prevent accumulation of static electrical charges, particularly in the fuel tank areas. This is extremely important when designing an all metal aircraft since the aircraft structure acts as a Faraday Cage, shielding all contents from lightning strikes.
3. Static discharge devices and lightning divertors must be located and installed correctly.
4. Fuel lines supplying rear fuselage mounted engines must be designed to ensure proper fire resistance and have the flexibility to resist rupture in a crash situation.
5. Fuel lines and main electrical leads must be segregated.
6. Main electrical power cables in the fuselage must be shrouded in fire resistive flexible conduit.
7. The hydraulic system must be designed properly and use fire resistive fluids. Such fluids presently in use have autoignition temperatures in excess of 1000°F (538°C) are only slightly flammable. (Older types of mineral oil based hydraulic fluids are still in wide-spread use, particularly in the military, and have been responsible for many serious fires).
8. Other consideration such as the improvements in the cargo compartment fire detection and extinguishing systems, escape system and devices as well as aircraft rescue and fire control.

### **8.3 Fuel-Structural Interaction – Basic Analytical Formulations**

Fuel with high temperature from the aircraft impacting the structure, it is necessary to develop fuel-structure interaction analysis, which includes fuel pressure load acting also at the interface. The structure equation is written as follows:

$$[M_e]\{\ddot{\delta}_e\} + [C_e]\{\delta'_e\} + [K_e]\{\delta_e\} = \{F_e\} + \{F_{e_e}^{pr}\} \tag{8.1}$$

The fuel pressure load vector  $\{F^{pr}\}$  at the interface  $S$  is obtained by integrating the pressure over the area of the surface:

$$\{F_{e_e}^{pr}\} = \int_S \{N'\} P \{n\} d(S) \tag{8.2}$$

where

- $\{N'\}$  = shape functions employed to discretize the displacement components  $u, v$  and  $w$  (obtained from the structural element)
- $\{n\}$  = normal at the fuel boundary

Substituting the finite element approximating function for pressure given by

$$\{F_{e_e}^{pr}\} = \int_S \{N\} \{N\}_p^T \{n\} d(S) \{P_e\} \tag{8.3}$$

By comparing the integral equation (8.3) with the matrix definition of  $\rho_0 [Re]^T$ , it becomes clear that:

$$\{F_{e_e}^{pr}\} = [R_e] \{P_e\} \tag{8.4}$$

where:

$$[Re]^T = \int_S \{N'\} \{N\}_p^T \{n\} d(S)$$

The substitution of (8.4) into (8.1) results in the dynamic elemental equation of the structure:

$$[M_e]\{\ddot{\delta}_e\} + [C_e]\{\delta'_e\} + [K_e]\{\delta_e\} - [R_e]\{P_e\} = \{F_e\} \tag{8.5}$$

### 8.3.1 Velocity Pressure Formulations

$$\nu_x = \{N\} T' \{\nu_{xe}\} \tag{8.6}$$

$$\nu_y = \{N\} T' \{\nu_{ye}\} \tag{8.7}$$

$$\nu_z = \{N\} T' \{\nu_{ze}\} \tag{8.8}$$

$$T = \{N\} T' \{T_e\} \tag{8.9}$$

$$P = \{N\} T' \{P_e\} \tag{8.10}$$

where

- $\{N\}_p$  = element shape function for velocities and temperature
- $\{N\}$  = element shape function for pressure
- $\{\nu_{xe}\}, \{\nu_{ye}\}, \{\nu_{ze}\}$  = nodal temperature vector
- $\{T_e\}$  = nodal temperature vector
- $\{P_e\}$  = nodal pressure vector

While  $v_x$ ,  $v_z$  and  $T$  are approximated using the same set of shape functions  $\{N\}_p$ , the pressure is interpolated using a different set of shape functions  $\{M\}$  which are at least one polynomial order less than  $\{N\}_p$ . This is a requirement based on the theoretical conditions for stability and convergence of the solutions. The time derivatives are written as, for example, using  $v_x$  as an example:

$$\frac{\partial v_x}{\partial t} = \{N\}_p^{T'} \{v_{xe}\}$$

$$\delta v_x = \{N\}_p^{T'} \{\delta v_{xe}\}$$

$$\{L\}(v_x) = \{L\}\{N\}^{T'} \{v_{xe}\} = [B_G] \{v_{xe}\} = \begin{bmatrix} [b_x] \\ [b_y] \\ [b_z] \end{bmatrix} \{v_{xe}\} \quad (8.11)$$

$$\{L\}^{T'} \{V\} = \{L\}^{T'} \{N\}^{T'} \begin{Bmatrix} \{v_{xe}\} \\ \{v_{ye}\} \\ \{v_{ze}\} \end{Bmatrix} = \begin{bmatrix} [b_x] & [b_y] & [b_z] \end{bmatrix} \begin{Bmatrix} \{v_{xe}\} \\ \{v_{ye}\} \\ \{v_{ze}\} \end{Bmatrix} \quad (8.12)$$

where

$$[b_x]^{T'} = \{b_x\} = \frac{\partial}{\partial x} \{N\} p$$

$$[b_y]^{T'} = \{b_y\} = \frac{\partial}{\partial y} \{N\} p$$

$$[b_z]^{T'} = \{b_z\} = \frac{\partial}{\partial z} \{N\} p$$

Let the matrix operator  $[L_x]$  applied to the variables be denoted by:

$$[L_x] \{V\} = [L_x] \{N\}^{T'} \begin{Bmatrix} \{v_{xe}\} \\ \{v_{ye}\} \\ \{v_{ze}\} \end{Bmatrix} = [B_x] \begin{Bmatrix} \{v_{xe}\} \\ \{v_{ye}\} \\ \{v_{ze}\} \end{Bmatrix} \quad (8.13)$$

The finite element equation (8.12) is written assuming  $\delta v_{xe}$  and  $\delta p_e$  are the virtual change in nodal velocity vector  $\{v_{xe}\}$  and nodal pressure  $\{p_e\}$ , which are not zero, as follows:

$$\begin{aligned}
 & \rho \int_{vol} \{N\}_p \{N\}_p^{T'} d(vol) \{\nu_{xe}\} + \rho \int_{vol} \{N\}_p \{N\}_p^{T'} [B_G] d(vol) \{\nu_{xe}\} \\
 & + \int_{vol} [B_G]^{T'} [D_\mu] [B_x] d(vol) \begin{Bmatrix} \{\nu_{xe}\} \\ \{\nu_{ye}\} \\ \{\nu_{ze}\} \end{Bmatrix} - \int_{vol} \{b_x\} \{M\}^{T'} d(vol) \{P_e\} \\
 & + \rho g_x \beta \int_{vol} \{N\} \{N\}^{T'} d(vol) \{T_e\} \tag{8.14} \\
 & = F_{bx} \int_{vol} \{N\}_p d(vol) + \rho g_x (1 + \beta T_0) \int_{vol} \{N\}_p d(vol) \\
 & + \{n\}^T \begin{Bmatrix} \sigma_x^s \\ \sigma_{xy}^s \\ \sigma_{xz}^s \end{Bmatrix} \int_{S2} \{N\}_p d(S2)
 \end{aligned}$$

$$\int_{vol} \{M\} [B_D] d(vol) \begin{Bmatrix} \{\nu_{xe}\} \\ \{\nu_{ye}\} \\ \{\nu_{ze}\} \end{Bmatrix} = 0 \tag{8.15}$$

The finite element equation can be written now as follows:

$$\begin{aligned}
 & [C_e^f] \{\nu_{xe}\} + \{[K_e^{sx}] + [K_e^{fx}]\} \begin{Bmatrix} \{\nu_{xe}\} \\ \{\nu_{ye}\} \\ \{\nu_{ze}\} \end{Bmatrix} + [K_e^{ex}] \{P_e\} + [K_e^{gx}] \{T_e\} \\
 & = [K_e^{bx}] + [K_e^{gx}] + [K_e^{sx}] \tag{8.16}
 \end{aligned}$$

$$[D_e]^T \begin{Bmatrix} \{\nu_{xe}\} \\ \{\nu_{ye}\} \\ \{\nu_{ze}\} \end{Bmatrix} = 0$$

where

$$\begin{aligned}
 [C_e^f] &= \rho \int_{vol} \{N\}_p \{N\}_p^T d(vol) && = \text{capacity matrix} \\
 [K_e^{sx}] &= \rho \int_{vol} \{N\}_p \{V\}^T [B_G] d(vol) && = \text{momentum matrix due to mass transport} \\
 [K_e^{fx}] &= \int_{vol} [B_G]^T [D] [B_x] d(vol) && = \text{momentum matrix due to diffusion} \\
 [K_e^{ex}] &= \int_{vol} b_x^T \{M\}^T d(vol) && = \text{pressure gradient matrix} \\
 [K_e^{gx}] &= \rho g_x \beta \int_{vol} \{N\}_p \{N\}_p^T d(vol) && = \text{buoyancy matrix} \\
 [F_e^{bx}] &= F_{bx} \int_{vol} \{N\}_p d(vol) && = \text{body force load vector due to non-gravity effects such as an electrostatic field} \\
 \{F_e^{gx}\} &= \rho g_x (1 + \beta T_0) \int_{vol} \{N\}_p d(vol) && = \text{buoyancy force load vector} \\
 \{F_e^{sx}\} &= \{n\}^T \left\{ \begin{array}{c} \sigma_x^s \\ \sigma_{xy}^s \\ \sigma_{xz}^s \end{array} \right\} \int_{vol} \{N\}_p d(S) && = \text{load vector for element face stresses} \\
 [D_e]^{T'} &= \int_{vol} \{m\} [B_d] d(vol) \begin{bmatrix} [D_e^x] \\ [D_e^y] \\ [D_e^z] \end{bmatrix} && = \text{divergence matrix}
 \end{aligned}$$

$[K_e^{fx}]$  is not a square matrix, and therefore, is further divided into submatrices, for notation purposes, as follows:

$$[K_e^{fx}] = [[K_e^{fx1}] [K_e^{fx2}] [K_e^{fx3}]] \quad (8.17)$$

The complete finite element discretized equations for the fuel-structure interaction problem are written in assembled form as:

$$\begin{bmatrix} [M_e] & [o] \\ [M^{fs}] & [M_e^p] \end{bmatrix} \begin{Bmatrix} \{\ddot{\delta}_e\} \\ \{\dot{P}_e\} \end{Bmatrix} + \begin{bmatrix} [C_e] & [o] \\ [o] & [C_e^p] \end{bmatrix} \begin{Bmatrix} \{\dot{\delta}_e\} \\ \{\dot{P}_e\} \end{Bmatrix} \tag{8.18}$$

$$\begin{bmatrix} [K_e] & [K^{fs}] \\ [o] & [K_e^p] \end{bmatrix} \begin{Bmatrix} \{\delta_e\} \\ \{P_e\} \end{Bmatrix} = \begin{Bmatrix} \{F_e\} \\ \{o\} \end{Bmatrix}$$

where

$$[M^{fs}] = \rho_o [R_e]^T$$

$$[K^{fs}] = -[R_e]$$

For a problem involving fuel-structure interaction, therefore, the fluid element will generate all the submatrices with superscript  $p$  in addition to the coupling submatrices  $\rho_o [R_e]^T$  and  $[R_e]$ . Submatrices without a superscript will be generated by the compatible structural element used in the model. Combining the momentum and continuity equations with to the energy equation, the coupled thermal flow equation is given below in a matrix form:

$$\begin{bmatrix} [C_e^f] & [0] & [0] & [0] & [0] \\ [0] & [C_e^f] & [0] & [0] & [0] \\ [0] & [0] & [C_e^f] & [0] & [0] \\ [0] & [0] & [0] & [0] & [0] \\ [0] & [0] & [0] & [0] & [C_e^f] \end{bmatrix} \begin{Bmatrix} \{\nu_{xe}\} \\ \{\nu_{ye}\} \\ \{\nu_{ze}\} \\ \{\dot{P}_e\} \\ \{\dot{T}_e\} \end{Bmatrix} + \begin{pmatrix} [K^{sx}] & [0] & [0] & [0] & [0] \\ [0] & [K^{sy}] & [0] & [0] & [0] \\ [0] & [0] & [K^{sz}] & [0] & [0] \\ [0] & [0] & [0] & [0] & [0] \\ [0] & [0] & [0] & [0] & [K^{tm}] \end{pmatrix} \begin{Bmatrix} \{\nu_{xe}\} \\ \{\nu_{ye}\} \\ \{\nu_{ze}\} \\ \{\dot{P}_e\} \\ \{\dot{T}_e\} \end{Bmatrix} \tag{8.19}$$

$$\begin{pmatrix} [K_e^{fx1}] & [K_e^{fx2}] & [K_e^{fx3}] & [K_e^{ex}] & [K_e^{gx}] \\ [K_e^{fy1}] & [K_e^{fy2}] & [K_e^{fy3}] & [K_e^{ey}] & [K_e^{gy}] \\ [K_e^{fz1}] & [K_e^{fz2}] & [K_e^{fz3}] & [K_e^{ez}] & [K_e^{gz}] \\ [K_e^{ex}]^T & [K_e^{cy2}]^T & [K_e^{cz3}]^T & [0] & [0] \\ [0] & [0] & [0] & [0] & [K_e^{tb}] \end{pmatrix} \begin{Bmatrix} \{\nu_{xe}\} \\ \{\nu_{ye}\} \\ \{\nu_{ze}\} \\ \{\dot{P}_e\} \\ \{\dot{T}_e\} \end{Bmatrix}$$

$$= \begin{Bmatrix} \{F_e^{bx}\} + \{F_e^{gx}\} + \{F_e^{prx}\} \\ \{F_e^{by}\} + \{F_e^{gy}\} + \{F_e^{pry}\} \\ \{F_e^{bz}\} + \{F_e^{gz}\} + \{F_e^{prz}\} \\ \{0\} \\ \{Q_e^g\} \end{Bmatrix}$$

The elements of the submatrices  $[K_e^{sx}]$ ,  $[K_e^{sy}]$ ,  $[K_e^{sz}]$ , and  $[K_e^{tm}]$  are functions of the element velocity vector  $\{V\}$ .

The matrix equation in (8.19) is highly non-linear, which requires interactive solutions.

The convergence criteria, element stiffness formulation and Newton-Raphson interaction are to be seen in the Appendix AI.

Some notations used above are defined below:

- $\rho$  = density
- $\beta$  = volume expansion coefficient
- $g_x, g_y, g_z$  = gravitational constants along the X, Y, Z global Cartesian coordinate directions
- $F_b, F_{by}, F_{bz}$  = body forces along the X, Y, Z global Cartesian coordinate directions
- $\nabla \times$  = divergence operator
- $\nabla$  = gradient operator

Second, consider the flow continuity equation:

$$\nabla \times \{V\} = 0 \tag{8.20}$$

Finally, consider the energy equation:

$$\rho c \left( \frac{\partial T}{\partial t} + \{V\}^T \{\nabla T\} \right) = \nabla \times ([D]\{\nabla T\}) + \bar{q}$$

where

$c$  = specific heat

$$[D] = \begin{bmatrix} K_{xx} & 0 & 0 \\ 0 & K_{yy} & 0 \\ 0 & 0 & K_{zz} \end{bmatrix}$$

$K_{xx}, K_{yy}, K_{zz}$  = thermal conductivities in the element  $x, y, z$  directions  
 $q$  = heat generation rate per unit volume

$$\{V\} = \begin{Bmatrix} \nu_x \\ \nu_y \\ \nu_z \end{Bmatrix} = \text{velocity components in the three orthogonal coordinate directions } (\nu_x = \nu_x(x, y, z, t), \nu_y = \nu_y(x, y, z, t), \nu_z = \nu_z(x, y, z, t))$$

$T$  = temperature ( $T = T(x, y, z, t)$ )

### 8.3.2 Stress Vector

$$\{\tau_x\} = \begin{Bmatrix} \sigma_x \\ \sigma_y \\ \sigma_z \end{Bmatrix} = \text{stress vector on a plane perpendicular to } x \text{ axis}$$

$$\{\tau_y\} = \begin{Bmatrix} \sigma_{xy} \\ \sigma_y \\ \sigma_{zy} \end{Bmatrix} = \text{stress vector on a plane perpendicular to } y \text{ axis}$$

$$\{\tau_z\} = \begin{Bmatrix} \sigma_{xz} \\ \sigma_{yz} \\ \sigma_z \end{Bmatrix} = \text{stress vector on a plane perpendicular to } z \text{ axis}$$

$t$  = time



**Table 8.2.** Development of wave equations

Fuel-pressure packing on structures with displacement components  $u, \nu, \omega$ . The Finite Element shape function is for the spatial variation of the pressure and displacement components are given by:

$$P = \{N\}_p^{T'} \{P_e\} \quad (a)$$

$$U = \{N'\}^T \{U_e\} \quad (b)$$

where

$$\begin{aligned} \{N\}_p &= \text{element shape function for pressure} \\ \{N'\} &= \text{element shape function for displacements} \\ \{P_e\} &= \text{nodal pressure vector} \\ \{\delta_e\} &= \{u_e\}, \{\nu_e\}, \{\omega_e\} = \text{nodal displacement component vectors} \end{aligned}$$

From (a) and (b), the second time derivative of the variables and the virtual change in the pressure can be written as follows:

$$\frac{\partial^2 P}{\partial t^2} = \{N\}_p^{T'} p \{\ddot{P}_e\} \quad (c)$$

$$\frac{\partial^2}{\partial t^2} \{\delta\} = \{\ddot{\delta}_e\} \quad (d)$$

$$\partial P = \{N\}_p^{T'} \{\delta P_e\} \quad (e)$$

Let the matrix operator  $\{L\}$  applied to the element shape functions  $\{N\}$  be denoted by:

$$[B] = \{L\} \{N\}_p^T \quad (e)$$

Substituting (a) through (f) into (i), the Finite Element statement of the wave equation is given by:

$$\begin{aligned} \int_{vol} \frac{1}{c^2} \{\delta P_e\}^{T'} \{N\}_p \{N\}_p^T d(vol) \{\ddot{P}_e\} + \int_{vol} \{\delta P_e\}^{T'} [B]^{T'} [B] d(vol) \{P_e\} \\ + \int_S \rho_o \{\delta P_e\}^{T'} \{N\} \{n\}^T \{N\}^{T'} d(S) \{U\} = \{0\} \end{aligned} \quad (g)$$

where

$$\begin{aligned} \{n\} &= \text{normal at the fuel boundary} \\ \text{virtual change in nodal pressure } \{\delta P_e\} &\neq 0 \end{aligned}$$

$$\begin{aligned} \frac{1}{c^2} \int_{vol} \{N\}_p \{N\}_p^{T'} d(vol) \{\ddot{P}_e\} + \int_{vol} [B]^{T'} [B] d(vol) \{P_e\} \\ + \rho_o \int_S \{N\}_p \{n\}^{T'} \{N\}^{T'} d(S) \{\delta\} = \{0\} \end{aligned} \quad (h)$$

The equation (h) can be written in matrix notation to get the discretized wave equation:

$$[M_e^P]\{\ddot{P}_e\} + [K_e^P]\{P_e\} + \rho_o[R_e]^{T'}\{\delta\} = \{0\} \quad (i)$$

where

$$[M_e^P] = \frac{1}{c^2} \int_{vol} \{N\}_p \{N\}_p^{T'} d(vol) \quad = \text{fuel mass matrix (fluid)}$$

$$[K_e^P] = [B]^{T'} [B] d(vol) \quad = \text{fuel stiffness matrix (fluid)}$$

$$\rho_o[R_e] = \rho_o \int_S \{N\}_p \{n\}^{T'} \{N\}^{T'} d(S) = \text{coupling mass matrix (fluid-structure interface)}$$

When the losses at the interface occurs, the discretized wave equation becomes:

$$[M_e^P]\{\ddot{P}_e\} + [C_e^P]\{\dot{P}_e\} + [K_e^P]\{P_e\} + \rho_o[R_e]^{T'}\{\delta_e\} = 0 \quad (j)$$

If  $D =$  Dissipation factor is:

$$D = [\delta P_e]^T \frac{\beta}{c} \int_S \{N\}_p \{N\}_p^T d(S) \{P_e\} \quad (k)$$

to account for the energy loss equation (h) is added to equation  $D$ , the loss activity boundary surface is absorbing boundary surface becomes:

$$[C_e^P]\{P_e\} = \frac{\beta}{c} \int_S \{N\}_p \{N\}_p^T d(S) \{P_e\} \quad (l)$$

$$[C_e^P] = \frac{\beta}{c} \int_S \{N\}_p \{N\}_p^T d(S) = (\text{fluid damping matrix})$$

$\frac{\beta}{c}$  and  $\{\delta P_e\}$  are constants over the surface of the element.  
 $\rho_o =$  density,  $\beta =$  volume expansion coefficient;

$$\{L\}^T = \left[ \frac{\partial}{\partial x}, \frac{\partial}{\partial y}, \frac{\partial}{\partial z} \right] = \text{vector of divergence}$$

$$\{n\} = \text{outward unit normal vector; } \{P_e\} = \frac{\partial P}{\partial t}$$

$$B = \frac{r}{\rho_o c} = \text{boundary absorption coefficient}$$

$r =$  damping resistance of the material at boundary surface

---

## 8.4 Output Quantities

The pressure gradient is evaluated at the element centroid using the computed nodal pressure values.

$$\frac{\partial P}{\partial x} = \left\{ \frac{\partial N}{\partial x} \right\}^T \{P_e\} \quad (8.22)$$

$$\frac{\partial P}{\partial y} = \left\{ \frac{\partial N}{\partial y} \right\}^T \{P_e\} \quad (8.23)$$

$$\frac{\partial P}{\partial z} = \left\{ \frac{\partial N}{\partial z} \right\}^T \{P_e\} \quad (8.24)$$

where  $\frac{\partial P}{\partial x}$ ,  $\frac{\partial P}{\partial y}$ ,  $\frac{\partial P}{\partial z}$  = gradients in  $x$ ,  $y$ , and  $z$  directions, respectively. Other terms are similarly defined.

The element fluid velocity is computed at the element centroid for the full harmonic analysis

$$V_x = \frac{j}{\rho_o \omega} = \frac{\partial P}{\partial x} \quad (8.25)$$

$$V_y = \frac{j}{\rho_o \omega} = \frac{\partial P}{\partial y} \quad (8.26)$$

$$V_z = \frac{j}{\rho_o \omega} = \frac{\partial P}{\partial z} \quad (8.27)$$

where

$V_x$ ,  $V_y$  and  $V_z$  = components of the fluid velocity in the  $x$ ,  $y$ , and  $z$  directions, respectively

$\omega$  =  $2\pi f$

$f$  = frequency of the oscillations of the pressure wave

$j$  =  $\sqrt{-1}$

The discrete time points are assumed  $0, \delta t, 2 \delta t \dots t$ , to establish the numerical equation of virtual work from which the unknown static and kinematic variables at  $t + \Delta t$  can be solved. The displacement-based Finite Element procedure has been employed numerically. In explicit time integration equilibrium is considered at time “ $t$ ”, where implicit time integration equilibrium is considered at time  $t + \Delta t$ . The Pressure  $P$  at time “ $t$ ” is used for virtual variation of the volumetric strain at time “ $t$ ” must be computed.

In order to reduce solution errors and in some cases instabilities, equilibrium iteration can be used. Equations are solved for incremental displacements. In the entire work 3D 20-noded elements are used both for fluid elements and structural elements of floors. For the columns and beams, 3D two-noded elements (Appendix I) have been adopted. The shape functions  $N$  for these elements are given in Tables 8.3 and 8.4. Various Gauss integration schemes associated with the two types of elements are considered. For

columns  $2 \times 2$ , the Gauss integration is used. The hourglass patterns correspond to zero eigen values. The idea is to remove hour glass instability. For 3D 20-noded elements  $\frac{\text{NO of zero Eigenvalues}}{\text{NO Degrees of Freedom}}$  is kept  $\frac{43}{60}$  and for 2-noded bar elements, the ratio is kept  $5/8$ .

## 8.5 Input Data and General Analysis of WTC-1 and WTC-2 (World Trade Center)

### 8.5.1 Geometrical Data

The World Trade Center and adjacent affected buildings were located on the West Side of New York, adjacent to Hudson River at the south tip of Manhattan. Here geometrical details are given for only two buildings, namely WTC-1 and WTC-2.

#### *WTC-1*

- (a) up to roof height = 1368 ft = 417 m  
total main height: Each floor height = 12 ft (3.675 m)  
total floors = 110  
H = effective height = 402.336 m
- (b) WTC-1  
Floor plan area:  
Larger  $\rightarrow$  207 ft (63.1 m)  $\times$  207 ft (63.1 m)  
Smaller  $\rightarrow$   
Regular service core  $\rightarrow$  87 ft (26.517 m)  $\times$  137 ft (41.7576) = 1107.31134 m<sup>2</sup>  
Corners chamfered 6' – 11' (2108 mm)

#### *WTC-2*

This building was 6 ft (1.829 m) less than WTC-1  
H = effective height = 400.5072 m.  
Up to roof height = 415.1376 m  
Areas (same as of WTC-1)

### 8.5.2 Aircraft Impact Areas and Speed

(a) *American Airlines, (Flight 11) and United Airlines (Flight 115)*

#### *Boeing 767-200 ER*

Maximum take-off weight	= 178,170 kg
Gross weight	= 124,284.3 kg
Max range	= 12,200 km
Cruise speed	= 850 km/hr (530 mph)
Wing span	= 156' – 1" (47.6 m)
Overall length	= 159' – 2" (48.5 m)
Interior cabin width	= 15' – 6" (4.7 m)

Aircraft area  $= 48.5 \times 47.6 = 2308.6 \text{ m}^2$   
 Flight 11, departed time: 7.59 a.m. and crashed time 8.46 a.m.  
 Flight 175, departed time: 8.14 a.m. and crashed time 9.03 a.m.

(b) *Impact Areas*

(i) *North Tower WTC-1*  $= 4 \times 12 = 48'$  (14.6304 m),  
 Height: Impact Area between  
 Maximum Impact Area  
 Impact between floor 98 and 94  $= 30 \text{ m}^2$   
 centred on north face  
 Speed at impact  $= 470 \text{ km/hr} = 131.6 \text{ m/s}$   
 (taken for the analysis)

(i) *South Tower WTC-2*  
 Floors under impact  $= 78 \text{ to } 84 = 6 \times 12 = 72'$  (21.9456 m)  
 Maximum Impact Area assumed as  $30 \text{ m}^2$   
 Speed at impact  $= 590 \text{ km/hr} = 165.2 \text{ m/s}$   
 (taken for the analysis)

(c) *Time Durations*

**WTC-1**  $\rightarrow$  **47 minutes** (2820 seconds) collapsed at 10.29 a.m.  
 Time duration 10.29–8.46 a.m.  $= 1 \text{ hr} - 43 \text{ minutes}$   
 $= 1.717 \text{ hr}$   
 $= 103.02 \text{ minutes}$   
 $= 6181.2 \text{ seconds}$

**WTC-2**  $\rightarrow$  **49 minutes** (2940 seconds) collapsed at 56 minutes after impact  
 i.e.  $9.03 + 56/60 = 11.223 = 9.063 \text{ a.m.}$ , time at which collapse occur

(d) *Load-Time Function*

The load-time function as explained in the Appendix I is to be created with  $\Delta t$ , the time interval for the dynamic Finite Element will be the base values against impact loads. Simpson rule or others can be used to develop the response of the entire structure of WTC-1 or WTC-2.

At the central zone, the impact corresponding to the air plane fuselage and engines is the worst zone. Away from the central zone, outer wing structures create also an impact zone.

(e) *Existing Loads on WTC-1 apart from Those Due to Aircraft Impact*

The upper 55 stories of the building's exterior-wall frame were explicitly modeled using beam and column elements. This encompassed the entire structure above the zone of impact and about 20 stories below. The lower 55 stories of

the exterior were modeled as a “boundary condition” consisting of a perimeter super-beam that was 52 inches deep (1321) and about 50 inches (5270) wide, supported on a series of springs. A base spring was provided at each column location to represent the axial stiffness of the columns from the 55th floor down to grade. The outrigger trusses at the top of the building were explicitly modeled, using truss-type elements. The interior core columns were modeled as spring elements.

An initial analysis of the building was conducted to stimulate the pre-impact condition. In addition to the weight of the floor itself (approximately 54 psf (259 kN/m<sup>2</sup>) at the building sides), a uniform floor loading of 12 psf (0.76 kN/m<sup>2</sup>) for partitions and an additional 20 psf was conservatively assumed to represent furnishings and contents.

At the impact area, all columns are damaged. The assumption is valid in the impact analysis.

#### *(f) Fireball and Temperature*

Fireballs erupted and jet fuel across the impact floors and down interior shaft ways igniting fire. The term fireball is used to describe deflagration or ignition of fuel vapour cloud. As a result, give raged shroud out the upper floors of the Towers. Program BANG-FR is invoked to get necessary quantities in terms of pressures of loads and are algebraically added to those pressures produced from aircraft-impact specifically floors receiving hot fuel and floors should be analysed using the above analysis. In this analysis for the jet-oil-Tower structure interaction, based on FEMA Report – 3000 gallons escaped with 4000 gallons remained on the impacted floor. The total peak rate of fire energy per Tower is assumed as 3–5 trillion Btu/hr (1–1.56 GW), with a ceiling gas temperature 1100°C (2000°F). growth of fire balls with final full size of 200 ft (60.96 m) occur after 2 seconds.

#### *(g) Concentrated Loads*

BANG-FR for fire analysis is initially concentrated on 80th floor level. The columns above the damage area are predicted to act as tension members, transferring around 10% of the load carried by the damaged columns upward to outrigger trusses and this load is assumed back on core columns.

#### *(h) Chunks Dismantled*

As predicted on site, chunks with dimensions around 12' (305 mm) have landed at a distance of 15 ft (4.572 m) from the face of the building. The distance is assumed always for the computation of forces of chunks. The maximum length and width as observed were 40 ft (12.2 m) and 30 ft (9.144 m).

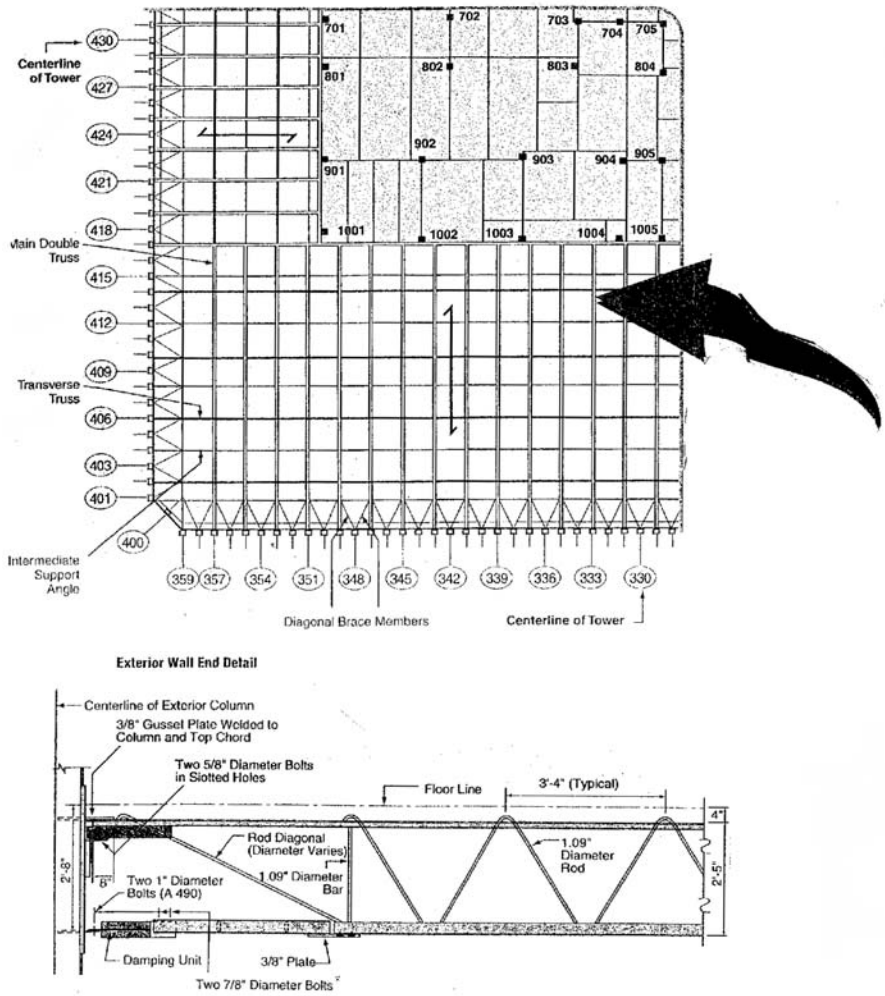
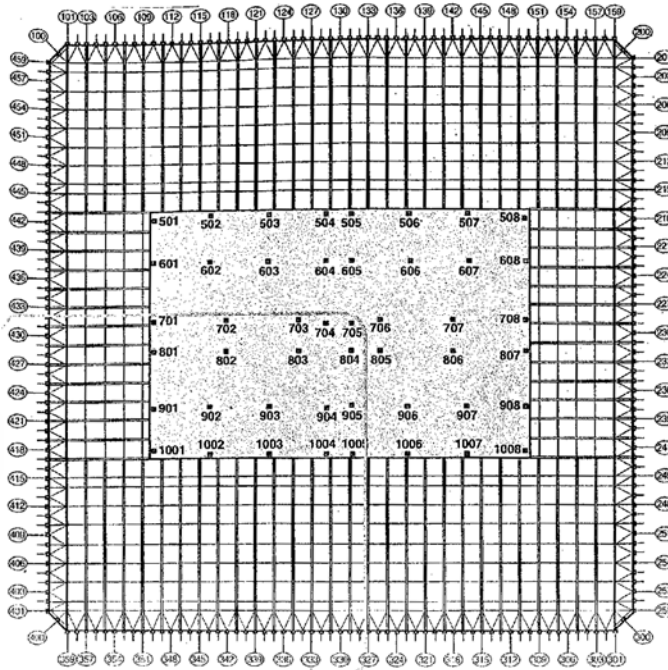
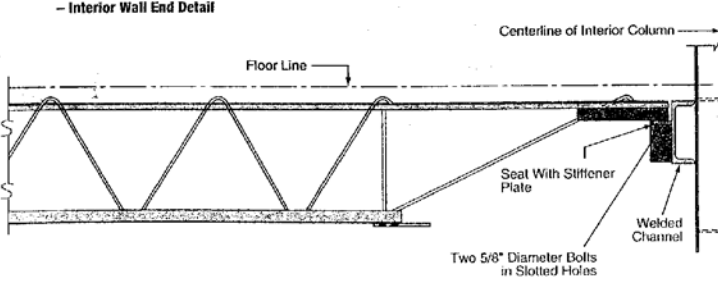


Fig. 8.1. Floor plan and cross section with exterior wall and detail (courtesy of FEMA, Washington; DC, USA)



- Interior Wall End Detail



**Fig. 8.2.** Floor plan and cross section with exterior wall and detail (courtesy of FEMA, Washington; DC, USA)



### 8.5.3 Connection Details, Structural Sizes, and Other Parameters

The behaviour of a typical fully rigid, partial strength wind-moment connection about the strong axis of the column was studied. The connection of the W18 × 50 girder to the W15 × 426 column between girder line 7–8 at frame line D on the 14 floor was modeled as a representative connection. The top and bottom moment plates (estimated as 5/8 inch × 6 inches × 24 inches (15.875 mm × 152 mm × 610 mm) and 3/8 inch × 10-1/2 inches × 24 inches (0.56 mm × 267 mm X × 610 mm), respectively, were welded to girder flanges with a 1/4-inch weld. The shear plate (estimated as 5/16 inch × 3 inches × 12 inches; 1.938 mm × 15 mm × 300 mm) was bolted to each girder web with four 7/8-inch-diameter (6.36 mm) bolts. The designs of the bolts are taken to be A 370 bolts.

Similarly, the behaviour of a typically fully rigid, partial-strength wind-moment connection about the weak axis of the column was studied. The connection of the W24 × 68 girder to the W14 × 426 column between girder line C–D at frame line 7 on the 15th floor was modeled as a representative connection. The top and bottom moment plates were estimated as 3/8 inch × 12 inches × 14 inches (9.5 × 300 × 355 mm) with a 1/4-inch (6 mm) weld with a 3/8-inch × 8-inch seat plate (12 mm × 125 mm × 355 mm). The connection capacity was estimated to be 7.500 kip/in (8011.5 KNm), thus confirming that the frame design was governed by stiffness and not strength.

#### 8.5.3.1 Columns, Plates, and Spandrels

- (a) The columns are built up by 4NO plates. 14'' (955.6 mm) × 14'' (355.6 mm) welded plates spaced 3' – 4'' (1016 mm).

Adjacent parameter columns are interconnected at each floor level by deep spandrel plates of 52'' (1320.8 mm) depth.

In alternative stories, an additional column can be found at the centre of each of the chamfered building corners.

A reference is made to Fig. 8.1. The Section A, the size is 13 1/2'' (343 mm) with top plate 355.6 – 343 = 12.6 mm, and the width of this section is 14'' (350.6 mm). The base of the exterior column is assumed to be 3NO 14'' × 14'' (356 × 356 mm) welded together.

The vertical plate thickness 2 NO 1/2'' (12 mm) = 25 total. Figures 8.1 and 8.2 show exterior and interior wall details for floor truss members, with details of end connections. Figure 8.3 shows the cross-section of the main trusses along with transverse trusses.

- (b) The floor section is shown in Fig. 8.4c, with concrete thickness of the metal deck. The main double truss has a total width of 2032 mm.
- (c) The estimated openings in the exterior walls of WTC-1 are shown in Table 8.3.

Typical 3D analysis models of flange and shear plate moment-connections in Figs. 8.4a and 8.4b are adopted in the FEMA report and have been

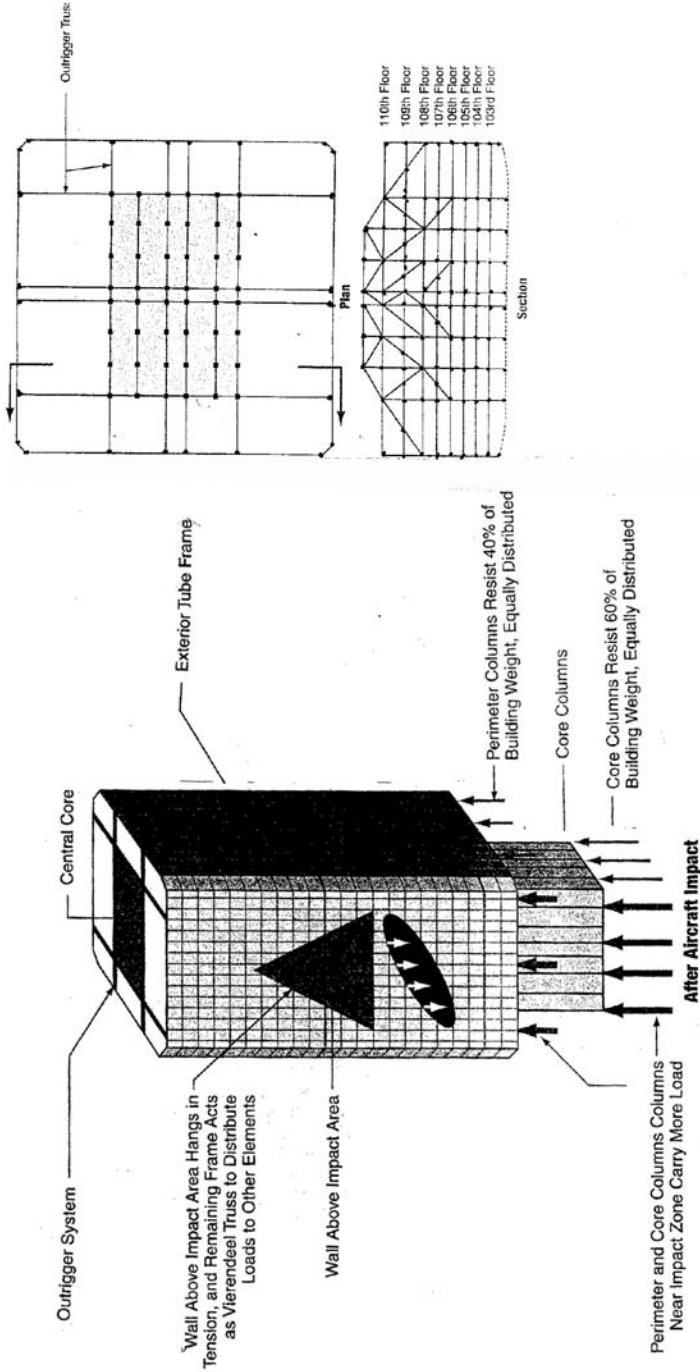
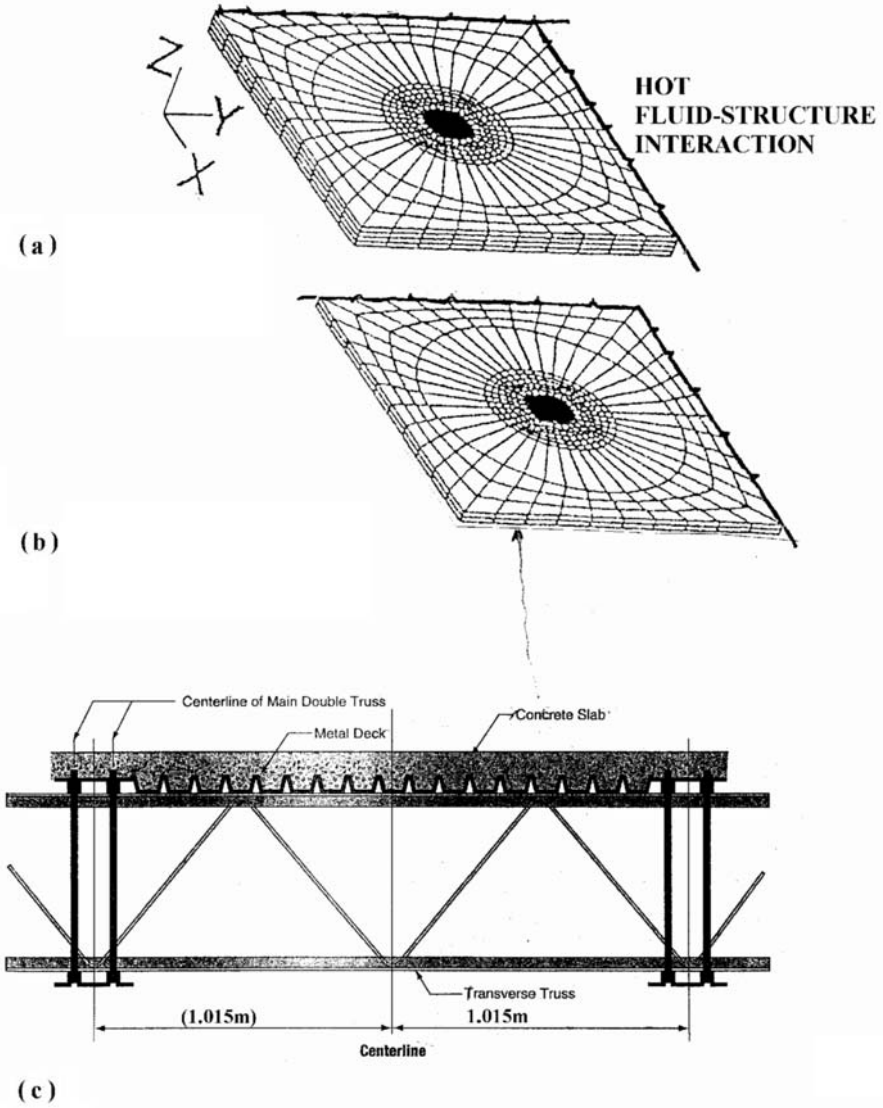


Fig. 8.3. Redistribution of load after aircraft impact (courtesy of FEMA, Washington; DC, USA)



**Fig. 8.4.** (a) 3D concrete floor – 3 layers thickness (full depth case); (b) 3D concrete plan slab – 2 layers thickness (half depth case); (c) cross-section to main double trusses supporting concrete floor (for (c) courtesy of FEMA, Washington, DC, USA)

**Table 8.3.** Critical temperatures for various types of steel

Steel	Temperature
Columns	538°C (1,000°F)
Beams	593°C (1,100°F)
Open Web Steel Joists	593°C (1,100°F)
Reinforcing Steel	593°C (1,100°F)
Prestressing Steel	426°C (800°F)

re-examined in the current analysis. the number of elements and nodes can be estimated from these figures for local analysis. They are given in the separate section in the text.

(d) Section properties (AISC Manual)

(i) *W14 426 columns*: weight  $w = 426$  lb

$F_y = 36$  ksi; Kh with respect to  $r_y$  axial load = 2560 kips

$F_{0y} = 50$  ksi; Kh with respect to  $r_y$  axial load = 3441 kips

$A = 125$  in<sup>2</sup>;  $K_w = 1.875$  in

$I_x = 6600$  in<sup>4</sup>;  $b_f = 16.695$  in<sup>4</sup>;  $I_y = 2360$  in<sup>4</sup>

$r_x = 4.34$  in;  $t_f = 3.035$  in

$\frac{r_y}{r_x} = 1.67$

bending factor =  $\begin{cases} B_x = 0.177 \\ B_y = 0.442 \end{cases}$

$F'_{ex} (K_x L)^2 / 10^2$  kips = 547

$F'_{ey} (K_y L)^2 / 10^2$  kips = 195

(ii) *W18 50 girders*: weight  $w = 50$ /ft

flange width =  $7\frac{1}{2}$ " ;  $A = 147$  in<sup>2</sup>

$L_c = 7.90$  ft  $d = 18$  in

$L_U = 11.0$  ft  $t_w = 0.355$

Span (ft) = 15  $b_f = 7.495$  in

Span (ft) = 44  $t_f = 0.570$  in

$F_y = 36$  ksi

$\Delta = 0.03$ " to  $2.64$ "

$S_x = 88.9$  in<sup>3</sup>

$v = 92$  kips

(iii) *14" × 14" Box Section Columns*

$t_w =$  wall inches =  $0.625$ " ( $5/8$ " )

area =  $32.4$  in<sup>2</sup>;  $I = 952$  in<sup>4</sup>;  $S = 136$  in<sup>3</sup>

$r = 5.42$ " ;  $J = 1530$  in<sup>4</sup>;  $Z = 161$  in<sup>3</sup>

(iv) *W24 68 Columns*

$$A = 20.1 \text{ m}^2$$

$$d = 23.73 \text{ in}; t_w = 0.415; b_f = 911 \text{ in}; t_f = 0.585 \text{ in}$$

$$I_{xy} = 18.30 \text{ in}^4; S = 154 \text{ in}^3; r_x = 955 \text{ in}; I_y = 70.4 \text{ in}^4; S_y = 15.3 \text{ in}^3;$$

$$r_y = 1.87$$

$$F_y = 20.2 \text{ ksi}$$

(v) *W14 193 Columns*

$$F_y = 36 \text{ ksi}$$

$$A = 56.8 \text{ in}^2$$

$$I_x = 2400 \text{ in}^4$$

$$I_y = 931 \text{ in}^4$$

$$r_y = 4.05 \text{ in}$$

$$\frac{r_x}{r_y} = 1.6$$

$$B_x = 0.183$$

$$B_y = 0.477$$

$$F'_{ex} (k_x L_x)^2 / 10^2 \text{ kips} = 438$$

$$F'_{ey} (k_y L_y)^2 / 10^2 \text{ kips} = 170$$

$$s = 54 \text{ in}^3; r_x = 955 \text{ in}; I_y = 70.4 \text{ in}^4; s_y = 15.3 \text{ in}^3; b_y = 1.89$$

$$d = 23.73 \text{ in}; t_w = 0.415; b_f = 911 \text{ in}; t_f = 0.585 \text{ in}$$

$$I_{xy} = 18.30 \text{ in}^4; s = 54 \text{ in}^3; r_x = 955 \text{ in}; I_y = 70.4 \text{ in}^4; s_y = 15.3 \text{ in}^3;$$

$$b_y = 1.89$$

#### 8.5.4 Critical Temperature for Steel

In building materials such as steel, a critical temperature is often referenced at which the integrity of fully-loaded structural members becomes questionable. The critical temperature for steel members varies with the type of steel structural member (e.g. beams, columns, bar joists, or reinforcing steel). North American Test Standards (e.g., ASTM E119) assume a critical temperature of 538°C (1000°F) for structural steel columns. The critical temperatures for columns and other steel structural elements are given in Table 8.3. The critical temperature is defined as approximately the temperature where the steel has lost approximately 50 percent of its yield strength from that at room temperature, in an actual structure, the actual impact of such heating of the steel will also depend on the actual imposed load, member end restraint (axial and rotational), and other factors.

To limit the loss of strength and stiffness, external fire protection is provided to the steel structural members to satisfy required fire resistance ratings. This is usually achieved by fire protecting the steel members to keep the temperature of the steel, in case of a fire, from reaching a critical limit. Traditionally, the amount of fire protection needed is based on the results of standard fire resistance tests.

The temperature attained in a fire-exposed steel member depends on the fire exposure, characteristics of the protection provided, and the size and mass of the steel. For steel members protected with direct-applied insulating materials, the role of the insulating materials is strongly dependent on their thermal conductivity and thickness.

The role of the fire exposure and size and mass of the steel can be demonstrated by analyzing the temperature rise in two protected steel columns with two different fire exposures. For this comparative analysis, the fire exposure associated with two standard fire resistance tests is selected, ASTM E 119 and UL 1709. The following two column sizes are selected for this comparative analysis:

- W14 × 193
- Steel box column, 36 inches × 16 inches, with a wall thickness of 7/8 inch for the 36-inch-wide side and 15/16 inch for the 16-inch-wide side. The failure or critical time for 36'' × 16'' box column UL 109 is 800°C, with time = 10 minutes. For column 96'' × 16'', E119, the temperature is around 600°C, with time = 20 minutes. For steel section W14 × 193 UL 1709, the temperature is 800°C, for critical time 7 minutes.

### 8.5.5 Walls with Opening

Table 8.4 gives walls opening and has to be taken in the finite Element Analysis throughout where they exist.

**Table 8.4.** Estimated openings in exterior walls of WTC-1

Floor	North Wall		South Wall		East Wall		West Wall		Total Area	
	ft <sup>2</sup>	(m <sup>2</sup> )	ft <sup>2</sup>	(m <sup>2</sup> )	ft <sup>2</sup>	(m <sup>2</sup> )	ft <sup>2</sup>	(m <sup>2</sup> )	ft <sup>2</sup>	(m <sup>2</sup> )
92	743	(69)	0	(0)	1,572	(146)	0	(0)	2,314	(215)
93	958	(89)	0	(0)	1,356	(126)	0	(0)	2,314	(215)
94	592	(55)	54	(5)	1,163	(108)	0	(0)	1,808	(168)
95	1,055	(98)	54	(5)	0	(0)	420	(39)	1,528	(142)
96	797	(74)	151	(14)	0	(0)	1,518	(141)	2,465	(229)
97	926	(86)	151	(14)	0	(0)	1,798	(167)	2,874	(267)
98	1,335	(124)	0	(0)	0	(0)	0	(0)	1,335	(124)
TOTAL	6,405	(595)	409	(38)	4,090	(380)	3,735	(347)	14,639	(1,360)

Note: Differences in totals are due to rounding in the conversion of square meters to square feet.

### 8.5.6 Stresses in Steel to Be Considered

Columns = 50 to 100 ksi in increment of 5 ksi

Core columns (Box sections A36 steel  $36'' \times 14'' - 16$  inches with plate thickness  $3/4$  to  $4''$ )

Maximum strain  $\epsilon = 0.002$  or  $\epsilon = 0.20$  in/in

Bolts: -ASTM A325 for A490 standards

$R_o$  = bearing capacity of a single bolt assumed =  $44 \times 3$  kips

$F_U A_y$  = shear capacity of a single bolt =  $52 \times 8$  kips

Floor truss seated with end connections at spandrel beam and core

$R_U$  ( $5/8''$  bolt) = 45 kips

shear capacity of a  $5/8''$  bolt A3 25 bolts =  $2 F_U A_x = 53 \times 9$  kips

block shear rupture

$R_U = 0 \times 6 F_U A_{nv} + F_U A_{nt}$

$A_{nv}$  = net shear area =  $0.5632$  in<sup>2</sup>

$R_U = 2 [0 \times 6(60)(0 \times 563) + 60(0 \times 563)] = 108$  kips

### 8.5.7 Data on Finite Elements and Their Geometry

#### 8.5.7.1 Typical Floor Elements

(a) *Concrete Deck Elements per Floor*

- (i) *Full-depth case*: 800 20-noded isoparametric elements  
Nodal points = 2100
- (ii) *Half-depth case*: 100 NO 20-noded isoparametric elements

(b) *Steel Elements of Floors*

Note: they are all idealised as 3D line elements of the degrees of freedom defined in Appendix I.

- (i) *Metal deck*: assumed as equivalent of concrete section to match with deck concrete increasing the floor depth by  $1/10 d$  with nodal points matching with those of concrete
- (ii) *3D line elements*: double trusses per floor = 1400 (3-noded) with variable lengths  $L$
- (iii) *3D line elements*: transverse trusses per floor = 13000 (3-noded)
- (iv) *and 3D truss diagonals in transverse trusses*: 25 mm  $\Phi$  bars = 11000 (3-noded)
- (v) *for local stresses investigation*: flange and shear plate connections = 7200 per truss – per floor – 4-noded isoparametric elements  
flange and seat moment connections = 54,000 per truss – per floor – 4-noded isoparametric elements

(c) *Outer Frame Wall*

3D – 3-noded line elements per tower = 450,000

(d) Core Frame Innerwall

3D – 3-noded line elements per tower = 250,000

8.5.8 Analysis of Hot Fuel-Floor Interaction

Although the above comprehensive data is given for the global Finite Element analysis of Twin Towers, New York, in this section only the hot-fuel-floor interaction is considered. The fastenings such as bolts, welds and bars in towers are treated as semi-rigid connections. Based on the above data provided by the FEMA, the maximum length of time for the finite element analysis for the fuel to heat up upto 1000°C is assumed to be in the range of 40 minutes to one hour while the plane is in the air. From the time of impact to the collapse scenario is also kept 60 minutes. The analysis from zero time to

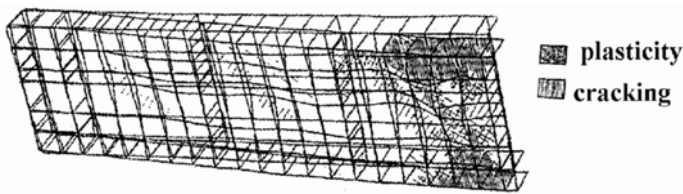


Fig. 8.5. Main double truss

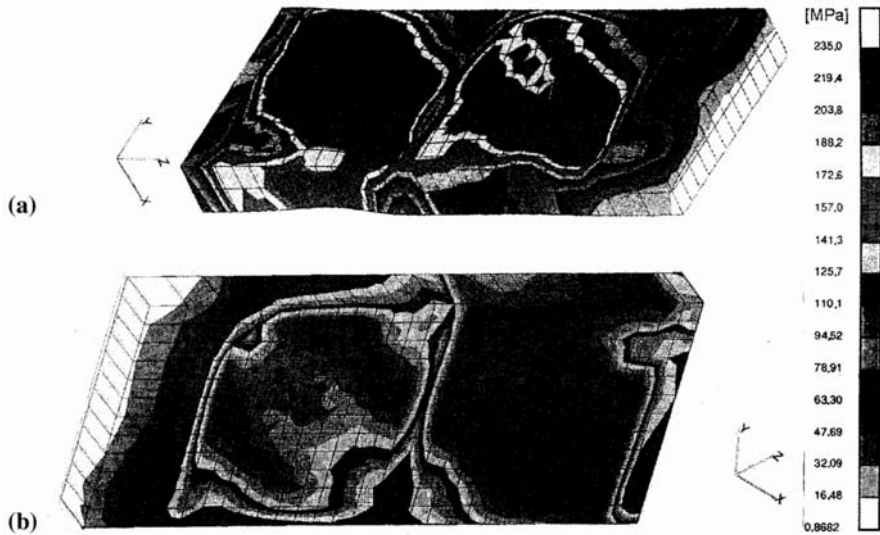


Fig. 8.6. Damage scenarios: (a)  $M_p = 250$  Mpa,  $P = 2000$  KN,  $\delta = 3.5$  cm,  $t = 5000$  seconds,  $a/b = 4$ , 3D half depth floor-damage scenario; (b)  $P = 5300$  KN,  $M_p = 350$  Mpa,  $\delta = 5.20$  cm,  $t = 5000$  second,  $a/b = 4$ , 3D full depth floor-damage scenario



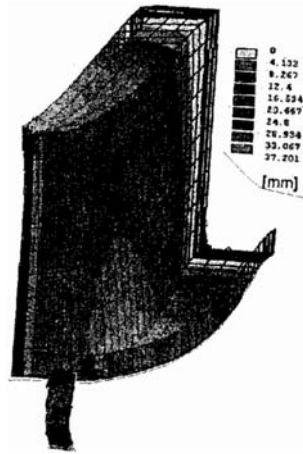


Fig. 8.7. Flanges seats damage scenario

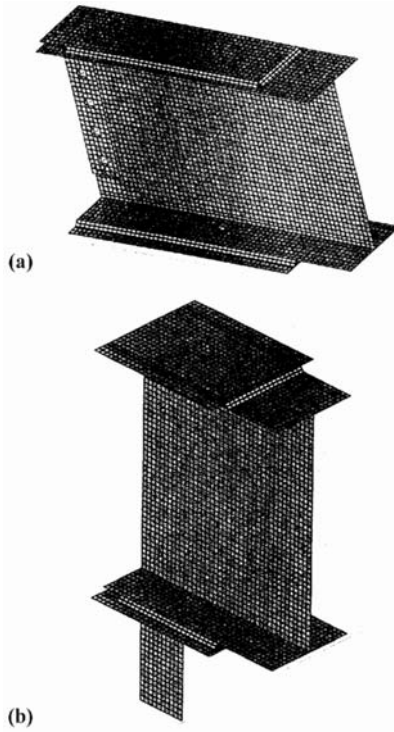


Fig. 8.8. (a) Flang and shear plate moment connection; (b) Flanges and seat moment connection 3-D Finite element analysis

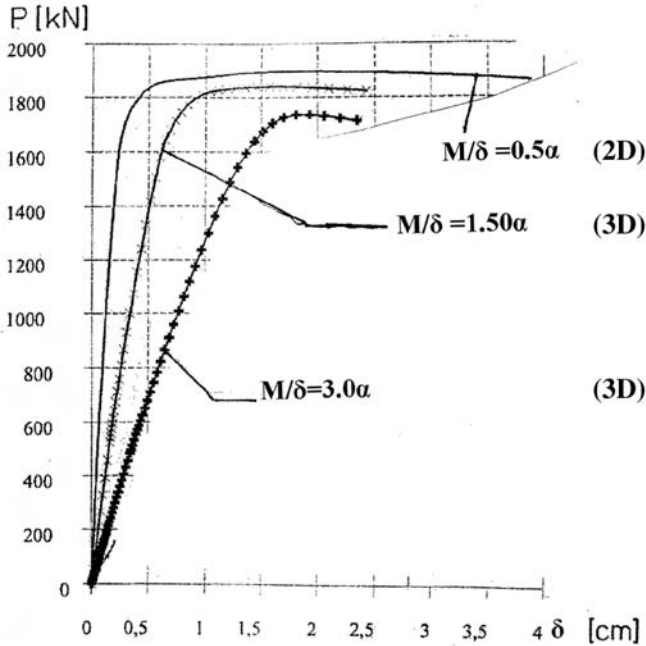
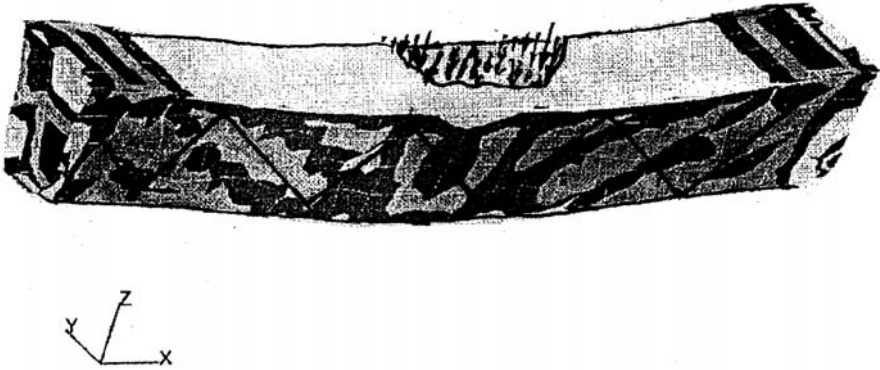


Fig. 8.9. Load-displacement relations for  $M/\delta$  ratios half-depth case

60 minutes assumes to have an aspect time  $\Delta t = \Delta T = 10$  seconds. At every interval of 360 seconds, the program stops to give away the results in terms of displacements velocities, accelerations and dynamic plasticity and cracking noted by the flag numbers. The total number of 600 increments are considered for the analysis and solution procedures. At the 10th incremental stage, the floor scenario in each case is shown in Fig. 8.4a and b with full depth and half depth collapse conditions for the full depth analysis, the truss given in Fig. 8.4a has been included only along with metal deck and concrete slab.

Figure 8.5 shows the collapse of the main double truss indicating steel plasticity in other areas and cracking in concrete deck. At the 500 incremental stage having 5000 seconds consumed to develop damage scenarios for the 2D and 3D cases as are shown in Fig. 8.6. Steel flanges have also been examined independently and the damage is indicated in Fig. 8.7. The original F.E. mesh schemes for the two different plate moment connections are shown in Fig. 8.8.

For the half depth case, the load displacement relations are plotted for various  $M/\delta$  ratios ranging between  $0.5\alpha$  to  $3.0\alpha$ . The plasticity has been achieved for  $M/\delta = 0.5\alpha$  at about 1900 kN. When  $M/\delta = 3.0\alpha$  in a case of half depth, the maximum collapse load reached at about 1700 kN and with a maximum displacement of 2.61 cm corresponding to the 500th incremental stage (Fig. 8.9). A similar analysis was carried out for a full depth case in which a transverse truss was included.

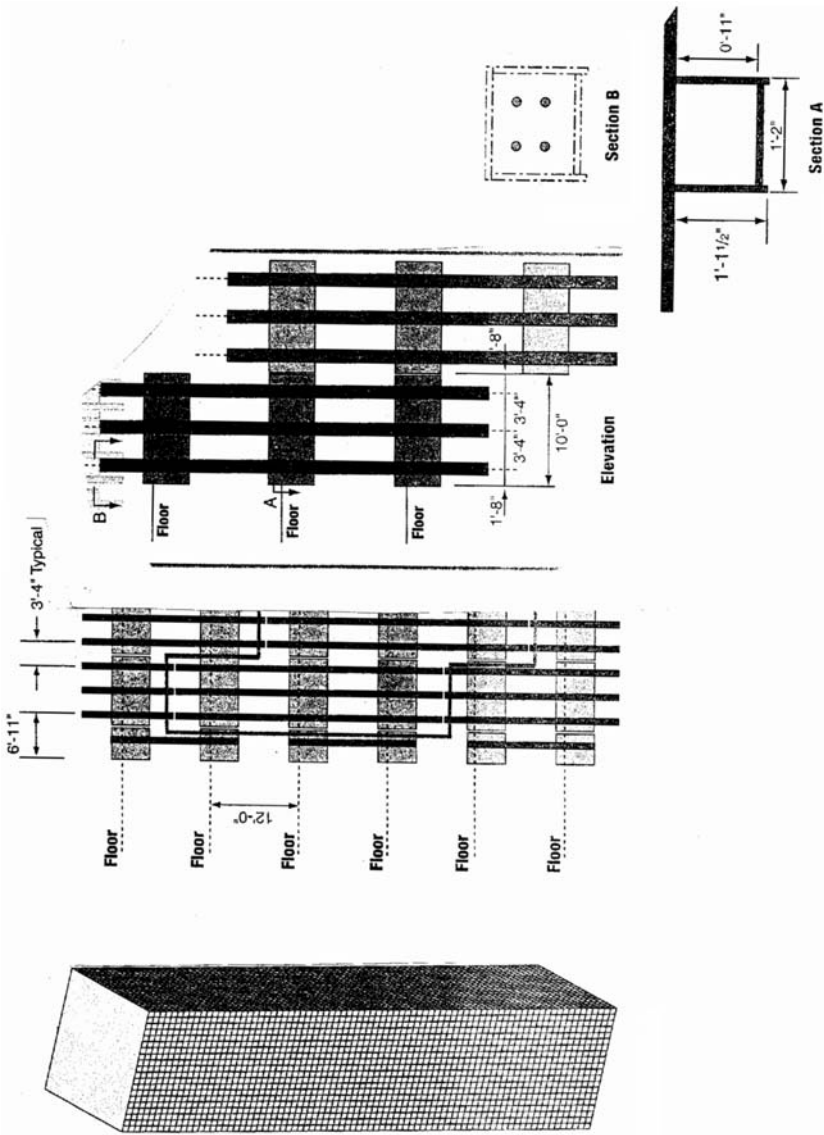


**Fig. 8.10.** Transverse truss-metal ties with plastic zones at 2000 kN damage scenario

The damage scenario is shown in Fig. 8.10. The main double truss reached plasticity at approximately 2000 KN corresponding to the failure stress of  $450 \text{ MN/m}^2$ . The plastic moment in the corner areas of the truss show excessive damage with multiple cleavages. The difference between the results of the half depth and full depth analysis indicate that excessive cracking in concrete floor slabs in half depth case which excludes the transverse truss. The results 60% more than the full depth when 3D F.E. analysis was considered in case of full depth analysis, the rupturing occurred in the transverse truss completely under the same load increment sequence. The depths of failure zones reached maximum to the bottom levels of the trusses.

The damage scenario is shown in Fig. 8.10. In all cases the concrete of the floor slabs had completely deteriorated with full depth cracks more than 250 mm wide. The floor levels and the element details are given in Fig. 8.11. The same finite element mesh scheme later on has been adopted in aircraft/fire global analysis. The  $350 \text{ mm} \times 350 \text{ mm}$  ( $14'' \times 14''$  box) columns have been analysed for the fuel-column-floor interaction analysis with length taken as given Fig. 8.12 with known floor heights. The boundary conditions of these box columns are shown in Fig. 8.12a. The maximum displacements in 3D analysis for  $x$ ,  $y$ ,  $z$  axes are plotted in Fig. 8.12b with the damage scenario as predicted in Fig. 8.12c. The damage scenario can also be demonstrated for the columns in terms of critical/collapse loads taking into consideration the buckling checking procedures. Plasticity of the points and ejection of the columns occurred at collapse conditions (loads) under specific time scale as shown in Fig. 8.3.

The critical/collapse loads versus time dependent displacements are also recorded simultaneously in Fig. 8.13. Initial observations of the result seem to be in line what were viewed as the disaster scenario of the Twin-Tower collapse. Nevertheless the data and the results will be kept awaiting for the confirmation of the final global analysis of the Twin Towers (WTC Building Complex) later on this text.



**Fig. 8.11.** Floor component: Details use as part of data by the F.E. analysis (based on FEMA Report 2002, Washington, D.C., U.S.A.)

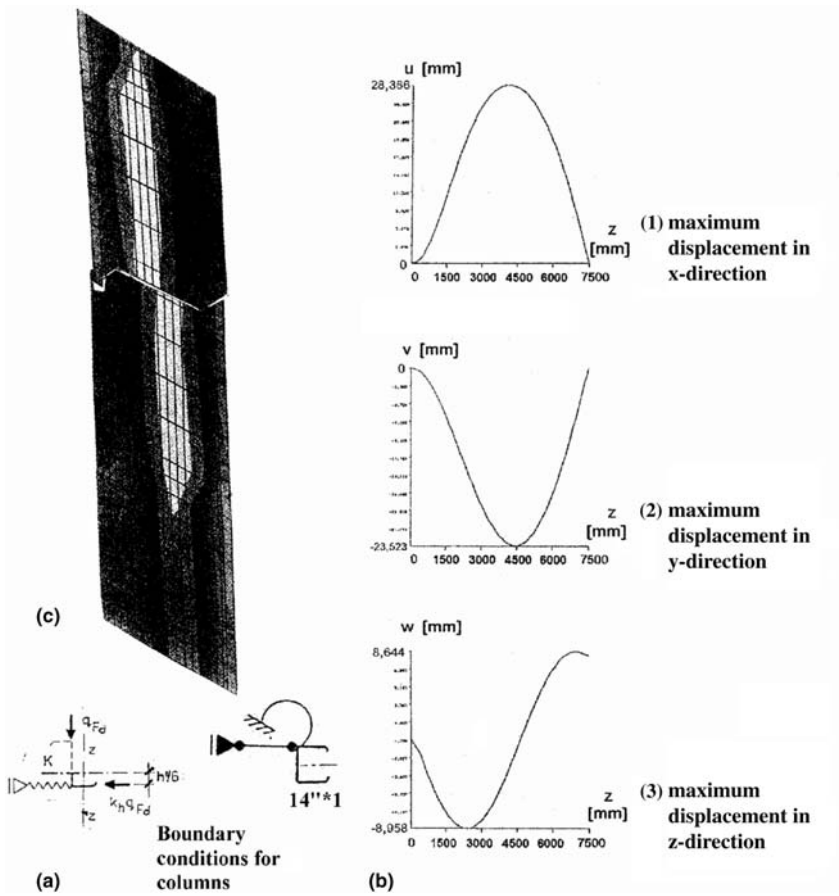


Fig. 8.12. Disaster scenario: 14'' x 14'' box columns, 7.5 m long with displacements in 3D space

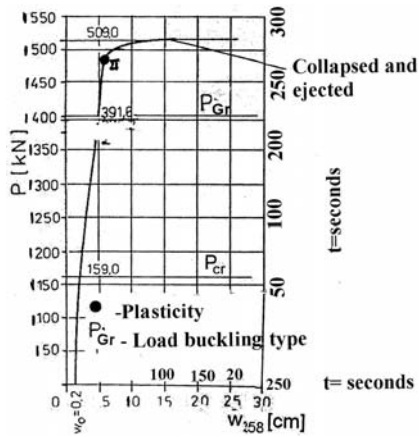


Fig. 8.13. Critical and collapse loads for 7.5 m columns 14'' x 14'' box type ( $W = 8 \rightarrow$  displacement)

## References

NFP A Codes, Standards, Recommended Practices and Manuals (see the latest NFP A Codes and Standards Catalog for availability of current editions of the following documents)

NFPA 12 A, Standard on Halon 1301 Fire Extinguishing Systems

NFPA 12 B, Standard on Halon 1211 Fire Extinguishing Systems

NFPA 70, National Electrical Code

NFPA 101, Code for Safety to Life for Fire in Buildings and Structures

NFPA 403, Manual for Aircraft Rescue and Fire Fighting Operational Procedures

NFPA 407, Standard for Aircraft Fuel Servicing

NFPA 408, Standard for Aircraft Hand Fire Extinguishers

NFPA 409, Standard on Aircraft Hangars

NFPA 410, Standard on Aircraft Maintenance

NFPA 412, Standard for Evaluating Foam Fire Fighting Equipment on Aircraft Rescue and Fire Fighting Vehicles

NFPA 414, Standard for Aircraft rescue and Fire Fighting Vehicles

NFPA 415, Standard on Aircraft Fueling Ramp Drainage

NFPA 416, Standard on Construction and Protection of Airport Terminal Buildings

NFPA 417, Standard on Construction and Protection of Aircraft Loading Walkways

NFPA 418, Standard on Roof-top Heliport Construction and Protection

NFPA 419, Guide for Master Planning Airport Water Supply Systems for Fire Protection

NFPA 421, Recommended Practice on Aircraft Interior Fire Protection Systems

NFPA 422M, Manual for Aircraft and Explosion Fire Investigators

NFPA 424, Recommended Practice for Airport/Community Emergency Planning

NFPA 1003, Standard for Airport Fire Fighter Professional Qualifications

“Aeronautics and Space”, Code of Federal Regulations, Title 14, Washington, D.C. (under continuous revision).

Federal Aviation Administration Advisory Circulars, U.S. Department of Transportation, Washington, D.C. (with the following designations and titles):

Aircraft Fire and Rescue Communications, 150/5210-7A, Mar. 16, 1972

Aircraft Fire and Rescue Facilities and Extinguishing Agents, 150/5210-6B, Jan. 25, 1973

Airport Fire and Rescue Vehicle Specification Guide, 150/5220-14, Mar. 15, 1979

Airport Fire Department Operating Procedures During Period of Low Visibility, 150/5210-0, Oct. 27, 1967

Airport Operations Manual, 150/5280-1, June 16, 1972

Fire and Rescue Service for Certificated Airports, 150/5210-12, Mar. 2, 1972

Fire Department Responsibility in Protecting Evidence at the Scene of an Aircraft Accident, 150/5200-12, Aug. 8, 1969

Fire Fighting Exemptions under the 1976 Amendment to the Federal Aviation Act, 150/5200-12, Aug. 8, 1969

Fire Fighting Exemptions under the 1976 Amendment to the Federal Aviation Act, 150/5280-3, Feb. 4, 1977

Fire Prevention During Aircraft Fueling Operations, 150/5230-3, Apr. 8, 1969

Hand Fire Extinguishers for Use on Aircraft, 150/5210-13, May 4, 1972

Heliport Design Guide, 150/5390-1B, Aug. 22, 1977

Response to Aircraft Emergencies, 150/5210-11, Apr. 15, 1969

Water Rescue Plans, Facilities, and Equipment, 150/5210-13, May 4, 1972

Water Supply Systems for Aircraft Fire and Rescue Protection, 150/5220-4, Dec. 7, 1967

Williams C, Laughlin J (eds.) (1978) Aircraft fire protection and rescue procedures. International Fire Service Training Association, Oklahoma State University, Stillwater, OK,

- [8.1] Belytschko T (1977) Methods and programs for analysis of fluid-structure systems, *J. Nuclear Eng. and Design* 42:41–52
- [8.2] Belytschko T (1974). In: Pilkey W et al. (eds.) *Transient analysis, structural mechanics computer programs*. University Press of Virginia, pp. 255–275
- [8.3] Kennedy JM, Belytschko T (1975) Energy source and fluid representation in a structural response code – STRAW. Argone Natl Lab., Rep. ANL-8140, May 1975
- [8.4] Chang UW, Glivigys J (1975) RECO-HEP: A two-dimensional computer code for calculating the primary system response in fast reactors, Argone Natl Lab., Rep. ANL-75-19, June 1975
- [8.5] Hofmann R (1976) STEALTH, A Lagrangian explicit finite difference code for solids, structural and thermohydraulic analysis, Electric Power Res. Institute, Vol. 1-4, Palo Alto, California, June 1976
- [8.6] Bathe KJ, Wilson EL (1976) *Numerical Methods in Finite Element Analysis*, Prentice-Hall, Englewood Cliffs, New Jersey
- [8.7] Bathe KJ (1975) ADINA – A finite element program for automatic dynamic incremental nonlinear analysis. Acoustics and Vibration Lab., Rep. ANL-82448-1, Department of Mechanical Engineering, MIT (Sept. 1975, revised May 1977)
- [8.8] Bathe KJ, Ramm E, Wilson EL (1975) Finite element formulations for large deformation dynamic analysis, *Int. J. Num. Meth. Eng.* 9:353–386
- [8.9] Malvern LE (1976) *Introduction to the Mechanics of a Continuous Medium*. Prentice-Hall, Englewood Cliffs, New Jersey
- [8.10] Bathe KJ (1976) Static and dynamic geometric and material nonlinear analysis using ADINA. Acoustics and Vibration Lab., Rep. ANL-82448-1, Department of Mechanical Engineering, MIT (May 1976, revised May 1977)
- [8.11] Crandall SH (1956) *Engineering analysis – A survey of numerical procedures*. McGraw-Hill, New York
- [8.12] Munro M, Piekarski K (1977) Stress-induced radial pressure gradients in liquid-filled multiple concentric cylinders. *J. App. Mech.* 44(2):218–221
- [8.13] Walker JS, Phillips JW (1977) Pulse propagation in fluid-filled tubes. *J. App. Mech.* 44(1):31–35
- [8.14] Romander CM, Cagliostro DJ, Florence AL (1976) Experiments on the response of flexible piping systems to interal pressure pulses. SRI Project PVD-1960, Stanford Research Institute, Menlo Park, California, April 1976
- [8.15] Allen HG (1969) *Analysis and design of structural sandwich panels*. Oxford
- [8.16] Appeltauer J, Kollar L (1999) Buckling of frames. In: Kollar L (ed.) *Structural stability in engineering practice*, E & FN Spon, pp. 129–186

- [8.17] Asztalos Z (1972) Buckling analysis of multistorey, one-bay frameworks using the continuum model, taking the axial deformations of the columns into account. *Magyar Építőipar*:471–474 (in Hungarian)
- [8.18] Barbero E, Tomblin J (1993) Euler buckling of thin-walled composite columns. *Thin-Walled Structures* 17:237–258
- [8.19] Barkan DD (1962) *Dynamics of bases and foundations*. McGraw-Hill, London
- [8.20] Beck H (1956) Ein neues Berechnungsverfahren für gegliederte Scheiben, dargestellt am Beispiel des Vierendeel-Trägers. *Der Bauingenieur* 31:436–443
- [8.21] Beck H, König G, Reech H (1968) Kenngrößen zur Beurteilung der Torsionssteifigkeit von Hochhäusern. *Beton und Stahlbetonbau* 63:268–277
- [8.22] Beck H, Shafer HG (1969) Die Berechnung von Hochhäusern durch Zusammenfassung aller aussteinenden Bauteile zu einem Balken. *Der Bauingenieur* 44:80–87
- [8.23] Bishop RED, Price WG (1977) Coupled bending and twisting of a Timoshenko beam. *J. Sound and Vibration* 50(4):469–477
- [8.24] Boughton J (1994) *Dynamic tests on a small-scale building model*. Manuscript. Building Research Establishment, Watford
- [8.25] Brohn DM, Cowan J (1977) Teaching towards an improved understanding of structural behaviour. *The Structural Engineer* 55(1):9–17
- [8.26] Brohn DM (1992) A new paradigm for structural engineering. *The Structural Engineer* 70(13):239–242
- [8.27] Coull A, Mukherjee PR (1978) Natural vibrations of shear wall buildings on flexible supports. *Earthquake Engineering and Structural Dynamics* 6:295–315
- [8.28] Council on Tall Buildings and Urban Habitat (1978) *Monograph on planning and design of tall buildings*. Vol CB: Structural design of tall concrete and masonry buildings. American Society of Civil Engineers
- [8.29] Council on Tall Buildings and Urban Habitat (1978) *Monograph on planning and design of tall buildings*. Vol SB: Structural design of tall steel buildings. American Society of Civil Engineers
- [8.30] Council on Tall Buildings and Urban Habitat, (1978) *Monograph on planning and design of tall buildings*. Vol SC: Structural buildings systems and concepts. American Society of Civil Engineers
- [8.31] Council on Tall Buildings and Urban Habitat (1978) *Monograph on planning and design of tall buildings*. Vol CB: Structural design of tall concrete and masonry buildings. American Society of Civil Engineers
- [8.32] Croll JGA, Walker AC (1972) *Elements of structural stability*. Macmillan, London
- [8.33] Csonka P (1956) Über proportionierte Rahmen. *Die Bautechnik* 33:19–20
- [8.34] Csonka P (1956) Simple procedure for multistorey frameworks under wind load. *Az MTA VI Oszt. Közl.*, Budapest, 35:209–219 (in Hungarian)
- [8.35] Ellis RB (1986) The significance of dynamic soil-structure interaction in tall buildings. *Proc. ICE*, Part 2, 81:221–242
- [8.36] Ellis RB, Ji T (1996) Dynamic testing and numerical modelling of the Cardington Steel Framed Building from construction to completion. *The Structural Engineer* 74(11):186–192



- [8.37] Eurocode 1 (1995) Actions on structures. Part 2.4: Wind actions. EN 1991. CEN/TC250/SCI Technical Secretariat, March 1995
- [8.38] Eurocode 2, Design of concrete structures. EN 1992
- [8.39] Eurocode 3, Design of steel structures. EN 1993
- [8.40] Eurocode 8, Design of structures for earthquake resistance. EN 1998
- [8.41] Bangash MYH (2001) Structural detail in steel, Thomas Telford
- [8.42] Bangash MYH (2003) Structural detail in concrete, Thomas Telford
- [8.43] Bangash MYH (2001) Manual of numerical methods in concrete, Thomas Telford
- [8.44] FEMA. World Trade Center building performance. Study: Data collection, preliminary observations and recommendations, Federal Emergency Agency, Washington, DC
- [8.45] Daniels BJ (1994) Serviceability testing at Cardington. Proc. 1st Cardington Conf. 16-17 November 1994, Cardington
- [8.46] De Wolf JT, Pelliccione JF (1979) Cross-bracing design, J. Structural Division, ASCE 105 (ST7):1379–1391
- [8.47] DIN 18800 (1990) Teil 2, Stahlbauten. Stabilitätsfälle. Knicken von Stassen und Stabwerken
- [8.48] Dowrick DJ (1976) Overall stability of structures. The Structural Engineer 54:399–409
- [8.49] Dulacka E, Kollar L (1960) Angenäherte Berechnung des Momentenzuwachses und der Stabilität von gedruckten Rahmenstielen. Die Bautechnik 37(3):98

# 9 Flying Debris – Elastic Scattering Approach

## 9.1 Introduction

Impact, blast and fire generate and scatter flying objects and debris. The scenario was witnessed in cases of WTC buildings and Oklahoma building. The object of the scattering method is to identify the form and location of unknown elements inside a given surrounding medium. This is done from measured wave reflection data in space and time. Hybrid finite element/difference method is developed in three dimensions, where scattering may be performed with time-periodic data or non periodic data in the form of short impulses. In this chapter non-periodic time-dependent wave equation solutions known as TIME DOMAIN have been adopted. The basic mathematical tool adopted an amounts numerically solving the time-dependended elastic wave equation with given material coefficients. Finally, the scattering phenomenon of objects has been devised to create an overall damage scenario.

### 9.1.1 Nomenclature

- B = Boundary
- [D] = material compliance matrix
- $h$  = mesh function
- $G$  = prestrain
- $I$  = Time interval  $(0, T)$
- $J = [J]$  = Time discretization, partition of time
- $K_h$  = finite element mesh
- [K] = element stiffness matrix
- $L$  = Length or size
- [ $M_1$ ] = mass;  $m$  = added mass
- $D\delta = \frac{\partial \delta}{\partial t}$
- $f$  = flow = density of materials
- $t$  = time variable
- $\vec{T}$  = Surface forces
- $T$  = final time
- $P^e$  = Ejecting Element Node Forces
- $v$  = velocity
- $\nu$  = Poisson's ratio

$\delta_{ij}$  = Kronecker Delta or Symbol

$\delta$  = displacement

$\tau$  = stress tensor

$\Omega_{\text{FEM}}$  = Finite Element Domain – unstructured mesh

$\Omega_{\text{FDM}}$  = Finite Difference Domain – structured mesh

$$M = \frac{\dot{E}}{2(1 + \dot{\nu})}$$

$$\lambda = \frac{\dot{E}\dot{\nu}}{(1 + \dot{\nu})(1 - 2\dot{\nu})}$$

## 9.1.2 Turbulence Modeling

### 9.1.2.1 Specific Nomenclature

$A$	constant
$C_D, C_M$	turbulence model constants
$c = 1 - Y_f/f$	progress variable
$c_p$	heat capacity at constant pressure
$Da$	Damköhler number
$D_L$	molecular diffusivity
$D_t$	turbulent diffusivity
$D_{t,0}$	steady turbulent diffusivity
$E_{\text{ign}}$	total energy supplied by a spark
$F$	equivalence ratio
$f$	mixture function
$h$	thermal energy
$Ka$	Karlovitz number
$k$	turbulent kinetic energy
$L$	turbulent length scale
$Le$	Lewis number
$P$	pressure
$Q_{\text{ign}}$	energy source term for ignition
$q_f$	lower calorific value
$Re_t$	turbulent Reynolds number
$\bar{r}_f$	radius of the leading edge of turbulent flame
$St$	mass stoichiometric coefficient
$T$	gas temperature
$t$	time
$t_r$	reaction time scale
$U_L$	laminar burning velocity
$U_t$	turbulent flame speed
$u_j, j = 1, 2, 3$	gas flow velocity components
$u'$	r.m.s. turbulent velocity
$W_t$	turbulent combustion velocity
$W$	reaction rate

$x_j, j = 1, 2, 3$  spatial coordinates  
 $Y_f$  fuel mass function

### Greek Symbols

$\delta_t$  turbulent flame thickness  
 $\varepsilon$  viscous dissipation rate  
 $\Theta$  activation temperature  
 $\kappa$  heat diffusivity  
 $\nu$  kinematic viscosity  
 $\rho$  density  
 $\tau_c$  chemical time scale  
 $\tau'$  time scale for development of turbulent diffusivity

### Subscripts and Superscripts

0 steady or unperturbed value  
b combustion products  
L Laminar  
t turbulent  
u unburned mixture

### Acronyms

**ATDC** after top dead centre  
**BTDC** before top dead centre  
**CAD** crank angle degree  
**TDC** top dead centre

## 9.2 Finite Element/Difference Method for Elastic Wave Equations

### 9.2.1 Elastic Wave Propagation

Wave propagation in a non-homogeneous isotropic elastic medium occupying a bounded domain  $\Omega \subset R^d$ ,  $d = 2, 3$ , with boundary  $B$ , is described by the elastic wave equation:

$$\begin{aligned} \rho \frac{\partial^2 \nu}{\partial t^2} - \nabla \times \tau &= f \text{ in } \Omega \times (0, T) \\ \tau_{ij} &= \lambda \sum_{k=1}^d \epsilon_{kk} \delta_{ij} + 2\mu \epsilon_{ij}, \\ \nu(\times 0) &= 0, \frac{\partial \delta}{\partial t}(\cdot, 0) = 0 \text{ in } \Omega, \\ \delta/B &= 0, \text{ on } B \times (0, T) \end{aligned} \tag{9.1}$$

where  $\delta(x, t) \subset R^d$  is the displacement satisfying homogeneous boundary and initial conditions,  $\rho(x)$  is the density of the elastic material depending on  $x \in \Omega$ ,  $t$  is the time variable,  $T$  is a final time, and  $f(x, t) \subset R^d$  is a given source function,  $\tau = \{\tau_{ij}\}$  is the stress tensor, and  $\epsilon = \{\epsilon_{ij}\}$  is the strain tensor with components

$$\epsilon_{ij} = \epsilon_{ij}(\delta) = \frac{1}{2} \left( \frac{\partial \delta_i}{\partial x_j} + \frac{\partial \delta_{ji}}{\partial x_i} \right), \tag{9.2}$$

and  $\delta_{ij}$  is the Kronecker symbol with  $\delta_{ij} = 1$  if  $i = j$  and  $\delta_{ij} = 0$ . Depending upon  $x$ , the coefficients of the elastic material for  $d = 3$  case are given as  $M(x)$  and  $\lambda(x)$ , where

$$\ddot{\mu} = \frac{\dot{E}}{2(1 + \dot{\nu})}, \lambda = \frac{\dot{E}\dot{\nu}}{(1 + \dot{\nu})(1 - 2\dot{\nu})} \tag{9.3}$$

where  $\dot{E}$  and  $\dot{\nu}$  are variables since debris contain various objects of different material properties, such as elastic module and Poisson’s ratios. Matrix [D] is the compliance matrix.

Tables 9.1 to 9.5 (from Appendix A.I.A) are considered for the analysis and give the material compliance matrices and shape functions, where two cases respectively are examined for variable  $E$  and constant  $\nu$  and variable  $E$  and  $\nu$  ratios. For concrete, steel and timber, the  $\nu$  values can be established.

concrete elements	$E = 20 \text{ GN (m}^2\text{)}, \nu = 0.2$
steel elements	$E = 200 \text{ GN (m}^2\text{)}, \nu = 0.3$
timber elements	$E = 8400 \text{ N (mm}^2\text{)}, \nu = 0.3 \text{ to } 0.5$

If the medium consists of all the objects in the debris, each zone is investigated and then it is adopted a compliance matrix comprising these elements with specific properties.

Figure 9.1 shows a column or rod elements with degrees of freedom shown there on. In Appendix I can be shown the stiffness matrix of the element  $[K_1]$  and the mass matrix  $[M_1]$  for the same elements, so that  $M_t$  is:

$$M_t = (\rho A + m)(I - \epsilon^{in}) = (\rho(x)A + m) \tag{9.4}$$

where

- $\rho = \rho(x)$  is the density
- $m =$  added mass for direct
- $\epsilon^{in} =$  prestrain = 0

Eliminating the strain the elastic wave equation takes the following form in the case  $d = 3$ :

$$\rho \frac{\partial^2 \delta}{\partial t^2} - \nabla \times (\mu \nabla v) - \nabla((\lambda + \mu) \nabla \times v) = f \tag{9.5}$$

together with boundary and initial conditions.

**Table 9.1.** [D] – variable Young’s modulus and constant Poisson’s ratio

---

$D_{11} = \frac{E_1(E')^3 - E_{cr}}{\nu''}$	$D_{12} = \frac{\nu E_1 E_2 (E')^2 + E_{cr}}{\nu''}$	$D_{13} = \frac{\nu E_1 E_3 (E')^2 + E_{cr}}{\nu''}$	$D_{14} = 0$	$D_{15} = 0$	$D_{16} = 0$
	$D_{22} = \frac{E_2 E_3 (E')^2 + E_{cr}}{\nu''}$	$D_{23} = \frac{\nu E_2 E_3 (E')^2 + E_{cr}}{\nu''}$	$D_{24} = 0$	$D_{25} = 0$	$D_{26} = 0$
		$D_{33} = \frac{E_3 (E')^3 - E_{cr}}{\nu''}$	$D_{34} = 0$	$D_{35} = 0$	$D_{36} = 0$
			$D_{44} = G_{12}$	$D_{45} = 0$	$D_{46} = 0$
				$D_{55} = G_{23}$	$D_{56} = 0$
					$D_{66} = G_{31}$

$$E_{cr} = \nu^2 E_1 E_2 E_3 E'$$

$$E' = (E_1 + E_2 + E_3)/3$$

$$\nu'' = (E')^3 - 2E_1 E_2 E_3 \nu^2 - E' \nu^2 (E_1 E_2 + E_1 E_3 + E_2 E_3)$$

$$G_{12} = E_{12}/2(1 + \nu)$$

$$E_{12} = (E_1 + E_2)/2$$

$$G_{23} = E_{23}/2(1 + \nu)$$

$$E_{23} = (E_2 + E_3)/2$$

$$G_{31} = E_{31}/2(1 + \nu)$$

$$E_{31} = (E_3 + E_1)/2$$


---

**Table 9.2.** [D] – variable Young’s modulus and Poisson’s ratio

---

$D_{11} = \frac{(1 - \nu_{23}\nu_{32})}{\bar{\nu}} E_1$	$D_{12} = \frac{(\nu_{12} + \nu_{12}\nu_{32})}{\bar{\nu}} E_2$	$D_{13} = \frac{(\nu_{13} + \nu_{12}\nu_{23})}{\bar{\nu}} E_3$	$D_{14} = 0$	$D_{15} = 0$	$D_{16} = 0$
$D_{21} = \frac{(\nu_{21} + \nu_{23}\nu_{31})}{\bar{\nu}} E_1$	$D_{22} = \frac{(1 - \nu_{13}\nu_{31})}{\bar{\nu}} E_2$	$D_{23} = \frac{(\nu_{23} + \nu_{13}\nu_{21})}{\bar{\nu}} E_3$	$D_{24} = 0$	$D_{25} = 0$	$D_{26} = 0$
$D_{31} = \frac{(\nu_{31} + \nu_{21}\nu_{32})}{\bar{\nu}} E_1$	$D_{32} = \frac{(\nu_{32} + \nu_{12}\nu_{31})}{\bar{\nu}} E_2$	$D_{33} = \frac{(1 - \nu_{12}\nu_{21})}{\bar{\nu}} E_3$	$D_{34} = 0$	$D_{35} = 0$	$D_{36} = 0$
$D_{41} = 0$	$D_{42} = 0$	$D_{43} = 0$	$D_{44}$	$D_{45} = 0$	$D_{46} = 0$
$D_{51} = 0$	$D_{52} = 0$	$D_{53} = 0$	$D_{54} = 0$	$D_{55}$	$D_{56} = 0$
$D_{61} = 0$	$D_{62} = 0$	$D_{63} = 0$	$D_{64} = 0$	$D_{65} = 0$	$D_{66}$

$$\bar{\nu} = 1 - \nu_{12}\nu_{21} - \nu_{13}\nu_{31} - \nu_{23}\nu_{32} - \nu_{12}\nu_{23}\nu_{31} - \nu_{21}\nu_{13}\nu_{32}$$

Due to symmetry of compliances, the following relations can be written:

$$E_1 \nu_{21} = E_2 \nu_{12} \quad D_{55} = G_{23}$$

$$E_2 \nu_{32} = E_3 \nu_{23} \quad D_{66} = G_{13}$$

$$E_3 \nu_{13} = E_1 \nu_{31}$$

The values of  $G_{12}$ ,  $G_{23}$  and  $G_{13}$  are calculated in terms of modulus of elasticity and Poisson’s ratio as follows:

$$G_{12} = \frac{1}{2} \left[ \frac{E_1}{2(1 + \nu_{12})} + \frac{E_2}{2(1 + \nu_{21})} \right] = \frac{1}{2} \left[ \frac{E_1}{2(1 + \nu_{12})} + \frac{E_2}{2 \left( \frac{E_1}{E_2} \right) + \nu_{12}} \right]$$

$$G_{23} = \frac{1}{2} \left[ \frac{E_2}{2(1 + \nu_{23})} + \frac{E_3}{2(1 + \nu_{32})} \right] = \frac{1}{2} \left[ \frac{E_2}{2(1 + \nu_{23})} + \frac{E_2}{2 \left( \frac{E_2}{E_3} \right) + \nu_{23}} \right]$$

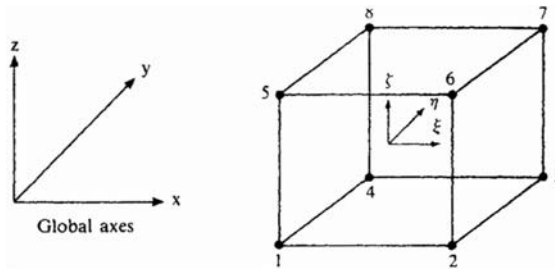
$$G_{13} = \frac{1}{2} \left[ \frac{E_3}{2(1 + \nu_{31})} + \frac{E_1}{2(1 + \nu_{13})} \right] = \left[ \frac{E_3}{2(1 + \nu_{31})} + \frac{E_2}{2 \left( \frac{E_3}{E_1} \right) + \nu_{31}} \right]$$

For isotropic cases:

$$E_1 = E_2 = E_3 = E$$

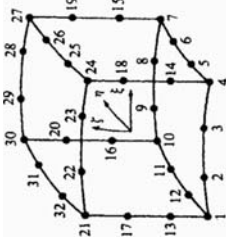
$$\nu_{12} = \nu_{13} = \nu_{23} = \nu_{21} = \nu_{31} = \nu_{32} = \nu$$

**Table 9.3.** Solid isoparametric elements eight-noded element



Node $i$	Shape functions $N_i(\xi, \eta, \zeta)$	Derivatives		
		$\frac{\partial N_i}{\partial \xi}$	$\frac{\partial N_i}{\partial \eta}$	$\frac{\partial N_i}{\partial \zeta}$
1	$\frac{1}{8}(1 - \xi)(1 - \eta)(1 - \zeta)$	$-\frac{1}{8}(1 - \eta)(1 - \zeta)$	$-\frac{1}{8}(1 - \xi)(1 - \zeta)$	$-\frac{1}{8}(1 - \eta)(1 - \xi)$
2	$\frac{1}{8}(1 + \xi)(1 - \eta)(1 - \zeta)$	$\frac{1}{8}(1 - \eta)(1 - \zeta)$	$-\frac{1}{8}(1 + \xi)(1 - \zeta)$	$-\frac{1}{8}(1 + \eta)(1 - \eta)$
3	$\frac{1}{8}(1 + \xi)(1 + \eta)(1 - \zeta)$	$\frac{1}{8}(1 + \eta)(1 - \zeta)$	$\frac{1}{8}(1 + \xi)(1 - \zeta)$	$-\frac{1}{8}(1 + \eta)(1 + \eta)$
4	$\frac{1}{8}(1 - \xi)(1 + \eta)(1 - \zeta)$	$-\frac{1}{8}(1 + \eta)(1 - \zeta)$	$\frac{1}{8}(1 - \xi)(1 - \zeta)$	$-\frac{1}{8}(1 - \eta)(1 + \eta)$
5	$\frac{1}{8}(1 - \xi)(1 - \eta)(1 + \zeta)$	$-\frac{1}{8}(1 - \eta)(1 + \zeta)$	$-\frac{1}{8}(1 - \xi)(1 + \zeta)$	$\frac{1}{8}(1 - \eta)(1 - \eta)$
6	$\frac{1}{8}(1 + \xi)(1 - \eta)(1 + \zeta)$	$\frac{1}{8}(1 - \eta)(1 + \zeta)$	$-\frac{1}{8}(1 + \xi)(1 + \zeta)$	$\frac{1}{8}(1 + \eta)(1 - \eta)$
7	$\frac{1}{8}(1 + \xi)(1 + \eta)(1 + \zeta)$	$\frac{1}{8}(1 + \eta)(1 + \zeta)$	$\frac{1}{8}(1 + \xi)(1 + \zeta)$	$\frac{1}{8}(1 + \eta)(1 + \eta)$
8	$\frac{1}{8}(1 - \xi)(1 + \eta)(1 + \zeta)$	$-\frac{1}{8}(1 + \eta)(1 + \zeta)$	$\frac{1}{8}(1 - \xi)(1 + \zeta)$	$\frac{1}{8}(1 - \eta)(1 + \eta)$

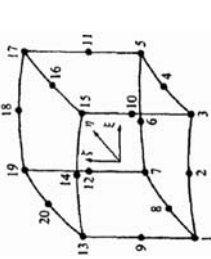
Table 9.4. Thirty-two-noded solid element



Node $i$	Shape functions		Derivatives	
	$N_i(\xi, \eta, \zeta)$	$\frac{\partial N_i}{\partial \eta}$	$\frac{\partial N_i}{\partial \xi}$	$\frac{\partial N_i}{\partial \zeta}$
23	$\frac{\eta}{64}(1 - \xi^2)(1 + 3\xi)(1 - \eta)(1 + \zeta)$	$-\frac{\eta}{64}(1 - \xi^2)(1 + 3\xi)(1 + \zeta)$	$\frac{\eta}{64}(3 - 2\xi - 9\xi^2)(1 - \eta)(1 + \zeta)$	$\frac{\eta}{64}(1 - \xi^2)(1 + 3\xi)(1 - \eta)$
24	$\frac{\eta}{64}(1 + \xi)(1 - \eta)(1 + \zeta)(\xi^2 + \eta^2 - \frac{19}{9} + \zeta^2)$	$\frac{\eta}{64}(1 + \xi)(1 - \eta)(2\xi + 3\xi^2 + \zeta^2 + \eta^2 - \frac{19}{9})$	$\frac{\eta}{64}(1 + \xi)(1 + \zeta)(2\eta^2 - 3\eta - \xi^2 - \zeta^2 + \eta^2 + \frac{19}{9})$	$\frac{\eta}{64}(1 + \zeta)(1 - \eta)(2\xi + 3\xi^2 + \zeta^2 + \eta^2 - \frac{19}{9})$
25	$\frac{\eta}{64}(1 - \eta^2)(1 - 3\eta)(1 + \xi)(1 + \zeta)$	$\frac{\eta}{64}(0\eta^2 - 2\eta - 3)(1 + \xi)(1 + \zeta)$	$\frac{\eta}{64}(1 - \eta^2)(1 - 3\eta)(1 + \zeta)$	$\frac{\eta}{64}(1 - \eta^2)(1 - 3\eta)(1 + \xi)$
26	$\frac{\eta}{64}(1 - \eta^2)(1 + 3\eta)(1 + \xi)(1 + \zeta)$	$\frac{\eta}{64}(3 - 2\eta - 9\eta^2)(1 + \xi)(1 + \zeta)$	$\frac{\eta}{64}(1 - \eta^2)(1 + 3\eta)(1 + \zeta)$	$\frac{\eta}{64}(1 - \eta^2)(1 + 3\eta)(1 + \xi)$
27	$\frac{\eta}{64}(1 + \xi)(1 + \eta)(1 + \zeta)(\xi^2 + \eta^2 + \zeta^2 - \frac{19}{9})$	$\frac{\eta}{64}(1 + \xi)(1 + \eta)(2\xi + 3\xi^2 + \eta^2 + \zeta^2 - \frac{19}{9})$	$\frac{\eta}{64}(1 + \xi)(1 + \zeta)(2\eta + 3\eta^2 + \xi^2 + \zeta^2 - \frac{19}{9})$	$\frac{\eta}{64}(1 + \xi)(1 + \eta)(2\xi^2 + 3\xi + \zeta^2 + \eta^2 - \frac{19}{9})$
28	$\frac{\eta}{64}(1 - \xi^2)(1 + 3\xi)(1 + \eta)(1 + \zeta)$	$\frac{\eta}{64}(1 - \xi^2)(1 + 3\xi)(1 + \zeta)$	$\frac{\eta}{64}(1 - \xi^2)(1 + 3\xi)(1 + \zeta)$	$\frac{\eta}{64}(1 - \xi^2)(1 + 3\xi)(1 + \eta)$
29	$\frac{\eta}{64}(1 - \xi^2)(1 - 3\xi)(1 + \eta)(1 + \zeta)$	$\frac{\eta}{64}(1 - \xi^2)(1 - 3\xi)(1 + \zeta)$	$\frac{\eta}{64}(1 - \xi^2)(1 - 3\xi)(1 + \zeta)$	$\frac{\eta}{64}(1 - \xi^2)(1 - 3\xi)(1 + \eta)$
30	$\frac{\eta}{64}(1 - \xi)(1 + \eta)(1 + \zeta)(\zeta^2 + \eta^2 + \xi^2 - \frac{19}{9})$	$\frac{\eta}{64}(1 - \xi)(1 + \eta)(2\xi - 3\xi^2 - \eta^2 - \zeta^2 + \frac{19}{9})$	$\frac{\eta}{64}(1 - \xi)(1 + \zeta)(2\eta + 3\eta^2 + \zeta^2 + \xi^2 - \frac{19}{9})$	$\frac{\eta}{64}(1 - \xi)(1 + \eta)(2\xi + 3\xi^2 + \zeta^2 + \eta^2 - \frac{19}{9})$
31	$\frac{\eta}{64}(1 - \eta^2)(1 + 3\eta)(1 - \xi)(1 + \zeta)$	$-\frac{\eta}{64}(1 - \eta^2)(1 + 3\eta)(1 + \zeta)$	$\frac{\eta}{64}(3 - 2\eta - 9\eta^2)(1 - \xi)(1 + \zeta)$	$\frac{\eta}{64}(1 - \eta^2)(1 + 3\eta)(1 - \xi)$
32	$\frac{\eta}{64}(1 - \eta^2)(1 - 3\eta)(1 - \xi)(1 + \zeta)$	$-\frac{\eta}{64}(0\eta^2 - 2\eta - 3)(1 - \xi)(1 + \zeta)$	$\frac{\eta}{64}(1 - \eta^2)(1 - 3\eta)(1 + \zeta)$	$\frac{\eta}{64}(1 - \eta^2)(1 - 3\eta)(1 - \xi)$



Table 9.5. Twenty-noded solid element



Node $i$	Shape functions		Derivatives	
	$N_i(\xi, \eta, \zeta)$	$\frac{\partial N_i}{\partial \xi}$	$\frac{\partial N_i}{\partial \eta}$	$\frac{\partial N_i}{\partial \zeta}$
1	$\frac{1}{8}(1-\xi)(1-\eta)(1-\zeta)(-\xi-\eta-\zeta-2)$	$\frac{1}{8}(1-\eta)(1-\zeta)(2\xi+\eta+\zeta+1)$	$\frac{1}{8}(1-\xi)(1-\zeta)(2\eta+\xi+\zeta+1)$	$\frac{1}{8}(1-\xi)(1-\eta)(2\zeta+\eta+\xi+1)$
2	$\frac{1}{4}(1-\xi^2)(1-\eta)(1-\zeta)$	$-\frac{1}{2}(1-\eta)(1-\zeta)\xi$	$-\frac{1}{4}(1-\xi^2)(1-\zeta)$	$-\frac{1}{4}(1-\xi^2)(1-\eta)$
3	$\frac{1}{8}(1+\xi)(1-\eta)(1-\zeta)(\xi-\eta-\zeta-2)$	$\frac{1}{8}(1-\eta)(1-\zeta)(2\xi-\eta-\zeta-1)$	$\frac{1}{8}(1+\xi)(1-\zeta)(2\eta-\xi+\zeta+1)$	$\frac{1}{8}(1+\xi)(1-\eta)(2\zeta-\xi+\eta+1)$
4	$\frac{1}{4}(1+\xi^2)(1-\eta^2)(1-\zeta)$	$\frac{1}{4}(1-\eta^2)(1-\zeta)$	$-\frac{1}{2}(1+\xi)(1-\zeta)\eta$	$-\frac{1}{4}(1-\eta^2)(1+\xi)$
5	$\frac{1}{4}(1+\xi)(1+\eta)(1-\zeta)(\xi+\eta-\zeta-2)$	$\frac{1}{4}(1+\eta)(1-\zeta)(2\xi+\eta-\zeta-1)$	$\frac{1}{4}(1+\xi)(1-\zeta)(2\eta+\xi-\zeta-1)$	$\frac{1}{4}(1+\xi)(1+\eta)(2\zeta-\xi-\eta+1)$
6	$\frac{1}{4}(1-\xi^2)(1+\eta)(1-\zeta)$	$-\frac{1}{2}(1+\eta)(1-\zeta)\xi$	$\frac{1}{4}(1-\xi^2)(1-\zeta^2)$	$-\frac{1}{4}(1-\xi^2)(1+\eta)$
7	$\frac{1}{4}(1-\xi)(1+\eta)(1-\zeta)(-\xi+\eta-\zeta-2)$	$\frac{1}{4}(1+\eta)(1-\zeta)(2\xi-\eta+\zeta+1)$	$\frac{1}{4}(1-\xi)(1-\zeta)(2\eta-\xi-\zeta-1)$	$\frac{1}{4}(1-\xi)(1+\eta)(2\zeta-\eta+\xi+1)$
8	$\frac{1}{4}(1-\xi)(1-\eta^2)(1-\zeta)$	$-\frac{1}{4}(1-\eta^2)(1-\zeta)$	$-\frac{1}{2}(1-\xi)(1-\zeta)$	$-\frac{1}{4}(1-\eta^2)(1-\xi)$
9	$\frac{1}{4}(1-\xi)(1-\eta)(1-\zeta^2)$	$-\frac{1}{4}(1-\xi^2)(1-\eta)$	$-\frac{1}{4}(1-\xi)(1-\zeta^2)$	$-\frac{1}{4}(1-\xi)(1-\eta)\zeta$
10	$\frac{1}{4}(1+\xi)(1-\eta)(1-\zeta^2)$	$\frac{1}{4}(1-\eta)(1-\zeta^2)$	$-\frac{1}{4}(1+\xi)(1-\zeta^2)$	$-\frac{1}{2}(1+\xi)(1-\eta)\zeta$
11	$\frac{1}{4}(1+\xi)(1+\eta)(1-\zeta^2)$	$\frac{1}{4}(1+\eta)(1-\zeta^2)$	$\frac{1}{4}(1+\xi)(1-\zeta^2)$	$-\frac{1}{2}(1+\xi)(1+\eta)\zeta$
12	$\frac{1}{4}(1-\xi)(1+\eta)(1-\zeta^2)$	$-\frac{1}{4}(1+\eta)(1-\zeta^2)$	$\frac{1}{4}(1-\xi)(1-\zeta^2)$	$-\frac{1}{2}(1-\xi)(1+\eta)\zeta$
13	$\frac{1}{8}(1-\xi)(1-\eta)(1+\zeta)(-\xi-\eta+\zeta-2)$	$\frac{1}{8}(1-\eta)(1+\zeta)(2\xi+\eta-\zeta+1)$	$\frac{1}{8}(1-\xi)(1+\zeta)(2\eta+\xi-\zeta+1)$	$\frac{1}{8}(1-\xi)(1-\eta)(2\zeta-\eta-\xi-1)$
14	$\frac{1}{4}(1-\xi^2)(1-\eta)(1+\zeta)$	$-\frac{1}{2}(1-\eta)(1+\zeta)\xi$	$-\frac{1}{4}(1-\xi^2)(1+\zeta)$	$\frac{1}{4}(1-\xi^2)(1-\eta)$
15	$\frac{1}{8}(1+\xi)(1-\eta)(1+\zeta)(\xi-\eta+\zeta-2)$	$\frac{1}{8}(1-\eta)(1+\zeta)(2\xi-\eta+\zeta-1)$	$\frac{1}{8}(1+\xi)(1+\zeta)(2\eta-\xi-\zeta+1)$	$\frac{1}{8}(1-\eta)(1+\xi)(2\zeta+\xi-\eta-1)$
16	$\frac{1}{4}(1+\xi)(1-\eta^2)(1+\zeta)$	$\frac{1}{4}(1-\eta^2)(1+\zeta)$	$-\frac{1}{2}(1+\xi)(1+\zeta)\eta$	$\frac{1}{4}(1+\xi)(1-\eta^2)$
17	$\frac{1}{4}(1+\xi)(1+\eta)(1+\zeta)(\xi+\eta+\zeta-2)$	$\frac{1}{4}(1+\eta)(1+\zeta)(2\xi+\eta+\zeta-1)$	$\frac{1}{4}(1+\xi)(1+\zeta)(2\eta+\xi+\zeta-1)$	$\frac{1}{4}(1+\xi)(1+\eta)(2\zeta+\eta+\xi-1)$
18	$\frac{1}{4}(1-\xi^2)(1+\eta)(1+\zeta)$	$-\frac{1}{2}\xi(1+\eta)(1+\zeta)$	$\frac{1}{4}(1-\xi^2)(1+\zeta)$	$\frac{1}{4}(1-\xi^2)(1+\eta)$
19	$\frac{1}{4}(1-\xi)(1+\eta)(1+\zeta)(-\xi+\eta+\zeta-2)$	$\frac{1}{4}(1+\eta)(1+\zeta)(2\xi-\eta-\zeta-1)$	$\frac{1}{4}(1-\xi)(1+\zeta)(2\eta-\xi+\zeta-1)$	$\frac{1}{4}(1-\xi)(1+\eta)(2\zeta-\xi+\eta-1)$
20	$\frac{1}{4}(1-\xi)(1-\eta^2)(1+\zeta)$	$-\frac{1}{4}(1-\eta^2)(1+\zeta)$	$-\frac{1}{2}(1-\xi)(1+\zeta)\eta$	$\frac{1}{4}(1-\xi)(1-\eta^2)$

**9.2.1.1 The Finite Element Method**

A hybrid finite element/difference method for time-domain elastic wave propagation is obtained by using continuous space-time piecewise linear finite elements on a partially structured mesh in space. The resulting scheme is efficiently implemented by (i) mass lumping in space and time making the scheme explicit in time, and (ii) using a fixed finite difference stencil on the structured mesh.

The computational space domain  $\Omega$  is decomposed into a finite element domain  $\Omega_{\text{FEM}}$  with an unstructured mesh and a finite difference domain  $\Omega_{\text{FDM}}$  with a structured mesh, with typically  $\Omega_{\text{FEM}}$  covering only a small part of the  $\Omega$ . In  $\Omega_{\text{FDM}}$  they are used quadrilateral elements in  $\mathbb{R}^2$  and hexahedra in  $\mathbb{R}^3$ . In  $\Omega_{\text{FEM}}$  it is used a finite element mesh  $K_h = [K_1]$  with elements  $K_1$  consisting of rectangles in  $\mathbb{R}^2$  and tetrahedra in  $\mathbb{R}^3$ . One associates with  $K_h$  a (continuous) mesh function  $h = h(x)$  representing the diameter of the element  $K_1$  containing  $x$ . For the time discretization  $J_\tau = \{J\}$  be a partition of the time interval  $I = (0, T)$  into time intervals  $J = (t_{k-1}, t_k)$  of uniform length  $\tau = t_k - t_{k-1}$ .

The following  $L_2$  inner products and norms are given:

$$\begin{aligned} ((p, q)) &= \int_{\Omega} \int_0^T pq dx dt, \|p\|^2 = ((p, p)) \\ (a, \beta) &= \int_{\Omega} a\beta dx, |a|^2 = (a, a). \end{aligned} \tag{9.6}$$

where

$$D\delta = \frac{\partial \delta}{\partial t} \tag{9.6a}$$

**9.2.1.2 The Basis for the Finite Element-Formulation**

To formulate the finite element method, the finite element trial space  $W_h^\delta$  is defined by:

$$W_h^\delta := \{w \in W^\delta : w|_{K_1 \times J} \in [P_1(K_1) \times P_1(J)]^3, \forall K_1 \in K_h, \forall J \in J_\tau\} \tag{9.7}$$

where

$$W^\delta := \{w \in [H^1(\Omega \times I)]^3 : w(\cdot, 0) = 0, w|_B = 0\}$$

Correspondingly, introducing the finite element test space  $W_h^a$  defined by:

$$W_h^a := \{w \in W^a : w|_{K_1 \times J} \in [P_1(K_1) \times P_1(J)]^3, \forall K_1 \in K_h, \forall J \in J_\tau\} \tag{9.8}$$

and

$$W^a := \{w \in [H^1(\Omega \times I)]^3 : w(\cdot, T) = 0, w|_B = 0\}$$

**Plate 9.1.** Side view of simulated aircraft impact into WTC 1 (Time = 0.20 s)

---

Computed debris scenario  
under air craft impact



The finite element method now gives as below the expression: Find  $w_h \in W_h$ , such that  $\forall \bar{a} \in W_h^a$

$$-((\rho D\delta, D\bar{a})) + ((\mu \nabla \delta_h^k, \nabla \bar{a})) = ((f^k, \bar{a})) \tag{9.9}$$

with again the initial condition  $D\delta(0) = (0)$  imposed in weak form through the variational formulation. The elastic wave formulation is given in Table 9.6.

Expanding as above  $\delta$  in terms of the standard continuous piecewise linear functions in space and in time and substituting this into (9.9), the following system of linear equations is obtained:

$$M_1(\delta^{k+1} - 2\delta^k + \delta^{k-1}) = \tau^2 F^k - \tau^2 K_1 \left( \frac{1}{6}\delta^{k-1} + \frac{2}{3}\delta^k + \frac{1}{6}\delta^{k+1} - \tau^2 D\delta^k \right) \tag{9.10}$$

with initial conditions  $\delta^0 = 0$  and  $\delta^1 \approx 0$ . Here,  $M_1$  is a (vector) mass matrix in space,  $K_1$  is a (vector) stiffness matrix corresponding to the Laplacian,  $D$  is a stiffness matrix corresponding to the divergence term,  $F^k$  is the load vector at time level  $t_k$ , corresponding to  $f(\cdot, \cdot)$  and  $\delta^k$  denotes the nodal values of  $\delta(\cdot, t_k)$ .

As above it can be obtained efficient explicit scheme by approximating  $M$  with a lumped mass matrix  $M_1^L$  and replacing the terms  $\frac{1}{6}\delta^{k-1} + \frac{1}{3}\delta^k + \frac{1}{6}\delta^{k+1}$  by  $\delta^k$ .

$$\begin{aligned} \delta^{k+1} &= \tau^2 (M^L)^{-1} F^k + 2\delta^k - \tau^2 (M^L)^{-1} K_1^k \\ &\quad - \tau^2 (M^L)^{-1} D\delta^k - \delta^{k-1} \end{aligned} \tag{9.11}$$

One now describes the hybrid finite element methods Table 9.7, hence, the communication between the finite element method on the unstructured part of the mesh with  $\Omega_{\text{FEM}}$  with the finite difference method on the structured part  $\Omega_{\text{FDM}}$ . One needs to pay particular attention to this condition, because the finite element method on  $\Omega_{\text{FEM}}$  and the difference method on  $\Omega_{\text{FDM}}$  are implemented differently in various modules. Technically, the communication is achieved by mesh overlapping. The structural cells created by (9.11). For example, for the two dimensional case  $d = 2$  and the three dimensional case  $d = 3$ , the interior nodes can be computed.

**Table 9.6.** A systematic hybrid elastic wave formulation

---

**Wave Equation in Elastodynamic**

Equations (9.1) to (9.5) indicate the entire process of the elastic wave phenomenon coupled to  $\tau$  by Hooke's Law:

$$\tau_{ij} = \sum_{k=1}^d \sum_{l=1}^d C_{ijkl} \epsilon_{kl} \tag{a}$$

where  $C$  is a cyclic symmetric tensor, satisfying:

$$C_{ijkl} = C_{klij} = C_{jkti} \tag{b}$$

If the constants  $C_{ijkl}(x)$  do not depend on  $x$ , the material of the body is said to be homogeneous. If the constants  $C_{ijkl}(x)$  do not depend on the choice of the coordinate system, the material of the body is said to be isotropic at the point  $x$ . otherwise, the material is anisotropic at the point  $x$ .

In the isotropic case,  $C$  can be written as:

$$C_{ijkl} = \lambda \delta_{ij} \delta_{kl} + \mu (\delta_{ij} \delta_{kl} + \delta_{il} \delta_{jk}) \tag{c}$$

where  $\delta_{ij}$  is Kronecker delta, in which case takes the form of Hooke’s Law:

$$\tau_{ij} = \lambda \delta_{ij} \sum_{k=1}^d \epsilon_{kk} + 2\mu \epsilon_{ij} \tag{d}$$

where  $\lambda$  and  $\mu$  are the Lamé coefficients, depending on  $x$ , given by:

$$\mu = \frac{\dot{E}}{2(1 + \dot{\nu})}, \lambda = \frac{\dot{E}\nu}{(1 + \dot{\nu})(1 - 2\nu)} \quad \text{as in (9.3)} \tag{e}$$

where  $\dot{E}$  is the modulus of elasticity (Young modulus), and  $\dot{\nu}$  is the Poisson’s ratio of the elastic material. We have that

$$\lambda > 0, \mu > 0 \Leftrightarrow \dot{E} > 0, 0 < \nu < 1/2 \tag{f}$$

Eliminating the strain tensor using Hooke’s law, we can verify the elastic wave equation in terms of  $\delta$  only. In the isotropic case, with  $d = 3$ , then it takes the following form:

$$\begin{aligned} \rho \frac{\partial^2 \delta_1}{\delta t^2} - \frac{\partial}{\partial x_1} \left( (\lambda + 2\mu) \frac{\partial \delta_1}{\partial x_1} + \lambda \frac{\partial \delta_2}{\partial x_2} + \lambda \frac{\partial \delta_3}{\partial x_3} \right) \\ - \frac{\partial}{\partial x_2} \left( \mu \left( \frac{\partial \delta_1}{\partial x_2} + \lambda \frac{\partial \delta_2}{\partial x_1} \right) \right) \end{aligned} \tag{g}$$

$$\begin{aligned} - \frac{\partial}{\partial x_3} \left( \mu \left( \frac{\partial \delta_1}{\partial x_3} + \lambda \frac{\partial \delta_3}{\partial x_1} \right) \right) = f_1 \ , \\ \rho \frac{\partial^2 \delta_2}{\delta t^2} - \frac{\partial}{\partial x_2} \left( (\lambda + 2\mu) \frac{\partial \delta_2}{\partial x_2} + \lambda \frac{\partial \delta_1}{\partial x_1} + \lambda \frac{\partial \delta_3}{\partial x_3} \right) \\ - \frac{\partial}{\partial x_1} \left( \mu \left( \frac{\partial \delta_1}{\partial x_2} + \lambda \frac{\partial \delta_2}{\partial x_1} \right) \right) \end{aligned} \tag{h}$$

$$\begin{aligned} - \frac{\partial}{\partial x_3} \left( \mu \left( \frac{\partial \delta_2}{\partial x_3} + \lambda \frac{\partial \delta_3}{\partial x_2} \right) \right) = f_2 \ , \end{aligned}$$

$$\begin{aligned} \rho \frac{\partial^2 \delta_3}{\delta t^2} - \frac{\partial}{\partial x_3} \left( (\lambda + 2\mu) \frac{\partial \delta_3}{\partial x_3} + \lambda \frac{\partial \delta_2}{\partial x_2} + \lambda \frac{\partial \delta_1}{\partial x_1} \right) \\ - \frac{\partial}{\partial x_2} \left( \mu \left( \frac{\partial \delta_3}{\partial x_2} + \lambda \frac{\partial \delta_2}{\partial x_3} \right) \right) \end{aligned} \tag{i}$$

$$\begin{aligned} - \frac{\partial}{\partial x_1} \left( \mu \left( \frac{\partial \delta_1}{\partial x_3} + \lambda \frac{\partial \delta_3}{\partial x_1} \right) \right) = f_3 \ , \end{aligned}$$

or in more compact form:

$$\rho \frac{\partial^2 \delta}{\delta t^2} - \nabla(\mu \nabla v) - \nabla((\lambda + \mu) \nabla v) = f \quad \text{as in (9.5)} \quad (j)$$

Inserting a Helmholtz decomposition:

$$\delta = \nabla \varphi + \nabla \times \psi \quad (k)$$

With a scalar potential  $\phi$  and a vector potential  $\psi$  into (9.9), it becomes:

$$\rho \frac{\partial^2 \delta}{\delta t^2} (\nabla \varphi + \nabla \times \psi) = \mu (\nabla \varphi + \nabla \times \psi) + (\lambda + \mu) \nabla (\nabla (\nabla \varphi + \nabla \times \psi)) \quad (l)$$

while by incorporating:

$$\begin{aligned} \nabla (\nabla \varphi) &= \Delta \varphi \\ \nabla (\nabla \times \psi) &= 0 \end{aligned} \quad (m)$$

reduces to

$$\nabla \left( \rho \frac{\partial^2 \varphi}{\delta t^2} - (\lambda + 2\mu) \Delta \varphi \right) + \nabla \times \left( \rho \frac{\partial^2 \psi}{\delta t^2} - \mu \Delta \psi \right) = 0 \quad (n)$$

if the potentials  $\phi$  and  $\psi$  satisfy the wave equations:

$$\frac{\partial^2 \varphi}{\delta t^2} - (\lambda + 2\mu) \Delta \varphi = 0 \quad (o)$$

$$\rho \frac{\partial^2 \psi}{\delta t^2} - \mu \Delta \psi = 0 \quad (p)$$

then  $\delta = \nabla \varphi + \nabla \times \psi$  satisfies (o). It is noted that  $v = \nabla \phi$  corresponds to a pressure wave with speed:

$$V_p = \left( \frac{\lambda + 2\mu}{\rho} \right)^{1/2} \quad (q)$$

and  $\delta = \nabla \times \psi$  to a shear wave with speed:

$$V_s = \left( \frac{\mu}{\rho} \right)^{1/2} \quad (r)$$

In the pressure wave displacement is parallel to the direction of wave propagation, and the shear wave is orthogonal to the direction of propagation.

To formulate in the finite element method, Equations (9.7) and (9.9) are derived. The finite element method reads. Find

$$\delta_h \in W_h^\delta \quad (s)$$

such that:

$$\begin{aligned} \left( \rho \frac{\delta_h^{k+1} - 2\delta_h^k + \delta_h^{k-1}}{\tau^2}, \delta \right) &+ (\mu \nabla \delta_h^k, \nabla \delta) \\ &+ (\lambda + \mu) \nabla \delta_h, \nabla \delta = (f^k, \delta) \quad \forall \delta \in W_h^\delta \quad (t) \\ \delta_h(0) &= \delta_h(0) = 0 \end{aligned}$$

For a **discrete scheme**, expanding  $\delta$  in terms of standard continuous piecewise linear function  $\Phi_i(x)$  in space and  $\Psi_i(x)$ , (9.10) is derived and the rest of the procedure as discussed. The explicit scheme is adopted.

---

**Table 9.7.** Explicit time integration

The finite element semi-discretisation of the momentum balance partial differential equation results in a system of ordinary differential equations in time. The full discretisation can be obtained by applying an appropriate integration method with respect to time.

In general, most multi-body contact problems fall into the category of wave propagation problems. Normally, in order to solve numerically this type of problems explicit time integration schemes are employed.

**Central Difference Time Integration Scheme**

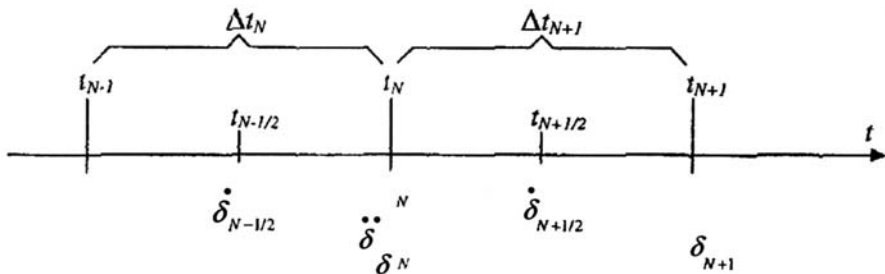
The displacement field

$$\delta = \delta(t) \tag{a}$$

is a one parameter function which determines the current position  $x(t)$  of material particles in explosion, with respect to their initial position  $X$  as follows:

$$x(t) = X + \delta(t) \tag{b}$$

if the response of the continuum is strongly non-linear, the central difference method is often applied with a varying time increment.



**Fig. 9.1.** Central difference integration scheme

Let  $\Delta t_{N+1}$  be the time increment between  $t_N$  and  $t_{N+1}$  with  $\delta_N = \delta(t_N)$  as illustrated in Fig. 9.1. The mid-step velocities are defined by:

$$t_{N-1/2} = \frac{1}{2}(t_{N-1} + t_N) \quad t_{N+1/2} = \frac{1}{2}(t_N + t_{N+1}) \tag{c}$$

and

$$\dot{\delta}_{N-1/2} = \dot{\delta}(t_{N-1/2}) \quad \dot{\delta}_{N+1/2} = \dot{\delta}(t_{N+1/2}) \tag{d}$$

The central difference formula for velocity is

$$\dot{\delta}_{N+1/2} = \frac{\delta_{N+1} - \delta_N}{\Delta t_{N+1}} \tag{e}$$

while the central difference formula for acceleration is

$$\ddot{\delta}_N = \frac{\dot{\delta}_{N+1/2} - \dot{\delta}_{N-1/2}}{\Delta t_{N+1/2}} \tag{f}$$

where

$$\Delta t_{N+1/2} = \frac{1}{2}(\Delta t_N + \Delta t_{N+1}) \quad (\text{g})$$

The finite element discretisation of the momentum balance equation for an undamped system can be expressed in its matrix form as follows:

$$M_1 \ddot{u}(t) + F^{\text{int}}(u(t)) = F^{\text{ext}}(t) \quad (\text{h})$$

where  $M_1$  is the mass matrix,  $F^{\text{int}}$  is the internal forces vector and  $F^{\text{ext}}$  is the external forces vector. Full discretisation of this second-order partial differential equation can be obtained by substituting the acceleration term with its finite difference approximation as follows:

$$M_1 = \frac{\dot{\delta}_{N+1/2} - \dot{\delta}_{N-1/2}}{\Delta t_{N+1/2}} + F_N^{\text{int}} = F_N^{\text{ext}} \quad (\text{i})$$

which yields:

$$\dot{\delta}_{N+1/2} = M_1^{-1}(F_N^{\text{ext}} - F_N^{\text{int}}) = \Delta t_{N+1/2} + \dot{\delta}_{N-1/2} \quad (\text{j})$$

and

$$\delta_{N+1} = \delta_N + \dot{\delta}_{N+1/2} \Delta t_{N+1/2} \quad (\text{k})$$

Subsequently, the internal and external forces vectors can be calculated as:

$$\begin{aligned} F_{N+1}^{\text{int}} &= F^{\text{int}}(\delta_{N+1}) \\ F_{N+1}^{\text{ext}} &= F^{\text{ext}}(\delta_{N+1}) \end{aligned} \quad (\text{l})$$

which accomplishes the  $N$ -th time step.

Computational domain can be grouped as follows:

- $\omega_o$ : Nodes interior to  $\Omega_{\text{FDM}}$  and lying on the boundary of  $\Omega_{\text{FEM}}$ ,
- $\omega_X$ : Nodes interior to  $\Omega_{\text{FEM}}$  and lying on the boundary of  $\Omega_{\text{FDM}}$ ,
- $\omega^*$ : Nodes interior to  $\Omega_{\text{FEM}}$  and not contained in  $\Omega_{\text{FDM}}$ ,
- $\omega'_D$ : Nodes interior to  $\Omega_{\text{FDM}}$  and not contained in  $\Omega_{\text{FEM}}$ ,

In each time-step of the explicit method scheme the communication carried out as follows:

- (1) Update the solution in the interior of  $\Omega_{\text{FDM}}$ , i.e., at nodes  $\omega'_D$  and  $\omega_o$  using the finite difference method.
- (2) Update the solution in the interior of  $\Omega_{\text{FEM}}$ , i.e., at nodes  $\omega^*$  and  $\omega_X$  using the finite element method.
- (3) Copy values at nodes  $\omega_X$  from  $\Omega_{\text{FEM}}$  to  $\Omega_{\text{FDM}}$ .
- (4) Copy values at nodes  $\omega_o$  from  $\Omega_{\text{FDM}}$  to  $\Omega_{\text{FEM}}$ .

The finite element method is formulated as a Galerkin method with piecewise linear approximation for the Jacobian equations expressing stationarity of the Lagrangian. The adaptivity is based on a posteriori error estimates involving Jacobian residuals and associated dual weights obtained from the solution an associated linearized dual problem involving the Hessian of the Lagrangian. With data depending on the quantity of interest (output). The size of the dual solution with the data expresses the sensitivity of the output to different perturbations. Of prime concern in adaptivity may be the sensitivity of the material coefficients to perturbations from (i)



discretisation of the Jacobian equations with finite elements/differences, and (ii) from errors in the measured data. It can be expected that the sensitivity should increase with increasing amount of (correct) wave reflection data.

If one restricts the output to be the Lagrangian itself, then the dual weights are obtained from the solution of the Jacobian equations, while more demanding outputs, such as more or less local mean values of the material coefficients, require the dual problem with the Hessian to be (approximately) solved.

### 9.2.1.3 Elastic Scattering of Debris

For the wave equation function  $\rho(x)$ ,  $M(x)$ , and  $\lambda(x)$  are necessary to be found. Preliminary equations can be written as:

$$\begin{aligned}
 E(\delta, \rho, \mu, \lambda) = & \frac{1}{2} \int_0^t \int_{\Omega} (\delta - \bar{\delta})^2 \delta_{\text{obs}} dx dt \\
 & + \frac{1}{2} \gamma_1 \int_{\Omega} |\nabla \rho|^2 dx + \frac{1}{2} \gamma_2 \int_{\Omega} |\nabla \mu|^2 dx + \frac{1}{2} \gamma_3 \int_{\Omega} |\nabla \lambda|^2 dx,
 \end{aligned}
 \tag{9.12}$$

where  $\bar{\delta}$  is observed data at  $x_{\text{obs}}$ ,  $\delta$  is satisfied and thus depends on  $\rho\mu$  and  $\lambda$ , and  $\gamma_i$ ,  $i = 1, 2, 3$  are regularized parameters.

$$\begin{aligned}
 L(u) = & E(\delta, \rho, \mu, \lambda) - ((\rho D\delta, Da) + (\mu \nabla \delta, \nabla a)) \\
 & + ((\lambda + \mu) \nabla \delta, \nabla a) - (f, a)
 \end{aligned}
 \tag{9.13}$$

where  $u = (\nu, \alpha, \rho, \mu, \lambda)$ , and search for a stationary point  $u$  satisfying  $\forall \bar{u}$ :

$$L'(u, \bar{u}) = 0
 \tag{9.14}$$

where  $L'(u; \cdot)$  is the Jacobian of  $L$  at  $u$ , and we assume that  $a(\cdot, T) = \bar{a}(\cdot, T) = 0$ ,  $a = 0$  and  $\delta(\cdot, T) = \bar{\delta}(\cdot, T) = 0$ , together with homogeneous boundary conditions.

The equation (9.14) expresses that in  $\Omega \times (0, T)$

$$\rho \frac{\partial^2 \delta}{\partial t^2} - \nabla(\mu \nabla \delta) - \nabla((\lambda + \mu) \nabla \delta) = f
 \tag{9.15}$$

$$\rho \frac{\partial^2 a}{\partial t^2} - \nabla(\mu \nabla a) - \nabla((\lambda + \mu) \nabla a) = -(\delta - \bar{\delta}) \delta_{\text{obs}}
 \tag{9.16}$$

$$-\gamma_1 \Delta \rho - \int_0^T \int_{\Omega} \frac{\partial \delta \partial a}{\partial t \partial t} dx dt = 0
 \tag{9.17}$$

$$-\gamma_2 \Delta \mu - \int_0^T \int_{\Omega} \nabla \delta \nabla a + \nabla \delta \nabla a dx dt = 0$$

$$-\gamma_3 \Delta \lambda + \int_0^T \int_{\Omega} \nabla \delta \nabla a dx dt = 0
 \tag{9.18}$$

together with homogenous boundary and initial conditions. Here (9.15) is the state equation for the state  $\nu$ , (9.16) is the adjoint state equation for the costate  $a$ , and (9.17 to 9.18) express the stationarity with respect to the parameters  $\rho$ ,  $\mu$  and  $\lambda$ .

**9.2.1.4 A Finite Element Method for Elastic Scattering**

One now defines  $U_h = W_h^\delta \times W_h^a \times V_h^3$  and seeks  $u_h \in U_h$  such that:

$$L' = (u_h; \bar{u}) = 0, \forall \bar{u} \in U_h \tag{9.19}$$

where now  $L$  is defined by (9.13) and the finite element spaces  $W_h^\delta$  and  $W_h^a$  are defined.

Program BANG-FIR is now invoked with scattering achieved under symbols  $o$ ,  $x$ ,  $*$  and  $'$ , various elements scattered can be identified.

**9.3 Three Dimensional Scattering of Elements Under Impact/Explosion/Fire**

Adaptive algorithm for computation of the parameter for ‘ $c$ ’ is used. Test cases of 2, 4 and 6 plane waves are performed. The method is as follows:

- (1) Choose an initial mesh  $K_h$  and an initial time partition  $J_k$  of the time interval  $[0, T]$ .
- (2) Compute the solution  $p$  on  $K_h$  and  $J_k$  of the forward problem (2.1.) with  $c = c^{(n)}$ .
- (3) Compute the solution  $\lambda$  of the adjoint problem

$$\frac{1\partial^2\lambda}{c^2\partial t^2} - \Delta\lambda = -(p - \tilde{p})\delta_{\text{obs}}, x \in \Omega, 0 < t < T \tag{9.20}$$

on  $K_h$  and  $J_k$ .

- (4) Update the velocity on  $K_h$  and  $J_k$  according to

$$c^{(n+1)}(x) = c^{(n)}(x) - a^{(n)} \frac{2}{c^{(n)3}} \int_0^T \frac{\partial\lambda(x, t)}{\partial t} \frac{\partial p(x, t)}{\partial t} dt \tag{9.21}$$

where  $a = 0.01$ .

- (5) Compute the error for  $c$ .
- (6) Refine all tetrahedra, where  $R_c\sigma_c > \varepsilon$ ,  $\varepsilon$  is a desired tolerance. Each isoparametric can be divided into 2, to 8 new isoparametric tetrahedra.
- (7) Construct a new mesh  $K_h$ : one connects a refined grid with the previous one, to maintain the consistency of the grid.

## 9.4 Debris Dispersion Relation Using Time-Dependent Elastic Waves

In this section it is necessary to present the dispersion relations for the time-dependent elastic wave equation. These relations allow one to get the information on the stability and accuracy properties of the numerical models.

Searching for a plane wave solution of the homogenous elastic equation in the form

$$\delta_1 = \delta_{1_0} e^{i(\omega t + k_1 x + k_2 y)} \quad (9.22)$$

$$\delta_2 = \delta_{2_0} e^{i(\omega t + k_1 x + k_2 y)} \quad (9.23)$$

one gets two dispersion relations by identifying eigenvalues of the problem:

$$AX = \rho \sin^2 \frac{\omega \tau}{2} X \quad (9.24)$$

where  $X = \delta_{1_0}, \delta_{2_0}$  and

$$A_1 = \frac{\tau^2}{h^2} \begin{pmatrix} (\lambda + 2\mu) \sin \frac{2k_1 h}{2} + \mu \sin \frac{2k_2 h}{2} & (\lambda + \mu) \sin \frac{k_1 h}{2} \sin \frac{k_2 h}{h} \cos \frac{k_1 h}{2} \cos \frac{k_2 h}{2} \\ (\lambda + \mu) \sin \frac{k_1 h}{2} \sin \frac{k_2 h}{h} \cos \frac{k_1 h}{2} \cos \frac{k_2 h}{2} & (\lambda + 2\mu) \sin \frac{2k_2 h}{2} + \mu \sin \frac{2k_1 h}{2} \end{pmatrix},$$

which gives

$$\begin{aligned} \rho \sin^2 \frac{\omega \tau}{2} &= \frac{\tau^2}{h^2} \left( (\lambda + 2\mu) \left( \sin^2 \frac{k_1 h}{2} + \sin^2 \frac{k_2 h}{2} \right) \right. \\ &\quad \left. - (\lambda + \mu) \sin^2 \frac{k_1 h}{2} \sin^2 \frac{k_2 h}{2} \right), \end{aligned} \quad (9.25)$$

$$\begin{aligned} \rho \sin^2 \frac{\omega \tau}{2} &= \frac{\tau^2}{h^2} \left( \mu \left( \sin^2 \frac{k_1 h}{2} + \sin^2 \frac{k_2 h}{2} \right) \right. \\ &\quad \left. + (\lambda + \mu) \sin^2 \frac{k_1 h}{2} \sin^2 \frac{k_2 h}{2} \right). \end{aligned} \quad (9.26)$$

### 9.4.1 Stability Criterion

To determine the time step restriction for stability of our explicit method, one assumes that  $\sin \frac{\omega t}{2} \leq 1$  and  $k_1 h = k_2 h = k_3 h = \pi$  corresponding to the highest spatial frequency resolved by the grid, and then deduces from (9.25 to 9.26) the CFL condition:

$$\tau \leq h \sqrt{\frac{\rho}{\lambda + 3\mu}} \quad (9.27)$$

### 9.4.2 Absorbing Boundary Conditions

One has also simulated a variation of the problem by applying absorbing boundary conditions at the boundary  $\Omega_{\text{FDM}}$ . It means, that these boundary

conditions approximate the solution of the boundaries. One uses the following boundary condition:

$$\left. \frac{\partial}{\partial t} u - \frac{\partial}{\partial x} u \right|_{x=0} = 0 \tag{9.28}$$

### 9.4.3 Neumann Boundary Conditions

The condition:

$$\tau_{ij} n_j = \overline{T}_i, x \in B \tag{9.29}$$

$$\lambda \delta_{ij} n_i \sum_{k=1}^d \epsilon_{kk} + 2\mu_{ij} n_i = \overline{T}_i \tag{9.30}$$

in this case, one seeks a solution  $u_i \in C^2(\Omega), i = 1, 2, 3$ . The explicit expression for the computations of the surface forces  $T_i \in C(B), i = 1, 2, 3$  at the boundary B in the three dimensional case take the following form:

$$\begin{aligned} \overline{T}_x &= (\lambda + 2\mu) \frac{\partial \delta_1}{\partial x_1} n_1 + \lambda \left( \frac{\partial \delta_2}{\partial x_2} + \frac{\partial \delta_3}{\partial x_3} \right) n_1 + \mu \left( \frac{\partial \delta_1}{\partial x_2} + \frac{\partial \delta_2}{\partial x_1} \right) n_2 + \mu \left( \frac{\partial \delta_1}{\partial x_3} + \frac{\partial \delta_3}{\partial x_1} \right) n_3, \\ \overline{T}_y &= (\lambda + 2\mu) \frac{\partial \delta_2}{\partial x_2} n_2 + \lambda \left( \frac{\partial \delta_1}{\partial x_1} + \frac{\partial \delta_3}{\partial x_3} \right) n_2 + \mu \left( \frac{\partial \delta_2}{\partial x_3} + \frac{\partial \delta_3}{\partial x_2} \right) n_3 + \mu \left( \frac{\partial \delta_2}{\partial x_1} + \frac{\partial \delta_1}{\partial x_2} \right) n_1, \\ \overline{T}_z &= (\lambda + 2\mu) \frac{\partial \delta_3}{\partial x_3} n_3 + \lambda \left( \frac{\partial \delta_1}{\partial x_1} + \frac{\partial \delta_2}{\partial x_2} \right) n_3 + \mu \left( \frac{\partial \delta_3}{\partial x_2} + \frac{\partial \delta_2}{\partial x_3} \right) n_2 + \mu \left( \frac{\partial \delta_3}{\partial x_1} + \frac{\partial \delta_1}{\partial x_3} \right) n_1. \end{aligned} \tag{9.31}$$

## 9.5 Debris Elements Forced by a 3-D Turbulent Flame

### 9.5.1 Introduction

A turbulent flame speed model is modified and implemented into program BNG-FR written in three-dimensional finite element or finite discrete element technique. The modifications are done to account for mixture inhomogeneity. Multidimensional numerical solutions are recognised. The mixtures, as discussed above consist of dirt, structural elements and the rest of debris. Since due to turbulent flame the commercial CFD code requires a revision to include these effects on kinetic energy of turbulence. Additional momentum is employed due to a specific turbulent component and the realistic equations are obtained to represent the true debris dynamics.

### 9.5.2 Turbulent Driven Debris Equations

The model yields the following closed balance equation for the mean progress variable

$$\frac{\partial \bar{\rho} \tilde{c}}{\partial t} + \frac{\partial \bar{\rho} \tilde{c}}{\partial x_j} (\bar{\rho} \tilde{u}_j \tilde{c}) = \frac{\partial}{\partial x_j} \left[ \bar{\rho} (\kappa + D_t) \frac{\partial \tilde{c}}{\partial x_j} \right] - \frac{\bar{\rho} \tilde{c}}{t_r (1 + D_t / \kappa_b)} \exp \left( -\frac{\Theta}{T} \right) + \quad (9.32)$$

$$A \rho_u u' \left[ \frac{L}{u' \tau_c} \right]^{1/4} \left\{ 1 + \frac{\tau'}{t} \left[ \exp \left( -\frac{t}{\tau'} \right) - 1 \right] \right\}^{1/2} |\nabla \tilde{c}|$$

$$|\nabla \tilde{c}| = \left\{ \sum_{j=t}^3 \left( \frac{\partial \tilde{c}}{\partial x_j} \right)^2 \right\}^{1/2} \quad (9.33)$$

where the following well-known approximation

$$D_t = D_{t,0} \left[ 1 - \exp \left( -\frac{t}{\tau'} \right) \right] \quad (9.34)$$

of time-dependent turbulent diffusivity  $D_t$  is used. Here,  $t$  is the time counted from ignition;  $x_j$  and  $u_j$  are the coordinates and flow velocity components, respectively;  $\rho$  is the gas density;  $\tau_c = \kappa_u / U_L^2$  and  $\tau' = D_{t,0} / u'^2$  are the chemical and turbulent time scales, respectively; subscripts  $u$  and  $b$  label the unburned and burned gas, respectively. The Reynolds averages, such as  $\bar{\rho} \tilde{c} = \overline{\rho c}$ , are used. The r.m.s. turbulent velocity  $u' = \sqrt{2\tilde{k}/3}$ , integral turbulent length scale  $L = C_D u'^3 / \tilde{\varepsilon}$ , and the steady turbulent diffusivity  $D_{t,0} = C_\mu \tilde{k}^2 / (\sigma_c \tilde{\varepsilon})$  are evaluated using, for example, the standard  $k - \varepsilon$  turbulent model, where  $C_D$ ,  $C_\mu$  and  $\sigma_c$  are constants, and  $k$  and  $\varepsilon$  are the turbulent kinetic energy and its dissipation rate, respectively. The Favre averaged temperature is linked with the progress variable as follows:

$$\tilde{T} = T_u (1 - \tilde{c} + \gamma \tilde{c}) \quad (9.35)$$

where  $\gamma = \rho_u / \rho_b$  is the heat release parameter.

In addition to two turbulence characteristics ( $k$  and  $\varepsilon$  or  $u'$  and  $L$ ), the BANG-FIR includes a single constant  $A$  and a set of physico-chemical characteristics must be calculated so that it yields the known value of  $U_L$  when  $u' = 0$ . It is worth noting that joint variations in  $\Theta$  and  $t_r$  weakly affect the turbulent combustion rate [predicted by the BANG-FIR, provided that this set of values of  $\Theta$  and  $t_r$  yields the correct value of  $U_L$  when  $u' = 0$ ].

Equations (9.32) and (9.33) are the core of the BANG-FIR. It is compatible both with another turbulence submodel, required to evaluate  $u'$ ,  $L$  and  $D_{t,0}$  locally, and with another thermo-chemical approximation, required to evaluate the temperature.

*Model Features.* To show the basic features of the model in a clear manner. One considers the limit behaviour of (9.32) in the simplest case of the planar one-dimensional flame.

*Weak Turbulence.* For the limit of weak turbulence ( $u' \rightarrow 0$ ), (9.32) is reduced to the standard balance equation of the thermal laminar flame theory.

$$\frac{\partial}{\partial t}(\rho c) + \frac{\partial}{\partial x}(\rho u c) = \frac{\partial}{\partial x} \left[ \rho \kappa \frac{\partial c}{\partial x} \right] + \frac{\rho(1-c)}{t_0} \exp\left(-\frac{\Theta}{T}\right) \quad (9.36)$$

The first, laminar-like, source term has been inserted into (9.32), in order to satisfy this limit behaviour.

*Strong Turbulence.* For this opposite limit case of strong turbulence ( $u' \gg U_L$  and  $D_t \gg D_L$ ), this source term is reduced by the ratio  $D_t/\kappa_b$  and the last source term is dominating. Then, (9.32), is reduced to:

$$\frac{\partial}{\partial t}(\bar{\rho}\tilde{c}) + \frac{\partial}{\partial x}(\bar{\rho}\tilde{u}\tilde{c}) = \frac{\partial}{\partial x} \left[ \bar{\rho}D_t \frac{\partial \tilde{c}}{\partial x} \right] + \rho_u U_t |\nabla \tilde{c}| \quad (9.37)$$

in the laboratory coordinate system or to:

$$\frac{\partial}{\partial t}(\bar{\rho}\tilde{c}) + \frac{\partial}{\partial x}(\bar{\rho}\tilde{u}\tilde{c}) = \frac{\partial}{\partial x} \left[ \bar{\rho}D_t \frac{\partial \tilde{c}}{\partial x} \right] + \rho_u U_t |\nabla \tilde{c}| \quad (9.38)$$

in the coordinate system moving with the speed:

$$U_t = U_{t,0} \left\{ 1 + \frac{\tau'}{t} \left[ \exp\left(-\frac{t}{\tau'}\right) - 1 \right] \right\}^{1/2} \quad (9.39)$$

from  $x = +\infty$  to  $x = -\infty$ . Here,  $\tilde{v} = \tilde{u} - U_t$ ,  $U_{t,0}$  is associated with the fully developed turbulent flame speed

$$U_{t,0} = Au' \times \text{Da}^{1/4} = Au' \times \left[ \frac{L}{u'\tau_c} \right]^{1/4} \quad (9.40)$$

where Da is the Damköhler number.

Two features of this strong turbulence limit behaviour are worth emphasizing. First, (9.38) is exactly the same as the standard balance equation of the turbulent diffusion theory. Therefore, (9.38) yields a permanent growth of the turbulent flame brush thickness  $\delta_\nu$ . this growth is controlled by the turbulent diffusion law in the case of a constant density. This trend is the peculiarity and the core of the reviewed elsewhere showing that such a regime of growing  $\delta_\nu$  occurs in many combustion devices.

Second, the turbulent flame speed  $U_t$  is incorporated into the model through (9.39) and (9.40), so the BANG-FIR is based on a certain submodel for the turbulent flame speed. Equation (9.39) accounts for the development of  $U$ , due to the fact that, as a kernel grows after ignition, it experiences a wider range of the turbulence serum. This submodel has been developed using certain ideas of Zimont. Equation (9.40) accounts for the effects of both turbulence and mixture characteristics on the fully developed flame speed. The same expression has been suggested by various authors using substantially different physical models, and has been found to be the best fit of an extensive experimental database associated with moderate turbulence. A very close expression ( $U_t \sim u'Ka^{-0.3}$  where  $\text{Ka} \sim R_t^{1/2}/Da$  and  $\text{Re}_t = u'L/\nu$  are the Karlovitz and Reynolds numbers, respectively,  $\nu$  is the kinematic viscosity of the mixture) well approximates extensive experimental databases

of Iverson R.M. [9.15] and Karpov et al. [9.19,9.22] in the case of near unity Lewis number,  $Le \cong 1$ .

Equation (9.40) predicts that the turbulent flame speed is controlled by the only physico-chemical characteristics of the mixture, which is a chemical time scale  $\tau_c$ . This feature is supported by the experimental investigations of Kido et al. [9.27] and offers the opportunity to account for two important effects. First, numerous experiments discussed elsewhere show that  $U_t$  is reduced by the Lewis number, the effect being very strong for lean hydrogen-air mixtures characterized by small  $Le$ . A submodel predicting these effects through the strong dependence of  $\tau_c$  ( $Le$ ) has been developed and can be incorporated into the program BANG-FIR.

Second, the ability to predict the effects of pressure on  $U_t$  appears to be of crucial importance for modeling SI engines. Both old experiments discussed elsewhere and recent investigations show that  $U_t$  is increased with pressure  $P$  despite the substantial decrease in  $U_L$ . For example, Kobayashi et al. [9.23] showed that  $U_t$  is roughly constant in the range of  $P = 1 - 30$  bar, despite the strong decrease in  $U_L$ . Numerous models employing  $U_L$  as the only physico-chemical characteristic of the mixture cannot predict such pressure effects. On the other hand, the BANG-FIR in (9.40) is in fact able to do so. Indeed, according to (9.40), the pressure may affect  $U_t$  only through  $\tau_c = \kappa_u/U_L^2$ . Since  $U_L \sim P^{-1/2}$  for the experiments of Takashi T. [9.16] and  $\kappa \sim P^{-1}$ , (9.40), predicts the constant  $\tau_c$  and  $U_t$  in line with the measurements.

$$\begin{aligned} \frac{\partial}{\partial t}(\bar{\rho}\tilde{c}) + \frac{\partial}{\partial x}(\bar{\rho}\tilde{v}\tilde{c}) &= \frac{\partial}{\partial x} \left[ \bar{\rho}(\kappa + D_i) \frac{\partial \tilde{c}}{\partial x} \right] + \\ &\frac{\bar{\rho}(1 - \tilde{c})}{t_0(1 + D_t/\kappa_b)} \exp\left(-\frac{\theta}{T}\right) \end{aligned} \quad (9.40a)$$

in the coordinate system moving where a speed  $U_t$  determined by (9.39), from  $x = +\infty$  to  $x = -\infty$  since the equation is similar to the standard balance equation of the thermal laminar flame theory (9.40), its steady limit solution can be easily obtained. It yields steady flame thickness.

$$\delta_t = \delta_L \left( 1 + \frac{D_{t,0}}{\kappa_b} \right) \quad (9.40b)$$

and the steady flame speed:

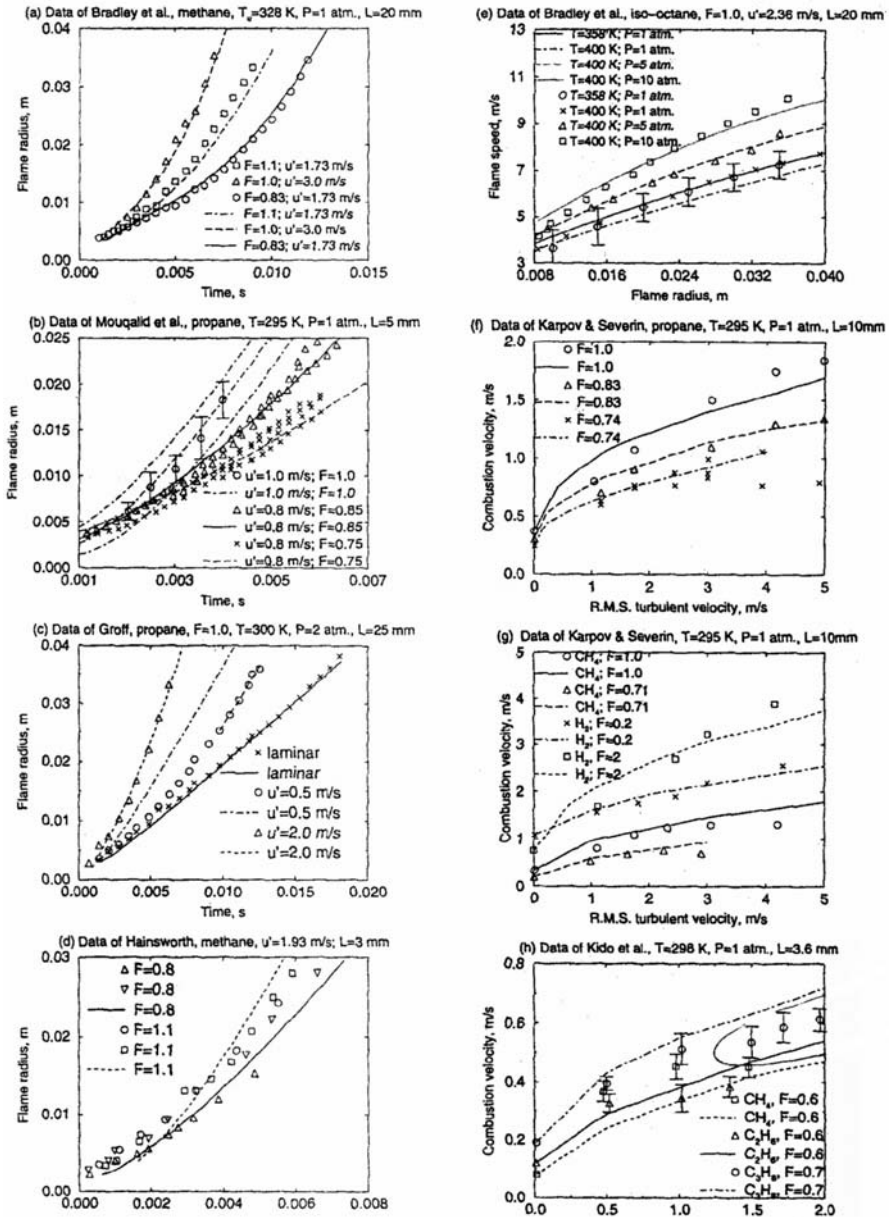
$$U_{t,0} = U_t + Au' \times Da^{1/4} \quad (9.40c)$$

in the laboratory coordinate system.

### Data

From the data already given, the following values are in addition  $P = 1.1$  40 bar. Based on  $k$ - $e$  turbulence model.

Plate 9.2. Flame radius versus flames-time and velocity





The turbulence characteristics are computed employing the version of the  $k$ - $\epsilon$  turbulence model implemented into the original code. For instance,  $u' = \sqrt{2\tilde{k}/3}$ ,  $L = C_d u'^3 / \tilde{\epsilon}$ ,  $\tau' = D_{t,0} / u'^2$ ,  $D_{t,0} = C_\mu \tilde{k}^2 / (\tilde{\epsilon} \sigma_c)$ , where  $C_\mu = 0.09$ ,  $\sigma_c = 0.9$ , and  $C_D = (9/4 C_\mu)^{3/4} = 0.302$ . The locally computed values of  $u'$ ,  $L$  and  $\tau'$  are used to calculate the time-dependent diffusivity and the mean reaction rate locally.

### *Analysis results*

Flame radius versus time versus flame speed for various forced out are plotted in Plate 9.2.

## 9.6 Development of Flight Model

This model now seeks to link the aerodynamics of debris elements with the damage caused when flying debris strikes a building or other structure. Initially, pieces of debris, such as stones or bits of steel, of which the three spatial dimensions are roughly equal, pieces of debris, will be examined, and later, some other shapes of debris will be introduced. The aerodynamic force on such an element in the direction of the blast vector can be written as:

$$\bar{T} = \frac{1}{2} \rho \nu^2 L^2 C = P^e \quad (9.41)$$

where  $\bar{T}$  is defined by (9.40) and  $\rho$  is the air density,  $\nu$  is the relative velocity between the blast and element,  $L$  is a typical dimension of the particle or debris and  $C_N$ , is a force coefficient that is assumed to be constant for the particular orientation of the element to the blast. In fact, most debris particles will have an irregular shape, and if the element is moved by the blast then  $C_N$ , is likely to change with time as the element rotates through different orientations defined by direction cosines, since elements come in all shapes and sizes, and the above theory can model this process.

If the element is at rest, perhaps lying on the ground or attached to a building, then  $\nu$  is equal to the blast speed  $\bar{U}$ . However, if the element starts moving in the blast wind direction,  $\nu$  will become less than  $\bar{U}$ , and the force  $\bar{T}$  correspondingly less. Loose materials will start to move under blast wind action if their blast loading exceeds the product of their weight and a “friction coefficient” having a wider definition than usual to account for the likelihood that elements may be trapped behind fixed connections. A broad distinction between “loose” objects with an effective friction coefficient of about unity, and “fixed” objects where the blast force required to break them loose is greater than their own weight will also be assumed. Let the ratio of these forces be defined as  $\bar{R}_1$ , which is the fixture strength integrity. For the great majority of real fixed objects, the value of  $\bar{R}_1$  is likely to be much greater than one, whereas for loose objects,  $\bar{R}_1$  will be of order unity.

The distinction becomes important when the conditions for flight to occur are considered. This will occur when the lift on an object exceeds its weight that is when:

$$\frac{1}{2} \rho_a \nu^2 L^2 C_L > M_1 g \quad (9.42)$$

or since

$$\begin{aligned} M_1 &= \rho_m L \\ \frac{1}{2} \rho_a \nu C_L &> \rho_m L g \end{aligned} \quad (9.43)$$

where  $\rho_m$  is the density of the material. At this stage it seems fair to note that “flight” for a piece of debris bears little resemblance to the flight of a streamlined object, such as an aerofoil or aircraft. To the level of accuracy, there is little distinction between  $C_l$ ,  $C_N$ , and  $C_D$ , and the use of a generalised force coefficient  $\bar{J}$  is more appropriate, of which the value will probably be close to unity for the typically bluff bodies involved. The effective friction coefficient of loose objects is now assumed to be about one. The following scenario can be set up: in the steadily increasing blast wind, very poorly restrained objects with  $\bar{R}_1 < 1$  (fixing strength less than their weight) will come loose from their fixings when  $1/2 \rho_a \bar{U}^2 \bar{T} > \rho_m L g \bar{R}_1$ , but the aerodynamic force will be insufficient for them to “fly”, and they will fall to the ground and remain there with now  $\bar{R}_1$  now equal to one until  $1/2 \rho_a \bar{U}^2 \bar{T} > \rho_m L g$  when they begin to move downwind and become a potential hazard. In reality, the value of  $\bar{R}_1$  depends on physical connections that vary.

Better restrained objects ( $\bar{R}_1 > 1$ ) will remain attached until

$$\frac{1}{2} \rho_a \bar{U}^2 \bar{T} > \rho_m L g \bar{R}_1 \quad (9.44)$$

they will also come loose, but since the value of  $\bar{U}$  at which this happens is higher than the minimum required for flight, they will travel further, accelerating towards the blast wind speed  $\bar{U}$ , losing relative speed and falling eventually to the ground if the initial value of  $\bar{R}_1$  was not much above one. In this model it is assumed that elements forming missiles reach a proportion of  $\nu_b$  the blast wind speed, ignoring for the moment how  $\nu_b$  might vary with the other parameters of the problem.

Although (9.44) has been written as an inequality, in the increased blast wind speed of a typhoon a simplest assumption would be that each object flies as soon as condition of the (9.44) is reached, so that the condition for flight becomes:

$$\frac{1}{2} \rho_a \bar{U}^2 \bar{T} > \rho_m L g \bar{R}_1 \quad (9.45)$$

or

$$\bar{U}^2 = 2(\rho_m / \rho_a)(\bar{R}_1 / \bar{T}) L g \quad (9.46)$$

in this scenario, blast wind speed increases steadily from a low rate, and as soon as (9.45) is satisfied for a particular element, that element becomes an

airborne missile. This implies that for fixed values of  $\overline{R_1}$  and  $\rho_m$ , smaller elements such as dust particles become airborne first, and that as blast wind speed regularly increases, larger and larger particles become missiles. Also heavier particles, higher  $\rho_m$ , require higher blast wind speed in order to become airborne.

A similar analysis can be performed for sheet materials, such as plywood, or steel columns, corrugated iron, typical of material torn from a building in high blast winds. This time the equation governing the flight criteria becomes:

$$\bar{U}^2 = 2(\rho_m/\rho_a)(\overline{R_1}/\bar{T})\bar{t}_h g M_1 \quad (9.47)$$

where  $\bar{t}_h$  is the depth of the section of elemental sheet. Whilst this equation resembles its equivalent for solid particles, (9.46), there is a crucial difference. This time, the initial flight speed is dependent, not on size, but on mass/unit area, the product of density and thickness. The analytical flight equation for flying rod missile of length  $L$  and diameter  $d$  can be written as:

$$\bar{U}^2 = \pi/2(\rho_m/\rho_a)(\overline{R_1}/\bar{T})dg \quad (9.48)$$

A similar flight equation can be written for particle of  $l_1$  or  $d_1$ , a diameter:

$$\bar{U}^2 = \pi/2(\rho_m/\rho_a)(\overline{R_1}/\bar{T})d_1g \quad (9.49)$$

## 9.7 Damage Function for a Scenario

When such a missile strikes a building, damage to the façade may or may not occur. Initially, it might be assumed that the amount of damage sustained is proportional to the missile kinetic energy. A constant of proportionality of unity will be used, remembering though that the actual damage sustained is likely to be a proportion of the missiles total kinetic energy. This is also true for the oozing out of damaged missiles. An expression for the “damage” caused by a single missile then becomes:

$$D_m = \frac{1}{2}\rho_m L^3 v_a^2 \bar{U}^2 \quad (9.50)$$

It is now possible to combine this with the flight condition for a solid three-dimensional object (9.45) and eliminate the typical missile dimension  $L$ . The damage function then becomes:

$$D_m = \frac{1}{16}\rho_m \{(\bar{T}\rho_a)/(\rho_m\overline{R_1})\}^3 v_a^2 \bar{U}^8 \quad (9.51)$$

Because of the composition of the flight condition (9.47) and (9.48) and their different dependence on  $\bar{U}$  for the sheets and rod missile types compared the solid objects, the damage function becomes a function of only  $\bar{U}^4$  in these cases. This very strong dependence on  $\bar{U}$  arises because for given missile density  $\rho_m$  each blast wind speed is associated with a particular missile size  $L$ , and as  $\bar{U}$  increases the damage inflicted by the corresponding missile size

**Table 9.8.** Final flight speeds (m/s) of elements and their kinetic energy J/m<sup>2</sup>

Element type	Theoretical final speed (m/s)	Blast wind speed (m/s)	KE(J/m <sup>2</sup> )
25 mm solid $\rho_m = 150 \text{ Kg/m}^3$	1.35	10	95
	2.31		
	3.80		
25 mm hollow $\rho_m = 94 \text{ Kg/m}^3$	1.22	20	1500
	2.65	40	2400
	4.35		
50 mm solid $\rho_m = 135 \text{ Kg/m}^3$	1.20	Multiplying factors	
	2.27		
	3.97		
50 mm hollow $\rho_m = 42 \text{ Kg/m}^3$	1.33	for 1.9 kg/m <sup>2</sup> for 10 m/s	
	2.45	for 1.5 kg/m <sup>2</sup> for 20 m/s	
	3.73		
100 mm solid $\rho_m = 114 \text{ Kg/m}^3$	1.01	for 30 kg/m <sup>2</sup> for 40 m/s	
	1.91		
	3.63		
100 mm hollow $\rho_m = 56 \text{ Kg/m}^3$	1.08	(a) stone size = 2 mm	
	1.98	KE = 0.00017 (J)	
	3.42		
100 mm hollow $\rho_m = 23.6 \text{ Kg/m}^3$	1.37	stone size = 9 mm	
	2.39	KE = 0.04 (J)	
	4.20		
200 mm hollow $\rho_m = 23.2 \text{ Kg/m}^3$	1.02	stone size = 37 mm	
	1.84	KE = 110 (J)	
	3.35		

also increases rapidly. It is instructive to examine some typical cases to see the implications of (9.50). Table 9.8 gives the values of the damage function for solid objects. At blast wind speeds of only 10 m/s the wooden missile will create “damage” of 0.05  $J$ , the stone 0.0017  $J$ . these levels of “damage” are probably below the threshold of real damage, though at higher speeds real damage becomes possible for solid objects as well as for sheets and rods. Average value  $\bar{R}_1 = 0.64$  for sheet material is considered. For rod material  $\bar{R}_1 = 0.5$  is considered a suitable figure for the analysis.

Let the ejecting force  $\{\Delta P_i^e\} = T_i$  and is now the impulse when multiplied by the time of ejection. This may be the impulsive force for any object of size 0.0001  $L$  to  $L = 4.57$  m, which is the column length, particularly in WTC in one floor area.

An impulse is defined as a force multiplied by time, such that:

$$\bar{T}_i(t) = \int F dt \tag{9.52}$$

where  $\bar{T}_i(t)$  is the impulse,  $F$  is the force and  $t$  is the time. The momentum of a body is the product of its mass and its velocity:

$$\text{momentum} = M_1\nu \tag{9.53}$$

where  $M_1$  is the mass and  $\nu$  is the velocity =  $dx/dt$ . Both velocity and momentum are vector quantities; their directions are the same. If a body is moving with a constant velocity, its momentum is constant. If velocity is to be changed, a force  $F$  must act on the body. It follows that a force  $F$  must act in order to change the momentum.

$$F = M_1d\nu/dt \tag{9.53a}$$

or

$$Fdt = M_1d\nu \tag{9.53b}$$

Figure 9.2 shows a missile projected at a velocity  $u$  from a position 0. At 0,  $x, \dot{x}$ , and  $\ddot{x}$  are all zero. The only force on the flight is equal to  $M_1g$ . Hence  $y$ , the acceleration in the vertical direction, is  $-g$ .

The general forms of the velocity and distance equations are:

$$\nu = u + gt \tag{9.54}$$

$$s = ut + \frac{1}{2}gt^2$$

$$\dot{x} = u \cos a, \dot{y} = u \sin a - gt \tag{9.55}$$

$$x = (u \cos a)t; y = (u \sin a)t - \frac{1}{2}gt^2 \tag{9.56}$$

$$\ddot{x} = 0; y = -g \tag{9.57}$$

By elimination of  $t$  from (9.24), the trajectory equation is written in a parabolic form as:

$$y = x \tan a - (gx^2 \sec^2 a/2u^2) \tag{9.58}$$

The velocity  $\nu$  of the missile during flight at any instant in time is given by:

$$\nu = \sqrt{(x^2 + y^2)}, \quad \text{with } a = \tan^{-1}(\dot{y}/\dot{x}) \tag{9.59}$$

$$\dot{y}/\dot{x} = (dy/dt)/(dx/dt) = dy/dx$$

the direction of the velocity at any instant is along the tangent to the path for that particular instant. If the missile is projected in a building from the aircraft at an angle below its level in order to hit the target at the ground level (the aircraft level is treated as horizontal), (9.50) becomes:

$$y = x \tan a - (gx^2 \sec^2 a/2u^2) \tag{9.60}$$

and all negative signs in (9.47) and in (9.48) related to  $g$  are *positive*.

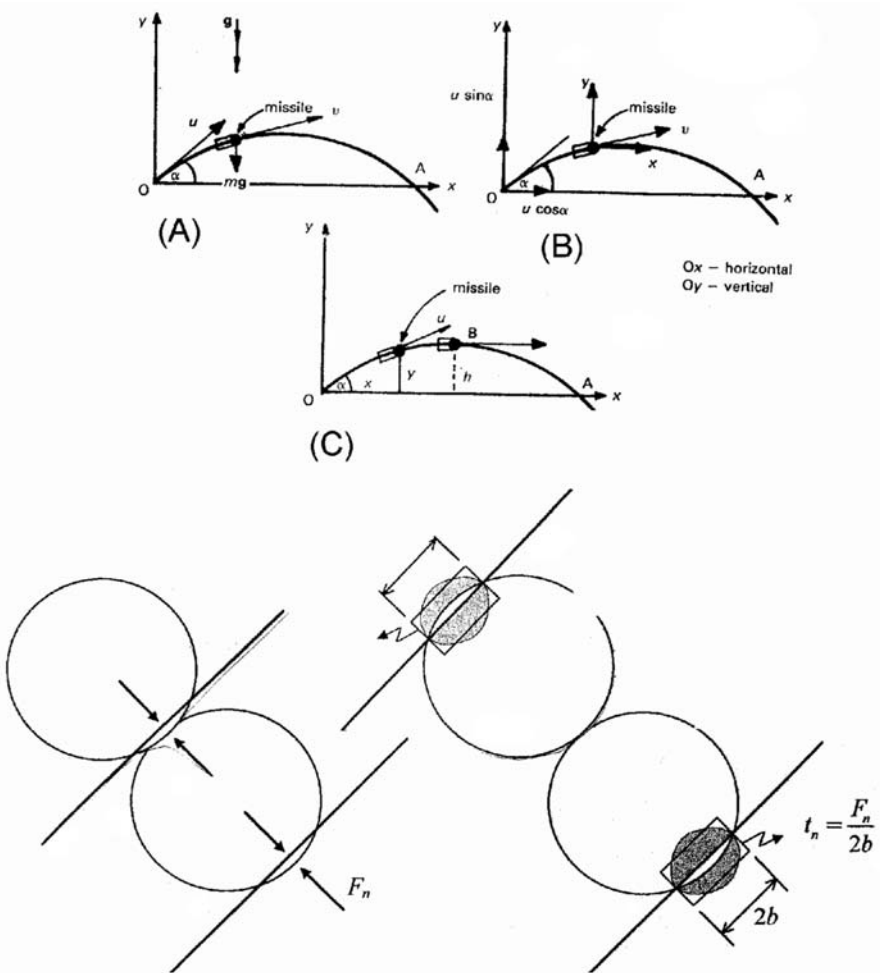


Fig. 9.2. Element of a debris plight

### 9.8 Test Example on WTC Tower Collapse

In this text it is recommended to examine the test data in Chap. 8 for dimensions, loadings and the oil/structure interaction. Apart from the given data, it is recommended to use four plane waves from left, right, top and bottom boundaries.

To get data for the reconstruction, it is solved the wave equation with four plane waves of the form with  $k = 100$ . The time interval is  $[0, 0.4]$  and is divided into four phases, 0.1 each: first, one plane wave starts at the left boundary  $x_1 = 0$  of  $\Omega$  and goes through the  $\Omega_{FEM}$  to the right boundary  $x_1 = 1$ , then at time 0.1 a second wave starts at the right boundary  $x_1 = 1$

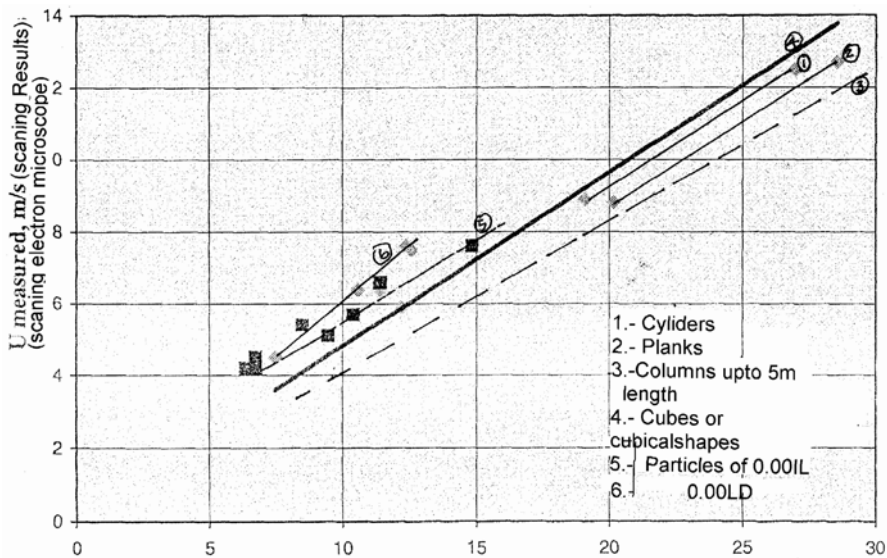


Fig. 9.3.  $\{2Lg(\rho_m/\rho_\alpha)\}^{1/2}$ , m/s (theoretical results)

of  $\Omega$  and goes to the left, and the third and fourth plane waves begin at time 0.2 and 0.3 at the top/bottom boundaries of  $\Omega_{FDM}$ , respectively, and goes to the top/bottom boundaries. They are used absorbing boundary conditions on the other boundaries. The observation points are placed around the object.

The data for the reconstruction is obtained by solving the direct problem with  $c = 2$  in the scatter and  $c = 1$  outside.

In Fig.9.3, it is presented the computed exact solution of the problem inside  $\Omega_{FEM}$  with four plane waves and absorbing boundary conditions at all the boundaries. the computer simulations of the reconstructed scatterer on the adaptive refined meshes are shown in Fig.9.3. First, it is computed parameter  $c$ , using the reconstruction algorithm on the coarse grid. Then, the coarse grid is refined by using the estimate, and the previously computed parameter  $c$  is interpolated into a new refined mesh. This value is used as starting value for computations of the new mesh. Next, all the steps of the reconstruction algorithm are performed and the previously described procedure of the interpolation of the computed parameter  $c$  is repeated into the refined mesh until the desired tolerance is achieved.

### 9.8.1 Additional Data Due to Explosion

Explosion at exterior face = 172.369 KN/m<sup>2</sup>

$\bar{t}_h$  varies 2.6 mm to 12 mm

$\nu = 0$  to 0.3

$\rho_m = 2224$  kg/m<sup>2</sup>

$$\rho = 1800 \text{ kg/m}^2$$

$$E_s \text{ for steel} = 209 \text{ GN/m}^2$$

$$\begin{aligned} \text{Explosion load} &= 33 \text{ tons of TNT for Oklahoma} \\ &= 0.6 \text{ tons of TNT for WTC Tower} \end{aligned}$$

$$c_D: \text{ drag coefficient} = 1.0$$

$$P_o: \text{ ambient atm. pressure} = 1 \text{ bar}$$

$$P_{so} = 6784 \frac{W}{R^3} + 93 \left( \frac{W}{R^3} \right)^{1/2}$$

$$k_B: \text{ short pulse duration}$$

$$= 10.23 \frac{W^{1/2}}{\sqrt{P_{SO}}}, P_{SO} < 70 \text{ bar}$$

$$= 20.77 \frac{W^{1/3}}{P_{SO}^{2/3}}, P_{SO} \geq 70 \text{ bar}$$

$$f_y = 400 \text{ N/m}^2; f_{dy} = 1.2 f_y = 552 \text{ N/m}^2$$

$$I: \text{ impulse load} = 5095 \text{ KPa} \cdot \text{ms}$$

$$t_R: 0.28 \text{ to } 0.3 \text{ seconds}$$

When the objects scatter, the direction cosine matrix is needed to position the flying objects in debris. The direction cosine matrix is given in Table 9.5, which can be linked up to any finite element program or finite discrete element program. A typical compliance material matrix [D] (Table 9.1 and 9.2) is chosen for the flying object in which E and V can be different for different material constituting the debris.

Referring to Table 9.5, when the incremental slip occurs under impact load, the bond between joint and member is broken. The element nodal force  $\bar{T}_i = \{\Delta P_i^c\}$  is the component of the impact force that ejects the elements of debris. The minimum  $L$  value chosen is  $0.001 L = dL$ . The maximum value  $L$  for the program BANG-FIR is taken to be  $L = 15 \text{ ft}$  (4.57 m).

### 9.8.1.1 Check on Turbulent Velocity Data

Plate 9.2 gives a relationship between flame radius and time and combustion velocities versus r.m.s. turbulent velocities. The data given is to be simulated into program BANG-FIR.

### 9.8.1.2 Scanning Approach of Existing Scenario

Finite element analysis is related to scanning method, which examines the existing data and then considers these relations to the initial flight speed of rectangular shapes and steel sheets. Figure 9.3 shows the flight speed for cube shapes and sheets. In WTC scenario, the total number of missiles generated is determined by the highest speed achieved. The time of exposure



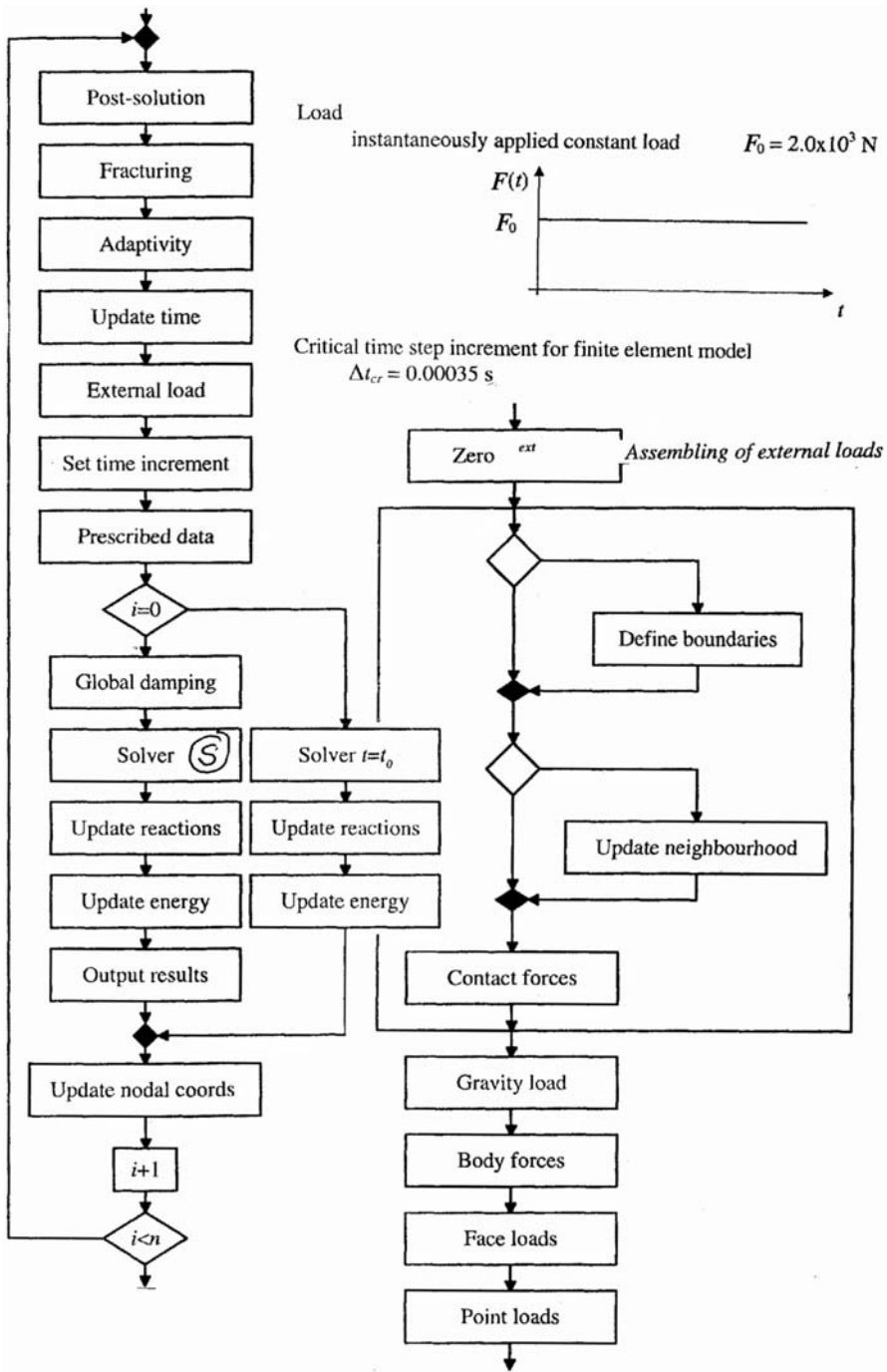
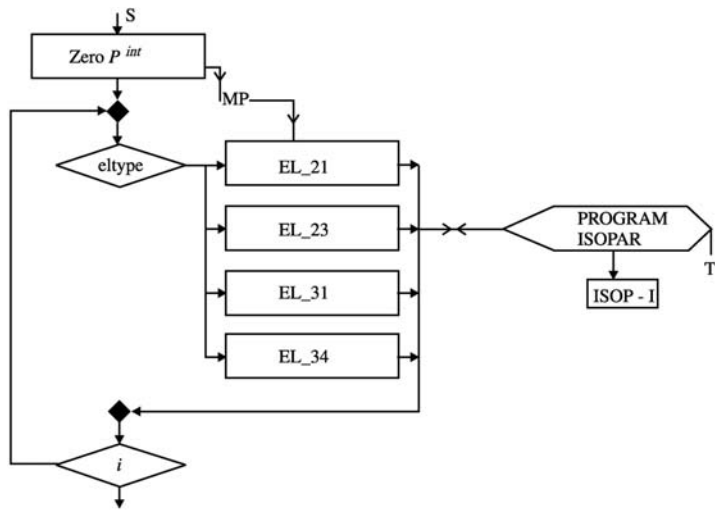


Fig. 9.4. Explicit solver: central difference time integration scheme



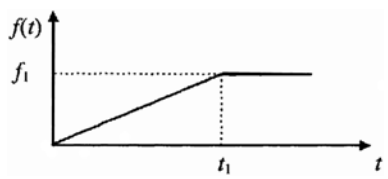
Material

- linear, elastic, isotropic – determination of outer boundaries
  - density – neighbourhood update: – body location mapping,
  - Young’s modulus – space bisection,
  - Poisson’s ratio – bounding box inter-section search,
- contact forces: – local resolution, – evaluation of contact tractions
- **Scan mapping and calculation**
  - **Data Assessment**

$\rho = 1.0 \times 10^3 \text{ kg/m}^3$   
 $E = 1.0 \times 10^{10} \text{ N/m}^2$   
 $\nu = 0.0$

Load II

Slowly applied load  
 $f_1 = 2.0 \times 10^3 \text{ N}$   
 $t_1 = 3.0 \text{ s}$



Critical time step increment for finite element model

$\Delta t_{cr} = 0.00035 \text{ s}$   
 Load III  
 impulse load

$f_1 = 2.0 \times 10^3 \text{ N}$   
 $t_1 = 0.001 \text{ s}$   
 $t_2 = 0.002 \text{ s}$

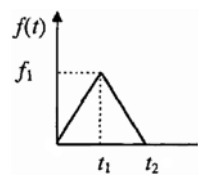


Fig. 9.5. Finite element post-solution – calculation of internal forces

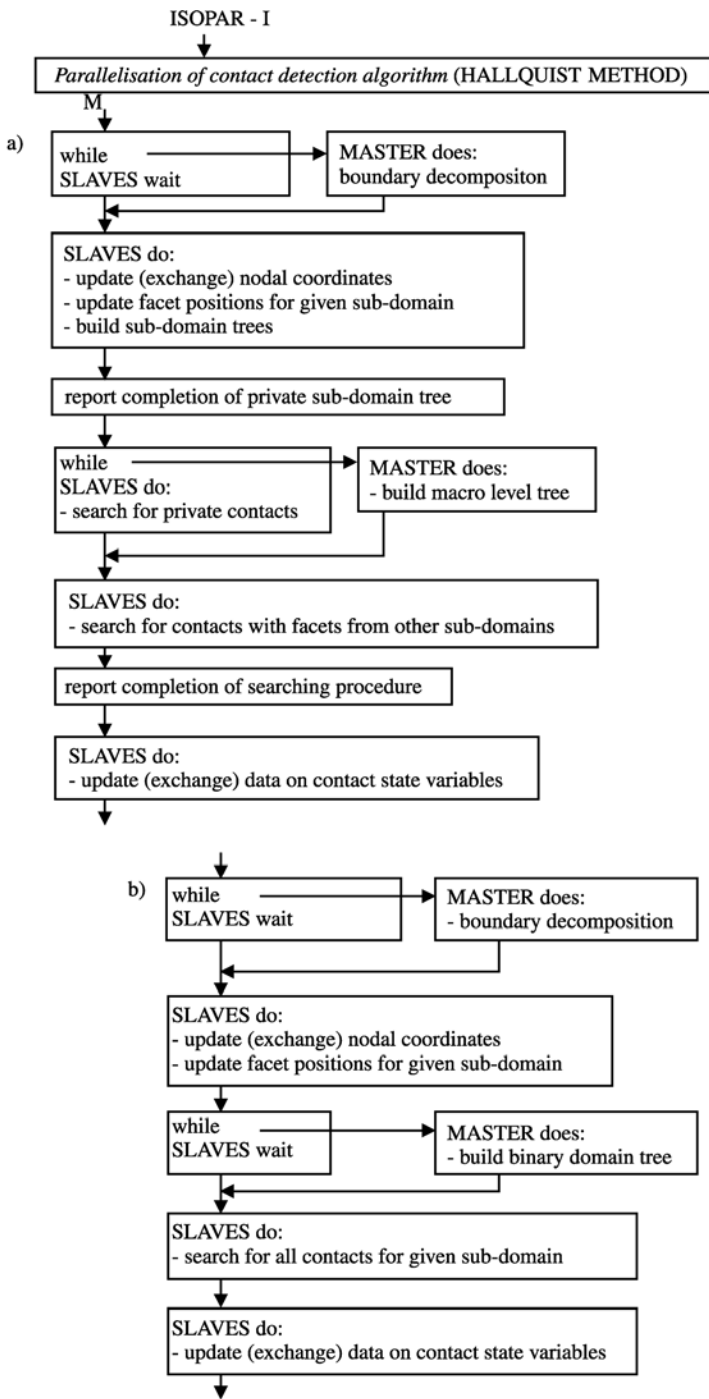


Fig. 9.6. Flow chart for program ISOPAR

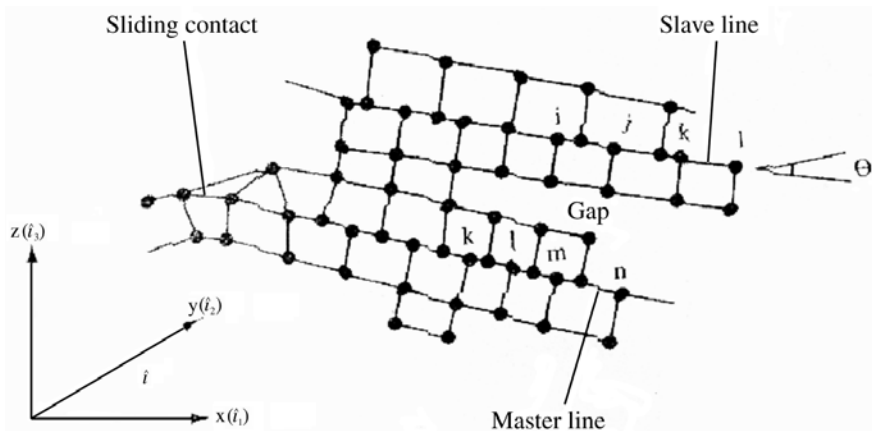
of the fire storm is important only in that it affects the reducing value of  $\bar{R}_1$ , as objects fatigue and break loose from their attachment or mountings. Estimates of the availability of missiles might best be determined by an analysis of the wreckage left in the aftermath of a typical disaster. For WTC scanning and the velocity values of  $\bar{U}$  (m/s) are compared with theoretical values of  $\left\{2Lg \rho_m/\rho_a\right\}^{1/2}$  m/s. They are plotted as in Fig.9.3. The results being straight-lines are truly established since the analysis is validated, no further tests are needed for other shapes or objects. The theoretical analysis is based on  $\left\{2Lg \rho_m/\rho_a\right\}^{1/2}$  has been adopted throughout.

Program ISOPAR has been modified on the lines suggested in Figs.9.4 to 9.6.

## Explanatory Notes on Analysis

### Hallquist et al. Method

Hallquist et al. [9.188] developed a useful concept of master and slave nodes sliding on each other. As shown in Fig.9.7, slave nodes are constrained to slide on master segments after impact occurs and must remain on a master segment until a tensile interface force develops. The zone in which a slave segment exists is called a slave zone. A separation between the slave and the master line is known as void. The following basic principles apply at the interface:



$k_n$  = Interface normal stiffness  $m \bar{U}$  material stiffness matrix  
 Values varied as  $10^3$  to  $10^6$  n/mm<sup>3</sup>

Fig. 9.7. Hallquist contact method (modified by Bangash)

Hallquist et al. [9.188] gave a useful demonstration of the identification of the contact point, which is the point on the master segment to the slave node  $n_s$ , and which finally becomes non-trivial during the execution of the analyses. When the master segment  $\hat{t}$  is given the parametric representation and  $t$  is the position vector drawn to the slave node  $n_s$ , the contact point co-ordinate must satisfy the following equations:

$$\frac{\partial \hat{r}}{\partial \xi}(\xi_c, \eta_c) \times [\hat{t} - \hat{r}(\xi_c, \eta_c)] = 0$$

$$\frac{\partial \hat{r}}{\partial \eta}(\xi_c, \eta_c) \times [\hat{t} - \hat{r}(\xi_c, \eta_c)] = 0$$

where  $(\xi_c, \eta_c)$  are the coordinates on the master surface segments  $S_i$ .

Where penetration through the master segment  $S_i$  occurs, the slave node  $n_s$  (containing its contact point) can be identified using the interface vector  $f_s$ .

$$f_s = -lk_i n_i \quad \text{if } l < 0$$

to the degree of freedom corresponding to  $n_s$ ,

$$f_m^i = N_i(\xi_c, \eta_c) f_s \quad \text{if } l < 0$$

where

$$l = \hat{n}_i [\hat{t} - \hat{r}(\xi_c, \eta_c)] < 0$$

a unit normal

$$\hat{n}_i = \hat{n}_i(\xi_c, \eta_c); \quad \hat{t}_i = \hat{n}_i \sum_{j=1}^n N_j (F_1)^j(t)$$

$$k_i = t f_{s_i} K_i A_i^2 / V_i$$

where

$$(F_1)^j(t) = \text{impact at the } j\text{th node}$$

$$K = \text{stiffness factor}$$

$$K_i, V_i, A_i = \text{bulk modulus, volume and face area, respectively}$$

$$f_{s_i} = \text{scale factor normally defaulted to 0.10}$$

$$N_i = \frac{1}{4}(1 + \xi \xi_i)(1 + \eta \eta_i) \text{ for a 4-node linear surface}$$

Bangash extended this useful analysis for other shape functions, such as  $N_i$  for 8-noded and 12-noded elements. On the basis of this theory and owing to the non-availability of the original computer source, a new sub-program CONTACT was written in association with the program ISOPAR. The sub-program CONTACT is in three dimensions.

$$\{\hat{\mathbf{F}}\Delta_N\} = [K_{\gamma\gamma}]_i \{U_\gamma\}_i = [\Sigma k] \{\Sigma \Delta_i, \Delta_j, \dots\} = \{\hat{\mathbf{F}}_{i,j}, \dots\} + \{\pm \mu \hat{\mathbf{F}}_n, \dots \pm k \Delta_i, \dots\}$$

$\Delta_{sl}$  = distance of sliding

$$= (\Delta_j - \Delta_i) - \frac{\mu |\hat{\mathbf{F}}_n|}{[K_{\gamma\gamma}]}$$

$\mu$  = friction

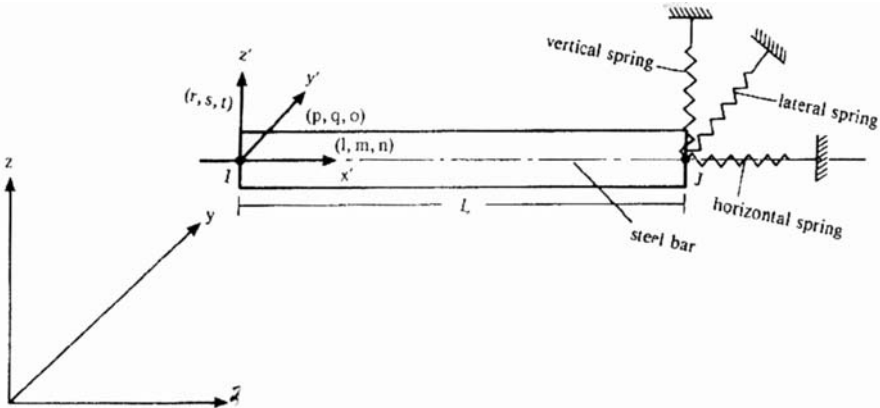
$$\{\hat{\mathbf{F}}_{SN}\} < \{\mu \hat{\mathbf{F}}_N\} \quad \text{no sliding}$$

$$\geq \{\mu \hat{\mathbf{F}}_N\} \quad \text{sliding}$$

$$= 0 \quad \text{contact broken}$$

$$\theta = \cos^{-1} \frac{X}{\gamma} \quad \text{or} \quad \sin^{-1} \frac{Y}{\gamma}$$

**Table 9.9.** Elements of debris with direction cosines



**Fig. 9.8.**

**Debris as a rod of length  $L$**

$L \neq$  varies from 5 m to 0.01 m

Let  $I$  and  $J$  (Fig.9.8) be line element nodes.  $x, y, z$  and  $x', y', z'$  are global and local co-ordinates. The direction cosines of the local axes  $(x', y', z')$  with respect to the global axes  $(x, y, z)$  are  $(l, m, n), (p, q, \theta), (r, s, t)$ . Let  $(I, J)$  be the line element nodes. the direction cosines are computed as follows:

$$\begin{aligned}
l &= (y_J - x_I)/L & m &= (y_J - x_I)/L \\
n &= (z_J - z_I)/L & p &= m/\sqrt{1-n^2} \\
q &= l/\sqrt{1-n^2} & r &= -l/\sqrt{1-n^2} \\
s &= -mn/\sqrt{1-n^2} & t &= \sqrt{1-n^2} \\
L &= \sqrt{(x_J - x_I)^2 + (y_J - y_I)^2 + (z_J - z_I)^2}
\end{aligned} \tag{a}$$

Let  $\Delta S_H$ ,  $\Delta S_V$  and  $\Delta S_L$  be the incremental slip in the horizontal, vertical and lateral directions of the steel element. The incremental relationship between the slip and the nodal displacements can be written as:

$$\begin{Bmatrix} \Delta S_H \\ \Delta S_V \\ \Delta S_L \end{Bmatrix} = \begin{bmatrix} -l & -m & -n & l & m & n \\ -p & -q & -\theta & p & q & \theta \\ -r & -s & -t & r & s & t \end{bmatrix} = \begin{Bmatrix} \delta_{ix} \\ \delta_{iy} \\ \delta_{iz} \\ \delta_{jx} \\ \delta_{jy} \\ \delta_{jz} \end{Bmatrix} \tag{b}$$

or

$$\{\Delta S\}_{H,V,L} = [T_b]_{l,m,n}^{r,s,t} \times \{\Delta U^e\} \tag{c}$$

where  $(T_b)$  is the transformation matrix and  $\{\Delta U^e\}$  are the global element displacements.

The local incremental bond stress and bond-slip may be written

$$\begin{Bmatrix} \Delta \sigma_{Hi} \\ \Delta \sigma_{Vi} \\ \Delta \sigma_{Li} \end{Bmatrix} = \begin{bmatrix} k_{Hi} & 0 & 0 \\ 0 & k_{Vi} & 0 \\ 0 & 0 & k_{Li} \end{bmatrix} = \begin{Bmatrix} \Delta S_{Hi} \\ \Delta S_{Vi} \\ \Delta S_{Li} \end{Bmatrix} \tag{d}$$

or  $K_H$ ,  $K_V$  and  $K_L$  are the spring constants or

$$\overline{T}_i = \Delta \sigma_{bi}^e = K_{bi} \Delta S_{Hi}^e \tag{e}$$

The ejecting nodal force vector can be written as

$$\Delta \overline{T}_i^e = \pi d L [T_b]^{T^n} \Delta \sigma_{bi}^e \tag{f}$$

and the element stiffness matrix assumes the form:

$$[K_L]_{6 \times 6} = \pi d L [T_b]^{T^n} k_{bi} [T_b]^{T^n} \tag{g}$$

where  $[T_b]$  is the transformation matrix given in (b).  $T''$  transpose

## Program BANG-FIR in Combination with BANG-BLAST and BANG-IMPACT

The finite finite element algorithms developed in this study in a new computer program aimed at solving transient, dynamic problems in continuum mechanics involving large number of contacting bodies. The program BANG-FIR is written using super computers with dynamic memory management, with highly post-solution procedures embodying algorithms designed to simulate the behaviour of all kinds of solid materials, thus enabling the accomplishment of one of the most important tasks that constitute the finite element method. The flow chart presented outlines the structure of the finite element post-solution procedure. The calculation and the assembling of the nodal forces is arranged according to the type of finite element used in discretisation. Scanning process examines pictorially the items in question. The position vectors are evaluated and is formed the input for the dynamic blast analysis BANG-BLAST linked with the program BANG-FIR, which considers all aspects of fire analysis, as described earlier. BANG-IMPACT plays a part in evaluating impact effects due to aircraft crashes. They are then linked to the program ISOPAR for the finite element analysis and the damage scenario. In some cases, “explicit solver” is asked for the central difference analysis, which is necessary together with the finite element analysis for dynamic elastic wave evaluation, for which the analytical model is given in this section. Where dynamic contact due to elements impacting themselves in the creation of damage scenario, MASTER AND SLAVE NODES are considered for contact detection and elemental damage analysis. The function of the PILE COLLECTION is involved to bring to rest all ejected elements during flights in WINDFIRE.

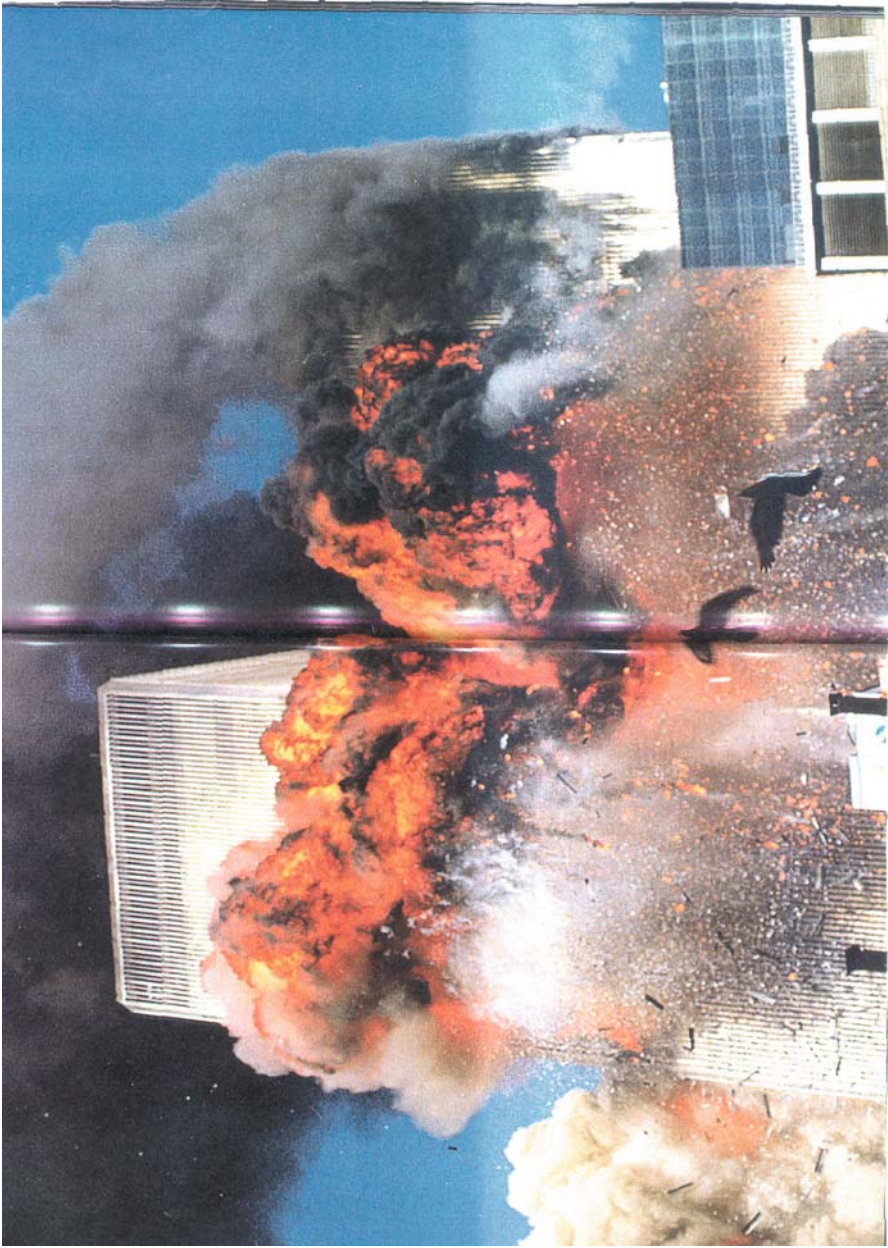
## Analysis of Results

Based on the numerical model and analysis described in this section, and fully tested, the combined design scenario covering aircraft impact, blast loads, fire load and zones of dismantling elements from the WTC-1, the program ISOPAR devised a disaster scenario, which is shown in Plate 9.3 and Plate 9.3.a. A great deal of similarity in various zones has been obtained. A number of assumptions on the geometry of dismantled elements are considered. It was difficult to simulate the dirt associated with fire. It was assumed that the dirt particle diameter was  $L = 0.001$  m as the minimum. The maximum length of the elements is approximately taken as around  $L \approx 5.0$  m. variable speeds and the nature of fire were considered. Chapter 8 gives also data that was included and for reasons of space could not be repeated: although the  $\Delta es$  as  $|e|$  scenarios are very similar, more research is needed to better approach the analytical results.

Plate 9.4 gives the computed version of the WTC disaster scenario based on the numerical model given in this chapter and program ISOPAR.



**Plate 9.3.** WTC-1 on fire – flume/smoke/fire scenario (courtesy FEMA, Washington D.C. 2002). Used as initial data for checking with PATRAN and BANG-FIRE

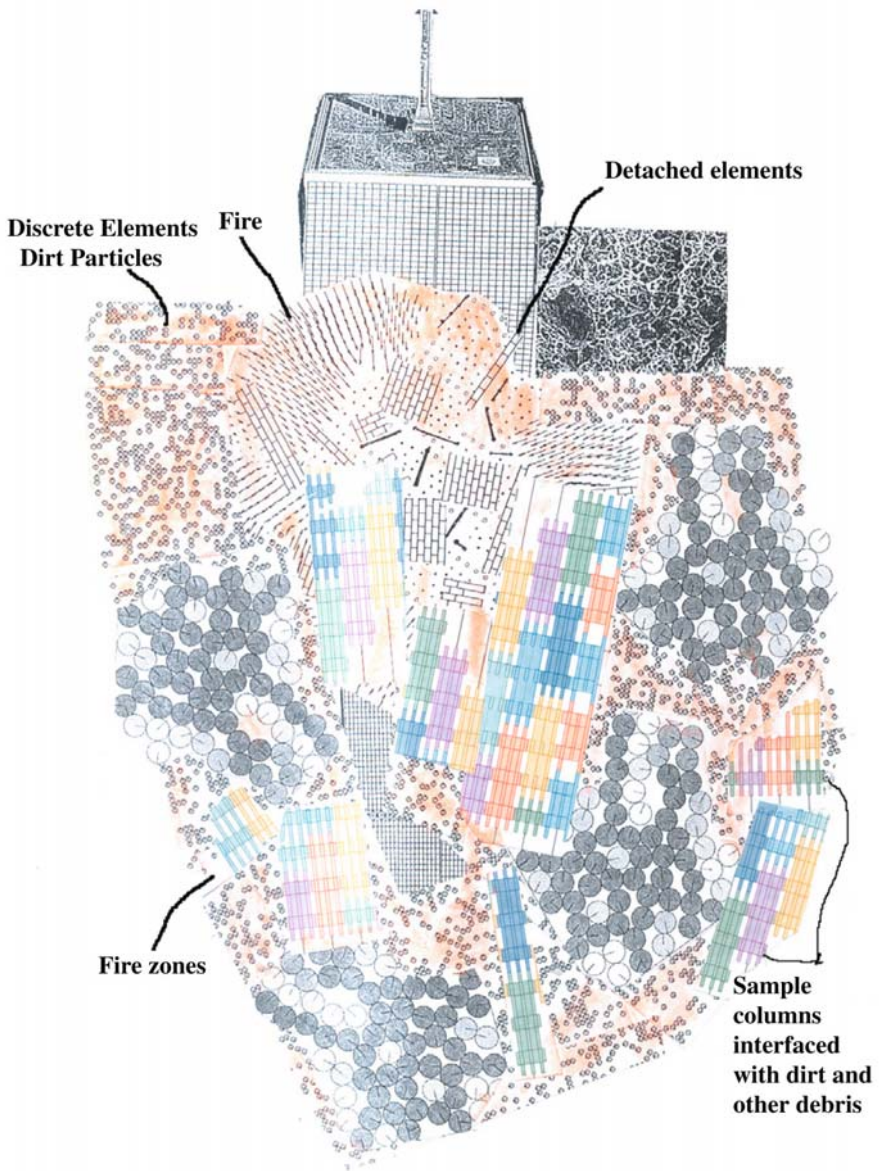


**Plate 9.3a.** WTC-1 on fire– dejected elements. Computational damage scenario – local face area (using finite element/PATRAN/FEMVIEW 2003)

---



**Plate 9.4.** Computed damage scenario using finite element/PATRAN-FRONTENDED (finite element linked with scanning) – fire and debris



## References

- [9.1] Talio KV, Colella P (1997) A multi-fluid CFD turbulent entrainment combustion model: formulation and one-dimensional results. SAE Paper No 972880
- [9.2] Lipatnikov AN, Chomiak J (1997) A simple model of unsteady turbulent flame propagation. SAE Paper No 972993
- [9.3] Zimont VL (1977) Computations of turbulent combustion of partially premixed gases, chemical physics of combustion and explosion processes. Combustion of multi-phase and gas systems, OLKhH, Chernogolovka, pp. 77–80 (in Russian)
- [9.4] Zimont VL, Polifke W, Bettelini M, and Weisenstein W (1997) An efficient computational model for premixed turbulent combustion at high Reynolds number based on a turbulent flame speed closure. Proc. Int. Gas Turbine and Aerospace Congress and Exhibition, Orlando
- [9.5] FIRE manual (1996) version 6.2b, AVL LIST GmbH, Graz
- [9.6] Bray KNC, Moss JB (1977) A unified statistical model for the premixed turbulent flame. *Acta Astronautica* 4:291–319
- [9.7] Hinze JO (1975) *Turbulence*, 2nd edn, McGraw-Hill, New York
- [9.8] Launder BE, Spalding DB (1972) *Mathematical models of turbulence*. Academic Press, London
- [9.9] Zel'dovich YaB, Barenblatt GI, Librovich VB, Makhviladze GM (1985) *The mathematical theory of combustion and explosions*. Prentice Hall, New York
- [9.10] Lipatnikov AN, Chomiak J (1997) Modeling of turbulent flame propagation. Annual Report 98/2, Chalmers University of Technology, Department of Thermo- and Fluid Dynamics, Göteborg
- [9.11] Prudnikov AG (1964) Combustion of homogenous fuel-air mixtures in turbulent flows. In: Raushenbakh BV et al. (eds.) *Physical basis of processes in combustion chambers of ate-breathing engines*. Mashinostroenie, Moscow, Chap. 5, pp. 255–347 (in Russian)
- [9.12] Kuznetsov VR (1976). *Izvestia Akademii Nauk SSSR, Mekhanika Zhikosti i Gaza* 5:3 (in Russian)
- [9.13] Frost VA (1977) Combustion and explosion. *Nauka*, Moscow, pp. 361–365 (in Russian)
- [9.14] Zimont VL (1979) Theory of turbulent combustion of a homogeneous fuel mixture at high Reynolds number. *Combustion, Explosions, and Shock Waves* 15:305–311
- [9.15] Iverson RM (2005) Debris-flow mechanics. In: Jakob M, Hungr O (eds.) *Debris-flow hazards and related phenomena*, Springer, pp. 105–134; Iverson RM (1997) The physics of debris flow. *Review of Geophysics* 35:245–296; Iverson RM, Schilling SP, Vallance JW (1998) Objective delineation of lahar-inundation hazard zones. *Geological Society of America Bulletin* 110(8):972–984
- [9.16] Takashi T (1981) Mechanical characteristics of debris flow. *J. of the Hydraulics Division, ASCE*, HY8:1153–1169
- [9.17] Gülder ÖL (1990) Turbulent premixed combustion modeling using fractal geometry. 23rd Symposium (Int.) on Combustion, The Combustion Institute, Pittsburgh, pp. 835–841

- [9.18] Asshurst WT, Checkel MD, Ting DS-K (1994) The eddy structure model of turbulent flamelet propagation. The expanding spherical and steady planar cases. *Combustion Science and Technology* 99:51–74
- [9.19] Karpov VP, Severin ES (1980) The influence of molecular transfer processes on turbulent combustion velocity, *Combustion, Explosions, and Shock Waves* 16:41–46
- [9.20] Lipatnikov AN, Chomiak J (1998) Lewis number effects in premixed turbulent combustion and highly perturbed laminar flames. *Combustion Science and Technology*
- [9.21] Kido H, Kitagawa T, Nakashima K, Kato K (1989) An improved model of turbulent mass burning velocity. *Memoirs of The Faculty of Engineering, Kyushu University* 49:229–247
- [9.22] Karpov VP, Lipatnikov AN, Zimont VL (1997) Flame curvature as a determinant of preferential diffusion effects in premixed turbulent combustion. In: Sirignano WA, Merzhanov AG, de Luca (ed.) *Advances in combustion science: In honor of Ya.B. Zel'dovich*, 1st edn, *Progress in Astronautics and Aeronautics*, Vol. 173, Chap. 14, pp. 235–250
- [9.23] Kobayashi H, Tamura T, Maruta K, Nioka T (1996) Burning velocity of turbulent premixed flames in a high-pressure environment. 26th Symposium (Int.) on Combustion, The Combustion Institute, Pittsburgh, pp. 389–396
- [9.24] Tachikawa M (1983) Trajectories of flat plates in uniform flow with application to wind-generated missiles, *J. Wind Eng., Ind. Aerodyn.* 14:443–453
- [9.25] Tachikawa M (1990) A method of estimating the distribution range of trajectories of windborne missiles, *J. Wind Eng., Ind. Aerodyn.* 29:175–184
- [9.26] Groff EG (1987) An experimental evaluation of entrainment flame propagation model. *Combustion and Flame* 67:153–162
- [9.27] Kido H, Huang S, Tanoue K, Nitta T (1994) Improvement of lean hydrocarbon mixtures combustion performance by hydrogen addition and its mechanisms. *JSME, Yokohama, COMODIA* 94:119–124
- [9.28] Bradley D, Lawes M, Speppard CGW (1994) Study of turbulence and combustion interaction: measurement and prediction of the rate of turbulent burning. Periodic Report 30.6.94 to 31.12.94, CEC JOULE Contract JOU2-CT92-0162, Leeds University
- [9.29] Bradley D, Lawes M, Scott MJ, Mushi, EMJ (1994) Afterburning in spherical premixed turbulent explosions. *Combustion and Flame* 99:581–590
- [9.30] Bradley D, Lawes M, Speppard CGW (1995) Study of turbulence and combustion interaction: measurement and prediction of the rate of turbulent burning. Periodic Report 30.6.95 to 31.12.95, CEC JOULE Contract JOU2-CT92-0162, Leeds University
- [9.31] Mouquallid M, Lecordier B, Trinite M (1994) High speed laser tomography analysis of flame propagation in a simulated internal combustion engine-applications to non-uniform mixture. *SAE Paper No 941990*
- [9.32] Pope SB, Cheng WK (1986) Statistical calculations of spherical turbulent flames. 21st Symposium (Int.) on Combustion, The Combustion Institute, Pittsburgh, pp. 1473–1481

- [9.33] Müller UC, Bolig M, Peters N (1997) Approximations for burning velocities and Markstein numbers of lean hydrocarbon and methanol flame. *Combustion and Flame* 108:349–356
- [9.34] Ozdor N, Dulger M, Sher E (1994) Cyclic variability in spark ignition engines. A literature survey. SAE Paper No 940987
- [9.35] Peters N (1986) Laminar flamelet concepts in turbulent combustion. Symposium (Int.) on Combustion, The Combustion Institute, Pittsburgh, pp. 1231–1249
- [9.36] Abdel-Gayed RG, Bradley D, Lawes M (1987) Turbulent burning velocities: a general correlation in terms of straining rates. Proc. The Royal Society on London A, pp. 414
- [9.37] Bray KNC (1987) Methods of including realistic chemical reaction mechanisms in turbulent combustion models. In: Complex chemical reaction systems. Mathematical Modeling and Simulation, Heidelberg, p. 356
- [9.38] Kuznetsov VR, Sabel'nikov VA (1990) Turbulence and combustion. Hemisphere Publ. Corp., New York
- [9.39] Zimont VL, Lipatnikov AN (1995) A numeric premixed turbulent combustion. *Chemical Reports* 14:993–1025
- [9.40] Karpov VP, Lipatnikov AN, Zimont VL (1996) An engineering model of premixed turbulent combustion. Symposium (Int.) on Combustion, The Combustion Institute, Pittsburgh, pp. 249–257
- [9.41] Lipatnikov AN (1997) Modeling of the influence properties on premixed turbulent combustion. Computation and analysis of combustion, In: Frolov SM, Givi P (eds.) Advanced computation and analysis of combustion, ENAS Publish, Moscow, pp. 335–359
- [9.42] Metghalchi M, Keck JC (1982) Burning velocity mixtures of air with methanol, iso-octane, and high pressure and temperature. *Combustion* 48:191–210
- [9.43] Grantner H, Nisbet J, Schwarz W (1996) The sional simulation of the entire engine cycle 4-valve SI engine. *Méthodologies Et Technique: Tion Numérique, Société Des Ingénieurs Automobiles*
- [9.44] Tatschi R, Wieser K, Reitbauer R (1994) Sional simulation of flow evolution. Mixture and combustion in a 4-valve SI engine. Private communication
- [9.45] Hicks RA, Lawes M, Sheppard CGW, Whitaker, BJ (1992) Multiple laser sheet imaging investigation of turbulent flame structure in a spark ignition engine. SAE Paper No 941992. Private communication
- [9.46] Al-Jabri KS et al. (1998) Behaviour of steel and composite beam-column connect fire. *Journal of Constructional Steel Research* 46(1–3), Paper 180
- [9.47] Allen LW (1970) Fire endurance of selected non-loadbearing concrete masonry, DBR Fire Study No 25, Division of Building Research, National Research Cou, Canada, Ottawa, Canada
- [9.48] Almand K (1989) The role of passive systems in fire safety design in buildings. *Fire and Engineering – International Symposium Papers*, The Warren University of Sydney, Australia, pp. 103–129
- [9.49] Anderberg Y (1986) Measured and predicted behaviour of steel beams and columns in fire. Lund Institute of Technology, Lund, Sweden
- [9.50] Anderberg Y (1988) Modeling and steel behaviour: *Fire Safety Journal* 13(1):17–26

- [9.51] Anderberg Y (1989) Fire engineering design based on PC. Nordic Mini-Seminar of Fire Resistance of Concrete Structures, Trondheim, Fire Safety Design, Lund, Sweden
- [9.52] Anderberg Y (1993) Computer simulations and a design method for fire exposed concrete columns. Report 92-50, Fire Safety Design, Lund, Sweden
- [9.53] Anderberg Y (1982) Fire resistance of concrete structures. Nordic Concrete Research Publication No. 1, Oslo, Reprinted as Report LUTVDG/(TVBB-3009), Lund University, Sweden
- [9.54] Andersen NE, Lauridsen DH (1999) TT-roof slabs. Hollow core concrete slabs. Technical Report X52650, Parts 1 and 2 respectively, Danish Institute of Fire Technology, Denmark
- [9.55] Armer GST, O'Dell T (eds.) (1996) Fire, static and dynamic tests of building structures. Proc. 2nd Cerdington Conf., E& F.N. Spon, London, UK
- [9.56] ASCE (1995) Standard for load and resistance factor design (LRFD) for engineered wood construction. AF& PA/ASCE 16-95, American Forest and Paper Association, American Society for Civil Engineers, New York, USA
- [9.57] ASFPCM (1988) Fire protection for structural steel in buildings. Association of Specialist Fire Protection Contractors and Manufacturers, UK
- [9.58] ASTM (1988) Standard tests methods for fire tests of building construction and materials. E119-88, American Society for Testing and Materials
- [9.59] ASTM (1988) Fire tests of through-penetration fire stops. E814-88, American Society for Testing and Materials
- [9.60] ASTM (1995) Fire tests of through-penetration fire stops. E814-88, American Society for Testing and Materials
- [9.61] Babrauskas V (1979) COMPF2: A program for calculating post-flashover fire temperatures. NBS Technical Note 991, National Bureau of Standards
- [9.62] Babrauskas V (1981) A closed form approximation for post flashover compartment fires. *Fire Safety Journal* 4:63–73
- [9.63] Babrauskas V (1995) Burning rates. In: SFPE handbook of fire protection engineering. 2nd edn, Society of Fire Protection Engineers, USA, Chap. 3.1
- [9.64] Babrauskas V, Grayson SJ (1992) Heat release in fires. Elsevier Applied Science
- [9.65] Babrauskas V, Williamson RB (1978) Post-flashover compartment fires – basis for a theoretical model. *Fire and Materials* 2(2):339–353
- [9.66] Babrauskas V, Williamson RB (1978) Temperature measurement in fire test furnaces – part I. *Fire Technology* 14(3):226–238
- [9.67] Babrauskas V, Williamson RB (1978) The historical basis of fire resistance testing – part I, *Fire Technology* 14(3):184–205
- [9.68] Babrauskas V, Williamson RB (1978) The historical basis of fire resistance testing – part II, *Fire Technology* 14(3):304–316
- [9.69] Bailey CG, Burgess IW, Plank RJ (1996) Analyses of the effects of cooling and fire spread on steel-flamed buildings. *Fire Safety Journal* 26:273–293
- [9.70] Bailey CG, Burgess IW, Plank RJ (1996) The lateral torsional buckling of unrestrained steel beams in fire, *Journal of Constructional Steel Research* 36(2):101–119

- [9.71] Barnfield JR, Porter AM (1984) Historic buildings and fire: fire performance of cast-iron structural elements, *The Structural Engineer* 62A(12): 373–380
- [9.72] Bazant ZP, Kaplan MF (1996) Concrete at high temperatures – material properties and mathematical models. Concrete Design and Construction Series, Longman Group Ltd., UK
- [9.73] Cooke GME (1996) A review of compartment fire tests to explore the behaviour structural steel. Fire, static and dynamic tests of building structures. Proc. 2nd Cardington Conf., E& F.N. Spon, London, pp. 17–31
- [9.74] Cooke GME (1997) The behaviour of sandwich panels exposed to fire. *Building Engineer* 72(6):14–29
- [9.75] Cooper LY (1997) The thermal response of gypsum panel steel stud wall systems exposed to fire environments. NISTR 6027, National Institute of Standards and Technology, USA
- [9.76] Cooper LY, Steckler KD (1996) Methodology for developing and implementing alternative temperature-time curves for testing the fire resistance of barriers for nuclear power plant applications. NISTR 5842, National Institute of Standards and Technology, USA
- [9.77] Cosgrove BW (1996) Fire design of single storey industrial buildings. Fire Engineering Research Report No 96/3, University of Canterbury, New Zealand
- [9.78] Cramer SM (1995) Fire endurance modelling of wood floor/ceiling assemblies. Proc. Fire and Materials Conf., Washington DC, USA, pp. 105–114
- [9.79] Cramer SM, Shrestha D, Mtenga PV (1993) Computation of memebr forces metal plate connected wood trusses. *Structural Engineering Review* 5(3):209–217
- [9.80] CSIRO, FIRECALC (1993) Division of Building Construction and Engineering, CSIR North Ryde, NSW, Australia
- [9.81] Custer RLP, Meacham BJ (1997) Introduction to performance-based fire safety. Society of Fire Protection Engineers and National Fire Protection Association
- [9.82] Deal S (1993) Technical reference guide for FPE tool version 3.2, NISTR 5486, National Institute of Standards and Technology, USA
- [9.83] DelSenno M, Cont S, and Piazza M (1998) Charring rate slowing by means of fibregla: reinforcing coatings. Proc. 4th World Conf. on Timber Engineering, Montreux, Switzerland, Vol. 2, pp. 230–237
- [9.84] DIN (1996) Baulicher Brandschutz im Industriebau, Teil 1, DIN 18230-1 (Structural Fire Protection in Industrial Building – Part I: Analytically Required Fire Resistance Tim), Deutsches Institut für Normung e.V, Berlin
- [9.85] Dotreppa J-C et al. (1996) Experimental research of the determination of the Ma parameters affecting the behaviour of reinforced concrete columns under fire condition. *Magazine of Concrete Research* 49(179):117–127
- [9.86] Drysdale D. (1998) An introduction to fire dynamics. 2nd edn, John Wiley & So., Chichester, UK
- [9.87] Dunn V (1988) Collapse of burning buildings: a guide to fireground safety. F Engineering, PenWell Books, New York, USA
- [9.88] ECI (1994) Eurocode 1: Basis of design and design actions on structures. Part 2-2: Actions structures exposed to fire. ENV 1991-2-2, European Committee for Standardization, Brussels, Belgium



- [9.89] ECCS (1983) Calculation of the fire resistance for composite concrete slabs with profiles steel sheet exposed to the standard fire. Publication No 32, European Commission for Constructional Steelwork, Brussels, Belgium
- [9.90] ECCS (1985) Design manual on the European recommendations for the fire safety of steel structures. European Commission for Constructional Steelwork, Brussels, Belgium
- [9.91] ECCS (1988) Calculation of the fire resistance of centrally-loaded composite steel-concrete columns exposed to the standard fire. Technical Note No 55, European Commission for Constructional Steelwork, Brussels, Belgium
- [9.92] ECCS (1995) Fire resistance of steel structures. ECCS Technical Note No 89, Technical Committee 3, European Commission for Constructional Steelwork, Brussels, Belgium
- [9.93] Ellinwood BR, Corotis RB (1991) Load combinations for buildings exposed to fires. *Engineering Journal*, American Institute of Steel Construction 28(1):37–44
- [9.94] El-Rimawi JA, Burgess IW, Plank RJ (1996) The treatment of strain reversal in structural members during the cooling phase of a fire. *Journal of Constructional Steel Research* 37(2):115–135
- [9.95] England JP, Young SA, Hui MC, Kurban N (2000) Guide for the design of fire resistant barriers and structures. Building Control Commission, Melbourne, Australia
- [9.96] FCRC (1996) Fire engineering guidelines. Fire Code Reform Centre, Sydney, Australia
- [9.97] Feasey R, Buchanan AH (1999) Post-flashover design fires. Fire Engineering Research Report 99/6, University of Canterbury, New Zealand
- [9.98] Feasey R, Buchanan AH (2000) Post-flashover fires for structural design, submitted to *Fire Safety Journal*
- [9.99] FIP/CEB (1975) Guides to good practice. FIP/CEB recommendations for the design of reinforced and prestressed concrete structural members for fire resistance. FIP/1/1. Fédération Internationale de la Précontrainte. Wexham Springs, Slough, UK
- [9.100] Fleischmann CM (1995) Analytical methods for determining fire resistance of concrete members. In: SFPE handbook of fire protection engineering. 2nd edn, Society of Fire Protection Engineers, USA, Chap. 4.10
- [9.101] Skinner P, Wallace M (2002) World Trade Center. The giants that defied the sky. White Star s.r.l., p. 123
- [9.102] The Daily Telegraph/The Independent (London)/The Times (London) (2001) Extract from features on WTC. September 16, 30 pp.
- [9.103] Hopkison J (2001) Fire-safety engineering: the consultant's view. *J. Instruct E* 79(19): 22–23, London, Oct. 2
- [9.104] Subramanian N (2002) Collapse of WTC. Its impact on skyscraper construction. *J. Indian Concrete* (March):165–169
- [9.105] Baker WE, Cox PA, Westine PS, Kulesz JJ (eds.) (1982) Explosion hazards and evaluation. Fundamental studies in engineering. Elsevier Scientific Publishing Company, NY
- [9.106] Bangash M (1993) Impact and explosion, analysis and design. CRC Press, Sect. 4.3
- [9.107] International Organization for Standardization (1999) Fire resistance tests – elements of building construction, ISO 834

- [9.108] National Fire Protection Association (1999) Standard methods of fire tests of building construction and materials. NFPA 251, Quincy, MA
- [9.109] U.S. Department of Energy (1996) Accident analysis for aircraft crash into hazardous facilities. DOE Standard 3014-96, October
- [9.110] Zalosh RG (2002) Explosion protection. In: SFPE handbook of fire protection engineering. 3rd edn, Quincy, MA
- [9.111] Bangash T (2003) PhD. Thesis, London University
- [9.112] AISC (2001) Manual of steel construction. LRFD, 3rd edn, Chicago
- [9.113] ASTM (2000) Standard test methods for fire tests of building construction and materials. ASTM E119, West Conshohocken, PA
- [9.114] Smith, D. (2002) Report from Ground Zero: The story of the rescue efforts at the World Trade Center. Viking Press
- [9.115] Worthington, Skilling, Helle, Jackson (1968) The World Trade Center Northeast Plaza building. Structural drawings
- [9.116] Zalosh RG (1995) Explosion protection. In: SFPE handbook of fire protection engineering. 2nd edn, Quincy, MA
- [9.117] Schleich J-B (2002) Auswirkungen des WTC-Schocks auf den europäischen Stahlgeschossbau, Stahlbau 71(4):289–293
- [9.118] Anon (2002) 11 September. The official report on WTC. The New Civil Engineer, May, pp. 5–7
- [9.119] BBC (2001) Planes attack US targets. A report on 9/11/2001. Sept., 12 pp.
- [9.120] Hunkele LM (2001) The Pentagon project. Civil Engineering (June):85
- [9.121] Mlakar PF et al. (2003) The Pentagon building performance report. ASCE, two Appendices, Jan., p. 61
- [9.122] Prieto R (2002) The 3Rs: lessons learned from September 11th. The Royal Academy of Engineering, London, Oct., p. 20
- [9.123] FEMA (Federal Emergency Agency) (2002) Data collection preliminary observations and recommendations. FEMA Region II, New York and ASCE, May, p. 435
- [9.124] Zhang JZ, Halliday MD, Poole P, Bowen P (1997) Crack closure in small fatigue cracks – a comparison of finite element predictions with in-situ scanning electron microscope measurements. Fatigue and Fracture Engineering Material & Structures 20(9):1279–1293
- [9.125] Lindholm BE (1994) System identification of finite element modeling parameters using experimental spatial dynamic modeling. Proc. SPIE – The International Society for Optical Engineering 2358:450–462
- [9.126] Szwerc RP, Hambric SA, Erickson MJ (1998) Comparison of experimental and finite element structural intensities on an aluminum ribbed panel. Proc. – National Conf. on Noise Control Engineering, pp. 359–364
- [9.127] Dobson CA, Siasias G, Phillips R, Langton CM, Fagan MJ (2002) Smoothing of pixelated finite element models of cancellous bone structures and the effect on the predicted structural properties of the bone. Proc. of The Institution of Mechanical Engineers, Part H: Journal of Engineering in Medicine 216(2):145–149
- [9.128] Silva LFM, Goncalves JPM, Oliveira FMF, de Castro PMST (2002) Multiple-site damage in riveted lap-joints: experimental simulation and finite element prediction. International Journal of Fatigue 22(4):319–338 (April)

- [9.129] Herr W, Halla JW. Jr, White TD, Johnson W (1995) Continuous deflection basin measurement and backcalculation under a rolling wheel load using a scanning laser technology. Proc. of The Transportation Congress, Vol. 1, pp. 600–611
- [9.130] Bissinger G, Ye K (2002) Automated hammer-impact modal analysis with a scanning laser vibrometer: working example – a violin. Proc. SPIE – The International Society for Optical Engineering 4062(I):943–949
- [9.131] Bissinger G., and Ye K., Automated hammer-impact modal analysis with a scanning laser vibrometer: Working example – A violin, Proc. Int. Modal Analysis Conf. – IMAC, Vol. 1, pp. 943–949, 2000
- [9.132] Steegen A, DeWolf I, Maex K, Ignat M (1993) Finite element simulations of the mechanical stress in and around narrow TISI2 lines. Materials Research Society Symposium – Proc., Vol. 518, Microelectromechanical Structures for Materials Research, pp. 227–232
- [9.133] LaPeter MC, Cudney HH, Wicks AL (1993) Investigation of distributed measurements for finite element model verification. Proc. SPIE – The International Society for Optical Engineering 1923(1):pp. 409–417,
- [9.134] Ikuta F, Horino T, Inoue T (1998) Computer simulation of residual stresses/distortion and structural change in the course of scanning induction hardening. Zairyo/Journal of The Society of Material Science, Japan 47(9):892–898 (Sept.)
- [9.135] Chen SH, GangaRao HVS (1998) Damage detection using scanning laser vibrometer. Proc. SPIE – The International Society for Optical Engineering 3411:473–484
- [9.136] Marchiando JF, Kopanski JJ, Albers J (2000) Limitations of the calibration curve method for determining dopant profiles from scanning capacitance microscope measurements. Journal of Vacuum Science and Technology B: Microelectronics and Nanometer Structures 18(1):414–417 (Jan.)
- [9.137] Castellini P, Esposito E, Paone N, Tomasini EP (1992) Non-invasive measurements of structural damage by laser scanning vibrometer: An experimental comparison among different exciters. Proc. SPIE – The International Society for Optical Engineering 3585:304–315
- [9.138] Commean PK, Simth KE, Vannier MW, Hildebolt CF, Pilgram TK (1996) Precision and accuracy of 3D lower extremity residual measurement systems. Proc. SPIE – The International Society for Optical Engineering 2710:494–510
- [9.139] Ohashi T, Sugawara H, Ishii Y, Sato M (1999) 3D stress analysis in cultured endothelial cells exposed to fluid shear stress. American Society of Mechanical Engineers, Bioengineering, Division (Publication) BED 43:121–122
- [9.140] Michel B, Vogel D, Schubert A, Auesperg J, Reichl H (1997) Microdac method – a powerful means for microdeformation analysis in electronic packaging. Applications of Experimental Mechanics to Electronic Packaging, American Society of Mechanical Engineers, EEP 22:117–123
- [9.141] Harbury HK, Porod W (1998) Parallel computation for electronic waves in quantum corrals. VLSI Design 6(1-4):47–51
- [9.142] Montgomery DE, West RL, Burdisso RA (1996) Acoustic radiation prediction of a compressor housing from three-dimensional experimental spatial dynamics modeling. Applied Acoustics 47(2):165–185 (Feb.)

- [9.143] Castellini P, Revel GM (2000) Defect detection and characterization by laser vibrometry and neural networks. Proc. SPIE – The International Society for Optical Engineering 4062:1818–1824
- [9.144] Bysh IN, Crocombe AD, Smith PA (1996) Determining the effective material properties of damaged particle-filled adhesives. Journal of Adhesion 58(3-4):205–226
- [9.145] Castellini P, Revel GM (2000) Defect detection and characterization by laser vibrometry and neural networks. Proc. Int. Modal Analysis Conf., IMAC, Vol. 2, pp. 1818–1824
- [9.146] Toi T, Motegi T, Okubo N (2000) Prediction of dynamic behaviors at unmeasurable part of micro-machine. Proc. SPIE – The International Society for Optical Engineering 4062: 448–453
- [9.147] Toi T, Motegi T, Okubo N (2000) Prediction of dynamic behaviors at unmeasurable part of micro-machine, Proc. Int. Modal Analysis Conf., IMAC, Vol. 1, pp. 448–453
- [9.148] Montgomery DE, West RL, Burdisso RA, Camargo HE (1994) Acoustic radiation prediction of a compressor from 3D experimental spatial dynamics modeling, Proc. SPIE – The International Society for Optical Engineering 2358:281–291
- [9.149] Cao TT, Zimmerman DC, James GH (1999) Identification of Ritz vectors from the space shuttle vertical stabilizer assembly test article. Proc. Int. Modal Analysis Conf., IMAC, Vol. 2, pp. 2005–2010
- [9.150] Montgomery DE, West RL (1996) Three-dimensional experimental spatial dynamics modelling of a reciprocating from compressor housing. Optics and Lasers in Engineering 25(4-5):265–288 (Oct.-Nov.)
- [9.151] Eagle S, Lakdawala H, Fedder GK (1999) Design and simulation of thermal actuators for STM applications in a standard CMOS process. Proc. SPIE – The International Society for Optical Engineering 3875:32–39
- [9.152] Zhang H, Minnetyan L, Chamis C.C (2002) Simulation of energy release rates and correlation with NDE test data. Proc. Int. SAMPE Symposium and Exhibition 47(1):131–144
- [9.153] Witz DC, Pandorf T, Portheine F, Radermacher K, Schiffers N, Prescher A, Weichert D, Niethard FU (2003) Concept and development of an orthotropic FE model of the proximal femur. Journal of Biomechanics 36(2):289–293 (Feb. 1)
- [9.154] Kristler LS (1994) Experimental investigation of the impact response of cylindrically curved laminated composite panels. Collection of Technical Papers – AIAA/ASME/ASCE/AHS/ABS Structures, Structural Dynamics & Materials Conference, No 14, AIAA-94-1604-CP, pp. 2292–2297
- [9.155] Wangg ZP, Ruiz C (1990) Damage process of ceramics in contact with metals. Materials Science & Engineering A: Structural Materials: Properties, Microstructure & Processing A 127(1):105–114 (July)
- [9.156] Hasko G, Dexter HB, Loos A, Kranuehl D (1994) Application of science-based RTM for fabricating primary aircraft structural elements. Journal of Advanced Materials 26(1):9–15 (Oct.)
- [9.157] Zachariah SG, Sanders JE, Turkiyyah GM (1996) Automated hexahedral mesh generation from biomedical image data: application in limb prosthetics. IEEE Transactions on Rehabilitation Engineering 42(2):91–102 (June)

- [9.158] Roschke PN (1995) Advisory system for design of highway safety structures. *Journal of Transportation Engineering* 117(4):418–434 (July-Aug.)
- [9.159] Lee S-H, Preissner C, Lai B, Cai Z, Shu D (2002) Enhancement of the vibration stability of a microdiffraction goniometer. *Proc. SPIE – The International Society for Optical Engineering* 4771:100–110
- [9.160] Jin S, Frank P (2000) Locating structural defects using deflection shapes. *Journal of Intelligent Material Systems and Structures* 11(8):613–630 (August)
- [9.161] Reynolds P, Hayward G (1998) Design and construction of a new generation of flexible ultrasonic transducer arrays. *Insight: Non-Destructive Testing and Condition Monitoring* 40(22):101–106 (Feb.)
- [9.162] Bose MRSC, Thomas G, Palaninathan R, Damodaran SP, Chellapandi P (2001) Buckling investigations on a nuclear reactor inner vessel model. *Experimental Mechanics* 41(2):114–150
- [9.163] Gao F, Poulet P, Yamada Y (2001) 3D simultaneous reconstruction of absorption and scattering coefficients in time-resolved optical tomography. *Proc. SPIE – The International Society for Optical Engineering* 4250:514–521
- [9.164] Faulkner MG, Amairaj JJ, Bhattacharyya A (2000) Experimental determination of thermal and electrical properties on Ni-Ti shape memory wires. *Smart Materials and Structures* 9(5):632–639 (Oct.)
- [9.165] Castellini P (2000) Laser vibration measurement for damage detection of composite materials: Advances in signal processing. *Proc. SPIE – The International Society for Optical Engineering* 4072:442–452
- [9.166] Hasko G, Dexter HB, Loos A, Kranuehl D (1994) Application of science-based RTM for fabricating primary aircraft structural elements. *Journal of Advanced Materials* 26(1):9–15 (Oct.)
- [9.167] Chen K-S, Ayon AA, Zhang X, Spearing SM (2002) Effect of process parameters on the surface morphology and mechanical performance of silicon structures after deep reactive ion etching (DRIE). *Journal of Microelectromechanical Systems* 11(3):264–275 (June)
- [9.168] Vogel D, Kuehnert R, Michel B (1999) Strain measurement in micrometrology. *Proc. SPIE – The International Society for Optical Engineering* 3897:224–238
- [9.169] Vogel D, Kuehnert R, Michel B (1994) Strain and displacement measurements for microsystems technology. *Proc. SPIE – The International Society for Optical Engineering* 2342:209–218
- [9.170] De Vita A, Charlier JC, Blasé X, Car R (1999) Electronic structure at carbon nanotube tips. *Applied Physics A: Materials Science & Processing* 68(3):283–286 (Mar.)
- [9.171] Esong IE, Elghazouli AY, Chryssanthopoulos MK (1998) Measurement techniques for buckling sensitive composite shells. *Strain* 34(1):11–17 (Feb.)
- [9.172] Sihiborn R (1998) Electrical modeling of anisotropically conductive adhesive interconnections for microwave applications. *Proc. Electronic Packaging Technology Conf., EPTC*, pp. 119–125
- [9.173] Castellini P, Revel G-M (2002) Experimental technique for structural diagnostic based on laser vibrometry and neural networks. *Shock and Vibration* 7(6):381–397

- [9.174] Secretan Y, Leclerc M, Duchesne S, Heniche M (2001) Une méthodologie de modélisation numérique de terrain pour la simulation hydrodynamique bidimensionnelle (A methodology to construct a numerical terrain model for two-dimensional hydrodynamic simulations), *Revue Des Sciences De l'Eau* 14(2):187–212 (in French)
- [9.175] Bouzakis K-D, Vidakis N, Kallinikidis D, Leyendecker T, Erkens G, Wenke G, Fuss H-G (1998) Fatigue failure mechanisms of multi- and monolayer physically vapour-deposited coatings in interrupted cutting processes. *Surface & Coatings Technology* 108-109(1-3):526–534 (Oct. 10)
- [9.176] Walker R, Gurary AI, Yuan C, Zadadzki P, Moy K, Salahaj T, Thomson AG, Kroll WJ, Stall RA, Schmaker NE (1995) Novel high temperature metal organ chemical vapor deposition rotating-disk reactor with multi-zone heating for gan related materials. *Materials Science & Engineering B: Solid-State Materials for Advanced Technology* B35(1-3):97–101 (Dec.)
- [9.177] Shinada S, Koyama F, Nishiyama N, Arai M, Matsutani A, Goto K, and Iga K (2002) Optical near field by vertical cavity surfaces emitting laser. *Electronics and Communications in Japan, Part II: Electronics* (English Translation of *Denshi Tsushin Gakkai Ronbunshi*) 85:43–53 (Feb.)
- [9.178] Tada Y, Fujino N (1996) Creation of FEM data by image processing and automatic meshing: automatic generation of FEM data for inverse problems. *Proc. Japan/Usa Symposium on Flexible Automation, Vol. 2*, pp. 971–974
- [9.179] Prangnell PB, Barnes SJ, Roberts SM, Withers PJ (1996) Effect of particle distribution on damage formation in particulate reinforced metal matrix composites deformed in compression. *Materials Science & Engineering A: Structure Materials: Properties, Microstructure and Processing* A220(1-2):41–56 (Dec. 15)
- [9.180] Shinada S, Koyama F, Suzuki K, Nishiyama N, Goto K, Iga K (1999) Micro-aperture surface emitting laser for near field optical data storage. *Pacific Rim Conf. on Lasers and Electro-Optics, CLEO-Technical Digest, Vol. 3*, pp. 618–619
- [9.181] Anon (2001) *Proc. of the ACM SIGGRAPH Conf. on Computer Graphics*, 573 p.
- [9.182] Kojima F, Okamoto J, Ohno Y (1997) Computational method for crack reconstruction of steam generator materials using FEM-BEM scheme in inverse applied electromagnetics. *Nippon Kikai Gakkai Ronbunshu, C Hen/Transactions of The Japan Society of Mechanical Engineers, Part C* 63(612):2650–2656 (Aug.) (in Japanese)
- [9.183] Kim C-H, Jeong H-M, Jeon J-U, Kim Y-K (2003) Silicon micro XY-stage with a large area shuttle and no-etching holes for SPM-based data storage. *Journal of Microelectromechanical Systems* 12(4):470–478 (Aug.)
- [9.184] Vignola J, Houston BH (1998) A three-dimensional velocity measurement of a periodically ribbed aircraft panel surface by optical vibrometry. *Proc. SPIE – The International Society for Optical Engineering* 3411:528–536
- [9.185] Hah D, Toshiyoshi H, Wu M-C (2002) Design of electrostatic actuators for MOEMS applications. *Proc. SPIE – The International Society for Optical Engineering* 4655:200–207
- [9.186] Ert T, Joy K, Varshney A (eds.) (2001) *Proc. IEEE Visualize Conference*, 519 p.

- [9.187] Bouzakis K-D, Vidakis N, Kallinikidis D, Leyendecker T, Erkens G, Wenke G, Fuss H-G (1999) Quantification of properties modification and cutting performance of  $(\text{Ti}_{1-x}\text{Al}_x)\text{N}$  coatings at elevated temperatures. *Surface & Coatings Technology* 120-121:34–43 (Nov.)
- [9.188] Hallquist JO et al. (2005) LS-DYNA – A computer package. Available at Lawrence Livermore Laboratory, California, U.S.A.; Modification by Bangash MYH (2001) *Manual of numerical methods in concrete*, Thomas Telford

# 10 Building Global Analysis for Damage Scenario

## 10.1 Introduction

The global concept is based on combining all elements including bracings shears and cores to form a single spatial cantilever with physical boundary conditions; the major contributions apart from axial and shear shall be the bending and torsional stiffnesses of the entire building.

In the lateral load analysis of buildings, wind, earthquake and blast forces are treated as equivalent static loads and are reduced to a series of horizontal concentrated loads applied to the building at each floor level. Portal and cantilever methods offer quick ways of analysis of a rigid bent with unknown sizes.

In the portal method, a wind bent is treated as a series of consecutive single-bay portal frames in the determination of axial stresses in the columns due to overturning effect. Interior columns are considered as part of two such portals, and the direct compression arising from the overturning effect on the leeward column of one portal is offset by the direct tension arising from the overturning effect on the windward column of the adjacent portal. If the widths of different portals are unequal, the distribution of blast shear resisted by each portal can be assumed proportional to the aisle widths to maintain the interior column free of direct stress. Alternately, the column shears can be assumed to be unaffected by aisle widths resulting in axial stresses in the interior columns. With the shears in each column known and the points of contraflexure pre-established, the moments in beams and columns are determined. Simple statics will yield axial and shear forces in beams and columns.

In the portal method it is assumed that (1) points of contraflexure are located at midpoints of girders and columns, and (2) the shear in columns is distributed in a rational manner. Under the second category, some engineers assume that the shear in exterior columns equals one-half the shear in an interior column, while some assume that the shear is distributed in proportion to the tributary bay width. For unequal bays, the former assumption results in direct stresses in the interior columns equal to the difference in girder shears on either side of the column. The latter assumption keeps the interior columns free from direct stresses.

The frame analysis for horizontal loads by the so-called cantilever method is obtained by assuming that (1) inflection points, i.e., hinges, form at midspan of each beam and at midheight of each column; and (2) the unit



direct stresses in the columns vary as the distance from the frame centroidal axis. It is usually further assumed that all columns in a story are of equal area. In this case the total column forces will vary as the distance from the centre of gravity of the bent. Using these assumptions the frame is rendered statically determinate and the direct forces, shears, and moments are determined by equilibrium considerations.

The lateral displacement of one floor relative to the floor below results from a combination of bending and shear deformation of the bent. The bending deformation or the chord drift, as it is sometimes called, is a consequence of axial deformation of the columns alone and is independent of the size, type, location, and arrangement of the web system. The shear deformation is due to the rotation of the joints in the frame, which causes bending of columns.

For the relatively short frames with height-to-width ratios less than 3, the deflection due to axial shortening of columns can be neglected and the deflection of the frame can be assumed to be entirely due to joint rotations. Its contribution to deflection can, however, be obtained by considering the frame as a cantilever with an equivalent moment of inertia  $I = 2\alpha d^2$  where  $\alpha$  is the area of exterior column and  $d$  is half the base of the portal frame. For taller frames, it is prudent to consider the axial deformation of the interior columns; the equivalent moment of inertia is determined by the relation  $I = \sum_1^n a_1 d_1^2$ , where  $a_1, a_2, \dots, a_n$  represent the areas of the columns and  $d_1, d_2, \dots, d_n$  represent their corresponding distances from the natural axis of the frame.

Deflection can occur due to column type rotation or girder rotation the framed tube system in its simplest form consists of closely spaced exterior columns tied at each floor level by relatively deep spandrels. The behaviour of the tube is in essence similar to that of a hollow perforated tube. The overturning moment under lateral load is resisted by compression and tension in the columns while the shear is resisted bending of columns and beams primarily in the two sides of the building parallel to the direction of the lateral load. The bending moments in the beams and columns of these frames, which are called the web frames, can be evaluated using either of the two approximate procedures, namely the portal or the cantilever analysis. It is perhaps more accurate to use the cantilever method because tube systems are predominantly used for very tall buildings in the 40- to 80-story range in which the axial forces in the columns play a dominant role. The moments in spandrels and columns as well as the racking components of the tube deflection can be evaluated by using the cantilever method.

As mentioned earlier, because of the continuity of closely spaced columns and spandrels around the corners of the building, the flange frames are coaxed into resisting the overturning moment. Whether or not all the flange columns, or only a portion thereof, contribute to the bending resistance is a function of shear rigidity of the tube. The frame tube system can have a single core, two cores or multi-cores.

## 10.2 Analysis of Buildings in Three-Dimensions

### 10.2.1 General Introduction

A framed tube is thin-walled structure, which can be defined as one, which is made up of thin plates joined along their edges. A precise quantitative definition for the thinness is not easy to give, except to say that the wall thickness is small compared to other cross-sectional dimensions, which are in turn small compared with the overall length of the structure. Shear walls of this type are extensively used in tall buildings, which typically exhibit another characteristic, namely that the walls are open sections, meaning that they do not have closed sections as, for example, box girders.

Compared to closed sections, open-section shear walls possess very little torsional rigidity and, therefore, must be given special consideration in their analysis and design. In a shear wall the shear stresses and strains are relatively much larger than those in solid rectangular columns. When shear walls twist, there is a so-called warping of the cross section.

The framed tube buildings are very slender with a high width ratio in excess of 8.0. As mentioned the framed tube can be multi-dimensional. Various structural flooring systems are included. In order to achieve composite behaviour sometimes an attempt is made to limit the number of shear walls by interconnecting them with heavy floor systems.

Non-linear analyses of two- or three-dimensional structures are achieved by modelling prototype structures as assemblages of line members and panels. The line members may have axial, flexural, shearing, and torsional properties, while the panels may carry in plane direct and shear stresses in addition to out-of-plane stress resultants. The analysis method employed is a matrix formulation of the stiffness or displacement type. In a general three-dimensional program, the coefficients, which relate the applied loading to six generalized displacements at the joint are calculated, and a set of non-linear simultaneous equations is set up for each loading. Solutions of these equations result in the displacements of the joints, which are then used to calculate internal loads and stresses in the structural elements.

Analytical solutions can be obtained for both frame or framed tube structures for high rise buildings which mostly analysed as 3D structures composed of relatively slender members which can be represented by properties a long centroidal axis. Surface systems such as slabs and walls or frames are treated as an assemblage of finite elements. Many computer packages have the capabilities for mixing up different element types and are useful in idealizing problems of complex shape. External influences such static, dynamic and blast loads temperature and fire can be considered in the design of such structures. The reader is advised to refer to the Appendix IA for options.

Generation options are available for convenience of inputting large amounts of data. Many computer programs have plotting capabilities for the undeformed and deformed shape of the structure for verification of the

model geometry and the structural behaviour of the system. The library of elements consists of elements from the basic linear element to the most sophisticated three-dimensional elements. Boundary elements in the form of spring supports can be incorporated. Loading options include gravity, thermal, in addition to the usual nodal loading consisting of either specified forces or displacements.

Among the dynamic analysis options, two of the most useful ones are eigen value analysis and response spectrum analysis. Wind, seismic and blast analyses by the response spectrum approach requires the undamped free vibration mode shapes and frequencies of the system. The response spectrum analysis is obtained by solving the dynamic equilibrium equations by using the modal superposition method.

Data preparation involves defining the basic geometric dimensions of the structure by establishing joints or nodes on the structure.

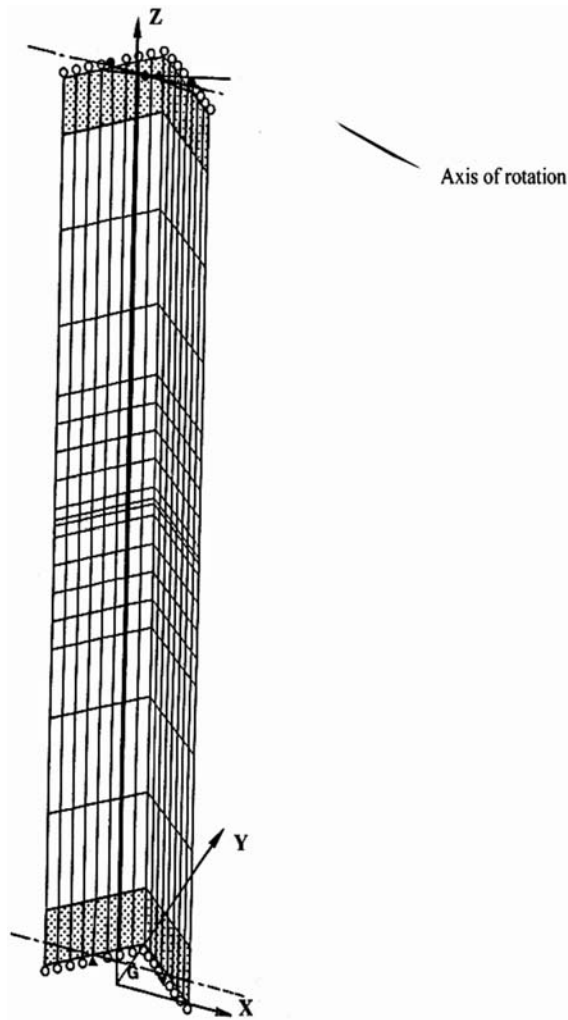
### **10.2.2 Finite Element Analysis of Framed Tubular Buildings Under Static and Dynamic Loads Influences**

A tube is a three-dimensional structure, and as such responds by bending about both its principle axes and rotation about a vertical axis. In analysing a quarter or half model, it is necessary to restrain the transverse bending and rotation of the tube. The kinematic restraints that preclude transverse movement and rotation of the model are shown in Fig. 10.1.

#### **10.2.2.1 Lumping Technique**

Many structural analysis have used lumping techniques to reduce the size of analytical models for computer analysis. The reduction in size was necessitated because, even with large-capacity computers, there just was no economical way of solving very tall buildings with large numbers of joints. Before the structural analysis raises their eyebrows in surprise, it is well to bear in mind that many notable buildings have been analysed using lumping techniques and they have been performing successfully over the years. Therefore, although the speed and capacity of modern mainframe computers are so vast as not to require lumping, introduction of desktop computers with relatively less capacity has once again required lumped computer modelling techniques. It is important to realise that as long as the essential features of the building are captured in the model, it makes very little difference whether a lumped or a full model is used for the analysis. Of course, there will be differences between the results of the two models, especially in regard to the stress resultants. Under impact and blast load effects, the authors found very little difference between the results of lumped and full models as discussed later on.

In this method of analysis, while looking at the entire structure, two floors are lumped into one floor, the moment of inertia and area of the girder in the lumped model should be twice their values in the prototype model. If  $n$



**Fig. 10.1.** Building frame in three-dimensions using global axes on sectional elevation

floors are lumped into one floor, the corresponding properties will be  $n$  times the prototype values. To keep the explanation simple, it is useful to introduce the following notations:

- $I_{cp}$  = moment of inertia of column in the unlumped model (prototype)
- $I_{cl}$  = moment of inertia of the column in the lumped model
- $L$  = length of girder which is the same in both models
- $h_{cp}$  = height of column in the unlumped model (prototype)
- $h_{cl}$  = height of column in the lumped model

For example, two stories are lumped together. Therefore, ratio of  $h_{cl}/h_{cp} = 2.0$ . In general, this ratio can be considered as  $n$ , where  $n$  is the model ratio. Equating stiffness ratios of column and beams between the two models gives

$$\frac{I_{cp}/h_{cp}}{I_{bp}/L} = \frac{I_{cl}/h_{cl}}{I_{bl}/L} \quad (10.1)$$

which simplifies to

$$I_{cl} = I_{cp} = \left( \frac{h_{cl}}{h_{cp}} \right) \left( \frac{I_{bl}}{I_{cl}} \right) \quad (10.2)$$

Since in the example the ratio of the heights of prototype and model columns is 2.0 and the moment of inertia of the model beam is twice that of the prototype, one gets

$$I_{cl} = I_{cp} = (2)^2 \quad (10.3)$$

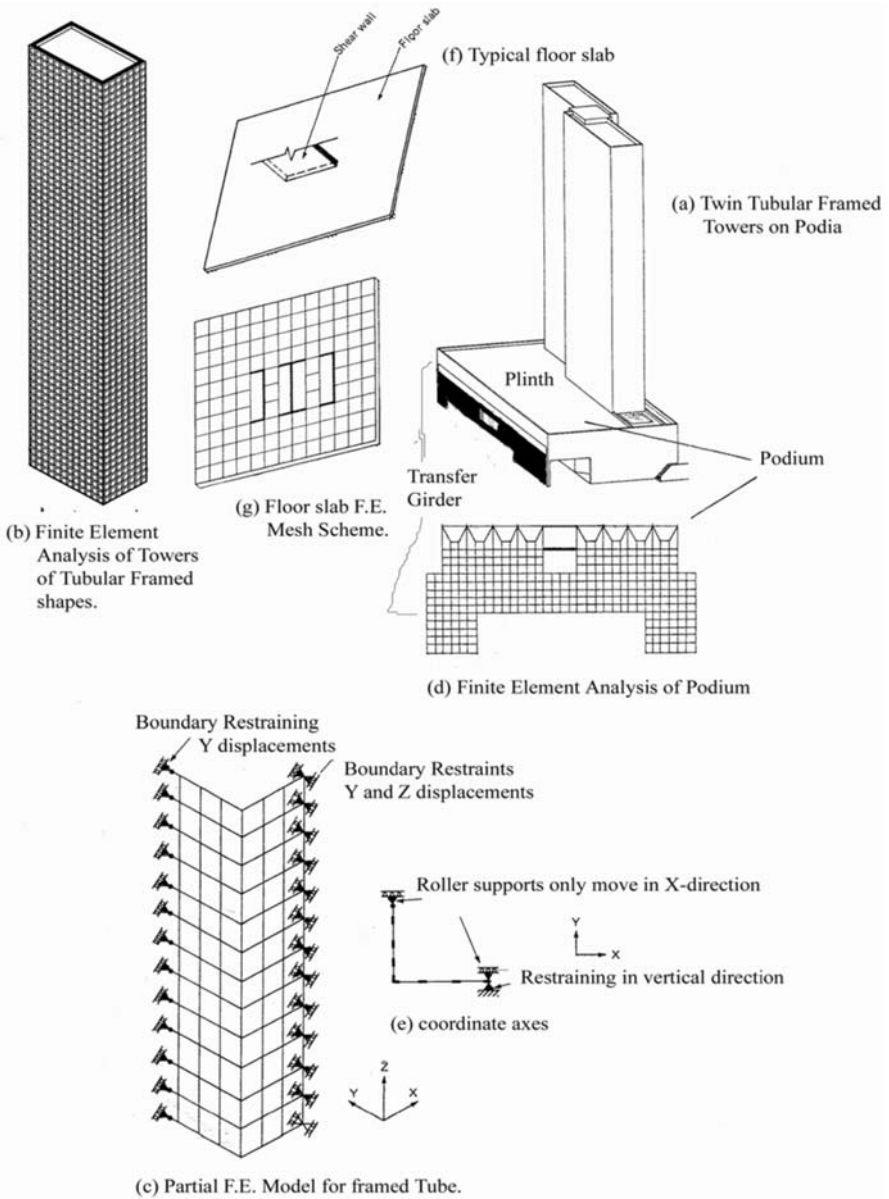
In the general case, the moment of inertia of the lumped model column works out to be  $n^2$  times the prototype value. Lumping of nontypical floors can also be accomplished by assuming locations of point of contraflexure at, say, one-third the height for the lower stories and by using the principle of virtual work to equate the deflection properties.

### 10.2.2.2 Dynamic Finite Element Analysis Using BANGF

A structure such as a building frame can be considered as an assemblage of linear members or elements, each element being three-dimensional, with its cross-sectional dimensions very small relative to its length. A surface structure such as a thin slab on the other hand, can be considered as made up of a network of three-dimensional elements. These elements differ from the beam elements because both their width and length are significant when compared to their thickness. All the three dimensions, namely, the length, width, and thickness need to be considered in the analysis. The whole structure can be treated as an assembly of structural elements of different types. It is only necessary for the engineer to discretize the structure into proper categories in order to gain computational economy. For dynamic finite element analysis, a reference is made to the Appendix I. Figure 10.1 shows a three dimensional framed building finite element mesh of a sectional scheme. Plates 10.1 and 10.2 show F.E. scheme on a Framed Tube Buildings. The mesh scheme given in Plate 10.2 is finally adopted for a tower such as WTC-1, which can be viewed with Plate 10.3 where the two towers are shown simultaneously under impact-cum-fire.

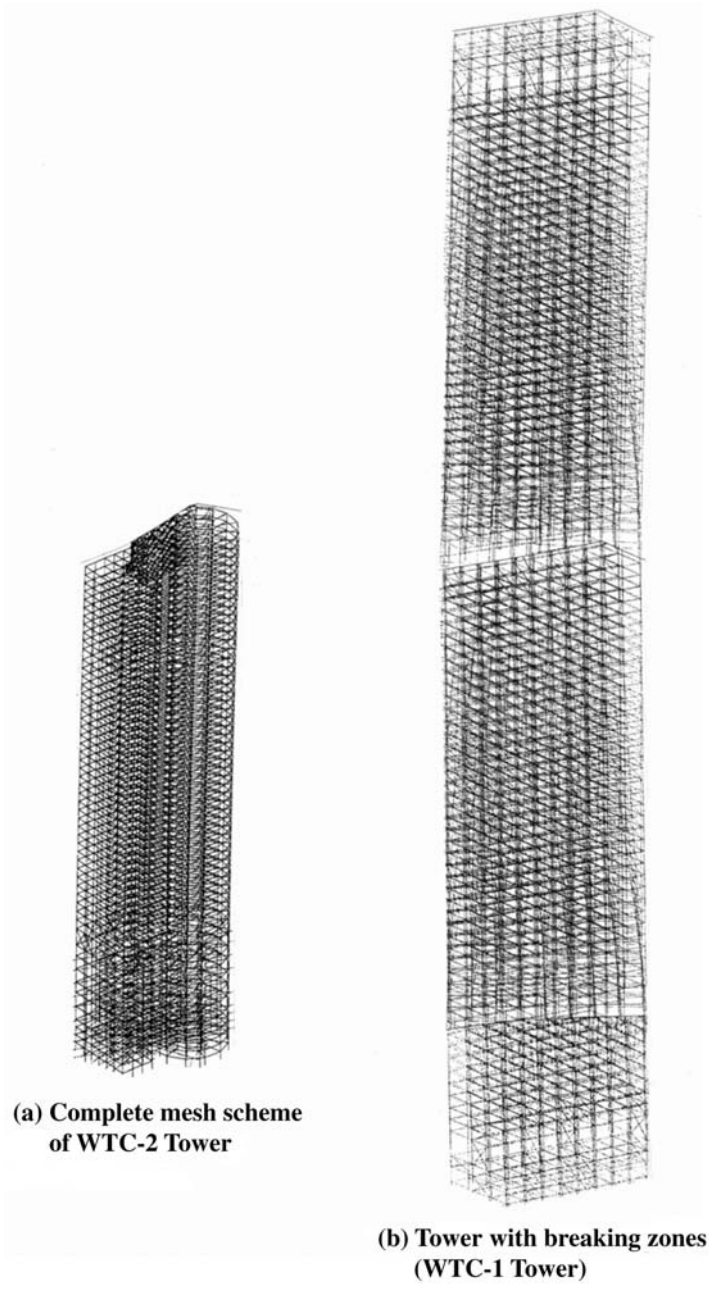
As shown in Fig.10.1 this is the initial optimum process in which the structure being analysed and subdivided into a system of finite elements. Depending on the type of structure, the element models can be line elements, two-dimensional plane stress or plane strain elements, flexural plate and shell elements, axisymmetric elements, general three-dimensional solid elements,

Plate 10.1. Finite element scheme on a framed tube type building



**Plate 10.2.** Three-dimensional F.E. mesh scheme for WTC-1 or WTC-2

---



**Plate 10.3.** Simultaneous views of Twin Towers under impact/fire (courtesy: ASCE, 2002, New York, U.S.A.; FEMA Report, 2002, Washington D.C., U.S.A.; New York Times, private communication)

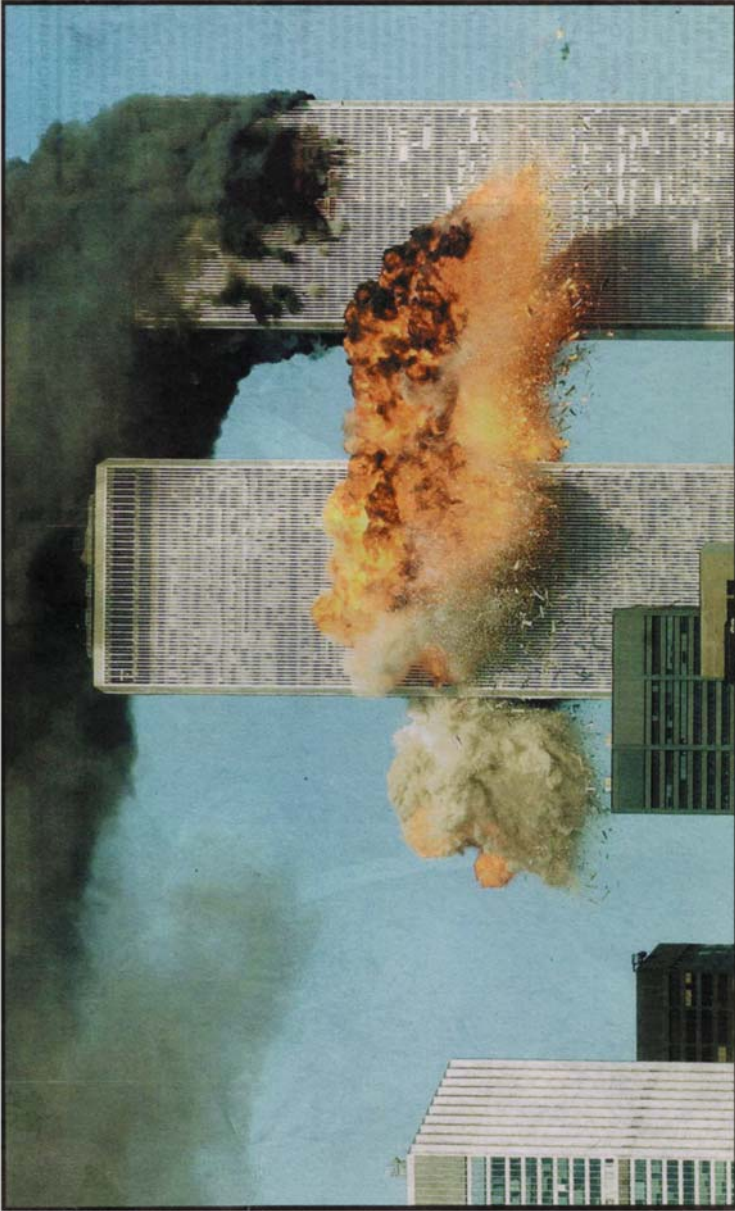




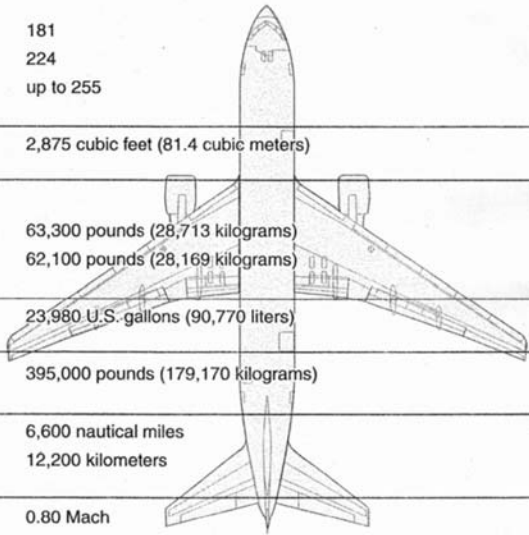
Plate 10.4. Aircraft information Boeing 767-200ER

# Aircraft Information

## Boeing 767-200ER

### General Specifications

<b>Passengers</b> Typical 3-class configuration Typical 2-class configuration Typical 1-class configuration	181 224 up to 255
<b>Cargo</b>	2,875 cubic feet (81.4 cubic meters)
<b>Engines' Maximum Thrust</b> Pratt & Whitney PW4062 General Electric CF6-80C2B7F	63,300 pounds (28,713 kilograms) 62,100 pounds (28,169 kilograms)
<b>Maximum Fuel Capacity</b>	23,980 U.S. gallons (90,770 liters)
<b>Maximum Takeoff Weight</b>	395,000 pounds (179,170 kilograms)
<b>Maximum Range</b> Typical city pairs: New York-Beijing	6,600 nautical miles 12,200 kilometers
<b>Typical Cruise Speed at 35,000 feet</b>	0.80 Mach 530 mph (850 km/h)
<b>Basic Dimensions</b> Wing Span Overall Length Tail Height Interior Cabin Width	156 feet 1 inch (47.6 meters) 159 feet 2 inches (48.5 meters) 52 feet (15.8 meters) 15 feet 6 inches (4.7 meters)



or any hybrid arrangements. For Tower Analysis, a single aircraft, Boeing 767 (Plate 10.4) is used.

The subdivision process is essentially a task that requires engineering judgment. During this process the engineer decides on the number, shape, size, and configurations of the elements with the purpose of simulating the structure as closely as possible. The principal objective of such a subdivision is to discretize the structure into sufficiently small elements such that their displacement can adequately reflect the true deflection pattern of the structure, keeping in mind at the same time that too fine a subdivision will lead to extra computational effort.

The underlying principle is to have an arrangement of finite elements that gives effective representation of the given structure for the particular problem considered. For the floor problem, the finite element idealization is based on the premise that the stress gradients in the vicinity of the shear wall are likely to be steep compared with their values elsewhere in the slab. It is natural to subdivide this area into smaller elements and to use coarser grids away from the regions of severe floor bending. This implies that for floors subjected to other types of imposed loads or displacements it may be necessary to use an entirely new arrangement of finite elements. Based on the expected mode of deformation of the floor, the analyst must decide what number, size, and layout of finite element will best represent the structural behaviour. One of the basic assumptions of the finite element method is introduced at this stage when the analyst chooses displacement functions to represent the actual distribution of the displacements. Usually in structural engineering problems, the displacement function is commonly assumed in a polynomial form with a limited number of terms. The displacement function in the form of a polynomial has certain advantages over other types of functions such as trigonometric formulations. First, even though the polynomial selected for structural analysis purposes is of finite order (i.e., it contains a limited number of terms), it can approximate fairly closely the true displacements for each element. Second, it is relatively easy to carry out the mathematical manipulations such as differentiation and integration. Third, by choosing polynomials we are assured that the displacement variation within an element is continuous without any kinks or other discontinuities. Interelement compatibility is not generally satisfied completely, but solutions sufficiently accurate for purposes of structural design are obtainable even without full displacement compatibility between elements. These are fully discussed in the Appendix I.

It is necessary to impose boundary conditions to the overall assembled stiffness matrix to remove the singularity of the matrix. The physical significance is that unless supports or kinematic constraints are imposed, the structure is free to experience unlimited rigid body motions. Boundary conditions can be thought of as restraints that arrest the rigid body motions.

The equilibrium equations are modified for appropriate boundary conditions and then solved for unknown displacements. In linear structural analysis

this is a relatively straightforward procedure, which uses techniques of matrix algebra.

By using the computed displacements, the nodal forces and hence the stresses at the nodes are calculated by multiplying the nodal displacements by the element stiffness matrix. Usually an average value of the nodal stresses is taken to provide the stress value for each element. Appendix I is referred to in all cases.

The blast loads do cause twisting of structural elements. The warping torsion of beams of solid cross-section and thin walled closed sections can easily be analysed sufficiently accurately by using the classical St. Venant's Torsion Theory. In solid sections the axial stresses as a result of warping is of a local nature while in thin-walled open-section beams, axial and tangential stresses appear in the cross section.

From the three-dimensional F.E. analysis, all stresses are computed. However, torsional analysis can be computed with a special care depending upon the building consisting of single, double or multi-core phenomena.

A central core with access openings can be considered as an example of this system. When such a core is subjected to torsion, it suffers warping displacements and may develop high axial stresses due to restraint at foundation. The St. Venant theory is inadequate for the analysis of such systems and a more appropriate theory, which takes into account the axial stresses has to be applied when torsional loads are present.

The central-core-supported structure offers open floor plans free of columns except at the perimeter, allowing partitioning to be placed to suit the individual needs of occupants, with the elevators and other building services and stairs centralized within the core, which serves also as the main structural element for supporting the vertical and horizontal loads. The core invariably has openings for access into elevator lobbies and stairs; therefore, its cross section can be considered open.

Torsion in high-rise buildings is usually the result of an eccentric disposal of the horizontal loading, from wind or earthquake or explosion with respect to the centre of reaction of the shear-resisting elements. This eccentricity can be caused by an orthogonally symmetrical core being offset horizontally from the centre of area of the building elevation, but of both transverse and tangential stress distribution.

Accidental load torsion has also started receiving considerable attention in recent years. For example, the city of Houston building code stipulates that unless wind tunnel procedures are used in determining wind loads, the primary frame should be designed to resist a torsional moment caused by 50 percent of wind load acting on half of the windward and leeward faces, with the full wind loading acting on the remaining portions of the windward and leeward faces.

Many cases arise in practice where external constraints cause some sections of the core to remain plane. For example, heavy foundation at the base of the core prevents warping, giving rise to warping axial stresses. These stresses

vary along the height and are accompanied by transverse shear stresses, which also vary from section to section. The transverse shear stresses are in addition to tangential shear stresses caused by pure twisting and jointly resist the applied torque at any section. At the foundation, since the warping of the cross section is prevented, the shear stress distribution is solely due to transverse bending of the core.

During twisting, the cross sections of the core undergo distortion, with different points on the cross section suffering different displacements along the longitudinal axis of the core. If this distortion or warping as it is called is not free to take place, longitudinal stresses directed along the  $z$  axis develop in the cross section. The foundation for a high-rise core is usually stiff and can be considered to restrain almost completely the vertical movement of the relatively light walls.

**10.2.2.3 Derivation of Equations for Building Cores Under Torsion Alone (Based on B. Taranath Method [10.57])**

It is proposed that all stresses in the finite element analysis can normally be computed. The effects of torsion or twist are algebraically added to them so that they represent the true scenario.

The structure is rendered statically determinate by introducing an “imaginary cut” along a line bisecting the imaginary core plate. The equilibrium equation is written for the core in terms of external transverse forces and equivalent shear forces applied along the cut edges of the core plate. The compatibility condition for the relative displacement at the cut section leads to the differential equation for the core beam assembly. The detailed steps are as follows.

The equilibrium equation for non-uniform torsion of a thin-walled core subjected to the action of external transverse loads and longitudinal shear forces applied along the edges can be shown to be

$$EI_{\omega} \frac{d^4\theta}{dz^4} - GJ \frac{d^2\theta}{dz^2} = m + \frac{dV}{dz} A \tag{10.4}$$

where

- $m$  = the external torsional moment at  $z$
- $dV/dz$  = the derivative of the shear forces  $V_z$  at section  $z$
- $A$  = twice the area of the enclosed contour between the core and the beam.

The vertical displacement  $\delta_{z,s}$  which results from warping of the thin-walled beam is expressed according to the equation

$$\delta_{z,s} = -\frac{d\theta}{dz} \omega_s \tag{10.5}$$

where  $d\theta/dz$  is the relative warping dependent upon the  $z$  coordinate and  $\omega_s$ , is the sectorial area which depends on the location of the point  $s$  on the contour.

The relative displacement at the cut section due to warding can be written thus

$$\begin{aligned}\Delta_1 &= \frac{d\theta}{dz}(\omega_L - \omega_k) \\ \Delta_1 &= -\frac{\partial\theta}{\partial z} A\end{aligned}\tag{10.6}$$

The relative displacement  $\Delta_2$  at the cut due to the flexibility of the beam under the application of a shear force  $V_z h$  is given by

$$\Delta_2 = \frac{V_z h}{G} \left( \frac{l^2 G}{12EI_b} + \frac{1.2}{A_b} \right)\tag{10.7}$$

where

$h$  = the story height

$l$  = the beam length

$I_b$  = moment of inertia of beam about the  $y$  axis

$A_b$  = the area of the beam

$E$  and  $G$  = the familiar material properties of the beam

For compatibility of displacement,  $\Delta_1 + \Delta_2 = 0$ ; I.e.,

$$\frac{d\theta}{dz} A + \frac{V_z h}{G} \left( \frac{l^2 G}{12EI_b} + \frac{1.2}{A_b} \right) = 0\tag{10.8}$$

Differentiating with respect to  $z$ , we have

$$\frac{d^2\theta}{dz^2} A + \frac{dV}{dz} \frac{h}{G} \left( \frac{l^2 G}{12EI_b} + \frac{1.2}{A_b} \right) = 0\tag{10.9}$$

These analyses are part of BANGF program.

#### 10.2.2.4 Core Interaction with Floor Systems for WTC-1

Structural Analysis and computer programs exist on the inter action problems of shear wall and floor systems. It pares the way to assess the effective width of the slab and to establish coupling stiffnesses in the finite element program.

However, comparatively little information is available for the structural analysis and design of floor coupled tall core structures subjected to torsional loads, in spite of the fact that the interacting forces developed in a coupling floor of a core structure are substantially larger than those developed in a cross-wall system. In a cross-wall system the coupling beam or slab resists the independent cantilever action of the frame by developing shear and bending stresses. A slab surrounding a core by comparison is subjected to very high bending and twisting actions due to the warping deformation of the core. Guided by the available results for the cross-wall systems and the deformation pattern of the floor around a core, it is natural to expect substantial

interacting forces around the core where the slab is rigidly connected to the core walls. It is concluded that torsion theory tacitly takes into account the in-plane action of the floors.

A finite element method is employed for evaluating the warping stiffness of the floor slab, which is then incorporated into a stiffness method analysis of torsion of the core system. A comparison of analytical results conducted on a model core structure is presented with comments on convergence characteristics of finite elements.

When the core undergoes warping deformation, the floor slab, which is rigidly connected to the core, is forced to bend out of plane in resisting the warping deformation of the core. The transverse displacement of the slab and the warping displacement of the core must be compatible at the profile of the core where the two systems are interconnected. The displacement pattern of the floor at points along its floor connection to the wall is, therefore, known from the warping displacement of the core. For a unit warping displacement of the core, the slab is displaced along the contact boundary in a manner similar to the warping coordinate diagram  $\omega_s$  of the core. This displacement gives rise to continuous interactive forces consisting of distributed axial forces and moments at the inner edges of the floor at the profile of the core. The problem of finding the warping stiffness of the floor, therefore, reduces to the determination of these interactive forces and moments. Incorporation of these forces and thus the warping stiffness of the floor in the torsion analysis of the core is greatly simplified by mathematically converting these forces into a bimoment function, as will be shown shortly.

The necessary force displacement relationship defines the slab warping stiffness Plate 10.2 shows forces and moments. The force resultants in terms of forces and moments are shown there in.

In general, the resulting force system, which consists are concentrated forces  $P_1, P_2, P_3, \dots, P_n$ , and moments  $M_1, M_2, M_3, \dots, M_n$  applied at the points  $k = 1, 2, 3, \dots, n$  of the cross section, is expressed as a bimoment by the relation

$$B_\omega = \sum_{k=1}^n P_k \omega_k + \sum_{k=1}^n M_k \frac{\partial \omega_k}{\partial s} \tag{10.10}$$

where

- $B_\omega$  = the warping stiffness of floor slab
- $\sum_{k=1}^n P_k \omega_k$  = the summation of the product of concentrated forces and the warping displacement
- $\sum_{k=1}^n M_k \frac{\partial \omega_k}{\partial s}$  = the summation of the concentrated transverse moments and the rate of change of warping function

Substituting for  $dt/dz$  in the equilibrium equation and using the notation

$$J_b = \frac{A}{\alpha h} \left\{ \frac{l^2 G}{12EI_b} + \frac{1.2}{A_b} \right\} \tag{10.10a}$$

or

$$EI_\omega \frac{d^4\theta}{dz^4} - G(J + J_b) \frac{d^2\theta}{dz^2} = m_z \quad (10.11)$$

For this purpose, it is only necessary to replace St. Venant's torsional constant  $J$  by the sum  $J + J_b$  as given by (10.11). The parameter  $k$  is now computed from the equation

$$k = l \sqrt{\frac{G(J + J_b)}{EI_\omega}} \quad (10.12)$$

The calculation of bimoment and axial forces follows the procedure as the torque moment  $M_1$  carried by the membrane shear stresses, which accompany the longitudinal stresses is given by

$$M_1 = -\frac{-E}{1 - \mu^2} I_\omega \frac{d^3\theta}{dz^3} \quad (10.13)$$

the torque  $M_2$  carried by St. Venant shear stresses is given by

$$M_2 = GJ \frac{d\theta}{dz} \quad (10.14)$$

where  $GJ$  is St. Venant torsional rigidity of the section.

Total torque

$$M = M_1 + M_2 = \frac{-EI_\omega}{1 - \mu^2} \frac{d^3\theta}{dz^3} + GJ \frac{d\theta}{dz} \quad (10.15)$$

Differentiating with respect to  $z$ , (10.12) is obtained (10.15) is then

$$\frac{EI_\omega}{1 - \mu^2} \frac{d^4\theta}{dz^4} - GJ \frac{d^2\theta}{dz^2} = m_z \quad (10.16)$$

or

$$\frac{d^4\theta}{dz^4} - \frac{k^2}{l^2} \frac{d^2\theta}{dz^2} = m_z$$

The longitudinal stresses and warping are related

$$\sigma_{z,s} = \frac{-E}{1 - \mu^2} \frac{d^2\theta}{dz^2} \omega_s \quad (10.17)$$

the quantity  $\int \sigma_{z,s} \omega_s t_s ds$  is a generalised for called BIMOMENT  $B_z$  and is easily obtained as

$$B_z = \frac{-EI_\omega}{1 - \mu^2} \frac{d^2\theta}{dz^2} \quad (10.18)$$

where  $I_\omega =$  warping moment of

$$\text{inertia} = \int \omega_s^2 t_s ds \quad (10.19)$$

$t_s$  = wall thickness of the element.

The longitudinal displacements can still be represented by

$$\delta_{z,s} = -\theta'_z \omega_k \quad (10.20)$$

where  $\theta'_z$  = unit warping displacement introducing longitudinal displacements and measure of cross-sectional distortion.

A typical finite element idealization for the floor is given in Plate 10.2. The floor is assumed to be free of any restraint as maybe imposed by perimeter columns, ties etc. Hence all the nodes except those corresponding to the profile of the core are assumed to be free. The next stage is to impose unit  $\theta'_z$  displacement at the inner boundary of the slab. For this purpose, transverse displacements perpendicular to the plane of the slab and equal in magnitude and sense to the warping function are introduced at the nodes common to the core and the slab (e.g., nodes  $N_1, N_2, \dots, N_n$  in Plate 10.5(i)c. In addition to these vertical displacements, the slopes  $\delta\omega/\delta x$  and  $\delta\omega/\delta y$  are made equal in magnitude and sense to the slope of the  $\omega_s$  diagram. Having thus given at the inner edge of the slab a displacement conforming to the warped outline of the core, the forces and transverse moments at the nodes are found from a finite element solution. The bimoment, which then corresponds to the required warping stiffness of the slab, is found from the relation given in (10.20)). The effect of the floor system, which is mathematically equivalent to the bimoment, is incorporated into the analysis by adding the bimoment to the appropriate elements of the stiffness matrix of the core. The stiffness coefficients for an open section need to be calculated first. One way is to invert the flexibility matrix and the other is to assume deformed shape of the members. In any case the following relationship is established:

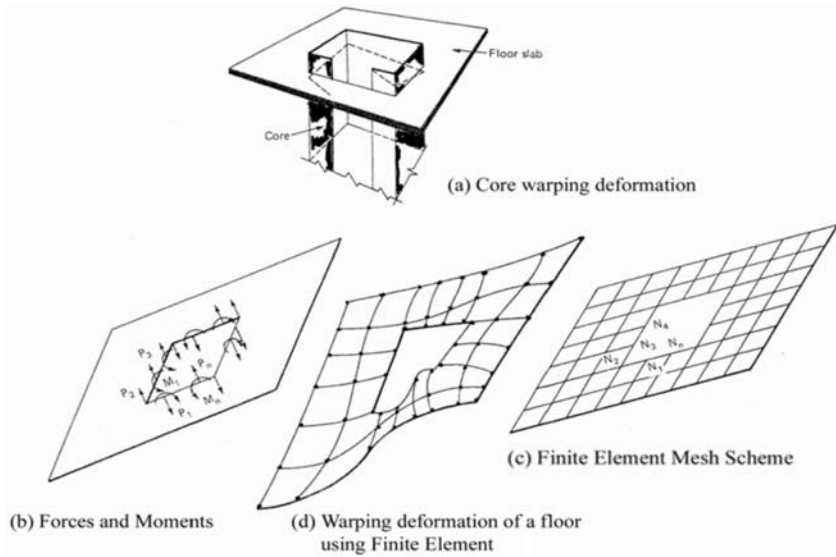
$$\begin{bmatrix} \theta_z \\ \theta'_z \\ \frac{B_z}{GJ} \\ \frac{M_z}{GJ} \end{bmatrix} = \begin{bmatrix} 1 & \frac{l}{k} \sinh \frac{kz}{l} & 1 - \cosh \frac{k}{l} z & z - \frac{l}{k} \sinh \frac{kz}{l} \\ 0 & \cosh \frac{kz}{l} & -\frac{k}{l} \sinh \frac{kz}{l} & 1 - \cosh \frac{kz}{l} \\ 0 & -\frac{l}{k} \sinh \frac{kz}{l} & \cosh \frac{kz}{l} & \frac{l}{k} \sinh \frac{kz}{l} \\ 0 & 0 & 0 & 1 \end{bmatrix} \begin{bmatrix} \theta_{0z} \\ \theta'_{0z} \\ \frac{B_0}{GJ} \\ \frac{M_0}{GJ} \end{bmatrix} \quad (10.21)$$

It is essential to find the elements of the first row of the stiffness matrix, which correspond to the torque and bimoment at each end of the beam required to produce a unit rotation of  $\theta = 1$  at  $z = 0$  while all the other three displacements are zero, it is necessary to introduce the appropriate boundary conditions in (10.22).

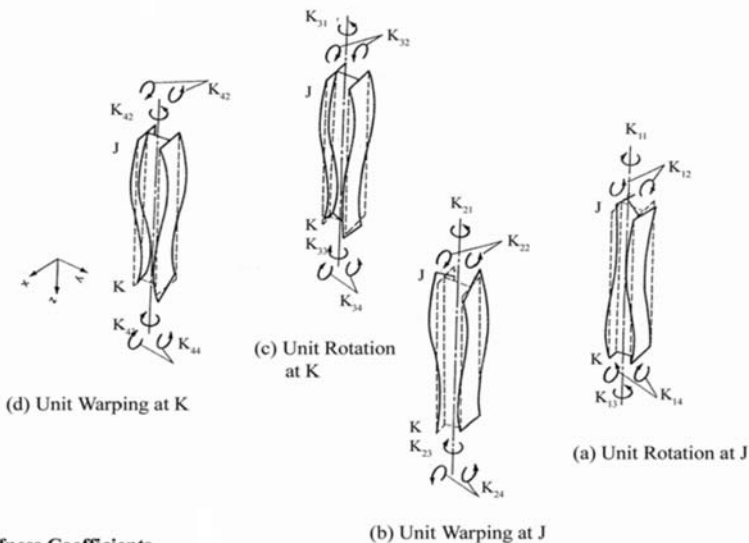
In (10.22) on the left hand column matrix, elements  $\theta_z = 0$  and  $\theta'_z = 0$  and on the right side in the column matrix  $\theta_o = 1$  and  $\theta'_o = 0$ . All other do not change. The four stress resultants or force resultants  $M_o$ ,  $B_o$ ,  $M_l$  and  $B_l$  at the two ends can be obtained. One has to know the member stiffness matrix for thin walled section subjected to torsion and shall take the form: these are shown in Plate 10.5(ii)c.



**Plate 10.5.** Warping phenomenon (courtesy and based on: Taranath BS (1998) Steel, concrete, and composite design of tall buildings, McGraw-Hill, New York, London. Chapter 10: Analysis technique)



**(i) Slab Deformation**



**(ii) Stiffness Coefficients**

**Note:** Computer program BANG-STAB, part of BANG-F has been developed using this analysis and variation from this analysis after modification to suit WTC Towers.

$$\left[ \frac{GJ}{2 + k \sinh k - 2 \cosh k} \right] \begin{bmatrix} \frac{k}{l} \sinh k & (1 - \cosh k) & -\frac{k}{l} \sinh k & (1 - \cosh k) \\ (1 - \cosh k) & \frac{l}{k}(k \cosh k - \sinh k) & -(1 - \cosh k) & \frac{l}{k}(\sinh k - k) \\ -\frac{k}{l} \sinh k & -(1 - \cosh k) & \frac{k}{l} \sinh k & -(1 - \cosh k) \\ (1 - \cosh k) & \frac{l}{k}(\sinh k - k) & -(1 - \cosh k) & \frac{l}{k}(k \cosh k - \sinh k) \end{bmatrix} \quad (10.22)$$

Assuming  $M, B, \theta, \theta'$  and  $I_\omega$  are replaced by  $V, M, \omega, \omega'$  and  $I_{xx}$  the matrix  $[K]$  of the element can be written in an expanded form for  $\sinh k$  and  $\cosh k$ . Take one element  $K_{11}$

$$K_{11} = \frac{GJk}{l(z + k \sinh k - 2 \cosh k)} \sinh k \quad (10.23)$$

when  $k = 0$

$$K_{11} = \frac{EI_\omega k^2 \left( \frac{k}{l} \right) \left( k + \frac{k^3}{6} + \frac{k^5}{120} \right)}{l^2 \left[ 2 + k \left( k + \frac{k^3}{6} + \frac{k^5}{120} \right) - 2 \left( 1 + \frac{k^2}{2} + \frac{k^4}{24} \right) \right]} = \frac{12EI_\omega}{l^3} \quad (10.24)$$

which is of the same form as the element corresponding to the shear force in the well-known beam stiffness matrix.

Where  $V =$  shear force and  $\omega' = d\omega/dz$  and all others have been defined.

Similarly for other stiffness values  $K_{21}, K_{22}, \dots, \omega'$  can be computed. Of the heavy foundation is at the base for shear core  $\theta = 0; \theta' = 0$  at the base. Where it is an elastic spring, an appropriate stiffness can be incorporated.

The final step will be the solution of (10.25) which are simultaneous equations:

$$\{F\} = [K]\{\theta\} \quad (10.25)$$

Combined load vector. The combined load vector is the sum of the applied loads at the joints and the equivalent joint loads due to member loads between the joints. The former is known immediately from the given loads on the structure, while the latter needs to be evaluated such as blast loads.

When the analysis is carried out on a regular basis, the torsional aspect shall be algebraically added. For a torsion alone case, rotations and stresses at various stages should be shown along the bimoment variation. Bimoments are plotted for full storey height of the building – considerable gain in strength and stiffness can be obtained by considering the warping stiffness of the floors.

### 10.2.2.5 Twin Core System – Method of Analysis (Based on B. Taranath [10.57])

In certain core systems, the combined floor space required to house the stairways, duct shafts, storage and mechanical equipment, etc., can become so large that it is not architecturally feasible or structurally economic to group the services within a single core. In such circumstances it is usual to use two

or more cores and distribute the services between them. The stiffness method of analysis explained in the previous section can be conveniently employed for the torsion analysis of such practical arrangement of cores.

This section presents a method for the analysis of twin-core structures interconnected either through beams only or beams and slabs. Analytical results are compared with available experimental results.

For a complete analysis of interconnected core systems subjected to loads producing both bending and torsion, it is necessary to resort to a three-dimensional analysis. However, leaving aside the bending part, the problem can be reduced to a unidirectional analysis. This simplification is achieved by considering the entire system of cores as a single thin-walled beam. All the elements of this beam are then considered to rotate about a common centre of rotation  $O$ , which is located from a consideration of the shear forces in the individual elements. The sectional properties of the complete system are found with respect to this centre of rotation, and the analysis is carried out as outlined earlier for single-core systems.

### Notations

$I_{\omega c}$	Sectorial moment of inertia of the core with respect to $O$
$I_{\omega A}$	Sectorial moment of inertia of the core with respect to $A$
$O$	Shear centre of the assembly of twin cores
$O_1$	Shear centre for single core
$(x_0, y_0)$	Coordinates of $O$
$(x_1, y_1)$	Coordinates of $O_1$
$X_1$	$(x_0 - y_A)$
$Y_1$	$(y_0 - y_A)$
$I_{\omega O}$	Sectorial moment of inertia of the cores
$I_{xx}, I_{yy}$	Moment of inertia of the core about its centroidal axis
$F_1, F_2$	Sectorial origins for the two cores
$S \times E$	Strain energy of the plate
$P \times E$	Potential energy
$E_{TOT}$	$SE + PE$

A system comprising two interconnected cores is shown in Plate 10.6. Although it is possible to consider more complicated systems, this plan form has been chosen.

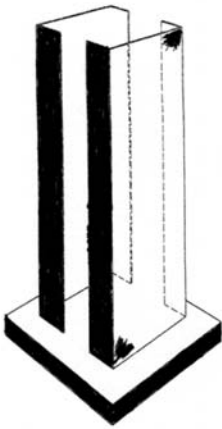
Torsional parameters  $\omega_s$  and  $f_\omega$  to calculate first  $I_\omega$  for each core.

Each core

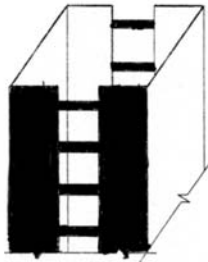
$$I_{\omega c} = I_{\omega O_1} + I_{xx}X_1^2 + I_{yy}Y_1^2 \quad (10.26)$$

In this example the two cores coincide  $y_1 = 0$  substituting into (10.26) and for two cores

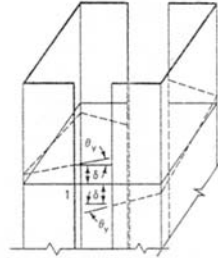
Plate 10.6. Twin cores



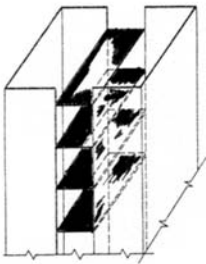
(i) Twin cores



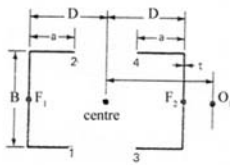
(ii) (a) Twin cores coupled with internal connected beams



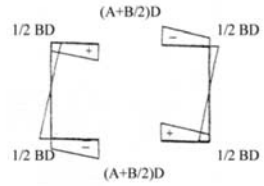
(ii) (b) Core warping rotations and deflections of beam ends



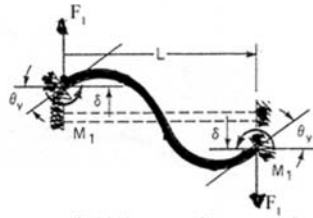
(iii) Twin cores coupled through slabs



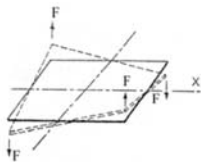
(i) (b) Dimensions of core



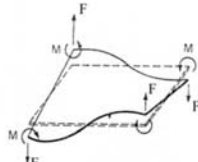
(i) (a) diagram and warping coordinates



(i) (c) Forces and moments due to core warping



(iii) (a) Slab subjected to corner forces F



(iii) (b) Slab subjected to corner forces F and moment M

$$I_{\omega}^0 = 2I_{\omega_c}^0 = 2[I_{\omega O_1} + I_{xx}X_1^2] \tag{10.27}$$

In order to determine parameters, sectoral origin for the two cores to be found first, while keeping in mind that sectoral static moment is zero

$$I_{\omega}^0 = \int_1^2 \omega_s^2 ds + \int_3^4 \omega_s^2 ds \tag{10.28}$$

Considering  $GJ$  for two cores are algebraically added, the value of  $k$  is then computed as to be used for the stiffness matrix as

$$k = \sqrt[3]{\frac{GJ}{EI_{\omega}^0}} \tag{10.29}$$

$h$  being the height of a storey.

The forces and moment in a beam (Plate 10.6(i)c) are given as

$$F_1 = \frac{12EI}{L^2} \left( \frac{2\delta}{L} + \delta_{\nu} \right) \tag{10.30}$$

$$M_1 = \frac{6EI}{L} \left( \frac{2\delta}{L} + \theta_{\nu} \right)$$

Consider the case when the two cores are interconnected at each floor level by two beams as in Plate 10.6(i)a. To find the warping stiffness of the beams it is required to find the force system, and hence the bimoment generated, when a unit  $\theta'_z$  displacement is given to the beams. From a consideration of  $\omega_{(s)}$  diagram for the cores, it is seen that unit  $\theta'_z$  corresponds to a vertical displacement equal to the magnitude of  $\omega$  at 1, and a rotation of  $\partial\omega/\partial x$  at each end of the beam. The warping stiffness  $B_{\omega}$  is found as:

$$B_{\omega} = 4 \left( P_1\omega_1 + M_1 \frac{\gamma\omega_1}{\gamma y} \right) \tag{10.31}$$

The stiffness of the individual storey segments are then assembled to give the complete stiffness matrix  $[K]$ . Appropriate boundary conditions are then introduced and equations are solved for the given load system. The stress resultants at each storey level are obtained from the known displacements and member given load system.

The potential energy for the four point loads at the corners is given by

$$P.E. = -4F \frac{\alpha}{2} \frac{b}{2} C = -F\alpha bC \tag{10.32}$$

Substituting for  $\omega$  in the expression for  $S.E.$ , the total energy

$$E_{TOT} = S.E. + P.E. = \int_{-\alpha/2}^{\alpha/2} \int_{-b/2}^{b/2} D_1(1 - \mu)C^2 dx dy - F\alpha bC \tag{10.33}$$

$$= D_1(1 - \mu)C^2\alpha b - F\alpha bC$$

Differentiating  $E_{TOT}$  with respect to  $C$  and equating to zero,  $C$  is found to be equal to  $F/2D_1(1 - \mu)$

$$\omega = Cxy = \frac{F}{2D(1 - \mu)} xy \quad (10.34)$$

and the value of  $F$  per unit displacement becomes equal to

$$F = \frac{8D_1(1 - \mu)}{\alpha b} \quad (10.35)$$

The required bimoment due to the four corner forces is given by

$$B_\omega = \sum_{i=1}^4 F_i \omega_i \quad (10.36)$$

Since  $\omega_1 = -\omega_2 = -\omega_3 = \omega_4$ ,

$$B_\omega = 4 \times \frac{8D_1(1 - \mu)}{\alpha b} \times \omega_1 \quad (10.37)$$

When the slab-core joint is rigid, then it is no longer possible to find the forces and moment at the corners analytically. However, using the finite element technique, these can be readily established and the appropriate value of stiffness found.

The nodes corresponding to the corners of the plate 1, 2, 3, and 4 are given a vertical displacement and rotation equal to the warping coordinate of  $\omega$  and the slope  $\partial\omega/\partial s$  at these points. From the finite element analysis the corner forces and moments can be computed.

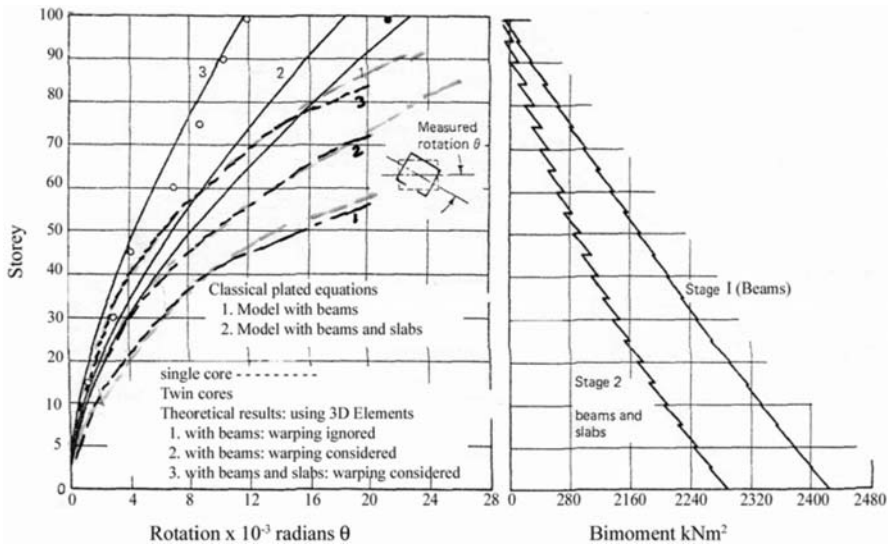
Equation (10.37) is modified to include bimoment and is given by:

$$B_\omega = \sum_{i=1}^4 \left( F_i \omega_i + M_i \frac{\partial \omega_i}{\partial s} \right) \quad (10.38)$$

The warping stiffness is added to the story stiffness to obtain the stiffness of modified story segment.

### 10.2.2.6 Application

The finite element analysis is applied to a 100 storey building assuming coupled with beams and floors as two case studies. The details of F.E. method is given in Appendix I. The above classical method of the twin core building is compared with the finite element method. Both methods are compared. The blast load of 1500 lb bomb of TNT as explained in earlier sections using displacements concept based on Simpson's Rule, is applied. Figure 10.2 shows a comparative study of results of both these analyses. A good agreement exists and the importance of taking the warping stiffness of beams and floor labs is emphasised more strikingly than in the case of single core, since the method shows a great deal of collaboration.



**Fig. 10.2.** Comparison of rotations for twin-core system subject to 1500 lb bomb, producing Torque

### 10.3 Multi Multiple-Core Systems (Based on B. Taranath [10.57])

In previous investigations of the three-dimensional behaviour of shear wall structures, it has generally been assumed that at each story a shear wall has, at the most, six degrees of freedom. While this is accurate for plane shear walls or those with a *T* or *L* section, the presence of shear walls with an open section, e.g., with a U or H shape, as often used for elevator shafts, introduces the additional possibility of warping displacements. This seventh degree of freedom and its associated actions can have a significant influence on the behaviour of the structure. It is necessary, therefore, that any method of analysis, which aims to predict satisfactorily the behaviour of such open-section systems must recognize the warping effect.

The method presented in this section considers the warping behaviour as well as the warping interaction between a multiple system of open-section shear wall structures interconnected by floor slabs. The finite element technique is employed to compute the out-of-plane stiffness of floor slabs, and using a stiffness matrix approach, the complete structure is studied in a unified manner.

#### *Method or Analysis*

It is convenient to develop the method of analysis with reference to a particular structural plan such as that of a hypothetical high-rise building. In order

to emphasize the warping phenomenon, all the shear walls are open sections. The shear walls are interconnected solely through a flat plate system, it being assumed that there are no columns or beams. The floor diaphragms are considered to be perfectly rigid in their own plane and are joined to the walls by a moment-resistant connection. The geometry of the plan, story height, member properties, elastic modulus, and Poisson's valid can be assumed constant or variable depending upon types of elements and their materials. Each element is treated as a three-dimensional element which can be a thin wall or prismatic. Plate 10.7 show the stiffness matrices  $[K]$  for both prismatic and thin wall type.

In the absence of a rigid floor diaphragm, each vertical element would have seven degrees of freedom at each end; six of these are the familiar translations and rotations about three orthogonal axes, while the remaining seventh is the warping displacement. These are shown numbered for a typical open-section member in Fig. 10.2. Thus the stiffness matrix for an open-section shear wall will be of the order of 14 by 14 (for seven degrees of freedom at each end). This matrix is obtained by combining the well known 12-by-12 stiffness matrix of a prismatic member of a space frame together with the 4-by-4 torque-bimoment matrix given earlier. The resulting matrix is henceforth referred to as the generalized member stiffness. The 12-by-12 stiffness matrix of a prismatic member and the 14-by-14 matrix for an open section are shown in Plate 10.7, wherein the actions and displacements are taken to be positive in the positive sense of the reference axes.

Because the floor slab is considered to be rigid in its own plane, the displacements are such that its plan shape and the geometrical dimensions remain unchanged. The floor slab can be considered to be displaced as an absolutely rigid body.

A matrix method is employed for the evaluation of each single storey segment. The transformation matrix of displacement nature  $T$  is given in terms of stiffness coordinates and each member stiffness is given as

$$[K] = [T^T][K][T] \quad (10.39)$$

where  $T''$  is the transpose of the matrix  $[T]$ .

Plate 10.8 shows typical segment consisting of 3 No. shear walls with the numbering scheme or sequence of displacement.


- $u_1, u_2$  = planar displacements of the slab referred to the origin
- $u_3, u_4, u_5$  = axial displacements
- $u_6$  to  $u_6$  = rotation of the shear walls about their own centroidal axes
- $u_{12}$  = rotation of the assembly about  $z$  axis
- $u_{13}$  to  $u_{15}$  = warping displacements of the three shear walls related to their shear centres

When a unit displacement is given to the top of the floor to be  $u_1$ , the corresponding forces are:

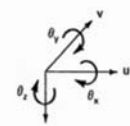


**Plate 10.7.** Stiffness matrices for thin-walled core elements (with compliments of the Tall Building Association of New York, U.S.A). From B. Taranath [10.57]

		u	v	w	$\theta_x$	$\theta_y$	$\theta_z$	u	v	w	$\theta_x$	$\theta_y$	$\theta_z$
		1	2	3	4	5	6	7	8	9	10	11	12
u	1	$\frac{12EI_y}{L^3}$	S										
v	2	0	$\frac{12EI_x}{L^3}$	Y									
w	3	0	0	$\frac{EA}{L}$	M								
$\theta_x$	4	0	0	$\frac{6EI_x}{L^2}$	0	$\frac{4EI_x}{L}$							
$\theta_y$	5	0	0	0	0	$\frac{4EI_y}{L}$							
$\theta_z$	6	0	0	0	0	0	$\frac{GJ}{L}$						
u	7	0	0	0	0	0	0	$\frac{12EI_y}{L^3}$					
v	8	0	0	0	0	0	0	0	$\frac{12EI_x}{L^3}$				
w	9	0	0	0	0	0	0	0	0	$\frac{EA}{L}$			
$\theta_x$	10	0	0	0	0	0	0	0	0	0	$\frac{4EI_x}{L}$		
$\theta_y$	11	0	0	0	0	0	0	0	0	0	0	$\frac{4EI_y}{L}$	
$\theta_z$	12	0	0	0	0	0	0	0	0	0	0	0	$\frac{GJ}{L}$



(b) Global coordinates

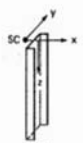


(c) Local coordinates


(a) Twelve by twelve stiffness matrix for prismatic three-dimensional element;

(b) coordinate axes; (c) positive sign convention.

		u	v	w	$\theta_x$	$\theta_y$	$\theta_z$	$\theta'_z$	u	v	w	$\theta_x$	$\theta_y$	$\theta_z$	$\theta'_z$
		1	2	3	4	5	6	7	8	9	10	11	12	13	14
u	1	$\frac{12EI_y}{L^3}$			S										
v	2	0	$\frac{12EI_x}{L^3}$		Y										
w	3	0	0	$\frac{EA}{L}$		M									
$\theta_x$	4	0	0	$\frac{6EI_x}{L^2}$	0	$\frac{4EI_x}{L}$									
$\theta_y$	5	0	0	0	0	$\frac{4EI_y}{L}$									
$\theta_z$	6	0	0	0	0	0	$S_{11}$								
$\theta'_z$	7	0	0	0	0	0	$S_{12}$	$S_{22}$							
u	8	0	0	0	0	0	0	0	$\frac{12EI_y}{L^3}$						
v	9	0	0	0	0	0	0	0	0	$\frac{12EI_x}{L^3}$					
w	10	0	0	0	0	0	0	0	0	0	$\frac{EA}{L}$				
$\theta_x$	11	0	0	0	0	0	0	0	0	0	0	$\frac{4EI_x}{L}$			
$\theta_y$	12	0	0	0	0	0	0	0	0	0	0	0	$\frac{4EI_y}{L}$		
$\theta_z$	13	0	0	0	0	0	0	0	0	0	0	0	0	$S_{11}$	
$\theta'_z$	14	0	0	0	0	0	0	0	0	0	0	0	0	0	$S_{22}$



(b)



(c)

Torque bimoment relation as between  $P_x$  and  $\theta'_z$

$$K_{11} = \alpha \frac{k}{\ell} \sinh k \quad K_{24} = \alpha \frac{k}{\ell} (\sinh k - k)$$

$$K_{12} = \alpha (1 - \cosh k)$$

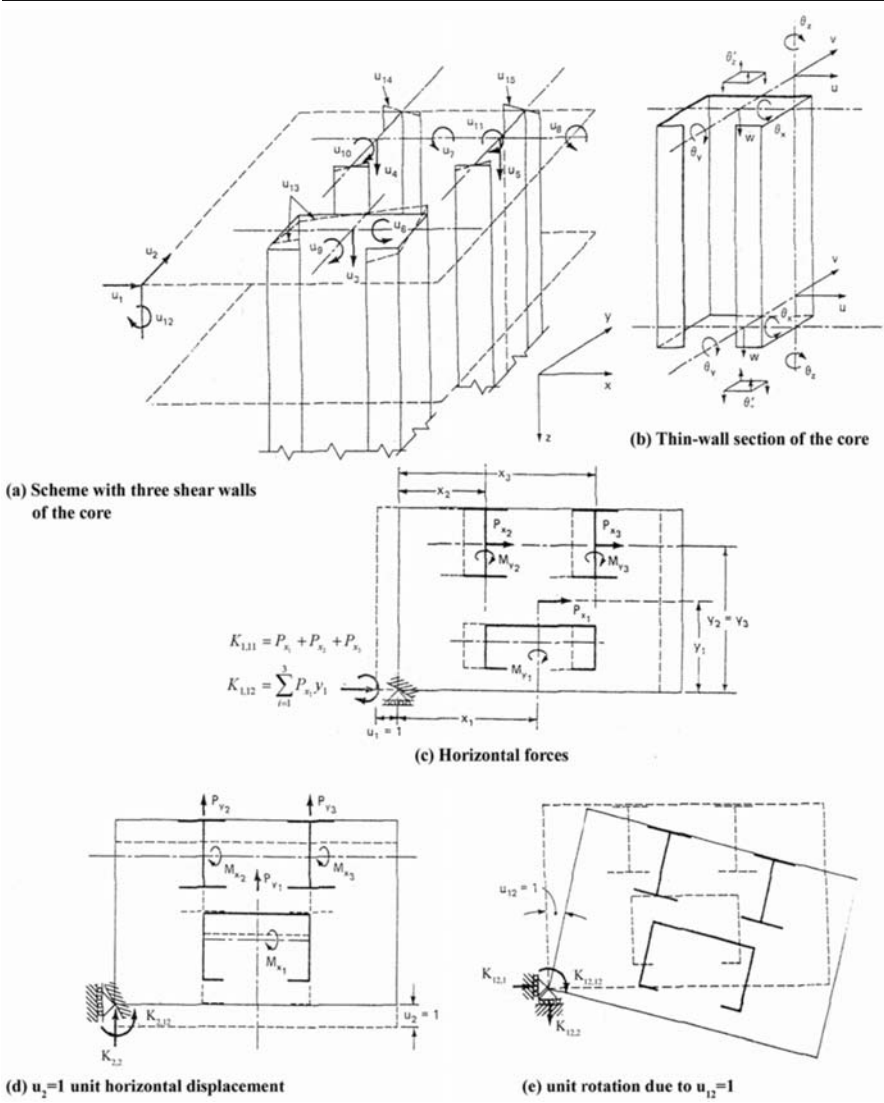
$$K_{22} = \alpha (k \cosh k - \sinh k)$$

where  $\alpha = \frac{GJ}{(2 + k \sinh k - 2 \cosh k)}$

(a) Fourteen by fourteen stiffness matrix for thin-walled open section;

(b) coordinate axes; (c) positive sign convention.

**Plate 10.8.** Shear walls (with compliments of the Tall Building Association of New York, U.S.A). From B. Taranath [10.57]



$$F_{x_1} + F_{x_2} + F_{x_3}$$

and a torque equal to

$$\sum_{i=1}^3 F_{x_i} \times y_i$$

The force and the torque correspond to the elements  $K_{1,1}$  and  $K_{1,12}$  of the segments of stiffness matrix. Moments  $M_{y_1}$ ,  $M_{y_2}$  and  $M_{y_3}$  are the elements of  $K_{1,9}$ ,  $K_{1,10}$  and  $K_{1,11}$  respectively. The storey stiffness matrix is shown in Plate 10.7 which shows non zero elements at the lower half of the quadrant.

Looking at the three shear walls (Plate 10.8), the remaining 12 displacements (axial deformation, rotations about centroidal axes and the warping about the shear centres) produce considerable bending and twisting of the floor slab.

Plate 10.8 shows various floor stiffnesses i.e., displacements, rotations and warping of the floor slab. The finite element idealisation of the floor slab is also given here in.

The nodes  $N_{11}, N_{12}, \dots, N_{11}, N_{21}, N_{22}, \dots, N_{27}$  and  $N_{31}, N_{32}, \dots, N_{37}$  corresponding to the profiles of the three shear walls are of particular importance in the finite element analysis, since the displacements and forces only at these nodes are of concern. A unit displacement corresponding to  $u_3 = 1$  is applied to the plate by giving the nodes  $N_{11}, N_{12}, \dots, N_{1,11}$  a vertical downward displacement of unity and a zero slope along the contour. The two groups of nodes  $N_{21}, N_{22}, \dots, N_{27}$  and  $N_{31}, N_{32}, \dots, N_{37}$  corresponding to the contours of the I-shaped walls are held down by imposing zero deflections and rotations along the contour. However, no moment restraint is imposed in the direction perpendicular to the contour of the walls. This freedom is necessary to conform with the assumption that the longitudinal moments in the thin-walled beam are negligible. The finite element analysis of the plate is carried out for the above displacements, and the forces and moments developed at each of the nodes are found. The next step is to evaluate the four generalized forces, namely the vertical force, moments  $M_x$  and  $M_y$ , and a bimoment  $B_z$  for each of the three shear walls. This is achieved by using an appropriate transformation matrix for each wall.

The core wall is marked for the nodes  $1, 2, 3, \dots, n$ . Using finite element solution, forces and moments of these nodes are known. In terms of  $F_z$ ,  $M_x$ ,  $M_y$  and  $B_z$ . Vertical displacement and rotation at each node is considered to be the combination of  $W$ ,  $\theta_x$ ,  $\theta_y$  and  $\theta'_z$  of the core.

The nodal displacements are now given in terms of core wall displacements.

Note: Adopt subscripts 'cr' for core  
Adopt subscripts 'sl' for slab

$$\begin{bmatrix} w_1 \\ \theta_{x_1} \\ \theta_{y_1} \\ w_2 \\ \theta_{x_2} \\ \theta_{y_2} \\ \dots \\ \dots \\ \dots \\ w_n \\ \theta_{x_n} \\ \theta_{y_n} \end{bmatrix} \begin{bmatrix} 1 & \xi_1 & -\zeta_1 & -\omega_1 \\ 0 & 1 & 0 & \frac{\partial \omega_1}{\partial y} \\ 0 & 0 & 1 & \frac{\partial \omega_1}{\partial x} \\ 1 & \xi_2 & -\zeta_2 & -\omega_2 \\ 0 & 1 & 0 & \frac{\partial \omega_2}{\partial y} \\ 0 & 0 & 1 & \frac{\partial \omega_2}{\partial x} \\ \dots & \dots & \dots & \dots \\ \dots & \dots & \dots & \dots \\ \dots & \dots & \dots & \dots \\ 1 & \xi_n & \zeta_n & \omega_n \\ 0 & 1 & 0 & \frac{\partial \omega_n}{\partial y} \\ 0 & 0 & 1 & \frac{\partial \omega_n}{\partial x} \end{bmatrix} \begin{bmatrix} w \\ \theta_x \\ \theta_y \\ \theta'_z \end{bmatrix} \tag{10.40}$$

or

$$\{\Delta_{sl}\} = [T]\{\delta\}_{cr} \tag{10.41}$$

where

- $\xi_i, \zeta_i$  = the x and y coordinates of the  $i$ th node referred to the centroidal axes of the core
- $\omega_i$  = the sectorial coordinate of the  $i$ th node referred to the shear centre of the core
- $\frac{\partial \omega_i}{\partial x} \frac{\partial \omega_i}{\partial y}$  = the rates of change of the sectorial coordinate along x and y directions, respectively
- $w_i$  = the vertical displacement of the  $i$ th node
- $\theta_{x_i}, \theta_{y_i}$  = the rotations at the  $i$ th node with respect to a set of local orthogonal axes at  $i$ , parallel to the centroidal axes of the core
- $W_1$  = the vertical displacement of the core
- $\theta_{X_1}, \theta_{Y_1}$  = the rotations of the core about its centroidal axes
- $\theta'_{z_1}$  = the warping displacement of the core referred to its shear centre
- $\{\Delta_{sl}\}$  = the vector of nodal displacements and rotations
- $[T]$  = the transformation matrix
- $\{\Delta_{cr}\}$  = the vector of the generalised displacements of the core.



Using the contragradient relationship that exists between stress resultants and displacements, the forces and moments at the nodes of the slab are expressed in terms of the generalized forces in the core:

$$[F]_{cr} = [T^*][F]_{sl} \tag{10.42}$$

where

- $[F]_{cr}$  = the vector of generalized forces in the core
- $[T^*]$  = the transpose of the transformation  $[T]$
- $[F]_{sl}$  = the vector of nodal forces and moments

Equation (10.42) when expanded takes the form

$$\begin{bmatrix} F_{z_1} \\ M_{x_1} \\ B_{z_1} \end{bmatrix} \begin{bmatrix} 1 & 0 & 0 & 1 & 0 & 0 & \dots & 1 & 0 & 0 \\ \xi_1 & 1 & 0 & \xi_2 & 1 & 0 & \dots & \xi_n & 1 & 0 \\ -\zeta_1 & 0 & 1 & -\zeta_2 & 1 & 0 & \dots & \zeta_n & 1 & 0 \\ \omega_1 & \frac{\partial \omega_1}{\partial y} & \frac{\partial \omega_1}{\partial x} & \omega_2 & \frac{\partial \omega_2}{\partial y} & \frac{\partial \omega_2}{\partial x} & \dots & \omega_n & \frac{\partial \omega_n}{\partial y} & \frac{\partial \omega_n}{\partial x} \end{bmatrix} \begin{bmatrix} p_1 \\ m_{x_1} \\ m_{y_1} \\ p_2 \\ m_{x_2} \\ m_{y_2} \\ \dots \\ \dots \\ \dots \\ p_n \\ m_{x_n} \\ m_{y_n} \end{bmatrix} \tag{10.43}$$

where

- $F_{z_1}$  = the vertical force in the core assumed to be acting uniformly over the cross section
- $M_{X_1}, M_{Y_1}$  = the transverse bending moments about the centroidal axes of the core
- $B_{z_1}$  = the bimoment referred to the core shear centre
- $p_i$  = the vertical force at the  $i$ th node of the slab
- $m_{x_1}, m_{y_1}$  = the transverse moments at the  $i$ th node about the  $x$  and  $y$  axes, respectively.

$F_{z_1}, M_{X_1}, M_{Y_1}$  and  $B_{z_1}$  are the required generalized stress resultants and  $p_i, m_{x_1}, m_{y_1}, \dots$ , etc., are the forces and moments at the nodes.

Having obtained the stiffness matrix for the slab, the next step is to add the appropriate elements of the slab and segment stiffnesses to form the modified story segment stiffness matrix.

*Assembly and Solution*

The final part of the analysis consists of assembling the modified story segment matrices to obtain the complete stiffness matrix of the structure. Advantage is taken of the band form and symmetry of the stiffness matrix and

the overall matrix is stored in the half-band form. Since the number of degrees of freedom is 15 at each story the dimensions of the stored matrix will be  $(15 \times NS)$  by 30. The solution is obtained for the required number of loading cases, and from the displacements thus obtained and the generalized member stiffness matrices. The stress resultants are found. Finally, the global load, stiffness and displacement relationships are obtained for the overall structures.

## 10.4 Local and Global Stability Analysis

When the impact/blast occurs, there can be problem of combined torsional-flexural buckling of the building comprising of the core, floors, columns and bracings. The elements of the building structures may be bolted or welded or in case of concrete connected with bars embedded to floors. The torsional buckling analysis can be combined with flexural buckling by adjusting the respective stiffness matrices. The torsional buckling is dealt with in detail already.

### 10.4.1 Flexural Buckling

The eigen value buckling (bifurcation) is vital where steel is fully or partially anchored to the other elements such as aluminium or concrete. The eigen value buckling by bifurcation is represented by

$$([K] + \lambda_{ei}[K]_s) \{\Psi\}_i = \{0\} \quad (10.44)$$

where

$[K]$  = stiffness matrix of the core complex

$[K]_s$  = stress stiffness matrix

$\lambda_{ei}$  = the  $i$ th eigen value (is to multiplyload which generated  $[K]_s$ )

$\{\Psi\}_i$  = the  $i$ th eigen vector of displacements

To reduce the solution of (10.44) to its static and dynamic buckling (master) degrees of freedom, the matrix  $[K]$  is reduced and  $[K]_s$  is reduced in a manner identical to that by which the mass matrix is reduced. Hence (10.44) becomes

$$([K]_R + \lambda_{ei}[K]_s) \{\Psi_i\}_R = \{0\} \quad (10.45)$$

where  $[K]_R = [K'_t]_R$  when blast problem is involved. The subscript 't' in  $[K'_t]_R$  is time dependent matrix.

Since the building structures have specific geometry, the geometric stiffness matrix is involved. At the plasticity situation, the dynamic plastic stiffness matrix will now be  $[K_t'^P]_R$ . The overall plastic buckling matrix is now given by

$$([K_t'^P]_R + \lambda_{ei}[K_G]) \{\Psi_i\}_R = 0 \quad (10.46)$$

where  $\lambda_{ei} = I + E_{ps}$  and  $E_{ps}$  = accuracy parameters.

### 10.4.2 Inclusion of Torsional Buckling

A reference is made to Sect.10.3. for the torsional phenomena. Assuming from the core–floor–bracings–complex has the final stiffness matrix  $[K]_{\text{TOR}}$ . This matrix is algebraically added to  $[K'_t{}^P]_R$ . Hence

$$[K_{\text{TOT}}] = [K'_t{}^P]_R + [K]_{\text{TOR}} + \lambda_{ei}[K_G], \{\Psi_i\}_R \tag{10.47}$$

The final buckling/torsional equation is given as

$$[K_{\text{TOT}}] \{\delta\}^* + \{F_T\} - \{R_T\} = 0 \tag{10.48}$$

where

- $\{F_T\}$  = total initial blast load vector on each element of the complex
- $\{R_T\}$  = total external blast load vector

$$\{\delta\}^* = \begin{Bmatrix} \delta_{un} \\ \delta_b \end{Bmatrix}; \quad \{F_T\} = \begin{Bmatrix} F_{un} \\ F_b \end{Bmatrix}; \quad \{R_T\} = \begin{Bmatrix} R_{un} \\ R_b \end{Bmatrix} \tag{10.49}$$

In (10.49) the subscript 'un' and 'b' are defined as

- un = quantities corresponding to unknown displacements
- b = quantities corresponding to restrained boundaries

In (10.47) if for simplicity reasons on mathematical equation

$$[K_l] = [K'_t{}^P]_R + [K]_{\text{TOR}} \tag{10.50}$$

Then without geometric stiffness

$$[K_l] \{\delta_{un}\} + \{F_{un}\} = 0 \tag{10.51}$$

When the influence of  $[K_G]$  is taken into consideration, the overall plastic buckling/torsional criterion can now be given as

$$([K_l] + \lambda[K_G]) F_T = 0 \tag{10.52}$$

where

- $\lambda = \lambda_{ei} \{\Psi_i\}_R$
- $[K_l]$  = total plastic stiffness matrix as a function of the current state of plastic deformation

The determinant

$$|K_l + \lambda K_G| = 0 \tag{10.53}$$

The essential equation is characteristically triangularised for the  $i$ th loading step. It is essential to notice a brief breakdown of the buckling phenomenon  $\{\Psi_i\}_R$  is related to the load vector  $F_T$  of the elements in (10.49) and

$$\{F_{un}\} = \int [B]^T [D] \{\varepsilon_o\} d_{et} [J] d\xi d\eta d\zeta \tag{10.54}$$



where

$$E = \text{strain in the element} = [B]\{\delta\} \quad (10.55)$$

$$\sigma = \text{stress in the element} = [D](\{\varepsilon\} - \{\varepsilon_0\}) \quad (10.56)$$

where  $\{\varepsilon_0\}$  = initial strain.

At individual anchoring (bolting or welding) level, the anchoring area element matrix is  $\{K_a\}$ , then anchoring shear forces  $\{\bar{S}\}$  can be written as

$$\{\bar{S}\} = [K_a]\{\delta_{un}\} \quad (10.57)$$

This is known as *sturm sequence approach*, which is a part of the dynamic finite element analysis. The matrices are further condensed by again reducing out those rows and columns of matrices that have a positive value on the main diagonal of stress geometric matrix. The matrices are inverted such that accuracy is archived having the lowest eigen value. A standard iteration procedure given in the Appendix I is adopted for the solutions of these matrices. The eigen vectors are then normalised such that each has the largest value of 1.0.

If this is archived, the output would give which element of the building structure will fail under blast loads. The output will also give buckling-torsional elements more under extreme stresses or strains. Where anchored, the elements output will identify elements intact (*b*-type) or unanchored (*un*-type). Subroutine BANBUCKL will be asked in the finite element analysis to produce results where necessary.

#### 10.4.2.1 Load Distribution from Blast Loads and Radius of Gyration

*Statement:* Blast load phenomenon is fully explained with this text.

For steel elements the calculations are easy but for the concrete elements the effects of cracking on elements stiffness may be taken into account. A reference is made to the Appendix I. Where the detailed effective analysis is not demanded, the following relation is considered while reducing the value  $I_g$  of the uncracked or gross second moment of area.

$$I_e = 0.8I_g \quad (10.58)$$

In addition to the above constants the radius of gyration  $i_p$  is required for the *stability* and *dynamic analysis*. Two cases are considered:

- (a) The load  $q(x, y)$  is the arbitrary distribution with arbitrary shape layout caused by impact/explosion

$$i_p = \sqrt{\frac{\int q(x, y)(x^2 + y^2)dA}{\int q(x, y)dA}} \quad (10.59)$$

(b) Where the forces are computed as nodal forces, then (10.59) assumes the form for the bracing element  $i$  as

$$i_p = \sqrt{\frac{\sum F_i (\hat{x}_i^2 + \hat{y}_i^2)}{\sum F_i}} \tag{10.60}$$

where  $F_{Ti}$  is the  $i$ th concentrated force or load due to explosion with and without fire  $x, y =$  coordinate axes.

## 10.5 Formation of Elastic–Plastic Joint Element Using Finite Element or Finite Discrete Element Analyses

### 10.5.1 Introduction

Masonry walls are included in certain tall core buildings. The structure, in general, consists of brick/block and mortar. The joint element is the mortar (Fig. 10.3) between bricks or blocks, Fig. 10.4 shows typical elastoplastic joint element with corresponding composite model.

By introducing a suitable number of members and assigning different material characteristics to each, a variety of sophisticated composite actions can be obtained. In a simplified manner, the joint element consists of three members forming truss structure. One vertical and two diagonal members. The angle  $\Phi_o$  is between vertical and diagonal members. The vertical member is denoted by III and diagonal members by I and II.

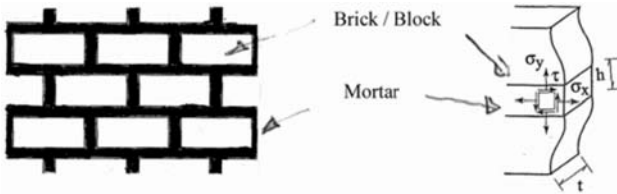


Fig. 10.3. Brick/block  $i$ th mortar layer

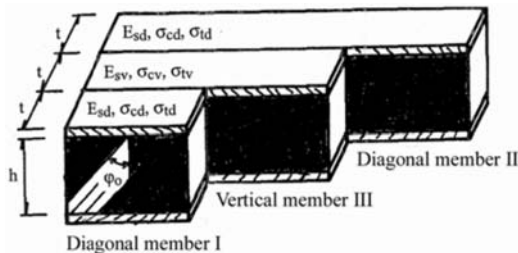
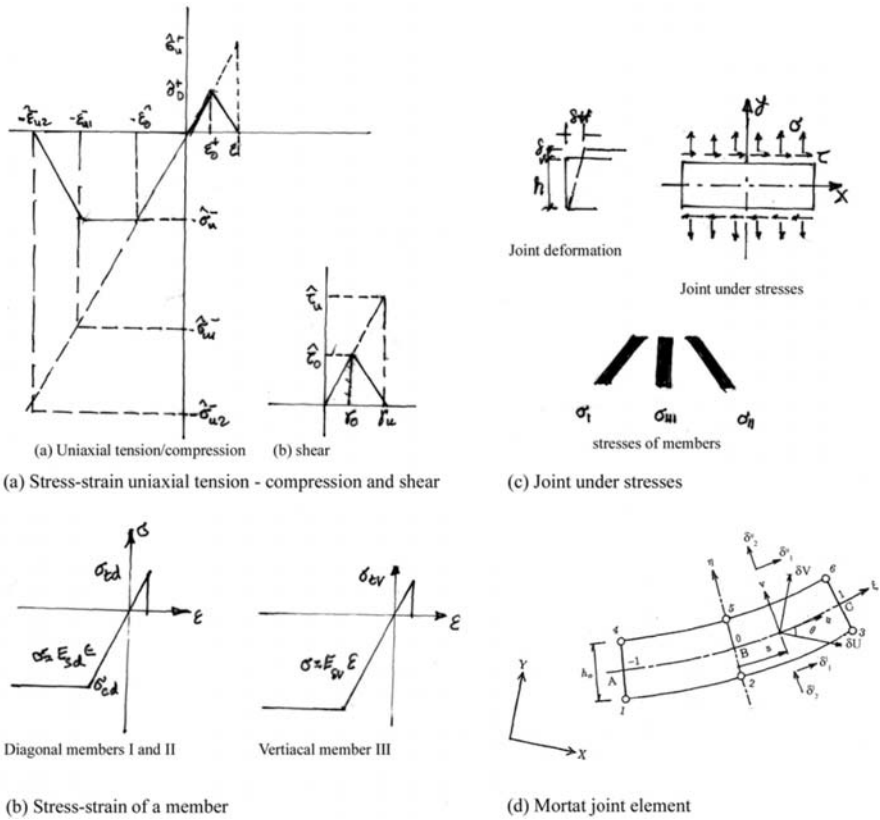


Fig. 10.4. Elastic–plastic joint element represented by truss–type member

Plate 10.10. Joint element analysis with mortar joint



Each member is assumed to have the same thickness,  $t$ , and the same height,  $h$ . However, each member can have different material properties:  $E_{sd}$ ,  $E_{sv}$  the stiffness,  $\sigma_{td}$ ,  $\sigma_{tv}$ , the tensile strength, and  $\sigma_{cd}$ ,  $\sigma_{cv}$  the compressive strength of the diagonal and the vertical members, respectively. The stress-strain relationships of all three members in tension and compression are shown in Plate 10.10. It is seen that beyond the proportional limits  $\sigma_{cd}$  and  $\sigma_{cv}$  the stress-strain lines under compression are assumed straight lines parallel to the  $\epsilon$ -axis, but beyond the proportional limits  $\sigma_{td}$  and  $\sigma_{tv}$  the stress-strain lines under tension are assumed to soon become zero.

### 10.5.2 The Damage Model

The damage model conceived has three internal variables  $DM_t$ ,  $DM_c$  and  $DM_s$  which mean damage induced can respectively tensile, compressive and shear. The stress strain relation can be written as

$$\{\varepsilon\} = [K^{-1}] \{\sigma\} \left\{ \frac{1(tr\{\sigma^+\})}{(1 - MD_{TS})(tr\{\sigma\})} + \frac{1(tr\{\bar{\sigma}\})}{(1 - MD_{cs})(tr\{\sigma\})} \right\} \quad (10.61)$$

where  $[K]$  is the material stiffness matrix.

The evolution laws of the damage variables  $DM_t$ ,  $DM_c$  and  $DM_s$  are defined by introducing three threshold values  $\bar{\sigma}_0^+$ ,  $\bar{\sigma}_0^-$  and  $\bar{\tau}_0$ . In order to calculate  $DM_{ts}$  and  $DM_{cs}$ , the elastic stresses strains its threshold value such that an increment in the corresponding may develop according to the relevant evolutions law.

The evolution law for  $M_{DT}$ ,  $M_{DC}$  and  $M_{DS}$  are governed by the following relationships:

$$M_{DT} = 1 - \frac{\hat{\sigma}_0^+ (\hat{\sigma}_u^+ - \hat{\sigma}^+)}{\hat{\sigma}^+ (\hat{\sigma}_{cu}^+ - \hat{\sigma}_0^+)} \quad (10.62)$$

$$M_{DC} = \begin{cases} 1 - \frac{\hat{\sigma}^-}{\hat{\sigma}} & f\hat{\sigma}^- \leq \hat{\sigma}_{u1}^- \\ 1 - \frac{\hat{\sigma}_0^- - (\hat{\sigma}_{u2}^- - \hat{\sigma}^-)}{\hat{\sigma}^- (\hat{\sigma}_{u2}^- - \hat{\sigma}_{u1}^-)} & f\hat{\sigma}^- > \hat{\sigma}_{u1}^- \end{cases} \quad (10.63)$$

$$M_{DS} = 1 - \frac{\hat{\tau} (\hat{\tau}_u - \hat{\tau})}{\hat{\tau} (\hat{\tau}_u - \hat{\tau}_0)} \quad (10.64)$$

where  $\wedge$ ,  $+$ ,  $-$  are the respective threshold limit.

The stress-strain curve for the masonry is shown in Plate 10.10a,b.

In the finite element analysis the fracture energy  $G_f$  can be obtained by

$$l_c \times g_f \quad (10.65)$$

where  $l_c$  = characteristic length of the finite element

$g_c$  = material energy dissipated per unit volume

$$= \int_0^\infty \sigma(\varepsilon) d\varepsilon \quad (10.66)$$

If ' $l$ ' depends on the size of the representative volume element which is the smallest value representing fracture, then parameter ' $\alpha$ ' can be obtained by substituting the stress-strain law into (10.66).

$$\alpha = \frac{l}{l_c} = \frac{2G_f E}{\hat{\sigma}_u + l_c \hat{\sigma}_0^+} \quad (10.67)$$

where  $l_c$  is function of the dimensions of the finite element such that its value is given as:

$$l_{c_{\min}} = \frac{2G_f E}{(\hat{\sigma}_0^+)^2} \tag{10.68}$$

To avoid the snap-back phenomenon,  $l_c >$  the critical value  $l_{c_{\min}}$ . The value  $E$  is the elastic modulus of the material.

The values of  $\sigma$  and  $\tau$  are given as

$$\sigma = (\sigma_I + \sigma_{II}) \cos^2 \varphi_0 + \sigma_{III} \tag{10.69}$$

$$\tau = (\sigma_I - \sigma_{II}) \sin \varphi_0 \cos \varphi_0 \tag{10.70}$$

The corresponding strains of truss members  $\varepsilon_I, \varepsilon_{II}, \varepsilon_{III}$  are obtained by

$$\begin{aligned} \varepsilon_I &= \sin \varphi_0 \cos \varphi_0 \gamma + \cos^2 \varphi_0 \varepsilon \\ \varepsilon_{II} &= -\sin \varphi_0 \cos \varphi_0 \gamma + \cos^2 \varphi_0 \varepsilon \\ \varepsilon_{III} &= \varepsilon \end{aligned} \tag{10.71}$$

Assuming  $\delta_V$  and  $\delta_H$  are the vertical and horizontal displacement of the joint element when it is subjected to  $\sigma$  and  $\tau$ , the formulation of the joint element for the finite element can be given in the following manner.

Plate 10.10, shows the joint element  $ABC = l_0$  with depth or height  $h_0$ . In joint element  $h_0 < l_0$ . Displacement on the upper surface ( $\delta_1^u, \delta_2^u$ ) and on the lower surface ( $\delta_1^l, \delta_2^l$ )

$$\begin{bmatrix} \delta_1^u & \delta_1^l \\ \delta_2^u & \delta_2^l \end{bmatrix} = \begin{bmatrix} NA(\xi) & 0 & NB(\xi) & 0 & NC(\xi) & 0 \\ 0 & NA(\xi) & 0 & NB(\xi) & 0 & NC(\xi) \end{bmatrix} \begin{Bmatrix} \delta_4 & \delta_1 \\ \delta'_4 & \delta'_1 \\ \delta_5 & \delta_2 \\ \delta'_5 & \delta'_2 \\ \delta_6 & \delta_3 \\ \delta'_6 & \delta'_3 \end{Bmatrix} \tag{10.72}$$

where

$$NA(\xi) = \xi(\xi - 1)/2, NB(\xi) = 1 - \xi^2, NC(\xi) = \xi(\xi + 1)/2, \tag{10.73}$$

respectively.

Displacements on the upper surface ( $u_u, u_u$ ) and on the lower surface ( $u_l, u_l$ ) in the  $\xi - \eta$  coordinate are obtained:

$$\begin{bmatrix} u_u & u_l \\ u_u & u_l \end{bmatrix} = \begin{bmatrix} \cos \theta & -\sin \theta \\ \sin \theta & \cos \theta \end{bmatrix} \begin{bmatrix} \delta_u & \delta_l \\ \delta'_u & \delta'_l \end{bmatrix} \tag{10.74}$$

If the height  $d_0$  is assumed to be sufficiently small, we have the strains of truss members  $\varepsilon_i$  as follows

$$\varepsilon_i = \frac{\cos \varphi_i}{h_0} \left[ -\sin \varphi_i - \cos \varphi_i \sin \varphi_i \cos \varphi_i \right] \begin{Bmatrix} \delta_1^l \\ \delta_2^l \\ \delta_1^u \\ \delta_2^u \end{Bmatrix} \quad (10.75)$$

where  $i = I, II, III$ .

The corresponding angles of truss members are  $\varphi_I, \varphi_{II}, \varphi_{III}$ .  $\varphi_I = \varphi_0$ ;  $\varphi_{II} = -\varphi_0$ ;  $\varphi_{III} = 0$

When the incremental strain  $\Delta\varepsilon_i$  and initial stress  $\sigma_{0i}$  in each member are known, the incremental strain energy  $\Delta U$  is given as

$$\Delta U = \sum_{i=1}^n \int \Delta U_i ds = \sum_{i=1}^n \int_{-1}^{+1} t \left| \frac{ds}{d\xi} \right| \left[ \sigma_{0i} \times \Delta\varepsilon_i + \frac{1}{2} E_{ti} (\Delta\varepsilon_i)^2 \right] h_0 d\xi \quad (10.76)$$

where

- $n$  = the number of truss members
- $t$  = thickness of the joint element
- $E_{ti}$  = the tangent modulus of the truss members

When  $\sigma \neq 0$  and  $\tau > 0$  – failure occurs in the first diagonal member I

- (a) At the point at which I fails, members II and III not yielded or failed. After member I failed, member III will fail when stress reaches

$$\tau = (\sigma_{tv} - \sigma) \tan \varphi_0 \quad (10.77)$$

- (b) After condition (a), member II will yield when

$$\tau = \sigma_{cd} \sin \varphi_0 \quad (10.78)$$

- (c) When  $\sigma < 0 < \tau > 0$ , diagonal member II will yield in compression, diagonal member I will fail in tension. In this condition, vertical member III yield in compression.

After member II yields, member III will yield when the stress reaches  $\tau$  given by (10.79).

$$\tau = 2\sigma_{cd} \sin \varphi_0 \cos \varphi_0 + \tan \varphi_0 (\sigma + \sigma_{cv}) \quad (10.79)$$

At the point at which member II yields, member I will not yet have reached its point ( $\sigma_{cd}$ ) or its breaking point ( $\sigma_{td}$ ). Consequently, when stress  $\sigma_I$  is  $-\sigma_{cd} \leq \sigma_I \leq \sigma_{td}$  it is equal to:

$$-\sigma_{cd} \leq \frac{\tau}{\sin \varphi_0 \cos \varphi_0} - \sigma_{cd} \leq \sigma_{td} \quad (10.80)$$

Here  $\tau < 0$  is omitted because the shape of the yielding conditions is symmetrical about the  $\sigma$ -axis. Figure 10.5 show the failure scenario. The yielding condition is represented by:

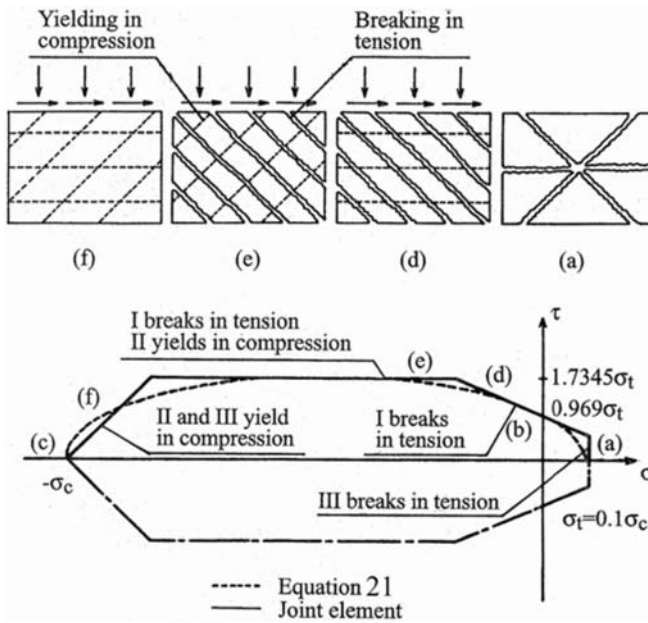


Fig. 10.5. Damage cases joint element

$$\frac{\tau}{\sigma_c} = \sqrt{-0.104 \left( \frac{\sigma}{\sigma_c} \right)^2 + 0.095 \left( \frac{\gamma}{\sigma_c} \right) + 0.0089} \quad (10.81)$$

Where detailed numerical figures are not known, the following should be adopted for the joint element.

- $t$  = thickness = 0.5 cm
- $h$  = height = 2.0 cm
- $E$  = Young's modulus =  $2.06 \times 10^4$  Nmm<sup>2</sup>
- $\nu$  = Poisson's Ratio = 0.16
- $\sigma_c$  = compressive strength = 20.6 N/mm<sup>2</sup>
- $\sigma_t$  = tensile strength = 2.06 N/mm<sup>2</sup>
- $\varphi_0$  = angle = 45°
- $E_{sd} = 0.862 E$  - diagonal member -  $E$  being equal to 4000 MPa
- $E_{sv} = 0.595 E$  - vertical member
- $\sigma_{cd}$  = comp. strength diagonal member =  $0.25 \sigma_c$
- $\sigma_{cv}$  = comp. strength vertical member =  $0.75 \sigma_c$
- $\sigma_{td}$  = tensile strength =  $0.945 \sigma_t$  - diagonal member
- $\sigma_{tv}$  = tensile strength =  $0.805 \sigma_t$  - vertical member
- $\varepsilon$  = strain = -0.0025

The European code EC6, the most general characteristic equation is given for mortar joint:

$$f_{\omega c,k} = K f_{bc}^{0.65} \times f_{mc}^{0.25} \quad (10.82)$$

where

$K$  depends on selected type of blocks  $\rightarrow 1$

$$\left. \begin{array}{l} f_{bc} = \text{mean compressive strength} \\ f_{mc} = \text{mean compressive strength} \\ \quad \text{of mortar} \end{array} \right\} \text{They need to be evaluated} \\ \text{experimentally for a case study}$$

Generally,  $f_{\omega c}$  can vary from 1.6 to 6.0 MPa.

Note: Where 3D finite element analysis is required, a reference is made to Appendix I.

## 10.6 Modelling and Behaviour of Masonry Walls

### 10.6.1 Introduction

A great number of factors determine the structural response of a masonry fire wall and it is this, which makes the prediction of structural behaviour so complex. Physical conditions such as wall geometry, boundary conditions, magnitude and location of applied loading all strongly influence results. High temperature mechanical material properties and thermal material properties also considerably alter response.

### 10.6.2 Thermal Bowing

In fire separating elements such as fire walls, heat is usually exposed to one face. This is particularly important in the case of masonry materials due to its generally low thermal conductivity, producing high thermal gradients over the cross section. If the wall is unrestrained this leads to differential thermal expansion of the material. With the hot face expanding more rapidly than the cool face, the unrestrained wall will tend to bow towards the fire. In cases of high slenderness ratio thermal displacements may be of a magnitude to cause instability buckling. Previous experimental investigations have revealed that this occurs when the lateral thermal displacement at the mid height of the wall reaches 90 per cent of the wall thickness. In tall cantilever fire walls thermal bowing may be of a magnitude to cause instability buckling under the self weight of the wall alone. The reduction of strength and modulus of the material on the face exposed to the fire can serve to reduce thermal bowing, depending on the magnitude of applied loading. The thermally degrading material on the fire exposed face will experience additional



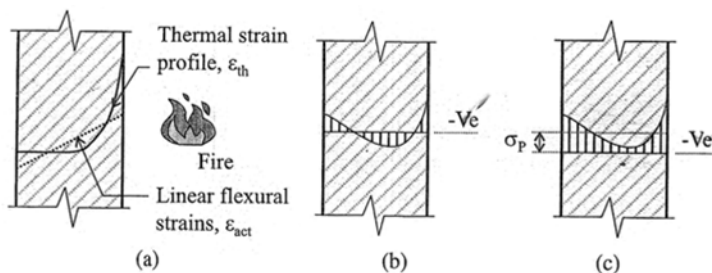


Fig. 10.6. The thermal and resulting linear flexural strain distributions

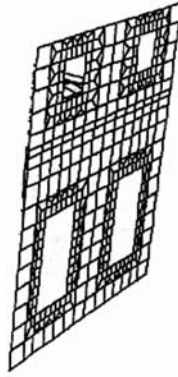
compressive strains when subject to axially applied loading, therefore counteracting thermal expansion. In some situations where, i) the magnitude of applied loading is high, ii) central lateral displacements are small, and iii) the material properties on the fire exposed face have significantly deteriorated, – the additional compressive strains may be sufficient to change the direction of the central displacement. This behaviour is known as reverse bowing, and eventual failure is normally due to crushing of the thermally degraded material on the fire-exposed face.

The thermal conductivity of a masonry material together with the normally high rate of temperature increase ensures a predominantly non-linear distribution of temperature through the thickness of the wall. This in turn leads to a non-linear application of thermal strains,  $\sigma_{th}$ . Due to the shearing transfer in a continuum material the resulting strain response leads to a linear distribution, adhering to the numerical stipulation that plane sections remain plane Fig. 10.6a. This effectively means that the applied thermal strains are incompatible with the linear flexural strains,  $\epsilon_{act}$ . Thus at any internal point the thermal strains cannot occur freely and are internally restrained producing thermal stresses  $\epsilon_{ths}$ . Figure 10.6b shows the thermal stresses which may exist in a non-loaded section, due to the application of thermal strains. Compressive stresses are experienced in the outer.

Sections, while tensile stresses exist in the central region of the wall. Thermal stresses are self equilibrating both axially and rotationally.

- (a) Tensile thermal stresses are often of a magnitude to cause cracking, and since thermal stresses are self equilibrating this effectively relieves compressive thermal stresses.
- (b) Thermal stresses  $\sigma_{ths}$ , produced by a non-linear temperature profile.
- (c) Thermal stresses in a wall subject to an applied axial load producing compressive stress,  $\sigma_P$ .

The effects of thermal stresses are largely influenced by the external loading system. In the case of a wall, which is subject to an axially applied load to produce uniform compressive stress  $\sigma_P$ , thermal stresses may never induce



**Fig. 10.7.** 3D Finite element mesh scheme or walls with openings

tensile stresses, but simply serve to reduce the compressive stresses in the central region of the wall thickness (Fig. 10.7).

$$\sigma_{ths} = D[\varepsilon_{act} - \varepsilon_{th}] \quad (10.82a)$$

where  $D$  is the elasticity matrix.

$$P_{ths} = \int \sigma_{ths} dx = 0 \quad (10.82b)$$

$$M_{ths} = \int \sigma_{ths} x dx = 0 \quad (10.82c)$$

### 10.6.3 Masonry Material Properties

In a load bearing structural concrete wall the material compressive strength  $f_c$ , strongly influences the magnitude of thermal bowing. A stressed material will experience less resultant thermal expansion than an unstressed material. The reduction in thermal expansion is proportional to the stress level, which is directly related to the compressive strength of the material. An increase in  $f_c$  results in a reduced stress level ( $\sigma/f_c$ ) leading to an effective increase in thermal expansion. This behaviour is due to the additional temperature related transient strain component, or load induced thermal strain (LITS).

### 10.6.4 Wall Geometry

The occurrence of instability buckling in a laterally deforming wall due to thermal bowing, is largely determined by the slenderness ratio (height to breadth ratio of the wall cross section). Boundary conditions also influence the event of buckling.

### 10.6.5 Boundary Conditions

Restrained boundary conditions can greatly increase fire resistance time. In the case of unrestrained thermal expansion, thermal bowing occurs freely. Where end fixities are present the thermal response is at least partially restrained causing induced loading and decreased thermal deformations.

### 10.6.6 Applied Loading on Walls

The effects of axially applied loading at higher temperatures are dependent on the wall “ $\lambda$ ”, material compressive strength and material type. Applied loading has a more profound effect on walls with lower  $\lambda$ . Increase applied loading has been shown to improve structured fire resistance times. Load eccentricity may have effect of prolonging degrading fire resistance time.

### 10.6.7 The Finite Element Model

Material non-linearity is approached using the tangent modulus method in order to obtain a converged solution. The smearing cracking model is simulated as it best suited to brittle nature of masonry material. The cracking and damage criteria are fully described in Appendix I. The interface element is given in Sect. 10.5.2. and else where in the text. This element is used as the main element connecting masonry using mortar.

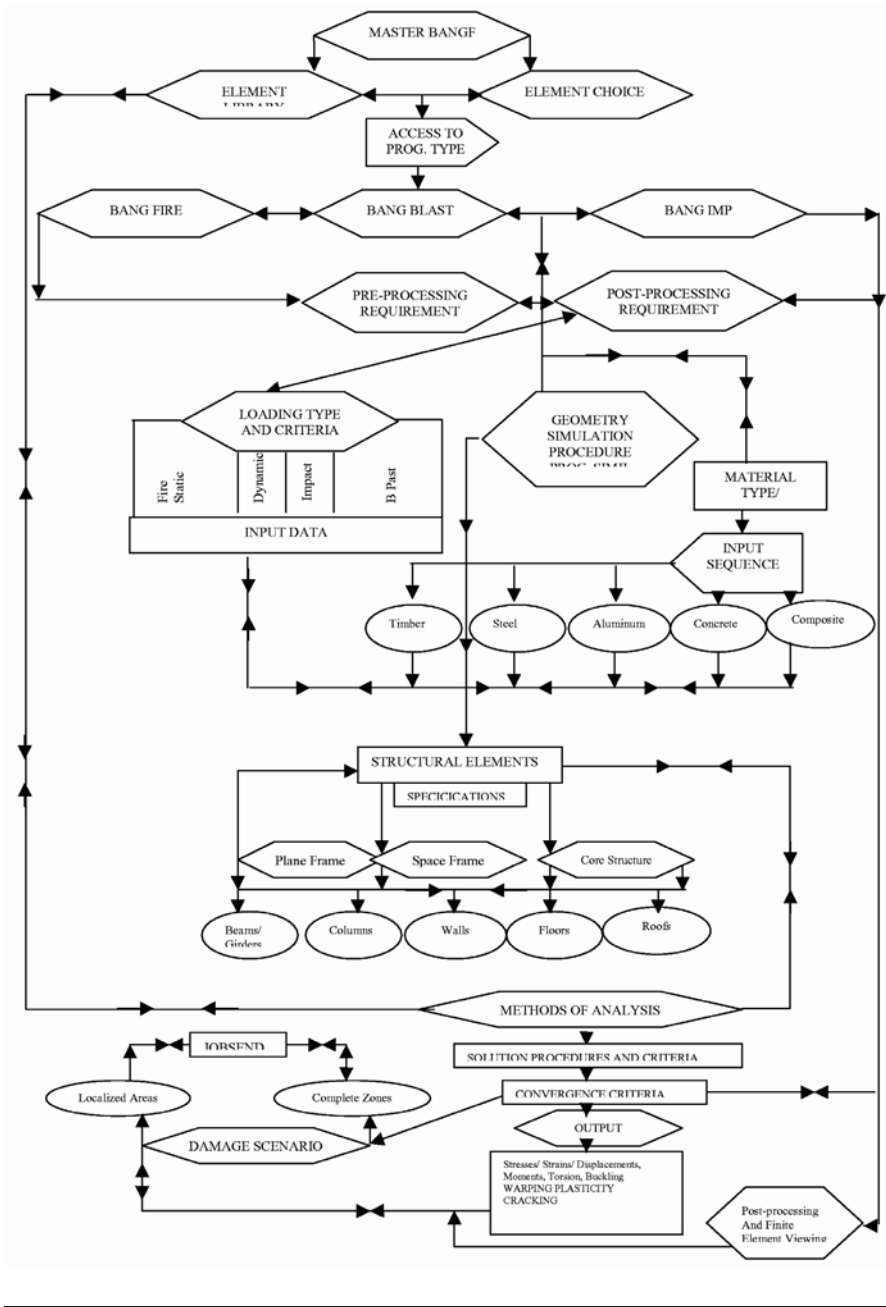
## 10.7 Global Analysis Based on PROGRAM BANGF

### 10.7.1 General Introduction

In order to prepare a clear-cut strategy, this section gives a comprehensive approach in the form of flow chart covering all possible scenario included in PROGRAM BANG-BLAST. Depending on the type of the external actions, the analysis could be either static or dynamic. For the purpose of the coverage for Blast Analysis, various materials and optional behaviours are included to cover for any single damage scenario. The flow chart for the BANG-F is shown in Plate 10.11, which gives the sequence of combining various scenarios wherever applicable. Some of the subroutines are given in the Appendix I.

Two cases, namely WTC-1/WTC-2 are examined using the finite element methods. The Alfred Murrah Building has been analysed by the second author, T. Bangash using the Discrete Element Method.

Plate 10.11. Flow chart for program BANGF (Global Finite Element Analysis)



## 10.8 Case Studies

### 10.8.1 Introduction

Numerous case studies can be considered. As mentioned in earlier sections several structures had been subject to impact/explosion and fire. Various techniques of analysing such structures have been fully described and as far as possible, several numerical models and analytical approaches are given in the text for individual isolated cases and for global structures which maybe subjected to aircraft/missile crashes, explosion and fire. The reader has been given choices to integrate cases, which need urgent considerations. At the time of writing of this book, several more disaster scenarios might have occurred and which couldn't be recorded. It is intended to present some well-known case studies, which might have hearing on identical disaster scenarios. The following well-known cases are identified:

- WTC Towers in New York, U.S.A.
- The Oklahoma City Building, Alfred Murrah Building, Oklahoma U.S.A.
- The Pentagon Building in Washington D.C., U.S.A.
- The HSBC Building in Istanbul, Turkey

### 10.8.2 WTC Towers Collapse in New York

Much has been said in this text about the collapse analysis of these towers. In this section a summary on the collapse of these towers is given prior to the engineering evaluation.

#### 10.8.2.1 How the Towers Collapsed

The top and both vertical edges of a masonry wall may be fixed, pinned or free, resulting in various permutations and combination of fixities. The bottom boundary condition can be assumed to be fixed in all circumstances. Axial and rotational restraint of the top boundary conditions will restrict vertical thermal expansion and the deformation of thermal bowing, imposing additional compressive stresses, which may prolong fire resistance.

#### *How the Towers Collapsed*

The federal investigation into the collapse of the World Trade Center towers on Sept. 11 has been unable to pinpoint what engineering elements were critical in the disintegration of the buildings or how best to resist a recurrence. Even so, the six-month study – conducted by the American Society of Civil Engineers and the Federal Emergency Management Agency -has revealed some disturbing facts about modem skyscrapers that are potentially worrisome for those who work or live in high-rise buildings around the country.

The most encouraging finding was that the impact forces of the huge jets that rammed into the towers were not the only ones, by themselves, to cause the collapse. Although the twin towers were designed to handle only the crash of a Boeing 707 flying at low approach speeds, the FEMA (1) [10.56] report indicates when put to the test on Sept. 11 they absorbed the shock of slightly heavier Boeing 767's flying at much higher speeds. Had no other stresses caused by explosion and fire been imposed on the structures, they could have remained standing indefinitely.

Unfortunately there was added stress effects, in the form of extremely hot fires that resulted when jet fuel ignited the contents of the buildings and planes. The flames softened the structural steel, triggering events that allowed the upper floors to cascade downward.

All three major defences against fire proved unequal to the task. The sprinkler systems were disabled by the impact of the planes. Firemen were unable to reach the inferno because emergency elevator's were damaged, and even if they had arrived in force, the standpipes they needed were almost certainly disabled. Finally, the fireproofing material sprayed on steel beams and trusses to protect against overheating failed to do so, probably because most of it was blasted off by the planes' impact. Whether better insulation is needed, at least for the most critical structural elements, will be one focus of additional inquiry.

The experts appointed were unable to determine whether the fires alone, without the impact of the airplanes, could have brought the towers down. But it is to learn that an adjacent 47-story building collapsed completely as a result of a fierce fire fed by diesel oil on the premises, and that another building suffered a partial collapse from fire. These are the first known instances of protected steel-frame structures collapsing from severe fire, suggesting that many modern buildings may be more vulnerable than anyone realised.

The investigation has put a spotlight on longstanding practices that will surely need revision in the wake of this disaster. It seems absurd that steel beams are tested for fire resistance, whereas the steel connections that hold them together are generally not. Nor is any analysis made of how an integrated structure, not just its individual components, will respond to fires, or how fires and structural damage interact.

A more thorough two-year investigation, to be conducted by the National Institute of Standards and Technology (NIST), is expected to give more definitive answers on the collapse scenario. Based on that inquiry, authorities hope to learn whether building codes and engineering practices will need to be upgraded. It will never be feasible to harden all civilian buildings to withstand a ferocious terrorist attack. But it should be possible to strengthen their vulnerable parts – and their ability to withstand extremely hot fires and other extraordinary stresses. At the time of the publications of this book, the report from NIST has been available now in draft form. The authors have contributed to some of the salient features. This report was devoid of flume, hot-fluid WTC structure interaction and analysis for the dismantling of elements. No debris analysis was included. This book covers these.

### 10.8.2.2 Blow by Blow Accounts

As someone stood staring in disbelief at the smoke pouring from one tower of the World Trade Center, it was with at first curiosity and then dumbfounded horror that he saw a silver, plane curl round from the East River, aim straight at the second tower and then a fireball erupt as it struck (Fig. 10.1).

It all happened in no more than a three or four seconds.

Standing on the top floor of a Times Square office block in mid-town Manhattan, he at first had a fleeting feeling of watching something pure Hollywood. That was how it was supposed to look, he knew full well he was watching events unfold of if historic, world-changing dimension.

Word of the fire in the first tower had spread around the elevator he was riding up to the top floor. A small knot of office staff, most clutching coffee cups and brown bags, joined him there to stare at the smoking building clearly visible from our 40th floor.

Televisions running in the background were reporting frantically that an airplane had hit the tower, but there was still uncertainty about whether this was terrorism or some kind of freak accident. The second plane ended that debate.

It was, in the annals of terrorism, an exquisitely choreographed operation. In the minutes before and after 8 am on Tuesday, four large passenger jets lifted off at major eastern airports, headed for California. It was the time of the morning when such airports are usually buzzing, when vacationers get an early start on long days of travel, and business travellers can leave the East Coast expecting to arrive in time for afternoon meetings.

The planes, two Boeing 767s and two 757s, each had just a pair of pilots and none had more than nine flight attendants on board. But all of them carried thousands of gallons of fuel. And once aloft, they were remarkably effective flying bombs. Just what happened on board the flights may not be clear for missing reasons.

### 10.8.2.3 Blow Accounts Versus Time Scenario for Aircraft

The blow accounts given on pages 23–24, Chap. 1, together with the time aspect is taken into consideration in the finish element analysis.

### 10.8.2.4 Problems Associated with the Collapse of the Towers

A reference is made to Chaps. 7, 8, and 9 on the major data and individual elemental analyses. Various result are highlighted. Some these are briefly given below part of the overall discussions:

When the buildings WTC came down, as gravitational potential energy unloaded, and its value computed is around  $6.8 \times 10^{11}$  J. (Compared to this, the energy of a severe earthquake would be 1017 J and the annual energy output

of a reasonably large power station would be 1016 J). As a matter of fact, the collapse created an earthquake of magnitude 2.4 on the Richter scale. However, unlike a normal earthquake, they were richer in low frequency energy and poorer in high frequency energy, the main reason for this being the gravitational potential energy due to the falling of building material. According to Prof. Mackin, of the University of Illinois at Urbana-Champaign, an aircraft has the equivalent power of a small-scale commercial power plant. The kinetic energy of a 767 jet at impact is of the order of 40 mega joules as shown below:

$$KE = \frac{1}{2}mv^2 \quad (10.83)$$

where

$$m = \text{mass} = 204 \times 10^3 \text{ kg}$$

$$\nu = \text{velocity} = 19.7 \text{ m/s}$$

$$KE = \text{kinetic energy} = 39.6 \times 10^6 \text{ J} \cong 40 \text{ MJ}$$

Though this energy is considerable, it is clear that the towers withstood this impact. Though damaged, Two WTC managed to remain standing for approximately one hour, and one WTC for 90 minutes. The elemental analyses show that it was not the impact, but the energy in the fuel that affected the structural integrity of the building. The energy content of fuel is approximately  $35 \times 10^6$  joules per litre. (Jet fuel may have even greater energy content). Assuming that the jet had 75,700 litres of fuel, (fuel capacity of 767 jet is 90,764 litres) and it detonated at once, the resulting energy would be  $792 \times 10^9$  joules. This would amount to the equivalent of 2,376,000 sticks of dynamite! (3 sticks of dynamite will have 1 mega joule of energy).

If one assumes that the jet liner with a weight of 205 tonne was traveling at cruising speed (850 km/hr) and dissipated all of its energy in one second, their torque on building shall be =  $F \times$  moment arm =  $857 \times 10^3$  KNm, where  $F = MV =$  momentum per second = 4018 KN. If the plane hits the 70th floor, the torque at the base will be  $857 \times 10^3$  KNm. Later on the global torque analysis given in the text could envisage the W.C. tower with standing this high impact. However, elemental analysis indicated that the impact of the plane crash destroyed a significant number of perimeter columns on several floors of the building, severely weakening the entire system. As the fire analysis indicates, as the fire raged in the upper floor, the heat gradually affected the remaining tower structure. The preliminary elemental analysis gives a firm belief that the steel core struts became weakened due to prolonged high temperatures fuelled by the large volumes of aviation fuel. The floor results showed from the elemental 3D finite element programs that when the fire reached  $815^\circ\text{C}$  ( $1500^\circ\text{F}$ ), the weakened struts collapsed due to the vertically directed collapsed mechanisms. This is the scientific explanation put forward for the catastrophic failure of the tower having intended to withstand an impact of aircraft such as that of a Boeing 767 jet aircraft.



The thermal environment within each tower is still a subject of discussion. Prior to the global analytical work on failure and collapsed scenario, it is essential the elemental analysis provided for components should be discussed in the light of program BANG-FIR.

Based on preliminary assumptions and analysis, mathematical and numerical models have been used to estimate the behaviour of the fires in the twin towers of the World Trade Center. The hijacked-plane collision with each tower produced significant structural damage, generated a spectacular external fireball, and started burning within the tower. The fuel consumed by the fireball was absorbed as an ignition source, but produced a pressure pulse that damaged windows and changed the ventilation for the fires. The subsequent fire in each tower generated a quasi-static, wind-blown smoke plume. The fire and smoke behaviour were simulated using the program BANG-FIR (FDS). Comparison of the observed plume trajectory with the simulated one causes to estimate the rate of energy supplied by the fire to the plume which was of the order of magnitude of a gigawatt (GW). The rate of energy supplied to the plume, plus the energy-loss rate, determine the total heat release rate (HRR), the most important single parameter for each tower fire. Two bounding scenarios for the *interior* damage and fuel distributions were considered by program BANG-FIR for the north tower. For each scenario, the simulated visible fire and smoke behaviour outside the tower were compared with known photographic, to determine which scenario seemed more appropriate. The simulations for the two scenarios also provided estimates of the likely thermal environment within each tower.

Because both towers were so completely destroyed when they collapsed, relatively little physical evidence remained for investigation. As a result, photographs have become the primary resource for providing initial estimates of the *exterior* damage to each building and of progression of the fire. These proved to be only source for comparing with numerical models. Wind, pressure and temperature as functions of height, obtained from the records of the Aircraft Communications Addressing and Reporting System (ACARS), were also found to be critical input for the study, in the finite element analysis provided by program BANG-BLAST and program BANG-FIR.

#### 10.8.2.5 Smoke Flame and Heat Analyses Release for Global Structures

The trajectory of the smoke plume was used, in principle, to estimate the magnitude of convective energy per time contributed to the smoke plume by the tower fires. This convective energy rate, the wind speed and direction, and atmospheric stability are the parameters known to govern a smoke-plume trajectory.

From photographs it was determined that the wind direction was almost exactly from the geographic North. We also established that the velocity of this wind was between 5 m/s and 10 m/s. The wind speed and direction were

verified by data from the Aircraft Communications Addressing and Reporting System (ACARS), which also provided data on temperature and pressure as functions of height. From these data, assuming a perfect gas, one can also calculate air density as a function of height, and these thermodynamic quantities determine the stability of the atmosphere. Commercial flights generally use ACARS to capture and report temperature, pressure and wind speed and direction data as functions of altitude. It shows these quantities on the morning of 9/11 as obtained from three flights, one from JFK airport in New York and the other two from Newark International in New Jersey. Hence the analysis has used 5 m/s as the wind velocity and a lapse rate approximately one half the adiabatic lapse rate, which was  $-1.0^{\circ}\text{C}$  per 100 m.

As explained earlier, a full fuel load for each plane would be approximately 90,800 L or 74,500 kg of jet fuel, as noted earlier, the planes carried only approximately 31,000 to 34,000 L or 26,000 to 28,000 kg of jet fuel (density  $\rho_{\text{fuel}} = 0.82 \text{ kg/L}$ ). The area of one floor of either tower was 4025 m<sup>2</sup>.

By contrast a second sophisticated model uses a strictly Eulerian, mixture-fraction formulation to describe the combustion. In this model, the flame sheet was found where stoichiometry occurs, and the heat from the exothermic reaction is released into the flow along the flame sheet using BANG-FIR. The radiative transport is also handled in a more sophisticated fashion. An approximate solution to the full radiation transport equation, that accounts for local absorption and re-radiation by the material in the computational domain, is used to calculate radiative fluxes and, therefore, heat transfer by radiation. This formulation allows the radiation coupling that generates new gaseous fuel at solid surfaces. This method is applied for floors in Chaps. 8 and 9.

Detailed descriptions of the mathematical models used in both versions, and of the methods used to validate them are presented. The quality and ease of use of this tool have significantly improved the ability to understand fire behaviour.

In the global analysis, the heat released per unit area in PROGRAM BANG-FIR is 2 MW/m<sup>2</sup>. It is assumed that the plane dumped its whole fuel load over only one to two floors, smashing all material on those floors to an averaged depth of around 0.8 cm with fuel load of 6.2 kg/m<sup>2</sup> as part of the input to BANG-FIR. At the burning rate with heat release rate of 2 MW/m<sup>2</sup> the scenario established in Chap. 9 is the final attempt with time 10 minutes to spread over greater area. The estimate is consistent with that given in FEMA study Report. Throughout it is assumed in BANG-FIR that the jet fuel would be consumed quickly relative to the duration of the tower fire.

### *Plume-Trajectory Scaling*

The mass, momentum and energy equations stated earlier can be simplified by assuming a steady, non-zero horizontal wind blowing over a fire of heat release rate  $Q$ , assumed to be constant.  $Q$  is the most important parameter characterizing an outdoor fire. Ambient stratification of the atmosphere,

which is related to the meteorological concept of potential temperature, is included in this model. The atmospheric stability at any height is determined by the local density (or temperature) gradient and is specified by the local buoyancy frequency  $N = \sqrt{(g/\rho(z))(d\rho(z)/dz)}$ . This frequency arises because the atmosphere is naturally stratified as a function of height, with the highest density air at ground level and smaller densities with increased height. The horizontal velocity is assumed to be uniform with height over the height of interest, although the more general theory allows for a velocity profile changing with height. Analytical scaling of the governing equations introduced in these papers yields the following important length scale:

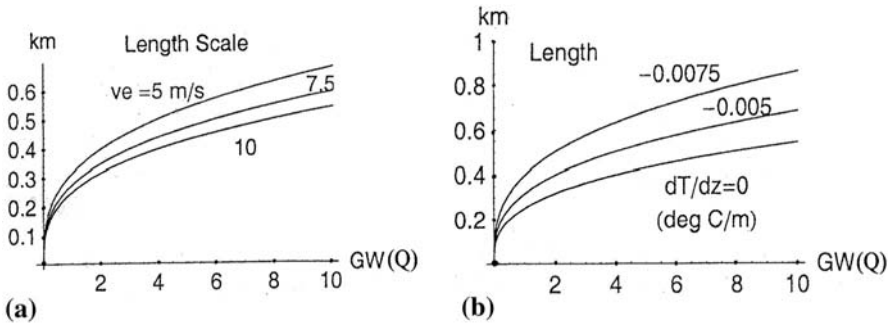
$$L = \left( \frac{Qg}{C_p T_\alpha \rho_\alpha V N^2} \right)^{1/3} \quad (10.84)$$

where  $U$  is the steady and uniform horizontal velocity,  $N$  is the buoyancy frequency defined above,  $C_p$  is the constant-pressure specific heat for air, and  $T_\alpha$  and  $\rho_\alpha$  are the ambient, ground-level temperature and density. This length must be interpreted as an estimate of the order of magnitude of the height above the fire to which the centerline of the plume will rise for the specified values of the fire size  $Q_1$  (GW) the wind speed  $V$  and the buoyancy frequency  $N$ . Because this relationship is derived from the governing equations, it should apply to the WTC tower fires as well as to oil-spill fires.

From BANG-FIR part I the characteristic length  $L$  is computed as a function of  $Q$  for different values of  $N$  and  $V$  for the tower of WTC. These plots indicate the sensitivity of the value  $L$  to changes in atmospheric stability and the wind speed.

Program BANG-FIR – part 2 used the thermal element model and was performed over a domain, which included the top portions of both towers and horizontal lengths in each direction equal to a few tower heights. With these computations, we attempted to bound the total quasi-steady convective heat release from the fires in each tower by comparison of the observed smoke plume trajectory with that determined by the simulations.

Based on FEMA, for most of the simulations reported here, a grid of 108 nodes in each direction ( $1.26 \times 10^6$  total cells) was used. Computations required about 15 CPU hours on a 1 GHz standard personal computer to simulate 500 s real time for the FDS1 computations and about 30 s real time for the FDS2 computations. The domain for the FDS1 computations was taken to be 600 m in both horizontal directions by 800 m in the vertical direction, evaluating a cell size of 5.6 m by 5.6 m by 7.4 m. The domain for the FDS2 simulations was approximately 84 m by 84 m by 70 m, giving a cell size of 0.78 m by 0.78 m by 0.65 m. It was noted from the calculations the steady state plume height increased very quickly with down wind distance. Where the rate of magnitude became smaller, the plume height was slow with down wind distance.



**Fig. 10.8.** Plume scaling length  $L$  as functions of the convective energy/time  $Q$  for  $Ve = 5$  m/s; (a)  $Q$  versus  $Ve$  with  $L$  scale, (b)  $L$  versus  $Q$  with  $dT/dz$  scale

### *Fire Simulation in the Global Analysis*

After the aircraft impact occurred, it is important to simulate fire in postulating interior and exterior damage of a WTC tower.

For both undamaged towers, the authors have modelled a story as having a total height of 3.66 m, with a floor/truss thickness/ceiling combination of 1.04 m. Only a portion of the height of each tower was included in the simulations. The model started two stories below the damaged ones and ended tell stories above, because buoyancy  $N$  causes the smoke and hot gas to rise. For the north tower, the model began at the 92nd story and included the 108th story. The south tower began at the 76th story and ended at the 93rd story. The outside walls of the undamaged stories of each tower were impenetrable, whereas the core was assumed to be open at both the top and bottom allowing gases to flow freely in and out. These were taken from the FEMA Report. A reference is made to the following data from FEMA Report together with plume scaling length versus several parameters indicated in Fig. 10.8.

The core which had a different orientation in the two towers as noted above, was modelled by two vertical shafts each extending 42 m in the direction of the long axis of the core, one having a width of 2.5 m and the other a width of 14.6 m, with a 7.4 m aisle separating the two. The larger shaft was taken to be hollow, with a slit of 3.2 m running vertically up the centre of both long faces of the shaft. These slits were constructed to represent openings shown by connecting floors vertically through the core, and can be regarded as a combination of designed vertical connections and damage produced connections. The core shaft was open at both the bottom and the top of the model. The slit size in the core shaft changes the interior ventilation for the model, and this interior ventilation should be varied systematically to determine its importance to the spread of smoke, hot gases and the fire. Only two cases were simulated, one with no slits in the core and the other with the 3.2 m slits as described above.

Damage and the fuel distribution on the inside of the tower must be postulated. As an attempt to bracket the interior damage, two very different damage scenarios exist for a segment of the north tower. For the first scenario, it was assumed that five floors were damaged and collapsed into a pile of combustible rubble from the force of initial impact, the north face, to the core. Therefore, the damage geometry was effectively one large open space with the rubble treated as a big rectangular block on the floor. We assumed that the internal combustible material was spread uniformly over all of the interior surfaces in the damaged area including the block, and all surfaces burned at the same rate. A reference is made to Chap. 9.

In a second case, it was postulated that the plane penetrated to the core of the north tower and that the floors remained standing up to the damage hole produced by the plane. In this case, most of the floor area, except for the plane hole remained as it was before the collision, and the fire burned over these long, narrow floors.

The design load for one floor of such a building is usually taken to be  $460 \text{ kg/m}^2$  with  $90 \text{ kg/m}^2$  due to partitions and  $370 \text{ kg/m}^2$  regarded as movable. Of this movable load, the combustible portion is generally taken to be 14 to  $18.5 \text{ kg/m}^2$ , but possibly ranging up to  $140 \text{ kg/m}^2$ , with an average load of  $46 \text{ kg/m}^2$  still being reasonable in an office building such as the WTC Towers. A very reasonable way to look at these fires is to consider the burning jet fuel to be the igniter of the existing fuel within the building. It must also be noted that the fuel loads might vary considerably with spatial location in each building.

## 10.9 World Trade Center (WTC 1 and WTC 2)

### 10.9.1 Data for Three-Dimensional Finite Element Modelling

The following summarises the basic geometric data for WTC 1 and WTC 2: (Note: The data is given for both towers. Where there is a difference, this has been identified).

- 1 Storey Height is generally 110 storeys plus 7 levels.
- 2 For WTC 1 roof height is 1368 ft (417 m) with 360' or 110 m Television Tower  
For WTC 2 roof height is 1362 ft (415 m)
- 3 Square floor plate 207'-2" (63.1 m): corners chamfered 6'-11" (2.13 m)  
Long on each side
- 4 Floor space at each level 207'  $\times$  207'
- 5 Rectangular service core 87' (26.5 m)  $\times$  137' (41.75 m)
- 6 Bearing wall (exterior wall module) Ref: Fig. 10.10

- 7 Welded columns 59 No columns 14" (358 mm)  
 Typical floor at each of the flat faces of the building square box section at 3'-4" (1.06 m) closed spaces Ref: Fig. 10.15
- 8 Adjacent perimeter column interconnected at each floor level 52" (1.321 m) deep spandrel plates
- 9 Plate thickness Exterior walls = 1/4" (6.3 mm)  
 Base of the column = 4" (100 mm)
- 10 Floor construction (a) 100 mm light weigh concrete with 38 mm – 22 gauge non-composite steel deck open web joist floor system  
 (b) Floor trusses  
 In pairs with spacing 6'-8' (2.03 m), Spanning 60' (18.276 m) and 35.0' (10.67 m) at the ends of each core

The following summarises carefully by studying literature and drawings of WTC 1 and WTC 2 the loads and material properties associated with these two towers:

- 1 Floor imposed load 100 lb/ft<sup>2</sup> (4.788 KN/m<sup>2</sup>)  
 Building corner load 55 lb/ft<sup>2</sup> 3.79 KN/m<sup>2</sup>)
- 2 Boeing 767 – 200ER Commercial Aircraft  
 (a) Maximum rated take off load/weight 3.95 × 10<sup>3</sup> lbf (376672 kg)
- 3 Basic dimensions of the aircraft 767-200 ER 159' (48.45 m) length × 156' (47.85 m) wide × 53' (16.155) high from ground
- 4 Rated cruise speed 530 miles/hr  
 Actual for WTC 1 470 miles/hr  
 Actual for WTC 2 590 miles/hr
- 5 Tower Impacted floors WTC 1 – Between floors 94 and 98  
 WTC 2 – Between floors 78 and 84
- 6 Impact Duration as reported (approx) WTC 1 → 10 seconds Average  
 WTC 2 → 8–10 seconds Average
- 7 Area Impacted 30 m<sup>2</sup> for WTC 1  
 35 m<sup>2</sup> for WTC 2

SEA LOAD-TIME FUNCTION FOR AN AIRCRAFT IN  
 APPENDIX I

- 8 Collapsed after impact                    WTC 1 → After 102 minutes in  
5 seconds  
WTC 2 → After 56 minutes in  
10 seconds
- 9 Approx. sealing gas                    1000°C–1100°C  
temperature
- 10 Approx. dead load                    88 lb/ft<sup>2</sup> (4.213 kN/m<sup>2</sup>)
- 11 Floor beams                            Exterior: W24 × 61  
Interior: W18 × 50
- 12 Steel plate thickness through       3/8" (9.5 mm) thick  
out in bolted joints                    12" (305 mm) × 6 1/2" (65 mm) PL
- 12 Bolts (as evident from               3/4" (19 mm) spaced along rows  
drawings)                                3 1/2" (90 mm)
- 13 Weld material                         Nominal yield strength = 50 Ksi  
(342 MN/m<sup>2</sup>)
- 14 Steel Grades 12ND                    42 Ksi (289.6 MN/m<sup>2</sup>) to 100 Ksi  
(684.5 MN/m<sup>2</sup>)
- 15 Metal Deck spanning                13'-4" (4.064 m)
  - (a) Parallel to the main trusses  
supported by transverse  
bridging trusses
  - (b) Intermediate deck, support       6'-8" (2.03 m)  
angles, spacing from  
transverse trusses
  - (c) Core concrete fill on metal       14" (350 mm) × 36" (915 mm) deep  
deck supported by floor  
framing of rolled sections,  
in turn, supported  
combined wide shaped  
flanges and columns of box  
sections
- 15 Outrigger truss system for        103 floor – 110 floor  
stiffening of frames
- 16 Structural tube framing base       3ND columns 14" (358 mm) box  
of the exterior wall frame            each joint to form base columns
- 17 Cantilever transfer girder        46' (14 m) span, 2 to column  
detail                                        continuous down. At continuous  
down = 4'-6" (1.37 m) 9 ft (2.74 m)  
depth near rafter with spacing  
6'-9" (2.057 m)

Note: For other material properties reference is made to Tables 10.1 to 10.8. In the finite element analyses where stresses, strains for each element reached. The limit values, the element has yielded. This is discussed later on in this section.

**Table 10.1.** Heat release rate for office module

Heat Release (KW)	Time (seconds)
0	0–1200
1000	420↑
2000	Slow – Rate ↑450–600
4000	↑480–660↓
6000	0550↑↓
7000	600

**Table 10.2.** Temperature–time ASTM E119

Temperature °C	Time Minutes
25	1.5
200	2.0
400	4.0
600	7.5
800	20
1000	60

**Table 10.3.** Stress-strain curve structured steel ASTM A36 steel at 600°C (1112F°)

Stress N/mm <sup>2</sup>	Strain ε in/in
0	0
100	0.08
130	0.02
150	0.12

**Table 10.4.** Critical temperature for various types of steel

Steel	Temperature
Columns	538°C
Beams	593°C
Open-web steel joists	593°C
Reinforcement	593°C
Pre-stress steel	426°C

**Table 10.5.** Strength–reduction factor Fyt/Fy at elevated temperature

Fyt/Fy	Temperature °C
1	0
0.9	200
0.8	300
0.7	400
0.4	600
0.2	700

**Table 10.6.** Young’s modulus at elevated temperature °C reduction values

E/E <sub>0</sub>	Temperature °C
1	0
0.97	50
0.95	100
0.85	300
0.82	400
0.63	500
0.20	600



**Table 10.7.** Box columns 14'' × 14'' temperature versus time based on E119

Temperature °C	Time (minutes)
100	5.0
200	7.5
300	10.0
400	12.5
600	15.0
700	20.0

**Table 10.8.** Warping and buckling

Warping $W_{vcb}$	$M_1/M_2$
1.0	-1.0
1.25	-0.5
2.25	+0.5
2.75	+1.0

## 10.10 Finite Element Modelling of WTC-1 or WTC-2

### 10.10.1 Introduction

In order to make more efficient use of the inelastic response of the building system and its damage scenario, the relevant numerical analysis and analytical work should be based on keeping in mind where the damaged areas were visible and where columns and floors statistical data in the FEMA Report have shown as disaster areas. This will be quite useful to check also the analytical results. Where the classification of the damage scenario is not clear, the normal course of finite element analysis shall be carried out. This section is entirely based on the WTC 1 and WTC 2 building collapse analysis. For the dynamic finite element analysis, a reference is made to Appendix I where derivations of various cases have been studied and analytical formulations are recorded.

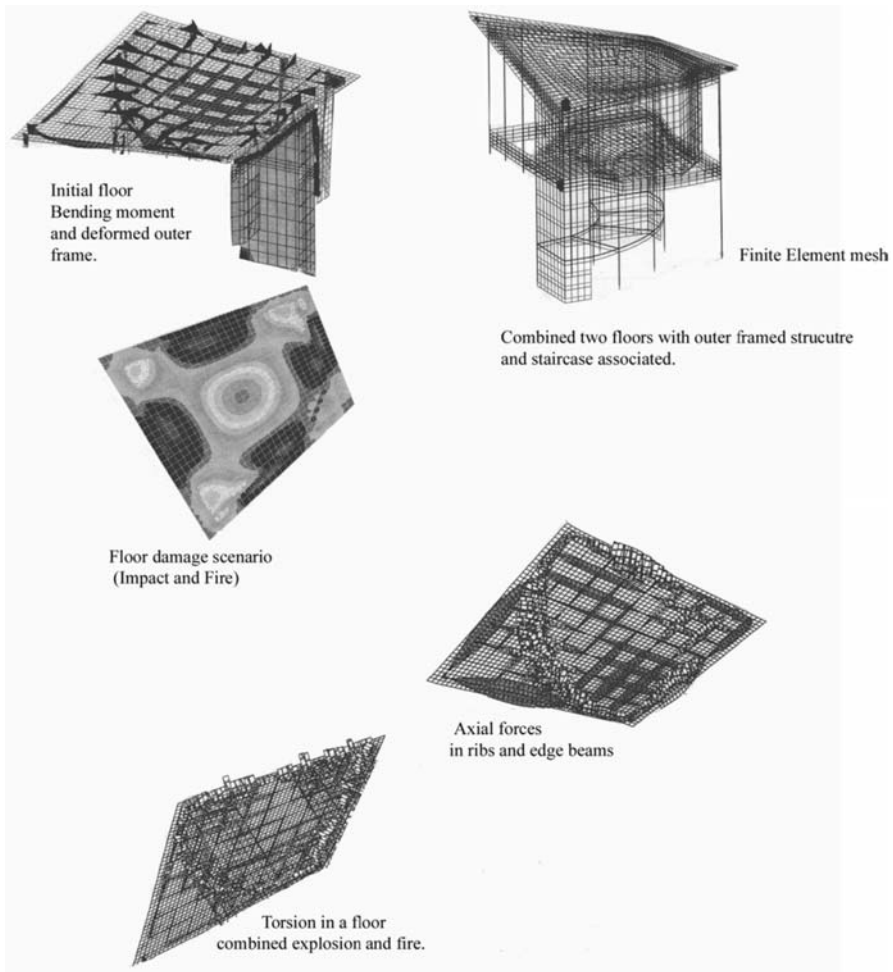
#### 10.10.1.1 Finite Element Analysis of WTC 1 and WTC 2: Basic Philosophy

Plate 10.2 shows a typical 3D finite element mesh scheme, comprising of 3D line elements and series of these elements are connected by nodal points through out in the WTC 1 framed building. The concrete floors have 4-noded is 0 parametric elements and their nodes are linked with 2 noded truss rods of the trusses. The same scheme is continuous for the supporting trusses in transverse directions.

Both towers and their tores are modelled explicitly. The steel connections such as moment and shear connections are spandrell-column connections in all major framing are also explicitly modelled. In the intermediate framing, beams are incorporated as grids.

Typical mess schemes are given in Fig. 10.09 to 10.12 for individual local F.E. analysis for buckling, warping and interactive analyses when members are under loads caused by either impact-cum-blasts.

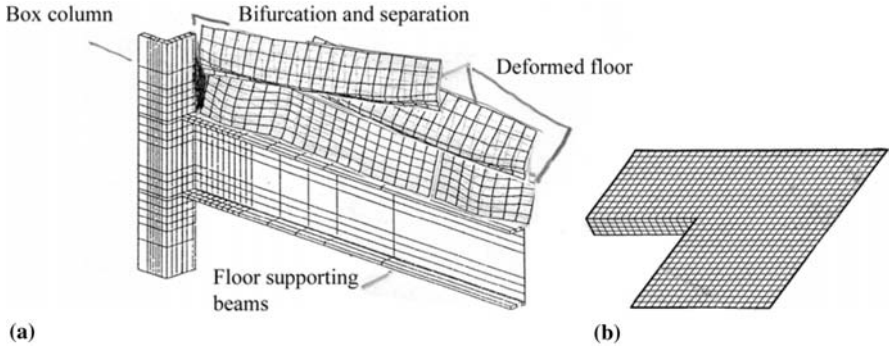
Basic formulations for the steel deck slab system are complex. In this analysis the system was modelled at each floor level as composite with clear



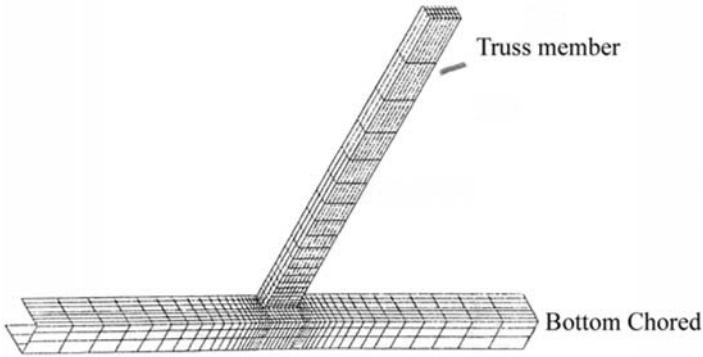
**Fig. 10.9.** Typical floor-core deformations

material properties. The elements refined systematically to obtain key out put data, specifically in the regions of heavy damage where F.E. mesh schemes were refined. PROGRAM BANG-BLAST has been used to carry out damage analysis using different models.

- (a) Impact from 767-200 ER.
- (b) Assessment of loose joints buckling and plasticity zones.
- (c) Blast load defined for WTC1 and WTC2.
- (d) (b) + (c) algebraically added results: check for any damage scenario defined by members crushing, yielding and cracking with and without buckling/warping.



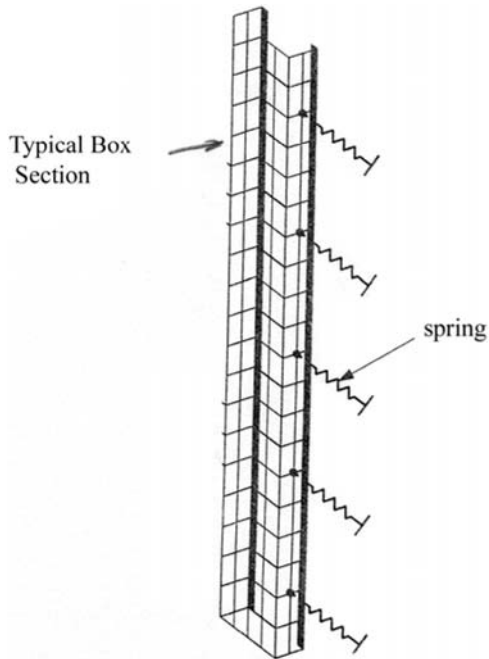
**Fig. 10.10.** (a) Floor on floor supporting beams with box columns – finite element mesh scheme; (b) Undeformed deck – mesh scheme 4 noded isoparametric elements



**Fig. 10.11.** Finite element mesh scheme for trusses

(e) (b) + (c) + fire ball loads. The fire ball investigation includes fuel - structural interaction. BANG-FIR is called upon in the main program. The out put is algebraically added to (a) + (b). Check by FLAG, whether or not damage scenario has further intensified or spread to other elements.

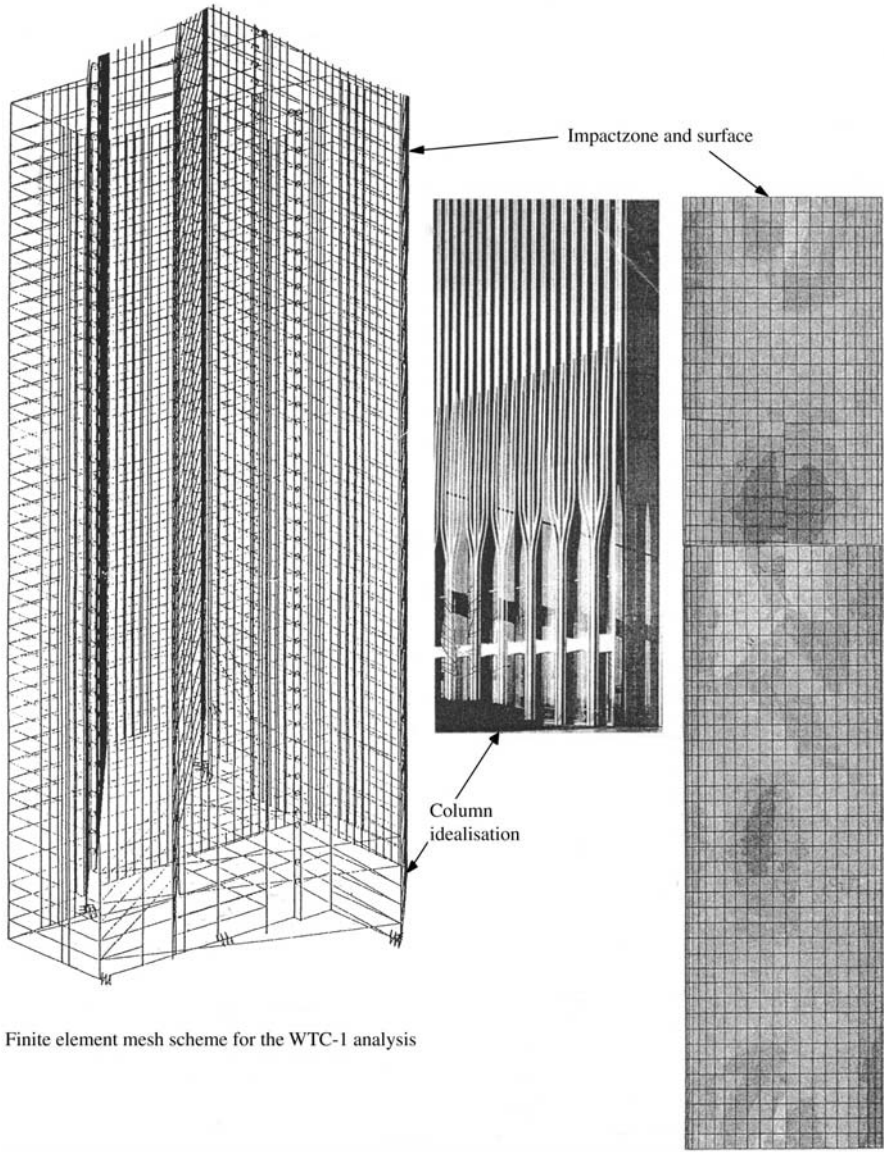
The jet fuel has been distributed over multiple floors, and some have been transported to other locations. Some have assumed been absorbed by carpeting or other furnishings, consumed in the flash fire in the aerosol, expelled and consumed externally in the fireballs, or flowed away from the fire floors. Accounting for these factors, it is believed that all of the jet fuel that remained on the impact floors was consumed in the first few minutes of the fire. The wind speed at heights equal to the upper stories of the towers was in the range of 10–20 mph. The outside temperatures over the height of the building were 20–21°C (68–70°F). These effects are considered in the loading cases.



**Fig. 10.12.** Box section column interacting with floor (half box is shown for F.E. mesh assessments)

The modelling suggests a peak total rate of fire energy output on the order of 3–5 trillion Btu/hr, around 1–1.5 gigawatts (GW), for each of the two towers. From one third to one half of this energy is assumed to flow out of the structures. This vented energy is the force that drove the external smoke plume. The vented energy and accompanying smoke from both towers combined into a single plume. The energy output from each of the two buildings is similar to the power output of a commercial power generating station. The modelling also suggests ceiling gas temperatures of  $1,000^{\circ}\text{C}$  ( $1,800^{\circ}\text{F}$ ), with an estimated value of plus or minus  $100^{\circ}\text{C}$  ( $200^{\circ}\text{F}$ ) or about  $900\text{--}1,100^{\circ}\text{C}$  ( $1,600\text{--}2,000^{\circ}\text{F}$ ). A major portion of the uncertainty in these estimates is due to the scarcity of data regarding the initial conditions within the building and how the aircraft impact changed the geometry and fuel loading. Temperatures may have been as high as  $900\text{--}1,100^{\circ}\text{C}$  ( $1,700\text{--}2,000^{\circ}\text{F}$ ) in some areas and  $400\text{--}800^{\circ}\text{C}$  ( $800\text{--}1,500^{\circ}\text{F}$ ) in others.

The viability of a 3–5 trillion Btu/hr (1–1.15 GW) fire depends on the fuel and air supply. The surface area of office contents needed to support such a fire ranges from about 30,000–50,000 square feet ( $2787\text{ m}^2\text{--}4645\text{ m}^2$ ) depending on the composition and final arrangement of the contents and the fuel loading present. Given the typical occupied area of a floor as approximately 30,000 square feet, it can be seen that simultaneous fire involvement of an area



Finite element mesh scheme for the WTC-1 analysis

Fig. 10.13. A damage scenario of WTC-1 at and around impact area

equal to 1–2 entire floors can produce such a fire. Fuel loads are typically described in terms of the equivalent weight of wood. Fuel loads in office-type occupancies typically range from about 4–12 psf (0.191/0.0515 kN/m<sup>2</sup>) with the mean slightly less than 8 psf (0.382 KN/m<sup>2</sup>). File rooms, libraries, and similar concentrations of paper.

Based on photographic evidence, the fire burned as a distributed collection of large but separate fires with significant temperature variations from space to space, depending on the type and arrangement of combustible material present and the available air for combustion in each particular space. Consequently, the temperature and related incident heat flux to the structural elements varied with both time and location. This information is not currently available, but has been modelled with advanced CFD fire models.

Damage caused by the aircraft impacts is believed to have disrupted the sprinkler and fire standpipe systems, preventing effective operation of either the manual or automatic suppression systems. Even if these systems had not been compromised by the impacts, they would likely have been ineffective. It is believed that the initial flash fires of jet fuel would have opened so many sprinkler heads that the systems would have quickly depressurised and been unable to effectively deliver water to the large area of fire involvement. Further, the initial spread of fires was so extensive as to make occupant use of small hose streams ineffective.

It is assumed that the structural joints, at the level of impact, are 95% in effective is the joints have failed. Areas outside impact zone, the strength reduction factor is, for the purpose of analysis, is 50% assumed to be 50%.

As stated earlier the impact of the aircraft into WTC 1 substantially degraded the strength of structure to withstand additional loading and also made the building more susceptible to fire-induced failure. Among the most significant factors:

1. The force of the impact and the resulting debris field and fireballs probably compromised spray-applied fire protection of some steel members in the immediate area of impact. The exact extent of this damage will probably never be known, but this likely resulted in greater susceptibility of the structure of fire-related failure.
2. Some of the columns were under elevated states of stress following the impact, due to the transfer of load from the destroyed and damaged elements.
3. Some portions of floor framing directly beneath the partially collapsed areas were carrying substantial additional weight from the resulting debris and, in some cases, were likely carrying greater loads than they were designed to resist.

As fire spread and raised the temperature of structural members, the structure was further, stressed and weakened, until it eventually was unable to support its immense weight. Although the specific chain of events that led to the eventual collapse will probably never be identified, the

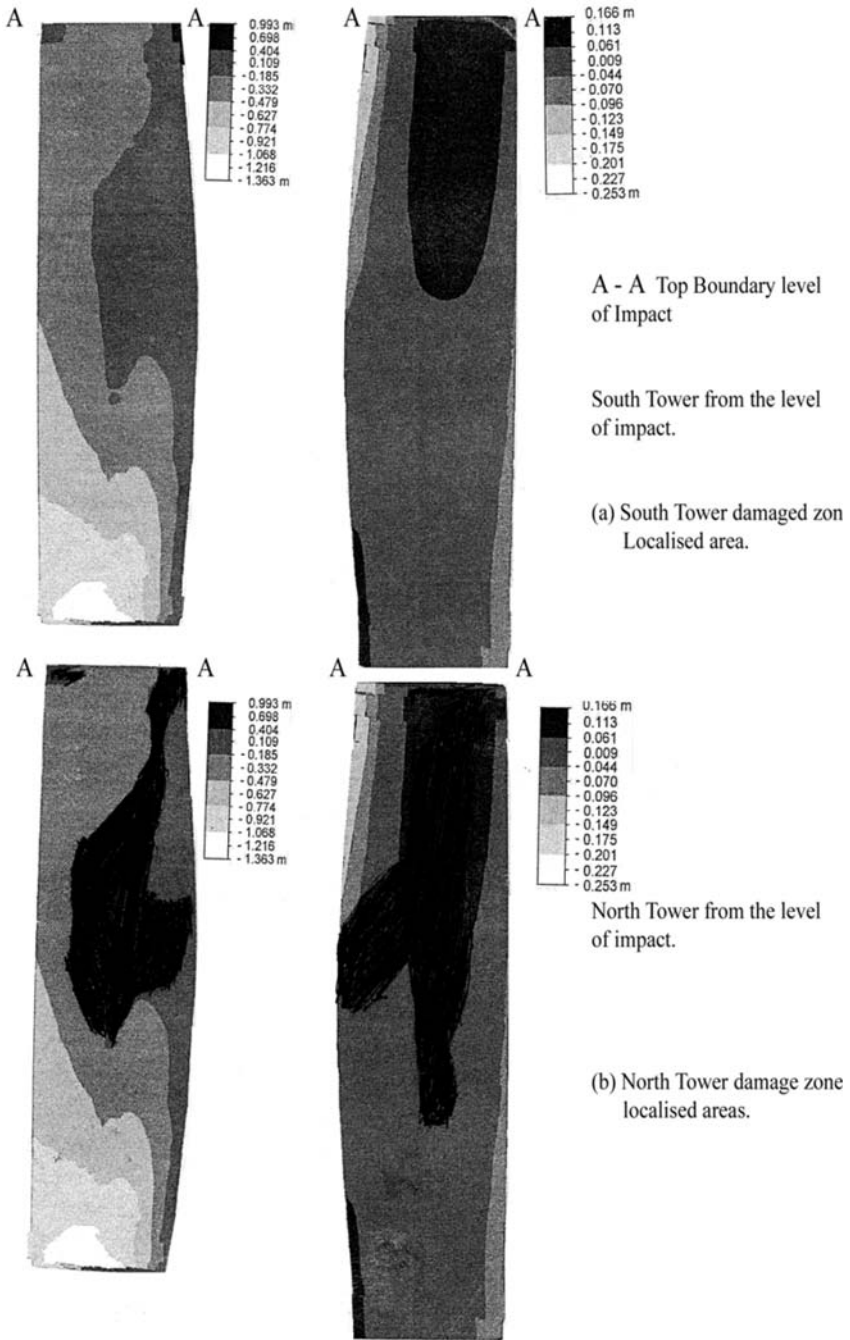


Fig. 13.a. WTC-1 and WTC-2 damage zones of localised areas under impact

following effects of fire on structures may each have contributed to the collapse in some way discussion of the structural effects of fire.

4. As floor framing and supported slabs above and in a fire area are heated, they expand. As a structure expands, it can develop additional, potentially large, stresses in some elements. If the resulting stress state exceeds the capacity of some members or their connections, this can initiate a series of failures.
5. As the temperature of floor slabs and support, framing increases, these elements can lose rigidity and sag into catenary action. As catenary action progresses, horizontal framing, elements and floor slabs become tensile elements, which can cause failure of end connections and allow supported floors to collapse onto the floors below. The presence of large amounts of debris on some floors of WTC 1 would have made them even more susceptible to this behaviour. In addition to overloading the floors below, and potentially resulting in a pancake-type collapse of successive floors, local floor collapse would also immediately increase the laterally unsupported length of columns, permitting buckling to begin. As indicated in Appendix B, the propensity of exterior columns to buckle would have been governed by the relatively weak bolted column splices between the vertically stacked prefabricated exterior wall units. This effect would be even more likely to occur in a fire that involves several adjacent floor levels simultaneously, because the columns could effectively lose lateral support over several stories.

These factors 1 to 5 taken from the FEMA report are in line with the analysis presented in the text.

### **Progression of Collapse**

As in WTC 1, a very large quantity of potential energy was stored in the building, during its construction. Once collapse initiated, much of this energy was rapidly released and converted into kinetic energy, in the form of the rapidly accelerating mass of the structure above the aircraft impact zone. The impact of this rapidly moving mass on the lower structure caused a wide range of structural failures in the floors directly at and below the aircraft impact zone, in turn causing failure of these floors. As additional floor plates failed, the mass associated with each of these floors joined that of the tower above the impact area, increasing the destructive energy on the floors immediately below. This initiated a chain of progressive failures that resulted in the total collapse of the building.

A review of aerial photographs of the site, following the collapse, as well as identification of pieces of structural steel from WTC 2, strongly suggests that while the top portion of the tower fell to the South and East, striking Liberty Street and the Bankers Trust building, the lower portion of the tower fell to the North and West, striking the Marriott Motel (WTC 3). Again, the



debris pattern spread laterally as far as approximately 400–500 feet from the base of the structure. These effects are not considered in two towers.

Construction of WTC 1 resulted in the storage of more than  $4 \times 10^{11}$  joules of potential energy over the 1,368-foot (417 m) height of the structure. Of this, approximately  $8 \times 10^9$  joules of potential energy were stored in the upper part of the structure, above the impact floors, relative to the lowest point of impact. Once collapse initiated, much of this potential energy was rapidly converted into kinetic energy. As the large mass of the collapsing floors above accelerated and impacted on the floors below, it caused an immediate progressive series of floor failures, punching each in turn onto the floor below, accelerating as the sequence progressed. As the floors collapsed, tins left tall freestanding portions of the exterior wall and possibly central core columns. As the unsupported height of these freestanding exterior wall elements increased, they buckled at the bolted column splice connections, and also collapsed. Perimeter walls of the building seen, to have peeled off and fallen directly away from the building face, while portions of the core fell in a somewhat random manner. The perimeter walls broke apart at the bolted connections, allowing individual prefabricated units that formed the wall or, in some cases, large assemblies of these units to fall to the street and onto neighbouring buildings below.

## 10.10.2 WTC 2

### 10.10.2.1 Initial Damage from Aircraft Impact

United Airlines Flight 175 struck the south face of WTC 2 approximately between the 78th and 84th floors. The zone impact extended from near the southeast corner of the building across much of the building face. The aircraft caused massive damage to the south face of the building in the zone of impact. At the central zone of impact corresponding to the airplane fuselage and engines, six of the prefabricated, three-column sections that formed the exterior walls were broken loose from the structure, with some of the elements apparently pushed inside the building envelope. Locally, as was the case in WTC 1, floors supported by these exterior wall sections appear to have partially collapsed. Away from this central zone, in the areas impacted by the outer wing structures, the exterior steel columns were fractured by impact. Evidence shows from 27 to 32 columns over a 5-storey range were destroyed along the south building face. Partial collapse of floors occurred over a horizontal length of approx. 70 ft (214 m) while floors in the other portions were intact. A landing gear from the aircraft crashed through the roof of WTC 2. The roof was located six blocks to the North. A portion of the fuselage was lying on the roof of WTC 5. There was a lot of debris in WTC 2 as well. This effect is not taken in the analysis.

The same types of structural behaviours and failure mechanisms previously discussed are equally likely to have occurred in WTC 2, resulting in the

initiation of progressive collapse, approximately 56 minutes (3360 seconds) after the aircraft impact. Review of video footage of the WTC 2 collapse suggests that it probably initiated with a partial collapse of the floor in the southeast corner of the building at approximately the 80th level. This appears to have been followed rapidly by collapse of the entire floor level along the east side as evidenced by a line of dust blowing out of the side of the building. As this floor collapse occurred, columns along the east face of the building appear to buckle in the region of the collapsed floor, beginning at the south side and progressing to the North, causing the top of the building to rotate toward the East and South and to begin to collapse downward. It should be noted that failure of core columns in the southeast corner of the building could have preceded and triggered these events.

### 10.10.3 Analysis of Results from the Global Analysis

The full simulation of the aircraft 767-200ER with a fuel-filled wings impacting WTC-1 Tower has been carried out. The key components were meshed out together with exterior walls columns wall panels and composite floors. The aircraft engine has a fine mesh of hybrid elements. At the impacting level both mesh schemes are provided with contact/gap elements For the purpose of interactive analysis Hallquist et al. method of master slave and nodes have been adopted. The slave nodes are constrained to slide on master segments after impact occurs and must remain on the master segment until tensile interface force develops. A zone in which a slave segment exists is known as SLAVE ZONE. A void exists between slave and master line. At impact level whether it is due to the aircraft or debris, it is necessary to update the location of each slave node by finding its closet master node or the one on which it lies. In the collapse analysis it becomes necessary that for each master segment one must find out the first slave zone that overlaps. Generate finally the existence of the tensile interface force. Constraints are imposed on global equations by the transformation of the nodal displacement components of the slave nodes among the contact interface. The slave nodes will have no normal degrees of freedom and the normal force components are distributed near by master nodes using explicit time integration in the finite element solution procedures.

There after the impact and release conditions are imposed. This method in the finite elements analysis identifies the contact point that can become trivial during the execution of the analyses. The impact of the aircraft developed a hole of not less than  $\leq 30\text{ m}^2$  by breaking the exterior columns and the floor slabs. The analysis shows, the area filled with hot fuel (800–1000°C) completely developed failure zones and some cases rupture columns and floors. The debris formed impacted the walls and created large spaces for ventilation, allowing 70 seconds to produce flume and fire, initially in the impacted areas. The fuel structure interaction analysis showed continuous damaging and enlarging deformations, particularly to the floors with

exterior columns bowed inward. The impact analysis further showed that the aircraft wing segments were fragmented ( $f_y > 550 \text{ MN/m}^2$ ) and penetrated. Columns and floor zones filled with spraying hot fuel moving down from floor to floor. The hot fuel-cum-debris was sufficient to create a surge of rapidly filling the floors (93rd–97th floors). Debris integrate at this level to dust ridden plume. The ventilation created in the wall (east and south side of the tower) due to debris impacted as well created plume and ignited mist out the entrance gash and blown out window elements. The fire ball resulted. The finite elements analysis, using 3D FEMVIEW and PATRON, indicated continuous debris filled smoke for around 6000 second after which the entire structure collapsed. When the instability analysis performed, the exterior columns showed more “bowing in” at least 25% more than the combined load conditions. Where the exterior columns are not affected (outside impacted zone), they displayed enough residual capacity. The impact analysis re-evaluated the results and vertical approach angle below horizontal  $13.6^\circ\text{C}$  (heading down ward) for WTC 1 Tower while maintaining  $180^\circ$  lateral approach angle and the vertical approach by  $8^\circ$  (heading downward) for WTC 2 Tower. In both cases the average roll angle taken to be  $32^\circ$ . The total time for load-time function diagram was 0.6 seconds for both towers. The progressive analysis of collapse involved different timings for the WTC-1 and WTC-2. The same aspect time,  $\Delta t = 200$  seconds plus, was considered. Not having enough information on the damage to the thermal insulation, it was assumed that aircraft and debris impact have damaged and dislodged the insulation due to inertia forced developed as a result.

BANG-FIRE results when algebraically added to those obtained from aircraft and debris impactive forces indicated that the floors influenced initially by such forces, the hot jet fuel interaction with steel and steel-concrete composites have damaged zones more than the temperature expansion phenomenon which was around 2 to 3%. The fuel temperature could not be less than  $900^\circ\text{C}$  for one hour at least, thus bringing the steelwork taking not more than  $600^\circ\text{C}$  would have contributed to the melting of the structural elements, the zones above the impact zone would be solid and undamaged, thus bring about the vertical collapse scenario. Since the ventilation created would have injected oxygen, thus causing fire which also created high temperatures to cause certain zones of WTC-1 and WTC-2 building structures the initiation of collapse. The temperature modelling alone without impact took almost twice the time of the collapse of WTC-1. Under combined impact fuel and fire loads generated the total collapse of WTC 2 in the specified time. This indicates that aircraft impact had substantially weakened the tower structures and joints welds etc. The impacts have caused greater instability without creating total collapse. The sagging of the floors had increased. Although the floors on the north side of the tower had sagged first, when the fuel plus fires moved toward south. Now the south side floors had sagged to the point where the south perimeter columns bowed inward. The finite element analysis showed that the south exterior wall had bowed inward by 1350 mm.

The robustness of the towers with that truss in particular was designed for normal loads with wind and earthquake effects. After seeing the tower WTC-1 with the core the floors and perimeter walls weakened major instability exhibited in the south wall. The hat truss could not be transferred the loads thereby causing the columns collapsed and the load via spandrels could not have been transferred. The upper section as predicted by the finite element like a high section started tilting and the upper section collapsed on to the floor in WTC-1. Top sway around 675 mm to the north. For maximum displacement value of the tower was achieved using hybrid finite element at 2.5 seconds. The impact position of UA Flight 175 was 7 m from the east corner of WTC-2. This is the off-centre called oblique impact produced torsion in the upper part and caused counter clock movement. The floors considered under direct impact were 77 to 85. The bulk of impact damage was according the finite element analysis was confirmed to six floor. The aircraft wing laden with fuel struck the tower WTC-2.

The heavier damage was discovered in 79th floor due to sheltering of aircraft engine and wings, especially damaged the floor slabs down to the building core. The fuselage when interacted with 80th and 81st floors, the damage scenario was worse. The impact showed the collapsed spandrels and cruised part of the 82nd floor slab with severed columns and the core. The photographs showed as within about one half of a second, dust and debris flew out of windows on the east and the north faces. Several small fireballs of atomized jet fuel burst from windows on the east face of the 81st and 82nd floors loading a large fireball that spanned the entire face. Almost simultaneously, three fireballs came from the east side of the north face. The largest came from the 80th through 82nd floors. A second, somewhat smaller one came from the 79th floor.

The finite element analysis showed only the same fuel-structure-interaction. The results were quite similar to WTC-1 except the physical conditions of the tower determined with inward bowing of columns. The tower lost in half the time the ability to support upper solid floors. The progressive analysis showed that the top of the tower continual tilted to the east and south. Using the aspect time  $\Delta t = 200$  s, the tower began to collapse at earlier time when compared with the WTC-1 tower. Due to oblique impact the impact damage was more severe to the WTC-2 core. The causes can be due jet fuel spray into the interior of the building causing rapid fire, sagging of the east floors, pulling forces to the east perimeter columns with reduced load carrying capacity and heavily weakened and unprotected steel yielded and plastic hinges developed at various positions.

#### 10.10.4 A Comparative Study of WTC-1 Tower Results

An independent assessment of the validity of tower step-by-step collapse scenarios is tabulated using both observed and computed simulated phenomena. The insulation ate assumed ineffective in floors covering impact zones.

<b>WTC-1 Tower</b>		
	<b>Observation</b>	<b>BANG-F Results</b>
1	The aircraft impact did occur at the tower and the tower did not collapse and with stood the impact at the initial time.	The computer simulation after impact showed no sign of major collapse. At increments, the tower still stood and resisted design loads on exterior column. In 20th incremental process, the results showed around 8% reduced margin.
2	The south wall bowed at 10.23 am inward along the entire south face of 94th floor to 100th floor. The maximum bowing based on FEMA Report was 55'' on the 97th floor.	The instability part of the analysis indicated that buckling occurred at the level of 97th floor around 1.375 m along with the tilt angle of around 10° in the direction of south. The total time registered to be 60,000 seconds.
3	At the structural collapse due to impact and fire, the top building section above impact zone tilted enormously in the south and no discernable east and west component in the tilt.	The analysis showed that thermal expansion was resisted by that truss. Core to the external walls, exterior columns splices and spandrel completely failed. The hot fuel structural composite slab interaction initiated the collapse of six floors. Debris impact created ventilation holes and fire analysis took over from fuel analysis, thus created maximum load on core and external walls which exceeded when the process reached at 750°C where this intervened and make the components declared failed and (major parts) when $T_{\theta} = 600^{\circ}\text{C}$ , the solid part of the building above impact zone tilted and the bottom structure acted as like "magma" thus creating opportunity for nearly vertical collapse.
4	As clouds and dust obscured. The view the building section began to fall down nearly vertically. At 102 minutes from the impact of the air craft, the collapse initiated.	The global instability segment within Program BANG-F, supported by program F-PATRAN to register viewing instantly, reached the limit over 1. South side bowed significantly. The program stopped at 6200 seconds from the time of impact. All elements collapsed. Flickering occurred at that level in F-PATRAN indicating the program collapsed and non-functional and finally stopped.

### 10.10.5 A Comparative Study of WTC-2 Tower Results

A similar approach was adopted for WTC-I towers. The tower remained upright – with significant reserve capacity after aircraft impact and the initiation of hot-fuel structural interaction. The east perimeter wall, as indicated by BANG-F showed inward bowing of around 250 mm at floor 80. The bowing was extended and instability to 78th to 83rd floors. When BANG-F called upon the F-BUCKL (for instability and for graphical view) and F-PATRAN, the results showed a greater tilt  $+8^\circ$  to the east prior to the significant downward movement of the building section above the level of impact. Around  $\theta = 30^\circ$  tilt was registered by the instability analysis. The time of collapse initiation registered by program BANG-F together with sub programs duly intervened for component failure at different times was 2880 seconds.

### 10.10.6 Practical Solution to Twin Towers

The geometry of the twin tower is assumed to alter. Sky bridges of intervals of 4 floors were introduced between WTC-1 and WTC-2. A total number of 25 sky bridges were adopted. A rigid frame concept was introduced. The aircraft impact plus fire plus hot fuel loads apart from usual design loads were considered. Various impact angles on south and north sides were considered for the aircraft impact while keeping the roll angle to be  $32^\circ$ . The collapse of one tower took 5 hours and 25 second when aircraft was only considered. On combined loading the disaster scenario for one of the rigid towers reached 2 hours and 25 minutes. The analyses was repeated by introducing the rigidity of escalators or moving walks, placed inclined positions to pave the way for the quick removal of the population. The new factor of safety against impact alone was 15, against – collapse time of  $15 - 2 = 13$  hours when instability analysis intervened. In association with the blast loading effects, the margin of safety was reduced to 7 against 5 hours and 25 minutes and 30 seconds. Only one tower failure phenomenon was considered with the out come showed five sky bridges failed. When escalators and moving walkways were ignored, it is concluded that sky bridges need to be introduced at suitable levels.

### 10.10.7 Conclusion and Future Recommendations

The comments examined what can be learned from the extreme events of 11 September 2001 for the future design of tall buildings and the appraisal of existing ones. The aim has been comprehensively examine the safety issues arising from such event and to direct and improve provisions for building infrastructure which can be sustain future malicious with reduced risk of loss of life.

A comprehensive study carried out, especially on WTC Towers gave an insight of the existing design and how it is related to the progressive collapse of the towers. Since no two buildings are identical, more case studies need to

be examined using international collaboration amongst respective professionals are needed to optimise occupant safety in extreme events. The following conclusions should be noted on the draft report.

(A) *Analysis*

1. A three-dimensional dynamics hybrid finite element analysis is required on tall buildings core and frames using the load-time functions of various known aircraft. In order to assist the designers the authors have prepared such load-time functions plotted for a number of known aircraft. This plot is given Plate 10.3. The buildings are made up of materials which can early be checked for the aircraft impact.
2. It is vital to analyse floors of steel, concrete and composite for damage scenarios caused by aircraft hot fluid interacting with these floors. The report is devoid of such recommendations.
3. From the hot oil-structural interaction, after the building was subjected to heavy impact from the aircraft, debris could result, they in turn produce impulsive loads and cause an impact to the exterior of the columns/walls and core. It is essential to have a through investigation of the debris impact which causes holes and air ventilation, as such would generate instant fire. BANG-FIRE Program can take such a case of instant fire. The structural integrity is vital.
4. Passive and Active fire protection shall form the basis of analysis. The passive fire could not be simulated due to shortage of time and must be pursued in using specific analytical approach.
5. During this analytical analysis at no stage thermal expansion is created any problem. Under such instant load, 2 to 3% of load caused by thermal expansion is in author's view, insignificant.
6. Due to aircraft impact, prior to the hot-fuel interaction the joints, according to analysis, were heavily loosened, and were failed fire together with hot fuel interaction presented a desired scenario.
7. The three dimensional dynamic instability (elastoplastic) analyses has produced using FEMVIEW and PATRAN, dismantled structural elements. The maximum defection of dismantling of a column element was 10m at ground level. This analysis is important for defection with debris dust is still in progress and the international community must show an interest in producing 3D model of Debris-Dust-Deflection (DDD) of structural elements. RROGRAM IMP interacting with DDD program have produced extremely clear scenario.

(B) *Design*

On the design and safety side, the new NIST is an excellent draft and raised there the same important issues. Looking at the various recommendations one has reasons to believe that the following needs urgent attentions:

1. Safety Cladding: The author's analysis indicates that use of laminated or toughened glass with fixing shall be designed to take into account of

the potential explosion loading. Wherever is possible SIFCON Layers are employed which have improved load-deflection characteristics and stress-strain properties in comparison with normal concrete. The SIFCON panel between laminated glasses subjected to blast loading provides 35% additional safety factor. Cladding and glazing of such a system cause less human injuries.

2. A comprehensive test program is needed to design and to create solutions with and without fire.
3. Security and Safety of Building Services: Design procedures supported by comprehensive and experimentation must produce robust and protected building services systems. The building must service complete “burn out” of contents.
4. Safety of Human Beings and Building Design: In order to reduce the probability of occurrence of extreme events, all designs must be carried out on time-load basis so as they have the potential to cause progressive collapse. Buildings above 25 storeys must be designed against impact and explosion with and without fire. Any height above 25 storeys buildings shall be provided with sky bridges, especially the buildings standing in parallel or on any axis. The sky bridges above 25 storeys shall be on the basis of 4 No: floors/sky bridge. In order to make the building robust, the sky bridge would provide “stiff frame” effects and offer opportunities to stay longer in order to carry out substantial evacuation. Using cross positioned escalators in between sky bridges must provide potential escape routes. The physical size of these sky bridges shall not be less than those of staircase widths. Entrances to buildings must have separate air distribution zones with separate air supply and extract. The layout of the building shall be such that terrorists cannot find escape routes on grounds. This will be treated as part of strategies of deterrence needed for the protection vital installations.

It is vital to ensure compartments in a building are gas tight and seals are sound on building completion, if new, by inspection, testing and certification.

## 10.11 Case Study: Alfred P. Murrah Building, Oklahoma, U.S.A.

### 10.11.1 Introduction

The truck bombing of the Alfred Murrah Building on 29th April 1995 caused a great deal of damage to the structure and its elements. From the characteristic of the bomb crater Corley G.W. determined explosion yield energy of 1814 kg (4000 lb) of TNT. It was a nine-storey office building. The site plan indicating column lines is shown in Fig. 10.14. The location of the building in the Oklahoma City is clearly visible in Fig. 10.15.





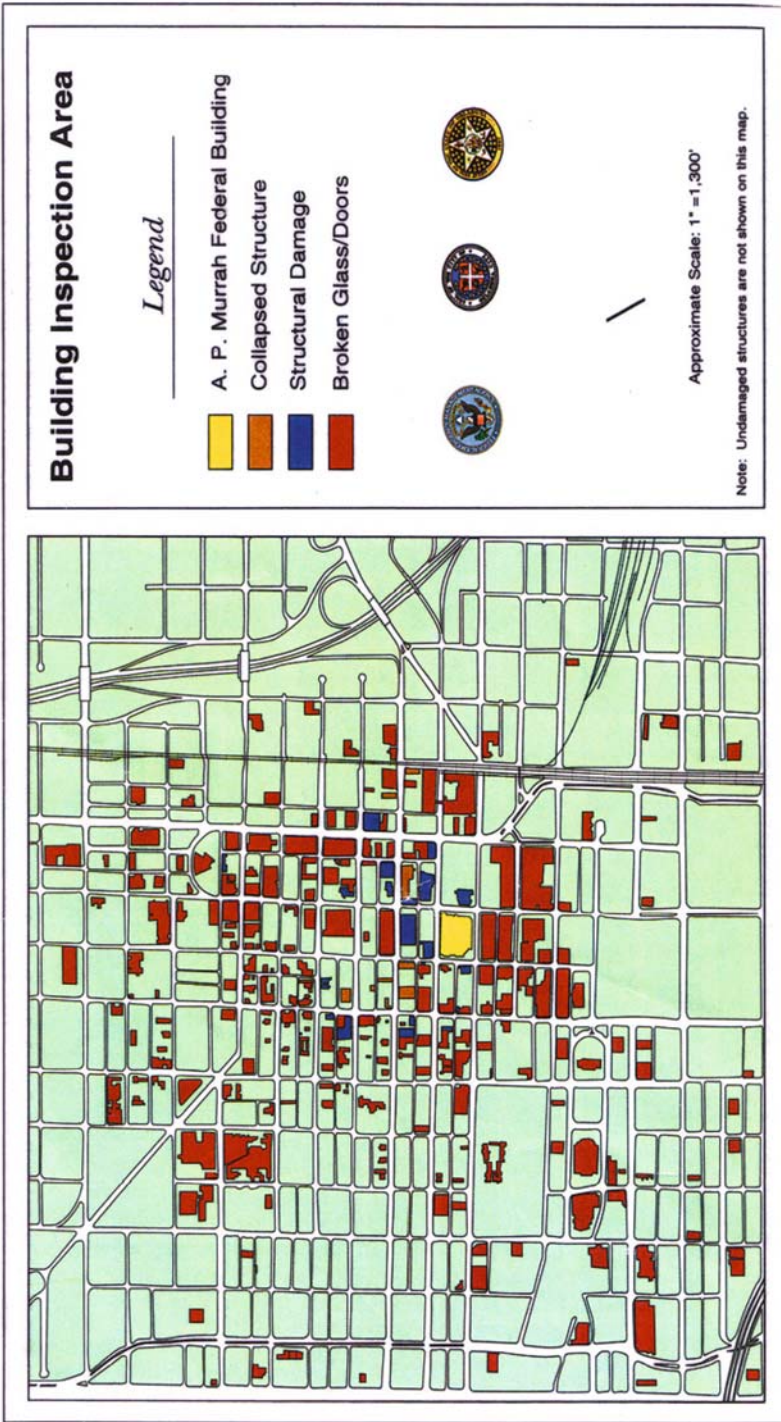


Fig. 10.15. Locations of Murrah Building and other damaged structures (with compliments of FEMA Report 2002, Washington D.C., U.S.A.)

While in Oklahoma City, the investigators took photographs; collected structural drawings, shop drawings, photographs, and samples of structural components, including concrete and reinforcing bars; and obtained an audio tape of the blast. The team also conducted interviews to obtain information concerning damage to buildings. Physical inspection of the structure was limited to visual observation from a distance of approximately 200 ft. (blm)

Following the site visit, samples of concrete and reinforcing bars taken from the site were tested to determine physical properties of materials used in the building. Work performed included developing the most probable response of the building to the blast and determining whether new technology can be used to enhance the resistance of buildings to blast, wind, earthquake, and other hazards.

On May 12, 1995, the BPAT visited the Oklahoma County Sheriffs Firing Range to interview personnel and view debris from the Murrah Building. During this visit, photographs taken soon after the explosion by several law enforcement organizations were reviewed. Also, several pieces of building debris were inspected.

Inspection of debris disclosed that there were a few 'chunk' samples, sections of spandrel beams, some large slab sections, and a few pieces of deformed reinforcing bar and it was confirmed that the concrete and the reinforcing bars had come from the Murrah Building. During the visit, locations were marked on six concrete debris samples where cores were to be taken. In addition, a seventh sample, a chunk of concrete was also marked for coring. Several sections of reinforcing bars were marked to be taken as samples.

On May 12, 1995, a concrete coring company took six 152-mm (6-in) cores from the marked areas. After the cores had been taken in the field, they were packed in a plastic cooler and shipped to Construction Technology Laboratories, Inc. (CTL), in Skokie, Illinois where selected samples were tested. Similarly, reinforcing bar samples were put in a heavy plastic shipping tube and sent to CTL for testing. All samples arrived at CTL on May 15, 1995. Chain-of-custody documentation was maintained for all samples.

In addition to conducting a visual inspection, the team reviewed photographs and videotapes recorded on April 19, 1995, and during the following rescue and recovery period. These records were useful in establishing the performance of the building.

The Kirkpatrick Engineering Consultants, Oklahoma, U.S.A. provided a full description of the design, construction, and condition of the Murrah Building prior to the tragic bombing (BPAT, 1996). The structure was a reinforced concrete frame with three rows of columns spaced at 6.1 m (20 ft) within each row. A large transfer girder at the third floor permitted the elimination of alternate exterior columns below. The building was designed and constructed in accordance with the applicable codes, but did not provide any deliberate resistance against a vehicular bomb attack. Additional information is given in companion papers (Corley et al. [10.1,10.4]).

An estimate is made of the blast loading and its direct effect on the structure of the building. First, the blast loading is calculated from the properties of the crater formed by the explosion. Then, the response of critical structural elements to the calculated loading is determined using approximate methods appropriate for this assessment. Critical elements include the principal exterior columns supporting the transfer girder and the floor slabs of the building.

Bangash T. [10.20] analysed this building using blast pressure loading described later on in this section. The blast pressure diagrams were adopted for slabs and columns together with building response given in Figs. 10.47 to 10.70. Simple Simpson's Rule was adopted in association with blast loads. Results obtained from FEM/DEM analysis (Ref. Appendix I) turned out to be remarkably accurate. The results were corroborated with visual disaster scenario and inspection of damaged components. A specially developed computer program using 'C' Language was developed and tested successfully with other case studies.

### 10.11.2 Experimental Validation of the Combined Finite-Discrete Element Modelling of Structures

#### 10.11.2.1 Introduction

The combined finite-discrete element suggested in earlier chapters was adopted to model the pre-failure and post failure transient dynamics of concrete structures. For this purpose a novel beam element is introduced in order to increase CPU and RAM efficiency. The accuracy and reliability of this element now need to be assessed when used in dynamic loading conditions. Experiments, which have already been undertaken at the Swiss Federal Institute of Technology, Zurich, are used for comparison and validation. The results indicate that the elements introduced is capable of accurately modelling inertia and contact effects in pre failure dynamics, up to collapse.

#### 10.11.2.2 Experimental Investigation and Data Used

The experiments undertaken at the Swiss federal Institute of Technology tested a total of twenty-four beams. The beams were hinged at one end whilst the other end was raised and then released to drop upon a shock absorber as shown in Fig. 10.16.

Beam B1 is chosen for the numerical simulation as this is in line with the stated aim of the paper. The properties of beam B1 are given by

depth $d = 0.3$ m	mass 300 kg/m
breadth $b = 0.4$ m	length 8.15 m
$EI = 32998$ kNm <sup>2</sup>	
concrete cube strength $f_{cu} = 30$ N/mm <sup>2</sup>	
reinforcement yield stress $f_{sy} = 550$ N/mm <sup>2</sup>	

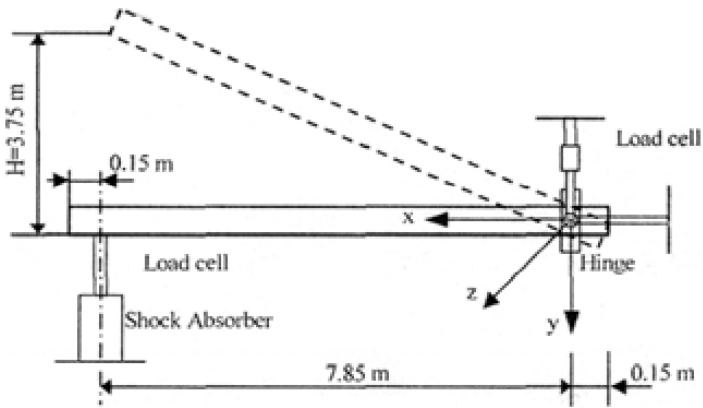


Fig. 10.16. Experimental set up for beam B1

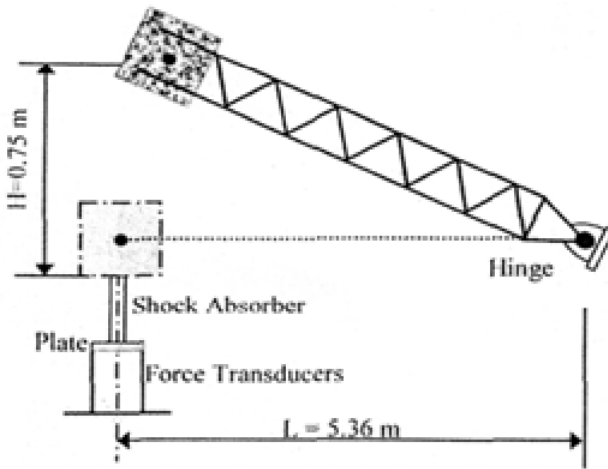


Fig. 10.17. Experimental set up to test shock absorber properties

The beam is raised by using of an overhead crane and then dropped from a height of 3.75 m onto a shock absorber. Only one single drop takes place. A ringfederpuffer (Spring) type shock absorber was used. This shock absorber can endure a maximum force of the order of 3000 kN. A small plate of mass 57 kg was placed at the base of the shock absorber. The impact force of the beam was measured using three force transducers positioned underneath the plate. The properties of this shock absorber were investigated using a truss with a concrete block positioned at its end, as shown in Fig. 10.17. The mass of the block and the truss were 997 kg – and 342 kg respectively. Three drops heights of 300, 650 and 750 mm were used.

*FEM/DEM Simulation for the Shock Absorber*

The first task of the rem/dem simulation was to accurately reproduce the properties of the shock absorber found in the experimental investigations. The FEM/DEM simulation of the impacting truss, described in the previous section is thus performed. The steel truss was modelled as a rigid beam with seven elements. The end node (node 0) was given greater mass, thus representing the mass of the concrete block.

A velocity field is applied along the truss with maximum velocity at node 0 and zero velocity at the hinge. Drop heights of 0.30, 0.65 and 0.75 m were simulated. The velocity formulation for the nodes along the truss is derived from the potential energy, which is given by

$$E_p = \int_0^L \frac{H}{L} x \rho g dx \tag{10.85}$$

By assuming that the energy losses before the moment of impact with the shock absorber together with strain energy of any elastic deformation before impact is negligible the kinetic energy at the moment of impact is given by

$$E_k = \int_0^L \frac{1}{2} \frac{\rho \nu^2}{L^2} x^2 dx = \frac{\nu^2}{L^2} \int_0^L \frac{1}{2} \rho x^2 dx \tag{10.86}$$

where  $\nu$  is the velocity of node 0.

By equating the kinetic and potential energies,  $E_k = E_p$ , the velocity at the moment of impact is obtained

$$\nu = \sqrt{\frac{\int_0^L \frac{H}{L} x \rho g dx}{\frac{1}{L^2} \int_0^L \frac{1}{2} \rho x^2 dx}} \tag{10.87}$$

The results for the force-time, displacement-time and force displacement properties for the shock absorber are compared in Figs. 10.18 to 10.20.

Figure 10.18 shows the force-time relationship of the shock absorber obtained for drop heights of 300, 650 and 750 mm. The experimental result for a drop height of 650 mm is also shown on the plot. A good agreement between both experimental and numerical plots is seen.

The displacement-time relationships for the same drop heights, of 300, 650 and 750 mm are plotted in Fig. 10.19. Here good agreement is also found between numerical and experimental results plotted for the drop height of 650 mm. Larger displacements are seen to occur as the drop height increases.

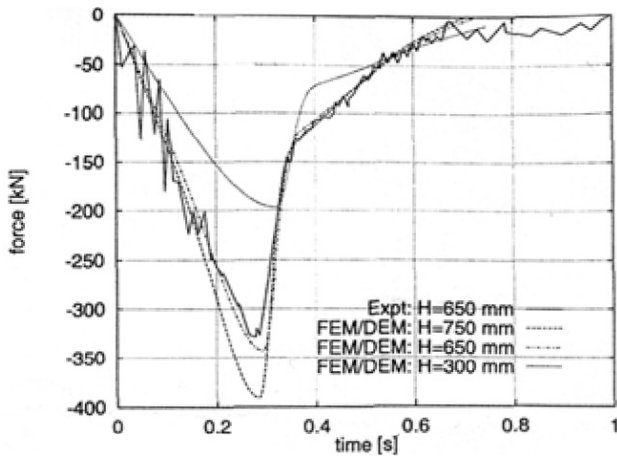


Fig. 10.18. Force-time relationship of the shock absorber for various drop heights

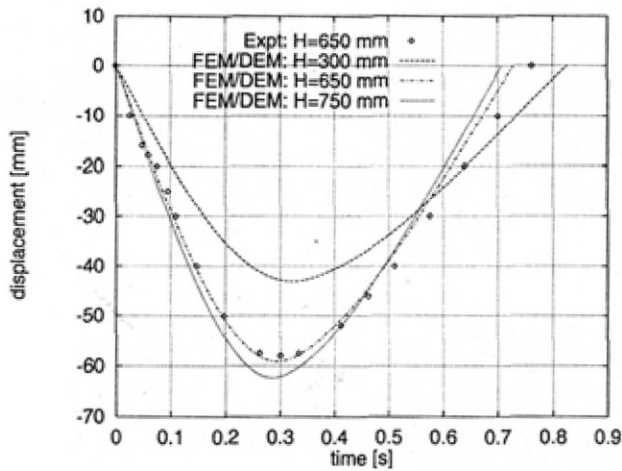


Fig. 10.19. Displacement-time relationship of the shock absorber for various drop heights

Figure 10.20 shows the force displacement relationship of the shock absorber. In this case the drop heights of 300, 650 and 750 mm were also investigated. Here the result for the drop height of 750 mm is compared with the experimental result. The comparison shows good agreement between the two.

*FEM/DEM Simulation for the Beam*

The above simulated force-displacement properties of the shock absorber are integrated with the FEM/DEM transient analysis of beam B1. The beam is discretized into 55 elements.

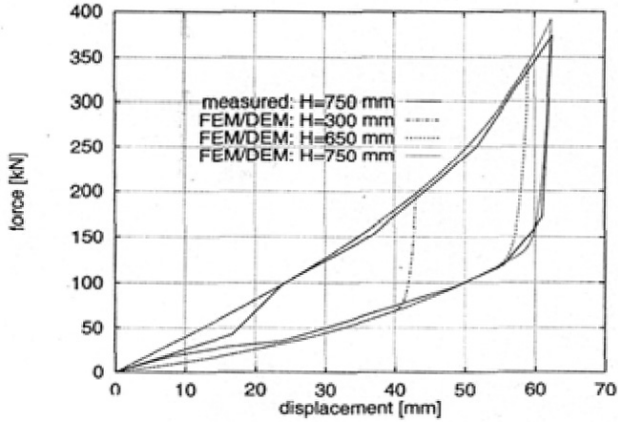


Fig. 10.20. Force-displacement relationship of the shock absorber for various drop heights

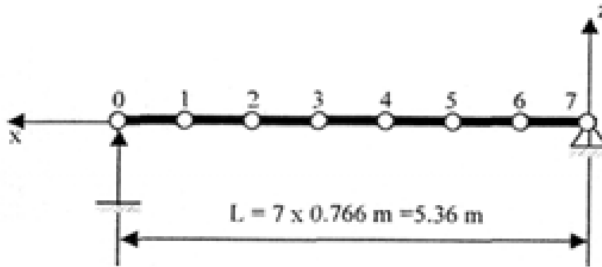


Fig. 10.21. Discretized truss

The finite element described is employed. The dropping action performed in the experiment is modelled by applying a velocity field along the beam at the instance of impact. The maximum velocity is applied at the free end and this decreases linearly along the beam with zero velocity at the hinge. Thus prior to impact the beam is assumed to rotate as a rigid body i.e. the strain energy,  $U$  due to elastic deformations prior to impact is assumed to be small compared to the available potential energy.

The potential energy,  $E_p$  for the complete beam length, shown in Fig. 10.21, is given by

$$E_p = \int_{-L/2}^{L/2} \rho g h dx \tag{10.88}$$

where  $\rho$  is the mass per unit length of the beam. The height of the beam,  $H$  at a distance  $x$  from the centre line is given by



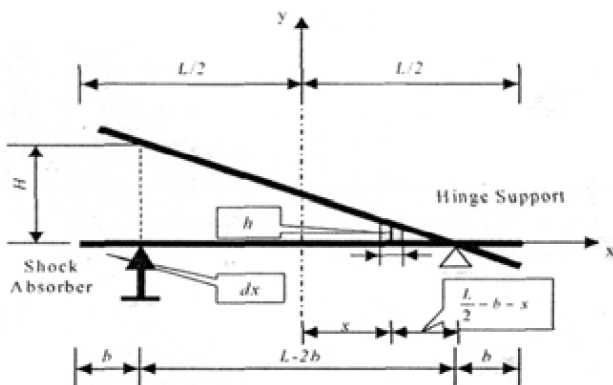


Fig. 10.22. Beam B1 at initial drop height

$$h = \frac{H}{L - 2b} \left( \frac{L}{2} - b - x \right) \tag{10.89}$$

Substituting (10.88) into (10.89) gives

$$E_p = \frac{\rho g H}{L - 2b} \int_{-L/2}^{L/2} \left( \frac{L}{2} - b - x \right) dx = \left( \frac{\rho g H}{L - 2b} \right) \left[ \frac{Lx}{2} - bx - \frac{x^2}{2} \right]_{-L/2}^{L/2} \tag{10.90}$$

Thus the potential energy is given by (Fig. 10.22)

$$E_p = \frac{\rho g H}{L - 2b} \left[ \frac{L^2}{2} - bL \right] \tag{10.91}$$

The kinetic energy for the whole beam length just prior to landing is calculated from the velocity field at the instant just before impact (Fig. 10.23)

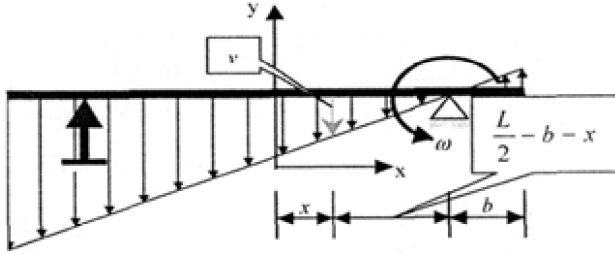
$$E_p = \int_{-L/2}^{L/2} \frac{1}{2} \rho \nu^2 \tag{10.92}$$

The velocity  $\nu$  at distance  $x$  from the centre line of the beam is given by

$$\nu = \omega \left( \frac{L}{2} - b - x \right) \tag{10.93}$$

Hence upon substituting (10.93) into (10.92) the kinetic energy can be found from

$$\begin{aligned} E_k &= \int_{-L/2}^{L/2} \frac{1}{2} \rho \omega^2 \left( \frac{L}{2} - b - x \right)^2 \\ &= \frac{1}{2} \rho \omega^2 \left[ \frac{L^2 x}{4} - \frac{Lx^2}{2} - bLx + \frac{x^3}{3} + b^2 x + bx^2 \right]_{-L/2}^{L/2} \end{aligned} \tag{10.94}$$



**Fig. 10.23.** Velocity field along beam B1 just prior to landing

This gives

$$E_k = \rho\omega^2 \left[ \frac{L^3}{3} + b^2L \right] \tag{10.95}$$

Equating the kinetic and potential energy,  $E_k = E_p$  gives the angular velocity as

$$\begin{aligned} \omega &= \sqrt{\frac{3gH}{L^2 - 3bL + 3b^2}} \\ &= \sqrt{\frac{3 \times 9.81 \times 3.75}{8.15^2 - (3 \times 0.15 \times 8.15) + (3 \times 0.15^2)}} = 1.32 \text{ rad/s} \end{aligned} \tag{10.96}$$

where  $L = 8.15$  m and  $b = 0.15$  m.

The net deflection of the beam is calculated by subtracting the deflection due to rigid body motion from the total deflection. Hence for any node along the beam the nodal deflection,  $w_2$  is calculated by subtracting the rigid body deflection,  $w_1$ , from the total deflection,  $w_3$ .

$$w_2 = w_3 - w_1 \tag{10.97}$$

The rigid body deflection is found from

$$\frac{\delta}{w_1} = \frac{x_h - x_n}{x_n} \tag{10.98}$$

where the suffix's  $h$  and  $n$  stand for the hinge and nodal  $x$  co-ordinate respectively.

The results from the rem/dem model for the deflection time relationship and the deflected form of the beam are shown in Figs.10.24 to 10.26. The deflection of the beam at points 2.5, 4.0 and 5.0 m from the beam is enumerated and compared with those of the experiment. This is shown in Fig. 10.24. Greater deflection is seen to result as the time increases. The value of the deflection is also higher for points farther along the beam. For all three  $x$  values along the beam excellent agreement is seen to exist between the two sets of results.

The deflected form of the beam is shown in Fig. 10.24 at various time steps after the beam had hit the shock absorber. At each time step the plastic hinge

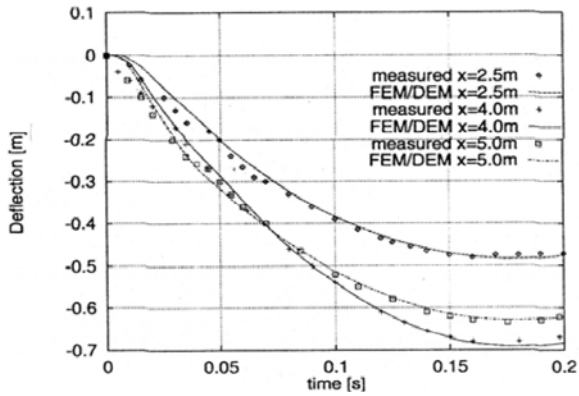


Fig. 10.24. Deflection-time relation at various points from the hinge

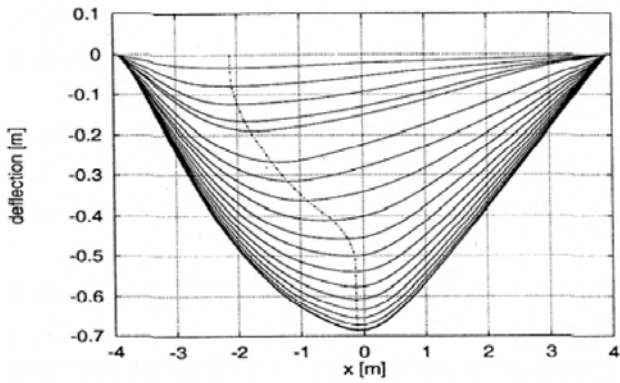


Fig. 10.25. Deflected form of beam B1

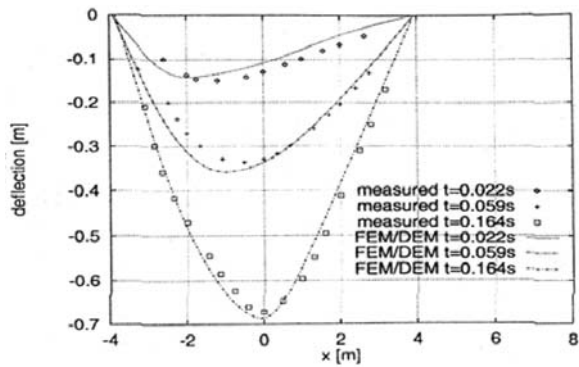


Fig. 10.26. Deflected form of beam B1 at various times

is seen to travel along the beam as the deflection increases with time. This is shown by the dotted line on the plot and is confirmed by experimental observations made at the Swiss Institute of Technology. Figure 10.26 shows the same output reproduced when the elapsed time after the drop was 0.022, 0.059 and 0.164 s. Experimental results for the same time periods are plotted on the same curve. The results are seen to concur favourably.

### 10.11.2.3 Conclusions

A simple element has been tested in combination with dynamic loading conditions. The FEM/DEM simulation first concentrated on accurately reproducing the properties of the shock absorber. These properties were then applied in the FEM/DEM analysis to simulate the beam impact. The results obtained from the analysis show good agreement with the experimental measurements and also validates the conclusion of the authors of the Swiss Institute's report that the plastic hinge moves along the beam as the deflection increases with time.

This shows that the simple element is highly effective when used in combination with dynamic loading conditions. Static condensation can be performed without matrix inversion; thus the CPU processing time is kept to the minimum.

It is worth noting that the procedures described in this paper are not aimed at truck beams and are limited therefore to thin beams. As the numerical experiments demonstrate, large displacements are by default taken into account, as is the standard approach with FEM/DEM. However this excludes finite strains.

In FEM/DEM lumped mass approach is used for the transient dynamic analysis, and there is no problem with using regular grids for individual beams. Also for contact detection and interaction regular grid is an optimal solution in terms of CPU and RAM. In other words where the structure is made of a large number of beams, columns, etc, in FEM/DEM modelling of collapse there is no reason why a particular beam should not have a regular grid. In this context, there was no need to speculate what would happen if element lengths were varied. Thus this was left outside the scope and practical purpose of this paper. However, should one use the element in the context different from FEM/DEM where using distorted grids over individual beams may be important, it advised that accuracy and convergence criteria be carefully examined.

### 10.11.3 Structural Layout of the Alfred P. Murrah Building

The Murrah Building comprised of a nine storey section either side of which was a single storey building as shown in Fig. 10.27. Figure 10.27 also shows a multi level underground car park in front of the south face of the Murrah Building. The structure was erected using a tower crane.

The full force of the bomb was taken by a nine storey section of the structure. This structure was an ordinary moment frame rising nine floors supported by columns as shown by Fig. 10.31. The north face was covered with one inch thick bronze insulated glass cladding. At each floor level a further quarter inch bronze tempered glass had been placed. The cladding curved inwards for the first two floors. The distance between the cladding and the exterior wall was 1.5 m (5 ft).

Circular vertical tubes were constructed at each corner of the building as part of the structure's ventilation system.

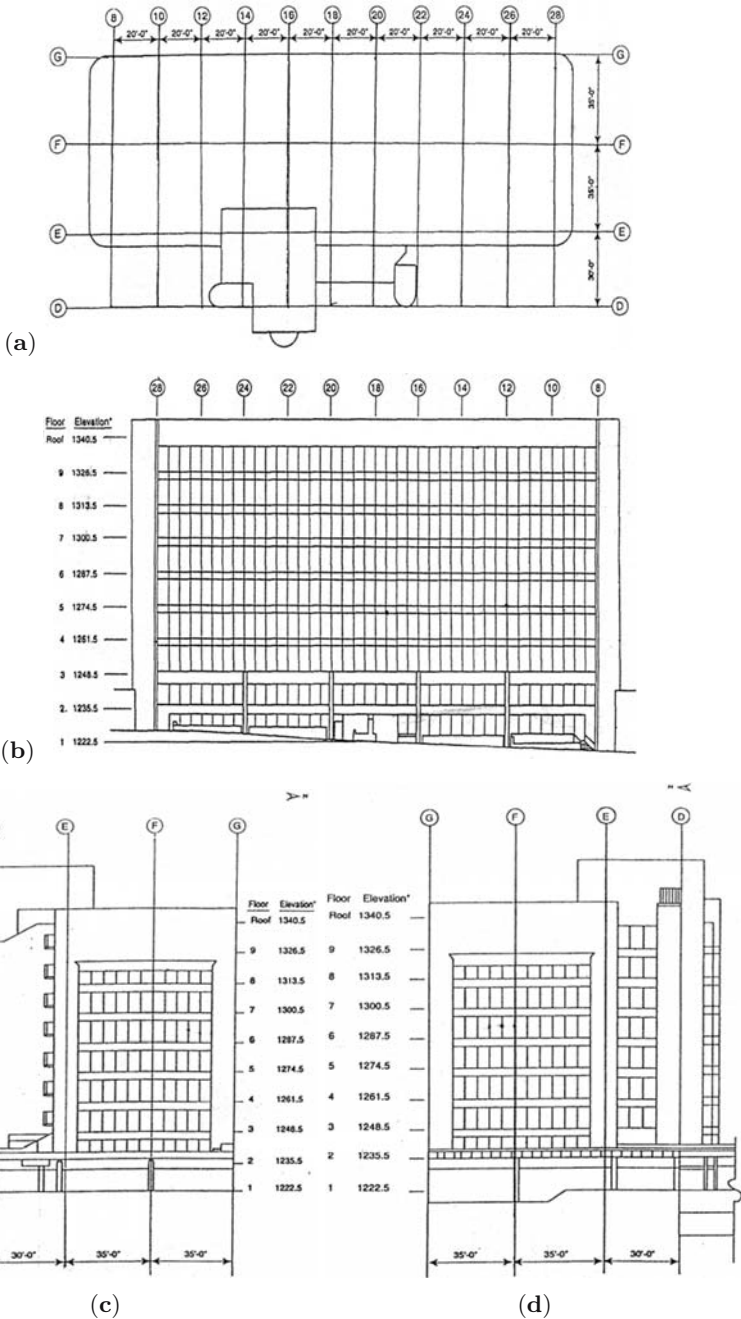
The floor spacing was 3.96 m except for the ninth floor, which was 4.27 m. The roof consisted of a mono filament membrane supported by a one inch thick vent board. Concrete roof pedestals existed for use with window washing mechanisms.

The east and west floors consisted of vertical board formed spandrels in between three 7.63 cm (3 in) concrete infill walls. These infill walls were made of granite stone with steel studs and drywall backing. The infill walls were also covered with the glass cladding.

Exposed precast concrete spandrels with in between glass cladding were to found on the southside face. Board formed core walls and shear walls were exposed on the southside.



**Fig. 10.27.** Architectural view of the Murrah Building (with compliments to ASCE, New York 2003; Kirkpatrick, Consulting Engineers, Oklahoma, U.S.A.)



**Fig. 10.28.** (a) Roof plan: nine-story portion of Murrah Building; (b) North elevation nine-story portion of Murrah Building; (c) East elevation: nine-story portion of Murrah Building; (d) West elevation: nine-story portion of Murrah Building

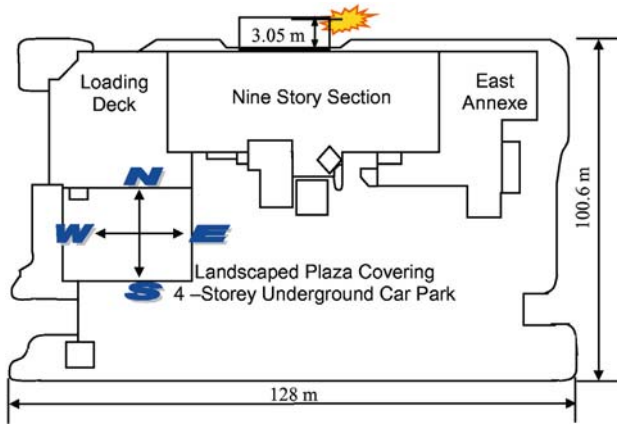


Fig. 10.29. Plan of the Murrah Building

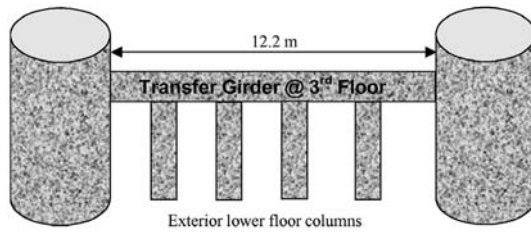


Fig. 10.30. Section through the Murrah Building

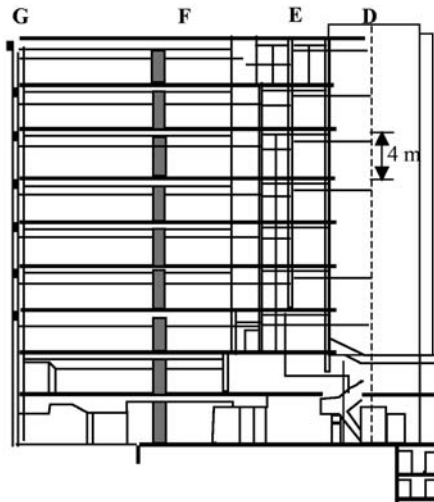
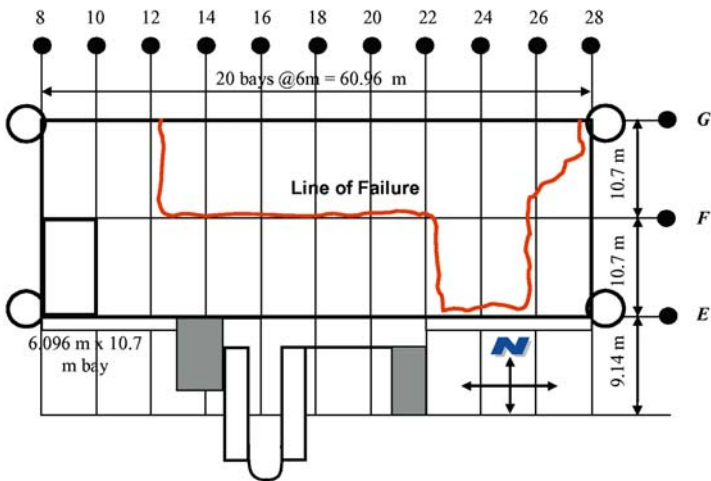


Fig. 10.31. Sectional elevation the Murrah Building (courtesy: Kirkpatrick Consultants, Oklahoma, U.S.A.)

Each floor is divided into ten bays spanning East to West and two bays spanning North to South. At the third floor a transfer girder of cross section 1.52 by 6.91 m supported intermediate columns from the upper floors. Columns spanning the first two floors in turn supported this transfer girder.

#### 10.11.4 Structural Damage to the Alfred P. Murrah Building

The explosion occurred 3.05 m away from the north side of building close to column G20. The failure line is marked on the floor plan as shown in Fig. 10.32.



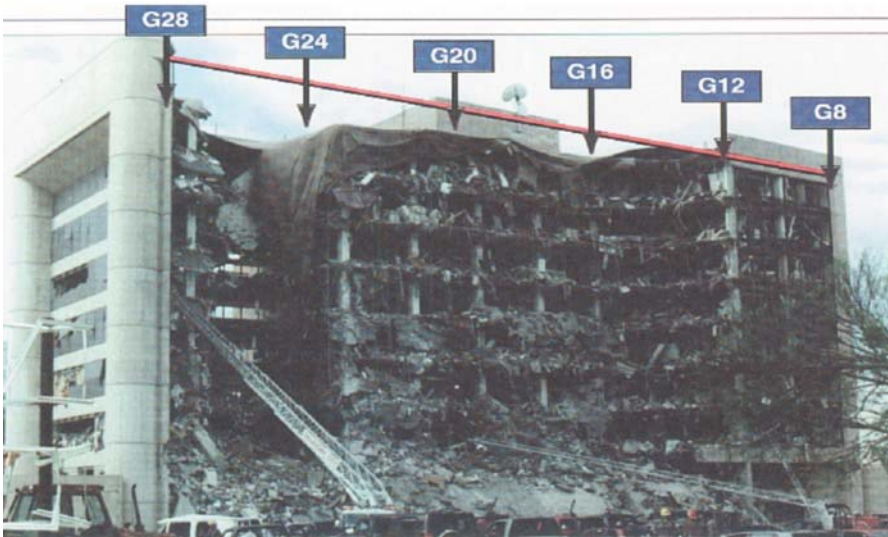
**Fig. 10.32.** Typical floor plan of the Murrah Building (courtesy: Kirkpatrick, Consulting Engineers, Oklahoma, U.S.A.)

The extent of the damage and progressive collapse is illustrated in Figs. 10.33 to 10.35.

Columns G 16, G20 and G24 collapsed resulting in the progressive failure of all the floors above. Eight out of the tell bars in the above floors failed. The failure line extended 10.67 m into the building between grid line G12 and G22. The failure of F24 resulted in the failure of a further two bars on the second and third floors extending 21.3 m between G22 and G26. Between column lines 8 and 12 the transfer girders, mullions, columns and spandrels remained undamaged. The glass cladding was completely destroyed. Figure 10.34 shows the destruction at the G column line.

Figures 10.35 and 10.36 shows the results of the progressive failure. As the upper floor failed the resulting mass falls on to the floor below. This induces failure on that level. The inertia created by the falling mass then induces destruction of the floors below.





**Fig. 10.33.** Damage to the north side of the Murrah Building (courtesy: Kirkpatrick, Consulting Engineers, Oklahoma, U.S.A., 2001)



**Fig. 10.34.** G column line (courtesy: ASCE, New York, U.S.A., 2001)



**Fig. 10.35.** Progressive collapse of the Murrah Building



**Fig. 10.36.** Progressive collapse (courtesy: FEMA, Washinton D.C., U.S.A. – private communication)



**Fig. 10.37.** Remains of the transfer girder

The failure of G16 and G24 was thought to be as a result of the inward rotation of the transfer girder between the second and third floor. Column F24 failed since unlike nearby columns it was not provided with additional lateral bracing from the lift core and stairway. Column F14 failed in shear.

The girder failed at the midspan where an intermediate column had been supported. The bottom reinforcement had been pulled out thus pulling out the connecting shear ties. The floor slab behind the girder had been pulled down by the failing columns. The relative good condition of the transfer beam showed that load transfer did not occur (Fig. 10.37).

Most of the failures were brittle and occurred mostly at the connections. This resulted in the progressive collapse of the higher floors as illustrated in figure. Only where the full force of the explosion was not felt, some ductility was observed. The collapse was deemed to have occurred in three seconds as a result of subsequent forensic investigations.

The south face (Fig. 10.38) did not endure the full force of the blast and in comparison suffered insignificant damage to the doorframes, glass cladding and mullions. Much of the buildings lateral stiffness was concentrated in the form of shear/core walls along column line E (referred to as the core section of the building) on the south face of the building. The investigating team concluded this to be a major reason why this side did not suffer as much damage as the north face.

The core section and to a lesser extent the circular shafts provided the lateral restraint and the team also concluded that no meaningful lateral or



**Fig. 10.38.** South side of the Murrah Building (courtesy: Kirkpatrick, Consulting Engineers, Oklahoma, U.S.A., 2001)

torsional displacement occurred as apart of the global response during collapse.

Of the end walls the east end wall endured most damage. All the granite infill panels failed in flexure and some were dislodged. The west wall endured a similar flexural failure pattern to its infill walls but most remained in place.

The interior ceiling, ductwork and floor panels failed. Columns along lines G and F failed either entirely or partially. Masonry partition walls in the core area also failed in particular on the first three floors.

#### **10.11.5 Structural Plans for the Floors of the Alfred P. Murrah Building**

The ground floor level will be assumed as fixed at the base with columns rising to the first floor. The first floor is idealised by the beam slab arrangement shown in Fig. 10.39. The letters B and S denote the beams and slabs respectively. The columns on the line F' extend from the ground floor upwards to beneath the first floor.

Figures 10.40 and 10.41 show the plans for the second and third floors respectively.

Figure 10.42 shows the roof plan. This beam and slab detailing shown is used for the fourth through to ninth floors.

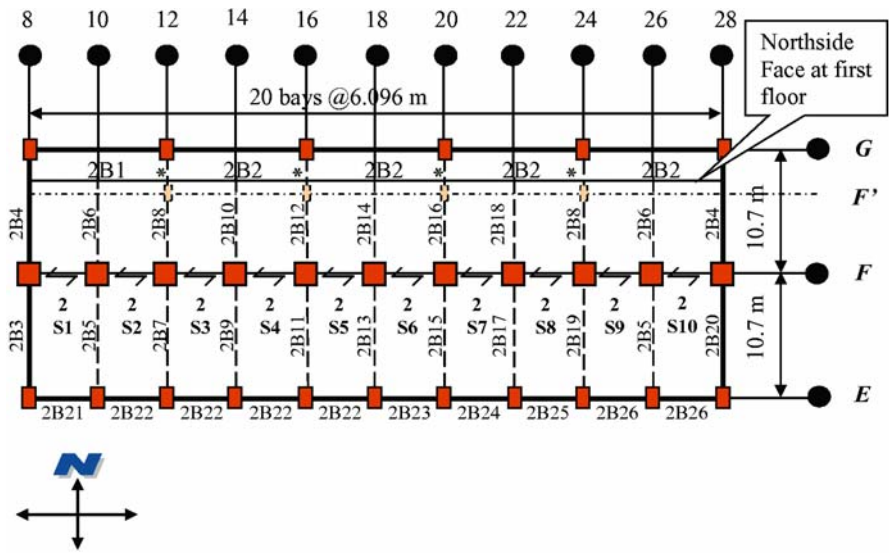


Fig. 10.39. Plan of the first floor (not to scale). Courtesy: Kirkpatrick Consultants, Oklahoma, U.S.A., 2002, T. Bangash, Ph.D. Thesis, London University, 2004

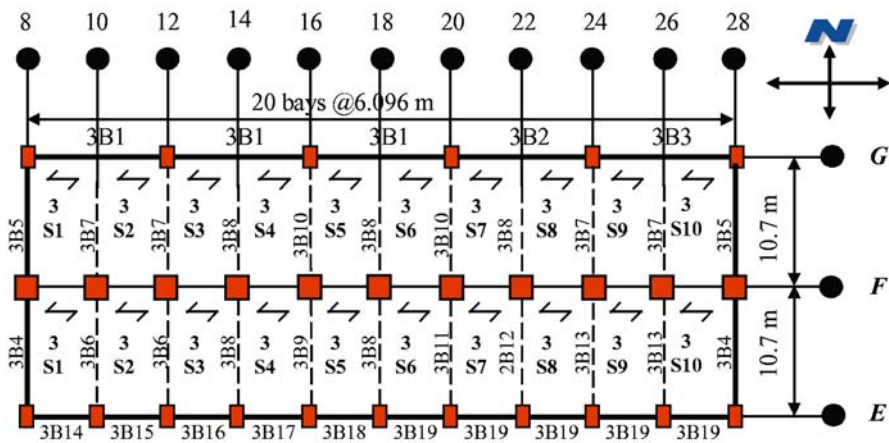


Fig. 10.40. Plan of the second floor (not to scale). Courtesy: Kirkpatrick Consultants, Oklahoma, U.S.A., 2002, T. Bangash, Ph.D. Thesis, London University, 2004

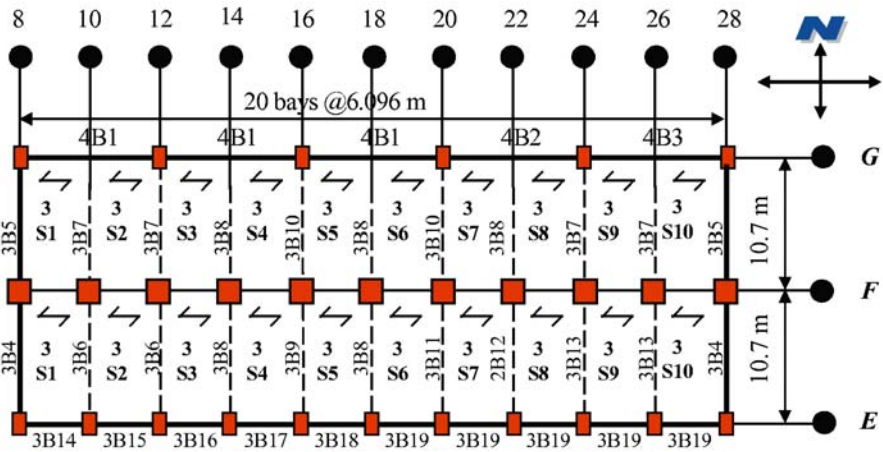


Fig. 10.41. Plan of the third floor (not to scale). Courtesy: Kirkpatrick Consultants, Oklahoma, U.S.A., 2002, T. Bangash, Ph.D. Thesis, London University, 2004

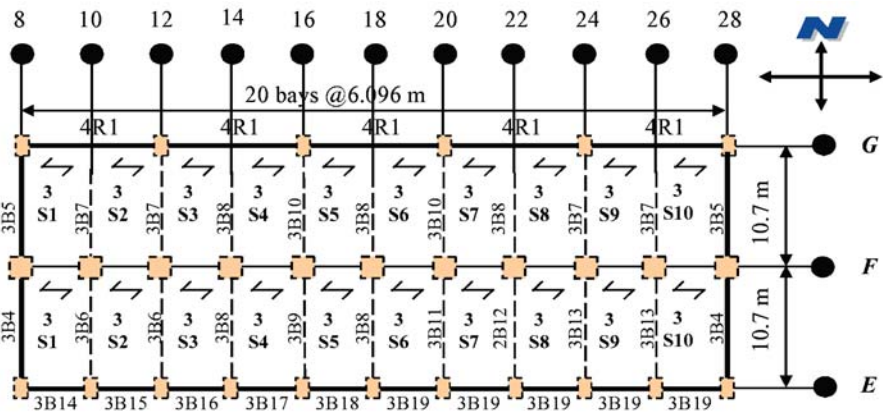


Fig. 10.42. Plan of the roof (not to scale). Courtesy: Kirkpatrick Consultants, Oklahoma, U.S.A., 2002, T. Bangash, Ph.D. Thesis, London University, 2004

### 10.11.6 Material Properties and Reinforcement Detailing

The concrete eight day compressive strength was 27.5 Mpa and the yield strength of the reinforcing bars were 413.7 Mpa. The density of the concrete samples tested at CRL ranged from 2346.8–2396.5 kg/m<sup>3</sup> (146.4 to 149.5 lb/ft<sup>3</sup>). The properties of the reinforcement samples tested are summarised in Table 10.9.

**Table 10.9.** Properties of the reinforcement samples

Parameter/BarSize	#8	#5
Design yield stress	413.7 MPa	413.7 MPa
Measured yield stress	495.061 MPa	449.554 MPa
Yield load	252.2 kN	89.9 kN
Ultimate load	377.64 kN	148.1 kN
Ultimate stress	737.765 kN	737.765 kN
Elongation	9.8%	11.1%
Modulus of elasticity	196507.5 MPa	196507.5 MPa

These parameters were compiled on the basis of the following conversion factors

$$1 \text{ ll/ft}^3 = 16.03 \text{ kg/m}^3$$

$$1 \text{ lb/ft}^2 = 0.006895 \text{ MPa}$$

$$1 \text{ lb} = 4.448 \text{ N}$$

The reinforcement use for the columns and there detailing is described and illustrated below in Fig. 10.43. The column heights are taken as 3.96 m for floor up to floor 9. The ninth floor columns are taken as 4.27 m.

(1) Conversion Table:

$$1'' = 25.4 \text{ mm}$$

$$1 \text{ ft} = 0.3048 \text{ m}$$

(2) Equivalent bars in S.I. units:

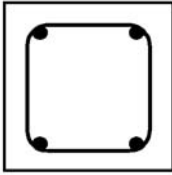
$$\#4 = 12 \text{ mm } \varnothing; \#5 = 16 \text{ mm } \varnothing; \#6 = 20 \text{ mm } \varnothing; \#7 = 22 \text{ mm } \varnothing;$$

$$\#3 = 10 \text{ mm } \varnothing; \#8 = 25 \text{ mm } \varnothing; \#9 = 29 \text{ mm } \varnothing; \#10 = 32 \text{ mm } \varnothing;$$

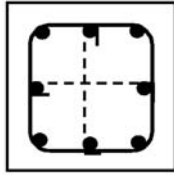
$$\#11 = 35 \text{ mm } \varnothing; \#14 = 43 \text{ mm } \varnothing; \#18 = 57 \text{ mm } \varnothing$$

Figures 10.44a to 10.44d show structural elements of the Murrah Buildings.

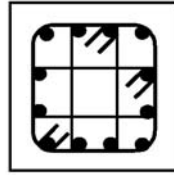
Square Columns



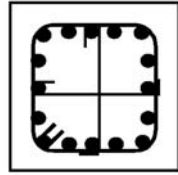
4 Bars



8 Bars

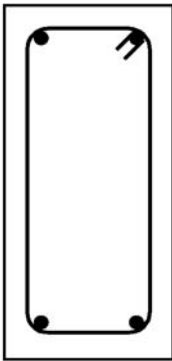


12 Bars

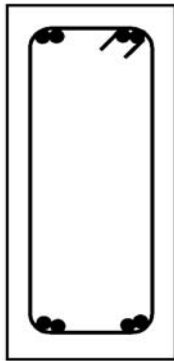


16 Bars

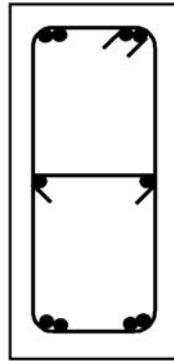
Rectangular Columns



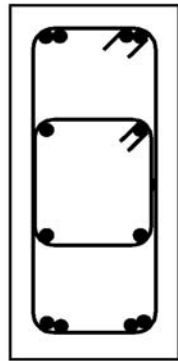
4 Bars



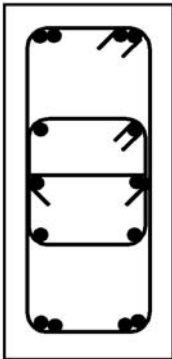
8 Bars



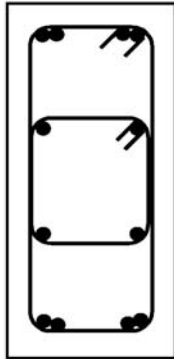
10 Bars



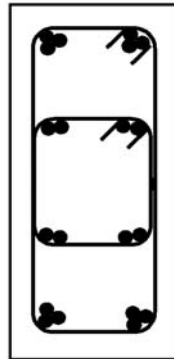
12 Bars



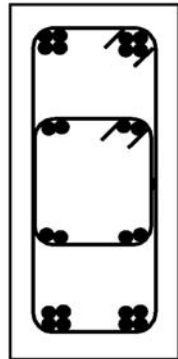
14 Bars



16 Bars



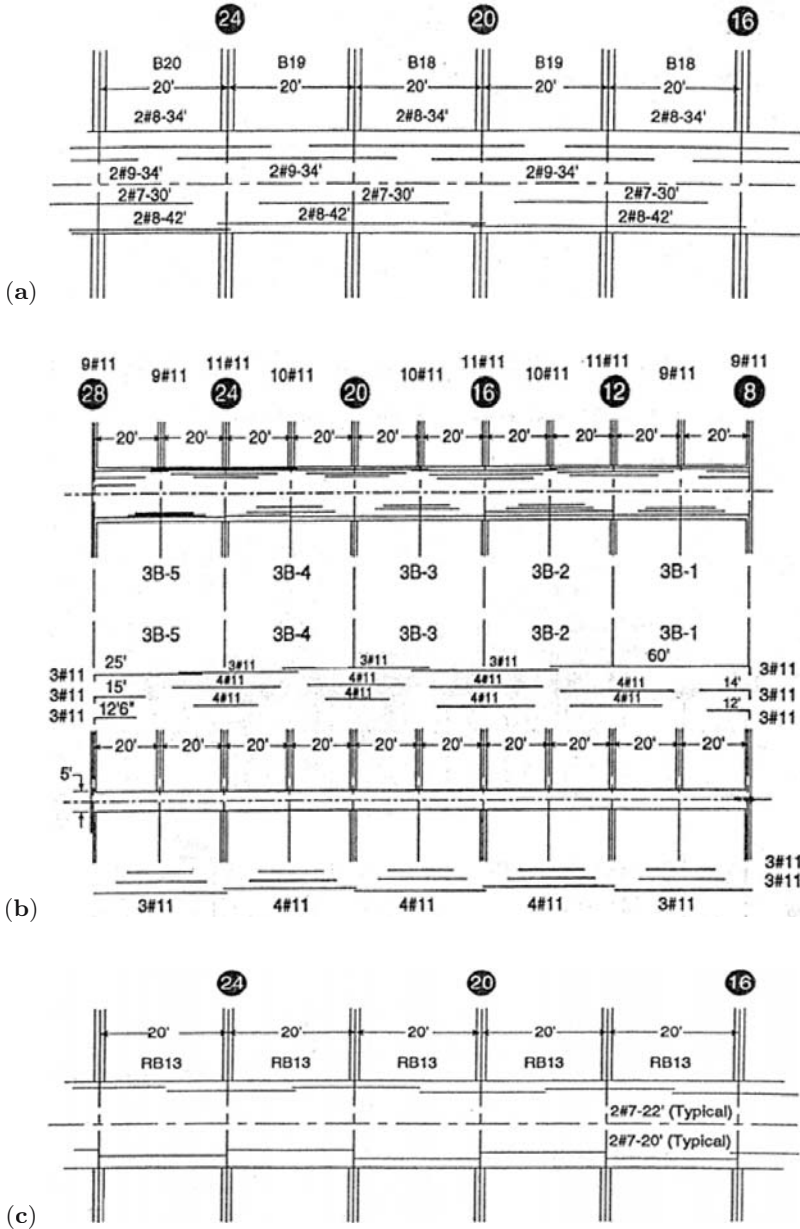
20 Bars



24 Bars

Fig. 10.43. Reinforcement detailing for the columns





**Fig. 10.44.** (a) Schematic of distorted section, showing reinforcing bar arrangement of spandrel girders on fourth through ninth floors at column line G; (b) schematic of reinforcement for transfer girder on third floor at column line G; (c) schematic of distorted section, showing reinforcing bar arrangement for roof girder at column line G

Reinforcement of splander beam along north face

T-beam (1)	Location (2)	Number-size (3)	Length (4)
18	Bottom at centerline	2-#7	30 ft 0 in.
	Bottom at column	2-#8	42 ft 0 in.
	Side face	2-#5	22 ft 0 in.
	Top at line	2-#8	34 ft 0 in.
	Stirrups	#6 at 17in.	
	Stirrups	#4 at 17in.	
19		See T-beam 18	
	Side face	2-#5	22 ft 0 in.
	Top at column line	2-#9	24 ft 0 in.
	Stirrups	#6 at 17in.	
	Stirrups	#4 at 17in.	
20	Bottom at centerline	2-#7×	30 ft 0 in.
	Bottom at centerline	2-#8×	42 ft 0 in.
	Side face	2-#5×	22 ft 0 in.
	Top of column line	2-#8×	34 ft 0 in.
	Stirrups	#6 at 17 in.	
	Stirrups	#4 at 17 in.	

Reinforcement of third-floor transfer girders

Column line (1)	Girder (2)	Location (3)	Number-size (4)	Length (5)
Between 16 and 20	3B-3	Bottom at centerline	3-#11	20 ft 0 in.
			3-#11	27 ft 0 in.
			4-#11	40 ft 0 in.
		Top at column line	4-#11	20 ft 0 in.
			4-#11	30 ft 0 in.
			3-#11	45 ft 0 in.
Between 20 and 24	3B-4	Stirrups	#6 at 6 in.	
		Bottom at centerline	Same as 3B-3	
			Top at column line	4-#11
			4-#11	32 ft 6 in.
			3-#11	45 ft 0 in.
	Stirrups	#6 at 6 in.		

Reinforcement of second floor spandrels

Beam (1)	Location (2)	Number-size (3)	Length (4)
2B-33	Bottom at span centerline	2-#7	26 ft 0 in.
		2-#8	41 ft 0 in.
	Top at column line	3-#9	22 ft 6 in.
	Top at span centerline	2-#6	22 ft 6 in.
	Stirrups	#5 at 22 in.	
2B-34	Same as 2B-33		

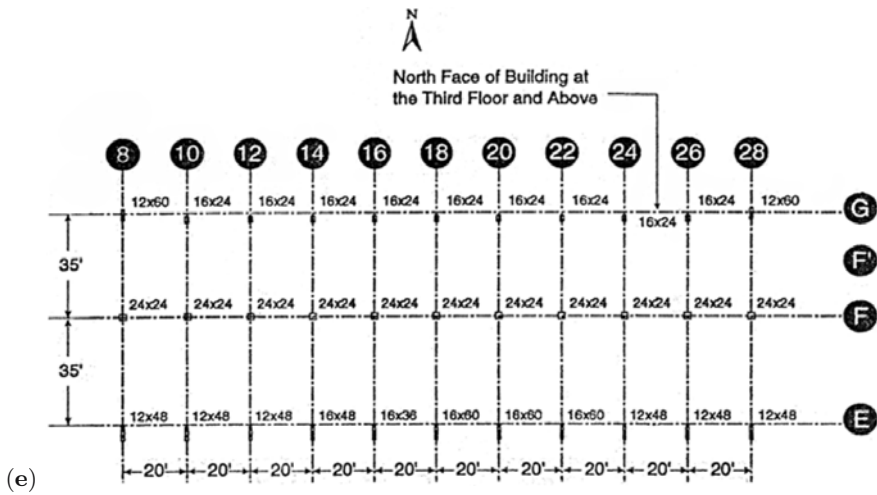
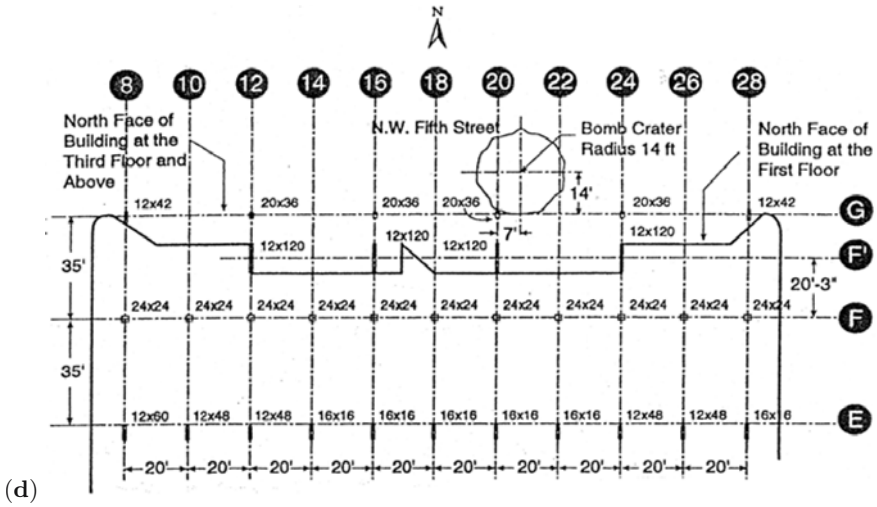


Fig. 10.44. (d) Column locations and dimensions: first floor; (e) column location and dimensions: second floor

Reinforcement of roof beams

Beam (1)	Location (2)	Number-size (3)	Length (4)
RB-4	Bottom short	2-#8	20 ft 0 in.
	Bottom at column (long)	3-#8	34 ft 0 in.
	Top at column line G	4-#8	10 ft 6 in.

Reinforcement of East-West spandrel in roof

Beam (1)	Location (2)	Number-size (3)	Length (4)
RB-13	Bottom at centerline side face	2-#7	20 ft 0 in.
	Top at column line	2-#7	22 ft 0 in.
	Stirrups	4-#5 at 24 in. each end	

Reinforcement of interior column 22

Floor (1)	Vertical bars (number-size) (2)	Ties (number and spacing) (3)
3-4	16-#11	#4 at 16 in. on center
4-5	12-#11	#4 at 16 in. on center
5-6	8-#10	#3 at 16 in. on center
6-7	4-#10	#3 at 16 in. on center
7-8	4-#9	#3 at 16 in. on center
8-9	4-#9	#3 at 16 in. on center
9-Roof	4-#8	#3 at 16 in. on center

Reinforcement of third-floor beams

Column line (1)	T-beam (2)	Location (3)	Number-size (4)	Length (5)
10, 12, 24 and 26	6	Bottom (short)	2-#7	22 ft 6 in.
		Bottom at column (long)	4-#8	33 ft 6 in.
		Top at column line G	4-#10	12 ft 0 in.
		Top at column line F	4-#11	12 ft 6 in.
		Stirrups	#4 at 9 in.	
16, 18, and 20	12	Bottom (short)	2-#7	22 ft 0 in.
		Bottom at column (long)	4-#8	33 ft 6 in.
		Top at column line G	3-#11	11 ft 0 in.
		Top at column line F	3-#10	22 ft 6 in.
		Stirrups	#4 at 9 in.	
14 and 22	10	Bottom (short)	2-#7	22 ft 0 in.
		Bottom at column (long)	4-#8	33 ft 6 in.
		Top at column line G	2-#10	11 ft 0 in.
		Top at column line F	4-#11	23 ft 0 in.

### 10.11.7 Numerical Simulation of Blast Loading

The Alfred P. Murrah Building is modelled as a rectangular structure of ten floors. As Fig. 10.38 shows the south side of the structure remained relatively intact after the blast loading. This part of the structure consisted of the core structure of the building including the lift shafts and stairwells. These acted as shear walls providing the principal lateral bracing against the explosion loading. The circular concrete air ducts at the four corners of the structure added to the structures overall stiffness. In order to accurately model the structures response behaviour to blast loading, the corner column nodes were fixed. In addition the nodes on the ground floor and the nodes representing the south face were also fixed.

The original structure had a seven foot square hole at each floor level. This was omitted from the model as its influence upon the overall structural behaviour is limited.

The material properties used in the modelling are described in Table 10.10. The size of element used and the reinforcement is described in Table 10.11.

**Table 10.10.** Input values for material properties

Property	Magnitude of property
Max concrete strain	0.0035
Concrete elastic modulus	25.0e+09 N/m <sup>2</sup>
Strength of concrete	540.2e+06 N/m <sup>2</sup>
Density of concrete	2.4e+03 kN/m <sup>2</sup>
Steel elastic modulus	210.0e+09 N/m <sup>2</sup>
Steel yield stress	560.0e+06 N/m <sup>2</sup>

**Table 10.11.** Element geometry and reinforcement used in the model

Structural element	$b$ (mm)	$h$ (mm)	$d_c$ (mm)	$A_0$ (mm <sup>2</sup> )	$A_1$ (mm <sup>2</sup> )	$A_2$ (mm <sup>2</sup> )	$A_3$ (mm <sup>2</sup> )
East/West outer wall	6.1e-01	8.9e-01	5e-02	9.82e-04	9.82e-04	1.29e-03	1.29e-03
North/South outer wall	5.7e-01	1.27e00	9.0e-02	2.01e-03	2.01e-03	1.206e-03	1.206e-03
Transfer girder	9.1e-01	1.52e00	1.0e-01	4.0125e-03	4.0125e-03	6.036e-03	6.036e-03
G column	5.1e-01	9.1e-01	5e-02	3.027e-03	3.027e-03	3.027e-03	3.027e-03
F' column	3.1e-01	3.2e00	2.2e-01	3.83e-03	3.83e-03	3.83e-03	3.83e-03
F column	6.1e-01	6.1e-01	4e-02	2.52e-03	2.52e-03	2.52e-03	2.52e-03
E column	4.1e-01	9.1e-01	5e-02	2.77e-03	2.77e-03	2.77e-03	2.77e-03

The blast pressure is applied along the local axis of the cross section of the element,  $a_1$  and  $a_2$ . These loads are over a specified time period using three factors, which modify the load according to the point in time. For example if the applied load is  $500 \text{ N/m}^2$  at a time  $t_1$ , then  $f_1$  would equal one. The values of  $f_2$  and  $f_3$  would be a fraction of one according to how the load decreased over time period  $t_1$  to  $t_2$ .

Two blast load scenarios were modelled and are described below in Figs. 10.45 and 10.46.

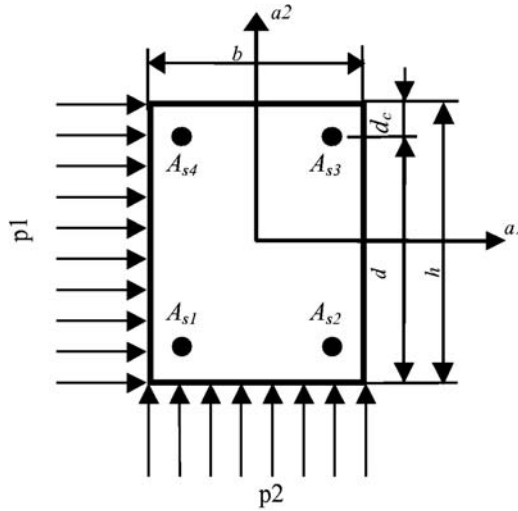


Fig. 10.45. Blast pressure loading

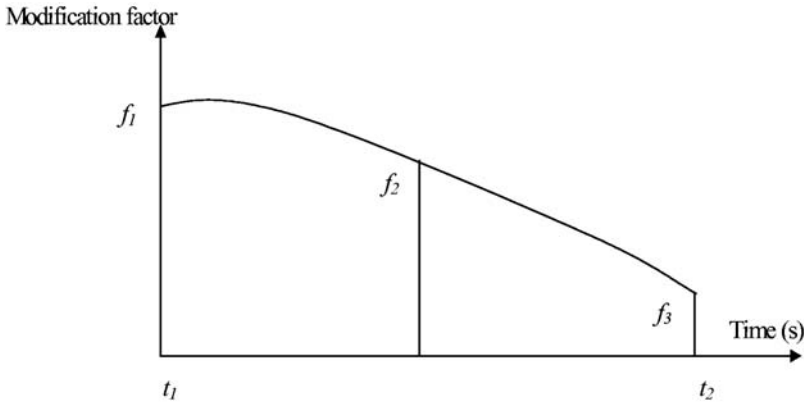


Fig. 10.46. Load modification factors

### LOAD CASE 1

In this case the load is applied across all of the floors at all levels and along the G line columns. The various blast pressure profiles are shown in Figs. 10.47 to 10.48. The duration of this simulation is 12 ms. Stages of the failure simulation are shown in Figs. 10.49 to 10.57.

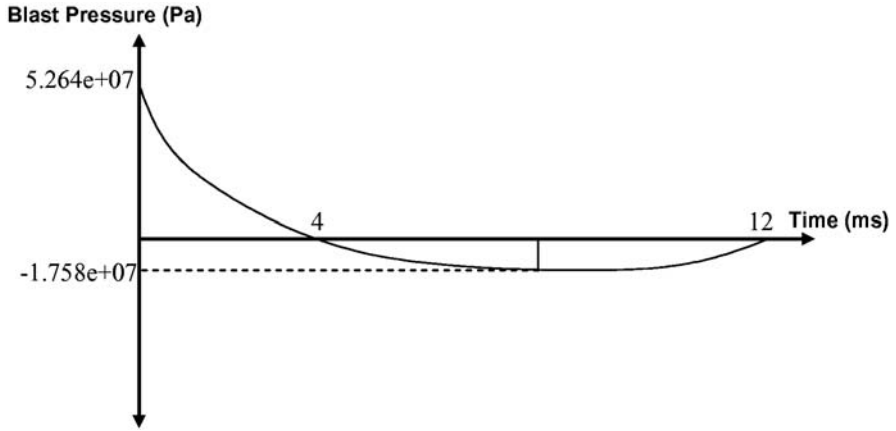


Fig. 10.47. Blast pressure loading for slabs

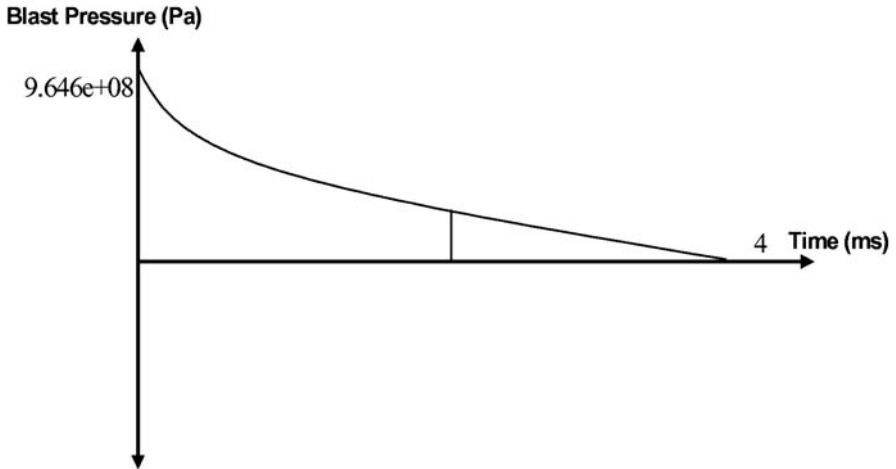
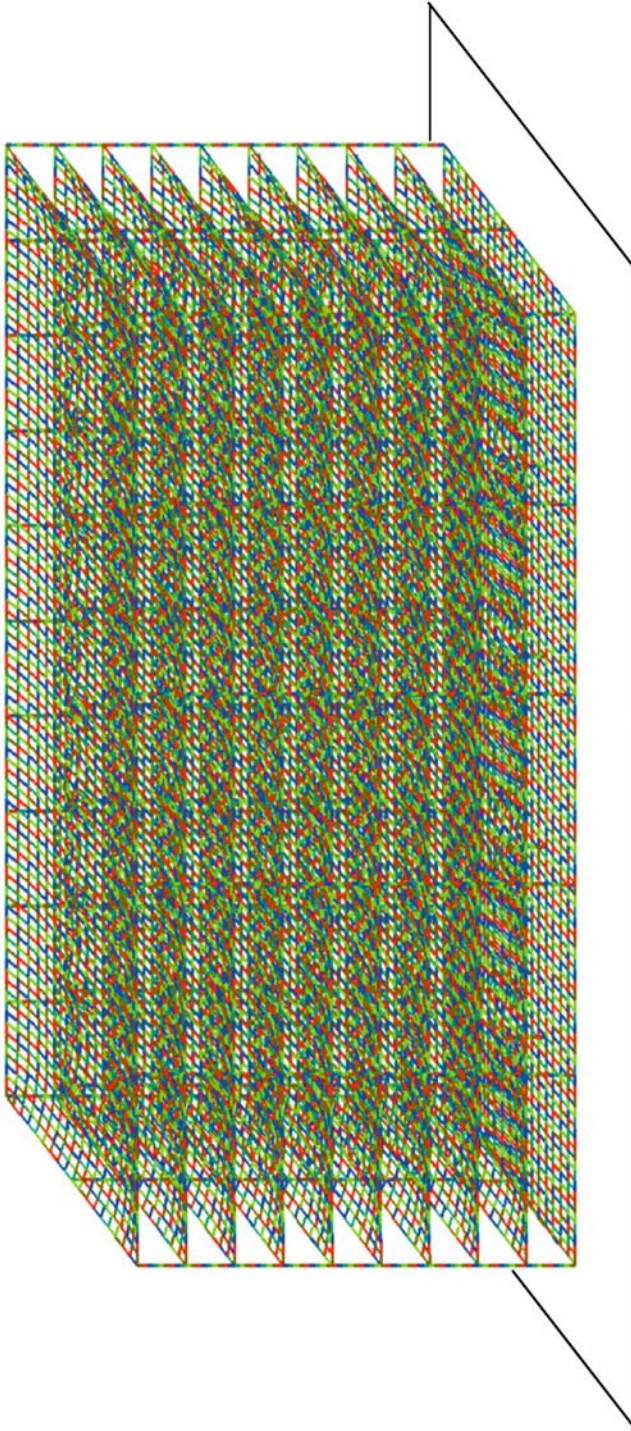


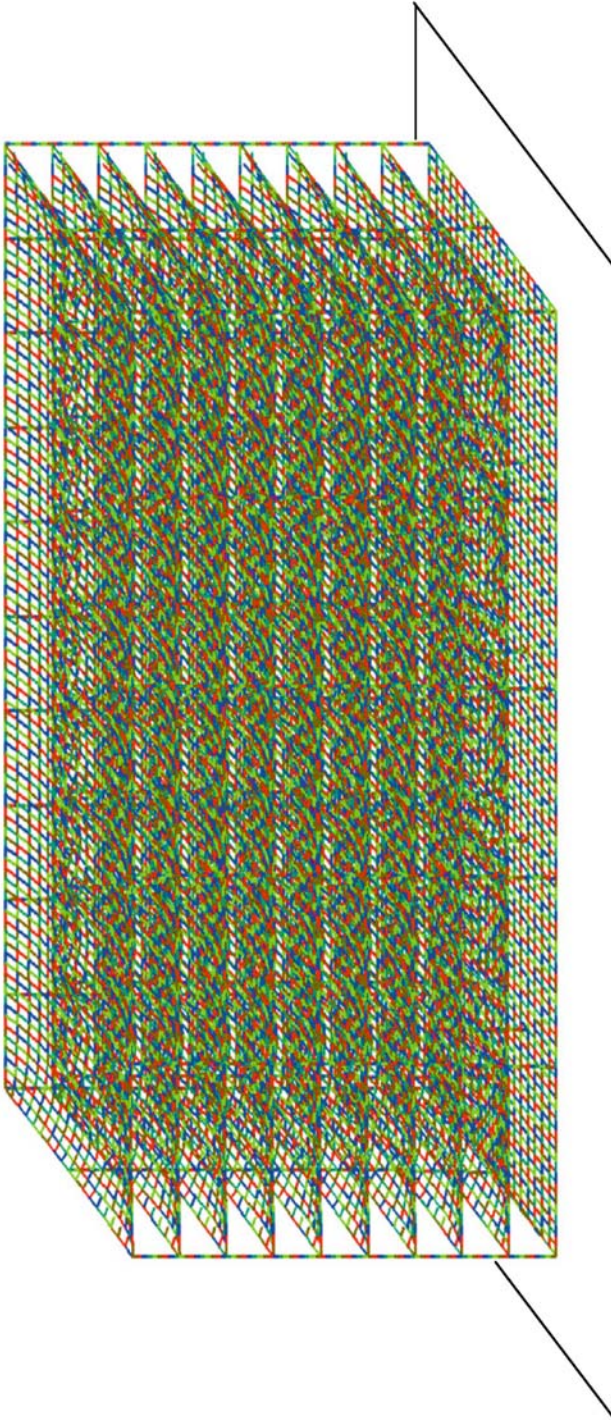
Fig. 10.48. Blast pressure load for columns



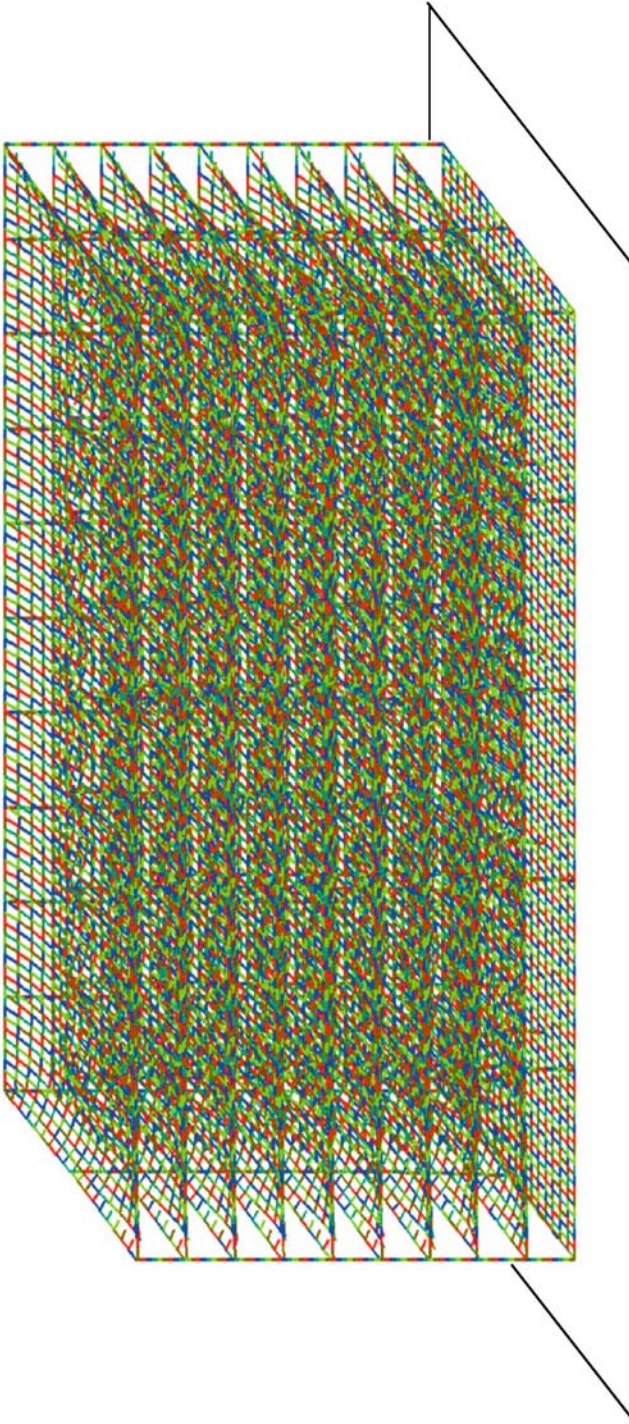




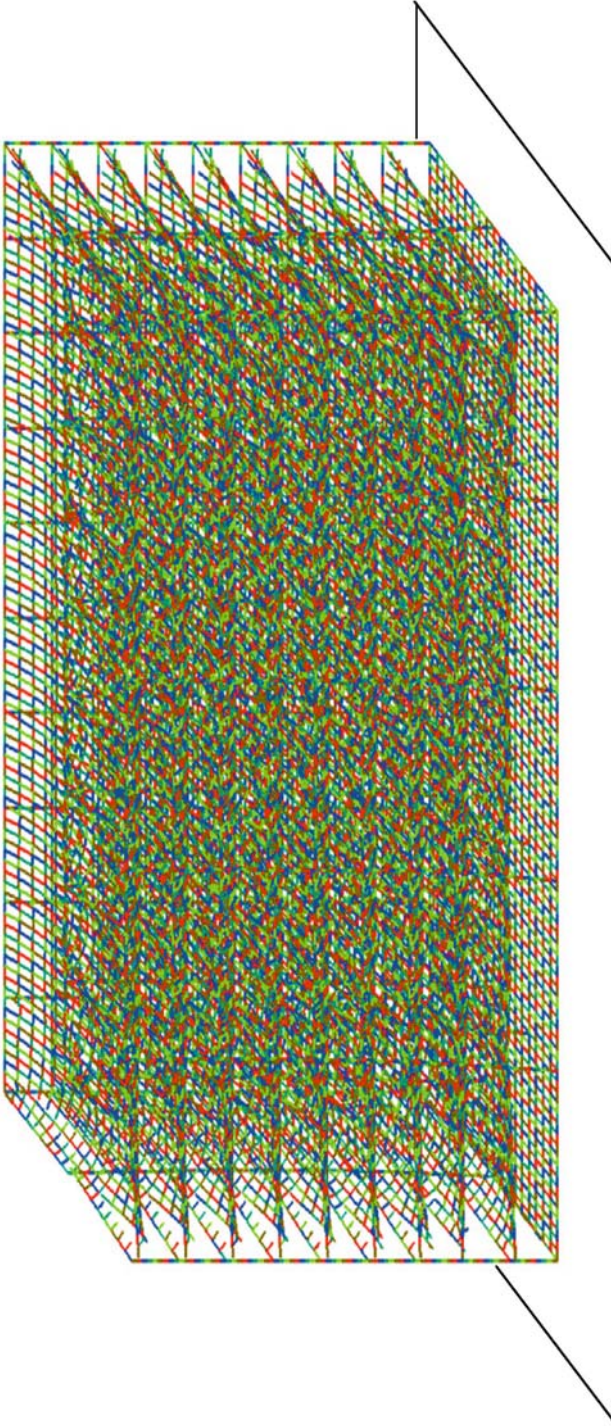
**Fig. 10.50.** Murrah building collapse sequence  $t = 0.3$  s. At this time the structure has begun to deform at the floor levels



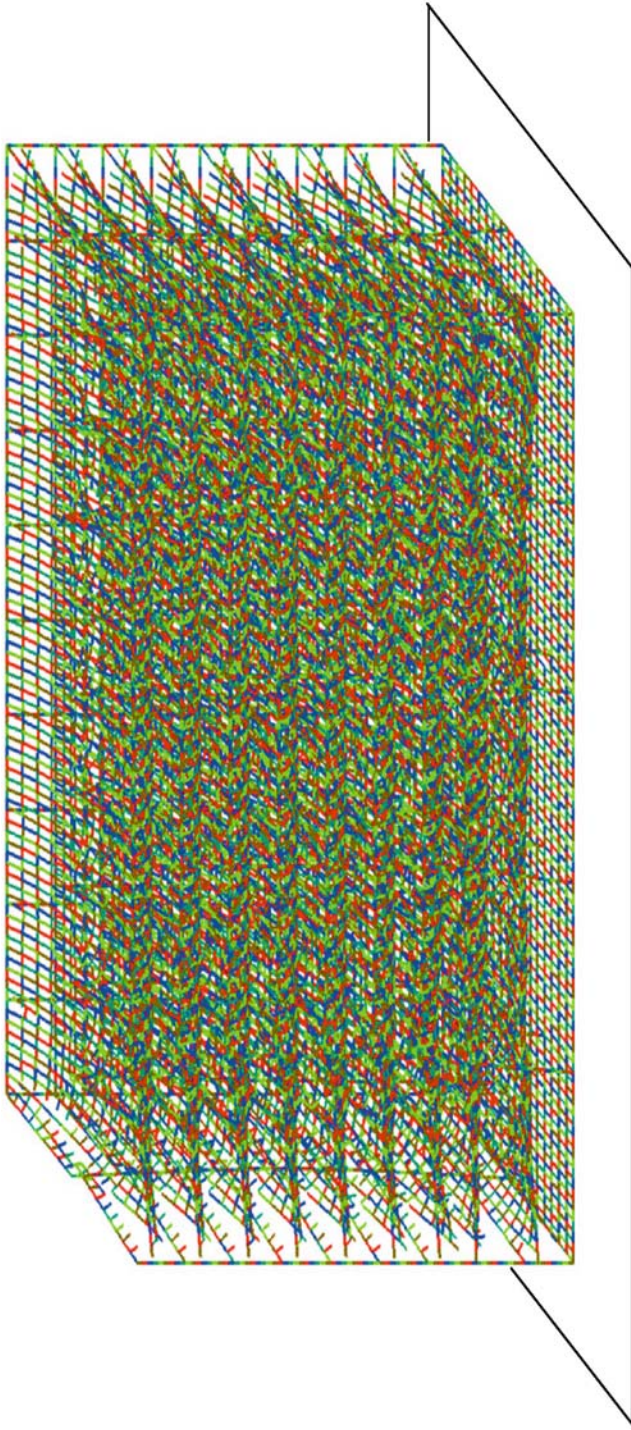
**Fig. 10.51.** Murrah building collapse sequence  $t = 0.45$  s. The structure is seen to further deform at the floor levels with same elements detaching at the fight rear (south face) circular vent shaft



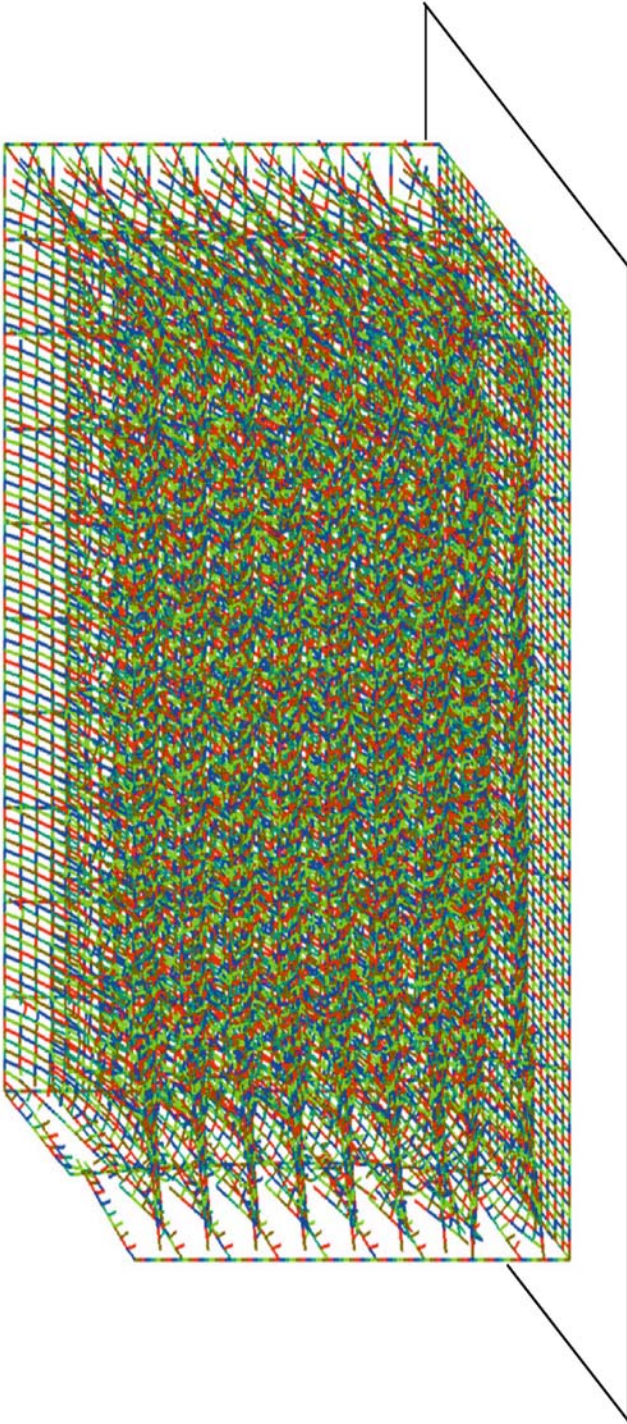
**Fig. 10.52.** Murrah building collapse sequence  $t = 0.55$  s. Further element detachment is seen on the south facing left side circular vent shaft



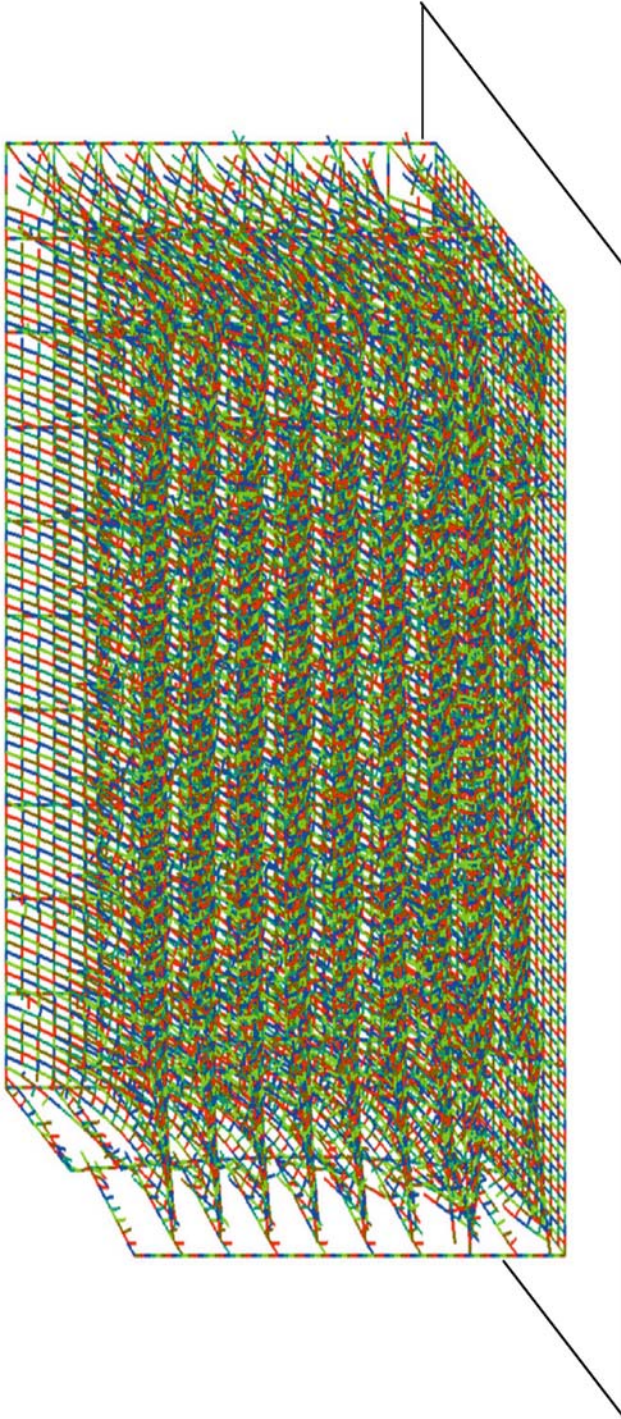
**Fig. 10.53.** Murrah building collapse sequence  $t = 0.65$  s. At this time the breakage at all floor levels is severe



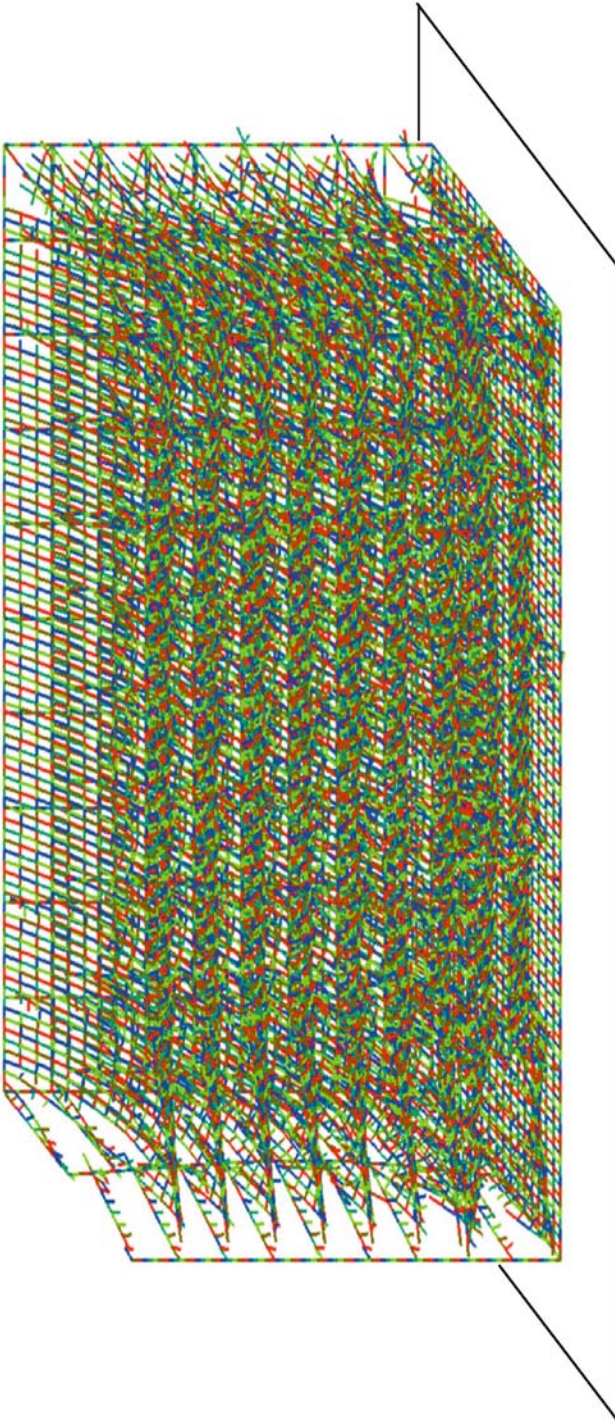
**Fig. 10.54.** Murrah building collapse sequence  $t = 0.8$ s. Further breakage occurs with the floors and columns showing major deflection. The east side face is now showing breakage at the roof level



**Fig. 10.55.** Murrah building collapse sequence  $t = 0.95$  s. More pronounced failure is beginning to occur



**Fig. 10.56.** Murrah building collapse sequence  $t = 1.1$  s. All the floors and columns are collapsing



**Fig. 10.57.** Murrah building collapse sequence  $t = 1.35$  s. Progressive failure has been shown to be induced



**LOAD CASE 2**

The load is applied across the floor area marked by the squared area shown in Fig. 10.58. The columns were not loaded. The blast load time function is shown in Fig. 10.59. The duration of this simulation is 12 milliseconds. Stages of the failure simulation are shown in Figs. 10.60 to 10.69.

The variation of velocity with time of node X positioned on the second floor is shown in the Fig. 10.70. The velocity is initially small during the elastic stage. At approximately 1.4 seconds the nodal velocity changes indicating it has impacted with another node. The velocity at this stage has increased approximately two fold. Hence the kinetic energy will have increased four fold. Thus in order to avoid structural collapse through progressive failure this energy needs to be dissipated in some way.

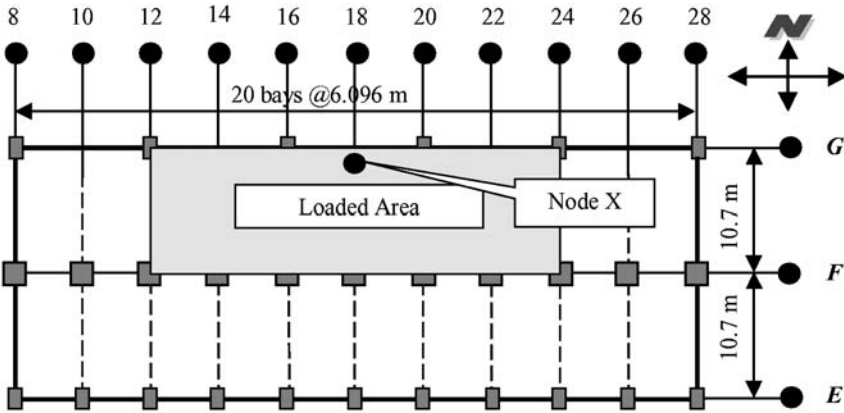


Fig. 10.58. Loaded area

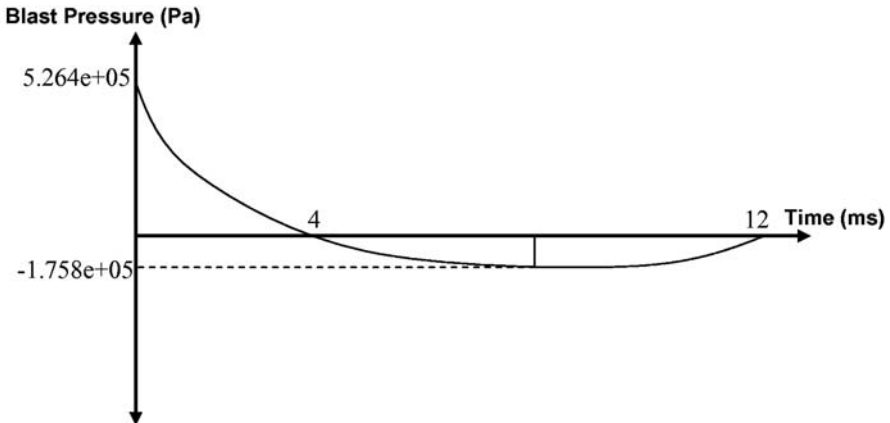
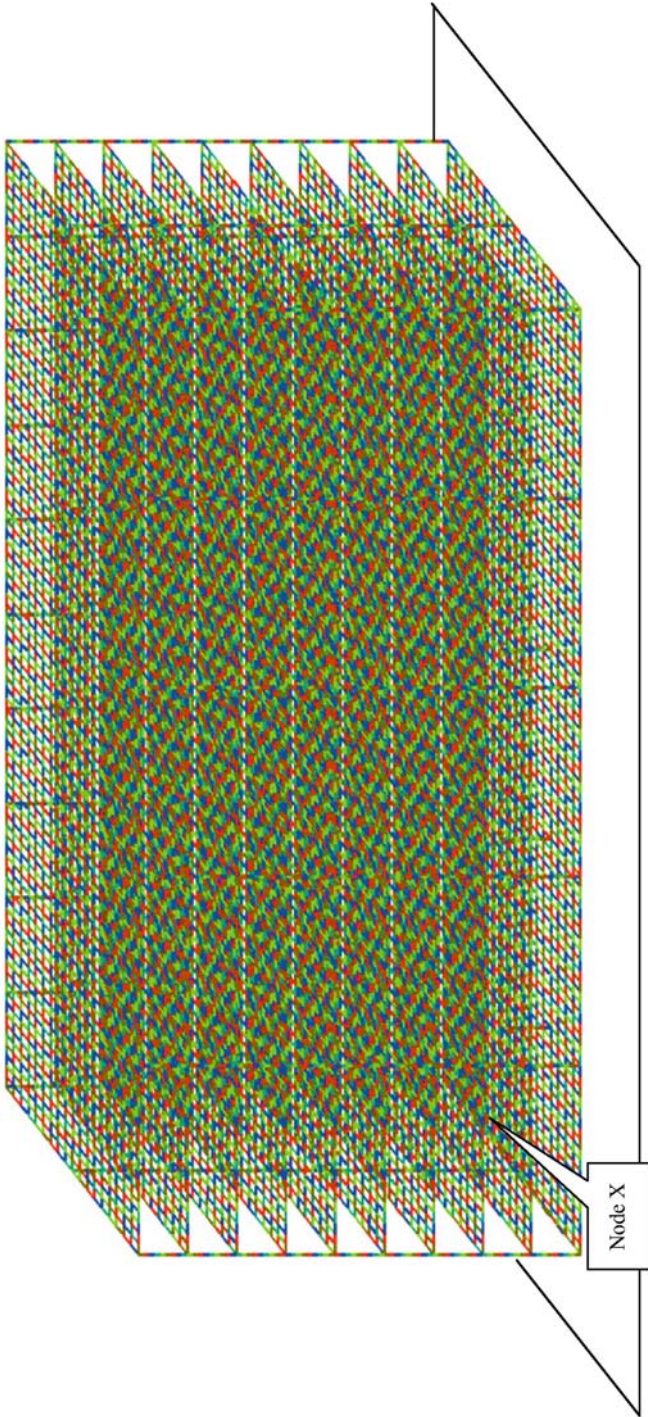
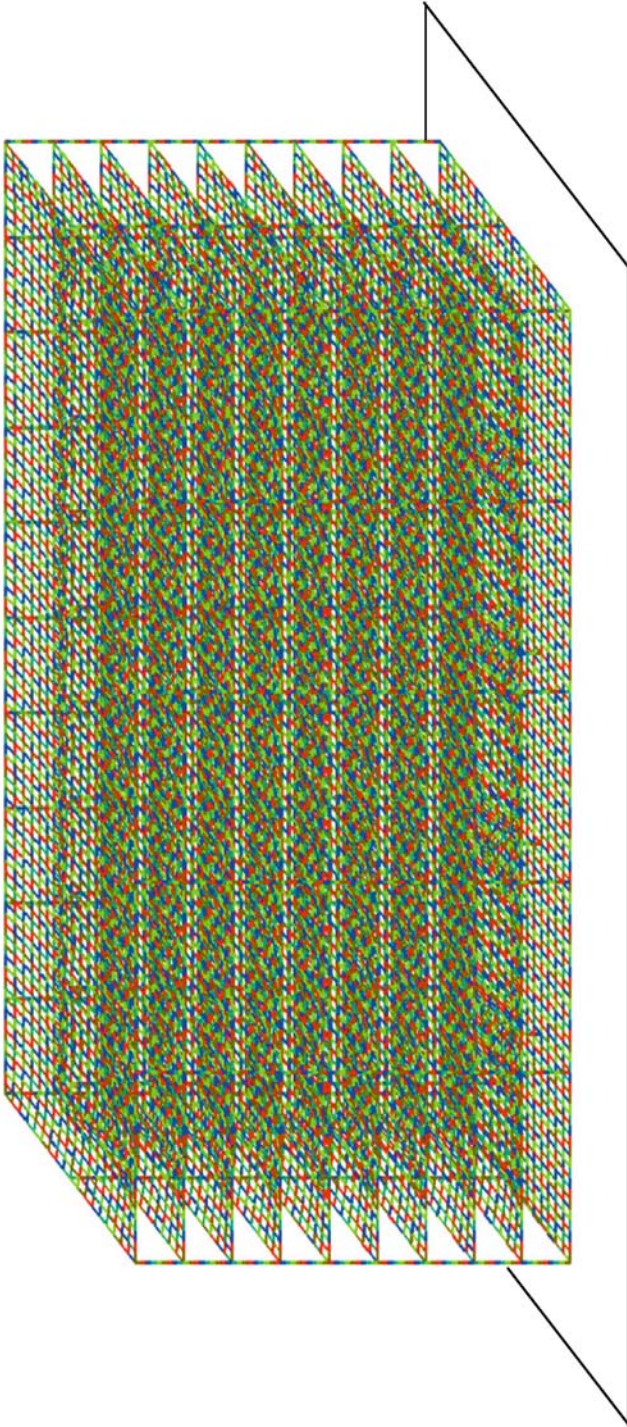


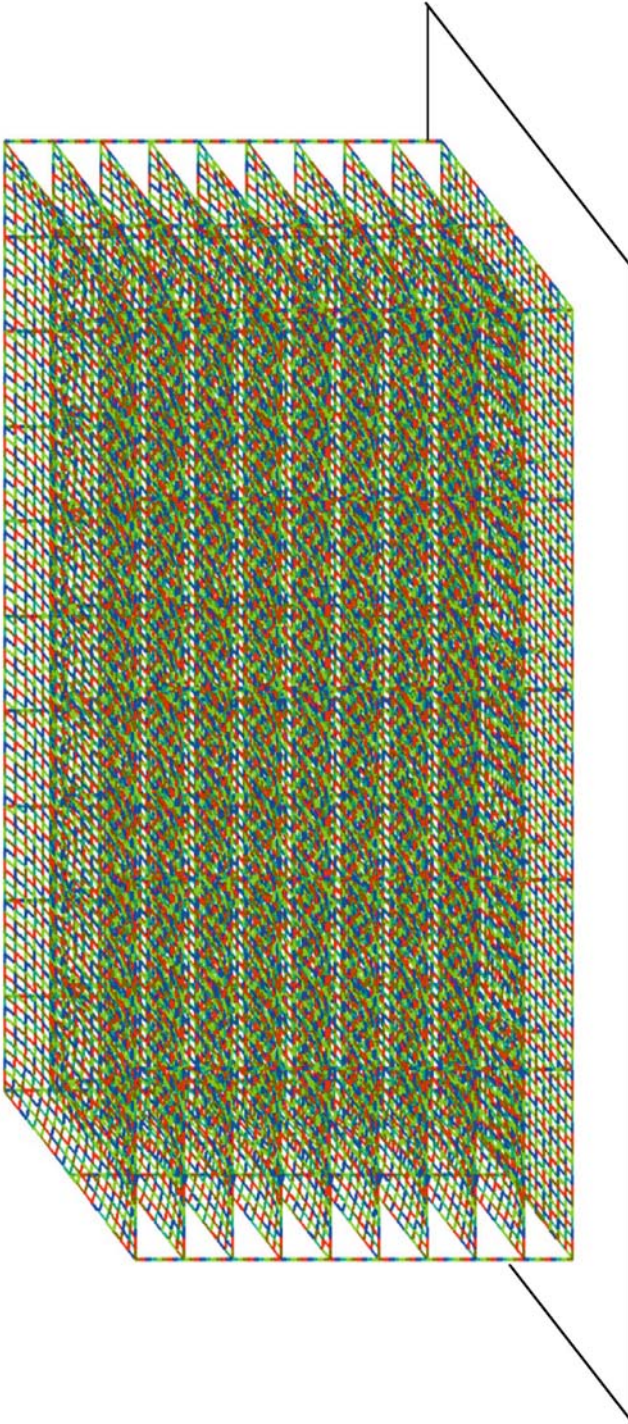
Fig. 10.59. Blast pressure profile for elements in the loaded area



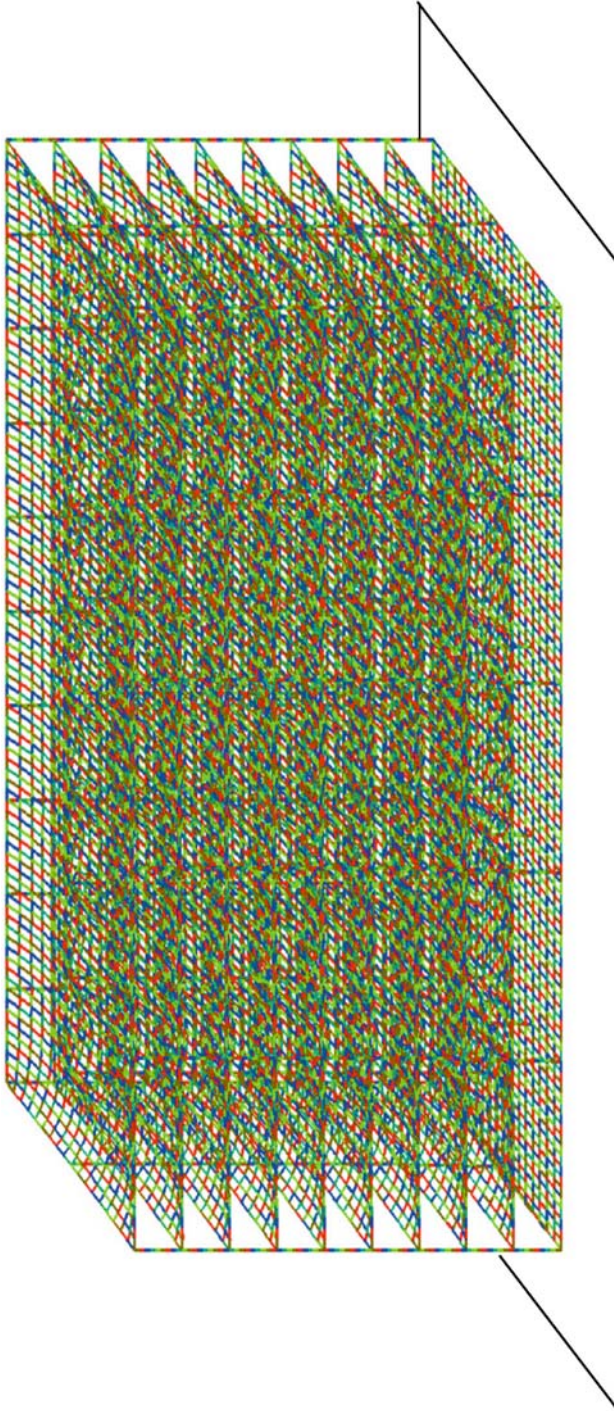
**Fig. 10.60.** Murrah building collapse sequence  $t = 0.0$ s. The structure before blast load application



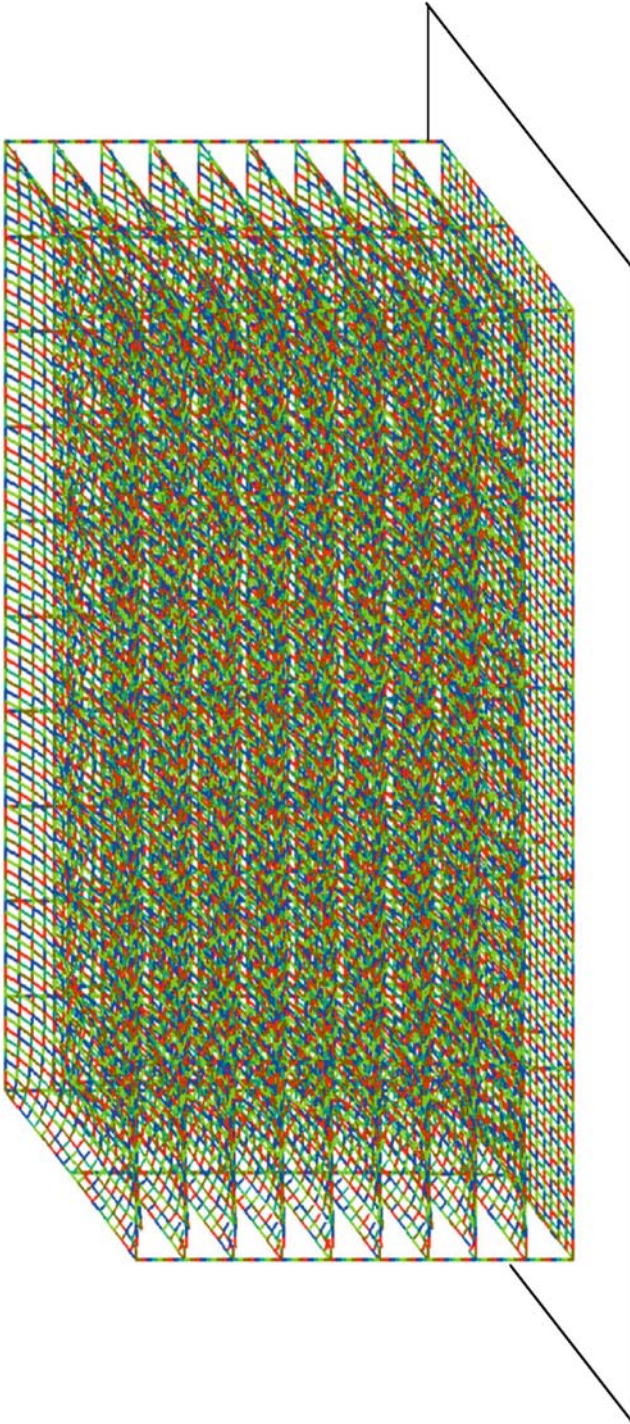
**Fig. 10.61.** Murrah building collapse sequence  $t = 0.225$  s. The lower floors are begin to deflect



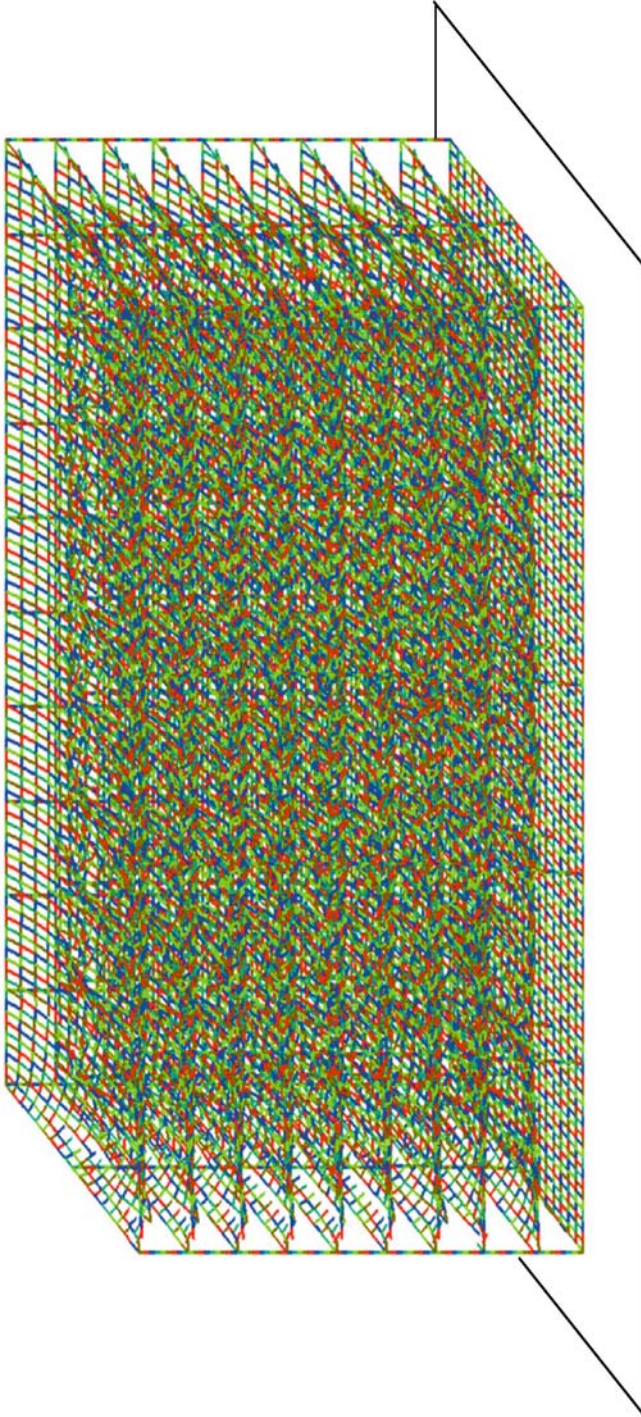
**Fig. 10.62.** Murrah building collapse sequence  $t = 0.3$  s. Deflection starts to occur at all floor levels



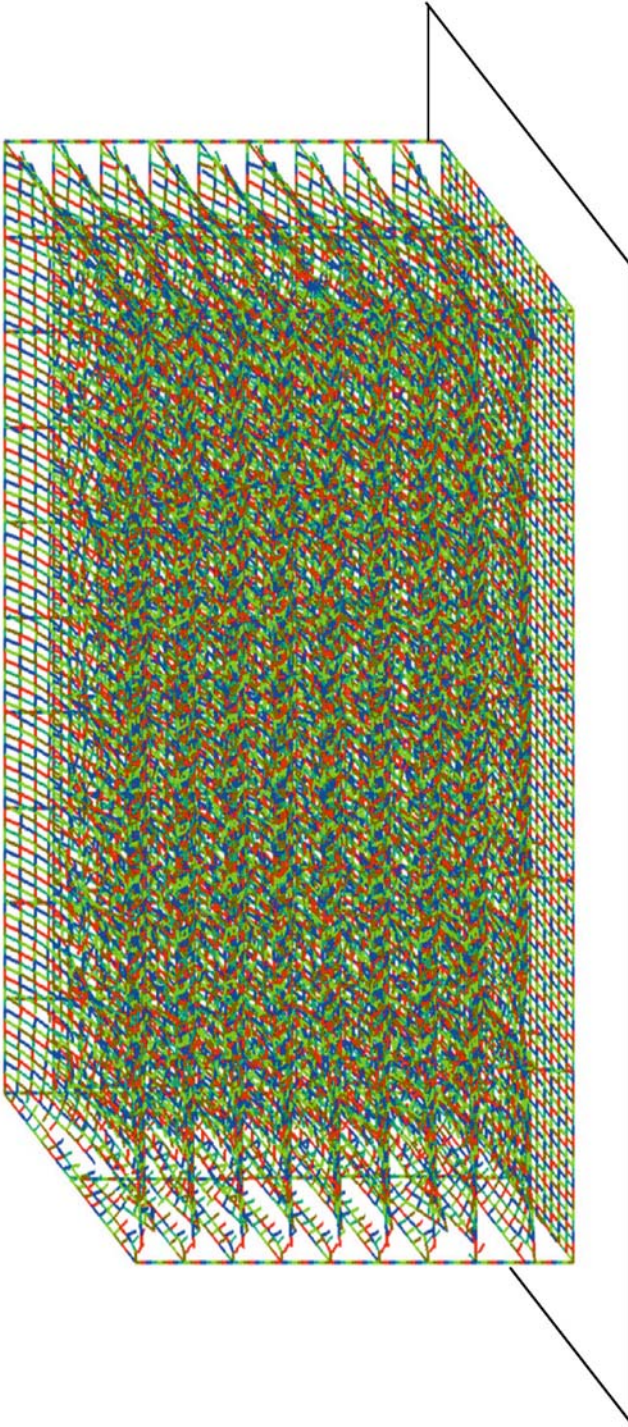
**Fig. 10.63.** Murrah building collapse sequence  $t = 0.45$  s. The deflected form is has become more pronounced



**Fig. 10.64.** Murrah building collapse sequence  $t = 0.525$  s. Failure at the front left hand corner (north side) between the column vent and the floor levels begins to occur

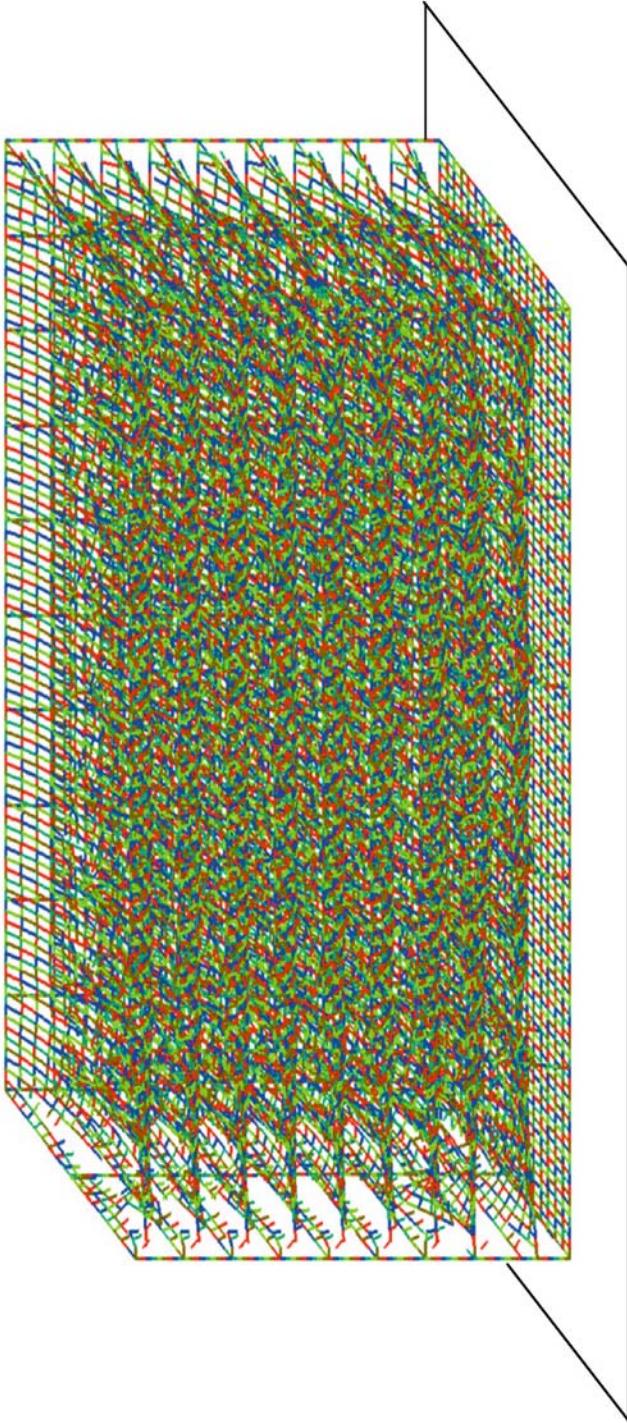


**Fig. 10.65.** Murrah building collapse sequence  $t = 0.6$  s. Failure increases towards the top of the building

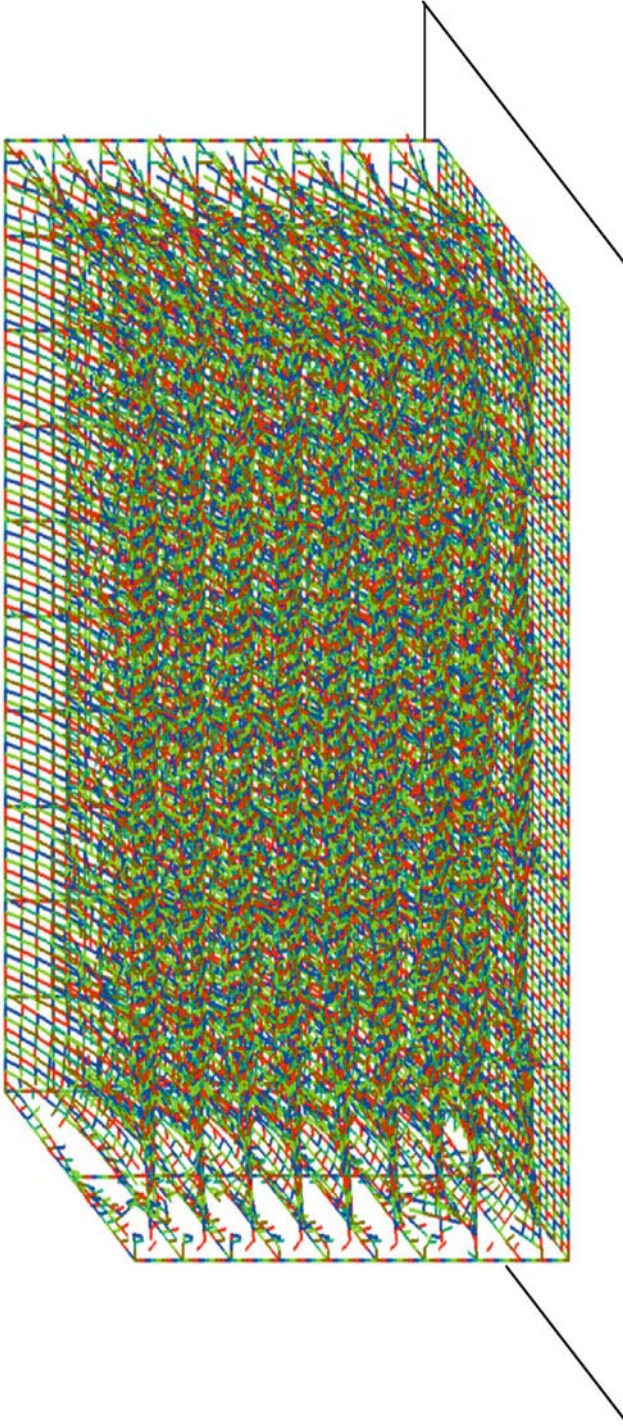


**Fig. 10.66.** Murrah building collapse sequence  $t = 0.675$  s. Further breakage is seen to occur inducing the start of progressive collapse

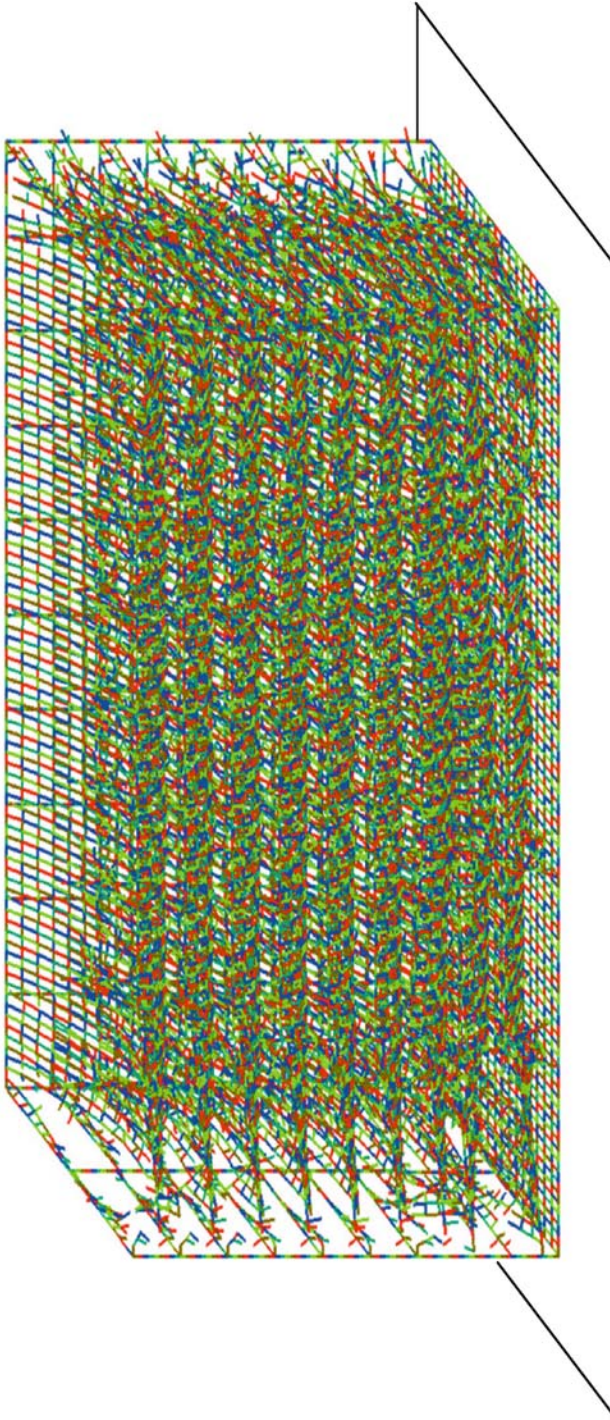




**Fig. 10.67.** Murrah building collapse sequence  $t = 0.75$  s. All floors are seen collapsing



**Fig. 10.68.** Murrah building collapse sequence  $t = 0.825$  s. The columns on the front left north side has completely disconnected



**Fig. 10.69.** Murrah building collapse sequence  $t = 0.9375$  s. Progressive collapse has occurred

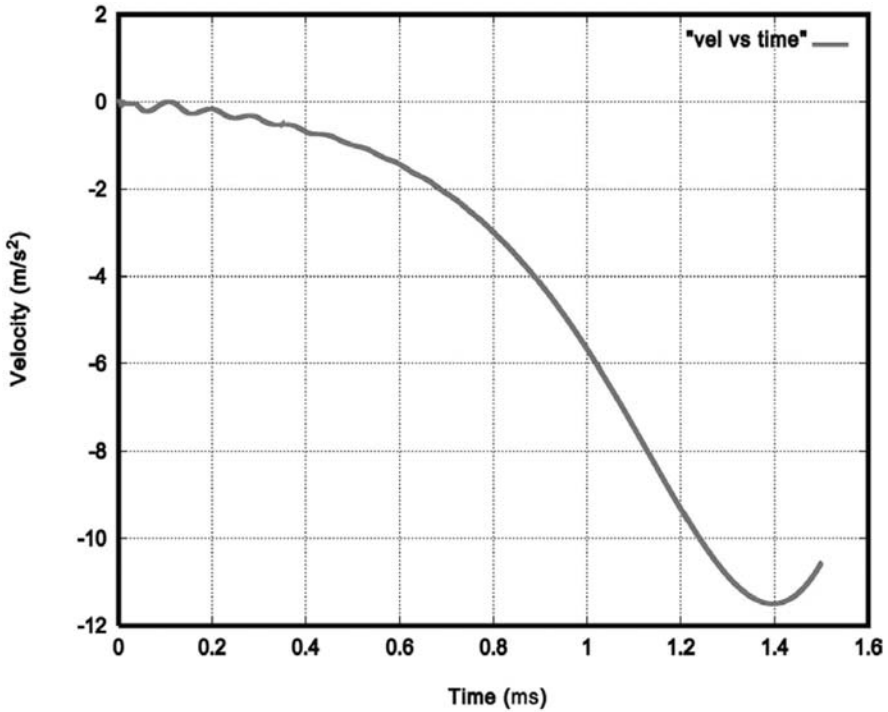


Fig. 10.70. Velocity versus time for node X

### 10.11.8 Conclusions

An element, which has been successfully tested for both dynamic and static situation has been applied to the numerical simulation of a full scale structure subjected to blast loading. By adopting a simplified approach the potential of the FEM/DEM modelling procedure is demonstrated, thus showing that this technology presents enormous opportunities, unforeseen benefits and potential breakthrough's for engineering modelling.

The results obtained present a good representation of the failure of the structure. These results were realised by incorporating membrane effects, strain stiffening, realistic stress strain curves for concrete and dynamically localised finite strains especially in the reinforcement. The results could be improved with greater knowledge of the magnitude and sequence of the loading, which is unknown. Alternatively further accuracy could be achieved by incorporating the coupling effects of the fluid structure interaction into the numerical simulation of the blast loading. Slab elements incorporating membrane effects could also be developed to provide greater flexibility in the modelling procedure.

This simulation indicates that a radical rethinking may be needed in the context of structural design. This is particularly true for tall buildings. Build-

ings cannot be made more resistant to progressive collapse simply by increasing the reinforcement or even employing stronger materials. The only approach is to come up with different structural concepts, perhaps incorporating new lightweight materials. Progressive collapse thus presents a new challenge in terms of structural concepts, structural systems and structural materials.

There are at present only two solutions to designing a structure to resist progressive collapse. The first is to avoid building such tall structures. The second is to offer complete shielding from any hazardous loading and in so doing protect from progressive collapse. Both of these solutions are not practical.

Thus new and different concepts in building design, structural materials, structural concepts etc are necessary to build robust structures which are more resistant to progressive collapse.

## References

- [10.1] Corley WG et al. (1996) The Oklahoma City bombing, improving building performance through multi-hazard mitigation. FEMA Bull 277, ASCE Press
- [10.2] Corley WG et al. (2001) Effects of structural integrity on damage from the Oklahoma City, USA bombing. Forensic Engineering, Thomas Telford, London
- [10.3] Corley WG et al. (1997) Using forensic engineering techniques to obtain data from the Oklahoma City bombing. In: Proc. 1st Forensic Engineering Congress, Reston, VA, ASCE Press
- [10.4] Corley WG et al. (1995): Blast loading and response of the Murrah Building. J. Performance of Constructed Facilities, ASCE Press, 12(3):100–112
- [10.5] Hinmann E (1997) Lessons from the Oklahoma City bombing-defensive design techniques. ASCE Press
- [10.6] Hinman EE (1995) Explosion and collapse: Disaster in milliseconds. Fire Engineering (Oct.)
- [10.7] Construction News (1995) Oklahoma blast forces unsettling design questions (May 1)
- [10.8] Times international index. Volumes from 1961–1997. Westminster Research Library, London
- [10.9] Holzer TL et al. (1995): Interpretation of seismographs of April 19 1995 Oklahoma City bombing. US Geological Survey, Menlo Pk, CA
- [10.10] Norville HS et al. (1995) Glass related injuries in the Oklahoma City bombing. J. Perf. Constr. Fac. 13(3):100–112, ASCE Press
- [10.11] ENR News (1995) Weighing future safety of Federal Buildings. McGraw-Hill Companies (May 8)
- [10.12] Ettouney M et al. (1996) Blast resistant design of commercial buildings. Practice Periodical on Structural Design and Construction 1(1) (Feb.) ASCE
- [10.13] Longinow A et al. (1996) Protecting vehicles against vehicle bomb attacks. Practice Periodical on Structural Design and Construction 1(1) (Feb.) ASCE
- [10.14] O'Connell J (1995) Supporting a fractured building. Fire Engineering (Nov.)
- [10.15] Brown MG (1995) The work of a task force: Dismantling a dying building. Fire Engineering (Nov.)
- [10.16] Carrl T (1995) USAR task force logistics. Fire Engineering (Nov.)
- [10.17] Massa R (1995) Vulnerability of buildings to bombs: Additional thoughts after Oklahoma City. Fire Engineering (Nov.)
- [10.18] Hammond DJ (1995) Engineering the collapse: Making the structure safe. Fire Engineering (Nov.)
- [10.19] Kirkpatrick Engineering Company (KEC) (2001) Engineering drawings of the Oklahoma Building, received by the Author
- [10.20] Bangash, T (2004) The combined finite/discrete element method in transient dynamics of reinforced concrete structures under blast loading. PhD Thesis, University of London
- [10.21] Pusgley A, Griffiths H, Saunders O (1968) Report of the inquiry into the collapse of flats at roman point. Canning Town, HMSO

- [10.22] Munjiza A (2002) Computational challenge of large scale discontinua. Keynote address, 3rd Int. Conf. on Discrete Element Methods, Sante Fe, American Society of Civil Engineers
- [10.23] Onate E, Zarate F (2000) Rotation-free triangular plate and shell elements. *Int. J. Numer. Meth. Eng.* 47:557–603
- [10.24] Flores FG, Oñate E (2001) A basic thin shell triangle with only translational DOFs for large strain plasticity. *Int. J. for Num. Methods in Engng.* 51(1):57–93
- [10.25] Corley G (2002) Disecting the collapses. *Civil Engineering Magazine V72 ASCE* 5:36–45
- [10.26] Munjiza A, Owen DRJ, Bicanic N (1995) A combined finite-discrete element method in transient dynamics of fracturing solids. *Int. J. Eng. Comput.* 12:145–174
- [10.27] Munjiza A, Andrews KRF (1998) NBS contact detection algorithm for bodies of similar size. *Int. J. Numer. Meth. Eng.* 43:131–149
- [10.28] Munjiza A, Owen DRJ, Crook AJL (1995) Energy and momentum preserving contact algorithm for general 2D and 3D contact problems. In: *Proc 4th International Conference Computational Plasticity – Fundamentals and Applications*. Barcelona, pp. 829–841
- [10.29] Munjiza A, Andrews KRF, White JR (1997) Discretized contact solution for combined finite-discrete method. 5th ACME Conference. London, UK, pp. 96–100
- [10.30] Munjiza A, Andrews KRF (2000) Penalty function method for in combined finite-discrete element systems comprising large number of separate bodies. *Int. J. Numer. Meth. Eng.* 49:1377–1396
- [10.31] Ammann W, Bachmann H, Muhlematter M (1982) *Versuche an Stahlbeton und Spannbetonbalken unter stoßartiger Beanspruchung. Teil 2 – Konzeption und Durchführung der Balkenversuche, Zusammenfassung der Versuchsergebnisse*. Birkhäuser Verlag, Institut für Baustatik und Konstruktion, Zürich
- [10.32] Ammann W, Bachmann H, Muhlematter M (1982) *Versuche an Stahlbeton und Spannbetonbalken unter stoßartiger Beanspruchung. Teil 3 – PI, P2 und BI bis B8*. Birkhäuser Verlag, Institut für Baustatik und Konstruktion, Zürich
- [10.33] Ammann W, Bachmann H, Muhlematter M (1982) *Versuche an Stahlbeton und Spannbetonbalken unter stoßartiger Beanspruchung. Teil 4 – B9 bis B21*. Birkhäuser Verlag Institut für Baustatik und Konstruktion, Zürich
- [10.34] Ammann W, Bachmann H, Muhlematter M (1982) *Versuche an Stahlbeton und Spannbetonbalken unter stoßartiger Beanspruchung. Teil 5 – Verhalten von zweifeldrigen Stahlbetonbalken bei Ausfall einer Unterstützung*. Birkhäuser Verlag, Institut für Baustatik und Konstruktion, Zürich
- [10.35] Ammann W, Bachmann H, Muhlematter M (1981) Experiments and numerical investigation of reinforced and pre-stressed concrete beams for shock loading. *Transaction of the 6th International Conference on Structural Mechanics in Reactor Technology*, Paris
- [10.36] SIA-162 Norm Ausgabe M (1989) *Betonbauten*. Schweizerischer Ingenieur und Architekten, Zürich
- [10.37] SIA-162/1 Norm Ausgabe M (1989) *Betonbauten Materialprüfung*. Schweizerischer Ingenieur und Architekten, Zürich

- [10.38] Ammann W, Bachmann H, Muhlematter M (1982) Stress-strain behaviour of non-prestressed and pre-stressed reinforcing steel at high strain rates. Proc BAM Concrete Structures under Impact and Impulsive Loading, Berlin
- [10.39] Bangash MYH (1989) Concrete and concrete structures – Numerical modelling and applications. Elsevier Science
- [10.40] McGrattan KB, Baum HR, Rehm RG, Hamins A, Forney GP (2000) Fire dynamics simulator – Technical reference manual. National Institute of Standards and Technology Report No. NISTIR 6467
- [10.41] McGrattan KB, Forney GP (2000) Fire dynamics simulator – User’s manual. National Institute of Standards and Technology Report No. NISTIR 6469
- [10.42] Forney GP, McGrattan KB (2000) User’s guide for smokeview version 1.0 – A tool for visualizing fire dynamics simulation data. National Institute of Standards and Technology Report No. NISTIR 6513
- [10.43] McGrattan KB, Baum HR, Rehm RG, Hamins A, Forney GP, Floyd JE, and Hostikka S (2001) Fire dynamics simulator (version 2) – Technical reference guide. National Institute of Standards and Technology Report No. NISTIR 6783
- [10.44] McGrattan KB, Forney GP, Floyd JE, Hostikka S (2001) Fire dynamics simulator (version 2) – User’s guide. National Institute of Standards and Technology Report No. NISTIR 6784
- [10.45] Forney GP, McGrattan KB (2001) User’s guide for smokeview version 2.0 – A tool for visualizing fire dynamics simulation data. National Institute of Standards and Technology Report No. NISTIR 6761
- [10.46] Federal Emergency Management Agency, Federal Insurance and Mitigation Administration, Washington, DC (2002) World Trade Center building performance study: Data collection, preliminary observations, and recommendations. FEMA Report 403
- [10.47] Arup Corporation (2001) Briefing 2 by the extreme events mitigation task force. Arup Report (Arup web site: [www.arup.com](http://www.arup.com))
- [10.48] Hart F, Henn W, Sontag H (1978) Multi-storey buildings in steel. English edn (ed. by G. Bernard Godfrey) Halsted Press, John Wiley & So., New York, pp. 162–164
- [10.49] Wyllie M (2001) private communication. National Weather Service, National Oceanographic and Atmospheric Administration (NOAA), Department of Commerce
- [10.50] Baum HR, Ezekoye OA, McGrattan KB, Rehm RG (1994) Mathematical modeling and computer simulation of fire phenomena. Theoretical and Computational Fluid Dynamics 6:125–139
- [10.51] Baum HR, McGrattan KB, Rehm RG (1994) Simulation of smoke plumes from large pool fires. J. Proc. Combo. Inst. 25:1463–1469
- [10.52] McGrattan KB, Baum HR, Walton WD, Trelles J (1997) Smoke plume trajectory from in situ burning of crude oil in Alaska – Field experiments and modeling of complex terrain. NIST Internal Report NISTIR 5958
- [10.53] Culver CG (1976) Survey of results for fire loads and live loads in office buildings. Final Report, NBS BSS 085, National Bureau of Standards
- [10.54] Trelles JJ, McGrattan KB, Baum HR (1999) Smoke transport by sheared winds. Combustion Theory and Modelling 3:323–341



- [10.55] Prasad K, Patnaik G, Kailasanath K (2002) A multiblock technique for simulating fire and smoke spread in large complex enclosures. To appear in Fire Safety Science, Proc. 7th Int. Symp.
- [10.56] FEMA (1) (2002) Federal Emergency Agency Report on WTC, Washington DC, U.S.A
- [10.57] Taranath BS (1998) Steel, concrete, and composite design of tall buildings, McGraw-Hill, New York, London, chapter 10

# Appendix I

## A.I.A Related Analysis and Computer Programs Based on Finite Element

**Table A.I.A.1.** [D] – variable Young’s modulus and constant Poisson’s ratio

---

$D_{11} = \frac{E_1(E')^3 - E_{cr}}{\nu''}$	$D_{12} = \frac{\nu E_1 E_2 (E')^2 + E_{cr}}{\nu''}$	$D_{13} = \frac{\nu E_1 E_3 (E')^2 + E_{cr}}{\nu''}$	$D_{14} = 0$	$D_{15} = 0$	$D_{16} = 0$
	$D_{22} = \frac{E_2 E_3 (E')^2 + E_{cr}}{\nu''}$	$D_{23} = \frac{\nu E_2 E_3 (E')^2 + E_{cr}}{\nu''}$	$D_{24} = 0$	$D_{25} = 0$	$D_{26} = 0$
		$D_{33} = \frac{E_3 (E')^3 - E_{cr}}{\nu''}$	$D_{34} = 0$	$D_{35} = 0$	$D_{36} = 0$
			$D_{44} = G_{12}$	$D_{45} = 0$	$D_{46} = 0$
				$D_{55} = G_{23}$	$D_{56} = 0$
					$D_{66} = G_{31}$

$$E_{cr} = \nu^2 E_1 E_2 E_3 E'$$

$$E' = (E_1 + E_2 + E_3)/3$$

$$\nu'' = (E')^3 - 2E_1 E_2 E_3 \nu^2 - E' \nu^2 (E_1 E_2 + E_1 E_3 + E_2 E_3)$$

$$G_{12} = E_{12}/2(1 + \nu)$$

$$E_{12} = (E_1 + E_2)/2$$

$$G_{23} = E_{23}/2(1 + \nu)$$

$$E_{23} = (E_2 + E_3)/2$$

$$G_{31} = E_{31}/2(1 + \nu)$$

$$E_{31} = (E_3 + E_1)/2$$


---

**Table A.I.A.2.** [D] – variable Young’s modulus and Poisson’s ratio

---

$D_{11} = \frac{(1 - \nu_{23}\nu_{32})}{\bar{\nu}} E_1$	$D_{12} = \frac{(\nu_{12} + \nu_{12}\nu_{32})}{\bar{\nu}} E_2$	$D_{13} = \frac{(\nu_{13} + \nu_{12}\nu_{23})}{\bar{\nu}} E_3$	$D_{14} = 0$	$D_{15} = 0$	$D_{16} = 0$
$D_{21} = \frac{(\nu_{21} + \nu_{23}\nu_{31})}{\bar{\nu}} E_1$	$D_{22} = \frac{(1 - \nu_{13}\nu_{31})}{\bar{\nu}} E_2$	$D_{23} = \frac{(\nu_{23} + \nu_{13}\nu_{21})}{\bar{\nu}} E_3$	$D_{24} = 0$	$D_{25} = 0$	$D_{26} = 0$
$D_{31} = \frac{(\nu_{31} + \nu_{21}\nu_{32})}{\bar{\nu}} E_1$	$D_{32} = \frac{(\nu_{32} + \nu_{12}\nu_{31})}{\bar{\nu}} E_2$	$D_{33} = \frac{(1 - \nu_{12}\nu_{21})}{\bar{\nu}} E_3$	$D_{34} = 0$	$D_{35} = 0$	$D_{36} = 0$
$D_{41} = 0$	$D_{42} = 0$	$D_{43} = 0$	$D_{44}$	$D_{45} = 0$	$D_{46} = 0$
$D_{51} = 0$	$D_{52} = 0$	$D_{53} = 0$	$D_{54} = 0$	$D_{55}$	$D_{56} = 0$
$D_{61} = 0$	$D_{62} = 0$	$D_{63} = 0$	$D_{64} = 0$	$D_{65} = 0$	$D_{66}$

$$\bar{\nu} = 1 - \nu_{12}\nu_{21} - \nu_{13}\nu_{31} - \nu_{23}\nu_{32} - \nu_{12}\nu_{23}\nu_{31} - \nu_{21}\nu_{13}\nu_{32}$$

Due to symmetry of compliances, the following relations can be written:

$$\begin{aligned} E_1\nu_{21} &= E_2\nu_{12} & D_{55} &= G_{23} \\ E_2\nu_{32} &= E_3\nu_{23} & D_{66} &= G_{13} \\ E_3\nu_{13} &= E_1\nu_{31} \end{aligned}$$

The values of  $G_{12}$ ,  $G_{23}$  and  $G_{13}$  are calculated in terms of modulus of elasticity and Poisson’s ratio as follows:

$$G_{12} = \frac{1}{2} \left[ \frac{E_1}{2(1 + \nu_{12})} + \frac{E_2}{2(1 + \nu_{21})} \right] = \frac{1}{2} \left[ \frac{E_1}{2(1 + \nu_{12})} + \frac{E_2}{2 \left( \frac{E_1}{E_2} \right) + \nu_{12}} \right]$$

$$G_{23} = \frac{1}{2} \left[ \frac{E_2}{2(1 + \nu_{23})} + \frac{E_3}{2(1 + \nu_{32})} \right] = \frac{1}{2} \left[ \frac{E_2}{2(1 + \nu_{23})} + \frac{E_2}{2 \left( \frac{E_2}{E_3} \right) + \nu_{23}} \right]$$

$$G_{13} = \frac{1}{2} \left[ \frac{E_3}{2(1 + \nu_{31})} + \frac{E_1}{2(1 + \nu_{13})} \right] = \left[ \frac{E_3}{2(1 + \nu_{31})} + \frac{E_2}{2 \left( \frac{E_3}{E_1} \right) + \nu_{31}} \right]$$

For isotropic cases:

$$\begin{aligned} E_1 &= E_2 = E_3 = E \\ \nu_{12} &= \nu_{13} = \nu_{23} = \nu_{21} = \nu_{31} = \nu_{32} = \nu \end{aligned}$$

$[D]$  – constant Young’s modulus and Poisson’s ratio

$$[D] = \frac{E}{(1 + \nu)(1 - 2\nu)} \begin{bmatrix} 1 - \nu & \nu & \nu & 0 & 0 & 0 \\ \nu & 1 - \nu & \nu & 0 & 0 & 0 \\ \nu & \nu & 1 - \nu & 0 & 0 & 0 \\ 0 & 0 & 0 & \frac{1 - 2\nu}{2} & 0 & 0 \\ 0 & 0 & 0 & 0 & \frac{1 - 2\nu}{2} & 0 \\ 0 & 0 & 0 & 0 & 0 & \frac{1 - 2\nu}{2} \end{bmatrix}$$

Bulk and shear moduli

$$[D] = \begin{bmatrix} K + \frac{4}{3}G & K - \frac{2}{3}G & K - \frac{2}{3}G & 0 & 0 & 0 \\ K - \frac{2}{3}G & K + \frac{4}{3}G & K - \frac{2}{3}G & 0 & 0 & 0 \\ K - \frac{2}{3}G & K - \frac{2}{3}G & K + \frac{4}{3}G & 0 & 0 & 0 \\ 0 & 0 & 0 & G & 0 & 0 \\ 0 & 0 & 0 & 0 & G & 0 \\ 0 & 0 & 0 & 0 & 0 & G \end{bmatrix}$$

For plane stress

$$[D] = \frac{E}{1 - \nu^2} \begin{bmatrix} 1 & \nu & 0 \\ \nu & 1 & 0 \\ 0 & 0 & \frac{1 - \nu}{2} \end{bmatrix}$$

For plane strain

$$[D] = \frac{E(1 - \nu)}{(1 + \nu)(1 - 2\nu)} \begin{bmatrix} 1 & \frac{\nu}{1 - \nu} & 0 \\ \frac{\nu}{1 - \nu} & 1 & 0 \\ 0 & 0 & \frac{1 - 2\nu}{2(1 - \nu)} \end{bmatrix}$$

For axisymmetric cases

$$[D] = \frac{E}{(1 + \nu)(1 - 2\nu)} \begin{bmatrix} 1 - \nu & \nu & \nu & 0 \\ \nu & 1 - \nu & \nu & 0 \\ \nu & \nu & 1 - \nu & 0 \\ 0 & 0 & 0 & \frac{1 - 2\nu}{2} \end{bmatrix}$$


---

**Table A.I.A.3.** Two-dimensional elastic beam (courtesy STRUCOM, London)

*Element matrices and load vectors*

The element stiffness matrix in element co-ordinates is:

$$[K_1] = \begin{bmatrix} \frac{AE}{L} & 0 & 0 & -\frac{AE}{L} & 0 & 0 \\ 0 & \frac{12EI}{L^3(1+\phi')} & \frac{6EI}{L^2(1+\phi')} & 0 & -\frac{12EI}{L^3(1+\phi')} & \frac{6EI}{L(1+\phi')} \\ 0 & \frac{6EI}{L^2(1+\phi')} & \frac{EI(4+\phi')}{L(1+\phi')} & 0 & -\frac{6EI}{L^2(1+\phi')} & \frac{EI(2-\phi')}{L(1+\phi')} \\ -\frac{AE}{L} & 0 & 0 & \frac{AE}{L} & 0 & 0 \\ 0 & -\frac{12EI}{L^3(1+\phi')} & \frac{6EI}{L^2(1+\phi')} & 0 & \frac{12EI}{L^3(1+\phi')} & -\frac{6EI}{L^2(1+\phi')} \\ 0 & \frac{6EI}{L^2(1+\phi')} & \frac{EI(2-\phi')}{L(1+\phi')} & 0 & -\frac{6EI}{L^2(1+\phi')} & \frac{EI(4+\phi')}{L(1+\phi')} \end{bmatrix}$$

where

$A$  = cross-sectional area

$E$  = Young's modulus

$L$  = element length

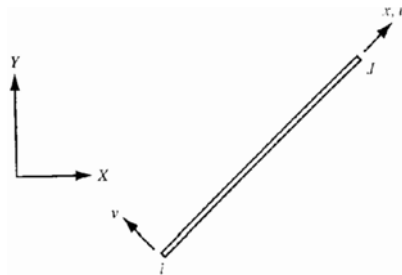
$I$  = moment of inertia

$$\phi' = \frac{12EI}{GA^s L^2}$$

$G$  = shear modulus

$$A^s = \frac{A}{F^s} = \text{shear area}$$

$F^s$  = shear deflection constant



**Fig. A.I.A.1.** Two-dimensional beam element centroidal axis

For uniform lateral pressure

$$P_1 = P_4 = 0$$

$$P_2 = P_5 = -\frac{PL}{2}$$

$$P_3 = -P_6 = -\frac{PL^2}{12}$$

$P$  = uniform applied pressure (units = force/length)

*Stress calculations*

The centroidal stress at end  $i$  is:

$$\sigma_i^{\text{dir}} = \frac{F_{x,i}}{A}$$

where

$\sigma_i^{\text{dir}}$  = centroidal stress

$F_{x,i}$  = axial force

The bending stress is

$$\sigma_i^{\text{bnd}} = \frac{M_i t}{2I}$$

where

$\sigma_i^{\text{bnd}}$  = bending stress at end  $i$

$M_i$  = moment at end  $i$

$t$  = thickness of beam in element  $z$  direction

**Table A.I.A.4.** Three-dimensional elastic beam (courtesy STRUCOM, London)

*Element matrices and load vectors*

All element matrices and load vectors are generated in the element co-ordinate system and must subsequently then be converted to the global co-ordinate system.

The element stiffness matrix is:

$$[K_1] = \frac{AE}{L} \begin{bmatrix} C_1 & 0 & 0 & -C_1 & 0 & 0 \\ 0 & 0 & 0 & 0 & 0 & 0 \\ 0 & 0 & 0 & 0 & 0 & 0 \\ -C_1 & 0 & 0 & C_1 & 0 & 0 \\ 0 & 0 & 0 & 0 & 0 & 0 \\ 0 & 0 & 0 & 0 & 0 & 0 \end{bmatrix}$$

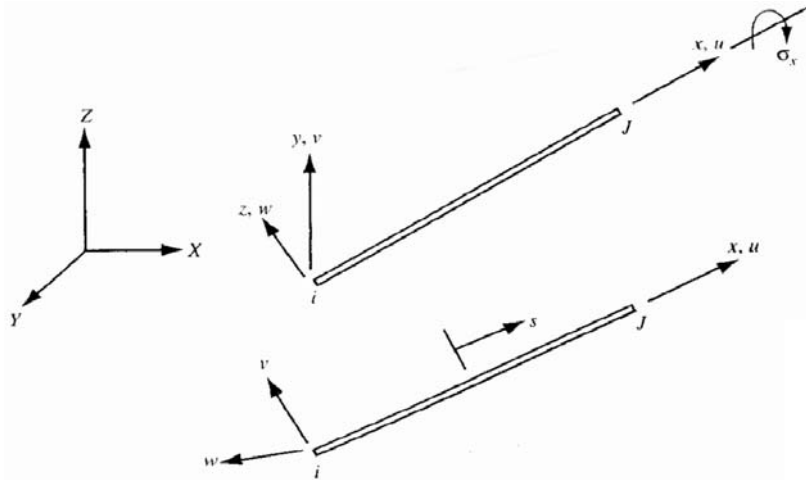


Fig. A.I.A.2. Three-dimensional elastic beam

where

- $A$  = element cross-sectional area
- $E$  = Young's modulus
- $L$  = element length
- $C_1$  = value given in the table below.

Value of stiffness coefficient ( $C_1$ )	
Previous iteration resulted in a tensile stress	Previous iteration resulted in a compressive stress
1.0	0.0
1.0	$1.0 \times 10^{-6}$
0.0	1.0
$1.0 \times 10^{-6}$	1.0

The element mass matrix is the same as the element stress stiffness matrix:

$$[S_1] = \frac{F}{L} \begin{bmatrix} 0 & 0 & 0 & 0 & 0 & 0 \\ 0 & C_2 & 0 & 0 & -C_2 & 0 \\ 0 & 0 & C_2 & 0 & 0 & -C_2 \\ 0 & 0 & 0 & 0 & 0 & 0 \\ 0 & -C_2 & 0 & 0 & C_2 & 0 \\ 0 & 0 & -C_2 & 0 & 0 & C_2 \end{bmatrix}$$







The element mass matrix in element co-ordinates is:

$$[M_1] = (\rho A + m)L(1 - \epsilon^{in})$$

$$\times \begin{bmatrix} 1/3 & 0 & 0 & 1/6 & 0 & 0 \\ 0 & A(r, \phi') & C(r, \phi') & 0 & B(r, \phi') & -D(r, \phi') \\ 0 & C(r, \phi') & E(r, \phi') & 0 & D(r, \phi') & -F(r, \phi') \\ 1/6 & 0 & 0 & 1/3 & 0 & 0 \\ 0 & B(r, \phi') & D(r, \phi') & 0 & A(r, \phi') & -C(r, \phi') \\ 0 & -D(r, \phi') & -F(r, \phi') & 0 & -C(r, \phi') & E(r, \phi') \end{bmatrix}$$

where

- $\rho$  = density
- $m$  = added  $m$
- $\epsilon^{in}$  = prestrain

$$A(r, \phi') = \frac{13/35 + 7/10\phi' + 1/3\phi'^2 + 6/5(r/L)^2}{(1 + \phi')^2}$$

$$B(r, \phi') = \frac{9/70 + 3/10\phi' + 1/6\phi'^2 - 6/5(r/L)^2}{(1 + \phi')^2}$$

$$C(r, \phi') = \frac{(11/210 + 11/120\phi' + 1/24\phi'^2 + (1/10 - 1/2\phi')(r/L)^2) L}{(1 + \phi')^2}$$

$$D(r, \phi') = \frac{(13/420 + 3/40\phi' + 1/24\phi'^2 - (1/10 - 1/2\phi')(r/L)^2) L}{(1 + \phi')^2}$$

$$E(r, \phi') = \frac{(1/105 + 1/60\phi' + 1/120\phi'^2 + (2/15 + 1/6\phi' + 1/3)(r/L)^2) L^2}{(1 + \phi')^2}$$

$$F(r, \phi') = \frac{(1/140 + 1/60\phi' + 1/120\phi'^2 + (1/30 + 1/6\phi' + 1/6\phi'^2)(r/L)^2) L^2}{(1 + \phi')^2}$$

$$r = \sqrt{\frac{I}{A}} = \text{radius of gyration}$$

The element pressure load vector in element coordinates is:

$$\{F_1^{pr}\} = [P_1 \ P_2 \ P_3 \ P_4 \ P_5 \ P_6]^T$$

$$F = \begin{cases} \text{for the first iteration: } AE\epsilon^{in} \\ \text{for all subsequent iterations: the axial force} \\ \text{in the element as computed in the previous} \\ \text{stress pass of the element (output quantity)} \\ \text{FORC} \end{cases}$$

$C_2$  = value given in the table below.





**Table A.I.A.7.** Analytical formulation of the steel anchors/studs

$$[K_{TOT}]\{\delta\}^* + \{F_T\} - \{R_T\} = 0$$

where

$$[K_{TOT}] = [K_l] + [K_a]$$

$$\{\delta\}^* = \begin{Bmatrix} \delta_{un} \\ \delta_b \end{Bmatrix} \quad \{F_T\} = \begin{Bmatrix} F_{un} \\ F_b \end{Bmatrix} \quad \{R_T\} = \begin{Bmatrix} R_{un} \\ R_b \end{Bmatrix}$$

$[K_{TOT}]$  = total stiffness matrix

$[K_l]$  = liner stiffness matrix

$[K_a]$  = a stud stiffness matrix

$\{F_T\}$  = total initial load vector

$\{R_T\}$  = total external load vector

Subscript

un = quantities corresponding to unknown displacement

b = quantities corresponding to restrained boundaries

$$[k_l]\{\delta_{un}\} + \{F_{un}\} = 0$$

$$\{\varepsilon\} = [B]\{\delta\}$$

$$\{\sigma\} = [D](\{\varepsilon\} - \{\varepsilon_0\})$$

$\{\bar{S}\}$  = anchor shear forces

$$= [K_a]\{\delta_{un}\}$$

$$\{F_{un}\} = \int_{\nu} [B]^T [D] \{\varepsilon_0\} d\nu = \int_{\nu} [B]^T [D] \{\varepsilon_0\} \det[J] d\xi d\eta d\zeta$$

The plastic buckling matrix is given by

$$(K + \lambda K_G) F_T = 0$$

where  $K$  = the elasto-plastic stiffness matrix as a function of the current state of plastic deformation; and  $K_G$  = the initial stress geometric stiffness matrix.

The determinant

$$|K + \lambda_c K_G| = 0$$

The essential equation is characteristically triangularised for the  $i$ th loading step as

$$(K^i + \lambda_c K_G^i) F_T^i = 0 \quad \lambda_c = 1 + E_{ps}$$

$E_{ps}$  is an accuracy parameter.

### A.I.A.1 Plastic Flow Rule and Stresses During Elastoplastic Straining

Many materials have been examined, including concrete. They behave elastically up to a certain stage of the loading beyond which plastic deformation takes place. During this plastic deformation the state of strain is not uniquely determined by the state of stress, as stated previously. In a uniaxial state of stress a simple rule is required to initiate yielding at any Gaussian point of the isoparametric element. In the multiaxial state of stress, there are an infinite number of possible combinations of stresses at which yielding starts. These can be examined by the flow rule. Moreover, the flow rule supplements the elastic constitutive relationship; and the plastic strain increments are related to the plastic stress increments during the occurrence of plastic flow.

The yield criterion described by a failure surface in a multi-dimensional stress space is given by Bangash

$$L_F(\sigma_{ij}^s, \varepsilon^P, S_H) = 0 \quad (\text{A.1})$$

where

$L_F$  = the yield function

$\sigma_{ij}^s$  = the multi-dimensional stress state

$\varepsilon^P$  = accumulated plastic strain

$S_H$  = strain hardening or softening parameter

The general form of the yield surface given by (A.1) allows either isotropic or kinematic hardening of the material. For a given previous history,  $L_F(\sigma_{ij})$  is always considered as a function of the current state of stress for which  $S_H$  is variable.

To give added generality, the plastic potential to which the normality principle is applicable is assumed as

$$L_Q(\sigma_{ij}^s, \varepsilon^P, SH_0) = 0 \quad (\text{A.2})$$

This allows non-associated plasticity to be dealt with and associated rules to be obtained as a special case by making

$$L_F = L_Q \quad (\text{A.3})$$

For a perfectly plastic material the yield surface of (A.1) remains constant. For a strain hardening material the yield surface must change with continued straining beyond the initial yield.

This phenomenon is included in (A.1) by allowing both  $L_F$  and  $S_H$  to be functions of the state of stress and the plastic deformation history. This means  $S_H$  will have a new value for every time dependent yielding. Further, if the material is unloaded and then loaded again, additional yielding cannot take place, unless the current value of  $S_H$  has been exceeded.

A unified approach for arriving at the incremental stress-strain equation based on (A.1) can be written in a combined tensor form in three dimensions as

$$f(\sigma, \varepsilon, \dot{\sigma}, \dot{\varepsilon}, S_H) = 0 \quad (\text{A.4})$$

where  $f$  is a definite representation of  $L_F$  and is a stress function. The only change is in the value of  $S_H$ , accounting for isotropic and anisotropic hardening, and allowing the function  $f$  to be dependent not only on the present state of stress or strain, but also on the hardening history according to previous states of stress and strain. The value of  $(\sigma, \dot{\sigma})$  and  $(\varepsilon, \dot{\varepsilon})$  must be in the plastic range, having total values of  $\sigma_{ij}^p$  and  $\varepsilon_{ij}^p$ , respectively.

When (A.4) is satisfied then the total differential of  $f$  is written as

$$df = \frac{\partial f}{\partial \sigma_{ij}^p} d\sigma_{ij}^p + \frac{\partial f}{\partial \varepsilon_{ij}^p} d\varepsilon_{ij}^p + \frac{\partial f}{\partial S_H} dS_H \quad (\text{A.5})$$

The yield condition with  $\varepsilon_{ij}^p$  and  $S_H$  held constant can be interpreted as a yield surface in the multidimensional stress space, and is in conformity with (A.1). When  $f < 0$  the condition indicates a purely elastic change towards the inside of the yield surface. In cases where plastic flow does not occur, the increments of plastic strain  $d\varepsilon_{ij}^p$  and the change of hardening parameter  $dS_H$  will be automatically zero, and hence, in the case of the unloading, (A.5) is reduced to

$$df = \frac{\partial f}{\partial \sigma_{ij}^p} d\{\sigma_{ij}^p\} < 0 \quad (\text{A.6})$$

When  $df = 0$ , which is the case for neutral loading, no plastic strain changes occur and the hardening factor remains unchanged, then

$$df = \frac{\partial f}{\partial \sigma_{ij}^p} d\{\sigma_{ij}^p\} = 0 \quad d\{\varepsilon_{ij}^p\} = 0 \quad (\text{A.7})$$

The quantity  $d\sigma_{ij}^p$  is tangent to the surface for neutral loading. For the vector products to be zero,  $\partial f / \partial \sigma_{ij}^p$  will be normal to the surface. When  $d\sigma_{ij}^p$  is pointing to the outside of the surface the vector product will be positive; and this constitutes loading, with plastic flow taking place such that

$$df = \frac{\partial f}{\partial \sigma_{ij}^p} d\{\sigma_{ij}^p\} > 0 \quad (\text{A.8})$$

The definition for the structural material stability postulates that during a load cycle that includes loading and unloading, the work performed has to be greater than zero, i.e.

$$d\varepsilon_{ij}^p d\sigma_{ij}^p \geq 0 \quad (\text{A.9})$$

From (A.8) and (A.9) for ideally plastic material the plastic strain increment  $d\varepsilon_{ij}^p$  is proportional to the stress gradient of the yield surface

$$d\varepsilon_{ij}^p = \frac{\partial f}{\partial \sigma_{ij}^p} d\lambda \quad (\text{A.10})$$

where  $d\lambda =$  a constant of proportionality.

The normality rule given by (A.10) shows that the plastic strain increment has the same direction as the normal surface  $f$  in the stress space. At this stage both isotropic and kinematic hardening cases can be included in (A.10).

In order to perform the plastic analysis, the loading path is discretised into several linear load steps. The increments in stresses and strains for each step are then related by the rate constitutive laws mentioned earlier. The assumption is that the extension in the linearised step can be regarded as infinitesimal, and (A.10), which is true for all infinitesimal increments of stresses and strains, can be employed for small increments. Concrete structures for nuclear and offshore installations require small increments. The total strain increment  $d\varepsilon'_{ij}$  is the algebraic sum of the increments in elastic and plastic strains  $d\bar{\varepsilon}_{ij}$  and  $d\varepsilon^P_{ij}$ , respectively. The equation for  $d\varepsilon'_{ij}$  can be written as

$$d\varepsilon_{ij} = d\bar{\varepsilon}_{ij} + d\varepsilon^P_{ij} = d\varepsilon^e_{ij} + d\varepsilon^T_{ij} + d\varepsilon^P_{ij} \tag{A.11}$$

The stresses can be written as

$$d\sigma'_{ij} = [D]d\varepsilon_{kl} \tag{A.12}$$

$$d\sigma_{ij} = [D]d\varepsilon_{kl} - d\lambda[D]^{-1} \frac{\partial f}{\partial \sigma_{kl}} \tag{A.13}$$

The plastic strain relationship is given as

$$d\varepsilon = [D^*]^{-1}d\{\sigma\} \tag{A.14}$$

The total strain increment  $\{\Delta\varepsilon\}_{TOT}$  becomes

$$\{\Delta\varepsilon\}_{TOT} = [D^*]^{-1}\{\Delta\sigma\} + \frac{\partial f}{\partial \sigma}d\lambda \tag{A.15}$$

When (A.5) is written in a compressed form as

$$df = \frac{\partial f}{\partial \{\sigma\}} d\{\sigma\} + \frac{\partial f}{\partial S_H} dS_H = 0 \tag{A.16}$$

Replacing the second term for the hardening characteristics by  $d\lambda$ , the following equations are obtained

$$\left\{ \frac{\partial f}{\partial \sigma} \right\}^T d\{\sigma\} - Cd\lambda = 0 \tag{A.17}$$

$$d\varepsilon_{TOT} = [D^*]^{-1}d\{\sigma\} + \left\{ \frac{\partial f}{\partial \sigma} \right\} d\lambda \tag{A.18}$$

$$0 = \left\{ \frac{\partial f}{\partial \sigma} \right\}^T d\{\sigma\} - Cd\lambda \tag{A.19}$$

Multiplying (A.18) with  $[D^*]$  throughout, (A.18) can be expressed as

$$d\{\sigma\} = [D^*]\{d\varepsilon\}_{TOT} - [D^*] \left\{ \frac{\partial f}{\partial \sigma} \right\} d\lambda \tag{A.20}$$



Equation (A.20) is then substituted into (A.19), and (A.21) is obtained

$$0 = \frac{\partial f^T}{\partial \sigma} [D^*] \{d\varepsilon\}_{TOT} - \left\{ \frac{\partial f}{\partial \sigma} \right\}^T [D^*] \left\{ \frac{\partial f}{\partial \sigma} \right\} d\lambda - C d\lambda \quad (A.21)$$

Equation (A.11) is then combined with (A.10), (A.18) and (A.6) to give the final value of  $d\lambda$

$$d\lambda = \frac{\left\{ \frac{\partial f}{\partial \sigma} \right\}^T [D^*] \{d\varepsilon\}_{TOT}}{C + \left\{ \frac{\partial f}{\partial \sigma} \right\}^T [D^*] \left\{ \frac{\partial f}{\partial \sigma} \right\}} \quad (A.22)$$

The factor  $C$  in (A.22) is an unknown factor defining the state of elasto-plasticity. When  $C = 0$ , (A.22) gives a value of  $d\lambda$  for a perfectly plastic situation with no hardening. The stress increments are given by:

$$\{d\sigma\}_{TOT} = [D^*] - \frac{[D^*] \left\{ \frac{\partial f}{\partial \sigma} \right\} \left\{ \frac{\partial f}{\partial \sigma} \right\}^T [D^*]}{C + \left\{ \frac{\partial f}{\partial \sigma} \right\}^T [D^*] \left\{ \frac{\partial f}{\partial \sigma} \right\}} \{d\varepsilon\}_{TOT} \quad (A.23)$$

for the elasto-plastic case,

$$\{d\sigma\}_{TOT} = [D^*] - [D_p] \{d\varepsilon\}_{TOT} \quad (A.24)$$

$$[D_p] = \frac{[D^*] \left\{ \frac{\partial f}{\partial \sigma} \right\} \left\{ \frac{\partial f}{\partial \sigma} \right\}^T [D]}{C + \left\{ \frac{\partial f}{\partial \sigma} \right\}^T [D] \left\{ \frac{\partial f}{\partial \sigma} \right\}} \quad (A.25)$$

The true stress increment in (A.25) is the difference between the stress increment  $[D_p] \{d\varepsilon\}_{TOT}$  and the algebraic sum of stresses  $[D] \{d\varepsilon\}$  due to elastic, creep, shrinkage, temperature, fatigue and other effects.

The matrix  $[D]$  has the flexibility to include any concrete failure models described elsewhere in this book.

The parameter  $C$  is given by Hill [A.1] as

$$C = 4/9 \sigma_{eq}^2 S_H \quad (A.26)$$

where  $S_H$  is the slope of the curve and represents hardening.

Where the influence of the studs, lugs and any other type of anchorages is to be included in the finite element analysis, the steps given in Table A.I.A.7 are considered together with solid, panel and line elements.

**1 Sample Cases**

**1.1 Plastic Potential of the Same Form as the Yield Surface**

$$f(J_2) = f(\sigma_{ij}) = \frac{3}{2} = \frac{3}{2} S_{ij} S_{ij} \tag{A.27}$$

where

$$S_{ij} = \sigma_{ij} - \frac{1}{3} \sigma_{kk} \delta_{ij}$$

$\delta_{ij}$  = the Kronecker delta.

Differentiating

$$\begin{aligned} \frac{\partial f}{\partial \sigma_{ij}} &= \frac{3}{2} \partial (S_{kl} S_{kl}) / \partial \sigma_{ij} \\ &= \frac{3}{2} S_{kl} \partial S_{mn} / \partial \sigma_{ij} = 3 S_{ij} \end{aligned} \tag{A.28}$$

The plastic strain increment is stated as

$$d\lambda \varepsilon_{ij}^P = \lambda S_{ij} \tag{A.29}$$

The equivalent plastic strain  $\lambda \bar{\varepsilon}^P$  can be obtained as

$$d\lambda \bar{\varepsilon}^P = \left( \frac{2}{3} d\varepsilon_{ij}^P d\varepsilon_{ij}^P \right)^{1/2} \tag{A.30}$$

where

$$d\lambda = \frac{3}{2} \frac{d\bar{\varepsilon}^P}{\sigma_{eq}}$$

**1.2 Von Mises Yield Surface Associated with Isotropic Hardening**

The yield function  $f$  is written as

$$f = \frac{T}{2} (\sigma_{ij}) - \frac{1}{3} \sigma_{eq}^2 \tag{A.31}$$

By differentiating, (A.31) becomes

$$df = (S_{ij} d\sigma_{ij}) - \frac{2}{3} \sigma_{eq} (\partial \sigma_{eq}) / (\partial \bar{\varepsilon}^P) \{d\bar{\varepsilon}^P\} \tag{A.32}$$

Using (A.6) onwards, the values of  $d\lambda$  and  $d\sigma$  given in (A.22) and (A.23) are given by

$$d\lambda = \left( [D^*]_{i,j,k,l} - \frac{[D^*] S_{mn} S_{pq} [D^*]_{pqkl}}{\sigma_{ij} [D^*]_{i,j,k,l} S_{kl} + \left(\frac{2}{3} \sigma_{eq}\right)^2 S_H} \right) \{d\varepsilon\}_{kl} \tag{A.33}$$

## Dynamic Analysis

Dynamic analysis is a subject by itself. In this text a specific approach to the dynamic analysis of concrete structures is discussed. The equations of motion are discretised in time. The direct integration technique and the Wilson- $\theta$  method are summarised. Where dynamic problems are tackled, the nonlinear equations of motion (coupled or uncoupled), have been solved using these methods.

### *Nonlinear Transient Dynamic Analysis*

The dynamic equilibrium at the nodes of a system of structural elements is formulated at a given time  $t$  as

$$[M]\{\ddot{U}_t\} + [C_1]\{\dot{U}_t\} + K'_t\{U_t\} = \{R_t\} \quad (\text{A.34})$$

where  $\{U_t\}$  and  $\{R_t\}$  are the vectors of displacement and specified load, respectively.  $[M]$  represents the mass matrix which is regarded as constant;  $[C_t]$  and  $[K'_t]$  are the damping and stiffness matrices, respectively. The subscript  $t$  is used for quantities at time  $t$  and a dot denotes a derivative with respect to time.

To formulate (A.34), discretisation with respect to time, using isoparametric finite elements, is performed. The simple applicable method is the numerical step-by-step integration of the coupled equations of motion, such as (A.34). The response, history is divided into time increments  $\Delta t$ , which are of equal length. The system is calculated for each  $\Delta t$ , with properties determined at the beginning of the interval. Only one matrix based on  $M$ , is excited. In addition, the direct integration technique allows a general damping matrix  $[C_t]$  (which has to be specified explicitly), to be used without resorting to complex eigenvalues.

### *Discretisation in the Time Domain*

The equation of motion formulated at time  $t = 0$ , is written in the form

$$[M]\{\ddot{U}_0\} + [C_0]\{\dot{U}_0\} + [K_0]\{U_0\} = \{R_0\} \quad (\text{A.35})$$

where the subscript zero has been introduced. At time  $t$ , all quantities are known. Equation (A.34) is specified as

$$[M]\{\ddot{U}_t\} + ([C_0] + [\Delta C_{0 \rightarrow t}])\{\dot{U}_t\} + ([K'_0] + [K_{0 \rightarrow t}])\{U_t\} = \{R_t\} \quad (\text{A.36})$$

or as

$$[M]\{\ddot{U}_t\} + [C_0]\{\dot{U}_t\} + [K_0]\{U_t\} = \{R_t\} + \{P_t\} = \{F\}_t \quad (\text{A.37})$$

where the initial load  $\{P_t\}$  is specified by

$$\{P_t\} = -[\Delta C_{0 \rightarrow t}]\{\dot{U}_t\} - [\Delta K_{0 \rightarrow t}]\{\delta_t\} \quad (\text{A.38})$$

To obtain the solution at time  $t + \Delta t$  the equation is stated as

$$\begin{aligned}
 & [M]\{\ddot{U}_{t+\Delta t}\} + [C_0]\{\dot{U}_{t+\Delta t}\} + [K_0]\{U_{t+\Delta t}\} \\
 & = \{R_{t+\Delta t}\} + \{P_t\} + \{\Delta P_{t \rightarrow t+\Delta t}\}
 \end{aligned}
 \tag{A.39}$$

$\{\Delta P_{t \rightarrow t+\Delta t}\}$  represents the influence of the nonlinearity during the time increment and is determined by iteration and satisfied for  $t + \tau$ , where  $\tau = \theta \Delta t$  ( $\theta > 1.37$  for an unconditionally stable method) applied to a linear problem.  $[\Delta C_{0 \rightarrow t}]$  and  $[\Delta K_{0 \rightarrow t}]$  represent the change of  $[C]$  and  $[K]$ , respectively, from  $t = 0$  to  $t$ .

To obtain the solution at time  $t + \Delta t$ , (A.40) can be written as

$$\begin{aligned}
 & [M]\{\ddot{U}_{t+\Delta t}\} + [C_0]\{\dot{U}_{t+\Delta t}\} + [K_0]\{U_{t+\Delta t}\} \\
 & = \{R_{t+\Delta t}\} + \{F_t\} + \{\Delta F_{t \rightarrow t+\Delta t}\}
 \end{aligned}
 \tag{A.40}$$

$\{\Delta P_{t \rightarrow t+\Delta t}\}$  represents the influence of the nonlinearity during the time increment  $t$  and is determined by iteration

$$\begin{aligned}
 \{\Delta P_{t \rightarrow t+\Delta t}\} & = -[\Delta C_{0 \rightarrow t}]\{\Delta \dot{U}_{t \rightarrow t+\Delta t}\} \\
 & \quad -[\Delta C_{t \rightarrow t+\Delta t}](\{\dot{U}\} + \{\Delta \dot{U}_{t \rightarrow t+\Delta t}\}) \\
 & \quad -[\Delta K_{0 \rightarrow t}]\{\Delta U_{t \rightarrow t+\Delta t}\} \\
 & \quad -[\Delta K_{t \rightarrow t+\Delta t}](\{U_t\} + \{\Delta U_{t \rightarrow t+\Delta t}\})
 \end{aligned}
 \tag{A.41}$$

$\{\Delta P_{t \rightarrow t+\Delta t}\}$  is calculated using the initial stress approach.

A modified Newton–Raphson or initial stress approach is adopted for solving these nonlinear equation.

### Reduced Linear Transient Dynamic Analysis

This is a reduced form of nonlinear transient dynamic analysis. This analysis is carried out faster than the nonlinear analysis since the matrix in (A.34) requires to be inverted once, and the analysis is reduced to a series of matrix multiplications and essential degrees of freedom (dynamic or master of freedoms) to characterise the response of the system. The analysis generally has restrictions such as constant  $[M]$ ,  $[C_t]$ ,  $[K_t]$  and time interval for all iterations and nodal forces applied at dynamic or master degrees of freedom.

### Quadratic Integration

$$\begin{aligned}
 & \left( \frac{1}{\Delta t^2} [M]_{\text{R}} + \frac{3}{2\Delta t} [\hat{C}_t]_{\text{R}} + [K_t]_{\text{R}} \right) \{U_t\} = \{F(t)\}_{\text{R}} \\
 & \quad + [M]_{\text{R}} \frac{1}{\Delta t^2} \left( 2\{U_{t-1}\}_{\text{R}} - \{U_{t-2}\}_{\text{R}} \right) \\
 & \quad + \frac{1}{\Delta t} \left( 2\{U_{t-1}\}_{\text{R}} - \frac{1}{2}\{U_{t-2}\}_{\text{R}} \right)
 \end{aligned}
 \tag{A.42}$$

The symbol R represents reduced matrices and vectors.

*Cubic Integration*

$$\begin{aligned}
& \left( \frac{2}{\Delta t^2} [M]_{\text{R}} + \frac{11}{6\Delta t} [C_t]_{\text{R}} + [K_t]_{\text{R}} \right) \{U_t\} = \{F(t)\} \\
& + [M]_{\text{R}} \frac{1}{\Delta t^2} \left( 5\{U_{t-1}\}_{\text{R}} - 4\{U_{t-2}\}_{\text{R}} + \{U_{t-3}\}_{\text{R}} \right) \\
& + [C_t]_{\text{R}} \frac{1}{\Delta t^2} \left( 3\{U_{t-1}\}_{\text{R}} - \frac{3}{2}\{U_{t-2}\}_{\text{R}} + \frac{1}{3}\{U_{t-3}\}_{\text{R}} \right)
\end{aligned} \tag{A.43}$$

*Mode Frequency Analysis*

The equation of motion for an undamped structure with no applied forces is written as

$$[M]\{\ddot{U}\} + [K'_t]\{U_t\} = \{0\} \tag{A.44}$$

$[K'_t]$  the structure stiffness matrix, may include stress-stiffening effects.

The system of equations is initially condensed down to those involved with the master (dynamic) degrees of freedom.

The number of dynamic degrees of freedom should at least be equal to two times the selected frequencies. The reduced form of (A.44) can be written as

$$[M]_{\text{R}}\{\ddot{U}_t\}_{\text{R}} + [K'_t]_{\text{R}}\{U_t\}_{\text{R}} = \{0\} \tag{A.45}$$

For a linear system, free vibrations of harmonic type are written as

$$\{U_t\}_{\text{R}} = \{\psi_i\}_{\text{R}} \cos \omega_i t \tag{A.46}$$

where  $\{\psi_i\}_{\text{R}}$  = the eigenvector representing the shape of the  $i$ th frequency;  $\omega_i$  = the  $i$ th frequency (radians/unit time); and  $t$  = time.

Equation (A.44) assumes the form

$$(-\omega_i^2 [M]_{\text{R}} + [K'_t]_{\text{R}})\{\psi_i\}_{\text{R}} = \{0\} \tag{A.47}$$

which is an eigenvalue problem with  $n$  values of  $\omega^2$  and  $n$  eigenvectors  $\{\psi_i\}_{\text{R}}$  which satisfy (A.47), where  $n$  is the number of dynamic degrees of freedom. Using standard iteration procedures, (A.47) will yield a complete set of eigenvalues and eigenvectors.

Each eigenvector  $\{\psi_i\}_{\text{R}}$  is then normalised such that:

$$\{\psi_i\}_{\text{R}}^{T''} [M]_{\text{R}} \{\psi_i\}_{\text{R}} = 1 \tag{A.48}$$

These  $n$  eigenvectors are now expanded to the full set of structure modal displacement degrees of freedom.

$$\{\psi_{\gamma'i}\}_{\text{R}} = [K_{\gamma'\gamma'}]^{-1} [K_{\gamma'\gamma}]\{\psi_i\}_{\text{R}} \tag{A.49}$$

where  $\{\psi_t\}_{\text{R}}$  = the slave degree of freedom vector of mode  $i$ ; and  $[K_{\gamma'\gamma}]$ ,  $[K_{\gamma'\gamma'}]$  = submatrix parts.

The above dynamic analysis approach is generally adopted for structures subjected to normal dynamic loads, wind, wave and seismic loads. The above analysis, with modifications, is also applied to missile and aircraft explosions/impact problems.

**Table A.I.A.8.** Summary of step-by-step integration method

*Initialisation*

- (1) Effective stiffness matrix

$$[K_0^*] = (6/\tau^2)[M] + (3/\tau)[C_0] + [K_0] \tag{A}$$

- (2) Triangularise  $[K_0^*]$

For each time step:

*Calculation of displacement  $\{U_{t+\tau}\}$*

- (1) Constant part of the effective load vector

$$\begin{aligned} \{R_{t+\tau}^*\} &= \{R_t\} + \theta(\{R_{t+\Delta t}\} - \{R_t\}) + \{F_t\} = [M] \\ &\times \left( \left( \frac{6}{\tau^2} \right) \{U_t\} + \frac{6}{\tau} \{\dot{U}_t\} + 2\{\ddot{U}_t\} \right) \\ &+ [C_0] \left( \frac{3}{\tau} \{U_t\} + 2\{\dot{U}_t\} + \frac{\tau}{2} \{U_t\} + \right) \end{aligned} \tag{B}$$

- (2) Initialisation  $i = 0, \quad \{\Delta P_{t \rightarrow t+\tau}^i\} = 0$

- (3) Iteration

- (a)  $i \rightarrow i + 1$

- (b) Effective load vector

$$\{R_{t+\tau_{TOT}}^*\} = \{R_{t+\tau}^*\} + \{\Delta P_{t \rightarrow t+\tau}^{i-1}\} \tag{C}$$

- (c) Displacement

$$\{U_{t+\tau}^i\}[K_0^*]\{U_{t+\tau}^i\} = \{R_{t+\tau_{TOT}}^*\} \tag{D}$$

- (d) Velocity  $\{\dot{U}_{t+\tau}^i\} + (3/\tau)(\{U_{t+\tau}^i\} - \{U_t\}) - 2\{\dot{U}_t\} - (\tau/2)\{\ddot{U}_t\}$

- (e) Change of initial load vector caused by the nonlinear behaviour of the material  $\{\Delta P_{t \rightarrow t+\tau}^i\}$

$$\begin{aligned} \{\Delta P_{t \rightarrow t+\tau}^i\} &= -[\Delta C_{0 \rightarrow t}]\{(\dot{U}_{t+\tau}^i\} - \{\dot{U}_t\}) - \{\Delta C_{t \rightarrow t+\tau}^i\}\{\dot{U}_{t+\tau}^i\} \\ &\times [\Delta K_{0 \rightarrow t}]\{(\{U_{t+\tau}^i\} - \{U_t\}) - \{\Delta K_{t \rightarrow t+\Delta t}^i\}\{U_{t+\tau}^i\}\} \end{aligned} \tag{E}$$

In fact,  $\{\Delta P_{t \rightarrow t+\tau}^i\}$  is calculated using the initial-stress method.

- (f) Iteration convergence

$$\| \{\Delta P_{t \rightarrow t+\tau}^i\} = \{\Delta P_{t \rightarrow t+\tau}^{i-1}\} \| / \| \{\Delta P_{t \rightarrow t+\tau}^i\} \| < \text{tol} \tag{F}$$

or analogously, on stresses.

*Note:*  $\{P\}$  could be any value of  $\{F\}$ .

*Calculation of velocity, acceleration*

Calculate new acceleration  $\{\ddot{U}_{t+\Delta t}\}$ , velocity  $\{\dot{U}_{t+\Delta t}\}$ , displacement  $\{U_{t+\Delta t}\}$  and initial load  $\{P_{t+\Delta t}\}$

$$\begin{aligned}
 \{\ddot{U}_{t+\Delta t}\} &= (6/\theta\tau^2)(\{U_{t+\tau}\} - \{U_t\}) - (6/\tau\theta)\{\dot{U}_t\} + \left(1 - \frac{3}{\theta}\right)\{\ddot{U}_t\} \\
 \{\dot{U}_{t+\Delta t}\} &= \{\dot{U}_t\} + \frac{\tau}{2\theta}\{\ddot{U}_t\} + \{\ddot{U}_{t+\Delta t}\} \\
 \{U_{t+\Delta t}\} &= \{U_t\} + \frac{\tau}{\theta}\{\dot{U}_t\} + (\tau^2/6\theta^2)(2\{\ddot{U}_t\} + \{\ddot{U}_{t+\Delta t}\}) \\
 \{P_{t+\Delta t}\} &= \{P_t\} + \{\Delta P_{t \rightarrow t+\tau}^i\}
 \end{aligned}
 \tag{G}$$

*Calculation by Quadratic Integration*

When the velocity varies linearly and the acceleration is constant across the time interval, appropriate substitutions are made into (A.34) giving

$$[f_1[M] + f_2[C_t] + [K'_t]\{U_t\} = \{F(t)\} + \{f_3([C_t], [M], U_t, U_{t2}, \dots)\} \tag{H}$$

where  $f_1, f_2, f_3 =$  functions of time.

This results in an implicit time integration procedure. The only unknown is  $\{U_t\}$  at each time point and this is calculated in the same way as in static analysis. Equation (H) is then written as:

$$\begin{aligned}
 &\left(\frac{2}{\Delta t_0 \Delta t_{01}}[M] + \frac{2\Delta t_0 + \Delta t_1}{\Delta t_0 \Delta t_{01}}[C] + [K'_t]\right)U_t \\
 &= \{F(t)\} + [M] \left(-\frac{2}{\Delta t_0 \Delta t_1}\{U_{t-1}\} - \frac{2}{\Delta t_1 \Delta t_{01}}\{U_{t-2}\}\right) \\
 &+ [C_t] \left(\frac{\Delta t_{01}}{\Delta t_0 \Delta t_1}\{U_{t-1}\} - \frac{\Delta t_0}{\Delta t_{01} \Delta t_1}\{U_{t-2}\}\right)
 \end{aligned}
 \tag{I}$$

where

$$\begin{aligned}
 \Delta t_0 &= t_0 - t_1 & t_0 &= \text{time of current iteration} \\
 \Delta t_1 &= t_1 - t_2 & t_1 &= \text{time of previous iteration} \\
 \Delta t_2 &= t_2 - t_3 & t_2 &= \text{time before previous iteration} \\
 & & t_3 &= \text{time before } t_2 \\
 \Delta t_2 &= \Delta t_0 + \Delta t_1 = t_0 - t_2
 \end{aligned}$$

*Calculation by Cubic Integration*

Equation (H) becomes cubic and hence is written as

$$\begin{aligned}
 (a_1([M] + a_2[C_t] + [K'_t])\{U_t\} &= \{F(t)\} \\
 &+ [M](a_3\{U_{t-1}\} - a_4\{U_{t-2}\} + a_5\{U_{t-3}\}) \\
 &+ [C](a_6\{U_{t-1}\} - a_7\{U_{t-2}\} + a_8\{U_{t-3}\})
 \end{aligned}
 \tag{J}$$

where  $a_1$  to  $a_8$  are functions of the time increments; these functions are derived by inverting a four by four matrix.

For clear-cut solutions, the size of the time step between adjacent iterations should not be more than a factor of 10 in nonlinear cases and should not be reduced by more than a factor of 2 where plasticity exists.

---

*Spectrum Analysis*

Spectrum analysis is an extension of the mode frequency analysis, with both base and force excitation options. The base excitation option is generally suitable for seismic and wave applications. A direction vector and a response spectrum table will be needed in addition to the data and parameters required for the reduced modal analysis. The response spectrum table generally includes displacements, velocities and accelerations. The force excitation is, in general, used for wind and space structures and missile/aircraft impact. It requires a force distribution and an amplitude multiplier table in addition to the data and parameters needed for the reduced modal analysis. A study of the mass distribution is made. Generally the masses are kept close to the reaction points on the finite element mesh rather than the (master) degrees of freedom. It is important to calculate the participation factors in relation to a given excitation direction. The base and forced excitations are given below:

$$\tilde{\gamma}_i = \{\psi_i\}_R^{T''} [M] \{\tilde{b}\} \quad \text{for the base excitation} \quad (\text{A.50})$$

$$\tilde{\gamma}_i = \{\psi_i\}_R^{T''} \{F_t\} \quad \text{for the force excitation} \quad (\text{A.51})$$

where  $\{\tilde{b}\}$  = the unit vector of the excitation direction; and  $\{F_t\}$  = an input force vector.

The values of  $\{\psi\}_R$  are normalised, and the reduced displacement vector is calculated from the eigenvector by using a mode coefficient  $\tilde{M}$ .

$$\{\tilde{U}\}_i = [\tilde{M}_i] \{\psi\}_i \quad (\text{A.52})$$

where  $\{\tilde{U}\}_i$  = the reduced displacement vector; and  $[\tilde{M}_i]$  = the mode coefficient and where (a) for velocity spectra

$$[\tilde{M}_i] = \frac{[V_{si}] \{\tilde{\gamma}_i\}}{\omega_i} \quad (\text{A.53})$$

( $V_{si}$  = spectral velocity for the  $i$ th mode); (b) for force spectra

$$[\tilde{M}_i] = \frac{[\bar{f}_{si}] \{\tilde{\gamma}_i\}}{\omega_i^2} \quad (\text{A.54})$$

( $\bar{f}_{si}$  = spectral force for the  $i$ th mode); (c)

$$[\tilde{M}_i] = \frac{[a_{si}] \{\tilde{\gamma}_i\}}{\omega_i^2} \quad (\text{A.55})$$

( $a_{si}$  = spectral acceleration for the  $i$ th mode); (d)

$$[\tilde{M}_i] = \frac{[U_{si}] \{\tilde{\gamma}_i\}}{\omega_i^2} \quad (\text{A.56})$$

( $U_{si}$  = spectral displacement for the  $i$ th mode).

$\{U\}_i$  may be expanded to compute all the displacements, as was done in the case of superelement and substructuring of the equation



$$\left[ \begin{array}{c|c} K & K_R \\ \hline K_R^{T''} & K_{RR} \end{array} \right] \left\{ \begin{array}{c} U \\ U_R \end{array} \right\} = \left\{ \begin{array}{c} F \\ F_R \end{array} \right\} \tag{A.56a}$$

as was done above.

$$\{U_{\gamma'}\}_i = [K_{\gamma',\gamma'}]^{-1}[K_{\gamma',\gamma}]\{U_i\}_R \tag{A.57}$$

where  $\{U_{\gamma'}\}_i$  = the slave degree of freedom vector of mode  $i$ ; and  $[K_{\gamma',\gamma'}]$ ,  $[K_{\gamma',\gamma}]$  = submatrix parts.

Sometimes an equivalent mass  $M_i^e$  is needed for the  $i$ th mode since it may not be a function of excitation direction. This  $M_i^e$  is computed as

$$[M_i^e] = 1/\{\psi_i\}_R^{T''} \{\psi_i\}_R \tag{A.58}$$

This is derived from the definition of the diagonal matrix of equivalent masses  $[M^e]$

$$[\psi]_R^{T''} [M^e][\psi]_R = [I] \tag{A.59}$$

where  $[I]$  = the identity matrix; and  $[\psi]_R$  = a square matrix containing all mode shape vectors.

Where damping is included, the damping ratio  $D_{Ri}$  for the data input, including damping  $C_e$ , is given for a matrix of coupling coefficients as

$$D_{Ri} = C_e\omega_i/2 \tag{A.60}$$

where  $\omega_i$  is the undamped natural frequency of the  $i$ th mode.

In between the modes  $i$  and  $j$ , a modified damping ratio  $D'_{Ri}$  is needed to take into account the concrete structures subjected to wave and seismic effects.

$$D'_{Ri} = D_{Ri} + 2/t_e\omega_i \tag{A.61}$$

where  $t_e$  is the duration.

### Impact/Explosion

Structural response of concrete structures subjected to relatively fast loading rates, such as those from missile and aircraft impact/explosion, bombs and nuclear detonations, etc., can be influenced by the effect of strain rate on the material properties. These material changes lead to an instantaneous change in the strength of materials. Chapter 6 invoked along with the above equations of motion. The normality rules and the proportionality factor  $d\lambda$  are used as given.

The  $d\lambda$  values are substituted into (A.13) to give an expression for the stress state of the form

$$d\sigma_{ij} = [D]\{d\epsilon_{kl}\} + \tilde{\gamma}_{ij}\{\tilde{\epsilon}\}^P \tag{A.62}$$

where, using Von Mises criterion,

$$\tilde{\gamma}_{ij} = \frac{[D^*]\{S_{mn}\}\{S_{kl}\}\{\bar{D}\}}{\alpha^*} \tag{A.63}$$

$$\begin{aligned} \alpha^* &= \frac{4}{9} \sigma_{\text{eq}}^2 \frac{\partial \sigma_{\text{eq}}}{\partial \varepsilon^{\text{P}}} + S_{ij}[D]\{S_{kl}\} \\ [D^*] &= D_{ijmn} \\ [\bar{D}] &= D_{pqkl} \end{aligned} \tag{A.64}$$

The term  $\gamma_{ij}\varepsilon^{\text{P}}$  can be implemented. Where deformation rates do not change too rapidly the term  $\gamma_{ij}\varepsilon^{\text{P}}$  is neglected. The rest of the procedure is the same as for general dynamic analysis.

*Mass Moments of Inertia*

The computation of the mass moments and products of inertia as well as the model centroids is described in this section. The model centroids are computed as

$$\begin{aligned} X_c &= A_x/M \\ Y_c &= A_y/M \\ Z_c &= A_z/M \end{aligned} \tag{A.65}$$

where typical terms are

- $X_c$  = X co-ordinate of model centroid
- $A_x = \sum_{i=1}^N m_i X_i$
- $N$  = number of elements
- $m_i$  = mass of element  $i$
- $X_i$  = X co-ordinate of the centroid of element  $i$
- $M = \sum_{i=1}^N m_i$  = mass of model centroid

The moments and products of inertia with respect to the origin are

$$I_{xx} = \sum_{i=1}^N m_i [(Y_i)^2 + (Z_i)^2] \quad I_{zz} = \sum_{i=1}^N m_i [(X_i)^2 + (Y_i)^2] \tag{A.66}$$

$$I_{yy} = \sum_{i=1}^N m_i [(X_i)^2 + (Z_i)^2] \quad I_{xy} = \sum_{i=1}^N m_i [(X_i)(Y_i)] \tag{A.67}$$

$$I_{yz} = \sum_{i=1}^N m_i [(Y_i)(Z_i)] \quad I_{xz} = \sum_{i=1}^N m_i [(X_i)(Z_i)] \tag{A.68}$$

where typical terms are  $I_{xx}$  = mass moment of inertia about the X axis through the model centroid and  $I_{xy}$  = mass product of inertia with respect to the X and Y axes through the model centroid.

The moment and products of inertia with respect to the model centroid (the components of the inertia tensor) are

$$\begin{aligned} I'_{xx} &= I_{xx} - M[(Y_c)^2 + (Z_c)^2] \\ I'_{yy} &= I_{yy} - M[(X_c)^2 + (Z_c)^2] \end{aligned} \tag{A.69}$$

$$\begin{aligned} I'_{zz} &= I_{zz} - M[(X_c)^2 + (Y_c)^2] \\ I'_{xy} &= I_{xy} - MX_cY_c \\ I'_{yz} &= I_{yz} - MY_cZ_c \end{aligned} \tag{A.70}$$

$$I'_{xz} = I_{xz} - MX_cZ_c$$

where typical terms are  $I'_{xx}$  = mass moment of inertia about the  $X$  axis through the model centroid and  $I'_{xy}$  = mass product of inertia with respect to the  $X$  and  $Y$  axes through the model centroid.

It may be seen from the above development that only the mass ( $m_i$ ) and the centroid ( $X_i$ ,  $Y_i$  and  $Z_c$ ) of each element are included. Effects which are not considered are

- (a) the mass being different in different directions
- (b) the presence of rotational inertia terms.

*Energies*

Energies are available by setting

$$E_e^{po} = \begin{cases} \frac{1}{2} \sum_{i=1}^{NINT} \{\sigma\}^T \{\varepsilon^{el}\} \text{vol}_i + E_e^{pl} & \text{if element allows only displacement and rotational degree of freedom (DOF), and either is non linear or uses integration points} \\ \frac{1}{2} \{u\}^T [K_e] \{u\} & \text{all other cases} \end{cases} \tag{A.71}$$

= potential energy

$$E_e^{ki} = \frac{1}{2} \{\dot{u}\}^T [M_e] \{\dot{u}\} \tag{A.72}$$

= kinetic energy

$$E_e^{pl} = \sum_{i=1}^{NINT} \sum_{j=1}^{NCS} \{\sigma\}^T \{\Delta\varepsilon^{pl}\} \text{vol}_i \tag{A.73}$$

= plastic energy

where

- $\{u\}$  = element DOF vector
- $\{\dot{u}\}$  = time derivative of element DOF vector
- $\{K_e\}$  = element stiffness/conductivity matrix
- $[M_e]$  = element mass matrix
- NINT = number of integration points
- NCS = total number of converged substeps
- $\{\sigma\}$  = stress vector
- $\{\varepsilon^{el}\}$  = elastic strain vector
- $\{\Delta\varepsilon^{pl}\}$  = plastic strain increment
- $vol_i$  = volume of integration points.

*Aircraft Impact*

The design and analysis of a containment vessel to withstand the effect of an aircraft crash or impact involves many complex parameters, including loadings and durations. Bangash [1.40] has produced modified force-time impact functions for various aircraft, and these are shown in Fig. A.I.1. First, the

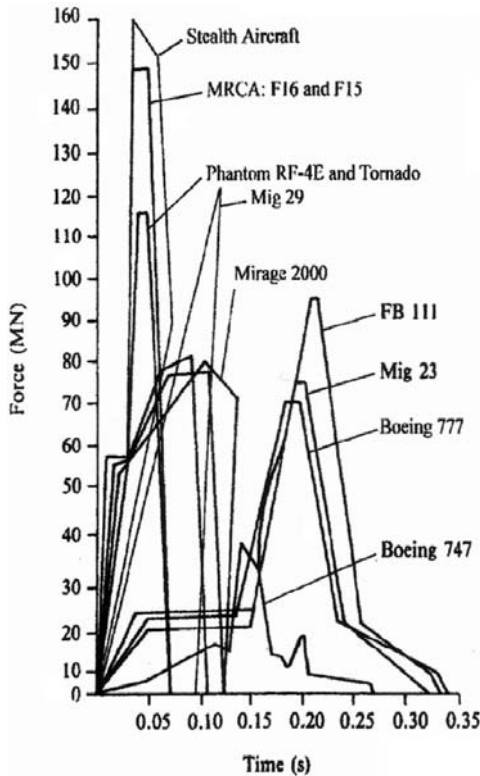


Fig. A.I.1. Force-time function for aircraft impact

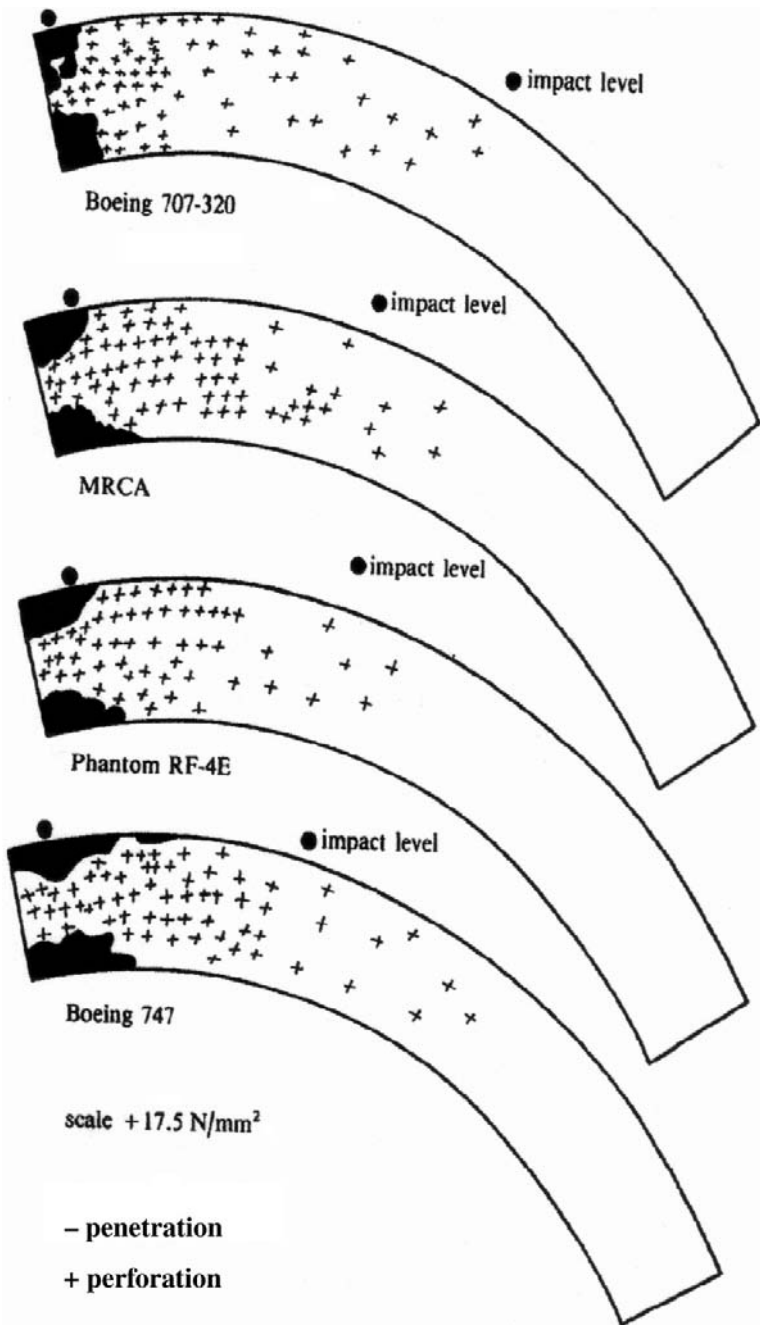


Fig. A.I.2. Stresses ( $\text{N/mm}^2$ ) is dome shell

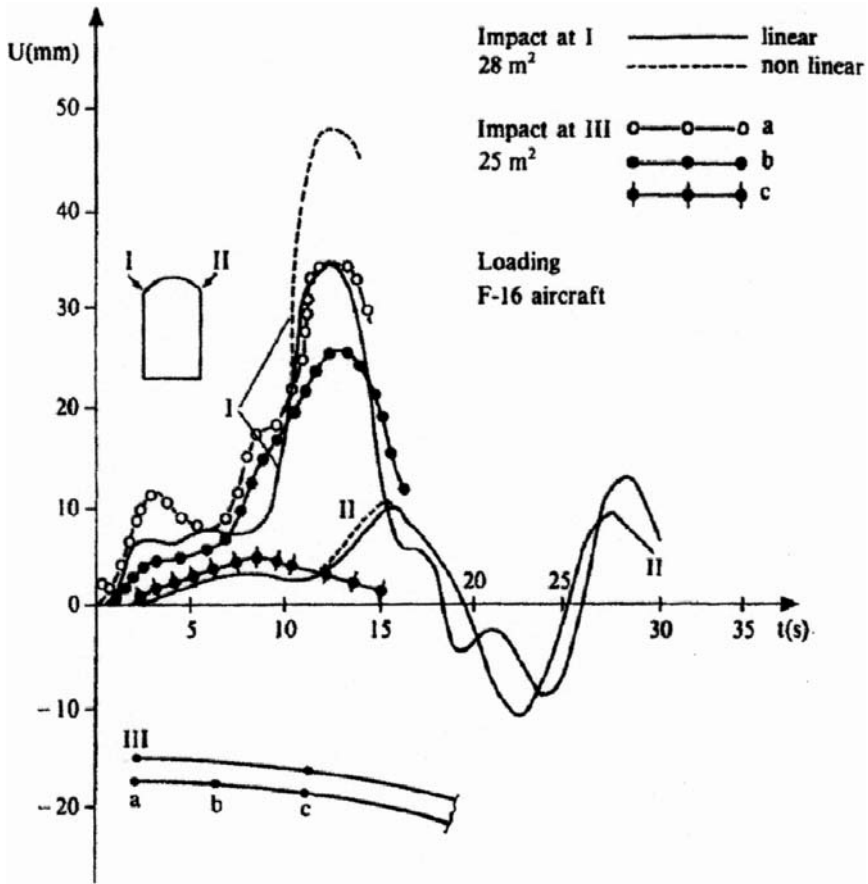


Fig. A.I.3. Linear and nonlinear displacement as a function of time

Bellefonte vessel parameters were chosen for the analysis. The impact point is chosen to be the apex of the vessel and at junction of the dome and the cylinder. Results are produced in the form of acceleration-time histories, displacements and stress stated for selected times and acceleration response spectra. Newmark and Wilson  $\theta$  direct integration methods are used for the analysis.

Crack propagation, and linear and nonlinear displacements for four aircraft are shown in Figs. A.I.2 to A.I.3a. The impact zones are shown in Fig. A.I.2 and also shows comparative results for penetrations and perforations based on both empirical and finite element analysis for a number of aircraft impact loads. The endochronic model is used throughout the analysis. A similar analysis was carried out for the Sizewell B vessel using load-time functions for Phantom and Tornado aircraft. The 'post-mortem' of the vessel is shown in Fig. A.I.4. The load-displacement as a function of time is given Fig. A.I.4.

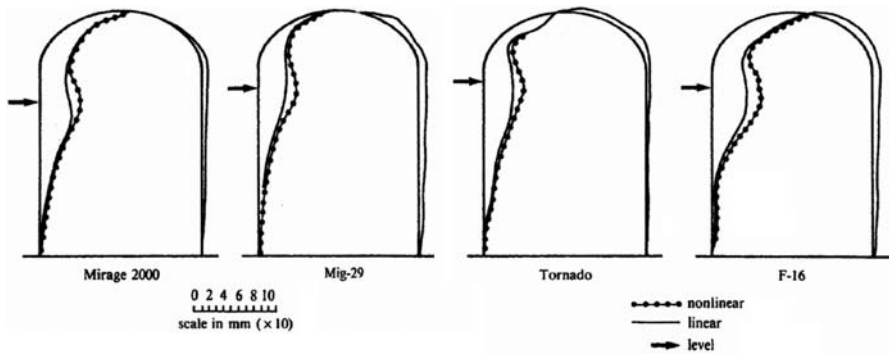


Fig. A.I.3a. Linear and nonlinear displacements for impacts due to four aircraft

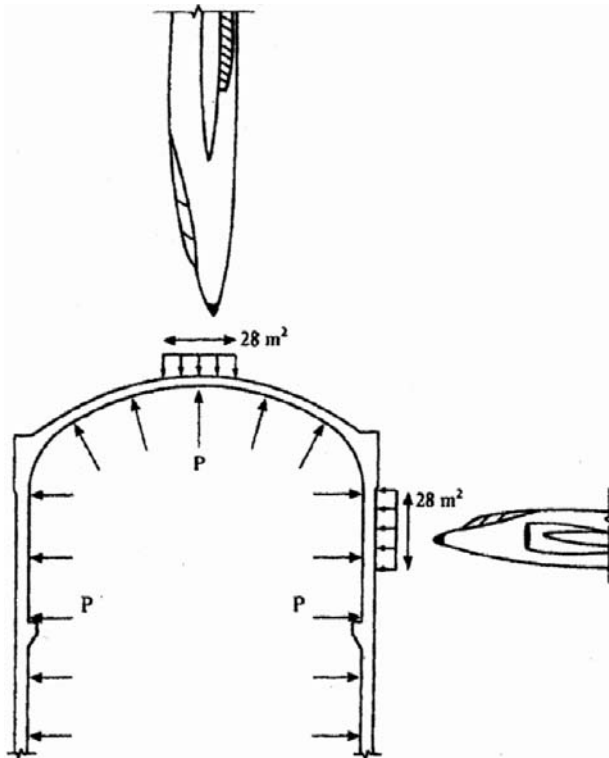


Fig. A.I.3b. Extreme loading condition

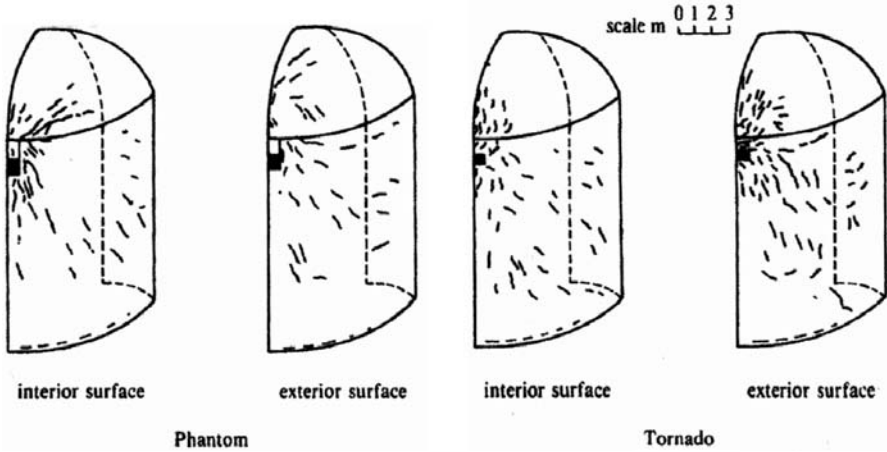


Fig. A.I.4. Phantom and Tornado aircraft impact 'post-mortem'

**I.1 General Steps of Crack Flow and Crack Calculations  
(Tests on PWR Containment Reactor Building)**

- (1) The load increment  $\{\Delta P_n\}$  is applied where  $n$  is the load increment.
- (2) The total is accumulated as  $\{P_n\} = \{P_{n-1}\} + \{\Delta P_n\}$ , and  $\{R\} = \{\Delta P_n\}$ , where  $\{R\}$  is the residual load vector.
- (3) Incremental displacement is computed as  $\{\Delta U_i\} = [K]_e^{-1}\{R\}$ , where  $i$  is the iteration.
- (4) Total displacements are now accumulated in the following form:  $\{U_i\} = \{U_{i-1}\} + \{\Delta U_i\}$ .
- (5) Strain increments are calculated from step 4 as  $\{\Delta \varepsilon_i\} = [B]\{\Delta U_i\}$ . The accumulated strains at this stage would then be written as

$$\{\varepsilon_i\} = \{\varepsilon_{i-1}\} + \{\Delta \varepsilon_i\}$$

- (6) The stress increments are calculated using the current nonlinear constitutive matrices of various models described earlier:  $\{\Delta \sigma_i\} = \{f(\sigma)\}\{\Delta \varepsilon\}$ . The accumulated stresses are computed as  $\{\sigma_i\} = \{\sigma_{i-1}\} + \{\Delta \sigma_i\}$ . In order to differentiate stresses at elastic and plastic conditions, a stress point indicator  $I_p$  is introduced.

- $I_p = 0$  (elastic point)
- $= 1$  (plastic point)
- $= 2$  (unloading from plastic state)

- (7) The stress increment is calculated using the elastic material matrix as  $\{\Delta \sigma'_i\} = [D']\{\Delta \varepsilon\}$ . Total stresses are given as  $\{\sigma'_i\}_T = \{\sigma_{i-1}\} - \{\Delta \sigma'_i\}$ .
- (8) The stress  $\{\sigma_i\}$  is now calculated using step 7:  $\{\sigma_i\} = \{f(\sigma'_i)\}$ ,  $\{\sigma_{i-1}\} = \{f(\sigma_{i-1}) - \text{any yield criterion required}\}$ .
- (9) If a plastic point is obtained, step 11 should be considered.



- (10) If  $\sigma_i \geq \sigma_y$  - plastic point ( $I_p = 1$ ), transition from elastic to plastic, calculate factor  $F_{\text{TP}}$ :

$$F_{\text{TP}} = \left( \frac{\sigma_y - \bar{\sigma}_{i-1}}{\sigma_i - \sigma_{i-1}} \right)$$

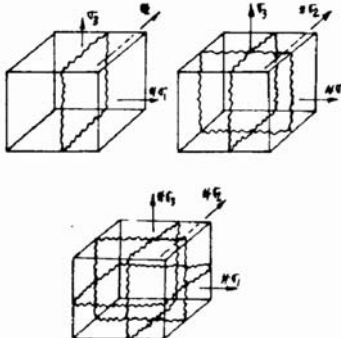
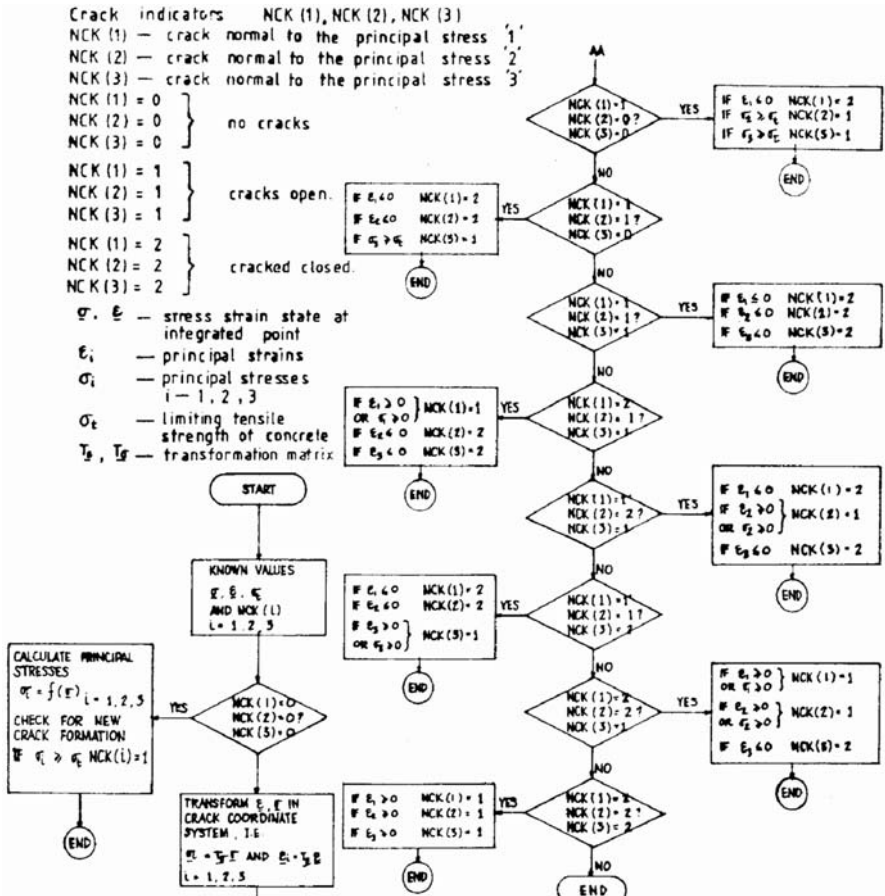
The stress at the yield surface  $\{\sigma_i\}_y^* = \{\sigma_{i-1}\} + F_{\text{TP}}^* \{\Delta\sigma_i\}$ . Elasto-plastic stress increments are calculated as  $\{\Delta\sigma_i\} = [D]_{\text{ep}} \{\sigma_i\}^* (1 - F_{\text{TP}}) \{\Delta\varepsilon\}$ . Total stress  $\{\sigma_i\}_T = \{\sigma_i\} + \{\Delta\sigma_i\}$ .

- (11) Plastic point from steps 9 and 10, check for unloading, i.e. if  $\bar{\sigma} \geq \sigma_y$  it is necessary to proceed to step 12. For the unloading case at this point, set  $I_p = 2$ , total stress  $\{\sigma_i\}_T$  then given by  $\{\sigma_i\} = \{\sigma_{i-1}\} + \{\Delta\sigma_i\}$ . Set  $\{\sigma_y\} = \{\bar{\sigma}_{i-1}\}$ , and the procedure is repeated for the additional increments.
- (12) Loading at this point  $\{\Delta\sigma_i\} = [D]_{\text{ep}} \{\bar{\sigma}_{i-1}\} \{\Delta\varepsilon\}$ . Total stress  $\{\sigma_i\}_T = \{\bar{\sigma}_{i-1}\} + \{\Delta\varepsilon\}$ .
- (13) Sometimes it is necessary to correct stresses from the equivalent stress-strain curve:  $\sigma_{\text{corr}} = \sigma_{i-1} + S_H \Delta\varepsilon_p$ , where  $\Delta\varepsilon_p = \sqrt{\frac{2}{3} \Delta\varepsilon_{ij}^p \Delta\varepsilon_{ij}^p}$  = equivalent plastic strain increment.  $S_H$  is the strain hardening parameter, such that  $\Delta\bar{\varepsilon}_p = \lambda$ .
- Equivalent stress, calculated from the current stress state, is given by  $\{\sigma_i\} = F_{\text{TP}} \{\sigma_i\}$ . The correct stress state, which is on the yield surface, will therefore be given as  $\{\sigma_i\} = F_{\text{TP}} \{\sigma_i\}$ . The total stresses are converted into equivalent nodal loads from  $\int_{\nu} [B]^T \{\sigma_i\} d \text{vol}$ , and the residual load vector is calculated from  $\{R\} = \{F_n\} - \int_{\nu} [B]^T \{\sigma_i\} d \text{vol}$ .
- (14) Check for convergence.

$$(\|R\|/\|F\|) \leq \text{TOL} \quad (\|\Delta U\|/\|U\|) \leq \text{TOL}$$

where TOL is chosen from 0.01 to 0.001;  $\|R\| = \sqrt{R_i^T R_i}$  is the Euclidean norm of the residuals;  $\|F\| = \sqrt{P^T P}$  is the Euclidean norm of the externally applied load; and  $\|\Delta U\| = \sqrt{\Delta U_i^T U_i}$  is the Euclidean norm. If convergence is not achieved, step 3 is invoked and all the steps repeated for the next iteration. If convergence is achieved, then proceed with the next load increment.

I.2 Flow Chart on Cracking Phenomenon



CRACK IN PRINCIPAL DIRECTIONS THREE AND ONE

$$D_{11}^m = D_{33}^m = D_{12}^m = D_{21}^m = 0$$

$$D_{13}^m = D_{31}^m = D_{23}^m = D_{32}^m = 0$$

$$D_{22}^m \quad D_{22} - D_{12} D_{12} \quad - D_{23} \quad D_{23}$$

$$D_{11} \quad D_{33}$$

$$D_{44}^m = \beta D_{44}$$

$$D_{55}^m = \beta D_{55}$$

$$D_{66}^m = \beta D_{66}$$

CRACKS IN ALL THREE PRINCIPAL DIRECTIONS

$$[D^m] = [0]$$

### I.3 Program ISOPAR to Print Displacements and (if ISTAT.NE.0) Velocities and Accelerations (Part of Bang-F)

*(Jointly developed by J. Tang and the author.)*

#### Part of PROG BANG-BLAST

```

IND.EQ.0, PRINT DISPL/VEL/ACC AT ALL NODES
IND.NE.0, PRINT DISPL/VEL/ACC ONLY AT NODES
          CONTAINED IN PRINTOUT BLOCKS

COMMON/EL/IND,ICOUNT,NPAR(20),NUMEG,NEGL,NEGNL,IMASS,IDAMP,ISTAT,
1         NDOFDM,KLIN,IEIG,IMASSN,IDAMPN
COMMON/PRCON/NPB,IDC,IVC,IAC,IPC,IPNODE(2,8)
DIMENSION DISP(NEQ),VEL(NEQ),ACC(NEQ),ID(NDOF,1)
DIMENSION D(6)

READ ID ARRAY INTO CORE

REWIND 8
NDBLK=NUMNP
READ(8)((ID(I,J),I=1,NDOF),J=1,NUMNP)

PRINT DISPLACEMENTS

IC=4
IF(IND.EQ.0) GO TO 10
IF(IND.EQ.0) GO TO 180
10 WRITE(6,2000)
   WRITE(1,2000)
   IC=IC+5
   DO 150 IB=1,NPB
     NODE1=IPNODE(1,IB)
     IF(NODE1.EQ.0) GO TO 150
     NODE2=IPNODE(2,IB)
     IF(IND.EQ.0)NODE1=1
     IF(IND.EQ.0)NODE2=NUMNP

   DO 100 II=NODE1,NODE2
     IC=IC+1
     IF(IC.LT.56) GO TO 105
     WRITE(6,2045)

   WRITE(1,2045)
   IC=4
105 DO 110 I=1,6
110 D(I)=0.
     DO 120 I=1,NDOF

```

```

      KK=ID(I,II)
      IL=I
      IF(NDOF.EQ.2) IL=I+1
120 IF(KK.NE.0)D(IL)=DISP(KK)
      WRITE(1,2010) II,D
100 WRITE(6,2010) II,D

      IF(IND.EQ.0) GO TO 180
      IF(IC.GE.55) GO TO 150
      IC=IC+1
      WRITE(6,2050)
      WRITE(1,2050)
150 CONTINUE
180 IF(ISTAT.EQ.0)RETURN
      PRINT VELOCITIES
305 IC=IC+5
      WRITE(6,2030)
      WRITE(1,2030)
308 DO 350 IB=1,NPB
      NODE1=IPNODE(1,IB)
      IF(NODE1.EQ.0) GO TO 350
      NODE2=IPNODE(2,IB)
      IF(IND.EQ.0) NODE1=1
      IF(IND.EQ.0) NODE2=NUMNP

      DO 300 II=NODE1,NODE2
      IC=IC+1
      IF(IC.LT.56) GO TO 307
      WRITE(6,2032)
      WRITE(1,2032)
      IC=4
307 DO 310 I=1,6
310 D(I)=0.
      DO 320 I=1,NDOF
      KK=ID(I,II)
      IL=I
      IF(NDOF.EQ.2) IL=I+1
320 IF(KK.NE.0) D(IL)=ACC(KK)
      WRITE(1,2010) II,D
300 WRITE(6,2010) II,D

      IF(IND.EQ.0) RETURN
      IF(IC.GE.55) GO TO 350
      IC=IC+1
      WRITE(6,2050)
      WRITE(1,2050)
350 CONTINUE

      RETURN

```

**Subroutine CRACKD (PROP,NCK,SIG,EPS,PS1,PS2,PS3,  
DC1,DC2,DC3) IMPLICIT REAL\*8(A-H,O-Z)**

SET UP MATERIAL MATRICES FOR CRACKED CONCRETE

```

COMMON/MTMD3D/D(6,6),STRESS(6),STRAIN(6),IPT,NEL
DIMENSION DD(6,6),PROP(1),NCK(1),SIG(1),EPS(1),
@      PS1(1),PS2(1),PS3(1),DC1(1),DC2(1),DC3(1)
CALL PRINCL (IPT,STRESS,PS1,PS2,PS3,DC1,DC2,DC3)
CALL RCMOD (PROP,D)
CALL DMAT (PROP,NCK)
DO 222 I=1,6

DO 222 J=1,6
222 DD(I,J)=0.0
  JJJ=1
  LL=0
  IF(NCK(1).EQ.1)LL=1
  IF(NCK(2).EQ.1)LL=2
  IF(NCK(3).EQ.1)LL=3
  IF(NCK(1).EQ.1).AND.NCK(2).EQ.1)LL=4
  IF(NCK(2).EQ.1).AND.NCK(3).EQ.1)LL=5
  IF(NCK(1).EQ.1).AND.NCK(3).EQ.1)LL=6
  IF(NCK(1).EQ.1).AND.NCK(2).EQ.1.AND.NCK(3).EQ.1)LL=7

  IF(LL.EQ.7) GOTO 99
  IF(JJJ.EQ.0) GOTO 200
  IF(LL.EQ.0) GOTO 999
  GOTO(113,114,115,116,117,118),LL

  ONLY ONE DIRECTION CRACKED

113 CONTINUE

  CRACK IN DIRECTION 1
  DD(1,1)=0.0
  DD(1,2)=0.0
  DD(1,3)=0.0
  DD(2,1)=0.0
  DD(2,2)=D(2,2)-D(1,2)*D(1,2)/D(1,1)
  DD(2,3)=D(2,3)-D(1,3)*D(1,2)/D(1,1)
  DD(3,1)=0.0
  DD(3,2)=DD(2,3)
  DD(3,3)=D(3,3)-D(1,3)*D(1,3)/D(1,1)
  DD(4,4)=PROP(12)*D(4,4)
  DD(5,5)=DD(5,5)
  DD(6,6)=PROP(12)*D(6,6)
  GOTO 121
114 CONTINUE

```

CRACK IN DIRECTION 2

```

DD(1,1)=D(1,1)-D(2,1)*D(2,1)/D(2,2)
DD(1,2)=0.0
DD(1,3)=D(1,3)-D(1,2)*D(2,3)/D(2,2)
DD(2,1)=0.0
DD(2,2)=0.0
DD(2,3)=0.0
DD(3,1)=DD(1,3)
DD(3,2)=0.0
DD(3,3)=D(3,3)-D(2,3)*D(2,3)/D(2,2)
DD(4,4)=PROP(12)*D(4,4)
DD(5,5)=PROP(12)*D(5,5)
DD(6,6)=D(6,6)
GOTO 121
115 CONTINUE

```

CRACK IN DIRECTION 3

```

DD(1,1)=D(1,1)-D(1,3)*D(1,3)/D(3,3)
DD(1,2)=D(1,2)-D(1,3)*D(2,3)/D(3,3)
DD(1,3)=0.0
DD(2,1)=DD(1,2)
DD(2,2)=D(2,2)-D(2,3)*D(2,3)/D(3,3)
DD(2,3)=0.0
DD(3,1)=0.0
DD(3,2)=0.0
DD(3,3)=0.0
DD(4,4)=D(4,4)
DD(5,5)=D(5,5)*PROP(12)
DD(6,6)=D(6,6)*PROP(12)
GOTO 121
116 CONTINUE

```

CRACKS IN TWO DIRECTIONS  
 CRACKS IN DIRECTIONS 1 & 2

```

DENOM=D(1,1)*D(2,2)-D(1,2)*D(2,1)
DD(1,1)=0.0
DD(1,2)=0.0
DD(1,3)=0.0
DD(2,1)=0.0
DD(2,2)=0.0
DD(2,3)=0.0
DD(3,1)=0.0
DD(3,2)=0.0
DD(3,3)=D(3,3)
1      -D(3,1)*(D(2,2)*D(1,3)-D(1,2)*D(2,3))/DENOM
2      -D(3,2)*(D(1,1)*D(2,3)-D(2,1)*D(3,1))/DENOM

```

```

DD(4,4)=PROP(12)*D(4,4)
DD(5,5)=PROP(12)*D(5,5)
DD(6,6)=PROP(12)*D(6,6)
GOTO 121
117 CONTINUE

CRACKS IN DIRECTIONS 3 & 2

DENOM=D(2,2)*D(3,3)-D(2,3)*D(3,2)
DD(1,1)=D(1,1)
1      -D(1,2)*(D(3,3)*D(2,1)-D(3,1)*D(2,3))/DENOM
2      -D(1,3)*(D(2,2)*D(3,1)-D(2,1)*D(3,2))/DENOM
DD(1,2)=0.0
DD(1,3)=0.0
DD(2,1)=0.0
DD(2,2)=0.0
DD(2,3)=0.0
DD(3,1)=0.0
DD(3,2)=0.0
DD(3,3)=0.0
DD(4,4)=PROP(12)*D(4,4)
DD(5,5)=PROP(12)*D(5,5)
DD(6,6)=PROP(12)*D(6,6)
GOTO 121
118 CONTINUE

CRACKS IN DIRECTIONS 1 & 3

DENOM=D(1,1)*D(3,3)-D(3,2)*D(1,3)
DD(1,1)=0.0
DD(1,2)=0.0
DD(1,3)=0.0
DD(2,1)=0.0
DD(2,2)=D(2,2)
1      -D(2,1)*(D(3,3)*D(1,2)-D(3,2)*D(1,3))/DENOM
2      -D(2,3)*(D(1,1)*D(3,2)-D(3,1)*D(1,2))/DENOM
DD(2,3)=0.0
DD(3,1)=0.0
DD(3,2)=0.0
DD(3,3)=0.0
DD(4,4)=PROP(12)*D(4,4)
DD(5,5)=PROP(12)*D(5,5)
DD(6,6)=PROP(12)*D(6,6)
121 CONTINUE
GOTO 99
200 CONTINUE
IF(LL.EQ.0) GOTO 999

GOTO(1,2,3,4,5,6),LL

```

```
1 CONTINUE
  DD(2,2)=D(2,2)
  DD(2,3)=D(2,3)
  DD(3,2)=DD(2,3)
  DD(3,3)=D(3,3)
  DD(4,4)=PROP(12)*D(4,4)
  DD(5,5)=PROP(12)*D(5,5)
  DD(6,6)=PROP(12)*D(6,6)
  GOTO 99
2 CONTINUE
  DD(1,1)=D(1,1)
  DD(1,3)=D(2,3)
  DD(3,1)=D(1,3)
  DD(3,3)=D(3,3)
  DD(4,4)=PROP(12)*D(4,4)
  DD(5,5)=PROP(12)*D(5,5)
  DD(6,6)=D(6,6)
  GOTO 99
3 CONTINUE
  DD(1,1)=D(1,1)
  DD(2,2)=D(2,2)
  DD(1,2)=D(1,2)
  DD(3,3)=D(3,3)
  DD(2,1)=DD(1,2)
  DD(4,4)=D(4,4)
  DD(5,5)=PROP(12)*D(5,5)
  DD(6,6)=PROP(12)*D(6,6)
  GOTO 99
4 CONTINUE
  DD(3,3)=D(3,3)
  DD(4,4)=PROP(12)*D(4,4)
  DD(5,5)=PROP(12)*D(5,5)
  DD(6,6)=PROP(12)*D(6,6)
  GOTO 99
5 CONTINUE
  DD(1,1)=D(1,1)
  DD(4,4)=PROP(12)*D(4,4)
  DD(5,5)=PROP(12)*D(5,5)
  DD(6,6)=PROP(12)*D(6,6)
  GOTO 99
6 CONTINUE
  DD(2,2)=D(2,2)
  DD(4,4)=D(4,4)
  DD(5,5)=D(5,5)
  DD(6,6)=D(6,6)
99 CONTINUE

  CRACKS IN ALL THREE DIRECTIONS
  TRANSFER DD TO D
```



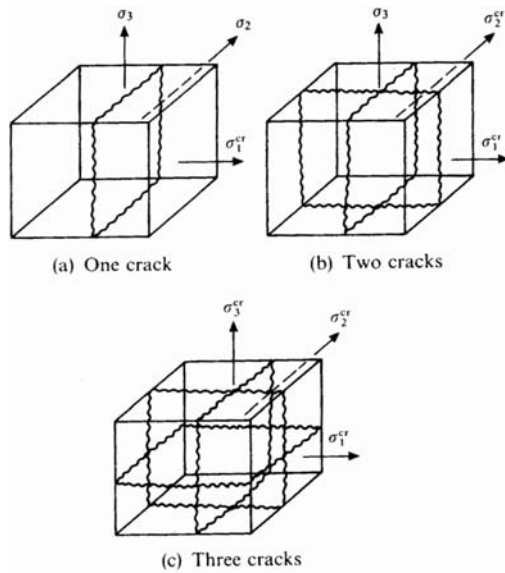
```

DO 101 J=1,6
DO 101 K=1,6
D(J,K)=DD(J,K)
101 CONTINUE
999 CONTINUE
RETURN
END
    
```

**Table A.I.1.** Computer program ISOPAR: Material models subroutines

*Cracks in all three principal directions*

$$[D^*] = [0]$$



*Material Matrix for Reinforcement*

```

IMPLICIT REAL*8(A-H,O-Z)
COMMON/MTMD3D/D(6,6),STRESS(6),STRAIN(6),IPT,NEL
DIMENSION PROP(1),DS(6,6),SIG(1),EPS(1),NCK(1),PSI(1),PS2(1),
1      PS3(1),DC1(1),DC2(1),DC3(1)
DO 111 II=1,6
DO 111 JJ=1,6
111 DS(II,JJ)=0.0
DS(1,1)=PROP(9)/PROP(6)*PROP(2)
DS(2,2)=PROP(10)/PROP(7)*PROP(2)
    
```

```

DS(3,3)=PROP(11)/PROP(8)*PROP(2)
CALL TESTCK(PROP,SIG,EPS,NCK.PS1,PS2,PS3,DC1,DC2,DC3)
IF(NCK(1).EQ.1.OR.NCK(2).EQ.1.OR.NCK(3).EQ.1)
@   GOTO 220
CALL DMAT(PROP,NCK)
220 DO 222 III=1,6
    DO 222 JJJ=1,6
222 D(III,JJJ)=D(III,JJJ)+DS(III,JJJ)
    RETURN
END

```

### *Orthotropic Variable-Modulus Model for Concrete*

```

IMPLICIT REAL*8(A-H,O-Z)
DIMENSION E(3),G(3,3),D(6,6),PROP(1)
DO 222 II=1,6
DO 222 JJ=1,6
222 D(II,JJ)=0.0
AA=(1.0-PROP(S))/(1.0 + PROP(5))*(1.0-2.0*PROP(5))
BB=PROP(5)/(1.0-PROP(5))
E(1)=PROP(12)*PROP(1)*PROP(6)+PROP(2)*PROP(9)
E(2)=PROP(12)*PROP(1)*PROP(7)+PROP(2)*PROP(10)
E(3)=PROP(12)*PROP(1)*PROP(8)+PROP(2)*PROP(11)
DO 7100 J=1,3
DO 7100 K=1,3
7100 G(J,K)=0.25*(AA*(E(J) + E(K)))-2.0*AA*BB*DSQRT(E(J)*E(K))
D(1,1)=AA*E(1)
D(1,2)=AA*BB*DSQRT(E(1)*E(2))
D(1,3)=AA*BB*DSQRT(E(1)*E(3))
D(2,1)=D(1,2)
D(2,2)=AA*E(2)
D(2,3)=BB*DSQRT(E(2)*E(3))
D(3,1)=D(1,3)
D(3,2)=D(2,3)
D(3,3)=AA*E(3)
D(4,4)=G(1,2)
D(5,5)=G(1,3)
D(6,6)=G(2,3)
RETURN
END

```

### *Ottoson Model*

```

IMPLICIT REAL*8(A-H,O-Z)
COMMON/MTMD3D/DEP(6,6),STRESS(6),STRAIN(6),IPT,NEL
DIMENSION PAR(3,5),FS(6,6),FSTPOS(6,6),PROP(1),SIG(1),
@   DVI1DS(6),DVJ2DS(6),DVJ3DS(6),DVTHDS(6)
OPEN(UNIT=5,FILE='PARAMETERS',STATUS='OLD')
READ(5,*,END=3700)((PAR(IF,JF),JF=1,5),IF=1,3)

```

```

3700 CLOSE(5)
    PK=PROP(3)/PROP(4)
    IP=0
    JP=0
    IF(PK.LE.0.08) IP=1
    IF(PK.EQ.0.10) IP=2
    IF(PK.GE.0.12) IP=3
    IF(PK.LT.0.10) JP=1
    IF(PK.GT.0.10) JP=2
    IF(IP.EQ.0) GOTO 3800
    A=PAR(IP,2)
    B=PAR(IP,3)
    PK1=PAR(IP,4)
    PK2=PAR(IP,5)
    GOTO 3900
3800 SUB1=PK-PAR(JP,1)
    SUB2=PAR(JP+1,1)-PAR(JP,1)
    A=SUB1*(PAR(JP+1,2)-PAR(JP,2))/SUB2+PAR(JP,2)
    B=SUB1*(PAR(JP+1,3)-PAR(JP,3))/SUB2+PAR(JP,3)
    PK1=SUB1*(PAR(JP+1,4)-PAR(JP,4))/SUB2+PAR(JP,4)
    PK2=SUB1*(PAR(JP+1,5)-PAR(JP,5))/SUB2+PAR(JP,5)
3900 VARI1=SIG(1)+SIG(2)+SIG(3)
    VARJ2=1.0/6.0*((SIG(1)-SIG(2))**2+(SIG(2)-SIG(3))**2+
    @ (SIG(3)-SIG(1))**2)+ SIG(4)**2+SIG(5)**2+SIG(6)**2
    VARI13=VARI1/3.0
    VI131=SIG(1)-VARI13
    VI132=SIG(2)-VARI13
    VI133=SIG(3)-VARI13
    VARJ3=VI131*(VI132*VI133-SIG(5)**2)-SIG(4)*(SIG(4)*VI133
    @ -SIG(5)*SIG(5))+ SIG(6)*(SIG(4)*SIG(5)-SIG(6)*VI132)
    VAR3TH=1.5*3.0**(0.5)*VARJ3/VARJ2**1.5
    IF(VAR3TH.GE.0.0) GOTO 4000
    ALAM=22.0/21.0-1.0/3.0*ACOS(-PK2*VAR3TH)
    TOTLAM=PK1*COS(ALAM)
    DFD3TH=PK1*PK2*VARJ2**0.5*SIN(ALAM)/(3.0*PROP(4)*
    @ SIN(ACOS(-PK2*VAR3TH)))
    GOTO 4100
4000 ALAM=1.0/3.0*ACOS(PK2*VAR3TH)
    TOTLAM=PK1*COS(ALAM)
    DFD3TH=PK1*PK2*VARJ2**0.5*SIN(ALAM)/(3.0*PROP(4)*
    @ SIN(ACOS(PK2*VAR3TH)))
4100 DFDI1=B/PROP(4)
    DFDJ2=A/PROP(4)**2+TOTLAM/(PROP(4)*VARJ2**0.5)
    DVI1DS(1)=1.0
    DVI1DS(2)=1.0
    DVI1DS(3)=1.0
    DVI1DS(4)=0.0
    DVI1DS(5)=0.0
    DVI1DS(6)=0.0

```

```

DVJ2DS(1)=1.0/3.0*(2.0*SIG(1)-SIG(2)-SIG(3))
DVJ2DS(2)=1.0/3.0*(2.0*SIG(2)-SIG(1)-SIG(3))
DVJ2DS(3)=1.0/3.0*(2.0*SIG(3)-SIG(1)-SIG(2))
DVJ2DS(4)=2.0*SIG(4)
DVJ2DS(5)=2.0*SIG(5)
DVJ2DS(6)=2.0*SIG(6)
DVJ3DS(1)=1.0/3.0*(VI131*(-VI132-VI133))+2.0*VI132*VI131
@      -2.0*SIG(5)**2+SIG(4)**2+SIG(6)**2
DVJ3DS(2)=1.0/3.0*(VI132*(-VI131-VI133))+2.0*VI131*VI133
@      -2.0*SIG(6)**2+SIG(4)**2+SIG(5)**2
DVJ3DS(3)=1.0/3.0*(VI133*(-VI131-VI132))+2.0*VI131*VI132
@      -2.0*SIG(4)**2+SIG(5)**2+SIG(6)**2
DVJ3DS(4)=-2.0*VI133*SIG(4)+2.0*SIG(5)*SIG(6)
DVJ3DS(5)=-2.0*VI131*SIG(5)+2.0*SIG(4)*SIG(6)
DVJ3DS(6)=-2.0*VI132*SIG(6)+2.0*SIG(4)*SIG(5)
CONVJ2=3.0*3.0**0.5/(2.0.VARJ2*1.2)
VJ3J2=VARJ3/VARJ2**0.5
DVTHDS(1)=CONVJ2*(-0.5*VJ3J2*(2.0*SIG(1)-SIG(2)-SIG(3))
      +DVJ3DS(1))
DVTHDS(2)=CONVJ2*(-0.5*VJ3J2*(2.0*SIG(2)-SIG(1)-SIG(3))
      +DVJ3DS(2))
DVTHDS(3)=CONVJ2*(-0.5*VJ3J2*(2.0*SIG(3)-SIG(1)-SIG(2))
      +DVJ3DS(3))
DVTHDS(4)=CONVJ2*(-3.0*VJ3J2*SIG(4)+DVJ3DS(4))
DVTHDS(5)=CONVJ2*(-3.0*V33J2*SIG(5)+DVJ3DS(5))
DVTHDS(6)=CONVJ2*(-3.0*VJ3J2.SICA6)+DVJ3DS(6)
DO 4200 IS=1,6
FS (IS, 1)=DFDI1*DVI1DS (IS)+DFDJ2*DVJ2DS (IS)+DFD3TH*DVTHDS (IS)
4200 FSTPDS (1, IS)=FS (IS, 1)
      RETURN
      END

```

**Table A.I.2.** Algorithm for principal stresses

Principal stresses and direction cosines D1, D2, D3 are the direction cosines of principal stresses PS1, PS2, PS3.

```

IF(X5.GE.X6.AND.X6.GE.X7) GOTO 430
IF(X5.GE.X7.AND.X7.GE.X6) GOTO 431
IF(X6.GE.X5.AND.X5.GE.X7) GOTO 432
IF(X6.GE.X7.AND.X7.GE.X5) GOTO 433
IF(X7.GE.X5.AND.X5.GE.X6) GOTO 434
IF(X7.GE.X5.AND.X6.GE.X5) GOTO 435
430 X1=X5
      X2=X6
      X3=X7
      GOTO 438
431 X1=X5
      X2=X7
      X3=X6

```

```

      GOTO 438
432 X1=X6
      X2=X5
      X3=X7
      GOTO 438
433 X1=X6
      X2=X7
      X3=X5
      GOTO 438
434 X1=X7
      X2=X5
      X3=X6
      GOTO 438
435 X1=X7
      X2=X6
      X3=X5
438 CONTINUE

```

```

      PRINCIPAL STRESSES
      PS1(IPT)=X1
      PS2(IPT)=X2
      PS3(IPT)=X3
      DO 440 IS=1,3
      GOTO (443,445,447),IS
443 AS1=G1-X1
      AS2=G2-X1
      AS3=G3-X1
      GOTO 444
445 AS1=G1-X2
      AS2=G2-X2
      AS3=G3-X2
      GOTO 444
447 AS1=G1-X3
      AS2=G2-X3
      AS3=G3-X3
444 CONTINUE
      AK=G4
      BK=G5
      CK=G6
      YAP1=AS2*CK-BK*AK
      YAP2=AK*AK-AS1*AS2
      IF(YAP1.EQ.0.0) YAP1=1.0
      IF(YAP2.EQ.0.0) YAP2=1.0
      BJM1=(BK*BK-AS2*AS3)/YAP1
      BJM2=(AS1*BK-AK*CK)/YAP2
      BJ1=BJM1*BJM1
      BJ2=BJM2*BJM2
      ZIP=DSQRT(BJ1+BJ2+1.0)

```

---

## A Computer Program for the Analysis of Concrete Elements Subject to Fire

This program was developed by R. Karuna for his MSc Thesis, City University, London, UK, 1996. Reproduced here by courtesy of R. Karuna.

Note that the author has assisted him in programming and analysis for two years.

### Part A

```
c PROGRAM FOR CALCULATING OVERALL STRESS OF
c PRESTRESSED CONCRETE BEAM DUE TO THE EFFECTS
c OF TEMPERATURE, PRESTRESS, POINT LOADS AND
c UNIFORMLY DISTRIBUTED LOAD.
```

```
REAL X(75),Y(75),D(75),TEa,e,H,Yj,B,T,SIGAV,
+SIGP,SIG,L,F(20),a(20),c,W,PREFOE,SA,NA,
+SEMO,ARE
```

```
WRITE(*,*) 'B=', 'T=', 'H=', 'Yj='
```

```
READ(*,*) B,T,H,Yj
```

```
WRITE(*,*) 'L=', 'c=', 'W='
```

```
READ(*,*) L,c,W
```

```
WRITE(*,*) 'e=', 'PREFOE=', 'SA='
```

```
READ(*,*) e,PREFOE,SA
```

```
WRITE(*,*) 'NO OF NODES'
```

```
WRITE(*,*) 'X=', 'Y='
```

```
WRITE(*,*) 'M=', 'F=', 'a='
```

```
CALL SEMO3(B,T,H,e,SA,NA,m1,ARE,D,AvE,SEMO)
```

```
WRITE(*,*) 'SEMO', 'NA', 'SA'
```

```
WRITE(*,*) SEMO,NA,SA
```

```
CALL tele(X,Y,B,T,H,Yj,D,SIGAV,L,F,
```

```
+W,a,c,SEMO,NA)
```

```
WRITE(*,*) 'SIGAV'
```

```
WRITE(*,*) SIGAV
```

```
CALL telep(B,H,T,e,Yj,0,TEa,SIGP,SA,
```

```
+PREFOE,NA,SEMO)
```

```
WRITE(*,*) 'SIGP'
```

```
WRITE(*,*) SIGP
```

```
SIG=SIGAV+SIGP
```

```
WRITE(*,*) 'SIG'
```

```
WRITE(*,*) SIG
```

```
END
```

```
c SUBROUTINE FOR CALCULATING AVERAGE STRESS
c OF CONCRETE BEAM DUE TO TEMPERATURE EFFECT.
```

```
SUBROUTINE tele(X,Y,B,T,H,Yj,D,SIGAV,L,F,
+W,a,c,SEMO,NA)
```

```
INTEGER I,N
```

```
REAL X(75),Y(75),D(75),Y1(75),F(20),W,
```

```
+TEa(20),E(20),SIGAV3,Yj,SIGAV,L,a(20),c,
```

```

+SIG 12(75),SIGAV1,SIGAV2,SIG3(75),H,MOM,
+SIGL1,SIGL2,SEMO,NA
ARE=B*H
READ(*,*) N
SUM12=0
SUM3=0
DO 10 1=1,N
READ(*,*) X(I)
READ(*,*) Y(I)
IF (X(I).LT.Y(I)) THEN
D(I)=X(I)
ELSE
D(I)=Y(I)
ENDIF
Y1(I)=Y(I)-NA
CALL DIRKF(B,D(I),T,TEa(I))
WRITE(*,*) ' TEa(I) '
WRITE(*,*) TEa(I)
CALL faxff(TEa(I),FACT,ecC,E(I))
WRITE(*,*) 'E(I) '
WRITE(*,*) E(I)
SIG12(1)=E(I)*7E-06*(TEa(I)-20)
SIG3(I)=(E(I)*7E-06*(TEa(I)-20)*Y1(I)*ARE*Yj)
+/(SEMO*N)
SUM12=SUM12+SIG12(1)
SUM3=SUM3+SIG3(1)
10 CONTINUE
SIGAV1=-SUM12/N
WRITE(*,*) 'SIGAV1'
WRITE(*,*) SIGAV1
SIGAV2=SUM12/N**2
WRITE(*,*) 'SIGAV2'
WRITE(*,*) SIGAV2
SIGAV3=SUM3/N**2
WRITE(*,*) 'SIGAV3'
WRITE(*,*) SIGAV3
CALL momt(F,a,l,c,MOM)
WRITE(*,*) 'MOM'
WRITE(*,*) MOM
SIGL1=-(MOM*Yj*10**3)/(SEMO)
WRITE(*,*) 'SIGL1'
WRITE(*,*) SIGL1
SIGL2=-(W*c*(L-c)*Yj*10**3)/(2*SEMO)
WRITE(*,*) 'SIGL2'
WRITE(*,*) SIGL2
SIGAV=SIGAV1+SIGAV2+SIGAV3+SIGL1+SIG12
WRITE(*,*) 'SIGAV'
WRITE(*,*) SIGAV

```

```

RETURN
END

c SUBROUTINE FOR CALCULATING TEMPERATURE OF A
c BEAM AT A PARTICULAR DEPTH FOR A GIVEN TIME
c OF FIRE EXPOSURE.
SUBROUTINE DIRKF (BX,DX,TX,TEa)
INTEGER I, J, K
REAL B(10), D(75), T(10), TE(10, 75, 10), TE1,
+TE2, TE3, TE4, TE5, TE6,
+TE7, TE8, D1, D2, T1, T2, B1, B2, TE57, TE13,
+TE86, TE24, TEa1, TEa2, TEa
OPEN(UNIT=9, FILE='TEMP2', STATUS='OLD')
REWIND 9
READ(9, *) (D(J), J=1, 19)
DO 10 J=1, 19
IF (DX.LT.D(J)) THEN
JD=J
GO TO 20
ENDIF
10 CONTINUE
20 READ(9, *) (T(K), K=1, 6)
DO 30 K=1, 6
IF (TX.LT.T(K)) THEN
KT=K
GO TO 40
ENDIF
30 CONTINUE
40 READ(9, *) (B(I), I=1, 8)
DO 50 I=1, 8
IF (BX.GT.B(I)) THEN
IB=I
GO TO 60
ENDIF
50 CONTINUE
60 AREAD(9, *) (((TE(I, J, K), J=1, 19), K=1, 6), I=1, 8)
TE1=TE(IB-1, JD, KT-1)
TE3=TE(IB-1, JD, KT)
TE4=TE(IB, JD, KT)
TE5=TE(IB-1, JD-1, KT)
TE6=TE(IB, JD-1, KT)
TE7=TE(IB-1, JD-1, KT-1)
TE8=TE(IB, JD-1, KT-1)
D1=D(JD-1)
D2=D(JD)
T1=T(KT-1)
T2=T(KT)
B1=B(IB-1)
B2=B(IB)

```



```

TE57=(TX-T2)*(TE5-TE7)/(T2-T1)+TE5
TE13=(TX-T2)*(TE3-TE1)/(T2-T1)+TE3
TE86=(TX-T2)*(TE6-TE8)/(T2-T1)+TE6
TE24=(TX-T2)*(TE4-TE2)/(T2-T1)+TE4

```

```

TEa1=(DX-D2)*(TE57-TE13)/(D1-D2)+TE13
TEa2=(DX-D2)*(TE86-TE24)/(D1-D2)+TE24
TEa=(BX-B1)*(TEa2-TEa1)/(B2-B1)+TEa1
CLOSE (9)
RETURN
END

```

- c SUBROUTINE FOR CALCULATING ELASTIC MODULES
- c OF CONCRETE FOR A PARTICULAR TIME OF FIRE
- c EXPOSURE.

```

SUBROUTINE faxff(TEa,FACT,ecC,E)
INTEGER I
REAL TE(20),FAC(20),FACT,ec(20),ecC,
+E,TEa
OPEN(UNIT=2,FILE='YONG',STATUS='OLD')
REWIND 2
READ(2,*) (TE(I),I=1,13)
READ(2,*) (FAC(I),I=1,13)
READ(2,*) (ec(I),I=1,13)
DO 10 I=1,13
IF (TEa.LT.TE(I)) THEN
ITE=I
GO TO 20
ENDIF
10 CONTINUE
20 TE2=TE(ITE-1)
TE1=TE(ITE)
FAC2=FAC(ITE-1)
FAC1=FAC(ITE)
ec2=ec(ITE-1)
ec1=ec(ITE)
FACT=(TEa-TE2)*(FAC1-FAC2)/(TE1-TE2)+FAC2
ecC=(TEa-TE2)*(ec1-ec2)/(TE1-TE2)+ec2
WRITE(*,*) 'FACT', 'ecC'
WRITE(*,*) FACT,ecC
E=(1.5*FACT*43.4)/ecC
CLOSE (2)
RETURN
END

```

- c SUBROUTINE FOR CALCULATING STRESS OF A CONCRETE
  - c BEAM DUE TO PRESTRESS WITH TEMPERATURE EFFECT.
- ```

SUBROUTINE telep(B,H,T,e,Yj,D,TEa,SIGP,SA,
+PREFOE,NA,SEMO)

```

```

INTEGER I
REAL TE(20),COE(20),COEF,FORC,B,H,ARE,Yj,SA,NA,
+SEMO, T,e,D,TEa,SIGP1,SIGP2,PREFOE,Et,SIGP3,SIGP
OPEN(UNIT=3,FILE='PRE',STATUS='OLD')
ARE=B*H
IF((H/2-e).LT.B/2)THEN
D=H/2-e
ELSE
D=B/2
ENDIF
CALL DIRKF(B,D,T,TEa)
WRITE(*,*)'TEa'
WRITE(*,*) TEa
READ(3,*)(TE(I),I=1,13)
READ(3,*)(COE(I),I=1,13)
DO 10 I=1,13
IF (TEa.LT.TE(I)) THEN
ITE=I
GO TO 20
ENDIF
10 CONTINUE
20 TE2=TE(ITE-1)
TE1=TE(ITE)
COE2=COE(ITE-1)
COE1=COE(ITE)
COEF=(TEa-TE2)*(COE1-COE2)/(TE1-TE2)+COE2
WRITE(*,*)'COEF'
WRITE(*,*) COEF
FORC=COEF*PREFOE
SIGP1=-FORC/ARE
WRITE(*,*)'SIGP1'
WRITE(*,*) SIGP1
SIGP2=(FORC*e*Yj)/SEMO
WRITE(*,*)'SIGP2'
WRITE(*,*)SIGP2
CALL STLYON(TEa,H,e,B,T,D,RATIO,Et)
WRITE(*,*)'Et'
WRITE(*,*) Et
SIGP3=-((Et*(TEa-20)*SA)/ARE)*6.5E-06
WRITE(*,*)'SIGP3'
WRITE(*,*) SIGP3
SIGP=SIGP1+SIGP2+SIGP3
CLOSE (3)
RETURN
END

```

- c SUBROUTINE FOR CALCULATING MOMENT OF
- c A BEAM AT A PARTICULAR DISTANCE FROM
- c THE SUPPORTS WITH NUMBER OF POINT LOADS

```

SUBROUTINE momt(F,a,L,c,MOM)
INTEGER I,M
REAL F(20),a(20),L,c,SUM1(20),
+MOM,SUM2(20),SUM11,SUM22
READ(*,*) M
SUM22=0
SUM11=0
DO 20 I=1,M
READ(*,*) F(I)

c SUBROUTINE FOR CALCULATING I-VALUE OF A PRESTRESSED
c CONCRETE BEAM FOR A GIVEN TIME OF FIRE EXPOSURE.
SUBROUTINE SEMO3(B,T,H,e,SA,NA,m1,ARE,D,AvE,SEMO)
REAL B,T,H,e,SA,NA,m1,ARE,
+SEMO,D,AvE
CALL NAXIS1(B,T,H,e,SA,m1,ARE,AvE,D,NA)
WRITE(*,*) NA
SEMO=(B*H**3)/12+B*H*(NA-H/2)**2t+(m1*SA-SA)*(H/2+e-NA)**2
WRITE(*,*) 'SEMO'
WRITE(*,*) SEMO
RETURN
END

c SUBROUTINE FOR CALCULATING NEUTRAL AXIS DEPTH
c OF A PRESTRESSED CONCRETE BEAM FOR A GIVEN
c TIME OF FIRE EXPOSURE.
SUBROUTINE NAXIS1(B,T,H,e,SA,m1,ARE,AvE,D,NA)
REAL X(75),Y(75),TEa,B,T,H,AvE,Et,SA,e,NA,m1,ARE,D
CALL CONYON(X,Y,B,T,AvE)
WRITE(*,*) 'AvE'
WRITE(*,*) AvE
CALL STLYON(TEa,H,e,B,T,D,RATIO,Et)
WRITE(*,*) 'Et'
WRITE(*,*) Et
m1=Et/AvE
ARE=B*H
NA=(ARE*H/2+(m1-1)*SA*(H/2+e))/(ARE+(m1-1)*SA)
WRITE(*,*) 'NA'
WRITE(*,*) NA
RETURN
END

c SUBROUTINE FOR CALCULATING AVERAGE ELASTIC
c MODULES OF CONCRETE BEAM FOR A PARTICULAR
c TIME OF FIRE EXPOSURE.
SUBROUTINE CONYON(X,Y,B,T,AvE)
INTEGER I,N
REAL X(75),Y(75),D(75),TEa(75),E(75),
+AvE,B,T

```

```

READ(*,*) N
SUM=0
DO 10 I=1,N
READ(*,*) X(I)
READ(*,*) Y(I)
IF (X(I).LT.Y(I)) THEN
D(I)=X(I)
ELSE
D(I)=Y(I)
ENDIF

CALL dirkf(B,D(I),T,TEa(I))
WRITE(*,*) TEa(I)
CALL faxff(TEa(I),FACT,ecC,E(I))
WRITE(*,*) E(I)
SUM=SUM+E(I)
10 CONTINUE
AvE=SUMN
WRITE(*,*) 'AvE'
WRITE(*,*) AvE
RETURN
END

```

### I.4 Superelement and Substructuring

In general terms, such formulations are described by the following:

$$\left[ \begin{array}{c|c} K & K_R \\ \hline K_R^{T''} & K_{RR} \end{array} \right] \left\{ \begin{array}{c} U \\ U_R \end{array} \right\} = \left\{ \begin{array}{c} F \\ F_R \end{array} \right\} \tag{A.74}$$

The subscript R represents reaction forces. The top half of (A.74) is used to solve for {U}:

$$\{U\} = -[K]^{-1}[K_R]\{U_R\} + [K]^{-1}\{F\} \tag{A.75}$$

The reaction forces {F<sub>R</sub>} are computed from the bottom half of the equation as

$$\{F_R\} = [K_R]^{T''}\{U\} + \{K_{RR}\}\{U_R\} \tag{A.76}$$

Equation (A.75) must be in equilibrium with (A.76).

For large structures with complicated features, a substructure (superelement) may be adopted on the lines suggested in (A.74). This superelement may then be used as a reduced element from the collection of elements. If subscripts  $\gamma$  and  $\gamma'$  represent the retained and removed degrees of freedom of the equations partitioned into two groups, then the expressions in (A.74) can be written as

$$\left[ \begin{array}{c|c} K_{\gamma\gamma} & K_{\gamma\gamma'} \\ \hline K_{\gamma'\gamma} & K_{\gamma'\gamma'} \end{array} \right] \left\{ \begin{array}{c} U_{\gamma} \\ U_{\gamma'} \end{array} \right\} = \left\{ \begin{array}{c} F_{\gamma} \\ F_{\gamma'} \end{array} \right\} \quad (\text{A.77})$$

Equation (A.77) when expanded assumes the following form:

$$\{F_{\gamma}\} = [K_{\gamma\gamma}]\{U_{\gamma}\} + [K_{\gamma\gamma'}]\{U_{\gamma'}\} \quad (\text{A.78})$$

$$\{F_{\gamma'}\} = [K_{\gamma'\gamma}]\{U_{\gamma}\} + [K_{\gamma'\gamma'}]\{U_{\gamma'}\} \quad (\text{A.79})$$

When a dynamic analysis is carried out, the subscript  $\gamma$ , (retained) represents the dynamic degrees of freedom.

When (A.79) is solved, the value of  $U_{\gamma'}$  is then written, similarly to (A.75).

$$\{U_{\gamma'}\} = [K_{\gamma'\gamma'}]^{-1}\{F_{\gamma'}\} + [K_{\gamma'\gamma'}]^{-1}[K_{\gamma'\gamma}]\{U_{\gamma}\} \quad (\text{A.80})$$

Substituting  $\{U_{\gamma'}\}$  into (A.77) gives:

$$\left[ [K_{\gamma\gamma}] - [K_{\gamma'\gamma}][K_{\gamma'\gamma'}]^{-1}[K_{\gamma'\gamma}] \right] \{U_{\gamma}\} = \left[ \{F_{\gamma}\} - [K_{\gamma'\gamma}][K_{\gamma'\gamma'}]^{-1}\{F_{\gamma'}\} \right] \quad (\text{A.81})$$

or

$$[\bar{K}]\{\bar{U}\} = \{\bar{F}\} \quad (\text{A.82})$$

where

$$[\bar{K}] = [K_{\gamma\gamma}] - [K_{\gamma'\gamma}][K_{\gamma'\gamma'}]^{-1}[K_{\gamma'\gamma}] \quad (\text{A.83})$$

$$\{\bar{F}\} = \{F_{\gamma}\} - [K_{\gamma'\gamma}][K_{\gamma'\gamma'}]^{-1}\{F_{\gamma'}\} \quad (\text{A.84})$$

$$\{\bar{U}\} = \{U_{\gamma}\} \quad (\text{A.85})$$

and  $[\bar{K}]$  and  $\{\bar{F}\}$  are generally known as the substructure stiffness matrix and load vector, respectively.

In the above equations, the load vector for the substructure is taken as a total load vector. The same derivation may be applied to any number of independent load vectors. For example, one may wish to apply thermal, pressure, gravity and other loading conditions in varying proportions. Expanding the right-hand sides of (A.78) and (A.79) gives:

$$\{F_{\gamma}\} = \sum_{i=1}^n \{F_{\gamma i}\} \quad (\text{A.86})$$

$$\{F_{\gamma'}\} = \sum_{i=1}^n \{F_{\gamma' i}\} \quad (\text{A.87})$$

where  $n$  = the number of independent load vectors.

Substituting into (A.82)

$$\{\bar{F}\} = \sum_{i=1}^n \{F_{\gamma\gamma' i}\} - [K_{\gamma'\gamma}][K_{\gamma'\gamma'}]^{-1} \sum_{i=1}^n \{F_{\gamma' i}\} \quad (\text{A.88})$$

### I.5 Large Strain

When the strains in a material exceed more than a few per cent, the changing geometry due to this deformation can no longer be neglected. Analyses which include this effect are called large strain, or finite strain, analyses. A large strain analysis is performed in a static and dynamic transient analysis.

The theory of large strain computations can be addressed by defining a few basic physical quantities (motion and deformation) and the corresponding mathematical relationship. The applied loads acting on a body make it move from one position to another. This motion can be defined by studying a position vector in the ‘deformed’ and ‘undeformed’ configuration. Say the position vectors in the ‘deformed’ and ‘undeformed’, state are represented by  $\{\mathbf{x}\}$  and  $\{\mathbf{X}\}$  respectively, then the motion (displacement) vector  $\{\mathbf{u}\}$  is computed by (Fig. A.I.5)

$$\{\mathbf{u}\} = \{\mathbf{x}\} - \{\mathbf{X}\} \tag{A.89}$$

The deformation gradient  $[F_d]$  is defined as:

$$[F_d] = \frac{\partial\{\mathbf{x}\}}{\partial\{\mathbf{X}\}} + [\mathbf{I}] = [\mathbf{R}][\mathbf{u}] \tag{A.90}$$

where  $[\mathbf{I}] =$  identity matrix.

The volume change at a point

$$\frac{dV}{dV_0} = \det[F] \tag{A.91}$$

where

$V_0 =$  original volume

$V =$  current volume

$[\mathbf{u}] =$  fight stretch shape change matrix

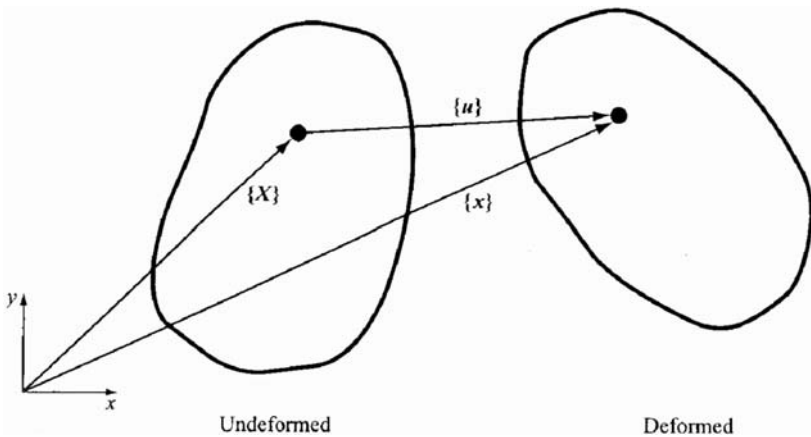


Fig. A.I.5. Position vectors and motion of a deforming body

Largestrain  $\{\varepsilon\}$  is written as

$$\{\varepsilon\} = \ln[\mathbf{u}] = \sum \ln(\lambda_i)\{e_i\}\{e_i\}^{\text{T}''} \quad (\text{A.92})$$

where

$\lambda_i$  = eigenvalues of  $[\mathbf{u}]$

$e_i$  = eigenvectors of  $[\mathbf{u}]$

$\mathbf{R}$  = rotation matrix  $\left([\mathbf{R}]^{\text{T}''}[\mathbf{R}] = [\mathbf{I}]\right)$

Element formulation using Lagrangian formulation technique

$$[\bar{\mathbf{K}}_i]\Delta u_i = [F^a] - [F_i^{\text{nr}}] \quad (\text{A.93})$$

where

$[\bar{\mathbf{K}}_i]$  = tangent matrix =  $[\mathbf{K}_i] + [S_i]$

$[\mathbf{K}_i]$  = usual stiffness matrix

$$= \int [B_i]^{\text{T}''} [D_i] [B_i] d(\text{vol}) \quad (\text{A.94})$$

$[S_i]$  = stress stiffness contribution or geometric stiffness

$$= \int [\mathbf{G}_i]^{\text{T}} [\tau_i] [\mathbf{G}_i] d(\text{vol}) \quad (\text{A.95})$$

where

$[\mathbf{G}_i]$  = matrix of shape function derivatives

$[\tau_i]$  = matrix for the current Cauchy stresses i.e. true stresses  $\sigma_i$

$$[F_i^{\text{nr}}] = \int [B_i]^{\text{T}''} \{\sigma_i\} d(\text{vol}) \quad (\text{A.96})$$

The increment of large strain  $[\Delta\varepsilon_n]$  is then written as

$$[\Delta\varepsilon_n] = [\mathbf{R}_{1/2}]^{\text{T}''} [\Delta\bar{\varepsilon}_n] [\mathbf{R}_{1/2}] \quad (\text{A.97})$$

where

$[\mathbf{R}_{1/2}]$  = rotational matrix from the polar decomposition of the deformation gradient evaluated at the midpoint configuration

$$[F_{1/2}] = [R_{1/2}][U_{1/2}] \quad (\text{A.98})$$

where

$$[F_{1/2}] = [I] + \frac{\partial\{U_{1/2}\}}{\partial X} \quad (\text{A.99})$$

Large deformation and large strains are obtained where these formulations are linked to the main analyses, static dynamic and blast type of loading are encountered.

### I.6 Criteria for Convergence and Acceleration

#### Convergence Criteria

To ensure convergence to the correct solution by finer sub-division of the mesh, the assumed displacement function must satisfy the convergence criteria given below:

- (a) Displacements must be continuous over element boundaries.
- (b) Rigid body movements should be possible without straining.
- (c) A state of constant strain should be reproducible.

Euclidean norm  $\psi_i/R_i \leq C$ . The term  $\psi_i$  represents the unbalanced forces and the norm of the residuals. With the aid of the iterative scheme described above, the unbalanced forces due to the initial stresses  $\{\sigma_0\}$  become negligibly small. As a measure of their magnitude, the norm of the vector  $\|\psi_i\|$  is used. The Euclidean norm and the absolute value of the largest component of the vector are written as

$$\begin{aligned} \|\psi_i\| &= (|\psi_1|^2 + \dots + |\psi_n|^2)^{1/2} \\ \|R_i\| &= (|\{R_i\}^T \{R_i\}|)^{1/2} \end{aligned} \tag{A.100}$$

the convergence criterion adopted is

$$\|\psi\| = \max_i |\psi_i| < C = 0.001 \tag{A.101}$$

#### Uniform Acceleration

Various procedures are available for accelerating the convergence of the modified Newton-Raphson iterations. Figures A.I.6a and b shows the technique

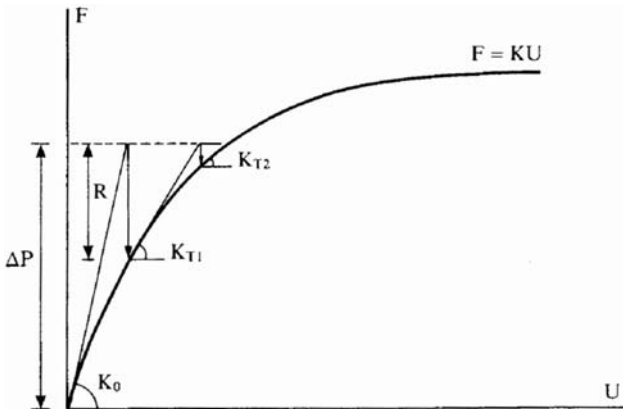


Fig. A.I.6a. Newton-Raphson method



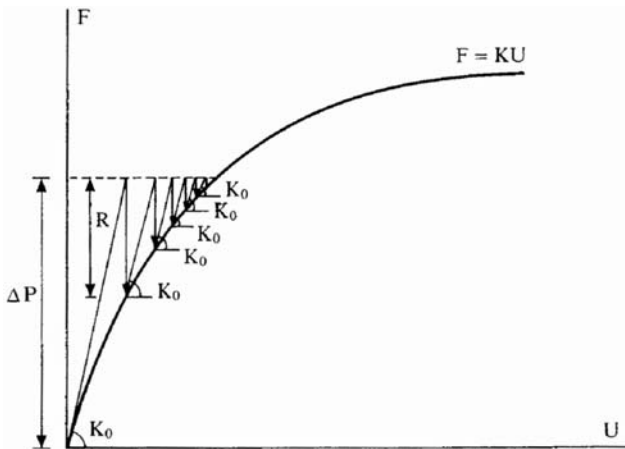


Fig. A.I.6b. Initial stress method

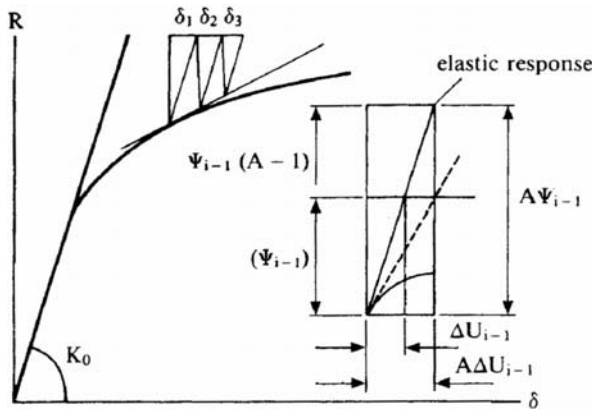


Fig. A.I.6c. Technique of computing acceleration factors

of computing individual acceleration factors,  $\delta_1$  and  $\delta_2$  are known. Then, assuming a constant slope of the response curve, and from similar triangles, the value of  $\delta_3$  is computed (Figs. A.I.6a to f).

$$\frac{\delta_1}{\delta_2} = \frac{\delta_2}{\delta_3} \quad \delta_3 = \delta_2 \frac{\delta_2}{\delta_1} \tag{A.102}$$

When  $\delta_3$  is added to  $\delta_2$ , then the accelerated displacement  $\delta'_2$  is expressed as

$$\delta'_2 = \delta_2 + \delta_3 = \delta_2 \left( 1 + \frac{\delta_2}{\delta_1} \right) = \alpha \delta_2 \tag{A.103}$$

where the acceleration factor  $\alpha$  is

$$\alpha = 1 + \frac{\delta_2}{\delta_1} \tag{A.104}$$

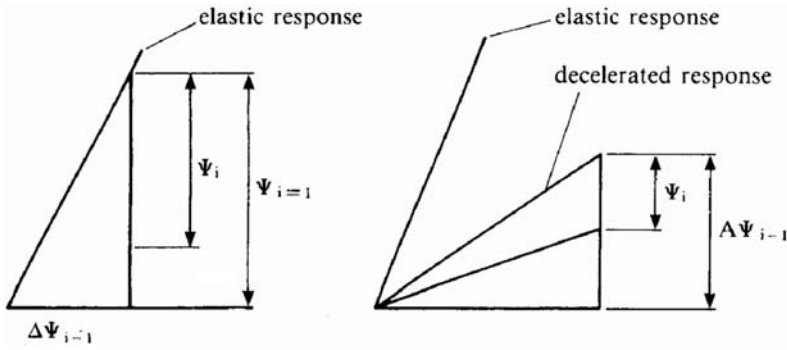


Fig. A.I.6d. Graphical representation

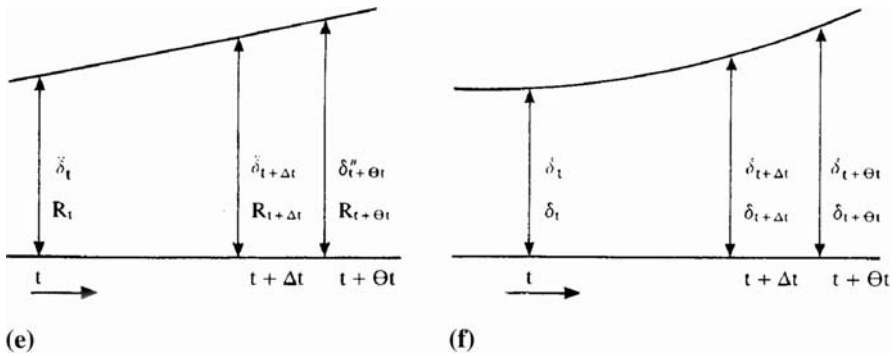


Fig. A.I.6e-f. (e) Linear acceleration and load assumptions of the Wilson  $\theta$  method; (f) Quadratic and cubic variation of velocity and displacement assumptions of the Wilson  $\theta$  method

Generally the range of  $\alpha$  is between 1 and 2. The value of  $\alpha = 1$  for zero acceleration, and the value of  $\alpha$  reaches the maximum value of 2 when the slope of the  $\delta - R$  curve approaches zero.

The acceleration factor  $\alpha$  is computed individually for every degree of freedom of the system. The displacement vector obtained from the linear stiffness matrix  $[k_0]$  is then multiplied by the  $[\alpha]$  matrix having the above constants on its diagonals. The remaining components of  $[\alpha]$  are zero. The accelerated displacement vector is then expressed as follows:

$$\{\Delta u'_i\} = [a_i - 1]\{\Delta u_i\} \tag{A.105}$$

From these accelerated displacements  $\{\Delta u'_i\}$ , the initial stresses  $\{\sigma_0\}$  are found and they are equilibrated with the forces  $\{\psi_i\}$ . They are then used for the next solution

$$\{\Delta \bar{u}_i\} = [k_0]^{-1}\{\psi_i\} \tag{A.106}$$

which results in a new set of acceleration factors. Now an estimate for the displacement increment is made in order to find the incremental stresses and total stresses.

Note:  $\Delta P$  is a specific value of  $F$ .

The residual forces needed to re-establish equilibrium can now easily be evaluated

$$\{\hat{\psi}_i\} = \int_{\nu} [B]^T \{\sigma_{0T}\} dV - \{R_i\} \quad (\text{A.107})$$

where  $\{R_i\}$  represents the total external load;  $dV$  is the volume.

A new displacement now results from

$$\{\Delta u_{i+1}\} = -[k_0]^{-1} \{\hat{\psi}_i\} \quad (\text{A.108})$$

In order to carry out these iterative steps, numerical integration is required. First of all the evaluation of  $\{\hat{\psi}_i\}$  from the initial stresses is required, and this requires integration over the elastic-plastic region only. The value of  $\{\hat{\psi}_i\}$  is computed by carrying out the integration over the entire domain of the analysis. Since these kinds of accelerated steps unbalance the equilibrium, therefore it has to be re-established by finding the residual forces  $\{\hat{\psi}_i\}$ . Since the state of stress produced by the accelerated displacements is not in balance with the residual forces of the previous iteration, the new residual forces  $\{\hat{\psi}_i\}$  of (A.108) must balance  $\{\sigma_T\}$  and  $\{R_i\}$ . Here the acceleration scheme is needed to preserve equilibrium, which will eventually make the equivalent forces over the whole region unnecessary. This is achieved by applying a uniform acceleration, i.e. the same acceleration factor  $\bar{A}$  to all displacements, found by averaging the individual factors  $\alpha_i$

$$\bar{A} = \frac{1}{n} \sum_{i=1}^n \alpha_i \quad (\text{A.108a})$$

The force-displacement equation is then written by multiplying both sides with the scalar quantity  $\bar{A}$  without disturbing the equilibrium.

$$\bar{A}\{\Delta u_i\} = [k_0]^{-1} \bar{A}\{\psi_i\}$$

Now to evaluate  $\{\psi_{i+1}\}$ , the previous value of  $\{\psi_i\}$  must be multiplied by  $\bar{A}$ , and the previously accelerated forces from the initial stresses  $\{\sigma_0\}$  must be included such that

$$\{\psi_{i+1}\} = \int_V [B]^T \{\sigma_0\} dV - (A-1)\{\psi_{i-1}\} \quad (\text{A.109})$$

## Part SUB-PROGRAM of BANG-FIRE

## Part B

```

c PROGRAMME FOR CALCULATING DEFLECTION OF
c A BEAM AT A DISTANCE FROM THE SUPPORT
c DUE TO POINT LOADS AND UNIFORMLY
c DISTRIBUTED LOAD FOR A PARTICULAR TIME
c OF FIRE EXPOSURE.
INTEGER I,M
REAL P(20),a(20),L,c,w,SUM1(20),A,Def,
+SUM4,SUM,SEMO,SUM2(20),AvE,H1,As,NA,m1,Def2,
+SUM3(20),B,T,H,Def1,SUM11,SUM22,SUM33,R2
WRITE(*,*) 'B=', 'T=', 'H=', 'H1=', 'As='
READ(*,*) B,T,H,H1,As
WRITE(*,*) 'L=', 'c=', 'w='
READ(*,*) L,c,w
WRITE(*,*) 'M='
WRITE(*,*) 'P=', 'a='
READ(*,*) M
SUM11=0
SUM22=0
SUM33=0
DO 10 I=1,M
READ(*,*) P(I)
READ(*,*) a(1)
SUM1(I)=P(I)*(c-a(I))**3/6
SUM2(I)=P(I)*(L-a(I))**3/(6*L)
SUM3(I)=P(I)*(L-a(I))/L
SUM11=SUM11+SUM1(I)
SUM22=SUM22+SUM2(I)
SUM33=SUM33+SUM3(I)
10 CONTINUE
SUM=SUM11-SUM22*c+SUM33*(c*L**2-c**3)/6
SUM4=w*c**4/24+w*c*L**3/24-w*L*c**3/12
WRITE(*,*) 'I', 'P', 'a'
DO 20 I=1,M
WRITE(*,*) I,P(I),a(I)'
20 CONTINUE
WRITE(*,*) 'SUM11', 'SUM22', 'SUM33',
+'SUM', 'SUM4'
WRITE(*,*) SUM11,SUM22,SUM33,SUM,SUM4
WRITE(*,*) 'NO OF NODES'
WRITE(*,*) 'X=', 'Y='
CALL SEMO2(B,T,H,H1,NA,m1,A,As,AvE,SEMO)
WRITE(*,*) 'SEMO', 'AvE'
WRITE(*,*) SEMO,AvE
WRITE(*,*) SEMO,AvE,SUM,SUM4
Def1=((SUM+SUM4)*10**9)/(AvE.SEMO)

```

```

WRITE(*,*) 'Def1'
WRITE (*,*) Def1
CALL CONYON(X,Y,B,T,A,H,NA,R2)
WRITE(*,*) 'R2'
WRITE(*,*) R2
WRITE(*,*) 'L,c,AvE,SEMO'
WRITE(*,*) L,c,AvE,SEMO
Def2=(R2*c*(L-c)*10**6)/(2*AvE*SEMO)
WRITE(*,*) 'Def2'
WRITE(*,*) Def2
Def=Def1+Def2
WRITE(*,*) 'Def'
WRITE(*,*) Def
END

SUBROUTINE DIRKF(BX,OX,TX,TEa)
INTEGER I,J,K
REAL B(75),D(75),T(75),TE(75,75,75),TE1,
+TE2,TE3,TE4,TE5,TE6,
+TE7,TE8,D1,D2,T1,T2,B1,B2,TE57,TE13,
+TE86,TE24,TEa1,TEa2,TEa
OPEN(UNIT=9,FILE='TEMP2',STATUS='OLD')
READ(9,*)(D(J),J=1,19)
DO 10 J=1,19
IF(DX.LT.D(J)) THEN
JD=J
GO TO 20
ENDIF
10 CONTINUE
20 READ(9,*) (T(K),K=1,6)
DO 30 K=1,6
IF (TX.LT.T(K)) THEN
KT=K
GO TO 40
ENDIF
30 CONTINUE
40 READ(9,*) (B(I),I=1,8)
DO 50 I=1,8
IF (BX.GT.B(I)) THEN
IB=I
GO TO 60
ENDIF
50 CONTINUE
60 READ(9,*) (((TE(I,J,K),J=1,19),K=1,6),I=1,8)
TE1=TE(IB-1,JD,KT-1)
TE2=TE(IB,JD,KT-1)
TE3=TE(IB-1,JD,KT)
TE4=TE(IB,JD,KT)
TE5=TE(IB-1,JD-1,KT)

```

```

TE6=TE(IB,JD-1,KT)
TE7=TE(IB-1,JD-1,KT-1)
TE8=TE(IB,JD-1,KT-1)
D1=D(JD-1)
D2=D(JD)
T1=T(KT-1)
T2=T(KT)
B1=B(IB-1)
B2=B(IB)
TE57=(TX-T2)*(TE5-TE7)/(T2-T1)+TE5
TE13=(TX-T2)*(TE3-TE1)/(T2-T1)+TE3
TE86=(TX-T2)*(TE6-TE8)/(T2-T1)+TE6
TE24=(TX-T2)*(TE4-TE2)/(T2-T1)+TE4
TEa1=(DX-D2)*(TE57-TE13)/(D1-D2)+TE13
TEa2=(DX-D2)*(TE86-TE24)/(D1-D2)+TE24
TEa=(BX-B1)*(TEa2-TEa1)/(B2-B1)+TEa1
WRITE(*,*)'TEa'
WRITE(*,*) TEa
CLOSE (9)
RETURN
END

```

```

SUBROUTINE faxff(TEa,FACT,ecC,E)
INTEGER I
REAL TE(20),FAC(20),ec(20),FACT,ecC,E
OPEN(UNIT)=2,FILE='YOUNG',STATUS='OLD')
READ(2,*) (TE(I),I=1,13)
READ(2,*) (FAC(I),I=1,13)
READ(2,*) (ec(I),I=1,13)
DO 10 I=1,13
IF (TEa.LT.TE(I)) THEN
ITE=I
GO TO 20
ENDIF
10 CONTINUE
20 TE2=TE(ITE-1)
TE1=TE(ITE)
FAC2=FAC(ITE-1)
FAC1=FAC(ITE)
ec2=ec(ITE-1)
ec1=ec(ITE)
WRITE(*,*)'TE1,TE2,FAC1,FAC2,ec1,ec2'
WRITE(*,*) TE1,TE2,FAC1,FAC2,ec1,ec2
FACT=(TEa-TE2)*(FAC1-FAC2)/(TE1-TE2)+FAC2
ecC=(TEa-TE2)*(ec1-ec2)/(TE1-TE2)+ec2
WRITE(*,*)'FACT','ecC'
WRITE(*,*) FACT,ecC
E=(1.5*FACT*25)/ecC
WRITE(*,*)'E'

```

```

WRITE(*,*) E
CLOSE (2)
RETURN
END

c SUBROUTINE FOR CALCULATING NEUTRAL AXIS DEPTH
c AND I-VALUE OF A CONCRETE BEAM FOR A
c PARTICULAR TIME OF FIRE EXPOSURE.
SUBROUTINE semo2(B,T,H,H1,NA,m1,A,As,AvE,SEMO)
REAL TEa,B,T,H,AvE,Et,As,H1,NA,m1,A,SEMO
CALL CONYON1(X,Y,B,T,AvE)
WRITE(*,*) AvE
CALL STLYON(TEa,H,H1,S,T,Et,D)
WRITE(*,*) Et
A=B*H
m1=Et/AvE
NA=(m1*As/B)*((1+(2*B*H1)/(m1*As))**0.5-1)
WRITE(*,*) 'NA'
WRITE(*,*) NA
SEMO=(B*NA**3)/3+m1*As*(H1-NA)**2
WRITE(*,*) 'SEMO'
WRITE(*,*) SEMO
RETURN
END

SUBROUTINE CONYON1(X,Y,B,T,AvE)
INTEGER I,N
REAL X(75),Y(75),D(75),TEa(75),E(75),
+AvE,B,T
READ(*,*) N
SUM=0
DO 10 I=1,N
READ(*,*) X(I)
READ(*,*) Y(I)
IF (X(I).LT.Y(I)) THEN
D(I)=X(I)
ELSE
D(I)=Y(I)
ENDIF
CALL DIRKF(B,D(I),T,TEa(I))
WRITE(*,*) TEa(I)
CALL faxff(TEa(I),FACT,ecC,E(I))
WRITE(*,*) E(I)
SUM=SUM+E(I)
10 CONTINUE
DO 20 I=1,N
WRITE(*,*) 'E', 'SUM'
WRITE(*,*) E(I),SUM
20 CONTINUE

```

```

AvE=SUM/N
WRITE(*,*)'AvE'
WRITE(*,*) AvE
RETURN
END

SUBROUTINE STLYON(TEa,H,H1,B,T,Et,C)
INTEGER I
REAL TE(20),RATO(20),Et,TEa,H1,H,D,RATIO
OPEN(UNIT=2,FILE='YONGST1',STATUS='OLD')
D=H-H1
WRITE(*,*)'D'
WRITE(*,*) D
CALL DIRKF(B,C,T,TEa)
WRITE(*,*)'TEa'
READ(2,*)(TE(I),1=1,13)
READ(2,*)(RATO(I),1=1,3)
GO 10 I=1,13
IF(TEa.LT.TE(I))THEN
ITE=I
GOTO 20
ENDIF
10 CONTINUE
20 TE2=TE(ITE-1)
TE1=TE(ITE)
RATO2=RATO(ITE-1)
RAT=1=RATO(ITE)
RATIO=(TEa-TE2)*(RATO1-RATO2)/(TE1-TE2)+RATO2
WRITE(*,*)'RATIO'
WRITE(*,*) RATIO
Et=210*10**3*RATIO
WRITE(*,*)'Et'
WRITE(*,*) Et
CLOSE(2)
RETURN
END

c SUBROUTINE FOR CALCULATING MOMENT DUE
c TO THERMAL STRESS FOR A PARTICULAR TIME
c OF FIRE EXPOSURE.
SUBROUTINE CONYON(X,Y,B,T,A,H,NA,R2)
INTEGER I,N
REAL X(75),Y(75),C(75),TEa(75),E(75),
+B,T,R2,R(75),Y1(75),A,H,NA
A=B*H
WRITE(*,*)'NA'
WRITE(*,*) NA
READ(*,*) N
R2=0

```



```

DO 10 I=1,N
READ(*,*) X(I)
READ(*,*) Y(I)
IF (X(I).LT.Y(I)) THEN
D(I)=X(I)
ELSE
D(I)=Y(I)
ENDIF
Y1(I)=Y(I)-NA
CALL DIRKF(B,D(I),T,TEa(I))
WRITE(*,*) TEa(I)
CALL faxff(TEa(I),FACT,ecC,E(I))
WRITE(*,*) E(I)
R(I)=E(I)*7E-06*(TEa(I)-20)*Y1(I)*A/N
R2=R2+R(I)
10 CONTINUE
DO 20 I=1,N
WRITE(*,*) 'I', 'R', 'YI'
WRITE(*,*) I,R(I),Y1(I)
20 CONTINUE
WRITE(*,*) 'R2'
WRITE(*,*) R2
RETURN
END

```

*Part C*

```

c PROGRAM FOR CALCULATING DESIGN MOMENT
c OF A CONCRETE BEAM FOR A PARTICULAR
c TIME OF FIRE EXPOSURE.
REAL X(75),Y(75),TEa,B,T,As,D1,Dis,
+H,Avfcut,Fyt,Mu1
WRITE(*,*) 'B=', 'T =', 'D1=', 'H=', 'As='
READ(*,*) B,T,D1,H,As
WRITE(*,*) 'NO OF NODES='
WRITE(*,*) 'X=', 'Y='
CALL consh(X,Y,B,T,Avfcut)
WRITE(*,*) 'Avfcut'
WRITE(*,*) Avfcut
CALL stlsh(TEa,D1,B,T,fyt)
WRITE(*,*) 'fyt'
WRITE(*,*) fyt
Dis=H-D1
WRITE(*,*) 'Dis'
WRITE(*,*) Dis
Mu1=fyt*As*(Dis-(fyt*As)/(2*Avfcut*B))
WRITE(*,*) 'Mu1'
WRITE(*,*) Mu1
END

```

```

SUBROUTINE consh(X,Y,B,T,Avfcut)
INTEGER I,N
REAL X(75),Y(75),D(75),TEa(75),fcut(75),
+Avfcut,B,T
READ(*,*) N
SUM=0
DO 10 I=1,N
READ(*,*) X(I)
READ(*,*) Y(I)
IF (X(J).LT.Y(I)) THEN
D(I)=X(I)
ELSE
D(I)=Y(I)
ENDIF
CALL DIRKF(B,D(I),T,TEa(I))
WRITE(*,*) 'TEa(I)'
WRITE(*,*) TEa(I)
CALL faxx(TEa(I),FACT,fcut(I))
WRITE(*,*) 'fcut(I)'
WRITE(*,*) fcut(I)
SUM=SUM+fcut(I)
10 CONTINUE
Avfcut=SUM/N
WRITE(*,*) 'Avfcut'
WRITE(*,*) Avfcut
RETURN
END

```

```

SUBROUTINE DIRKF(BX,DX,TX,TEa)
INTEGER I,J,K
REAL B(75),D(75),T(75),TE(75,75,75),TE1,
+TE2,TE3,TE4,TE5,TE6,
+TE7,TE8,D1,D2,T1.T2,B1,B2,TE57,TE13,
+TE86,TE24,TEa1,TEa2,TEa
OPEN(UNIT=9.FILE='TEMP2',STATUS='OLD')
READ(9,*) (D(J),J=1.19)
DO 10 J=1.19
IF (DX.LT.D(J)) THEN
JD=J
GO TO 20
ENDIF
10 CONTINUE
20 REAO(9,*) (T(K),K=1,6)
DO 30 K=1,6
IF (TX.LT.T(K)) THEN
KT=K
GO TO 40
ENDIF

```

50 CONTINUE

```

READ(9,*) (((TE(I, J, K), J=1.19), K=1, 6), I=1, 6)
TE1=TE(IB-1, JD, KT-1)
TE2=TE(IB, JD, KT-1)
TE3=TE(IB-1, JD, KT)
TE4=TE(IB, JD, KT)
TE5=TE(IB-1, JD-1, KT)
TE6=TE(IB, JD-1, KT)
TE7=TE(IB-1, JD-1, KT-1)
TE8=TE(IB, JD-1, KT-1)
D1=D(JD-1)
D2=D(JD)
T1=T(KT-1)
T2=T(KT)
B1=B(IB-1)
B2=B(IB)
TE57=(TX-T2)*(TE5-TE7)/(T2-T1)+TE5
TE13=(TX-T2)*(TE3-TE1)/(T2-T1)+TE3
TE86=(TX-T2)*(TE6-TE8)/(T2-T1)+TE6
TE24=(TX-T2)*(TE4-TE2)/(T2-T1)+TE4
TEa1=(DX-D2)*(TE57-TE13)/(D1-D2)+TE13
TEa2=(DX-D2)*(TE86-TE24)/(D1-D2)+TE24
TEa=(BX-B1)*(TEa2-TEa1)/(B2-B1)+TEa1
CLOSE (9)
RETURN
END

```

Corresponding temperature (Tea)

|      |      |     |     |     |     |     |     |     |     |     |     |     |     |     |     |     |     |     |     |
|------|------|-----|-----|-----|-----|-----|-----|-----|-----|-----|-----|-----|-----|-----|-----|-----|-----|-----|-----|
| 20   | 20   | 20  | 20  | 20  | 20  | 20  | 20  | 20  | 20  | 20  | 20  | 20  | 20  | 20  | 20  | 20  | 20  | 20  | 20  |
| 860  | 675  | 530 | 430 | 350 | 290 | 240 | 200 | 160 | 140 | 110 | 90  | 70  | 50  | 40  | 30  | 30  | 30  | 30  | 30  |
| 975  | 750  | 630 | 530 | 450 | 380 | 330 | 280 | 250 | 220 | 190 | 170 | 150 | 140 | 120 | 100 | 100 | 100 | 100 | 100 |
| 1000 | 850  | 730 | 610 | 530 | 450 | 400 | 350 | 310 | 280 | 260 | 240 | 220 | 200 | 200 | 190 | 190 | 190 | 190 | 190 |
| 1025 | 870  | 750 | 670 | 600 | 540 | 480 | 440 | 400 | 360 | 330 | 310 | 290 | 270 | 260 | 240 | 240 | 240 | 240 | 240 |
| 1070 | 900  | 800 | 710 | 650 | 600 | 550 | 500 | 460 | 430 | 400 | 370 | 350 | 340 | 320 | 300 | 300 | 300 | 300 | 300 |
| 20   | 20   | 20  | 20  | 20  | 20  | 20  | 20  | 20  | 20  | 20  | 20  | 20  | 20  | 20  | 20  | 20  | 20  | 20  | 20  |
| 900  | 720  | 570 | 460 | 380 | 320 | 270 | 230 | 190 | 160 | 140 | 120 | 110 | 100 | 100 | 100 | 100 | 100 | 100 | 100 |
| 950  | 800  | 660 | 550 | 460 | 390 | 340 | 290 | 260 | 230 | 200 | 190 | 170 | 160 | 150 | 140 | 140 | 140 | 140 | 140 |
| 1020 | 880  | 750 | 640 | 550 | 480 | 420 | 370 | 340 | 300 | 280 | 260 | 240 | 230 | 220 | 200 | 200 | 200 | 200 | 200 |
| 1060 | 940  | 800 | 700 | 620 | 550 | 500 | 460 | 430 | 390 | 360 | 340 | 330 | 320 | 310 | 300 | 300 | 300 | 300 | 300 |
| 1100 | 950  | 830 | 730 | 680 | 610 | 600 | 520 | 490 | 460 | 440 | 420 | 400 | 390 | 380 | 370 | 370 | 370 | 370 | 370 |
| 20   | 20   | 20  | 20  | 20  | 20  | 20  | 20  | 20  | 20  | 20  | 20  | 20  | 20  | 20  | 20  | 20  | 20  | 20  | 20  |
| 910  | 760  | 620 | 500 | 400 | 350 | 300 | 260 | 230 | 200 | 180 | 170 | 150 | 140 | 120 | 100 | 100 | 100 | 100 | 100 |
| 970  | 840  | 700 | 590 | 490 | 420 | 370 | 340 | 300 | 270 | 260 | 240 | 220 | 200 | 190 | 180 | 180 | 180 | 180 | 180 |
| 1060 | 910  | 790 | 670 | 580 | 510 | 460 | 430 | 400 | 360 | 350 | 330 | 310 | 300 | 290 | 280 | 280 | 280 | 280 | 280 |
| 1100 | 960  | 840 | 730 | 650 | 590 | 550 | 520 | 500 | 470 | 460 | 440 | 430 | 420 | 400 | 390 | 390 | 390 | 390 | 390 |
| 1100 | 1000 | 870 | 760 | 700 | 650 | 620 | 590 | 560 | 540 | 520 | 510 | 500 | 480 | 460 | 440 | 440 | 440 | 440 | 440 |
| 20   | 20   | 20  | 20  | 20  | 20  | 20  | 20  | 20  | 20  | 20  | 20  | 20  | 20  | 20  | 20  | 20  | 20  | 20  | 20  |
| 950  | 800  | 660 | 530 | 430 | 370 | 350 | 320 | 300 | 280 | 260 | 250 | 230 | 220 | 200 | 180 | 180 | 180 | 180 | 180 |
| 1010 | 870  | 730 | 620 | 520 | 470 | 450 | 420 | 400 | 390 | 370 | 360 | 350 | 340 | 330 | 320 | 320 | 320 | 320 | 320 |
| 1080 | 940  | 820 | 700 | 620 | 560 | 530 | 510 | 500 | 480 | 460 | 460 | 450 | 440 | 430 | 420 | 420 | 420 | 420 | 420 |
| 1100 | 1000 | 900 | 790 | 700 | 660 | 640 | 610 | 600 | 590 | 580 | 570 | 560 | 550 | 540 | 530 | 530 | 530 | 530 | 530 |
| 1100 | 1030 | 930 | 830 | 750 | 700 | 660 | 640 | 640 | 620 | 610 | 600 | 600 | 590 | 580 | 570 | 570 | 570 | 570 | 570 |

```

20 20 20 20 20 20 20 20 20 20 20 20 20 20 20 20 20 20
970 820 690 560 460 420 380 360 340 320 310 305 300 290 280 270 270 270
830 900 760 650 560 530 500 480 460 450 440 430 420 410 405 400 400 400
1100 970 850 740 660 630 600 580 560 550 540 530 525 520 515 510 510 510
1100 1020 920 820 760 730 700 690 680 670 660 650 645 640 630 625 625 625
1100 1040 940 840 780 750 730 710 700 700 690 670 665 660 655 650 650 650

```

```

20 20 20 20 20 20 20 20 20 20 20 20 20 20 20 20 20 20
990 860 730 600 510 470 450 440 420 410 400 400 390 380 370 360 360 360
1070 940 800 700 630 600 580 570 560 550 540 535 530 525 520 510 510 510
1100 1000 890 780 720 680 670 660 650 640 635 630 625 620 615 610 610 610
1100 1040 940 860 820 780 760 760 740 730 725 720 715 715 710 710 710 710
1100 1050 950 880 840 800 780 780 760 750 740 735 730 725 720 720 720 720

```

Factors from 'Ecro Code'

Data (PRE) for reduction factor in strength of prestressing steel with temperature.

Temperature (TEa)

```

20 100 200 300 400 500 600 700 800 900 1000 1100 1200

```

```

SUBROUTINE faxx(TEa,FACT,fcut)
  INTEGER I
  REAL TE(20),FAC(20),FACT,TEa,fcut
  OPEN(UNIT=2,FILE='YONGHZ',STATUS='OLD')
  READ(2,*) (TE(I),I=1,13)
  READ(2,*) (FAC(I),I= 1,13)
  DO 10 I=1,13
  IF (TEa.LT.TE(I)) THEN
  ITE=I
  GO TO 20
  ENDIF
10 CONTINUE A:
20 TE2=TE(ITE-1) A:
  TE1=TE(ITE)
  FAC2=FAC(ITE-1)
  FAC1=FAC(ITE)
  WRITE(*,*) 'FAC1,FAC2'
  WRITE (*,*) FAC1,FAC2
  FACT=(TEa-TE2)*(FAC1-FAC2)/(TE1-TE2)+FAC2
  fcut=44 *FACT

```

```

SUBROUTINE stlsh(TEa,D1,B,T,fyT)
  INTEGER I
  REAL TE(20),RAT0(20),fyT,TEa,B,D1
  OPEN(UNIT=3,FILE='STRTHHZ',STATUS='OLD')
  D=D1
  CALL dirkf(B,D,T,TEa)
  WRITE(*,*) 'TEa'
  WRITE(*,*) TEa
  READ(3,*)(TE(I),I=1.13)

```

```

READ(3,*)(RATO(I),I=1.13)
DO 10 I=1,13
IF(TEa.LT.TE(I))THEN
ITE=I
GOTO 20
ENDIF
10 CONTINUE
TE2=TE(ITE-1)
TE1=TE(ITE)
RATO2=RATO(ITE-1)
RATO1=RATO(ITE)
RATIO=(TEa-TE2)*(RATO1-RATO2)/(TE1-TE2)+RATO2
WRITE(*,*)'RATIO'
WRITE(*,*) RATIO
fyt=480*RATIO
WRITE(*,*)'fyt'
WRITE(*,*) fyt
CLOSE (3)
RETURN
END

```

*Part D*

Data (TEMP2) sheet for temperature of various width and time of fire exposure of beam at various depths from exposed surface.

Depth from exposed surface (D)

0. 10. 20. 30. 40. 50. 60. 70. 80. 90. 100. 110. 120. 130. 140. 150. 175. 200. 250.

Time of fire exposure (T)

0.0 1.0 1.5 2.0 3.0 4.0

Width of beam (B)

500.0 400.0 300.0 250.0 200.0 150.0 125.0 100

Reduction factor (COE)

1.00 0.99 0.87 0.72 0.46 0.22 0.10 0.08 0.05 0.03 0.00 0.00 0.00

Data (YONGST) for reduction factor in elastic modules of prestressing steel with temperature.

Temperature (TEa)

20 100 200 300 400 500 600 700 800 900 1000 1100 1200

Reduction factor (RATO)

1.00 0.98 0.95 0.88 0.81 0.54 0.41 0.10 0.07 0.03 0.00 0.00 0.00

Data (YONG) for reduction factor of concrete strength and strain with temperature.

Temperature (TEa)

20 100 200 300 400 500 600 700 800 900 1000 1100 1200

Reduction factor (FAC)

1.00 0.97 0.94 0.91 0.85 0.74 0.60 0.43 0.27 0.15 0.06 0.02 0.00

Strain value (ec)

0.0025 0.0035 0.0045 0.0060 0.0075 0.0095 0.0125 0.0140 0.0145 0.0150 0.0150 0.0150 0.0150

Data (STRTH) for reduction factor of steel strength with temperature.

Temperature (TEa)

20 100 200 300 400 500 600 700 800 900 1000 1100 1200

Reduction factor (RATO)

1.00 1.00 1.00 1.00 1.00 0.78 0.47 0.23 0.11 0.06 0.04 0.02 0.00

Data (YONGST1) for reduction factor of steel young modules with temperature.

Temperature (TEa)

20 100 200 300 400 500 600 700 800 900 1000 1100 1200

Reduction factor (RATIO)

1.00 1.00 0.90 0.80 0.70 0.60 0.31 0.13 0.09 0.07 0.04 0.02 0.00

Factors from 'Analysis of prestressed concrete structures exposed to fire' by Hertz.

Data (EstHZ) for reduction factor of elastic modules of steel with temperature.

Temperature

20 100 200 300 400 500 600 700 800 900 1000 1100 1200

Reduction factor

1.000 0.998 0.936 0.829 0.714 0.457 0.243 0.129 0.050 0.025 0.000 0.000 0.000

Data (EvalHZ) for reduction factor of elastic modules of concrete with temperature.

Temperature

20 100 200 300 400 500 600 700 800 900 1000 1100 1200

Reduction factor

1.00 1.00 0.650 0.364 0.186 0.043 0.100 0.000 0.000 0.000 0.00 0.00 0.00

Data (STRTHHZ) for reduction factor of steel strength with temperature.  
Temperature

20 100 200 300 400 500 600 700 800 900 1000 1100 1200

Reduction factor

1.00 0.95 0.875 0.775 0.65 0.475 0.27 0.125 0.05 0.025 0.0 0.0 0.0

Data (YONGHZ) for reduction factor of concrete strength with temperature.  
Temperature

20 100 200 300 400 500 600 700 800 900 1000 1100 1200

Reduction factor

1.00 0.975 0.85 0.825 0.66 0.325 0.10 0.08 0.03 0.0 0.0 0.0 0.00

Factors from 'Computer assisted analysis of the fire resistance of steel and composite concrete structures' (C.E.C agreement No. 7210-SA/502)

Data (Evalue) for reduction factor in elastic modules of concrete with temperature.

Temperature

20 100 200 300 400 500 600 700 800 900 1000 1100 1200

Reduction factor

1.00 0.865 0.695 0.520 0.360 0.235 0.130 0.080 0.040 0.020 0.00 0.00 0.00

*Part E*

Sample output for Deflection program.

Script started on Fri May 12 13:07:21 1995]1;shiplake

(shiplake)1 Script% a.out

B=T=H=H1=As=

285mm

1h

580mm

531mm

1631mm\*\*2

L=c=w=

8m

4m

11000 N/m

M=

P=a=

0

IPa

SUM11SUM22SUM33SUMSUM4

0. 0. 0. 0. 586667.

NO OF NODES

X=Y=

15

47.5

58

TEa

314.000

314.000

TE1,TE2,FAC1,FAC2,ec1,ec2

400.000 300.000 0.850000 0.910000 7.50000E-03 6.00000E-03

FACTecC

0.901600 6.21000E-03

E

5444.44

5444.44

47.5

58

TEa

314.000

314.000

TE1,TE2,FAC1,FAC2,ec1,ec2

400.000 300.000 0.850000 0.910000 7.50000E-03 6.00000E-03

FACTecC

0.901600 6.21000E-03

E

5444.44

5444.44

142.5

58

TEa

259.000

259.000

TE1,TE2,FAC1,FAC2,ec1,ec2

300.000 200.000 0.910000 0.940000 6.00000E-03 4.50000E-03

FACTecC

0.922300 5.38500E-03

E

6422.70

6422.70

47.5

174

TEa

314.000



314.000  
TE1,TE2,FAC1,FAC2.ec1,ec2  
400.000 300.000 0.850000 0.910000 7.50000E-03 6.00000E-03  
FACTecC  
0.901600 6.21000E-03  
E  
5444.44  
5444.44

47.5

174

TEa  
314.000  
314.000  
TE1,TE2,FAC1,FAC2,ec1,ec2  
400.000 300.000 0.850000 0.910000 7.50000E-03 6.00000E-03  
FACTecC  
0.901600 6.21000E-03  
E  
5444.44  
5444.44

142.5

174

TEa  
56.2500  
56.2500  
TE1,TE2,FAC1.FAC2,ec1,ec2  
100.0000 20.0000 0.970000 1.00000 3.50000E-03 2.50000E-03  
FACTecC  
0.986406 2.95312E-03  
E  
12525.8  
12525.8

47.5

290

TEa  
314.000  
314.000  
TE1,TE2,FAC1,FAC2.ec1,ec2  
400.000 300.000 0.850000 0.910000 7.50000E-03 6.00000E-03  
FACTecC  
0.901600 6.21000E-03  
E  
5444.44  
5444.44

47.5

290

TEa  
314.000  
314.000

```

TE1,TE2,FAC1,FAC2,ec1,ec2
  400.000 300.000 0.850000 0.910000 7.50000E-03 6.00000E-03
FACTecC
  0.901600 6.21000E-03
E
  5444.44
  5444.44
142.5
290
TEa
  56.2500
  56.2500
TE1,TE2,FAC1,FAC2,ec1,ec2
  100.0000 20.0000 0.970000 1.00000 3.50000E-03 2.50000E-03
FACTecC
  0.986406 2.95312E-03
E
  12525.8
  12525.8
47.5
406
TEa
  314.000
  314.000
TE1,TE2,FAC1,FAC2,ec1,ec2
  400.000 300.000 0.850000 0.910000 7.50000E-03 6.00000E-03
FACTecC
  0.901600 6.21000E-03
E
  5444.44
  5444.44
47.5

```

Table for variation of steel strength with time

$B = 285 \text{ mm}, H = 580 \text{ mm}, H1 = 531 \text{ mm}, L = 8000 \text{ mm}, A_s = 1631 \text{ mm}^2$

| Times (h) | EC coefficient strength (MPa) | HZ coefficient strength (MPa) |
|-----------|-------------------------------|-------------------------------|
| 0         | 420                           | 420                           |
| 0.5       | 420                           | 379.3                         |
| 1         | 420                           | 322.9                         |
| 1.5       | 390                           | 278.3                         |
| 2         | 358.4                         | 224                           |
| 2.5       | 317.2                         | 192.6                         |
| 3         | 263.4                         | 157.1                         |



```

84 10 CONTINUE
85 PRINT 220,TIME,KTIME
86 200 FORMAT(/////1X,75(1HF)/2HF,F/F* MAXIMAL TEMPERATURES/'F*,
87 1 18A4/' F MAX=',F8.3,1CX,'YMAX=',F8.3/'F')
88 210 FORMAT('F',13(I5,F5,0))
89 220 FORMAT(2H F/2H F/'F MAX-TIME',F7.2,10X,'NUMBER OF'
90 1 'TIME INCREMENTS',I5/2H F/2H F/2H F,75(1HF))
91 230 FORMAT('F',18F7.C)
92 RETURN
93 END
94
95 SUBROUTINE OUT2(IX,IY,NN,NE,X,Y,TIME,KTIME,DELTI,T,TT,TMAX,FLOW,
96 1 TFIRE,NODT,AXIAL)
97 C-----THIS ROUTINE PRINTS NODAL TEMPERATURES AND VOID AIR TEMPERATURES
98 DIMENSION X(NN),Y(NN),TT(NN),TMAX(NN),FLOW(NN)
99 LOGICAL TMAX,AXIAL,LDUM,LEN
100 COMMON/ENCON/H(50),TAIR(2)
101 COMMON/ENCLOS/LEN,NENC,NENCNG(2),IGREN(2,4),NNODEN(2)
102 1 INODEN(100);XSYM(7);YSYM(2)
103 COMMON/TOUT/II,TOUT(100),TIMMAX,DTMAX,TIMFAC,KTMAX,KUPDA
104 TIME1=TIME-DELTI
105 DO 5 IJ=1,NN
106 IF(TMAX(IJ) GOTO 5
107 C-----IF THE NODAL TEMPERATURES DECREASES SET TMAX=.TRUE. AND PRINT
108 C-----MAX TEMPERATURE TT
109 IF(TT(IJ).GT.1.001*T(IJ))
110 1 PRINT 200,IJ,TT(IJ),TIME1,DELTI
111 IF(TT(IJ).GT.1.001*T(IJ))TMAX(IJ)=.TRUE.
112 TT(IJ)=AMAX1(TT(IJ),T(IJ))
113 5 CONTINUE
114 C-----IF TIME=TOUT PRINT ALL TEMPERATURES
115 IF((TIME-TOUT(II)).LT.-1.E-4) GOTO 70
116 PRINT 100,TIME,KTIME,TFIRE,NODT
117 IF(.NOT.LEN) GOTO 30
118 PRINT 300
119 DO 20 I=1,NENC
120 20 PRINT 310,I,TAIR(I)
121 30 CONTINUE
122 II1=II+1
123 IDUM1=1-IY
124 LDUM=IY.LT.7
125 DO 10 I=1,IX
126 IDUM1=IDUM1+IY
127 IDUM2=IDUM1 +IY-1
128 SUBROUTINE BRBCA(BR,BC,EPSIG,BET,BAR,NUM1,N3,ING1)
129 C-----FORM BOUNDARY RADIATION AND CONVECTION MATRICES
130 DIMENSION BR(NUM1,2),BC(NUM1,2),BAR(NB,NUM1)
131 BR(1,1)=0.
132 BR(1,2)=.33333333*BAR(ING1,2)
133 NUM1=NUM1-1
134 IF(NUM1.EQ.1) GOTO 20
135 DO 10 I=2,NUM1
136 BR(I,1)=.16666667*BAR(ING1,I)
137 BR(I,2)=.33333333*(BAR(ING1,I)+BAR(ING1,I+1))
138 10 CONTINUE
139 20 CONTINUE
140 BR(NUM1,1)=.16666667*BAR(ING1,NUM1)
141 BR(NUM1,2)=.33333333*BAR(ING1,NUM1)
142 C
143 DO 30 I=1,NUM1
144 DO 30 J=1,2
145 BC(I,J)=BET*BR(I,J)
146 BR(I,J)=EPSIG*BR(I,J)
147 30 CONTINUE
148 RETURN
149 END
150

```

```

224     SUBROUTINE BRBC(BR,BC,TR,TC,TRD, TCD, NUMI, DTA, NN, MAX, FLOW, TG,
225     1   T, INGI)
226 C-----THIS ROUTINE CALCULATES EXTERNAL HEAT FLOW BY RADIATION AND
227 C-----CONVECTION AND ADDS THE CORRESPONDING CONTRIBUTIONS TO THE
228 C-----VECTOR DATA FOR CALCULATION OF CRITICAL TIME INCREMENT
229     DIMENSION BR(NUMI, 2), BC(NUMI, 2), DTA(NN), FLOW(NN), T(NN)
230     1, TR(NUMI), TC(NUMI), TRD(NUMI), TCD(NUMI)
231     PARAMETER NB=10, NNP=30, NNB2=2*NNB
232     COMMON/BNOD/NUMB(NB), NBOUND(NB, NNB), BAREA(NB, NNB),
233     1   EPSG(NB), BETA(NB), CPG(NB), FA(NB)
234     LOGICAL FA
235 C
236 C-----FIRST NODE
237 C
238     NODE=NBOUND(ING1, 1)
239     TR2=TR(1)
240     TC2=TC(1)
241     TR3=TR(2)
242     TC3=TC(2)
243     TRCD2=TRD(1)
244     TCD2=TCP(1)
245     TRD3=TRD(2)
246     TCD3=TCD(2)
247     BR2=BR(1, 2)
248     BC2=BC(1, 2)
249     BR3=BR(2, 1)
250     BC3=BC(2, 1)
251     FLW=BR2*TR2+BC2*TC2
252     FLW=FLW+BR3*TR3
253     FLW=FLW+5C3*TC3
254     DA=BR2*TRD2+BC2*TCD2
255     DA=DA+BR3*TRD3

     SUBROUTINE PTBNDB(T, TFIRE)
C-----SET PRESCRIBED NODAL BOUNDARY TEMPERATURE
     DIMENSION T(1)
     PARAMETER NB=10, NNB=30, NNB2=2*NNB
     COMMON/PTE/NPTNG, NPTG(NB)
     COMMON/BNOD/NUMB(NP), NBOUND(NB, NNB), BAREA(NB, NNB), TH(NB),
     1   EPSG(NB), BETA(NB), CPG(NB), FA(NB)
     COMMON/UNIT/SIGMA, TABS, TINIT, TAMB, TAMB4
     LOGICAL FA
C-----
     IF(NPTNG.EQ.0) RETURN
C-----EACH PRESCRIBED TEMPERATURE BOUNDARY NODE GROUP
     DO 10 IB=1, NPTNG
     TG=TAMB
     INGI=NPTG(IB)
     IF(FA(ING1)) TG=TFIRE
     NUMI=NUMB(ING1)
     DO 10 I=1, NUMI
     NODE=NBOUND(ING1, 1)
     T(NODE)=TG
10    CONTINUE
     RETURN
     END

     SUBROUTINE RADVEC(F, ETA, N, Q)
C-----THIS ROUTINE FORMS THE LOCAL ENCLOSURE SURFACE RADIATION HEAT
C-----EXCHANGE VECTOR Q=E*ETA
     DIMENSION Q(1), ETA(1), E(N, N)
     QTOT=0.
     DO 20 I=1, N
     QT=0.
     DO 10 J=1, N
10    QT=QT+E(I, J)*ETA(J)
     QTOT=QTOT+QT

```

```

20  Q(I)=QT
    RETURN
220  FORMAT(/'TOTAL RADIATION HEAT EXCHANGE',E11.3)
    END

    SUBROUTINE REG2(NN,NE,NR,N,KTOP,X,Y,NODEL,MNODEL)
C-----THIS SUBROUTINE FORMS VECTOR OF REGION NUMBERS N OF EACH ELEMENT
    DIMENSION X(NN),Y(NN),N(NE),KTOP(4,NE),NODEL(4,NN),MNODEL(NN)
    PARAMETER MNR=10
    COMMON/RGEO/ELFICT(MNR),ET(MNR),SRDIAC(4,MNR)
    LOGICAL ELFICT
    EPS=1.E-7
    DO 10 I=1,NE

        N(I)=1
        IF(NR.EQ.1) GOTO 10
        ND1=KTOP(1,I)
        ND2=KTOP(4,I)
        DO 5 J=2,NR
            IF((X(ND1)-SRDIAC(3,J)).GT.-EPS) GOTO 5
            IF((Y(NC1)-SRDIAC(4,J)).GT.-EPS) GOTO 5
            IF((X(ND2)-SRDIAC(1,J)).LT.EPS) GOTO 5
            IF((Y(NC2)-SRDIAC(2,J)).LT.EPS) GOTO 5
            N(I)=J
        5  CONTINUE
    10  CONTINUE
        DO 40 T=1,NN
            II=0
        20  DO 30 IE=1,NE
                N1=N(IE)
                IF(ELFICT(N1)) GOTO 30
                DO 20 J=1,4
                    IF(KTOP(J,IF).NF.I) GOTO 20
                    II=II+1
                NODEL(II,I)=IE
                IF(II.EQ.4) GOTO 30
        20  CONTINUE
        30  CONTINUE
            MNODEL(I)=II
        40  CONTINUE
        RETURN
    END

589  SUBROUTINE ENCON1
590  C-----THIS ROUTINE FORMS CONVECTION ARRAY H
591  PARAMETER NB=10,NNB=30,NNB2=2*NNB
592  COMMON/BNOD/NUMB(NB),NBOUND(NB,NNB),BAREA(NB,NNB),TH(NB),
593  1  EPSG(NB),BETA(NB),CPG(NB),FA(NB)
594  COMMON/ENCLOS/LEN,NENC, NENCNG(2),IGREN(2,4),NNODEN(2),
595  1  INODEN(100),XSYM(2),YSYM(2)
596  COMMON/ENCON/H(50),TAIR(2)
597  COMMON/DUMMY/HZ(25),DUM 2(25)
598  LOGICAL LEN
599  LOGICAL XSYM,YSYM,SYM
600  INTEGER EN
601  IND=1
602  C-----FORM ZONE CONVECTION ARRAY
603  C-----EACH VOID
604  DO 150 EN=1,NENC
605  SYM=XSYM(EN).OR.YSYM(EN)
606  IN=0
607  NENG=NENCNG(EN)
608  C-----EACH NODE GROUP
609  DO 10 IG=1,NENG
610  I1=IGREN(EN,IG)
611  NUMI=NUMB(I1)
612  BE=BETA(I1)

```

```

613 C-----EACH ZONE
614     DO 10 I=2,NUMI
615     IN=IN+1
616     10 HZ(IN)=BE*BAREA(I1,1)
617 C-----FORM NODE CONVECTION ARRAY
618     CALL HTRANS(HZ,H(IND),IN,SYM)
619     N=IN
620     IF(SYM) N=N+1
621     IND=IND+N
622     150 CONTINUE
623     RETURN
624     END
625
2013     SUBROUTINE TIME
2014 C-----READ TIME INTEGRATION CONTROL DATA
2015     COMMON/TOUT/II,TOUT(100),TIMMAX,DTMAX,TIMEAC,KTMAX,KUPDA
2016     PRINT 200
2017 C-----
2018     READ 100,NT,TIMMAX,DTMAX,TIMFAC,KTMAX,KUPDA
2019 C-----
2020     IF(DTMAX.EQ.0) DTMAX= TIMMAX
2021     IF(TIMFAC.EQ.0) TIMFAC=.8
2022     IF(KTMAX.EQ.0) KTMAX=1000
2023     IF(KUPDA.EQ.0) KUPDA=1
2024 C-----
2025     READ 100,(TOUT(I),1=1,NT)
2026 C-----
2027     PRINT 210,TIMMAX,DTMAX,TIMFAC,KTMAX,KUPDA
2028     PRINT 220,(TOUT(I),1=1,NT)
2029     100 FORMAT()
2030     220 FORMAT('PRINT OUT TIMES',3X,8G7.2/(19X,8G7.2))
2031     200 FORMAT('/'TIME'/' *****/)
2032     210 FORMAT('MAXIMUM TIME=',G8.3/' MAXIMUM TIME INCREMENT=',G8.3/
2033     1 'CRITICAL TIME INCREMENT FACTOR=',G8.3/
2034     2 'MAXIMUM NUMBER OF TIME INCREMENTS=',I5/
2035     3 'NUMBER OF STEPS BETWEEN UPDATING OF CONDUCTION MATRIX=',I5)
2036     RETURN
2037     END
708     SUBROUTINE ENRAD1(X,Y)
709 C-----FORM RADIATION MATRICES FOR EACH VOID AND STORE THEM IN
710 C-----THE VECTOR E.
711 C-----CALCULATE VIEW-FACTOR MATRIX VIEW AND ZONE AREA VECTOR D
712     DIMENSION X(1),Y(1),A(25,25),B(25,25)
713     PARAMETER NB=10,NNB=30,NNB2=2*NNB
714     COMMON/BNOD/NUM B(NB),N BOUND(NB,NNB),BAREA(NB, NNB),
715     1 EPSG(NB),BETA(NB),CPG(NB),FA(NB)
716     COMMON/ENCLOS/LEN,NENC,NENCNG(2),IGREN(2,4),NNODEN(2),
717     1 INODEN(100),XSYM(2),YSYM(2)
718     COMMON/ENRAD/E(1000)
719     COMMON/UNIT/SIGMA,TABS
720     COMMON/DIM/MAXNG,MAXNOD
721     COMMON/DUMMY/D(25),DUM2(25)
722     DIMENSION VIEW(25,25)
723     EQUIVALENCE (A(1),VIEW(1))
724     DATA IND,IE/0,11
725     LOGICAL LEN
726     LOGICAL XSYM,YSYM,SYM
727     INTEGER EN
728 C-----EACH VOID
729     DO 150 EN=1,NENC
730     CALL VIEWFC(X,Y,D,EN,VIEW,MAXNOD)
731 C-----FORM THE MATRICES A AND B
732     NENG=NENONG(EN)
733     IN=0
734 C-----EACH NODE GROUP
735     DO 120 IG=1,NENG
736     I1=IGREN(EN,IG)

```

```

737     NUMI=NUMB(I1)
738 C-----EACH ZONE
739     DO 120 I=2,NUMI
740     IN=IN+1
741     JN=0
742     DO 120 JG=1,NENG
743     J1=IGREN(EN,JG)
744     NUMJ=NUMB(J1)
745     EPSJ=EPSG(J1)
746     DO 120 J=2,NUMJ
747     JN=JN+1
748     B(IN,JN)=VIEW(IN,JN)*SIGMA
749     A(IN,JN)=-VIEW(tN,JN), (1.-EPSJ)/EPSJ/D(JN)
750     IF B(IN.NE.JN) GOTO 120
751     B(IN,JN)=-SIGMA+B(IN,JN)
752     A(IN,JN)=1./EPSJ/D(JN)+A(IN,JN)
753 120 CONTINUE
754     N=IN
755 C-----INVERT A AND STORE RESULT IN A
756     CALL INVER(A,N,MAXNOD)
757 C-----MULTIPLY A AND B AND STORE RESULT IN A
758     CALL MULT(A,B,N,MAXNOD)
759     SYM=.FALSE.
760     IF(XSYM(EN).OR.YSYM(EN)) SYM=.TRUE.
761     NZ=N
762     IF(SYM) N=N+1
763 C-----TRANSFORM THE LOCAL RADIATION MATRICE A AND STORE THE RESULT IN
764 C-----VECTOR E
765 C-----B IS EMPLOYED AS A DUMMY MATRIX
766     CALL ETRANS(A,B,E(IE),N,NZ,SYM,MAXNOD)
767     IE=IE+N*N
988     SUBROUTINE FQBND(B,FLOW,DTA,NN,MAX,TFIRE)
989 C-----THIS ROUTINE PREPARES CALCULATION OF PRESCRIBED BOUNDARY FLOW
990     DIMENSION T(NN),DTA(NN),FLOW(NN)
991     PARAMETER NB=10,NNB=30,NNB2=2*NNB
992     COMMON/FQB/NFQNG,NFQG(NB),TR(NNB),TC(NNB)
993     1 BR(NNB2),BC(NNB2),TRD(NNB),TCD(NNB)
994     COMMON/BNOD/NUMB(NB),NBOUND(NB,NNB),BAREA(NB,NNB),
995     1 EPSG(NB),BETA(NB),CPG(NB),FA(NB)
996     COMMON/UNIT/SIGMA,TABS,TINIT,TAMB,TAMB4
997     LOGICAL FA
998 C-----NULL FLOW VECTOR
999     DO 777 I=1,NN
1000 777 FLOW(I)=0,
1001 C-----RETURN IF NO PRESCRIBED BOUNDARY FLOW
1002     IF(NFQNG.EQ.0) RETURN
1003     TF4=(TFIRE+TABS)**4
1004     IND=1
1005 C-----EACH BOUNDARY FLOW NODE GROUP
1006     DO 30 IB=1.NFQNG
1007     TG4=TAMB4
1008     TG=TAMB
1009     ING1=NFQG(IB)
1010     IF(FA(ING1)) TG=TFIRE
1011     IF(FA(ING1)) TG4=TF4
1012     NUMI=NUMB(ING1)
1013     CP=CPG(ING1)
1014     DO 20 I=1.NUMI
1015     NODE=NBOUND(ING1,I)
1016     TNODE=T(NODE)
1017     TNABS=TNODE+TABS
1018 C-----RADIATION
1019     TRD(I)=4.*TNABS**3
1020     TR(I)= TG4-TNABS**4
1021 C-----CONVECTION
1022     DUM=TG-TNODE
1023     TCD(I)=CP*ABS(DUM)**(CP-1.)

```



## A.I.B Computer Program Based on FEM/DEM

### Finite Discrete Element PROGRAM [A.2]

```

/* File Y1.c==Y1BEAM.c */
#include "Yproto.h"
/*****PRIVATE*****/
/* OUTPUT */
static INT i1num[100]; /* numbers for space saving format */
static DBL d1num[100]; /* numbers for space saving format */
static CHR c1code[500]; /* coded i1para in space saving format */

static void YaOutput(prefix,index,suffix,ndigit,
                    nelem,nnode,
                    dsizsp,dsizve,
                    d1ba1x,d1ba1y,d1ba1z,d1ba2x,d1ba2y,
                    d1ba2z,d1B,d1D,d1H,
                    d1A0,d1A1,d1A2,d1A3,d1P00,
                    d1P01,d1P02,d1P03,d1U0,d1U1,
                    d1ncix,d1nciy,d1nciz,d1nccx,d1nccy,
                    d1nccz,d1ncfx,d1ncfy,d1ncfz,d1ncmx,
                    d1ncmy,d1ncmz,d1ncox,d1ncoy,d1ncoz,
                    d1ncvx,d1ncvy,d1ncvz,d1ne1x,d1ne1y,
                    d1ne1z,d1ne2x,d1ne2y,d1ne2z,
                    i1elty,i2elto)
CHR *prefix; INT index; CHR *suffix; INT ndigit;
INT nelem; INT nnode;
DBL dsizsp; DBL dsizve;
DBL *d1ba1x; DBL *d1ba1y; DBL *d1ba1z; DBL *d1ba2x; DBL *d1ba2y;
DBL *d1ba2z; DBL *d1B; DBL *d1D; DBL *d1H;
DBL *d1A0; DBL *d1A1; DBL *d1A2; DBL *d1A3; DBL *d1P00;
DBL *d1P01; DBL *d1P02; DBL *d1P03; DBL *d1U0; DBL *d1U1;
DBL *d1ncix; DBL *d1nciy; DBL *d1nciz; DBL *d1nccx; DBL *d1nccy;
DBL *d1nccz; DBL *d1ncfx; DBL *d1ncfy; DBL *d1ncfz; DBL *d1ncmx;
DBL *d1ncmy; DBL *d1ncmz; DBL *d1ncox; DBL *d1ncoy; DBL *d1ncoz;
DBL *d1ncvx; DBL *d1ncvy; DBL *d1ncvz; DBL *d1ne1x; DBL *d1ne1y;
DBL *d1ne1z; DBL *d1ne2x; DBL *d1ne2y; DBL *d1ne2z;
int *i1elty; INT **i2elto;

{ DBL xc,yc,zc,s1,s2,s3,a1x,a1y,a1z,a2x,a2y,a2z,a3x,a3y,a3z;
  INT npar,ipar,ielem,n0,n1; FILE *fout;

  npar=13;
  if(CHRCmp(prefix,"a1_",3)==0) /* output animation */
  { fout=OpenFile("a1_",index,suffix, "w");
    if(fout!=FILENULL)
    { for (ielem=0;ielem<nelem;ielem++)
      { n0=i2elto[0][ielem];
        n1=i2elto[1][ielem];

```

```

V3DAdd(xc,yc,zc,d1nccx[n1],d1nccy[n1],d1nccz[n1],
      d1nccx[n0],d1nccy[n0],d1nccz[n0]);
V3DSca(xc,yc,zc,RP5);
V3DAdd(a1x,a1y,a1z,d1nccx[n1],d1nccy[n1],d1nccz[n1],
      -d1nccx[n0],-d1nccy[n0],-d1nccz[n0]);
V3DNor(s1,a1x,a1y,a1z);
V3DTranToG1(a2x,a2y,a2z,d1ba1x[ielem],d1ba1y[ielem],
      d1ba1z[ielem],d1ne1x[n0],d1ne1y[n0],d1ne1z[n0],
      d1ne2x[n0],d1ne2y[n0],d1ne2z[n0]);
V3DTranToG1(a3x,a3y,a3z,d1ba2x[ielem],d1ba2y[ielem],
      d1ba2z[ielem],d1ne1x[n0],d1ne1y[n0],d1ne1z[n0],
      d1ne2x[n0],d1ne2y[n0],d1ne2z[n0]);
V3DDot(s2,a2x,a2y,a2z,a1x,a1y,a1z);
V3DDot(s3,a3x,a3y,a3z,a1x,a1y,a1z);
if(s2<R0)s2=-s2;
if(s3<R0)s3=-s3;
if(s2>s3)
{ V3DCro(a3x,a3y,a3z,a1x,a1y,a1z,a2x,a2y,a2z);
  V3DCro(a2x,a2y,a2z,a3x,a3y,a3z,a1x,a1y,a1z);
}
else
{ V3DCro(a2x,a2y,a2z,a3x,a3y,a3z,a1x,a1y,a1z);
  V3DCro(a3x,a3y,a3z,a1x,a1y,a1z,a2x,a2y,a2z);
}
V3DNor(s2,a2x,a2y,a2z);
V3DNor(s3,a3x,a3y,a3z);

i1num[0]=ndigit;
i1num[1]=npar;
d1num[3]=xc/dsizsp;
d1num[4]=yc/dsizsp;
d1num[5]=zc/dsizsp;
d1num[6]=a1x;
d1num[7]=a1y;
d1num[8]=a1z;
d1num[9]=a2x;
d1num[10]=a2y;
d1num[11]=a2z;
d1num[12]=s1/dsizsp;
for(ipar=3;ipar<npar;ipar++)
{ d1num[ipar]=MAXIM((-R1),MINIM(d1num[ipar],R1));
}
codeDBLtoINT(d1num,i1num);
i1num[2]=i1elty[ielem];
codeINTtoCHR(c1code,i1num);
CHRw(fout,c1code); CHRwcr(fout);
}
fclose(fout);
} } }

```

```

static void GauslIntegrateRectangle(
    dfac,dE,dcoFc,dcoEc,
    epst,kaptx,kapty,
    d0fax,d0mx,d0my,dU,d1xcor,d1ycor
    )
    DBL dfac;      DBL dE;      DBL dcoFc;      DBL dcoEc;
    DBL epst;      DBL kaptx;      DBL kapty;
    DBL *d0fax; DBL *d0mx; DBL *d0my; DBL *dU; DBL *d1xcor; DBL *d1ycor;
{
    DBL ksig[4]; DBL etag[4];
    DBL shf0, shf1, shf2, shf3;
    DBL shf0k, shf1k, shf2k, shf3k;
    DBL shf0e, shf1e, shf2e, shf3e;
    DBL scale,xgas, ygas, xgask, ygask, xgase, ygase;
    DBL jacg, epsg; DBL sigg;
    DBL force; DBL momx; DBL momy;
    INT iga;

    ksig[0]=-MYRGAUSP4NOD;
    ksig[1]= MYRGAUSP4NOD;
    ksig[2]= MYRGAUSP4NOD;
    ksig[3]=-MYRGAUSP4NOD;
    etag[0]=-MYRGAUSP4NOD;
    etag[1]=-MYRGAUSP4NOD;
    etag[2]= MYRGAUSP4NOD;
    etag[3]= MYRGAUSP4NOD;

    force=R0; momx=R; momy=R0;
    for(iga=0;iga<4;iga++)
    { shf0=RP25*(R1-ksig[iga])*(R1-etag[iga]);
      shf1=RP25*(R1+ksig[iga])*(R1-etag[iga]);
      shf2=RP25*(R1+ksig[iga])*(R1+etag[iga]);
      shf3=RP25*(R1-ksig[iga])*(R1+etag[iga]);
      shf0k=-RP25*(R1-etag[iga]);
      shf1k= RP25*(R1-etag[iga]);
      shf2k= RP25*(R1+etag[iga]);
      shf3k=-RP25*(R1+etag[iga]);
      shf0e=-RP25*(R1-ksig[iga]);
      shf1e=-RP25*(R1+ksig[iga]);
      shf2e= RP25*(R1+ksig[iga]);
      shf3e= RP25*(R1-ksig[iga]);
      xgas=shf0*d1xcor[0] +shf1*d1xcor[1]+shf2*d1xcor[2]+shf3*d1xcor[3];
      ygas=shf0*d1ycor[0] +shf1*d1ycor[1]+shf2*d1ycor[2] +shf3*d1ycor[3];
      xgask=shf0k*d1xcor[0]+shf1k*d1xcor[1]+shf2k*d1xcor[2]
        +shf3k*d1xcor[3];
      ygask=shf0k*d1ycor[0]+shf1k*d1ycor[1]+shf2k*d1ycor[2]
        +shf3k*d1ycor[3];
      xgase=shf0e*d1xcor[0]+shf1e*d1xcor[1]+shf2e*d1xcor[2]

```

```

        +shf3e*d1xcor[3];
ygate=shf0e*d1ycor[0]+shf1e*d1ycor[1]+shf2e*d1ycor[2]
        +shf3e*d1ycor[3];
jacg=xgask*ygate-ygask*xgase;
epsg=epst+kaptx*ygas-kpty*xgas;
/* sigg=dE*epsg-epsg*epsg*((dcoFc-dE*dcoEc)/(dcoEc*dcoEc));
if((*dU)<(-dcoEc))
{ scale>(*dU)/(-dcoEc)-R1;
  if(scale>RP5) scale=RP5;
  sigg=sigg*(R1-1.5*scale);
}
if(sigg>R0)sigg=R0;
*/
sigg=R0;
if(epsg<R0)
{ scale=-epsg/dcoEc;
  sigg=-dcoFc*(R2*scale-scale*scale);
}
if((*dU)<(-dcoEc))
{ scale=-R1>(*dU)/dcoEc;
  if(scale<R0) scale=R0;
  if(scale>RP5) scale=RP5;
  scale=scale*R2;
  sigg=sigg*(R1-scale*scale);
}
force=force+sigg*jacg;
momx=momx+sigg*jacg*ygas;
momy=momy-sigg*jacg*xgas;
}
*d0fax=*d0fax+dfac*force;
*d0mx= *d0mx+dfac*momx;
*d0my=*d0my+dfac*momy;
}

static void ConcreteForce(
        dE,dcoFc,dcoEc,
        epst,kaptx,kpty,
        d0fax,d0mx,d0my,dU,d1xcor,d1ycor
        )
    DBL dE;      DBL dcoFc;   DBL dcoEc;
    DBL epst;    DBL kaptx;   DBL kpty;
    DBL *d0fax; DBL *d0mx;   DBL *d0my; DBL *dU; DBL *d1xcor; DBL *d1ycor;
{
    DBL xcor[4]; DBL ycor[4]; DBL epsc[4];
    DBL facti,factj,fact;
    INT ncompr,nten,icom,iten,icor,jcor;

    ncompr=0;
    nten=0;

```

```

icom=-1;
iten=-1;
for(icor=0;icor<4;icor++)
{ epsc[icor]=epst+kaptx*d1ycor[icor]-kapy*d1xcor[icor];
  if(epsc[icor]<R0)
  { ncompr=ncompr+1;
    if(icom<0)icom=icor;
    if(epsc[icor]<(*dU)(*dU)=epsc[icor];
  }
  else
  { nten=nten+1;
    if(iten<0) iten=icor;
  } }
if(ncompr==0)
{ epsc[0]=R0;
}
else if(ncompr==1)
{ xcor[0]=d1xcor[icom];
  ycor[0]=d1ycor[icom];
  xcor[1]=d1xcor[icom];
  ycor[1]=d1ycor[icom];
  jcor=icom+1; if(jcor>3)jcor=0;
  DBLget0point(facti,factj,fact,epsc[icom],epsc[jcor]);
  xcor[2]=d1xcor[icom]*facti+d1xcor[jcor]*factj;
  ycor[2]=d1ycor[icom]*facti+d1ycor[jcor]*factj;
  jcor=icom-1; if(jcor<0)jcor=3;
  DBLget0point(facti,factj,fact,epsc[icom],epsc[jcor]);
  xcor[3]=d1xcor[icom]*facti+d1xcor[jcor]*factj;
  ycor[3]=d1ycor[icom]*facti+d1ycor[jcor]*factj;
  GausIntegrateRectangle(
      R1,dE,dcoFc,dcoEc,
      epst,kaptx,kapy,
      dOfax,d0mx,d0my,dU,xcor,ycor
  );
}
else if(ncompr==2)
{ xcor[0]=d1xcor[icom];
  ycor[0]=d1ycor[icom];
  icor=icom+1; if(icor>3)icor=0;
  xcor[1]=d1xcor[icor];
  ycor[1]=d1ycor[icor];
  jcor=icor+1; if(jcor>3)jcor=0;
  DBLget0point(facti,factj,fact,epsc[icor],epsc[jcor]);
  xcor[2]=d1xcor[icor]*facti+d1xcor[jcor]*factj;
  ycor[2]=d1ycor[icor]*facti+d1ycor[jcor]*factj;
  jcor=icor-1; if(jcor<0)jcor=3;
  DBLget0point(facti,factj,fact,epsc[icor],epsc[jcor]);
  xcor[3]=d1xcor[icor]*facti+d1xcor[jcor]*factj;
  ycor[3]=d1ycor[icor]*facti+d1ycor[jcor]*factj;
}

```

```

GausIntegrateRectangle(
    R1,dE,dcoFc,dcoEc,
    epst,kaptx,kapty,
    dOfax,d0mx,d0my,dU,xcor,ycor
    );
}
else
{ for(icor=0;icor<4;icor++)
  { xcor[icor]=d1xcor[icor];
    ycor[icor]=d1ycor[icor];
  }
  GausIntegrateRectangle(
      R1,dE,dcoFc,dcoEc,
      epst,kaptx,kapty,
      dOfax,d0mx,d0my,dU,xcor,ycor
      );

  if(nten>0)
  { xcor[0]=d1xcor[iten];
    ycor[0]=d1ycor[iten];
    xcor[1]=d1xcor[iten];
    ycor[1]=d1ycor[iten];
    jcor=iten+1; if(jcor>3)jcor=0;
    DBLgetOpoint(facti,factj,fact,epsc[iten],epsc[jcor]);
    xcor[2]=d1xcor[iten]*facti+d1xcor[jcor]*factj;
    ycor[2]=d1ycor[iten]*facti+d1ycor[jcor]*factj;
    jcor=iten-1; if(jcor<0)jcor=3;
    DBLgetOpoint(facti,factj,fact,epsc[iten],epsc[jcor]);
    xcor[3]=d1xcor[iten]*facti+d1xcor[jcor]*factj;
    ycor[3]=d1ycor[iten]*facti+d1ycor[jcor]*factj;
    GausIntegrateRectangle(
        -R1,dE,dcoFc,dcoEc,
        epst,kaptx,kapty,
        dOfax,d0mx,d0my,dU,xcor,ycor
    );
  } }
}
static void GetSectionForce(
    dbeB,dbeD,dbeH,dbsA0,dbsA1,
    dbsA2,dbsA3,dcoE,dcoFc,dcoEc,
    dstE,dstEc,dstY,depst,dkaptx,dkapty,
    dOfax,d0mx,d0my,dOP0,
    dOP1,dOP2,dOP3,dU
    )
DBL dbeB;   DBL dbeD;   DBL dbeH;   DBL dbsA0;   DBL dbsA1;
DBL dbsA2;   DBL dbsA3;   DBL dcoE;   DBL dcoFc;   DBL dcoEc;
DBL dstE;   DBL dstEc;   DBL dstY;   DBL depst;   DBL dkaptx;   DBL dkapty;
DBL *dOfax;   DBL *d0mx;   DBL *d0my;   DBL *dOP0;
DBL *dOP1;   DBL *dOP2;   DBL *dOP3;   DBL *dU;
{ DBL scale,xcor,ycor,epsc,barEt,barEe,sign;
  DBL d1xcor[4];

```

```

DBL d1ycor[4];
DBL d1bsP[4];
DBL d1bsA[4];
INT ibar;

(*d0fax)=R0;
(*d0mx)=R0;
(*d0my)=R0;
xcor=dbeB*RP5;
ycor=dbeH*RP5;
d1xcor[0]=-xcor; d1xcor[1]= xcor; d1xcor[2]=xcor; d1xcor[3]=-xcor;
d1ycor[0]=-ycor; d1ycor[1]=-ycor; d1ycor[2]=ycor; d1ycor[3]= ycor;
d1bsP[0]=*d0P0; d1bsP[1]=*d0P1; d1bsP[2]=*d0P2; d1bsP[3]=*d0P3;
d1bsA[0]=dbsA0; d1bsA[1]=dbsA1; d1bsA[2]=dbsA2; d1bsA[3]=dbsA3;
for(ibar=0;ibar<4;ibar++)
{ xcor=d1xcor[ibar];
  if(xcor<R0)
  { xcor=xcor+dbeD;
  }
  else
  { xcor=xcor-dbeD;
  }
  ycor=d1ycor[ibar];
  if(ycor<R0)
  { ycor=ycor+dbeD;
  }
  else
  { ycor=ycor-dbeD;
  }
  barEt=depst+dkaptx*ycor-dkapy*xcor;
  barEe=barEt-d1bsP[ibar];
  sigm=barEe*dstE;
  if(sigm>dstY)
  { sigm=dstY;
    d1bsP[ibar]=barEt-dstY/dstE;
  }
  else if(sigm<(-dstY))
  { sigm=-dstY;
    d1bsP[ibar]=barEt+dstY/dstE;
  }
  (*d0fax)=(*d0fax)+sigm*d1bsA[ibar];
  (*d0mx)=(*d0mx)+sigm*d1bsA[ibar]*ycor;
  (*d0my)=(*d0my)-sigm*d1bsA[ibar]*xcor;
}
(*d0P0)=d1bsP[0];
(*d0P1)=d1bsP[1];
(*d0P2)=d1bsP[2];
(*d0P3)=d1bsP[3];
ConcreteForce( dcoE,dcoFc,dcoEc,

```

```

depst,dkaptx,dkapty,
d0fax,d0mx,d0my,dU,d1xcor,d1ycor);
}

static void Ylload( nelelem,nnode,
                   dcoRo,dtime,
                   d1ba1x,d1ba1y,d1ba1z,d1ba2x,d1ba2y,
                   d1ba2z,d1bp1, d1bp2, d1bpt1,d1bpt2,
                   d1bpf1,d1bpf2,d1bpf3,d1B,d1H,
                   d1ncix,d1nciy,d1nciz,d1ncfx,d1ncfy,
                   d1ncfz,d1ncmx,d1ncmy,d1ncmz,d1ne1x,
                   d1ne1y,d1ne1z,d1ne2x,d1ne2y,d1ne2z,
                   d1nmar,d1nmas,
                   i1nnel,i2elto)
INT nelelem; INT nnode;
DBL dcoRo; DBL dtime;
DBL *d1ba1x; DBL *d1ba1y; DBL *d1ba1z; DBL *d1ba2x; DBL *d1ba2y;
DBL *d1ba2z; DBL *d1bp1; DBL *d1bp2; DBL *d1bpt1; DBL *d1bpt2;
DBL *d1bpf1; DBL *d1bpf2; DBL *d1bpf3; DBL *d1B; DBL *d1H;
DBL *d1ncix; DBL *d1nciy; DBL *d1nciz; DBL *d1ncfx; DBL *d1ncfy;
DBL *d1ncfz; DBL *d1ncmx; DBL *d1ncmy; DBL *d1ncmz; DBL *d1ne1x;
DBL *d1ne1y; DBL *d1ne1z; DBL *d1ne2x; DBL *d1ne2y; DBL *d1ne2z;
DBL *d1nmar; DBL *d1nmas;
INT *i1nnel; INT **i2elto;

{ INT ipas,n0,n1,n2,inode,ielem;
  DBL a1x,a1y,a1z,a2x,a2y,a2z;
  DBL rix,riy,riz,ri,ksi,fact,p1,p2;

  for(inode=0;inode<nnode;inode++)
  { d1ncfx[inode]=R0;
    d1ncfy[inode]=R0;
    d1ncfz[inode]=R0;
    d1ncmx[inode]=R0;
    d1ncmy[inode]=R0;
    d1ncmz[inode]=R0;
    d1nmas[inode]=R0;
    d1nmar[inode]=R0;
    i1nnel[inode]=0;
  }
  for(ielem=0;ielem<nelem;ielem++)
  { n0=i2elto[0][ielem];
    n1=i2elto[1][ielem];
    i1nnel[n0]=i1nnel[n0]+1;
    i1nnel[n1]=i1nnel[n1]+1;
    V3DAdd(rix,riy,riz,d1ncix[n1],d1nciy[n1],d1nciz[n1],
           -d1ncix[n0],-d1nciy[n0],-d1nciz[n0]);
    V3DNor(ri,rix,riy,riz);
    d1nmas[n0]=d1nmas[n0]+ri*d1B[ielem]*d1H[ielem]*RP5*dcoRo;
  }
}

```



```

d1nmas[n1]=d1nmas[n1]+ri*d1B[ielem]*d1H[ielem]*RP5*dcoRo;
d1nmar[n0]=d1nmar[n0]+d1B[ielem]*d1H[ielem]*dcoRo*ri*ri*ri/R12;
d1nmar[n1]=d1nmar[n1]+d1B[ielem]*d1H[ielem]*dcoRo*ri*ri*ri/R12;
if(((d1bpt2[ielem]-d1bpt1[ielem]>EPSILON)&&
    ((dtime-d1bpt1[ielem]>EPSILON)&&
    ((d1bpt2[ielem]-dtime)>EPSILON)))
{ ksi=R2*(dtime-RP5*(d1bpt1[ielem]+d1bpt2[ielem]))/
  (d1bpt2[ielem]-d1bpt1[ielem]);
  fact=(R1-ksi)*(R1+ksi)*d1bpf2[ielem]-
    d1bpf1[ielem]*RP5*(R1-ksi)*ksi+
    d1bpf3[ielem]*RP5*ksi*(R1+ksi);
  p1=fact*d1bp1[ielem];
  p2=fact*d1bp2[ielem];
  for(ipas=0; ipas<2; ipas++)
  { V3DTranToGl(a1x,a1y,a1z,d1ba1x[ielem],d1ba1y[ielem],
    d1ba1z[ielem],d1ne1x[n0],d1ne1y[n0],d1ne1z[n0],
    d1ne2x[n0],d1ne2y[n0],d1ne2z[n0]);
    V3DTranToGl(a2x,a2y,a2z,d1ba2x[ielem],d1ba2y[ielem],
    d1ba2z[ielem],d1ne1x[n0],d1ne1y[n0],d1ne1z[n0],
    d1ne2x[n0],d1ne2y[n0],d1ne2z[n0]);
    d1ncfx[n0]=d1ncfx[n0]+RP25*ri*(p1*d1H[ielem]*a1x+p2*
      d1B[ielem]*a2x);
    d1ncfy[n0]=d1ncfy[n0]+RP25*ri*(p1*d1H[ielem]*a1y+p2*
      d1B[ielem]*a2y);
    d1ncfz[n0]=d1ncfz[n0]+RP25*ri*(p1*d1H[ielem]*a1z+p2*
      d1B[ielem]*a2z);
    d1ncfx[n1]=d1ncfx[n1]+RP25*ri*(p1*d1H[ielem]*a1x+p2*
      d1B[ielem]*a2x);
    d1ncfy[n1]=d1ncfy[n1]+RP25*ri*(p1*d1H[ielem]*a1y+p2*
      d1B[ielem]*a2y);
    d1ncfz[n1]=d1ncfz[n1]+RP25*ri*(p1*d1H[ielem]*a1z+p2*
      d1B[ielem]*a2z);
    n2=n0; n0=n1; n1=n2;
  } } }
for(inode=0; inode<nnode; inode++)
{ d1ncfx[inode]=R0;
  d1ncfy[inode]=R0;
  d1ncfz[inode]=R0;
  d1ncmx[inode]=R0;
  d1ncmy[inode]=R0;
  d1ncmz[inode]=R0;

}
}
static void Ylforce( nelelem,n0node,datetime,
  dcoE, dcoEc, dcoFc, dcoKs, dcoRo,
  dstE, dstEc, dsty ,
  d1ba1x,d1ba1y,d1ba1z,d1ba2x,d1ba2y,
  d1ba2z,d1B, d1D, d1H,d1A0,

```

```

d1A1,d1A2,d1A3,d1P00,d1P01,
d1P02,d1P03,d1P10,d1P11,d1P12,
d1P13,d1U0, d1U1,
d1ncix,d1nciy,d1nciz,d1nccx,d1nccy,
d1nccz,d1ncfx,d1ncfy,d1ncfz,d1ncmx,
d1ncmy,d1ncmz,d1ncox,d1ncoy,d1ncoz,
d1ncvx,d1ncvy,d1ncvz,d1ne1x,d1ne1y,
d1ne1z,d1ne2x,d1ne2y,d1ne2z,d1nmar,
d1nmas,d1nrad,d1sepm,
i1nnel,i1noty,i2elto)
INT nelelem; INT *n0node; DBL datime;
DBL dcoE; DBL dcoEC; DBL dcoFC; DBL dCoKS; DBL dcoRo;
DBL dstE; DBL dstEc; DBL dstY;
DBL *d1balx; DBL *d1ba1y; DBL *d1ba1z; DBL *d1ba2x; DBL *d1ba2y;
DBL *d1ba2z; DBL *d1B; DBL *d1D; DBL *d1H; DBL *d1A0;
DBL *d1A1; DBL *d1A2; DBL *d1A3; DBL *d1P00; DBL *d1P01;
DBL *d1P02; DBL *d1P03; DBL *d1P10; DBL *d1P11; DBL *d1P12;
DBL *d1P13; DBL *d1U0; DBL *d1U1;
DBL *d1ncix; DBL *d1nciy; DBL *d1nciz; DBL *d1nccx; DBL *d1nccy;
DBL *d1nccz; DBL *d1ncfx; DBL *d1ncfy; DBL *d1ncfz; DBL *d1ncmx;
DBL *d1ncmy; DBL *d1ncmz; DBL *d1ncox; DBL *d1ncoy; DBL *d1ncoz;
DBL *d1ncvx; DBL *d1ncvy; DBL *d1ncvz; DBL *d1ne1x; DBL *d1ne1y;
DBL *d1ne1z; DBL *d1ne2x; DBL *d1ne2y; DBL *d1ne2z; DBL * d1nmar;
DBL *d1nmas, DBL *d1nrad,
DBL *d1sepm;
INT *i1nnel; INT *i1noty; INT **i2elto;

{ INT nnode, ipas, n0, n1, n2, inode, ielem;
DBL a1x, a1y, a1z, a2x, a2y, a2z;
DBL e01x, e01y, e01z, e02x, e02y, e02z;
DBL fax0, fax1, fax, mx, my, mz, m1, m2, m3, sx, sy, sz;
DBL phx, phy, phz, ph1, ph2, ph3, epst, kapt1, kapt2;
DBL rc, ri, va, rcx, rcy, rcz, rrx, rry, rrz, rix, riy, riz, vcx, vcy, vcz;
DBL ox, oy, oz, oex, oey, oez, o1, o2, o3;
DBL ero;
static INT icount=0;

nnode=*n0node;
ero=SQRT(dcoE*dcoRo);
/* for(ielem=0;ielelem<nelelem;ielelem++) */
for(ielem=0;ielelem<nelelem;ielelem++)
{ if((nnode>19626)&&(ielelem==33968))
{ n0=n1;
}
n0=i2elto[0][ielelem];
n1=i2elto[1][ielelem];
V3DAdd(rix,riy,riz,d1ncix[n1],d1nciy[n1],d1nciz[n1],
-d1ncix[n0],-d1nciy[n0],-d1nciz[n0]);
V3DAdd(rcx,rcy,rcz,d1nccx[n1],d1nccy[n1],d1nccz[n1],

```

```

        -d1nccx[n0], -d1nccy[n0], -d1nccz[n0]);
V3DNor(ri,rix,riy,riz);
V3DNor(rc,rcx,rcy,rcz);
V3DAdd(vcx,vcy,vcz,d1ncvx[n1],d1ncvy[n1],d1ncvz[n1],
        -d1ncvx[n0],-d1ncvy[n0],-d1ncvz[n0]);
V3DDot(va,vcx,vcy,vcz,rcx,rcy,rcz);
V3DCro(oex,oez,oez,rcx,rcy,rcz;vcx,vcy;vcz);
V3DSca(oex,oez,oez,R1/rc);
for(ipas=0;ipas<2;ipas++)
{ e01x=d1ne1x[n0];
  e01y=d1ne1y[n0];
  e01z=d1ne1z[n0];
  e02x=d1ne2x[n0];
  e02y=d1ne2y[n0];
  e02z=d1ne2z[n0];
  V3DTranToGl(a1x,a1y,a1z,d1ba1x[ielem],d1ba1y[ielem],
              d1ba1z[ielem],e01x,e01y,e01z,e02x,e02y,e02z);
  V3DTranToGl(a2x,a2y,a2z,d1ba2x[ielem],d1ba2y[ielem],
              d1ba2z[ielem],e01x,e01y,e01z,e02x,e02y,e02z);
  V3DAdd(rix,riy,riz,d1ncix[n1],d1nciy[n1],d1nciz[11],
        -d1ncix[n0],-d1nciy[n0],-d1nciz[n0]);
  V3DAdd(rcx,rcy,rcz,d1nccx[n1],d1nccy[n1],d1nccz[n1],
        -d1nccx[n0],-d1nccy[n0],-d1nccz[n0]);
  V3DSca(rix;riy,riz,R1/ri);
  V3DSca(rcx,rcy,rcz,R1/rc);
  V3DTranToGl(rrx,rry,rrz,rix,riy,riz,
              e01x,e01y,e01z,e02x,e02y,e02z);
  V3DCro(phx,phy,phz,rrx,rry,rrz,rcx,rcy,rcz);
  V3DTranToLoc(ph1,ph2,ph3,phx,phy,phz,a1x,a1y,a1z,a2x,a2y,a2z);
  V3DAdd(ox,oy,oz,oex,oez,oez,
        -d1ncox[n0],-d1ncoy[n0],-d1ncoz[n0]);
  V3DTranToLoc(o1,o2,o3,ox,oy,oz,a1x,a1y,a1z,a2x,a2y,a2z);
  kapt1=R2*ph1/ri;
  kapt2=R2*ph2/ri;
  epst=(rc-ri)/ri;

if(ipas==0)
{ GetSectionForce(
  d1B[ielem],d1D[ielem],d1H[ielem],d1A0[ielem],d1A1[ielem],
  d1A2[ielem],d1A3[ielem],dcoE,dcoFc,dcoEc,
  dstE,dstEc,dstY,epst+d1sepm[ielem],kapt1,kapt2,
  &fax0,&m1,&m2,&d1P00[ielem],&d1P01[ielem]),
  &(d1P02[ielem]),&(d1P03[ielem]),&(d1U0[ielem]));
}
else
{ GetSectionForce(
  d1B[ielem],d1D[ielem],d1H[ielem],d1A0[ielem],d1A1[ielem],
  d1A2[ielem],d1A3[ielem],dcoE,dcoFc,dcoEc,
  dstE,dstEc,dstY,epst-d1sepm[ielem],-kapt1,-kapt2,

```

```

&fax1,&m1,m2,&(d1P10[ielem]),&(d1P11[ielem]),
&(d1P12[ielem]),&(d1P13[ielem]),&(d1U1[ielem]));
m1=-m1; m2=-m2;
}
m1=m1+dcoKs*ri*d1B[ielem]*d1H[ielem]*d1H[ielem]*o1*ero/R4;
m2=m2+dcoKs*ri*d1H[ielem]*d1B[ielem]*d1B[ielem]*o2*ero/R4;
V3DTranToGl(mx,my,mz,m1,m2,R0,a1x,a1y,a1z,a2x,a2y,a2z);
VB3DCro(sx,sy,sz,mx,my,mz,rcx,rcy,rcz);
V3DSca(sx,sy,sz,R1/rc);
d1ncfx[n0]=d1ncfx[n0]+sx;
d1ncfy[n0]=d1ncfy[n0]+sy;
d1ncfz[n0]=d1ncfz[n0]+sz;
d1ncfx[n1]=d1ncfx[n1]-sx;
d1ncfy[n1]=d1ncfy[n1]-sy;
d1ncfz[n1]=d1ncfz[n1]-sz;
d1ncmx[n0]=d1ncmx[n0]+mx;
d1ncmy[n0]=d1ncmy[n0]+my;
d1ncmz[n0]=d1ncmz[n0]+mz;
n2=n0; n0=n1; n1=n2;
}
d1sepm[ielem]=d1sepm[ielem]+
RP4*(fax1-fax0)/(dcoE*d1B[ielem]*d1H[ielem]);
fax=RP5*(fax0+fax1);
fax=fax+R1P4*dcoKs*d1H[ielem]*d1B[ielem]*va*ero;
d1ncfx[n0]=d1ncfx[n0]-fax*rcx;
d1ncfy[n0]=d1ncfy[n0]-fax*rcy;
d1ncfz[n0]=d1ncfz[n0]-fax*rcz;
d1ncfx[n1]=d1ncfx[n1]+fax*rcx;
d1ncfy[n1]=d1ncfy[n1]+fax*rcy;
d1ncfz[n1]=d1ncfz[n1]+fax*rcz;
}
for(ielem=0;ielem<nelem;ielem++)
{ n0=i2elto[0][ielem];
n1=i2elto[1][ielem];
if((d1U0[ielem]<(-R1PS*dcoEc))||
(DABS(d1P00[ielem])>dstEc)|| (DABS(d1P01[ielem])>dstEc)||
(DABS(d1P02[ielem])>dstEc)|| (DABS(d1P03[ielem])>dstEc)
{ d1U0[ielem]=R0;
i1noty[n0]=0;
d1nrad[n0]=R0;
if(i1nnel[n0]>1)
{ i1noty[nnode]=0; /* broken node zero radius */
d1nrad[nnode]=R0;
i1nnel[n0]=i1nnel[n0]-1;
i1noty[n0]=0;
d1nrad[n0]=R0;
d1nccx[nnode]=d1nccx[n0];
d1nccy[nnode]=d1nccy[n0];
d1nccz[nnode]=d1nccz[n0];

```

```

d1ncix [nnode]=d1ncix [n0];
d1nciy [nnode]=d1nciy [n0];
d1nciz [nnode]=d1nciz [n0];
d1ncox [nnode]=d1ncox [n0];
d1ncoy [nnode]=d1ncoy [n0];
d1ncoz [nnode]=d1ncoz [n0];
d1ncvx [nnode]=d1ncvx [n0];
d1ncvy [nnode]=d1ncvy [n0];
d1ncvz [nnode]=d1ncvz [n0];
d1ncfx [nnode]=d1ncfx [n0];
d1ncfy [nnode]=d1ncfy [n0];
d1ncfz [nnode]=d1ncfz [n0];
d1ncmx [nnode]=d1ncmx [n0];
d1ncmy [nnode]=d1ncmy [n0];
d1ncmz [nnode]=d1ncmz [n0];
d1nmar [nnode]=d1nmar [n0];
d1nmas [nnode]=d1nmas [n0];
d1nelx [nnode]=d1nelx [n0];
d1neiy [nnode]=d1neiy [n0];
d1nelz [nnode]=d1nelz [n0];
d1ne2x [nnode]=d1ne2x [n0];
d1ne2y [nnode]=d1ne2y [n0];
d1ne2z [nnode]=d1ne2z [n0];

i2elto [0] [ielem]=nnode;
nnode=nnode+1;
} }
if( (d1U1 [ielem]<(-R1P5*dcoEc)) ||
    (DABS(d1P10 [ielem])>dstEc) || (DABS(d1P11 [ielem])>dstEc) ||
    (DABS(d1P12 [ielem])>dstEc) || (DABS(d1P13 [ielem])>dstEc))
{ d1U1 [ielem]=R0;
  i1noty [n1]=0;
  d1nrad [n1]=R0;
  if(i1nnel [n1]>1)
  { i1noty [nnode]=0;
    d1nrad [nnode]=R0;
    i1nnel [n1]=i1nnel [n1]-1;
    i1noty [n1]=0;
    d1nrad [n1]=R0;
    d1nccx [nnode]=d1nccx [n1];
    d1nccy [nnode]=d1nccy [n1];
    d1nccz [nnode]=d1nccz [n1];
    d1ncix [nnode]=d1ncix [n1];
    d1nciy [nnode]=d1nciy [n1];
    d1nciz [nnode]=d1nciz [n1];
    d1ncox [nnode]=d1ncox [n1];
    d1ncoy [nnode]=d1ncoy [n1];
    d1ncoz [nnode]=d1ncoz [n1];
    d1ncvx [nnode]=d1ncvx [n1];

```

```

d1ncvy [nnode]=d1ncvy [n1];
d1ncvz [nnode]=d1ncvz [n1];
d1ncfx [nnode]=d1ncfx [n1];
d1ncfy [nnode]=d1ncfy [n1];
d1ncfz [nnode]=d1ncfz [n1];
d1ncmx [nnode]=d1ncmx [n1];
d1ncmy [nnode]=d1ncmy [n1];
d1ncmz [nnode]=d1ncmz [n1];
d1nmar [nnode]=d1nmar [n1];
d1nmas [nnode]=d1nmas [n1];
d1ne1x [nnode]=d1ne1x [n1];
d1ne1y [nnode]=d1ne1y [n1];
d1ne1z [nnode]=d1ne1z [n1];
d1ne2x [nnode]=d1ne2x [n1];
d1ne2y [nnode]=d1ne2y [n1];
d1ne2z [nnode]=d1ne2z [n1];
i2elto [1] [ielem]=nnode;
nnode=nnode+1;
} } }
*n0node=nnode;
}
static void Y1ContactNBS(
    ncel,nnode,
    dcs,dxmin,dymin,dzmin,
    dpenks,dpenmu,dpenpe,d1nccx,d1nccy,
    d1nccz,d1ncfx,d1ncfy,d1ncfz,d1ncmx,
    d1ncmy,d1ncmz,d1ncox,d1ncoy,d1ncoz,
    d1ncvx,d1ncvy,d1ncvz,d1nmas,d1nrad,
    i1noty,i1xf,i1yf,i1zf,i1xn,i1yn,i1zn )

    INT ncel;    INT nnode;
    DBL dcs;    DBL dxmin;    DBL dymin;    DBL dzmin;
    DBL dpenks;    DBL dpenmu;    DBL dpenpe;
    DBL *d1nccx;    DBL *d1nccy;    DBL *d1nccz;    DBL *d1ncfx;    DBL *d1ncfy;
    DBL *d1ncfz;    DBL *d1ncmx;    DBL *d1ncmy;    DBL *d1ncmz;    DBL *d1ncox;
    DBL *d1ncoy;    DBL *d1ncoz;    DBL *d1ncvx;    DBL *d1ncvy;    DBL *d1ncvz;
    DBL *d1nmas;    DBL *d1nrad;
    INT *i1noty;    INT *i1xf;    INT *i1yf;    INT *i1zf;    INT *i1xn;
    INT *i1yn;    INT *i1zn;

{ INT ic,it,ix,iy,iz,ixx,iyy,izz,ixt,iyt,izt,iyc,izc,in,jn,kn;

    DBL dxc;    DBL dyc;    DBL dzc;    DBL dxt;    DBL dyt;    DBL dzt;
    DBL drt;    DBL drc;    DBL kro;
    DBL h1;    DBL h2;    DBL h3;    DBL hx;    DBL hy;
    DBL hz;    DBL p;    DBL px;    DBL py;    DBL pz;
    DBL rx;    DBL ry;    DBL rz;    DBL v;    DBL vn;
    DBL vx;    DBL vy;    DBL vz;    DBL forcen;    DBL forcef;
    DBL fx;    DBL fy;    DBL fz;    DBL tmpx;    DBL tmpy;

```

```

DBL tmpz; DBL mas; DBL stif; DBL pen;      DBL area;

ncel=ncel-2;
for(kn=0;kn<nnode;kn++)                    /* make z layers */
{ ix=((INT)((d1nccx[kn]-dxmin)/dcs));
  iy=((INT)((d1nccy[kn]-dymin)/dcs));
  iz=((INT)((d1nccz[kn]-dzmin)/dcs));
  if((ix>1)&&(iy>1)&&(iz>1)&&(ix<ncel)&&(iy<ncel)&&(iz<ncel))
  { i1zn[kn]=i1zf[iz];
    i1zf[iz]=kn;
  } }
for(kn=0;kn<nnode;kn++)                    /* a loop over non empty z layers */
{ ix=((INT)((d1nccx[kn]-dxmin)/dcs));
  iy=((INT)((d1nccy[kn]-dymin)/dcs));
  iz=((INT)((d1nccz[kn]-dzmin)/dcs));
  if((ix>1)&&(iy>1)&&(iz>1)&&(ix<ncel)&&(iy<ncel)&&(iz<ncel))
  { if(i1zf[iz]<nnode)
    { i1zf[iz]=i1zf[iz]+nnode;
      for(izz=(iz-1);izz<=iz;izz++)        /* make y rows */
      { jn=i1zf[izz];
        if(jn>=nnode)jn=jn-nnode;
        while(jn>=0)
        { iy=((INT)((d1nccy[jn]-dymin)/dcs));
          i1yn[jn]=i1yf[iy];
          i1yf[iy]=jn;
          jn=i1zn[jn];
        } }
        jn=i1zf[iz];
        if(jn>=nnode)jn=jn-nnode;
        while(jn>=0)                        /* a loop over non empty y rows */
        { iy=((INT)((d1nccy[jn]-dymin)/dcs));
          if(i1yf[iy]<nnode)
          { i1yf[iy]=i1yf[iy]+nnode;
            for(iyy=(iy-1);iyy<=(iy+1);iyy++)
            { in=i1yf[iyy];                  /* make x heaps */
              if(in>=nnode)in=in-nnode;
              while(in>=0)
              { ix=((INT)((d1nccx[in]-dxmin)/dcs));
                i1xn[in]=i1xf[ix];
                i1xf[ix]=in;
                in=i1yn[in];
              } }
              in=i1yf[iy];
              if(in>=nnode)in=in-nnode;
              while(in>=0)                  /* a loop over non empty x heaps */
              { ix=((INT)((d1nccx[in]-dxmin)/dcs));
                if(i1xf[ix]<nnode)
                { ic=i1xf[ix];
                  i1xf[ix]=i1xf[ix]+nnode;
                }
              }
            }
          }
        }
      }
    }
  }
}

```

```

while(ic>=0)
{ iyc=((INT)((d1nccy[ic]-dymin)/dcs));
  izc=((INT)((d1nccz[ic]-dzmin)/dcs));
  if((izc==iz)&&(iyc==iy))
  { dxc=d1nccx[ic];
    dyc=d1nccy[ic];
    dzc=d1nccz[ic];
    drc=d1nrad[ic];
    for(ixx=(ix-1);ixx<=(ix+1);ixx++)
    { it=i1xf[ixx];
      if(it>=nnode)it=it-nnode;
      while(it>=0)
      { ixt=((INT)((d1nccx[it]-dxmin)/dcs));
        iyt=((INT)((d1nccy[it]-dymin)/dcs));
        izt=((INT)((d1nccz[it]-dzmin)/dcs));
        if((it!=ic)&&
          ((i1noty[it]>0)|| (i1noty[ic]>=0))&&
          ((izt<iz)|| (iyt<iy)|| ((iyt==iy)&&(ixt<=ix))))
        { dxt=d1nccx[it];
          dyt=d1nccy[it];
          dzt=d1nccz[it];
          drt=d1nrad[it];
          V3DAdd(px,py,pz,dxc,dyc,dzc,-dxt,-dyt,-dzt);
          V3DNor(p,px,py,pz);
          pen=R1-p/(drc+drt);
          if(pen>R0)
          { area=MINIM(drc,drt);
            area=area*area;
            stif=dpenpe*area/(drc+drt);
            mas=MINIM(d1nmas[it],d1nmas[ic]);
            kro=R2*dpenks*SQRT(stif*mas);
            V3DBet(rx,ry,rz,dxc,dyc,dzc,dxt,dyt,dzt,
              (drt/(drc+drt)),(drc/(drc+drt)));
            V3DCro(hx,hy,hz,d1ncox[it],d1ncoy[it],
              d1ncoz[it],(rx-dxt),(ry-dyt),(rz-dzt));
            V3DCro(h1,h2,h3,d1ncox[ic],d1ncoy[ic],
              d1ncoz[ic],(rx-dxc),(ry-dyc),(rz-dzc));
            vx=h1+d1ncvx[ic]-hx-d1ncvx[it];
            vy=h2+d1ncvy[ic]-hy-d1ncvy[it];
            vz=h3+d1ncvz[ic]-hz-d1ncvz[it];
            V3DDot(vn,vx,vy,vz,px,py,pz);
            V3DAdd(vx,vy,vz,vx,vy,vz,
              -vn*px,-vn*py,-vn*pz);
            V3DNor(v,vx,vy,vz);
            forcen=stif*pen-vn*kro;
            if(forcen<R0) forcen=R0;
            forcef=v*kro;
            if(forcef>(forcen*dpenmu))forcef
              =forcen*dpenmu;
          }
        }
      }
    }
  }
}

```



```

V3DAdd(fx,fy,fz,forcen*px,forcen*py,
forcen*pz,-forcef*vx,-forcef*vy,
-forcef*vz);
V3DCro(tmpx,tmpy,tmpz,
rx-dxc,ry-dyc,rz-dzc,fx,fy,fz);
d1ncfx[ic]=d1ncfx[ic]+fx;
d1ncfy[ic]=d1ncfy[ic]+fy;
d1ncfz[ic]=d1ncfz[ic]+fz;
d1ncmx[ic]=d1ncmx[ic]+tmpx;
d1ncmy[ic]=d1ncmy[ic]+tmpy;
d1ncmz[ic]=d1ncmz[ic]+tmpz;
V3DCro(tmpx,tmpy,tmpz,
rx-dxt,ry-dyt,rz-dzt,fx,fy,fz);
d1ncfx[it]=d1ncfx[it]-fx;
d1ncfy[it]=d1ncfy[it]-fy;
d1ncfz[it]=d1ncfz[it]-fz;
d1ncmx[it]=d1ncmx[it]-tmpx;
d1ncmy[it]=d1ncmy[it]-tmpy;
d1ncmz[it]=d1ncmz[it]-tmpz;
    } }
    it=i1xn[it];
  } } }
  ic=i1xn[ic];
} }
in=i1yn[in];
}
for(iyy=(iy-1);iyy<=(iy+1);iyy++) /* delete x heaps */
{ in=i1yf[iyy];
  if(in>=nnode)in=in-nnode;
  while(in>=0)
  { ix=((INT)((d1nccx[in]-dxmin)/dcs));
    i1xf[ix]=-1;
    in=i1yn[in];
  } } }
  jn=i1zn[jn];
}
for(izz=(iz-1);izz<=iz;izz++) /* delete y rows */
{ jn=i1zf[izz];
  if(jn>=nnode)jn=jn-nnode;
  while(jn>=0)
  { iy=((INT)((d1nccy[jn]-dymin)/dcs));
    i1yf[iy]=-1;
    jn=i1zn[jn];
  } } } } }
for(kn=0;kn<nnode;kn++) /* delete z layers */
{ iz=((INT)((d1nccz[kn]-dzmin)/dcs));
  if((iz>1)&&(iz<ncl))i1zf[iz]=-1;
}
}
}

```

```

static void Y1Move(                                     /* Move elements */
    nnode,
    dt, dtime, dagrax,dagray,dagraz,
    d1nccx,d1nccy,d1nccz,d1ncfx,d1ncfy,
    d1ncfz,d1ncmx,d1ncmy,d1ncmz,d1ncox,
    d1ncoy,d1ncoz,d1ncvx,d1ncvy,d1ncvz,
    d1ne1x,d1ne1y,d1ne1z,d1ne2x,d1ne2y,
    d1ne2z,d1nmar,d1nmas,d1pnft,d1pnfx,
    d1pnfy,d1pnfz,d1pnf1,d1pnf2,d1pnf3,
    d1pnt1,d1pnt2,d1pn1x,d1pn1y,d1pn1z,
    d1pn2x,d1pn2y,d1pn2z,i1noty
)
INT nnode;
DBL dt;      DBL dtime;  DBL dagrax;  DBL dagray;  DBL dagraz;
DBL *d1nccx; DBL *d1nccy; DBL *d1nccz; DBL *d1ncfx; DBL *d1ncfy;
DBL *d1ncfz; DBL *d1ncmx; DBL *d1ncmy; DBL *d1ncmz; DBL *d1ncox;
DBL *d1ncoy; DBL *d1ncoz; DBL *d1ncvx; DBL *d1ncvy; DBL *d1ncvz;
DBL *d1ne1x; DBL *d1ne1y; DBL *d1ne1z; DBL *d1ne2x; DBL *d1ne2y;
DBL *d1ne2z; DBL *d1nmar; DBL *d1nmas; DBL *d1pnft; DBL *d1pnfx;
DBL *d1pnfy; DBL *d1pnfz; DBL *d1pnf1; DBL *d1pnf2; DBL *d1pnf3;
DBL *d1pnt1; DBL *d1pnt2; DBL *d1pn1x; DBL *d1pn1y; DBL *d1pn1z;
DBL *d1pn2x; DBL *d1pn2y; DBL *d1pn2z; INT *i1noty;

{ INT inode, inoty, ihys;
  DBL aX,aY,aZ,fX,fY,fZ,vX,vY,vZ,dfix;
  DBL en1x,en1y,en1z,en2x,en2y,en2z,en3x,en3y,en3z,s;
  DBL t1,t2,f1,f2,f3,ksi,fact,ek,ew,tmp;

  ek=R0;
  for(inode=0;inode<nnode;inode++)
  { if(d1nmas[inode]<EPSILON)
    { CHRw(stderr, "XXX");
      d1nmas[inode]=1.0e+09;
      d1nmar[inode]=20000.0;
    }
    inoty=UNMARKEDINT(i1noty[inode]);
    ek=ek+RP5*d1nmas[inode]*(d1ncvx[inode]*d1ncvx[inode]+
      d1ncvy[inode]*d1ncvy[inode]+d1ncvz[inode]*d1ncvz[inode])+
      RP5*d1nmar[inode]*(d1ncox[inode]*d1ncox[inode]+
      d1ncoy[inode]*d1ncoy[inode]+d1ncoz[inode]*d1ncoz[inode]);
    d1ncvx[inode]=d1ncvx[inode]+dagrax*dt;
    d1ncvy[inode]=d1ncvy[inode]+dagray*dt;
    /* d1ncvz[inode]=d1ncvz[inode]+dagraz*dt*(17.82+d1nccz[inode])/100.0;
    */
    d1ncvz [inode]=d1ncvz[inode]+dagraz*dt;
    V3DTranToLoc(vX,vY,vZ,d1ncvx[inode],d1ncvy[inode],d1ncvz[inode],
      d1pn1x[inoty],d1pn1y[inoty],d1pn1z[inoty],
      d1pn2x[inoty],d1pn2y[inoty],d1pn2z[inoty]);
    V3DTranToLoc(fX,fY,fZ,d1ncfx[inode],d1ncfy[inode],d1ncfz[inode],

```

```

    d1pn1x[inoty],d1pn1y[inoty],d1pn1z[inoty],
    d1pn2x[inoty],d1pn2y[inoty],d1pn2z[inoty]);
dfix=d1pnft[inoty];
aX=d1pnfx[inoty]; aY=d1pnfy[inoty]; aZ=d1pnfz[inoty];
f1=d1pnf1[inoty]; f2=d1pnf2[inoty]; f3=d1pnf3[inoty];
t1=d1pnt1[inoty]; t2=d1pnt2[inoty];
fact=R0;
if(((t2-t1)>EPSILON)&&((dtime-t1)>EPSILON)&&((t2-dtime)>EPSILON))
{ ksi=R2*(dtime-RP5*(t1+t2))/(t2-t1);
  fact=(R1-ksi)*(R1+ksi)*f2-
    f1*RP5*(R1-ksi)*ksi+f3*RP5*ksi*(R1+ksi);
}
aX=aX*fact;
aY=aY*fact;
aZ=aZ*fact;

if(dfix<R200) /* supplied force */
{ vX=vX+((aX+fX)/d1nmas[inode])*dt;
}
else if(dfix<R300) /* supplied acceleration */
{ vX=vX+(aX+fX/d1nmas[inode])*dt;
}
else /* supplied velocity */
{ vX=aX;
}
dfix=dfix-R100;
if(dfix>R100) dfix=dfix-R100;
if(dfix>R100) dfix=dfix-R100;
if(dfix<R20) /* supplied force */
{ vY=vY+((aY+fY)/d1nmas[inode])*dt;
}
else if(dfix<R30) /* supplied acceleration */
{ vY=vY+(aY+fY/d1nmas[inode])*dt;
}
else /* supplied velocity */
{ vY=aY;
}
dfix=dfix-R10;
if(dfix>R10) dfix=dfix-R10;
if(dfix>R10) dfix=dfix-R10;
if(dfix<R1P5) /* supplied force */
{ vZ=vZ+((aZ+fZ)/d1nmas[inode])*dt;
}
else if(dfix<R2P5) /* supplied acceleration */
{ vZ=vZ+(aZ+fZ/d1nmas[inode])*dt;
}
else /* supplied velocity */
{ vZ=aZ;
}

```



```

d1pn1x,d1pn1y,d1pn1z,d1pn2x,d1pn2y,
d1pn2z,i1noty,i1elty,i2elto
)
INT nrnd;    CHR *prefix; INT *i0ndex; CHR *suffix; INT ndigit;
INT nelem;   INT *n0node; INT nstep;   INT nnoty;
DBL dadt;    DBL datime;  DBL dacoks;   DBL dacomu;  DBL dacope;
DBL dagrax;  DBL dagray;  DBL dagraz;
DBL dcoE;    DBL dcoEc;   DBL dcoFc;   DBL dcoKs;   DBL dcoRo;
DBL dstE;    DBL dstEc;   DBL dstY;
DBL dsizsp;  DBL dsizve;
DBL *d1ba1x; DBL *d1ba1y; DBL *d1ba1z; DBL *d1ba2x; DBL *d1ba2y;
DBL *d1ba2z; DBL *d1bp1;  DBL *d1bp2;  DBL *d1bpt1; DBL *d1bpt2;
DBL *d1bpf1; DBL *d1bpf2; DBL *d1bpf3;
DBL *d1B;    DBL *d1D;    DBL *d1H;    DBL *d1A0;
DBL *d1A1;   DBL *d1A2;   DBL *d1A3;   DBL *d1P00;  DBL *d1P01;
DBL *d1P02;  DBL *d1P03;  DBL *d1P10;  DBL *d1P11;  DBL *d1P12;
DBL *d1P13;  DBL *d1U0;   DBL *d1U1;
DBL *d1nccx; DBL *d1nccy; DBL *d1nccz; DBL *d1ncix; DBL *d1nciy;
DBL *d1nciz; DBL *d1ncfx; DBL *d1ncfy; DBL *d1ncfz; DBL *d1ncmx;
DBL *d1ncmy; DBL *d1ncmz; DBL *d1ncox; DBL *d1ncoy; DBL *d1ncoz;
DBL *d1ncvx; DBL *d1ncvy; DBL *d1ncvz; DBL *d1ne1x; DBL *d1ne1y;
DBL *d1ne1z; DBL *d1ne2x; DBL *d1ne2y; DBL *d1ne2z; DBL *d1nmar;
DBL *d1nmas; DBL *d1pnft; DBL *d1pnfx; DBL *d1pnfy; DBL *d1pnfz;
DBL *d1pnf1; DBL *d1pnf2; DBL *d1pnf3; DBL *d1pnt1; DBL *d1pnt2;
DBL *d1pn1x; DBL *d1pn1y; DBL *d1pn1z; DBL *d1pn2x; DBL *d1pn2y;
DBL *d1pn2z; INT *i1noty; INT *i1elty; INT **i2elto;
{ DBL ew;
  DBL *d1nrad; DBL *d1sepm;
  INT *i1nnel; INT *i1xf; INT *i1yf; INT *i1zf; INT *i1xn; INT *i1yn;
  INT *i1zn;
  INT irnd,istep,inode,ielem,ncel,nn;
  DBL ri,rix,riy,riz,dcs, zdefl;
  DBL dxmin; DBL dymin; DBL dzmin;
  DBL dxmax;
  i1nnel=INT1NULL;
  d1nrad=DBL1NULL;
  d1sepm=DBL1NULL;
/* TformINT1(FILENULL,0,2*(*n0node),&i1nnel); xxxx ok
TformDBL1(FILENULL,RO,(*n0node),&d1nrad);
TformDBL1(FILENULL,RO,(nelem),&d1sepm); */
TformINT1(FILENULL,0,5*(*n0node),&i1nnel);
TformDBL1(FILENULL,RO,5*(*n0node),&d1nrad);
TformDBL1(FILENULL,RO,(5*nelem),&d1sepm);
for(ielem=0;ielem<nelem;ielem++)
{ V3DAdd(rix,riy,riz,d1ncix[i2elto[1][ielem]],
  d1nciy[i2elto[1][ielem]],d1nciz(i2elto[1][ielem]),
  -d1ncix[i2elto[0][ielem]],-d1nciy[i2elto[0][ielem]],
  -d1nciz[i2elto[0][ielem]]);
  V3DNor(ri,rix,riy,riz);

```

```

    if(d1nrad[i2elto[0][ielem]]
        <(ri*RP4))d1nrad[i2elto[0][ielem]]=ri*RP4;
    if(d1nrad[i2elto[1][ielem]]
        <(ri*RP4))d1nrad[i2elto[1][ielem]]=ri*RP4;
}
dcs=d1nrad[0];
for(inode=1;inode<(*n0node);inode++)
{ dcs=MAXIM(dcs,d1nrad[inode]);
}
dcs=R2*dcs;
dxmin=-dsizsp-(R3*dcs);
dymin=-dsizsp-(R3*dcs);
dzmin=-dsizsp-(R3*dcs);
dxmax=dsizsp+(R3*dcs);
ncel=((INT)((dxmax-dxmin)/dcs));
nn=MAXIM(ncel,(*n0node));
nn=nn+7;
i1xf=INT1NULL;
i1yf=INT1NULL;
i1zf=INT1NULL;
i1xn=INT1NULL;
i1yn=INT1NULL;
i1zn=INT1NULL;
TformINT1(FILENULL,-1,nn,&i1xf);
TformINT1(FILENULL,-1,nn,&i1yf);
TformINT1(FILENULL,-1,nn,&i1zf);
TformINT1(FILENULL,-1,nn,&i1xn);
TformINT1(FILENULL,-1,nn,&i1yn);
TformINT1(FILENULL,-1,nn,&i1zn);
ew=R0;
for(irnd=0;irnd<nrnd;irnd++)
{ CHRw(stderr,"      STARTED IRND,nnode,time=");
  INTw(stderr,irnd,5); INTw(stderr,(*n0node),7); CHRwsp(stderr);
  DBLw(stderr,datetime,15);
  CHRwcr(stderr);
  for(istep=0;istep<nstep;istep++)
  { Ylload(nelem,(*n0node),
    dcoRo, datetime,
    d1ba1x,d1ba1y,d1ba1z,d1ba2x,d1ba2y,
    d1ba2z,d1bp1 ,1lbp2 ,d1bpt1,d1bpt2,
    d1bpf1,d1bpf2,d1bpf3,d1B ,d1H ,
    d1ncix,d1nciy,d1nciz,d1ncfx,d1ncfy,
    d1ncfz,d1ncmx,d1ncmy,d1ncmz,d1ne1x,
    d1ne1y,d1ne1z,d1ne2x,d1ne2y,d1ne2z,
    d1nmar,d1nmas,i1nne1,i2elto);
    Ylforce(nelem,n0node,datetime,
    dcoE ,dcoEc ,dcoFc , dcoKs,dcoRo,
    dstE ,dstEc ,dstY ,
    d1ba1x,d1ba1y,d1ba1z,d1ba2x,d1ba2y,

```

```

d1ba2z,d1B ,d1D ,d1H,d1A0,
d1A1,d1A2,d1A3,d1P00,d1P01,
d1P02,d1P03,d1P10,d1P11,d1P12,
d1P13,d1U0 ,d1U1,
d1ncix,d1nciy,d1nciz,d1nccx,d1nccy,
d1nccz,d1ncfx,d1ncfy,d1ncfz,d1ncmx,
d1ncmy,d1ncmz,d1ncox,d1ncoy,d1ncoz,
d1ncvx,d1ncvy,d1ncvz,d1ne1x,d1ne1y,
d1ne1z,d1ne2x,d1ne2y,d1ne2z,d1nmar,
d1nmas,d1nrad,d1sepm,
i1nnel,i1noty,i2elto):
/* YlContactNBS(
nn,(*n0node),
dcs ,dxmin, dymin, dzmin,
dacoks,dacomu,dacope,d1nccx,d1nccy,
d1nccz,d1ncfx,d1ncfy,d1ncfz,d1ncmx,
d1ncmy,d1ncmz,d1ncox,d1ncoy,d1ncoz,
d1ncvx,d1ncvy,d1ncvz,d1nmas,d1nrad,
i1noty,i1xf , i1yf, i1zf , i1xn,
i1yn ,i1zn); */
YlMove((*n0node),
dadt,datetime, dagrax, dagray,dagraz,
d1nccx,d1nccy,d1nccz,d1ncfx,d1ncfy,
d1ncfz,d1ncmx,d1ncmy,d1ncmz,d1ncox,
d1ncoy,d1ncoz,d1ncvx,d1ncvy,d1ncvz,
d1ne1x,d1ne1y,d1ne1z,d1ne2x,d1ne2y,
d1ne2z,d1nmar,d1nmas,d1pnft,d1pnfx,
d1pnfy,d1pnfz,d1pnf1,d1pnf2,d1pnf3,
d1pnt1,d1pnt2,d1pn1x,d1pn1y,d1pn1z,
d1pn2x,d1pn2y,d1pn2z,i1noty);
datetime=datetime+dadt;
}
if ((*i0ndex)>=0)
{ if (CHRcmp(prefix,"a1",2)==0)
{ YaOutput(prefix,(*i0ndex),suffix,ndigit,
nelem,(*n0node),
dsizsp,dsizve,
d1ba1x,d1ba1y,d1ba1z,d1ba2x,d1ba2y,
d1ba2z,d1B ,d1D ,d1H,
d1A0,d1A1,d1A2,d1A3,d1P00,
d1P01,d1P02,d1P03,d1U0,d1U0,
d1ncix,d1nciy,d1nciz,d1nccx,d1nccy,
d1nccz,d1ncfx,d1ncfy,d1ncfz,d1ncmx,
d1ncmy,d1ncmz,d1ncox,d1ncoy,d1ncoz,
d1ncvx,d1ncvy,d1ncvz,d1ne1x,d1ne1y,
d1ne1z,d1ne2x,d1ne2y,d1ne2z,
i1elty,i2elto);
(*i0ndex)=(*i0ndex)+1;
} } }

```

```

FREE(i1zn);
FREE(i1yn);
FREE(i1xn);
FREE(i1zf);
FREE(i1yf);
FREE(i1xf);
FREE(d1sepm);
FREE(d1nrad);
FREE(i1nnel);
i1xf=INT1NULL;
i1yf=INT1NULL;
i1zf=INT1NULL;
i1xn=INT1NULL;
i1yn=INT1NULL;
i1zn=INT1NULL;
d1sepm=DBL1NULL;
d1nrad=DBL1NULL;
i1nnel=INT1NULL;
}

```

```

/***** PUBLIC *****/
void YIDYNAM( finp,fcheck,yl      /** dynamics of line elements **/
)
FILE *finp; FILE *fcheck; YL yl;
{ int iword;
  CHR word[50];
  CHR prefix[10];      /* output file extension */
  CHR suffix[10];     /* output file name */
  INT index;          /* output file index */
  INT ndigit;        /* number of digits for coded output */
  INT narnd,natis;
  DBL datst,datim;
  DBL dabox,dagrx,dagry,dagrz;
  DBL daiks,daimu,daipe;
  DBL dacEm,dacEc,dacFc,dacKs,dacRo,dasEm,dasEc,dasYs;

  CHRw(stderr,"***** Y IS PROCESSING LINE ELEMENTS (YIDYNAM) *****");
  CHRwcr(stderr);

  index=-1;
  CHRr(finp,word);
  CHRw(fcheck,word); CHRwcr(fcheck);
  while(CHRcmp(word,"#END",4)!=0)
  { CHRw(fcheck,word); CHRwcr(fcheck);
    if(CHRcmp(word,"#NARND",6)==0)      /* number of rounds */
    { INTr(finp,&narnd);
      }
  }
}

```



```

else if(CHRCmp(word,"#NATIS",6)==0) /*number of steps each round*/
{ INTr(finp,&natis);
}
else if(CHRCmp(word,"#FOUT",5)==0) /* output file */
{ CHRr(finp,prefix); INTr(finp,&index); CHRr(finp,suffix);
  INTr(finp,&ndigit);
}
else if(CHRCmp(word,"#DATST",6)==0) /* current time step */
{ DBLr(finp,&datst);
}
else if(CHRCmp(word,"#DATIM",6)==0) /* current time step */
{ DBLr(finp,&datim);
}
else if(CHRCmp(word,"#DAGR X",6)==0) /* acceleration gravity x */
{ DBLr(finp,&dagr x);
}
else if(CHRCmp(word,"#DAGR Y",6)==0) /* acceleration gravity y */
{ DBLr(finp,&dagr y);
}
else if(CHRCmp(word,"#DAGR Z",6)==0) /* acceleration gravity z */
{ DBLr(finp,&dagr z);
}
else if(CHRCmp(word,"#DACEC",6)==0) /* concrete epsilon cu */
{ DBLr(finp,&dacEc);
}
else if(CHRCmp(word,"#DACEM",6)==0) /* concrete elastic modulus */
{ DBLr(finp,&dacEm);
}
else if(CHRCmp(word,"#DACFC",6)==0) /* concrete fcu */
{ DBLr(finp,&dacFc);
}
else if(CHRCmp(word,"#DACKS",6)==0) /* concrete ksi 0.0-1.0 */
{ DBLr(finp,&dacKs);
}
else if(CHRCmp(word,"#DACRO",6)==0) /* concrete densiti kg/m3 */
{ DBLr(finp,&dacRo);
}
else if(CHRCmp(word,"#DASEC",6)==0) /* steel Elastic modulus */
{ DBLr(finp,&dasEc);
}
else if(CHRCmp(word,"#DASEM",6)==0) /* steel Elastic modulus */
{ DBLr(finp,&dasEm);
}
else if(CHRCmp(word,"#DASYS",6)==0) /* steel Yield stress */
{ DBLr(finp,&dasYs);
}
else if(CHRCmp(word,"#DAIKS",6)==0) /* penetration ksi 0.0-1.0 */
{ DBLr(finp,&daiks);
}

```

```

else if(CHRCmp(word,"#DAIMU",6)==0) /* penetration mu 0.0-1.0 */
{ DBLr(finp,&daimu);
}
else if(CHRCmp(word,"#DAIPE",6)==0) /* penetration penalty N/m2 */
{ DBLr(finp,&daipe);
}
else
{ CHRw(stderr,"YIMOVE: unknown name: ");
  CHRw(stderr,word);
  CHRwcr(stderr);
  exit(1);
}
  CHRr(finp,word);
}
YlDynamics(narnd,prefix,(&index),suffix,ndigit,
  y1->nelem,&(y1->nnode),natis,y1->nnoty,
  datst,datim,daiks,daimu,daipe,
  dagrxdagry,dagrzdacEm,dacEc,dacFc,dacKs,dacRo,
  dasEc,dasEm,dasYs,
  y1->dsizsp,y1->dsizve,
  y1->d2bc[0],y1->d2bc[1],y1->d2bc[2],y1->d2bc[3],y1->d2bc[4],
  y1->d2bc[5],y1->d2b1[0],y1->d2b1[1],y1->d2b1[2],y1->d2b1[3],
  y1->d2b1[4],y1->d2b1[5],y1->d2b1[6],
  y1->d2bc[6],y1->d2bc[7],y1->d2bc[8],
  y1->d2bc[9],y1->d2bc[10],y1->d2bc[11],y1->d2bc[12],
  y1->d2bs[0],y1->d2bs[1],
  y1->d2bs[2],y1->d2bs[3],y1->d2bs[4],y1->d2bs[5],y1->d2bs[6],
  y1->d2bs[7],y1->d2bs[8],y1->d2bs[9],
  y1->d2ncc[0],y1->d2ncc[1],y1->d2ncc[2],y1->d2ncc[3],y1->d2ncc[4],
  y1->d2ncc[5],y1->d2ncf[0],y1->d2ncf[1],y1->d2ncf[2],y1->d2ncf[3],
  y1->d2ncf[4],y1->d2ncf[5],y1->d2ncv[0],y1->d2ncv[1],y1->d2ncv[2],
  y1->d2ncv[3],y1->d2ncv[4],y1->d2ncv[5],y1->d2nce[0],y1->d2nce[1],
  y1->d2nce[2],y1->d2nce[3],y1->d2nce[4],y1->d2nce[5],y1->d2nma[0],
  y1->d2nma[1],y1->d2pn[0],y1->d2pn[1],y1->d2pn[2],y1->d2pn[3],
  y1->d2pn[4],y1->d2pn[5],y1->d2pn[6],y1->d2pn[7],y1->d2pn[8],
  y1->d2pn[9],y1->d2pn[10],y1->d2pn[11],y1->d2pn[12],y1->d2pn[13],
  y1->d2pn[14],y1->i1noty,y1->i1elty,y1->i2elto);
}

```

## A.I.C Rules for Impact/Explosion and Load Distribution – Time Function

### A.I.C.1 Trapezium Rule

One knows that higher-order differences are negligible for small  $h$  in the case of well behaved functions. Neglecting the second and higher-order differences in and putting  $n = 1$ , one obtains

$$\int_{x_0}^{x_0+h} y dx = h \left( f_0 + \frac{1}{2} \Delta f_0 \right) \quad (\text{A.I.C.1})$$

$$= \frac{h}{2} (f_1 + f_0)$$

Equation (A.I.C.1) is called the *trapezium rule*. Geometrically, we replace the portion of the curve between the points  $[x_0, f(x_0)]$  and  $[x_0 + h, f(x_0 + h)]$  by the line segment joining them (Fig. A.I.C.1).

In this rule, the area under the *curve AEB* between the ordinates at  $x_0$  and  $x_0 + h$  is replaced by that under the *chord AB*; i.e. by the area of the *trapezium ABCD*.

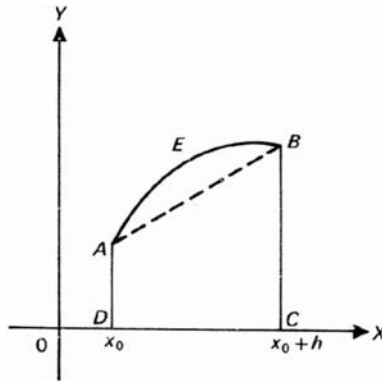


Fig. A.I.C.1. Trapezium rule

#### A.I.C.1.1 Trapezoidal Rule

Let the area between the ordinates at  $x_0$  and  $x_0 + nh$  be divided into  $n$  strips at  $x_0, x_0 + h, \dots, x_0 + nh (= x_1)$ . Applying the trapezium rule to each strip and summing up, we get

$$\int_{x_0}^{x_1} y dx = \frac{h}{2} (f_1 + f_0) + \frac{h}{2} (f_1 + f_2) + \dots + \frac{h}{2} (f_{n-1} + f_n) \tag{A.I.C.2}$$

$$= h \left[ \frac{1}{2} (f_1 + f_n) + (f_1 + f_2 + \dots + f_{n-1}) \right]$$

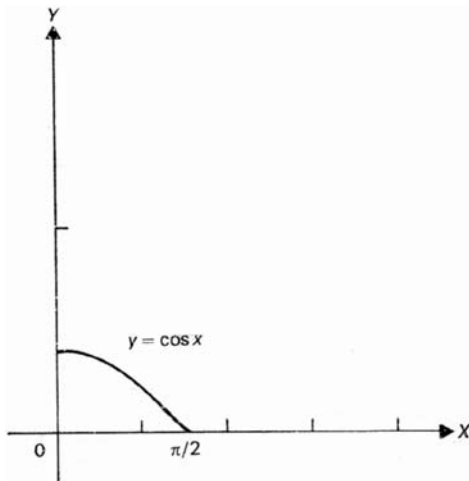
Equation (A.I.C.2) is called the *trapezoidal rule*.

*Example*

Evaluate numerically

$$\int_0^{\pi/4} \cos x dx ,$$

by dividing the interval into 3 strips.



**Fig. A.I.C.2.** Graph of  $\cos x$  over  $[0, \pi/2]$

In Fig. A.I.C.2  $f(x) = \cos x$  and  $h = (\pi/4 - 0)/3 = 0.2618$  (correct to four decimal places);

$$x_0 = 0, \quad f_0 = f(0) = 1$$

$$x_1 = 0.2618, \quad f_1 = f(x_1) = 0.9659$$

$$x_2 = 0.5236, \quad f_2 = f(x_2) = 0.8660$$

$$x_3 = \frac{\pi}{4} = 0.7854, \quad f_3 = f(x_3) = 0.7071$$

Using the trapezoidal rule (A.I.C.2), one finds

$$\int_0^{\pi/4} \cos x \, dx = h \left[ \frac{1}{2} (f_0 + f_3) + (f_1 + f_2) \right] = 0.7030$$

### Error in the Trapezium Rule

If one neglects the second and higher-order differences, the leading error term is  $-(1/12)h\Delta^2 f_0$ .

### Program TRAIL

Program TRAIL has been developed which is based on Trapezoidal Rule. This program is linked with PROGRAM BLAST for loading the WTC Buildings.

### Program (FORTRAN) TRAIL

Trapezoidal integral rule

```

C *****
  REAL FUNCTION F(X)
  REAL X
  F = EXP(-X/2)
  RETURN
  END
C *****
  EXTERNAL F
  REAL A,B,H,P
  INTEGER N,I
  PRINT *,' *****'
  PRINT *,' *'
  PRINT *,' *          TRAPEZOIDAL INTEGRAL RULE'
  PRINT *,' *'
  PRINT *,' *****'
  PRINT *,' ENTER INITIAL VALUE:'
  READ(*,*)A
  PRINT *,' ENTER FINAL VALUE:'
  READ(*,*)B
  PRINT *,' NUMBER OF STRIPS:'
  READ(*,*)N
  H = (B - A)/N
  P = (F(A) + F(B))/2
  DO 100 I = 1, N - 1
    P = P + F(A + I*H)
100 CONTINUE
  WRITE(*,50) H*P
50  FORMAT('INTEGRAL IS = ',F12.8)
  STOP
  END

```

### A.I.C.2 Simpson’s Rule

Let  $n = 2$  the one can write the integral as

$$\int_{x_0}^{x_0+2h} ydx = h \int_0^2 ydk = h \left[ 2f_0 + \frac{2^2}{2} \Delta f_0 + \left( \frac{2^3}{3} - \frac{2^2}{2} \right) \frac{\Delta^2 f_0}{2!} \right] \tag{A.I.C.3}$$

Here one has to neglect the third and higher-order differences. By replacing  $\Delta f_0$  and  $\Delta^2 f_0$  in terms of the functional values, then

$$\int_{x_0}^{x_0+2h} ydx = \frac{h}{3} [f_0 + 4f_1 + f_2] \tag{A.I.C.4}$$

Equation (A.I.C.4) expresses the integral in terms of the ordinates at the three points  $x_0, x_0 + h, x_0 + 2h$ . Hence, the formula determines the areas of two strips at a time. In general, the given interval is divided into an *even* number of *equal* intervals.

One has truncated the series in (A.I.C.4) at  $\Delta^2 f_0$ . It has now been approximated the function  $f(x)$  by a *quadratic curve* (or a parabola).

This equation can be extended to an area subdivided into  $n$  strips, where  $n$  is *even*. Summing up all the integrals, the integral is represented as

$$\int_{x_0}^{x_0+nh} ydx = \frac{h}{3} [(f_0 + f_n) + 4(f_1 + f_3 + \dots + f_{n-1}) + 2(f_2 + f_4 + \dots + f_{n-2})] \tag{A.I.C.5}$$

Equation (A.I.C.5) is called *Simpson’s one-third rule*.

The first term neglected now is the involving  $\Delta^4 f_0$  due to the coefficient of  $\Delta^3 f_0$  being zero. The term containing  $\Delta^4 f_0$  is  $-(h/90)\Delta^4 f_0$ . This is the error term in Simpson’s rule.

**A.I.C.3 Program SIMPSON**

Program SIMPSON based on Simpson's rule has been developed as an alternative to Program TRAIL and has been used with Blast load - Time function for the Oklahoma Building in Oklahoma, U.S.A. using PROGRAM C.

```

C *****
  REAL FUNCTION F(X)
  REAL X
  F = EXP(-X/2)
  RETURN
  END
C *****
  EXTERNAL F
  REAL A,B,H,P,I
  INTEGER N,R,Z
  PRINT *,' *****'
  PRINT *,' *'
  PRINT *,' *          SIMPSON'S METHOD OF INTEGRATION          *'
  PRINT *,' *'
  PRINT *,' *****'
  PRINT *,'ENTER INITIAL VALUE:
  READ(*,*)A
  PRINT *,'ENTER FINAL VALUE:
  READ(*,*)B
  PRINT *,'NUMBER OF STRIPS:
  READ(*,*)N
  H = (B - A)/N
  P = F(A) + F(B)
  Z = 4
  DO 40 R = 1, N - 1
    P = P + Z*F(A + R*H)
    Z = 6 - Z
40  CONTINUE
  I = H*P/3
  WRITE(*,50) I
50  FORMAT('INTEGRAL = ',F12.8)
  STOP
  END

```

## References

- [A.1] Hill R (1959) The mathematical theory of plasticity. Oxford at the Clarendon Press
- [A.2] Bangash T (2004) Ph.D. Thesis, London University



# Index

- ABAQUS gap contact element 356
- abnormal loads 67
- absolute pressure 93
- absorbing boundary conditions 492
- accidental load torsion 540
- accumulated stresses 689
- ACE formulae 409
- aerodynamics 46
- aggressor 52
- air blast 78
- air bombs 16
- Air Force 394
- aircraft 16, 23, 576
- aircraft area 454
- Aircraft Communications Addressing and Reporting System (ACARS) 579
- aircraft engine 597
- aircraft impact 23, 388, 685
- aircraft impact areas 453
- aircraft impact on structures 386
- aircraft/missile impact and fire IX
- aircraft/missile impact data VII, 49, 367
- Al-Khobar 14
- Alfred Murrah Building V, VIII, 2, 572, 601, 604, 613
- Alfred Murrah Building prior to the tragic bombing (BPAT) 604
- aluminium panels 10
- ambient temperature 185
- American code 158
- American practice 126
- analyses release 578
- analysis of results from the global analysis 595
- analytical scaling 580
- analytical tools 49
- anchorages 674
- angle of the shock plane 91
- ANSYS contact elements 353
- anti-fragmentation film 59
- anti-tank weapons 16
- assembly and solution 559
- atmospheric pressure 97
- atomized jet fuel 597
- aviation fuels 441
- Ballistic Research Laboratory formula (BRL) 422
- BANBUCKL 562
- BANG-FIRE 596, 600
- BANG-IMPACT 513
- basement 26
- basic heat transfer analysis 206
- basic parameters 77
- basis for the finite element-formulation 483
- beam type continuous 26
- beams 131, 296, 297, 462
- beams/slabs 165
- Bechtel formula 408
- behaviour of masonry walls 569
- bending moment and shear diagrams 275
- bifurcation 560
- bilinear blast loading 99
- bimoment 544, 556
- Bishopsgate 7
- blast 67
- blast duration 241
- blast effects 1
- blast evading V
- blast load V, VII, 69, 233, 562
- blast load on buildings 69

- blast loading VI, 229
- blast loads and modelling 72
- blast modelling V
- blast parameters 315
- blast pressure load for columns 632
- blast pressure loading 631
- blast pressure loading for slabs 632
- blast resistant glass window panes 331
- blast response resistance VI, 289
- blast wave energy 78
- blast wave location 75
- blast wave scaling laws V, 76
- blast waves VI
- blast wind 76, 87
- blast zone 10
- blast-fire structural interaction 333
- blow accounts 576
- blowdown 99
- blunt-nosed bodies 407
- Boeing 707 575
- bomb blast V, 77
- Bomb Blast at Lisburn, Northern Ireland 12
- bomb crater 601
- bomb damage 1
- bomb detonation 9
- bomb explosion 1, 2
- bomb gas impulse 97
- bombs V, 394
- box section column interacting with floor 589
- bracings 529
- British practice 126
- brittle hardness 423
- building design 601
- building frame 533
- building geometry 9
- building structures 406
- building sub-systems 2
- buildings 16, 67, 69, 95, 103, 531
- buildings on fire 205
- buoyancy force 447
- calculation by cubic integration 680
- calculation by quadratic integration 680
- calculation of fire resistance of steel members 139
- Calder and Goldsmith velocity model 422
- calorific values 47, 107
- Canary Wharf Building 217
- cantilever method 529
- cantilever with distributed load 258
- cantilever with end point load 254
- case with 1 element 255, 259
- case with 2 elements 255, 259, 262
- case with 3 elements 263
- case with 4 elements 256, 260, 266
- case with 5 elements 269
- category rotation 299
- central difference formula 488
- Chang formulae 415
- characteristic fire loads 109
- charts VI
- check for convergence 690
- chronological events 23
- chunks dismantled 455
- circular reinforced concrete slabs 414
- circular shafts 620
- civilian and military aircraft VII
- CKW-BRL formula 410
- (CKW)-BRL formula 411
- cladding 9
- classification 52
- closed sections 531
- closely spaced columns 530
- clouds 12
- coefficient of expansion 185
- collapse 18
- collapse debris impact 18
- collapse scenario 16
- column collapses 191
- column type rotation 530
- column-water interaction 149
- columns 155, 184, 458, 462, 529
- columns and slab construction 7
- combined finite discrete element method 249
- combustion 579
- compartment sizes 111
- composite concrete 216
- composite wave 79
- comprehensive 3D analysis VIII

- compression members 131, 185  
 compressive strength 136  
 compressive stress 418  
 computational domain 489  
 computed simulated phenomena 597  
 computer programmes 46  
 computer subroutines 211  
 computerised database of terrorist activities 54  
 concrete and reinforcing steel 132  
 concrete beams and columns 211  
 concrete slab 159, 413  
 concrete structures 406  
 concrete targets 417  
 concrete-plank flooring 11  
 conduction 116  
 configuration factor 120  
 conical missile 420  
 connection details 458  
 construction technique V  
 Construction Technology Laboratories, Inc. (CTL) 604  
 contact between contactor and target node 342  
 contact between spheres 345  
 contact element 333  
 contact with the box 348  
 contactor 342  
 continuity of closely spaced columns 530  
 continuous beam slab 164  
 continuous beams and slabs 162  
 continuous slab 168  
 contour profile 154  
 conventional-bearing framed structures 1  
 convergence criteria 448  
 core interaction 542  
 cored structures VIII  
 cores 529  
 corner forces 551  
 counter clock movement 597  
 coupled tall core 542  
 cracking 170  
 crater 605  
 crater depth 421  
 crater radius 421  
 creep of concrete 135  
 criteria for convergence and acceleration 713  
 critical damping 285  
 critical elements 605  
 critical force 285  
 critical temperature 462, 585  
 critical/collapse loads 468  
 cross-wall systems 542  
 cubic integration 678  
 curves range-weapon 291  
 damage 10, 22, 617  
 damage cases 568  
 damage curves 290  
 damage function for a scenario 500  
 damage model 565  
 damage scenario VII, VIII, 26, 28, 465  
 damage-distance relation 78  
 Damköhler number 495  
 damped structure 233  
 damping coefficient 281  
 damping constant 283  
 damping of stress waves 80  
 damping of the stretching movement of the element 282  
 damping resistance 451  
 data due to explosion 504  
 data on civilian and military aircraft 368  
 data on major explosives 40  
 data on major explosives elements 41  
 database 16  
 DDD program 600  
 de Marre modified formula 424  
 debris 3, 14, 475, 597  
 debris as a rod of length 511  
 debris dispersion 492  
 debris elements 493  
 debris field 591  
 debris scenario 484  
 decay period 117  
 decelerating aircraft 26  
 deflection 91, 170, 173, 291  
 deflection angle 94  
 deflection using four elements 257, 260  
 deflection using one element 259  
 deflection using two elements 259

- deformation waves 78
- deleting cell lists 347
- DELFT interface fraction type element 351
- delivery mode 54
- density 87, 122
- density of the concrete 160
- design guide 128
- design methodology V
- design of structural elements VI, 289
- detection of contact 341
- detection systems 46
- determinate beams 184
- Dietrich, Furste (DF)-BRL formula 411
- difference method 477, 485
- different loadings 165
- diffraction 71
- dimensional analysis 416
- dimensional changes 205
- dimensionless parameters 152
- direct forces 530
- direct impact 367
- direct impulse/impact scaling 81
- direct integration 687
- direct measurement/assessment 106
- direction of the velocity 502
- discret element method VI
- discrete element method 572
- discrete scheme 487
- discrete time points 452
- discretisation 489
- discretisation in the time domain 676
- displacement 539, 566
- displacement of the core 543
- displacement-time relationship 607, 608
- dissipation factor 451
- distillation range 441
- distributed loads 172
- distribution 539
- divergence matrix 447
- Docklands 7
- Docklands Light Railway 10
- drag coefficient 88
- drag energy 87
- drop height 607
- ductile failure 423
- Duhamel Integral 246
- Duhamel's integral method 247
- duration 73, 82
- dust 597
- dynamic analysis 676
- dynamic finite element 534, 562
- dynamic finite element technology 249
- dynamic load factor (DLF) 231, 234
- dynamic pressure 85
- dynamic-design factors 296, 297
- earthquake 23
- elastic 418
- elastic analysis 304
- elastic properties 128
- elastic scattering 475, 491
- elastic wave equations 477
- elastic wave propagation 477
- elastic-plastic response 231
- elastic-plastic solution for bending of blast-loaded beams 291
- elastoplastic straining 671
- element accuracy 252
- element forces and moments 283
- element rotational velocity 280, 281
- element technology 249
- elements 529, 568
- elements of debris 511
- elevator 18
- emissivity 118, 141
- emitter temperature 120
- empirical and code analytical equations 139
- empirical constant 290
- endochronic model 687
- endurance of steel beams 144
- energies 684
- engine company operations 51
- equivalent load factor 75
- equivalent nodal loads 690
- equivalent spring system 284
- equivalent stress 690
- equivalent velocity of stretch 284
- error convergence result 272
- Eurocode 130, 569
- Eurocode EC3 Part 1.2 197
- existing loads 454

- existing scenario 505
- expansion joint 29
- explicit scheme 485
- explicit time integration 488
- explosion IX, 14, 46, 103
- explosion caused by impact-cum-fire 45
- explosion in air VI, 83
- explosion of a cylindrical charge 80
- explosion of a spherical charge 80
- explosion protection 46
- explosion-cum-fire VIII
- explosive and crater formation 44
- explosive load 67
- explosive load on buildings 67
- explosive SEMTEX 329
- explosives and bombs 67
- explosives and charge factors 68
- exposed to fire 171
- exterior walls 7
- external cladding 11
- external fireball 578
- external loads 172, 175
- external transverse loads 541
- extreme events 601
  
- F.E. method 551
- facility security protection plan 59
- FEM/DEM analysis 605, 613
- FEM/DEM lumped mass 613
- FEM/DEM simulation for the beam 608
- FEM/DEM simulation for the shock absorber 607
- FEM/DEM transient analysis 608
- FEMA 16, 575, 581
- FEMA study 579
- fertilizer-based 3
- finite difference analysis 139
- finite discrete element 563
- finite element VI, 330, 464, 477, 491, 563
- finite element analysis 139, 205
- finite element analysis parameters 327
- finite element idealization 539
- finite element mesh scheme for trusses 588
- finite element method 483
  
- finite element model 572
- finite element post-solution 507
- finite element technique VII, VIII
- finite/discrete element VI
- finite/discrete element technique VIII
- fire 103, 104
- fire damage 29
- fire dynamics 103
- fire engineering 46
- fire exposed face 569
- fire fighting 49
- fire growth rates for  $t^2$  fires 113
- fire hazard 441
- fire initiated by the fuel 26
- fire load 112
- fire loading 192
- fire protection 144
- fire resistance 104, 111, 146, 147, 169, 216
- fire resistance of concrete members 158
- fire simulation 581
- fire temperature 122, 173, 183
- fire using three-dimensional finite element analysis 211
- fire walls 569
- fireball 23, 28, 455, 578, 597
- fireproofing material 575
- firing debris VII
- flame height 46
- flammability limits 441
- flash fire 588
- flash fires of jet fuel 591
- flash points 441
- flat-nosed bodies 407
- flexural buckling 560
- flexural strain 570
- flight model 498
- floor construction 583
- floor elements 464
- floor on floor supporting beams with box columns 588
- floor slab 553
- floor structures 229
- floor systems 542
- flow chart 573
- flow chart on cracking phenomenon 691

- fluid velocity 452
- flying debris 10, 475
- foam agents 46
- foam blocks 443
- foot mode 54
- force displacement relationship 274
- force-displacement equation 716
- force-time history 84
- force-time relationship 608
- forced vibration 232
- forces and moments along the element 278
- forensic 10
- formulae for deformable missiles impacting on concrete targets 419
- foundation structures 229
- framed and core systems VIII
- framed structures VIII
- framed tubular buildings 532
- frames 7
- frequency 386
- frequency of a tall structure 386
- fuel 23
- fuel distribution 582
- fuel lines 443
- fuel loading 589
- fuel-structure interaction 441, 443, 597
- full-scale prototype building 211
- fully developed period 117
- fuselage 597
  
- Galerkin method 489
- gap element VII, 333
- Gaussian point 671
- general steps of crack flow and crack calculations 689
- generalised displacements 557
- generic blast resistant window system 329
- geometry of finite elements 464
- girder 529
- glass VII, 9
- glass and glazing 319
- glass cladding 614
- glazing materials VII
- global analysis 529, 581
- global analysis based on program BANGF 572
- global axis 278
- global finite element analysis of doors and windows 328
- global force 346
- global response 621
- global stability analysis 560
- graphs VI
- gravitational potential energy 577
- Great Eastern Enterprise 10
- grid 492
- growth period 117
- gyration 562
  
- Haldar, Miller, and Hatami method 416
- Hallquist contact method 509
- Hallquist et al. method 349
- hard missiles 416
- hardened framed structures 1
- hardening buildings 321
- hat truss 597
- heat flow 208
- heat release rate 114, 578, 585
- heat transfer 116
- heat transfer analyses 144
- heated perimeter 141, 146, 147
- heated perimeter of steel 149
- heavier shrapnel 7
- heavy, sealed windows 50
- Helmholtz decomposition 487
- hemi-spherical blast 9
- high temperatures 136
- high-rise buildings 540
- high-risk areas 2
- hijacked-plane collision 578
- HMX 67
- hollow columns 148
- Hooke's law 486
- horizontal loads 529
- hot fuel interaction VII
- hot fuel-floor interaction 465
- hot gases 39
- Hughes formulae 416
- hybrid finite element 485
- hybrid finite element/difference method VII

- hydraulic system 443
- hydrodynamic wave 79
- idealized blast load impulse 237
- ignition 441
- impact 81, 103
- impact and blast load effects 532
- impact angles 599
- impact areas 454
- impact fire explosion 16
- impact floors 18
- impact response 413
- impact velocity 407
- impact-cum-explosion VIII
- impact-cum-fire VIII, 46
- impact/explosion 682
- impactors VII, 394
- implementation 341
- impulse 81
- impulse and momentum 367
- impulse of the incident pressure 87
- impulse versus pressure 292
- incident pressure VI
- incident pressure versus range 75
- incident waves 96
- incremental strain 567
- indeterminate beams 184
- ingredients of explosives and their properties 43
- initial damage from aircraft impact 594
- initial stress method 714
- initial vector 278
- instability buckling 571
- installation 59
- insulation 597
- insulation properties 224
- insulation thickness 144
- integerised relative co-ordinates 339
- integration points 685
- intense heat and smoke 50
- internal blast VI
- internal blast load modelling 95
- IRS formula for total protection of a target 409
- IRS formulae 409
- ISO 123
- isodamage curves 290
- isoparametric element 671
- isotropic hardening 675
- IStructE method 171
- Jacobian equations 489
- Jeanes' graph 150, 152
- Jewish Community Centre 7
- joint element 563
- joists 462
- Kar steel target formula 423
- kinetic energy 87, 607, 610, 684
- ladder company operations 52
- Lambert model 424
- large strain 711
- larger shaft 581
- Lie's graph 150, 152
- lighting divertors 443
- lightweight concrete 145, 155
- limit state 179
- limit state and plastic analysis 139
- limited means of ventilation 50
- limiting temperature criterion 131
- linear deflection profile 386
- live load densities 48
- load distributions 85
- load energy density 119
- load modelling VI
- load modification factors 631
- load vector 447
- load-range-time relation 75
- load-time function VII, 98, 306, 388
- load-time function – rectangular 306
- load-time function – triangular 306
- load-time relationships for blasts in open air 86
- loadings 105
- loads for chemical explosions 82
- loads for nuclear explosions 82
- local effects 406
- local stability analysis 560
- local stresses investigation 464
- locate a fire 51
- Love wave 79
- lower surface 566
- LS-DYNA gap/contact elements 362
- luminous flames 119
- lumping technique 532

- Mach number 85, 87, 94  
 major explosive elements 39  
 Malhotra's method 150  
 Malhotra's quasi-steady state approach 150  
 managers and security staff 55  
 Manchester Bomb Blast 10  
 masonry column 138  
 masonry material 570  
 masonry material properties 571  
 masonry walls 569  
 masonry/brick/block 137  
 mass matrix 489  
 mass moments of inertia 683  
 mass of model centroid 683  
 MASTER AND SLAVE NODES 513  
 master segment 510  
 material coefficients 489  
 material density 420  
 material energy 565  
 material properties 127, 129, 330, 624  
 materials 24, 49  
 maximum dynamic load 237  
 maximum response 245  
 McMahon, Meyers, Sen model 419  
 mechanic of fluids 46  
 membrane effects 653  
 mesh scheme 571  
 method or analysis 552  
 methods of analysis VI, 229  
 methods of analysis and design 139, 230  
 military 394  
 missile length 420  
 missile shape factor 407  
 missiles 16, 394, 420  
 mitigation 1  
 mode frequency analysis 678  
 model core structure 543  
 model features 494  
 model of Wolf et al. 389  
 modelling of masonry walls 569  
 modelling prototype structures VIII  
 modes and tactics 52  
 modes and tactics: flow chart A 56  
 modes and tactics: flow chart B 57  
 modes and tactics: flow chart C 58  
 modified Ballistic Research Laboratory formula 410  
 modified Barr, Carter, Howe, and Neilson formulae 414  
 modified CEA-EDF formula 414  
 modified Kar formula 412  
 modified Kar formulae 417  
 modified NDRC formula 408  
 modified Stone and Webster 411  
 modulus of elasticity 134, 185  
 moment and products of inertia 684  
 moment vector 346  
 moment-resistant connection 553  
 moments 530, 551  
 momentum 367, 502  
 momentum balance 489  
 momentum matrix 447  
 mono filament membrane 614  
 mortars 16  
 multi multiple-core systems 552  
 multi-bay-multi-storey framed buildings 192  
 natural response period 233  
 Navy missiles 394  
 NBS algorithm 341  
 NBS contact detection 334  
 NBS contact detection algorithm for 3D problems 337  
 NDRC formula 406  
 NDRC formula for penetration 407  
 NDRC formula for perforation 407  
 negative moment due to fire 164  
 Neumann boundary conditions 493  
 Newton-Raphson method 713  
 non-aluminized explosive mixtures 42  
 nonlinear constitutive matrices 689  
 nonlinear transient dynamic analysis 676  
 normal and oblique impact VII  
 normal concrete 145, 155  
 normal shock reflection 93  
 normally reflected blast parameters 316  
 nose-shaped coefficient 417  
 numerical simulation of blast loading 630  
 numerical solution method 240



- oblique impact 382
- oblique reflection 94
- oblique shock VI, 89
- observed simulated phenomena 597
- Oklahoma City 601
- one-way slab 162, 296, 297
- open air explosions 83
- open-section shear walls 531
- opening factor 122
- openings 463, 581
- operating guidelines 51
- outer frame wall 464
- outrigger truss 584
- overpressure 78, 81, 82
- overturning moment 530
  
- peak displacement 386
- peak impulsive load 73
- peak pressure VI, 314
- penalty function method 344
- penetration VII, 406, 409, 410
- Pentagon V, 24, 26, 27
- perforation VII, 406, 408–410
- perforation energy 425
- permanent deformation of pipe 426
- Perry and Brown formulae 417
- Petry formula 412
- Phantom aircraft 689
- physical boundary 529
- P-i* curves for elastic and plastic cases 292
- piecewise linear functions 485
- plastic 418, 468
- plastic analysis 179, 183, 197, 304, 305
- plastic buckling matrix 560
- plastic energy 684
- plastic films 10
- plastic flow rule 671
- plastic hinge 611
- plastic point 689, 690
- plastic strain relationship 673
- plate thickness 583
- plates 458
- plugging 423
- plume-trajectory scaling 579
- point of intersection between contacting nodes 343
  
- Poisson's ratio 479
- polycarbonates 59
- polynomial 539
- portal frames 192
- positive moment due to fire 164
- post-flashover design fires 116
- post-mortem 689
- post-shock temperatures 88
- potential energy 550, 607, 609, 610, 684
- potential temperature 580
- pre-flashover design fires 116
- prediction of gas pressure impulse 99
- pressure 76
- pressure at ambient temperature 97
- pressure gradient 447, 452
- pressure-time history 97
- pressure-time relation VI, 72
- prestressed concrete 171
- prestressed concrete beam 176
- prevent penetration 409
- principal lateral bracing 630
- prismatic member 553
- probability methods 104
- profiled steel sheet 216
- program BANG-BLAST 513, 572, 587
- program BANG-FIR 494–496, 513, 578, 579
- program BANGF VIII, 534, 573
- program FEMVIEW VII, 600
- program ISOPAR 211, 513, 692
- program SIMPSON 768
- program TRAIL 766
- progression of collapse 593
- progressive collapse 617, 620
- projectile 412
- projectile penetration 443
- propagation of flame 441
- protected steel 143
- protected steel members 142
- protection 148
- protective design technologies 1
- puttins block 10
  
- quadratic integration 677
- quasi-static pressure 97

- radiant heat flux 120
- radiation 117
- radiation heat transfer 46
- radius of gyration 562
- raised floors 7
- ramp-function load 231, 238
- range 290
- range of fire load density 112
- Rankine-Hugonist equation 88
- rarefaction 85
- rarefaction waves 78
- rated cruise speed 583
- Rayleigh wave 79
- RC-framed basement 9
- RDX 67
- recoilless guns 16
- recommended values for characteristic fire loads 108
- rectangular pulse 245
- rectangular pulse load 244
- reduced linear transient dynamic analysis 677
- reduction of strength 569
- reflected waves 96
- reflection coefficient 94
- reinforced concrete 171
- reinforced concrete columns 158
- reinforced concrete frame 26
- reinforced concrete slabs 416
- reinforced concrete wall 300
- reinforced-concrete buildings 2
- reinforcement detailing 624
- reinforcing steel 462
- residual velocity of the missile 415
- residual vibration 245
- resistance of the slab 314
- resistance required 314
- resistance-weapon 291
- response analysis equations 232
- response solution method 240
- restraints 105, 165
- reverberation phase 96
- reverberation time 96
- Reynolds number 495
- Riera model 388
- rigid body deflection 611
- rigid body motion 611
- rigidity of escalators 599
- rigidity of moving walks 599
- risk analysis 104
- rockets 16, 394
- rolled-steel frame 329
- roof 9
- roof structures 229
- rotational stiffness 286
- rotational velocity 286, 287
- rotations of the core 557
- Rotz damage model 420
- rubble-covered columns 3
- rupture VII, 441
- safety factors 109
- safety of human beings 601
- scabbing VII, 406
- scabbing thickness 411, 420
- scaled distance 81
- scaling of the overpressure 81
- scanning approach 505
- scattering flying objects VII, 475
- scattering of debris 490
- schematic of distorted section 626
- secant modulus 418
- sectorial coordinate 557
- security camera 26
- security of building services 601
- selection 62
- shafts 18
- shape factors 141, 143, 144
- shape functions 444
- shear stress 418
- shear walls VIII, 531, 553
- shear-resisting elements 540
- shears 169, 291, 529, 530
- sheet materials 500
- sheetings 10
- shells 16
- shield design 321
- shock absorber 608
- shock front VI
- shock loading VI, 244
- shock overpressure 98
- shock plane 91
- shock pulse duration 73
- shock reflection VI, 93
- shock spectrum location 245

- shock wave peak pressure versus slant range 92
- shock waves 39
- short frames 530
- side-on blast parameters 317
- side-on blast pressure 318
- SIFCON 60
- SIFCON layers 601
- siliceous aggregate concrete 136
- simplified missile analysis 376
- simply supported beam under distributed load 262
- simply-supported unstrained beams 162
- Simpson's rule 551, 605, 767
- single-bay portal frames 529
- site problems and management 56
- sky bridges 599
- slab construction 50
- slab warping 543
- slabs 3, 26, 293, 294
- slabs simply supported on shorter sides 298
- slenderness ratio 569
- slow speed indentation 420
- smoke 12, 28, 104
- smoke flame 578
- smoke plume 589
- snap-back phenomenon 566
- 'sof-shock' glass 7
- solid isoparametric elements 480
- solid missiles 417
- solid steel missiles 408
- South Quay Plaza 9
- South Quay Waterside 9
- space domain 483
- spalling VII, 406
- spandrel beam 3
- spandrels 458, 597
- spatial cantilever 529
- special application of Duhamel Integral for impulse load 246
- specific heat 127, 136
- specific heat capacity 87
- specific heat of the concrete 160
- specific limit energy 424
- spectrum analysis 681
- speed 453
- speed-of-sound 91
- spherical missile 422
- spherical-ended bodies 407
- splander beam 627
- sprinkler systems 46
- SRI equation 423
- St. Mary Axe 7
- stability criterion 492
- stagnation pressure VI, 88
- stand-off damage assessment 302
- stand-off distance 315, 327
- Staples Corner 10
- static condensation 272
- static discharge devices 443
- statistical survey 106, 109
- steel 127, 462, 464
- steel and composite beams and columns 211
- steel and concrete elements VII
- steel at elevated temperatures 129
- steel beam 184
- steel box column 463
- steel columns 145–147
- steel frame 2, 10
- steel pipe missiles 409
- steel plates 423
- steel structural members 462
- steel targets 420
- steel temperature 185
- steel-framed structure 12, 18
- steel-trussed footbridge 10
- step-function load 231, 234
- step-function with time 239
- Stevenson's direct head-on impact model 388
- stiffness coordinates 553
- stiffness of the beam element 286
- Stone and Webster formula 410
- storage building 120
- strain increment 689
- strain rate 283
- strain stiffening 653
- strain tensor 486
- strategy 50
- strength reduction 183
- strength reduction coefficient 170

- strength–reduction factor 585  
 stress increment 689  
 stress resultants 550  
 stress vector 449  
 stress waves VI  
 stress waves and blast waves 78  
 stress-strain curve 585  
 stress-strain curves for a mild steel  
     132  
 stresses 175, 291, 464  
 strong turbulence 495  
 structural cells 485  
 structural damage 16, 22  
 structural element VI, 289  
 structural form 9  
 structural integrity V, 1  
 structural material stability 672  
 structural response 229  
 structural response analysis to blast  
     loading 230  
 structural response of buildings 95  
 structural sizes 458  
 structural tube framing 584  
 structures 16  
 sturm seugence 562  
 sub-basement 26  
 substructuring 709  
 sufficient buckling 191  
 superelement 709  
 support conditions 252  
 surface waves 78  
 surveillance mode 53  
 suspended ceilings 7
- tables VI  
 tabulated cases 192  
 tactics 50, 52  
 Takeda, Tachikawa, and Fujimoto  
     formula 416  
 tall exposed columns 3  
 tangent modulus 418  
 target node 342  
 target penetration 424  
 TASEF-2 211  
 Taub and Curtis model 424  
 technique of computing acceleration  
     factors 714
- temperature 91, 129, 455  
 temperature distribution 176  
 temperature range 128  
 temperature-time 124, 126  
 temperature-time curves 125  
 temperature-time relation VI, 46, 117  
 tension members 130  
 terrorist activities and threat 54  
 terrorist bombings 1  
 terrorist bombs 39, 68  
 tests on PWR containment reactor  
     building 689  
 Thames Quay 9  
 thermal bowing 569  
 thermal conductivity 127, 136, 570  
 thermal conductivity of the concrete  
     160  
 thermal displacements 569  
 thermal fire resistance 160, 161  
 thermal gradients 569  
 thermal properties 205  
 thermal strains 570  
 thermal stresses 570  
 thermochemistry 46  
 thick concrete 411  
 thickness 408  
 thickness of the shock front 88  
 thin-walled 541  
 thirty-two-noded solid element 481  
 Thomas Telford House 10  
 threats 52  
 three dimensional scattering 491  
 three dimensional scattering of elements  
     491  
 three-dimensional finite element  
     modelling 582  
 three-dimensions 531, 533  
 3D finite element analysis VIII  
 3D implementation into the combined  
     FEM/DEM method 337  
 3D structures 531  
 threshold limit 565  
 time 122  
 time dependent displacements 468  
 TIME DOMAIN VII, 475  
 time durations 454  
 time increment 488

- time of drag 73
- time scenario 576
- time-load basis 601
- tinted glass 10
- TNT 14, 71, 551
- Tornado aircraft 689
- torsion 540
- torsional buckling 561
- torsional moment 540
- torsional parameters 548
- total deflection 257
- total pressure 314
- total strain increment 673
- tower components VII
- transfer beam 620
- transfer girders 627
- transformation factor 305
- transformation factors for beams and one-way slabs 295
- transformation matrix 557
- transient 87
- transient over pressure V
- translating impact forces 1
- translation and rotation 276
- transverse waves 78
- trapezium rule 764
- trapezoidal rule 764
- travel distance 110
- triangular pressure-pulse function 299
- triangular pulse load 246
- tributary bay 529
- truss-metal ties 468
- t*-squared fires 112
- turbulence model 496
- turbulence modeling 476
- turbulent diffusion theory 495
- turbulent driven debris equations 493
- turbulent flame 493
- turbulent velocity 505
- twenty-noded solid element 482
- twisting actions 542
- 2D nature 334
- types of classification – dynamic 233
- types of classification – impulsive *I* 233
- types of classification – quasi-static 233
- ultimate moment capacity 419
- ultimate rotational capacity 419
- ultimate strength of concrete 134
- underground explosions 83
- underwater explosions 83
- uniform acceleration 713
- unprotected steel 597
- unprotected steel columns 149
- unprotected steel members 140
- upper surface 566
- US Army Corps of Engineers' formula 407
- use of characteristic fire load density 106
- various loading 252
- vehicle barrier 62
- vehicle bomb V, 1, 61, 299
- velocity pressure 444
- vented energy 589
- ventilation 581
- vertical displacement 556, 557
- very sharp-nosed bodies 407
- vicious device 7
- von Mises yield 675
- wall panels 14
- walls 463
- warping 531, 542
- warping deformation 543
- warping stiffness 543
- warping stiffness of beams 551
- wave displacement 487
- wave equations 450
- weak turbulence 494
- weapon yield 290
- welded columns 583
- wet wing construction 442
- window pane 327
- windows 10, 330
- windstorm 23
- Winfrith perforation energy model 425
- wing structure 442
- wings 597

- World Trade Center V, VII, VIII, 3, 16, 49, 453
- WTC Towers 18, 574, 599
- WTC Towers – finite element analysis 465, 586
- WTC Towers – finite element modelling 586
- WTC Towers collapse 23, 503, 576
- WTC Towers impacted floors 583
- WTC-1 453, 454, 572, 582, 593
- WTC-1 – damage scenario 590
- WTC-2 453, 454, 572, 582, 594
- WTC-1 Tower results – comparative study 597
- YIELD 67
- yield condition 672
- yield criterion 671
- yield surface 671
- Young’s modulus 418, 479